Transactions of the ASME®

Technical Editor, **LEON M. KEER (1993)**

The Technological Institute
Northwestern University
Evanston, IL 60201

APPLIED MECHANICS DIVISION

Chairman, **MICHAEL J. FORRESTAL**
Secretary, **L. B. FREUND**
Associate Technical Editors,
R. M. BOWEN (1994)
S. K. DATTA (1993)
G. J. DVORAK (1993)
M. E. FOURNEY (1994)
C. O. HORGAN (1992)
R. L. HUSTON (1994)
D. J. INMAN (1992)
J. T. C. LIU (1993)
R. M. McMEEKING (1994)
A. K. NOOR (1994)
J. W. RUDNICKI (1992)
W. N. SHARPE, JR. (1994)
C. F. SHIH (1993)
J. G. SIMMONDS (1992)
P. D. SPANOS (1992)
K. R. SREENIVASAN (1992)
Z. WARHAFT (1992)

BOARD ON COMMUNICATIONS
Chairman and Vice-President
R. E. NICKELL
Members-at-Large
W. BEGELL, T. F. CONRY, T. DEAR, R. L. KASTOR, R. MATES, E. M. PATTON, R. E. REDER, R. D. ROCKE, A. VAN DER SLUYS, A. J. WENNERSTROM, W. O. WINER, B. ZIELS

President, **A. E. BERGLES**
Exec. Dir.
D. L. BELDEN
Treasurer, **ROBERT A. BENNETT**

PUBLISHING STAFF
Mng. Dir., Publ.,
CHARLES W. BEARDSLEY
Managing Editor,
CORNELIA MONAHAN
Production Editor, **JUDY SIERANT**
Prod. Asst., **MARISOL ANDINO**

Transactions of the ASME, Journal of Applied Mechanics (ISSN 0021-8936) is published quarterly (Mar., June, Sept., Dec.) for $160.00 per year by The American Society of Mechanical Engineers, 345 East 47th Street, New York, NY 10017. Second class postage paid at New York, NY and additional mailing offices. POSTMASTER: Send address changes to Transactions of the ASME, Journal of Applied Mechanics, c/o THE AMERICAN SOCIETY OF MECHANICAL ENGINEERS, 22 Law Drive, Box 2300, Fairfield, NJ 07007-2300.

CHANGES OF ADDRESS must be received at Society headquarters seven weeks before they are to be effective. Please send old label and new address.

PRICES: To members, $29.00, annually; to nonmembers, $160.00. Add $20.00 for postage to countries outside the *United States and Canada.*

STATEMENT from By-Laws. The Society shall not be responsible for statements or opinions advanced in papers or . . . printed in its publications (B7.1, Par. 3).

COPYRIGHT © 1990 by The American Society of Mechanical Engineers. Reprints from this publication may be made on condition that full credit be given the TRANSACTIONS OF THE ASME, JOURNAL OF APPLIED MECHANICS, and the author, and date of publication be stated.

INDEXED by Applied Mechanics Reviews and Engineering Information, Inc.

Journal of Applied Mechanics

Published Quarterly by The American Society of Mechanical Engineers

VOLUME 57 • NUMBER 4 • DECEMBER 1990

TECHNICAL PAPERS

805 **Diffusion of Self-Equilibrating End Loads in a Stretched Elastoplastic Circular Cylinder**
D. Durban and W. J. Stronge

810 **Equilibrium Path Bifurcation Due to Strain-Softening Localization in Ellipsoidal Region** (90-WA/APM-30)
Z. P. Bažant

815 **Micromechanics of an Extrusion in High-Cycle Fatigue With Creep** (90-WA/APM-43)
T. H. Lin, S. R. Lin, and X. Q. Wu

821 **Finite Dynamic Motions of Thin Rate-Dependent Sheets**
J. A. Blume

828 **Analysis and Application of a Coupled Thermoviscoplasticity Theory** (90-WA/APM-35)
H. Ghoneim

836 **A Mechanism for Shear Band Formation in the High Strain-Rate Torsion Test**
Timothy J. Burns

845 **Elastic Field Due to a Dynamically Transforming Spherical Inclusion** (90-WA/APM-47)
Y. Mikata and S. Nemat-Nasser

850 **On Bonded Inclusions With Circular or Straight Boundaries in Plane Elastostatics** (90-WA/APM-24)
T. Honein and G. Herrmann

857 **A General Theory on Media With Randomly Distributed Inclusions: Part I—The Average Field Behaviors** (90-WA/APM-34)
B. Wang

863 **Force on a Piezoelectric Screw Dislocation** (90-WA/APM-38)
Y. E. Pak

870 **Incident Wave and Dislocation Acceleration Effects in Dislocation Emission From Cracks** (90-WA/APM-39)
L. M. Brock and J. S. Wu

877 **Self-Similar Solution in Problems of Hydraulic Fracturing** (90-WA/APM-31)
N. C. Huang, A. A. Szewczyk, and Y. C. Li

882 ***Stress Intensity Factor and Energy Release Rate for Interfacial Cracks Between Dissimilar Anisotropic Materials***
Kuang-Chong Wu

887 **Analysis of Branched Interface Cracks**
D. J. Mukai, R. Ballarini, and G. R. Miller

894 **Correspondence Relations for the Interface Crack in Monoclinic Composites Under Mixed *Loading***
Kuang-Chong Wu and Shyh-Jye Hwang

901 **On Measuring the Near-Tip Plastic Strain Singularity** (90-WA/APM-46)
Sundar M. Kamath and Kyung S. Kim

906 **A General Algorithm for Multidimensional Cauchy Principal Value Integrals in the Boundary Element Method**
M. Guiggiani and A. Gigante

916 **Thermal Stresses in an Anisotropic Plate Disturbed by an Insulated Elliptic Hole or Crack** (90-WA/APM-29)
Chyanbin Hwu

923 **Lamb Wave Propagation in Anisotropic Laminates**
G. R. Liu, J. Tani, K. Watanabe, and T. Ohyoshi

930 **Strain-Induced Elastic Anisotropy Measured With Ultrasonic Waves**
Kazuyuki Sasaki, Yukio Iwashimizu, and Osami Kobori

937 **On the Wave Propagation in Elastic Multilayer Periodic Media With Nonlocal Interactions**
J. L. Nowinski

941 **Thermal Dynamic Problems of Reinforced Composite Cylinders**
Victor Birman

948 **A Three-Dimensional Constitutive Theory for Fiber Composite Laminated Media** (90-WA/APM-32)
R. Christensen and E. Zywicz

956 **Effect of Interphases on Micro and Macromechanical Behavior of Hexagonal-Array Fiber Composites** (90-WA/APM-44)
J. D. Achenbach and H. Zhu

964 **A New Method for Determination of Bending Rigidities of Thin Anisotropic Plates** (90-WA/APM-27)
M Grédiac and A. Vautrin

969 **Relationship Between the Elastic Buckling of Square Tubes and Rectangular Plates**
S. Li and S. R. Reid

974 **Plane Contact of an Elastic Layer Supported by a Winkler Foundation**
J. P. Dempsey, Z. G. Zhao, L. Minnetyan, and H. Li

981 **Buckling and Post-Buckling Behavior of Elliptical Plates: Part I — Analysis** (90-WA/APM-36)
Herzl Chai

(Contents continued on Inside Back Cover)

Downloaded 04 May 2010 to 171.66.16.49. Redistribution subject to ASME license or copyright; see http://www.asme.org/terms/Terms_Use.cfm

989 **Buckling and Post-buckling Behavior of Elliptical Plates: Part II — Results** (90-WA/APM-37)
Herzl Chai

995 **Free Vibration and Tension Buckling of Circular Plates With Diametral Point Forces** (91-APM-24)
E. F. Ayoub and A. W. Leissa

1000 **Analytical Estimation for Static Deformation of Wire Ropes With Fibrous Core**
K. Kumar and J. E. Cochran, Jr.

1004 **The Maggi or Canonical Form of Lagrange's Equations of Motion of Holonomic Mechanical Systems**
John G. Papastavridis

1011 **Equivalence of Stochastic Averaging and Stochastic Normal Forms**
N. S. Namachchivaya and Gerard Leng

1018 **The Generalized Cell Mapping Method in Nonlinear Random Vibration Based Upon Short-Time Gaussian Approximation** (90-WA/APM-28)
J. Q. Sun and C. S. Hsu

1026 **A Study of Belleville Spring and Diaphragm Spring in Engineering** (90-WA/APM-45)
Ye Zhiming and Yeh Kaiyuan

1032 **Density Effects in Two-Dimensional Bins**
N. P. Kruyt

1036 **Gravity-Driven Granular Flows of Smooth, Inelastic Spheres Down Bumpy Inclines**
M. W. Richman and R. P. Marciniec

1044 **Flows Inside and Around a Vaporizing/Condensing Drop Translating in an Electric Field**
H. D. Nguyen and J. N. Chung

1056 **Effect of Finite Thickness Flexible Boundary Upon the Stability of a Poiseuille Flow**
Mauro Pierucci and Pedro G. Morales

1061 **Transient Stokes Flow in a Channel Driven by Moving Sleeves** (90-WA/APM-48)
P. Carbonaro and Erik B. Hansen

1066 **On the Disturbance of a Thin Layer of Liquid by a Moving Obstruction**
Roger F. Gans and Chung-Hai Wang

1073 **Rate of Flow in a Curved Concentric Pipe of Circular Cross-Section**
M. A. Ebadian

BRIEF NOTES

Dynamic Plastic Response of Circular Plates With Transverse Shear 1077
Q. M. Li and Y. G. Huang

A Central Crack in a Finite Rectangular Plate With Four Hinged Edges Under the Opening Mode 1079
S. W. Ma and Y. G. Tseui

Analytical Solution for a Pinched Laminated Cylinder 1082
K. Bhaskar and T. K. Varadan

Finite Element Transient Response of Composite and Sandwich Plates With A Refined Higher-Order Theory 1084
Mallikarjuna and T. Kant

Shearing Stress Intensity Factors of a Cracked and Perforated Plate 1087
Fu Bin and Zhang Xiangzhou

1088 On Kinematical Assumptions of Refined Theories of Plates: A Survey
G. *Jemielita*

1091 On the Propagation Pressure of Buckles in Cylindrical Confined Shells
F. S. Li and S. Kyriakides

1094 On the Spatial Chaos, Asymptotic Modal Analysis, and Turbulence
Earl H. Dowell and Lawrence N. Virgin

1097 Monte Carlo Simulation of Coupled Nonlinear Oscillators Under Random Excitations
Wenglung Li and R. A. Ibrahim

1099 Flexure of a Pressurized Tube
D. J. Steigmann

ERRATA

1076 **Errata on *Crack Extension Force in a Piezoelectric Material*, by Y. E. Pak, and published in the September 1990 issue.**

DISCUSSION

1101 ***Torsional Response of Rectangular Composite Laminates* by C.-L. Tsai, I. M. Daniel, and G. Yaniv—Discussion by Yi-Yuan Yu**

BOOK REVIEWS

1102 ***The Behavior of Thin Walled Structures, Beams, Plates, and Shells*, by J. R. Vinson** . . . Reviewed by **S. Abrate**

1102 ***Mécanique Vibratoire*, by Del Pedro and Pahud** . . . Reviewed by **S. Abrate**

1102 ***Knowledge-Based Control with Application to Robots*, by C. W. de Silva and A. G. J. MacFarlane** . . . Reviewed by **C. B. Brown**

(Contents continued on p. 827)

Downloaded 04 May 2010 to 171.66.16.49. Redistribution subject to ASME license or copyright; see http://www.asme.org/terms/Terms_Use.cfm

ANNOUNCEMENTS AND SPECIAL NOTES

814	11th ASME Freeman Scholar Program in Fluids Engineering
820	I.U.T.A.M. Symposium — Call for Proposals
869	Change of Address Form
900	18th International Congress of Theoretical and Applied Mechanics — Call for Papers
1055	First U. S. National Congress on Computational Mechanics — Announcement
1103	Books Received by the Office of the Technical Editor
1104	Worldwide Mechanics Meetings List
1006	Author Index

Downloaded 04 May 2010 to 171.66.16.49. Redistribution subject to ASME license or copyright; see http://www.asme.org/terms/Terms_Use.cfm

Diffusion of Self-Equilibrating End Loads in a Stretched Elastoplastic Circular Cylinder

D. Durban
Faculty of Aerospace Engineering,
Technion,
Haifa 32000, Israel

W. J. Stronge
Department of Engineering,
University of Cambridge,
Cambridge CB2 1PZ,
U.K.

Low rates of axial diffusion are discovered for asymmetric instantaneous self-equilibrating disturbances imposed at the end of an initially stretched circular cylinder. The diffusion rates are evaluated within the framework of continuum plasticity for materials represented by the isotropic J_2 flow theory. Over most of the initial stress range, a lower bound on the decay rate is provided by an eigenvalue associated with flexure. There is almost no decay for this component of a disturbance when the axial stretch is small in comparison with the stretch at necking.

1 Introduction

A preliminary analysis of axial decay rates for suddenly applied self-equilibrating disturbances imposed at the end of a finitely strained, elastoplastic circular cylinder was presented by Durban and Stronge (1988a). This end disturbance on an indefinitely long cylinder was formulated as a linear eigenvalue problem within the framework of an incremental theory for continuum plasticity. Using the eigenfunction expansion method it was possible to evaluate the smallest rate of axial diffusion, thus providing an estimate of the validity of Saint-Venant's principle in finite strain plasticity. While that study was restricted to the subspace of axially symmetric eigenfunctions, nevertheless it revealed the sensitivity of the lowest decay rate to initial axial stress.

More recent investigations (Durban and Stronge, 1988b, 1988c) on the analogous elastic and elastoplastic plane-strain problem have shown the importance of examining the complete eigenfunction space, allowing for competition among the corresponding eigenvalues over the entire elastoplastic range. A particularly striking discovery was the very low decay rate of the first antisymmetric eigenfunction at small values of initial stretch.

Therefore, we are reconsidering the circular cylinder end problem without the restriction of axially symmetric behavior. The problem formulation closely follows the (1988a) paper and the analysis proceeds along the line of the more general plane-strain problem (1988b, 1988c). A semi-infinite circular cylinder in a stress state of uniform axial tension σ is subjected to an instantaneous end disturbance. The uniform component of the imposed surface traction is assumed to be sufficiently large to ensure continuous plastic loading everywhere within the body. The nonuniform, self-equilibrating part of the end disturbance induces in the body a strain rate field which decays exponentially with distance from the end. That field is governed by a nonhomogeneous rate boundary value problem which can be approached by the eigenfunction expansion method. Here we examine these eigenfunctions and their associated eigenvalues with emphasis on the rate of diffusion away from the end.

We begin with a mathematical description of the problem and consider materials represented by the J_2 flow theory of plasticity along with the elastic incompressibility constraint. Combining the constitutive relations with the equilibrium rate equations leads to four linear partial differential equations for three velocity components and the hydrostatic stress rate. These equations are supplemented by homogeneous stress-free boundary conditions at the cylindrical surface.

The eigenfunctions, introduced in Section 3, admit a separation of variables representation whereby each eigencomponent has a trigonometic circumferential term and is assumed to decay exponentially with distance from the end. We show that the governing field equations are reduced to four ordinary differential equations for the radial profiles of the velocities and the hydrostatic stress rate. That system has an exact analytical solution expressed by modified Bessel functions. Compliance with the stress-free boundary conditions generates the transcendental equation for the associated eigenvalues.

Sample calculations of the eigenvalues for strain-hardening solids are presented in Section 4 over the entire elastoplastic range. We examine in particular the behavior of the first eigenvalue since this determines the smallest rate of axial diffusion. This is the eigenvalue with the smallest positive real part so it provides a quantitative assessment of the validity of Saint-Venant's principle for the stretched elastoplastic circular cylinder.

The main result reported in this paper is that among all eigenfunctions, the first eigenvalue is associated with a flexural eigenfunction except near necking. Initially at low to intermediate levels of tension stress σ, the first eigenvalue is real

Contributed by the Applied Mechanics Division of THE AMERICAN SOCIETY OF MECHANICAL ENGINEERS for publication in the JOURNAL OF APPLIED MECHANICS.

Discussion on this paper should be addressed to the Technical Editor, Leon M. Keer, The Technological Institute, Northwestern University, Evanston, IL 60208, and will be accepted until two months after final publication of the paper itself in the JOURNAL OF APPLIED MECHANICS. Manuscript received and accepted by the ASME Applied Mechanics Division, Oct. 18, 1988.

Copyright © 1990 by ASME
Downloaded 03 May 2010 to 171.66.16.244. Redistribution subject to ASME license or copyright; see http://www.asme.org/terms/Terms_Use.cfm

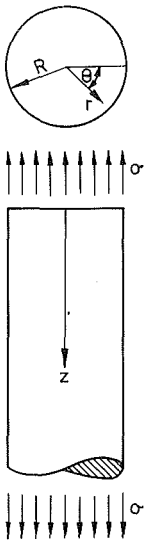


Fig. 1 Semi-infinite circular cylinder under uniform axial stress $\sigma_z = \sigma$. R is the current deformed radius.

and increases with σ. This behavior implies a purely exponential nonoscillatory decay of the first eigencomponent. A particularly striking observation is the low rate of axial diffusion at small values of σ. That result is supported by a rigorous asymptotic expansion. Above a critical value of σ, the first eigenvalue becomes complex and remains so, with little change in the real part, up to the necking stress σ_u. Over most of the range $0 \le \sigma \le \sigma_u$ the first asymmetric eigenvalue has a smaller real part than the first axially symmetric eigenvalue discussed by Durban and Stronge (1988a). That picture is inverted as the necking stress is approached; within a finite band near σ_u, the first axially symmetric eigenvalue has the smallest real part.

The paper concludes with some general observations on Saint-Venant's principle at finite strains. It is suggested that bifurcation points along the primary loading path are preceded by very low rates of diffusion of self-equilibrating eigencomponents.

2 The Mathematical Model

An elastoplastic, incompressible, semi-infinite circular cylinder (Fig. 1) is in a state of uniform axial tension $\sigma_z = \sigma$. Now consider an instantaneous surface disturbance that is imposed over the end $z = 0$. That disturbance is composed of a uniform component—sufficiently large to ensure continuous plastic loading—and a nonuniform but self-equilibrating part which is expected to decay with distance along the z-axis.

We will examine the axial decay rate of the nonuniform surface tractions imposed over the end using the standard eigenfunction expansion method. Material behavior is governed by the J_2 flow theory of plasticity which has an invariant form for incompressible materials,

$$\overset{\nabla}{\mathbf{S}} = \frac{2}{3} E\mathbf{D} - \frac{E - E_t}{\sigma_e^2}\mathbf{S}\mathbf{S}\cdot\cdot\mathbf{D}. \tag{1}$$

This equation relates the Jaumann rate of the deviatoric stress $\overset{\nabla}{\mathbf{S}}$ to the Eulerian strain rate tensor $\mathbf{D}$, deviatoric stress $\mathbf{S}$, elastic modulus E, effective stress σ_e, and tangent modulus E_t (a known function of σ_e). The effective stress $\sigma_e = \left[\frac{3}{2}\mathbf{S}\cdot\cdot\mathbf{S}\right]^{1/2}$. In our problem $\sigma_e \equiv \sigma$ and the tensorial equation (1) can be separated into six scalar relations

$$\overset{\nabla}{\Sigma}_r = \dot{\pi} + \frac{2}{3}\epsilon_r + \frac{1}{3}(1 - \eta_t)\epsilon_z \tag{2a}$$

$$\overset{\nabla}{\Sigma}_\theta = \dot{\pi} + \frac{2}{3}\epsilon_\theta + \frac{1}{3}(1 - \eta_t)\epsilon_z \tag{2b}$$

$$\overset{\nabla}{\Sigma}_z = \dot{\pi} + \frac{2}{3}\eta_t\epsilon_z \tag{2c}$$

$$\overset{\nabla}{\Sigma}_{r\theta} = \frac{2}{3}\gamma_{r\theta} \qquad \overset{\nabla}{\Sigma}_{rz} = \frac{2}{3}\gamma_{rz} \qquad \overset{\nabla}{\Sigma}_{\theta z} = \frac{2}{3}\gamma_{\theta z} \tag{3}$$

where $(\Sigma_r, \Sigma_\theta, \ldots) = (\sigma_r/E, \sigma_\theta/E, \ldots)$ are nondimensionalized stress components, $\pi = (\Sigma_r + \Sigma_\theta + \Sigma_z)/3$ is the hydrostatic stress, $\eta_t = E_t/E$, and the strain rate components are given by the usual expressions,

$$\epsilon_r = u_{,r} \qquad \epsilon_\theta = \frac{u}{r} + \frac{1}{r}v_{,\theta} \qquad \epsilon_z = w_{,z} \tag{4}$$

$$\gamma_{r\theta} = \frac{1}{2}\left(\frac{1}{r}u_{,\theta} + v_{,r} - \frac{v}{r}\right) \qquad \gamma_{rz} = \frac{1}{2}(u_{,z} + w_{,z})$$

$$\gamma_{\theta z} = \frac{1}{2}\left(v_{,z} + \frac{1}{r}w_{,\theta}\right) \tag{5}$$

with (u, v, w) standing for the perturbed velocity field induced by the nonuniform part of the end disturbance. (Note that the stresses Σ_r, Σ_θ, . . . are here slightly different from those in (1988a), since we have nondimensionalized with respect to $2E/3$.)

Equilibrium requirements for the instantaneous response of the body are given by the equation

$$\nabla\cdot(\overset{\nabla}{\boldsymbol{\sigma}} - \mathbf{D}\cdot\boldsymbol{\sigma} + \boldsymbol{\sigma}\cdot\boldsymbol{\Omega} + \mathbf{I}\cdot\cdot\mathbf{D}\boldsymbol{\sigma}) = \mathbf{0} \tag{6}$$

where ∇ is the gradient operator, $\boldsymbol{\sigma}$ is the Cauchy stress tensor, $\mathbf{I}$ is the second-order unit tensor, and $\boldsymbol{\Omega}$ is the spin tensor defined by

$$\boldsymbol{\Omega} = \frac{1}{2}(\nabla\mathbf{V} - \mathbf{V}\nabla), \tag{7}$$

where $\mathbf{V}$ is the velocity vector. Recalling that for incompressible materials $\mathbf{I}\cdot\cdot\mathbf{D} = 0$, and noting that the only active component of $\boldsymbol{\sigma}$ is $\sigma_z = \sigma$, we obtain from equation (6) the three equilibrium rate equations

$$\overset{\nabla}{\Sigma}_{r,r} + \frac{1}{r}(\overset{\nabla}{\Sigma}_r - \overset{\nabla}{\Sigma}_\theta) + \frac{1}{r}\overset{\nabla}{\Sigma}_{r\theta,\theta} + \overset{\nabla}{\Sigma}_{rz,z} + \bar{\sigma}\omega_{zr,z} = 0 \tag{8}$$

$$\overset{\nabla}{\Sigma}_{r\theta,r} + \frac{2}{r}\overset{\nabla}{\Sigma}_{r\theta} + \frac{1}{r}\overset{\nabla}{\Sigma}_{\theta,\theta} + \overset{\nabla}{\Sigma}_{\theta z,z} - \bar{\sigma}\omega_{\theta z,z} = 0 \tag{9}$$

$$\overset{\nabla}{\Sigma}_{rz,r} + \frac{1}{r}\overset{\nabla}{\Sigma}_{rz} + \frac{1}{r}\overset{\nabla}{\Sigma}_{\theta z,\theta} + \left(\overset{\nabla}{\Sigma}_z - \bar{\sigma}\epsilon_z\right)_{,z} - \bar{\sigma}\left(\gamma_{rz,r} + \frac{1}{r}\gamma_{rz}\right) - \bar{\sigma}\left(\frac{1}{r}\gamma_{\theta z}\right)_{,\theta} = 0 \tag{10}$$

where $\bar{\sigma} = \sigma/E$, and the spin components are defined by

$$\omega_{r\theta} = \frac{1}{2}\left(-\frac{1}{r}u_{,\theta} + v_{,r} + \frac{v}{r}\right) \qquad \omega_{\theta z} = \frac{1}{2}\left(-v_{,z} + \frac{1}{r}w_{,\theta}\right)$$

$$\omega_{zr} = \frac{1}{2}(u_{,z} - w_{,r}). \tag{11}$$

Combining equations (8)–(10) with the constitutive relations (2)–(3), and using the kinematic connections (4)–(5) and (11), we arrive at three linear partial differential equations for the velocity components (u, v, w) and the hydrostatic stress rate $\dot{\pi}$. A fourth equation is provided by the incompressibility constraint $\epsilon_r + \epsilon_\theta + \epsilon_z = 0$ or, via equation (4),

$$u_{,r} + \frac{u}{r} + \frac{1}{r}v_{,\theta} + w_{,z} = 0. \tag{12}$$

Altogether there are four equations in four unknown functions. This system is supplemented by the stress-free boundary conditions over the cylindrical surface,

Downloaded 03 May 2010 to 171.66.16.244. Redistribution subject to ASME license or copyright; see http://www.asme.org/terms/Terms_Use.cfm

$$\mathbf{e}_r \cdot (\overset{\nabla}{\sigma} - \mathbf{D}\cdot\sigma + \sigma\cdot\Omega + \epsilon_t\sigma) = \mathbf{0} \quad \text{at } r = R \tag{13}$$

where $\mathbf{e}_r$ is the radial unit vector. For the simple primary state of uniaxial tension we find, from equation (13), the three homogeneous boundary conditions

$$\overset{\nabla}{\Sigma}_r = 0 \qquad \overset{\nabla}{\Sigma}_{r\theta} = 0 \qquad \overset{\nabla}{\Sigma}_{rz} - \bar{\sigma}\gamma_{rz} = 0 \quad \text{at } r = R. \tag{14}$$

These conditions are easily transformed with the aid of the constitutive and kinematic relations to linear conditions in terms of velocity components and hydrostatic stress rate. Note, incidentally, that the second and third of equation (14) imply the vanishing of the shear strain rates ($\gamma_{r\theta}$, γ_{rz}) at the boundary $r = R$.

The exact details of the nonuniform boundary tractions imposed at $z = 0$ need not be specified. Our interest is confined to the eigenfunctions and their associated eigenvalues produced by the homogeneous system of equations (8)–(10), (12), in conjunction with the stress-free boundary conditions (14). Of course, this set of eigenfunctions could be used to solve the nonhomogeneous rate boundary value problem for any imposed end disturbance.

3 The Eigenfunctions

Now assume that the perturbed field induced by the nonuniform part of the surface disturbance admits an eigenfunction representation with a typical eigencomponent described by

$$\begin{aligned} u &= U(r)e^{-kz}\cos m\theta \qquad v = V(r)e^{-kz}\sin m\theta \\ w &= W(r)e^{-kz}\cos m\theta \qquad \dot{\pi} = P(r)e^{-kz}\cos m\theta \end{aligned} \tag{15}$$

where m is an integer, (U, V, W, P) are unknown functions of r, and k is the associated eigenvalue.

The equilibrium rate equations (8)–(10) are reduced, for each eigenfield equation (15) to the system of ordinary differential equations,

$$2\left[U'' + \frac{1}{r}U' - \left(\frac{m^2+2}{2}\right)\frac{1}{r^2}U + \frac{1}{2}\left(1+\frac{3}{2}\bar{\sigma}\right)k^2U\right] + m\left(\frac{1}{r}V' - \frac{3}{r^2}V\right) - \left(2-\eta_t-\frac{3}{2}\bar{\sigma}\right)kW' + 3P' = 0 \tag{16}$$

$$-m\left(\frac{1}{r}U' + \frac{3}{r^2}U\right) + V'' + \frac{1}{r}V' - (1+2m^2)\frac{1}{r^2}V + \left(1+\frac{3}{2}\bar{\sigma}\right)k^2V + \left(2-\eta_t-\frac{3}{2}\bar{\sigma}\right)(mk)\frac{1}{r}W - 3m\left(\frac{1}{r}\right)P = 0 \tag{17}$$

$$-\left(1-\frac{3}{2}\bar{\sigma}\right)k\left(U' + \frac{1}{r}U + m\frac{V}{r}\right) + \left(1-\frac{3}{2}\bar{\sigma}\right)\left(W'' + \frac{W'}{r} - m^2\frac{W}{r^2}\right) + (2\eta_t - 3\bar{\sigma})k^2W - 3kP = 0, \tag{18}$$

where a prime indicates differentiation with respect to the radial coordinate. Similarly, the incompressibility constraint equation (12) becomes

$$U' + \frac{1}{r}U + m\frac{V}{r} - kW = 0. \tag{19}$$

At $r = R$, the stress free boundary conditions equations (14) take the form,

$$2U' - (1-\eta_t)kW + 3P = 0 \tag{20}$$

$$-m\frac{U}{r} + V' - \frac{V}{r} = 0 \tag{21}$$

$$-kU + W' = 0. \tag{22}$$

As expected, the radial profiles of the eigencomponents equations (15) are determined by the linear eigenvalue equations (16)–(19) along with the homogeneous boundary conditions (20)–(22). Nontrivial solutions for the system only occur for certain discrete eigenvalues, k. The eigenvalues depend on material properties, initial stress $\bar{\sigma}$, and circumferential wave number m.

Equations (16)–(19) admit a general solution in terms of modified Bessel functions. The algebra involved in deriving that solution is formidable, but it may be verified by direct substitution that the solid cylinder solution is

$$U = 3C_1\left[\left(\frac{k^2}{\alpha_1}\right)I_{m+1}(\alpha_1 r) + \left(\frac{mk^2}{\alpha_1^2}\right)\frac{1}{r}I_m(\alpha_1 r)\right] + 3C_2\left[\left(\frac{k^2}{\alpha_2}\right)I_{m+1}(\alpha_2 r) + \left(\frac{mk^2}{\alpha_2^2}\right)\frac{1}{r}I_m(\alpha_2 r)\right] + C_3\frac{1}{r}I_m(\beta r) \tag{23}$$

$$V = -3C_1\left(\frac{mk^2}{\alpha_1^2}\right)\frac{1}{r}I_m(\alpha_1 r) - 3C_2\left(\frac{mk^2}{\alpha_2^2}\right)\frac{1}{r}I_m(\alpha_2 r) - C_3\left[\frac{\beta}{m}I_{m+1}(\beta r) + \frac{1}{r}I_m(\beta r)\right] \tag{24}$$

$$W = 3C_1kI_m(\alpha_1 r) + 3C_2kI_m(\alpha_2 r) \tag{25}$$

$$P = C_1A_1I_m(\alpha_1 r) + C_2A_2I_m(\alpha_2 r) \tag{26}$$

where C_1, C_2, C_3 are integration constants, and

$$\alpha_1^2 = \frac{1-3\eta_t + i\sqrt{3(1+3\eta_t)(1-\eta_t) - 9\bar{\sigma}^2}}{2-3\bar{\sigma}}k^2 \tag{27a}$$

$$\alpha_2^2 = \frac{1-3\eta_t - i\sqrt{3(1+3\eta_t)(1-\eta_t) - 9\bar{\sigma}^2}}{2-3\bar{\sigma}}k^2 \tag{27b}$$

$$\beta = ik\sqrt{\left(1+\frac{3}{2}\bar{\sigma}\right)} \tag{28}$$

$$A_1 = \left(1-\frac{3}{2}\bar{\sigma}\right)\alpha_1^2 - \left(1-2\eta_t+\frac{3}{2}\bar{\sigma}\right)k^2 \tag{29a}$$

$$A_2 = \left(1-\frac{3}{2}\bar{\sigma}\right)\alpha_2^2 - \left(1-2\eta_t+\frac{3}{2}\bar{\sigma}\right)k^2. \tag{29b}$$

The complete solution of equations (16)–(19) contains three more independent functions involving the modified Bessel functions K_m and K_{m+1}. That branch of the solution is unbounded at the origin $r = 0$; consequently, it has been omitted from the present discussion. The full solution would be needed for the analogous tube problem.

Finally, we substitute solution (23)–(26) in the boundary conditions (20)–(22). The resulting homogeneous algebraic system for constants C_1, C_2, C_3, has a nontrivial solution only when the determinant of the system vanishes. This requirement can be written as

$$\det(Q_{ij}) = 0, \tag{30}$$

where

$$Q_{11} = -\left(\frac{2k^2}{\alpha_1 R}\right)I_{m+1}(\alpha_1 R) + \left[2m(m-1)\left(\frac{k}{\alpha_1 R}\right)^2 + B_1\right]I_m(\alpha_1 R) \tag{31a}$$

$$Q_{12} = -\left(\frac{2k^2}{\alpha_2 R}\right)I_{m+1}(\alpha_2 R) + \left[2m(m-1)\left(\frac{k}{\alpha_2 R}\right)^2 + B_2\right]I_m(\alpha_2 R) \tag{31b}$$

$$Q_{13} = 2\beta^2\left[\left(\frac{1}{\beta R}\right)I_{m+1}(\beta R) + \frac{m-1}{(\beta R)^2}I_m(\beta R)\right] \tag{31c}$$

Downloaded 03 May 2010 to 171.66.16.244. Redistribution subject to ASME license or copyright; see http://www.asme.org/terms/Terms_Use.cfm

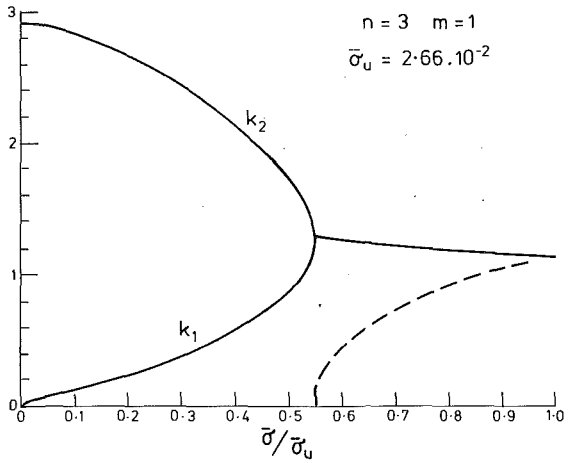


Fig. 2(*a*) Variation of the first asymmetric eigenvalue k_1 with applied uniform tension for $n=3$. The solid and chained curves represent the real and imaginary parts of the eigenvalues, respectively.

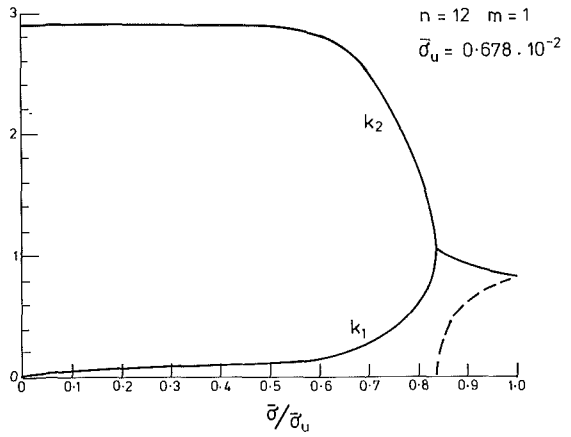


Fig. 2(*b*) Variation of the first asymmetric eigenvalue k_1 with applied uniform tension for $n=12$. The solid and chained curves represent the real and imaginary parts of the eigenvalues, respectively.

$$Q_{21} = -2m\left[\left(\frac{k^2}{\alpha_1 R}\right) I_{m+1}(\alpha_1 R) + (m-1)\left(\frac{k}{\alpha_1 R}\right)^2 I_m(\alpha_1 R)\right] \tag{31d}$$

$$Q_{22} = 2m\left[\left(\frac{k^2}{\alpha_2 R}\right) I_{m+1}(\alpha_2 R) + (m-1)\left(\frac{k}{\alpha_2 R}\right)^2 I_m(\alpha_2 R)\right] \tag{31e}$$

$$Q_{23} = \frac{2\beta^2}{m}\left\{\left(\frac{1}{\beta R}\right) I_{m+1}(\beta R) - \left[\frac{m(m-1)}{(\beta R)^2} + \frac{1}{2}\right] I_m(\beta R)\right\} \tag{31f}$$

$$Q_{31} = \frac{k}{\alpha_1}(\alpha_1^2 - k^2)\left[I_{m+1}(\alpha_1 R) + \left(\frac{m}{\alpha_1 R}\right) I_m(\alpha_1 R)\right] \tag{31g}$$

$$Q_{32} = \frac{k}{\alpha_2}(\alpha_2^2 - k^2)\left[I_{m+1}(\alpha_2 R) + \left(\frac{m}{\alpha_2 R}\right) I_m(\alpha_2 R)\right] \tag{31h}$$

$$Q_{33} = -\frac{k}{R} I_m(\beta R) \tag{31i}$$

and

$$B_1 = \left(1 - \frac{3}{2}\bar{\sigma}\right)(k^2 - \alpha_2^2) \qquad B_2 = \left(1 - \frac{3}{2}\bar{\sigma}\right)(k^2 - \alpha_1^2). \tag{32}$$

The transcendental equation (30) can be solved numerically to obtain the eigenvalues, k, for each integer, m. The solution of the limiting axially symmetric case (Durban and Stronge, 1988a) is obtained directly from equations (23)–(26) with $m=0$ and $C_3=0$.

In passing, it is worth mentioning that each eigencomponent equation (15) produces a self-equilibrating surface field at the end $z=0$. This can be proved by a standard technique similar to the one used in the plane-strain analysis (1988b).

4 Numerical Results and Discussion

Sample calculations of the eigenvalues from equation (30) were performed with the Ramberg-Osgood stress-strain relation

$$ln\lambda = \bar{\sigma} + \frac{3}{7} e_o^{1-n} \bar{\sigma}^n \tag{33}$$

where e_o and n are material constants and λ is the axial stretch. The tangent modulus of curve (33) is simply

$$\eta_t = \frac{E_t}{E} = \frac{d\bar{\sigma}}{dln\lambda} = \left[1 + \frac{3n}{7}\left(\frac{\bar{\sigma}}{e_o}\right)^{n-1}\right]^{-1} \tag{34}$$

and the necking load, defined by the stress where $\bar{\sigma} = \eta_t$, is given approximately by

$$\frac{\sigma_u}{E} \equiv \bar{\sigma}_u \approx \left(\frac{7}{3n} e_o^{n-1}\right)^{1/2}. \tag{35}$$

Note that the current deformed radius of the cylinder R is related to the original undeformed radius R_o by

$$R = R_o \lambda^{-1/2}. \tag{36}$$

A characteristic value of $e_o = 0.005$ has been used in the computations along with the representative values of $n=3$ and $n=12$ for the hardening parameter.

At a given value of initial stress $\bar{\sigma}$ there is an infinite number of eigenvalues, k, for each wave number, m. Of particular interest, however, is the first eigenvalue—the one with the smallest positive real part—since it provides a lower bound on the axial rate of decay of the nonuniform part of the end disturbance. A straightforward search procedure has been employed to trace that first eigenvalue for each wave number, m, over the loading range of $0 \le \bar{\sigma} \le \bar{\sigma}_e$. Only symmetric cases where $m \ge 1$ were investigated since the axisymmetric case ($m=0$) has already been studied (1988a).

Figures 2(*a*)–2(*b*) display the typical variation of the real and imaginary parts of the first asymmetric eigenvalue, k_1 with the background tension stress, σ. The eigenvalues with the smallest real part have been found to be given always by $m=1$. Initially, for small values of $\bar{\sigma}$, the root is real indicating a purely exponential nonoscillatory decay of the associated eigenfunctions. The values of k_1 in that range of axial stress, are considerably below the first eigenvalue for the axisymmetric eigenfunction. It appears that there is almost no decay at all at very small levels of $\bar{\sigma}$. These findings are supported by an asymptotic analysis for the eigenvalue equation (30). Thus, for small values of k and with $m=1$, we can use expansions that are valid for $|z| << 1$,

$$I_1(z) \approx \frac{z}{2}\left(1 + \frac{z^2}{8} + \ldots\right) \qquad I_2(z) \approx \frac{z^2}{8}\left(1 + \frac{z^2}{12} + \ldots\right). \tag{37}$$

Inserting these approximations in equations (30)–(31), after some algebraic manipulations we find the following asymptotic expression

$$(k_1 R)^2 \approx \frac{4\bar{\sigma}\left(1 - \frac{3}{2}\bar{\sigma}\right)}{(1+3\bar{\sigma})\eta_t - \left[1 + \frac{3}{2}\bar{\sigma}(1+\bar{\sigma})\right]\bar{\sigma}}. \tag{38}$$

Results evaluated from equation (38) with the aid of equation (34) are in close agreement with the numerical solution, shown in Figs. 2(*a*)–2(*b*), up to values of $k_1 R \approx 0.3$. At low values of

Downloaded 03 May 2010 to 171.66.16.244. Redistribution subject to ASME license or copyright; see http://www.asme.org/terms/Terms_Use.cfm

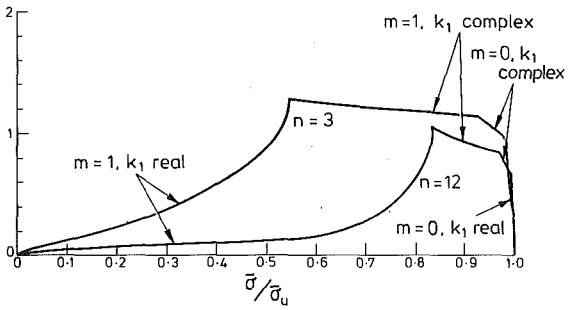


Fig. 3 Variation of the real part of the smallest eigenvalue with initial tension stress σ. Asymmetric eigenfunctions are described by $m=1$ and symmetric eigenfunctions by $m=0$.

2(*a*)-2(*b*), up to values of $k_1R \approx 0.3$. At low values of stress, where $\eta_l \approx 1$ and $\bar{\sigma} \ll 1$, approximation (38) can be reduced further to

$$k_1R \approx 2\sqrt{\bar{\sigma}} = 2\sqrt{\Delta} \tag{39}$$

where $\Delta \approx \lambda - 1$ is the linear elastic strain. The analogous plane-strain result in the present notation reads (1988b, 1988c)

$$k_1h \approx \sqrt{3\Delta}, \tag{40}$$

where h is the deformed half-thickness of the strip. Both results, equations (39) and (40), relate to purely elastic behavior; they can be regarded as critical second-order effects not given by the linear theory of elasticity.

The value of k_1 increases with increasing stress up to a sharp branching point (Figs. 2(*a*)-2(*b*)) where k_1 becomes complex. For tensile stress above the branching point, the real part decreases slightly while the imaginary part rapidly increases with increasing stress. It is interesting to note that the second asymmetric eigenvalue k_2 for $m=1$, decreases monotonously from the linear elastic value of $k_2 \approx 2.90$; at the branching point it merges with the first eigenvalue, k_1. The second eigenvalue is purely real from zero stress up the branching point.

Finally, an estimate of the validity of Saint-Venant's principle for the circular cylinder problem is obtained by comparing the first eigenvalues of the asymmetric subspace (Figs. 2(*a*)-2(*b*)) and the symmetric subspace (1988a). Selecting the eigenvalue with smallest real part we arrive at the picture shown in Fig. 3; over most of the range of initial stress the smallest eigenvalue is indeed associated with an asymmetric ($m=1$) eigenfunction. Near the necking stress, however, the smallest eigenvalue is associated with a symmetric ($m=0$) eigenfunction. The stress level at which this transition occurs appears to increase with n (Fig. 3).

We have seen already in equations (38)-(39) that the first asymmetric eigencomponent diffuses very slowly when the axial stress is small. Likewise, near the ultimate stress ($\sigma = \sigma_u$) there is almost no decay of the first symmetric eigencomponent as shown by the asymptotic expansion (1988a)

$$k_1R \approx \sqrt{8n(1-\bar{\sigma}/\bar{\sigma}_u)}. \tag{41}$$

Since both extreme points ($\sigma = 0$ and $\sigma = \sigma_u$) are associated with the existence of instabilities (buckling of the semi-infinite cylinder as the compressive stress vanishes and necking at maximum tension force), Saint-Venant's principle apparently fails at points of bifurcation. That failure is preceded by low rates of diffusion as the bifurcation stress is approached.

A similar observation has been made for the analogous plane-strain problem (1988b, 1988c); for small stress we have expression (40), which is associated with an antisymmetric eigenfunction. Near necking the first eigenvalue, associated with a symmetric eigenfunction, admits an asymptotic expression, which resembles equation (41)

$$k_1h \approx \sqrt{3n(1-\bar{\sigma}/\bar{\sigma}_u)}. \tag{42}$$

In this expression, $\bar{\sigma}_u$ is the plane-strain necking stress.

It is worth noting that the decay rate is real for a stress near either the elastic (39)-(40) or plastic (41)-(42) instability condition; i.e., the associated velocity field is a very slowly decaying nonoscillatory function of z.

Acknowledgment

Part of this work was supported by the V.P.R.—Aeronautical Engineering Research Fund, Technion, Haifa.

References

Durban, D., and Stronge, W. J., 1988a, "On the Validity of Saint Venant's Principle In Finite Strain Plasticity," ASME JOURNAL OF APPLIED MECHANICS, Vol. 55, pp. 11-16.

Durban, D., and Stronge, W. J., 1988b, "Diffusion Of Self-Equilibrating End Loads In Plane Strain Plasticity," *J. Mech. Phys. Solids*, Vol. 36, pp. 459-476.

Durban, D., and Stronge, W. J., 1988c, "Diffusion Of Self-Equilibrating End Loads In Elastic Solids, ASME JOURNAL OF APPLIED MECHANICS, Vol. 55, pp. 492-495.

Downloaded 03 May 2010 to 171.66.16.244. Redistribution subject to ASME license or copyright; see http://www.asme.org/terms/Terms_Use.cfm

Equilibrium Path Bifurcation Due to Strain-Softening Localization in Ellipsoidal Region

Z. P. Bažant
Department of Civil Engineering,
Northwestern University,
Evanston, IL 60208
Mem. ASME

A preceding study of the loss of stability of a homogeneous strain state in infinite homogeneous solid due to localization of strain into an ellipsoidal region is complemented by determining the condition of bifurcation of equilibrium path due to ellipsoidal localization mode. The bifurcation occurs when the tangential moduli matrix becomes singular, which coincides with Hill's classical bifurcation condition for localization into an infinite layer. The bifurcation is normally of Shanley type, occurring in absence of neutral equilibrium while the controlled displacements at infinity increase. During the loading process with displacement increase controlled at infinity, this type of bifurcation precedes the loss of stability of equilibrium due to an ellipsoidal localization mode, except when the tangential moduli change suddenly (which happens, e.g., when the slope of the stress-strain diagram is discontinuous, or when temperature is increased).

Introduction

Strain softening due to distributed cracking may cause strain-localization instabilities. For uniaxial behavior and for bending, the localization instabilities were analyzed in 1974 by Bažant (1976). In multidimensional situations, the simplest localization instabilities are the localization into a planar band or into an ellipsoid, which were analyzed by Rudnicki and Rice (1975), Rice (1976), and Rudnicki (1977). These pioneering studies were limited to localizations in an infinite space and to von Mises or Drucker-Prager plasticity. Recently, Bažant (1988d) extended these classical works to ellipsoidal localization in a material with an arbitrary constitutive law and, for the cases of localizations into planar bands as well as circular or spherical regions, to finite bodies. He also went beyond the conditions of critical state and obtained the conditions of stability. A detailed study of the effects of various material parameters as well as body size on the critical states has been presented by Bažant and Lin (1989). For a more detailed literature review, see Bažant (1988d) and Bažant and Lin (1989).

The interest in the solutions of localization in ellipsoidal regions stems from the fact that, in contrast to the solutions for infinite bands, they can be used as approximate solutions of localization in finite bodies. If the body is finite, localization into an infinite band cannot represent and exact solution because, for example, the fixed boundary conditions cannot be satisfied at the location where the localization band intersects the boundary.

In particular, we will focus on localization into ellipsoidal regions for which analytical solutions can be found. Except for the special case of cylindrical and spherical localization regions, these solutions are available only for an infinite solid, and generally cannot satisfy the boundary conditions for a finite body. However, in contrast to the infinite localization band, they can at least satisfy the boundary conditions approximately, provided the body is sufficiently large compared to the size of the localization ellipsoid. This is due to the fact that the stresses, strains, and displacements in the analytical solution for the ellipsoidal localization region in an infinite solid decay rapidly with the distance from the ellipsoid, thus becoming negligible at a certain sufficient distance from the ellipsoid. If the boundary lies beyond that distance, the solution is nearly vanishing at the boundary and can, therefore, be used as an approximate solution for a finite body.

The previous studies of strain localization into ellipsoidal regions have been restricted to instabilities, which occur at constant load and represent a state of neutral equilibrium or limit of stability. Localizations, however, can also occur in a stable fashion as a bifurcation of equilibrium response path at increasing load, similarly to Shanley-type instability of plastic column. The objective of this paper is to extend the previous general stability analysis of Bažant (1988b) and Bažant and Lin (1989) to bifurcations of Shanley type, at which the ellipsoidal localization region is stable and the loading increases during bifurcation.

Eshelby's Solution

We consider an ellipsoidal hole (Fig. 1(*b*)) in an infinite homogeneous elastic space characterized by the elastic moduli

Contributed by the Applied Mechanics Division of THE AMERICAN SOCIETY OF MECHANICAL ENGINEERS for presentation at the Winter Annual Meeting, Dallas, Texas, Nov. 25–30, 1990.

Discussion on this paper should be addressed to the Technical Editor, Leon M. Keer, The Technological Institute, Northwestern University, Evanston, IL 60208, and will be accepted until two months after final publication of the paper itself in the JOURNAL OF APPLIED MECHANICS. Manuscript received by the ASME Applied Mechanics Division, Aug. 30, 1988; final revision, Dec. 14, 1989.

Paper No. 90-WA/APM-30.

Copyright © 1990 by ASME
Downloaded 03 May 2010 to 171.66.16.244. Redistribution subject to ASME license or copyright; see http://www.asme.org/terms/Terms_Use.cfm

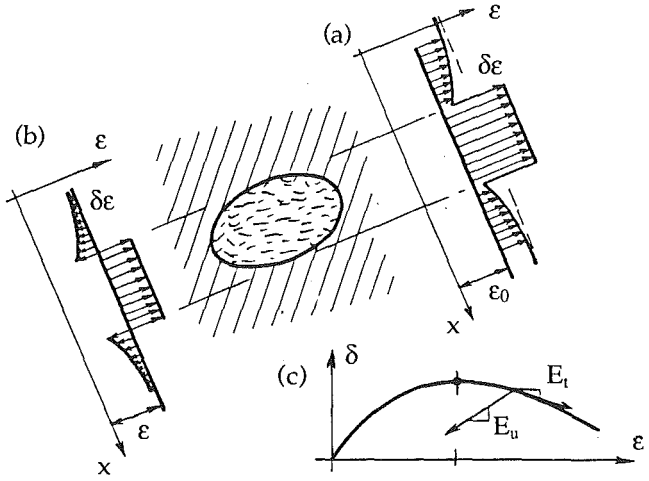


Fig. 1 Strain increment distribution for localization during loading into an ellipsoidal region, and stress-strain diagram (E_t – D_{IIII})

matrix $\mathbf{D}_u$. We imagine to fit and glue into this hole an ellipsoidal plug made of the same material. To fit, the plug must first be deformed by a uniform strain, ϵ^0, called the eigenstrain (note that an ellipsoid can be transformed to any other ellipsoid by uniform strain). The eigenstrain is then imagined unfrozen. This causes the plug with ellipsoidal hole to undergo strain increment, ϵ^e, in order to establish equilibrium with the surrounding infinite space. According to the famous Eshelby's (1957) theorem, the strain ϵ^e in the plug is uniform and is expressed as

$$\epsilon^e_{ij} = S_{ijkm}\epsilon^0_{km} \tag{1}$$

in which S_{ijkm} are the components of a fourth-rank tensor which depend only on the aspect ratios a_1/a_2, a_3/a_2 of the principal axes of the ellipsoid, as well as on the elastic moduli; the latin lower case subscripts refer to cartesian coordinates x_i (i = 1, 2, 3), and repeated subscripts imply summation over 1, 2, 3. Eshelby's coefficients S_{ijkm} are generally calculated as elliptic integrals (Mura, 1982). Always, $S_{ijkm} = S_{jikm} = S_{ijmk}$, but in general $S_{ijkm} \neq S_{kmij}$. For arbitrary anisotropic material properties, the expressions for coefficients S_{kmij} were derived by Kinoshita and Mura (1971) and Lin and Mura (1973). For convenience we rewrite equation 1 in a matrix form:

$$\boldsymbol{\epsilon}^e = \mathbf{Q}_u\boldsymbol{\epsilon}^0 \tag{2}$$

in which $\mathbf{Q}_u$ is a (6 × 6) square matrix formed from coefficients S_{ijkm} (see Bažant, 1988d), and $\boldsymbol{\epsilon}^0$ and $\boldsymbol{\epsilon}^e$ are (6 × 1) column matrices of the eigenstrains and the equilibrium strains in the ellipsoidal region.

According to Hooke's law, the stress in the ellipsoidal plug, $\boldsymbol{\sigma}^e$, which is uniform, may be expressed as $\boldsymbol{\sigma}^e = \mathbf{D}_u(\boldsymbol{\epsilon}^e - \boldsymbol{\epsilon}^0)$. From equation 2, $\boldsymbol{\epsilon}^0 = \mathbf{Q}_u^{-1}\boldsymbol{\epsilon}^e$, and so

$$\boldsymbol{\sigma}^e = \mathbf{D}_u(\mathbf{I} - \mathbf{Q}_u^{-1})\boldsymbol{\epsilon}^e \tag{3}$$

in which $\mathbf{I}$ = unit (6 × 6) matrix.

Review of Ellipsoidal Localization Instability

For the readers' convenience, let us first briefly outline a simplified version of the analysis from Bažant (1988d). We consider an infinite strain-softening solid (without any hole) which is initially in an initial equilibrium state of uniform initial strain, $\boldsymbol{\epsilon}$, and uniform initial stress, $\boldsymbol{\sigma}$, balanced by loads applied at infinity. We seek the condition under which the initial state loses stability in a mode in which the strain localizes into an ellipsoidal region (Fig. 1(*a*)) without changing the prescribed stresses (or the prescribed displacements) at infinity. If these variations can happen while maintaining equilibrium, we have a state of neutral equilibrium which represents the limit of stability, i.e., the critical state.

Due to localization, the strain and stress in the infinite continuum outside the ellipsoidal region becomes nonuniform; while according to Eshelby's theorem, the stress and strain inside the ellipsoidal region will remain uniform (Fig. 1(*b*)). The strains can become discontinuous across the ellipsoidal interface. On the other hand, the normal and shear stress components acting on this surface must remain continuous in order to maintain equilibrium.

It must now be recognized that a material in a strain-softening state can deform not only according to the matrix of tangential moduli for further loading (i.e., strain-softening), which is indefinite, but also according to the matrix of elastic moduli for unloading, which is positive definite. Because the stresses inside the ellipsoidal region decrease if there is strain softening at further loading, and because the stress components on the ellipsoidal interface must be continuous across the interface, the stresses immediately outside the ellipsoidal region must decrease if the stresses or displacements at infinity are fixed. So, immediately outside the ellipsoidal region, there can be unloading, i.e., the material can behave elastically. In fact, there must be unloading at least somewhere outside the ellipsoidal region, for if there were none, the strain variations would be non-negative everywhere along any straight line through the ellipsoid, and positive inside the ellipsoid; their integral from $-\infty$ to ∞ along such a line would be nonzero and thus incompatible with the boundary condition of constant displacements at infinity. The same must be true for the boundary condition of constant stresses at all infinitely remote points because integration of strains along any closed infinitely remote contour indicates that this boundary condition implies constant displacement at infinity. (Later, we will see that in the bifurcation problem, the situation is different: There need not be any unloading since bifurcation can occur while the displacements at infinity increase.)

According to equation (3), the stress variations inside the ellipsoidal region that correspond to Eshelby's solution for the outside are $\delta\boldsymbol{\sigma}^e = \mathbf{D}_u(1 - \mathbf{Q}_u^{-1})\delta\boldsymbol{\epsilon}^e$ in which $\mathbf{D}_u$ represents the matrix of the elastic moduli for unloading from the current state characterized by initial strain $\boldsymbol{\epsilon}$. This matrix is positive definite, and it is also isotropic if the material is isotropic. The vector of surface tractions that must be transmitted from the ellipsoidal region to the outside in order to provide the correct boundary conditions for the Eshelby's solution for the outside is $\delta\mathbf{p}^e = -\delta\boldsymbol{\sigma}^e\mathbf{n}$, where $\mathbf{n}$ is the unit vector of the normals to the ellipsoidal surface, pointed outward from the ellipsoid. Therefore,

$$\delta\mathbf{p}^e = -\mathbf{D}_u(\mathbf{I} - \mathbf{Q}_u^{-1})\delta\boldsymbol{\epsilon}^e\mathbf{n}. \tag{4}$$

At the same time, the stress variations inside the ellipsoidal region may be expressed as $\delta\boldsymbol{\sigma}^e = \mathbf{D}_t\delta\boldsymbol{\epsilon}^e$, in which $\mathbf{D}_t$ is the (6 × 6) matrix of tangential moduli for further loading from the current state of strain $\boldsymbol{\epsilon}$. This matrix is not positive definite if the initial state is in the strain-softening range, and, in general, is anisotropic (as a manifestation of stress-induced anisotropy). Based on the stress variations inside the ellipsoidal region, the vector of surface tractions acting on the surface of the ellipsoid must be $(\mathbf{D}_t\delta\boldsymbol{\epsilon}^e)\,\mathbf{n}$, and the vector of surface tractions applied from the ellipsoidal region on the outside must be

$$\delta\mathbf{p}^e = -\mathbf{D}_t\delta\boldsymbol{\epsilon}^e\mathbf{n}. \tag{5}$$

Substituting equation (5) into equation (4), one obtains for the strain variations $\delta\boldsymbol{\epsilon}^e$ in the ellipsoidal localization region the condition:

$$\delta\mathbf{X}\,\mathbf{n} = \mathbf{0}, \text{ with } \delta\mathbf{X} = \mathbf{Z}\,\delta\boldsymbol{\epsilon}^e, \tag{6}$$

in which

$$\mathbf{Z} = \mathbf{D}_t - \mathbf{D}_u(\mathbf{I} - \mathbf{Q}_u^{-1}), \tag{7}$$

where $\mathbf{Z}$ is a (6 × 6) matrix depending only on the loading

Downloaded 03 May 2010 to 171.66.16.244. Redistribution subject to ASME license or copyright; see http://www.asme.org/terms/Terms_Use.cfm

and unloading stiffness matrices of the material in its current state.

Vector $\delta\mathbf{X}$ is the same for all the points of the ellipsoidal surface because the strain $\delta\epsilon^e$ in the ellipsoidal region is homogeneous, both according to Eshelby's solution for the outside and the assumed strain-softening deformation inside. Equation (6) represents a system of three homogeneous linear algebraic equations for the three components of $\mathbf{n}$. These equations must be satisfied not just for one vector, $\mathbf{n}$, but for infinitely many vectors of all the normals, $\mathbf{n}$, of the ellipsoidal surface. This is possible if and only if $\delta\mathbf{X} = \mathbf{0}$. Therefore.

$$\mathbf{Z}\delta\epsilon^e = \mathbf{0}. \tag{8}$$

This is a system of six homogeneous linear algebraic equations for the six components of column matrix $\delta\epsilon^e$. Thus, a localization instability is possible if and only if the determinant of this equation system vanishes, i.e.,

$$\det \mathbf{Z} = 0. \tag{9}$$

This condition, representing a condition of neutral equilibrium, was obtained in Bažant (1988d) by analyzing the positive definiteness of the second-order work in the infinite solid, which showed that the states in the loading process preceding the attainment of this condition are stable, and the subsequent states are unstable. The special case of equation (9) for Drucker-Prager plasticity was obtained by Rudnicki (1977).

Using the thermodynamic stability condition from Bažant (1988a, b), Bažant (1988d) further showed that the initial state of uniform strain ϵ is unstable if matrix $\mathbf{Z}$ is not positive definite, and is stable (with regard to the ellipsoidal localization mode) if matrix $\mathbf{Z}$ is positive definite.

The critical state condition in equation (8) ignores second-order nonlinear geometric effects. As is well known from various three-dimensional stability problems (Biot, 1965; Bažant 1971), the nonlinear geometric effects can have influence on three-dimensional instabilities only if they occur at stresses that are of the same order of magnitude as the tangential moduli. For a material with a stress-strain diagram that lacks a prolonged plastic plateau (Fig. 1(*c*)), this situation arises only if the instability occurs very near the peak of the stress-strain diagram. Since Eshelby's theorem is limited to small-strain elasticity, we must exclude this case from our analysis (as done by Rudnicki, 1977). Our solution will be applicable only to postpeak states at which the tangential modulus E_t (Fig. 1(*c*)) is of a higher order of magnitude than the stresses. Thus, if we find the bifurcation to occur at the peak stress, it means that according to finite strain theory it should occur near the peak stress.

Bifurcation Analysis

For inelastic structures, the condition of stable equilibrium does not necessarily indicate which equilibrium path will be followed by the structure under a given loading process. It can happen that, after a bifurcation of the equilibrium path, the states on all the equilibrium branches emanating from the bifurcation point are stable, yet only one of them can be followed by the structure. Which one is followed is decided by the condition of stable path (Bažant 1988a,b), which differs from the condition of stable equilibrium if the structure is inelastic. (An example of such behavior is Shanley's bifurcation at the tangent modulus load of an elastoplastic column.) We will now show that, for ellipsoidal localizations, the bifurcation of equilibrium path happens earlier and can take place during a succession of stable equilibrium states at increasing load, i.e., in absence of neutral equilibrium.

The loss of stability due to strain localization is considered to occur while the remote displacements, strains, and stresses are constant (Fig. 1(*b*)). Bifurcation of the equilibrium path, on the other hand, can occur while the remote displacements, strains, and stresses increase (Fig. 1(*c*)). In this manner, it can happen that the strains increase everywhere, but the increase inside the ellipsoidal region is larger than outside, so that the strain localizes simultaneously with the progress of loading; see Fig. 1(*a*). For the mode of instability (Fig. 1*b*), matrix $\mathbf{D}_t$ of the moduli for loading applies for the interior of the ellipsoid, and matrix $\mathbf{D}_u$ of the moduli for unloading applies for the exterior. But in the bifurcation mode (Fig. 1*a*), matrix $\mathbf{D}_t$ applies for both the interior and the exterior of the ellipsoid.

As shown in Bažant (1988d, equation 12), the second-order work for an arbitrary deviation from the initial uniform equilibrium state with loading inside and unloading outside the ellipsoid is $\delta^2 W = (1/2)\,\delta\epsilon^T \mathbf{Z}\,\delta\epsilon\, V$, where V = volume of the ellipsoidal region and $\delta\epsilon$ is the (6×1) column matrix of arbitrary homogeneous strain increments inside the ellipsoid. According to the derivation of equation (1), one can check that the second-order work done along the equilibrium path when loading takes place both inside and outside the ellipsoid is $\delta^2 W = (1/2)\,\delta\epsilon^T \mathbf{Z}_t\,\delta\epsilon\, V$ where $\mathbf{Z}_t$ is obtained from $\mathbf{Z}$ (equation (7) by replacing $\mathbf{D}_u$ with $\mathbf{D}_t$. Therefore, $\mathbf{Z}_t = \mathbf{D}_t(\mathbf{I} + \mathbf{Q}_t^{-1} - \mathbf{I})$ or

$$\mathbf{Z}_t = \mathbf{D}_t\mathbf{Q}_t^{-1}, \tag{10}$$

where $\mathbf{Q}_t$ is the matrix of Eshelby's coefficients based on $\mathbf{D}_t$.

Assuming $\mathbf{D}_t$ to vary during the loading process continuously, the first bifurcation of the equilibrium path is obtained when $\delta^2 W = 1/2\,\delta\epsilon^T \mathbf{Z}_t\,\delta\epsilon\, V = 0$ for some nonzero vector $\delta\mathbf{e}$. This case occurs when the matrix equation

$$\mathbf{Z}_t\delta\epsilon = \mathbf{0} \tag{11}$$

admits a nonzero solution $\delta\mathbf{e}$. This means that matrix $\mathbf{Z}_t$ given by equation (10) is singular.

Matrix $\mathbf{Q}_t$ relates the equilibrium strain of an elastic plug of moduli, $\mathbf{D}_t$, in an infinite space of moduli, $\mathbf{D}_t$, to the eigenstrain, $\delta\epsilon^0$, by which the plug must be deformed to fit it into an ellipsoidal hole in the infinite space; $\delta\epsilon = \mathbf{Q}_t\delta\epsilon^0$. From this physical meaning it is clear that if $\mathbf{D}_t$ is positive definite, then a finite $\delta\epsilon$ can be produced only by a finite $\delta\epsilon^0$, and if $\mathbf{D}_t$ is nearly singular (a state near the peak of the stress-strain diagram), then a finite $\delta\epsilon$ can occur even for a vanishingly small $\delta\epsilon^0$. Therefore, if $\mathbf{D}_t$ is positive definite, so must be $\mathbf{Q}_t^{-1}$, and if $\mathbf{D}_t$ is singular, so must be $\mathbf{Q}_t^{-1}$. Hence, in view of equation (10), singularity of matrix $\mathbf{Z}_t$ implies the tangential moduli matrix $\mathbf{D}_t$ to be singular, i.e.,

$$\det \mathbf{D}_t = 0. \tag{12}$$

This is equivalent to the well-known bifurcation condition for an infinite localization band in an infinite solid (Rudnicki and Rice, 1975). Equation (11) is satisfied at the peak point of the stress-strain diagram and represents the condition which separates the strain-hardening regime of material ($\mathbf{D}_t$ positive definite) from the strain-softening regime ($\mathbf{D}_t$ indefinite).

So we must conclude that, during a loading process in which the displacements are continuously increased at infinity, localization of homogeneous strain into an ellipsoidal region must begin as soon as $\mathbf{D}_t$ loses positive definiteness, i.e., as soon as strain softening begins, same as localization into an infinite band.

Let us now discuss the type of bifurcation. In view of equation (10), equation (11) for eigenvector $\delta\epsilon^*$ of matrix $\mathbf{Z}$ may be written as

$$\mathbf{D}_t\mathbf{x}^* = \mathbf{0}, \tag{13}$$

in which $\mathbf{x}^* = \mathbf{Q}_t^{-1}\,\delta\epsilon^*$ or

$$\delta\epsilon^* = \mathbf{Q}_t\mathbf{x}^*, \tag{14}$$

and $\mathbf{x}^*$ is the eigenvector of matrix $\mathbf{D}_t$ corresponding to zero eigenvalue.

Two cases may now be distinguished: (1) Either the eigenvector $\delta\epsilon^*$ lies in the sector of loading, or (2) it does not.

Downloaded 03 May 2010 to 171.66.16.244. Redistribution subject to ASME license or copyright; see http://www.asme.org/terms/Terms_Use.cfm

If it does, then the bifurcation state would be a state of neutral equilibrium, which represents the limit of stability. In previous work (Bažant 1988d, Bažant and Lin 1989), however, it was found that, except for the limit case of an infinite layer (which is equivalent to an ellipsoid for which the two ratios of its axes tend to infinity), the limit of stability does not occur when $\det \mathbf{D}_t = 0$ but only later, when matrix $\mathbf{D}_t$ becomes indefinite (i.e., at a certain finite distance after the peak of the stress-strain diagram).

It follows that the eigenvector $\delta\epsilon^*$ must lie outside the loading sector. So the actual increment $\delta\epsilon^{ep}$ along the equilibrium path cannot coincide with $\delta\epsilon^*$ because it would imply unloading, which we have ruled out. Therefore, the actual $\delta\epsilon^{ep}$ musts lie at the boundary of the loading sector and must differ from the eigenvector $\delta\epsilon^*$. Hence, $\mathbf{Z}_t\, \delta\epsilon^p \neq 0$ and, furthermore, $\mathbf{D}_t\, \mathbf{x}^{ep} \neq \mathbf{0}$ where $\mathbf{x}^{ep} = \mathbf{Q}_t^{-1}\, \delta\epsilon^p$. This means that the increment $\delta\epsilon^{ep}$ along the equilibrium path must be happening at increasing boundary displacements (or increasing strains) at infinity, i.e., neutral equilibrium does not exist. This is obviously the Shanley type of bifurcation, in which the bifurcation state and all the immediate postbifurcation states are stable (Bažant 1988a, b).

For an infinite localization band in an infinite solid, by contrast, the first bifurcation is not of Shanley type. It occurs at neutral equilibrium and represents the onset of instability.

Comments

As shown by Rudnicki (1977) for Drucker-Prager plasticity and by Bažant (1988d) and Bažant and Lin (1989) for general material properties, the loss of stable equilibrium with localization into an ellipsoidal region can occur only when matrix $\mathbf{D}_t$ becomes indefinite, i.e., when the material enters a strain-softening state. This occurs at a finite distance after the peak point of the stress-strain diagram, at which the tangential modulus is nonzero and negative. We now find, however, that along the equilibrium path the localization into an ellipsoidal region occurs already when matrix $\mathbf{D}_t$ becomes semi-definite, i.e., at the peak-stress state, which always precedes the state of stability loss.

The classical bifurcation condition of Hill (1962), which serves as the basis of the method of linear comparison solid, also indicates that singularity of matrix $\mathbf{D}_t$ is the condition of first bifurcation; see also Rudnicki and Rice (1975), Rice (1976), Leroy and Ortiz (1988), and de Borst (1988). Hill's bifurcation condition, however, has been proven only for localization into an infinite planar band in an infinite space. The boundary conditions of such a localization mode cannot be accommodated for finite bodies. The present analysis proves that Hill's bifurcation condition (i.e., $\det \mathbf{D}_t = 0$) is also correct for localization into ellipsoidal regions, although the mode of localization is different.

Note that Hill's case of localization into an infinite layer is obtained as the limiting case of ellipsoidal localization when two axes of the ellipsoid tend to infinity. The fact that this limiting case agrees with Hill's case was numerically verified in Bažant (1988d) and Bažant and Lin (1989).

The foregoing analysis, which led to the bifurcation condition $\det \mathbf{D}_t = 0$, shows only when localization can occur. To show that it must occur, Bažant's (1988a,b) path-stability criterion requires it to prove that, for the conditions of prescribed displacements at infinity, the value of $\delta^2 W$ is smaller for the localizing path than for the nonlocalized path (in which the strain field remains uniform). The calculation of $\delta^2 W$ along the equilibrium path can be done numerically and will not be illustrated in the present paper.

The preceding analysis shows that the case of stability loss with localization into an ellipsoidal domain can never occur in a continuous loading process in which the displacement at infinity are controlled. Localization along the equilibrium path, without any loss of stability, always precedes such instability. So, can the solution of stability loss have, in this case, any practical application? It can—either if the tangential moduli matrix $\mathbf{D}_t$ changes suddenly during the loading process (which happens, e.g., for bilinear stress-strain diagrams), or if the uniform strain state in the strain-softening range at incipient instability is reached by some other type of process. Examples are processes in which some displacements inside the body are controlled, or processes in which a finite sudden change of $\mathbf{D}_t$ is caused by a change of temperature, change in moisture content or pore pressure, crystallographic conversion, chemical conversion, irradiation, etc., or processes in which $\mathbf{D}_t$ is changed due to hysteretic cycles.

Conclusion

A bifurcation of equilibrium path characterized by localization of initially homogeneous strain into an ellipsoidal region takes place when the matrix of incremental moduli becomes singular. This coincides with Hill's classical bifurcation condition for localization of strain into an infinite layer, which represents a condition of neutral equilibrium and stability limit. By contrast, the ellipsoidal bifurcation is of Shanley type, occurring in a stable manner while the controlled displacements at infinity increase. If the incremental material moduli vary continuously during the loading process, this bifurcation always precedes the loss of stability of equilibrium in the ellipsoidal localization mode. Such a loss of stability of an initially uniform strain field can nevertheless occur simultaneously with the first bifurcation if the matrix of incremental moduli changes suddenly.

Acknowledgment

The paper was written during the author's stay as NATO Senior Guest Scientist at Ecole Normale Supérieur (E.N.S.) de Cachan, Université Paris 6, France. Partial financial support for the background analysis of ellipsoidal localizations was obtained under AFOSR contract No. F49620-87-C-0030DEF with Northwestern University, and final revisions were made under support from NSF S&T Center for Advanced Cement-Based Materials at Northwestern University (NSF grant DMR-8808432).

References

Bažant, Z. P., 1971, "A Correlation Study of Incremental Deformations and Stability of Continuous Bodies," ASME Journal of Applied Mechanics, Vol. 38, pp. 919–928.

Bažant, Z. P., 1988a, "Stable Path of Structures with Plasticity or Damage," *J. of Eng. Mech.* ASCE 114 (Dec.); based on Report No. 87-10/498s, Department of Civil Engineering, Northwestern University, Evanston, IL, Oct. 1987.

Bažant, Z. P., 1988b, "Stable States and Stable Paths of Propagation of Damage Zones," Preprints, France-U.S. CNRS-NSF Workshop on "Localization of Damage and Size Effect Due to Distributed Cracking," held at E.N.S. de Cachan, *Université Paris 6, J. Mazars and Z. P. Bažant, eds.*, publ. by Elsevier, New York.

Bažant, Z. P., 1988c, "Softening Instability: Part I—Localization Into a Planar Band," ASME Journal of Applied Mechanics, Vol. 55, pp. 517–522.

Bažant, Z. P., 1988d, "Softening Instability: II. Localization Into Ellipsoidal Regions," ASME Journal of Applied Mechanics, Vol. 55, pp. 523–529.

Bažant, Z. P., and Lin, F.-B., 1989, "Stability Against Localization of Softening into Ellipsoids and Bands: Parameter Study," *Int. J. of Solids and Structures*, Vol. 25, No. 12, pp. 1483–1498; based on Report No. 87-7/498s, Department of Civil Engineering, Northwestern University, Evanston, IL, July 1987

Biot, M. A., 1965, *Mechanics of Incremental Deformations*, John Wiley and Sons, New York.

de Borst, R., 1987, "Stability and Uniqueness in Numerical Modelling of Concrete Structures," *IABSE Colloquium on Computational Mechanics of Concrete Structures—Advances and Applications*, Delft, Aug. 1987, pp. 161—176.

Eshelby, J. D., 1957, "The Determination of the Elastic Field of an Ellipsoidal Inclusion and Related Problems," *Proc. Roy. Soc., London*, Vol. A241, p. 376.

Downloaded 03 May 2010 to 171.66.16.244. Redistribution subject to ASME license or copyright; see http://www.asme.org/terms/Terms_Use.cfm

Hill, R., 1961, "Bifurcation and Uniqueness in Non-Linear Mechanics of Continua," *Problems of Continuum Mechanics*, Philadelphia, PA, Soc. of Industr. and Appl. Math., pp. 155–164.

Hill, R., 1962, "Uniqueness Criteria and Extremum Principles in Self-Adjoint Problems of Continuum Mechanics," *J. of the Mech. Phys. of Solids*, Vol. 10, pp. 184–194.

Kinoshita, N., and Mura, T., 1971, "Elastic Fields of Inclusions in Anisotropic Media," *Phys. Stat. Solidi.*, Vol. 5(a), pp. 757–768.

Leroy, Y.,. and Ortiz, M., 1988, "Finite Element Analysis of Strain-Localization in Frictional Materials," Report, Brown University, Providence, R.I.

Lin, S. C., and Mura, T., 1973, "Elastic Fields of Inclusions in Anisotropic Media (II)," *Phys. Stat. Solidi*, Vol. 15(a), pp. 281–282.

Rice, J. R., 1976, "The Localization of Plastic Deformation," *Proc. 14th Intern. Congress of Theor. and Appl. Mech.*, Delft, The Netherlands, Vol. 1, pp. 207–220.

Rudnicki, J. W., and Rice, J. R., 1975, "Conditions for the Localization of Deformation in Pressure-Sensitive Dilatant Materials," *J. Mech. Phys. Solids*, Vol. 23, pp. 371–394.

Rudnicki, J. W., 1977, "The Inception of Faulting in a Rock Mass with a Weakened Zone," *J. of Geophysical Research*, Vol. 82, No. 5, pp. 844–854.

Downloaded 03 May 2010 to 171.66.16.244. Redistribution subject to ASME license or copyright; see http://www.asme.org/terms/Terms_Use.cfm

Micromechanics of an Extrusion in High-Cycle Fatigue With Creep

T. H. Lin
Department of Civil Engineering,
University of California,
Los Angeles, CA 90024-1593
Fellow ASME

S. R. Lin
The Aerospace Corporation,
Structural Technology Department,
El Segundo, CA 90295-2641

X. Q. Wu
Department of Civil Engineering,
University of California,
Los Angeles, CA 90024-1593

Extrusions and intrusions often are sites of fatigue cracks. The extent of extrusions is important in fatigue crack initiation. Metals often are subject to fatigue loadings at elevated temperatures. At temperatures below one half of the melting temperature slip is the main mechanism of inelastic deformation. In this study, an aluminum polycrystal loaded in this temperature range is considered. A most favorably oriented crystal located at a free surface of a f.c.c. polycrystal subject to creep under cyclic tension and compression of high-cycle fatigue is considered. An extrusion in this crystal is shown to be produced by a positive slip in one thin slice "P" and a negative slip in a closely located slice "Q". An initial tensile strain $\epsilon^{I}_{\alpha\alpha}$ in the thin slice "R" sandwiched between P and Q causes a positive initial shear stress $\tau^{I}_{\alpha\beta}$ in P and a negative one in Q. It is shown that the extrusion growth causes a tensile strain in R, which can activate a second slip system giving a creep strain with a tensor component $\epsilon_{\alpha\alpha}$. It has the same effect as the initial strain $\epsilon^{I}_{\alpha\alpha}$ in causing this difference in shear stresses in P and Q and gives much additional extrusion growth. The extent of intrusion and extrusion is important in this study of crack initiation.

Introduction

A single crystal test at room temperature (Taylor, 1938) has shown that, under stress, slip occurs along certain directions on certain planes. Slip, the result of displacement of dislocations, has been found to depend on the resolved shear stress and not on the normal stress on the sliding plane. This dependency of slip on the resolved shear stress, known as Schmid's law, has been shown by Parker (1961) to hold also under cyclic loadings. Deformation of single crystals at elevated temperatures (Johnson et al., 1953, 1955) also occurs by slip in primarily the same slip systems that are operative at room temperature. This slip was found to depend on the resolved shear stress. This agrees with Gilman's (1969) observation that this dislocation velocity varies with the resolved shear stress.

Following the clue provided by the observation of extrusions and intrusions in fatigue specimens (Forsyth, 1954), a number of distinguished investigators (Mott, 1958; Cottrell and Hull, 1957; Thompson, 1959; McEviley and Machlin, 1959; Wood, 1956) and others have proposed different theories of fatigue crack initiation. The above early fatigue crack initiation theories primarily consider the paths of dislocation movement without considering the resolved shear stress induced by this movement. This seems to be the main cause for these theories to be not quite satisfactory, as pointed out by Kennedy (1961).

Contributed by the Applied Mechanics Division of THE AMERICAN SOCIETY OF MECHANICAL ENGINEERS for presentation at the Winter Annual Meeting, Dallas, Texas, Nov. 25-30, 1990.

Discussion on this paper should be addressed to the Technical Editor, Leon M. Keer, The Technological Institute, Northwestern University, Evanston, IL 60208, and will be accepted until two months after final publication of the paper itself in the JOURNAL OF APPLIED MECHANICS. Manuscript received by the ASME Applied Mechanics Division, Mar. 8, 1989; final revision, Jan. 18, 1990.

Paper No. 90-WA/APM-43.

Lin and Ito (1969) proposed the first quantitative micromechanic theory of fatigue crack initiation. This theory calculates the stress fields produced by slip in fatigue bands and has been shown to agree with nearly all experimental observations (Lin, 1977, 1981). This theory is briefly reviewed here and is applied to the present analysis.

Initial defects always exist in metals and cause an initial stress field. Let the initial resolved shear stress be denoted by τ^I. During loading, when the resolved shear stress in some region reaches the critical shear stress τ^c, slip occurs. After unloading, this slip remains and induces a residual resolved shear stress τ^R. The resolved shear stress due to loading is denoted by τ^A. The total shear stress after reloading is

$$\tau = \tau^I + \tau^R + \tau^A. \tag{1}$$

Consider a most favorably oriented crystal at a free surface of a f.c.c. polycrystal as shown in Fig. 1. For an extrusion to start in a thin slice R sandwiched between two slices P and Q, positive shear must occur in P and negative in Q. The initial shear stress field τ^I, favorable for this sequence of slip, clearly is one having positive shear stress in P and negative in Q. Such an initial stress field can be provided by an initial tensile strain $\epsilon^I_{\alpha\alpha}$ in R. The repetition of Greek subscripts does not denote summation. This positive $\epsilon^I_{\alpha\alpha}$ can be provided by a row of interstitial dislocation dipoles and a negative $\epsilon^I_{\alpha\alpha}$ by vacancy dislocation dipoles as shown by Lin and Ito (1969b).

A tensile loading τ_{22} on the polycrystal (Fig. 1) produces a positive τ^A in the whole crystal. Taking τ^I to be positive in P and negative in Q, we have $\tau^I + \tau^A$ in P reaching the critical shear stress τ^c first; and hence, P slides. Due to the continuity of stress field, slip in P relieves not only the positive shear stress in P but also in Q (Lin and Ito, 1969a; Lin, 1977). Hence,

Copyright © 1990 by ASME
Downloaded 03 May 2010 to 171.66.16.244. Redistribution subject to ASME license or copyright; see http://www.asme.org/terms/Terms_Use.cfm

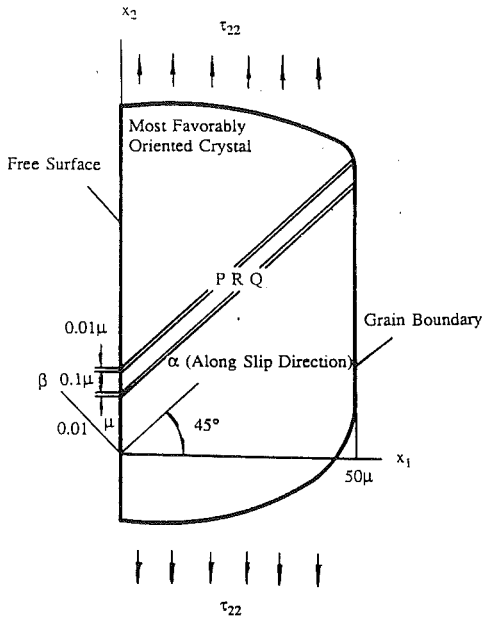


Fig. 1 Most favorably oriented crystal at free surface

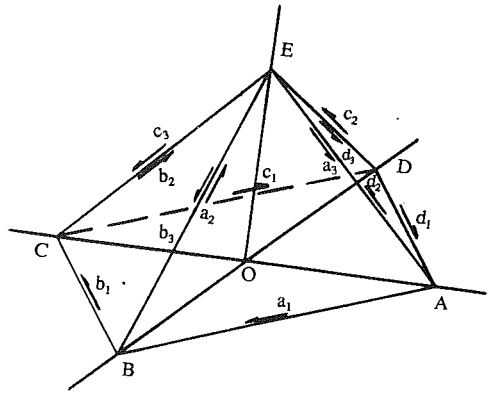


Fig. 2 Crystallographic directions of a f.c.c. crystal

this slip increases the negative resolved shear stress in Q to cause Q to slide more readily in the reverse loading. The negative slip in Q relieves the negative shear stress not only in Q, but also in P, thus causing P more readily to slide in the next forward loading. This process is repeated for every cycle thus providing a natural gating mechanism for a monotonic buildup of local slip strain $\epsilon^c_{\alpha\beta}$ in P and Q, pushing R out of the free surface and starts an extrusion. Interchanging the signs of the initial stresses in P and Q initiates an intrusion instead of an extrusion. This theory is extensively supported by metallurgical observations (Lin, 1977).

Extent of Extrusion

The buildup of this local slip strain $\epsilon^c_{\alpha\beta}$ in P and Q is caused by the positive and negative initial shear stresses $\tau^I_{\alpha\beta}$ which, in turn, is caused by $\epsilon^I_{\alpha\alpha}$ in R. If R were cut out, this free length of R would be longer than the slot cut by an amount referred to as the "static extrusion" (Mughrabi et al., 1983). This $\epsilon^I_{\alpha\alpha}$ causes an initial compression $\tau^I_{\alpha\alpha}$ in R. As the extrusion grows under cyclic loading, the slice R increases in length. This elongation causes the compression to decrease. A question has been raised as to whether the extrusion growth will cease after the extrusion has reached the static extrusion. Lin et al. (1989) have shown that the residual tensile stress $\tau^R_{\alpha\alpha}$ caused by elongation in R due to extrusion can cause changes of resolved shear stresses in all 12 slip systems. The resolved shear stress in one slip system may reach the critical and slide. The creep strain $\epsilon^c_{\xi\eta}$ caused by slip in this system has a tensor component $\epsilon^c_{\alpha\alpha}$ just like $\epsilon^I_{\alpha\alpha}$ in causing the positive and negative $\tau^I_{\alpha\beta}$, respectively, in P and Q. This secondary slip has been shown by Lin et al. (1989) to increase greatly the extent of extrusion and intrusion in time-independent slip. The present paper shows that this secondary slip also increases this extent of intrusion and extrusion in fatigue with creep.

Residual Stress Field Caused by Creep Strain

The creep rate depends on the resolved shear stress τ which is given in equation (1) as the sum of the initial, applied, and residual shear stresses. To calculate τ, the analogy of creep strain and applied force is applied (Lin, 1968). It has been shown that the equivalent body force per unit volume along the x_i-axis due to creep strain ϵ^c_{ij} is

$$F_i = -(\lambda\delta_{ij}\epsilon^c_{kk,j} + 2G\epsilon^c_{ij,j}), \tag{2}$$

where λ and G are Lame's constants and δ_{ij} is the Kronecker delta. The repetition of a Latin subscript denotes summation and the subscript after a comma denotes differentiation, with respect to the coordinate variable. The equivalent surface force per unit area along the x_i-axis also has been shown as

$$S_i = (\lambda\epsilon^c_{kk}\delta_{ij} + 2G\epsilon^c_{ij})\nu_j, \tag{3}$$

where ν_j is the cosine of the angle between the exterior normal to the surface and the x_j-axis.

From a given ϵ^c_{ij}, we obtain F_i and S_i from equations (2) and (3). Then we apply this F_i and S_i to the body and obtain the strain distribution ϵ_{ij} in this body by *elastic* solution. The residual stress field in this body is then

$$\tau^R_{ij} = \lambda\delta_{ij}\epsilon_{kk} + 2G\epsilon_{ij} - \lambda\delta_{ij}\epsilon^c_{kk} - 2G\epsilon^c_{ij}. \tag{4}$$

This analogy becomes Duhamel's analogy for thermal stress (Lin, 1968), if the creep strain ϵ^c_{ij} is replaced by thermal strain ϵ^T_{ij}.

The lengths of the slices P, Q, and R along the x_3-direction are much larger than the thickness; the thickness also is much smaller than their inclined lengths as shown in Fig. 1. Hence, strains in the major central portion of the slices are taken to be of generalized plane strain, i.e.,

$$u_i = u_i(x_1, x_2) \quad i = 1,2,3. \tag{5}$$

This gives

$$\tau_{ij} = 2G\left[\frac{\nu}{1-2\nu}\delta_{ij}\theta + \frac{1}{2}(u_{i,j} + u_{j,i})\right], \tag{6}$$

where $\theta = u_{1,1} + u_{2,2}$ and ν is Poisson's ratio. Substitution of the expression into the conditions of equilibrium yields

$$\nabla^2 u_i + \frac{1}{1-2\nu}\frac{\partial\theta}{\partial x_i} + \frac{F_i}{G} = 0, \quad i = 1,2 \tag{7}$$

and

$$\nabla^2 u_3 + \frac{F_3}{G} = 0 \tag{8}$$

where

$$\nabla^2 = \frac{\partial^2}{\partial x_1^2} + \frac{\partial^2}{\partial x_2^2}.$$

F_i and F_3 can be either the applied forces or the equivalent forces.

Equations (7) and (8) are not coupled and can be solved separately. Lin and Lin (1974) and Lin et al. (1989) have shown the solution of this stress field caused by F_i by using Airy's stress functions. The solution of the displacement fields and then the stress fields caused by F_3 has also been shown by Lin et al. (1989). Consequently, the stress fields caused by the equivalent forces due to creep strain can readily be calculated.

Downloaded 03 May 2010 to 171.66.16.244. Redistribution subject to ASME license or copyright; see http://www.asme.org/terms/Terms_Use.cfm

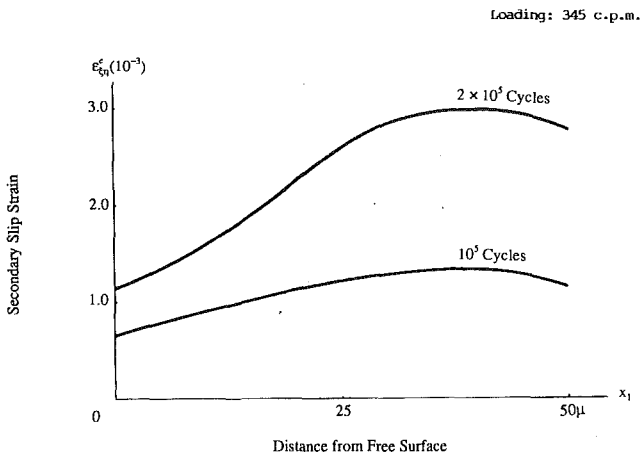


Fig. 3 Creep strain distribution of secondary slip

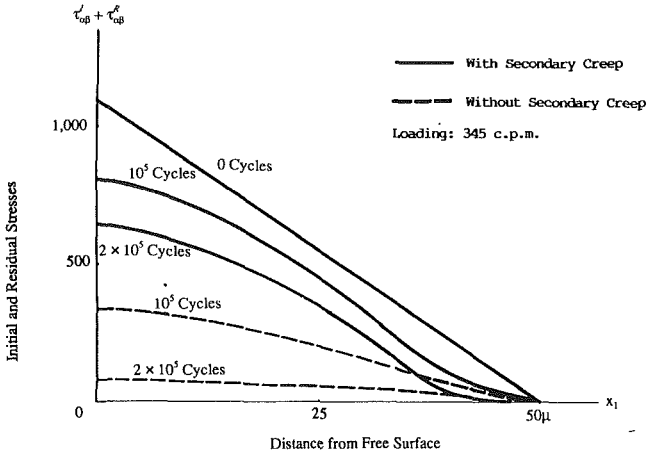


Fig. 4 Initial and residual stress distribution in P and Q (P and Q opposite sign)

The creep strain can be regarded as an eigenstrain in Mura's noteworthy book of *Micromechanics of Defects in Solids* (Mura, 1982). Methods shown in his book will give the same numerical results.

The 12 slip systems of a f.c.c. crystal are shown in Fig. 2. The most favorable slip system in the most favorably oriented crystal making 45 deg with the direction of loading is identified with a_2 (Fig. 2). During fatigue loading, this buildup of large, local creep shear strain $\epsilon_{\alpha\beta}$ in P and Q causes R to elongate, inducing an appreciable direct stress $\tau_{\alpha\alpha}$. It has been shown by Lin et al. (1989) that there are four slip systems c_1, c_3, d_1, and d_2 equally favorable under $\tau_{\alpha\alpha}$. Among the four, c_3 is the most favorable under this applied load τ_{22}. Hence, c_3 is considered to be active in R.

The normal to the slip plane β and the slip direction α of the slip system a_2 lie in the x_1x_2-plane. The equivalent forces F_i caused by slip $\epsilon^c_{\alpha\beta}$ in the a_2-slip system are in this plane. Hence, plane-strain solution satisfying the differential equation (7) was used (Lin and Lin, 1974). However, the slip direction ξ and the normal to the slip plane η of the c_3 slip system are not in the x_1x_2-plane. The equivalent forces caused by slip $\epsilon^c_{\xi\eta}$ in the c_3 slip system does not lie in the x_1x_2-plane. Hence the equivalent force has a component F_3. Then the stress fields caused by the components $F_i (i = 1, 2)$ lying in the plane are solved by equation (7) and those caused by the component F_3 are solved by equation (8) (Lin et al., 1989). This shows how this residual stress caused by creep in the primary slip system $\epsilon^c_{\alpha\beta}$ and those in the secondary slip system $\epsilon^c_{\xi\eta}$ are analytically calculated.

Numerical Calculations

The dimensions of the most favorably oriented crystal at the free surface of a polycrystal of pure aluminum are shown in Fig. 1. The thickness in P and Q is 0.01μ (micron), and the thickness in R is 0.1μ along the x_2-direction. As shown in Fig. 4, the initial shear stress in P, Q is taken to vary linearly from 0 at the interior boundary to 1.1×10^4 Pa (1.6 psi) at the free surface. This is expressed as

$$\tau^I_{\alpha\beta}(s) = 1.1\times 10^4\left(1 - \frac{s}{50\sqrt{2}\mu}\right)\text{Pa}$$

where s is the distance from the free surface along the α-direction. From equilibrium conditions,

$$\frac{0.1\mu}{\sqrt{2}}\tau^I_{\alpha\alpha}(s) = -2\int_0^S \tau^I_{\alpha\beta}(s)ds = -2.2\times 10^4\left(s - \frac{s^2}{100\times\sqrt{2}\mu}\right)\text{Pa}$$

$$\epsilon^I_{\alpha\alpha}(s) = \frac{-(1-\nu^2)}{E}\tau_{\alpha\alpha} = 0.412\times 10^{-5}\left(s - \frac{s^2}{100\times\sqrt{2}\mu^{-1}}\right)\mu^{-1}.$$

The static extrusion is then

$$\int_0^{50\sqrt{2}\mu} \epsilon^I_{\alpha\alpha}(s)ds = 0.687\times 10^{-2}\mu.$$

The creep strain $\epsilon^c_{\alpha\beta}$ at this free surface corresponding to the foregoing static extrusion is 0.486 μ. The single crystal creep property is taken from tests of pure aluminum at 204.4°C (400°F) performed by Johnson et al. (1953, 1955) and is represented approximately by a linear relation (Lin and Lin, 1978, 1980).

$$\dot{\epsilon}^c_{\alpha\beta} = 3.26\times 10^{-7}\text{m}^2/\text{N}[\tau_{\alpha\beta} - 1.3167 \times 10^6\text{N/m}^2(190.1\text{ psi})]/\text{min}$$

where the dot on top denotes the time derivative and $\tau_{\alpha\beta}$ is the resolved shear stress in N/m^2 in the active slip system. Creep strain is highly localized in slip bands (Brown, 1952). The creep rate in this band is much higher than the average rate of the whole crystal and is assumed to be 1000 times that of the crystal giving

$$\dot{\epsilon}^c_{\alpha\beta} = 3.26\times 10^{-4}\text{m}^2/\text{N}(\tau_{\alpha\beta} - 1.3167\times 10^6\text{N/m}^2)/\text{min}. \quad (9)$$

Referring to Fig. 1, the thin slices P, Q, and R are divided along their lengths into thin parallelogram grids. For numerical calculation, the creep strain in each grid is assumed to be constant. Hence, there is no creep strain gradient and no equivalent body force in each grid. However, each grid is subject to a set of equivalent surface forces on the boundary. The average residual resolved shear stress in the ith grid, caused by constant creep strain $\epsilon^c_{\alpha\beta}$ in the jth grid, or $\epsilon^c_{\xi\eta}$ in the kth grid, was then calculated using the generalized plane-strain semi-infinite solid solution given by equations (7) and (8) (Lin et al., 1989), and is denoted by $-C(i, \alpha\beta; j, \alpha\beta)$ or $-C(i, \alpha\beta; k, \xi\eta)$. With $\epsilon^c_{\alpha\beta}$ occurring only in P, Q and $\epsilon^c_{\xi\eta}$ in R, the residual resolved shear stress in the ith grid due to creep strain $\epsilon^c_{\alpha\beta}$ and $\epsilon^c_{\xi\eta}$ is then written as

$$\tau^R_{\alpha\beta_i} = -C(i,\alpha\beta;\ j,\alpha\beta)\epsilon^c_{\alpha\beta_j} - C(i,\alpha\beta;\ k,\xi\eta)\epsilon^c_{\xi\eta_k}$$
$$\tau^R_{\xi\eta_i} = -C(i,\xi\eta;\ j,\alpha\beta)\epsilon^c_{\alpha\beta_j} - C(i,\xi\eta;\ k,\xi\eta)\epsilon^c_{\xi\eta_k}. \quad (10)$$

The repetition of subscript "j" denotes summation covering all grids with $\epsilon^c_{\alpha\beta}$ and "k" summation covering all grids with $\epsilon^c_{\xi\eta}$. The resolved shear stress in the ith grid is written as

Downloaded 03 May 2010 to 171.66.16.244. Redistribution subject to ASME license or copyright; see http://www.asme.org/terms/Terms_Use.cfm

$$\tau_{\alpha\beta_i} = \tau^I_{\alpha\beta_i} + \tau^A_{\alpha\beta_i} + \tau^R_{\alpha\beta_i}$$
$$\tau_{\xi\eta_i} = \tau^I_{\xi\eta_i} + \tau^A_{\xi\eta_i} + \tau^R_{\xi\eta_i}. \tag{11}$$

From equations (9) through (11) we can write

$$\dot{\epsilon}^c_{\alpha\beta_i} = 3.26\times10^{-4}\text{m}^2/\text{N}(\tau_{\alpha\beta} - 1.3167\times10^6\text{N/m}^2(190.1\text{ psi})/\text{min}$$
$$= 3.26\times10^{-4}\text{m}^2/\text{N}[\tau^I_{\alpha\beta_i} + \tau^A_{\alpha\beta_i} - C(i,\alpha\beta;\ j,\alpha\beta)\epsilon^c_{\alpha\beta}$$
$$- C(i,\alpha\beta;\ k,\xi\eta)\epsilon^c_{\xi\eta_k} - 1.3167\times10^6\text{N/m}^2(190.1\text{ psi})]. \tag{12}$$

A similar equation can be written for $\dot{\epsilon}^c_{\xi\eta_i}$.

From the foregoing, the creep strain rates in grids with resolved shear stress greater than this critical 1.3167×10^6N/m^2 (190.1 psi) can be determined.

Write equation (12) in matrix form

$$\{\dot{\epsilon}\} = [A]\{\epsilon\} + \{B(t)\} \tag{13}$$

subject to the initial condition $\{\epsilon(t_o)\} = \{\epsilon_o\}$ where { } denotes column matrix and [ ] square matrix.

$$B_i = 3.26\times10^{-4}/\text{N}(\tau^I_{\alpha\beta_i} + \tau^A_{\alpha\beta_i} - 1.316\times10^6\text{N/m}^2)/\text{min} \tag{14}$$

The series solution of equation (13) is given by Frazer et al. (1963). The complementary solution of equation (13) is given as

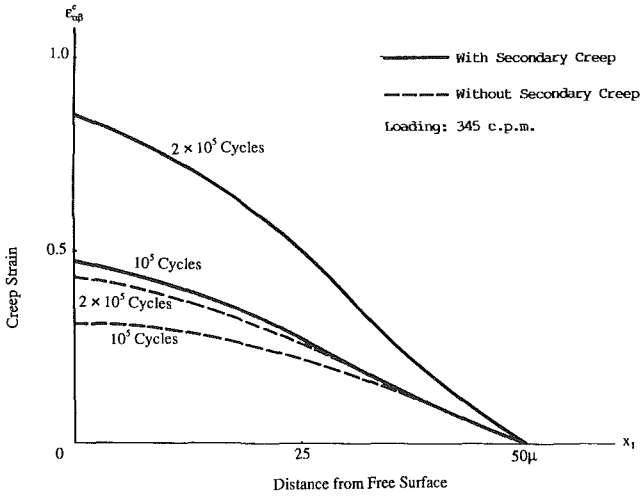


Fig. 5 Creep strain distribution

$$\{\epsilon_c\} = e^{[A](t-t_o)}\{\epsilon_o\}$$
$$= \{[I] + [A](t-t_o) + \ldots + \frac{1}{p!}[A]^p(t-t_o)^p + \ldots]\}\{\epsilon_o\} \tag{15}$$

where ϵ_o is the creep strain at t_o, e is the base of the natural logorithm, and $[I]$ is the identity matrix. The particular solution is obtained by multipying equation (13) by $e^{-[A]t}$. This gives

$$\frac{d}{dt}(e^{-[A]t}\{\epsilon_p\}) = e^{-[A]t}\{B(t)\}$$

and

$$\{\epsilon_p\} = \int_{t_o}^{t} e^{-[A](s-t)}\{B(s)\}ds.$$

The cyclic loading is taken to be rectangular: i.e., tension and compression are applied instantaneously and remain constant during each half cycle.

$$\{\epsilon_p\} = -\{[I] - e^{[A](t-t_o}\}[A]^{-1}\{B\}$$
$$\{\epsilon_p\} = \{I(t-t_o) + \frac{1}{2!}[A](t-t_o)^2 + \ldots. + \frac{1}{p!}[A]^{p-1}(t-t_o)^p$$
$$+ \ldots\}\{B\}, \tag{16}$$

to calculate the creep strain distribution in a given time interval 0 to T. This interval is divided into N steps with $\Delta t = T/N$. The Δt is chosen to be small enough, so the maximum eigenvalue of $[A]\Delta t$ is less than unity. Then the matrix $[A]^n\ (t - t_o)^n$ approaches a zero matrix as "n" approaches infinity. The series solution of equations (15) and (16) will converge.

For each time-step Δt, take the first p-terms of $\{\epsilon_c\}$ and $\{\epsilon_p\}$ to obtain the creep strains. The smaller the Δt and the more terms p used, the more accurate will be the results. In the previous work (Lin and Lin, 1979, 1982), the creep strain rate was assumed to be constant in Δt. The solution corresponds to $p = 1$. It has been found that using this series solution reduces the numerical calculation by more than six times for the same accuracy in evaluating the creep strain distributions. In the present example, the magnitude of applied load was 2.7326×10^6 N/m^2(380 psi) giving $\tau^A = 1.366 \times 10^6$ N/m^2 (190 psi). Two loading frequencies were calculated; one is 0.345 cycles/min and the other is 345 cycle/min. In the high-frequency loading, the half period was equally divided into ten time increments and three terms in the series solution were used. The creep strain in the second slip system $\epsilon^c_{\xi\eta}$ in R versus

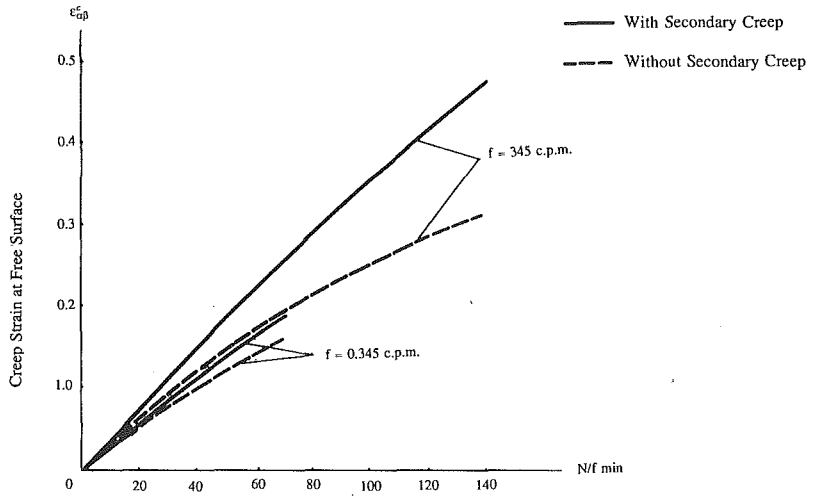


Fig. 6 Creep strain at free surface versus loading time

Downloaded 03 May 2010 to 171.66.16.244. Redistribution subject to ASME license or copyright; see http://www.asme.org/terms/Terms_Use.cfm

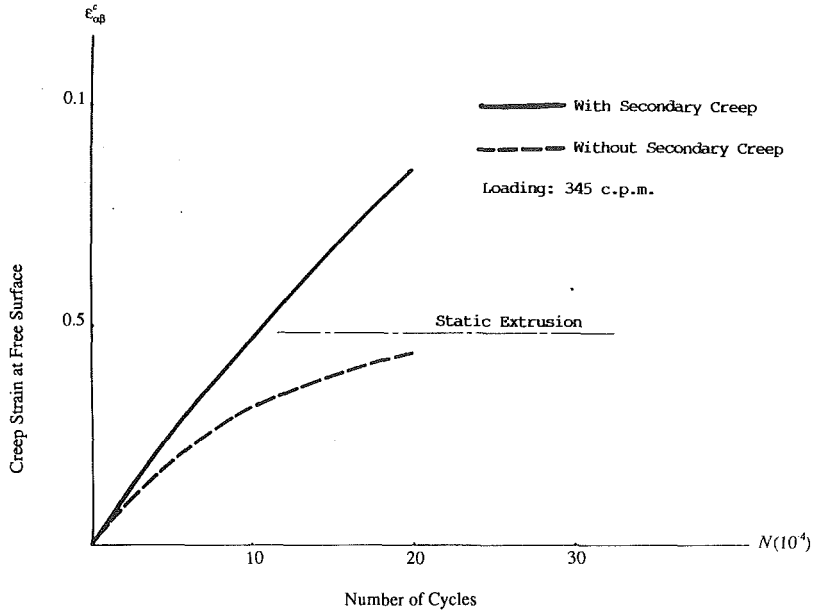


Fig. 7 Creep strain buildup at free surface versus loading time *N/f*

the distance from the free surface at different cycles of loading under a frequency of 345 cycles per minute was calculated and is shown in Fig. 3. The creep strain $\epsilon^c_{\xi\eta}$ in the second slip system causes some $\epsilon^c_{\alpha\alpha}$, which in turn cause additional positive $+\tau^R_{\alpha\beta}$ in P and negative $-\tau^R_{\alpha\beta}$ in Q. The creep rate in P and Q depends on the sum of the initial and the residual shear stresses $\tau^I_{\alpha\beta} + \tau^R_{\alpha\beta}$ in P and Q. This sum at different stages of loading is shown in Fig. 4. Note that this sum decreases considerably slower in the cases with the secondary slip $\epsilon^c_{\xi\eta}$ than the case without. When this sum approaches zero, the extrusion approaches static extrusion and ceases to grow. The creep shear strain distributions $\epsilon^c_{\alpha\beta}$ in P and Q at different cycles of loading were calculated for the cases with and without secondary slip and are shown in Fig. 5. The $\epsilon^c_{\alpha\beta}$'s at the free surface versus cycles of loading are shown in Fig. 6 this strain versus loading time N/f is shown in Fig. 7. Note that with no secondary slip, the extrusion growth ceases when the extrusion approaches the static extrusion. The creep strain $\epsilon^c_{\alpha\beta}$ in P and Q at the free surface, which represents the amount of extrusion or intrusion with the secondary slip, is much higher than that without the secondary slip. Calculations also have been made at a frequency of loading of 10 cycles/min, and the creep strain in P and Q versus N/f have been found to be essentially the same as that at 345 cycles/min. In the high-cycle range, the creep strain depends mainly on the time of loading. Similar calculations were made on a low frequency loading 0.345 cycles/min. The creep strain at this low frequency depends on the number of cycles as well as N/f the time of loading.

Conclusions

The amount of creep shear strains $\epsilon^c_{\alpha\beta}$ in P and Q at the free surface is a measure of the amount of extrusion and intrusion and, hence, is taken as a measure of fatigue crack initiation. The calculated results indicate that this surface creep strain depends only on the time of loading N/f in high-frequency range and becomes dependent also on the number of loading cycles in the low, frequency range.

Creep strain in the secondary slip system has a *tensor* component $\epsilon^c_{\alpha\alpha}$ which has the same effect in causing the different resolved shear stresses $\tau^I_{\alpha\beta}$ in P and Q as $\tau^I_{\alpha\alpha}$. Hence, this creep strain $\epsilon^c_{\alpha\beta}$ in P and Q with this secondary slip is much larger than that without. Without the secondary slip, the extrusion ceases when it reaches the static extrusion. However, with the secondary slip, extrusion grows considerably beyond the static extrusion. This may be a main cause for the extent of extrusion to be much more in a face-centered polycrystal than that in a hexagonal polycrystal. The stress intensity factor of crack depends on the extent of extrusion or intrusion. Hence, this extent is important for the study of fatigue crack initiation.

Acknowledgments

The support of the U.S. Office of Naval Research through Contract N00014-86-K-0153 and the interest of the scientific officer, Dr. Yapa Rajapakse, are gratefully acknowledged.

References

Brown, A. F., 1952, "Surface Effects in Plastic Deformation of Metals," *Advances in Physics*, pp. 427–479.

Cottrell, A. H., and Hull, D., 1957, "Extrusion and Intrusions by Cyclic Slip in Copper," *Proc. Roy. Soc., London*, Vol. A242, p. 211.

Forsyth, P. J. E., and Stubbington, C. A., 1955, "The Slip Band Extrusion Effect Observed in Some Aluminum Alloys Subjected to Cyclic Stresses," *J. Inst. Metals*, Vol. 83, p. 395.

Frazer, R. A., Duncan, W. J., and Collar, A. R., 1938, *Elementary Matrices and Some Applications to Dynamics and Differential Equations*, Cambridge University Press, p. 45.

Gilman, J. J., 1969, *Micromechanics of Flow in Solids*, McGraw-Hill, New York, pp. 176–179.

Johnson, R. D., Shober, R. R., and Schope, A. D., 1953, "The Creep of Single Crystals of Aluminum," National Advisory Committee for Aeronautics, Technical Note 2945.

Johnson, R. D., Young, A. P., and Schope, A. D., 1955, "Plastic Deformation of Aluminum Single Crystals at Elevated Temperatures," National Advisory Committee for Aeronautics, Technical Note 3351.

Kennedy, A. J., 1963, *Process of Creep and Fatigue of Metals*, John Wiley and Sons, New York, pp. 331–343.

Lin, T. H., 1968, *Theory of Inelastic Structures*, John Wiley and Sons, New York, Chapter 2.

Lin, T. H., 1977, "Micromechanics of Deformation of Slip Bands Under Monotonic and Cyclic Loadings," *Reviews of the Deformation Behavior of Materials*, P. Felham, ed., Freund Publishing House, Tel-Aviv.

Lin, T. H., 1981, "Micromechanic of Fatigue Crack Initiation: Theory and Experimental Observation," *Mechanics of Fatigue*, AMD-Vol. 47, T. Mura, ed., ASME, New York, pp. 41–109.

Lin, T. H., and Ito, Y. M., 1969a, "Mechanism of a Fatigue Crack Nucleation Mechanism," *J. Mech. Phys. Solids*, Vol. 17, pp. 511–523.

Lin, T. H., and Ito, Y. M., 1969b, "Fatigue Crack Nucleation in Metals," *Proc. U.S. Nat. Acad. of Sciences*, Vol. 62, pp. 631–638.

Lin, T. H., and Lin, S. R., 1979, "Micromechanics Theory Crack Initiation Applied to Time-Dependent Fatigue," *ASTM STP 675*, pp. 707–728.

Lin, T. H., and Lin, S. R., 1982, "Fatigue Crack Initiation with Creep,"

Downloaded 03 May 2010 to 171.66.16.244. Redistribution subject to ASME license or copyright; see http://www.asme.org/terms/Terms_Use.cfm

Defects and Fracture, G-C. Shih and H. Zorski, eds., Martinas Nijhoff, pp. 3–13.

Lin, T. H., Lin, S. R., and Wu, X. Q., 1989, "Micromechanics of an Extrusion in High-Cycle Fatigue," *Phil. Mag. A*, Vol. 59, No. 6, pp. 1263–1276.

McEviley, J., Jr., and Machlin, E. S., 1959, "Critical Experiments on the Nature of Fatigue in Crystalline Materials," *Proc. Int. Conf. on the Atomic Mechanism of Fracture*, Technology Press, M.I.T. Press, and John Wiley and Sons.

Mott, N. F., 1958, "Origin of Fatigue Cracks," *ACTA Metallurigica*, Vol. 6, p. 195.

Mughrabi, H. R., Wang, Differt, K., and Essmann, U., 1983, "Fatigue Crack Initiation by Cyclic Slip Irreversibilities in High-Cyclic Fatigue," *Fatigue Mechanics*, ASTM-STP Vol. 811, pp. 5–45.

Mura, T., 1982, *Micromechanics of Defects in Solids*, Martinus Nijhoff, Chapter 1.

Parker, E. R., 1961, *Theories of Fatigue: Mechanical Behavior of Materials in Elevated Temperatures*, J. E. Dorn, ed., McGraw-Hill, New York, pp. 129–148.

Taylor, G. I., 1938, "Plastic Deformation of Metals," *J. Inst. Metals*, Vol. 62, p. 307.

Thompson, N., Wadsworth, N. J., and Louat, N., 1955, "The Origin of Fatigue Fracture in Copper," *Phil. Mag.*, Vol. 1, p. 113.

Thompson, N., 1959, *Proc., Int. Conf. on the Atomic Mechanism of Fracture*, Technology Press, M.I.T., and John Wiley and Sons.

Wood, W. A., 1956, "Mechanism of Fatigue," *Fatigue in Aircraft Structures*, A. M. Freundental, ed., Academic Press, New York, pp. 1–19.

Downloaded 03 May 2010 to 171.66.16.244. Redistribution subject to ASME license or copyright; see http://www.asme.org/terms/Terms_Use.cfm

J. A. Blume
Division of Engineering,
Brown University,
Providence, RI 02912
Assoc. Mem. ASME

Finite, Dynamic Motions of Thin Rate-Dependent Sheets

The transient response of a thin sheet comprised of a rate-dependent solid is determined. The material is assumed to be incompressible, and the constitutive response is governed by a nonlinearly viscous power-law model. The sheet has axially symmetry, but an otherwise arbitrarily varying thickness. Axially symmetric, finite, dynamic motions of the sheet are identified.

Introduction

In this paper, the finite, transient response of an axially symmetric, thin sheet comprised of a rate-dependent, incompressible solid is determined. A Lagrangian formulation, coupled with a theory of generalized plane stress, is employed. The dependence of the motion on the initial thickness profile of the sheet is explored.

Because of its importance in connection with sheet metal forming, plane-stress motions in plastically deforming materials have been the subject of extensive research activity. The prediction of necking in such sheets is a main objective, and several studies, including those by Stören and Rice (1975), Needleman (1976), and Rice (1976), have been carried out using plane-stress approximative assumptions. Needleman and Tvergaard (1977), and Hutchinson, Neale, and Needleman (1978) did studies in both three-dimensional and plane-stress settings, and discuss the validity of the plane-stress theory. Dynamic instabilities of plastically deforming solids were considered by Taylor, Harlow, and Ainsden (1978).

In this paper, a simple material model is used to describe the dynamic response of finitely-deforming, rate-dependent sheets. In uniaxial tension, the Cauchy stress τ is proportional to the rate of strain raised to a power. Using generalized plane stress, axially symmetric motions of a sheet of arbitrary undeformed cross-section are analytically determined.

1 Notation Preliminaries on Finite Deformations of Rate-Dependent Solids

Throughout this paper, lower case and capital letters in boldface designate vectors and (second-order) tensors, respectively. The same letter in lightface appearing with one or more subscripts will signify the appropriate components of the vector or tensor in either cylindrical or Cartesian coordinates.

If $\mathcal{R}$ is the region in three-space occupied by a solid in its reference configuration, a motion is a mapping $\hat{\mathbf{y}}$ described by

$$\mathbf{y}=\hat{\mathbf{y}}(\mathbf{x},t)=\mathbf{x}+\mathbf{u}(\mathbf{x},t) \text{ on } \mathcal{R},\ (t>0), \tag{1}$$

where $\mathbf{x}$ is the position vector of a material point in $\mathcal{R}$, $\hat{\mathbf{y}}(\mathbf{x},t)$ is the position vector of its deformation image at time t, and $\mathbf{u}$ is the associated displacement field. The region occupied by the body at time t will be called $\mathcal{R}_t$, and at each t, the mapping from $\mathcal{R}$ to $\mathcal{R}_t$ is assumed to be one-to-one. The motion $\hat{\mathbf{y}}$ of $\mathcal{R}$ is taken to be twice jointly continuously differentiable with respect to position and time.

This work is concerned with motions of an *incompressible* solid, which can sustain only locally volume-preserving deformations. The mapping (equation) (1) is locally-volume preserving if and only if

$$J\equiv \det \mathbf{F}=1,\ \mathbf{F}=\nabla\hat{\mathbf{y}}. \tag{2}$$

Here, $\mathbf{F}$ is the deformation gradient tensor and J is the Jacobian.

The letter $\mathbf{D}$ denotes the rate-of-deformation tensor, so that

$$\mathbf{D}(\mathbf{y},t)=\operatorname{sym}\nabla\mathbf{v}(\mathbf{y},t) \text{ on } \mathcal{R}_t,\ t>0, \tag{3}$$

in which $\mathbf{v}$ is the Eulerian velocity field:

$$\mathbf{v}(\mathbf{y},t)=\dot{\hat{\mathbf{y}}}(\hat{\mathbf{x}}(\mathbf{y},t),t) \text{ on } \mathcal{R}_t,\ t>0. \tag{4}$$

Here the dot denotes the derivative with respect to time ($\mathbf{x}$ fixed), and $\hat{\mathbf{x}}(\mathbf{y},t)$ is the inverse of $\hat{\mathbf{y}}(\mathbf{x},t)$ at time t: $\hat{\mathbf{x}}(\hat{\mathbf{y}}(\mathbf{x},t),t)=\mathbf{x}$ for all $\mathbf{x}$ in $\mathcal{R}$. The rate of deformation tensor is thus expressible as

$$\mathbf{D}(\hat{\mathbf{y}}(\mathbf{x},t),t)=\frac{1}{2}\{\dot{\mathbf{F}}(\mathbf{x},t)\mathbf{F}^{-1}(\mathbf{x},t)+\mathbf{F}^{-T}(\mathbf{x},t)\dot{\mathbf{F}}^{T}(\mathbf{x},t)\}. \tag{5}$$[1]

This, together with the constraint of local volume-preservation (2) can be found to imply that

$$\operatorname{trace}\mathbf{D}=0 \text{ on } \mathcal{R}_t,\ t>0. \tag{6}$$

If $\boldsymbol{\sigma}$ is the Piola stress tensor accompanying the motion (1), the equations of motion, in absence of body forces, demand that

$$\operatorname{div}\boldsymbol{\sigma}=\rho\ddot{\mathbf{y}},\ \boldsymbol{\sigma}\mathbf{F}^{T}=\mathbf{F}\boldsymbol{\sigma}^{T} \text{ on } \mathcal{R}, \tag{7}$$

with ρ designating the reference mass density. The mass density for the solid at hand is assumed to be constant. The

Contributed by the Applied Mechanics Division of THE AMERICAN SOCIETY OF MECHANICAL ENGINEERS for publication in the JOURNAL OF APPLIED MECHANICS.

Discussion on this paper should be addressed to the Technical Editor, Leon M. Keer, the Technological Institute, Northwestern University, Evanston, IL 60208, and will be accepted until two months after final publication of the paper itself in the JOURNAL OF APPLIED MECHANICS. Manuscript received and accepted by the ASME Applied Mechanics Division, June 12, 1989.

[1] If $\mathbf{F}^{T}$ stands for the transpose of $\mathbf{F}$, while $\mathbf{F}^{-1}$ is its inverse and $\mathbf{F}^{-T}$ denotes the transposed inverse of $\mathbf{F}$.

Copyright © 1990 by ASME
Downloaded 03 May 2010 to 171.66.16.244. Redistribution subject to ASME license or copyright; see http://www.asme.org/terms/Terms_Use.cfm

Eulerian version of equation (7) may be written in terms of the Cauchy stress field τ, which is linked to the Piola stress tensor through

$$\tau(\mathbf{y},t)=\sigma(\mathbf{x},t)\mathbf{F}^T(\mathbf{x},t),\ \mathbf{y}=\hat{\mathbf{y}}(\mathbf{x},t). \tag{8}$$

The equations of motion are alternately cast as

$$\operatorname{div}\tau(\mathbf{y},t)=\rho\left\{\frac{\partial}{\partial t}\mathbf{v}(\mathbf{y},t)+[\nabla\mathbf{v}(\mathbf{y},t)]\mathbf{v}(\mathbf{y},t)\right\},$$

$$\tau(\mathbf{y},t)=\tau^T(\mathbf{y},t)\ \text{for all}\ \mathbf{y}\in\mathcal{R}_t, \tag{9}$$

with $\mathbf{v}$ again signifying the Eulerian velocity field. In arriving at the above, the local volume preservation of the motion and the conservation of mass postulate have been used in writing ρ for the current mass density.

The stress response of the materials at hand is assumed to be well described by a purely rate-dependent, power-law type constitutive model. In particular, if ν and γ are material constants with $\nu>0$ and $\gamma>-1$, then

$$\tau=-p\mathbf{1}+\nu d^{\gamma}\mathbf{D}\ \text{on}\ \mathcal{R}_t, \tag{10}$$

where p is the pressure field which accommodates the constraint of incompressibility, $\mathbf{1}$ is the identity tensor, and

$$d=|\mathbf{D}|=\sqrt{D_{ij}D_{ij}}\ \text{on}\ \mathcal{R}_t. \tag{11}$$

Note that the second of equation (9) is satisfied automatically. Although the parameter γ is dimensionless, the constant ν has the peculiar units of time raised to the power $(\gamma-1)$, multiplied by mass/length. Typically, for describing the behavior of metals at very high strain rates, γ is close to -1.

On account of equations (8) and (5), the Piola stress for such materials may be written as

$$\sigma=-p\mathbf{F}^{-T}+\frac{1}{2}\nu d^{\gamma}\{\dot{\mathbf{F}}\mathbf{C}^{-1}-(\mathbf{F}^{-T})^{\cdot}\}\ \text{on}\ \mathcal{R},\ \mathbf{C}=\mathbf{F}^T\mathbf{F}. \tag{12}$$

It is convenient to express the equations of motion in dimensionless form. To this end, if l and v are, respectively, a characteristic length and velocity of a given boundary value problem, one defines dimensionless independent variables $\bar{\mathbf{x}}$ and $\bar{t}$ through

$$\bar{\mathbf{x}}=\mathbf{x}/l,\ \bar{t}=\frac{tv}{l}, \tag{13}$$

and dimensionless dependent variables $\bar{\mathbf{y}}$, $\bar{\sigma}$, and $\bar{p}$, by

$$\bar{\mathbf{y}}(\bar{\mathbf{x}},\bar{t})=\frac{1}{l}\mathbf{y}(\bar{\mathbf{x}}l,\bar{t}l/v),\ \bar{\sigma}(\bar{\mathbf{x}},\bar{t})=\frac{1}{v^2\rho}\sigma(\bar{\mathbf{x}}l,\bar{t}l/v),$$

$$\bar{p}(\bar{\mathbf{x}},\bar{t})=\frac{1}{v^2\rho}p(\bar{\mathbf{x}}l,\bar{t}l/v). \tag{14}$$

The constitutive law (12) may thus be written in dimensionless form as

$$\bar{\sigma}=-\bar{p}\bar{\mathbf{F}}^{-T}+\frac{1}{2}\bar{\nu}\bar{d}^{\gamma}\{\dot{\bar{\mathbf{F}}}\bar{\mathbf{C}}^{-1}-(\bar{\mathbf{F}}^{-T})^{\cdot}\}\ \text{on}\ \mathcal{R},\ \bar{\mathbf{C}}=\bar{\mathbf{F}}^T\bar{\mathbf{F}}. \tag{15}$$

Here, the dot denotes differentiation with respect to $\bar{t}$,

$$\bar{\mathbf{F}}=\nabla_{\bar{\mathbf{x}}}\bar{\mathbf{y}},\ \bar{d}=\frac{1}{2}|\dot{\bar{\mathbf{F}}}(\mathbf{x},t)\bar{\mathbf{F}}^{-1}(\mathbf{x},t)+\bar{\mathbf{F}}^{-T}(\mathbf{x},t)\dot{\bar{\mathbf{F}}}^T(\mathbf{x},t)|, \tag{16}$$

and $\bar{\nu}$ is a dimensionless viscosity-like material parameter, given by

$$\bar{\nu}=\frac{\nu v^{\gamma-1}}{\rho l^{\gamma+1}}. \tag{17}$$

When $\gamma=0$, so that the constitutive law at hand describes a Newtonian fluid, $1/\bar{\nu}$ is the standard Reynolds number. The equations of motion (7), become

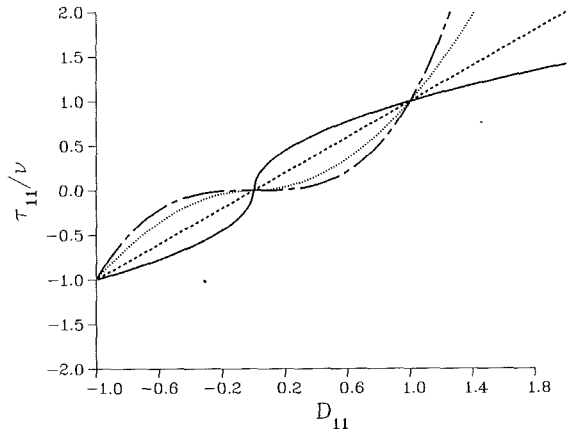


Fig. 1 Response of the power-law viscous solids in uniaxial stress; $\gamma=-.9$: solid line, $\gamma=0$: dashed line, $\gamma=1$: dotted line, $\gamma=2$: broken dashed line

$$\operatorname{div}_{\bar{\mathbf{x}}}\bar{\sigma}=\ddot{\bar{\mathbf{y}}},\ \bar{\sigma}\bar{\mathbf{F}}^T=\bar{\mathbf{F}}\bar{\sigma}^T\ \text{on}\ \mathcal{R}. \tag{18}$$

In addition, if $\bar{\tau}$ is a dimensionless Cauchy stress tensor, then one has from equation (8)

$$\bar{\tau}(\bar{\mathbf{y}},\bar{t})\equiv\frac{1}{v^2\rho}\tau(\bar{\mathbf{y}}l,\bar{t}l/v)=\sigma(\bar{\mathbf{x}},\bar{t})\bar{\mathbf{F}}^T(\bar{\mathbf{x}},\bar{t}). \tag{19}$$

In the analyses that follow, the nondimensional variables introduced previously will be used, and to avoid cumbersome notation, ν, $\mathbf{x}$, t, $\hat{\mathbf{y}}$, σ, p, and τ will be written in place of $\bar{\nu}$, $\bar{\mathbf{x}}$, $\bar{t}$, $\bar{\mathbf{y}}$, $\bar{\sigma}$, $\bar{p}$, and $\bar{\tau}$, with the understanding that the former now refer to the associated *dimensionless* quantities.

In order to understand the behavior of the material model, consider a state of *uniaxial stress*. In this case, only one stress component, say τ_{11}, is nonzero; all others vanish identically. One motion and pressure field which corresponds to such a state is

$$\hat{y}_1(\mathbf{x},t)=\lambda(t)x_1,\ \hat{y}_2(\mathbf{x},t)=\lambda^{-1/2}(t)x_2,\ \hat{y}_3(\mathbf{x},t)=\lambda^{-1/2}(t)x_3,$$

$$p(\mathbf{x},t)=-\frac{1}{2}\nu\left(\frac{3}{2}\right)^{\gamma/2}\left|\frac{\dot{\lambda}}{\lambda}\right|^{\gamma}\frac{\dot{\lambda}}{\lambda}. \tag{20}$$

Here, $\lambda>0$ for $t>0$, and λ is a twice continuously differentiable function of time. The associated spatial velocity field has the components

$$v_1(\mathbf{y},t)=\frac{\dot{\lambda}(t)}{\lambda(t)}y_1,\ v_2(\mathbf{y},t)=-\frac{1}{2}\frac{\dot{\lambda}(t)}{\lambda(t)}y_2,$$

$$v_3(\mathbf{y},t)=-\frac{1}{2}\frac{\dot{\lambda}(t)}{\lambda(t)}y_3, \tag{21}$$

and only the on-diagonal components of the rate-of-deformation tensor $\mathbf{D}$ are nonzero:

$$D_{11}=\frac{\dot{\lambda}(t)}{\lambda(t)},\ D_{22}=D_{33}=-\frac{1}{2}D_{11}. \tag{22}$$

One has

$$\tau_{11}=\bar{\nu}\frac{\dot{\lambda}}{\lambda}\left|\frac{\dot{\lambda}}{\lambda}\right|^{\gamma}\equiv\bar{\nu}D_{11}|D_{11}|^{\gamma},\ \bar{\nu}=\nu\left(\frac{3}{2}\right)^{\gamma/2+1}. \tag{23}$$

Plots of D_{11} versus τ_{11} are given in Fig. 1.

2 Problem Formulation

If (r,θ,z) are cylindrical coordinates of the point with position $\mathbf{x}$ in Euclidean three-space, the solid initially occupies the disk-shaped region $\mathcal{R}$, described by

$$\mathcal{R}=\{\mathbf{x}\,|-h(r)<z<h(r),\ 0\le r\le 1,\ 0\le\theta<2\pi\}. \tag{24}$$

Here, $h(r)$ is a continuously differentiable, positive-valued

Downloaded 03 May 2010 to 171.66.16.244. Redistribution subject to ASME license or copyright; see http://www.asme.org/terms/Terms_Use.cfm

function of the in-plane radius r. Note that the normalizing dimension of the problem is taken as the disk radius. We assume that

$$h(r) \ll 1, \quad \left|\frac{dh}{dr}\right| \ll 1, \; 0 \le r \le 1, \tag{25}$$

so that the disk is thin and the function $h(r)$ is *slowly varying*.

The faces of the plate, $z = \pm h(r)$, are traction-free while the edge, $r = 1$, is subjected to a time-dependent radial pressure with magnitude $f(t)$. If $\mathbf{n}$ is the outer unit normal vector to the boundary of $\mathcal{R}$, the nominal stress therefore obeys

$$\boldsymbol{\sigma}\mathbf{n} = \mathbf{0} \text{ on } z = \pm h(r), \; \boldsymbol{\sigma}\mathbf{n} = f\mathbf{n} \text{ on } r = 1. \tag{26}$$

The cylindrical components of $\mathbf{n}$ on the faces of the disk are

$$n_r = \frac{h'(r)}{\sqrt{1+[h'(r)]^2}}, \; n_\theta = 0,$$
$$n_z = \pm \frac{1}{\sqrt{1+[h'(r)]^2}}, \; h'(r) \equiv \frac{dh}{dr}(r), \tag{27}$$

where the plus or minus sign holds according as $\mathbf{n}$ is the outer unit normal vector to the upper or lower face of $\mathcal{R}$. Using equations (27) and (26), one finds that the nominal stress components conform to

$$\begin{aligned} &\pm\sigma_{rr}(r,z,t)h'(r) - \sigma_{rz}(r,z,t) = 0, \\ &\pm\sigma_{\theta r}(r,z,t)h'(r) - \sigma_{\theta z}(r,z,t) = 0, \\ &\pm\sigma_{zr}(r,z,t)h'(r) - \sigma_{zz}(r,z,t) = 0, \text{ on } z = \pm h(r), \; (0 \le r \le 1). \end{aligned} \tag{28}$$

Since $\mathbf{n}$ has components $n_r = 1$, $n_\theta = n_z = 0$ on the disk edge, the second of equation (26) demands that

$$\begin{aligned} &\sigma_{rr}(1,z,t) = f(t), \; \sigma_{\theta r}(1,z,t) = \sigma_{zr}(1,z,t) = 0 \\ &\qquad -h(1) \le z \le h(1), \; t > 0. \end{aligned} \tag{29}$$

Initially, the disk is undeformed, so that any motion $\hat{\mathbf{y}}$ of $\mathcal{R}$ must obey

$$\begin{aligned} &\hat{\mathbf{y}}(\mathbf{x},t) = \mathbf{x} \text{ for all } \mathbf{x} \in \mathcal{R}, \text{ or} \\ &\hat{R}(r,z,t) = r, \; \hat{Z}(r,z,t) = z \text{ at } t = 0, -h(r) \le z \le h(r), \; 0 \le r \le 1. \end{aligned} \tag{30}$$

Here, $\hat{R} = \hat{R}(r,z,t)$ is the radial component of $\hat{\mathbf{y}}$, while $\hat{Z} = \hat{Z}(r,z,t)$ is the component of $\hat{\mathbf{y}}$ in the z-direction. Although $\hat{R} = 0$ when $r = 0$ and $\hat{Z} = 0$ when $z = 0$, $\hat{R}$ and $\hat{Z}$ are otherwise nonvanishing and suitably smooth.

The symmetries inherent in the problem give

$$\begin{aligned} &\hat{R}(r,z,t) = \hat{R}(r,-z,t), \; \hat{Z}(r,z,t) = -\hat{Z}(r,-z,t), \\ &\qquad -h(r) < z < h(r), \; r > 0, \end{aligned} \tag{31}$$

as well as

$$\begin{aligned} &\sigma_{rr}(r,z,t) = \sigma_{rr}(r,-z,t), \\ &\sigma_{\theta\theta}(r,z,t) = \sigma_{\theta\theta}(r,-z,t), \; \sigma_{zz}(r,z,t) = \sigma_{zz}(r,-z,t), \\ &\sigma_{rz}(r,z,t) = -\sigma_{rz}(r,-z,t), \; \sigma_{zr}(r,z,t) = -\sigma_{zr}(r,-z,t); \end{aligned} \tag{32}$$

all other stress components vanish. The second of (28) is thus automatically satisfied, as are the the last of (29).

At this point, it is useful to recall that for axially symmetric motions, the component versions of the balance of linear momentum equations in the first of (18) reduce to

$$\begin{aligned} &\frac{\partial}{\partial r}\sigma_{rr} + \frac{1}{r}(\sigma_{rr} - \sigma_{\theta\theta}) + \frac{\partial}{\partial z}\sigma_{rz} = \frac{\partial^2 \hat{R}}{\partial t^2}, \\ &\frac{\partial}{\partial r}\sigma_{zr} + \frac{\partial}{\partial z}\sigma_{zz} + \frac{1}{r}\sigma_{zr} = \frac{\partial^2 \hat{Z}}{\partial t^2}. \end{aligned} \tag{33}$$

Using plane-stress approximative assumptions, motions of the plate that are axially symmetric as well as symmetric about the plane $z = 0$ will be calculated. Let Π stand for the midplane ($z = 0$) of $\mathcal{R}$, and if g is a function defined on $\mathcal{R}$, $\mathring{g}$ will be used to denote its restriction to Π. The aim of the following is to characterize the deformation parameter $\mathring{R}$, along with the stress components $\mathring{\sigma}_{rr}$ amd $\mathring{\sigma}_{\theta\theta}$ by assuming that the thickness averages of the in-plane stress components are well approximated by their midplane values, and that the midplane value of the out-of-plane stress component, σ_{zz} is approximately zero. Thus, it is assumed that

$$\begin{aligned} &\mathring{\sigma}_{zz} \approx 0, \; \frac{1}{2h(r)}\int_{-h(r)}^{h(r)} \sigma_{rr}(r,z,t)\,dz \approx \mathring{\sigma}_{rr}(r,t), \\ &\frac{1}{2h(r)}\int_{-h(r)}^{h(r)} \sigma_{\theta\theta}(r,z,t)\,dz \approx \mathring{\sigma}_{\theta\theta}(r,t) \text{ on } \Pi. \end{aligned} \tag{34}$$

The motivation for these assumptions comes from (25), the third of (28), and the second of (33).

Integrating the first of the equations of motion equation (33) through the thickness of $\mathcal{R}$ leads to

$$\int_{-h(r)}^{h(r)} \left\{\frac{\partial}{\partial r}\sigma_{rr} + \frac{1}{r}(\sigma_{rr} - \sigma_{\theta\theta}) - \frac{\partial^2 \hat{R}}{\partial t^2}\right\} dz + \sigma_{rz}\Big|_{z=-h(r)}^{z=h(r)} = 0. \tag{35}$$

The first of (28) and the assumptions of (34) enable

$$\frac{\partial}{\partial r}\mathring{\sigma}_{rr} + + \frac{1}{r}(\mathring{\sigma}_{rr} - \mathring{\sigma}_{\theta\theta}) + \frac{h'}{h}\mathring{\sigma}_{rr} = \frac{\partial^2 \mathring{R}}{\partial t^2} \text{ on } \Pi. \tag{36}$$

With a view towards expressing the stresses $\mathring{\sigma}_{rr}$ and $\mathring{\sigma}_{\theta\theta}$ in terms of the deformation parameter $\mathring{R}$, note that equation (31) implies that the nonzero cylindrical components of the midplane deformation gradient tensor $\mathring{\mathbf{F}}$ are

$$\mathring{F}_{rr} = \mathring{R}_{,r}, \; \mathring{F}_{\theta\theta} = \mathring{R}/r, \; \mathring{F}_{zz} = \mathring{\lambda} \equiv \partial\hat{Z}(r,0,t)/\partial z \text{ on } \Pi. \tag{37}$$

Here, $\mathring{\lambda}$ is the midplane value of the out-of-plane stretch, $\partial\mathring{R}/\partial r \equiv \mathring{R}_{,r}$, and $\partial\mathring{R}/\partial t \equiv \mathring{R}_{,t}$. Incompressibility demands that $\det \mathring{\mathbf{F}} = 1$ on Π, whence

$$\mathring{\lambda} = \frac{r}{\mathring{R}_{,r}\mathring{R}} \text{ on } \Pi. \tag{38}$$

Therefore, $\mathring{\lambda}$ is fully determined by the function $\mathring{R}(r,t)$.

The stress components are now found on Π from (15) as

$$\begin{aligned} &\mathring{\sigma}_{rr} = \left\{-\mathring{p} + \nu d^\gamma \frac{\mathring{R}_{,rt}}{\mathring{R}_{,r}}\right\}\frac{1}{\mathring{R}_{,r}}, \; \mathring{\sigma}_{\theta\theta} = \left\{-\mathring{p} + \nu d^\gamma \frac{\mathring{R}_{,t}}{\mathring{R}}\right\}\frac{r}{\mathring{R}}, \\ &\mathring{\sigma}_{33} = \left\{-\mathring{p} - \nu d^\gamma\left[\frac{\mathring{R}_{,t}}{\mathring{R}} + \frac{\mathring{R}_{,rt}}{\mathring{R}_{,r}}\right]\right\}\frac{\mathring{R}\mathring{R}_{,r}}{r}, \end{aligned} \tag{39}$$

and

$$d = \sqrt{2\left[\left(\frac{\mathring{R}_{,rt}}{\mathring{R}_{,r}}\right)^2 + \left(\frac{\mathring{R}_{,t}}{\mathring{R}}\right)^2 + \frac{\mathring{R}_{,rt}\mathring{R}_{,t}}{\mathring{R}_{,r}\mathring{R}}\right]} \text{ on } \Pi. \tag{40}$$

The last of (39), in conjunction with the plane-stress assumption appearing in the first of (34) enables one to express the midplane pressure field $\mathring{p}$ as

$$\mathring{p} = -\nu d^\gamma\left[\frac{\mathring{R}_{,t}}{\mathring{R}} + \frac{\mathring{R}_{,rt}}{\mathring{R}_{,r}}\right] \text{ on } \Pi, \tag{41}$$

whence,

$$\begin{aligned} &\mathring{\sigma}_{rr} = \nu d^\gamma\left[\frac{\mathring{R}_{,t}}{\mathring{R}} + 2\frac{\mathring{R}_{,rt}}{\mathring{R}_{,r}}\right]\frac{1}{\mathring{R}_{,r}}, \\ &\mathring{\sigma}_{\theta\theta} = \nu d^\gamma\left[2\frac{\mathring{R}_{,t}}{\mathring{R}} + \frac{\mathring{R}_{,rt}}{\mathring{R}_{,r}}\right]\frac{r}{\mathring{R}}. \end{aligned} \tag{42}$$

Downloaded 03 May 2010 to 171.66.16.244. Redistribution subject to ASME license or copyright; see http://www.asme.org/terms/Terms_Use.cfm

On entering (40) and (42) into (36), one is led to a nonlinear, partial differential equation of motion for $\mathring{R}$ with variable coefficients. This equation involves two derivatives of $\mathring{R}$ with respect to r, and two derivatives with respect to time.

In order find solutions to the partial differential equation for $\mathring{R}$, set

$$\mathring{R}(r,t) = A(t)q(r),\ 0 \le r \le 1,\ t > 0, \tag{43}$$

with A and q twice differentiable. Other than the vanishing of q at $r=0$, neither q nor A may have any zeros. It is assumed, without loss of generality, that $A>0$ for $t \ge 0$ and $q>0$ for $0<r\le 1$. The functions A and q will be determined by the equation of motion mentioned previously. Unless one finds that this equation demands $q(r)=r$ for $(0\le r\le 1)$ and $A(t)=1$ at $t=0$, the above separated form for $\mathring{R}$ will be in conflict with the initial condition (30), which demands that the disk be initially undeformed. It will emerge from what follows that for certain choices of the initial disk profile $h(r)$, these initial conditions can be satisfied exactly. For other choices of h, the solutions obtained via the variable separation cannot conform the initial condition, and these results may be interpreted as descriptive of the large-time behavior of the disk.

Combining (43) with (40), one finds

$$d = \sqrt{6}\left|\frac{\dot{A}}{A}\right| \quad \dot{A} \equiv \frac{dA}{dt}. \tag{44}$$

and (42) leads to

$$\mathring{\sigma}_{rr} = \frac{m(t)}{q'(r)},\ \mathring{\sigma}_{\theta\theta} = r\frac{m(t)}{q(r)} \text{ on } \Pi,$$

$$q' \equiv \frac{dq}{dr},\ m = \frac{3\nu 6^{\gamma/2}}{A}\left|\frac{\dot{A}}{A}\right|^{\gamma}\left(\frac{\dot{A}}{A}\right). \tag{45}$$

The above, in conjunction with the first of (29), implies that

$$m(t) = q'(1)f(t),\ t>0. \tag{46}$$

Because A will be determined from the equation of motion, the edge load f required to sustain motions of the form (43) will also be a consequence of the analysis. Owing to the positivity of A and ν, the edge load is tensile or compressive according as the radial velocity $\dot{A}$ is positive or negative.

Substitution from (43) and (45) into the equilibrium equation (36) and rearranging leads to the following pair of ordinary differential equations for q and A:

$$-r[qq'' + (q')^2] + qq' + r\frac{h'}{h}qq' - \alpha r q^2 (q')^2 = 0,\ 0 \le r \le 1, \tag{47}$$

and

$$\ddot{A}A = \beta\left|\frac{\dot{A}}{A}\right|^{\gamma}\left(\frac{\dot{A}}{A}\right),\ \beta = \alpha 3\nu 6^{\gamma/2}. \tag{48}$$

In the above, α is a constant separation parameter. Note that (48) can be written as

$$\frac{d}{dt}\left\{\frac{1}{2}\dot{A}^2\right\} = \beta\left|\frac{\dot{A}}{A}\right|^{\gamma+2}, \tag{49}$$

and since ν is positive by assumption, the radial speed $|\dot{A}|$ of the disk is monotone increasing, decreasing, or is constant, according as the separation parameter α is positive, negative, or zero.

If one sets

$$s(r) = q(r)q'(r),\ 0 \le r \le 1, \tag{50}$$

in the spatial equation (47), then the latter reduces to the first-order Ricatti equation,

$$s' - \left(\frac{1}{r} + \frac{h'}{h}\right)s + \alpha s^2 = 0. \tag{51}$$

The case in which $\alpha = 0$ corresponds to the quasi-static case, since (48) demands that $\ddot{A} = 0$ for all time, and

$$A(t) = c_1 t + c_2 \text{ for all } t>0,\ c_1,\ c_2 \text{ constant}. \tag{52}$$

The solution to (51) when $\alpha = 0$ is given by

$$s(r) = crh(r). \tag{53}$$

Here, c is a constant. Bearing in mind that $\mathring{R}(0,t)=0$, one finds on integrating equation (50) that

$$q(r) = \sqrt{2c\int_0^r lh(l)dl}. \tag{54}$$

The constant c can be taken as unity without loss of generality. Consequently, one has from (43)

$$\mathring{R}(r,t) = [c_1 t + c_2]\sqrt{2\int_0^r lh(l)dl}. \tag{55}$$

This solution can satisfy the initial condition $\mathring{R}(r,0) = r$ exactly only if the undeformed disk profile is independent of r: $h(r) = h_o = \text{constant}$. If this is not the case, the solution given above might correspond to the large-time behavior of the sheet.

According to (55) and (38), the out-of-plane stretch $\mathring{\lambda}$ is given by

$$\mathring{\lambda}(r,t) = \frac{1}{A^2(t)h(r)}. \tag{56}$$

The boundary $z = h(r)$ is thus approximately mapped to the plane $y_3 = Z = \mathring{\lambda}(r,t)h(r) = A^{-2}(t)$, regardless of the initial thickness profile h. The sheet is transformed into one which is approximately flat.

As far as the stresses are concerned in this quasi-static case, the nominal and Cauchy stresses are found from equations (55), (42), and (8):

$$\mathring{\sigma}_{rr} = m(t)\ \frac{rh(r)}{\sqrt{2\int_0^r lh(l)dl}},\ \mathring{\sigma}_{\theta\theta} = \frac{m(t)r}{\sqrt{2\int_0^r lh(l)dl}},$$

$$\tau_{rr} = \tau_{\theta\theta} = m(t)A(t), \tag{57}$$

with m given by (52) and the last of (45). Note that the Cauchy stresses are constant.

Turning next to the dynamic case, assume that $\alpha \ne 0$. Equation (51) is solved by setting

$$s(r) = \frac{w'(r)}{\alpha w(r)},\ 0 \le r \le 1, \tag{58}$$

with w a nonvanishing, suitably smooth function of r. This substitution reduces equation (51) to

$$w''(r) - \left(\frac{1}{r} + \frac{h'(r)}{h(r)}\right)w'(r) = 0, \tag{59}$$

and one has

$$w(r) = c\int_0^r lh(l)dl + d,\quad c,\ d \text{ constant}, \tag{60}$$

so that (58) and (50) and the fact that $q(0)=0$ demand

$$q(r) = \sqrt{\frac{2}{\alpha}\ \log\left\{c\int_0^r lh(l)dl + 1\right\}},\ 0 \le r \le 1. \tag{61}$$

In order for equation (61) to be meaningful, $c \ne 0$ and the sign of c must correspond to the sign of α, with

$$c > -\frac{1}{\int_0^1 lh(l)dl}. \tag{62}$$

The initial condition $\mathring{R}(r,0) = A(0)q(r) = r$ for all r between 0 and 1 can be satisfied identically in this case only if

Downloaded 03 May 2010 to 171.66.16.244. Redistribution subject to ASME license or copyright; see http://www.asme.org/terms/Terms_Use.cfm

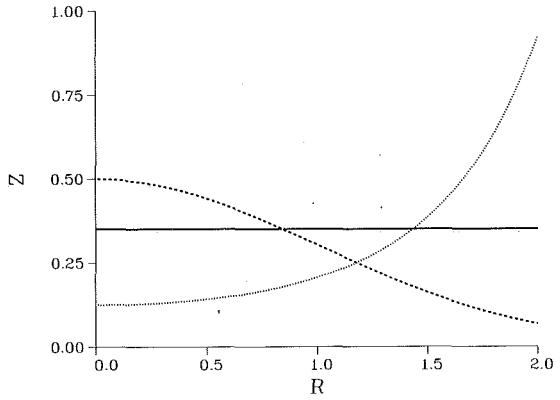


Fig. 2 Disk shapes described by $h(r)=k_1\exp\{k_2r^2\}$; $k_2=0$: solid line, $k_2>0$: dotted line, $k_2<0$, dashed line

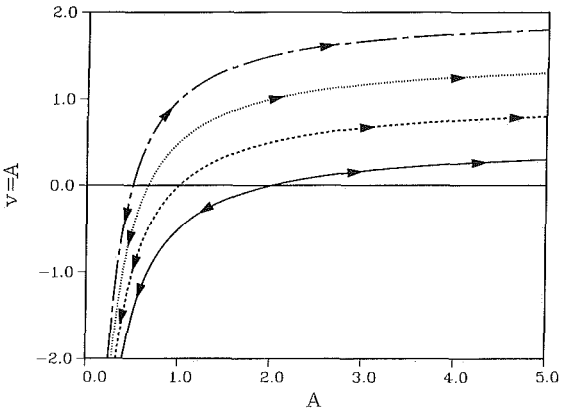


Fig. 3 Phase-plane trajectories for $\gamma=0$ and $\beta=1$

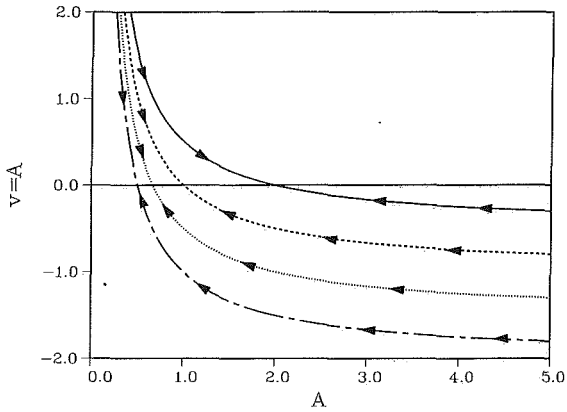


Fig. 4 Phase-plane trajectories for $\gamma=0$ and $\beta=-1$

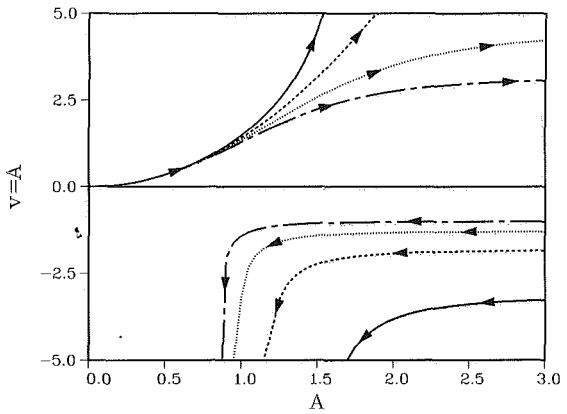


Fig. 5 Phase-plane trajectories for $\gamma=2$ and $\beta=1$

$$h(r)=k_1e^{k_2r^2},\ (0\le r\le 1), \tag{63}$$

in which k_1 and k_2 are constants; $k_1>0$. According as k_2 is positive, negative, or zero, h given above describes one of the shapes shown in Fig. 2. For the disk profile in (63), in order that $\mathring{R}(r,0)=r$, one may choose $A(t)=1$ at $t=0$, and $\alpha=k_2$. If the initial disk thickness profile is *not* given by the above formula, the following results might be interpretable as descriptive of the long-time behavior of the disk.

Solution of the temporal equation (48) in the dynamic case ($\alpha\neq 0$) will be put off until later. For now, note that the out-of-plane stretch $\mathring{\lambda}$ is found from (61), (43), and (38) to conform to

$$\mathring{\lambda}(r,t)=\frac{\alpha}{A^2(t)h(r)}\left[\int_0^r lh(l)dl+\frac{1}{c}\right]. \tag{64}$$

The image of the faces of the sheet, $z=\pm h(r)$, are approximately carried onto the boundary described by

$$Z=\hat{Z}(r,\pm h(r),t)\approx$$
$$\mathring{\lambda}(r,t)h(r)=\pm\frac{\alpha}{A^2(t)}\left[\int_0^r lh(l)dl+\frac{1}{c}\right]. \tag{65}$$

Owing to the fact that $R=\mathring{R}(r,t)=A(t)q(r)$, one has from (61) and (65) the following expression for the thickness Z of the deformed disk as a function of radial distance R at time t:

$$Z=\pm\frac{\alpha}{2cA^2}e^{1/2\alpha R^2/A^2},\ (0\le R\le A(t)q(1)). \tag{66}$$

As in the quasi-static case, the plane-stress approximations predict that the profile of the deformed disk is independent of the initial disk thickness $h(r)$. As was mentioned earlier, A is either monotonically increasing, monotonically decreasing, or is constant. In the case of increasing A, the disk edges will be extended and the disk will be thinned and flattened. If A is decreasing, the disk is thickened as its radius is reduced.

The in-plane stress components are determined with the aid of (45), (61), and (8) as

$$\mathring{\sigma}_{rr}=m(t)\frac{rh(r)}{\alpha q(r)[\int_0^r lh(l)dl+1/c]},\ \mathring{\sigma}_{\theta\theta}=\frac{m(t)r}{q(r)},$$
$$\tau_{rr}=\tau_{\theta\theta}=m(t)A(t); \tag{67}$$

the Cauchy stresses are again constant.

The autonomous, second-order equation (48) for A admits an implicit solution that is well interpreted with the aid of the phase plane. Bearing in mind that $\gamma>-1$ by assumption, note that equation (48) can be written as

$$\frac{d}{dt}\left\{\dot{A}\,|\dot{A}|^{-\gamma}+\beta\frac{1-\gamma}{1+\gamma}A^{-(1+\gamma)}\right\}=0\ (\gamma\neq 1),$$
$$\frac{d}{dt}\left\{\log|\dot{A}|+\frac{1}{2}\beta A^{-2}\right\}=0\ (\gamma=1). \tag{68}$$

Thus, if

$$v(t)=\dot{A}(t), \tag{69}$$

the phase-plane trajectories of a solution A to (48) are described by the curves

$$v|v|^{\gamma}+\beta\frac{1-\gamma}{1+\gamma}A^{-(1+\gamma)}=d\ (\gamma\neq 1),$$
$$\log|v|+\frac{1}{2}\beta A^{-2}=d\ (\gamma=1) \tag{70}$$

in the (A,v)-plane, with d constant.

Downloaded 03 May 2010 to 171.66.16.244. Redistribution subject to ASME license or copyright; see http://www.asme.org/terms/Terms_Use.cfm

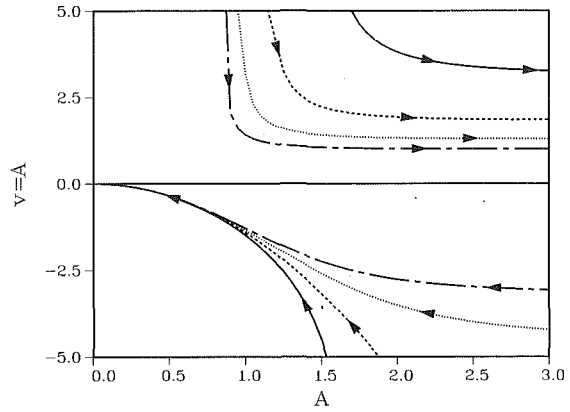


Fig. 6 Phase-plane trajectories for $\gamma = 2$ and $\beta = -1$

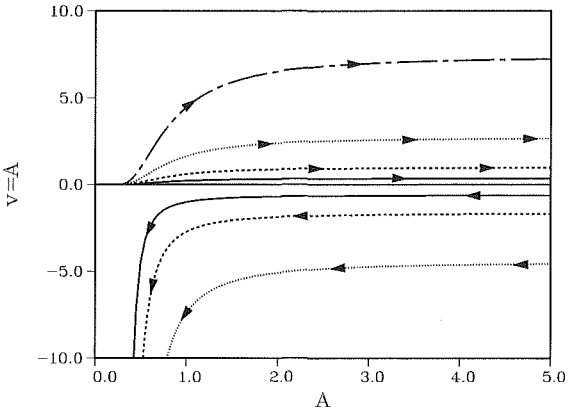


Fig. 7 Phase-plane trajectories for $\gamma = 1$ and $\beta = 1$

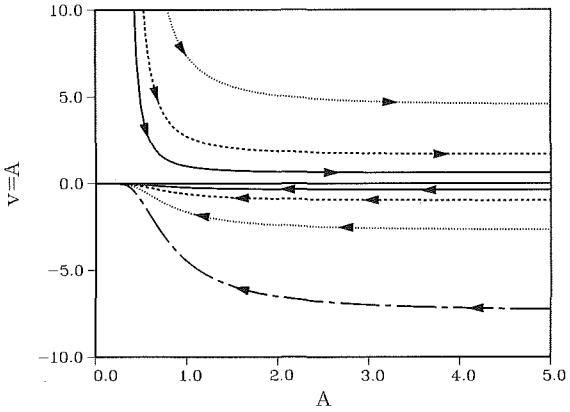


Fig. 8 Phase-plane trajectories for $\gamma = 1$ and $\beta = -1$

The critical points in the phase plane are those that correspond to solutions of (48) that obey $\ddot{A} = \dot{A} = 0$; $A =$ constant. Evidently, such solutions exist and the constant value of $A > 0$ is arbitrary. Thus, critical points of the phase plane lie along the entire positive A-axis for any value of $\gamma > -1$. Because of (45) and (46), the upper half of the phase plane ($v > 0$) corresponds to a tensile edge load, while the lower half plane ($v < 0$) corresponds to a compressive edge load.

Phase plane trajectories are shown in Figs. 3–8. There are three separate cases to consider. The first of these is the case in which $(-1 < \gamma < 1)$. Here, the phase plane trajectories intersect the critical line $v = 0$. Solutions to equation (48) follow the trajectories away from this line if β is positive. For $v = \dot{A} > 0$ (corresponding to a tensile edge load), v tends toward a constant positive value for large time, while A grows without bound. In contrast, if $v < 0$, so that the edge load is compressive, $v \to -\infty$ and A remains bounded as $t \to \infty$.

For $(-1 < \gamma < 1)$ and $\beta < 0$, solutions to (48) move along their phase plane trajectories toward the line $v = 0$, although one can show that $v = 0$ cannot occur in finite time. Thus, as $t \to \infty$ in this case, both A and v approach finite values.

Next, consider the case in which $\gamma > 1$. We suppose first that β is positive. If $v > 0$, then one of either v or A grows without bound, while the other approaches a constant limit. In the lower half plane, however, all trajectories lead to constant values of A while v tends toward negative infinity.

If $\gamma > 1$ and $\beta < 0$, solutions that move on trajectories in the upper half plane have $v \to \infty$ and A approaching a finite limit as $t \to \infty$. In the lower half plane, all solutions approach $v = A = 0$.

When $\gamma = 1$ and $\beta > 0$, solutions that follow trajectories in the upper half plane have velocities that tend toward a constant value as $t \to \infty$, while $A \to \infty$. In the lower half plane, $v \to -\infty$ and A approaches a constant value as $t \to \infty$.

Finally, the behavior of $A(t)$ in the case in which $\gamma = 1$ and $\beta < 0$ is shown in Fig. 8. For large times, velocities tend toward a constant value as A grows without bound (in the upper half of the phase plane) or approach a finite bound (for $v < 0$).

One can show using a continuity argument on (48) that if $\dot{A} \equiv v = 0$ at some instant of time, then $v = 0$ for all time. According to (45) and (46), this corresponds to traction-free edges on the disk. Further, if $v \neq 0$ at some time, then the velocity will never vanish in finite time.

If $\gamma \neq 1$, the first of (70) can be integrated to give the implicit, integral expression for $A(t)$:

$$\pm \int_{A_o}^{A} \left\{ \frac{1}{d \mp \beta \dfrac{1-\gamma}{1+\gamma} a^{-(1+\gamma)}} \right\}^{\frac{1}{1-\gamma}} da = t. \tag{71}$$

Here, A_o is a constant which corresponds to the value of A at time $t = 0$. If the edge load is tensile, so that the radial velocity is positive, then the upper signs in (71) hold; the lower signs correspond to compressive edge loads. If the edges are traction-free, then the velocity is *zero* and (71) must be replaced by $A = A_o$ for all time.

Next, let $\gamma = 1$, so that the phase plane trajectory equations are those appearing in the second of (70). This equation can be integrated to give

$$e^{-d} \int_{A_o}^{A} e^{1/2\beta a^{-2}} da = \pm t. \tag{72}$$

As before, the sign in (72) is chosen according to the direction of the edge load: the upper sign corresponds to tensile edge load, and the lower holds if the loading is compressive. In the tensile case, A becomes unbounded as t grows large. When the loading is compressive, A goes to zero as t tends toward infinity if $\beta > 0$.

The behavior of the edge load $f(t)$ that is required to sustain these motions is found from equations (45) and (46), and the phase plane diagrams. It is seen that $|f(t)| \to 0$ as $t \to \infty$ in all cases, with the exception of those situations in which A approaches a constant limit and $|v|$ tends toward infinity as t gets large. In these cases, one finds that $|f(t)|$ grows without bound.

3 Discussion

The plane-stress assumptions introduced in these analyses are most likely to be valid in the cases in which A grows with

Downloaded 03 May 2010 to 171.66.16.244. Redistribution subject to ASME license or copyright; see http://www.asme.org/terms/Terms_Use.cfm

time, so that the edge load is tensile. Compressive edge loads lead to a thickening of the disk, and in this situation, the plane-stress approximations are subject to some question. In the compressive case, one might expect buckling of the disk to occur; this cannot be predicted using the symmetry assumptions of (31). These, in addition to the separated form of $\dot{R}$ that is assumed, also preclude the occurrence of necking in the sheet.

In the tensile edge load case, one might use the solutions obtained here to obtain a time-to-failure of the disk. If one assumes that the disk ruptures when its minimum thickness attains a preassigned critical vale H_*, then the (dimensionless) time t_* to reach H_* is found from equation (71) to be given by

$$\int_{A_o}^{H_*} \left\{ \frac{1}{d-\beta \dfrac{1-\gamma}{1+\gamma} a^{-(1+\gamma)}} \right\}^{\frac{1}{1-\gamma}} da = t_*. \tag{73}$$

Acknowledgment

The support of the Army Research Office is gratefully acknowledged.

References

Hutchinson, J. W., Neale, K. W., and Needleman, A., 1978, "Sheet Necking—I. Validity of the Plane Stress Assumptions of the Long-wavelength Approximation," *Mechanics of Sheet Metal Forming*, D. P. Koistinen and N.-M. Wang, eds., Plenum, New York, pp. 111–126.

Needleman, A., and Tvergaard, V., 1977, "Necking of Biaxially Stretched Elastic-Plastic Circular Plates," *Journal of the Mechanics and Physics of Solids*, Vol. 25, pp. 159–183.

Needleman, A., "Necking of Pressurized Spherical Membranes," *Journal of the Mechanics and Physics of Solids*, Vol. 24, pp. 339–359.

Rice, J. R., 1976, "The Localization of Plastic Deformation," *Proceedings of the 14th International Congress of Theoretical and Applied Mechanics*, W. T. Koiter, ed., Vol. 1, pp. 207–220.

Stören, S., and Rice, J. R., 1975, "Localized Necking in Thin Sheets," *Journal of the Mechanics and Physics of Solids*, Vol. 23, pp. 421–441.

Taylor, J. W., Harlow, F. H., and Ainsden, A. A., 1978, "Dynamic Plastic Instabilities in Stretching Plates and Shells," ASME JOURNAL OF APPLIED MECHANICS, Vol. 45, pp. 105–113.

Downloaded 03 May 2010 to 171.66.16.244. Redistribution subject to ASME license or copyright; see http://www.asme.org/terms/Terms_Use.cfm

Analysis and Application of a Coupled Thermoviscoplasticity Theory

H. Ghoneim
Associate Professor,
Department of Mechanical Engineering,
Rochester Institute of Technology,
Rochester, NY 14623
Mem. ASME

Coupled thermoviscoplasticity equations are developed based on the rational theory of thermodynamics. A power-form internal state variable constitutive equation is proposed. Limitation of the proposed constitutive equation is discussed and simulation results of cyclic loading of 1070 steel at different temperatures and strain rates are presented. The developed coupled equations and the proposed constitutive equation are implemented into a finite element program which is used to investigate the thermomechanical problem of cyclic loading of a constrained-ended cylinder.

Introduction

Modeling of the thermomechanical behavior of metallic parts at elevated temperature and high strain rates requires the combined application of the theories of thermodynamics, continuum mechanics, and viscoplasticity—the theory of coupled thermoviscoplasticity. Hetnarski et al. (1986) acknowledged this fact and suggested that implementation of the coupled thermoviscoplasticity theory to solve thermomechanical problems required: (1) the application of the rational theory of thermodynamics, (2) a viscoplastic constitutive equation which takes into account the temperature and rate effects, and (3) a numerical tool, such as the finite element method, in order to utilize the developed equations to solve realistic boundary value problems. Cernocky and Krempl (1980) presented a coupled thermoviscoplasticity theory based on the overstress constitutive equation and applied it to investigate special types of loadings: pure torsion, uniaxial loading, and cyclic loading. Rubin (1982) developed coupled thermoviscoplasticity equations using a thermoelastic-viscoplastic constitutive equation based on a modification of the inviscid theory of plasticity. Only analytical solutions of simple problems were presented. Lehmann and Bix (1985) defined a coupled thermoviscoplasticity theory and applied it to investigate the necking process in a uniaxial testing problem. The constitutive law and boundary conditions he adopted were very simplified. Allen (1986) developed coupled thermoviscoplasticity equations based on the rational theory of thermodynamics. He adopted the constitutive equation of Bodner and Partom (1975) and his applications were limited to the one-dimensional tensile loading of a uniaxial bar. In a similar analysis, Ghoneim (1986) presented coupled thermoviscoplasticity equations and applied them to solve the problem of dynamic loading of a thick-walled cylinder as well as compression of a constrained-ended cylinder (Ghoneim and Matsuoka, 1987). However, the viscoplastic constitutive equation he adopted was limited to perfectly-viscoplastic (no hardening) materials.

In this paper, a brief analysis of the development of coupled thermoviscoplasticity equations is presented, a viscoplastic constitutive equation based on the internal state variable theory is proposed, and the coupled equations are implemented into a finite element program and applied to solve the thermomechanical problem of cyclic loading of a constrained-ended cylinder. The analysis throughout the paper is restricted to infinitesimal deformations. Extension of the analysis to large deformations will be the subject of future work.

The Coupled Thermomechanical Equations

The coupled thermomechanical equations of a continuous media is defined, in general, by the balance of momenta equations and the conservation of energy:

$$\sigma_{ij,i}+\rho f_j=\rho a_j,\ \sigma_{ij}=\sigma_{ji} \tag{1}$$

$$\rho \dot{e}=\sigma_{ij}\dot{\epsilon}_{ij}-q_{i,i}+\rho r \tag{2}$$

where ϵ_{ij}. . .the strain tensor,
f_j. . .the body force vector,
a_j. . .the acceleration vector,
e. . .the specific internal energy,
q_j. . .the heat flux vector per unit area of the boundary surface,
r. . .the specific heat supply rate, and
ρ. . .the mass density.

These thermocoupled equations are restricted, for any thermodynamic process, by any form of the second law of thermodynamics, e.g., Clausius-Duhem inequality:

$$\rho \dot{s}-\rho r/T+(q_i/T)_{,i}\geq 0 \tag{3}$$

where s is the specific entropy and T is the absolute temperature.

Contributed by the Applied Mechanics Division of THE AMERICAN SOCIETY OF MECHANICAL ENGINEERS for presentation at the Winter Annual Meeting, Dallas, Texas, Nov. 25-30, 1990.

Discussion on this paper should be addressed to the Technical Editor, Leon M. Keer, The Technological Institute, Northwestern University, Evanston, IL 60208, and will be accepted until two months after final publication of the paper itself in the JOURNAL OF APPLIED MECHANICS. Manuscript received by the ASME Applied Mechanics Division, May 2, 1989; final revision, Dec. 1, 1989.

Paper No. 90-WA/APM-35.

Copyright © 1990 by ASME
Downloaded 03 May 2010 to 171.66.16.244. Redistribution subject to ASME license or copyright; see http://www.asme.org/terms/Terms_Use.cfm

In order to completely define a thermomechanical problem constitutive assumptions, which describe the material response and abide by certain physical and mathematical restrictions (axioms of constitutive theory), are required (Eringen, 1967). Considering that the thermomechanical state at a material point is completely defined by the current values of the independent variables σ_{ij}, T, $T_{,i}$, and $\alpha_{ij}^{(k)}$, where $\alpha_{ij}^{(k)}$ is a set of internal state variables, we can postulate the following general constitutive relations:

$$\epsilon_{ij}^{e} = \hat{\epsilon}_{ij}^{e}(\sigma_{ij}, T, T_{,i}, \alpha_{ij}^{(k)})$$
$$\psi = \hat{\psi}(\sigma_{ij}, T, T_{,i}, \alpha_{ij}^{(k)})$$
$$s = \hat{s}(\sigma_{ij}, T, T_{,i}, \alpha_{ij}^{(k)})$$
$$q_i = \hat{q}_i(\sigma_{ij}, T, T_{,i}, \alpha_{ij}^{(k)})$$

where ψ is Gibb's function ($\psi = e - sT - 1/\rho\ \sigma_{ij}\epsilon_{ij}^{e}$), ϵ_{ij}^{e} is the elastic strain tensor, and $\alpha_{ij}^{(k)}$ is defined by an evolution equation of the form:

$$\dot{\alpha}_{ij}^{(k)} = \hat{\alpha}_{ij}^{(k)}(\sigma_{ij}, T, T_{,i}, \alpha_{ij}^{(k)}). \tag{4}$$

It is understood that the internal state variables can be second-rank tensors, vectors, and/or scalars. For the sake of brevity, the internal state variables are represented, in general, by second-rank tensors. Inclusion of vectors and scalars is straightforward.

Invoking the axiom of admissibility (Eringen, 1967) and using the separability of the strain tensor $\epsilon_{ij} = \epsilon_{ij}^{e} + \epsilon_{ij}^{vp}$ where ϵ_{ij}^{vp} is the viscoplastic strain, we can show:

$$\epsilon_{ij}^{e} = -\rho \frac{\delta\psi}{\delta\sigma_{ij}}$$

$$s = -\frac{\delta\psi}{\delta T}$$

$$\psi = \hat{\psi}(\sigma_{ij}, T, \alpha_{ij}^{(k)}). \tag{5}$$

Consequently, if we assume Fourier's law, $q_i = -kT_{,i}$, it becomes clear that the only constitutive relation required to completely define the thermomechanical problem is equation (5), which can be postulated as:

$$\psi = -\frac{1}{2\rho} C_{ijlm}(T)\sigma_{ij}\sigma_{lm} + C_v T(1 - \ln T/T_0) - \frac{1}{\rho}\gamma_{ij}\sigma_{ij}(T - T_0) + \frac{1}{2\rho} A_{ijlm}^{(k)}\alpha_{ij}^{(k)}\alpha_{lm}^{(k)} \tag{6}$$

where C_{ijlm} is the elastic compliance tensor, C_v is the specific heat at constant deformation and internal state variables, γ_{ij} is the thermal expansion tensor, and $A_{ijlm}^{(k)}$ is a set of material tensors. Assumption of the constitutive equation (6) is partially based on some past knowledges of the nature of ψ such as the separability of ψ into an elastic and an inelastic part (Kelly, 1976). A thermodynamic potential function (Helmholtz free energy), similar to equation (6), has been independently proposed by Freed and Chaboche (1989).

For the special case $A_{ijlm}^{(k)} = a^{(k)}\delta_{il}\delta_{jm}$ and $\gamma_{ij} = \gamma\delta_{ij}$, which is true for isotropic materials, and in the absence of the heat supply rate, the first and second laws of thermodynamics can be expressed as, respectively:

$$-kT_{,ii} + \rho C_v\dot{T} = -T\dot{\sigma}_{ii}\gamma - T\left(\frac{\delta C_{ijlm}}{\delta T}\dot{\sigma}_{ij} + \frac{\delta^2 C_{ijlm}}{2\delta^2 T}\dot{T}\sigma_{ij}\right)\sigma_{lm} + \sigma_{ij}\dot{\epsilon}_{ij}^{vp} - a^{(k)}\alpha_{ij}^{(k)}\dot{\alpha}_{ij}^{(k)} \tag{7}$$

$$\sigma_{ij}\dot{\epsilon}_{ij}^{vp} - a^{(k)}\alpha_{ij}^{(k)}\dot{\alpha}_{ij}^{(k)} + \frac{k}{T}T_{,i}^{2} \geq 0. \tag{8}$$

It may be worth mentioning that the right-hand side of equation (7) represents the rate of mechanical energy generation. The first and second terms stand for the reversible part due to dilatation and the temperature dependency of the elastic compliance tensor, the third for the irreversible viscoplastic part, and the fourth for the energy stored due to microstructural effects.

Equations (1) and (7) are the coupled thermomechanical equations which are not restricted to any specific evolution equations provided that the second law of thermodynamics, equation (8), is not violated. A specific postulated form of equation (4), which is appropriate for certain classes of viscoplastic materials within a certain range of thermomechanical loading, is discussed in the next section.

The Viscoplastic Constitutive Equation

The theory of viscoplasticity is concerned with the time/rate-dependent plastic behavior of some materials. A comprehensive review, analysis, and discussion of the current development of the theory are presented by Chaboche (1989). A branch of the theory is the internal state variable theory (Bodner and Partom, 1975; Miller, 1976; Hart, 1976) which has been an area of active research ever since: it is a unified theory which does not separate plastic and creep effects, it is partially based on microstructural observations, and it need not admit a yield surface and is consequently numerically more manageable and easier to be implemented into standard computational methods, such as the finite element method. Discontinuity at the yield surface and enforcing the consistency rule present numerical difficulties (Ghoneim and Chen, 1983). The internal state variable theory, in general, adopts a couple of internal state variables that embody microstructural effects and requires a kinetic equation which relates the stress to the viscoplastic strain rate (equivalent to the flow rule in the inviscid theory of plasticity) as well as evolution equations (4) for the internal state variables.

A power form similar to the one developed by Walker (1981) is adopted for the kinetic equation. Two internal state variables are considered: the drag stress, D, and the back (deviatoric) stress, B_{ij},

$$\dot{\epsilon}_{ij}^{vp} = \frac{3}{2}\dot{\epsilon}_0\left(\frac{\tau}{D}\right)^{n}\left(\frac{S_{ij} - B_{ij}}{\tau}\right) \tag{9}$$

where

τ. . .is the effective stress, $\tau = \sqrt{1.5(S_{ij} - B_{ij})(S_{ij} - B_{ij})}$,
S_{ij}. . .is the deviatoric stress tensor, $S_{ij} = \sigma_{ij} - \sigma_{ll}\delta_{ij}/3$,
n. . .is a temperature-dependent material parameter, and
$\dot{\epsilon}_0$. . .is a scale factor.

Although many formulas (James et al., 1987) have been suggested for the kinetic equation, the power form has its experimental supportive evidence (Jahnston and Gilman, 1959) and enjoys a lucid interpretation of the parameters involved: n is a strain-rate sensitivity parameter, and $\dot{\epsilon}_0$ represents the maximum admissible strain rate as will be demonstrated later. However, the power form equation (9), is valid only over a specific range of strain rates and temperature.

Evolution equations for the internal state variables can be proposed in a very general form: convolution form of Stieltjes intergral (Ghoneim et al., 1983),

$$\alpha = \int_{-\infty}^{\bar{\xi}} g(\xi - \bar{\xi})\frac{\delta w}{\delta\xi}\, d\xi \tag{10}$$

where α is a generic state variable taken as scalar for the ease of argument, ξ is a time and/or deformation variable with $\bar{\xi}$ as its present value, g is a weighting function, and w is a variable which is a function of σ_{ij}, T, and/or the remaining internal state variables (aside from α). Equation (10) implies

Downloaded 03 May 2010 to 171.66.16.244. Redistribution subject to ASME license or copyright; see http://www.asme.org/terms/Terms_Use.cfm

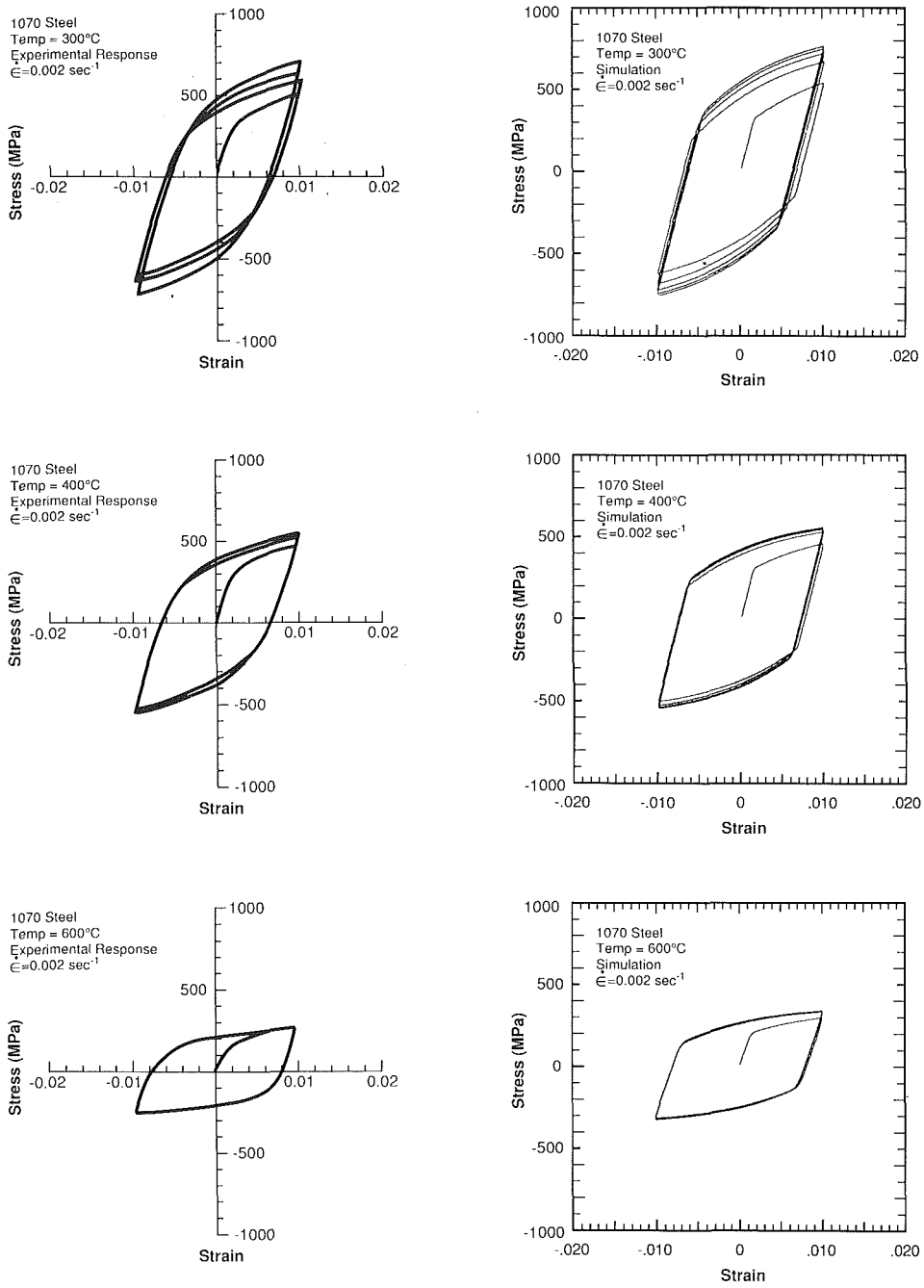


Fig. 1 Experimental and predicted isothermal cyclic stress response at different strain rates and temperatures

that α depends on the past history, with respect to ξ, of w. If an exponential decaying function is adopted for g, a more convenient and simpler (Maxwell Differential) form (Christensen, 1971) may replace equation (10):

$$\frac{\delta\alpha}{\delta\xi} + g_2(T)\alpha = g_1(T)\frac{\delta w}{\delta\xi}. \tag{11}$$

This form, equation (11), has been extensively used for the evolution of the internal state variables and is called, for obvious reasons, the hardening-recovery format. If ξ is chosen as the real time, t, equation (11) indicates that recovery occurs with time regardless of the deformation which excludes dynamic recovery. On the other hand, if ξ is chosen as a deformation related parameter, equation (11) signifies that recovery occurs with deformation which excludes static recovery. A proper choice of ξ must combine both time and deformation. However, since static effects are not addressed in this paper, we have selected ξ to be the accumulative viscoplastic strain, $\xi = \epsilon^{vp} = \int_0^t \sqrt{1.5\,\dot{\epsilon}_{ij}^{vp}\dot{\epsilon}_{ij}^{vp}}\,dt$. Consequently, equation (11) becomes:

$$\frac{\delta\alpha}{\delta\epsilon^{vp}} + g_2\alpha = g_1\frac{\delta w}{\delta\epsilon^{vp}}$$

or

$$\dot{\alpha} + g_2\dot{\epsilon}^{vp}\alpha = g_1\dot{w}.$$

For the specific material that is investigated in this paper (1070 steel), best simulation results are obtained when w, for isotropic hardening, is the accumulative viscoplastic strain, $\dot{w} = \dot{\epsilon}^{vp}$, and when w represents some measure of the viscoplastic work for kinematic hardening, $\dot{w} = (\tau/D)\dot{\epsilon}^{vp} = (\dot{\epsilon}^{vp}/$

Downloaded 03 May 2010 to 171.66.16.244. Redistribution subject to ASME license or copyright; see http://www.asme.org/terms/Terms_Use.cfm

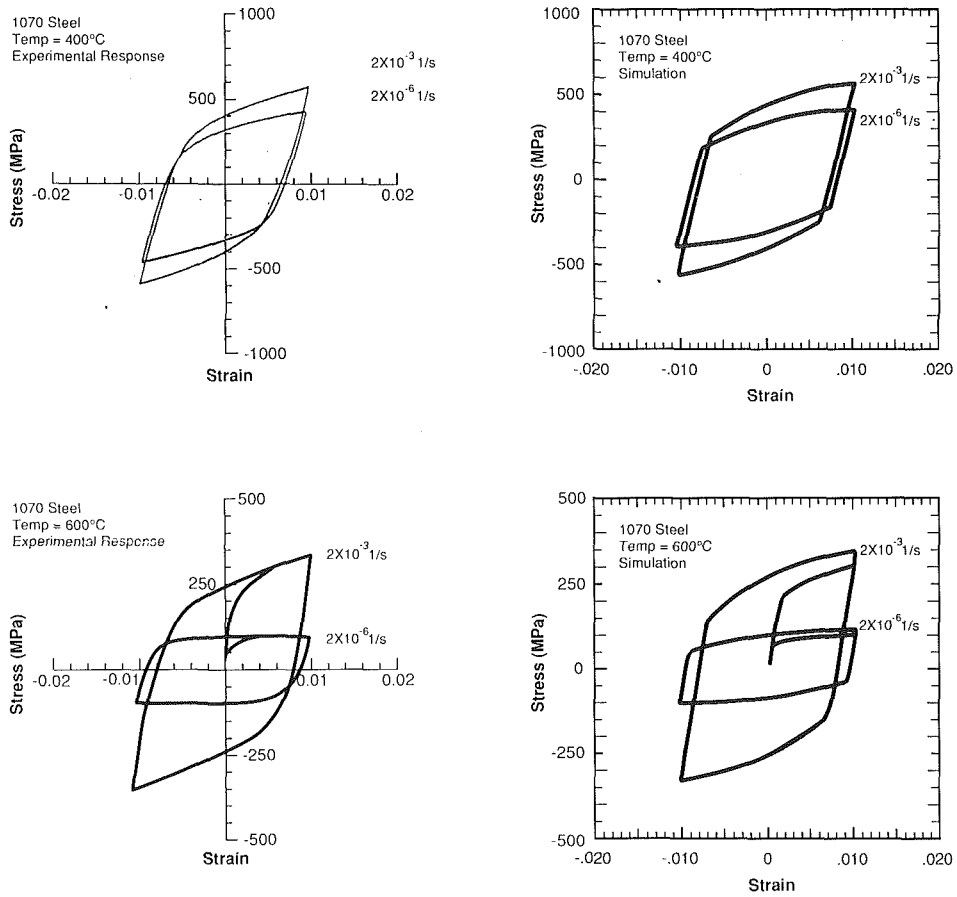


Fig. 2 Experimental and predicted saturation stress loops of isothermal cyclic at (*a*) $T = 400°C$ (*b*) $T = 600°C$

$\dot{\epsilon}_0)^{\left(\frac{1}{n}\right)} \dot{\epsilon}^{vp}$. This implies that for 1070 steel kinematic hardening is strain-rate dependent. Consequently, evolution equations for the back and drag stresses become, respectively:

$$\dot{B}_{ij} + b_2 \dot{\epsilon}^{vp} B_{ij} = b_1 \dot{\epsilon}^{vp}_{ij} (\tau/D) \tag{12}$$

$$\dot{D} + d_2 \dot{\epsilon}^{vp} D = d_1 \dot{\epsilon}^{vp} \tag{13}$$

where b_2 and d_2 are recovery parameters and b_1 and d_1 are hardening parameters. All four parameters are, in general, functions of temperature. It must be pointed out that evolution equations (12) and (13) are special forms of the general equation (11), and that selection of the physical nature of ξ and w is not restricted to our choice as long as it leads to satisfaction of Clausius-Duhem inequality as well as good simulation results.

Equations (9), (12), and (13) constitute the proposed viscoplastic constitutive equations. Simulation results of isothermal cyclic of 1070 steel at different temperatures (300, 400, and 600°C) together with the corresponding experimental results (Slavik and Sehitoglu, 1986) are displayed in Fig. 1. The stable loops of experimental (Sehitoglu and Slavik, 1987) and predicted results of isothermal cyclic loading at 400°C and 600°C for two different strain rates, $2E\text{-}3$ and $2E\text{-}6$ s^{-1}, are shown in Fig. 2. In general, simulation results depict some of the salient features of the experimental results: strain-rate sensitivity decreases with decreasing temperature, and hardening increases with increasing strain rate and/or decreasing temperature. However, it is the fair quantitative agreement between the experimental and the simulation results that is encouraging.

For simulation, the following material functions and constants are adopted:

$$n(T) = (n_0 - 1)\left(\frac{T_0}{T}\right)^m + 1$$

with $n_0 = 21$, $m = 5$, and $T_0 = 670\ K$;

$$b_1 = b_0 \exp\left(\frac{Q}{R}\right)_b \left(\frac{T_0 - T}{T_0 T}\right)$$

with $b_0 = 26$ Gpa and $\left(\frac{R}{Q}\right)_b = 1500\ K$;

$$d_2 = d_0 \exp\left(\frac{Q}{R}\right)_d \left(\frac{T - T_0}{T_0 T}\right)$$

with $d_0 = 30$ and $\left(\frac{R}{Q}\right)_d = 1500\ K$;

$$D_i(T) = d_3 - d_4(T - T_0) - u(T - T_0) d_5 (T - T_0)$$

with $d_3 = 300$ Mpa, $d_4 = 0.125$ Mpa/K, $d_5 = 0.375$ Mpa/K, and $u(T)$ is the unit step function; $\dot{\epsilon}_0 = 0.002\ s^{-1}$, $b_2 = 130$, and $d_1 = 12$ Mpa.

In addition, the modulus of elasticity, E, is taken as a function of T;

$$E = E_0 - u(T - T_0) E_1 (T - T_0),$$

with $E_0 = 200$ Gpa, and $E_1 = 250$ Mpa/K.

The aforementioned material functions and constants, except for b_1, b_2, d_1, and d_2, are directly and completely obtained from two sets of experiments (stress-strain results): isothermal monotonic loading at two different temperatures and strain rates. Determination of b_1, b_2, d_1, and d_2 is more involved and requires three isothermal cyclic loading experiments at two different temperatures and strain rates. Details of the assessment of the material constants are not discussed in this paper.

Downloaded 03 May 2010 to 171.66.16.244. Redistribution subject to ASME license or copyright; see http://www.asme.org/terms/Terms_Use.cfm

It may be worth mentioning that the adopted material functions are general and depend on the material under consideration.

It is understood that inequality equation (8) must be satisfied throughout any thermomechanical process which imposes some restrictions on the material constants. Substituting from equations (9), (12), and (13) into (8), taking into consideration that the last term is always positive, we get:

$$(\sigma_{ij} - a_1 b_1 B_{ij}\beta)\,\dot{\epsilon}_{ij}^{vp} + a_1 b_2 B_{ij} B_{ij}\,\dot{\epsilon}^{vp} - a_2 D\,\dot{\epsilon}^{vp}(d_1 - d_2 D) \geq 0 \quad (14)$$

where

$$\beta = \frac{\tau}{D} = \left(\frac{\dot{\epsilon}^{vp}}{\dot{\epsilon}_0}\right)^{\frac{1}{n}}.$$

For the special case $a_1 = 1/b_1$ and $a_2 = 0$, equation (14) becomes

$$(\sigma_{ij} - \beta B_{ij})\,\dot{\epsilon}_{ij}^{vp} + \frac{b_2}{b_1} B_{ij} B_{ij}\,\dot{\epsilon}^{vp} \geq 0. \quad (15)$$

It can be shown that equation (15) is always satisfied if $\beta \leq 1$ or $\dot{\epsilon}^{vp} \leq \dot{\epsilon}_0$. This confirms that applications of the power form equation (9) must be limited to a certain range of strain rates and indicates that $\dot{\epsilon}_0$ must be assigned the upper limit value of this range.

The coupled equations (1) and (7), together with the proposed viscoplastic equations (9), (12), and (13), completely define the thermomechanical equations. In the next section a finite element program implementing these equations is developed and applied to solve the problem of cyclic loading of a constrained-ended circular.

Finite Element Implementation

For quasi-static infinitesimal deformation problems, the coupled thermomechanical equations (1) and (7), in the absence of body forces and after some manipulations, can be expressed as, respectively:

$$\sigma_{ij,i} = (D_{ijlm}(T)\{\epsilon_{lm} - \epsilon_{lm}^{vp} - \gamma(T - T_0)\delta_{lm}\})_{,i} = 0 \quad (16)$$

$$-kT_{,ii} + \rho C_v \dot{T} = \dot{q}^{vp} - \dot{q}^{\alpha} - \dot{q}^{d} - \dot{q}^{E}, \quad (17)$$

where

$\dot{q}^{vp} = \sigma_{ij}\dot{\epsilon}_{ij}^{vp}$. . .rate of viscoplastic energy dissipation,

$\dot{q}^{\alpha} = B_{ij}\dot{B}_{ij}/b_1$. . .rate of energy stored due to microstructural effects,

$\dot{q}^{d} = \gamma_1 \dot{\epsilon}_{mm} T$. . .rate of dilatational elastic energy,

$\dot{q}^{E} = \gamma_2 \dot{\sigma}_{ij}\epsilon_{ij}^{e} T + \gamma_2^2 \dot{T}\sigma_{ij}\epsilon_{s}{}^{e}{}_{ij} T$. . .rate of elastic energy generated due to the temperature dependency of the elastic modulus, and

where D_{ijlm}, is the elastic tensor ($D_{ijlm} = C_{ijlm}^{-1}$), $\gamma_1 = \dfrac{\gamma E}{1-2\nu}$, $\gamma_2 = u(T - T_0)\dfrac{E_1}{E}$, and ν is Poisson's ratio.

A more condensed and convenient form for the finite element analysis of equations (16) and (17) is

$$\nabla.\sigma = \nabla.([\mathbf{D}]\{\epsilon - \epsilon^{vp} - \gamma(T - T_0)\delta\}) \quad (18)$$

$$-k\nabla^2 T + \rho C_v \dot{T} = \dot{q}^{vp} - \dot{q}^{\alpha} - \dot{q}^{d} - \dot{q}^{E}. \quad (19)$$

Note that in this section, σ, ϵ, and δ are vectors that represent σ_{ij}, ϵ_{ij}, and the Kroneckar Delta function, δ_{ij}, respectively.

Application of Galerkin finite element method (Zienkiewicz, 1977) to the rate form of equations (18) and to (19) yields, respectively:

$$[\mathbf{K}]\dot{\mathbf{U}} = \dot{\mathbf{F}}^{b} + \dot{\mathbf{F}}^{vp} + \dot{\mathbf{F}}^{th} + \dot{\mathbf{F}}^{E} = \dot{\mathbf{F}} \quad (20)$$

$$[\mathbf{C}]\dot{\mathbf{T}} + [\mathbf{S}]\mathbf{T} = \dot{\mathbf{Q}}^{vp} - \dot{\mathbf{Q}}^{\alpha} - \dot{\mathbf{Q}}^{d} - \dot{\mathbf{Q}}^{E} + \dot{\mathbf{Q}}^{s} = \dot{\mathbf{Q}}, \quad (21)$$

where

$[\mathbf{K}] = \int_A [\mathbf{B}]^T [\mathbf{D}]_0 [\mathbf{B}] dA$. . .the stiffness matrix,

$[\mathbf{C}] = \rho C_v \int_A \Psi\Psi^T dA$. . .the consistency matrix,

$[\mathbf{S}] = k\int_A [\nabla\Psi][\nabla\Psi]^T dA$. . .the conductivity matrix,

$\dot{\mathbf{F}}^{b} = \int_S \Psi(\mathbf{n}.\sigma) dS$. . .boundary traction nodal force vector,

$\dot{\mathbf{F}}^{vp} = \int_A [\mathbf{B}]^T [\mathbf{D}]_0 \dot{\epsilon}^{vp} dA$. . .nodal force vector which accounts for viscoplastic effects,

$\dot{\mathbf{F}}^{th} = \gamma_1 \int_A [\mathbf{B}]^T [\Psi] dA\dot{\mathbf{T}}$. . .nodal force vector which accounts for thermal strain effects,

$\dot{\mathbf{F}}^{E} = \int_A [\mathbf{B}]^T [\mathbf{D}]_1 \{T\dot{\epsilon}^{e} - (T - T_0)\dot{\epsilon}^{e}\} dA$. . .nodal force vector which accounts for the temperature dependency of the modulus of elasticity,

$\dot{\mathbf{Q}}^{vp} = \int_A \Psi \dot{q}^{vp} dA$. . .rate of heat supply vector due to viscoplastic deformation,

$\dot{\mathbf{Q}}^{\alpha} = \int_A \Psi \dot{q}^{\alpha} dA$. . .rate of heat supply vector due to microstructural effects,

$\dot{\mathbf{Q}}^{d} = \int_A \Psi \dot{q}^{d} dA$. . .rate of heat supply vector due to dilatation,

$\dot{\mathbf{Q}}^{E} = \int_A \Psi \dot{q}^{E} dA$. . .rate of heat supply vector due to temperature dependency of E,

$\dot{\mathbf{Q}}^{s} = \int_S \Psi h(T - T_0) dS$. . .rate of heat supply vector due to heat convection across the boundaries, and

where Ψ is the shape function vector, $[\mathbf{B}]$ is the strain-displacement matrix, and h is the coefficient of heat convection of the ambient air. Note that because of the linear temperature dependency of the modulus of elasticity, E, the elastic matrix

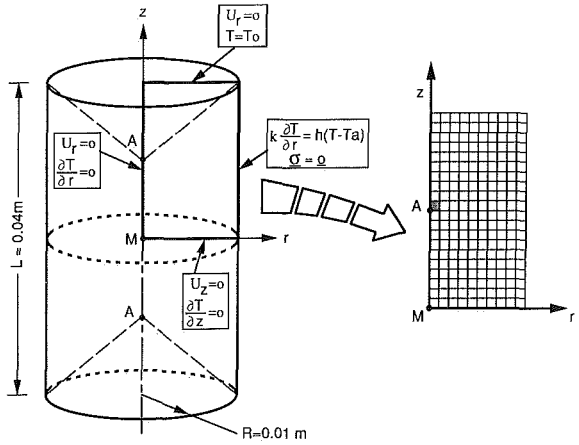


Fig. 3 Schematic of the cylinder, the boundary conditions, and the mesh used for the finite element simulation

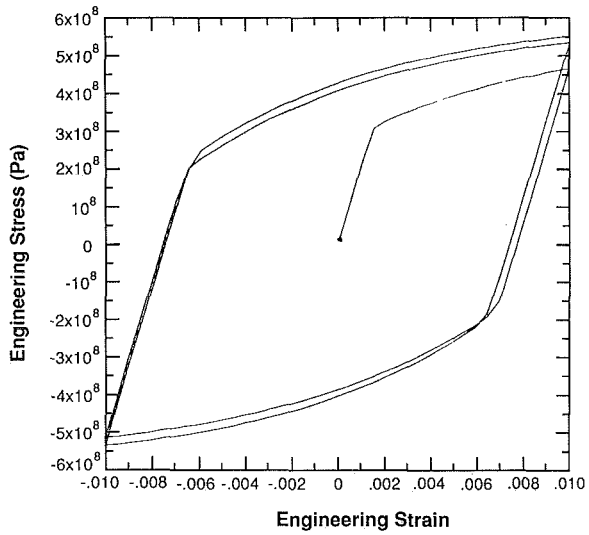
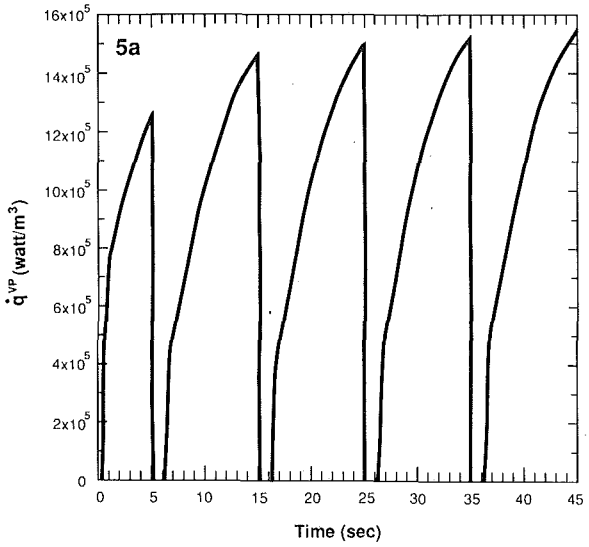
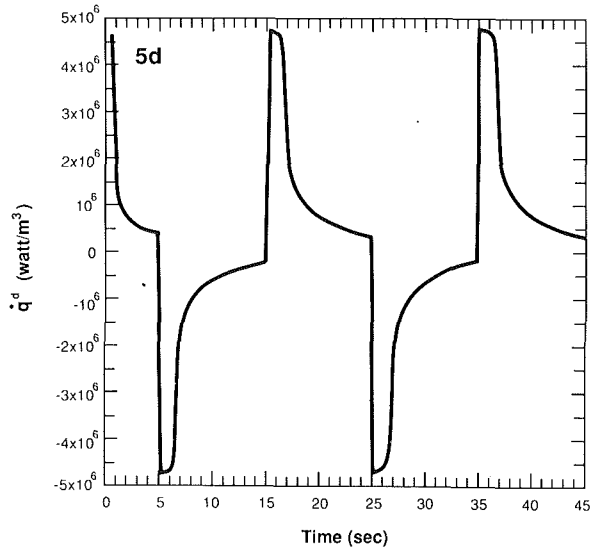
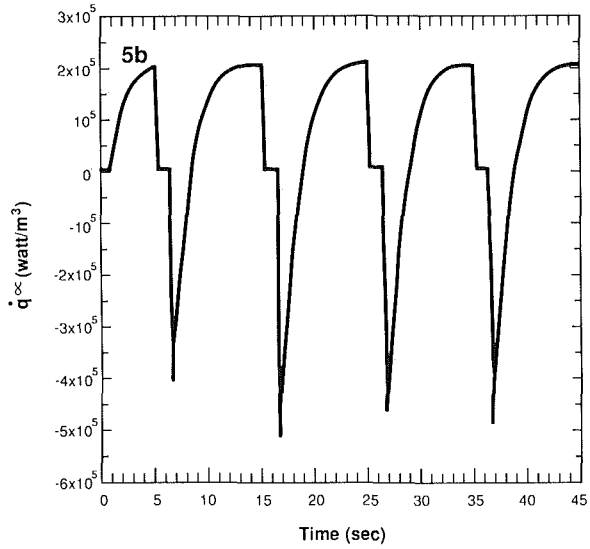


Fig. 4 Predicted stress response of the finite element simulation

Downloaded 03 May 2010 to 171.66.16.244. Redistribution subject to ASME license or copyright; see http://www.asme.org/terms/Terms_Use.cfm







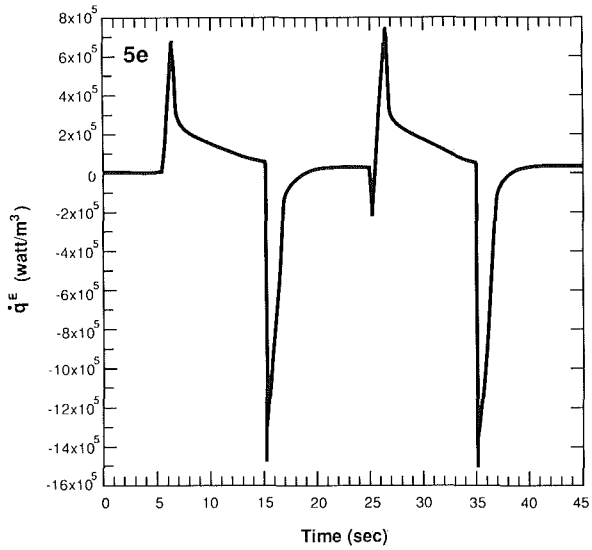
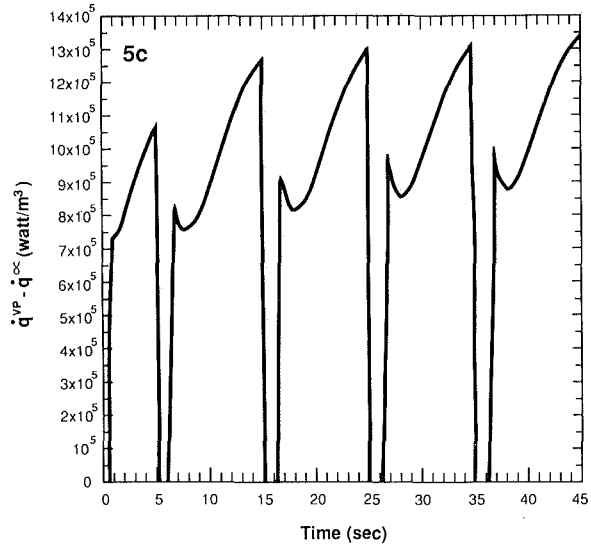


Fig. 5 Evolution of the different types of the rate of mechanical energy generation



[D] is a linear function of temperature as well, i.e., $[\mathbf{D}] = [\mathbf{D}]_0 - [\mathbf{D}]_1 T$. Also, the second term in the expression of $\dot{q}^E$ is assumed negligible and is dropped, which is acceptable for the material (1070 steel) and temperature range under consideration.

Using the "θ" method (Zienkiewicz, 1977) for the time marching solution of equations (20) and (21), we get, respectively:

$$[\mathbf{K}]\mathbf{U}^{j+1} = [\mathbf{K}]\mathbf{U}^{j} + \Delta t \mathbf{F}^{\theta} \tag{22}$$

$$[\mathbf{A}]\mathbf{T}^{j+1} = [\mathbf{H}]\mathbf{T}^{j} + \Delta t \mathbf{Q}^{\theta} \tag{23}$$

where $[\mathbf{A}] = [\mathbf{C}] + \Delta t\theta[\mathbf{S}]$

$[\mathbf{H}] = [\mathbf{C}] - \Delta t(1-\theta)[\mathbf{S}]$

$\mathbf{F}^{\theta} = \theta\mathbf{F}^{j+1} + (1-\theta)\mathbf{F}^{j}$

$\mathbf{Q}^{\theta} = \theta\mathbf{Q}^{j+1} + (1-\theta)\mathbf{Q}^{j}$

where Δt is the time increment, $\Delta t = t^{j+1} - t^{j}$, and θ is a weighting parameter ($0 \leq \theta \leq 1$). Equations (22) and (23) can be expressed as, respectively:

Downloaded 03 May 2010 to 171.66.16.244. Redistribution subject to ASME license or copyright; see http://www.asme.org/terms/Terms_Use.cfm

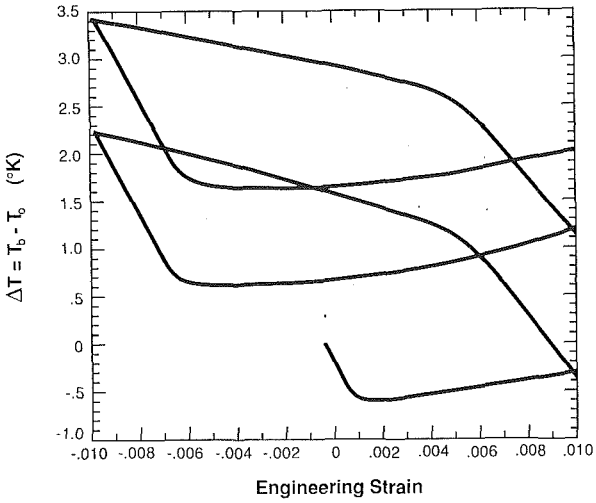
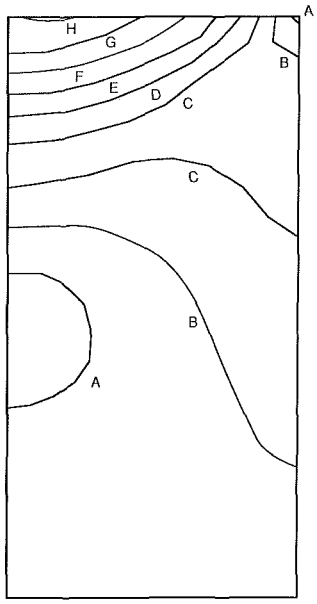


Fig. 6 Predicted temperature rise of the finite element simulation



Effective Stress (Pa)

A	3.9E8
B	3.8E8
C	3.6E8
D	3.4E8
E	3.2E8
F	3.0E8
G	2.8E8
H	2.6E8

Fig. 7 Contour plot of the effective stress

$$[\mathbf{K}]\mathbf{U}^{j+1} = \mathbf{N}_1 \tag{24}$$

$$[\mathbf{A}]\mathbf{T}^{j+1} = \mathbf{N}_2. \tag{25}$$

Equations (24) and (25) are solved using the fixed-point iteration method enhanced by the Aitken acceleration technique (Chow and Kay, 1984). Note that $\mathbf{N}_1$ and $\mathbf{N}_2$ contain all the nonlinearities, consequently, [K] and [A] are constructed and decomposed using the LU decomposion only once, and whenever the boundary conditions are changed. This algorithm turns out to be very efficient for the problem of cyclic loading of a constrained-ended cylinder presented in the next section.

Finite Element Simulation

Cyclic loading of a constrained-ended cylinder is a common test problem in the field of mechanics. Consequently, it is viewed as a good candidate for the investigation of thermomechanical coupling effects: prediction of temperature rise due to cyclic loading, and the effect of this temperature rise and the thermal boundary conditions on the mechanical response (stress-strain).

A cylindrical sample of 1070 steel, 4 cm in height and 1 cm in radius, is chosen for the finite element simulation. Dimensions, boundary conditions, and the finite element mesh (200 four-noded isoparametric elements) are shown in Fig. 3. Note that due to symmetry, only one quarter of the r-z cross-sectional plane is considered. Values of $\theta = 0.5$ (Crank-Nicolson) and $\theta = 0.667$ (Galerkin) have been experimented with. Both values render almost the same results (no significant difference). In addition to the material properties adopted in the one-dimensional simulation of 1070 steel, the following material constants are considered:

$$\nu = 0.3 \qquad \rho = 9500 \text{ kg/m}^3$$
$$C_v = 525 \text{ J/(kg K)} \qquad k = 21.7 \text{ W/(m K)}.$$

The convection coefficient h is assumed constant, $h = 10$ W/(m^2 K). Although this assumption is incorrect and the value is crude, it is acceptable for the problem under consideration where heat convection plays an insignificant role—numerical experimentation with $h = 100$ W/(m^{2}K) has not altered the results. Simulation of cyclic loading is conducted for the same combination of strain rates and temperatures adopted in the one-dimensional simulation case. Samples of the results for the case of engineering strain rate of 0.002 s^{-1} and ambient temperature of 400°C are displayed in Figs. 4–8.

Figure 4 displays the predicted engineering stress-strain response for three cycles. Comparison with the corresponding one-dimensional isothermal simulation results (Fig. 1) demonstrates that for this case of loading, the coupling effect on the mechanical response (stress-strain) is negligible.

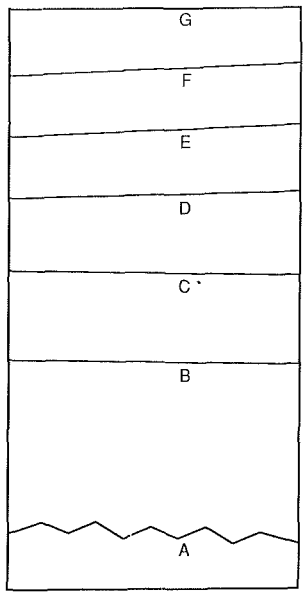
Evolution of the different types of the rate of mechanical energy generated ($\dot{q}^{vp}$, $\dot{q}^{\alpha}$, $\dot{q}^{d}$, $\dot{q}^{E}$) with time, at the centroid of the shaded element in Fig. 3, is displayed in Fig. 5. It can be observed that:

1 Both $\dot{q}^{vp}$(Fig. 5(*a*)) and $\dot{q}^{\alpha}$ (Fig. 5(*b*)) are primarily generated during viscoplastic deformation.

2 The rate of viscoplastic energy dissipation, $\dot{q}^{vp}$, is always positive, while $\dot{q}^{\alpha}$ can be positive or negative. However, the net effect, $\dot{q}^{vp} - \dot{q}^{\alpha}$, is always positive (Fig. 5(*c*)), which satisfies the second law of thermodynamics, equation (8).

3 Both $\dot{q}^{d}$ (Fig. 5(*d*)) and $\dot{q}^{E}$ (Fig. 5(*e*)) are primarily generated during the short periods of elastic loading resulting in a periodic impulse energy generation.

4 During tension, $\dot{q}^{d}$ (Fig. 5(*d*)) is positive which implies, from equation (17), a negative heat supply and vice versa, i.e., during tension the material expands and absorbs energy while during compression it contracts and generates energy. On the



Temperature rise (°K)

A	3.0
B	2.5
C	2.0
D	1.5
E	1.0
F	0.5
G	0.0

Fig. 8 Contour plot of the temperature rise

Downloaded 03 May 2010 to 171.66.16.244. Redistribution subject to ASME license or copyright; see http://www.asme.org/terms/Terms_Use.cfm

other hand, $\dot{q}^E$ is opposite to and smaller in magnitude than $\dot{q}^d$ (Fig. 5(e)).

Temperature change during cyclic loading is displayed in Fig. 6. Temperature change of the cylindrical sample (Fig. 3) is represented by $\Delta T = T_b - T_0$, where T_b is the bulk temperature,

$$T_b = \left(\int_V T dV \right) / V,$$

where V is the volume of the cylindrical sample. Clearly, the temperature change follows the loading cycle. During elastic tensile (compression) loading the dilatational energy generation dominates resulting in a temperature drop (rise), and during the viscoplastic portion of loading $\dot{q}^{vp}$ dominates causing a temperature rise. Since both $\dot{q}^d$ and $\dot{q}^E$ are not dissipative in nature, energy generated by them during tensile loading is, more or less, recovered during compression rendering a net power dissipation equal to $(\dot{q}^{vp} - \dot{q}^{\alpha})$. This results in a net temperature rise of approximately 1 K/cycle.

Contour plots of the effective stress, τ, and the temperature change, $T - T_0$, at the end of the third cycle are shown in Figs. 7 and 8, respectively. Figure 7 depicts that the effective stress is maximum at the constrained edges and points A (Fig. 3). Also, since the effective stress is proportional to the viscoplastic strain rate, it can be inferred from the contour plot (Fig. 7) that viscoplastic deformation initiates at the constrained edges and points A (Fig. 3) then propagates along the surface of the cones displayed in Fig. 3. Temperature contours in Fig. 8 clearly show that heat convection through the cylindrical surface is negligible, and that heat is predominantly dissipated by conduction through the constrained ends.

Summary and Conclusions

Coupled thermoviscoplasticity equations are developed based on the rational theory of thermodynamics. A power-form internal state variable viscoplastic constitutive equation is proposed. Analysis of the proposed constitutive equation demonstrates that at high strain rates the power form may violate the second law of thermodynamics, and that within a certain range of strain rates and temperatures it can simulate isothermal cyclic loading of 1070 steel fairly well. Analysis of the corresponding boundary value problem of cyclic loading of a constrained-ended cylinder using finite element suggests that thermomechanical coupling does not affect the mechanical response (stress-strain), at strain rate of 0.002 sec^{-1} and ambient temperature of 400°C; however, temperature rise as much as 1 K/cycle can be experienced by the cylinder due to mechanical heat generation.

References

Allen, D. H., 1986, "Predicted Axial Temperature Gradient in a Viscoplastic Uniaxial Bar Due to Thermoelastic Coupling," *International Journal of Numerical Methods in Engineering*, Vol. 23, pp. 903–917.

Bodner, S. R., and Partom, Y., 1975, "Constitutive Equations for Elastic-Viscoplastic Strain-Hardening Materials," ASME JOURNAL OF APPLIED MECHANICS, Vol. 42, pp. 385–389.

Cernocky, E. P., and Krempl, E., 1980, "A Theory of Thermoviscoplasticity Based on Infinitesimal Total Strain," *International Journal of Solids and Structures*, Vol. 16, pp. 723–741.

Chaboche, J. L., 1989, "Constitutive Equations for Cyclic Plasticity and Cyclic Viscoplasticity," *International Journal of Plasticity*, Vol. 5, pp. 247–302.

Chow, Y. K., and Kay, S., 1984, "On the Aitken Acceleration Method for Non-linear Problems," *Computers and Structures*, Vol.19, pp. 757–761.

Christensen, R. M., 1971, *Theory of Viscoelasticity*, Academic Press, New York, pp. 16–17.

Eringen, A. Cemal, 1967, *Mechanics of Continua*, John Wiley and Sons, New York, pp. 145–156.

Freed, A. D., and Chaboche, J. L.,1989, "Viscoplasticity: A Thermodynamic Formulation," submitted to the ASME JOURNAL OF APPLIED MECHANICS.

Ghoneim, H., 1986, "Thermoviscoplasticity by Finite Element: Dynamic Loading of a Thick-Walled Cylinder," *Journal of Thermal Stresses*, Vol. 9, pp. 345–358.

Ghoneim, H., and Chen, Y., 1983, "A Viscoelastic-Viscoplastic Constitutive Equation and Its Finite Element Implementation," *Computers and Structures*, Vol. 17, pp. 499–509.

Ghoneim, H., and Matsuoka, S., 1987, "Thermoviscoplasticity by Finite Element: Tension and Compression Tests," *International Journal of Solids and Structures*, Vol. 23, No. 8, pp. 1133–1143.

Ghoneim, H., Matsuoka, S., and Chen, Y., 1983, "Viscoplastic Modeling With Strain Rate History Dependency," ASME JOURNAL OF APPLIED MECHANICS, Vol. 50, pp. 465–468.

Hart, E. W., 1976, "Constitutive Equations for the Nonelastic Deformation of Metals," ASME *Journal of Engineering Materials and Technology*, Vol. 98, pp. 193–202.

Hetnarski, R. B., Ghoneim, H., and Paul, D. B., 1986, "Constitutive Modeling and Thermoviscoplasticity," *Third Symposium on Nonlinear Constitutive Relations for High Temperature Applications*, The University of Akron, Ohio.

James, G. H., Ibrie, P. K., Hill, P. S., Allen, D. H., and Haisler, W. E., 1987, "An Experimental Comparison of Current Viscoplastic Models at Elevated Temperature," *ASME Journal of Engineering Materials and Technology*, Vol. 109, pp. 130–139.

Kelly, M. James, 1976, "Dislocation Models in Continuum Laws," *Constitutive Equations in Viscoplasticity*, ASME, New York, AMD-Vol. 21, pp. 33–49.

Johnston, W. G., and Gilman, J. J., 1959, "Dislocation Velocities, Dislocation Densities, and Plastic Flow in Lithium Flouride Crystals," *Journal of Applied Physics*, Vol. 30, pp. 129–144.

Lehmann, T., and Bix, U., 1985, "On the Influence of Coupling of Thermal and Mechanical Processes in the Necking Problem in Uniaxial Testing," *Journal of Thermal Stresses*, Vol. 8, pp. 153–165.

Miller, A., 1976, "An Inelastic Constitutive Model for Monotonic Cyclic and Creep Deformation," *ASME Journal of Engineering Materials and Technology*, Vol. 98, pp. 97–113.

Rubin, M. B., 1982, "A Thermoelastic -Viscoplastic Model With a Rate-Dependent Yield Strength," ASME JOURNAL OF APPLIED MECHANICS, Vol. 49, pp. 305–311.

Sehitoglu, H., and Slavik, D., 1987, "Critical Experiments in Thermomechanical Loading," *Proceeding of Second International Conference on Low Cycle Fatigue and Elasto-Plastic Behavior of Materials*, Munich, Germany.

Slavik, D., and Sehitoglu, H., 1986, "Constitutive Models Suitable for Thermal Loading," *ASME Journal of Engineering Materials and Technology*, Vol. 108, pp. 303–312.

Walker, K. P., 1981, "Research and Development Program for Non-linear Structural Modeling with Advanced Time-Temperature Dependent Constitutive Relationships," Report PWA-5700-50, NASA CR-165533.

Zienkiewicz, O. C., 1977, *The Finite Element Method*, 3rd ed., McGraw-Hill, London.

Downloaded 03 May 2010 to 171.66.16.244. Redistribution subject to ASME license or copyright; see http://www.asme.org/terms/Terms_Use.cfm

A Mechanism for Shear Band Formation in the High Strain-Rate Torsion Test

Timothy J. Burns
Center for Computing and Applied Mathematics,
National Institute of Standards and Technology,[1]
Gaithersburg, MD 20899
Mem. ASME

A numerical study of a one-dimensional model of the high strain-rate torsion test shows that a moving boundary of rigid unloading, starting from the ends of the thin-walled tubular specimen, is a plausible mechanism for adiabatic shear band formation during the test. Even though the dimensionless thermal diffusivity parameter is very small, the moving boundary is due to heat transfer from the specimen through its ends, which are assumed to be isothermal heat sinks. The mathematical model is based on a physical model of thermoelastic-plastic flow and a phenomenological Arrhenius model for the plastic flow surface. The numerical technique used is the semi-discretization method of lines.

1 Introduction

It has been known for a long time that, during the late stages of large-strain plastic deformation at high strain rate, such as occurs during penetration of armor by ballistic impact or during high-speed machining, the accumulated permanent strain can become highly localized (see, e.g., the review by Rogers, 1979). Zener and Hollomon (1944) proposed that the basic mechanism for this localization is a dynamic instability, caused by adiabatic heating. Unfortunately, although this strain localization is believed to be driven by shear stress, a penetration event or a rapid machining process involves a large mean compressive stress as well, which makes detailed analysis of such a deformation formidable.

Thus, it is not surprising that a great deal of interest has been stimulated by the high strain rate torsional Kolsky bar experimental work of Costin et al., (1979), Hartley et al., (1987), and most recently, Marchand and Duffy (1988), who observed the formation of a single shear band in thin-walled steel tubes under loading conditions which were essentially the same as occur in rapid simple shear (see, e.g., Shrivastava et al., 1982). Successively improved measurements of the local temperature rise, as the deformation localized into a single adiabatic shear band, were also obtained. In addition, Marchand and Duffy (1988) recorded the evolution in time of the inhomogeneous strain distribution. This was done by photographing an originally horizontal grid pattern, which had been etched on the outer walls of the tubes parallel their axes prior to the tests, at different times during the experiments. On the basis of the experimental results, the authors concluded that shear strain localization at high strain rate can be divided into three stages, associated with strains γ_I and γ_{II}, with $\gamma_I < \gamma_{II}$. During the first stage, for nominal plastic shear strains $\gamma < \gamma_I$, the grid lines were observed to remain straight while they tilted to an angle δ uniformly around the tubular samples, where $\gamma = \tan \delta$. During the second stage, for $\gamma_I \le \gamma \le \gamma_{II}$, the grid lines were observed to curve, so that the deformation had begun to localize uniformly around the samples. For nominal shear strains satisfying $\gamma > \gamma_{II}$, the flow stress was observed to drop rapidly, the shear bands were observed to narrow considerably down to about 20 μm in the HY-100, and a strong dependence of shear strain on the circumferential coordinate around the tubes was observed. Marchand and Duffy believed that the flanges on their thin-walled tubes provided isothermal heat sinks, and that the stress remained homogeneous throughout their tests, except at very early time and after a narrow shear band formed.

Marchand and Duffy cited the papers of Litonski (1977), Wright and Walter (1987), and Molinari and Clifton (1987) as providing numerical predictions which are qualitatively consistent with their experimental results. In Litonski (1977) and in Molinari and Clifton (1987), the assumptions were made that the center of the thin-walled tube was thinner than the outer portions of the tube, and that the load was in equilibrium during the test, so that the shear stress was different in the thinner and thicker portions of the tube, and dynamical effects and heat conduction were neglected. Both papers also considered constitutive models for plastic flow which included strain and strain-rate hardening and thermal softening. The computational results in both studies indicated that the strain localized in the thinner, weaker part of the tube, once the load-displacement curve for the simulation changed from strain hardening to strain softening. Related computational results, in which heat conduction was also included, were reported by Shawki et al., (1983) and Clifton et al., (1984).

[1]Formerly National Bureau of Standards.

Contributed by the Applied Mechanics Division of THE AMERICAN SOCIETY OF MECHANICAL ENGINEERS for publication in the JOURNAL OF APPLIED MECHANICS.

Discussion on this paper should be addressed to the Technical Editor, Leon M. Keer, The Technological Institute, Northwestern University, Evanston, IL 60208, and will be accepted until two months after final publication of the paper itself in the JOURNAL OF APPLIED MECHANICS. Manuscript received by the ASME Applied Mechanics Division, June 15, 1989; final revision, Oct. 23, 1989.

Copyright © 1990 by ASME
Downloaded 03 May 2010 to 171.66.16.244. Redistribution subject to ASME license or copyright; see http://www.asme.org/terms/Terms_Use.cfm

In Wright and Walter (1987) (also see Wright and Walter, 1989), an analysis was given for the case of a strain-rate hardening and thermal-softening material, so that strain-hardening effects were neglected. The deformation was treated as antisymmetric, one-dimensional shearing of a thin layer with thermally insulated boundaries, and no variation in layer thickness was assumed. Instead, the problem was treated as homogeneous simple shear, with a small symmetric perturbation in temperature, so that the calculated deformation also localized in the center of the shear layer. Their numerical calculations, which also included heat transport by conduction, indicated that, after a rapid transition to a localized deformation pattern in the center of the shear layer, the strain rate became time independent, while the temperature continued to increase, and the stress continued to decrease, but both at a lower rate than before. Related computational results, in which strain-hardening effects were also included, were reported by Batra (1987) and by Batra and Kim (1989).

In contrast to the adiabatic temperature boundary conditions used in the studies just cited, Wright (1987) took a different approach to the late-time behavior of shear band formation. He assumed that the temperature boundary conditions were isothermal and that eventually saturation occurred, so the material ceased to strain harden. In this case, he set the evolution terms in his one-dimensional model equations for the deformation equal to zero, with the result that stress, velocity, and temperature became independent of the time. The temperature boundary conditions forced the reference solution to be inhomogeneous. More recently, Chen, et al. (1989) and Maddocks and Malek-Madani (1989) studied the stability of this late-stage steady shearing morphology. Since Marchand and Duffy (1988) observed a variation of shear strain with location on the tube circumference during Stage III in their high strain rate torsion tests it follows that, beyond a certain stage, the deformation process can no longer be modeled as one-dimensional, and none of the foregoing analyses continues to be directly applicable.

The purpose of this paper is to propose a different, nonsteady mechanism which can account for the formation of a single adiabatic shear band in the experimental torsion tests cited above. Under the assumptions that during a high strain-rate torsion test there is a small perturbation from room temperature in the initial temperature distribution and the boundaries of the thin-walled tube are isothermal heat sinks, it will be shown by comparison of two simulations of a problem which was identical, except that the temperature boundary conditions were isothermal heat sinks in the first and adiabatic in the second, that an inwardly moving boundary of rigid unloading, caused by heat conduction through the tube ends once the deformation process becomes unstable, is a plausible mechanism for adiabatic shear band formation during the test. As with the analyses cited above, this work is only directly applicable while the torsion test remains essentially one-dimensional.

2 Approximate One-Dimensional Problem

Before it is deformed, suppose a tube of ductile metal has length $d=2.5$ mm, uniform wall thickness $H=0.4$ mm, and uniform circular cross-sectional radius $R_0=9.7$ mm from the tube axis to the midpoint of the wall, so that its initial dimensions correspond to those in the samples studied experimentally by Marchand and Duffy (1988). When such a thin-walled tube is loaded in torsion, it was assumed here that the subsequent evolution of the deformation process is governed by the model of thermodynamically irreversible, isotropically elastic, thermoelastic-plastic flow derived by Wallace (1985) (also see Wallace, 1981).

Let the position of the tube in the undeformed configuration be given by cylindrical coordinates (R, Θ, Z), with its axis coincident with the Z-axis from $Z=0$ to $Z=d$, and let the corresponding cylindrical coordinate system in the current configuration be denoted by (r, θ, z). Let $\xi(Z, t)$ denote the angle of twist per unit length, relative to the end $Z=0$ of the tube through which the ring of material at Z has been rotated by the torsional loading process, so that $\xi(Z, 0)=0$. It was assumed here that the point on the midwall of the tube initially at $\mathbf{P}=(R_0, \Theta, Z)$, $0\le\Theta<2\pi$, $0\le Z\le d$, was moved by the deformation at time t to point $\mathbf{p}=(r, \theta, z)$, where

$$r=R_0, \quad \theta=\Theta+Z\xi(Z, t), \quad z=Z.$$

Also, the only nonzero components of the Cauchy stress tensor referred to the current (r, θ, z) coordinates were assumed to be $\sigma\langle\theta z\rangle=\sigma\langle z\theta\rangle=\tau$ (see McMeeking, 1982), where τ is related to the applied torque Γ by $\Gamma=2\pi R_0^2 H\tau$ (see Hartley and Duffy, 1985), and angular brackets denote physical components of a tensor. Define the shear strain γ and strain rate $\dot\gamma$ by

$$\gamma=\frac{\partial}{\partial Z}[R_0 Z\xi(Z,t)], \quad \dot\gamma=\frac{\partial}{\partial Z}[R_0 Z\dot\xi(Z,t)],$$

where the dot denotes the material time derivative. It was assumed here that $\dot\gamma=\dot\gamma^e+\dot\gamma^p$, i.e., that the total strain rate decomposes into a sum of elastic and plastic contributions (see, e.g, Wallace, 1985). The only nonzero components of the deformation rate tensor $\mathbf{D}$, referred to the current configuration, were assumed to be $D\langle\theta z\rangle=D\langle z\theta\rangle=\dot\gamma/2$ (see McMeeking, 1982; Shrivastava, et al., 1982).

The measure of deformation of most interest during the first two stages of the experiments of Marchand and Duffy (1988) was the twist $s(Z, t)$ at time t undergone by the circular ring of material in the tube labeled by the Lagrangian axial coordinate Z, since this was the variable which determined the instantaneous location of each of the grid lines etched on the tube prior to a test. For the deformation assumed here this was the arclength from $\mathbf{p}(Z, 0)=\mathbf{P}$ to $\mathbf{p}(Z, t)$, so that $s(Z, t)=R_0 z\xi(Z, t)$. The only nonzero component of the velocity $\mathbf{v}$ was thus the angular speed $v=v\langle\theta\rangle$, where

$$v=R_0 Z\dot\xi. \tag{1}$$

The twist and the angular speed were thus related by $\partial s(Z, t)/\partial t=v(Z, t)$.

It was shown by Shrivastava et al. (1982) that, as long as the strain in a torsion test remains uniform around the circumference of a tube, then for each fixed value of the angular material variable Θ, the test can be modeled as one-dimensional shear. Specializing the equations in Wallace (1985) to this case, the mathematical model of the torsion test was reduced to a set of five evolution equations in one material variable, consisting of an equation for the total twist s, a scalar equation for conservation of momentum, an equation for the evolution of the shear stress τ, an equation for the evolution of the temperature field T in the axial direction of the tube, and an equation for the evolution of the plastic shear strain γ^p.

The criterion for when plastic flow occurred, i.e., for when $\dot\gamma^p>0$, was an extension of the von Mises yield criterion. Wallace (1985) generalized this criterion to a flow surface, such that $\tau=k(\gamma^p, \dot\gamma^p, V, S)$ anywhere in the material where plastic flow takes place. This allowed for strain hardening, a strain rate effect, and a dependence on the thermoelastic state (V, S). In the approximation used here, the specific volume V (and thus the mass density ρ) does not change, and the specific entropy S is a function of the temperature T. Therefore, the von Mises flow surface could be written in the form

$$\tau=K(\gamma^p, \dot\gamma^p, T). \tag{2}$$

It was assumed that $\partial K/\partial\dot\gamma^p>0$, so that equation (2) could be inverted and written in the form

$$\dot\gamma^p=\Phi(\tau, \gamma^p, T). \tag{3}$$

Downloaded 03 May 2010 to 171.66.16.244. Redistribution subject to ASME license or copyright; see http://www.asme.org/terms/Terms_Use.cfm

The criterion for whether or not plastic flow takes place at a given material point at a given time was then given by

$$\dot{\gamma}^p = \begin{cases} \Phi(\tau, \gamma^p, T) & \text{if } \tau = K(\gamma^p, \dot{\gamma}^p, T) \\ 0 & \text{if } \tau < K(\gamma^p, 0, T). \end{cases} \tag{4}$$

The evolution equations were scaled and nondimensionalized as follows. Let $\hat{Z} = Z/d$, $\hat{t} = \dot{\gamma}_0 t$, $\hat{s} = s/d$, $\hat{v} = v/v_0 = v/(\dot{\gamma}_0 d)$, $\hat{\tau} = \tau/\tau_0$, $\hat{T} = (T - T_0)/T_0$, $\hat{\gamma}^p = \gamma^p$, $\hat{\Phi}(\hat{\tau}, \hat{\gamma}^p, \hat{T}) = \Phi(\tau, \gamma^p, T)/\dot{\gamma}_0$, and $\hat{K}(\hat{\gamma}^p, \hat{\gamma}^p, \hat{T}) = K(\gamma^p, \dot{\gamma}^p, T)/\tau_0$. Dropping the hats over the variables, the resulting equations were

$$\begin{aligned} \frac{\partial s}{\partial t} &= v, \\ \phi \frac{\partial v}{\partial t} &= \frac{\partial \tau}{\partial Z}, \\ \zeta \frac{\partial \tau}{\partial t} &= \frac{\partial v}{\partial Z} - \Phi(\tau, \gamma^p, T), \\ \frac{\partial T}{\partial t} &= \lambda \frac{\partial^2 T}{\partial Z^2} + \mu \tau \Phi(\tau, \gamma^p, T), \\ \frac{\partial \gamma^p}{\partial t} &= \Phi(\tau, \gamma^p, T), \end{aligned} \tag{5}$$

when plastic flow was occurring, so that $\tau = K(\gamma^p, \dot{\gamma}^p, T)$ and $\dot{\gamma}^p > 0$. When the material was unloading, so that $\tau < K(\gamma^p, 0, T)$ and $\dot{\gamma}^p = 0$, the resulting equations were the same, except that $\Phi = 0$.

The dimensionless groups of parameters ζ, ϕ, λ, and μ were defined by

$$\zeta = \frac{\tau_0}{G}, \quad \phi = \frac{\rho \dot{\gamma}_0^2 d^2}{\tau_0}, \quad \lambda = \frac{\kappa}{\rho_0 C \dot{\gamma}_0 d^2}, \quad \mu = \frac{\tau_0}{\rho C T_0}. \tag{6}$$

The shear modulus G for the structural steel HY-100 was assumed to be the handbook value for iron of 81 GPa. The strain rate assumed here was $\dot{\gamma}_0 = 1600\ \text{s}^{-1}$, and the tests were assumed to take place at room temperature, $T_0 = 300\ K$. The length scale d was the tube gauge length, $d = 2.5$ mm. The stress scale τ_0 was taken to be the stress level which gives the yield stress τ_y when the strain equals the yield strain γ_y, assuming the material behaves according to a power-law hardening rule for small strain, i.e., in dimensional form, $\tau = \tau_0 \gamma^n$, where $\tau_0 = \tau_y \gamma_y^{-n}$. The values chosen here for the three parameters defining τ_0 were those reported by Machand and Duffy (1988) for high strain-rate tests on HY-100 steel, $\tau_y = 463$ MPa, $\gamma_y = 0.012$, and $n = 0.107$, which gave a value for the stress scale of $\tau_0 = 743$ MPa. The density scale ρ was taken to be the typical value for steel of 7800 kg/m^3. The values for the heat capacity C and the thermal conductivity κ were taken to be the typical values for iron of 500 J/(kg K) and 54 W/(m K), respectively. These parameter values yielded orders of magnitude for the dimensionless groups, equation (6), of $\zeta \approx 10^{-2}$, $\phi \approx 10^{-4}$, $\lambda \approx 10^{-3}$, and $\mu \approx 10^{0}$. The inertia coefficient ϕ is the ratio of the momentum flux to the shear stress (Burns, 1989a), which was shown by Oswatitsch (1963) to define the Reynolds number for a fluid shear flow. The torsion tests of Marchand and Duffy can thus be interpreted as plastic shear experiments at very low Reynolds number.

To complete the specification of the problem, boundary and initial conditions needed to be specified, and a model for the flow surface (2) or (3) was required. In most of the computer simulations to date of shear band formation, the boundary conditions on the temperature have been assumed to be adiabatic, i.e., no heat flux through the boundaries,

$$\frac{\partial T}{\partial Z}(0,t) = \frac{\partial T}{\partial Z}(1,t) = 0. \tag{7}$$

It was assumed here, however, that the two ends of the thin-walled tube were constant-temperature heat sinks, given in dimensionless form by the boundary conditions

$$T(0, t) = T(1, t) = 0. \tag{8}$$

It follows from the expression for the velocity component in the θ-direction, equation (1), that one boundary condition must be $v(0, t) = 0$, so that it is not appropriate to specify a boundary condition on the stress at $Z = 0$. Corresponding to the test conditions described in Costin et al. (1979), Hartley et al. (1987), and Marchand and Duffy (1988), the remaining boundary condition was that the rate of twist $R_0 Z \xi$ of the end of the tube corresponding to $Z = 1$ was constant, which was given in dimensionless form by $v(1, t) = 1$. The initial conditions used will be discussed in Section 4. In the next section, the specific model derived for the plastic flow surface will be described.

3 Plastic Flow Surface Model

An Arrhenius model of the flow surface was chosen for the numerical simulations. In dimensional variables, it was assumed to have the form

$$\dot{\gamma}^p = \dot{\gamma}_r \exp\left(-\frac{\Delta H(\tau)}{kT}\right) \tag{9}$$

where $\Delta H(\tau)$ is the activation enthalpy for the plastic deformation process, k is Boltzmann's constant, T is the dimensional temperature, and $\dot{\gamma}_r$ is a term which was assumed to be constant and defined below. It was assumed that $\Delta H(\tau)$ could be linearized about the reference value of the flow stress, $\tau = \tau_0$ (see e.g., Kocks et al., 1975; Estrin and Kubin, 1980), so that

$$\Delta H(\tau) \approx \Delta H(\tau_0) - \Delta V(\tau - \tau_0), \tag{10}$$

where $\Delta V = -\partial(\Delta H)/\partial \tau|_{\tau = \tau_0}$ is the apparent activation area Δa times the magnitude b of the Burgers vector $\mathbf{b}$, so that it has the dimensions of a volume. The pre-exponential term $\dot{\gamma}_r$, was assumed to be given in terms of the constant reference conditions τ_0, $\dot{\gamma}_0$, and T_0 by

$$\dot{\gamma}_r = \dot{\gamma}_0 \exp\left(\frac{\Delta H(\tau_0)}{kT_0}\right). \tag{11}$$

To account for strain hardening, it was assumed the strain-hardening behavior followed the power-law rule $\tau = \tau_r(\gamma^p) = \tau_0(\gamma_y + \gamma^p)^n$, where γ_y, τ_0, and n have been defined and given numerical values in the preceding section. Then the constant reference stress τ_0 in the last term in equation (10) was replaced by this power-law rule, so that, using the dimensionless variables defined in the preceeding section, the linearized Arrhenius model had the form

$$\dot{\gamma}^p = \Phi(\tau, \gamma^p, T) = \exp\left\{\frac{\beta T + \alpha[\tau - \tau_r(\gamma^p)]}{1 + T}\right\}. \tag{12}$$

The model equation (12) contains four dimensionless groups of parameters. Two of these are the yield strain γ_y and the strain-hardening exponent n, which have already been discussed previously. The remaining two are a temperature coefficient β, where $\beta = \Delta H(\tau_0)/(kT_0)$, and a stress coefficient α, where $\alpha = \Delta V \tau_0/(kT_0)$. By equation (11), $\beta = \ln(\dot{\gamma}_r/\dot{\gamma}_0)$. Kocks et al., (1975, p. 243) gave the estimated bounds on β of $8 < \beta < 40$, where the lower bound corresponds to a strain rate of the order of magnitude of 10^2. The order of magnitude of the strain rates in the present study was assumed to be 10^3, and a value of $\beta = 40$ was chosen in order to get a reasonable value for α.

It was decided to fit the remaining parameter, α, by requiring that a homogeneous, adiabatic deformation of the thin-walled tube, at a constant strain rate of $\dot{\gamma}_0 = 1600\ \text{s}^{-1}$, attain its maximum stress when $\gamma^p = 0.25$, corresponding to a typical strain value at which a stress maximum was observed by Marchand and Duffy (1988, Tab. 4) in their experiments. The approximate value of the coefficient was found to be $\alpha = 55$,

Downloaded 03 May 2010 to 171.66.16.244. Redistribution subject to ASME license or copyright; see http://www.asme.org/terms/Terms_Use.cfm

which gave a peak stress of approximately 580 MPa, which is about six percent lower than the average of the peak stresses reported by Marchand and Duffy. As a consistency check on the order of magnitude of α, first solve for τ as a function of the other variables in equation (12),

$$\tau = K(\gamma^p, \dot{\gamma}^p, T) = \tau_r(\gamma^p) + \frac{(1+T)}{\alpha}\ln\dot{\gamma}^p - \frac{\beta}{\alpha}T. \tag{13}$$

Then the mean apparent strain-rate sensitivity parameter, $m = \partial\tau/\partial\ln\dot{\gamma}^p$ (see, e.g., Eleiche 1981), is given at constant temperature and plastic strain by $m = (1+T)/\alpha$. Thus, m is essentially $1/\alpha \approx 10^{-2}$. (Alternatively, since m is usually more readily available, α could have been determined from m, and then β could have been fit from the peak in the shear stress versus shear strain curve, as above.)

4 Computational Results

Results of two computer simulations will be presented here. As discussed in the Introduction, Marchand and Duffy (1988) concluded that there were three stages of shear strain localization in their torsion tests. In the final stage, Stage III, for a given axial location Z, the total twist was found to depend on the circumferential variable Θ, so there was no hope that the simple one-dimensional mathematical model derived here could simulate the observed late-time behavior. The yield criterion, equation (4), was replaced by the Arrhenius model, equation (12), so that, computationally, the material always deformed in the plastic regime. Since α and β were relatively large coefficients of approximately the same order of magnitude, it was reasoned that the Arrhenius plastic flow model should behave computationally as follows. Define the small parameter ϵ by $\epsilon = 1/\alpha$, and rewrite equation (12) in the form

$$\dot{\gamma}^p = \exp\left\{\frac{\nu T + [\tau - \tau_r(\gamma^p)]}{\epsilon(1+T)}\right\}, \tag{14}$$

where $\nu = \beta/\alpha \approx 1$. Solving for τ as in equation (13),

$$\tau = \tau_r(\gamma^p) + \epsilon(1+T)\ln\dot{\gamma}^p - \nu T, \tag{15}$$

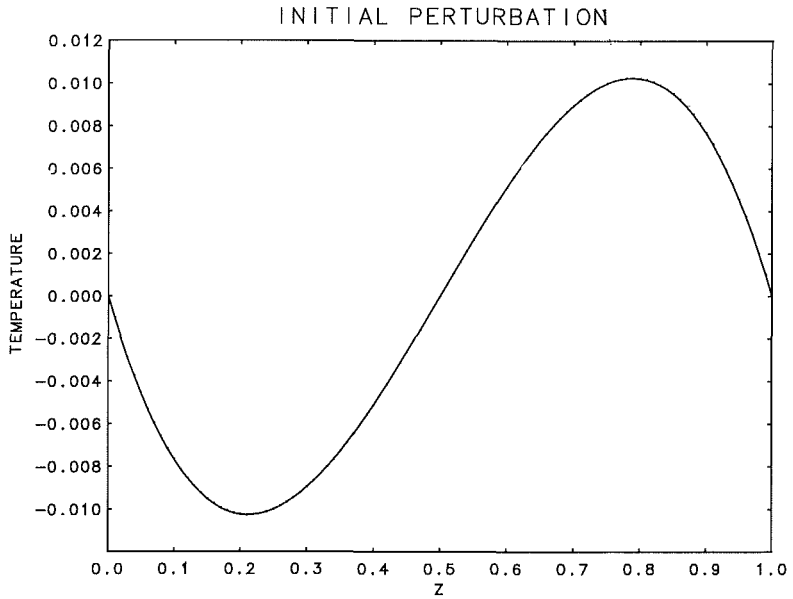


Fig. 1 Initial dimensionless temperature distribution used in both simulations. Maximum and minimum temperature corresponded to approximately 3 K above and below room temperature, respectively.

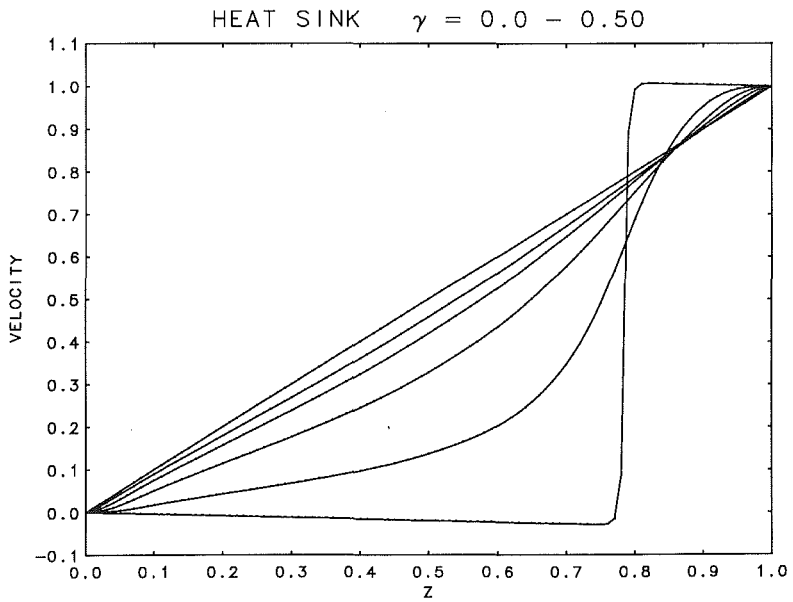


Fig. 2 Plots of twist rate v, as a function of the axial material coordinate Z, for nominal strain values of 0.0–0.50, in increments of 0.10 (see text)

Downloaded 03 May 2010 to 171.66.16.244. Redistribution subject to ASME license or copyright; see http://www.asme.org/terms/Terms_Use.cfm

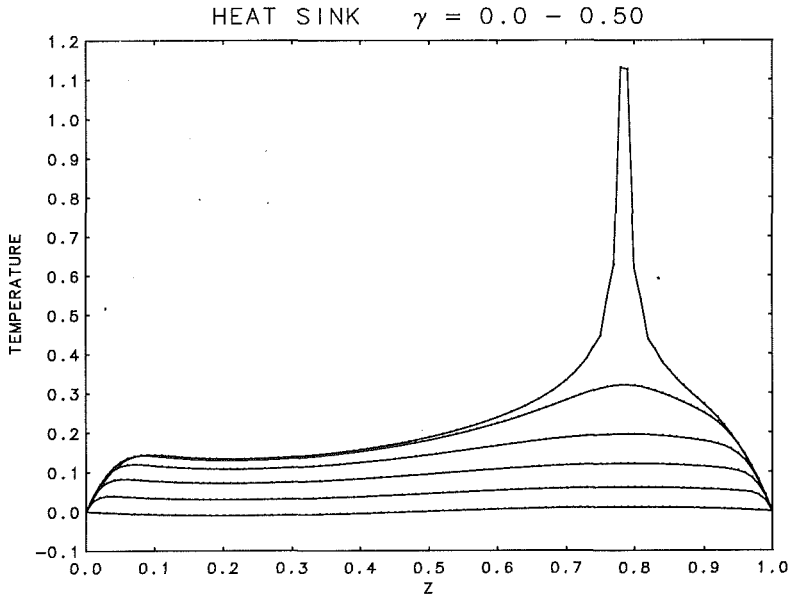


Fig. 3 Plots of dimensionless temperature T, as a function of the axial material coordinate Z, for nominal strain values of 0.0–0.50, in increments of 0.10

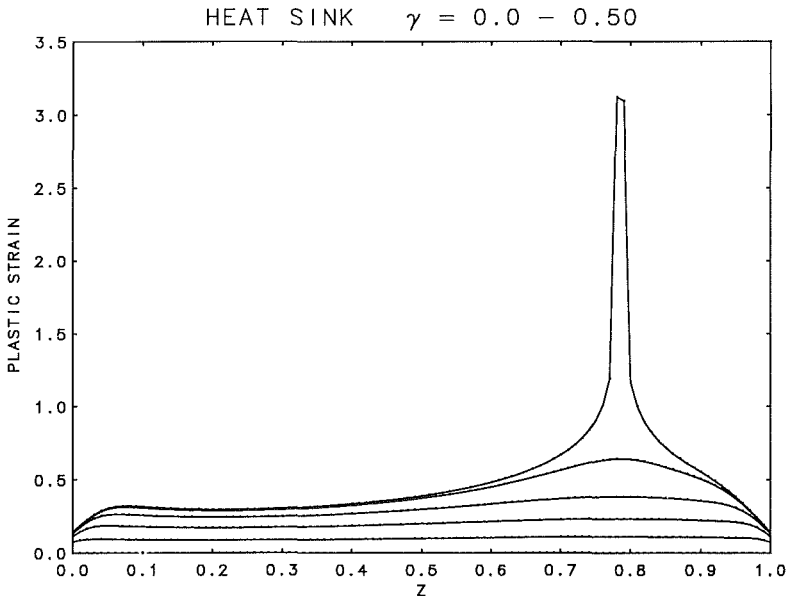


Fig. 4 Plots of plastic strain γ^p, as a function of the axial material coordinate Z, for nominal strain values of 0.0–0.50, in increments of 0.10

it follows that $\tau \approx \tau_r - \nu T$ as $\epsilon \to 0$, unless $\dot{\gamma}^p = O(\exp - 1/\epsilon)$. By equation (14), this latter condition will be satisfied when τ drops below $\tau_r - \nu T$, i.e., when $[\tau - (\tau_r - \nu T)]/(1 + T)$ is negative and $O(1)$ in ϵ. When this condition is satisfied, clearly $0 < \dot{\gamma}^p \ll 1$. Thus, the Arrhenius model equation (12) should give a good approximation to the unloading behavior, $\dot{\gamma}^p = O$.

The method of lines code MOL1D (Hyman (1979)) was chosen for the computer simulations. This software uses a finite difference semi-discretization of the partial derivatives with respect to the material variable Z, to convert the problem into a coupled system of ordinary differential equations (ODE's), and then solves the ODE's using Hindmarsh's (1975) version of the backward-difference method of Gear (1971) for stiff ODE's. This code was chosen because the time derivatives of two of the equations in (5) are multiplied by small parameters, and because the temperature evolution equation is parabolic, so that the resulting system of ODE's can be stiff (see Gear, 1971). Wright and Walter (1987), (1989), and Batra and Kim (1988) used versions of the method of lines based on Gear's method and a semi-discretization using the finite element method.

The initial time in the calculations was simplified by making the assumption that, in dimensional variables, $\tau = \tau_y$ and $\gamma = 0$ at $t = 0$. The calculations were all run on a uniform spatial grid of 101 points, so that the mesh width was 25 μm, and the applied dimensional strain rate was $\dot{\gamma}_0 = 1600\ s^{-1}$. The dimensionless parameters in the problem were then as follows, $\alpha = 55$, $\beta = 40$, $\zeta = 0.92 \times 10^{-2}$, $\phi = 0.17 \times 10^{-3}$, $\lambda = 0.14 \times 10^{-2}$, $\mu = 0.64$. Also, the function τ_r was given by $\tau_r = (0.012 + \gamma^p)^n$, where $n = 0.107$. The initial twist and plastic strain fields were assumed to be identically equal to zero; the initial stress was set equal to $(0.012)^n \approx 0.62$; and the initial velocity was assumed to increase linearly from 0 at $Z = 0$ to 1 at $Z = 1$, $v(Z, 0) = Z$, corresponding to a homogeneous initial strain rate of $\dot{\gamma} = 1$. Thus, if the deformation were to remain homogeneous, then

Downloaded 03 May 2010 to 171.66.16.244. Redistribution subject to ASME license or copyright; see http://www.asme.org/terms/Terms_Use.cfm

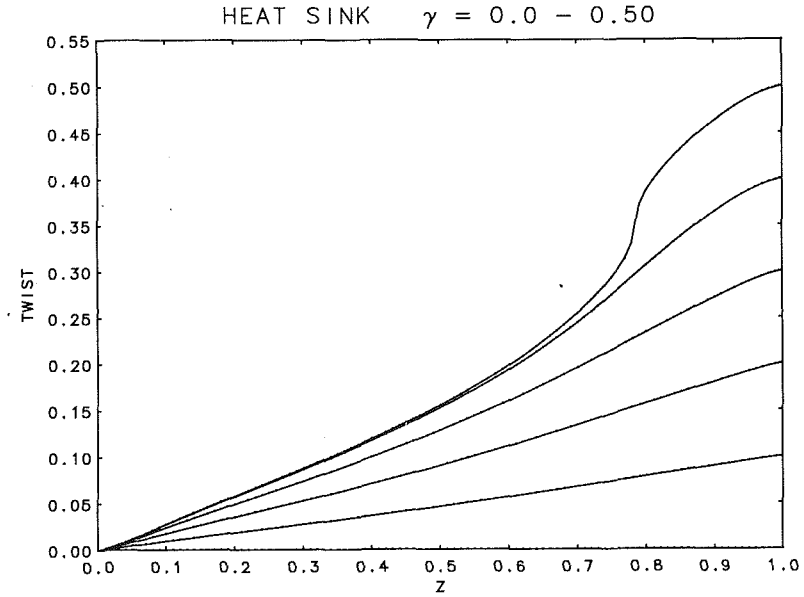


Fig. 5 Plots of total twist (arclength) *s* (see text), as a function of the axial material coordinate *Z*, for nominal strain values of 0.0–0.50, in increments of 0.10

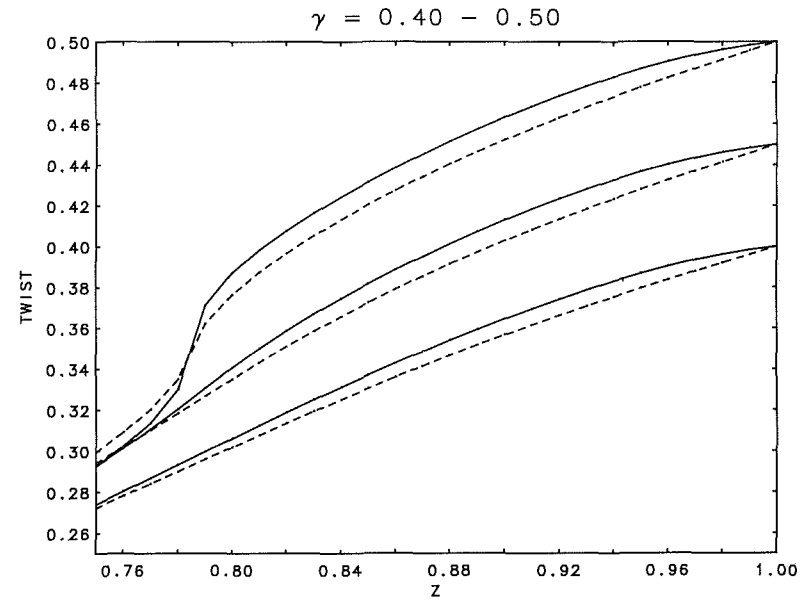


Fig. 6 Comparison of two computer simulations of twist versus *Z* for nominal strain values of 0.4, 0.45, and 0.5, in the region of the adiabatic shear band. Solid curve corresponds to heat sink boundary conditions; dashed curve corresponds to adiabatic boundary conditions. Notice that the band formed earlier and the strain gradient was larger inside the band in the heat sink case.

$\gamma(Z, t)=t$, so the dimensionless time variable would be the same as the homogeneous strain. The terminology "nominal strain" will be used next to mean the twist at the right-hand end of the tube, $s(1, t)=[s(1, t)-s(0, t)]$. This was the dimensionless time, and is what the shear strain would have equaled under conditions of homogeneous simple shear, with adiabatic boundary conditions in temperature. In the following discussion and above most of the figures, this nominal strain is denoted by γ.

The initial temperature distribution for both calculations was given by

$$T(Z, 0)=-\frac{16}{75}Z\left(Z-\frac{1}{2}\right)(Z-1),$$

which has a minimum and a maximum on $0<Z<1$ of approximately -0.01 and 0.01 at $Z\approx 0.21$ and 0.79, respectively (see Fig. 1), which corresponded to respective minimum and maximum dimensional temperature perturbations of 3 K below and above the ambient value of 300 K. In the first calculation, the heat sink temperature boundary conditions, equation (8), were used, while in the second calculation, the adiabatic boundary conditions, equation (7), were used. Plots of velocity, temperature, plastic strain, and twist, for nominal strain values of 0-0.5, in increments of 0.1, are given for the heat sink case in Figs. 2 through 5. In Figs. 6 and 7, a comparison is made between the twist and plastic strain fields simulated in the two calculations, in the neighborhood of the shear band. The stress was found to remain homogeneous in Z throughout both calculations, with its peak occurring at approximately $\gamma^p=0.25$

Downloaded 03 May 2010 to 171.66.16.244. Redistribution subject to ASME license or copyright; see http://www.asme.org/terms/Terms_Use.cfm

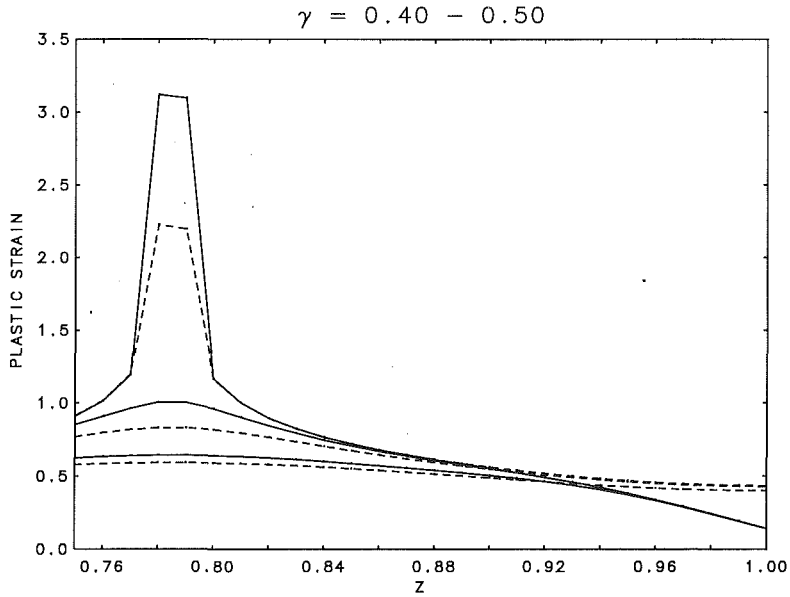


Fig. 7 Comparison of two computer simulations of plastic strain versus Z for nominal strain values of 0.4, 0.45, and 0.5, in the region of the adiabatic shear band. Solid curve corresponds to heat sink boundary conditions; dashed curve corresponds to adiabatic boundary conditions. Notice that, in the heat sink case, unloading occurred earlier, and from the boundaries inward towards the region of localization, with the result that the accumulated plastic strain was larger.

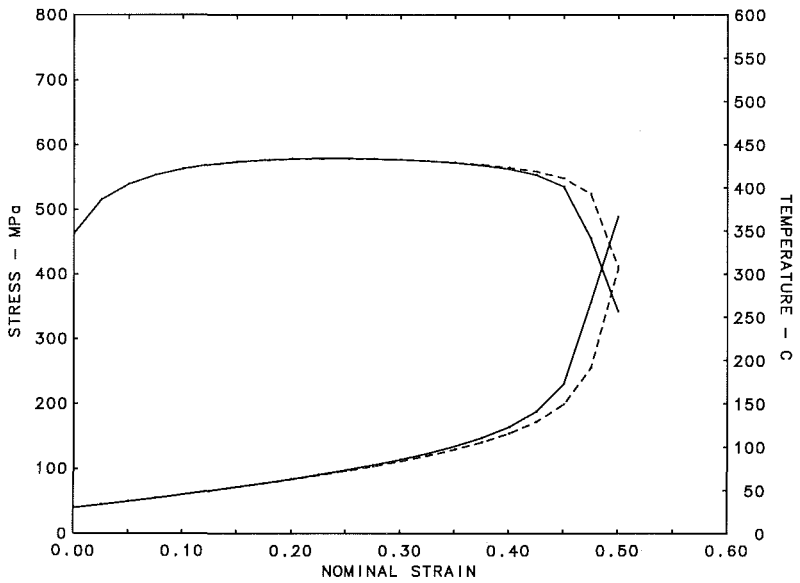


Fig. 8 Comparison, in dimensional variables, of stress in MPa (upper curves, scale on left) and peak temperature in degrees C (lower curves, scale on right) versus nominal strain in the two calculations; solid curve corresponds to heat sink boundary conditions, and dashed curve corresponds to adiabatic boundary conditions.

(Fig. 8); this supports taking the "quasi-static" asymptotic limit $\phi \to 0$ in equation (5), with ϵ held fixed in equation (14) (see Burns, 1985, 1989a).

While the differences between the two calculations were not great, the corresponding peak plastic strain was found to be about 1/3 larger in the heat sink case (Fig. 7), and the shear band thickness in both cases was found to be no greater than two computational mesh widths (Fig. 7 and 9), which means it was less than 50 μm. To resolve this width any finer would require doubling or tripling the fixed mesh width. The band width measured by Marchand and Duffy during Stage III was found to be about 20 μm. At $\gamma = 0.5$, the corresponding dimensional temperature in the heat sink case was calculated to be approximately 366°C. This is about 1/5 less than the measured peak values reported by Marchand and Duffy (1988, Tab. 5) during Stage III. The temperature and peak plastic strain values would have continued to grow had the calculations been run to a higher nominal strain. A final value of $\gamma = 0.5$ was chosen here, to agree with a typical maximum nominal strain achieved in the tests of Marchand and Duffy (1988, Tab. 4 and 5), In Fig. 8, the stress, which was always homogeneous in Z, and the peak temperature from the two simulations are plotted against the nominal strain in dimensional variables. The overall features of the two sets of curves are in good

Downloaded 03 May 2010 to 171.66.16.244. Redistribution subject to ASME license or copyright; see http://www.asme.org/terms/Terms_Use.cfm

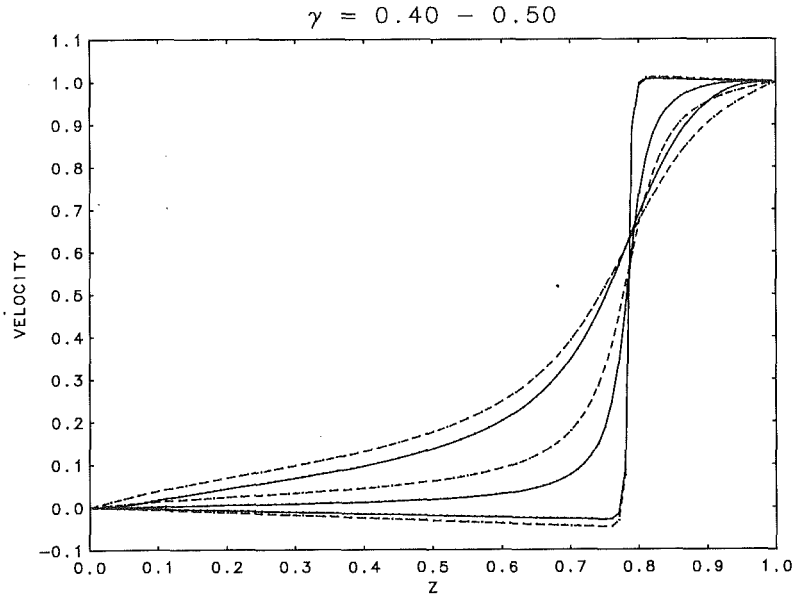


Fig. 9 *Comparison of the computed twist rates versus Z for nominal strain values of 0.4, 0.45, and 0.5, in the two simulations. Solid curve corresponds to heat sink boundary conditions; dashed curve corresponds to adiabatic boundary conditions. Notice that, in both cases, the unloading was rigid, i.e., to a good approximation, $\partial v/\partial Z = 0$. However, in the heat sink case, the unloading occurred earlier, and propagated from the boundaries inward, in contrast with the adiabatic case, where the unloading occurred later, and simultaneously outside the region of localization.*

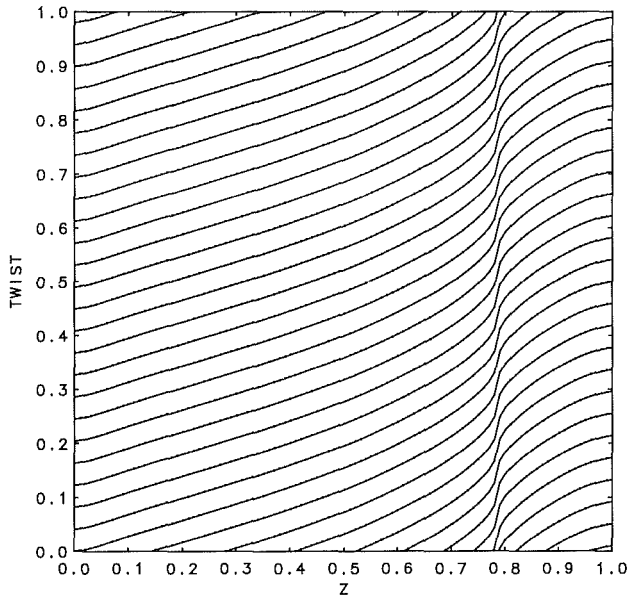


Fig. 10 **Parallel copies of the graph of twist versus *Z* at a nominal strain of 0.5 (top curve in Fig. 5), plotted on a scale of .98 lines per centimeter**

qualitative agreement with those obtained from experiment by Marchand and Duffy (1988, Fig. 12), until well into Stage III of the localization process. In Fig. 10, the twist versus Z at a nominal strain of 0.5 (the top curve in Fig. 5) has been plotted parallel to itself at a density of 98 lines per centimeter, to coincide with the corresponding experimental photographs published by Marchand and Duffy (1988, especially Fig. 13(3)). Once again, the good qualitative and approximate quantitative agreement with experiment is encouraging. It should be remembered, however, that the model used here cannot account for the late-time dependence of the twist field on the Langrangian material coordinate Θ.

The most interesting difference between the two calculations was that the details of the shear band evolution were found to be different in the two cases (Figs. 7 through 9). In both cases, when unloading occurred, it appeared to be rigid, in the sense that $\partial v/\partial Z \approx 0$ (see Fig. 9, which compares the computed twist rates in the two simulations at strains of 0.4, 0.45, and 0.5). This supports taking the asymptotic limit $\zeta \to 0$ in equation (5), as is often done in interpreting data from the torsion test (see, e.g., McMeeking (1982), Shrivastava et al., (1982), Hartley and Duffy, 1985). In the adiabatic case, however, rigid unloading was found to occur simultaneously away from a small neighborhood of the region of strain localization, while in the heat sink case, rigid unloading started earlier, at both ends of the tube, which were cooler, and moved inward, towards the region of localization. This can be seen in Fig. 7, and most clearly in Fig. 9. In the heat sink case, this moving boundary of rigid unloading was caused by conductive heat transfer through the isothermal tube boundaries. Even though the dimensionless thermal diffusivity parameter λ (equation (6)) was very small ($\approx 10^{-3}$), the ends of the tube necessarily remained at a lower temperature, so that once the deformation process became unstable, the flow surface for the material closest to the tube ends was at a higher stress state. Stress equilibrium then caused this region to unload first; next, the material adjacent to the unloaded region began to unload, and so on. This had the effect of concentrating the plastic work into a smaller region earlier than in the adiabatic case, which accounts for the larger final strain and temperature in this case.

5 Discussion and Concluding Remarks

Two computer simulations of a one-dimensional model of the high strain-rate torsion test have been presented, using an Arrhenius model of the plastic flow surface for HY-100 steel, based on the experimental data of Marchand and Duffy (1988). The first simulation treated the flanges on the thin-walled tubes as isothermal heat sinks, while the second simulation treated

Downloaded 03 May 2010 to 171.66.16.244. Redistribution subject to ASME license or copyright; see http://www.asme.org/terms/Terms_Use.cfm

the flanges as adiabatic insulators. It has been demonstrated that, in the heat sink case, the mechanism for localization into a single adiabatic shear band is different from that in the adiabatic case. Assuming that the flanges on the tubes are better approximated as heat sinks, as Marchand and Duffy believed was true for their experiments, it has thus been shown that a plausible mechanism for shear band formation during the high strain-rate torsion test is a moving boundary of rigid unloading, starting from the ends of the tube, caused by heat conduction through the tube flanges.

Even if there were more than one peak in the assumed initial temperature distribution, localization would have occurred in the hottest region of the material once the deformation became unstable, so that once again a single shear band would have formed (Burns, 1988b)), except in the unlikely case that there were identically equal peaks in the initial temperature distribution. Also, based on additional unpublished numerical work, if it were assumed that there was initially a temperature gradient across the tube, so that one flange was hotter than the other (perhaps due to thermoelastic effects during the initial loading process), then the deformation would still be found to localize, in both the adiabatic and heat sink cases, but with the difference that, in the adiabatic case, localization would occur right at the end of the tube adjacent to the hotter flange, while in the heat sink case, heat conduction through the flange would cause localization to occur inside the tube, some distance away from the hotter flange. Finally, if the calculations were run further in time, the stress would have begun to drop off less rapidly and the temperature would have begun to increase less rapidly with increasing nominal strain, which was not observed in the experiments, indicating that the one-dimensional model would no longer be useful as a model of the torsion test.

As discussed in Section 4, the Arrhenius model used here in equation (14) had the form $\dot{\gamma}^p = \exp\,[f(\tau, \gamma^p, T)/\epsilon T]$, where ϵ was a small dimensionless parameter. Because of this, it would have been nice to connect the strain localization problem discussed here with some of the modeling of thermal explosions which has been done in the mathematical theory of combustion, using activation-energy asymptotics (see, e.g., Kapila, 1983). This did not appear to be possible, for the following reason. The simulations indicated that it was valid to assume that $\zeta = 0$ in equation (5). Because of this, in the region where plastic flow occurred, the plastic strain rate did not grow like $\exp 1/\epsilon$, so that the temperature did not increase as rapidly as in a thermal explosion, i.e., like the solution of

$$\dot{T} = \frac{\epsilon}{b}\,(1 + b - T)\exp\left(\frac{T-1}{\epsilon T}\right), \quad T(0) = 1,$$

as $\epsilon \to 0$, for some positive constant b.

Acknowledgments

It is a pleasure to acknowledge helpful conversations with R. C. Batra of the University of Missouri-Rolla, J. Duffy of Brown University, D. G. Lasseigne of Old Dominion University, P. H. Leo of the University of Minnesota, and T. W. Wright of the U. S. Army Ballistics Research Laboratory. Also, helpful suggestions on improving the exposition of this paper by J. T. Fong of the National Institute of Standards and Technology and an unknown referee are gratefully acknowledged.

References

Batra, R. C., 1987, "The Initiation and Growth of, and the Interaction Among, Adiabatic Shear Bands in Simple and Dipolar Materials," *Int. J. Plasticity*, Vol. 3, pp. 75–89.

Batra, R. C., and Kim, C. H., 1989, "Adiabatic Shear Banding in Elastic-Viscoplastic Nonpolar and Dipolar Materials," *Int. J. Plasticity*, Vol. 5, to appear.

Burns, T. J., 1985, "Approximate Linear Stability Analysis of a Model of Adiabatic Shear Band Formation," *Quart. Appl. Math.*, Vol. 43, pp. 65–84.

Burns, T. J., 1989a, "Similarity and Bifurcation in Unstable Viscoplastic Shear," *SIAM J. Appl. Math.*, Vol. 49, pp. 314–329.

Burns, T. J, 1989b, "A Mechanism for High-Strain-Rate Shear Band Formation," *Proceedings of the American Physical Society Topical Conference on Shock Compression of Condensed Matter*, Albuquerque, New Mexico, August 14–18, 1989, ed. by S. C. Schmidt et al., to appear.

Clifton, R. J., Duffy, J., Hartley, K. A., and Shawki, T. G., 1984, "On Critical Conditions for Shear Band Formation at High Rates," *Scripta Metall.*, Vol. 18, pp. 443–448.

Chen, H. Tz., Malek-Madani, R., and Douglas, A. S., 1989, "An Asymptotic Stability Condition for Inhomogenous Simple Shear," *Quart. Appl. Math.*, Vol. 47, pp. 247–262.

Costin, L. S., Crisman, E. E., Hawley, R. H., and Duffy, J., 1979, "On the Localization of Plastic Flow in Mild Steel Tubes under Dynamic Torsional Loading," *Inst. Phys. Conf. Ser. No. 47*, Oxford, U.K., pp. 90–100.

Eleiche, A. M, 1981, "Strain-rate History and Temperature Effects on the Torsional-shear Behavior of a Mild Steel," *Experimental Mech.*, Vol. 21, pp. 285–294.

Estrin, Y., and Kubin, L. P., 1980, "Criterion for Thermomechanical Instability of Low Temperature Plastic Deformation," *Scripta Metall.*, Vol. 14, pp. 1359–1364.

Gear, C. W., 1971, *Numerical Initial Value Problems in Ordinary Differential Equations*, Prentice-Hall, Englewood Cliffs, N.J.

Hartley, K. A., and Duffy, J., 1985, "The Torsional Kolsky (Split-Hopkinson) Bar," *Metals Handbook*, Vol. 8, American Society for Metals, Metals Park, Ohio, pp. 218–228.

Hartley, K. A., Duffy, J., and Hawley, R. H., 1987, "Measurement of the Temperature Profile During Shear Band Formation in Steels Deforming at High Strain Rates," *J. Mech. Phys. Solids*, Vol. 35, pp. 283–301.

Hindmarsh, A. C., 1975, *GEARB: Solution of Ordinary Differential Equations Having Banded Jacobian*, Lawrence Livermore National Labortatory Report UCID-30059, Rev. 1, Livermore, CA.

Hyman, J. M,. 1979, *MOL1D: A General Purpose Subroutine Package for the Numerical Solution of Partial Differential Equations*, Los Alamos National Laboratory Manual LA-7595-M, Los Alamos, N.M.

Kapila, A. K., 1983, *Asymptotic Treatment of Chemically Reacting Systems*, Pitman, Boston.

Kochs, U. F., Argon, A. S., and Ashby, M. F., 1975, *Thermodynamics and Kinetics of Slip*, Pergamon Press, Oxford, U.K.

Likonski, J., 1977, "Plastic Flow of a Tube under Adiabatic Torsion," *Bull. Acad. Polonaise Sci.*, Vol. 25, pp. 7–14.

Marchand, A., and Duffy, J., 1988, "An Experimental Study of the Formation Process of Adiabatic Shear Bands in a Structural Steel," *J. Mech. Phys. Solids*, Vol. 36, pp. 251–283.

Maddocks, J. H., and Malek-Madani, R., 1989, "Stability of Localized Steady-State Solutions in Thermoplasticity," to appear.

McMeeking, R. M., 1982, "The Finite Strain Tension Torsion Test of a Thin-Walled Tube of Elastic-Plastic Material," *Int. J. Solids Structures*, Vol. 18, pp. 199–204.

Molinari, A., and Clifton, R. J., 1987, "Analytical Characterization of Shear Localization in Thermoviscoplastic Materials," ASME JOURNAL OF APPLIED MECHANICS, Vol. 54, pp. 806–812.

Oswatitsch, K. A., 1963, "Der gegenwärtige Stand der Strömungslehre," *Österr. Ing. Zeit.*, Vol. 6, pp. 421–426.

Rogers, H. C., 1979, "Adiabatic Plastic Deformation," *Ann. Rev. Mat. Sci.*, Vol. 9, pp. 283–311.

Shawki, T. G., Clifton, R. J., and Majda, G., 1983, "Analysis of Shear Strain Localization in Rate Sensitive Materials," Technical Report DAAG-29-81-0121/3, Division of Engineering, Brown University, Providence, R.I.

Shrivastava, S. C., Jonas, J. J., and Canova, G., 1982, "Equivalent Strain in Large Deformation Torsion Testing: Theoretical and Practical Considerations," *J. Mech. Phys. Solids*, Vol. 30, pp. 75–90.

Wallace, D. C., 1981, "Irreversible Thermodynamics of Flow in Solids," *Phys. Rev.*, Vol. B22, pp. 1477–1486.

Wallace, D. C., 1985, *Thermoelastic-Plastic Flow in Solids*, Los Alamos National Laboratory Report LA-10119, Los Alamos, N.M.

Wright, T. W., 1987, "Steady Shearing in a Viscoplastic Solid," *J. Mech. Phys. Solids*, Vol. 35, pp. 269–282.

Wright, T. W., and Batra, R. C., 1985, "The Initiation and Growth of Adiabatic Shear Bands," *Int. J. Plasticity*, Vol. 1, pp. 205–212.

Wright, T. W., and Walter, J. W., 1987, "On Stress Collapse in Adiabatic Shear Bands," *J. Mech. Phys. Solids*, Vol. 35, pp. 701–720.

Wright, T. W., and Walter, J. W., 1989, "Adiabatic Shear Bands in One Dimension," U.S. Army Ballistics Research Laboratory Memorandum Report BRL-MR-3759, Aberdeen Proving Ground, Md., to appear in *Proc. of 4th Oxford Conference on Mechanical Properties at High Rates of Strain*.

Zener, C., and Hollomon, J. H., 1944, "Effect of Strain Rate Upon Plastic Flow of Steel," *J. Appl. Phys.*, Vol. 15, pp. 22–32.

Downloaded 03 May 2010 to 171.66.16.244. Redistribution subject to ASME license or copyright; see http://www.asme.org/terms/Terms_Use.cfm

Y. Mikata[1]
Assoc. Mem. ASME

S. Nemat-Nasser
Fellow ASME

Center of Excellence for Advanced Materials,
Department of Applied Mechanics
and Engineering Sciences,
University of California, San Diego,
La Jolla, CA 92093

Elastic Field Due to a Dynamically Transforming Spherical Inclusion

As a first step towards a systematic study of the interaction between a stress-pulse traveling in transformation toughened ceramics and possible phase transformation of zirconia particles, a dynamic inclusion problem is investigated. An exact closed-form solution is obtained for the case of a spherical inclusion. With this result, the dynamic Eshelby tensors for the inside and outside fields of the spherical inclusion are defined and determined. It is confirmed that the static Eshelby tensor is obtained as a static limit of the dynamic Eshelby tensor. It is found in the numerical results that the frequency of the dynamic inclusion has a relatively large influence on the amplitudes of the stress components inside and outside the inclusion.

1 Introduction

Transformation toughening of ceramics has attracted considerable attention (see Chen and Reyes Morel (1986), Garvie, Hannink, and Pascoe (1975), Lange (1982), and Marshall and James (1986)) in recent years. The key mechanism in this toughening is the stress-induced phase transformation of a zirconia particle, which is accompanied by volumetric expansion. Due to this expansion, the composite material consisting of a zirconia particle within a brittle matrix becomes more resistant to fracturing. While this problem has been studied for quasi-static loadings (see Budiansky, Hutchinson, and Lambropoulos (1983), Lambropoulos (1986), and McMeeking and Evans (1982)), the corresponding dynamic case has remained essentially untouched.

As a first step toward understanding the effect of a traveling stress pulse on phase transformation of the zirconia particle, a dynamic inclusion problem is investigated. Here we use the term "inclusion" to denote a subset of a matrix, which has an eigenstrain (or transformation strain), but has the same elastic properties as the matrix (see Eshelby (1957)). Our objective is to determine the elastic field in and around the inclusion which is embedded in an infinite isotropic elastic matrix, and which is experiencing spatially uniform time-harmonic transformation strains. In principle, any form of transformation strain in time can be dealt with by using superposition of time-harmonic transformation strains. In practice, however, this would be very complicated, and often the frequency response is used directly to extract needed physical information. Indeed, since in certain cases the phase transformation is reversible (see Marshall and James (1986)), the time-harmonic solution provides direct useful information. The formal solution of this problem leads to an integral (see Mura (1982)) whose evaluation, in general, is very difficult. Some attempts (see Fu and Mura (1982)) have been made to evaluate this integral asymptotically in the Rayleigh limit in an effort to determine the elastodynamic field of an ellipsoidal inhomogeneity (see Fu and Mura (1983)).

As will be shown in this paper, the integral can be evaluated analytically in a closed form for a spherical inclusion. Even though the calculation is fairly straightforward, to the best of the authors' knowledge, it seems to have remained unnoticed. With this result, the dynamic Eshelby tensor, which is a dynamic analogue of Eshelby's static tensor (see Eshelby (1957, 1959)) is defined and determined for the spherical inclusion.

The time-harmonic solution for a dynamically transforming inclusion is a fundamental problem with broad applications. Even though in this investigation dynamic phase transformation is emphasized in order to motivate the considered problem and provide a concrete example, the solution has relevance to other problems, such as thermal stresses under a rapidly changing temperature field, and dynamic plasticity of heterogeneous solids.

2 Dynamic Inclusion Problem

Consider an infinite (i.e., R^3) isotropic elastic medium containing a region Ω (see Fig. 1) with an eigenstrain (or transformation strain) e^*_{ij}. The governing equations for determining the elastic fields in R^3 are

$$\begin{aligned} \sigma_{ij,j} &= \rho \ddot{u}_i, \\ \sigma_{ij} &= C_{ijkl}(e_{kl} - e^*_{kl}), \\ e_{kl} &= \frac{1}{2}(u_{k,l} + u_{l,k}), \end{aligned} \tag{1}$$

where ρ is the mass density and C_{ijkl} is the elasticity tensor of the medium

$$C_{ijkl} = \mu(\delta_{ik}\delta_{jl} + \delta_{il}\delta_{jk}) + \lambda\delta_{ij}\delta_{kl}. \tag{2}$$

[1]Presently, Assistant Professor, Department of Mechanical Engineering and Mechanics, Old Dominion University, Norfolk, VA 23529-0247.

Contributed by the Applied Mechanics Division of THE AMERICAN SOCIETY OF MECHANICAL ENGINEERS for presentation at the Winter Annual Meeting, Dallas, Texas, Nov. 25–30, 1990.

Discussion on this paper should be addressed to the Technical Editor, Leon M. Keer, The Technological Institute, Northwestern University, Evanston, IL 60208, and will be accepted until two months after final publication of the paper itself in the JOURNAL OF APPLIED MECHANICS. Manuscript received by the ASME Applied Mechanics Division, July 11, 1988; final revision, Feb. 13, 1989.

Paper No. 90-WA/APM-47.

Copyright © 1990 by ASME
Downloaded 03 May 2010 to 171.66.16.244. Redistribution subject to ASME license or copyright; see http://www.asme.org/terms/Terms_Use.cfm

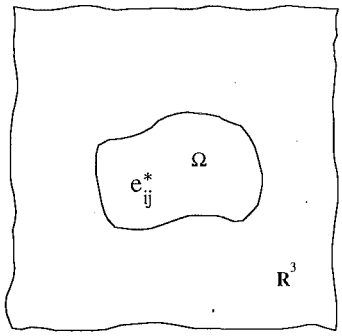


Fig. 1 Inclusion Ω with eigenstrain e^*_{ij}

The following eigenstrain is considered:

$$e^*_{kl}(\mathbf{x},t) = e^*_{kl}(\mathbf{x})e^{-i\omega t},$$

$$e^*_{kl}(\mathbf{x}) = \begin{cases} e^{\Omega}_{kl}(\mathbf{x}), & \mathbf{x}\in\Omega \\ 0, & \mathbf{x}\in R^3-\Omega, \end{cases} \tag{3}$$

where ω denotes an angular frequency and t measures time. Since the eigenstrain equation (3) has a harmonic dependence on time, the solution can be expressed as

$$u_i(\mathbf{x},t) = \bar{u}_i(\mathbf{x})e^{-i\omega t}, \tag{4}$$

with similar expressions for the stress and strain fields. Upon substitution of equation (4) into equation $(1)_1$, we have

$$\sigma_{ij,j} + \rho\omega^2 u_i = 0 \tag{5}$$

with equations $(1)_{2,3}$ retaining their initial form. Here, we have omitted the time factor $e^{-i\omega t}$, and have dropped the superposed bars; thus every quantity in equation (5) is a spatial part of the solution. Equation (5) can be solved by Fourier transform method (see Mura (1982)) and the corresponding displacement field is given by

$$u_i(\mathbf{x}) = -\int_{-\infty}^{\infty} d\mathbf{x}' C_{jlmn} e^*_{mn}(\mathbf{x}') g_{ij,l}(\mathbf{x}'-\mathbf{x}), \tag{6}$$

$$g_{ij}(\mathbf{x}'-\mathbf{x}) = \frac{1}{4\pi\rho\omega^2 r}\left[\beta^2\delta_{ij}e^{i\beta r} - r\frac{\partial^2}{\partial x_i \partial x_j}\left\{\frac{1}{r}\left(e^{i\alpha r}-e^{i\beta r}\right)\right\}\right], \tag{7}$$

and

$$r = |\mathbf{x}'-\mathbf{x}|,\ \alpha^2 = \frac{\rho\omega^2}{\lambda+2\mu},\ \beta^2 = \frac{\rho\omega^2}{\mu}. \tag{8}$$

If $e^{\Omega}_{kl}(\mathbf{x})$ in equation (3) is constant over Ω, then substituting equation (3) into equation (6), we have

$$u_i(\mathbf{x}) = -C_{mnkl}e^{\Omega}_{kl}\int_{\Omega} d\mathbf{x}' g_{im,n}(\mathbf{x}'-\mathbf{x}). \tag{9}$$

3 Elastic Field Inside the Inclusion

Equation (9) can be rewritten as

$$u_i(\mathbf{x}) = \frac{1}{\rho\omega^2} C_{mnkl}e^{\Omega}_{kl} g_{imn}(\mathbf{x}), \tag{10}$$

$$g_{imn}(\mathbf{x}) = -\frac{1}{4\pi}\left[\delta_{im}\beta^2\frac{\partial}{\partial x_n}f(\mathbf{x},\beta) - \frac{\partial^3}{\partial x_i \partial x_m \partial x_n}\{f(\mathbf{x},\alpha)-f(\mathbf{x},\beta)\}\right], \tag{11}$$

$$f(\mathbf{x},k) = \int_{\Omega} d\mathbf{x}' \frac{e^{ikr}}{r}. \tag{12}$$

Consider now a spherical inclusion Ω with a radius a. Then equation (12) becomes

$$f(\mathbf{x},k) = \begin{cases} f^{in}(\mathbf{x},k), & \mathbf{x}\in\Omega \\ f^{out}(\mathbf{x},k), & \mathbf{x}\in R^3-\Omega, \end{cases} \tag{13}$$

where

$$f^{in}(\mathbf{x},k) = -4\pi\left[\frac{1}{k^2} + \frac{e^{ika}}{k^3}(ika-1)\frac{\sin kx}{x}\right], \tag{14}$$

$$f^{out}(\mathbf{x},k) = -\frac{4\pi}{k^3}(ka\cos ka - \sin ka)\frac{e^{ikx}}{x}, \tag{15}$$

and

$$x = |\mathbf{x}|. \tag{16}$$

In this section, we concentrate on the elastic field inside the inclusion Ω. By substituting equation (14) into equation (11), we have

$$g_{imn}(\mathbf{x}) = \delta_{im}\beta^2\phi^{in}(\beta)I^{in}_{,n}(\mathbf{x},\beta) - \phi^{in}(\alpha)I^{in}_{,lmn}(\mathbf{x},\alpha) + \phi^{in}(\beta)I^{in}_{,lmn}(\mathbf{x},\beta), \tag{17}$$

where

$$\phi^{in}(k) = \frac{e^{ika}}{k^3}(ika-1), \tag{18}$$

$$I^{in}(\mathbf{x},k) = kj_o(kx) = \frac{\sin kx}{x}. \tag{19}$$

Here, $j_o(kx)$ is the spherical Bessel function of order zero. By using equations (2) and (17), equation (10) is rewritten as

$$u_i(\mathbf{x}) = J^{in}_{ikl}(\mathbf{x})e^{\Omega}_{kl},\ \mathbf{x}\in\Omega, \tag{20}$$

where

$$J^{in}_{ikl}(\mathbf{x}) = \frac{1}{\rho\omega^2}\Big[\mu\beta^2\phi^{in}(\beta)\{\delta_{ik}I^{in}_{,l}(\mathbf{x},\beta)+\delta_{il}I^{in}_{,k}(\mathbf{x},\beta)\} - 2\mu\{\phi^{in}(\alpha)I^{in}_{,ikl}(\mathbf{x},\alpha)-\phi^{in}(\beta)I^{in}_{,ikl}(\mathbf{x},\beta)\} + \lambda\delta_{kl}\{\beta^2\phi^{in}(\beta)I^{in}_{,i}(\mathbf{x},\beta) - \phi^{in}(\alpha)I^{in}_{,imm}(\mathbf{x},\alpha)+\phi^{in}(\beta)I^{in}_{,imm}(\mathbf{x},\beta)\}\Big]. \tag{21}$$

The strain field $e_{ij}(\mathbf{x})$ is obtained through equation (20) as

$$e_{ij}(\mathbf{x}) = M^{in}_{ijkl}(\mathbf{x})e^{\Omega}_{kl},\ \mathbf{x}\in\Omega, \tag{22}$$

where

$$M^{in}_{ijkl}(\mathbf{x}) = \frac{1}{2\rho\omega^2}\Big[\mu\beta^2\phi^{in}(\beta)\{\delta_{ik}I^{in}_{jl}(\mathbf{x},\beta)+\delta_{jk}I^{in}_{,il}(\mathbf{x},\beta)+\delta_{il}I^{in}_{,jk}(\mathbf{x},\beta) + \delta_{jl}I^{in}_{,ik}(\mathbf{x},\beta)\} - 4\mu\{\phi^{in}(\alpha)I^{in}_{,ijkl}(\mathbf{x},\alpha)-\phi^{in}(\beta)I^{in}_{,ijkl}(\mathbf{x},\beta)\} + 2\lambda\delta_{kl}\{\beta^2\phi^{in}(\beta)I^{in}_{,ij}(\mathbf{x},\beta)-\phi^{in}(\alpha)I^{in}_{,ijmm}(\mathbf{x},\alpha) + \phi^{in}(\beta)I^{in}_{,ijmm}(\mathbf{x},\beta)\}\Big]. \tag{23}$$

$M^{in}_{ijkl}(\mathbf{x})$ is the dynamic version of Eshelby's tensor for the inside of the sphere. As is seen from equation (23), unlike the static case (see Eshelby (1957)) this tensor varies over the inclusion Ω. The derivatives of $I^{in}(\mathbf{x},k)$, which are needed for the evaluation of J^{in}_{ikl} and M^{in}_{ijkl}, are calculated through equation (19) as

$$\begin{aligned} &I^{in}_{,i}(\mathbf{x},k) = x_i K^{in}_1, \\ &I^{in}_{,ij}(\mathbf{x},k) = \delta_{ij}K^{in}_1 + x_i x_j K^{in}_2, \\ &I^{in}_{,ijk}(\mathbf{x},k) = (x_i\delta_{jk}+x_j\delta_{ki}+x_k\delta_{ij})K^{in}_2 + x_i x_j x_k K^{in}_3, \\ &I^{in}_{,ijkl}(\mathbf{x},k) = (\delta_{ij}\delta_{kl}+\delta_{jk}\delta_{li}+\delta_{ik}\delta_{jl})K^{in}_2, \\ &+(x_i x_j\delta_{kl}+x_j x_k\delta_{li}+x_k x_i\delta_{ij}+x_i x_i\delta_{jk}+x_i x_k\delta_{jl}+x_j x_i\delta_{ik})K^{in}_3 \\ &\qquad + x_i x_j x_k x_l K^{in}_4, \end{aligned} \tag{24}$$

Downloaded 03 May 2010 to 171.66.16.244. Redistribution subject to ASME license or copyright; see http://www.asme.org/terms/Terms_Use.cfm

where

$$K_1^{in} = -\frac{k^2}{x} j_1(kx) = k\frac{\cos kx}{x^2} - \frac{\sin kx}{x^3},$$

$$K_2^{in} = \frac{k^3}{x^2} j_2(kx) = -k^2\frac{\sin kx}{x^3} - 3k\frac{\cos kx}{x^4} + 3\frac{\sin kx}{x^5},$$

$$K_3^{in} = -\frac{k^4}{x^3} j_3(kx) = -k^3\frac{\cos kx}{x^4} + 6k^2\frac{\sin kx}{x^5} + 15k\frac{\cos kx}{x^6} - 15\frac{\sin kx}{x^7},$$

$$K_4^{in} = \frac{k^5}{x^4} j_4(kx) = k^4\frac{\sin kx}{x^5} + 10k^3\frac{\cos kx}{x^6} - 45k^2\frac{\sin kx}{x^7} - 105k\frac{\cos kx}{x^8} + 105\frac{\sin kx}{x^9}. \tag{25}$$

4 Elastic Field Outside the Inclusion

In the same manner as in Section 3, we obtain the displacement and strain fields outside the inclusion as

$$u_i(\mathbf{x}) = J_{ikl}^{out}(\mathbf{x}) e_{kl}^{\Omega}, \quad \mathbf{x}\in R^3 - \Omega, \tag{26}$$

$$e_{ij}(\mathbf{x}) = M_{ijkl}^{out}(\mathbf{x}) e_{kl}^{\Omega}, \quad \mathbf{x}\in R^3 - \Omega, \tag{27}$$

where $J_{ikl}^{out}(\mathbf{x})$ and $M_{ijkl}^{out}(\mathbf{x})$ are defined in exactly the same manner as those in equations (21) and (23) except for the change in the superscript (i.e., in → out), and

$$\phi^{out}(k) = \frac{1}{k^3}(ka\cos ka - \sin ka), \tag{28}$$

$$I^{out}(\mathbf{x},k) = ikh_0^{(1)}(kx) = \frac{e^{ikx}}{x}. \tag{29}$$

Here, $h_o^{(1)}(kx)$ is the spherical Hankel function of the first kind of order zero. The derivatives of $I^{out}(\mathbf{x}, k)$ are calculated in a similar manner as those in equation (24), and

$$K_1^{out} = -\frac{ik^2}{x} h_1^{(1)}(kx) = \left[\frac{ik}{x^2} - \frac{1}{x^3}\right] e^{ikx},$$

$$K_2^{out} = \frac{ik^3}{x^2} h_2^{(1)}(kx) = \left[-\frac{k^2}{x^3} - \frac{3ik}{x^4} + \frac{3}{x^5}\right] e^{ikx},$$

$$K_3^{out} = -\frac{ik^4}{x^3} h_3^{(1)}(kx) = \left[-\frac{ik^3}{x^4} + \frac{6k^2}{x^5} + \frac{15ik}{x^6} - \frac{15}{x^7}\right] e^{ikx},$$

$$K_4^{out} = \frac{ik^5}{x^4} h_4^{(1)}(kx) = \left[\frac{k^4}{x^5} + \frac{10ik^3}{x^6} - \frac{45k^2}{x^7} - \frac{105ik}{x^8} + \frac{105}{x^9}\right] e^{ikx}. \tag{30}$$

In the original paper by Eshelby (1957), Eshelby's tensor was defined only for the inside of the inclusion. We can, however, call $M_{ijkl}^{out}(\mathbf{x})$ as the dynamic Eshelby tensor for the outside of the sphere.

5 Static Limit

The static Eshelby tensor can be obtained from the dynamic Eshelby tensor in the limit of $\omega \to 0$. To do this we need the asymptotic expressions of K_1^{in} ($i = 1 \sim 4$) in equation (25) as $k \to 0$; these are:

$$K_1^{in} = -\frac{k^3}{3},$$

$$K_2^{in} = \frac{k^5}{3\cdot 5},$$

$$K_3^{in} = -\frac{k^7}{3\cdot 5\cdot 7}, \quad \text{as } k\to 0$$

$$K_4^{in} = \frac{k^9}{3\cdot 5\cdot 7\cdot 9}, \tag{31}$$

Substituting equations (18), (24), and (31) into equation (23) we obtain, after some algebraic manipulation,

$$\lim_{\omega\to 0} M_{ijkl}^{in}(\mathbf{x}) = \frac{5\nu - 1}{15(1-\nu)}\delta_{ij}\delta_{kl} + \frac{4-5\nu}{15(1-\nu)}(\delta_{ik}\delta_{jl} + \delta_{il}\delta_{jk}) \tag{32}$$

which is the static Eshelby tensor given in Mura (1982).

In a similar manner, the static Eshelby tensor for the outside of the sphere can be obtained. To this end, we first report the asymptotic expressions of K_i^{out} ($i = 1 \sim 4$) in equation (30) as

$$K_1^{out} = -\frac{1}{x^3} - \frac{k^2}{2x},$$

$$K_2^{out} = \frac{3}{x^5} + \frac{k^2}{2x^3}, \quad \text{as } k\to 0$$

$$K_3^{out} = -\frac{15}{x^7} - \frac{3k^2}{2x^5},$$

$$K_4^{out} = \frac{105}{x^9} + \frac{15k^2}{2x^7}, \tag{33}$$

Substituting equations (24), (28), and (33) into equation (23) after changing the superscript "in" to "out," we find

$$\lim_{\omega\to 0} M_{ijkl}^{out}(\mathbf{x}) = \frac{a^3}{6}\Bigg[D_{ijkl} + \frac{1}{1-\nu}\left\{-A_{ijkl}\left(\frac{1}{x^3} - \frac{3a^2}{5x^5}\right) + 3B_{ijkl}\left(\frac{1}{x^5} - \frac{a^2}{x^7}\right) - 3C_{ijkl}\left(\frac{5}{x^7} - \frac{7a^2}{x^9}\right)\right\} + \frac{\nu}{(1-\nu)(1-2\nu)}\delta_{kl}\left\{-A_{ijmm}\left(\frac{1}{x^3} - \frac{3a^2}{5x^5}\right) + 3B_{ijmm}\left(\frac{1}{x^5} - \frac{a^2}{x^7}\right) - 3C_{ijmm}\left(\frac{5}{x^7} - \frac{7a^2}{x^9}\right)\right\}\Bigg], \tag{34}$$

where

$$A_{ijkl} = \delta_{ij}\delta_{kl} + \delta_{ik}\delta_{jl} + \delta_{il}\delta_{jk},$$

$$B_{ijkl} = x_ix_j\delta_{kl} + x_jx_k\delta_{li} + x_kx_l\delta_{ij} + x_ix_l\delta_{jk} + x_ix_k\delta_{jl} + x_jx_l\delta_{ik},$$

$$C_{ijkl} = x_ix_jx_kx_l,$$

$$D_{ijkl} = \frac{2}{x^3}\left(\delta_{ik}\delta_{jl} + \delta_{il}\delta_{jk} + \frac{2\nu}{1-2\nu}\delta_{ij}\delta_{kl}\right) - \frac{3}{x^5}\left(x_ix_k\delta_{jl} + x_ix_l\delta_{jk} + x_jx_k\delta_{il} + x_jx_l\delta_{ik} + \frac{4\nu}{1-2\nu}x_ix_j\delta_{kl}\right). \tag{35}$$

6 Numerical Results and Discussion

Let us consider the following eigenstrain:

$$e_{kl}^{\Omega} = e^{\Omega}\delta_{kl}. \tag{36}$$

Substituting equations (22) and (27) along with equation (36) into equation $(1)_2$, we obtain

$$\frac{\sigma_{ij}(\mathbf{x})}{\mu e^{\Omega}} = 2M_{ijkk}^{in} + \frac{\lambda}{\mu}M_{kkmm}^{in}\delta_{ij} - \left(2 + \frac{3\lambda}{\mu}\right)\delta_{ij}, \quad \mathbf{x}\in\Omega,$$

$$\frac{\sigma_{ij}(\mathbf{x})}{\mu e^{\Omega}} = 2M_{ijkk}^{out} + \frac{\lambda}{\mu}M_{kkmm}^{out}\delta_{ij} \quad \mathbf{x}\in R^3 - \Omega. \tag{37}$$

Equations $(37)_1$ and $(37)_2$ represent the spatial part of a non-dimensionalized stress field both inside and outside the inclu-

Downloaded 03 May 2010 to 171.66.16.244. Redistribution subject to ASME license or copyright; see http://www.asme.org/terms/Terms_Use.cfm

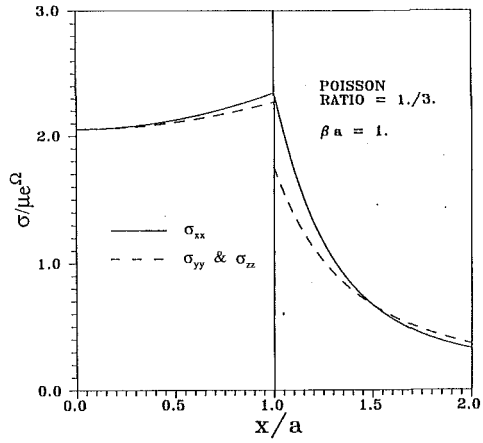


Fig. 2 Stress amplitude distributions along x-axis for $\beta a = 1$

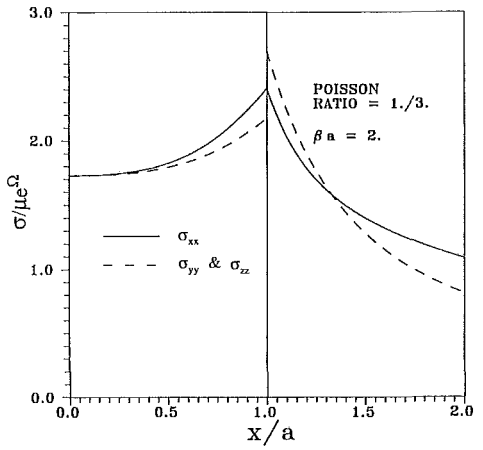


Fig. 3 Stress amplitude distributions along x-axis for $\beta a = 2$

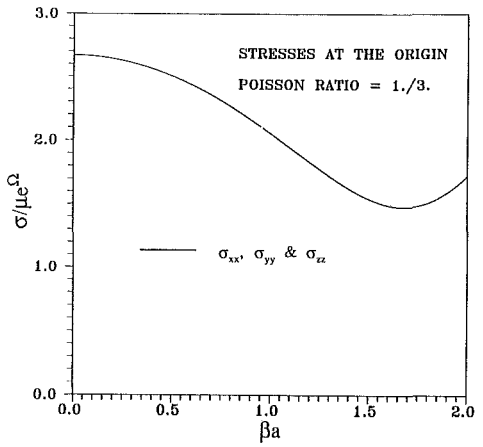


Fig. 4 Stress amplitude variations with βa at the origin

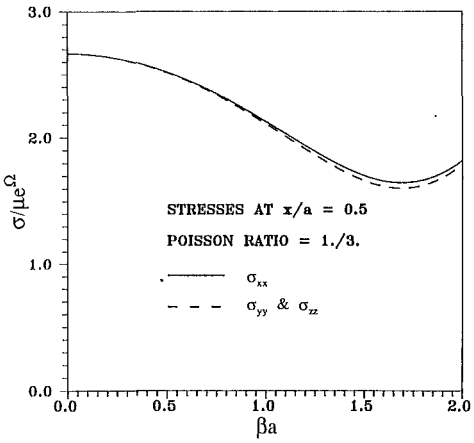


Fig. 5 Stress amplitude variations with βa at $x/a = 0.5$

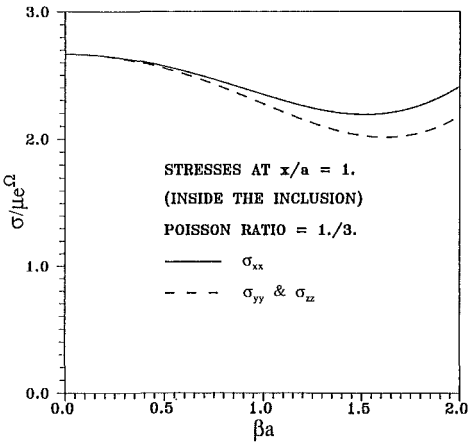


Fig. 6a Stress amplitude variations with βa at $x/a = 1$ (inside the inclusion)

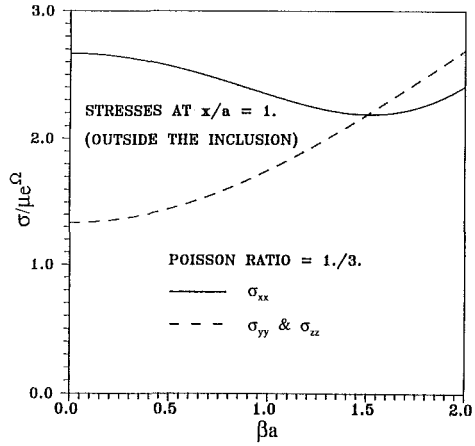


Fig. 6b Stress amplitude variations with βa at $x/a = 1$ (outside the inclusion)

sion. By using equations (23) and $(37)_1$, the stresses at the origin are evaluated as

$$\frac{\sigma_{ij}(0)}{\mu e^{\Omega}} = -2\,\frac{1+\nu}{1-2\nu}\,\delta_{ij}\left[\frac{1}{3}\,\frac{1+\nu}{1-\nu}\,e^{i\alpha a}(i\alpha a-1)+1\right]. \qquad (38)$$

In Figs. 2 and 3, the nondimensionalized stress amplitudes (i.e., the absolute values of equations $(37)_1$ and $(37)_2$) are shown along the x-axis for $\beta a = 1$ and 2, respectively. Poisson's ratio is taken as 1/3 here and throughout the following numerical examples. It is seen from Figs. 2 and 3 that the stress amplitudes are largest at the boundary of the spherical inclusion. In Figs. 4–6, the nondimensionalized stress amplitudes are shown for various values of the nondimensional wave number βa at the origin, at $x/a = 0.5$, and at the boundary $x/a = 1$, respectively. The calculation of Fig. 4 is based on equation (38). It is found from Figs. 4–6 that the stress amplitudes at different places have similar variations with respect to $\beta a \in [0, 2]$, except for σ_{yy} and σ_{zz} just outside the inclusion.

Downloaded 03 May 2010 to 171.66.16.244. Redistribution subject to ASME license or copyright; see http://www.asme.org/terms/Terms_Use.cfm

Acknowledgment

This work has been supported by the U.S. Army Research Office under Contract No. DAAL-03-86-K-0169 to the University of California, San Diego.

References

Budiansky, B., Hutchinson, J. W., and Lambroupoulos, J. C., 1983, "Continuum Theory of Dilant Transformation Toughening in Ceramics," *Int. J. Solids Structures*, Vol. 19, No. 4, pp. 337–355.

Chen, I-Wei, and Reyes Morel, P. E., 1986, "Implications of Transformation Plasticity in ZrO_2-Containing Ceramics: I, Shear and Dilatation Effects," *J. Am. Ceram. Soc.*, Vol. 69, No. 3, pp. 181–189.

Eshelby, J. D., 1957, "The Determination of the Elastic Field of an Ellipsoidal Inclusion, and Related Problems," *Proc. Roy. Soc. London*, Vol. A241, pp. 376–386.

Eshelby, J. D., 1959, "The Elastic Field Outside an Ellipsoidal Inclusion," *Proc. Roy. Soc. London*, Vol. A252, pp. 561–569.

Fu, L. S., and Mura, T., 1982, "Volume Integrals of Ellipsoids Associated wtih the Inhomogeneous Helmholtz Equation," *Wave Motion*, Vol. 4, pp. 141–149.

Fu, L. S., and Mura, T., 1983, "The Determination of the Elastodynamic Field of an Ellipsoidal Inhomogeneity," ASME JOURNAL OF APPLIED MECHANICS, Vol. 50, pp. 390–396.

Garvie, R. C., Hannink, R. H., and Pascoe, R. T., 1975, "Ceramic Steel," *Nature*, Vol. 258, pp. 703–704.

Lambropoulos, J. C., 1986, "Effect of Nucleation on Transformation Toughening," *J. Am. Ceram. Soc.*, Vol. 69, No. 3, pp. 218–222.

Lange, F. F., 1982, "Transformation Toughening," Part 1–5, *J. Mater. Sci.*, Vol. 17, pp. 225–263.

Marshall, D. B., 1986, "Strength Characteristics of Transformation-Toughened Zirconia," *J. Am. Ceram. Soc.*, Vol. 69, No. 3, pp. 173–180.

Marshall, D. B., and James, M. R., 1986, "Reversible Stress-Induced Martensitic Transformation in ZrO_2," *J. Am. Ceram. Soc.*, Vol. 69, No. 3, pp. 215–217.

McMeeking, R. M., and Evans, A. G., 1982, "Mechanics of Transformation-Toughening in Brittle Materials," *J. Am. Ceram. Soc.*, Vol. 65, No. 5, pp. 242–246.

Mura, T., 1982, *Micromechanics of Defects in Solids*, Martinus Nijhoff Publishers.

Downloaded 03 May 2010 to 171.66.16.244. Redistribution subject to ASME license or copyright; see http://www.asme.org/terms/Terms_Use.cfm

On Bonded Inclusions With Circular or Straight Boundaries in Plane Elastostatics

T. Honein
Graduate Student.

G. Herrmann
Professor of Applied Mechanics,
Fellow ASME.

Division of Applied Mechanics,
Stanford University,
Stanford, CA 94305-4040

It is shown that the solution, in plane elastostatics, for an infinite domain with a bonded circular inclusion (heterogeneous problem), may be obtained from the solution of the corresponding homogeneous problem merely by substitution into a simple algebraic expression (heterogenization). This relation is universal in the sense of being independent of the loading considered. The case of two half-planes occupied by two dissimilar materials and bonded along a straight boundary is obtained as a limiting case.

Introduction

In a recent paper (Honein and Herrmann, 1988) the authors have shown that the problem of plane elastostatics for a circular disk and that for an infinite region with a circular hole, subjected either to the same traction or same displacement along the common boundary, are related by an involution. Also, it was shown in the same paper that the solution of either problem, with singularities within the region, is related to the corresponding problem for the complete infinite region (subjected to the same singularities). Thus, knowing the solution for an infinite region, the solution for an infinite region with a circular hole can be obtained by mere substitution into a simple algebraic expression, assuming, of course, that all singularities lie outside the prospective hole. If all singularities, assumed now self-equilibrating, reside within a circular region, then the solution for the disk is obtained by substitution into the same expression.

The purpose of the present paper is to extend the above mentioned results to the case when, instead of a hole, a circular elastic inclusion perfectly bonded to the matrix is present.

Thus, we propose to show that the solution, in plane linear elastostatics, of an infinite body (matrix) containing a perfectly bonded elastic circular inclusion, when all singularities reside either outside or inside the inclusion, can be reduced to the corresponding problem of an infinite homogeneous material subjected to the same singularities. The solution is obtained by substitution into a simple algebraic expression. This expression is universal in the sense of being independent of the loading considered.

It was decided in formulating the aforementioned problems to employ the Kolosov-Muskhelishvili representation, thus allowing for lucidity and compactness. After a brief review in Section 1 of fundamental relations of plane elastostatics using this formalism, we proceed to derive in Subsection 2.1 the transformation giving the solution of the heterogeneous problem in terms of the homogeneous one, when all singularities reside within the matrix. The corresponding transformation, when all singularities lie inside the inclusion, is derived in Subsection 2.2. These transformations are given in terms of complex potentials and the expressions for the stresses are obtained in Section 3. The case of two dissimilar elastic materials occupying two half-planes and bonded along a straight boundary is obtained as a limiting case in Section 4. Several specific examples to illustrate this new procedure are presented in Section 5 and some conclusions are drawn in Section 6.

1 Review of Fundamental Relations of Plane Elastostatics

In this section we review very briefly the basic relations of plane elastostatics using the Kolosov-Muskhelishvili formalism. For details the reader is referred to Muskhelishvili (1953) or Sokolnikoff (1983).

We consider a linear elastic body (homogeneous and isotropic) occupying an open region D of $\mathbf{R}^2$ with piecewise smooth boundary ∂D consisting of a finite number of contours Γ_j, $j = 1, 2, \ldots, n$. A point on one of these contours shall be specified by prescribing the arc length s measured from a reference point on that contour.

Let $t_\alpha(s)$ ($\alpha = 1, 2$) denote the components of traction at a point of the boundary with respect to a Cartesian system of coordinates, Ox_1x_2. If one defines (see Sokolnikoff, 1983)

$$f_1 + if_2 = i\int_0^s [t_1(\lambda) + it_2(\lambda)]d\lambda$$

where the sense of integration is always such that the material is on the left as λ increases, then the first boundary value problem of plane elastostatics is reduced to the determination

Contributed by the Applied Mechanics Division of THE AMERICAN SOCIETY OF MECHANICAL ENGINEERS for presentation at the Winter Annual Meeting, Dallas, Texas, Nov. 25–30, 1990.

Discussion on this paper should be addressed to the Technical Editor, Leon M. Keer, The Technological Institute, Northwestern University, Evanston, IL 60208, and will be accepted until two months after final publication of the paper itself in the JOURNAL OF APPLIED MECHANICS. Manuscript received by the ASME Applied Mechanics Division, Nov. 15, 1988; final revision, June 10, 1989.

Paper No. 90-WA/APM-24.

Copyright © 1990 by ASME
Downloaded 03 May 2010 to 171.66.16.244. Redistribution subject to ASME license or copyright; see http://www.asme.org/terms/Terms_Use.cfm

of the complex Kolosov-Muskhelishvili potentials, $\phi(z)$, $\psi(z)$. These are subjected to the boundary condition

$$\phi(z)+z\overline{\phi'(z)}+\overline{\psi(z)}=f_1+if_2+\text{constant on } \partial D$$

where the constants have different values on each of the contours forming the boundary ∂D. The components of stress in polar coordinates are related to ϕ and ψ by

$$\sigma_{rr}+\sigma_{\theta\theta}=2[\phi'(z)+\overline{\phi'(z)}]=4\ \mathrm{Re}[\phi'(z)] \tag{1a}$$

$$\sigma_{\theta\theta}-\sigma_{rr}+2i\sigma_{r\theta}=2[\bar{z}\phi''(z)+\psi'(z)]e^{2i\theta} \tag{1b}$$

where Re designates the real part of the argument.

The components of displacement u_α in Cartesian coordinates are given by

$$2\mu(u_1+iu_2)=\kappa\phi(z)-z\overline{\phi'(z)}-\overline{\psi(z)}$$

and in polar coordinates by

$$2\mu(u_r+iu_\theta)=e^{-i\theta}(\kappa\phi(z)-z\overline{\phi'(z)}-\overline{\psi(z)}) \tag{2}$$

where μ is the shear modulus and

$$\kappa = 3-4\nu, \qquad \text{for plane strain, and}$$

$$\kappa = \frac{3-\nu}{1+\nu} \qquad \text{for plane stress,}$$

ν being Poisson's ratio.

2 Derivation of the Transformation

2.1 All Singularities are in the Matrix. We consider now a circular elastic inclusion perfectly bonded to an infinite matrix subjected to an elastic field whose sources are in the matrix (including infinity) so that the elastic field is free of singularities inside or on the boundary of the circular inclusion (see Fig. 1).

We propose to express the solution to this problem in terms of the corresponding much simpler problem of an infinite homogeneous body subjected to the same loading. It will be shown that the transformation leading from one solution to the other is essentially a very simple algebraic operation. Moreover, the interfacial stresses in the heterogeneous problem are shown to be just linear combinations of the stresses at the center and on the prospective circular boundary of the homogeneous problem.

The elastic moduli of the inclusion are denoted by μ_I, κ_I, while those of the matrix are designated by μ_M, κ_M, μ being the shear modulus, and κ as defined in the previous section.

In the paper by Honein and Herrmann (1988) some notions were introduced which are essential to the following developments. These notions are recalled briefly here. Let u be a function of polar coordinates r, θ. The Kelvin transformation in the plane is defined by

$$\tilde{u}(r,\theta)=u\left(\frac{a^2}{r},\theta\right).$$

The importance of this transformation lies in the fact that if u is a harmonic function on the disk $r<a$, then $\tilde{u}$ is a harmonic function on the region $r>a$ and vice versa. If u is regarded as the real part of a holomorphic function

$$f(z)=u(r,\theta)+iv(r,\theta),$$

then the "hat" transformation is defined by

$$\hat{f}(z)=\overline{f(a^2/\bar{z})}=u(a^2/r,\theta)-iv(a^2/r,\theta)=\tilde{u}(r,\theta)-i\tilde{v}(r,\theta).$$

The hat transformation maps holomorphic functions defined on $r<a$ into holomorphic functions defined on $r>a$, including the point at infinity and vice versa. Both the Kelvin and the "hat" transformations are involutions (i.e., each is its own inverse).

Also, it was shown in the same paper that if (ϕ, ψ) is a solution for the infinite plane subjected to singularities residing in the region $r>a$, then the solution when a traction-free hole or a fixed rigid inclusion, with boundary $r=a$, is introduced:

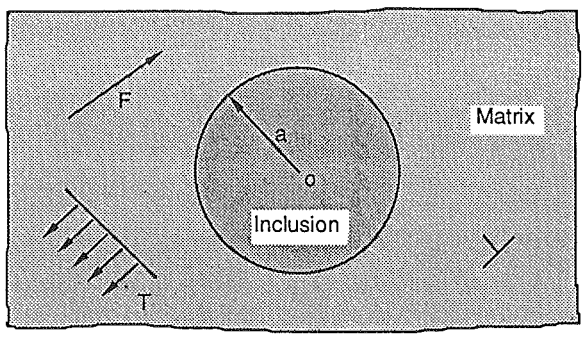


Fig. 1 A circular elastic inclusion of radius *a* free of singularities, and perfectly bonded to an infinite matrix which is subjected to arbitrary loading

$$\phi_o^*(z)=\phi(z)-\frac{1}{\alpha}\hat{f}(z)$$

$$\psi_o^*(z)=\psi(z)-\alpha\hat{\phi}(z)-\frac{a^2}{z}K-\frac{a^4}{\alpha z^3}\hat{f}'(z),$$

where

$$f(z)=\psi(z)+\frac{a^2}{z}(\phi'(z)-K),$$

$\alpha=1$ for the hole and $\alpha=-\kappa$ for the rigid inclusion. $K=\phi'(0)=\frac{I(0)}{4}+i\frac{2\mu}{1+\kappa}\omega(0)$ where I is the first stress invariant and ω is the rotation defined by

$$\omega=\frac{1}{2}\left(\frac{\partial u_2}{\partial x_1}-\frac{\partial u_1}{\partial x_2}\right).$$

ϕ may be chosen such that $\phi'(0)$ is real, a choice that does not affect the state of stress and leads to a floating rigid inclusion.

It is conceivable that the solution, when a perfectly bonded circular elastic inclusion rather than a hole is introduced, may be obtained by appropriately weighting the different terms in the previous expression. This is indeed the case and we have the following result:

Theorem A. The solution for the inclusion problem, when all singularities are in the matrix, is related to that of the corresponding homogeneous problem (ϕ, ψ) (i.e., when the complete region is occupied by the matrix material) by:

$$\phi_I(z)=(1-\alpha)\phi(z)+(\alpha-\gamma)\phi'(0)z$$

$$\psi_I(z)=(1-\alpha)\psi(z)+(\alpha-\beta)f(z)$$

$$\phi_M(z)=\phi(z)-\beta\hat{f}(z)$$

$$\psi_M(z)=\psi(z)-\alpha\hat{\phi}(z)-\beta\frac{a^4}{z^3}\hat{f}'(z)+(\alpha-2\gamma)\frac{a^2}{z}\phi'(0)$$

where

$$f(z)=\psi(z)+\frac{a^2}{z}[\phi'(z)-\phi'(0)].$$

ϕ is chosen such that $\phi'(0)$ is real.

α, β, and γ are the following combinations of the material moduli

$$\alpha = \frac{\mu_M\kappa_I-\mu_I\kappa_M}{\mu_I+\mu_M\kappa_I}$$

$$\beta = \frac{\mu_M-\mu_I}{\mu_M+\mu_I\kappa_M}$$

Downloaded 03 May 2010 to 171.66.16.244. Redistribution subject to ASME license or copyright; see http://www.asme.org/terms/Terms_Use.cfm

$$\gamma = \frac{\mu_M(\kappa_I - 1) - \mu_I(\kappa_M - 1)}{2\mu_I + \mu_M(\kappa_I - 1)},$$

a being the radius of the inclusion.

It should be emphasized that, in all the considerations, the center of the inclusion is taken to be the origin.

Proof. Note that by assumption ϕ and ψ are analytic throughout the disk $r < a$ which is free of singularities. Since the singularity of f at the origin is removable, f is also analytic throughout the disk $r < a$. Now, the "hat" transformation maps analytic functions on the disk $r < a$ to analytic functions on the region $r > a$ including the point at infinity. Hence, the additional terms do not introduce any new singularities. They are due only to the change of the elastic field at the interface when the inclusion has been introduced. We will now prove that they are the terms needed to ensure continuity of traction and displacement across the interface.

(*a*) *Continuity of Displacement.*

(i) For $r = a^-$ (from the inclusion side)

$$2\mu_I(u_1 + iu_2) = \kappa_I\phi_I(z) - z\overline{\phi_I'(z)} - \overline{\psi_I(z)}.$$

Upon substitution of ϕ_I and ψ_I by their expressions, we obtain

$$u_1 + iu_2|_{r=a^-} = \frac{1}{2\mu_I}\Big[\kappa_I(1-\alpha)\phi(z) - (1-\beta)(\overline{\psi(z)} + z\overline{\phi'(z)}) + [(\alpha-\gamma)\kappa_I + \gamma - \beta]\phi'(0)z\Big].$$

(ii) For $r = a^+$ (from the matrix side),

$$2\mu_M(u_1 + iu_2) = \kappa_M\phi_M(z) - \overline{z\phi_M'(z)} - \overline{\psi_M(z)}.$$

Upon substitution of ϕ_M and ψ_M by their expressions, we obtain

$$u_1 + iu_2|_{r=a^+} = \frac{1}{2\mu_M}[(\kappa_M + \alpha)\phi(z) - (\kappa_M\beta + 1)(\overline{\psi(z)} + z\overline{\phi'(z)}) + (2\gamma - \alpha + \kappa_M\beta)\phi'(0)z].$$

By comparing the corresponding coefficients it is readily seen that

$$u_1 + iu_2|_{r=a^-} = u_1 + iu_2|_{r=a^+}.$$

Hence, the displacement field is continuous across the interface.

(*b*) *Continuity of Traction.* The continuity of the traction can be proved similarly; one has only to show that the expression

$$\phi(z) + z\overline{\phi'(z)} + \overline{\psi(z)}$$

is continuous across the boundary which can be done following similar lines of argument. This concludes the proof of the theorem.

Remarks.

(1) For the case of identical materials:

$$\alpha = 0; \quad \beta = 0; \quad \gamma = 0$$

then

$$\phi_I = \phi = \phi_M$$
$$\psi_I = \psi = \psi_M$$

and the formulae reduce to those for the homogeneous problem.

(2) The two cases of a circular hole ($\mu_I = 0$) and of a rigid inclusion ($\mu_I = \infty$) are special cases. For a circular hole:

$$\alpha = 1; \quad \beta = 1; \quad \gamma = 1,$$

while for a rigid inclusion:

$$\alpha = -\kappa_M; \quad \beta = -1/\kappa_M; \quad \gamma = (1 - \kappa_M)/2,$$

and the expression reduces to that obtained earlier by the authors (Honein and Herrmann, 1988).

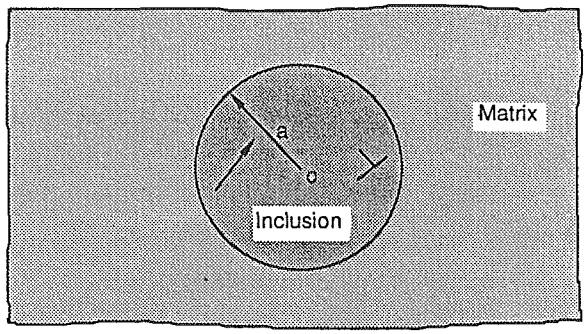


Fig. 2 A circular elastic inclusion of radius *a* subjected to arbitrary loading and perfectly bonded to an infinite matrix which is free of singularities

(3) Actually, there are only two independent combinations of the material moduli which are relevant, since we have

$$\gamma = \frac{\alpha - \beta}{(1-\beta) - \beta(1-\alpha)}.$$

Obviously, the choice of the parameters is not not unique and other composite parameters may be used (see Dundurs, 1967).

(4) The choice that $\phi'(0)$ is real does not affect the state of stress, it corresponds to taking the rotation at the origin to be zero. In the general case, the expression given in Theorem A must read:

$$\phi_I(z) = (1-\alpha)\phi(z) + \frac{\alpha - \gamma}{1 - \alpha\beta}[\beta(1-\alpha)\phi'(0) + (1-\beta)\overline{\phi'(0)}]z$$
$$\psi_I(z) = (1-\alpha)\psi(z) + (\alpha - \beta)f(z)$$
$$\phi_M(z) = \phi(z) - \beta\hat{f}(z)$$
$$\psi_M(z) = \psi(z) - \alpha\hat{\phi}(z) - \beta\frac{a^4}{z^3}\hat{f}'(z) + \frac{a^2}{z}(-\gamma\phi'(0) + (\alpha - \gamma)\overline{\phi'(0)}).$$

2.2 All Singularities are Inside the Inclusion. In this subsection we consider a circular elastic inclusion perfectly bonded to an infinite matrix subjected to an elastic field whose sources are inside the inclusion (see Fig. 2).

We propose to express the solution for this problem in terms of the corresponding much simpler homogeneous problem of a complete infinite region occupied by the inclusion material and subjected to the same singularities. These singularities need not be self-equilibrating and as such they might introduce logarithmic singularities in the complex potentials. Hence, even though the sources of the elastic field are confined to the disk $r < a$, the complex potentials might not be analytic in the region $r > a$, including the point at infinity. In order to be able to apply the "hat" transformation, these logarithmic terms should be subtracted from the complex potentials, and the manipulations are performed on the remaining terms. More precisely, if we stipulate that the stress field vanishes at infinity, then the complex potentials (for the homogeneous problem) have the form (Muskhelishvili, 1953)

$$\phi(z) = A\log\frac{a}{z} + \phi_0(z)$$
$$\psi(z) = B\log\frac{a}{z} + \psi_0(z)$$

where

$$\mu_I[u_1 + iu_2] = -\pi i(\kappa_I A + \bar{B}).$$
$$F_1 + iF_2 = 2\pi(A - \bar{B}).$$

F_1 and F_2 are the resultants of the tractions t_1 and t_2, respectively, along the circular boundary, and $[u_1 + iu_2]$ denotes the discontinuity in the displacement along the circle when traversed counterclockwise a full circuit. $\phi_0(z)$ and $\psi_0(z)$ are analytic in the region $r > a$ including the point at infinity.

The counterpart of Theorem A now reads:

Downloaded 03 May 2010 to 171.66.16.244. Redistribution subject to ASME license or copyright; see http://www.asme.org/terms/Terms_Use.cfm

Theorem B. The solution for the inclusion problem, when all singularities are in the inclusion, is related to that of the corresponding homogeneous problem (i.e., when the complete region is occupied by the inclusion material) by

$$\phi_M(z) = C\log\frac{a}{z} + (1-\alpha^*)\phi_0(z)$$

$$\psi_M(z) = D\log\frac{a}{z} + (1-\alpha^*)\psi_0(z) + (\alpha^*-\beta^*)g(z)$$

$$-\frac{a^2}{z}\frac{\beta^*}{1+\beta^*}\left((\hat{\psi}_0)'(0) - \beta^*\overline{(\hat{\psi}_0)'(0)}\right) + \frac{a^2}{z^2}\left(C + (\beta^*-1)A\right)$$

$$\phi_I(z) = \phi(z) - \beta^*\hat{g}(z) + \beta^*\bar{A}\frac{z^2}{a^2} + z\frac{\beta^{*2}}{\beta^{*2}-1} \times \left(\beta^*(\hat{\psi}_0)'(0) - \overline{(\hat{\psi}_0)'(0)}\right)$$

$$\psi_I(z) = \psi(z) - \alpha^*\hat{\phi}_0(z) - \beta^*\frac{a^4}{z^3}\hat{g}' - \beta^*\frac{a^2}{z}(\hat{\psi}_0)'(0) - 2\beta^*\bar{A}$$

where α^* and β^* are obtained from α and β, respectively, by interchanging the subscripts I and M.

C and D are complex numbers defined by

$$\mu_M[u_1 + iu_2] = -\pi i(\kappa_M C + \bar{D})$$

$$F_1 + iF_2 = 2\pi(C - \bar{D})$$

and $g(z) = \psi_0(z) + a^2\phi_0'(z)/z$. Note that

$$(\hat{\psi}_0)'(0) = <\sigma_{rr}> + i<\sigma_{r\theta}> = -<\sigma_{\theta\theta}> + i<\sigma_{r\theta}>$$

where $< h >$ designates the mean value of h along the circular boundary, i.e.,

$$<h> = \frac{1}{2\pi}\int_0^{2\pi} h(a,\theta)\, d\theta.$$

For the proof one notices first that the expression given for the complex potentials satisfies the required general form. Note in this regard that the singularity at the origin, of the term $\frac{a^4}{z^3}\hat{g}' + \frac{a^2}{z}(\hat{\psi}_0)'(0)$ which appears in the expression for $\psi_I(z)$, is removable. Then one shows continuity of displacement and traction across the interface as done in the proof of Theorem A. Finally, the expression for $(\hat{\psi}_0)'(0)$ can be obtained by applying the residue theorem to equations (1) (see Honein and Herrmann, 1988).

3 The Stress Field

The displacement and stress fields are expressed in terms of the complex potentials by equations (1) and (2). These equations combined with the transformations given in Theorems A and B permit one to express the elastic field of the heterogeneous problem in terms of that of the homogeneous one (heterogenization).

Here, for example, we give the components of stress inside and outside the inclusion for the heterogeneous problem in terms of those for the homogeneous one when all singularities are within the matrix. This corresponds to the expression given in Theorem A.

Thus, one obtains for the stresses inside the inclusion.

$$2\sigma_{rr}^I = (2-\alpha-\beta)\sigma_{rr} + (\beta-\alpha)\sigma_{\theta\theta} + (\alpha-\gamma)I(0) + \frac{\alpha-\beta}{2}\frac{a^2}{r^2}(I - I(0)) - \frac{\alpha-\beta}{2}\left(\frac{a^2}{r} - r\right)\frac{\partial I}{\partial r}$$

$$2\sigma_{\theta\theta}^I = (2-\alpha-\beta)\sigma_{\theta\theta} + (\beta-\alpha)\sigma_{rr} + (\alpha-\gamma)I(0) - \frac{\alpha-\beta}{2}\frac{a^2}{r^2}(I - I(0)) + \frac{\alpha-\beta}{2}\left(\frac{a^2}{r} - r\right)\frac{\partial I}{\partial r}$$

$$\sigma_{r\theta}^I = (1-\beta)\sigma_{r\theta} - (\alpha-\beta)\frac{a^2}{r^2}\Omega - \frac{\alpha-\beta}{4}\left(\frac{a^2}{r} - r\right)\frac{\partial I}{r\partial\theta}$$

where $I = \sigma_{rr} + \sigma_{\theta\theta}$ is the first stress invariant and Ω designates a weighted rotation defined by $\Omega = \frac{2\mu_M}{1+\kappa_M}\omega$. Recall that the choice $\omega(0) = 0$ determines Ω uniquely.

The stresses inside the matrix are given by

$$2\sigma_{rr}^M = 2\sigma_{rr} + \beta\frac{a^2}{r^2}\left(4 - \frac{3a^2}{r^2}\right)(\tilde{\sigma}_{\theta\theta} - \tilde{\sigma}_{rr}) + \left(-\beta + (\beta-\alpha)\frac{a^2}{2r^2}\right)\tilde{I} + \left(\beta + (\alpha-\beta-2\gamma)\frac{a^2}{2r^2}\right)I(0) - \beta\frac{a^2}{r}\left(\frac{a^2}{r} - r\right)\frac{\partial\tilde{I}}{\partial r} + \beta\left(\frac{a^2}{r} - r\right)\left[\frac{a^2}{r^2}\left(\frac{\partial\tilde{\sigma}_{\theta\theta}}{\partial r} - \frac{\partial\tilde{\sigma}_{rr}}{\partial r}\right) + \frac{1}{2}\left(\frac{a^2}{r} - r\right)\frac{\partial^2\tilde{I}}{\partial r^2}\right]$$

$$2\sigma_{\theta\theta}^M = 2\sigma_{\theta\theta} + 3\beta\frac{a^4}{r^4}(\tilde{\sigma}_{\theta\theta} - \tilde{\sigma}_{rr}) + \left(-\beta + (\alpha-\beta)\frac{a^2}{2r^2}\right)\tilde{I} + \beta\left(\frac{a^2}{r} - r\right)\left(2 + \frac{a^2}{r^2}\right)\frac{\partial\tilde{I}}{\partial r} + \left(\beta + (\beta-\alpha+2\gamma)\frac{a^2}{2r^2}\right)I(0) - \beta\left(\frac{a^2}{r} - r\right)\left[\frac{a^2}{r^2}\left(\frac{\partial\tilde{\sigma}_{\theta\theta}}{\partial r} - \frac{\partial\tilde{\sigma}_{rr}}{\partial r}\right) + \frac{1}{2}\left(\frac{a^2}{r} - r\right)\frac{\partial^2\tilde{I}}{\partial r^2}\right]$$

$$\sigma_{r\theta}^M = \sigma_{r\theta} - \beta\frac{a^4}{r^4}\tilde{\sigma}_{r\theta} + (\beta-\alpha)\frac{a^2}{r^2}\tilde{\Omega} + \beta\left(\frac{a^2}{r} - r\right)\left[\frac{a^2}{2r^3}\left(\frac{\partial\tilde{\sigma}_{\theta\theta}}{\partial\theta} - \frac{\partial\tilde{\sigma}_{rr}}{\partial\theta}\right) + \frac{1}{4}\left(\frac{a^2}{r} - r\right)\frac{\partial^2\tilde{I}}{\partial\theta\partial r} - \frac{1}{4}\left(1 + \frac{a^2}{r^2}\right)\frac{\partial\tilde{I}}{\partial\theta}\right].$$

For the case of a circular hole or a rigid circular inclusion, these expressions reduce to the ones obtained earlier by the authors (Honein and Herrmann, 1988) if one takes into account the equilibrium and compatibility equations.

The interface stresses are obtained as

$$4\sigma_{\theta\theta}^I = 3(\beta-\alpha)\sigma_{rr} + (4-3\alpha-\beta)\sigma_{\theta\theta} + (3\alpha-\beta-2\gamma)I(0)$$

$$4\sigma_{rr}^I = 4\sigma_{rr}^M = (4-\alpha-3\beta)\sigma_{rr} + (\beta-\alpha)\sigma_{\theta\theta} + (\alpha+\beta-2\gamma)I(0)$$

$$4\sigma_{\theta\theta}^M = (\alpha-9\beta)\sigma_{rr} + (4+\alpha+3\beta)\sigma_{\theta\theta} + (3\beta-\alpha+2\gamma)I(0)$$

$$\sigma_{r\theta}^I = \sigma_{r\theta}^M = (1-\beta)\sigma_{r\theta} + (\beta-\alpha)\Omega.$$

We note that for the case of a traction-free circular hole ($\alpha = \beta = \gamma = 1$), the expression for the hoop stress is given by

$$\sigma_{\theta\theta}^M = -2\sigma_{rr} + 2\sigma_{\theta\theta} + I(0) = 4\sigma_{\theta\theta} - 2I + I(0),$$

which is a formula simpler than the one obtained earlier by Kienzler and Zhuping (1987). These authors did not recognize that the integral in their expression can be evaluated by applying the mean value theorem for harmonic functions to the first stress invariant $I = \sigma_{rr} + \sigma_{\theta\theta}$, and is simply the value of I at the center of the circle.

The interface stresses, corresponding to the case discussed in Theorem B, are given by

$$4\sigma_{rr}^I = 4\sigma_{rr}^M = (4-\alpha^*-3\beta^*)\sigma_{rr} + (\beta^*-\alpha^*)\sigma_{\theta\theta} + 4\beta^*\frac{\beta^*-1}{\beta^*+1}<\sigma_{rr}> + \frac{4}{a}\,\mathrm{Re}(\beta^* B e^{i\theta} - \alpha^* A e^{-i\theta})$$

$$4\sigma_{\theta\theta}^I = (\alpha^*-9\beta^*)\sigma_{rr} + (4+\alpha^*+3\beta^*)\sigma_{\theta\theta} - 4\beta^*\frac{3\beta^*+1}{\beta^*+1}<\sigma_{\theta\theta}> + \frac{4}{a}\,\mathrm{Re}(\alpha^* A e^{-\theta} + 3\beta^* B e^{i\theta})$$

$$\sigma_{r\theta}^I = \sigma_{r\theta}^M = (1-\beta^*)\sigma_{r\theta} + (\beta^*-\alpha^*)\Omega^* + \beta^*<\sigma_{r\theta}> - \frac{1}{a}\,\mathrm{Im}(\alpha^* A e^{-i\theta} + \beta^* B e^{i\theta})$$

Downloaded 03 May 2010 to 171.66.16.244. Redistribution subject to ASME license or copyright; see http://www.asme.org/terms/Terms_Use.cfm

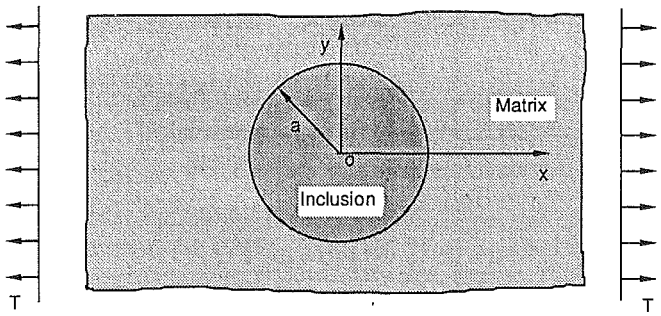


Fig. 3 A circular elastic inclusion perfectly bonded to an infinite matrix which is subjected to uniform remote tension T along the x-axis

$$4\sigma^M_{\theta\theta} = 3(\beta^* - \alpha^*)\sigma_{rr} + (4 - 3\alpha^* - \beta^*)\sigma_{\theta\theta}$$
$$+ 4\beta^* \frac{\beta^* - 1}{\beta^* + 1} < \sigma_{\theta\theta} > + \frac{4}{a} \operatorname{Re}((4 - 3\alpha^*)Ae^{-i\theta} - 4Ce^{-i\theta} - \beta^* Be^{i\theta})$$

Here Ω^* denotes a weighted rotation defined by $\Omega^* = \frac{2\mu_I}{1 + \kappa_I}\omega$.

4 Two Dissimilar Materials Occupying Half-Planes

As mentioned previously, the case of two dissimilar materials occupying two half-planes and bonded along the common straight boundary can be obtained by a limiting procedure. To this end we consider the expressions given in Theorem A, fix a tangent to the circle, and let the radius tend to infinity.

The net result, when all the singularities reside in the material labeled by M and when the common boundary is along the x-axis, is the following transformation leading from the solution of the homogeneous problem (when the material M occupies the complete plane) to that of the heterogeneous one

$$\phi_I(z) = (1 - \alpha)\phi(z)$$
$$\psi_I(z) = (1 - \alpha)\psi(z) + (\alpha - \beta)f(z)$$
$$\phi_M(z) = \phi(z) - \beta\overline{f(\bar{z})}$$
$$\psi_M(z) = \psi(z) - \alpha\overline{\phi(\bar{z})} + \beta z\overline{f'(\bar{z})}$$

where $f(z) = \psi(z) + z\phi'(z)$. This is valid under the assumption that the stress field vanishes at infinity and ϕ must be chosen such that the rotation vanishes at infinity.

The stress field corresponding to the foregoing transformation is obtained as

$$4\sigma^I_{xx} = (4 - 3\alpha - \beta)\sigma_{xx} + 3(\beta - \alpha)\sigma_{yy} - 2(\alpha - \beta)y\frac{\partial I}{\partial y}$$

$$4\sigma^I_{yy} = (\beta - \alpha)\sigma_{xx} + (4 - \alpha - 3\beta)\sigma_{yy} + 2(\alpha - \beta)y\frac{\partial I}{\partial y}$$

$$\sigma^I_{xy} = (1 - \beta)\sigma_{xy} + (\alpha - \beta)\Omega + \frac{\alpha - \beta}{2}y\frac{\partial I}{\partial x}$$

$$4\sigma^M_{xx} = 4\sigma_{xx} + (\alpha + 3\beta)\tilde{\sigma}_{xx} + (\alpha - 9\beta)\tilde{\sigma}_{yy}$$
$$- 4\beta y\left(\frac{\partial \tilde{\sigma}_{yy}}{\partial y} - \frac{\partial \tilde{\sigma}_{xx}}{\partial y} + y\frac{\partial^2 \tilde{I}}{\partial y^2} + 3\frac{\partial \tilde{I}}{\partial y}\right)$$

$$4\sigma^M_{yy} = 4\sigma_{yy} + (\beta - \alpha)\tilde{\sigma}_{xx} - (\alpha + 3\beta)\tilde{\sigma}_{yy}$$
$$+ 4\beta y\left(\frac{\partial \tilde{\sigma}_{yy}}{\partial y} - \frac{\partial \tilde{\sigma}_{xx}}{\partial y} + y\frac{\partial^2 \tilde{I}}{\partial y^2} + \frac{\partial \tilde{I}}{\partial y}\right)$$

$$\sigma^M_{xy} = \sigma_{xy} - \beta\tilde{\sigma}_{xz} + (\alpha - \beta)\tilde{\Omega}$$
$$+ \beta y\left(\frac{\partial \tilde{\sigma}_{yy}}{\partial x} - \frac{\partial \tilde{\sigma}_{xx}}{\partial x} + \frac{\partial}{\partial y}\left(y\frac{\partial \tilde{I}}{\partial x}\right)\right).$$

Here, the "~" transformation is simply a reflection with respect to the x-axis, i.e., $\tilde{u}(x,y) = u(x,-y)$.

The interface stresses are obtained as

$$4\sigma^M_{yy} = 4\sigma^I_{yy} = (\beta - \alpha)\sigma_{xx} + (4 - \alpha - 3\beta)\sigma_{yy}$$
$$4\sigma^I_{xx} = (4 - 3\alpha - \beta)\sigma_{xx} + 3(\beta - \alpha)\sigma_{yy}$$
$$4\sigma^M_{xx} = (4 + \alpha + 3\beta)\sigma_{xx} + (\alpha - 9\beta)\sigma_{yy}$$
$$\sigma^M_{xy} = \sigma^I_{xy} = (1 - \beta)\sigma_{xy} + (\alpha - \beta)\Omega.$$

5 Examples

(a) Elastic Inclusion Under Remote Uniaxial Tension. As our first example, we consider a circular elastic inclusion perfectly bonded to a matrix which is subjected to uniform tension T at infinity along the x-axis (see Fig. 3).

The solution of the corresponding homogeneous problem is trivially given as

$$\phi(z) = \frac{T}{4}z; \quad \psi(z) = -\frac{T}{2}z.$$

An immediate application of the formulae giving in Subsection 2.1 yields $\left(\text{after putting } f(z) = -\frac{T}{2}z\right)$ the solution of the heterogeneous problem as:

$$\phi_I(z) = (1 - \gamma)\frac{T}{4}z$$

$$\psi_I)(z) = -(1 - \beta)\frac{T}{2}z$$

$$\phi_M(z) = \frac{T}{4}\left(z + \frac{2\beta a^2}{z}\right)$$

$$\psi_M(z) = -\frac{T}{2}\left(z + \gamma\frac{a^2}{z} - \beta\frac{a^4}{z^3}\right).$$

This corresponds to the same solution obtained by Muskhelishvili (1953, pp. 215–217) essentially by guessing.

The stresses inside the inclusion are obtained as

$$2\sigma^I_{rr} = T[(1 - \gamma) + (1 - \beta)\cos 2\theta)]$$

$$2\sigma^I_{\theta\theta} = T[(1 - \gamma) - (1 - \beta)\cos 2\theta)]$$

$$2\sigma^I_{r\theta} = -T(1 - \beta)\sin 2\theta,$$

and those inside the matrix are given by

$$2\sigma^M_{rr} = T\left(1 - \frac{\gamma a^2}{r^2}\right) + T\left(1 - \frac{4\beta a^2}{r^2} + \frac{3\beta a^4}{r^4}\right)\cos 2\theta$$

$$2\sigma^M_{\theta\theta} = T\left(1 + \frac{\gamma a^2}{r^2}\right) - T\left(1 + \frac{3\beta a^4}{r^4}\right)\cos 2\theta$$

$$2\sigma^M_{r\theta} = -T\left(1 + \frac{2\beta a^2}{r^2} - \frac{3\beta a^4}{r^4}\right)\sin 2\theta.$$

(b) Point Force at the Center of the Inclusion. As a second example we consider the same elastic circular inclusion, subjected this time to a point force acting at the origin and having F_1 and F_2 as components with respect to a Cartesian coordinate system (see Fig. 4). It is known (see Sokolnikoff, 1983) that the complex potentials in the homogeneous body corresponding to this point force are given by

$$\phi(z) = \frac{F_1 + iF_2}{2\pi(1 + \kappa_I)}\log\frac{a}{z}$$

$$\psi(z) = -\frac{\kappa_I(F_1 - iF_2)}{2\pi(1 + \kappa_I)}\log\frac{a}{z}.$$

Downloaded 03 May 2010 to 171.66.16.244. Redistribution subject to ASME license or copyright; see http://www.asme.org/terms/Terms_Use.cfm

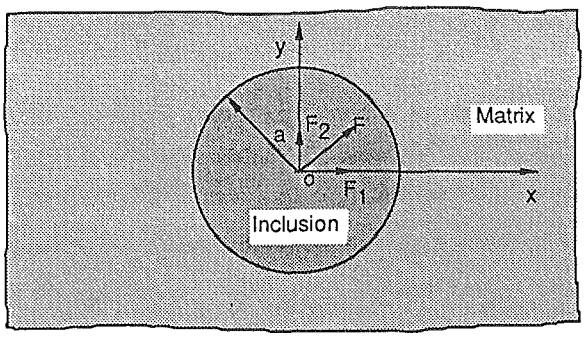


Fig. 4 A circular elastic inclusion subjected to a point force at its center and perfectly bonded to an infinite matrix

It is seen by inspection that

$$\phi_0(z)=0 \quad \psi_0(z)=0.$$

A direct application of the formulae given in Subsection 2.2 yields the solution as:

$$\phi_M(z)=\frac{F_1+iF_2}{2\pi(1+\kappa_M)}\log\frac{a}{z}$$

$$\psi_M(z)=-\frac{\kappa_M(F_1-iF_2)}{2\pi(1+\kappa_M)}\log\frac{a}{z}+\frac{F_1+iF_2}{2\pi}\frac{a^2}{z^2}\left(\frac{1}{1+\kappa_M}+\frac{\beta^*-1}{1+\kappa_I}\right)$$

$$\phi_I(z)=\frac{F_1+iF_2}{2\pi(1+\kappa_I)}\log\frac{a}{z}+\beta^*\frac{F_1-iF_2}{2\pi(1+\kappa_I)}\frac{z^2}{a^2}$$

$$\psi_I(z)=-\frac{\kappa_I(F_1-iF_2)}{2\pi(1+\kappa_I)}\log\frac{a}{z}-\beta^*\frac{F_1-iF_2}{\pi(1+\kappa_I)}.$$

The stresses inside the inclusion are given by

$$\sigma^I_{rr}=\frac{F_1\cos\theta+F_2\sin\theta}{2\pi(\kappa_I+1)}\left(-\frac{\kappa_I+3}{r}+\frac{2\beta^*r}{a^2}\right)$$

$$\sigma^I_{\theta\theta}=\frac{F_1\cos\theta+F_2\sin\theta}{2\pi(\kappa_I+1)}\left(\frac{\kappa_I-1}{r}+\frac{6\beta^*r}{a^2}\right)$$

$$\sigma^I_{r\theta}=\frac{F_1\sin\theta-F_2\cos\theta}{2\pi(\kappa_I+1)}\left(\frac{\kappa_I-1}{r}+\frac{2\beta^*r}{a^2}\right).$$

And for the stresses inside the matrix,

$$\sigma^M_{rr}=(F_1\cos\theta+F_2\sin\theta)\left\{-\frac{\kappa_M+3}{\kappa_M+1}\frac{1}{2\pi r}+\left(\frac{1}{1+\kappa_M}+\frac{\beta^*-1}{1+\kappa_M}\right)\frac{a^2}{\pi r^3}\right\}$$

$$\sigma^M_{\theta\theta}=(F_1\cos\theta+F_2\sin\theta)\left\{\frac{\kappa_M-1}{\kappa_M+1}\frac{1}{2\pi r}-\left(\frac{1}{1+\kappa_M}+\frac{\beta^*-1}{1+\kappa_I}\right)\frac{a^2}{\pi r^3}\right\}$$

$$\sigma^M_{r\theta}=(F_1\sin\theta-F_2\cos\theta)\left\{\frac{\kappa_M-1}{\kappa_M+1}\frac{1}{2\pi r}+\left(\frac{1}{1+\kappa_M}+\frac{\beta^*-1}{1+\kappa_I}\right)\frac{a^2}{\pi r^3}\right\}.$$

This solution is in agreement with the results obtained by Dokos (1949) (see also Dundurs, 1963).

(c) A Concentrated Moment in a Half-Plane. As our third example we consider a concentrated moment of intensity $2\pi\Gamma$ and at a distance d from the x-axis which separates a material M occupying the lower half-plane from a material I occupying the upper half-plane. These materials are perfectly bonded and the concentrated moment is in the material M and acts at the point $(0, -d)$ with respect to a Cartesian coordinate system (see Fig. 5).

The solution of the homogeneous problem (i.e., when the material M occupies the complete plane is given by (see Sokolnikoff, 1983))

$$\phi(z)=0; \quad \psi(z)=\frac{i\Gamma}{z+id}.$$

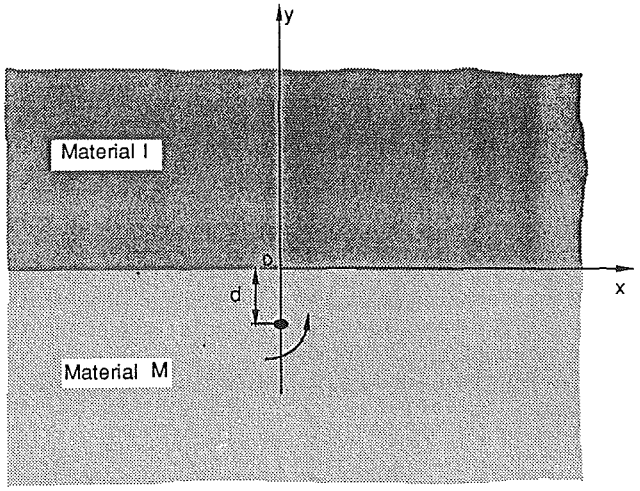


Fig. 5 A concentrated moment at a distance d from the boundary of two half-planes formed of two different elastic materials and bonded along the common interface

A direct application of the formulae given in Section 4 yields the solution for the heterogeneous problem as

$$\phi_I(z)=0 \quad \psi_I(z)=(1-\beta)\frac{i\Gamma}{z+id}$$

$$\phi_M(z)=\beta\frac{i\Gamma}{z-id}$$

$$\psi_M(z)=\frac{i\Gamma}{z+id}+\beta\frac{i\Gamma z}{(z-id)^2}.$$

The stress field is easily obtained as

$$\sigma^I_{xx}=-\sigma^I_{yy}=\frac{2(1-\beta)\Gamma x(y+d)}{(x^2+(y+d)^2)^2}$$

$$\sigma^I_{xy}=\frac{\Gamma(1-\beta)((y+d)^2-x^2)}{(x^2+(y+d)^2)^2}$$

$$\sigma^M_{xx}=-\frac{4\beta\Gamma xy(x^2-3(d-y)^2)}{(x^2+(y-d)^2)^3}+\frac{2\Gamma x(y+d)}{(x^2+(y+d)^2)^2}+\frac{6\beta\Gamma x(d-y)}{(x^2+(y-d)^2)^2}$$

$$\sigma^M_{yy}=\frac{4\beta\Gamma xy(x^2-3(d-y)^2)}{(x^2+(y-d)^2)^3}-\frac{2\Gamma x(y+d)}{(x^2+(y+d)^2)^2}+\frac{2\beta\Gamma x(d-y)}{(x^2+(y-d)^2)^2}$$

$$\sigma^M_{xy}=\frac{4\beta\Gamma y(d-y)(3x^2-(d-y)^2)}{(x^2+(y-d)^2)^3}-\frac{\Gamma(x^2-(y+d)^2)}{(x^2+(y+d)^2)^2}+\frac{\beta\Gamma(x^2-(y-d)^2)}{(x^2+(y-d)^2)^2}.$$

It is interesting to note that the stress field in the inclusion corresponds to a concentrated moment at the same location but whose intensity is magnified by a factor $(1-\beta)$. This is due to the fact that the first stress invariant for such singularity vanishes. It also holds for a center of dilatation.

6 Conclusions

In this paper the problem of a circular elastic inclusion perfectly bonded to a matrix of infinite extent and subjected to arbitrary loading has been solved explicitly in terms of the solution for the corresponding homogeneous problem. It is to be noted that the transformation leading from the solution for the homogeneous problem to that for the heterogeneous one is very simple, essentially algebraic and universal in the sense of being independent of the loading considered.

The exact solution for a single inclusion advanced here may

Downloaded 03 May 2010 to 171.66.16.244. Redistribution subject to ASME license or copyright; see http://www.asme.org/terms/Terms_Use.cfm

be employed as a building block for expressing approximately (but with arbitrary accuracy) solutions for two or more inclusions or plane boundaries in terms of the corresponding homogeneous problem. One such procedure, which will be presented in a forthcoming paper, uses the Schwarz alternating method (see Sokolnikoff, 1983).

Acknowledgments

This work was performed with the support of the U.S. Department of Energy and the National Science Foundation. This support is gratefully acknowledged.

The authors would also like to thank J. Dundurs for helpful discussions.

References

Dokos, S. J., 1949, "A Force Applied in the Median Plane at the Center of a Circular Insert in a Plate," ASME JOURNAL OF APPLIED MECHANICS, Vol. 16, pp. 411–412.

Dundurs, J., 1963, "Concentrated Force in an Elastically Embedded Disk," ASME JOURNAL OF APPLIED MECHANICS, Vol. 30, pp. 568–570.

Dundurs, J., 1967, "Effect of Elastic Constants on Stress in a Composite under Plane Deformation," *Journal of Composite Materials*, Vol. 1, pp. 310–322.

Honein, T., and Herrmann, G., 1988, "The Involution Correspondence in Plane Elastostatics for Regions Bounded by a Circle," ASME JOURNAL OF APPLIED MECHANICS, Vol. 55, pp. 566–573.

Kienzler, R., and Zhuping, D., 1987, "On the Distribution of Hoop Stresses Around Circular Holes in Elastic Sheets," ASME JOURNAL OF APPLIED MECHANICS, Vol. 54, pp. 110–114.

Muskhelishvili, N. I., 1953, *Some Basic Problems of the Mathematical Theory of Elasticity*, Noordhoff, Groningen, Holland.

Sokolnikoff, I. S., 1983, *Mathematical Theory of Elasticity*, Krieger Publishing Company, Fla.

Downloaded 03 May 2010 to 171.66.16.244. Redistribution subject to ASME license or copyright; see http://www.asme.org/terms/Terms_Use.cfm

A General Theory on Media with Randomly Distributed Inclusions: Part I—The Average Field Behaviors

B. Wang[1]
Laboratory of Nonlinear Mechanics of Continuous Media,
Institute of Mechanics,
CAS, Beijing 100080,
People's Republic of China

In this paper, a theory is developed to calculate the average strain field in the materials with randomly distributed inclusions. Many previous researches investigating the average field behaviors were based upon Mori and Tanaka's idea. Since they were restricted to studying those materials with uniform distributions of inclusions they did not need detailed statistical information of random microstructures, and could use the volume average to replace the ensemble average. To study more general materials with randomly distributed inclusions, the number density function is introduced in formulating the average field equation in this research. Both uniform and nonuniform distributions of inclusions are taken into account in detail.

1 Introduction

Since the materials with randomly distributed inclusions are widely used in engineering, many studies have been done on these materials. Here, by inclusion, we mean a rather general concept, which may refer to the transformation inclusion, inhomogeneity and defect, etc. In this paper, a theory is developed to calculate the average field value in a general material with randomly distributed inclusions.

Many researches on these materials focus on predicting their thermal, electrical, and mechanical properties. Among these are the self-consistent scheme and the variational principle proposed by Hashin and Shtrikman (1963), etc. Many approaches did not require detailed statistical information of the microstructures, since they assumed that the composites were statistically homogeneous, i.e., the inclusions distributed uniformly in the matrix. Another field of research which has received more and more attention recently is to calculate the average field created by a random distribution of inclusions, which is also essential for predicting the effective properties. A distinguished work has been done by Mori and Tanaka (1973) who calculated the average stress in the matrix created by the transformation inclusions, and then their idea has been used by many researchers, for example, Takao et al. (1982), Benveniste (1987), and Norris (1989). Tandon and Weng (1986a,b) applied the Mori-Tanaka method to calculate the average stress in the constituents of short-fiber composites. All the above studies are based on the assumption that the inclusions are uniformly distributed in an infinite matrix, and they can use the volume average to replace the ensemble average. Since the random microstructures of materials have significant effects on the average field behaviors, it naturally arises how to describe the random microstructures and incorporate the detailed statistical information in the analysis for a general class of materials with randomly distributed inclusions. To describe the random microstructures, many scientists have used the concept of the multipoint correlation function. Unfortunately, it is extremely hard to obtain the correlation function higher than three order from experiment. Therefore, in this research we use a rather different method, named for the Poisson Point Field Model, to describe the random microstructures of the materials. By introducing the number density function, which can be easily obtained from experiment, the average field equations are formulated for a general class of materials with randomly distributed inclusions.

The two cases of inclusion distributions are studied in detail. One is that the ellipsoidal inclusions distribute in the whole space uniformly. In this case we have obtained the same result with Mori and Tanaka (1973) when the inclusions are the aligned transformation inclusions, and the same result with Tandon and Weng (1986a) when the inclusions are the aligned short fibers, but we have a different result from Tandon and Weng (1986b) for randomly-oriented fibers. The other case is that the inclusions distribute in a finite region both uniformly and nonuniformly. In this paper although the higher-order moment equations of the strain field have been obtained, we

[1]Presently at: Department of Engineering Mechanics, Tsinghua University, Beijing 100084, People's Republic of China.

Contributed by the Applied Mechanics Division of THE AMERICAN SOCIETY OF MECHANICAL ENGINEERS for presentation at the Winter Annual Meeting, Dallas, Texas, Nov. 25–30, 1990.

Discussion on this paper should be addressed to the Technical Editor, Leon M. Keer, The Technological Institute, Northwestern University, Evanston, IL 60208 and will be accepted until two months after final publication of the paper itself in the JOURNAL OF APPLIED MECHANICS. Manuscript received by the ASME Applied Mechanics Division, Mar. 10, 1989; final revision, Jan. 15, 1990.

Paper No. 90-WA/APM-34.

Copyright © 1990 by ASME
Downloaded 03 May 2010 to 171.66.16.244. Redistribution subject to ASME license or copyright; see http://www.asme.org/terms/Terms_Use.cfm

only investigate the average field behaviors. The fluctuation of the strain field will be discussed in the following paper.

2 Poisson Point Field Model

The material we consider is an infinite matrix containing a finite region V in which a large number of inclusions, with eigenstrain ϵ^* are randomly distributed. According to Mura (1982), the perturbation of strain field created by a single inclusion is

$$\Delta\epsilon_{ij}(\mathbf{x}) = \int_{u(r)} K_{ijkl}(\mathbf{x}-\mathbf{x}')C_{klmn}\epsilon^*_{mn}d\mathbf{x}', \tag{1}$$

where $u(\mathbf{r})$ is the region occupied by an inclusion whose center is at $\mathbf{r}$, and

$$K_{ijkl}(\mathbf{x}-\mathbf{x}') = -\frac{1}{4}\Big[G_{jk,il}(\mathbf{x}-\mathbf{x}')+G_{ik,jl}(\mathbf{x}-\mathbf{x}') + G_{jl,ik}(\mathbf{x}-\mathbf{x}')+G_{il,jk}(\mathbf{x}-\mathbf{x}')\Big], \tag{2}$$

where $G_{ij}(\mathbf{x}-\mathbf{x}')$ is the Green's function for an infinite homogeneous body with elastic constants $\mathbf{c}$.

By introducing the concept of eigenstrain, any kind of inclusion can be equivalent to a distribution of body force in the form. If there are N_v inclusions in the volume V, the total perturbation of strain field is given by

$$\epsilon_{ij}(\mathbf{x}) = \sum_{\beta=1}^{N_v}\int_{u(r_\beta)} K_{ijkl}(\mathbf{x}-\mathbf{x}')C_{klmn}\epsilon^*_{mn}d\mathbf{x}', \tag{3}$$

where $u(\mathbf{r}_\beta)$ is the region occupied by the βth inclusion. If Φ and $\mathbf{a}$ are denoted as orientation and size of inclusion, respectively, $\epsilon_{ij}(\mathbf{x})$ is determined by N_v, Φ, $\mathbf{a}$, $\mathbf{r}_\beta$ ($\beta = 1, \ldots, N_v$) which are all random variables. By random variables we mean that even if the material is of the same kind, they would have different values for different specimens, but they should obey some statistical laws for the same kind of material. The following assumptions, which are called the Poisson Point Field Model, are taken to describe the distribution of inclusion number N_v, from which the distribution of inclusion position $\mathbf{r}_\beta$ can be derived. Compared with N_v and $\mathbf{r}_\beta$, inclusion orientation and size are easy to cope with.

Assumptions:

(1) In volume v, the number of inclusions obeys the Poisson distribution with parameter $\lambda(\mathbf{r})$, i.e., for $n = 0, 1, 2, \ldots$

$$P_r[N_v = n] = (n!)^{-1}\Big[\int_v \lambda(\mathbf{r})d\mathbf{r}\Big]^n \exp\Big[-\int_v \lambda(\mathbf{r})d\mathbf{r}\Big], \tag{4}$$

where $\Pr(N_v = n]$ is the probability of $N_v = n$, and $\lambda(\mathbf{r})$, which is called the number density function, is the ensemble average density of inclusions at the point $\mathbf{r}$.

(2) $\{Nv; v \subset V\}$ has independent increments in regions with a restriction for the intersection of them, i.e., for $v = v_1, v_2, \ldots, v_k$,

$$P_r[N_{v_1} = n_1, N_{v_2} = n_2, \ldots, N_{v_k} = n_k] = \prod_{i=1}^{k} P_r[N_{v_i} = n_i]. \tag{5}$$

According to this model, only one function $\lambda(\mathbf{r})$ is needed to describe the distribution of N_v and $\mathbf{r}_\beta$ ($\beta = 1, \ldots, N_v$), and $\lambda(\mathbf{r})$ has definite physical meaning which can be obtained through experiment measurement. If the inclusions are uniformly distributed in volume V, $\lambda(\mathbf{r})$ keeps constant, and is equal to the average number in unit volume. With the changeable function $\lambda(\mathbf{r})$, the model represents a wide variety of materials with inclusions.

By using equations (4) and (5), the probability density function of $\mathbf{r}_\beta$ ($\beta = 1, \ldots, k$) can be derived. According to the characteristic of Poisson distribution, the probability density function of any Poisson point $\mathbf{r}_\beta$ is

$$f(\mathbf{r}_\beta) = \frac{\lambda(\mathbf{r}_\beta)}{\int_v \lambda(\mathbf{r}_\beta)d\mathbf{r}_\beta}, \tag{6}$$

and if there are k inclusions in volume V, they should be statistically independent with each other. The joint probability density function $f(\mathbf{r}_1, \mathbf{r}_1, \ldots, \mathbf{r}_k)$ is

$$f(\mathbf{r}_1, \mathbf{r}_2, \ldots, \mathbf{r}_k) = \prod_{\beta=1}^{k}\frac{\lambda(\mathbf{r}_\beta)}{\int_v \lambda(\mathbf{r})d\mathbf{r}}. \tag{7}$$

In order to investigate the statistical properties of random strain field, the characteristic function should be introduced, which is defined as

$$M(\alpha) = <\exp(\mathbf{i}\ \alpha\ \epsilon)>, \tag{8}$$

where α is a constant tensor, $\mathbf{i}$ is the imaginary unit, and the symbol $< >$ means taking the average with respect to all random variables. By substituting equation (3) into equation (8) and using the properties of conditional average, equation (8) becomes

$$M(\alpha) = E^{\mathbf{a}}\Big\{E^{\Phi}\Big\{P_r(N_v=0) + \sum_{k=1}^{\infty} P_r(N_v=k)E^{\mathbf{r}\beta} \times\Big[\exp\Big(\mathbf{i}\sum_{\beta=1}^{k}\alpha\Delta\epsilon\Big)\,|(N_v=k)\Big]\Big\}\Big\}, \tag{9}$$

where $E^{\mathbf{a}}$, E^{Φ}, $E^{\mathbf{r}\beta}$ mean the averages with respect to $\mathbf{a}$, Φ, $\mathbf{r}_\beta$, respectively, and the symbol $|(N_v = k)$ means the condition of $N_v = k$. Using equation (7), we can obtain

$$E^{\mathbf{r}\beta}\Big[\exp\Big(\mathbf{i}\sum_{\beta=1}^{k}\mathbf{a}\ \Delta\epsilon\Big)|(N_v=k)\Big] = \Big[\Big(\int_v \lambda(\mathbf{r})\ d\mathbf{r}\Big)^{-1}\int_v \lambda(\mathbf{r})\exp(\mathbf{i}\ \alpha\ \Delta\epsilon)d\mathbf{r}\Big]^k. \tag{10}$$

By substituting equations (4) and (10) into equation (9), the characteristic function is given by

$$M(\alpha) = E^{\mathbf{a}}\Big\{E^{\Phi}\Big\{\exp\int_v \lambda(\mathbf{r})[\exp(\mathbf{i}\alpha\ \Delta\epsilon) - 1]d\mathbf{r}\Big\}\Big\}. \tag{11}$$

By using the characteristic function, the average equation of the random strain field can be obtained in the form

$$<\epsilon_{ij}> = (-\mathbf{i})\frac{\partial M(\alpha)}{\partial a_{ij}}(a_{ij}=0) = E^{\mathbf{a}}\Big\{E^{\Phi}\Big[\int_v \lambda(\mathbf{r})\Delta\epsilon_{ij}d\mathbf{r}\Big]\Big\}. \tag{12}$$

Substitution of equation (1) into equation (12) yields

$$<\epsilon_{ij}> = E^{\mathbf{a}}\Big\{E^{\Phi}\Big[\int_v \lambda(\mathbf{r})\int_{u(r)} K_{ijkl}(\mathbf{x}-\mathbf{x}')C_{klmn}\epsilon^*_{mn}d\mathbf{x}'d\mathbf{r}\Big]\Big\}, \tag{13}$$

where $u(\mathbf{r})$ is the region occupied by an inclusion with its center at $\mathbf{r}$. The higher-order moment equations can also be obtained easily; we will discuss them in the following paper. Although we have derived equation (13), which is simple and useful under the assumption of Poisson point field, it can be proved as follows that equation (13) can be used for more general cases, even for the non-Poisson point field.

If we take the average of equation (3) directly, it becomes

$$<\epsilon_{ij}> = <\sum_{\beta=1}^{N_v}\int_{u(r_\beta)} K_{ijkl}(\mathbf{x}-\mathbf{x}')C_{klmn}\epsilon^*_{mn}d\mathbf{x}'>. \tag{14}$$

When N_v becomes large, the fluctuation of N_v can be neglected, and we can take the average value $<N_v>$ instead,

$$<N_v> = \int_v \lambda(\mathbf{r})d\mathbf{r}. \tag{15}$$

Thus, equation (14) becomes

$$<\epsilon_{ij}> = <N_v><\int_{u(r)} K_{ijkl}(\mathbf{x}-\mathbf{x}')C_{klmn}\epsilon^*_{mn}d\mathbf{x}'>, \tag{16}$$

Downloaded 03 May 2010 to 171.66.16.244. Redistribution subject to ASME license or copyright; see http://www.asme.org/terms/Terms_Use.cfm

where the second pair of brackets on the right-hand side means the average with respect to the position, orientation, and size of a single inclusion. Many inclusions distribute randomly in a specimen; their positions can be treated as trial results of a single inclusion distribution. This means that the frequency distribution is known according to a representative specimen. Therefore, according to the frequency distribution the probability density function of the inclusion position $\mathbf{r}$ can be expressed in the form

$$f(\mathbf{r})=\frac{\lambda(\mathbf{r})}{\int_v(\mathbf{r})\,d\mathbf{r}}. \tag{17}$$

By substituting equations (15) and (17) into equation (16) and using the properties of conditional expectation, we find

$$<\epsilon_{ij}>=E^{\Phi}\{E^{\Phi}[\int_v\lambda(\mathbf{r})\int_{u(r)}K_{ijkl}(\mathbf{x}-\mathbf{x}')C_{klmn}\epsilon^*_{mn}d\mathbf{x}'d\mathbf{r}]\}, \tag{18}$$

which is the same result as equation (13).

Through the above discussion, we can conclude that if the inclusion positions form Poisson point field, equation (18) is exactly correct, and if the inclusion number in V is quite large, equation (18) is a good approximation for any kind of random distribution of inclusions. For simplicity, we neglect the randomness of inclusion size $\mathbf{a}$ in the following and assume that the eigenstrain ϵ^* keeps constant. Then equation (18) becomes

$$<\epsilon_{ij}>=E^{\Phi}[C_{klmn}\epsilon^*_{mn}\int_v\lambda(\mathbf{r})\int_{u(r)}K_{ijkl}(\mathbf{x}-\mathbf{x}')d\mathbf{x}'d\mathbf{r}]. \tag{19}$$

3 A Uniform Distribution of Inclusions in an Infinite Matrix

In this part of the article, the spheroidal inclusions are considered to distribute uniformly in an infinite matrix, and the average strain fields both in the inclusions and in the matrix are obtained, respectively. Two kinds of inclusions are considered. One is the transformation inclusion, which has the same elastic constants with the matrix has but acquire uniform transformation strain, and the other is the inhomogeneous inclusion, which has the different elastic constants with the matrix. Some previous results have been obtained again by using the method developed in this paper.

3.1 The Average Strain Within an Inclusion. To calculate the average strain at $\mathbf{x}$ within an inclusion, the essential requirement is that there is an inclusion at $\mathbf{x}$. Then, due to the nonintersecting property of inclusions, the density function $\lambda(\mathbf{r})$ becomes

$$\lambda(\mathbf{r})=\begin{cases}\delta(\mathbf{r}-\mathbf{x}) & \mathbf{r}\in U(\mathbf{x})\\ n & \text{others},\end{cases} \tag{20}$$

where $U(\mathbf{x})$ is the spheroidal region whose shape is similar to $u(\mathbf{x})$ and whose center is at $\mathbf{x}$, n is the average number of inclusions in unit volume, and for any continuous function $\delta(\mathbf{r}-\mathbf{x})$ is defined by

$$\int_v\delta(\mathbf{r}-\mathbf{x})\Phi(\mathbf{r})d\mathbf{r}=\Phi(\mathbf{x}). \tag{21}$$

Substitution of equation (20) into equation (19) yields

$$<\epsilon^I(\mathbf{x})>=E^{\Phi}\{[\int_{U(\mathbf{x})}\delta(\mathbf{r}-\mathbf{x})\int_{u(\mathbf{r})}\mathbf{K}(\mathbf{x}-\mathbf{x}')d\mathbf{x}'d\mathbf{r}+n\int_{v-U(\mathbf{x})}\times\int_{u(\mathbf{r})}\mathbf{K}(\mathbf{x}-\mathbf{x}')d\mathbf{x}'d\mathbf{r}]:\mathbf{C}:\epsilon^*\}, \tag{22}$$

where $<\epsilon^I(\mathbf{x})>$ is the average strain field within an inclusion. Since $U(\mathbf{x})$ and $u(\mathbf{r})$ are spheroidal inclusions, the first integral on the right-hand side can be written in the form (Eshelby, 1957)

$$\int_{U(\mathbf{x})}\delta(\mathbf{r}-\mathbf{x})\int_{u(\mathbf{r})}\mathbf{K}(\mathbf{x}-\mathbf{x}')d\mathbf{x}'d\mathbf{r}=\int_{u(\mathbf{x})}\mathbf{K}(\mathbf{x}-\mathbf{x}')d\mathbf{x}'=\mathbf{S}:\mathbf{B}, \tag{23}$$

where $\mathbf{S}$ is the Eshelby's tensor and $\mathbf{B}$ is the elastic compliance tensor of matrix. The second integral becomes

$$\int_{v-U(\mathbf{x})}\int_{u(r)}\mathbf{K}(\mathbf{x}-\mathbf{x}')d\mathbf{x}'d\mathbf{r}=\int_v\int_{u_0}\mathbf{K}(\mathbf{x}-\mathbf{r}-\mathbf{y})d\mathbf{y}d\mathbf{r}-\int_{U(\mathbf{x})}\int_{u_0}\mathbf{K}(\mathbf{x}-\mathbf{r}-\mathbf{y})d\mathbf{y}d\mathbf{r}, \tag{24}$$

where $\mathbf{x}'=\mathbf{r}+\mathbf{y}$, and u_0 is the region occupied by an inclusion with its center at zero. According to Kunin (1983), when V tends to infinity, it becomes

$$\int_v\mathbf{K}(\mathbf{x}-\mathbf{x}')d\mathbf{x}'=\mathbf{B}. \tag{25}$$

By changing the order of the integrals in equation (24), it becomes

$$\int_{v-U(\mathbf{x})}\int_{u(\mathbf{r})}K(\mathbf{x}-\mathbf{x}')d\mathbf{x}'d\mathbf{r}=v_0(\mathbf{I}-\mathbf{S}):\mathbf{B}, \tag{26}$$

where v_0 is the average volume of an inclusion, and $\mathbf{I}$ is the identity tensor. Substitution of equations (23) and (26) into equation (22) leads to

$$<\epsilon^I>=E^{\Phi}[C_f\epsilon^*+(1-C_f)\mathbf{S}:\epsilon^*], \tag{27}$$

where $C_f\,(=nv_0)$ is the volume fraction of inclusions.

3.2 The Average Strain in the Matrix. In such a case, the essential requirement is that there is no inclusion at $\mathbf{x}$. The number density function takes the form

$$\lambda(\mathbf{r})=\begin{cases}0 & \mathbf{r}\epsilon u(\mathbf{x})\\ n & \text{others}.\end{cases} \tag{28}$$

By substituting equation (28) into equation (19) and following the same procedure as above, one can obtain

$$<\epsilon^M(\mathbf{x})>=E^{\Phi}[C_f(\mathbf{I}-\mathbf{S}):\epsilon^*], \tag{29}$$

where $<\epsilon^M(\mathbf{x})>$ is the average strain in the matrix. Combining equation (27) with equation (29) gives

$$C_f<\epsilon^I(\mathbf{x})>+(1-C_f)<\epsilon^M(\mathbf{x})>=C_fE^{\Phi}(\epsilon^*), \tag{30}$$

which could be obtained through the volume average (see Mura, 1982). But in this approach, $<\epsilon^I>$ and $<\epsilon^M>$ are obtained through the ensemble average process. Therefore, this coincidence means the ensemble average of the strain field equals to the volume averages for uniform distributions of inclusions.

3.2.1 Transformation Inclusions. In such a case, it is considered that the elastic constants are uniform throughout the whole space and every inclusion acquires uniform transformation strain ϵ^*. If all the inclusions are unidirectionally distributed, equation (29) becomes

$$<\epsilon^M_{ij}(\mathbf{x})>=C_f(\mathbf{I}_{ijkl}-\mathbf{S}^L_{ijkl})\,\epsilon^*_{kl}, \tag{31}$$

which is the same result with Mori and Tanaka's result (1973), and $\mathbf{S}^L_{ijkl}$ are the components of the Eshelby's tensor in the ellipsoidal local coordinate system, which are referred to Tandon et al. (1986a) for spheroidal inclusions. For random-oriented spheroidal inclusions, the eigenstrain is axially symmetric with respect to the symmetric axis of inclusion and ($\mathbf{e}_1$, $\mathbf{e}_2$, $\mathbf{e}_3$) is denoted as the fixed coordinate system. The local coordinate system can be established by ($\mathbf{e}^L_1$, $\mathbf{e}^L_2$, $\mathbf{e}^L_3$), where $\mathbf{e}^L_1$ is the symmetric axis and $\mathbf{e}^L_3$ lies in the ($\mathbf{e}_1$, $\mathbf{e}_2$) plane with no loss in generality. Thus, the strain components in the matrix, with respect to the fixed coordinate system, are given by

$$\epsilon^M_{\alpha\beta}(\mathbf{x})=C_fT_{\alpha i}T_{\beta j}(\epsilon^{*L}_{ij}-\mathbf{S}^L_{ijkl}\,\epsilon^{*L}_{kl}), \tag{32}$$

where ϵ^{*L} is the eigenstrain in the local coordinate system, and

$$T_{ai}=\begin{bmatrix}\sin\theta\cos\Phi & -\cos\theta\cos\Phi & \sin\Phi\\ \sin\theta\sin\Phi & -\cos\theta\sin\Phi & -\cos\Phi\\ \cos\theta & \sin\theta & 0\end{bmatrix}. \tag{33}$$

The average strain in the matrix is given by

$$<\epsilon^M_{\alpha\beta}>=\frac{1}{2\pi}\int_0^{\pi}\int_0^{\pi}\epsilon^M_{\alpha\beta}\sin\theta\,d\theta\,d\Phi=\frac{1}{3}\epsilon_{kk}\delta_{\alpha\beta}, \tag{34}$$

Downloaded 03 May 2010 to 171.66.16.244. Redistribution subject to ASME license or copyright; see http://www.asme.org/terms/Terms_Use.cfm

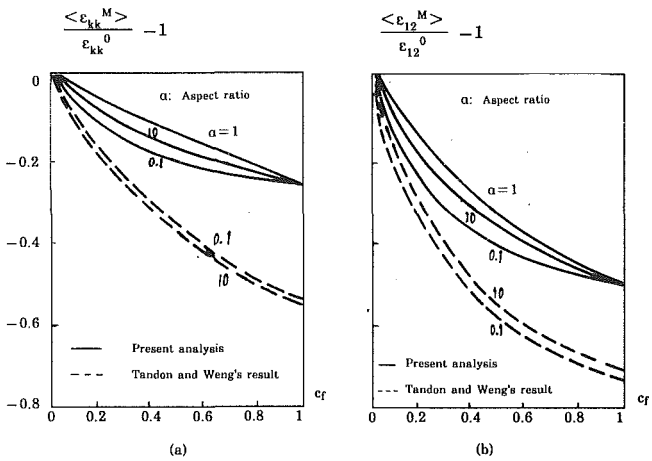


Fig. 1 The variation of (*a*) hydrostatic and (*b*) deviatoric perturbed stress components

where

$$\epsilon_{kk} = C_f[(1 - S^L_{1111} - 2S^L_{2211})\epsilon^{*L}_{11} + 2(1 + S^L_{1122} - S^L_{2222} - S^L_{2233})\epsilon^{*L}_{22}]. \quad (35)$$

3.2.2 Inhomogeneous Inclusions. In this case, the elastic constants of inclusions are different from those of the matrix. The inclusions and matrix are assumed to be linearly isotropic and perfectly bonded with the elastic moduli C^1 and C^0, respectively. A surface traction now prescribed on the boundary is a uniform stress σ^0. By using Eshelby's equivalent inclusion principle (1957), the relation between the eigenstrain ϵ^* and the internal strain ϵ^I can be established by

$$\mathbf{C}^1:\epsilon^I = \mathbf{C}^0:(\epsilon^I - \epsilon^*). \quad (36)$$

From equation (36) one obtains

$$\epsilon^* = -\mathbf{B}^0:(\mathbf{C}^1 - \mathbf{C}^0):\epsilon^I, \quad (37)$$

where $\mathbf{B}^0 = (\mathbf{C}^0)^{-1}$. To obtain the average strain in the constituents of composite with randomly-oriented inclusions, the conditional average strain $\mathbf{E}(\epsilon|\Phi)$ should first be obtained for a given orientation Φ. Combining equations (29), (30), and (37) gives

$$E(\epsilon^M|\Phi) = \epsilon^0 + C_f(\mathbf{I} - \mathbf{S}):[(\mathbf{C}^1 - \mathbf{C}^0)^{-1}:\mathbf{C}^0 - \mathbf{S}]^{-1}:E(\epsilon^M|\Phi), \quad (38)$$

where $\epsilon^0 = \mathbf{B}^0:\sigma^0$. For aligned inclusions Φ can be taken as zero and the components of $\mathbf{S}$ are those in the local coordinate system with no loss in generality. Equation (38) gives the same result as Tandon and Weng (1986a). But for randomly-oriented inclusions, their result is given by

$$<\epsilon^M> = \epsilon^0 + C_f E^\Phi\{(\mathbf{I} - \mathbf{S}):[(\mathbf{C}^1 - \mathbf{C}^0)^{-1}:\mathbf{C}^0 - \mathbf{S}]^{-1}\}:<\epsilon^M>, \quad (39)$$

where

$$<\epsilon^M> = E^\Phi[(\epsilon^M|\Phi)], \quad (39a)$$

and the assumption is contained in equation (39) that $\mathrm{E}(\epsilon^M|\Phi)$ is statistically independent of Φ. Through equation (38), the result is given by

$$<\epsilon^M> = E^\Phi\{\{\mathbf{1} - C_f(\mathbf{I} - \mathbf{S}):[(\mathbf{c}^1 - \mathbf{c}^0)^{-1}:\mathbf{c}^0 - \mathbf{S}]^{-1}\}^{-1}\}:\epsilon^0. \quad (40)$$

In order to shed some light on the difference between equations (39) and (40), we present some numerical results for the average strain in the matrix. The material constants used in numerical computations are those of glass/epoxy, i.e.,

$$k_0 = 3.07 \text{ GPa}, \quad \mu_0 = 1.02 \text{ GPa}$$
$$k_1 = 40.2 \text{ GPa}, \quad \mu_1 = 30.2 \text{ GPa} \quad (41)$$

where k_0, k_1 are bulk moduli of matrix and inclusions, and μ_0, μ_1 are shear moduli of matrix and inclusions. The variations of average perturbed strain ($<\epsilon^M> - \epsilon^0$) in the matrix are shown in Fig. 1, where α is the aspect ratio of spheroidal inclusion.

4 A Random Distribution of Inclusions in a Finite Region

The material considered in this part is an infinite matrix containing an ellipsoidal region in which a large number of inclusions distribute randomly. The aim is to investigate the average strain field both inside the ellipsoidal region and outside it.

4.1 The Inclusions Distribute Uniformly in an Ellipsoidal Region V. By uniform distribution we mean the number density function $\lambda(\mathbf{r})$ keeps constant inside the region V, i.e.,

$$\lambda(\mathbf{r}) = n \text{ (constant)}. \quad (42)$$

Substitution of equation (42) into equation (19) yields

$$<\epsilon_{ij}> = nE^\Phi[C_{klmn}\epsilon^*_{mn}\int_V\int_{u(\mathbf{r})} K_{ijkl}(\mathbf{x} - \mathbf{x}')d\mathbf{x}'\,d\mathbf{r}]. \quad (43)$$

By taking $\mathbf{x}' = \mathbf{r} + \mathbf{y}$ and changing the order of integration in equation (43), it becomes

$$<\epsilon_{ij}> = nE^\Phi[C_{klmn}\epsilon^*_{mn}\int_{u_0}\int_V K_{ijkl}(\mathbf{x} - \mathbf{y} - \mathbf{r})d\mathbf{r}d\mathbf{y}]. \quad (44)$$

Since V is an ellipsoidal region and if $\mathbf{x} - \mathbf{y}$ is inside the region V, the average strain inside the region V can be obtained in the form

$$<\epsilon^I_{ij}> = C_f S_{ijkl}(V)E^\Phi(\epsilon^*_{kl}), \quad (45)$$

where $S_{ijkl}(V)$ is the Eshelby's tensor in connection with the ellipsoidal region V. Equation (45) is true regardless of the shape of inclusion, and it leads to the conclusion that to calculate the average strain field inside an ellipsoidal region containing a uniform distribution of inclusions, one can treat the ellipsoidal region as a big inclusion with the eigenstrain $\mathbf{C}_1\mathbf{E}^\Phi(\epsilon^*)$.

From the foregoing discussion, the question arises naturally: To calculate the average strain field outside the ellipsoidal region, could one treat the ellipsoidal region as a big inclusion with the eigenstrain $\mathbf{C}_f\mathbf{E}^\Phi(\epsilon^*)$? Now, we try to answer this question. For simplicity, a spherical region containing spherical inclusions is considered in detail. From equation (44), one obtains

$$<\epsilon^M_{ij}(\mathbf{x})> = n\epsilon^*_{kl}\int_{u(x)} D_{ijkl}(\mathbf{z})d\mathbf{z}, \quad (46)$$

where $\mathbf{z} = \mathbf{x} - \mathbf{y}$, and $\mathbf{D}$ is expressed in terms of potentials Φ and Ψ (Eshelby, 1959) as

$$D_{ijkl}(\mathbf{x}) = \frac{1}{8\pi(1-\gamma)}\{\Psi_{,klij} - 2\gamma\delta_{kl}\Phi_{,ij} - (1-\gamma)[\Phi_{,kj}\delta_{il} + \Phi_{,ki}\delta_{jl} + \Phi_{,lj}\delta_{ik} + \Phi_{,li}\delta_{jk}]\}, \quad (47)$$

with

$$\Phi = \frac{4\pi a^3}{3}\times\frac{1}{|\mathbf{x}|} \text{ and } \Psi = \frac{4\pi a^3}{3}|\mathbf{x}| + \frac{4\pi a^5}{15}\times\frac{1}{|\mathbf{x}|}, \quad (48)$$

where a is the radius of the region V. The integral in equation (46) can be done directly by integration of expression (47) (Willis and Acton, 1976). Rodin and Hwang (1989) obtained the same result as a consequence of a more general formula. By using their result, equation (46) becomes

$$<\epsilon^M_{ij}(x> = C_f\left[D_{ijkl}(\mathbf{x})\epsilon^*_{kl} + \frac{3b^2a^3}{10(1-\gamma)|\mathbf{x}|^5}f_{ijkl}(\mathbf{n})\epsilon^*_{kl}\right], \quad (49)$$

Downloaded 03 May 2010 to 171.66.16.244. Redistribution subject to ASME license or copyright; see http://www.asme.org/terms/Terms_Use.cfm

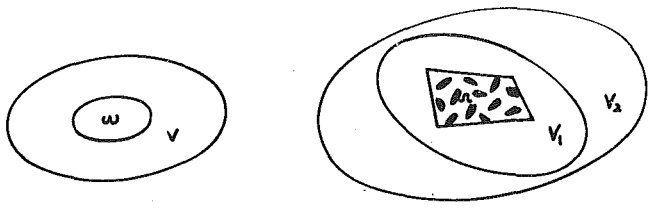


Fig. 2 Schematic of the integral domain between two ellipsoidal regions

where b is the radius of inclusion, $n_i = x_i / |\mathbf{x}|$ and

$$f_{ijkl}(\mathbf{n}) = 5n_in_jn_kn_l - 5(\delta_{ij}n_kn_l + \delta_{ik}n_jn_l + \delta_{jk}n_in_l - \delta_{il}n_jn_k - \delta_{kl}n_in_j - \delta_{jl}n_in_k) + \delta_{ij}\delta_{kl} + \delta_{ik}\delta_{jl} + \delta_{jk}\delta_{il}. \quad (50)$$

Equation (49) leads to an interesting conclusion: If the second term in equation (49) is neglected, equation (49) is the just result obtained by treating V as a big inclusion with the eigenstrain $\mathbf{C}_f\epsilon^*$. However, the second term in equation (49) depends on $a^2b^3/|\mathbf{x}|^5$ only when $|\mathbf{x}|$ becomes rather large, and it can be approximately neglected. That means that in a general case, one cannot treat the region as a big inclusion with the eigenstrain $C_f\ \epsilon^*$ in calculating the average strain field at $\mathbf{x}$ outside the region containing inclusions, but if $\mathbf{x}$ is far way from the region, the region can be replaced by a big inclusion approximately.

Tanaka and Mori (1972) have calculated the volume integral of the elastic field inside an ellipsoidal region around an ellipsoidal inclusion (Fig. 2(*a*)) and obtained

$$\int_{v-w}\epsilon d\mathbf{x} = 0. \quad (51)$$

Now, let us consider the volume integral of the elastic field around a region containing a random distribution of inclusions (Fig. 2(*b*)), i.e.,

$$\int_{V_2-V_1} <\epsilon(\mathbf{x})> d\mathbf{x} = \int_{V_2} <\epsilon(\mathbf{x})> d\mathbf{x} - \int_{V_1} <\epsilon(\mathbf{x})> d\mathbf{x}, \quad (52)$$

where V_1, V_2 are ellipsoidal regions. Substitution of equation (19) into equation (52) gives

$$\int_{V_2-V_1} <\epsilon(\mathbf{x})> d\mathbf{x} = E^{\Phi}\{[\int_{V_2} d\mathbf{x}\int_{\Omega}\lambda(\mathbf{r})d\mathbf{r}\int_{u(\mathbf{r})}\mathbf{K}(\mathbf{x}-\mathbf{x}')d\mathbf{x}' - \int_{V_1} d\mathbf{x}\int_{\Omega}\lambda(\mathbf{r})d\mathbf{r}\int_{u(\mathbf{r})}\mathbf{K}(\mathbf{x}-\mathbf{x}')d\mathbf{x}']:C:\epsilon^*\}. \quad (53)$$

If we let $\mathbf{x}' = \mathbf{y} + \mathbf{r}$ and change the order of integration in equation (53), we find

$$\int_{V_2-V_1} <\epsilon(\mathbf{x})> d\mathbf{x} = V_F E^{\Phi}\{[\mathbf{S}(V_2) - \mathbf{S}(V_1)]:\epsilon^*\}, \quad (54)$$

where V_F is the average total volume occupied by inclusions in Ω, i.e.,

$$V_F = v_0\int_{\Omega}\lambda(\mathbf{r})d\mathbf{r}, \quad (55)$$

and $\mathbf{S}(V_2)$ and $\mathbf{S}(V_1)$ are Eshelby's tensors in connection with V_2 and V_1, respectively. Equation (54) leads to the interesting conclusions: If V_1, V_2 are ellipsoidal regions, the volume integral of $<\epsilon>$ over $V_2 - V_1$ is proportional to the average volume occupied by all inclusions. It is independent of the absolute position and size of V_1 and V_2 as long as $V_2 \supset V_1$, independent of the position distribution of inclusions, and independent of the shape of Ω. It depends only on the shape of V_1 and V_2 and it vanishes when V_1 and V_2 are similar in shape and have the same orientation. The above properties of the integration in the domain are extensions of results obtained by Tanaka and Mori (1972) in studying the single inclusion problem.

4.2 Nonuniform Distribution of Inclusions. In this part, we consider that inclusions distribute in an ellipsoidal region Ω. The number density function $\lambda(\mathbf{r})$ is considered as an arbitrary smooth function and can be expanded in the Maclauren series in the form

$$\lambda(\mathbf{r}) = \sum_{N=0}^{\infty}\sum_{\alpha=0}^{\infty}\sum_{\beta=0}^{\infty}\sum_{\gamma=0}^{\infty}\frac{1}{\alpha!\beta!\gamma!}\frac{\partial^N f(0)}{\partial r_1^{\alpha}\partial r_2^{\beta}\partial r_3^{\gamma}}r_1^{\alpha}r_2^{\beta}r_3^{\gamma}, \quad (56)$$

where $\mathbf{r} = \mathbf{r}_1\mathbf{i} + \mathbf{r}_2\mathbf{j} + \mathbf{r}_3\mathbf{k}$, and the summation convention in this formula implies that $\alpha + \beta + \gamma = N$.

4.2.1 The Average Strain Field Outside the Ellipsoidal Region Ω. Substitution of equation (56) into equation (19) yields

$$<\epsilon_{ij}(\mathbf{x})> = \sum_{N=0}^{\infty}\sum_{\alpha=0}^{\infty}\sum_{\beta=0}^{\infty}\sum_{\gamma=0}^{\infty}\frac{1}{\alpha!\beta!\gamma!}\frac{\partial^N f(0)}{\partial r_1^{\alpha}\partial r_2^{\beta}\partial r_3^{\gamma}}E^{\Phi}[C_{klmn}\epsilon^*_{mn} \times \int_{\Omega}r_1^{\alpha}r_2^{\beta}r_3^{\gamma}\,d\mathbf{r}\int_{u(\mathbf{r})}K_{ijkl}(\mathbf{x}-\mathbf{x}')d\mathbf{x}']. \quad (57)$$

If the inclusion size is rather small, one can obtain approximately

$$\int_{u(\mathbf{r})}K_{ijkl}(\mathbf{x}-\mathbf{x}')d\mathbf{x}' = v_0K_{ijkl}(\mathbf{x}-\mathbf{r}), \quad (58)$$

where v_0 is the volume of an inclusion. By substituting equation (58) into equation (57), it follows

$$<\epsilon_{ij}(\mathbf{x})> = \sum_{N=0}^{\infty}\sum_{\alpha=0}^{\infty}\sum_{\beta=0}^{\infty}\sum_{\gamma=0}^{\infty}\frac{1}{\alpha!\beta!\gamma!}\frac{\partial^N F(0)}{\partial r_1^{\alpha}\partial r_2^{\beta}\partial r_3^{\gamma}}E^{\Phi}\,[D_{ijmn}(\mathbf{x})\epsilon^*_{mn}], \quad (59)$$

where

$$D_{ijmn}(\mathbf{x}) = \frac{1}{8\pi(1-\gamma)}[\Psi_{,mnij} - 2\gamma\delta_{mn}\Phi_{,ij} - (1-\gamma)(\Phi_{,mj}\delta_{ni} + \Phi_{,mi}\delta_{jn} + \Phi_{,nj}\delta_{im} + \Phi_{,ni}\delta_{jm})], \quad (60)$$

with

$$\Phi(\mathbf{x}) = \int_{\Omega}r_1^{\alpha}r_2^{\beta}r_3^{\gamma}\,|\mathbf{x}-\mathbf{r}|\,d\mathbf{r},\ \Psi(\mathbf{x}) = \int_{\Omega}\frac{r_1^{\alpha}r_2^{\beta}r_3^{\gamma}}{|\mathbf{x}-\mathbf{r}|}\,d\mathbf{r}. \quad (61)$$

According to Ferrers (1877) and Dyson (1981) (see Mura, 1982, p. 82), the above integrals can be expressed in terms of the elliptic integrals. After some mathematical calculation, it is obtained that

$$\Psi(\mathbf{x}) = I(\alpha,\beta,\gamma) = a_1^{\alpha}\alpha_2^{\beta}a_3^{\gamma}\left\{\sum_{n=0}^{\alpha/2}\frac{\alpha!x_1^{\alpha-2n}x_2^{\beta}x_3^{\gamma}}{2^{2n}n!(n+1)!(\alpha-2n+2)!a_1^2} \times\int_c^{\infty}\frac{s^nU^{n+1}(s)(a_1^2+s)}{(a_1^2+s)^{\alpha}(a_2^2+s)^{\beta}(a_3^2+s)^{\gamma}\Delta(s)}\,ds + \sum_{n=0}^{\beta/2}\frac{\beta!x_1^{\alpha}x_2^{\beta-2n}x_3^{\gamma}}{2^{2n}n!(n+1)!(\beta-2n+2)!a_2^2}\int_c^{\infty} \times\frac{s^nU^{n+1}(s)(a_2^2+s)}{(a_1^2+s)^{\alpha}(a_2^2+s)^{\beta}(a_3^2+s)^{\gamma}\Delta(s)} + \sum_{n=0}^{\gamma/2}\frac{\gamma!x_1^{\alpha}x_2^{\beta}x_3^{\gamma-2n}}{2^{2n}n!(n+1)!(\gamma-2n+2)!a_3^2} \times\int_c^{\infty}\frac{s^nU^{n+1}(s)(a_3^2+s)}{(a_1^2+s)^{\alpha}(a_2^2+s)^{\beta}(a_3^2+s)^{\gamma}\Delta(s)}\,ds\right\}, \quad (62)$$

and

$$\Phi(\mathbf{x}) = x_ix_jI(\alpha,\beta,\gamma) - 2[x_1I(\alpha+1,\ \beta,\ \gamma) + x_2I(\alpha,\ \beta+1,\ \gamma) + x_3I(\alpha,\ \beta,\ \gamma+1)] + I(\alpha+2,\ \beta,\ \gamma) + I(\alpha,\ \beta+2,\gamma) + I(\alpha,\ \beta\gamma+2), \quad (63)$$

Downloaded 03 May 2010 to 171.66.16.244. Redistribution subject to ASME license or copyright; see http://www.asme.org/terms/Terms_Use.cfm

where

$$U(s) = 1 - \left(\frac{x_1^2}{a_1^2+s} + \frac{x_2^2}{a_2^2+s} + \frac{x_3^2}{a_3^2+s)}\right), \quad \Delta(s) = \sqrt{(a_1^2+s)(a_2^2+s)(a_3^2+s)}, \tag{64}$$

and c is the largest positive root of $U(c) = 0$.

4.2.2 The Average Strain Field Inside the Ellipsoidal Region Ω. If we let $\mathbf{x}' = \mathbf{y} + \mathbf{r}$ and change the order of integration in equation (19), it becomes

$$<\epsilon_{ij}(\mathbf{x})> = E^{\Phi}[C_{klmn}\epsilon^*_{mn} \int_{u_0} d\mathbf{y} \int_{\Omega}\lambda(\mathbf{r})K_{ijkl}(\mathbf{x}-\mathbf{y}-\mathbf{r})d\mathbf{r}]. \tag{65}$$

If it is assumed that $\lambda(\mathbf{r})$ is a polynomial of $\mathbf{r}$ with degree n. According to Eshelby (1961), the first-order integration will give a polynomial function of $\mathbf{x} - \mathbf{y}$ with degree n, since $\mathbf{x} - \mathbf{y}$ is inside the ellipsoidal region Ω, and u_0 is also an ellipsoidal inclusion. The average strain field $< \epsilon_{ij}(\mathbf{x}) >$ inside the ellipsoidal region Ω can be proved to be a polynomial function of $\mathbf{x}$ with degree n. This conclusion is similar to that obtained by Eshelby (1961) in calculating the internal strain field for a single inclusion with a polynomial eigenstrain.

5 Conclusions and Discussions

Our major purpose is to seek an efficient model for general materials with randomly distributed inclusions and to incorporate detailed statistical information of the random microstructures in deriving the average strain field in such materials. The main results are summarized as follows.

1 By introducing the number density function of inclusions, the present analysis can easily evaluate the average strain field in more complicated materials, such as those with nonuniform distribution of inclusions.

2 One must be cautious in taking the orientation average for randomly oriented inclusions. The suggestion of the author is that one should first evaluate the aligned inclusion problem, then the average value can be obtained by taking orientation average, which is same with Christensen (1979).

3 When the inclusions distribute randomly in a finite ellipsoidal region, we have obtained the average strain fields inside the region and outside the region. The properties of the integration of the average strain in the domain between two ellipsoidal regions around an inclusion concentrated region are similar with those obtained by Tanaka and Mori (1972) for a single inclusion problem.

Although the theory can be extended to evaluate the polynomial eigenstrain problem, one must bear in mind that the present analysis is restricted to the constant eigenstrain problem. Therefore, it would only give approximate results for inhomogeneous inclusions.

Acknowledgment

The author expresses his gratitude to Dr. Gregory J. Rodin for providing a copy of his manuscript and to Prof. G. Weng for helpful comments on this paper.

References

Benveniste, Y., 1987, "A New Approach to the Application of Mori-Tanaka's Theory in Composite Materials," *Mechanics of Materials*, Vol. 6, pp. 147–157.

Christensen, R. M., 1979, *Mechanics of Composite Materials*, John Wiley and Sons, New York, pp. 124–130.

Eshelby, J. D., 1957, "The Determination of the Elastic Field of an Ellipsoidal Inclusion and Related Problems," *Proc. Royal Soc. London*, Vol. A241, p. 376.

Eshelby, J. D., 1959, "The Elastic Field Outside an Ellipsoidal Inclusion," *Proc. Royal Soc. London*, Vol. A252, p. 561.

Eshelby, J. D., 1961, "Elastic Inclusions and Inhomogeneities," *Progress in Solid Mechanics 2*, I. N. Sneddon and R. Hill, eds., North-Holland, Amsterdam, pp. 89–140.

Hashin, Z., and Shtrikman, S., 1963, "A Variational Approach to the Elastic Behavior of Multiphase Materials," *Journal of the Mechanics and Physics of Solids*, Vol. 13, pp. 119–134.

Kunin, I. A., 1983, *Elastic Media with Microstructures II. Three-Dimensional Problems*, Springer-Verlag, Berlin, pp. 91–94.

Mori, T., and Tanaka, K., 1973, "Average Stress in Matrix and Average Energy of Materials with Misfitting Inclusions," *Acta Metall.*, Vol. 21, pp. 571–574.

Mura, T., 1982, *Micromechanics of Defects in Solids*, Martinus Nijhoff, The Hague, Netherlands.

Norris, A. N., 1989, "An Examination of the Mori-Tanaka Effective Medium Approximation for Multiphase Composites," ASME JOURNAL OF APPLIED MECHANICS, Vol. 56, pp. 83–88.

Rodin, G. J., and Hwang, Y. L., 1989, "On the Problem of Linear Elasticity for Infinite Region Containing Finite Number of Non-Intersecting Spherical Inhomogeneities," to be published.

Tanaka, K., and Mori, T., 1972, "Note on Volume Integrals of the Elastic Field Around an Ellipsoidal Inclusion," *J. Elasticity*, Vol. 2, pp. 199–200.

Takao, Y., Chou, T. W., and Taya, M., 1982, "Effective Longitudinal Young's Modulus of Misoriented Short Fiber Composites," ASME JOURNAL OF APPLIED MECHANICS, Vol. 49, pp. 536–540.

Tandon, G. P., and Weng, G. J., 1986a, "Stress Distribution in and Around Spheroidal Inclusions and Voids at Finite Concentration," ASME JOURNAL OF APPLIED MECHANICS, Vol. 53, pp. 511–518.

Tandon, G. P., and Weng, G. J., 1986b, "Average Stress in the Matrix and Effective Moduli of Randomly Oriented Composites," *Composites Science and Technology*, Vol. 27, pp. 111–132.

Willis, J. R., and Acton, J. R., 1976, "The Overall Elastic Moduli of a Dilute Suspension of Spheres," *Q. J. Mech. Appl. Math.*, Vol. 29, p. 163.

Downloaded 03 May 2010 to 171.66.16.244. Redistribution subject to ASME license or copyright; see http://www.asme.org/terms/Terms_Use.cfm

Force on a Piezoelectric Screw Dislocation

Y. E. Pak
Grumman Corporation Research Center,
Bethpage, NY 11714-3580
Mem. ASME

A screw dislocation in a hexagonal crystal exhibiting piezoelectric behavior is analyzed in the framework of linear elasticity theory. Considered is a straight dislocation with the Burgers vector normal to the isotropic basal plane. In addition to having a discontinuous displacement and a discontinuous electric potential across the slip plane, the dislocation is subjected to a line force and a line charge at the core. The solution is obtained in a closed form by means of a semi-inverse method. The electric enthalpy which takes the place of the internal energy is calculated for the screw dislocation considered in the analysis. The interaction energy for two different internal stress-field systems is derived to calculate the force acting on an electroelastic singularity. Both the standard method and a generalized path-independent integral is used to calculate the force on a piezoelectric screw dislocation subjected to external mechanical and electrical loads. Also calculated are the force between two parallel screw dislocations and the image force due to a free surface.

Introduction

Dislocations in electronic materials can adversely influence the performance of electronic devices. In some of the electronic materials exhibiting piezoelectric behavior, the deformation and the electrical fields produced by the dislocations can affect the conductivity and other electrical properties (Farvacque et al., 1977). Considered in this paper is a simple continuum model of a single screw dislocation in a hexagonal piezoelectric crystal. The analysis is carried out in the framework of linear elasticity theory. Although a continuum model does not apply in the core region and fails to describe short-range effects, it can provide a useful description of long-range distortions produced by a dislocation. Mathematical modeling of lattice defects, such as dislocations in a continuum solid, can be quite complex. This is especially true in analyzing piezoelectric materials because they exhibit anisotropic behavior as well as coupling behavior between the mechanical and the electrical fields. Various authors (Saada, 1971; Faivre and Saada, 1972; Barnett and Lothe, 1975) have extended Stroh's (1958) formulation of dislocations in anisotropic linear crystals to include piezoelectric effects. Merten (1964) has investigated the properties of a screw dislocation in a cubic piezoelectric crystal. Here, a particular case of a screw dislocation in a hexagonal piezoelectric crystal is analyzed. The dislocation line is assumed to be straight and perpendicular to the isotropic basal plane. In this configuration, only the out-of-plane deformation (perpendicular to the basal plane) is coupled with the in-plane electrical fields. Therefore, the problem reduces to an antiplane problem of elastostatics coupled with a plane problem of electrostatics. In the analysis, an infinitely long screw dislocation suffering a finite discontinuity in the displacement and in the electric potential across the slip plane is modeled. The displacement jump across the slip plane corresponds to the Burgers vector **b**, which is perpendicular to the basal plane. The jump in the electric potential ("electric-potential-dislocation") corresponds to the electric dipole layer along the slip plane (Barnett and Lothe, 1975). The dislocation core is subjected to a line force and a line charge, with the latter modeling the line charge density produced along the core. It should be noted here that the line force does not correspond to any real crystal defect. It is, however, included in the analysis for the sake of completeness. The solution to this problem is obtained in a closed form following the methodology introduced by Eshelby et al. (1953) and later elaborated by Hirth and Lothe (1982).

It is well known that formation and movement of dislocations are intimately related to the plastic deformation of crystalline solid. Therefore, it is of interest to study how lattice defects such as dislocations interact with other defects and external loads. Eshelby (1951, 1956) has introduced an ingenious method of calculating the "force" acting on elastic singularities by examining the energetics of the system in consideration. This force is defined as the negative gradient of the total energy of the body with respect to the change in position of the defect within the body. Eshelby has shown that the force on a defect can be given as an integral over any surface enclosing it. This force, however, differs from the actual physical force that acts on the mass. It is a force that acts on configurations such as dislocations, voids, cracks, etc.; hence the name "configurational force" or "material force."

Contributed by the Applied Mechanics Division of THE AMERICAN SOCIETY OF MECHANICAL ENGINEERS for presentation at the Winter Annual Meeting, Dallas, Texas, Nov. 25-30, 1990.

Discussion on this paper should be addressed to the Technical Editor, Leon M. Keer, The Technological Institute, Northwestern University, Evanston, IL 60208, and will be accepted until two months after final publication of the paper itself in the JOURNAL OF APPLIED MECHANICS. Manuscript received by the ASME Applied Mechanics Division, July 6, 1989; final revision, Dec. 20, 1989.

Paper No. 90-WA/APM-38.

Copyright © 1990 by ASME
Downloaded 03 May 2010 to 171.66.16.244. Redistribution subject to ASME license or copyright; see http://www.asme.org/terms/Terms_Use.cfm

We will make an attempt to generalize Eshelby's method of calculating this force by taking into account the effects of electrical fields that are present in materials exhibiting piezoelectric behavior.

In this paper, we will try to address two problems related to a screw dislocation in a piezoelectric crystal, namely (1) determining the state of deformation and electrical fields produced by a single straight dislocation in an otherwise perfect piezoelectric crystal, and (2) studying how this defect, the source of internal stress and fields, interacts with other defects and external loads.

Governing Equations

In this section, we will consider the thermodynamics and the variational principle to derive necessary governing equations and boundary conditions for a static linear elastic piezoelectric material as introduced by Tiersten (1969). The work done per unit volume in a piezoelectric solid can be expressed as

$$du = \sigma_{ij} d\varepsilon_{ij} + E_i dD_i, \tag{1}$$

where u is the internal energy density, σ_{ij} is the stress tensor, ε_{ij} is the strain tensor, D_i is the electric displacement vector, and E_i is the electric field vector. If we choose E_i instead of D_i to be the independent field variable, we have to introduce another thermodynamic potential called electric enthalpy density,

$$h = u - D_i E_i. \tag{2}$$

The change in the electric enthalpy density can now be written as

$$dh = \sigma_{ij} d\varepsilon_{ij} - D_i dE_i. \tag{3}$$

For a linear elastic piezoelectric material occupying region V bounded by surface S, Hamilton's principle can be stated as

$$\delta \int_V h \, dV - \int_V (f_i \delta u_i - q_b \delta\phi) dV - \int_S (T_i \delta u_i - q_s \delta\phi) dS = 0, \tag{4}$$

where f_i is the body force, u_i is the displacement, q_b is the body charge, T_i is the applied surface traction, q_s is the applied surface charge, and ϕ is the electric potential whose negative of the gradient is the electric field,

$$E_k = -\phi_{,k}. \tag{5}$$

In this formulation, the displacement and the electric potential are taken to be the independent field variables. For linear elastic piezoelectric materials, the electric enthalpy density is expressed as

$$h(\varepsilon_{ij}, E_i) = \frac{1}{2} C_{ijkl} \varepsilon_{ij} \varepsilon_{kl} - \frac{1}{2} \epsilon_{ij} E_i E_j - e_{ikl} \varepsilon_{kl} E_i, \tag{6}$$

where C_{ijkl} are the elastic moduli measured in a constant electric field, ϵ_{ij} are the dielectric constants measured at constant strain, e_{ikl} are the piezoelectric constants, and ε_{ij} is the strain tensor,

$$\varepsilon_{ij} = \frac{1}{2}(u_{i,j} + u_{j,i}). \tag{7}$$

Generally valid symmetry conditions for the material constants are

$$C_{ijkl} = C_{jikl} = C_{jilk} = C_{klij},\ e_{kij} = e_{kji},\ \epsilon_{ij} = \epsilon_{ji}. \tag{8}$$

With these symmetry relations, ε_{ij} in equation (6) can be replaced by $u_{i,j}$.

The variational formulation for the piezoelectric continuum provides the following results:

Governing field equations,

$$\begin{aligned} \sigma_{ij,j} + f_i &= 0 \\ D_{i,i} &= q_b, \end{aligned} \tag{9}$$

boundary conditions,

$$\begin{aligned} \sigma_{ij} n_j &= T_i \\ D_i n_i &= -q_s, \end{aligned} \tag{10}$$

and constitutive equations,

$$\begin{aligned} \sigma_{ij} &= \frac{\partial h}{\partial \varepsilon_{ij}} = C_{ijkl}\varepsilon_{kl} - \epsilon_{kij} E_k \\ D_i &= -\frac{\partial h}{\partial E_i} = e_{ikl}\varepsilon_{kl} + \epsilon_{ik} E_k, \end{aligned} \tag{11}$$

where n_i is the outer unit normal vector to S.

Screw Dislocation Problem

For a special case of a piezoelectric material representing a transversely isotropic medium belonging to a hexagonal crystal class 6 mm, the constitutive relations equation (11) are of the form (Berlincourt et al., 1964)

$$\begin{Bmatrix} \sigma_{xx} \\ \sigma_{yy} \\ \sigma_{zz} \\ \sigma_{zy} \\ \sigma_{zx} \\ \sigma_{xy} \end{Bmatrix} = \begin{bmatrix} c_{11} & c_{12} & c_{13} & 0 & 0 & 0 \\ c_{12} & c_{11} & c_{13} & 0 & 0 & 0 \\ c_{13} & c_{13} & c_{33} & 0 & 0 & 0 \\ 0 & 0 & 0 & c_{44} & 0 & 0 \\ 0 & 0 & 0 & 0 & c_{44} & 0 \\ 0 & 0 & 0 & 0 & 0 & \tfrac{1}{2}(c_{11} - c_{12}) \end{bmatrix} \begin{Bmatrix} \varepsilon_{xx} \\ \varepsilon_{yy} \\ \varepsilon_{zz} \\ 2\varepsilon_{zy} \\ 2\varepsilon_{zx} \\ 2\varepsilon_{xy} \end{Bmatrix} - \begin{bmatrix} 0 & 0 & e_{31} \\ 0 & 0 & e_{31} \\ 0 & 0 & e_{33} \\ 0 & e_{15} & 0 \\ e_{15} & 0 & 0 \\ 0 & 0 & 0 \end{bmatrix} \begin{Bmatrix} E_x \\ E_y \\ E_z \end{Bmatrix} \tag{12}$$

$$\begin{Bmatrix} D_x \\ D_y \\ D_z \end{Bmatrix} = \begin{bmatrix} 0 & 0 & 0 & 0 & e_{15} & 0 \\ 0 & 0 & 0 & e_{15} & 0 & 0 \\ e_{31} & e_{31} & e_{33} & 0 & 0 & 0 \end{bmatrix} \begin{Bmatrix} \varepsilon_{xx} \\ \varepsilon_{yy} \\ \varepsilon_{zz} \\ 2\varepsilon_{zy} \\ 2\varepsilon_{zx} \\ 2\varepsilon_{xy} \end{Bmatrix} + \begin{bmatrix} \epsilon_{11} & 0 & 0 \\ 0 & \epsilon_{11} & 0 \\ 0 & 0 & \epsilon_{33} \end{bmatrix} \begin{Bmatrix} E_x \\ E_y \\ E_z \end{Bmatrix}. \tag{13}$$

In these constitutive equations, the x-y plane is the isotropic basal plane we will refer to as in-plane and the z-direction is the out-of-plane direction. Consider a screw dislocation which is assumed to be straight and infinitely long in the z-direction and suffers a finite discontinuity in the displacement and electric potential across the slip plane, $x > 0$, $y = 0$ (Fig. 1). In this configuration, the piezoelectric boundary value problem simplifies considerably because there exists only the out-of-plane displacement, u_z, which couples only with the in-plane electric fields, E_x and E_y, such that

$$u_x = u_y = 0,\ u_z = u_z(x,y), \tag{14}$$

$$E_x = E_x(x,y),\ E_y = E_y(x,y),\ E_z = 0. \tag{15}$$

In this case, if neither body forces nor body charges are present, the governing equations (9) simplify to

$$\begin{aligned} c_{44} \nabla^2 u_z + e_{15} \nabla^2 \phi &= 0 \\ e_{15} \nabla^2 u_z - \epsilon_{11} \nabla^2 \phi &= 0, \end{aligned} \tag{16}$$

Downloaded 03 May 2010 to 171.66.16.244. Redistribution subject to ASME license or copyright; see http://www.asme.org/terms/Terms_Use.cfm

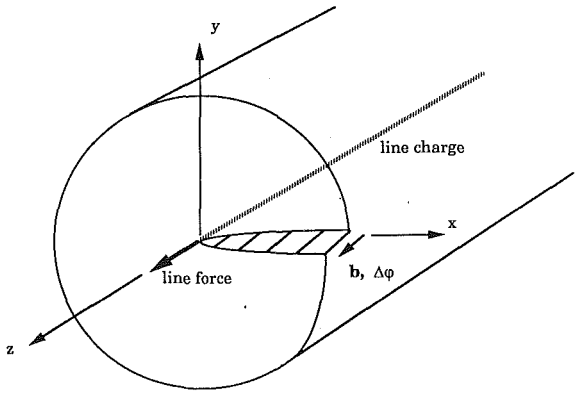


Fig. 1 Screw dislocation in a piezoelectric crystal subjected to a line force and a line charge

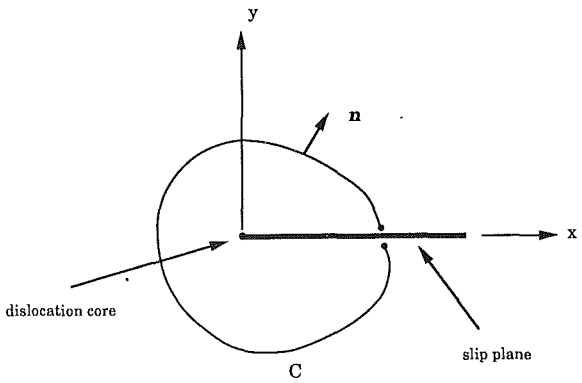


Fig. 2 Contour C used to define Burgers vector

where ∇^2 is the two-dimensional Laplacian operator

$$\nabla^2 \equiv \frac{\partial^2}{\partial x^2} + \frac{\partial^2}{\partial y^2}. \tag{17}$$

These simplified governing equations can be made to decouple and become

$$\begin{aligned} \nabla^2 u_z &= 0 \\ \nabla^2 \phi &= 0. \end{aligned} \tag{18}$$

The coupling between the mechanical fields and the electrical fields occurs only through the constitutive equations,

$$\begin{aligned} \sigma_{zx} &= c_{44}\frac{\partial u_z}{\partial x} + e_{15}\frac{\partial \phi}{\partial x} \\ \sigma_{zy} &= c_{44}\frac{\partial u_z}{\partial y} + e_{15}\frac{\partial \phi}{\partial y} \\ D_x &= e_{15}\frac{\partial u_z}{\partial x} - \epsilon_{11}\frac{\partial \phi}{\partial x} \\ D_y &= e_{15}\frac{\partial u_z}{\partial y} - \epsilon_{11}\frac{\partial \phi}{\partial y}. \end{aligned} \tag{19}$$

The solution to governing equations (18) can be found by letting u_z and ϕ be the real part of some analytic functions such that

$$\begin{aligned} u_z &= \mathrm{Re}U(Z) \\ \phi &= \mathrm{Re}\Phi(Z), \end{aligned} \tag{20}$$

where $Z = x + iy$ is a complex variable. The stresses and the electric displacements can then be expressed in terms of these functions

$$\begin{aligned} \sigma_{zx} &= \mathrm{Re}[c_{44}U'(Z) + e_{15}\Phi'(Z)] \\ \sigma_{zy} &= -\mathrm{Im}[c_{44}U'(Z) + e_{15}\Phi'(Z)] \\ D_x &= \mathrm{Re}[e_{15}U'(Z) - \epsilon_{11}\Phi'(Z)] \\ D_y &= -\mathrm{Im}[e_{15}U'(Z) - \epsilon_{11}\Phi'(Z)], \end{aligned} \tag{21}$$

where Re and Im denote the real and the imaginary part of the complex functions, respectively. The prime indicates differentiation with respect to Z. Since the logarithm function satisfies the Laplace equations (18) as well as the jump conditions across the slip plane, we choose these complex functions to be

$$\begin{aligned} U(Z) &= A \log Z \\ \Phi(Z) &= B \log Z, \end{aligned} \tag{22}$$

where A and B are complex constants:

$$\begin{aligned} A &= A_1 + iA_2 \\ B &= B_1 + iB_2. \end{aligned} \tag{23}$$

There are four unknown constants, A_1, A_2, B_1, and B_2 which will be determined by the displacement and electric potential jump conditions across the slip plane and the force and charge balance conditions at the core.

Let us consider a contour C with the outer normal unit vector, n_i, surrounding the dislocation core as shown in Fig. 2. The z-component of the Burgers vector is equal to the jump in the displacement across the slip plane ($x > 0$, $y = 0$), i.e.,

$$b = \int_C \frac{\partial u_z}{\partial x_j}\, dx_j = \Delta u_z = u_z(x,0^-) - u_z(x,0^+), \tag{24}$$

where Δ denotes the jump across the slip plane. This condition gives

$$A_2 = -\frac{b}{2\pi}. \tag{25}$$

Similarly, the jump in the electric potential, $\Delta\phi$, across the slip plane is

$$\Delta\phi = \int_C \frac{\partial \phi}{\partial x_j}\, dx_j = \phi(x,0^-) - \phi(x,0^+), \tag{26}$$

which provides

$$B_2 = -\frac{\Delta\phi}{2\pi}. \tag{27}$$

We now have to consider the force and the charge balance to obtain two more equations to determine the unknown constants, A_1 and B_1. The z-component of the traction integrated along the contour C must balance the line force p, applied at the core in the z-direction:

$$-p = \oint_C \sigma_{zj} n_j\, dl. \tag{28}$$

If we deform the contour C to become an infinitely narrow rectangle in the limit containing the dislocation and the line force (Fig. 3), with the use of equation (21) the balance equation (28) becomes

$$\begin{aligned} p &= \oint_C \sigma_{zy}\, dx \\ &= -\oint_C \mathrm{Im}[c_{44}U_z'(Z) + e_{15}\Phi'(Z)]dx \\ &= -\mathrm{Im}[c_{44}\Delta U_z + e_{15}\Delta\Phi(Z)] \\ &= -2\pi[c_{44}A_1 + e_{15}B_1]. \end{aligned} \tag{29}$$

Similarly for the charge balance, we apply Gauss's law for dielectrics on the same rectangular contour enclosing the dislocation and the line charge q,

$$\begin{aligned} q &= \oint_C D_i n_i\, dl \\ &= -\oint_C D_y\, dx \end{aligned}$$

Downloaded 03 May 2010 to 171.66.16.244. Redistribution subject to ASME license or copyright; see http://www.asme.org/terms/Terms_Use.cfm

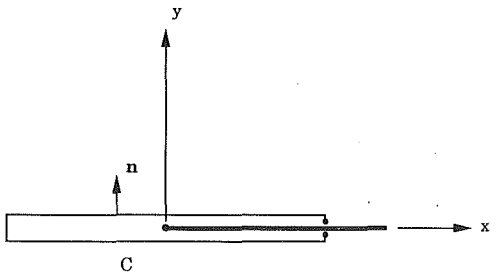


Fig. 3 Deformation of contour C to an infinitely narrow rectangle

$$= \oint_C \mathrm{Im}[e_{15}U_z'(Z) - \epsilon_{15}\Phi'(Z)]dx \tag{30}$$
$$= \mathrm{Im}[e_{15}\Delta U_z - \epsilon_{11}\Delta\Phi]$$
$$= 2\pi[e_{15}A_1 - \epsilon_{11}B_1].$$

From these balance conditions, we obtain A_1 and B_1 as follows

$$A_1 = \frac{-\epsilon_{11}p + e_{15}q}{2\pi(c_{44}\epsilon_{11} + e_{15}^2)}$$

$$B_1 = -\frac{e_{15}p + c_{44}q}{2\pi(c_{44}\epsilon_{11} + e_{15}^2)}. \tag{31}$$

All the field variables can now be expressed in terms of the mechanical and the electrical dislocations and line loads:

$$u_z = \frac{1}{2\pi}\left[b\tan^{-1}\frac{y}{x} + \left(\frac{\epsilon_{11}p - e_{15}q}{c_{44}\epsilon_{11} + e_{15}^2}\right)\log\frac{1}{r}\right]$$

$$\phi = \frac{1}{2\pi}\left[\Delta\phi\tan^{-1}\frac{y}{x} + \left(\frac{e_{15}p + c_{44}q}{c_{44}\epsilon_{11} + e_{15}^2}\right)\log\frac{1}{r}\right] \tag{32}$$

$$\gamma_{zx} = \frac{1}{2\pi(x^2+y^2)}\left[\left(\frac{-\epsilon_{11}p + e_{15}q}{c_{44}\epsilon_{11} + e_{15}^2}\right)x - by\right]$$

$$\gamma_{zy} = \frac{1}{2\pi(x^2+y^2)}\left[bx + \left(\frac{-\epsilon_{11}p + e_{15}q}{c_{44}\epsilon_{11} + e_{15}^2}\right)y\right] \tag{33}$$

$$E_x = \frac{1}{2\pi(x^2+y^2)}\left[\left(\frac{e_{15}p + c_{44}q}{c_{44}\epsilon_{11} + e_{15}^2}\right)x + \Delta\phi y\right]$$

$$E_y = \frac{1}{2\pi(x^2+y^2)}\left[-\Delta\phi x + \left(\frac{e_{15}p + c_{44}q}{c_{44}\epsilon_{11} + e_{15}^2}\right)y\right] \tag{34}$$

$$\sigma_{zx} = -\frac{1}{2\pi(x^2+y^2)}\left[px + (c_{44}b + e_{15}\Delta\phi)y\right]$$

$$\sigma_{zy} = \frac{1}{2\pi(x^2+y^2)}\left[(c_{44}b + e_{15}\Delta\phi)x - py\right] \tag{35}$$

$$D_x = \frac{1}{2\pi(x^2+y^2)}\left[qx + (-e_{15}b + \epsilon_{11}\Delta\phi)y\right]$$

$$D_y = \frac{1}{2\pi(x^2+y^2)}\left[(e_{15}b - \epsilon_{11}\Delta\phi)x + qy\right]. \tag{36}$$

Here, γ_{zx} and γ_{zy} are the antiplane engineering shear strains. These elastic and electrical fields exhibit classical screw dislocation behavior with $1/r$ singularity near the core. They also exhibit the line force and the line charge behavior of elasto and electrostatics, respectively. It is interesting to note that the strains are not affected by the electric potential jump, $\Delta\phi$, and at the same time the electric fields are not affected by the dislocation. This is due to the fact that the displacement and the electric potential are the independent field variables that are decoupled in the governing equations for the orientation of the dislocation considered in the analysis. These results also show that a line charge produces deformation but does not produce stresses because there are no mechanical constraints preventing the material from deforming. Similarly, the line load produces electric fields but not the electric displacements because the electric displacement produced by the deformation is counteracted by the one from the electric field. In the case of a continuous displacement and a continuous electric potential across the slip plane, the solution becomes electroelastic Green's function for the antiplane piezoelectric problem under consideration.

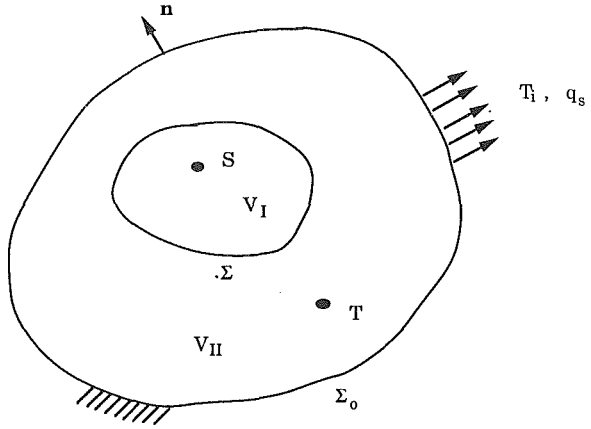


Fig. 4 Electro-elastic singularities S and T in a piezoelectric crystal

The electric enthalpy associated with this dislocation can be calculated using the solution just obtained. Because the quantities in the expression for the electric enthalpy density are continuous across the slip plane, the integral can be performed over a concentric cylindrical region surrounding the dislocation core with the inner and the outer radii of r_i and r_o, respectively. The integration can also be performed along a contour surrounding this cylindrical region with the use of divergence theorem. Both methods yield the identical result

$$H = \frac{1}{4\pi}\left[c_{44}b^2 + 2e_{15}b\Delta\phi - \epsilon_{11}\Delta\phi^2 + \frac{(\epsilon_{11}p^2 - 2e_{15}pq - c_{44}q^2)}{(c_{44}\epsilon_{11} + e_{15}^2)}\right]\log\frac{r_o}{r_i}. \tag{37}$$

From equation (37) one can see the coupling of energy between the mechanical and the electrical dislocations and between the mechanical and the electrical line loads, as well as the self-energy due to each of them separately.

Piezoelectric Interaction Energy

Let us consider two stress-field systems, S and T, both of which represent electroelastic singularities corresponding to the physical defects in a linear elastic piezoelectric crystal (Fig. 4). We can let T also represent the external mechanical and electrical loads. The mechanical load is applied in the form of traction at the surface, and the electrical load is applied in the form of surface charge equal to the negative of the normal component of electric displacement at the surface. We are interested in calculating the force acting on S due to the stresses and the electrical fields generated by T. We can also introduce a body force, f_i^S, and a body charge, q_b^S, associated with S since we are interested in calculating the force acting on a dislocation with a line force and a line charge "attached' to it. These body loads are assumed to be contained within Σ.

The total interaction electric enthalpy, H_{tot}, consists of stored interaction electric enthalpy, H_{int}, plus the potential energy of the external body and surface forces, H_{ext}. The total interaction enthalpy can be written as

Downloaded 03 May 2010 to 171.66.16.244. Redistribution subject to ASME license or copyright; see http://www.asme.org/terms/Terms_Use.cfm

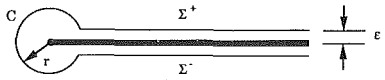


Fig. 5 Contour surrounding dislocation core and slip plane

$$H_{\text{tot}} = H_{\text{int}} + H_{\text{ext}}$$
$$= \int_{V_I + V_{II}} \left[\frac{1}{2} (\sigma_{ij}^S \, {}^T_{ij} - D_i^S E_i^T) + \frac{1}{2} (\sigma_{ij}^T \, {}^S_{ij} - D_i^T E_i^S) \right] dV$$
$$+ \int_{V_I} [-f_i^S u_i^T + q_b^S \phi^T] dV \tag{38}$$
$$+ \int_{\Sigma_o} [-u_i^S T_i^T + \phi^S q_s^T] dS.$$

With the use of divergence theorem and the following relationship,

$$\sigma_{ij}^S \varepsilon_{ij}^T - D_i^S E_i^T = \sigma_{ij}^T \varepsilon_{ij}^S - D_i^T E_i^S, \tag{39}$$

the stored interaction enthalpy can be rewritten as

$$H_{\text{int}} = \int_{V_I} [(\sigma_{ij}^S \varepsilon_{ij}^T + D_i^S \phi_{,i}^T)] dV$$
$$+ \int_{V_{II}} [(\sigma_{ij}^T \varepsilon_{ij}^S + D_i^T \phi_{,i}^S)] dV$$
$$= \int_{\Sigma} [\sigma_{ij}^S u_i^T + D_j^S \phi^T - \sigma_{ij}^T u_i^S - D_j^T \phi^S] dS \tag{40}$$
$$+ \int_{V_I} [f_i^S u_i^T - q_b^S \phi^T] dV$$
$$+ \int_{\Sigma_o} [u_i^S \sigma_{ij}^T + \phi^S D_j^T] n_j dS.$$

Upon substitution of equations (40) into (38), the work done by the external loads cancel out and the total electric enthalpy becomes

$$H_{\text{tot}} = \int_{\Sigma} [\sigma_{ij}^S u_i^T + D_j^S \phi^T - \sigma_{ij}^T u_i^S - D_j^T \phi^S] dS, \tag{41}$$

where Σ is any surface enclosing S. In the case of T representing only the external loads, the expression above can be evaluated on Σ_o.

Force on a Dislocation

We can now evaluate the total interaction electric enthalpy and calculate the force acting on a dislocation subjected to a line force, p_i^S, and a line charge q^S, at the core. Choosing a contour surrounding the dislocation, as shown in Fig. 5, we obtain the following results. On a contour C with vanishingly small radius r, the first two terms of equation (41) become

$$\lim_{r \to 0} \int_C [\sigma_{ij}^S u_i^T + D_j^S \phi^T] n_j \, dS = -p_i^S u_i^T + q^S \phi^T \tag{42}$$

and the last two terms of the same equation become

$$\lim_{r \to 0} \int_C [-\sigma_{ij}^T u_i^S - D_j^T \phi^S] n_j \, dS \sim \lim_{r \to 0} r \log r = 0. \tag{43}$$

In the last operation, we require that the dislocation line contains at most a logarithmic singularity. We assumed that the fields associated with T are continuous in the neighborhood of the contour C. We now calculate the contributions from the integrals on contours Σ^+ and Σ^- as $\varepsilon \to 0$. Since σ_{ij}^S, u_i^T, D_j^S, and ϕ^T are continuous across the slip plane, the contributions due to the first two terms of equation (41) cancel. With the jump conditions on u_i^S and ϕ^S, the last two terms become

$$-\int_{\Sigma^+ + \Sigma^-} [\sigma_{ij}^T u_i^S + D_j^T \phi^S] n_j \, dS$$
$$= b_i \int_{\Sigma^+} \sigma_{ij}^T n_j \, dS + \Delta\phi \int_{\Sigma^+} D_j^T n_j \, dS. \tag{44}$$

The total interaction energy for a piezoelectric dislocation interacting with another stress system T can now be written as

$$H_{\text{tot}} = b_i \int_{\Sigma^+} \sigma_{ij}^T n_j \, dS + \Delta\phi \int_{\Sigma^+} D_j^T n_j \, dS - p_i^S u_i^T + q^S \phi^T. \tag{45}$$

The last two terms correspond to the work done by the body force and the body charge of S against the displacement and the electric potential of T. This expression is valid for both screw and edge dislocations in any linear elastic piezoelectric crystals. Faivre and Saada (1972) derived a similar result by considering the internal energy instead of the electric enthalpy. By calculating the change in the total energy with respect to a small movement of the dislocation line, we can obtain the expression for the force acting on a dislocation S due to a stress-field system T. The change in H_{int} resulting from moving a unit length of dislocation in the x_k direction by an amount $\delta\xi$ is

$$\delta H_{\text{int}} = [b_i \sigma_{ij}^T + \Delta\phi D_j^T] \epsilon_{jkl} \delta\xi_k s_l, \tag{46}$$

where ϵ_{jkl} is an alternating tensor and s_l is a unit vector parallel to the dislocation line. Likewise the change in H_{ext} is

$$\delta H_{\text{ext}} = \left[-p_i^S \frac{\partial u_i^T}{\partial x_k} + q^S \frac{\partial \phi^T}{\partial x_k} \right] \delta\xi_k. \tag{47}$$

The general expression for the force acting on a dislocation in a piezoelectric crystal with a line load and a line charge "attached" to it is

$$F_k = \lim_{\delta\xi \to 0} -\frac{\partial H_{\text{tot}}}{\delta\xi_k} = -(b_i \sigma_{ij}^T + \Delta\phi D_j^T) \epsilon_{jkl} s_l + p_i^S u_{i,k}^T + q^S E_k^T. \tag{48}$$

This is the well-known Peach-Koehler force generalized to include piezoelectric effects and body forces. It is interesting to note that while $p_i^S u_{i,k}^T$ is not the actual physical force experience by the dislocation (but rather a generalized thermodynamic force), $q^S E_k^T$ is the actual physical electrostatic force acting on the charged dislocation. For infinite screw and edge dislocations along the z-axis with the Burgers vector b_z, b_x, and b_y, respectively, the generalized Peach-Koehler forces are

$$F_x = b_z \sigma_{zy}^T + \Delta\phi D_y^T + p_z^S \gamma_{zx}^T + q^S E_x^T$$
$$F_y = -b_z \sigma_{zx}^T - \Delta\phi D_x^T + p_z^S \gamma_{zy}^T + q^S E_y^T, \tag{49}$$
$$F_x = b_x \sigma_{xy}^T + \Delta\phi D_y^T + p_x^S u_{x,x}^T + p_y^S u_{y,x}^T + q^S E_x^T$$
$$F_y = -b_x \sigma_{xx}^T - \Delta\phi D_x^T + p_x^S u_{x,y}^T + p_y^S u_{y,y}^T + q^S E_y^T, \tag{50}$$
$$F_x = b_y \sigma_{yy}^T + \Delta\phi D_y^T + p_x^S u_{x,x}^T + p_y^S u_{y,x}^T + q^S E_x^T$$
$$F_y = -b_y \sigma_{xy}^T - \Delta\phi D_x^T + p_x^S u_{x,y}^T + p_y^S u_{y,y}^T + q^S E_y^T, \tag{51}$$

where γ_{ij}^T in equation (49) are the antiplane shear strains.

We can also calculate the force on an elastic singularity by evaluating a path-independent surface integral introduced by Eshelby and later independently by Rice (1968). Pak (1987) has generalized this integral for piezoelectric materials which takes the form of

$$F_k = \int_S [h\delta_{jk} - \sigma_{ij} u_{i,k} + D_j E_k] n_j \, dS, \tag{52}$$

where δ_{jk} is Kronecker delta. To obtain a solution for a piezoelectdric screw dislocation subjected to constant external loads, σ_{zx}^T, σ_{zy}^T, D_x^T, and D_y^T, we can superpose a constant field solution to the dislocation solution obtained previously. Evaluating the x and the y-component of this integral on a circular contour surrounding a piezoelectric screw dislocation, we arrive at

Downloaded 03 May 2010 to 171.66.16.244. Redistribution subject to ASME license or copyright; see http://www.asme.org/terms/Terms_Use.cfm

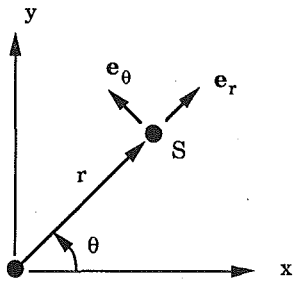


Fig. 6 Two parallel screw dislocations *S* and *T* in *x-y* plane

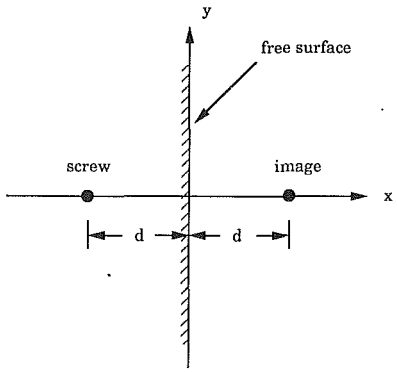


Fig. 7 Screw dislocation near a free boundary, and its image dislocation

$$F_x = b_z\sigma_{zy}^T + \Delta\phi D_y^T + \frac{p(\epsilon_{11}\sigma_{zx}^T + e_{15}D_x^T)}{c_{44}\epsilon_{11} + e_{15}^2} + \frac{q(c_{44}D_x^T - e_{15}\sigma_{zx}^T)}{c_{44}\epsilon_{11} + e_{15}^2}$$

$$F_y = -b_z\sigma_{zx}^T - \Delta\phi D_x^T + \frac{p(\epsilon_{11}\sigma_{zy}^T + e_{15}D_y^T)}{c_{44}\epsilon_{11} + e_{15}^2} + \frac{q(c_{44}D_y^T - e_{15}\sigma_{zy}^T)}{c_{44}\epsilon_{11} + e_{15}^2}. \tag{53}$$

These results are identical to equation (49) with γ_{ij}^T and E_i^T expressed in terms of the applied mechanical and electrical loads via constitutive relations equations (19).

Force Between Two Parallel Screw Dislocations

Once we have the solution to a single screw dislocation, we can superpose the solutions to obtain the solution for two screw dislocations parallel to each other. Then, using the generalized Peach-Koehler force expression given in equation (49), we can calculate the interaction forces between two piezoelectric screw dislocations. If we let T represent a dislocation at the origin and S represent a dislocation at some point (r, θ) in the x-y plane as shown in Fig. 6, the cylindrical components of the force acting on S due to T can be expressed as

$$F_r = b^S\sigma_{z\theta}^T + \Delta\phi^S D_\theta^T + p^S\gamma_{zr}^T + q^S E_r^T$$
$$F_\theta = -b^S\sigma_{zr}^T - \Delta\phi^S D_r^T + p^S\gamma_{z\theta}^T + q^S E_\theta^T. \tag{54}$$

Due to the cylindrical symmetry of the fields generated by a screw dislocation, the interaction forces between two screw dislocations depend only on the distance between them. Because we have a θ component of the force as well as a radial one, dislocation can move spirally toward or away from each other depending on whether the radial force is repulsive or attractive. Substituting the solutions equations (33)–(36) in equations (54), we obtain the force in an explicit form

$$F_r = \frac{1}{2\pi r}\left[c_{44}b^S b^T + e_{15}b^S\Delta\phi^T + e_{15}b^T\Delta\phi^S - \epsilon_{11}\Delta\phi^S\Delta\phi^T + \frac{-\epsilon_{11}p^S p^T + e_{15}p^S q^T + e_{15}p^T q^S + c_{44}q^S q^T}{c_{44}\epsilon_{11} + e_{15}^2}\right]$$

$$F_\theta = \frac{1}{2\pi r}\left[b^S p^T + b^T p^S - \Delta\phi^S q^T - \Delta\phi^T q^S\right]. \tag{55}$$

The expression for F_θ shows that, if a line force, a line charge, and a jump in the electric potential do not exit, the forces are then purely radial. In equations (55) for the radial force, a positive term contributes to the repulsive force and a negative term to an attractive one. The radial force expressions also contain some well-known results; two parallel screw dislocations with the same Burgers vector and two parallel line charges with a like charge repel each other. It is interesting to note that two line forces applied in the same direction attract each other. This is due to the fact that the potential energy of a line force decreases as it moves closer to the other; it gets displaced in the same direction as its force. The radial force expression also shows that two "electric-potential-dislocations" of the same sign, generating clockwise tangential electric fields, attract each other, possibly because the tangential fields between them annihilate each other, decreasing the electrical energy.

One can also calculate the image force acting on a dislocation near a traction-free, $\sigma_{ij}n_j = 0$, and a charge-free, $D_i n_i = 0$, boundary. For the configuration shown in Fig. 7 with a piezoelectric screw dislocation located at $(-d, 0)$, the image fields due to the free boundary can be obtained from equations (33)–(36) by reversing the signs of b and $\Delta\phi$ but keeping the same signs for p and q. Then from equation (49), the force due to the image fields can be obtained as

$$F_x = \frac{1}{4\pi d}\left[c_{44}b^2 + 2e_{15}b\Delta\phi - \epsilon_{11}\Delta\phi^2 + \frac{\epsilon_{11}p^2 - 2e_{15}pq - c_{44}q^2}{c_{44}\epsilon_{11} + e_{15}^2}\right] \tag{56}$$

$F_y = 0$.

The same result can be obtained from equation (55) with the appropriate sign changes. It is interesting to note that, just as in the purely elastic case, the force expression above is identical to the prelogarithmic energy factor given in equation (37) divided by the length parameter d. If we have, instead of a free boundary a material with higher elastic and dielectric constants interfacing at the boundary, we would expect to see the force acting in the opposite direction.

Concluding Remarks

The solution to a screw dislocation problem in a hexagonal piezoelectric crystal was obtained in a closed form. It was shown that for a particular case of a straight dislocation with the Burgers vector normal to the isotropic basal plane, the mechanical and the electrical fields decouple in the governing equations and the problem reduces to solving the Laplace equations in the displacement and the electric potential. Following the method of Eshelby, the energetics of the system is considered to calculate the force acting on an electro-elastic singularity in a piezoelectric material. It also was demonstrated that the path-independent integral (widely known as the J-integral), generalized to include piezoelectric effects, provides the Peach-Koehler force acting on the dislocation. The force between two parallel screw dislocations and the image force due to the presence of a free surface also were calculated. Since the electrical quantities can change in sign and in direction, their presence can either increase or decrease the interaction forces acting on piezoelectric dislocations. In the limiting case of vanishing electrical quantities, all the results obtained in this paper reduce to those for a purely elastic screw dislocation.

Downloaded 03 May 2010 to 171.66.16.244. Redistribution subject to ASME license or copyright; see http://www.asme.org/terms/Terms_Use.cfm

Acknowledgment

This work was supported by the Independent Research and Development Program at Grumman Corporate Research Center. Some of the algebraic calculations were performed on a MacIntosh II personal computer, using Mathematica, a symbolic manipulation software.

References

Barnett, D. M., and Lothe, J., 1975, "Dislocations and Line Charges in Anisotropic Piezoelectric Insulators," *Phys. Stat. Sol.* (*b*), Vol. 67, p. 105.

Berlincourt, D. A., Curran, D. R., and Jaffe, H., 1964, "Piezoelectric and Piezomagnetic Materials and Their Function in Transducers," *Physical Acoustics*, Vol. 1A, W. P. Mason, ed., Academic Press, New York, p. 177.

Eshelby, J. D., 1951, "The Force on an Elastic Singularity," *Phil. Trans. Roy. Soc.*, Vol. A244, No. 877, p. 87.

Eshelby, J. D., Read, W. T., and Shockley, W., 1953, *Acta Met.*, Vol. 1, p. 251.

Eshelby, J. D., 1956, "The Continuum Theory of Lattice Defects," *Solid State Physics*, Vol. 3, p. 79.

Faivre, G., and Saada, G., 1972, "Dislocations in Piezoelectric Semiconductors," *Phys. Stat. Sol.* (*b*), Vol. 52, p. 127.

Farvacque, J. L., Doukhan, J. C., von Alpen, U., and Gmelin, E., 1977, "Screw-Dislocation-Induced Scattering Processes and Acceptor States in Te," *Phys. Stat. Sol* (*b*), Vol. 79, p. 763.

Hirth, J. P., and Lothe, J., 1982, *Theory of Dislocations*, John Wiley and Sons, New York, p. 436.

Merten, L., 1964, "Modell einer Schraubenversetzung in piezoelektrischen Kristallen. I," *Phys. Kondens. Materie*, Vol. 2, pp. 53–65.

Pak, Y. E., 1987, "Crack Extension Force in a Piezoelectric Material," Advanced Development Report 20-11-87.1, Grumman Aerospace Corporation.

Rice, J. R., 1968, "A Path-Independent Integral and the Approximate Analysis of Strain Concentration by Notches and Cracks," ASME JOURNAL OF APPLIED MECHANICS, Vol. 35, p. 379.

Saada, G., 1971, "Dislocations dans les Cristaux Piézoélectriques," *Phys. Stat. Sol.* (*b*), Vol. 44, p. 717.

Stroh, A. N., 1958, "Dislocations and Cracks in Anisotropic Elasticity," *Phil. Mag.*, Vol. 3, p. 625.

Tiersten, H. F., 1969, *Linear Piezoelectric Plate Vibrations*, Plenum Press, New York.

Downloaded 03 May 2010 to 171.66.16.244. Redistribution subject to ASME license or copyright; see http://www.asme.org/terms/Terms_Use.cfm

Incident Wave and Dislocation Acceleration Effects in Dislocation Emission From Cracks

L. M. Brock
Mem. ASME

J.-S. Wu

Department of Engineering Mechanics,
University of Kentucky,
Lexington, KY 40506

Some previous transient analyses of dislocation emission from dynamically loaded cracks have treated glide at constant speeds, and have invoked an emissions criterion that allows the dislocation force to exceed the yield stress level during glide. In the context of nonstrain-hardening plasticity, this analysis requires that the force remain at the yield stress level. For an exact solution to the problem of screw dislocation emission from a crack subjected to plane SH-wave diffraction, the result is an equation of motion for the dislocation, which can be integrated exactly. The dislocation is found to accelerate during glide to a high but subcritical speed, before decelerating to its arrest position. A general incident SH-wave is considered, but is then specialized to the cases of a step-stress and a sinusoidal wave. Calculations on the basis of material and wave parameters show that purely brittle fracture can be difficult to achieve, and that wavelength/frequency cutoffs exist, beyond which emission cannot occur.

Introduction

Rice and Thomson (1974) and Ohr (1985) have examined quasi-static models for the emission of dislocations from elastic crack edges, while Brock (1989a) and Brock and Wu (1989a,b) have extended such models to dynamic loading and transient situations. The transient work, hereafter referred to as B-BW when cited together, examined exact solutions for screw dislocations, emitted from cracks subjected to incident SH-waves, in light of a dislocation force-based emissions criterion similar to those used in the quasi-static studies. It was found that the emitted dislocations always arrested, and that the emission process would generally occur prior to the attainment of crack edge conditions suitable for brittle fracture.

Glide occurred in B-BW at constant, subcritical speeds, and the emissions criterion required only that the dislocation force not fall below the yield stress level during glide. The constant speed assumption followed the well-known results of Johnston and Gilman (1959), while the mild force requirement was based on the idea (Mura, 1982) that dislocation motion can be associated with micromechanical strain hardening. Brock and Wu (1989a) noted that, in fact, these two aspects were coupled by the form of the dislocation force function. Finally, only step-stress SH-waves were treated, so that insight into the effects of more general incident wave properties, such as wavelength/frequency, was not possible.

The present analysis, therefore, reconsiders the work of B-BW: A more general incident SH-wave form is treated, the possibility of nonconstant speed glide is allowed and, more in accordance with classical nonstrain-hardening plasticity (Hill, 1967), the dislocation force is required to remain at the yield stress level during emission. Glide speeds are, however, still subcritical, a requirement based on the observation, e.g., (Mura, 1982; Brock, 1989a) that the glide plane-stress singularity order drops when a screw dislocation moves with the shear wave speed.

The exact solution to the basic emission problem is considered in the next two sections. The modified emissions criterion is then invoked, giving rise to an equation of motion for the screw dislocation, analogous to those for crack propagation (Freund, 1972). The behavior predicted by the equation is then studied. In particular, the cases of step-stress and sinusoidal incident SH-waves are examined. For this analysis, the semi-infinite crack model common (Achenbach, 1973) to transient analyses of fracture is employed. Such a model assumes that the critical event—emission here—occurs prior to the arrival of waves from the other edge of the actual crack. It will be seen that the assumption is justified here even for crack lengths which are several orders of magnitude less than the incident wavelength.

Basic Problem

Consider an unbounded, linearly elastic, homogeneous, isotropic solid containing a crack defined by Cartesian coordinates as $y = 0, x < 0$. The solid is undisturbed save for an incident plane SH-wave

Contributed by the Applied Mechanics Division of THE AMERICAN SOCIETY OF MECHANICAL ENGINEERS for presentation at the Winter Annual Meeting, Dallas, Texas, Nov. 25–30, 1990.

Discussion on this paper should be addressed to the Technical Editor, Leon M. Keer, the Technological Institute, Northwestern University, Evanston, IL 60208, and will be accepted until two months after final publication of the paper itself in the JOURNAL OF APPLIED MECHANICS. Manuscript received and accepted by the ASME Applied Mechanics Division, Mar. 16, 1989.

Paper No. 90-WA/APM-39.

Copyright © 1990 by ASME
Downloaded 03 May 2010 to 171.66.16.244. Redistribution subject to ASME license or copyright; see http://www.asme.org/terms/Terms_Use.cfm

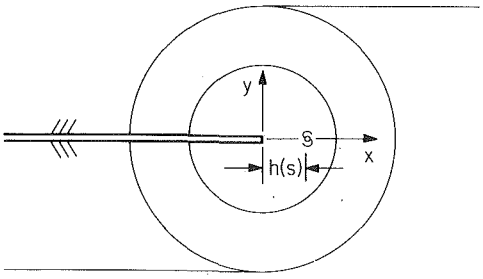


Fig. 1 Wave patterns, due to diffraction-emission process

$$\mu w_i = -\int_0^{s-y} g(u)\,du \quad (s \geq y), \tag{1}$$

where s is the time multiplied by the shear wave speed, μ is the shear modulus, and w_i is the displacement out of the xy-plane. The function $g(u)$ is the traction σ_{yz} produced a distance u behind the wavefront; it is piecewise continuous but, for now, otherwise arbitrary. As equation (1) indicates, the wave is traveling in the positive y-direction, and at $s = 0$ is diffracted by the crack. A mode III state results, and at $s = s_o > 0$, a right-handed screw dislocation with Burgers vector magnitude b is generated at the crack edge. The dislocation moves along the positive x-axis so that its position is always given by $y = 0$, $x = h(s)$. Here, $h(s)$ is single-valued and continuous, with properties

$$h(s) \equiv 0 (s \leq s_o),\ 0 \leq \dot{h} < 1 (s \geq s_o) \tag{2}$$

where $(\cdot)$ denotes s-differentiation. Thus, $\dot{h}$ is the dislocation emission speed nondimensionalized with respect to the shear wave speed; as equation (2) indicates, it is subcritical and nonnegative, but is otherwise arbitrary. It would appear that we must have $g > 0$ in order to produce a right-handed screw dislocation; however, the precise requirements for g will be discussed later.

This diffraction-emission process generates the wave pattern indicated schematically in Fig. 1. Only the displacement $w(x, y, s)$ out of the xy-plane exists, and can be written by superposition as

$$w = w_i + W_i + w_b + W_b \tag{3}$$

where w_b is the dislocation-generated contribution and (W_i, W_b) arise in order to cancel, respectively, the (w_i, w_b)-induced tractions from the crack surfaces. Each of the functions satisfies the equations

$$\frac{\partial}{\partial x}\sigma_{xz} + \frac{\partial}{\partial y}\sigma_{yz} = \mu\ddot{w},\ \sigma_{xz} = \mu\frac{\partial w}{\partial x},\ \sigma_{yz} = \mu\frac{\partial w}{\partial y} \tag{4}$$

for all $s > 0$ everywhere except perhaps the crack surface and dislocation slip zone.

Problems of the type involving (w_i, W_i) have been treated by Achenbach (1970), and expressions for the tractions on the plane ahead of the crack generated. These can be written for all $s > 0$ as

$$\sigma_{yz} = g(s) \quad (x < 0) \tag{5a}$$

$$\sigma_{yz} = \frac{1}{\pi\sqrt{x}}\int_0^{s-x} du\sqrt{u}\,\frac{g(s-x-u)}{u+x}\,du \quad (s \geq x > 0) \tag{5b}$$

for w_i and W_i, respectively. For what follows, equation (5) is sufficient, but in the case of w_b, the complete solution is needed. Fortunately, this can be obtained by simple manipulations of results by either Eshelby (1953) or Brock (1986):

$$\frac{2\pi}{b}w_b = y\int_{s_o}^{t^*}\frac{\dot{h}T\,dt}{R^2\sqrt{(T^2-R^2)}},\ T = s-t,\ T_o = s-s_o. \tag{6}$$

Here, $T_o > r$, $h = h(t)$ and

$$t^* = s - R(t^*),\ R(t) = \sqrt{[(x-h)^2+y^2]},\ r = R(s_o) = \sqrt{(x^2+y^2)} \tag{7}$$

while b is the Burgers vector magnitude.

By following and then specializing the analysis of Brock (1989), who treated the more general problem of nonrectilinear screw dislocation motion near a growing crack, an exact expression for W_b can be obtained. For present purposes, however, only the traction σ_{yz} generated by W_b ahead of the crack is required. How this traction is obtained, after Brock (1989a), is outlined in the next section.

Crack Plane Traction

From the work of Achenbach (1970), the necessary traction can be obtained by Green's function methods (Carrier and Pearson, 1976) as the solution to an Abel integral equation. Its general form is (Brock and Wu, 1989a,b)

$$\frac{1}{\mu}\sigma_{yz} = \frac{1}{\pi\sqrt{(\eta-\xi)}}\int_L^{\xi}\frac{\partial w_b}{\partial y}\left(\frac{v-\xi}{\sqrt{2}},\ 0,\ \frac{v+\xi}{\sqrt{2}}\right)\frac{\sqrt{(\xi-v)}}{\eta-v}\,dv,$$

$$L = \frac{s_o\xi}{\sqrt{2\xi - s_o}} \quad (s \geq x > 0) \tag{8}$$

where

$$\sqrt{2}\eta = s + x,\ \sqrt{2}\xi = s - x \tag{9}$$

are characteristic variables which arise naturally in the integral equation solution. The integrand function arguments correspond to $(x, 0, s)$, and $\eta = (\xi, L)$ are the $\xi\eta$-plane trajectories of, respectively, the crack edge and the intersection of the cylindrical shear wave radiating from the dislocation and the crack surfaces.

Evaluation of equation (8) requires, in view of equation (6), double integration and that w_b be differentiated with respect to y, and then y set to zero. For the constant-$\dot{h}$ case (B-BW), this is easily done because the singular integration ($T = R$ when $t = t^*$) can be carried out analytically. In the present case, we avoid the necessity of differentiating equation (6) by for the moment leaving these two steps as formal operations (Sneddon, 1972). Therefore, instead of equation (8), we deal with the related quantity

$$\frac{1}{\mu}\sigma_{yz}^{\epsilon} = \frac{1}{\pi\sqrt{(\eta-\xi)}}\int_{L_\epsilon}^{\xi}\frac{\partial w_b}{\partial \epsilon}\left(\frac{v-\xi}{\sqrt{2}},\ \epsilon,\ \frac{v+\xi}{\sqrt{2}}\right)\frac{\sqrt{(\xi-v)}}{\eta-v}\,dv,$$

$$\sqrt{2}L_\epsilon = \frac{\epsilon^2 + \sqrt{2}s_o\xi}{\sqrt{2\xi - s_o}}. \tag{10}$$

Here, $\epsilon > 0$ is an arbitrary real number, and $\eta = L_\epsilon$ is the trajectory of the dislocation-induced cylindrical wave intersection with the plane $y = \epsilon$. Equations (8) and (10) are, of course, identical when $\epsilon \to 0$.

At this point, it is convenient to work with the variables (x, s), and so we introduce equation (9) and the integration variable change $\sqrt{2}z = \xi - v$. In view of equation (6), it can then be shown that equation (10) becomes

$$\frac{2\pi^2}{\mu b}\sigma_{yz}^{\epsilon} = \frac{1}{\sqrt{x}}\int_0^{z_\epsilon}\frac{\sqrt{z}}{x+z}\frac{\partial}{\partial\epsilon}\epsilon\int_{s_o}^{t^*}\frac{\dot{h}(U-z)}{\sqrt{[2(U+H)]}}\frac{1}{\sqrt{(z^*-z)}}$$

$$\times\frac{dt}{(z+h)^2+\epsilon^2},\ U = T - x \tag{11}$$

where we now have

$$z^* = \frac{U^2 - h^2 - \epsilon^2}{2(U+h)},\ t^* = s - x - z - R(t^*),$$

$$z_\epsilon = \frac{(T_o - x)^2 - \epsilon^2}{2(T_o - x)} \tag{12}$$

and R is evaluated at $y = \epsilon$. It is easily shown that $t^*(z_\epsilon) =$

Downloaded 03 May 2010 to 171.66.16.244. Redistribution subject to ASME license or copyright; see http://www.asme.org/terms/Terms_Use.cfm

s_o, $z^*(s_o) = z_\epsilon$ while $z^* < 0$. Thus, the differentiation can be placed outside the double integration, and the order of integration reversed to give

$$\frac{2\pi^2}{\mu b}\sigma^\epsilon_{yz} = \frac{1}{\sqrt{x}}\frac{\partial}{\partial\epsilon}\epsilon\int_{s_o}^{t_o^*}\frac{\dot{h}dt}{\sqrt{[2(U+h)]}}$$

$$\int_0^{z^*}\frac{U-z}{x+z}\sqrt{\left(\frac{z}{z^*-z}\right)}\frac{dz}{(z+h)^2+\epsilon^2} \tag{13}$$

$$t_o^* = s-x-R_o(t_o^*),\ R_o(t) = \sqrt{(h^2+\epsilon^2)}. \tag{14}$$

The z-integration is along the branch cut $0 < z < z^*$ of the integrand, which itself exhibits simple poles at $z = -x < 0$ and $z = -h \pm i|\epsilon|$, and behaves as $0(z^{-2})$, when $|z| \to \infty$. Cauchy residue theory can be used, therefore, so that equation (13) becomes

$$\frac{2\pi}{\mu b}\sigma^\epsilon_{yz} = \frac{1}{\sqrt{x}}\frac{\partial}{\partial\epsilon}\int_{s_o}^{t_o^*}\frac{h\sqrt{R_o}}{r}\sin\left(\Omega-\frac{1}{2}\Omega_o\right)dt$$

$$-\frac{\partial}{\partial\epsilon}\epsilon\int_{s_o}^{t_o^*}\frac{\dot{h}Tdt}{R^2\sqrt{(T^2-R^2)}} \tag{15}$$

where R is again evaluated at $y = \epsilon$, and

$$h-x = R\cos\Omega,\ h = R_o\cos\Omega_o,\ \epsilon = R\sin\Omega = R_o\sin\Omega_o. \tag{16}$$

Introduction of the integration variable $u = h(t)$ in the first integral in equation (15) produces a result with no explicit dependence on $\dot{h}$, and dependence on t_o^* only through the quantity $h(t_o^*)$. Moreover, it can be shown that

$$\frac{\partial}{\partial\epsilon}\frac{\sqrt{R_o}}{R}\sin\left(\Omega-\frac{1}{2}\Omega_o\right) = \frac{-\partial}{\partial h}\frac{\sqrt{R_o}}{R}\cos\left(\Omega-\frac{1}{2}\Omega_o\right), \tag{17a}$$

$$\frac{dt_o^*}{d\epsilon} = \frac{\sin\Omega_o(t_o^*)}{1-\dot{h}(t_o^*)\cos\Omega_o(t_o^*)}, \tag{17b}$$

while the integrand of the second integral in equation (15) is not singular at $t = (s_o, t_o^*)$. Thus, the first integration in equation (15) can be performed analytically, and differentiation of both this result and the second integral is straightforward. Then, setting $\epsilon = 0$ yields for $y = 0$, $0 < x < T_o$ the expression

$$\frac{2\pi}{\mu b}\sigma_{yz} = \frac{1}{x-h^*}\left(\frac{h^*}{x}\right) + \int_{s_o}^{t_o^*}\frac{\dot{h}Tdt}{(x-h)^2\sqrt{[T^2-(x-h)^2]}} \tag{18}$$

where now

$$h^* = h(t^*),\ t^* = s-x-h^*. \tag{19}$$

This completes the assembly of expressions required for studying the emission process. In the next section, they are viewed in terms of an emission criterion.

The Criterion for Dislocation Emission

It is generally held (Dundurs, 1968; Mura, 1982; Hirth and Lothe, 1982) that dislocation motion by glide cannot occur until the dislocation force overcomes the lattice friction, which is identified with the material yield stress (Shaw, 1984). Rice and Thomson (1974), Ohr (1985), and B-BW have adopted this idea for both quasi-static and transient emission studies, under the assumption that an emitted dislocation does not travel far from the crack edge. For the transient case, a characteristic length may not be present in the geometry until wave reflections occur, so that the requirement

$$h/s_o \ll 1 \tag{20}$$

is imposed (B-BW). That is, the dislocation travel distance after emission ($s > s_o$) is much smaller than the distance traveled by a shear wave in the interval between wave diffraction and emission ($0 < s < s_o$).

The dislocation force on the glide plane per unit of length of dislocation edge, F, can be obtained from the Peach-Koehler formulas (Hirth and Lothe, 1982) as

$$\frac{F}{b} = \sigma_{yz} \tag{21}$$

where σ_{yz} is the total due to w and is evaluated at the dislocation. Despite the singularity there due to the w_b-contribution, a finite result can be obtained by approaching this position along a path perpendicular to the glide plane (Dundurs, 1968). We, therefore, perform this limiting process for the w_b-contribution, while merely setting $y = 0$, $x = h(s)$ in the contribution equations (5) and (18). In view of equations (2) and (20) and continuity, both $h(s)$ and T_o are much smaller than either s or s_o. Consequently, equation (21) gives

$$\frac{F}{b} = \frac{H_o}{\pi\sqrt{h}} - \frac{\mu b}{4\pi}\sqrt{\left(\frac{1+\dot{h}}{1-\dot{h}}\right)}\frac{1}{h},$$

$$H_o = P(s_o),\ P(s) = \int_0^s\frac{g(u)}{\sqrt{(s-u)}}du \tag{22a-c}$$

where we have also used the mean value theorem-based relation $\dot{h}(s) = \dot{h}(\bar{t})T_o$, $s_o < \bar{t} < s$. This assumes, of course, that $\dot{h}$ is also continuous for T_c near zero where, in view of equation (20), equation (22a) is to hold. For the step-stress case $g(u) = \tau$, equation (22a) is identical in form to the constant-$\dot{h}$ force (B-BW). Moreover, the nature of the h-dependence is identical to that arising in the quasi-static force (Ohr, 1985).

As indicated at the outset, B-BW required only that the force not fall below the yield stress level during dislocation motion. Thus, equating either F/b or its quasi-static counterpart to the yield stress σ resulted in a quadratic equation for the values $\sqrt{h}$ at which dislocation motion ceased, and thereby guaranteed dislocation arrest. The square of the larger root was treated as the arrest distance, while the square of the smaller root could not exceed the dislocation core radius r_c (Hirth and Lothe, 1982). This requirement followed from the idea (Ohr, 1985) that the applied stress term (H_o here) in the force must overcome the resistance to glide represented by the dislocation term (the b-term here) within this distance if emission is to be said to have occurred. Thus, a micromechanically-scaled zone of attraction exists at the crack edge. Moreover, this requirement is consistent with a view that perhaps the position of the continuum representation of the dislocation should be defined only to within an uncertainty no larger than the core radius.

In the present analysis, F/b is to equal σ during glide, a condition which equation (22a) obviously cannot satisfy for constant $\dot{h}$. Because $\dot{h}$ here does not have to be constant, equation (22a) gives, in effect, an equation of motion. This equation makes sense only when $H_o > 0$, which means that, while the incident wave stress g may change sign, its weighted time history H_o must be positive. If a left-handed screw dislocation were to be generated, then the requirement would of course be $H_o < 0$, and (b, σ) would be replaced in all the previous work by $(-b, -\sigma)$. With this understanding, solving the equation $F/b = \sigma$ gives

$$\dot{h} = \frac{h(2\alpha-\sqrt{h})^2-\beta^2}{h(2\alpha-\sqrt{h})^2+\beta^2},\ 2\alpha = \frac{H_o}{\pi\sigma},\ \beta = \frac{1}{4\pi}\frac{\mu}{\sigma}b. \tag{23}$$

Examination of equation (23) shows that $|\dot{h}| < 1$ for $h \geq 0$, and that $\dot{h}$ vanishes at the four roots $\sqrt{h} = \sqrt{h_i}$, where

$$\sqrt{h_1} = \alpha-p_+,\ \sqrt{h_2} = \alpha-p_-,\ \sqrt{h_3} = \alpha+p_-,\ \sqrt{h_4} = \alpha+p_+,$$

$$p_\pm = \sqrt{(\alpha^2\pm\beta)}. \tag{24}$$

The root $\sqrt{h_1}$ has no physical significance because it is negative, while $(\sqrt{h_2}, \sqrt{h_3})$ will have none unless $\alpha^2/\beta > 1$. For the special case $g(u) = \tau$ and constant $\dot{h}$, it can be shown (B-BW) that equation (23) gives $\alpha^2/\beta \gg 1$, because $\tau/\sigma < 0\ (10^{-1})$ for a high but reasonable stress while $\sigma/\mu < 0\ (10^{-2})$ for many

Downloaded 03 May 2010 to 171.66.16.244. Redistribution subject to ASME license or copyright; see http://www.asme.org/terms/Terms_Use.cfm

metallic solids (Guy, 1960). Thus, for the moment we will assume that ($\sqrt{h_2}$, $\sqrt{h_3}$) are real. Then, $\sqrt{h_1} < 0 < \sqrt{h_2} < \sqrt{h_4}$, and it can be shown that $\dot{h} > 0$ for $h_2 < h < h_3$. Finally, setting $\dot{h} = 0$ in equation (22*a*) and solving $F/b = \sigma$ for $\sqrt{h}$ gives the solutions ($\sqrt{h_2}$, $\sqrt{h_3}$). This behavior would suggest that dislocation emission begins at zero speed, and that arrest occurs at $y = 0$, $x = h_3$ after deceleration to zero speed. That is, h_1 is the length of the crack edge attraction/uncertainty zone, and h_3 is the arrest distance.

We will, for the time being, however, assume that emission initiates at a finite speed. That is, $\dot{h}(s_o) = c$, where $0 < c < 1$ is the speed nondimensionalized with respect to the shear wave speed. The positive behavior of $\dot{h}$ for $h_2 < h < h_3$ suggests, then, that the zone length must now be some value h_o, where $h_2 < h_o < h_3$. Because this length should not exceed the core radius r_c,

$$h_o = \lambda r_c (0 < \lambda \leq 1) \tag{25}$$

where λ is an arbitrary, dimensionless parameter. Because $h_2 < h_o < h_3$ and must satisfy equation (23) with $\dot{h} = c$, equation (25) can be used to obtain the relations

$$H_o = 2\pi\sigma\sqrt{(\lambda r_c)}A,\ 2A = 1 + kB,$$

$$B = \frac{1}{4\pi\lambda}\frac{\mu b}{\sigma r_c},\ k = \sqrt{\left(\frac{1+c}{1-c}\right)} \tag{26a-d}$$

for s_o. Substitution of this result into equation (24) gives

$$\sqrt{h_1} = -\sqrt{(\lambda r_c)}e_1,\ \sqrt{h_i} = \sqrt{(\lambda r_c)}e_i (i = 2,3,4) \tag{27a}$$

$$e_1 = Q_+ - A,\ e_2 = A - Q_-,\ e_3 = A + Q_-,\ e_4 = A + Q_+,$$

$$Q_\pm = \sqrt{(A^2 \pm B)} \tag{27b}$$

Because $k > 1$ ($0 < c < 1$), while $b/r_c = 0$ (1) (Rice and Thomson, 1974) and $\mu/\sigma \geq 0$ (10^2) (Guy, 1960) for metallic solids, it is easily shown that $h_3 \gg \lambda r_c > h_2$.

At this point we note that if the dimensionless parameter λ is introduced into the quasi-static formulations by Ohr (1985), one can obtain the arrest distance expressions

$$h_3 = \frac{1}{\lambda r_c}\left(\frac{\mu}{\sigma}\frac{b}{r\pi}\right)^2,\ h_3 = \frac{1}{\lambda r_c}\left(\frac{\mu}{\sigma}\frac{kb}{4\pi}\right)^2 \tag{28a,b}$$

from, respectively, Ohr's work and the B-BW results (with $\dot{h} = c$). Comparison of equation (28) with equation (27*a*) for h_3 shows that both transient analyses produce a dislocation speed-dependent dynamic overshoot effect, but that the effect for constant $\dot{h}$ is more pronounced.

Further Study of Equation of Motion: Sinusoidal Wave

Because s does not appear explicitly, the equation of motion equation (23) describes for $\lambda r_c < h < h_3$ a phase space (h, $\dot{h}$) diagram for the dislocation. By setting $d\dot{h}/dh = 0$ in view of equation (27), we find that $\dot{h}$ achieves a maximum value $\dot{h}_m$ for $h = h_m$, where

$$h_m = \lambda r_c A^2 (\lambda r_c < h_m < h_3),\ \dot{h}_m = \frac{(Q_+ Q_-)^2}{A^4 + B^2} < 1. \tag{29}$$

The forms of equation (27) suggest in view of equation (29) that $\sqrt{h_m}$ is roughly the average of $\sqrt{h_2}$ and $\sqrt{h_3}$; because $h_2 < \lambda r_c \ll h_3$, this implies that the dislocation attains a maximum subcritical speed at roughly one quarter of the arrest distance.

Separation of variables in equation (23) and integration gives an equation for s as a function of h, valid for $\lambda r_c < h < h_3$:

$$\frac{1}{\lambda r_c}(s - s_o) = z - 1 + B\ln\left(\frac{\sqrt{z} - e_2}{1 - e_2}\right)^{k_2}\left(\frac{e_3 - 1}{e_3 - \sqrt{z}}\right)^{k_3}$$

$$\times\left(\frac{e_4 - \sqrt{z}}{e_4 - 1}\right)^{k_4}\left(\frac{1 + e_1}{\sqrt{z} + e_1}\right)^{k_1} (1 < z < e_3^2) \tag{30a}$$

$$z = \frac{h}{\lambda r_c},\ k_i = \frac{e_i}{Q_+}\ (i = 1,4,),\ k_i = \frac{e_i}{Q_-}\ (i = 2,3) \tag{30b}$$

Here we have used the observation that (h_3, h_m) $\gg \lambda r_c$ to justify identification of the emission instant s_o with the attraction zone location $y = 0$, $x = \lambda r_c$, not the crack edge itself. Substitution of $h = h_3$ ($z = e_3^2$) into equation (30*a*) gives $s \to \infty$. That is, dislocation arrest occurs only after an infinitely long period of deceleration to zero speed. This result is in contrast to the constant-$\dot{h}$ results (B-BW), which gave a finite arrest time. Similarly, substitution of $h = h_2$ ($z = e_2^2$) into equation (30*a*) gives $s \to -\infty$, an unfortunate result which cannot actually occur because equation (30*a*) holds for $h > \lambda r_c$, where $\lambda r_c > h_2$. However, if we were to set $c = 0$ in all the previous results, it would be discovered that $h_2 = \lambda r_c$. This implies that we must have $c > 0$ in order to have a physically meaningful result.

To determine c, we use the fact that, while equation (30*a*) is an excellent approximation for the dislocation motion apart from the attraction zone, it is still, nevertheless, inconsistent with the basic problem solution behavior, which describes dislocation motion beginning at the crack edge when $s = s_o$. We, therefore, require that equation (30*a*) also hold for $s = s_o$, $z = 0$. Because the integrations leading to equation (30*a*) are in the Cauchy principal value sense, the logarithmic arguments are actually absolute values, so that we can obtain

$$1 + \ln\left(\frac{1}{e_2} - 1\right)^{k_2}\left(1 - \frac{1}{e_3}\right)^{-k_3}\left(1 - \frac{1}{e_1}\right)^{k_4}$$

$$\times\left(1 + \frac{1}{e_1}\right)^{-k_1} = 0. \tag{31}$$

Equation (31) can be solved numerically in view of equation (27*b*) for c.

In regard to the infinite arrest time, it could be argued, by analogy with the emission initiation at the crack edge, that the dislocation is arrested if it lies within an attraction/uncertainty zone surrounding the point $y = 0$, $x = h_3$ no larger than the core diameter in length. That is, the dislocation is arrested when $h = h_3 - \nu r_c$, where ν is a dimensionless parameter and $0 < \nu < 1$. In view of equations (23)–(28) and (30*a*), this definition would produce a finite arrest time s^* but, hopefully, a small value $\dot{h} = \dot{h}_3$. If for purposes of illustration we choose $\nu = \lambda$, then equations (23) and (30*a*) give, respectively,

$$\frac{1}{\lambda}(t^* - t_o) = e_3^2 - 2$$

$$+ B\ln\left(\frac{a - e_2}{1 - e_2}\right)^{k_2}\left(\frac{e_3 - 1}{e_3 - a}\right)^{k_3}\left(\frac{e_4 - a}{e_4 - 1}\right)^{k_4}\left(\frac{1 + e_1}{a + e_1}\right)^{k_1} \tag{32a}$$

$$\dot{h}_3 = \frac{a^2(2A - a)^2 - B^2}{a^2(2A - a)^2 + B^2},\ a = \sqrt{(e_3^2 - 1)},\ t^* = \frac{s^*}{r_c},\ t_o = \frac{s_o}{r_c}. \tag{32b-e}$$

With these general results available, we now consider the special case of the sinusoidal incident SH-wave

$$g(u) = \tau\sin\pi\frac{u}{L}\ (0 < \tau < \sigma) \tag{33}$$

where τ is the amplitude and L is the wavelength. Equation (22*c*) now becomes

$$P(s) = \tau\sqrt{L}\, I\left(\frac{s}{L}\right),\ I(\omega) = \sqrt{\omega}\int_0^{\pi/2}$$

$$\sqrt{(1 + \sin u)}\sin(\omega\pi\sin u)\, du \tag{34}$$

whereupon equation (26*a*) gives the implicit relation

$$\left|I\left(t_o\frac{r_c}{L}\right)\right| = 2\pi\sqrt{\left(\lambda\frac{r_c}{L}\right)}\frac{\sigma}{\tau}A \tag{35}$$

Downloaded 03 May 2010 to 171.66.16.244. Redistribution subject to ASME license or copyright; see http://www.asme.org/terms/Terms_Use.cfm

Table 1 Dislocation emission parameters

λ	c	$\dot{h}_m$	d_m	d^*	Δt	$\dot{h}_3$
1.0	$0(10^{-8})$	0.982	$4.16(10^2)$	$1.58(10^3)$	$2.04(10^3)$	0.013
0.5	$0(10^{-15})$	0.995	$8.12(10^2)$	$3.12(10^3)$	$3.67(10^3)$	0.0062
0.3	$0(10^{-28})$	0.998	$1.34(10^3)$	$5.28(10^3)$	$5.82(10^3)$	0.0037

Table 2(*a*) t_0 for $\tau/\sigma = 0.1$

		$\lambda = 1.0$	0.5	0.3
$L/r_c =$	10^8	$9.85(10^6)$	—	—
	10^9	$4.55(10^7)$	$5.69(10^7)$	$6.72(10^7)$
	10^{10}	$2.11(10^8)$	$2.63(10^8)$	$3.11(10^8)$
	10^{11}	$9.78(10^8)$	$1.22(10^9)$	$1.44(10^9)$
	10^{12}	$4.54(10^9)$	$5.67(10^9)$	$6.7(10^9)$
	10^{23}	$2.11(10^{10})$	$2.63(10^{10})$	$3.11(10^{10})$
	10^{14}	$9.78(10^{10})$	$1.22(10^{11})$	$1.44(10^{11})$

Table 2(*b*) t_0 for $\tau/\sigma = 0.01$

		$\lambda = 1.0$	0.5	0.3
$L/r_c =$	10^{10}	$9.85(10^8)$	—	—
	10^{11}	$4.55(10^9)$	$5.69(10^9)$	$6.73(10^9)$
	10^{12}	$2.11(10^{10})$	$2.63(10^{10})$	$3.11(10^{10})$
	10^{13}	$9.78(10^{10})$	$1.22(10^{11})$	$1.44(10^{11})$
	10^{14}	$4.54(10^{11})$	$5.67(10^{11})$	$6.7(10^{11})$

Table 2(*c*) t_0 for $\tau/\sigma = 0.001$

		$\lambda = 1.0$	0.5	0.3
$L/r_c =$	10^{12}	$9.85(10^{10})$	—	—
	10^{13}	$4.55(10^{11})$	$5.69(10^{11})$	$6.73(10^{11})$
	10^{14}	$2.11(10^{12})$	$2.63(10^{12})$	$3.11(10^{12})$

for s_o. In view of the earlier discussion of H_o, the plot of $I(\omega)$ in Fig. 2 indicates the ranges of potential s_o-values for which right-handed ($I > 0$) and left-handed ($I < 0$) screw dislocations will be emitted. We now examine the dimensionless parameters c, $\dot{h}_m$, $\dot{h}_3$, t_o and

$$d_m = \frac{\dot{h}_m}{r_c},\ d^* = \frac{\dot{h}_3}{r_c},\ \Delta t = t^* - t_o \tag{36}$$

for various values of $\lambda (0 < \lambda < 1)$, the dimensionless loading parameter τ/σ ($0 < \tau/\sigma < 0.1$), the dimensionless wavelength parameter L/r_c, and the typical values

$$\frac{b}{r_c} = 0.5,\ \frac{\sigma}{\mu} = 0.001. \tag{37}$$

In B-BW, it was noted that if the attraction/uncertainty zone size is a material property of emission, then λ becomes a specified constant and, consequently, that the calculated arrest distance $\dot{h}_3$ becomes independent of τ, cf. equation (28). It was also noted, however, that such a view does not imply the possibility of spontaneous emission for, as indicated by equations (22*b*,*c*), (26), and (34), $s_o \to \infty$ when $\tau = 0$.

In Table 1, the parameters c, $\dot{h}_3$, $\dot{h}_m$, d_m, Δt, d^* are arrayed versus λ. It is seen that the nondimensionalized distances (d_m, d^*) associated with maximum dislocation speed and arrest, respectively, vary inversely with λ, as does the nondimensionalized maximum speed $\dot{h}_m$ itself. Indeed, the $\dot{h}_m$-values indicate that the maximum dislocation speed is nearly critical. Of even more interest is the observation that both c, $\dot{h}_3 \ll 1$. It was hoped that $\dot{h}_3$ would be small but, in view of the consequences of actually setting $c = 0$ noted above, the result for c seems surprising. However, for equation (27*b*) and the parameter values chosen here, it can be shown that the dimensionless power k_2 of the logarithmic argument in equation (30*a*) which vanishes at $z = e_2^2 (h = h_2)$ is itself $\lambda 0(10^{-13})$. One consequence of c's behavior is that equation (27) and the quasi-static result equation (28*a*) give essentially identical values for $\dot{h}_3$.

In Tables 2(*a*–*c*), the data from Table 1 is used to display t_o for various combinations of (λ, L/r_c, τ/σ). This parameter

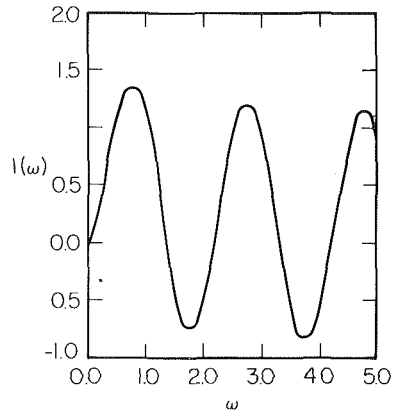


Fig. 2 Plot of sinusoidal wave function $I(\omega)$

apparently varies inversely with λ and τ/σ, but directly with L/r_c. No entries appear for $L/r_c < 0(10^8)$ when $\tau/\sigma = 0.1$ and $\lambda = 1$ because equation (35) cannot then be solved; that is, L/r_c exhibits an emission cutoff value for a given (λ, τ/σ). Indeed, Tables 2(*a*–*c*) show that this cutoff rises as both (λ, τ/σ) decrease. As an example, take the cutoff noted above: Because the shear wave speed and Burgers vector magnitudes for most metallic solids are, respectively, $0(10^3)$m/sec and $0(10^{-4})\mu$m, an incident wavelength sufficient for emission is theoretically $>0(1)$cm or, correspondingly, the incident wave frequency theoretically should be $<0(10^2)$KHZ.

Table 1 and Tables 2(*a*–*c*) together show that the difference between the times of arrest and emission initiation (Δt) is orders of magnitude smaller that the times themselves (t_o, t^*), and that $t_o/d^* \gg 1$. These results are consistent with the assumption equation (20) and also justify the assumption $\alpha^2/\beta > 1$. In view of the shear wave speed r_c magnitudes noted above, Tables 1 and 2(*a*–*c*) give emission initiation times of $0(10^{-1}) - 0(10^4)\mu$sec after SH-wave diffraction, and arrest distances of $0(10^{-1})\mu$m. The corresponding range of incident wavelengths L is $0(10^{-2}) - 0(10^4)$m so that the semi-infinite crack model is apparently justified for crack lengths several orders of magnitude smaller than the incident wavelength. Finally, comparison of Tables 2(*a*–*c*) with Fig. 2 shows in light of equation (35) that only right-handed screw dislocations ($I > 0$) are emitted for the parameters chosen here.

Further Study of Equation of Motion: Step-Stress Wave

We now consider the step-stress incident wave

$$g(u) = \tau (0 < \tau < \sigma) \tag{38}$$

which was treated in B-BW, where τ is the stress magnitude. Equation (26*a*) now gives the explicit result

$$t_o = \lambda \left(\pi \frac{\sigma}{\tau}\right)^2 A^2. \tag{39}$$

For the same input parameters (save L, of course) employed in the previous section, Table 1 is again valid. For t_o, however, equation (39) gives the data displayed in Table 3. There it is seen that the conclusions concerning (λ, τ/σ) noted for the sinusoidal wave case are also valid here. However, Table 3 gives much smaller values for t_o for the same (λ, τ/σ). This is appropriate, since an incident wave with a stress jump should have a more severe effect on the crack edge than a continuous wave of the same amplitude.

Although this paper focuses on emission itself, we now briefly examine its ramifications for brittle fracture.

Brittle Fracture Considerations

The dynamic stress intensity factor for a semi-infinite Mode III crack is given by

Downloaded 03 May 2010 to 171.66.16.244. Redistribution subject to ASME license or copyright; see http://www.asme.org/terms/Terms_Use.cfm

Table 3 t_0 **for step-stress incident wave**

		$\lambda = 1.0$	0.5	0.3
$\tau/\sigma =$	0.1	$4.11(10^5)$	$8.01(10^5)$	$1.32(10^6)$
	0.01	$4.11(10^7)$	$8.01(10^7)$	$1.32(10^8)$
	0.001	$4.11(10^9)$	$8.01(10^9)$	$1.32(10^{10})$

Table 4 t_c **for sinusoidal incident wave**

L/r_c	t_c
10^8	—
10^9	$5.4(10^8)$
10^{10}	$2.1(10^9)$
10^{11}	$9.3(10^9)$
10^{12}	$4.3(10^{10})$

$$K_3 = \lim_{x \to 0^+} \sqrt{(2\pi x)}\,\sigma_{yz}(x,0,s) \tag{40}$$

(Rice, 1968). In view of equations (1), (3)–(6), (18), and (40), it can be shown that for $0 < s < s_o$,

$$K_3 = \sqrt{\left(\frac{2}{\pi}\right)} P(s). \tag{41}$$

If fracture is to initiate prior to dislocation emission, then a suitable state must be attained at some instant s_c, $0 < s_c < s_o$. If a critical stress intensity factor criterion is adopted, then equation (41) gives

$$\left| I\left(t_c \frac{r_c}{L}\right) \right| = \sqrt{\left(\frac{2}{\pi}\frac{r_c}{L}\right)} \frac{\sigma}{\tau} k_c,$$

$$k_c = \frac{K_3^c}{\sigma\sqrt{r_c}},\ t_c = \frac{s_c}{r_c} < t_o \tag{42a-c}$$

for the sinusoidal wave case equation (33), where k_c is a dimensionless constant, K_3^c is the critical mode III intensity factor, and t_o satisfies equation (35). For materials of the type equation (37), we also find that

$$\sigma = 40 \text{ MPa},\ \mu = 4 \text{ GPa},\ K_3^c = 2.9(10^5)\text{N/m}^{3/2},\ b = 3\,\text{Å} \tag{43}$$

whereupon equation (42*a*) generates the information displayed in Table 4. There it is seen that s_c varies directly with incident wavelength, but that equation (42*a*) cannot be satisfied for $L/r_c < 0(10^9)$. That is, purely brittle fracture theoretically cannot occur if the wavelength is too short (frequency is too high). Comparison of Table 4 with Tables 2(*a–c*) shows that $t_o < t_c$ for $\tau/\sigma = 0.1$, but at lower τ/σ one can have $t_c < t_o$. Thus, lower-amplitude sinusoidal waves may create a stress state more amenable to purely brittle fracture, but the conditions for dislocation emission are met sooner when the amplitude nears the yield stress.

For the step-stress case, equation (42*a*) gives in view of equation (38) the explicit result

$$t_c = \frac{\pi}{2}\left(\frac{\sigma}{2\tau}\right)^2 k_c^2 \tag{44}$$

so that the condition $s_c < s_o$ becomes, in view of equation (39),

$$c > \frac{M^2 - 1}{M^2 + 1},\ M = 4\pi\left(\lambda \frac{r_c}{b}\right)\frac{\sigma}{\mu}\left(\frac{1}{\sqrt{(2\pi)}} k_c - 1\right). \tag{45}$$

For the same values equations (37) and (43) used earlier, it can be shown that equation (45) gives $c > 0.98$ when $\lambda = 1.0$, for example. This result contradicts Table 1, and thereby suggests that purely brittle fracture for the step-stress incident SH-wave is always difficult to achieve.

In view of this tendency for emission to precede brittle fracture, we return to equation (40) and find that for $s > s_o$,

$$K_3 = \sqrt{\left(\frac{2}{\pi}\right)} P(s) - \frac{\mu b}{\sqrt{(2\pi)}} \frac{\sqrt{(1+h)}}{h},\ h = h(s). \tag{46}$$

In principle, $P(s)$ could change its sign for $s > s_o$, so that the two terms in K_3 could have the same sign. Thus, the magnitude of K_3 would be enhanced, whereas Majumdar and Burns (1981) and Thomson and Sinclair (1982) found that nontransient dislocation emission invariably relaxed the stress intensity factor, giving rise to the concept of dislocation shielding. In either instance here, equation (46) demonstrates that the effect is temporary; for $s > s^*$ we have $\dot{h} \to 0$ and $h \to h_3$. Equation (46) also shows that $|K_3| \to \infty$ at $s = s_o$ ($h = 0$). This is a consequence of the singularity induced by the classical (Love, 1944) continuum representation of the dislocation, and implies that equation (46) should be employed for $s \gg s_o$.

Discussion

The present work extended previous (B-BW) transient analyses of dislocation emission from dynamically loaded cracks by allowing dislocation acceleration, by considering the role of incident wave properties, and by, in the spirit of nonstrain-hardening plasticity, requiring that the dislocation force remain at the yield stress level during emission. The extension used the exact solution for a screw dislocation leaving a crack loaded by the diffraction of a general plane SH-wave to produce an equation of motion for the dislocation. In terms of incident wave and material properties, the equation described a dislocation which leaves the crack edge with almost zero speed, accelerates rapidly to a near critical speed, and then decelerates to arrest in a finite distance. Mathematically, the dislocation speed asymptotically approaches zero, but it was shown here in terms of micromechanically-scaled attraction/uncertainty zones that arrest occurs for practical purposes in a finite time.

The very form of the dislocation force allowed some insight: It depends on a weighted time history of the applied stress on the crack plane, so that the sign of the stress and the Burgers vector need not be consistent at the instant of emission. Moreover, as predicted by B-BW, constant-speed emission cannot in fact occur unless the force is allowed to exceed the yield stress level, i.e., micromechanical strain hardening takes place.

Among the quantities prescribed by the motion equation were the instant of emission, the arrest distance and the distance at which maximum speed is attained, and the maximum speed. These were studied for two important incident wave forms, the step-stress wave and the sinusoidal wave. It was found that, appropriately, the former generally caused emission to occur more rapidly for the same stress amplitude and, indeed, that if its wavelengths were too small (frequencies too high), the latter might not cause emission at all. That is, emission exhibited a cutoff wavelength/frequency.

A dynamic stress intensity factor-based brittle fracture criterion was also invoked, and found to predict that the step-stress wave invariably causes emission to occur prior to fracture. The sinusoidal incident wave also exhibited a wavelength/frequency cutoff for brittle fracture, but whether or not dislocation emission or purely brittle fracture occurred first was otherwise influenced by its amplitude. In particular, the chances of the latter occurring first increase as the amplitude is decreased far enough below the yield stress. Examination of the intensity factor itself also revealed that emission can either enhance or relax the crack edge stress field, but that the effect in either case fades as dislocation arrest occurs.

It was also noted here that the arrest distance for the emitted dislocation is essentially identical to its quasi-static counterpart, as opposed to the constant-speed result (B-BW). Thus, an interesting feature of the emission process is that its major result, the final location of a dislocation, can be calculated adequately by a quasi-static analysis, yet the process itself is associated with strong accelerations and very high (albeit temporarily so) speeds.

In closing, it should be remarked that the screw dislocation

Downloaded 03 May 2010 to 171.66.16.244. Redistribution subject to ASME license or copyright; see http://www.asme.org/terms/Terms_Use.cfm

case was chosen here because it allows the use of simple, often closed-form, mathematical results. In particular, the equation of motion could be integrated exactly by separation of variables, because time did not appear explicitly. Work (Brock, 1989b) on constant-speed emission models for edge dislocations generated by Mode I and II cracks indicates that, while the time-dependence property is general, the easy separability found for the screw dislocation-Mode III case is not. Nevertheless, the current results will allow physical insight into the edge dislocation cases. The analysis presented here is admittedly theoretical, but is based on standard models for dislocations and cracks, standard emission criteria, and exact solutions. Moreover, some effort was made to ascertain the magnitudes of physical quantities. While the ideal nature of the mathematical problem limit their applicability, they do allow some conclusions which seem appropriate and, hopefully, will shed some light on aspects of elastic crack edge response under dynamic loading which may not be apparent.

References

Achenbach, J. D., 1970, "Extension of a Crack by a Shear Wave," *Zeitschrift fur angewandte Mathematik und Physik*, Vol. 21, pp. 887–900.

Achenbach, J. D., 1973, *Wave Propagation in Elastic Solids*, North-Holland/American Elsevier, Amsterdam.

Brock, L. M., 1986, "A Transient Three-Dimensional Analysis of Non-uniform Dislocations Distribution Growth by Climb and Glide over Non-planar Surfaces," *Proceedings of the Royal Society, London*, Vol. A407, pp. 299–311.

Brock, L. M., 1989a, "An Exact Transient Analysis of Dislocation Emission and Fracture," *Journal of the Mechanics and Physics of Solids*, Vol. 37, pp. 47–69.

Brock, L. M., 1989b, "Transient Analyses of Dislocation Emission in the Three Modes of Fracture," *International Journal of Engineering Science*, Vol. 27, pp. 1479–1495.

Brock, L. M., and Wu, J., 1989a, "Transient Analysis of Dislocation Emission from a Growing Crack," *Journal of the Mechanics and Physics of Solids*, Vol. 37, pp. 583–601.

Brock, L. M., and Wu, J.-S., 1989b, "An Exact Transient Study of Dislocation Emission and its Effects on Dynamic Fracture Initiation," ASME JOURNAL OF APPLIED MECHANICS, Vol. 56, pp. 571–576.

Dundurs, J., 1968, "Elastic Interaction of Dislocations with Inhomogeneities," *Mathematical Theory of Dislocations*, ASME, New York.

Eshelby, J. D., 1953, "The Equation of Motion of a Dislocation," *Physical Review*, Vol. 90, pp. 248–255.

Freund, L. B., 1972, "Crack Propagation in an Elastic Solid Subjected to General Loading—II. Non-uniform Rate of Extension," *Journal of Mechanics and Physics of Solids*, Vol. 20, pp. 141–152.

Guy, A. G., 1960, *Elements of Physical Metallurgy*, Addison-Wesley, Reading, Mass.

Hill, R., 1967, *The Mathematical Theory of Plasticity*, Clarendon Press, Oxford, U.K.

Hirth, J. P., and Lothe, J., 1982, *Theory of Dislocations*, 2nd ed., John Wiley and Sons, New York.

Johnston, W. G., and Gilman, J. J., 1959, "Dislocation Velocities, Dislocation Densities, and Plastic Flow in Lithium Fluoride Crystals," *Journal of Applied Physics*, Vol. 30, pp. 129–144.

Love, A. E. H., 1944, *A Treatise on the Mathematical Theory of Elasticity*, 4th ed., Dover, New York.

Majumdar, B. S., and Burns, S. J., 1981, "An Elastic Theory of Dislocations, Dislocation Arrays, and Inclusions Near a Sharp Crack," *Acta Metallurgica*, Vol. 29, pp. 579–588.

Mura, T., 1982, *Micromechanics of Defects in Solids*, Martinus Nijhoff, The Hague.

Ohr, S. M., 1985, "An Electron Microscope Study of Crack Tip Deformation and its Impact on the Dislocation Theory of Fracture," *Materials Science and Engineering*, Vol. 72, pp. 1–35.

Rice, J. R., 1968, "Mathematical Analysis in the Mechanics of Fracture," *Fracture*, Vol. II, H. Liebowitz, ed., Academic Press, New York.

Rice, J. R., and Thomson, R., 1974, "Ductile Versus Brittle Behaviour of Crystals," *Philosophical Magazine*, Vol. 29, pp. 73–97.

Shaw, M. C., 1984, "A Critical Review of Mechanical Failure Criteria," ASME *Journal of Engineering Materials and Technology*, Vol. 106, pp. 219–226.

Sneddon, I. N., 1972, *The Use of Integral Transforms*, McGraw-Hill, New York.

Thomson, R., and Sinclair, J. E., 1982, "Mechanics of Cracks Screened by Dislocations," *Acta Metallurgica*, Vol. 30, pp. 1325–1334.

Downloaded 03 May 2010 to 171.66.16.244. Redistribution subject to ASME license or copyright; see http://www.asme.org/terms/Terms_Use.cfm

N. C. Huang
Professor,
Mem. ASME

A. A. Szewczyk
Professor,
Mem. ASME

Y. C. Li
Graduate Student.

Department of Aerospace and
Mechanical Engineering,
University of Notre Dame,
Notre Dame, IN 46556

Self-Similar Solution in Problems of Hydraulic Fracturing[1]

The problem of hydraulic fracturing in geological materials is investigated based on a model of the growth of a finite crack in an infinite and linearly elastic medium induced by fluid pressure. The fluid is injected into the crack through an injection well at the center of the crack. The surface of the crack is considered to be impermeable. Flow is present in the crack as the crack propagates. In this study, the fluid is considered to be inviscid and incompressible. Assumptions of a one-dimensional flow in the fracture and a plane-strain deformation of the medium are imposed. At the crack tip, the value of stress intensity factor is considered to be constant during crack propagation. Self-similarity is found in the solution. Crack length, crack profile, fluid pressure, and other related physical characteristics are evaluated as functions of time.

Introduction

Hydraulic fracture is concerned with the propagation of cracks in geological materials induced by hydraulic pressure. The technology involved in hydraulic fracturing has major applicational value and economic significance in a number of industries. It can be used, for instance, in secondary oil recovery, geothermal energy exploration, and underground disposal of hazardous waste. The problem of the flow of fracturing fluid in a propagating crack has been studied by several authors. The two-dimensional theory of hydraulic fracture propagation was analyzed by Biot, Masse, and Medlin (1982) using a Lagrangian formuation associated with the principle of virtual work. In their work, the leak-off of fracturing liquid from the crack surface is included. The crack length, crack width, and hydraulic pressure in the crack are considered to be power functions of time. This work was later generalized by Advani, Torok, and Lee (1986) to a case of a three-dimensional crack, where in the solution, the physical and geometrical parameters are expressed as power functions of time. Similarity solutions for wedge-shaped hydraulic fractures under a constant inlet pressure was studied by Nilson (1988). Both laminar and turbulent flows in the fracture are included in his analysis. The problem of the hydraulic fracture growth with impermeable crack surface was studied by Spence and Sharp (1985). A self-similar solution associated with power functions or exponential functions of time was found. In all the aforementioned work, the fracturing liquid is treated as viscous and the flow in the crack is considered to be of Poiseulle's type. Poiseulle's equation for steady flow between parallel plates are used in the derivation of the governing equations for unsteady motion of fluid in a crack of variable cross-section. Thus, the results may be effective only if the flow in the fracture is almost steady and the variation of the fracture profile is moderate.

In this study, the problem of the growth of hydraulic fracture is considered. It is treated as a finite two-dimensional crack with impermeable surface in an infinite and linearly elastic medium. The crack growth is induced by the pressure in an inviscid and incompressible fluid which is injected into the fracture through an injection well at the center of the crack. The flow of the fracturing fluid in the crack is considered to be one-dimensional and unsteady. The governing equations are derived based on the conservation principles of the fluid and the plane-strain deformation of the medium. A fracture criterion of constant stress intensity factor is used for crack propagation in the geological material. Since the theory is based on the equations of unsteady flow in the crack, it is self-consistent and rigorous. The assumption of Poiseulle's flow in the fracture used in the previous work is relaxed here. Numerical solution of the problem is sought by an iterative process. It is found that under a specific pressure distribution function, self-similarity exists in the solution of the problem where power functions of time are found. The power parameters for different physical quantities are dependent on each other and their values are determined by the fracture criterion of the medium.

Basic Equations

This study deals with a two-dimensional finite crack of initial length, $2a_0$, in an infinite and linearly elastic medium. An injection well is located at the center of the crack as shown in

[1]This work is sponsored by Research grants A-88-12-00013 from Shell Development Company and 88-25-1-ART0205 from Amoco Production Company with the University of Notre Dame.

Contributed by the Applied Mechanics Division of THE AMERICAN SOCIETY OF MECHANICAL ENGINEERS for presentation at the Winter Annual Meeting, Dallas, Texas, Nov. 25–30, 1990.

Discussion on this paper should be addressed to the Technical Editor Leon M. Keer, The Technological Institute, Northwestern University, Evanston, IL 60208, and will be accepted until two months after final publication of the paper itself in the JOURNAL OF APPLIED MECHANICS. Manuscript received by the ASME Applied Mechanics Division, June 12, 1989; final revision, Jan. 21, 1990.

Paper No. 90-WA/APM-31.

Copyright © 1990 by ASME
Downloaded 03 May 2010 to 171.66.16.244. Redistribution subject to ASME license or copyright; see http://www.asme.org/terms/Terms_Use.cfm

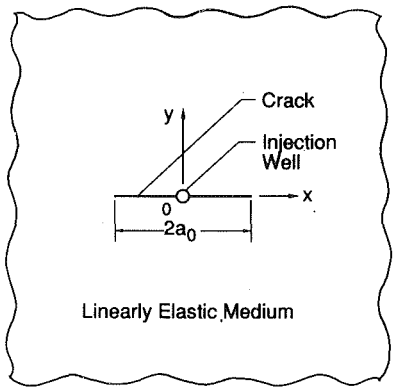


Fig. 1 Geometry of the problem

Fig. 1. In this analysis, it is assumed that the size of the injection well is so small compared with the initial crack length that it does not produce any effect on the crack growth. The crack is subjected to an internal pressure from the hydraulic pressure applied to the injection well. As the crack propagates, fracturing fluid flows into the crack. At any time t, the crack length is $2a(t)$. The origin $x = 0$ is set at the center of the crack. The pressure distribution in the crack is denoted by $p(x,t)$. Due to symmetry, the right half of the crack in the region, $0 \le x \le a(t)$, is considered in this analysis.

The crack opening displacement is denoted by $v(x,t)$ and the flow rate is $q(x,t)$. If the crack surface is impermeable and the flow in the crack is inviscid, incompressible, and one-dimensional, the conservation of mass requires that

$$\frac{\partial q}{\partial x}+2\frac{\partial v}{\partial t}=0. \tag{1}$$

The fluid velocity $u(x,t)$ is related to $q(x,t)$ and $v(x,t)$ by

$$u(x,t)=\frac{q(x,t)}{2v(x,t)}. \tag{2}$$

Since $v[a(t),t]=0$, the following boundary condition is valid:

$$q[a(t),t]=0. \tag{3}$$

From equations (1), (2), and (3), it is found that

$$u(x,t)=\frac{1}{v(x,t)}\int_x^{a(t)}\frac{\partial v}{\partial t}\,dx. \tag{4}$$

It can be shown that

$$u[a(t),t]=\frac{da}{dt}. \tag{5}$$

Let the mass of the fluid per unit volume be ρ. Conservation of linear momentum leads to the following equation:

$$\frac{\partial q}{\partial t}+2\frac{v}{\rho}\frac{\partial p}{\partial x}+\frac{\partial}{\partial x}(uq)=0. \tag{6}$$

From equations (1), (2), and (6), the following Euler's equation for an unsteady one-dimensional flow is obtained

$$\frac{\partial u}{\partial t}+\frac{1}{\rho}\frac{\partial p}{\partial x}+\frac{1}{2}\frac{\partial u^2}{\partial x}=0. \tag{7}$$

In the following, $p(0, t)$ is denoted by $p_0(t)$. Equation (7) can be integrated as

$$p(x,t)=p_0(t)-\rho\left[\int_0^x\frac{\partial u}{\partial t}\,dx+\frac{1}{2}u^2(x,t)-\frac{1}{2}u^2(0,t)\right]. \tag{8}$$

The medium is considered to be linearly elastic with shear modulus μ and Poisson's ratio ν. The crack opening displacement is related to the pressure distribution in the crack by

$$v(x,t)=\frac{1-\nu}{\pi\mu}\int_0^{a(t)}p(z,t)\ln\left|\frac{[a^2(t)-z^2]^{1/2}+[a^2(t)-x^2]^{1/2}}{[a^2(t)-z^2]^{1/2}-[a^2(t)-x^2]^{1/2}}\right|dz. \tag{9}$$

The stress intensity factor, $K(t)$, is related to the pressure distribution by

$$K(t)=2\left[\frac{a(t)}{\pi}\right]^{1/2}\int_0^{a(t)}\frac{p(x,t)}{[a^2(t)-x^2]^{1/2}}\,dx. \tag{10}$$

For geological materials under hydraulic pressure, the following fracture criterion may be employed. When the value of $K(t)$ reaches the fracture toughness K_c, the crack grows continuously. In this study, K_c is considered to be a material constant which is independent of the crack length. Hence, during crack growth,

$$K(t)=K_c. \tag{11}$$

Thus, equation (10) becomes

$$2\left[\frac{a(t)}{\pi}\right]^{1/2}\int_0^{a(t)}\frac{p(x,t)}{[a^2(t)-x^2]^{1/2}}\,dx=K_c. \tag{12}$$

Crack growth terminates when equation (12) cannot be reached. This fracture criterion has also been used by Nilson (1988) for the study of hydraulic fractures.

Finally, the crack volume is given by

$$Q(t)=2\int_0^{a(t)}v(x,t)\,dx \tag{13}$$

The following dimensionless parameters are used in the analysis:

$$\xi(\bar t)=\frac{x}{a(t)},\quad \bar t=\frac{4\pi\mu^2}{(1-\nu)^2K_c^2}\left[\frac{\pi\mu}{(1-\nu)\rho}\right]^{1/2}t,$$

$$\bar a(\bar t)=\frac{4\pi\mu^2}{(1-\nu)^2K_c^2}a(t),\quad \bar v(\xi,\bar t)=\frac{4\pi\mu^2}{(1-\nu)^2K_c^2}v(x,t),$$

$$\bar p(\xi,\bar t)=\frac{1-\nu}{\pi\mu}p(x,t),\quad \bar u(\xi,\bar t)=\left[\frac{(1-\nu)\rho}{\pi\mu}\right]^{1/2}u(x,t),$$

$$\bar Q(\bar t)=\frac{8\pi^2\mu^4}{(1-\nu)^2K_c^4}Q(t). \tag{14}$$

The governing equations (4), (8), (9), (12), and (13) can be written as

$$\bar u(\xi,\bar t)=\frac{\bar a(\bar t)}{\bar v(\xi,\bar t)}\int_\xi^1\frac{\partial\bar v(\xi,\bar t)}{\partial\bar t}\,d\xi, \tag{15}$$

$$\bar p(\xi,\bar t)=\bar p_0(\bar t)-\left[\bar a(\bar t)\int_0^\xi\frac{\partial\bar u(\xi,\bar t)}{\partial\bar t}\,d\xi+\frac{1}{2}\bar u^2(\xi,\bar t)-\frac{1}{2}\bar u^2(0,\bar t)\right], \tag{16}$$

$$\bar v(\xi,\bar t)=\bar a(\bar t)\int_0^1\bar p(\zeta,\bar t)\ln\left|\frac{(1-\zeta^2)^{1/2}+(1-\xi^2)^{1/2}}{(1-\zeta^2)^{1/2}-(1-\xi^2)^{1/2}}\right|d\zeta, \tag{17}$$

$$[\bar a(\bar t)]^{1/2}\int_0^1\frac{\bar p(\xi,\bar t)}{(1-\xi^2)^{1/2}}\,d\xi=1, \tag{18}$$

$$\bar Q(\bar t)=\bar a(\bar t)\int_0^1\bar v(\xi,\bar t)\,d\xi, \tag{19}$$

where $\bar p_0(\bar t)=\bar p(0,\bar t)$. Note that in the evaluation of the partial derivatives with respect to $\bar t$ in equations (15) and (16) it is necessary to treat ξ as a function of $\bar t$.

Self-Similar Solution

In this study, the following self-similar solutions are considered:

Downloaded 03 May 2010 to 171.66.16.244. Redistribution subject to ASME license or copyright; see http://www.asme.org/terms/Terms_Use.cfm

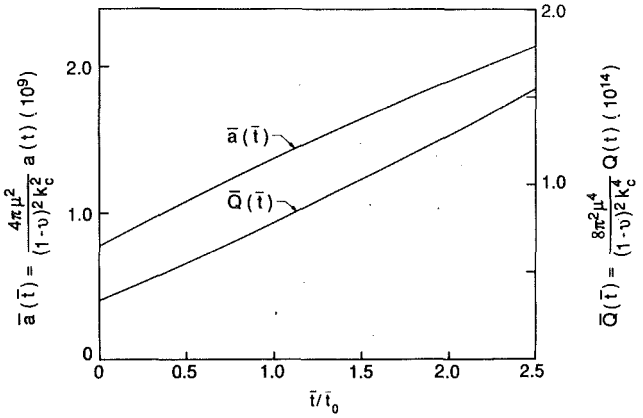


Fig. 2 $a(\bar{t})$ and $Q(\bar{t})$; curves for $\bar{Q}(0) = 0.3445 \times 10^{14}$ and $\bar{t}_0 = 0.3525 \times 10^{12}$

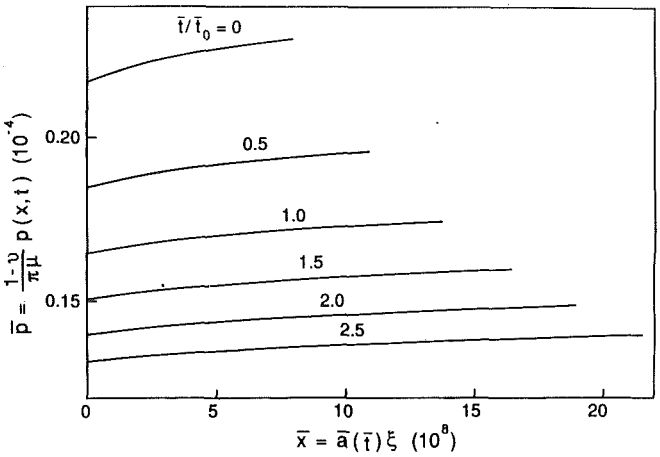


Fig. 3 $\bar{p}$ distribution curves for $\bar{Q}(0) = 0.3445 \times 10^{14}$ and $\bar{t}_0 = 0.3525 \times 10^{12}$

$$\tilde{Q}(\bar{t}) = \alpha^2 a^{*4}\,\tilde{Q}(\bar{t}+\bar{t}_0)^{\alpha},\quad \bar{a}(\bar{t}) = a^*(\bar{t}+\bar{t}_0)^{\lambda},$$
$$\tilde{v}(\xi,\bar{t}) = \alpha^2 a^{*3}\,\tilde{v}(\xi)(\bar{t}+\bar{t}_0)^{\beta},$$
$$\tilde{p}(\xi,\bar{t}) = \alpha^2 a^{*2}\tilde{p}(\xi)(\bar{t}+\bar{t}_0)^{\gamma},$$
$$\tilde{u}(\xi,\bar{t}) = \alpha\, a^*\,\tilde{u}(\xi)\,(\bar{t}+\bar{t}_0)^{\delta}, \tag{20}$$

where $\bar{t}_0$ and a^* are constants to be determined. From equations (15)–(19), it is found that

$$\alpha = \frac{6}{5},\ \beta = \frac{2}{5},\ \gamma = -\frac{2}{5},\ \delta = -\frac{1}{5},\ \lambda = \frac{4}{5}. \tag{21}$$

Equations (15), (16), (17), and (19) can be reduced to

$$\tilde{u}(\xi) = \frac{1}{\tilde{v}(\xi)}\int_{\xi}^{1}\tilde{v}(\zeta)d\zeta + \frac{\lambda}{\alpha}\xi, \tag{22}$$

$$\tilde{p}(\xi) = \tilde{p}_0 - \left[\frac{\lambda+\delta}{\alpha}\int_0^{\xi}\tilde{u}(\zeta)d\zeta - \frac{\lambda}{\alpha}\xi\tilde{u}(\xi) + \frac{1}{2}\tilde{u}^2(\xi) - \frac{1}{2}\tilde{u}^2(0)\right], \tag{23}$$

$$\tilde{v}(\xi) = \int_0^1 \tilde{p}(\zeta)\ln\left|\frac{(1-\zeta^2)^{1/2}+(1-\xi^2)^{1/2}}{(1-\zeta^2)^{1/2}-(1-\xi^2)^{1/2}}\right| d\zeta, \tag{24}$$

$$\tilde{Q} = \int_0^1 \tilde{v}(\xi)\,d\xi, \tag{25}$$

where $\tilde{p}_0 = \tilde{p}(0)$. Equation (18) leads to the following equation for determining a^*:

$$a^* = \left[\frac{36}{25}\int_0^1 \frac{\tilde{p}(\xi)}{(1-\xi^2)^{1/2}}\,d\xi\right]^{-2/5}. \tag{26}$$

To determine $\bar{t}_0$ the following initial condition is employed

$$\bar{a}(0) = \bar{a}_0. \tag{27}$$

It is found from equations (20) and (26) that

$$\bar{t}_0 = \frac{6}{5}\,\bar{a}_0^{5/4}\left[\int_0^1 \frac{\tilde{p}(\xi)}{(1-\xi^2)^{1/2}}\,d\xi\right]^{1/2}, \tag{28}$$

where $\bar{a}_0$ is related to the half initial crack length a_0 by

$$\bar{a}_0 = \frac{4\pi\mu^2}{(1-\nu)^2 K_c^2}a_0. \tag{29}$$

Method of Solution

Equations (22)–(25) are solved numerically by iteration. For a given value of $\tilde{p}_0$, the following crack opening displacement

$$\tilde{v}(\xi) = \pi\tilde{p}_0(1-\xi)^{1/2} \tag{30}$$

is first used to find $\tilde{u}(\xi)$ through equation (22). It is found that

$$\tilde{u}(\xi) = \begin{cases} \dfrac{1}{2(1-\xi^2)^{1/2}}\left[\dfrac{\pi}{2} - \xi(1-\xi^2)^{1/2} - \sin^{-1}\xi\right] + \dfrac{\lambda}{\alpha}\xi & \text{for } 0 \le \xi < 1 \\ \dfrac{\lambda}{\alpha} & \text{for } \xi = 1. \end{cases} \tag{31}$$

Hence, $\tilde{p}(\xi)$ and $\tilde{v}(\xi)$ can be determined according to equations (23) and (24), respectively. The integrals in equations (23) and (24) are evaluated numerically. Piecewise quadratic approximation is used for calculating the integral in equation (24), where the integrand is singular at $\zeta = \xi$. After $\tilde{v}(\xi)$ is found, $\tilde{u}(\xi)$ is determined according to equation (22), where numerical integration is employed. Note that at $\xi = 1$, $\tilde{u}(1) = \lambda/\alpha$. The iterative process continues until the relative error in $\tilde{u}(\xi)$ in two successive iterations is smaller than an assigned tolerance ϵ. Finally, $\tilde{Q}$, a^*, and t_0 can be calculated according to equations (25), (26), and (28), respectively.

Numerical Results

The following physical and geometrical constants and tolerance are employed in the computation:

$$a_0 = 60 \text{ in},\ \mu = 0.87\times10^6 \text{ psi},\ \nu = 0.15,$$
$$K_c = 10^3 \text{ psi} - \text{in}^{1/2},\ \rho = 9.35\times10^{-5}\text{lb s}^2/\text{in}^4,\ \epsilon = 10^{-4}.$$

It is found that for $\bar{Q}(0) = 0.3445\times10^{14}$, $\bar{t}_0 = 0.3525\times10^{12}$ which corresponds to $Q(0) = 0.3975$ in^2 and $t_0 = 0.1444$s. The self-similar solution can be obtained in three to four iterations.

In Fig. 2, $\bar{a}(\bar{t})$ and $\bar{Q}(\bar{t})$ curves are shown. It is seen from equation (20) that in the self-similar solution, $\bar{a}(\bar{t})$ grows as $(\bar{t}+\bar{t}_0)^{4/5}$ and $\bar{Q}(\bar{t})$ grows as $(\bar{t}+\bar{t}_0)^{6/5}$. The $\bar{p}$ distribution curves are shown in Fig. 3 for $\bar{t}/\bar{t}_0 = 0$, 0.5, 1.0, 1.5, 2.0, and 2.5. It is seen that the pressure in the crack increases with x and decreases with t. Note that $\bar{p}(0, 0) = 0.2169 \times 10^{-4}$, which corresponds to $p(0, 0) = 69.74$ psi. It is interesting to note that the pressure distribution in the self-similar solution increases from the well to the tip of the crack. This result stems from the assumption of inviscid flow in the fracture. Since the flow velocity decreases with increasing x, pressure increases with x due to Bernoulli's effect. If an assumption of visions flow in the fracture is employed, as a result of energy dissipation, the pressure will indeed decrease as the value of x increases. The initial pressure distribution for different values of $\bar{Q}(0)$ are shown in Fig. 4. The self-similarity will not exist under the fracture criterion of equation (11) if the initial pressure distribution in the crack does not follow the distribution shown in Fig. 4. It is seen from Fig. 4 that when $\bar{Q}(0)$ increases,

Downloaded 03 May 2010 to 171.66.16.244. Redistribution subject to ASME license or copyright; see http://www.asme.org/terms/Terms_Use.cfm

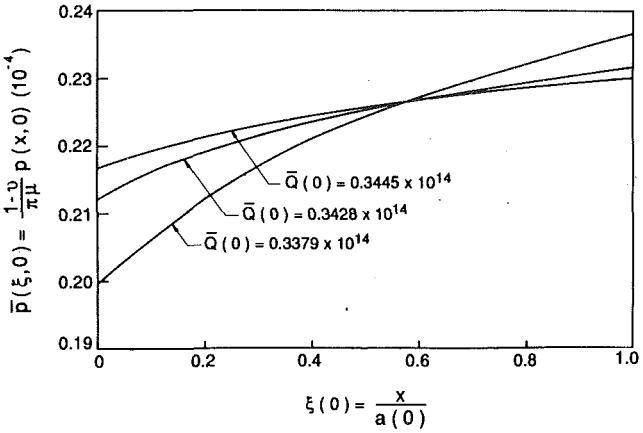


Fig. 4 $\bar{p}$ distribution curves at $t = 0$ for different values of $\bar{Q}(0)$

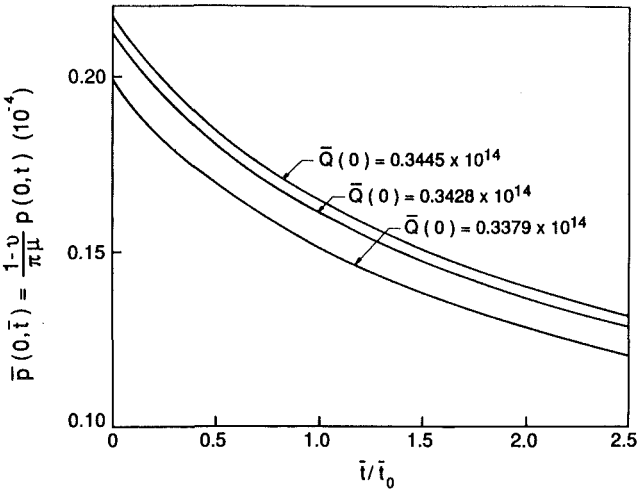


Fig. 5 $\bar{p}(0, \bar{t})$ curves for different values of $\bar{Q}(0)$

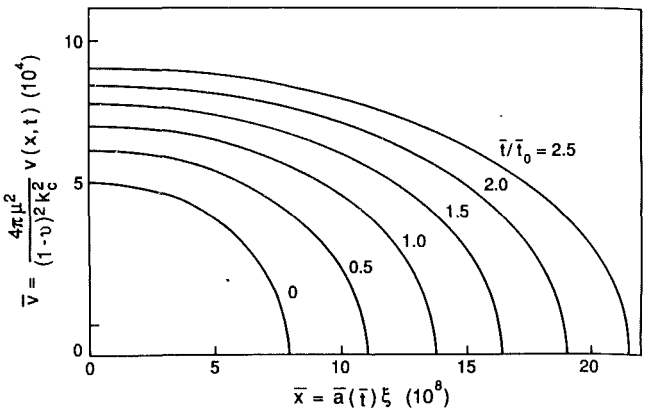


Fig. 6 $\bar{v}$ distribution curves for $\bar{Q}(0) = 0.3445 \times 10^{14}$ and $\bar{t}_0 = 0.3525 \times 10^{12}$

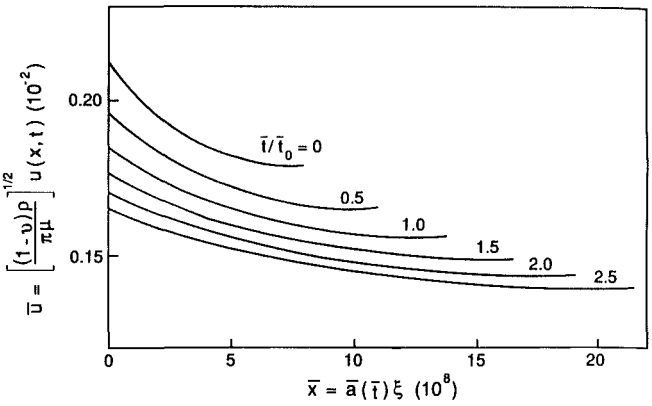


Fig. 7 $\bar{u}$ distribution curves for $\bar{Q}(0) = 0.3445 \times 10^{14}$ and $\bar{t}_0 = 0.3525 \times 10^{12}$

the $\bar{p}(\xi,0)$ distribution curve becomes more flat. The uniform initial pressure distribution occurs when the value of $\bar{Q}(0)$ is the largest. In this case, $\bar{p}(\xi, \bar{t}) = \tilde{p}_0$ with $\tilde{p}_0$ approaching infinity. From equations (26) and (28), it is found that

$$a^* = \left(\frac{18\pi}{25}\tilde{p}_0\right)^{-2/5} \tag{32}$$

and

$$\bar{t}_0 = \frac{6}{5}\bar{a}^{-5/4}\left(\frac{\pi}{2}\tilde{p}_0\right)^{1/2}. \tag{33}$$

When the value of $\tilde{p}_0$ approaches infinity, $\bar{t}_0$ also approaches infinity, but a^* approaches zero. It can be shown that at any finite time, the value of $\bar{p}(\xi, \bar{t})$ will approach a constant

$$\bar{p}(\xi, \bar{t}) = \frac{2}{\pi}\bar{a}_0^{-1/2}. \tag{34}$$

This is a case of the crack growth with infinitesimal rate where the pressure distribution in the crack remains uniform. In other words, the only self-similar solution with uniform pressure distribution in the crack is the solution with practically no crack growth.

The pressure drop at the well due to a self-similar crack growth is shown in Fig. 5. The crack profiles at different times are shown in Fig. 6. It is seen that the pressure distribution in the crack is almost uniform, and the shape of the crack is almost elliptical. It remains so since similarity guarantees the profiles be "similar" in form with the difference of a coordinate scale change. In the case of uniformly distributed pressure, under a constant stress intensity factor, the pressure is inversely proportional to the square root of crack length. Hence, it is evident that the pressure drops as crack grows. Finally, the fluid velocity distributions in the crack are shown in Fig. 7. At the crack tip, the fluid velocity is equal to the speed of the crack growth. Since the crack width decreases rapidly near the crack tip, a slight increase in fluid velocity near the tip is observed. It can be shown that $\frac{d\tilde{u}}{d\xi}(1) = \frac{1}{6}$. In the case of similar solutions for the velocity distribution, the velocity profiles at all values of the spatial coordinate along the crack can be made congruent if they are plotted in coordinates which have been made dimensionless with reference to the scale factors.

The quest for similar solutions in such complex fluid-solid interaction problem is particularly important to the mathematical character of the solution. In such cases where similar solutions exist and can be determined considerable mathematical simplification results in the problem. The solutions themselves represent physically meaningful results for one realizable fluid-solid interaction phenomenon.

Conclusion and Discussions

It is found that under the criteria of constant fracture toughness and the assumption of inviscid fracture flow, the self-similar hydraulic fracture growth is always associated with the decrease in pressure at the well-bore while the pressure distribution shows an increasing value from the crack center to the crack tip. The crack length grows with the power 0.8 of

Downloaded 03 May 2010 to 171.66.16.244. Redistribution subject to ASME license or copyright; see http://www.asme.org/terms/Terms_Use.cfm

$\bar{t} + \bar{t}_0$ and the crack volume grows with the power 1.2 of $\bar{t} + \bar{t}_0$.

In our study, the effect of confining pressure is not considered. However, our results can also be applied to the case with confining pressure if $p(x,t)$ is interpreted as the difference of the actual hydraulic pressure and the confining pressure.

This analysis is based on an assumption of impermeable crack surface. If the medium is porous, the fluid may leak into the medium through the crack surface. If Darcy's law is adopted for the flow in the medium and fluid is assumed to be incompressible, then the pressure in the medium would satisfy the two-dimensional diffusion equation. Since the pressure in the medium and the pressure in the crack are related to each other through either the continuity condition or a jump condition due to the presence of a wall of deposit on the surface of the crack, they must have the same power of time. The diffusion equation will lead to the condition

$$\gamma - 1 + 2\lambda = 0 \tag{35}$$

for self-similar solution. Although in the case of leak-off equations (15) and (16) must be modified, equation (21) still holds. It is found that the values of γ and λ given in equation (21) do not satisfy equation (35). Therefore, the self-similar solution does not exist in the case of leak-off of the fracturing liquid from the crack surface.

In reality, the problem is more complicated in view of the viscosity of the fluid in the fracture. In this case, the solution is no longer self-similar. In the region near the crack tip, the crack opening displacement is so small that the flow cannot reach the crack tip. However, the self-similarity solution presented here will give us a better understanding about the physical insight of the problem.

Acknowledgment

The authors wish to express their thanks to Dr. J. Shlyapobersky of Shell Development Company and Dr. P. D. Pattillo of Amoco Production Company for their encouragement and valuable discussions.

References

Advani, S. H., Torok, J. S., and Lee, J. K., 1986, "Explicit Approximate Solutions Associated with the Mechanics of Hydraulic Fracturing," ASME JOURNAL OF APPLIED MECHANICS, Vol. 53, pp. 462–465.

Biot, M. A., Masse, L., and Medlin, W. L., 1982, "A Two-Dimensional Theory of Fracture Propagation," SPE 11067, Society of Petroleum Engineers of AIME, pp. 1–15.

Nilson, R. H., 1988, "Similarity Solutions for Wedge-Shaped Hydraulic Fractures Driven into a Permeable Medium by a Constant Inlet Pressure," *International Journal for Numerical and Analytical Methods in Geomechanics*, Vol. 12, pp. 477–495.

Spence, D. A., and Sharp, P., 1985, "Self-Similar Solutions for Elastohydrodynamic Cavity Flow," *Proceedings of the Royal Society, London*, Vol. A400, pp. 289–313.

Downloaded 03 May 2010 to 171.66.16.244. Redistribution subject to ASME license or copyright; see http://www.asme.org/terms/Terms_Use.cfm

Stress Intensity Factor and Energy Release Rate for Interfacial Cracks Between Dissimilar Anisotropic Materials

Kuang-Chong Wu
Associate Professor,
Institute of Applied Mechanics,
National Taiwan University,
Taipei, Taiwan 10764

The framework of fracture mechanics analysis for interface cracks as outlined by Willis (1971) is recast into a form resembling the customary framework for cracks in homogeneous materials. Based on the complex-valued "stress concentration vector" introduced by Willis, a new definition of real-valued stress intensity factors is introduced. The definition is an extension to that for cracks in homogeneous materials and reduces to the one given recently by Rice for isotropic interface cracks. In terms of the new stress intensity factors, tractions ahead of the crack and the relative crack face displacements given by Willis are rewritten into real-form expressions. The energy release rate obtained by Willis is also expressed into a real form in terms of the stress intensity factors. The validity of using the stress intensity factors as parameters controlling fracture is discussed along the line advanced by Rice (1988).

1 Introduction

The plane problem of a crack lying between dissimilar isotropic materials was first studied by Williams (1959). Williams showed that the stresses possessed singularities of the types $r^{-1/2\pm i\gamma}$, where r is the radial distance from the crack tip and γ is a bimaterial constant. Due to the presence of these singularities, the stresses exhibit violent oscillation in the immediate vicinity of the crack tip. England (1965) investigated the problem of a finite crack between dissimilar isotropic media and showed that with the singularities derived by Williams, the upper and lower crack faces would wrinkle and overlap near the crack tips.

Rice and Sih (1965) analyzed similar problems and derived the expressions of the stress fields near the crack tip. They introduced a complex stress intensity factor $k=k_1+ik_2$. The complex stress intensity factor k does not possess the same physical significance as those for homogeneous cracks. In fact, k_1 and k_2 are related to both shear and tensile stress components. The physical units of the complex stress intensity factor are also complex, and are different from those of the classical stress intensity factors, Recently, Rice (1988) re-examined the elastic fracture mechanics concepts for the isotropic interface crack. The validity of using a complex stress intensity factor, K, given as k multiplied by a factor as a crack-tip characterizing parameter was discussed. Rice showed that for two loadings to produce the same value of K for different crack lengths, not only the magnitude but the direction of the loading would have to be altered. Definitions of stress intensity factors of classical type $K=K_I+iK_{II}$ are given by Rice by introducing an intrinsic material length scale $\hat{r}$.

The problem studied by England (1965) was extended for dissimilar anisotropic materials by Clements (1971) and Willis (1971). They showed that the oscillatory behavior of the stresses and the phenomenon of interpenetration of the crack faces were also present near the crack tips for anisotropic interface cracks. Willis further defined a complex "stress concentration vector," **k**, to characterize the fields near the crack tips and derived a simple expression for the energy release rate in terms of the stress concentration vector.

It is shown in this paper that based on the stress concentration vector, real-valued stress intensity factors **K** of classical type proposed by Rice (1988) can be extended for anisotropic bimaterial cracks. In terms of the stress intensity factors, tractions ahead of the crack, and the relative crack-face displacements given by Willis, can be rewritten into real-form expressions. The energy release rate derived by Willis can also be expressed into a real form in terms of the stress intensity factors. It is shown that the energy release rate is independent of the length parameter, $\hat{r}$. Finally, conditions under which the crack-tip fields would exist are investigated for plane-strain problems following the concept of Rice (1988).

2 Background

In this section, relevant results of (Willis, 1971) are given. Consider a crack of length L between material I and II in

Contributed by the Applied Mechanics Division of THE AMERICAN SOCIETY OF MECHANICAL ENGINEERS for publication in the JOURNAL OF APPLIED MECHANICS.

Discussion on this paper should be addressed to the Technical Editor, Leon M. Keer, The Technological Institute, Northwestern University, Evanston, IL 60208, and will be accepted until two months after final publication of the paper itself in the JOURNAL OF APPLIED MECHANICS. Manuscript received by the ASME Applied Mechanics Division, Nov. 2, 1988; final revision, Sept. 5, 1989.

Copyright © 1990 by ASME
Downloaded 03 May 2010 to 171.66.16.244. Redistribution subject to ASME license or copyright; see http://www.asme.org/terms/Terms_Use.cfm

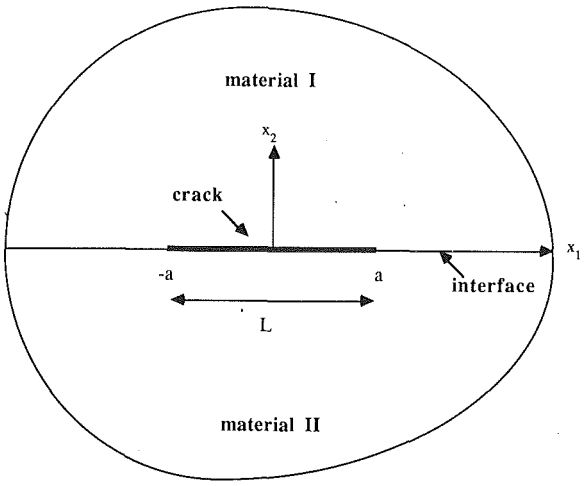


Fig. 1 An interface crack of length L, located on $x_2=0$, $|x_1|<a$, in an infinite anisotropic bimaterial

an infinite body as shown in Fig. 1. The interface crack is assumed to be loaded by tractions on the crack faces. Near the right tip, the stress $t_i=\sigma_{i2}$ ahead of the crack along the interface can be expressed as

$$\mathbf{t}=\frac{1}{2\pi\sqrt{r}}(\mathbf{A}^T+\mathbf{A})\bar{\mathbf{V}}\Lambda\left(\left(\frac{r}{L}\right)^{-i\gamma}\right)\mathbf{k}, \tag{1}$$

where r is the distance from the crack tip, $\mathbf{A}$ is a Hermitian matrix determined by the elastic constants of the bimaterial, $\mathbf{k}$ is the complex stress concentration vector, the matrix V is given by

$$\mathbf{V}=[\mathbf{v}_+,\ \mathbf{v}_-,\ \mathbf{v}_0], \tag{2}$$

and the diagonal matrix $\Lambda(c)$ is defined as

$$\Lambda(c)=\text{diag}[c,\ \bar{c},\ 1]. \tag{3}$$

In equation (2), the complex vectors $\mathbf{v}_+$, $\mathbf{v}_-$, $\mathbf{v}_0$ are the eigenvectors of the following equation:

$$(\mathbf{A}^{\mathrm{T}}-e^{2\pi\lambda_\xi}\mathbf{A})\mathbf{v}_\xi=0,\ (\xi=+,\ -,\ 0) \tag{4}$$

where $\lambda_\pm=\pm\gamma$, $\lambda_0=0$. The complex vectors $\mathbf{v}_+$, $\mathbf{v}_-$, $\mathbf{v}_0$ are normalized so that

$$\bar{\mathbf{v}}_\alpha^T\mathbf{A}\mathbf{v}_\beta=\delta_{\alpha\beta}. \tag{5}$$

From equations (4) and (5), it can be shown that

$$\mathbf{v}_-=e^{-\pi\gamma}\bar{\mathbf{v}}_+,\ \bar{\mathbf{v}}_0=\mathbf{v}_0. \tag{6}$$

From equation (6), the fact that $\mathbf{t}$ of equation (1) is real implies that the components of the complex stress concentration vector satisfy

$$k_-=e^{\pi\gamma}\bar{k}_+,\ \bar{k}_0=k_0. \tag{7}$$

The relative crack-face displacement $\Delta\mathbf{u}=\mathbf{u}(r,\ \pi)-\mathbf{u}(r,\ -\pi)$ is given by

$$\Delta\mathbf{u}=\sqrt{\frac{2}{\pi}}\bar{\mathbf{V}}\Lambda\left(\frac{\cosh(\pi\gamma)}{1-2i\gamma}\left(\frac{r}{L}\right)^{-i\gamma}\right)\mathbf{k}. \tag{8}$$

The energy release rate is given by

$$\mathcal{G}=\bar{\mathbf{k}}^T\Lambda\mathbf{k}, \tag{9}$$

where

$$\Lambda=\frac{1}{\sqrt{2\pi}}\text{diag}\left[\frac{1}{2}(1+e^{2\pi\gamma}),\ \frac{1}{2}(1+e^{-2\pi\gamma}),\ 1\right]. \tag{10}$$

3 Stress Intensity Factors of Classical Type

In this section, real-valued stress intensity factors of classical type are introduced based on the complex stress concentration vector defined by Willis (1971). Furthermore, equations (1), (8), and (9) are cast into real forms in terms of the stress intensity factors.

The explicit solution of γ has been obtained by Ting (1986) as

$$\gamma=\frac{1}{2\pi}\log\frac{1+\beta}{1-\beta}, \tag{11}$$

where

$$\beta=\left\{-\frac{1}{2}tr[(\mathbf{W}\mathbf{D}^{-1})^2]\right\}^{1/2}, \tag{12}$$

where $-\mathbf{W}$ and $-\mathbf{D}$ are the real imaginary parts of a complex matrix $\mathbf{M}$, i.e.,

$$\mathbf{M}=-(\mathbf{W}+i\mathbf{D}). \tag{13}$$

The matrix $\mathbf{D}$ is symmetric and positive definite and $\mathbf{W}$ is antisymmetric. The matrix $\mathbf{A}$ in equation (4) is related to the matrix $\mathbf{M}$ by

$$\mathbf{A}=-i\sqrt{2\pi}(\mathbf{M}^{-1})^T. \tag{14}$$

Let

$$\mathbf{M}^{-1}=\tilde{\mathbf{W}}+i\tilde{\mathbf{D}}, \tag{15}$$

where $\tilde{\mathbf{D}}$ is a symmetric and positive definite matrix and $\tilde{\mathbf{W}}$ is an antisymmetric matrix. The matrix $\mathbf{A}$ can be expressed as

$$\mathbf{A}=\sqrt{2\pi}(\tilde{\mathbf{D}}+i\tilde{\mathbf{W}}). \tag{16}$$

The Matrices $\tilde{\mathbf{W}}$, $\tilde{\mathbf{D}}$ can be shown to be related to and $\mathbf{W}$ $\mathbf{D}$ by

$$\tilde{\mathbf{W}}\tilde{D}^{-1}=-\mathbf{D}^{-1}\mathbf{W}, \tag{17}$$

$$\tilde{\mathbf{D}}^{-1}=\mathbf{W}\mathbf{D}^{-1}\mathbf{W}+\mathbf{D}. \tag{18}$$

In the discussions to be followed, it is more convenient to use a different set of complex vectors $\mathbf{q}_j$ given by

$$\mathbf{Q}=[\mathbf{q}_1,\ \mathbf{q}_2,\ \mathbf{q}_3]=(2\pi)^{1/4}\mathbf{V}\Gamma, \tag{19}$$

where

$$\Gamma=\text{diag}[\sqrt{1-\beta},\ \sqrt{1+\beta},\ 1]. \tag{20}$$

From equations (4) and (5), it can be shown that

$$\bar{\mathbf{Q}}\ =\ =\mathbf{Q}\hat{I}, \tag{21}$$

$$\bar{\mathbf{Q}}^T\tilde{\mathbf{D}}\mathbf{Q}\ =\ =\mathbf{I}, \tag{22}$$

$$\bar{\mathbf{Q}}^T\tilde{\mathbf{W}}\mathbf{Q}\ =\ i\beta\text{diag}[1,\ -1,\ 0], \tag{23}$$

where

$$\hat{\mathbf{I}}=\begin{bmatrix}0&1&0\\1&0&0\\0&0&1\end{bmatrix}. \tag{24}$$

From equations (22) and (23), we have

$$(\bar{\mathbf{Q}}^T)^{-1}\text{diag}[1,\ -1,\ 0]\bar{\mathbf{Q}}^T=-i\mathbf{P}, \tag{25}$$

where

$$\mathbf{P}=\frac{1}{\beta}\tilde{\mathbf{W}}\tilde{\mathbf{D}}^{-1}. \tag{26}$$

It follows from equation (25) that

$$(\bar{\mathbf{Q}}^T)^{-1}\text{diag}[1,1,0]\bar{\mathbf{Q}}^T=-\mathbf{P}^2. \tag{27}$$

A matrix $\mathbf{R}$ that will appear frequently in later discussions is introduced here. The matrix $\mathbf{R}$ is defined by

$$\mathbf{R}[c]=(\bar{\mathbf{Q}}^T)^{-1}\Lambda(c)(\bar{\mathbf{Q}}^T). \tag{28}$$

The matrix $\mathbf{R}$ has the following properties:

$$\mathbf{R}[1]=\mathbf{I}, \tag{29}$$

$$\mathbf{R}[c]\mathbf{R}(e)=\mathbf{R}[ce], \tag{30}$$

Downloaded 03 May 2010 to 171.66.16.244. Redistribution subject to ASME license or copyright; see http://www.asme.org/terms/Terms_Use.cfm

$$\mathbf{R}[c]^T\tilde{\mathbf{D}}^{-1}\mathbf{R}[e]=\tilde{\mathbf{D}}^{-1}\mathbf{R}[\bar{c}e]. \tag{31}$$

In deriving equation (31), equation (21) and equation (22) have been used. Let us express $\Lambda(c)$ as

$$\Lambda(c)=\mathbf{I}+i\Im[c]\text{diag}[1,-1,0]-(1-\Re[c])\text{diag}[1,1,0], \tag{32}$$

where $\Re$, $\Im$ denote the real and the imaginary part, respectively. From equations (25) and (27), $\mathbf{R}$ can be expressed in the following explicit real form:

$$\mathbf{R}[c]=\mathbf{I}+\Im[c]\mathbf{P}+(1-\Re[c])\mathbf{P}^2. \tag{33}$$

Note that as $\mathbf{P}$ is dimensionless, the argument c in $\mathbf{R}$ must also be dimensionless to avoid ambiguity of summation or subtraction of quantities with different dimensions. As a result, the matrix $\mathbf{R}$ is also dimensionless.

As the components of the complex stress concentration vector $\mathbf{k}$ satisfy equation (7), we can let

$$\mathbf{k}=\left(\frac{\pi}{8}\right)^{1/4}\mathbf{\Gamma}\mathbf{Q}^T\mathbf{K}(L), \tag{34}$$

where $\mathbf{K}(L)$ is real. With equations (16), (19), (21), and (34), equation (1) can be rewritten as

$$\mathbf{t}=\frac{1}{\sqrt{2\pi r}}\mathbf{R}\left[\left(\frac{r}{L}\right)^{i\gamma}\right]\mathbf{K}(L). \tag{35}$$

Following the concepts of Rice (1988), a material length $\hat{r}$ is introduced such that equation (35) becomes

$$\mathbf{t}=\frac{1}{\sqrt{2\pi r}}\mathbf{R}\left[\left(\frac{r}{\hat{r}}\right)^{i\gamma}\right]\mathbf{K}, \tag{36}$$

where $\mathbf{K}$ is related to $\mathbf{K}(L)$ by

$$\mathbf{K}=\mathbf{R}\left[\left(\frac{\hat{r}}{L}\right)^{i\gamma}\right]\mathbf{K}(L). \tag{37}$$

Equation (36) implies

$$\mathbf{K}=\sqrt{2\pi r}\mathbf{R}\left[\left(\frac{r}{\hat{r}}\right)^{-i\gamma}\right]\mathbf{t}. \tag{38}$$

Since $\mathbf{R}$ in equation (38) is dimensionless, $\mathbf{K}$ has the same units of stress times square root of length as the classical stress intensity factors for homogeneous cracks. In fact, if $\gamma=0$, equation (36) becomes

$$\mathbf{t}=\frac{1}{\sqrt{2\pi r}}\mathbf{K}, \tag{39}$$

and the usual definition of the stress intensity factors is recovered.[1] Thus, $\mathbf{K}$ will be defined as the stress intensity factors for interface cracks. The necessary and sufficient condition for $\gamma=0$ is shown by Ting (1986) and Bassani and Qu (1989) to be

$$\mathbf{W}=\mathbf{0}. \tag{40}$$

Homogeneous materials obviously satisfy equation (40). Other examples of bimaterials satisfying condition of equation (40) are given by Anderson (1988) and Bassani and Qu (1989). If $\gamma\neq 0$, the stress intensity factors $\mathbf{K}$ and the modes of loading, however, are intermixed. Indeed, for an interface crack loaded in Mode I, all three stress intensity factors are generally nonzero.

Similarly, the relative crack-face displacement of equation (8) can be expressed as

$$\Delta\mathbf{u}=\sqrt{\frac{2r}{\pi}}\tilde{\mathbf{D}}^{-1}\mathbf{R}\left[\frac{\cosh(\pi\gamma)}{1+2i\gamma}\left(\frac{r}{\hat{r}}\right)^{i\gamma}\right]\mathbf{K}, \tag{41}$$

[1] K_1 here is associated with Mode II loading and K_2 with Mode I loading.

The energy release rate of equation (9) can also be expressed in terms of a real-form quadratic in K_i as

$$\mathcal{G}=\frac{1}{4}\mathbf{K}^T\tilde{\mathbf{D}}^{-1}\mathbf{K}. \tag{42}$$

For special bimaterials satisfying $\gamma=0$, from equation (40) and equation (18), we have

$$\tilde{\mathbf{D}}^{-1}=\mathbf{D}, \tag{43}$$

and equation (42) becomes

$$\mathcal{G}=\frac{1}{4}\mathbf{K}^T\mathbf{D}\mathbf{K}. \tag{44}$$

Equation (44) is essentially the expression obtained by Anderson (1988).

Note that equation (42) is independent of choices of the material length $\hat{r}$. Suppose $\hat{r}_1$ and $\hat{r}_2$ are two different lengths chosen and $\mathbf{K}_1$ and $\mathbf{K}_2$ are the corresponding stress intensity factors, we have

$$\mathbf{K}_1=\mathbf{R}\left[\left(\frac{\hat{r}_1}{\hat{r}_2}\right)^{i\gamma}\right]\mathbf{K}_2. \tag{45}$$

It follows from equation (31) that

$$\mathbf{K}_1^T\tilde{\mathbf{D}}^{-1}\mathbf{K}_1=\mathbf{K}_2^T\tilde{\mathbf{D}}^{-1}\mathbf{K}_2. \tag{46}$$

Thus, the energy release rate is independent of $\hat{r}$.

The stress concentration vector for an interface crack located on $-a<x_1<a$ subjected to the traction $\mathbf{T}$ on the upper crack face and $-\mathbf{T}$ on the lower face is given by Willis (1971) as

$$\mathbf{k}=\frac{1}{\sqrt{L}}\int_{-a}^{a}\sqrt{\frac{a+x_1}{a-x_1}}\mathbf{\Lambda}_+\mathbf{V}^T\mathbf{T}(x_1)dx_1, \tag{47}$$

where $L=2a$ and

$$\mathbf{\Lambda}_+=\text{diag}\left[e^{-\pi\gamma}\left(\frac{a+x_1}{a-x_1}\right)^{i\gamma}, e^{\pi\gamma}\left(\frac{a+x_1}{a-x_1}\right)^{-i\gamma}, 1\right). \tag{48}$$

From equation (34), we have

$$\mathbf{K}(L)=\left(\frac{8}{\pi}\right)^{1/4}(Q^T)^{-1}\mathbf{\Gamma}^{-1}\mathbf{k}. \tag{49}$$

Substitution of equation (47) into equation (49) leads to

$$\mathbf{K}(L)=\frac{1}{\sqrt{\pi a}}\int_{-a}^{a}\sqrt{\frac{a+x_1}{a-x_1}}\mathbf{R}\left[\cosh(\pi\gamma)\left(\frac{a+x_1}{a-x_1}\right)^{i\gamma}\right]\mathbf{T}(x_1)dx_1. \tag{50}$$

The stress intensity factor $\mathbf{K}$ of equation (37) is given by

$$\mathbf{K}=\frac{1}{\sqrt{\pi a}}\int_{-a}^{a}\sqrt{\frac{a+x_1}{a-x_1}}\mathbf{R}\left[\cosh(\pi\gamma)\left(\frac{L}{\hat{r}}\right)^{-i\gamma}\times\left(\frac{a+x_1}{a-x_1}\right)^{i\gamma}\right]\mathbf{T}(x_1)dx_1. \tag{51}$$

For uniform tractions, equation (51) gives

$$\mathbf{K}=\sqrt{\pi a}\mathbf{R}\left[(1+2i\gamma)\left(\frac{L}{\hat{r}}\right)^{-i\gamma}\right]\mathbf{T}. \tag{52}$$

For isotropic bimaterials, Rice (1988) points out that if $\hat{r}$ is taken to be a constant independent of the crack length, the loadings yielding the same stress intensity factors for different crack lengths are different both in magnitude and direction. Consider two cracks of lengths L_1 and L_2 loaded by $\mathbf{T}^{(1)}$ and $\mathbf{T}^{(2)}$, respectively. Rice (1988) shows that the magnitudes of the loadings $T^{(1)}$ and $T^{(2)}$ are related by

Downloaded 03 May 2010 to 171.66.16.244. Redistribution subject to ASME license or copyright; see http://www.asme.org/terms/Terms_Use.cfm

$$T^{(2)} = T^{(1)} \sqrt{\frac{L_1}{L_2}}, \tag{53}$$

and the corresponding phase angles ψ_1 and ψ_2 by

$$\psi_1 = \psi_2 + \gamma \log\left(\frac{L_1}{L_2}\right), \tag{54}$$

where

$$\psi = \tan^{-1}\left(\frac{T_1}{T_2}\right). \tag{55}$$

The situation is more complicated for general anisotropic bimaterials. Indeed, from equation (52), the loadings are related by

$$\mathbf{T}^{(2)} = \sqrt{\frac{L_1}{L_2}} \mathbf{R}\left[\left(\frac{L_1}{L_2}\right)^{-i\gamma}\right]\mathbf{T}^{(1)}. \tag{56}$$

The magnitudes of the loadings are no longer related by the square-root dependence. Similar discussion based on Willis' original formulation (1971) has been given by Anderson (1988).

With equation (52) substituted into equation (41), the relative crack-face displacements near the tip are

$$\Delta\mathbf{u} = \sqrt{Lr}\tilde{\mathbf{D}}^{-1}\mathbf{R}\left[\cosh(\pi\gamma)\left(\frac{r}{L}\right)^{i\gamma}\right]\mathbf{T}. \tag{57}$$

The energy release rate is obtained by substituting equation (52) into equation (42). The resulting expression is

$$\mathcal{G} = \frac{\pi a}{4}\mathbf{T}^T\mathbf{R}^T\left[(1+2i\gamma)\left(\frac{L}{\hat{r}}\right)^{-i\gamma}\right]\tilde{\mathbf{D}}^{-1}\mathbf{R}\left[(1+2i\gamma)\left(\frac{L}{\hat{r}}\right)^{-i\gamma}\right]\mathbf{T}. \tag{58}$$

The expression of $\mathcal{G}$ can be further simplified by using equation (31) as

$$\begin{aligned}\mathcal{G} &= \frac{\pi a}{4}\mathbf{T}^T\tilde{\mathbf{D}}^{-1}\mathbf{R}[1+4\gamma^2]\mathbf{T}, \\ &= \frac{\pi a}{4}\mathbf{T}^T\tilde{\mathbf{D}}^{-1}(\mathbf{I}-4\gamma^2\mathbf{P}^2)\mathbf{T}.\end{aligned} \tag{59}$$

4 Plane-Strain Deformation

Consider materials for which the x_3-axis is a twofold symmetry axis (or, equivalently, there is a reflection plane normal to the x_3-axis). For these materials, there is no coupling of the displacement u_3 with u_1 and u_2; any two-dimensional problems reduces to one of plane strain ($u_3 = 0$) and one of antiplane strain ($u_1 = u_2 = 0$). For this class of materials, it can be shown that $M_{13} = M_{23} = 0$ (Stroh, 1958). For two-dimensional plane-strain problems, the expressions of the crack-tip fields and energy release rate derived in the previous section can be further simplified.

For plane-strain problems, from equation (12), the parameter β is given by

$$\beta = \frac{W_{21}}{\sqrt{D}}, \tag{60}$$

where $D = \det[\mathbf{D}]$. The matrix $\mathbf{P}^2$ can be shown to be

$$\mathbf{P}^2 = -\mathbf{I}. \tag{61}$$

Equation (33) can thus be simplified as

$$\mathbf{R}[c] = \Re[c]\mathbf{I} + \Im[c]\mathbf{P}. \tag{62}$$

From equation (18), equation (61) implies that the matrix $\tilde{\mathbf{D}}^{-1}$ is given by

$$\tilde{\mathbf{D}}^{-1} = \frac{1}{\cosh^2(\pi\gamma)}\mathbf{D}. \tag{63}$$

The expressions of the stresses ahead of the crack, the relative crack face displacements, and the stress intensity factors can be simplified using equation (62). The crack-face displacements for uniform loading of equation (57) can be cast into the following simple form:

$$\Delta\mathbf{u} = \frac{\sqrt{Lr}}{\cosh(\pi\gamma)}\left(\cos\left[\gamma\log\left(\frac{r}{L}\right)\right]\mathbf{D} - \frac{1}{\beta}\sin\left[\gamma\log\left(\frac{r}{L}\right)\right]\mathbf{W}\right)\mathbf{T}. \tag{64}$$

The energy release rate also becomes

$$\mathcal{G} = \frac{1}{4\cosh^2(\pi\gamma)}\mathbf{K}^T\mathbf{D}\mathbf{K}. \tag{65}$$

For isotropic bimaterial media under plane-strain deformation, the matrices $\mathbf{W}$ and $\mathbf{D}$ are given by (Ting, 1986)

$$\mathbf{W} = \beta\left(\frac{1-\nu}{\mu} + \frac{1-\nu'}{\mu'}\right)\begin{pmatrix}0 & -1\\ 1 & 0\end{pmatrix}, \tag{66}$$

$$\mathbf{D} = \left(\frac{1-\nu}{\mu} + \frac{1-\nu'}{\mu'}\right)\begin{pmatrix}1 & 0\\ 0 & 1\end{pmatrix}, \tag{67}$$

where

$$\beta = \frac{\mu'(1-2\nu) - \mu(1-2\nu')}{2(\mu'(1-\nu) + \mu(1-\nu'))}. \tag{68}$$

From equation (65), the energy release rate is given by

$$\mathcal{G} = \frac{1}{4\cosh^2(\pi\gamma)}\left(\frac{1-\nu}{\mu} + \frac{1-\nu'}{\mu'}\right)(K_1^2 + K_2^2). \tag{69}$$

This is the same result as obtained by Malyshev and Salganik (1965). Substituting equation (67) and equation (66) into equation (52) yields

$$K_1 = \sqrt{\pi a}\left(\Re\left[(1+2i\gamma)\left(\frac{L}{\hat{r}}\right)^{-i\gamma}\right]T_1 + \Im\left[(1+2i\gamma)\left(\frac{L}{\hat{r}}\right)^{-i\gamma}\right]T_2\right), \tag{70}$$

$$K_2 = \sqrt{\pi a}\left(-\Im\left[(1+2i\gamma)\left(\frac{L}{\hat{r}}\right)^{-i\gamma}\right]T_1 + \Re\left[(1+2i\gamma)\left(\frac{L}{\hat{r}}\right)^{-i\gamma}\right]T_2\right). \tag{71}$$

The expressions are the same as the stress intensity factors given by Rice (1988).

5 Discussions

The use of the stress intensity factor $\mathbf{K}$ as possible fracture parameters, of course, requires that the crack-tip fields of equation (36) and equation (41) do indeed exist. The issue is addressed in this section. For simplicity, the discussion is restricted to plane-strain deformation under uniform loading.

It is well known that the traction-free assumption results in a contradictory situation of part of the crack faces coming into contact. The extent to which this contact problem influences the crack-tip fields obviously depends on the size of the contact zone, r_c. If r_c is small compared to the crack length, it is then expected that the traction-free crack-tip fields would still be valid at distances much larger than r_c but smaller than the crack length (Rice, 1988, Anderson, 1988). The size of the contact zone can be estimated by setting Δu_2 predicted by equation (64) equal to zero (Rice, 1988). The resulting equation is

$$\cos\left[\gamma\log\left(\frac{r_c}{L}\right)\right](D_{12}T_1 + D_{22}T_2) - \sqrt{D}\sin\left[\gamma\log\left(\frac{r_c}{L}\right)\right]T_1 = 0, \tag{72}$$

Downloaded 03 May 2010 to 171.66.16.244. Redistribution subject to ASME license or copyright; see http://www.asme.org/terms/Terms_Use.cfm

where equation (60) has been used. Introduce an effective magnitude of the loading as

$$\tilde{T} = \frac{1}{\sqrt{D}}[(D_{12}T_1 + D_{22}T_2)^2 + DT_1^2]^{1/2},$$
$$= \left(\frac{D_{22}}{D}\mathbf{T}^T\mathbf{D}\mathbf{T}\right)^{1/2} \tag{73}$$

and an effective phase angle as

$$\tilde{\psi} = \sin^{-1}\frac{T_1}{\tilde{T}}. \tag{74}$$

For isotropic bimaterials, $\tilde{T}$ is simply the actual magnitude of the loading and $\tilde{\psi}$ is the same as the phase angle ψ of the loading. One can write equation (72) as

$$\cos\left[\gamma\log\left(\frac{r_c}{L}\right) + \tilde{\psi}\right] = 0. \tag{75}$$

The solution of r_c is then given by

$$\frac{r_c}{L} = \exp\left[-\frac{1}{\gamma}\left(\tilde{\psi} + \frac{\pi}{2}\right)\right]. \tag{76}$$

According to equation (76), the size of the contact zone depends on γ and $\tilde{\psi}$. If γ is taken to be positive, r_c would be small as long as γ is small and $\tilde{\psi} + \frac{\pi}{2}$ is positive and large compared to γ. If the magnitude of the loading is held constant and the phase angle ψ is restricted to change from $-\frac{\pi}{2}$ to $\frac{\pi}{2}$, for $D_{12} \geq 0$ the corresponding range $\tilde{\psi}$ can be shown to be

$$-\frac{\pi}{2} \leq \tilde{\psi} \leq \tilde{\psi}_0, \quad \text{for } -\psi_0 \leq \psi \leq \frac{\pi}{2}, \tag{77}$$

$$-\frac{\pi}{2} \leq \tilde{\psi} \leq -\tilde{\psi}_0, \quad \text{for } -\frac{\pi}{2} \leq \psi \leq -\psi_0, \tag{78}$$

where

$$\tilde{\psi}_0 = \sin^{-1}\left[\sqrt{\frac{D}{D_{11}D_{22}}}\right], \tag{79}$$

$$\psi_0 = \sin^{-1}\left[\frac{D_{22}}{\sqrt{D_{22}^2 + D_{12}^2}}\right]. \tag{80}$$

For $D_{12} < 0$, the range is given by

$$-\tilde{\psi}_0 \leq \tilde{\psi} \leq \frac{\pi}{2}, \quad \text{for } -\frac{\pi}{2} \leq \psi \leq \psi_0, \tag{81}$$

$$\tilde{\psi}_0 \leq \tilde{\psi} \leq \frac{\pi}{2}, \quad \text{for } \psi_0 \leq \psi \leq \frac{\pi}{2}. \tag{82}$$

For $D_{12} \geq 0$, the critical value of $\tilde{\psi} = -\frac{\pi}{2}$ occurs as loading is applied in the direction of $\psi = -\psi_0$. As long as ψ is sufficiently larger than $-\psi_0$, the size of the contact zone would be small. For $D_{12} < 0$, the critical value is $\tilde{\psi} = -\tilde{\psi}_0$ when $\psi = -\frac{\pi}{2}$. If the magnitude of D_{12} is large, the size of the contact zone may be small for full range of ψ. Under these circumstances, the crack-tip fields for the "traction-free" interface crack can still exist and the stress intensity factors or the energy release rate can be used as proper parameters controlling fracture.

References

Anderson, P. M., 1988, "Small Scale Contact Conditions for the Linear-Elastic Interface Crack," ASME JOURNAL OF APPLIED MECHANICS, Vol. 55, pp. 814–817.

Bassani, J. L., and Qu, J., 1989, "On Elasticity Solutions for Cracks on Bimaterial and Bicrystal Interfaces," *Materials Sci. and Eng.*, Vol. A107, pp. 177–184.

Clements, D. L., 1971, "A Crack Between Dissimilar Anistropic Media," *Int. J. Eng. Sci.*, Vol. 9, pp. 257–265.

England, A. H., 1965, "A Crack Between Dissimilar Media," ASME JOURNAL OF APPLIED MECHANICS, Vol. 32, pp. 400–402.

Malyshev, B. M., and Salganik, R. L., 1965, "The Strength of Adhesive Joints Using the Theory of Cracks," *Int. J. Fracture*, Vol. 1, pp. 114–127.

Rice, J. R., and Sih, G., 1965, "Plane Problems of Cracks in Dissimilar Media," ASME JOURNAL OF APPLIED MECHANICS, Vol. 32, pp. 418–423.

Rice, J. R., 1988, "Elastic Fracture Mechanics Concepts for Interfacial Cracks," ASME JOURNAL OF APPLIED MECHANICS, Vol. 55, pp. 98–103.

Ting, T. C. T., 1986, "Explicit Solution And Invariance of the Singularities at An Interface Crack in Anisotropic Composite," *Int. J. Solids Structures*, Vol. 22, pp. 965–983.

Williams, M. L., 1959, "The Stresses Around A Fault Or Crack in Dissimilar Media," *Bull. Seism. Soc. Am.*, Vol. 49, pp. 199–204.

Willis, J. R., 1971, "Fracture Mechanics of Interfacial Cracks," *J. Mech. Phys. Solids*, Vol. 19, pp. 353–368.

Downloaded 03 May 2010 to 171.66.16.244. Redistribution subject to ASME license or copyright; see http://www.asme.org/terms/Terms_Use.cfm

D. J. Mukai
Graduate Student,
Department of Civil Engineering,
University of Washington, FX-10
Seattle, WA 98195

R. Ballarini
Assistant Professor,
Department of Civil Engineering,
Case Western Reserve University,
Cleveland, OH 44106

G. R. Miller
Associate Professor,
Department of Civil Engineering,
University of Washington, FX-10
Seattle, WA 98195
Assoc. Mem. ASME

Analysis of Branched Interface Cracks

A solution is presented for the problem of a finite length crack branching off the interface between two bonded dissimilar isotropic materials. Results are presented in terms of the ratio of the energy release rate of a branched interface crack to the energy release rate of a straight interface crack with the same total length. It is found that this ratio reaches a maximum when the interface crack branches into the softer material. Longer branches tend to have smaller maximum energy release rate ratio angles indicating that all else being equal, a branch crack will tend to turn back parallel to the interface as it grows.

1 Introduction

The interface crack problem was addressed in the late 1950's by Williams (1959). Williams used an eigenfunction expansion technique to solve the interface crack problem and discovered complex singularities and rapid oscillating stresses near the crack tip. Williams also estimated the oscillatory region to be very small.

In the mid 1960's, various workers (England (1965), Erdogan (1965), Rice and Sih (1965)) came up with closed-form solutions to the interface problem. These solutions verified Williams' (1959) finding of complex singularities and rapidly oscillating stresses near the crack tip. England (1965) also pointed out that the complex singularities lead to the physical impossibility of the crack faces interpenetrating near the crack tips. Like Williams (1959), these workers found the region where these phenomena occur was very small.

In the mid-1970's Comninou (1977) put forth an alternate solution that addressed the difficulties at the crack tip. Comninou resolved the problems at the crack tip by solving the interface crack problem assuming there is a small contact zone near the crack tips. This zone was found to be extremely small. While calculations were carried out for a limited range of Dundurs' constants (Dundurs 1969), Comninou's work provides a rational explanation of the oddities occurring near the crack tips.

Lately, the interface crack problem has received renewed attention. Gautensen and Dundurs (1987) have solved the problem formulated by Comninou (1977) using quickly convergent series. Unlike Comninou's (Comninou (1977) results which were carried out for only severe material mismatches, Gautesen and Dundurs obtain results covering all material combinations. Symington (1987) has completed Williams' (Williams 1959) eigenfunction analysis by finding a set of integer eigenvalues left out by Williams. Rice (1988) has proposed that the peculiarities at the crack tip are not too critical. In an argument similar to the concept of small-scale yielding, he asserts that the complex stress intensity factors will be indicative of the general state of the crack tip even if they do not correctly represent the state immediately surrounding the crack tip. Rice also provides a framework to interpret the complex intensity factor in terms of the classical form stress intensity factors K_I and K_{II}. He also includes an interesting discussion of the interaction of the crack length and load phase angle influence. Hutchinson, Mear, and Rice (1987) have looked at a crack completely in one body but very near the interface. Their solution, based on dimensional arguments, energy considerations, and the representation of the crack as a distribution of dislocations, examines criteria for crack growth parallel to the material interface. Park and Earmme (1986) use various integrals to describe the interface crack tip characteristics and include a discussion of the properties of these integrals. Shih and Asaro (1988) have investigated the interface crack with plasticity. They find that the pathological features of the linear elastic analyses are lessened by nonlinear behavior and that the linear elastic solutions are good in regions not immediately around the crack tip. Delale and Erdogan (1988) have looked at the interface crack by modeling the interface as a transition material; they put the crack in a thin third layer between the two half-spaces. They present some results regarding the direction of maximum K_I of the crack. Generally, K_I is larger as the crack tends toward the softer material. He and Hutchinson (1988) have performed an analysis very similar to the present one for the case of a branched semi-infinite crack.

Contributed by the Applied Mechanics Division of THE AMERICAN SOCIETY OF MECHANICAL ENGINEERS for publication in the JOURNAL OF APPLIED MECHANICS.

Discussion on this paper should be addressed to the Technical Editor, Leon M. Keer, The Technological Institute, Northwestern University, Evanston, IL 20208, and will be accepted until two months after final publication of the paper itself in the JOURNAL OF APPLIED MECHANICS. Manuscript received and accepted by the ASME Applied Mechanics Division, Feb. 22, 1989.

Copyright © 1990 by ASME
Downloaded 03 May 2010 to 171.66.16.244. Redistribution subject to ASME license or copyright; see http://www.asme.org/terms/Terms_Use.cfm

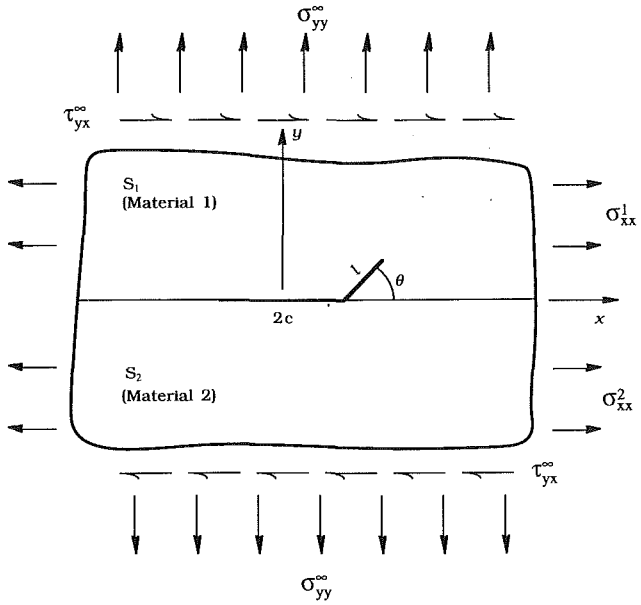


Fig. 1 A branched interface crack

They have presented extensive results on the initial branching angle, couched in terms of strain energy release rates.

In this paper, the branching of a finite length crack is analyzed. For small branch lengths the asymptotic results of He and Hutchinson are reproduced. For longer branch lengths the behavior changes as the global portion of the stress field influences further branch growth. Based on the obtained results, some conjectures are made concerning the fate of branching cracks.

2 Formulation

The problem configuration is depicted in Fig. 1, which shows the main crack, the branch crack, the loading at infinity, and the coordinate system. In the upper half-plane (S_1), the shear modulus is μ_1 and Poisson's ratio is ν_1. In the lower half-plane (S_2), the shear modulus is μ_2 and Poisson's ratio is ν_2. The boundary conditions for this problem require that both the main and branch cracks are traction-free and that at infinity the stresses approach σ^{∞}_{yy} and τ^{∞}_{yx}. Single-valuedness of the displacements at infinity is also required.

Some techniques useful for dealing with interface boundary conditions which are used in the problem formulation are presented first. These results follow directly from the formulation used by Clements (1971) to treat interface cracks in anisotropic materials.

In terms of the Muskhelishvili (1953) potentials, the stresses and displacements in isotropic elastic bodies may be expressed as follows:

$$(\sigma_{yy}-i\tau_{yx})_i=\Phi_i(z)+\overline{\Phi_i(z)}+z\overline{\Phi_i'(z)}+\overline{\Psi_i(z)} \tag{1}$$

$$(\sigma_{yy}+\sigma_{xx})_i=2[\Phi_i(z)+\overline{\Phi_i(z)}] \tag{2}$$

$$2\mu_i\left(\frac{\partial u}{\partial x}-i\frac{\partial v}{\partial x}\right)_i=\kappa_i\Phi_i(z)-[\overline{\Phi_i(z)}+z\overline{\Phi_i'(z)}+\overline{\Psi_i(z)}] \tag{3}$$

in which the subscript $i(i=1, 2)$ denotes "in region i", Φ_1, Ψ_1 correspond to the potentials for the upper half-plane and Φ_2, Ψ_2 correspond to the potentials for the lower half-plane. Moreover, z is the complex variable $x+iy$, the prime denotes differentation with respect to z, an overbar denotes conjugation, $\kappa=3-4\nu$ for plane strain, and $\kappa=\dfrac{3-\nu}{1+\nu}$ for plane stress.

For interface problems, it is convenient to introduce additional potentials as follows. Making use of the fact that if $f(z)$ is analytic for z in region R, then $f(z)\equiv\overline{f(\bar{z})}$ is analytic for $\bar{z}$ in region R, the following *analytic* jump potentials are constructed:

$$\Omega_s=\begin{cases}\Phi_1(z)-[\overline{\Phi_2}(z)+z\overline{\Phi_2'}(z)+\overline{\Psi_2}(z)] & z\in S_1\\ \Phi_2(z)-[\overline{\Phi_1}(z)+z\overline{\Phi_1'}(z)+\overline{\Psi_1}(z)] & z\in S_2\end{cases} \tag{4a}$$

$$\Omega_D=\begin{cases}\dfrac{\kappa_1}{2\mu_1}\Phi_1(z)+\dfrac{1}{2\mu_2}[\overline{\Phi_2}(z)+z\overline{\Phi_2'}(z)+\overline{\Psi_2}(z)] & z\in S_1\\ \dfrac{\kappa_2}{2\mu_2}\Phi_2(z)+\dfrac{1}{2\mu_1}[\overline{\Phi_1}(z)+z\overline{\Phi_1'}(z)+\overline{\Psi_1}(z)] & z\in S_2.\end{cases} \tag{4b}$$

Note that in terms of these jump potentials, the interface conditions can be expressed as:

$$(\sigma_{yy}-i\tau_{yx})_2-(\sigma_{yy}-i\tau_{yx})_1=\Omega_{S2}(x)-\Omega_{S1}(x) \tag{5a}$$

$$\left(\frac{\partial u}{\partial x}-i\frac{\partial v}{\partial x}\right)_2-\left(\frac{\partial u}{\partial x}-i\frac{\partial v}{\partial x}\right)_1=\Omega_{D2}(x)-\Omega_{D1}(x). \tag{5b}$$

The Ω potentials thus represent the jump in traction (Ω_S) and displacement (Ω_D) across the interface. The inverse relationship between the jump and Muskhelishvili potentials is determined algebraically from equations (4):

$$\Phi_1(z)=Q_1\left[\frac{1}{2\mu_2}\Omega_{S1}(z)+\Omega_{D1}(z)\right] \tag{6a}$$

$$\Psi_1(z)=Q_2\left[\frac{-\kappa_2}{2\mu_2}\bar{\Omega}_{S2}(z)+\bar{\Omega}_{D2}(z)\right]-\Phi_1(z)-z\Phi_1'(z) \tag{6b}$$

$$\Phi_2(z)=Q_2\left[\frac{1}{2\mu_1}\Omega_{S2}(z)+\Omega_{D2}(z)\right] \tag{6c}$$

$$\Psi_2(z)=Q_1\left[\frac{-\kappa_1}{2\mu_1}\bar{\Omega}_{S1}(z)+\bar{\Omega}_{D1}(z)\right]-\Phi_2(z)-z\Phi_2'(z) \tag{6d}$$

where

$$Q_1=\frac{2\mu_1\mu_2}{\mu_1+\kappa_1\mu_2} \tag{7a}$$

$$Q_2=\frac{2\mu_1\mu_2}{\mu_2+\kappa_2\mu_1}. \tag{7b}$$

This formulation allows for straightforward development of the various interaction potentials derived below.

3 Solution

The solution is obtained by a Green's function technique based on distributing dislocation singularities along the branch. The solution for the interaction between an interface crack and a dislocation is found by superposing the solutions for: (1) a dislocation in S_1 near an interface; (2) two perfectly bonded semi-infinite bodies loaded at infinity with σ_{yy} and τ_{yx}; and (3) an interface crack loaded with the negative of the stresses produced by (1) and (2). This solution for a single dislocation interacting with an interface crack (with the appropriate far-field loading) is then modified to model a distribution of dislocations along the branch, and by requiring zero tractions along the branch face a singular integral equation is obtained for the unknown dislocation distribution. The relevant physical quantities can be calculated after numerically solving the integral equation.

Most of the component solutions to be superposed are well-known. Nevertheless, it is convenient to rederive them here using the framework presented in Section 2. This will provide a consistent formulation, as well as a demonstration of the generality of the approach.

Consider first a dislocation near an interface (see Head,

Downloaded 03 May 2010 to 171.66.16.244. Redistribution subject to ASME license or copyright; see http://www.asme.org/terms/Terms_Use.cfm

1953; Dundurs and Sendeckyj (1965) located at a point z_0 in the upper half-plane. The continuity of tractions and displacements across the interface in combination with equation (5) implies the following boundary conditions on the jump potentials:

$$\left.\begin{aligned}\Omega^D_{S1}-\Omega^D_{S2}=0\\ \Omega^D_{D1}-\Omega^D_{D2}=0\end{aligned}\right\}\ |x|<\infty, y=0. \tag{8}$$

The singular portion of the jump potentials can be obtained directly by transforming the known singular potentials for a dislocation in a homogeneous full-plane into jump potentials. For a full-plane dislocation in region 1 we have:

$$\Phi^D_{1,\ \text{Singular}}=\frac{A}{z-z_0} \tag{9a}$$

$$\Psi^D_{1,\ \text{Singular}}=\frac{\overline{A}}{z-z_0}+A\frac{\overline{z_0}}{(z-z_0)^2} \tag{9b}$$

$$\Phi^D_{2,\ \text{Singular}}=\Psi^D_{2,\ \text{Singular}}=0 \tag{9c}$$

in which $A=\mu_1 e^{i\theta}\{[u_r]+i[v_\theta]\}/i\pi(\kappa_1+1)$, with $[u_r]$ and $[v_\theta]$ representing the jumps in the tangential and normal displacements accrued upon circling the dislocation. The corresponding Ω potentials are determined from equation (4):

$$\Omega^D_{S1,\ \text{Singular}}=\frac{A}{z-z_0} \tag{10a}$$

$$\Omega^D_{S2,\ \text{Singular}}=-\left[\frac{A}{z-\overline{z}_0}+\overline{A}\frac{z_0-\overline{z}_0}{(z-\overline{z}_0)^2}\right] \tag{10b}$$

$$\Omega^D_{S1,\ \text{Singular}}=\frac{\kappa_1}{2\mu_1}\frac{A}{z-z_0} \tag{10c}$$

$$\Omega^D_{S2,\ \text{Singular}}=\frac{1}{2\mu_1}\left[\frac{A}{z-\overline{z}_0}+\overline{A}\frac{z_0-\overline{z}_0}{(z-\overline{z}_0)^2}\right]. \tag{10d}$$

Obviously, the boundary conditions given by equation (8) are not satisfied. To patch up the interface boundary conditions, potentials of the following form are added, which are analytic in their respective regions:

$$\Omega^D_{S1,\ \text{Continuation}}=\Omega^D_{S2,\ \text{Singular}};\ z\in S_1 \tag{11a}$$

$$\Omega^D_{S2,\ \text{Continuation}}=\Omega^D_{S1,\ \text{Singular}};\ z\in S_2 \tag{11b}$$

with similar expressions for the displacement jump potentials. Using equation (6) to invert these to regular potentials gives the additional terms to be added to the singular potentials in equation (9) to give the desired solution (i.e., $\Phi^D=\Phi^D_{\text{Continuation}}+\Phi^D_{\text{Singular}}$, etc.):

$$\Phi^D_{1,\ \text{Continuation}}=A\left[\frac{(\alpha-\beta)}{(1+\beta)(z-\overline{z}_0)}\right]+\overline{A}\left[\frac{(\alpha-\beta)(z_0-\overline{z}_0)}{(1+\beta)(z-\overline{z}_0)^2}\right] \tag{12a}$$

$$\Psi^D_{1,\ \text{Continuation}}=\overline{A}\left[\frac{(\alpha+\beta)}{(1-\beta)(z-\overline{z}_0)}\right]-\Phi^D_{1,\ \text{Continuation}}-z\Phi^{D\prime}_{1,\ \text{Continuation}} \tag{12b}$$

$$\Phi^D_{2,\ \text{Continuation}}=A\left[\frac{1+\alpha}{(1-\beta)(z-z_0)}\right] \tag{12c}$$

$$\Psi^D_{2,\ \text{Continuation}}=A\left[\frac{(1+\alpha)(\overline{z_0}-z_0)}{(1+\beta)(z-z_0)^2}\right]+\overline{A}\left[\frac{(1+\alpha)}{(1+\beta)(z-z_0)}\right]-\Phi^D_{2,\ \text{Continuation}}-z\Phi^{D\prime}_{2,\ \text{Continuation}} \tag{12d}$$

where α and β are Dundurs' (Dundurs, 1969) constants defined by:

$$\alpha=\frac{\mu_2(\kappa_1+1)-\mu_1(\kappa_2+1)}{\mu_2(\kappa_1+1)+\mu_1(\kappa_2+1)} \tag{13a}$$

$$\beta=\frac{\mu_2(\kappa_1-1)-\mu_1(\kappa_2-1)}{\mu_2(\kappa_1+1)+\mu_1(\kappa_2+1)}. \tag{13b}$$

The constant potentials corresponding to the far-field loading can be derived from the jump potentials by simply starting with constant Ω's, which automatically satisfy the interface conditions, and inverting to determine the corresponding Φ's. The details of this operation are in the Appendix; the results are as follows:

$$\Phi^\infty_1=\frac{\sigma^\infty_{yy}+\sigma^\infty_{xx1}}{4}+i\left[\frac{(\beta-1)\tau^\infty_{yx}}{2}+\frac{1-\alpha}{2}IC_S\right] \tag{14a}$$

$$\Psi^\infty_1=\frac{\sigma^\infty_{yy}-\sigma^\infty_{xx1}}{2}+i\tau^\infty_{yx} \tag{14b}$$

$$\Phi^\infty_2=\frac{\sigma^\infty_{yy}+\sigma^\infty_{xx2}}{4}+i\left[-\frac{(\beta+1)\tau^\infty_{yx}}{2}+\frac{1-\alpha}{2}IC_S\right] \tag{14c}$$

$$\Psi^\infty_2=\frac{\sigma^\infty_{yy}-\sigma^\infty_{xx2}}{2}+i\tau^\infty_{yx} \tag{14d}$$

in which the arbitrary constant IC_S does not affect the stresses and is related to a rigid body rotation. For convenience, it is chosen so the Imag $\{\Phi_{1,\ \text{Far Field}}\}=0$. This gives Imag $\{\Phi_{2,\ \text{Far Field}}\}=\dfrac{\alpha-\beta}{1-\alpha}\tau_{yx}$.

In determining the relations (14), it turns out that the $x-$direction stresses are related:

$$\sigma_{xx2}=\frac{4\beta-2\alpha}{1-\alpha}\sigma^\infty_{yy}+\frac{1+\alpha}{1-\alpha}\sigma_{xx1} \tag{15}$$

This result for σ_{xx2} and σ_{xx1} is typical of interface problems (see, e.g., Dundurs (1969)). Since this analysis will be considering branches which are not strictly parallel to the x-axis, these x-direction stresses are important: They cannot be ignored as in the normal interface crack problem. Since it is generally not possible to have these stresses vanish in both regions simultaneously, some choice must be made for their values. The choice made here is to take $\sigma_{xx2}=-\sigma_{xx1}$, which implies that the net force on a vertical cut is zero. It was verified using a finite element analysis of bonded interface bodies of finite dimensions that there exists a region at the center of the specimens near the interface where the tensile stress parallel to the interface in one body is equal and opposite to the tensile stress parallel to the interface in the other body. Thus, the present choice of x-direction stresses would be appropriate for interface cracks far from free boundaries with no applied x-direction tractions.

It is now necessary to introduce the main crack. The stresses due to the dislocation near an interface and the far-field loading will be removed from the crack faces by the following potentials:

$$\Phi^C=\Phi^C_{\text{Dislocation}}+\Phi^C_{\text{Far Field}} \tag{16a}$$

$$\Psi^C=\Psi^C_{\text{Dislocation}}+\Psi^C_{\text{Far Field}} \tag{16b}$$

where $\Phi^C_{\text{Dislocation}}$ removes the stresses on the crack face due to the dislocation and $\Phi^C_{\text{Far Field}}$ removes the stresses due to the far-field loading.

Downloaded 03 May 2010 to 171.66.16.244. Redistribution subject to ASME license or copyright; see http://www.asme.org/terms/Terms_Use.cfm

To obtain these potentials, first consider the interface crack under arbitrary crack face loading (the standard solution has been presented by many investigators e.g., England, 1965; Erdogan, 1965; Rice and Sih, 1965). For a crack on an interface, the interface boundary conditions are:

$$(\sigma_{yy}-i\tau_{yx})_1-(\sigma_{yy}-i\tau_{yx})_2=0 \quad |x|<\infty,\ y=0 \tag{17a}$$

$$(u'-iv')_1-(u'-iv')_2=0 \quad |x|>c \tag{17b}$$

$$\sigma_{yy}-i\tau_{yx}=f(x) \quad |x|<c. \tag{17c}$$

These boundary conditions, in terms of the standard potentials, are somewhat cumbersome. However, as shown by equation (6), in terms of the jump potentials the first boundary condition is simply:

$$\Omega_{S1}(x)-\Omega_{S2}(x)=0 \quad |x|<\infty. \tag{18}$$

Using an argument similar to the one in the far-field solution (see the Appendix), since Ω_S is analytic everywhere and bounded, by Liouville's theorem it must be constant. Moreover, for zero stress at infinity, $\Omega_S=0$.

The second boundary condition in terms of the jump potentials is:

$$\Omega_{D1}(x)-\Omega_{D2}(x)=0 \quad |x|>c. \tag{19}$$

The third boundary condition in terms of the jump potentials is:

$$Q_1\Omega_{D1}(x^+)+Q_2\Omega_{D2}(x^-)=f(x^+)=f(x) \quad |x|<c \tag{20a}$$

$$Q_2\Omega_{D2}(x^-)+Q_1\Omega_{D1}(x^+)=f(x^-)=f(x) \tag{20b}$$

or

$$\Omega_D^+ + m\Omega_D^- = \frac{1}{Q_1}f(x) \quad ;|x|<c \tag{21a}$$

$$m=\frac{Q_2}{Q_1}=\frac{1+\beta}{1-\beta}. \tag{21b}$$

These last two boundary conditions (equations (19) and (21*a*)) define a Hilbert problem, with the well-known solution:

$$\Omega_D(z)=\frac{X(z)}{2\pi i}\int_{-c}^{+c}\frac{1}{Q_1}\frac{f(x)}{X^+(x)(x-z)}\,dx+X(z)P(z) \tag{22}$$

in which

$$X(z)=(z-c)^{\gamma-1}(z+c)^{-\gamma}$$

$$\gamma=\frac{1}{2}-\frac{i}{2\pi}\log m=\frac{1}{2}+i\epsilon$$

$$\epsilon=\frac{1}{2\pi}\log\frac{1}{m}$$

and $P(z)$ is a polynomial determined by far-field behavior. After Ω_D is obtained, the jump potentials can be inverted back to standard potentials using equation (6).

To remove the stresses on the crack caused by the dislocation solution, the integration in equation (22) is carried out with $f(x)$ equal to the opposite of the tractions due to a dislocation near the interface. These tractions are obtained by substituting equations (9) and (12) into equation (1):

$$\sigma_{yy}-i\tau_{yx}=A\left[\frac{1+\alpha}{1-\beta}\left(\frac{1}{x-z_0}\right)+\frac{1+\alpha}{1+\beta}\left(\frac{1}{x-\bar{z}_0}\right)\right]$$

$$+\bar{A}\left[\frac{1+\alpha}{1+\beta}\frac{(z_0-\bar{z}_0)}{(x-\bar{z}_0)^2}\right]. \tag{23}$$

The resulting jump potentials are

$$\Omega^C_{S,\ \text{Dislocation}}=0 \tag{24a}$$

$$\Omega^C_{D,\ \text{Dislocation}}=\frac{-2A}{1+m}\frac{1}{Q_1}\left[\frac{1+\alpha}{1-\beta}F(z,z_0)+\frac{1+\alpha}{1+\beta}F(z,\bar{z}_0)\right]$$

$$-\frac{2\bar{A}}{1+m}\frac{1}{Q_1}(z_0-\bar{z}_0)\left[\frac{1+\alpha}{1+\beta}G(z,\bar{z}_0)\right]$$

$$+X(z)P(z) \tag{24b}$$

in which

$$F(z,a)=\frac{1}{2}\frac{1}{(z-a)}\left[1-\frac{X(z)}{X(a)}\right] \tag{25a}$$

$$G(z,a)=\frac{\partial F(z,a)}{\partial a}. \tag{25b}$$

Inverting these to standard potentials gives:

$$\Phi^C_{1,\ \text{Dislocation}}=-\frac{2A}{1+m}\left[\frac{1+\alpha}{1-\beta}F(z,z_0)+\frac{1+\alpha}{1+\beta}F(z,\bar{z}_0)\right]$$

$$-\frac{2\bar{A}}{1+m}(z_0-\bar{z}_0)\left[\frac{1+\alpha}{1+\beta}G(z,\bar{z}_0)\right] \tag{26a}$$

$$\Psi^C_{1,\ \text{Dislocation}}=-\frac{2mA}{1+m}(\bar{z}_0-z_0)\left[\frac{1+\alpha}{1+\beta}\overline{G(\bar{z},\bar{z}_0)}\right]$$

$$-\frac{2m\bar{A}}{1+m}\left[\frac{1+\alpha}{1-\beta}\overline{F(\bar{z},z_0)}+\frac{1+\alpha}{1+\beta}\overline{F(\bar{z},\bar{z}_0)}\right]$$

$$-\Phi^C_{1,\ \text{Dislocation}}-z\Phi^{C\prime}_{1,\ \text{Dislocation}} \tag{26b}$$

$$\Phi^C_{2,\ \text{Dislocation}}=-\frac{2mA}{1+m}\left[\frac{1+\alpha}{1-\beta}F(z,z_0)+\frac{1+\alpha}{1+\beta}F(z,\bar{z}_0)\right]$$

$$-\frac{2m\bar{A}}{1+m}(z_0-\bar{z}_0)\left[\frac{1+\alpha}{1+\beta}G(z,\bar{z}_0)\right] \tag{26c}$$

$$\Psi^C_{2,\ \text{Dislocation}}=--\frac{2A}{1+m}(\bar{z}_0-z_0)\left[\frac{1+\alpha}{1+\beta}\overline{G(\bar{z},\bar{z}_0)}\right]$$

$$-\frac{2\bar{A}}{1+m}\left[\frac{1+\alpha}{1-\beta}\overline{F(\bar{z},z_0)}+\frac{1+\alpha}{1+\beta}\overline{F(\bar{z},\bar{z}_0)}\right]$$

$$-\Phi^C_{2,\ \text{Dislocation}}-z\Phi^{C\prime}_{2,\ \text{Dislocation}}. \tag{26d}$$

Each of the potentials in equation (26) contains an $X(z)P(z)$ term following inversion. However, requiring that the stresses vanish at infinity and requiring that there be no net displacement at infinity (no net $1/z$ term) leads to all the $P(z)$'s being zero.

Removal of the constant far-field tractions is simply the standard interface problem. After performing the necessary integrals in equation (22), the Ω potentials are:

$$\Omega^C_{S,\ \text{Far Field}}=0 \tag{27a}$$

$$\Omega^C_{D,\ \text{Far Field}}=-\frac{\sigma^\infty_{yy}-i\tau^\infty_{yx}}{(1+m)Q_1}+\frac{\sigma^\infty_{yy}-i\tau^\infty_{yx}}{(1+m)Q_1}[z+(2\gamma-1)c]X(z)$$

$$+P(z)X(z) \tag{27b}$$

Again, $P(z)$ is determined by far-field behavior and turns out to be zero. Inverting to standard potentials gives the fol-

Downloaded 03 May 2010 to 171.66.16.244. Redistribution subject to ASME license or copyright; see http://www.asme.org/terms/Terms_Use.cfm

lowing result, which is of course identical to the previous solutions mentioned earlier:

$$\Phi_{1,\text{ Far Field}}^{C} = \frac{\sigma_{yy}^{\infty} - i\tau_{yx}^{\infty}}{(1+m)}\,[X(z)\{z-(1-2\gamma)c\}-1] \tag{28a}$$

$$\Psi_{1,\text{ Far Field}}^{C} = \frac{m(\sigma_{yy}^{\infty}+i\tau_{yx}^{\infty})}{(1+m)}\,[\bar{X}(Z)\{z - (1-2\bar{\gamma})c\}-1]-\Phi_1 - z\Phi_1' \tag{28b}$$

$$\Phi_{2,\text{ Far Field}}^{C} = \frac{m(\sigma_{yy}^{\infty}-i\tau_{yx}^{\infty})}{(1+m)}\,[X(z)\{z-(1-2\gamma)c\}-1] \tag{28c}$$

$$\Psi_{2,\text{ Far Field}}^{C} = \frac{\sigma_{yy}^{\infty}-i\tau_{yx}^{\infty}}{(1+m)}\,[\bar{X}(z)\{z-(1-2\bar{\gamma})c\}-1]-\Phi_2 - z\Phi_2'. \tag{28d}$$

The final potentials that give the solution to the interaction between a discrete dislocation and an interface crack subjected to uniform far-field stresses are:

$$\Phi_1 = \Phi_1^D + \Phi_1^{\infty} + \Phi_1^C \tag{29a}$$

$$\Psi_1 = \Psi_1^D + \Psi_1^{\infty} + \Psi_1^C \tag{29b}$$

where the Dislocation (D) potentials, the infinity (∞) potentials and the Crack (C) potentials are all defined above. For the no interface case ($\alpha=\beta=0$) the present solution reduces analytically to Lo's (Lo, 1978) solution.

Replacing the discrete dislocation with a continuous distribution of dislocations enables the modeling of the crack branch. Requiring the traction to be zero on the branch leads to an integral equation in terms of the unknown dislocation density. After nondimensionalizing and separating the kernel into singular and regular parts, the following Cauchy-type integral equation is arrived at:

$$\int_{-1}^{1}\frac{D(t)}{t-s}\,dt + \frac{l/c}{2}\int_{-1}^{1}[\tilde{K}_1(s,t)D(t) + \tilde{K}_2(s,t)\bar{D}(t)]dt = -f(s) \tag{30}$$

in which $D(t) = \mu_1 e^{i\theta}\partial/\partial t\{[u_r]+i[v_\theta]\}/i\pi(\kappa_1+1)$ along the line $z_0 = 1 + te^{i\theta}$, $[u_r]$ and $[v_\theta]$ are the jumps in the tangential and normal displacements across the dislocation line, $\tilde{K}_1$ and $\tilde{K}_2$ are the kernels resulting from the potentials derived earlier, and $f(s)$ is the known traction along the branch line $z = 1 + se^{i\theta}$ due to the main crack loaded at infinity.

This equation is solved numerically using piecewise continuous polynomials in the manner of Gerasoulis (1982). Once the dislocation densities have been determined numerically, the stress intensity factors are obtained directly from the dislocation density at the tip of the branch crack in the normal fashion (e.g., Bryant, Miller, and Keer, 1984). In applying the numerical scheme, the integration point at the base of the branch crack is eliminated. Ignoring the integration point at the "knee" of the branched crack is an approximate method of incorporating the fact that the singularity at this end of the crack is less than one half. In their asymptotic analysis, He and Hutchinson (1988) investigated the effect of neglecting this integration point as opposed to including the actual singularity explicitly and found the effect to be minimal. Although it does not necessarily follow that the minimal effect of ignoring the integration point in the asymptotic problem holds true for the finite length crack problem, for those cases where one would expect the most problems (short branch lengths) the calculated results match those of He and Hutchinson quite well. Thus, despite the approximate nature of the handling of the junction of the main crack with the branch, the numerical solution provides accurate results for the branching problem.

4 Numerical Results and Conclusions

Although shear loading at infinity is included in the formulation of the problem, it is not included in the numerical results since the resulting large contact zones at the crack tips change the requirements of the solution procedure quite drastically. For this reason, the integral equation (30) was solved numerically for pure tensile load at infinity only (σ_{yy}^{∞}). Although results are presented as follows for a small set of material parameters, calculations were actually carried out over the entire α,β plane, with some not unexpected numerical difficulties arising in the vicinity of extreme material mismatches. The presented results are representative of these more wide-ranging calculations.

For purposes of linking up to the asymptotic results of He and Hutchinson (1988), the parameter of interest is taken as $\mathcal{G}/\mathcal{G}_0$; the ratio of the energy release rate at the tip of the branch to the energy release rate at an equivalent unbranched interface crack. For this analysis, $\mathcal{G}$ corresponds to the strain energy release rate of a branch crack tip in material 1 and $\mathcal{G}_0$ corresponds to the strain energy release rate at the tip of an interface crack of total length $2c' = 2c + l$. The expressions for $\mathcal{G}$, $\mathcal{G}_0$, and $\mathcal{G}/\mathcal{G}_0$ are:

$$\mathcal{G} = \left[\frac{1-\nu_1}{2\mu_1}\right](K_I^2 + K_{II}^2) \tag{31a}$$

$$\mathcal{G}_0 = \left[\frac{1-\nu_1}{\mu_1} + \frac{1-\nu_2}{\mu_2}\right]\frac{(\sigma_{yy}^2+\sigma_{yx}^2)(1+4\epsilon^2)\pi c'}{4\cosh^2(\pi\epsilon)} \tag{31b}$$

$$\frac{\mathcal{G}}{\mathcal{G}_0} = (1+\alpha)\frac{\cosh^2\pi\epsilon}{(1+4\epsilon^2)(\sigma_{yy}^{\infty 2}+\tau_{yx}^{\infty 2})}\left[\left(\frac{K_I}{\sqrt{\pi c'}}\right)^2 + \left(\frac{K_{II}}{\sqrt{\pi c'}}\right)^2\right]. \tag{31c}$$

As the length of the branch becomes very small relative to the main crack, it is expected that the present results should in some sense approach those of the semi-infinite crack. However, as explained below, the present results can be directly compared to He and Hutchinson's (1988) asymptotic results only for $\beta=0$. Figure 2 shows the dependence of the strain energy release, rate, $\mathcal{G}/\mathcal{G}_0$ on the branch angle, θ for $\alpha=0.5$, $\beta=0$, and $1/c=0.0001$. The $\mathcal{G}/\mathcal{G}_0$ results in Fig. 2 indeed agree well with those of He and Hutchinson (1988), as expected.

For $\beta\neq 0$, there are some interesting problems regarding the loading parameter. As shown by Rice (1988), the far-field loading and crack length are coupled in the expression for the complex intensity factor $K = K_1 + iK_2 = (k_1 + ik_2)\sqrt{\pi}\cos(\pi\epsilon)$, where $k_1 + ik_2$ is the complex intensity factor of Sih and Rice (1964). Since He and Hutchinson (1988) used $\gamma = \tan^{-1}K_2/K_1$

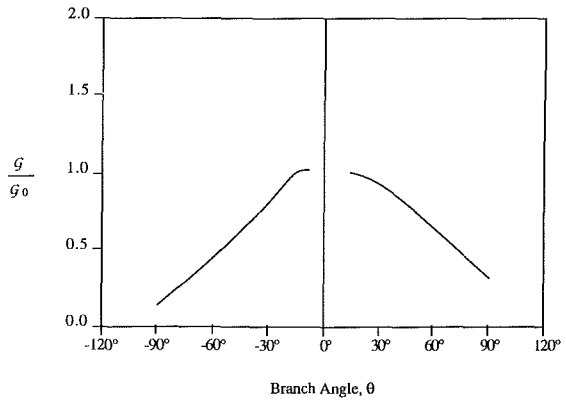


Fig. 2 Strain energy release rate ratio, $\mathcal{G}/\mathcal{G}_0$, versus extension angle, θ, for $l/c = 0.001$, $\alpha = 0.5$, $\beta = 0$ (e.g., $\Gamma = 3$, $\nu_1 = \nu_2 = 0.5$)

Downloaded 03 May 2010 to 171.66.16.244. Redistribution subject to ASME license or copyright; see http://www.asme.org/terms/Terms_Use.cfm

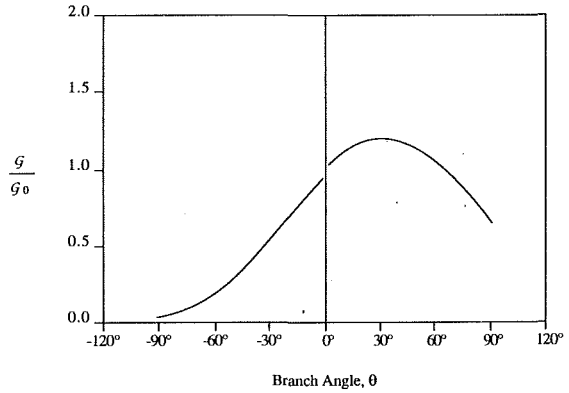


Fig. 3 Strain energy release rate ratio, $\mathcal{G}/\mathcal{G}_0$, versus extension angle, θ, for $l/c = 0.001$, $\nu_1 = \nu_2 = 0.3$, $\Gamma = 3$ ($\alpha = 0.5$, $\beta = 0.14286$)

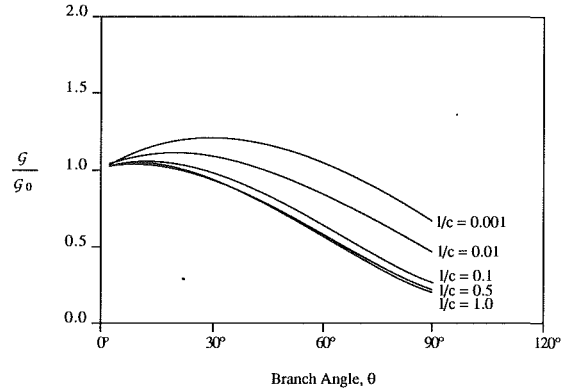


Fig. 5 Strain energy release rate ratio, $\mathcal{G}/\mathcal{G}_0$, versus extension angle, θ, for $\nu_1 = \nu_2 = 0.3$, $\Gamma = 3$, $l/c = 0.001, 0.01, 0.1, 0.5, 1$ ($\alpha = 0.5$, $\beta = 0.14286$)

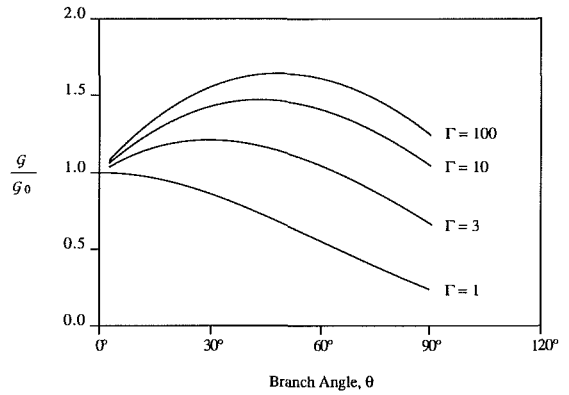


Fig. 4 Strain energy release rate ratio, $\mathcal{G}/\mathcal{G}_0$, versus extension angle, θ, for $l/c = 0.001$, $\nu_1 = \nu_2 = 0.3$, $\Gamma = 1, 3, 10, 100$ ($\alpha = 0, 0.5, 0.81818, 0.98020$; $\beta = 0, 0.14286, 0.23377, 0.28006$)

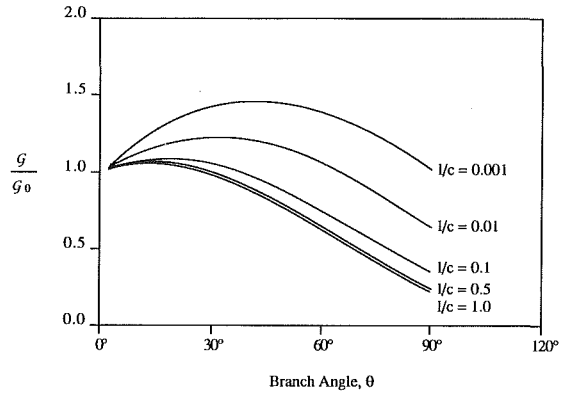


Fig. 6 Strain energy release rate ratio, $\mathcal{G}/\mathcal{G}_0$, versus extension angle, θ, for $\nu_1 = \nu_2 = 0.3$, $\Gamma = 10$, $l/c = 0.001, 0.01, 0.1, 0.5, 1$ ($\alpha = 0.81818$, $\beta = 0.23377$)

as their loading factor, it is not possible to match their loading parameters uniquely for $\beta \neq 0$. Specifically, the loading parameter used here, $\Psi = \tan^{-1}\sigma^{\infty}_{yx}/\sigma^{\infty}_{yy}$, is related to He and Hutchinson's parameter, γ, by:

$$\Psi = \gamma + \tan^{-1} 2\epsilon - \epsilon \log 2c. \tag{32}$$

In the present analysis, the salient length parameter is the ratio of the branch crack length to the main crack length, l/c, and the absolute value of c is arbitrary. Since the value of c is arbitrary Ψ and γ cannot be related in a definitive manner. Equation (32) shows that for $\beta = 0$, ϵ will be 0 and Ψ is equivalent to γ, and thus the results in Fig. 2 can be directly compared to He and Hutchinson's. Conversely for $\beta \neq 0$, $\Psi \neq \gamma$, the two loading parameters are different. As noted by Rice (1988), ϵ is usually very small. However, because of the ϵ log $2c$ term in equation (32), this does not ensure that $\Psi \cong \gamma$. If ϵ log $2c << 1$, then $\Psi \cong \gamma$.

Figure 3 shows that for the case of the crack growing into the softer material, the maximum $\mathcal{G}/\mathcal{G}_0$, $\mathcal{G}/\mathcal{G}_{0\max}$, occurs at an angle somewhat off the interface and in the softer material ($\theta > 0$). Although it is not shown by these figures, the angle at which K_I is maximized in the softer material corresponds to a nearly zero value for K_{II}. These results are typical for different l/c and Γs($\Gamma = \mu_2/\mu_1$), and are consistent with the observations of He and Hutchinson concerning the tendency of branching to occur in the softer material provided the material toughnesses are comparable. Subsequent results are presented for θ in the soft material only.

Figure 4 shows $\mathcal{G}/\mathcal{G}_0$ versus θ for various Γ and $l/c = 0.001$. Notice that as Γ increases, so does $\mathcal{G}/\mathcal{G}_{0\max}$. The angle that maximizes $\mathcal{G}/\mathcal{G}_0$, $\theta_{\max}$, also increases as Γ increases. Again, both these trends agree with He and Hutchinson's (1988) results for $\gamma \neq 0$, although for the reasons given above, direct comparison is no longer possible. It should be noted that the in-plane stresses, σ_{xx}, are increased also by increasing material mismatch, although these stresses appear to have only secondary influence on the branch behavior.

Figures 5 and 6 show the influence of finite main crack size by considering $\mathcal{G}/\mathcal{G}_0$ versus θ for various l/c values. In both Fig. 5 and 6, l/c increases, $\mathcal{G}/\mathcal{G}_{0\max}$ decreases towards a value of unity, while the branch angle corresponding to maximum energy release rate decreases. (Note, however, that in calculating $\mathcal{G}/\mathcal{G}_0$, $\mathcal{G}_0$ is adjusted to be the strain energy release rate for a crack of length $2c + l$. Thus, $\mathcal{G}_{\max}$ itself is not necessarily decreasing with increasing branch length, since $\mathcal{G}_0$ is increasing with l. In fact, $\mathcal{G}_{\max}$ reaches a minimum and then starts to increase again as l/c is increased). Using $\mathcal{G}/\mathcal{G}_{0\max}$ as a crack growth criterion, the decreasing $\theta_{\max}$ with increasing branch length can be taken as an indication that the branch would tend to turn back parallel to the interface as it grows (this rough method for predicting crack trajectories does not always work; see Rubinstein, 1989). Given the further result that the maximum energy release rate at the branch tip approaches that of the interface crack itself as the branch grows, then together this would imply that in a limited sense branching is irrelevant, since the driving force would be similar whether branching occurs or not. The critical issue, however, remains the relative toughnesses of the materials involved.

The primary conclusions to be drawn from the present analysis are that branching from an interface is a viable mode of crack growth, and that such branching is likely to occur initially at an angle somewhere between 10 deg and 47 deg in the softer of the two materials, provided the material toughnesses are similar. As the branch extends its growth characteristics will be altered, resulting in a tendency to return to a path parallel

Downloaded 03 May 2010 to 171.66.16.244. Redistribution subject to ASME license or copyright; see http://www.asme.org/terms/Terms_Use.cfm

to the interface, with a driving force similar to that of an unbranched crack.

Acknowledgments

This material is based upon work supported by the National Science Foundation under Grant No. MSM-8657628, and by NASA-Lewis under Grant No. NAG3-856.

References

Bryant, M. D., Miller, G. R., and Keer, L. M., 1984, "Line Contact Between A Rigid Indenter and a Damaged Elastic Body," ASME JOURNAL OF APPLIED MECHANICS, Vol. 37, pp. 467–478.

Clements, D. L., 1971, "A Crack Between Dissimilar Anisotropic Media," *International Journal of Engineering Science*, Vol. 9, pp. 257–265.

Comninou, M., 1977, "The Interface Crack," ASME JOURNAL OF APPLIED MECHANICS, Vol. 44, pp. 631–636.

Delale, F., and Erdogan, F., 1988, "On the Mechanical Modeling of the Interfacial Region in Bonded Half-Planes," ASME JOURNAL OF APPLIED MECHANICS, Vol. 55, pp. 317–324.

Dundurs, J., 1969, Discussion of "Edge-Bonded Dissimilar Orthogonal Elastic Wedges Under Normal and Shear Loading," ASME JOURNAL OF APPLIED MECHANICS, Vol. 36, pp. 650–652.

Dundurs, J., and Sendeckyj, G. P., "Behavior of an Edge Dislocation near a Bimaterial Interface," *Journal of Applied Physics*, Vol. 36, pp. 3353–3354.

England, A. H., 1965, "A Crack Between Dissimilar Media," ASME JOURNAL OF APPLIED MECHANICS, Vol. 32, pp. 400–402.

Erdogan, F., 1965, "Stress Distribution in Bonded Dissimilar Materials With Cracks," ASME JOURNAL OF APPLIED MECHANICS, Vol. 32, pp. 403–410.

Gautesen, A. K., and Dundurs, John, 1987, "The Interface Crack in a Tension Field," ASME JOURNAL OF APPLIED MECHANICS, Vol. 54, pp. 93–98.

Gerasoulis, A., 1982, "The Use of Piecewise Quadratic Polynomials for the Solution of Singular Integral Equations of Cauchy Type," *Computational Mathematics with Applications*, Vol. 8, pp. 15–22.

He, M. Y., and Hutchinson, J. W., 1988, "Kinking of a Crack Out of an Interface," *Harvard Report Mech-13*, Cambridge, Mass.

Head, A. K., 1953, "Edge Dislocations in Inhomogeneous Media," *Proceedings of the Physical Society, London*, Vol. B66, p. 793-801.

Hutchinson, J. W., Mear, M., and Rice, J. R., 1987, "Crack Paralleling an Interface Between Dissimilar Materials," ASME JOURNAL OF APPLIED MECHANICS, Vol. 54, pp. 828–832.

Lo, K. K., 1978, "Analysis of Branched Cracks," ASME JOURNAL OF APPLIED MECHANICS, Vol. 45, pp. 797–802.

Muskhelishvili, N. I., 1953, *Singular Integral Equations*, Noordhoff, Groningen.

Park, J. H., Earmme, Y. Y., 1986, "Application of Conservation Integrals to Interfacial Crack Problems," *Mech. Mater.*, Vol. 5, pp. 261–276.

Rice, J. R., 1988, "Elastic Fracture Mechanics Concepts for Interfacial Cracks," ASME JOURNAL OF APPLIED MECHANICS, Vol. 55, pp. 98–103.

Rice, J. R., and Sih, G. C., 1965, "Plane Problems of Cracks in Dissimilar Media," ASME JOURNAL OF APPLIED MECHANICS, Vol. 32, pp. 418–423.

Rubinstein, A. A., 1989, "Analysis of a Crack Path in a Heterogeneous Stress Field," *Proceedings of the First Pan American Conference of Applied Mechanics*, Rio de Janeiro, Brazil, Jan. 3-6, 1989.

Shih, C. F., and Asaro, R. J., 1988, "Elastic-Plastic Analysis of Cracks on Bimaterial Interfaces: Part 1—Small Scale Yielding," ASME JOURNAL OF APPLIED MECHANICS, Vol. 55, pp. 299–316.

Sih, G. C., and Rice, J. R., 1964, "The Bending of Plates of Dissimilar Materials With Cracks," ASME JOURNAL OF APPLIED MECHANICS, Vol. 31, pp. 477–482.

Symington, M. F., 1987, "Eigenvalues for Interface Cracks in Linear Elasticity," ASME JOURNAL OF APPLIED MECHANICS, Vol. 54, pp. 973–974.

Williams, M. L., 1959, "Stresses Around a Fault or Crack in Dissimilar Media," *Bulletin of the Seismological Society of America*, Vol. 49, pp. 199–204.

APPENDIX

The boundary conditions for the interface body (no crack) under remote stress are:

$$\left.\begin{aligned}\Omega_{S1}-\Omega_{S2}=0\\ \Omega_{D1}-\Omega_{D2}=0\end{aligned}\right\}\ |x|<\infty, y=0. \tag{A1}$$

As pointed out earlier, Ω_{S1}, Ω_{D1} and Ω_{S2}, Ω_{S2} are analytic in their respective regions. Moreover, since these two potentials are equal along the region boundary (as given by the above boundary condition), it can be concluded that Ω_S and Ω_D are analytic everywhere. By Liouville's theorem, since Ω_S and Ω_D are analytic everywhere and bounded, they must be constant. Thus, set:

$$\Omega_S^\infty = C_S = RC_S + iIC_S \tag{A2a}$$

$$\Omega_D^\infty = C_D = RC_D + iIC_D \tag{A2b}$$

in which RC_S, IC_S, RC_D, and IC_D are real constants.

Inverting relations equation (A2) to Muskhelishvili (1953) potentials gives:

$$\Phi_1^\infty = Q_1\left[\frac{1}{2\mu_2}C_S + C_D\right] \tag{A3}$$

$$\Psi_1^\infty = Q_2\left[\frac{-\kappa_2}{2\mu_2}\overline{C_S} + \overline{C_D}\right] - Q_1\left[\frac{1}{2\mu_2}C_S + C_D\right] \tag{A3b}$$

$$\Phi_2^\infty = Q_2\left[\frac{1}{2\mu_1}C_S + C_D\right] \tag{A3c}$$

$$\Psi_2^\infty = Q_1\left[\frac{-\kappa_1}{2\mu_1}\overline{C_S} + \overline{C_D}\right] - Q_2\left[\frac{1}{2\mu_1}C_S + C_D\right]. \tag{A3d}$$

The two complex constants C_S and C_D are determined from the conditions at infinity:

$$\sigma_{yy}^\infty - i\tau_{yx}^\infty = \Phi_i^\infty + \overline{\Phi_i^\infty} + \overline{\Psi_i^\infty} \tag{A4a}$$

$$\sigma_{yy}^\infty - \sigma_{xx1}^\infty = 2(\Phi_1^\infty + \overline{\Phi_1^\infty}) \tag{A4b}$$

$$\sigma_{yy}^\infty - \sigma_{xx2}^\infty = 2(\Phi_2^\infty + \overline{\Phi_2^\infty}) \tag{A4c}$$

Inverting these leads to the expressions in equation (14).

Downloaded 03 May 2010 to 171.66.16.244. Redistribution subject to ASME license or copyright; see http://www.asme.org/terms/Terms_Use.cfm

Kuang-Chong Wu
Associate Professor.

Shyh-Jye Hwang
Graduate Student.

Institute of Applied Mechanics,
National Taiwan University,
Taipei, Taiwan 10765
Republic of China

Correspondence Relations for the Interface Crack in Monoclinic Composites Under Mixed Loading

A correspondence is established between the problem of an interface crack in monoclinic composites and that of an interface crack in isotropic composites. The interface crack considered is subjected to a combined tension-compression, in-plane shear and antiplane shear loading at the crack faces. Under the applied loading, the interface crack is assumed to be partially opened. Through the correspondence, quantities of interest such as stress intensity factors, sizes of the contact zones, for monoclinic composites can be obtained from the results of the isotropic interface crack problem.

1 Introduction

The traction-free conditions on the crack faces of an interface crack generally lead to a physically unacceptable phenomenon of crack face interpenetration. One of the models to remove the phenomenon of crack face overlapping was proposed by Comninou (1977). The model assumes that frictionless contact zones exist behind the tips of an interface crack. The cases of an interface crack in an isotropic bimaterial under uniform pure tension, pure shear, and combined tension-compression and shear were treated numerically by Comninou (1977, 1978, 1979). Gautesen and Dundurs (1988) showed that the integral equations formulated by Comninou could be solved exactly for uniform loading and accurate results were derived for the whole range of mismatch in the elastic constants of the two materials.

The model proposed by Comninou (1977) was applied to a interface crack between anisotropic composites by Wang and Choi (1983a, 1983b). A particular high-modulus, graphite-exopy fiber-reinforced composite laminated plate with fiber orientation of [±45 deg] was solved numerically by Wang and Choi (1983a, 1983b).

Wu (1989b) proposed accurate approximations for the stress intensity factors of a partially opened interface crack under a combined tension-shear field and a combined compression-shear field. The approximations are applicable to isotropic as well as to anisotropic materials. The approximation derived by Wu, however, is limited to materials in which the in-plane shear deformation and antiplane shear deformation are uncoupled.

In this paper we show that a correspondence exists between the interface crack problem for monoclinic composites as considered by Wang and Choi and that for isotropic composites. Through such a correspondence, solutions for the anisotropic interface crack can be expressed in terms of those for the isotropic interface crack. The derivation of this paper follows Stroh's formulation (1958) for anisotropic elasticity problems. The plan of the paper is as follows. First Stroh's formulation is outlined in Section 2. The correspondence is established in Section 3. The stress intensity factors and the energy release rate for the anisotropic interface crack under uniform mixed loading are derived in Section 4 using the correspondence relations. Finally, numerical results of the stress intensity factors and the energy release rate are presented for $[\pm\theta]$ composite system and [30 deg/θ] composite systems. In the following discussions, summation is implied for repeated indices unless noted otherwise and boldfaced symbols denote matrices.

2 Stroh's Formulations

The equations of equilibrium in terms of the displacements are given by

$$C_{ijkl}\frac{\partial^2 u_k}{\partial x_l \partial x_j}=0 \tag{1}$$

where **C** is the elasticity tensor. The solutions to equation (1) are assumed to have the form:

$$u_k = a_k f(z) \tag{2}$$

where $z=x_1+px_2$ and p and a_k are the eigenvalues and eigenvectors to be determined, and the function f is an arbitrary function of z. With equation (2) in equation (1), we have

$$[C_{i1k1}+(C_{i1k2}+C_{i2k1})p+C_{i2k1}p^2]a_k=0. \tag{3}$$

Let

$$\begin{aligned} C_{i1k1} &= Q_{ik} \\ C_{i1k2} &= R_{ik} \\ C_{i2k2} &= S_{ik}. \end{aligned}$$

Contributed by the Applied Mechanics Division of THE AMERICAN SOCIETY OF MECHANICAL ENGINEERS for publication in the JOURNAL OF APPLIED MECHANICS.

Discussion on this paper should be addressed to the Technical Editor, Leon M. Keer, The Technological Institute, Northwestern University, Evanston, IL 60208, and will be accepted until two months after final publication of the paper itself in the JOURNAL OF APPLIED MECHANICS. Manuscript received by the ASME Applied Mechanics Division, Aug. 28, 1989; final revision, Nov. 20, 1989.

Copyright © 1990 by ASME
Downloaded 03 May 2010 to 171.66.16.244. Redistribution subject to ASME license or copyright; see http://www.asme.org/terms/Terms_Use.cfm

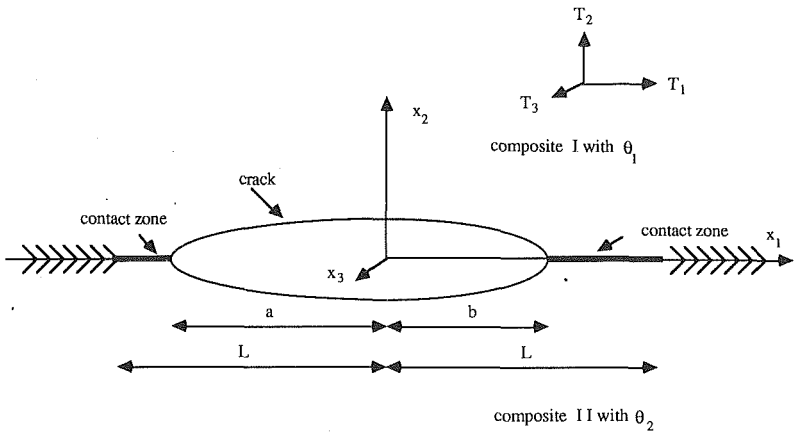


Fig. 1 Partially opened interface crack between dissimilar anisotropic composites

From the symmetry of elasticity constants, $C_{i2k1}=C_{k1i2}=R_{ki}$. Equation (3) can be expressed in the matrix form as

$$[\mathbf{Q}+(\mathbf{R}+\mathbf{R}^T)p+\mathbf{S}p^2]a=0 \tag{4}$$

where $\mathbf{I}$ is the unity matrix. For nontrivial solutions of a_k in equation (4),

$$\det[\mathbf{Q}+(\mathbf{R}+\mathbf{R}^T)p+\mathbf{S}p^2]=0. \tag{5}$$

Equation (5) is a sextic equation of p. It can be shown that if the strain energy is positive definite, the roots of the equations must be complex (Eshelby et al., 1953). Since the coefficients in equation (5) are real, it follows that the roots of p and the corresponding eigenvectors $\mathbf{a}$ must appear as two sets of complex quantities, one set being conjugate to the other. If we denote p_α, $\alpha=1, 2, 3$, as the eigenvalues for which the imaginary parts are positive and define a matrix $\mathbf{A}$ such that the columns of $\mathbf{A}$ are the eigenvectors corresponding to p_α, the complete solutions of the displacements can then be expressed as

$$u_k=2\Re[A_{ka}f_a(z_a)] \tag{6}$$

where $z_\alpha=x_1+p_\alpha x_2$, and $\Re$ denotes the real part.

From the stress-strain relations, the stresses can be expressed as

$$\sigma_{i1}=-2\Re[p_\alpha B_{i\alpha}g_\alpha(z_\alpha)] \tag{7}$$

$$\sigma_{i2}=2\Re[B_{i\alpha}g_\alpha(z_\alpha)] \tag{8}$$

where

$$g_\alpha(z)=\frac{df(z_\alpha)}{dz_\alpha}$$

and

$$B_{i\alpha}=(R_{ki}+p_\alpha S_{ik})A_{k\alpha} \text{ (no sum on } \alpha). \tag{9}$$

Of particular importance in the following discussions is the complex matrix $\mathbf{AB}^{-1}$. It is shown by Ting (1986) that the matrix can be expressed by

$$\mathbf{AB}^{-1}=\mathbf{U}-i\mathbf{L}^{-1} \tag{10}$$

where $\mathbf{L}$ and $\mathbf{U}$ are real matrices. The matrix $\mathbf{L}$ is symmetric and positive definite and the matrix $\mathbf{U}$ is antisymmetric. The materials of interest here are monoclinic materials symmetric with respect to the x_1-x_3 plane. For such materials Ting (1989) shows that

$$U_{13}=L_{12}=L_{23}=0. \tag{11}$$

The fact will be used to derive correspondence relations between the problem of interface cracks in monoclinic composites and that of interface cracks in isotropic composites.

3 Correspondence Relations

Consider an interface crack of length $2L$ shown in Fig. 1. The interface crack is assumed to lie between material I made of a composite with fiber orientation θ_1 measured counterclockwise from the positive x_3-axis in the x_1-x_3 plane and material II with fiber orientation θ_2. The tractions are assumed to be applied to the crack faces. The region where the crack faces are fully opened extends from $-a$ to b along the x_1-axis. A superscript prime is used to indicate quantities associated with material II.

For the anisotropic bimaterial system considered here, an important matrix is given by (Ting, 1986)

$$\mathbf{M}=\mathbf{AB}^{-1}-\overline{\mathbf{A}}'\overline{\mathbf{B}}'^{-1}. \tag{12}$$

From equation (10), the matrix $\mathbf{M}$ can be expressed by

$$\mathbf{M}=-(\mathbf{W}+i\mathbf{D}) \tag{13}$$

where

$$\mathbf{W}=\mathbf{U}'-\mathbf{U} \tag{14}$$

$$\mathbf{D}=\mathbf{L}^{-1}+\mathbf{L}'^{-1}. \tag{15}$$

Since $\mathbf{U}'$, $\mathbf{U}$ are antisymmetric and $\mathbf{L}'$, $\mathbf{L}$ are symmetric, the matrix $\mathbf{W}$ is antisymmetric and the matrix $\mathbf{D}$ is symmetric. The inverse matrix of $\mathbf{M}$ denoted by $\mathbf{N}$ can be expressed as

$$\mathbf{N}=\tilde{\mathbf{W}}+i\tilde{\mathbf{D}} \tag{16}$$

where $\tilde{\mathbf{W}}$ is antisymmetric and $\tilde{\mathbf{D}}$ is symmetric. Due to the property described by equation (11), it can be shown that

$$\tilde{W}_{13}=\tilde{D}_{12}=\tilde{D}_{23}=0. \tag{17}$$

Let the inverse matrix of $\tilde{\mathbf{D}}$ be denoted by $\tilde{\mathbf{E}}$. From equation (17), one has

$$\tilde{E}_{12}=\tilde{E}_{23}=0 \tag{18}$$

$$\tilde{E}_{22}=\frac{1}{\tilde{D}_{22}} \tag{19}$$

$$\tilde{\mathbf{e}}=\tilde{\mathbf{d}}^{-1} \tag{20}$$

where $\tilde{\mathbf{e}}$ and $\tilde{\mathbf{d}}$ are two by two matrices obtained by deleting the second column and row from $\tilde{\mathbf{E}}$ and $\tilde{\mathbf{D}}$, respectively.

As shown by Willis (1971) and Clements (1971), the tractions on the upper crack face, $\mathbf{T}$ can be expressed as

$$\mathbf{N}\mathbf{\Phi}^+-\overline{\mathbf{N}}\mathbf{\Phi}^-=-\mathbf{T}. \tag{21}$$

$\mathbf{\Phi}(z)$ is a sectionally analytic function of $z=x_1+ix_2$ and $\mathbf{\Phi}^+$, $\mathbf{\Phi}^-$ denote the limiting values of $\mathbf{\Phi}(z)$ as $y\to 0^+$ and $y\to 0^-$, respectively. Substitution of equation (16) into equation (21) yields

Downloaded 03 May 2010 to 171.66.16.244. Redistribution subject to ASME license or copyright; see http://www.asme.org/terms/Terms_Use.cfm

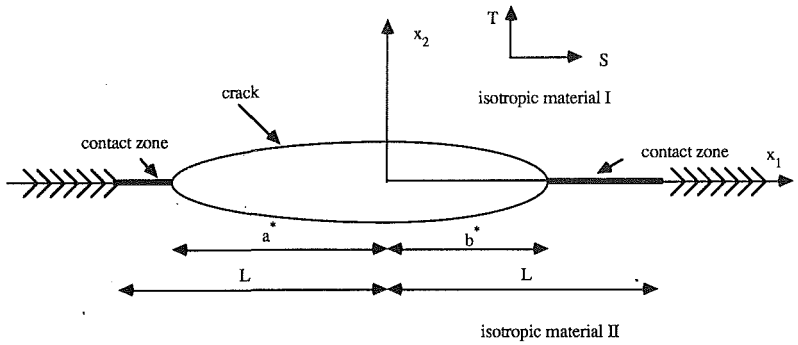


Fig. 2 Partially opened interface crack between dissimilar isotropic materials

$$\tilde{\mathbf{W}}(\boldsymbol{\Phi}^+ - \boldsymbol{\Phi}^-) + i\tilde{\mathbf{D}}(\boldsymbol{\Phi}^+ + \boldsymbol{\Phi}^-) = -\mathbf{T} \tag{22}$$

The dislocation density α defined by

$$\alpha = \frac{\partial}{\partial x_1}(\mathbf{u}' - \mathbf{u}) \tag{23}$$

is related to the analytic function $\boldsymbol{\Phi}$ by (Willis, 1971)

$$\alpha = -(\boldsymbol{\Phi}^+(x_1) - \boldsymbol{\Phi}^-(x_1)). \tag{24}$$

Equation (24) implies that the function $\boldsymbol{\Phi}$ can be represented by the following integral of Cauchy's type:

$$\boldsymbol{\Phi}(z) = -\frac{1}{2\pi i}\int_{-L}^{L}\frac{1}{s-z}\alpha ds. \tag{25}$$

The Plemelj formulae for Cauchy integrals give

$$\boldsymbol{\Phi}^+(x_1) + \boldsymbol{\Phi}^-(x_1) = -\frac{1}{\pi i}\int_{-L}^{L}\frac{1}{s-x_1}\alpha ds \tag{26}$$

Substitution of equations (24) and (26) into equation (22) leads to

$$\tilde{\mathbf{W}}\alpha + \frac{1}{\pi}\tilde{\mathbf{D}}\int_{-L}^{L}\frac{1}{s-x_1}\alpha ds = \mathbf{T}. \tag{27}$$

Equation (27) is a set of integral equations relating the dislocations densities and the tractions on the crack faces. The set of the integral equations is an extension to that given by Comninou (1979) for the isotropic interface crack problem.

Let

$$\hat{\mathbf{w}} = (\tilde{W}_{21},\ \tilde{W}_{23})^T \tag{28}$$

$$\hat{\alpha} = (\alpha_1,\ \alpha_3)^T \tag{29}$$

$$\hat{\mathbf{T}} = (T_1,\ T_3)^T. \tag{30}$$

Equation (27) can be separated into the following two sets of equations:

$$-\hat{\mathbf{w}}\alpha_2 + \frac{1}{\pi}\tilde{\mathbf{d}}\int_{-L}^{L}\frac{1}{s-x_1}\hat{\alpha}ds = \hat{\mathbf{T}} \tag{31}$$

$$\hat{\mathbf{w}}^T\hat{\alpha} + \frac{\tilde{D}_{22}}{\pi}\int_{-a}^{b}\frac{1}{s-x_1}\alpha_2 ds = T_2. \tag{32}$$

If we regard α_2 as a known function in equation (31), then equation (31) can be considered as a set of Cauchy singular integral equations. The solution to the singular equations can be shown to be

$$\hat{\alpha} = -\frac{1}{\pi\sqrt{L^2 - x_1^2}}\tilde{\mathbf{e}}\hat{\mathbf{w}}\int_{-L}^{L}\frac{\sqrt{L^2-s^2}}{s-x_1}\alpha_2 ds - \frac{1}{\pi\sqrt{L^2-x_1^2}}\tilde{\mathbf{e}}\int_{-L}^{L}\frac{\sqrt{L^2-s^2}}{s-x_1}\hat{\mathbf{T}}ds. \tag{33}$$

Substitution of equation (33) into equation (32) yields

$$-\frac{\beta^2\tilde{D}_{22}}{\pi\sqrt{L^2-x_1^2}}\int_{-L}^{L}\frac{\sqrt{L^2-s^2}}{s-x_1}\alpha_2 ds + \frac{\tilde{D}_{22}}{\pi}\int_{-a}^{b}\frac{1}{s-x_1}\alpha_2 ds = T_2 + \frac{1}{\pi\sqrt{L^2-x_1^2}}\int_{-L}^{L}\frac{\sqrt{L^2-s^2}}{s-x_1}\hat{\mathbf{w}}^T\tilde{\mathbf{e}}\hat{\mathbf{T}}ds \tag{34}$$

where

$$\beta^2 = \frac{1}{\tilde{D}_{22}}\hat{\mathbf{w}}^T\tilde{\mathbf{e}}\hat{\mathbf{w}}. \tag{35}$$

It can be shown (Wu, 1989) that for isotropic bimaterials,

$$\tilde{W}_{23} = \tilde{E}_{13} = 0 \tag{36}$$

$$\tilde{D}_{22} = \tilde{D}_{11} = C. \tag{37}$$

Thus, for interface cracks in isotropic bimaterials under plane-strain loading $T_1 = S$ and $T_2 = T$ as shown in Fig. 2, equation (34) becomes

$$-\frac{\beta^2 C}{\pi\sqrt{L^2-x_1^2}}\int_{-L}^{L}\frac{\sqrt{L^2-s^2}}{s-x_1}\alpha_2^* ds + \frac{C}{\pi}\int_{-a^*}^{b^*}\frac{1}{s-x_1}\alpha_2^* ds = T + \frac{\beta}{\pi\sqrt{L^2-x_1^2}}\int_{-L}^{L}\frac{\sqrt{L^2-s^2}}{s-x_1}Sds \tag{38}$$

where the relation

$$\beta = \frac{\tilde{W}_{21}}{\tilde{D}_{22}} \tag{39}$$

for isotropic bimaterials has been used. In equation (38), a superscript * is used to denote the solutions for the isotropic interface crack. Equation (38) is the same as that given by Comninou (1979). Comparison between equation (34) and equation (38) reveals that equation (34) can be transformed into equation (38) by the following replacements:

$$\tilde{D}_{22} \to C \tag{40}$$

$$T_2 \to T \tag{41}$$

$$\frac{1}{\beta}\hat{\mathbf{w}}^T\tilde{\mathbf{e}}\hat{\mathbf{T}} \to S. \tag{42}$$

Thus, the solutions of a, b, and α_2 to equation (34) can be obtained from the solutions for isotropic interface cracks through the transformations given by equations (40)–(42). The solutions of a, b, and α_2 can then be expressed as

$$a = a^*(T, S, \beta) \tag{43}$$

$$b = b^*(T, S, \beta) \tag{44}$$

$$\alpha_2 = \alpha_2^*(T, S, \beta). \tag{45}$$

Equation (41) also implies that contact stresses σ_{22} is the same as that for the corresponding isotropic problem. In fact, the

Downloaded 03 May 2010 to 171.66.16.244. Redistribution subject to ASME license or copyright; see http://www.asme.org/terms/Terms_Use.cfm

stress σ_{22} outside the crack along the interface is also the same since

$$\begin{aligned}\sigma_{22} &= -\frac{\tilde{D}_{22}}{\pi}\int_{-a}^{b}\frac{\alpha_2}{s-x}ds \\ &= -\frac{C}{\pi}\int_{-a^*}^{b^*}\frac{\alpha_2^*}{s-x}ds \\ &= \sigma_{22}^*. \end{aligned} \tag{46}$$

We next turn our attention to the stress intensity factors for the right crack tip. The crack opening displacements, $\Delta\mathbf{u}$, as the right tip is approached are given by Wu (1989) as

$$\Delta\mathbf{u} = \sqrt{\frac{2(L-x_1)}{\pi}}\tilde{\mathbf{E}}\mathbf{K}. \tag{47}$$

In equation (47),

$$\mathbf{K} = (K_{II}, K_I, K_{III})^T \tag{48}$$

are the stress intensity factors. It is shown by Wu (1989) that the stress intensity factor K_I is related to K_{II} and K_{III} by the following equation:

$$K_I = -\frac{1}{\tilde{E}_{22}}(\tilde{E}_{21}K_{II} + \tilde{E}_{23}K_{III}). \tag{49}$$

As shown in equation (17), $\tilde{E}_{21} = \tilde{E}_{23} = 0$, it follows that K_I is identically zero. With $K_I = 0$ and $\tilde{E}_{21} = \tilde{E}_{23} = 0$, equation (47) is simplified into

$$\Delta\hat{\mathbf{u}} = \sqrt{\frac{2(L-x_1)}{\pi}}\tilde{\mathbf{e}}\hat{\mathbf{K}} \tag{50}$$

where

$$\Delta\hat{\mathbf{u}} = (u_1, u_3)^T \tag{51}$$

$$\hat{\mathbf{K}} = (K_{II}, K_{III})^T. \tag{52}$$

The dislocation density $\hat{\alpha}$ corresponding to equation (50) is

$$\hat{\alpha} = \frac{1}{\sqrt{2\pi(L-x_1)}}\tilde{\mathbf{e}}\hat{\mathbf{K}}. \tag{53}$$

The stress intensity factors K_{II} and K_{III} can therefore be determined by

$$\hat{\mathbf{K}} = \lim_{x_1 \to L}\sqrt{2\pi(L-x_1)}\tilde{\mathbf{d}}\hat{\alpha}. \tag{54}$$

Substitution of equation (33) into equation (54) leads to

$$\hat{\mathbf{K}} = \frac{1}{\sqrt{\pi L}}\hat{\mathbf{w}}\int_{-L}^{L}\sqrt{\frac{L+s}{L-s}}\alpha_2 ds + \frac{1}{\sqrt{\pi L}}\int_{-L}^{L}\sqrt{\frac{L+s}{L-s}}\hat{\mathbf{T}}ds. \tag{55}$$

For isotropic interface cracks, equation (55) becomes

$$K_{II}^* = \frac{\beta C}{\sqrt{\pi L}}\int_{-L}^{L}\sqrt{\frac{L+s}{L-s}}\alpha_2^* ds + \frac{1}{\sqrt{\pi L}}\int_{-L}^{L}\sqrt{\frac{L+s}{L-s}}Sds. \tag{56}$$

Invoking the transformations of equation (40) and equation (42), equation (56) yields

$$\frac{\tilde{E}_{22}}{\beta}(K_{II}^* - K_{II}^{(h)}) = \frac{1}{\sqrt{\pi L}}\int_{-L}^{L}\sqrt{\frac{L+s}{L-s}}\alpha_2 ds \tag{57}$$

where

$$K_{II}^{(h)} = \frac{1}{\sqrt{\pi L}}\int_{-L}^{L}\sqrt{\frac{L+s}{L-s}}Sds \tag{58}$$

is the stress intensity factor for a crack in a homogeneous medium under in-plane shear S. Substituting equation (57) in to equation (55), one has

$$\hat{\mathbf{K}} = \frac{\tilde{E}_{22}}{\beta}\hat{\mathbf{w}}(K_{II}^* - K_{II}^{(h)}) + \hat{\mathbf{K}}^{(h)} \tag{59}$$

where

$$\hat{\mathbf{K}}^{(h)} = \frac{1}{\sqrt{\pi L}}\int_{-L}^{L}\sqrt{\frac{L+s}{L-s}}\hat{\mathbf{T}}ds \tag{60}$$

are the mode II and III stress intensity factors for a crack in a homogeneous medium under in-plane shear T_1 and antiplane shear T_3, respectively.

The energy release rate for the interface crack is given by (Wu, 1989)

$$G = \frac{1}{4}\hat{\mathbf{K}}^T\tilde{\mathbf{e}}\hat{\mathbf{K}}. \tag{61}$$

With equation (59) substituted into equation (61) and the relation

$$K_{II}^{(h)} = \frac{1}{\beta}\hat{\mathbf{w}}^T\tilde{\mathbf{e}}\hat{\mathbf{K}}^{(h)}, \tag{62}$$

it can be shown that

$$G = \frac{\tilde{E}_{22}}{4}[(K_{II}^*)^2 - (K_{II}^{(h)})^2] + G^{(h)} \tag{63}$$

where

$$G^{(h)} = \frac{1}{4}(\hat{\mathbf{K}}^{(h)})^T\tilde{\mathbf{e}}\hat{\mathbf{K}}^{(h)}. \tag{64}$$

Equation (59) and equation (63) are for the right tip. It can be shown that these equations are also valid for the left tip provided that all quantities in those equations be referred to the left tip.

4 Uniform Loading

As mentioned previously, the exact solution for the isotropic interface crack under uniform mixed loading has been found by Gautesan and Dundurs (1988). The corresponding exact solution for the anisotropic interface crack can be obtained by using the relations equations (40)–(42). The form of the solution of the mode II stress intensity factor provided by Gautesan and Dundurs appears, however, somewhat complicated. A simple and yet accurate approximation for the mode II stress intensity factor at the right tip is proposed by Wu (1989b) as

$$K_{II}^* = \sqrt{(1+4\gamma^2)(T^2+S^2)\pi L} \tag{65}$$

where

$$\gamma = \frac{1}{2\pi}\log\left(\frac{1+\beta}{1-\beta}\right) \tag{66}$$

for loading with $T > 0$. The approximation is exact for pure tension (Comninou, 1977). The maximum deviation of the approximation from the exact solution occurs when the loading is of pure shear and the bimaterial constant $\beta = 0.5$. In that case the relative error is about 3 percent. For loading with $T < 0$, the results of Gautesan and Dundurs show that

$$K_{II}^* = S\sqrt{\pi L} \tag{67}$$

Downloaded 03 May 2010 to 171.66.16.244. Redistribution subject to ASME license or copyright; see http://www.asme.org/terms/Terms_Use.cfm

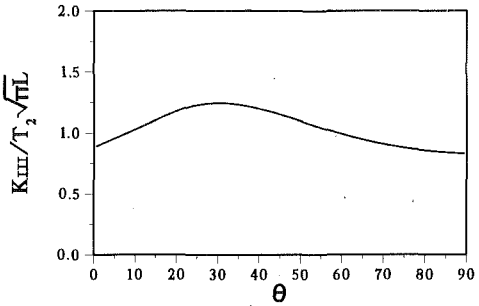


Fig. 3 Stress intensity factor $K_{III}(L)$ for $[\pm\theta]$ composite system under pure tension

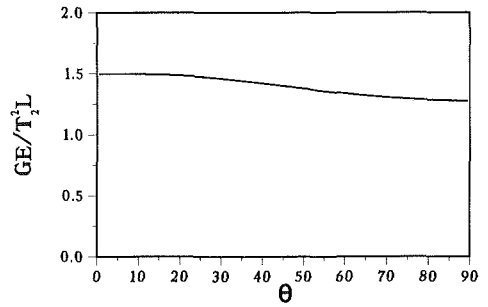


Fig. 4 Energy release rate for $[\pm\theta]$ composite system under pure tension

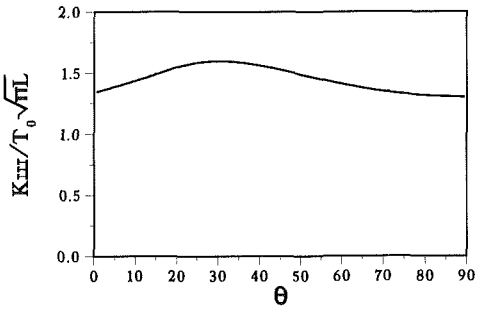


Fig. 5 Stress intensity factor $K_{III}(L)$ for $[\pm\theta]$ composite system under $T_2 = T_3 = T_0$

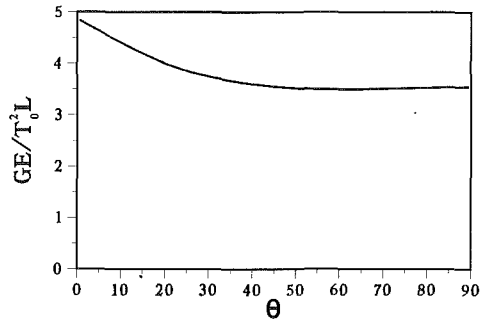


Fig. 6 Energy release rate for $[\pm\theta]$ composite system under $T_2 = T_3 = T_0$

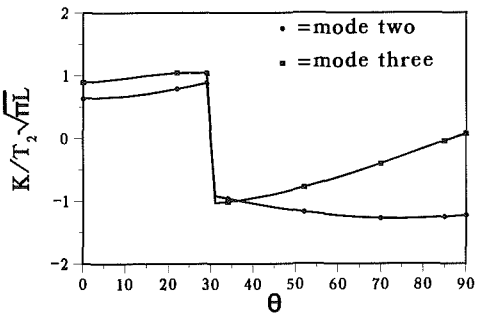


Fig. 7 Stress intensity factors $K_{II}(L)$ and $K_{III}(L)$ for [30 deg/θ] composite system under pure tension

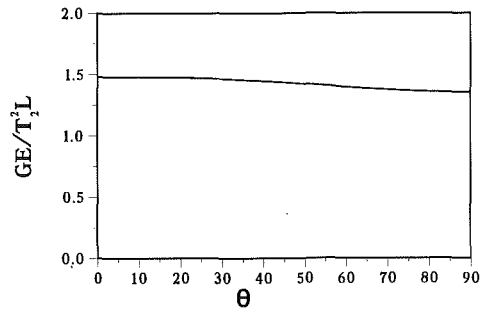


Fig. 8 Energy release rate for [30 deg/θ] composite system under pure tension

to a very good approximation. Substitution of equations (65) and (67) into equation (59) yields

$$\frac{1}{\sqrt{\pi L}}\hat{\mathbf{K}}(L)=\frac{\tilde{E}_{22}}{\beta}\hat{\mathbf{w}}\left(\sqrt{(1+4\gamma^2)(T^2+S^2)}-S\right)+\hat{\mathbf{T}} \tag{68}$$

for $T_2 > 0$ and

$$\frac{1}{\sqrt{\pi L}}\hat{\mathbf{K}}(L)=\hat{\mathbf{T}} \tag{69}$$

for $T_2 < 0$.

The corresponding energy release rate for $T_2 > 0$ is given by

$$\frac{G(L)}{\pi L}=\frac{\tilde{E}_{22}}{4}[(1+4\gamma^2)T^2+4\gamma^2S^2]+\frac{1}{4}\hat{\mathbf{T}}^T\tilde{\mathbf{e}}\hat{\mathbf{T}}. \tag{70}$$

Since $\gamma < 0.175$ ($\beta < 0.5$), equation (70) is well approximated by

$$\frac{G(L)}{\pi L}=\frac{1}{4}\mathbf{T}^T\tilde{\mathbf{E}}\mathbf{T}. \tag{71}$$

The above expression is nearly the same as that for the "fully opened" interface crack given by Wu (1990). This is a somewhat surprising result since the size of the contact zones can be comparable to the crack length and the nature of the solutions can be quite different for the two cases. For $T_2 < 0$, the energy release rate can be approximated by

$$G(L)=G^{(h)}. \tag{72}$$

For the left tip, Wu (1989) shows that the K_{II}^* is the negative of that for the right tip. Thus, for the left tip,

$$\frac{1}{\sqrt{\pi L}}\hat{\mathbf{K}}(-L)=-\frac{\tilde{E}_{22}}{\beta}\hat{\mathbf{w}}\left(\sqrt{(1+4\gamma^2)(T^2+S^2)}+S\right)+\hat{\mathbf{T}} \tag{73}$$

for $T_2 > 0$ and

$$\frac{1}{\sqrt{\pi L}}\hat{\mathbf{K}}(-L)=-\frac{2\tilde{E}_{22}}{\beta}\hat{\mathbf{w}}S+\hat{\mathbf{T}} \tag{74}$$

for $T_2 < 0$. Note that although the stress intensity factors are different in general for the right and the left tips, the energy release rate for the two tips are the same. The conclusion has been reached by Wu (1989).

Simplifications of equation (68) and equation (73) can be made if either $\tilde{W}_{23}$ or $\tilde{W}_{23}$ vanishes. For example, if $\tilde{W}_{21} = 0$, equation (35) gives

$$\beta^2=\tilde{E}_{22}\tilde{E}_{33}\tilde{W}_{23}^2. \tag{75}$$

From equation (42),

$$S=\frac{\tilde{W}_{23}\tilde{E}_{33}T_3}{\beta}=\sqrt{\frac{\tilde{E}_{33}}{\tilde{E}_{22}}}T_3. \tag{76}$$

Downloaded 03 May 2010 to 171.66.16.244. Redistribution subject to ASME license or copyright; see http://www.asme.org/terms/Terms_Use.cfm

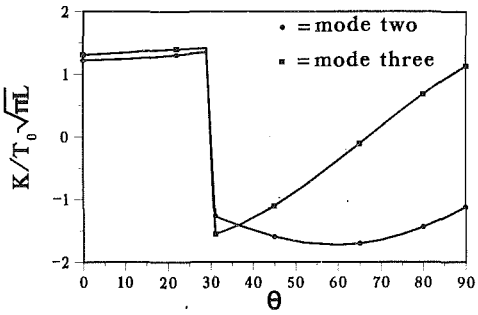


Fig. 9 Stress intensity factors $K_{II}(L)$ and $K_{III}(L)$ for [30 deg/θ] composite system under $T_1 = T_2 = T_3 = T_0$

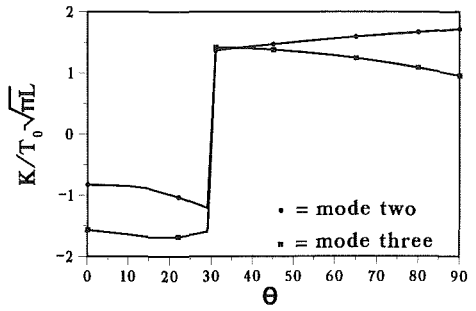


Fig. 10 Stress intensity factors $K_{II}(-L)$ and $K_{III}(-L)$ for [30 deg/θ] composite system under $T_1 = T_2 = T_3 = T_0$

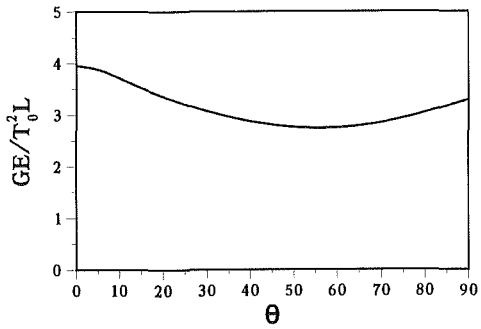


Fig. 11 Energy release rate for [30 deg/θ] composite system under $T_1 = T_2 = T_3 = T_0$

From equation (68), the stress intensity factors for the right tip become

$$K_{II}(L) = T_1\sqrt{\pi L} \tag{77}$$

$$\frac{K_{III}(L)}{\sqrt{\pi L}} = \sqrt{\frac{\tilde{E}_{22}}{\tilde{E}_{33}}}\sqrt{(1+4\gamma^2)(T^2+S^2)}. \tag{78}$$

From equation (73) the stress intensity factors for the left tip are

$$K_{II}(-L) = K_{II}(L) \tag{79}$$

$$K_{III}(-L) = -K_{III}(L). \tag{80}$$

If $T=0$, equation (78) can be further simplified as

$$K_{III}(L) = \sqrt{1+4\gamma^2}\,T_3\sqrt{\pi L}. \tag{81}$$

Note that the stress intensity factor equation (81) depends only on the bimaterial constant γ. The stress intensity factors for the left tip are simply the negative of those for the right tip.

5 Numerical Results

In this section, the numerical results of the stress intensity factors and the energy release rates are given for two composite systems: [$\pm\theta$] and [30 deg/θ] under uniform loading. The elastic constants used for the anisotropic composites are:

$$E_L = 20E,\ E_T = E_z = 2.1E$$

$$G_{LT} = G_{Lz} G_{Tz} = 0.85E$$

$$\nu_{LT} = \nu_{Lz} = \nu_{Tz} = 0.21$$

where the subscripts L, T, and z refer to longitudinal, transverse, and through-thickness directions, respectively, and $E = 6895$ Mpa.

We first consider [$\pm\theta$] composite system. Due to symmetry properties of the system, it can be shown that $\tilde{W}_{12} = \tilde{E}_{13} = 0$. From previous discussion, we need only to consider $K_{III}(L)$. The values of $K_{III}(L)$ for pure tensile loading are shown in Fig. 3. It should be noted that for pure tensile loading, equation (68) is exact. The curve of $K_{III}(L)$ is discontinuous at $\theta = 0$ deg or $\theta = 90$ deg, which corresponds to a homogeneous material, and attains a maximum at $\theta = 30$ deg. The energy release rate as displayed in Fig. 4, however, is continuous at $\theta = 0$ deg or $\theta = 90$ deg and is a decreasing function of θ. This case has also been treated by Wang and Choi (1983a). In their treatment, the cracks faces are assumed to be fully opened and the stress field near the crack tips is approximated by the square root singularity. Since the characteristics of the contact zone model local to the crack tips are altered in their approximation, the stress intensity factors given by Wang and Choi are different from the exact values shown here. But the total energy release rates computed from the approximate model of Wang and Choi are in reasonable agreement with the exact values. Numerical calculations were also performed for the system under a combined tensile and antiplane shear loading. The results are shown in Fig. 5 for K_{III} and in Fig. 6 for the energy release rate.

We next consider [30 deg/θ] composite system. The stress intensity factors for the system under pure tension are shown in Fig. 7 for the right tip and the corresponding energy release rates are shown in Fig. 8. the stress intensity factors for the left tip are the negative of those for the right tip. For reason stated previously, the curves of the stress intensity factors are discontinuous as $\theta = 30$ deg. The sign of the stress intensity factors changes from positive to negative, indicating a change in the shear directions near the crack tips, across $\theta = 30$ deg. The numerical results for the loading case $T_1 = T_2 = T_3 = T_0$ are shown in Fig. 9 for the stress intensity factors for the right tip and in Fig. 10 for the left tip. The corresponding energy release rates are shown in Fig. 11. it should be noted that although the stress intensity factors for the two tips are different, the energy release rates are the same for the two tips.

6 Acknowledgment

The authors wish to thank an anonymous reviewer for suggesting the current title and for bringing to their attention that equation (11) has been shown rigorously by Ting (1989).

References

Clements, D. L., 1971, "A Crack between Dissimilar Anisotropic Media," *Int. J. Eng. Sci.*, Vol. 9, pp. 257–265.

Comninou, M., 1977, "The Interface Crack," ASME JOURNAL OF APPLIED MECHANICS, Vol. 44, pp. 631–636.

Comninou, M., 1978, "The Interface Crack in a Shear Field," ASME JOURNAL OF APPLIED MECHANICS, Vol. 45, pp. 287–290.

Comninou, M., and Schmueser, D., 1979, "The Interface Crack in a Combined Tension-compression and Shear Field," ASME JOURNAL OF APPLIED MECHANICS, Vol. 46, pp. 345–358.

Gautesen, A. K., and Dundurs, J., 1988, "The Interface Crack under Combined Loading," ASME JOURNAL OF APPLIED MECHANICS, Vol. 55, pp. 580–586.

Stroh, A. N., 1958, "Dislocations and Cracks in Anisotropic Elasticity," *Philos. Mag.*, Vol. 7, pp. 625–646.

Downloaded 03 May 2010 to 171.66.16.244. Redistribution subject to ASME license or copyright; see http://www.asme.org/terms/Terms_Use.cfm

Ting, T. C. T., 1986, "Explicit Solution and Invariance of the Singularities at an Interface Crack in Anisotropic Composite," *Int. J. Solids Structures*, Vol. 22, No. 9, pp. 965–983.

Ting, T. C. T., 1989, "The Eigenvectors of the S matrix and Their Relations with Line Dislocations and Forces in Anisotropic Elastic Solids," *Micromechanics and Inhomogeneities*, The Toshio Mura Anniversary Volume, G. J. Weng, M. Taya, and H. Abe, eds., Springer-Verlag, New York, pp. 449–467.

Wang, S. S., and Choi, I., 1983, "The Interface Crack Between Dissimilar Anisotropic Materials," ASME JOURNAL OF APPLIED MECHANICS, Vol. 50, pp. 169–178.

Wang, S. S., and Choi, I., 1983, "The Interface Crack Behavior in Dissimilar Anisotropic Composites Under Mixed Loading," ASME JOURNAL OF APPLIED MECHANICS, Vol. 50, pp. 179–183.

Willis, J. R., 1971, "Fracture Mechanics of Interfacial Cracks," *J. Mech. Phys. Solids*, Vol. 19, pp. 353–368.

Wu, K. C., 1990, "Stress Intensity Factor and Energy Release Rate for Interfacial Cracks Between Dissimilar Anisotropic Materials," ASME JOURNAL OF APPLIED MECHANICS, Vol. 57, pp. 882–886.

Wu, K. C., 1989, "The Contact Zone Model for Interface Cracks," submitted to ASME JOURNAL OF APPLIED MECHANICS.

Downloaded 03 May 2010 to 171.66.16.244. Redistribution subject to ASME license or copyright; see http://www.asme.org/terms/Terms_Use.cfm

On Measuring the Near-Tip Plastic Strain Singularity

Sundar M. Kamath
I.B.M. General Technology Division,
East Fishkill, NY 12533

Kyung S. Kim
Professor,
Division of Engineering,
Brown University,
Providence, RI 02912
Mem. ASME

A recently developed experimental method, stress intensity factor tracer, is extended to measure the strength, J, of the HRR singularity for near-tip plastic deformation. Focal-plane mapping of the HRR field shows that the light intensity, I, collected on a finite area of the focal plane has a simple relationship with J as $I = \beta J^{2n/(2n+1)}$. *The constant, β, is a product of several experimental parameters and "n" is the hardening parameter of a power-law hardening material. The focal-plane mapping technique is also capable of estimating the shape and size of the HRR-field dominant region for a relatively thin (< 10 mm) metallic specimen. In addition, a continuous trace of the J variation can be monitored using a single, stationary photodetector. Because the measurement value of this method is independent of crack-tip motion, the transition of HRR singularity from stationary to moving can also be studied. In this paper, the theoretical analysis of the method is presented.*

Introduction

Nonlinear deformation around the crack tip for stationary and propagating cracks has been of great interest. In particular, elastic-plastic deformations that lead to subsequent unstable crack growth have been an important subject to be investigated. Such a deformation analysis would provide the understanding of fracture processes in many classes of structural materials for engineering importance.

Among the near-tip nonlinear deformation patterns, a diffuse-type plastic zone of a stationary crack has been approximately, but with fairly good accuracy, characterized by Hutchinson (1968) and Rice and Rosengren (1968), (HRR) singular field. This type of characterization is quite applicable to a broad class of elastic-plastic materials for which the Ramberg-Osgood (1943) type power-law hardening stress-strain relation gives an accurate description of their mechanical responses. Such a material class includes various alloys of structural metals—steel (excluding mild steel), aluminum, copper, etc. A similar analysis for growing cracks has been made by, for example, Rice (1982).

In this paper, we extended the applicability of an optical method, stress intensity factor tracer (SIFT), to such a nonlinear near crack-tip deformation field. Theoretical analysis of focal plane mapping of the nonlinear field reveals that the optical intensity of light in SIFT measures the nonlinear strain singularity strength "J". The relationship turns out to be $I = \beta J^{2n/(2n+1)}$, where I is the light intensity of the SIFT system, β is a constant, and n is the hardening parameter. In addition to these conclusive results, details for the optical mapping of the HRR field have been analyzed. Therefore, this technique can be used to study the nature of the HRR field, i.e., its radial and angular dependence, as well as transition in the singularity, as a function of material yield and hardening behavior and slow crack growth for plane stress prevailing fracture experiments. Furthermore, this analysis shows that SIFT has a potential to measure the transition of crack growth from stationary to growing states for ductile fracture experiments. Previously, the time of such a transition could not be sharply detected for ductile crack growth initiation. Such a sharp detection of crack growth initiation is very important in studying initiation toughness of materials under dynamic loading.

Analysis

Discussion of the SIFT method by Kim (1985) was restricted to linear elastic deformation response under plane-stress conditions. We now consider an extension of the same theory to elastic-plastic constitutive behavior. The class of elastic-plastic deformation that is of interest here is mainly power-law strain hardening (Ramberg-Osgood model) plasticity for which asymptotic crack-tip solutions, commonly known as the HRR (Hutchinson-Rice-Rosengren) singularity field exist. The in-plane HRR strain field, $\epsilon_{ij}(r, \theta)$, is given by

$$\epsilon_{ij} \cong \alpha \frac{\sigma_0}{E} \left[\frac{JE}{\alpha \sigma_0^2 I_n r} \right]^{\frac{n}{n+1}} E_{ij}(n,\theta) \qquad (1)$$

where (r, θ) indicates polar coordinate of a near tip position, α is an empirical constant (typically 0.02), n is an inverse measure of strain hardening, and E, σ_0 represents Young's modulus and yield stress, respectively. J is the strain singularity factor represented by the J-integral around the crack tip, while I_n is a nondimensionalized constant (Hutchinson, 1968) and

Contributed by the Applied Mechanics Division of THE AMERICAN SOCIETY OF MECHANICAL ENGINEERS for presentation at the Winter Annual Meeting, Dallas, Texas, Nov. 25–30, 1990.

Discussion on this paper should be addressed to the Technical Editor, Leon M. Keer, The Technological Institute, Northwestern University, Evanston, IL 60208, and will be accepted until two months after final publication of the paper itself in the JOURNAL OF APPLIED MECHANICS. Manuscript received by the ASME Applied Mechanics Division, Mar. 18, 1988; final revision, July 27, 1989.

Paper No. 90-WA/APM-46.

Copyright © 1990 by ASME
Downloaded 03 May 2010 to 171.66.16.244. Redistribution subject to ASME license or copyright; see http://www.asme.org/terms/Terms_Use.cfm

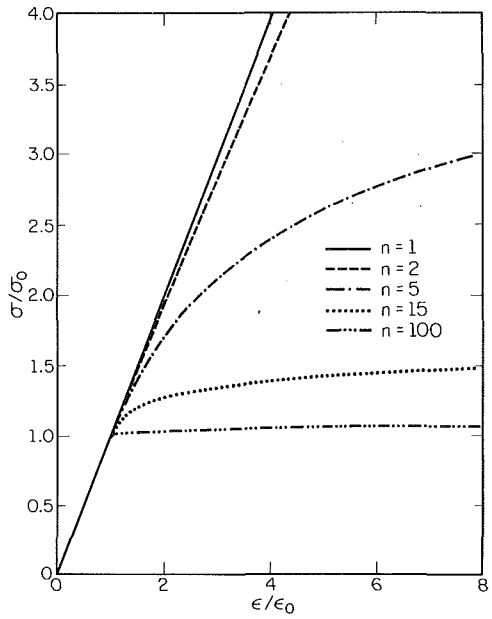


Fig. 1 Normalized stress-strain curves for various n (strain hardening exponent) values

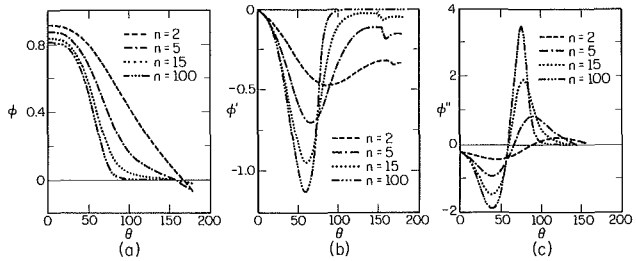


Fig. 2 (a) Angular variation of ϕ ($= E_{rr} + E_{\theta\theta}$) ($b$) first derivative ϕ', and (c) second derivative ϕ''

$E_{ij}(n, \theta)$ is a nondimensionalized function. Numerical values of I_n and E_{ij} have been tabulated by Shih (1963) for various n and θ in plane-strain and plane-stress conditions. Stress-strain curves of typical n's employed in numerical calculation are shown in Fig. 1. Because of plastic incompressibility, in plane stress deformation, the u_3 or out-of-plane component of displacement at one free surface was approximately given by

$$u_3(\underline{x}) = \epsilon_{33} d/2 \approx -(\epsilon_{rr} + \epsilon_{\theta\theta}) d/2 \tag{2}$$

where d is thickness. In terms of the HRR field quantities, this expression becomes

$$u_3(\underline{x}) = \frac{\alpha\sigma_0 d}{2E}\left[\frac{JE}{\alpha\sigma_0^2 I_n r}\right]^{\frac{n}{n+1}} \phi(n,\theta) \tag{3}$$

where

$$\phi(n,\theta) = E_{rr}(n,\theta) + E_{\theta\theta}(n,\theta). \tag{4}$$

The function ϕ and its derivatives ϕ', ϕ'', necessary for further theoretical development of optical mapping are shown in Fig. 2 for various n values. ϕ' and ϕ'' are obtained by numerical differentiation and smoothing of ϕ which is given by Shih (1983).

Now consider a focal plane mapping of such a deformation field. A schematic of the focal plane mapping of the reflecting surface of an elastic-plastic fracture specimen is shown in Fig. 3. As shown in the figure, a light ray of collimated incident beam, reflected from the generic point $\underline{x}$, will pass the mapping $\underline{x}^*$ on the focal plane because of the deflection caused by out-of-plane displacement, $u_3(\underline{x})$, of the specimen side surface.

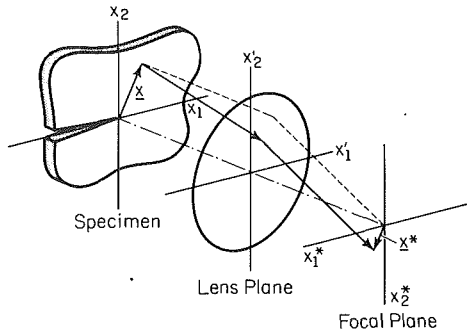


Fig. 3 Schematic of the focal plane mapping

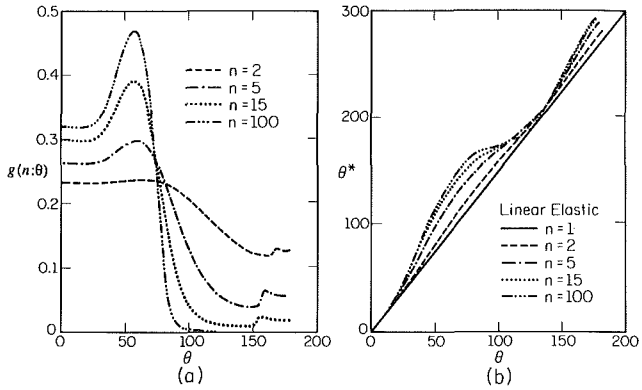


Fig. 4 (a) Angular dependence of focal plane radial mapping for HRR field ($\hat{r}^* = Ag(\theta)\hat{r}^{-2n+1/n+1}$) and ($b$) focal plane angular mapping for HRR field

From the theory of focal plane mapping (Kim, 1985), the mapping is expressed by

$$\underline{x}^* = -2f \text{grad}\, u_3(\underline{x}) \tag{5}$$

where f is the focal length of the converging lens. Then, from equations (3), (4), and (5) we can get the expression

$$\hat{x}_i^* = A \frac{\partial}{\partial \hat{x}_i}\left[\frac{\phi(n,\theta)}{\hat{r}^{n/n+1}}\right] \tag{6}$$

where $\hat{}$ denotes normalization with respect to thickness d and

$$A = \frac{\alpha\sigma_0 f}{Ed}\left[\frac{JE}{\alpha\sigma_0^2 I_n d}\right]^{\frac{n}{n+1}}. \tag{7}$$

Or the mapping can also be expressed in polar coordinates as

$$\hat{r}^* = Ag(n,\theta)(\hat{r})^{-\frac{2n+1}{n+1}} \tag{8}$$

$$\theta^* = \theta - \tan^{-1}\left(\frac{n+1}{n} \cdot \frac{\phi'}{\phi}\right) \tag{9}$$

$$g(n,\theta) = \left[\left(\frac{n}{n+1}\phi\right)^2 + \phi'^2\right]^{1/2} \tag{10}$$

The mapping functions, $g(n, \theta)$ and $\theta^*(n, \theta)$, are shown in Fig. 4.

Once the mapping function is established, the relationship between light intensities (per unit area), Ω and Ω^*, on the two planes is given by Kim (1985)

$$\Omega^* = \Omega \frac{r}{r^*} \cdot \frac{\partial(r,\theta)}{\partial(r^*,\theta^*)}. \tag{11}$$

From equations (8) and (9), and assuming uniform incident intensity Ω_0, equation (11) becomes for single branch of one-to-one mapping,

Downloaded 03 May 2010 to 171.66.16.244. Redistribution subject to ASME license or copyright; see http://www.asme.org/terms/Terms_Use.cfm

$$\frac{\Omega^*}{\Omega_0} = A^{\frac{2n+2}{2n+1}} k(\theta^*, n) \hat{r}^{*\,-\frac{6n+4}{2n+1}} \tag{12}$$

where $k(\theta^*, n)$ is a nondimensionalized function given by

$$k(\theta^*, n) = \frac{n+1}{2n+1} \cdot g^{\frac{6n+4}{2n+1}} \Big/ \left\{ g - \frac{n}{n+1} (\phi\phi'' - \phi'^2) \right\}. \tag{13}$$

A similar intensity ratio in the case of the K_I-field can be defined using the results from Kim (1985), which is

$$\frac{\Omega_K^*}{\Omega_0} = \frac{4}{9} \frac{1}{d^2} \left(\frac{K_I \nu f}{\sqrt{2\pi E}} \right)^{4/3} \cdot (\hat{r}^*)^{-10/3} \tag{14}$$

where ν is Poisson's ratio. This enters because in reflection, the shadow-optic coefficient c is simply ν/E.

The final result that is of interest is the relation between total light intensity for an aperture on the focal plane and the strength of the HRR singularity in the specimen or object plane. Total intensity is simply given by an area integral,

$$I = \int_{\Gamma^*} \Omega^* ds^* \tag{15}$$

where Γ^* is the light collecting area on the focal plane. Using equation (12) we have

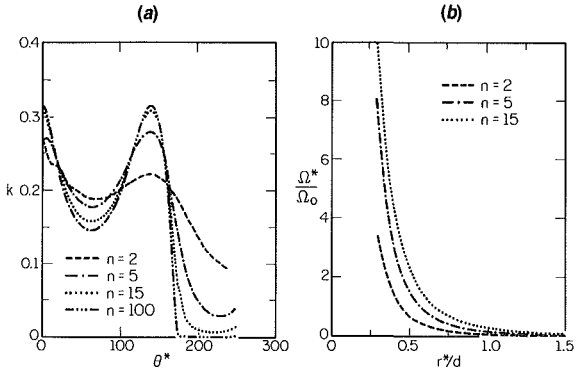


Fig. 5 (*a*) Angular variation of light intensity on the focal plane for HRR field (see equation (12)) and (*b*) radial variation of light intensity on the focal plane for HRR field

$$I = \beta J^{\frac{2n}{2n+1}}. \tag{16}$$

Here, β is a product of various experimental parameters, and is defined by

$$\beta = \Omega_0 \left(\frac{\alpha\sigma_0}{E} \right)^{\frac{2}{2n+1}} (fd)^{\frac{2n+2}{2n+1}} \left(\frac{1}{\sigma_0} \right)^{\frac{2n}{2n+1}} H \tag{17}$$

$$H = \int_{\Gamma^*} k(\theta^*, n) (r^*)^{-\frac{4n+3}{2n+1}} dr^* d\theta^*. \tag{18}$$

Discussion

In time-dependent fracture studies, the near-tip nonlinear deformation associated with the transition from a stationary to a growing crack is of great interest. Unlike a brittle initiation of crack growth, even detection of the time of such a transition event with submicrosecond accuracy is generally difficult, because the fracture process zone is imbedded in the plastic deformation field. Only an observation very close to the fracture process zone can provide such accurate information. This kind of observation is possible with the focal plane mapping (or SIFT) methods as applied to brittle fracture studies (Kamath, 1987). In order to extend the method to nonlinear fracture, we have to understand the focal plane mapping of near-tip plastic deformation. The theoretical basis of the experimental technique for the HRR mapping was derived in the previous section. The detailed behavior of the HRR focal plane mapping depends on various material parameters as will be discussed.

Figure 4(*a*) gives an idea of the radial mapping on the focal plane. It is seen that radial distances ($\propto g(n, \theta)$) in equation (8) are also mapped in a nonuniform manner depending upon angular location, as a consequence of plasticity development near the crack tip. Such a mapping leads to highly nonuniform variation of focal plane intensity. The influence of strain hardening on the angular mapping is quite nonlinear, as shown in Fig. 4(*b*), whereas a constant magnification ($\theta^* = 1.5\theta$) is applied in the linear elastic case (Kim, 1985). The nonlinear mapping is especially evident around $\theta \cong 70$ deg which is also where the plane-stress plastic-zone radius reaches a maximum. The angular dependence of focal plane intensity (actually the factor $k(\theta^*, n)$ in equation (12) is displayed in Fig. 5(*a*), and

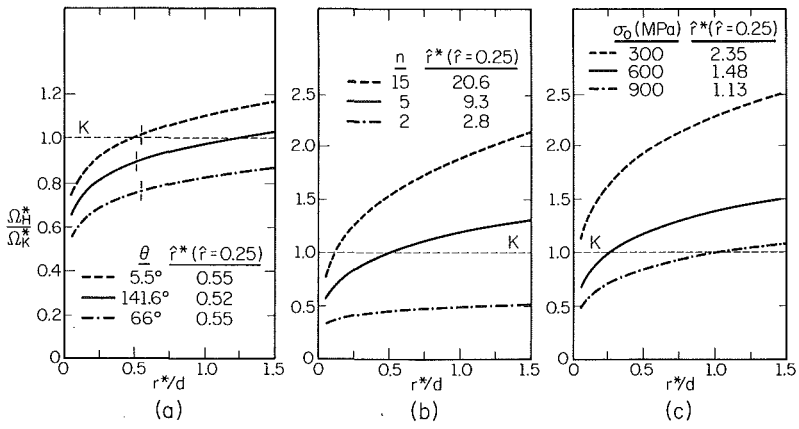


Fig. 6 (*a*) Focal plane light intensity of HRR field normalized by *K* field intensity at three extreme angles (ν = 0.3, α = 0.02, E = 210 GPa, σ_0 = 300 MPa, d = 10 mm, f = 1.2 m, K_I = 100 MPa $\sqrt{\text{m}}$); (*b*) the normalized intensity at minimum θ^* (~65) for different strain hardening (ν = 0.3, α = 0.02, E = 210 GPa, σ_0 = 550 MPa, d = 6.25 mm, f = 5 m, K_I = 75 MPa $\sqrt{\text{m}}$); (*c*) the normalized intensity at minimum θ^* (= 64.3 deg) for different yield strengths (ν = 0.3, α = 0.02, E = 210 GPa, n = 5, d = 10 mm, f = 2 m, K_I = 75 MPa $\sqrt{\text{m}}$)

Downloaded 03 May 2010 to 171.66.16.244. Redistribution subject to ASME license or copyright; see http://www.asme.org/terms/Terms_Use.cfm

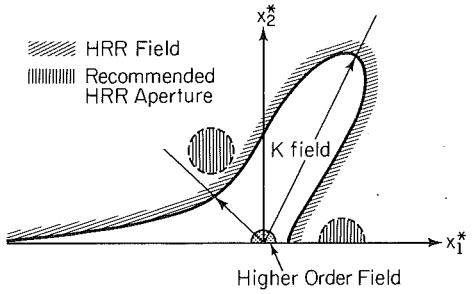


Fig. 7 The region of HRR dominance on the focal plane and the recommended HRR aperture

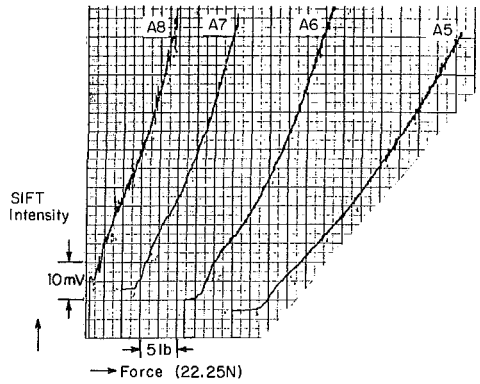


Fig. 8(*a*)

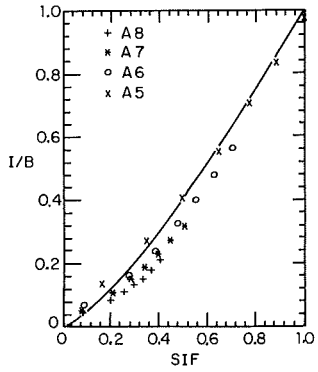


Fig. 8(*b*)

Fig. 8 SIFT test on blunt notch 3-point PMMA SENB specimen; (*a*) force versus SIFT intensity for different apertures (Apertures have ( ) shape and $A_5 > A_6 > A_7 > A_8$ for their size) and (*b*) comparison of theory with experiment ($K_I \in$ MPa $\sqrt{\text{m}}$)

the radial dependence is shown in Fig. 5(*b*). Distinct maxima at ~0 deg and ~140 deg are observed giving the impression of a 3-lobed intensity image on the focal plane. These aspects of the mapping must obviously be taken into account in the design of suitable light collecting systems in an experimental setup. Further illustration of this point is provided in Fig. 6(*a*) in which the focal plane intensity is normalized with respect to the intensity for K_I-field (from equations (7), (12), and (14)) using $J \cong K_I^2/E$ for equations (7) and (12). The extreme values of θ^*, namely near (0 deg or 5.5 deg) and 141.6 deg are at two of the lobes or extremities. The HRR field exists for normalized intensities greater than 1, which occurs at $\hat{r}^* \sim 0.5$ for 5.5 deg and the loading (K_I) and properties chosen for the material. Also indicated in Fig. 6(*a*) are the focal plane radii corresponding to $r/d = 0.25$. The plane stress region is generally assumed to exist for $r/d > 0.25$.

The influence of material hardening behavior and yield strength on the extent of the HRR field relative to the K_I-field can be similarly analyzed. For instance, three levels of hardening are considered in Fig. 6(*b*). Intensity ratios were calculated for material properties listed in the figure caption, and at $\theta^* \sim (60 \text{ deg} - 66 \text{ deg})$ where $k(\theta^*, n)$ is at the first minimum (Fig. 5(*a*)). It is seen that the HRR-field predominates for low hardening (larger n), while the K_I-field is strongly maintained for high hardening levels.The effect of strengthening the material (Fig. 6(*c*)) is very similar to increasing strain hardening, as may be expected. Thus, K_I-field dominance is greatest for high yield strengths, whereas the HRR field characterization becomes significant at lower strengths. Again, the vertical lines on the curves in Fig. 6(*c*) correspond to the presumed plane stress limit of $r/d = 0.25$.

Based on the above analysis, the region of HRR dominance on the focal plane is schematically presented in Fig. 7. As shown in the figure, the region of HRR dominance is close to the focal point at $\theta^* = 0$ deg and $\theta^* \cong 140$ deg. It is far from the focal point at $\theta^* \cong 66$ deg and $\theta^* \geq 180$. Therefore, the best practical geometry of the aperture to measure the HRR singularity is indicated in the figure as "recommended HRR aperture."

Even though the theoretical prediction of the light intensity distribution in the HRR and K field is clear, real focal plane light intensity distribution is far more complicated. This is because the plane-stress HRR dominant region is, sometimes, extremely small or even does not exist on the specimen plane. Instead, the near-tip three-dimensional deformation field dominates in many cases. If so, the prediction should be based on fully three-dimensional numerical calculations and we lose the sense of using single parameter characterization of the field. For a real experiment with a laboratory specimen, deviation of the Ω–J relation from the theoretical prediction is caused by many different reasons. These include crack-tip bluntness, near-tip three-dimensional deformation, etc. If a laboratory specimen is loaded gradually, the nonideal near-tip mapping sweeps out and the K field zone on the focal plane grows out to reach the aperture. Therefore, the I–K relation initially deviates from the relationship, $I = BK^{4/3}$, where $B = \frac{4}{9}\Omega_0 D(cfd/\sqrt{2\pi})^{4/3}$, $D = \int_\Gamma^* (r^*)^{-10/3} ds^*$, but it approaches the relationship as the load is increased. Figure 8 shows the experimental I–K relation compared with the relationship, $I = BK^{4/3}$. The initial deviation, which is believed to be caused by crack-tip bluntness and three-dimensional deformation, is clearly shown in the figure. Details of aperture shapes and specimen characteristics are shown in Table 1.

Table 1 Focal plane aperture dimensions (nominal)

Aperture type	Inner radius (mm)	Outer radius (mm)
A_5	1.75	3.25
A_6	1.25	2.75
A_7	1.00	2.50
A_8	0.75	2.25

Notes:
(a) Actual dimensions were: nominal ±0.03 mm.
(b) Aperture area is covered by (inner radius $< r^* <$ outer radius, and $-\pi/4 < \theta^* < \pi/4$, $3\pi/4 < \theta^* < 5\pi/4$).
(c) The 3-point bending specimen is made of PMMA. Specimen dimension is given as thickness = 6.25 mm, beam width = 50 mm, notch depth = 25 mm and outer span of loading = 200 mm.
(d) Focal length = 1.2 m and stress optic constant = 1.08×10^{-10} Pa^{-1}.

Conclusions

An extension of the SIFT focal plane mapping theory to characterize HRR singularly fields has been found to be feasible. Thus, a simple relation, equation (16) was obtained relating light intensity on the focal plane to the strength J of the HRR singularity in terms of the hardening exponent and var-

Downloaded 03 May 2010 to 171.66.16.244. Redistribution subject to ASME license or copyright; see http://www.asme.org/terms/Terms_Use.cfm

ious experimental parameters. The technique could be used to study the nature of the HRR field, i.e., its radial and angular dependence, as well as transitions in the singularity, as a function of material yield and hardening behavior and slow crack growth, so long as plane stress deformation prevails. In other words, it is so if relatively thin (5–10 mm) sheets of appropriate metallic or polymeric materials are used. Also, in principle, the theoretical formulation could be suitably modified for the quasi-static growing crack field and used to generate J-resistance curves experimentally under monotonic, uninterrupted loading. A stationary photodetector could be used to measure light intensity (or J) while stable crack growth could be monitored using techniques like the crack-tip position tracer described elsewhere (Kamath, 1987). However, a practical difficulty might arise in opaque samples due to loss of reflectivity if plastic deformation is excessive.

Acknowledgment

This is based on Chapter 2 of SMK's Ph.D. thesis submitted to the University of Illinois at Urbana-Champaign. The authors are grateful to IBM for SMK's IBM Graduate Fellowship and to the Research Board and the Department of Theoretical and Applied Mechanics of the University of Illinois at Urbana-Champaign for their support for the experiment.

References

Hutchinson, J. W., 1968, "Singular Behavior at the End of a Tensile Crack in a Hardening Material," *Journal of Mechanics and Physics of Solids*, Vol. 16, pp. 13–31.

Kamath, S. M., 1987, "Some Aspects of the Mechanics and Mechanisms of Dynamic Brittle Fracture," Ph.D. Thesis, University of Illinois at Urbana-Champaign, University Microfilms International Order No. 8721673.

Kim, K.-S., 1985, "A Stress Intensity Factor Tracer," ASME JOURNAL OF APPLIED MECHANICS, Vol. 52, pp. 291–297.

Ramberg, W., and Osgood, W. R., 1943, "Description of Stress-Strain Curves by Three Parameters," NACA TN 902.

Rice, J.R., 1982, "Elastic-Plastic Crack Growth," *Mechanics of Solids* (Hill 60th Anniversary Volume), Pergamon Press, pp. 539–562.

Rice, J. R., and Rosengren, G. F., 1968, "Plane Strain Deformation Near a Crack Tip in a Power-Law Hardening Material," *Journal of the Mechanics and Physics of Solids*, Vol. 16, pp. 1–12.

Shih, C. F., 1983, "Tables of Hutchinson-Rice-Rosengren Singular Field Quantities," Brown University, Report MRL E-147, June.

Downloaded 03 May 2010 to 171.66.16.244. Redistribution subject to ASME license or copyright; see http://www.asme.org/terms/Terms_Use.cfm

A General Algorithm for Multidimensional Cauchy Principal Value Integrals in the Boundary Element Method

M. Guiggiani
Researcher.

A. Gigante
Graduate Student.

Dipartimento di Costruzioni Meccaniche e Nucleari,
Universita degli Studi di Pisa,
56126 Pisa PI, Italy

This paper presents a new general method for the direct *evaluation of Cauchy principal value integrals in several dimensions, which is an issue of major concern in any boundary element method analysis in applied mechanics. It is shown that the original Cauchy principal value integral can be transformed into an element-by-element sum of regular integrals, each one expressed in terms of intrinsic (local) coordinates. The actual computation can be performed by standard quadrature formulae and can be easily included in any existing computer code. The numerical results demonstrate the accuracy and efficiency of the method, along with its insensitivity to the mesh pattern. This new method has full generality and, therefore, can be applied in any field of applied mechanics. Moreover, there are no restrictions on the numerical implementation, as the singular integrals may be defined on surface elements or internal cells of any order and type.*

1 Introduction

Boundary element method (BEM) formulations are now available for many relevant linear problems of applied mechanics (e.g., elastostatics, elastodynamics, plate bending, etc.) and also for a number of nonlinear problems, such as elastoplasticity, etc. A brief survey on the recent developments of the BEM can be found in Cruse (1987).

As is well known, the BEM can offer substantial computational advantages over other numerical techniques. However, in order to achieve an efficient numerical implementation of general validity, a number of issues have to be dealt with using special attention.

One of the typical and most significant issues of almost all BEM analyses is the evaluation of singular integrals only existing in the Cauchy principal value (CPV) sense. As a matter of fact, due to the strong singularity of some kernel functions, surface CPV integrals naturally arise in many boundary integral equations. Moreover, in order to solve nonlinear problems, the boundary integral equations have to be augmented with some relation for interior points, such as the relation for interior strain or stress in elastoplasticity. These relations do require the evaluation of domain integrals defined in the CPV sense (e.g., Brebbia et al., 1984, pp. 255–261).

Apart from pure analytical integration, which has obvious limitations (low order elements), many other methods have been devised so far to deal with *surface integrals* defined in the CPV sense. However, all these methods have the common feature of avoiding the direct computation of CPV integrals by employing known elementary solutions of the boundary integral equation, such as the rigid-body motion in elastostatics (Lachat and Watson, 1976), the inflating mode in axisymmetric elasticity (Sarihan and Mukherjee, 1982), or others (Nishimura and Kobayashi, 1989).

This indirect approach clearly lacks generality, as in some cases (notably, time-harmonic elastodynamics and acoustics) convenient elementary solutions of the boundary integral equation are not available. To overcome this problem, Rizzo et al. (1985) and Bui et al. (1985) proposed to combine integral equations of two different problems—the original problem and a "companion" problem—thus obtaining a new boundary integral equation free of CPV integrals. A similar idea was also applied in axisymmetric elasticity by Rizzo and Shippy (1986). However, this generalized indirect approach considerably increases the analytical complexity of the BEM formulation, as it requires two different sets of kernel functions. More details can be found, e.g., in a recent review paper (Guiggiani, 1990).

The evaluation of *domain integrals* defined in the CPV sense—typically the inelastic strain integrals of elastoplasticity—still largely relies on analytical (Matsumoto and Yuuki, 1988) or semi-analytical integration (Telles and Brebbia, 1981; Telles, 1983). Unfortunately, these techniques are applicable only in plane problems using piecewise constant or, at most, linear internal cells. A somewhat more general indirect method based on the application of a constant inelastic strain field was proposed by Telles and Brebbia (1979). Such procedure allows

Contributed by the Applied Mechanics Division of THE AMERICAN SOCIETY OF MECHANICAL ENGINEERS for publication in the JOURNAL OF APPLIED MECHANICS.

Discussion on this paper should be addressed to the Technical Editor, Leon M. Keer, The Technological Institute, Northwestern University, Evanston, IL 60208, and will be accepted until two months after final publication of the paper itself in the JOURNAL OF APPLIED MECHANICS. Manuscript received by the ASME Applied Mechanics Division, May 5, 1989; final revision, Nov. 1, 1989.

Copyright © 1990 by ASME
Downloaded 03 May 2010 to 171.66.16.244. Redistribution subject to ASME license or copyright; see http://www.asme.org/terms/Terms_Use.cfm

for the computation of the CPV domain integrals together with the corresponding free terms even on higher-order internal cells. However, in order to apply this method, the entire body must be covered with cells. To avoid this disadvantage a somewhat more involved implementation may be used (Telles and Brebbia, 1979). However, to date, this procedure has never been used in actual computations.

These techniques to circumvent the direct evaluation of CPV integrals do provide, when applicable, a rigorous solution to the problem. However, they have also induced the erroneous belief that CPV integrals "*must* be computed in an indirect manner" since they "*cannot* be numerically evaluated with reasonable efficiency and accuracy," to cite but a few sentences still reported in the recent BEM literature.

The problem of the evaluation of CPV integrals has also led to a number of approximate or even incorrect approaches. For instance, in some inelastic implementations employing higher-order cells, the singular integrand is made bounded by excluding a ball of *finite* radius. Clearly, this method may be regarded only as an approximation. In other cases, CPV integrals are manipulated in the same manner as weakly singular integrals; that is, with no proper consideration of the limiting process involved in any CPV definition. Thus, one of the fundamental aspects was completely overlooked leading to erroneous results.

A first contribution to the *direct* numerical evaluation of CPV integrals in the BEM, with proper consideration of the limiting process involved, was presented in Guiggiani and Casalini (1987) and Casalini and Guiggiani (1988). It was shown that general contour CPV integrals typical of plane or axisymmetric BEM formulations can be easily reduced to regular ones, before computing them by, e.g., standard Gaussian quadrature formulae. This procedure can be applied whatever the type and order of the shape functions employed (therefore, it does not suffer the limitations of Kutt's formulae for finite part integrals that are only applicable on straight linear boundary elements, as pointed out in Guiggiani (1988)). The direct approach has been also extended to the Galerkin version of the BEM (Parreira and Guiggiani, 1989).

One of the aims of the present paper is to show that the difficulty in directly computing any type of CPV integrals arising in the BEM is only apparent. It will be demonstrated that CPV integrals defined either on (curved) surface elements or (distorted) internal cells can be always transformed in ordinary integrals through simple (although rigorous) manipulations. Therefore, the results given in Guiggiani and Casalini (1987) are generalized, with relevant additional work, to the case of singular integrals in several dimensions (Mikhlin, 1965).

The proposed approach allows the actual computation to be performed by simple applications of standard Gaussian formulae and does not involve abandoning a standard BEM code structure.

This new general method for the evaluation of CPV integrals should greatly enhance the BEM applicability, as it is valid whatever the problem under consideration. As a consequence, elementary solutions to circumvent the CPV evaluation are no longer required. Further, analytical (or semi-analytical) integration can be definitely abandoned, thus allowing boundary elements and internal cells of *any order and type* to be easily and correctly employed in all BEM analyses.

To cite but a few examples, traction boundary integral equations (Bonnet, 1986, 1989; Zhang and Achenbach, 1989) and displacement discontinuity methods (e.g., Cruse, 1988) for three-dimensional static and dynamic crack analysis, linear and nonlinear plate bending, design sensitivity analysis in nonlinear problems (Mukherjee and Chandra, 1988), and some novel formulations for stress analysis (Okada et al., 1988, 1989) are all important fields that may take advantage from the application of the proposed method for the direct treatment of CPV integrals.

It is also worth noting that in adaptive methods employing hierarchical shape functions (an emerging field for the BEM) the problem unknowns are no longer nodal values. Therefore, the use of the rigid-body motion in elastostatics is no longer an easy task. On the other hand, the direct evaluation of CPV integrals with the proposed method is straightforward.

The proposed approach has rigorous mathematical bases. However, numerical results are given to show its effectiveness and efficiency. As expected, results have been shown to be very accurate and absolutely insensitive to the mesh pattern around the singularity.

2 Principal Value Integrals in the BEM

2.1 Boundary Integral Equations. The starting point of any BEM analysis is an integral equation, for scalar problems, or a coupled set of integral equations, for vector problems such as elastostatics, time-harmonic elastodynamics, etc. In cartesian coordinates, a general form for two and three-dimensional vectorial problems may be the following

$$u_i(\mathbf{y}) + \int_S T_{ij}(\mathbf{y},\mathbf{x}) u_j(\mathbf{x}) dS(\mathbf{x}) = \int_S U_{ij}(\mathbf{y},\mathbf{x}) t_j(\mathbf{x}) dS(\mathbf{x}), \quad (1)$$

where all indices are dropped in case of scalar problems. In equation (1), the regular surface S (in the sense of Kellog, i.e., possibly with a finite number of edges and vertices) represents the boundary of an open region V of the Euclidian space. A similar formulation can be given for axisymmetric problems, with S representing the contour of the meridian section.

In the integral identity equation (1), the source point $\mathbf{y} \in V$ while the field (integration) point $\mathbf{x} \in S$. U_{ij} are the fundamental solutions of the linear, second-order governing differential equations for the boundary value problem of interest. The other kernel functions T_{ij} may be regarded as generalized normal derivatives of U_{ij}. In case of elastostatic problems, equation (1) is the well-known Somigliana's identity, where u_j and t_j are the displacement and traction components, respectively.

If $r = |\mathbf{x} - \mathbf{y}|$ represents the distance between the source point $\mathbf{y}$ and a field point $\mathbf{x}$, the kernels U_{ij} show a weak singularity when $\mathbf{x} \to \mathbf{y}$, while the kernels T_{ij} have a *strong singularity* of order $(1/r)$, in two-dimensional and axisymmetric problems, and of order $(1/r^2)$ in three-dimensional problems.

In the interest of what is to follow, it is important to examine in some details the limiting form of equation (1) as the interior point $\mathbf{y}$ is taken to a boundary point (see, e.g. Brebbia et al., 1984, p. 191). The point $\mathbf{y}$ can be surrounded by an external small volume v_ϵ of arbitrary shape s_ϵ, thus letting the point $\mathbf{y}$ to be an internal point for the new region $V + v_\epsilon$. It is *usual* in the BEM to take as v_ϵ the external part of a sphere (a circle in two dimensions) at $\mathbf{y}$ and of radius ϵ. With reference to Fig. 1, equation (1) can be written

$$u_i(\mathbf{y}) + \int_{S - e_\epsilon + s_\epsilon} T_{ij}(\mathbf{y},\mathbf{x}) u_j(\mathbf{x}) dS(\mathbf{x}) = \int_{S - e_\epsilon + s_\epsilon} U_{ij}(\mathbf{y},\mathbf{x}) t_j(\mathbf{x}) dS(\mathbf{x}). \quad (2)$$

Letting $\epsilon \to 0$, the following boundary integral equation arises

$$c_{ij}(\mathbf{y}) u_j(\mathbf{y}) + \oint_S T_{ij}(\mathbf{y},\mathbf{x}) u_j(\mathbf{x}) dS(\mathbf{x}) = \int_S U_{ij}(\mathbf{y},\mathbf{x}) t_j(\mathbf{x}) dS(\mathbf{x}) \quad (3)$$

where the so-called free-term coefficients c_{ij} are given by the limit of the integral on the surface s_ϵ of v_ϵ.

The boundary integral equation for nonlinear problems (e.g., elastoplasticity) also contains a volume integral (see, e.g., Telles, 1983) which, however, shows a weak singularity.

It is important to note that, owing to the chosen shape of v_ϵ (a circle or a sphere) which enforces the *symmetry* with respect to $\mathbf{y}$ of the vanishing neighborhood e_ϵ on S, the surface

Downloaded 03 May 2010 to 171.66.16.244. Redistribution subject to ASME license or copyright; see http://www.asme.org/terms/Terms_Use.cfm

integral on the left-hand side of equation (3) has been defined in the sense of a Cauchy principal value and, therefore, it must be considered that way hereafter. As a matter of fact, although the limit on $S - e_\epsilon + s_\epsilon$ taken as a whole is independent on the shape of v_ϵ, the values of the free-term coefficients and of the singular integrals, taken separately, do actually depend upon the shape of v_ϵ.

After the introduction of the shape functions $N^c(\xi)$ of the intrinsic coordinate(s) $\xi = (\xi_1, \xi_2)$ to represent the geometry and the boundary fields in terms of nodal values, the usual discretized version of equation (3) is obtained

$$u_j^{pa}\left[N^a(\xi(\mathbf{y}))c_{ij}(\mathbf{y}) + \oint_{S_p} T_{ij}(\mathbf{y},\mathbf{x})N^a(\xi(\mathbf{x}))dS(\mathbf{x})\right] =$$

$$- \sum_{\substack{b \\ (b,c)\neq(p,a)}}\sum_{c} u_j^{bc}\int_{R_b} T_{ij}(\mathbf{y},\mathbf{x}(\xi))N^c(\xi)J^b(\xi)d\xi$$

$$+ \sum_b\sum_c t_j^{bc}\int_{R_b} U_{ij}(\mathbf{y},\mathbf{x}(\xi))N^c(\xi)J^b(\xi)d\xi. \qquad (4)$$

Contrary to normal practice, in equation (4) the indication of CPV integrals has not been omitted. It is important to remember that, notwithstanding the introduction of the one-to-one mapping between the boundary points and the intrinsic coordinate(s) ξ, the symmetry of the vanishing neighborhood hidden in any CPV definition must be maintained. Therefore, any manipulation of the CPV integrals in the local parameter space of the intrinsic coordinates ξ needs special attention, as will be shown next.

In equation (4), S_p indicates the set of *all* adjacent elements connected to the singular (collocation) point $\mathbf{y}$, and N^a collects all shape functions that do not vanish as $\mathbf{x} \to \mathbf{y}$ (usually $N^a(\xi(\mathbf{y})) = 1$). R_b is the image of the boundary element S_b in the parameter space ξ (e.g., a 1, $[-1, 1]\times[-1, 1]$ square). The other symbols have their usual meaning.

The problem is now reduced to the evaluation of all the integral coefficients in equation (4). In this paper focus is on the *direct* evaluation of the terms in square brackets, each one formed by the sum of a CPV integral on S_p and a c_{ij} coefficient.

2.2 Relations for Interior Points (Nonlinear Problems). Of fundamental importance for the stepwise solution of, for example, inelastic problems is the calculation of stresses (or strains) at internal points $\mathbf{y}$. The proper integral equation, in rate form, reads (e.g., Telles, 1983)

$$\dot\sigma_{ij}(\mathbf{y}) = \int_S D_{ijk}(\mathbf{y},\mathbf{x})\,\dot t_k(\mathbf{x})dS(\mathbf{x}) - \int_S S_{ijk}(\mathbf{y},\mathbf{x})\,\dot u_k(\mathbf{x})dS(\mathbf{x})$$

$$+ \int_V B_{ijkl}(\mathbf{y},\mathbf{x})\dot\sigma^o_{kl}(\mathbf{x})dV(\mathbf{x}) + E_{ijkl}\dot\sigma^o_{kl}(\mathbf{y}) \qquad (5)$$

where the volume integral of the initial stress term is defined in the principal value sense (consistently with jump terms E_{ijkl}).

3 Strongly Singular Integrals on Surface Elements

In what follows surface CPV integrals as in equation (4), typical of any three-dimensional BEM formulation, will be analyzed and a general method for their direct evaluation will be presented.

Owing to the definition of CPV, the singular integral over the surface S_p has to be written in the following form

$$\oint_{S_p} T_{ij}(\mathbf{y},\mathbf{x})N^a(\xi(\mathbf{x}))dS(\mathbf{x})$$

$$:= \lim_{\epsilon\to 0}\left\{\int_{S_p - e_\epsilon} T_{ij}(\mathbf{y},\mathbf{x})N^a(\xi(\mathbf{x}))dS(\mathbf{x})\right\} \qquad (6)$$

where e_ϵ indicates, as above, that part of the boundary in which the points are at a distance $\le \epsilon$ from the singular point $\mathbf{y}$ (Fig. 1).

To represent the geometry of the boundary we can introduce, as usual in the BEM, a suitable piecewise parametric representation of intrinsic coordinates $\xi = (\xi_1, \xi_2)$

$$x_i(\xi) = N^c(\xi)x_i^c, \quad i = 1,2,3 \qquad (7)$$

in terms of local shape functions and nodal values, thus subdividing the boundary S in a number of either quadrilateral or triangular curved boundary elements (of any order).

Here attention is restricted to S_p. Let us indicate by ${S_p}^m$ those elements belonging to S_p ($S_p = \cup_m {S_p}^m$). Therefore, after the introduction of the parametric representations (7), expression (6) becomes (Fig. 2)

$$\lim_{\epsilon\to 0}\left\{\sum_m \int_{{S_p}^m - {e_\epsilon}^m} T_{ij}(\mathbf{y},\mathbf{x})N^a(\xi(\mathbf{x}))dS(\mathbf{x})\right\}$$

$$= \lim_{\epsilon\to 0}\left\{\sum_m \int_{{R^m} - {\sigma_\epsilon}^m} T_{ij}(\mathbf{y},\mathbf{x}(\xi))N^a(\xi)J^m(\xi)d\xi\right\} \qquad (8)$$

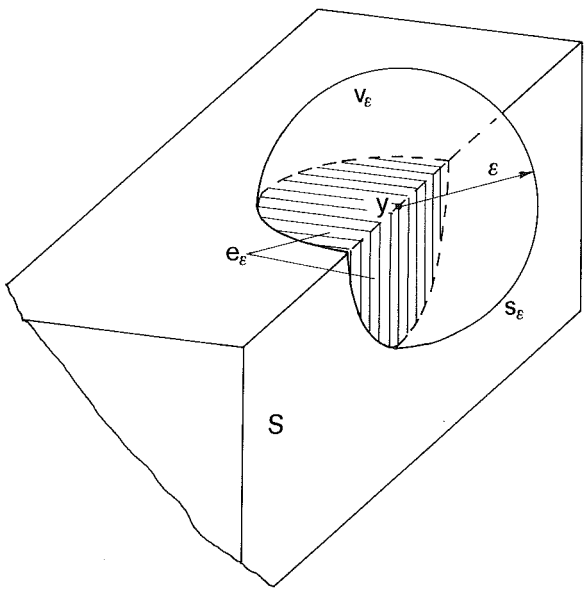


Fig. 1 Singular point y on the boundary S: illustration of the limiting procedure

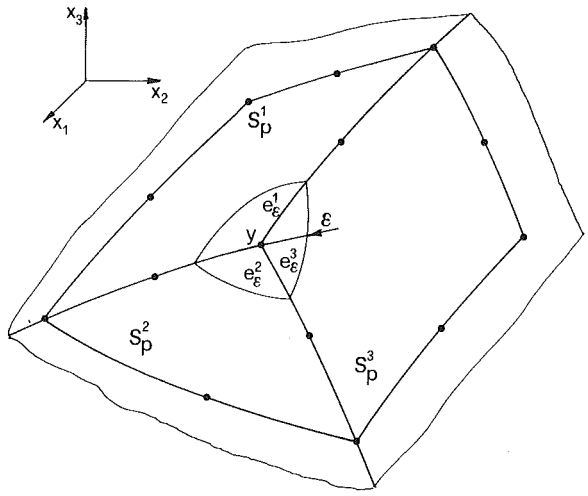


Fig. 2 Adjacent elements connected to the singular point: definition of CPV surface integral

Downloaded 03 May 2010 to 171.66.16.244. Redistribution subject to ASME license or copyright; see http://www.asme.org/terms/Terms_Use.cfm

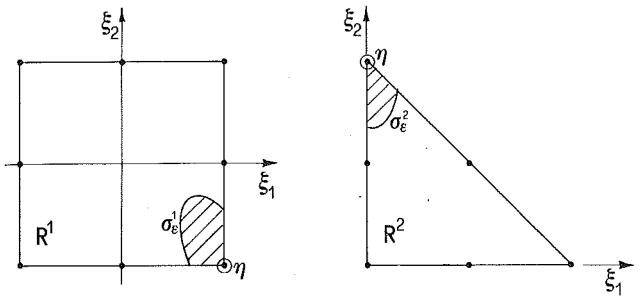


Fig. 3 Image in the local parameter plane of the surface element with the corresponding vanishing neighborhood; (*a*) quadrilateral element, (*b*) triangular element

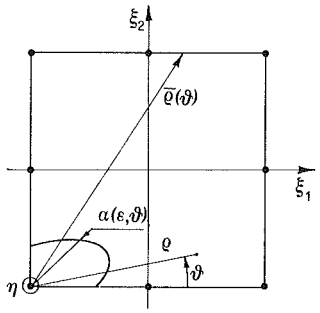


Fig. 4 Polar coordinates in the local plane

where e_ϵ^m represents that part of e_ϵ on $S_p{}^m$. The plane region R^m (of standard shape) is the image of the surface element $S_p{}^m$ in the transformed plane (ξ_1, ξ_2), and, accordingly, $\sigma_\epsilon{}^m$ is *the image* of e_ϵ^m (Fig. 3). Notice that, in general, σ_ϵ^m has *not* a circular shape (although its polar radius still tends to zero with ϵ). As will be shown next, the effect of the coordinate transformations on the image of the circular neighborhood e_ϵ is a very important, often overlooked matter.

Obviously, in equation (8) all elements $S_p{}^m$ round the pole $\mathbf{y}$ must be taken together, as any single contribution is unbounded in the limit.

3.1 Asymptotic Expression of the Integrand Function. A close examination of the expressions of the kernel functions $T_{ij}(\mathbf{y}, \mathbf{x})$ for *all* relevant fields (e.g., Brebbia et al., 1984) reveals that they have some common features. In particular, they are made up of two parts. A part multiplied by $dr/dn = r_{,h}n_h = 0(r)$, which, therefore, does not show a strong singularity and can be integrated in the standard way, and the truly singular remainder which, typically, has the form

$$T^*_{ij} = \frac{1}{r^2}\left\{n_j(\mathbf{x})\,\frac{x_i - y_i}{r} - n_i(\mathbf{x})\,\frac{x_j - y_j}{r}\right\}, \tag{9}$$

where $n_i(\mathbf{x})$ is the generic component of the outward unit normal vector at S.

Even in cases where it is not apparent, like time-harmonic elastodynamics, it can be demonstrated (Rizzo et al., 1985; Bonnet, 1986) that the asymptotic behavior in the vicinity of the singularity is exactly represented by terms in the above form. Indeed, the elastodynamic kernels have the same asymptotic behavior of the corresponding static kernels.

From the above considerations it follows that the use in the subsequent analysis of T^*_{ij} (equation (9)) in place of T_{ij} does not imply any loss of generality.

It is convenient to introduce in each R^m, a polar coordinate system (ρ, ϑ) centered at η, image of the singular point $\mathbf{y}$ (Fig. 4)

$$\begin{aligned}\xi_1 &= \eta_1 + \rho\,\cos\vartheta\\ \xi_2 &= \eta_2 + \rho\,\sin\vartheta\end{aligned} \tag{10}$$

thus having $d\xi_1 d\xi_2 = \rho d\rho d\vartheta$.

The integral on each element $S_p{}^m$ is now considered separately, provided the limit process has not been performed yet (its value would be unbounded)

$$\int_{R^m - \sigma_\epsilon{}^m} T^*_{ij}(\mathbf{y}, \mathbf{x}(\xi)) N^a(\xi) J^m(\xi)\, d\xi = \int_{\vartheta_1{}^m}^{\vartheta_2{}^m} \int_{\alpha^m(\epsilon,\vartheta)}^{\bar{\rho}^m(\vartheta)} F^m{}_{ij}(\rho,\vartheta)\, d\rho d\vartheta \tag{11}$$

where $F^m{}_{ij}(\rho, \vartheta) = T^*_{ij}(\mathbf{y}, \mathbf{x}(\xi(\rho, \vartheta)))N^a(\xi(\rho, \vartheta))J^m(\xi(\rho, \vartheta))\rho$. In expression (11), $\rho = \bar{\rho}^m(\vartheta)$ and $\rho = \alpha^m(\epsilon, \vartheta)$, $\vartheta_1{}^m \le \vartheta \le \vartheta_2{}^m$, are the equations in polar coordinates of the boundary of R^m and $\sigma_\epsilon{}^m$, respectively (Figs. 3 and 4). Their explicit expressions will be given next. Since ϵ has, for the moment, a finite value, any proper manipulation must take its value into account.

By employing a Taylor expansion in the neighborhood of the singular point (Aliabadi et al., 1985), it is easy to establish formulae of the form (the index m has been omitted for brevity)

$$\begin{aligned} x_i - y_i &= \left.\frac{\partial x_i}{\partial \xi_1}\right|_{\xi=\eta}(\xi_1 - \eta_1) + \left.\frac{\partial x_i}{\partial \xi_2}\right|_{\xi=\eta}(\xi_2 - \eta_2) + 0(\rho^2) = \\ &= \rho\left[\left.\frac{\partial x_i}{\partial \xi_1}\right|_{\xi=\eta}\cos\vartheta + \left.\frac{\partial x_i}{\partial \xi_2}\right|_{\xi=\eta}\sin\vartheta\right] + 0(\rho^2) \end{aligned} \tag{12}$$

where the derivatives, all evaluated at η, are promptly obtained from expressions (7).

Let, for brevity,

$$A_i(\vartheta) = \left[\left.\frac{\partial x_i}{\partial \xi_1}\right|_{\xi=\eta}\cos\vartheta + \left.\frac{\partial x_i}{\partial \xi_2}\right|_{\xi=\eta}\sin\vartheta\right],\ i = 1,2 \text{ or } 3 \tag{13a}$$

and

$$A(\vartheta) = \left\{\sum_{i=1}^{3}[A_i(\vartheta)]^2\right\}^{1/2}. \tag{13b}$$

From equations (12) and (13) and the definition of r, the following relations can be easily obtained

$$r^2(\rho,\vartheta) = \rho^2 A^2(\vartheta) + 0(\rho^3) \tag{14}$$

and

$$\frac{x_i - y_i}{r} = r_{,i} = \frac{A_i(\vartheta)}{A(\vartheta)} + 0(\rho) \tag{15}$$

where the explicit expressions of all functions on the right-hand side are known.

It is now possible to give explicitly the asymptotic expression of the singular integrand function F_{ij} in expression (11). From equations (9), (13), (14), and (15) it follows

$$\begin{aligned} F_{ij}(\rho,\vartheta) &= \frac{1}{\rho}\{f_{ij}(\vartheta) + 0(\rho)\} = \\ &= \frac{1}{\rho}\left\{\frac{n_j(\mathbf{y})A_i(\vartheta) - n_i(\mathbf{y})A_j(\vartheta)}{A^3(\vartheta)}\,N^a(\eta)J(\eta) + 0(\rho)\right\}. \end{aligned} \tag{16}$$

The knowledge of the (regular) function $f_{ij}(\vartheta)$ plays a key role in the present analysis. As a matter of fact, from equation (16) it immediately follows that $[F_{ij}(\rho, \vartheta) - f_{ij}(\vartheta)/\rho] = 0(1)$ as $\rho \to 0$.

Notice that, while some quantities (namely, n_i, N^a, and J) have simply assumed their value at the singular point, the asymptotic expression of the kernel function T^*_{ij} necessarily must depend on the angle ϑ (Mikhlin, 1965).

3.2 Vanishing Neighborhood in the Local Plane. As previously mentioned the contour of the region σ_ϵ^m, image of e_ϵ^m in the local parameter plane, is determined by an equation in the form $\rho = \alpha^m(\epsilon, \vartheta)$ (see equations (11) and Figs. 3 and 4). Its explicit asymptotic expression is now derived.

Downloaded 03 May 2010 to 171.66.16.244. Redistribution subject to ASME license or copyright; see http://www.asme.org/terms/Terms_Use.cfm

The contour of the neighborhood e_ϵ of radius ϵ on S is given by the equation

$$\epsilon^2 = (x_k - y_k)(x_k - y_k), \quad \mathbf{x},\mathbf{y} \in S \tag{17}$$

that is, in the ξ-plane (see equations (12) and (13))

$$\epsilon^2 = \rho^2 A^2(\vartheta) + 0(\rho^3). \tag{18}$$

Therefore, the contour of σ_ϵ^m, image of e_ϵ^m, is given by the equation (the index m is omitted for brevity)

$$\rho = \alpha(\epsilon,\vartheta) = \frac{\epsilon}{A(\vartheta)} + 0(\epsilon^2) = \epsilon\beta(\vartheta) + 0(\epsilon^2). \tag{19}$$

It can be demonstrated that, as ϵ approaches zero, equation (19) represents, in general, the equation of an *ellipse*. Notice that $\beta(\vartheta)$ depends only on the local characteristics in $\mathbf{y} = \mathbf{x}(\eta)$ of the one-to-one mapping between S_p^m and R^m (see equations (13)).

The explicit knowledge of $\beta(\vartheta)$ is the second key ingredient of the present approach to the direct evaluation of multidimensional CPV integrals. As a matter of fact, it carries all the information required to properly perform the limit process in the ξ-plane.

3.3 Final Formula for CPV Integrals. Let us consider the original CPV surface integral

$$I_S = \text{⨍}_{S_p} T^*_{ij}(\mathbf{y},\mathbf{x}) N^a(\xi(\mathbf{x})) dS(\mathbf{x})\}$$

$$:= \lim_{\epsilon\to 0}\left\{\sum_m \int_{S_p{}^m - e_\epsilon^m} T^*_{ij}(\mathbf{y},\mathbf{x}) N^a(\xi(\mathbf{x})) dS(\mathbf{x})\right\}. \tag{20a}$$

After the introduction of the parametric representation on each element the singular integral becomes

$$I_S = \lim_{\epsilon\to 0}\left\{\sum_m \int_{R^m - \sigma_\epsilon{}^m} T^*_{ij}(\mathbf{y},\mathbf{x}(\xi)) N^a(\xi) J^m(\xi) d\xi\right\} \tag{20b}$$

and, in local polar coordinates

$$I_S = \lim_{\epsilon\to 0}\left\{\sum_m \int_{\vartheta_1 m}^{\vartheta_2 m} \int_{\alpha^m(\epsilon,\vartheta)}^{\bar\rho^m(\vartheta)} F^m{}_{ij}(\rho,\vartheta) d\rho d\vartheta\right\}. \tag{20c}$$

Adding and subtracting on each element around $\mathbf{y}$ the corresponding asymptotic expression $f^m{}_{ij}(\vartheta)/\rho$ of the integrand function (see equation (16)), the original CPV integral results in an alternative form more suitable for actual computation

$$I_S = \left\{\sum_m \int_{\vartheta_1 m}^{\vartheta_2 m} \int_0^{\bar\rho^m(\vartheta)} \left[F^m{}_{ij}(\rho,\vartheta) - \frac{f^m{}_{ij}(\vartheta)}{\rho}\right] d\rho d\vartheta\right\} +$$

$$+ \lim_{\epsilon\to 0}\left\{\sum_m \int_{\vartheta_1 m}^{\vartheta_2 m} f^m{}_{ij}(\vartheta) \ln\left[\frac{\bar\rho^m(\vartheta)}{\alpha^m(\epsilon,\vartheta)}\right] d\vartheta\right\} \tag{20d}$$

where, due to the simplicity of the integrand, in the last term the integration with respect to ρ has been already performed. Notice that the first integral on the r.h.s. has now a regular integrand function and, therefore, the limiting process has been already performed.

If the asymptotic expression (19) for $\alpha^m(\epsilon, \vartheta)$ is now considered, the CPV integral I_S can be rewritten in the following form where all integrals are regular and, therefore, any limit process is no longer present

$$I_S = \sum_m \left\{\int_{\vartheta_1 m}^{\vartheta_2 m} \int_0^{\bar\rho^m(\vartheta)} \left[F^m{}_{ij}(\rho,\vartheta) - \frac{f^m{}_{ij}(\vartheta)}{\rho}\right] d\rho d\vartheta +\right.$$

$$\left. + \int_{\vartheta_1 m}^{\vartheta_2 m} f^m{}_{ij}(\vartheta) \ln\left[\frac{\bar\rho^m(\vartheta)}{\beta^m(\vartheta)}\right] d\vartheta\right\}. \tag{20e}$$

In the derivation of the last expression of I_S, the following property has been used

$$\lim_{\epsilon\to 0} (\ln\epsilon)\left\{\sum_m \int_{\vartheta_1 m}^{\vartheta_2 m} f^m{}_{ij}(\vartheta) d\vartheta\right\} = 0. \tag{21}$$

As a matter of fact, if equation (21) did not hold, an inconsistency would result (Gigante, 1989).

Therefore, in expression (20*e*) the original CPV integral on S_p has been expressed as a sum of double and one-dimensional *regular* integrals, each one in terms of local coordinates.

The expressions of all the functions involved have been given explicitly. Further, each term in the final sum refers to (the image in the local parameter plane of) one element at the time, thus allowing the computation to be performed in an *element-by-element* fashion (with obvious simplifications in the computer code structure). The parametric representation of surface elements in terms of intrinsic coordinates (ξ_1, ξ_2) and, then, the introduction of local polar coordinates are usually operations in the BEM.

Expression (20*e*)—deeply rooted in the classical theory of multidimensional singular integrals (Mikhlin, 1965)—is the fundamental result of the present paper.

It is important to note that in equation (20*e*) not only the singularity has been subtracted out, but also the limit process has been performed taking into account (through the functions $\beta^m(\vartheta)$) the distorted shape of each σ_ϵ^m in the corresponding ξ-plane. Numerical examples (see below) confirm that disregarding these terms leads to incorrect results.

Expression (20*e*) has a general validity. It can be applied in BEM formulations for *all* relevant fields in applied mechanics and *whatever* the surface elements employed. It is also worth remembering that it is an exact restatement of the original CPV integral I_S, as in its derivation from equation (20*a*) no approximations have been introduced.

The actual computation can be easily performed by using, e.g., Gauss-Legendre quadrature formulae. As shown in the numerical examples, a low order is sufficient to obtain good accuracy.

3.4 Free-Term Coefficients. As stated at the end of Section 2.2, any BEM implementation requires the knowledge of both CPV integrals and c_{ij} coefficients.

If $\mathbf{y}$ is a smooth boundary point, that is with only one tangent plane, the free-term coefficients are given by the well-known expression $c_{ij} = 0.5\delta_{ij}$.

In general, however, the point $\mathbf{y}$ may lie on an *edge* (two tangent planes) or may be a point in a *vertex* (three or more tangent planes). The computation of c_{ij} coefficients in non-smooth boundary points was treated in some details by Hartmann (1980, 1981) for elastostatic problems. Here we develop further the work of Hartmann to allow the actual computation of c_{ij} coefficients for any three-dimensional BEM implementation.

As previously mentioned, the kernel functions T_{ij} for all relevant fields share some common features, at least in their asymptotic behavior near the singular point $\mathbf{y}$. As an important consequence, the c_{ij} coefficients for, e.g., time-harmonic elastodynamics are exactly equal to the corresponding coefficients in elastostatics.

In general, the asymptotic behavior of kernels T_{ij} can be represented by terms like $dr/dn = r_{,h}n_h$ multiplied by some combination of $r_{,k}$, and by terms in the form $n_j r_{,i} - n_i r_{,j}$ (as in equation (9)). Of course, all terms are also multiplied by $1/r^2$.

As observed by Hartmann (1980), on the characteristic surface $\Omega(\mathbf{y})$, $dr/dn = -1$ and $n_j r_{,i} - n_i r_{,j} = 0$, and, therefore, $\tilde T_{ij} = r^2 T_{ij}$ always reduces to some simple combinations of $r_{,k}$, $k = 1, 2, 3$.

It is useful to introduce in the Euclidian space a system of spherical coordinates (r, ϑ, φ) centered at $\mathbf{y}$, thus having $r_{,1} = \cos\varphi\sin\vartheta$, $r_{,2} = \sin\varphi\sin\vartheta$ and $r_{,3} = \cos\vartheta$.

According to equation (16) in Hartmann (1980), the free-term coefficients are given by

Downloaded 03 May 2010 to 171.66.16.244. Redistribution subject to ASME license or copyright; see http://www.asme.org/terms/Terms_Use.cfm

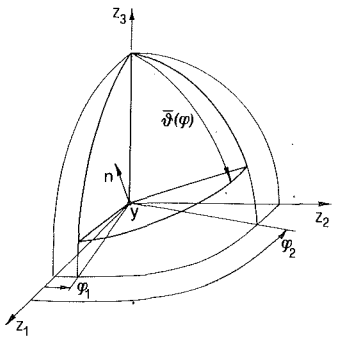


Fig. 5 Geometry of a nonsmooth boundary point

$$c_{ij}(\mathbf{y}) = \int_{\Omega(\mathbf{y})} \tilde{T}_{ij}(\vartheta,\varphi)\sin\vartheta d\vartheta d\varphi \tag{22}$$

where $\Omega(\mathbf{y})$ is the solid angle formed by the tangent planes at $\mathbf{y}$ and, in full generality, $\tilde{T}_{ij}(\vartheta, \varphi) = p_{ij}(\vartheta)q_{ij}(\varphi)$, with p_{ij} and q_{ij} simple known trigonometric functions (see, e.g., equation (19) in Hartmann, 1980).

If, without loss of generality the spherical coordinates are referred to a cartesian system (z_1, z_2, z_3) with its third axis coinciding with one of the edges at $\mathbf{y}$ (Fig. 5), expression (21) can be given the following more explicit form

$$c_{ij}(\mathbf{y}) = \int_{\varphi_1}^{\varphi_2}\int_0^{\bar{\vartheta}(\varphi)} p_{ij}(\vartheta)q_{ij}(\varphi)\sin\vartheta d\vartheta d\varphi \tag{23}$$

where (Gigante, 1989)

$$\bar{\vartheta}(\varphi) = \arccos\left\{\left[\frac{(n_1\cos\varphi + n_2\sin\varphi)^2}{(n_1\cos\varphi + n_2\sin\varphi)^2 + n_3^2}\right]^{1/2}\right\} \tag{24}$$

and n_i is the unit normal vector that identifies the "third" plane (Fig. 5), that is the plane that does not contain the z_3-axis.

The extension to the case of vertices having more than three tangent planes is straightforward.

In the general case, c_{ij} values can be computed by numerical integration of equation (23). Closed-form expressions for c_{ij} can be obtained when $\bar{\vartheta}(\varphi)$ = constant, that is where $\bar{\vartheta} = \pi$ (general edge) and $\bar{\vartheta} = \pi/2$ (a "quite" general vertex with three tangent planes). The corresponding expressions for elastic problems are reported in the Appendix.

Since the values of c_{ij} depend not only on the measure of the solid angle $\Omega(\mathbf{y})$ but also on the orientation of $\Omega(\mathbf{y})$, their values in the global reference system can be obtained from equation (23) through a simple tensor transformation.

4 Strongly Singular Integrals Over Internal Cells

In some important cases, such as inelastic problems, it is required to evaluate domain integrals defined in the Cauchy principal value sense.

As a matter of fact, for the stepwise solution of these nonlinear problems it is necessary to augment the boundary integral equation by equations in the form of equation (5), where the volume integral has a kernel function B_{ijkl} with a singularity of order $1/r^2$ for two-dimensional and axisymmetric problems, and of order $1/r^3$, for three-dimensional problems.

In equation (5) it is implicit in the definition of the free terms E_{ijkl} (Bui, 1978) that the principal value of the integral

$$\int_V B_{ijkl}(\mathbf{y},\mathbf{x})\dot{\sigma}^o{}_{kl}(\mathbf{x})dV(\mathbf{x}) \tag{25}$$

must be taken (e.g., Telles, 1983).

Taking elastoplasticity as an example, the kernel functions that appears in equation (25) are of the following form (e.g., Brebbia et al., 1984), p. 262)

$$B_{ijkl} = \frac{1}{4a\pi(1-\nu)r^b}\Big\{(1-2\nu)[\delta_{ik}\delta_{lj} + \delta_{jk}\delta_{li} - \delta_{ij}\delta_{lk} + b\delta_{ij}r_{,k}r_{,l}] + b[\delta_{li}r_{,j}r_{,k} + \delta_{jk}r_{,l}r_{,i} + \delta_{ik}r_{,l}r_{,j} + \delta_{jl}r_{,i}r_{,k}) + b\delta_{kl}r_{,i}r_{,j} - bcr_{,i}r_{,j}r_{,k}r_{,l}\Big\} \tag{26}$$

where $a = 2, 1$; $b = 3, 2$; $c = 5, 4$ for three-dimensional and plane-strain problems, respectively.

However, although the specific expression may change when considering different problems, in the present analysis it is only relevant that all such kernels are made up of the singular term $1/r^b$ multiplied by either constants or terms in the form of $r_{,i}$.

Of course, only that part of the domain V in which nonzero inelastic strains are expected to develop has to be discretized using internal cells.

For the definition of the CPV integral I_V only the internal region V_p corresponding to all adjacent cells $V_p{}^m$ connected to the singular point $\mathbf{y}$ needs to be considered

$$\begin{aligned} I_V &= \int_{V_p} B_{ijkl}(\mathbf{y},\mathbf{x})M^a(\xi(\mathbf{x}))dV(\mathbf{x}) \\ &:= \lim_{\epsilon\to 0}\left\{\int_{V_p - e_\epsilon} B_{ijkl}(\mathbf{y},\mathbf{x})M^a(\xi(\mathbf{x}))dV(\mathbf{x})\right\} \\ &= \lim_{\epsilon\to 0}\left\{\sum_m \int_{V_p{}^m - e_\epsilon^m} B_{ijkl}(\mathbf{y},\mathbf{x})M^a(\xi(\mathbf{x}))dV(\mathbf{x})\right\} \\ &= \lim_{\epsilon\to 0}\left\{\sum_m \int_{R^m - \sigma_\epsilon^m} B_{ijkl}(\mathbf{y},\mathbf{x}(\xi))M^a(\xi)J^m(\xi)d\xi\right\} \end{aligned} \tag{27}$$

where $M^a(\xi)$ collects all shape functions that equal 1 at $\mathbf{y}$. In equation (27) each cell V_p^m has been mapped, as usual in the BEM, in a region R^m of standard shape. Accordingly, each part e_ϵ^m of the vanishing sphere (circle in two dimensions) e_ϵ centered at $\mathbf{y}$ corresponds in the parameter ξ-space to a region σ_ϵ^m of distorted shape.

For *any kind* of interpolation functions $M^a(\xi)$ or cell shapes, it is possible to apply to CPV integral in equation (27) a procedure similar to the one previously illustrated for surface singular integrals in three dimensions.

The method is presented for both two-dimensional (or axisymmetric) and three-dimensional problems.

4.1 Two-Dimensional Internal Cells (Plane and Axisymmetric Problems. Two-dimensional internal cells, either quadrilateral or triangular, are very similar to three-dimensional boundary elements. Therefore, in the parameter plane (ξ_1, ξ_2) they result in regions like in Fig. 3. Further, polar coordinates (ρ, ϑ) centered at the singular point η (image of $\mathbf{y}$) can be defined as shown in Fig. 4.

As an important consequence, Taylor expansions (14) for r^2 and equation (15) for $r_{,i}$ are also valid for plane cells, provided the index k now ranges from 1 to 2. The same observation also applies to equation (19) that defines the shape of σ_ϵ^m.

Let $G^m{}_{ijkl}(\rho, \vartheta) = B_{ijkl}(\mathbf{y}, \mathbf{x}(\xi(\rho, \vartheta)))\, M^a(\xi(\rho, \vartheta))\, J^m(\xi(\rho, \vartheta))\rho$, that is the integrand function in equation (27) after the introduction of polar coordinates; from equations (14) and (15) and the expression (26) it is now easy to establish formulae of the form

$$G^m{}_{ijkl}(\rho,\vartheta) = \frac{1}{\rho}\{g^m{}_{ijkl}(\vartheta) + 0(\rho)\} \tag{28}$$

that gives the asymptotic expression of the integrand function in polar coordinates in the parameter plane.

Therefore, the CPV integral equation (27) can be expressed in terms of *regular* integrals by the formula

Downloaded 03 May 2010 to 171.66.16.244. Redistribution subject to ASME license or copyright; see http://www.asme.org/terms/Terms_Use.cfm

$$I_V=\left\{\sum_m\int_{\vartheta_1 m}^{\vartheta_2 m}\int_0^{\bar\rho^m(\vartheta)}\left[G^m{}_{ijkl}(\rho,\vartheta)-\frac{g^m{}_{ijkl}(\vartheta)}{\rho}\right]d\rho d\vartheta+\right.$$
$$\left.+\int_{\vartheta_1 m}^{\vartheta_2 m} g^m{}_{ijkl}(\vartheta)\ln\left[\frac{\bar\rho^m(\vartheta)}{\beta^m(\vartheta)}\right]d\vartheta\right\} \tag{29}$$

where the same basic procedure used for surface integrals has been applied.

All the observations made for expression (20*e*) also apply to equation (29). However, it is worth noting the full generality of expression (29), as it is valid for cells of any order, and also its simplicity as it requires only standard operations in the BEM. It is also worth remembering that no approximations have been introduced so far.

The actual computation can be performed by employing, e.g., Gauss-Legendre quadrature formulae.

4.2 Three-Dimensional Internal Cells. The above treatment can be entirely extended to three-dimensional internal cells. The main difference is the introduction of spherical coordinates $(\rho, \vartheta, \varphi)$, still centered at η image of $\mathbf{y}$, in place of polar ones. Therefore, in each R^m

$$\xi_1=\eta_1+\rho\sin\vartheta\cos\varphi$$
$$\xi_2=\eta_2+\rho\sin\vartheta\sin\varphi$$
$$\xi_3=\eta_3+\rho\cos\vartheta \tag{30}$$

thus having $d\xi_1 d\xi_2 d\xi_3 = \rho^2\sin\vartheta d\rho d\vartheta$.

Similarly to equation (13), let us define

$$A_i(\vartheta,\varphi)=$$
$$\left[\left.\frac{\partial x_i}{\partial\xi_1}\right|_{\xi=\eta}\sin\vartheta\cos\varphi+\left.\frac{\partial x_i}{\partial\xi_2}\right|_{\xi=\eta}\sin\vartheta\sin\varphi+\left.\frac{\partial x_i}{\partial\xi_3}\right|_{\xi=\eta}\cos\vartheta\right]$$
$$i=1,2,3 \tag{31a}$$

and

$$A(\vartheta,\varphi)=\left\{\sum_{i=1}^{3}[A_i(\vartheta,\varphi)]^2\right\}^{1/2} \tag{31b}$$

which allows us to write

$$x_i-y_i=\rho A_i(\vartheta,\varphi)+0(\rho^2),\ i=1,2,3. \tag{32}$$

Therefore, a formula formally equivalent to equation (15) holds for each $r_{,i}$, while

$$r^3(\vartheta,\varphi)=\rho^3A^3(\vartheta,\varphi)+0(\rho^4). \tag{33}$$

Taking into consideration expression (26), it is now easy to obtain formulae formally equivalent to equation (28), that is

$$G^m{}_{ijkl}(\rho,\vartheta,\varphi)=\frac{1}{\rho}\{g^m{}_{ijkl}(\vartheta,\varphi)+0(\rho)\} \tag{34}$$

where $G^m{}_{ijkl}(\rho,\vartheta,\varphi)=B_{ijkl}(\mathbf{y},\mathbf{x}(\xi(\rho,\vartheta,\varphi)))\,M^a(\xi(\rho,\vartheta,\varphi))\,J^m(\xi(\rho,\vartheta,\varphi))\sin\vartheta\,\rho^2$ represents the integrand function after the introduction of spherical coordinates in the parameter space (ξ_1, ξ_2, ξ_3).

In three-dimensional problems, each σ_ϵ^m in equation (27) is part of an *ellipsoid* centered at η and whose equation reads $\rho=\alpha(\epsilon,\vartheta,\varphi)=\epsilon\beta(\vartheta,\varphi)+0(\epsilon^2)$ and is formally equivalent to equation (19).

The final results for three-dimensional CPV integrals over hexahedral (higher-order) cells reads

$$I_V=\left\{\sum_m\int_{\vartheta_1 m}^{\vartheta_2 m}\int_{\varphi_1 m}^{\varphi_2 m}\int_0^{\bar\rho^m(\vartheta,\varphi)}\left[G^m{}_{ijkl}(\rho,\vartheta,\varphi)-\frac{g^m{}_{ijkl}(\vartheta,\varphi)}{\rho}\right]d\rho d\vartheta d\varphi+\right.$$
$$\left.+\int_{\vartheta_1 m}^{\vartheta_2 m}\int_{\varphi_1 m}^{\varphi_2 m} g^m{}_{ijkl}(\vartheta,\varphi)\ln\left[\frac{\bar\rho^m(\vartheta,\varphi)}{\beta^m(\vartheta,\varphi)}\right]d\vartheta d\varphi\right\} \tag{35}$$

where all functions are known in closed form. A similar expression can be obtained for tetrahedral cells.

All the observations made on the final formula equation (29) for plane cells also apply to relation (35) for volume cells.

To the authors' best knowledge, expressions (29) and (35) are so far the first rigorous answer to the problem of the direct evaluation of CPV integrals over (higher-order) internal cells.

A comparison between expressions (29) and (35) reveals that they have the same formal structure, thus showing that the extension from two to three geometrical dimensions does not involve special problems. On the other hand, a comparison between expression (20*e*) for surface integrals and the corresponding formula for (one-dimensional) contour integrals (i.e., expression (13) in Guiggiani and Casalini (1987)) immediately shows that the former cannot be regarded as a simple extension of the latter. As stated by Mikhlin (1965), indeed, the number of independent variables is not irrelevant in this matter, and a distinction must be drawn between the case of one and several variables.

5 Numerical Examples

Two types of tests have been performed on the present method for the direct evaluation of CPV integrals. Eight-node quadrilateral surface elements and internal cells were used because they have sufficiently high order to test in full generality all the aspects of the proposed approach.

All computations were performed in single-precision arithmetic (7-digit accuracy) on a MICROVAX II.

5.1 Plane Region (Two-Dimensional Internal Cells). The first test was carried out on a plane region V in the form of a square ($V=[-1,1]\times[-1,1]$). The region was represented by four eight-node *distorted* cells, thus resembling part of a two-dimensional body covered by higher-order internal cells. The singular point $\mathbf{y}$ was located at the node connected to all four cells. The coordinates of the singular point in the four cases of Fig. 6 were chosen as to have very graded meshes

Case (a): $\mathbf{y}=(0.6, 0)$;

Case (b): $\mathbf{y}=(0.6, 0.5)$;

Cases (c) and (d): $\mathbf{y}=(-0.3, 0.2)$, but with different meshes.

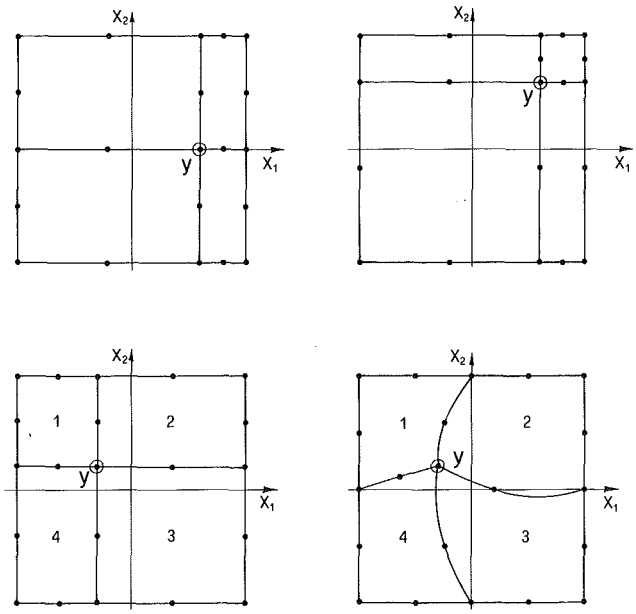


Fig. 6 Distorted meshes for testing the integration procedure; (*a*) y = (0.6, 0), (*b*) y = (0.6, 0.5), (*c*) and (*d*) y = (−0.3, 0.2)

Downloaded 03 May 2010 to 171.66.16.244. Redistribution subject to ASME license or copyright; see http://www.asme.org/terms/Terms_Use.cfm

Table 1 Numerical results for the CPV integral of equation (36) obtained with three values of the order n for the four cases of Fig. 6

Order n	Case (a) $\mathbf{y}=(0.6,0)$	Case (b) $\mathbf{y}=(0.6,0.5)$	Case (c) $\mathbf{y}=(-0.3,0.2)$	Case (d) $\mathbf{y}=(-0.3,0.2)$
4	−2.112146	−1.935989	0.8789888	0.8850154
6	−2.114198	−1.935728	0.8790181	0.8790102
8	−2.114175	−1.935709	0.8790181	0.8790138
Exact	−2.114175	−1.935711	0.8790179	0.8790179

Table 2 Numerical values (n = 8) of both double and one-dimensional regular integrals on each element in the final formula (36) for CPV integral for Cases (c) and (d) of Fig. 6

Element		Case (c)	Case (d)
1	2D	0.0	0.0216495
	1D	0.2020145	0.2722356
2	2D	0.0	0.4726095
	1D	0.1948843	−0.7523720
3	2D	0.0	0.7437897
	1D	0.3564001	0.0880795
4	2D	0.0	0.0624216
	1D	0.1257192	−0.0293996
Total		0.8790181	0.8790138

Without loss of generality the following Cauchy principal value was considered

$$I_V = \int_V \frac{1}{r^2}\frac{x_1 - y_1}{r}\, dx_1 dx_2 = \int_V \frac{r_{,1}}{r^2}\, dx_1 dx_2. \qquad (36)$$

The CPV integral equation (36) was chosen for the purpose of comparisons since it can be integrated in closed form as shown in Theocaris et al. (1980).

Notice, however, that the integrand function in equation (36) shows all the relevant features of any CPV integral arising in the BEM. Therefore, notwithstanding the apparent simplicity, this example provides a significant test for the method under investigation.

Each quadrilateral cell was mapped onto a $[-1, 1] \times [-1, 1]$ square, as usually done in the BEM. Similarly to expression (16), in each square in the plane of intrinsic coordinates the asymptotic expression of the integrand function in equation (36) was readily obtained by means of formulae like equations (14) and (15) (with the index k now ranging from 1 to 2). Moreover, on each local square, the image of the corresponding part of the vanishing neighborhood had an equation $\rho = \epsilon\, \beta\, (\vartheta)$ with an explicit expression like equation (19).

A final formula similar to equation (20*e*) (or equation (29)) was easily established and, therefore, the actual computation of the original two-dimensional CPV integral equation (36) was reduced to the evaluation of an element-by-element sum of regular integrals.

Each cell was divided into two triangular subcells and the corresponding two-dimensional regular integrals were evaluated by $n \times n$ Gauss-Legendre product rules. The same order n was also used in the Gauss formula for the one-dimensional integral.

Table 1 gives the numerical results obtained for the four cases shown in Fig. 6 and n = 4, 6, and 8, together with the corresponding exact values. Notice that order 6 is sufficient to have an accuracy of five significant digits (error ≤ 0.001 percent), thus confirming the effectiveness of the proposed approach.

Examples (*c*) and (*d*) in Fig. 6 have the singular point $\mathbf{y}$ in the same position but different meshes. Table 2 gives the numerical values (n = 8) of the double and one-dimensional regular integrals on each cell for both examples. It is worth noting that the single contributions are very different in the two cases. Nevertheless, the final results show almost the same accuracy. This result confirms that the proposed method for evaluating CPV integrals does provide the correct answer independently of the mesh employed.

Table 2 also shows that the contribution of the one-dimensional integrals is not negligible, in general. Indeed, when dealing with CPV integrals it is not sufficient to subtract out the singularity. Also the distortion due to the mapping in the shape of the image of the vanishing neighborhood must be taken into account through $\beta(\vartheta)$.

5.2 Surface Elements in Three Dimensions (Elastic Problems). As a more practical example, let us consider a three-dimensional body. Geometry and discretization are shown in Fig. 7. This example was chosen because there are distorted surface elements.

For the purpose of comparison, the body was supposed to be elastic (Young modulus = $2.0\ 10^6$, Poisson ratio = 0.3). As is well known, in this case the sums of CPV surface integrals and free-term coefficients (equation (4)) can be evaluated also in an indirect manner by using the rigid-body motion technique.

Results are reported for the singular point $\mathbf{y}$ located at three different nodes, namely nodes 1, 2, and 3 in Fig. 7. Notice that node 1 is in a smooth boundary point, node 2 is on an edge (two tangent planes), and node 3 is in a vertex (three tangent planes). In each case, integration referred to all adjacent elements connected to $\mathbf{y}$ (see equation (4)).

The direct evaluation of CPV surface integrals was performed using formula (20*e*). Gauss quadrature formulae of order 6 × 6 and 6 were used. Only true singular integrals were considered, that is those with kernels with different indices. The free-term coefficients c_{ij} were computed accordingly to formula (23).

The results obtained with both the (classical) indirect and the (new) direct approaches are displayed in Tables 3–5 for each case. The comparison shows that the results agree at least within 3 significant digits.

Direct computations of the CPV integrals with Gauss formulae of higher order (up to 12) were also done for a better check on the actual accuracy. It was found that with formulae of order 6 × 6 and 6 (as in Tables 3–5) an accuracy of at least six significant digits was always achieved. Therefore, the slight discrepancies in Tables 3–5 are probably due to numerical errors in the indirect (rigid-body motion) approach. It is believed that the direct approach provides not only a method of full generality, but also of higher reliability as the accuracy can be checked more easily.

6 Conclusions

In this paper a new method for the evaluation of Cauchy principal value integrals in the boundary element method has been presented in full detail. The procedure has general validity. It can be applied to singular integrals defined over surface elements and internal cells of any type and order. Therefore, advanced BEM implementations (even with hierarchical shape functions) can now be easily and correctly developed for a larger class of problems of applied mechanics.

The proposed approach basically reduces any CPV integral to the computation of a sum of regular integrals, each one relative to one element (or cell) at a time, and it simply requires

Downloaded 03 May 2010 to 171.66.16.244. Redistribution subject to ASME license or copyright; see http://www.asme.org/terms/Terms_Use.cfm

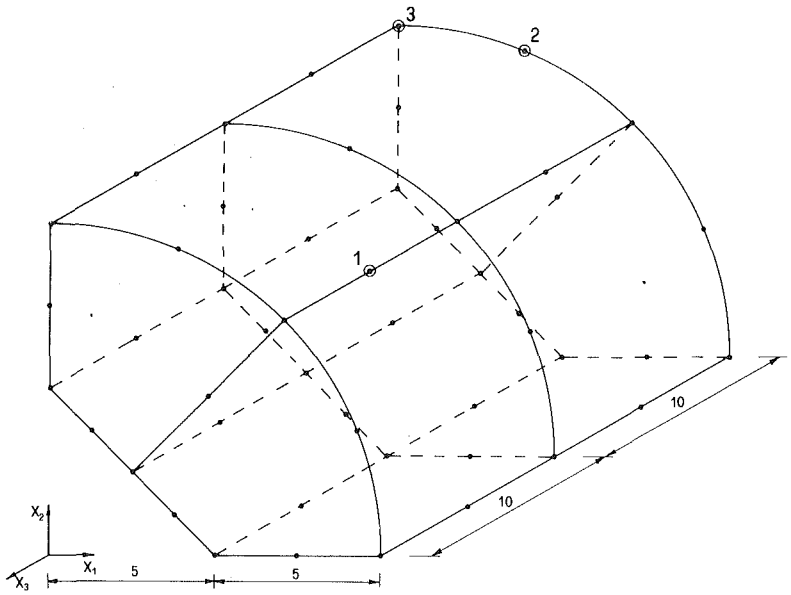


Fig. 7 Three-dimensional body: geometry and discretization

Table 3 Singular point on a *smooth* boundary point (node 1 in Fig. 7): numerical results for CPV integrals on surface elements and comparison with classical rigid-body motion technique

Kernel	CPV integral	+	Free-term	=	Total	Rigid-body motion
T_{12}	0.0360954		0.0		0.0360954	0.0360773
T_{13}	0.0		0.0		0.0	0.0000062
T_{23}	0.0		0.0		0.0	−0.0000059
T_{21}	0.0360954		0.0		0.0360954	0.0361121
T_{31}	0.0		0.0		0.0	−0.0000008
T_{32}	0.0		0.0		0.0	−0.0000022

Table 4 Singular point on an *edge* (node 2 in Fig. 7): numerical results for CPV integrals on surface elements and comparison with classical rigid-body motion technique

Kernel	CPV integral	+	Free-term	=	Total	Rigid-body motion
T_{12}	0.0100554		0.0		0.0100554	0.0100704
T_{13}	−0.0055337		−0.0435043		−0.0490380	−0.0490610
T_{23}	−0.0132945		−0.1050285		−0.1183230	−0.1183140
T_{21}	0.0100548		0.0		0.0100548	0.0100645
T_{31}	0.0062665		−0.0435043		0.0372378	−0.0372365
T_{32}	0.0150633		0.1050285		−0.0899652	−0.0898988

Table 5 Singular point on a *vertex* (node 3 in Fig. 7): numerical results for CPV integrals on surface elements and comparison with classical rigid-body motion technique

Kernel	CPV integral	+	Free-term	=	Total	Rigid-body motion
T_{12}	0.0069475		−0.0568410		−0.0498935	−0.0498569
T_{13}	0.0014441		0.0568410		0.0582851	0.0582699
T_{23}	−0.0105778		−0.0568410		−0.0674188	−0.0674180
T_{21}	−0.0080940		−0.0568410		−0.0649350	−0.0649039
T_{31}	−0.0028251		0.0568410		0.0540159	0.0540012
T_{32}	0.0098415		−0.0568410		−0.0469995	−0.0469672

standard operations in the BEM. The numerical tests have shown that the actual computation can be performed by means of Gaussian quadrature formulae of low order.

Full details for the direct computation of free-term coefficients in the general case have been also provided.

Acknowledgments

The financial support of the Italian Ministry of Education (M.P.I.) and National Research Council (C.N.R.) is gratefully acknowledged. M. G. also acknowledges receipt of an AGARD travel grant. The authors wish to thank Drs. M. Bonnet, P. Casalini, and W. S. Hall for their valuable comments on the manuscript.

References

Aliabadi, M. H., Hall, W. S., and Phemister, T. G., 1985, "Taylor Expansions for Singular Kernels in the Boundary Element Method," *International Journal for Numerical Methods in Engineering*, Vol. 21, pp. 2221–2236.

Bonnet, M., 1986, "Méthodes des Equations Intégrales Régularisées en Elastodynamique," Ph.D. Thesis, Ecole Nat. des Ponts et Chaussées.

Bonnet, M., 1989, "Regular Boundary Integral Equations for Three-Dimensional Finite or Infinite Bodies With or Without Curved Cracks in Elastodynamics," *Boundary Element Techniques: Applications in Engineering*, C. A. Brebbia and N. Zamani, eds., Computational Mechanics Publications, Southampton, U.K, pp. 171–188.

Brebbia, C. A., Telles, J. C. F., and Wrobel, L. C.,. 1984, *Boundary Element Techniques*, Springer-Verlag, Berlin.

Bui, H. D., 1978, "Some Remarks About the Formulation of Three-Dimensional Thermoelastoplastic Problems by Integral Equations," *International Journal of Solids and Structures*, Vol. 14, pp. 935–939.

Bui, H. D., Loret, B., and Bonnet, M., 1985, "Régularisation des Équations Intégrales de l'élastostatique et de l'élastodynamique," *Compte Rendus Acad. Sci. Paris*, t. 300, Série II, no. 14, pp. 633–636.

Casalini, P., and Guiggiani, M., 1988, "New Developments in the Boundary Element Method for Plane and Axisymmetric Elasticity," *Advanced Boundary Element Methods*, T. A. Cruse, ed., Springer-Verlag, Berlin, pp. 81–91.

Cruse, T. A., 1987, "Recent Advances in Boundary Element Analysis Method," *Computer Methods in Applied Mechanics and Engineering*, Vol. 62, pp. 227–244.

Cruse, T. A., 1988, *Boundary Element Analysis in Computational Fracture Mechanics*, Kluwer Academic Publishers, Dordrecht.

Gigante, A., 1989, "Sviluppo del Metodo Degli Elementi al Contorno Tramite la Definizione di Nuove Tecniche per la Valutazione di Integrali a Valor Principale," (in Italian), Thesis, Universitá degli Studi di Pisa, Italy.

Guiggiani, M., 1988, letter to the editor, *International Journal for Numerical Methods in Engineering*, Vol. 26, pp. 1683–1684.

Guiggiani, M., 1990, "The Evaluation of Cauchy Principal Value Integrals in the Boundary Element Method—A Review," *Computers and Mathematics with Applications*, Special Issue on BIEM/BEM, in press.

Guiggiani, M., and Casalini, P., 1987, "Direct Computation of Cauchy Principal Value Integrals in Advanced Boundary Elements," *International Journal for Numerical Methods in Engineering*, Vol. 24, pp. 1711–1720.

Hartmann, F., 1980, "Computing C-Matrix in Non-Smooth Boundary Points," *New Developments in Boundary Element Methods*, C. A. Brebbia, ed., Butterworths, London, pp. 367–379.

Hartmann, F., 1981, "The Somigliana Identity on Piecewise Smooth Surfaces," *J. of Elasticity*, Vol. 11, pp. 403–423.

Lachat, J. C., and Watson, J. O., 1976, "Effective Numerical Treatment of Boundary Integral Equations: A Formulation for Three-Dimensional Elasto-

Downloaded 03 May 2010 to 171.66.16.244. Redistribution subject to ASME license or copyright; see http://www.asme.org/terms/Terms_Use.cfm

statics," *International Journal for Numerical Methods in Engineering*, Vol. 10, pp. 991–1005.

Matsumoto, T., and Yuuki, R., 1988, "Accurate Boundary Element Analysis of Two-dimensional Elasto-Plastic Problems," *Boundary Element Methods in Applied Mechanics*, M. Tanaka and T. A. Cruse, eds., Pergamon Press, Oxford, pp. 205–214.

Mikhlin, S. G., 1965, *Multidimensional Singular Integrals and Integral Equations*, Pergamon Press, Oxford.

Mukherjee, S., and Chandra, A., 1988, "A Boundary Element Formulation for Design Sensitivities in Materially Nonlinear Problems," *Boundary Element Methods in Applied Mechanics*, M. Tanaka and T. A. Cruse, eds., Pergamon Press, Oxford.

Nishimura, N., and Kobayashi, S., 1989, "A Boundary Integral Equation Method for Consolidation Problems," *International Journal of Solids and Structures*, Vol. 25, pp. 1–21.

Okada, H., Rajiyah, H., and Atluri, S. N., 1988, "A Novel Displacement Gradient Boundary Element Method for Elastic Stress Analysis With High Accuracy," ASME JOURNAL OF APPLIED MECHANICS, Vol. 55, pp. 786–794.

Okada, H., Rajiyah, H., and Atluri, S. N., 1989, "Non-Hyper-Singular Integral-Representations for Velocity (Displacement) Gradients in Elastic/Plastic Solids (Small or Finite Deformations)," *Computational Mechanics*, Vol. 4, pp. 165–175.

Parreira, P., and Guiggiani, M., 1989, "On the Implementation of the Galerkin Approach in the Boundary Element Method," *Computers and Structures*, Vol. 33, pp. 269–279.

Rizzo, F. J., and Shippy, D. J., 1986, "A Boundary Element Method for Axisymmetric Elastic Bodies," *Developments in Boundary Element Methods-4*, P. K. Banerjee and J. O. Watson, eds., Elsevier Applied Science Publishers, Barking, Essex, England, pp. 67–90.

Rizzo, F. K., Shippy, D. J., and Rezayat, M., 1985, "A Boundary Integral Equation Method for Radiation and Scattering of Elastic Waves in Three Dimensions," *International Journal for Numerical Methods in Engineering*, Vol. 21, pp. 115–129.

Sarihan, V., and Mukherjee, S., 1982, "Axisymmetric Viscoplastic Deformation by the Boundary Element Method," *International Journal of Solids and Structures*, Vol. 18, pp. 1113–1128.

Telles, J. C. F., 1983, *The Boundary Element Method Applied to Inelastic Problems*, Springer-Verlag, Berlin.

Telles, J. C. F., and Brebbia, C. A., 1979, "On the Application of the Boundary Element Method to Plasticity," *Applied Mathematical Modelling*, Vol. 3, pp. 466–470.

Telles, J. C. F., and Brebbia, C. A., 1981, "The Boundary Element Method in Plasticity," *Applied Mathematical Modelling*, Vol. 5, pp. 275–281.

Theocaris, P. S., Ioakimidis, N. I., and Kazantzakis, J. G., 1980, "On the Numerical Evaluation of Two-Dimensional Principal Value Integrals," *International Journal for Numerical Methods in Engineering*, Vol. 15, pp. 629–634.

Zhang, Ch., and Achenbach, J. D., 1989, "A New Boundary Integral Equation Formulation for Elastodynamic and Elastostatic Crack Analysis," ASME JOURNAL OF APPLIED MECHANICS, Vol. 56, pp. 284–290.

APPENDIX

Free-Term Coefficients in Some Particular Cases

Referring to Fig. 5, there are two important cases in which $\bar{\vartheta}(\varphi) = \text{constant}$. More precisely, when $\vartheta = \pi$, that is whenever the singular point **y** lies on an edge (two tangent planes), and when $\vartheta = \pi/2$, that is when **y** lies on a vertex with one plane normal to the other two. In these cases, often encountered in practical calculations, closed-form expressions for the free-term coefficients $c_{ij}(\mathbf{y})$ can be obtained from equation (23).

As an example, the c_{ij} coefficients for three-dimensional elastic (static or time-harmonic) problems are reported

$$c_{11} = C\left\{\left(\frac{\varphi_2-\varphi_1}{2} + \frac{\sin(2\varphi_2)-\sin(2\varphi_1)}{4}\right)(2-3\cos\bar{\vartheta}+\cos^3\bar{\vartheta}) + a(\varphi_2-\varphi_1)(1-\cos\bar{\vartheta})\right\}$$

$$c_{22} = C\left\{\left(\frac{\varphi_2-\varphi_1}{2} - \frac{\sin(2\varphi_2)-\sin(2\varphi_1)}{4}\right)(2-3\cos\bar{\vartheta}+\cos^3\bar{\vartheta}) + a(\varphi_2-\varphi_1)(1-\cos\bar{\vartheta})\right\};$$

$$c_{33} = C\{(\varphi_2-\varphi_1)(1-\cos^3\bar{\vartheta}) + a(\varphi_2-\varphi_1)(1-\cos\bar{\vartheta})\};$$

$$c_{12} = c_{21} = C\left(\frac{\sin^2\varphi_2-\sin^2\varphi_1}{2}\right)(2-3\cos\bar{\vartheta}+\cos\bar{\vartheta}));$$

$$c_{13} = c_{31} = C(\sin\varphi_2-\sin\varphi_1)\sin^3\bar{\vartheta};$$

$$c_{23} = c_{32} = C(\cos\varphi_1-\cos\varphi_2)\sin^3\bar{\vartheta};$$

where

$$C = \frac{1}{8\pi(1-\nu)};\ \text{and}\ a = (1-2\nu).$$

Downloaded 03 May 2010 to 171.66.16.244. Redistribution subject to ASME license or copyright; see http://www.asme.org/terms/Terms_Use.cfm

Thermal Stresses in an Anisotropic Plate Disturbed by an Insulated Elliptic Hole or Crack

Chyanbin Hwu
Associate Professor,
Institute of Aeronautics and Astronautics,
National Cheng Kung University,
Tainan, Taiwan, 70101

The solutions presented in the literature for the thermal stresses under uniform heat flow disturbed by an insulated elliptic hole are for an isotropic or orthotropic medium. However, the solution for the latter cannot be specialized to the former due to the repeated eigenvalue of the elastic constants of isotropic materials, which also restricts the application to other degenerate materials. Based upon the Stroh formalism, a simple and compact version of general solutions for plane anisotropic thermoelasticity is given in this paper. Some new identities concerning the eigenvalues and eigenvectors are developed, which are the keys for the present solutions to be valid in any kind of anisotropic materials including degenerate materials. The hoop stress around the elliptic hole is given in an explicit form. The effect of geometry, heat flow, elastic and thermal anisotropy, and heat conductivity can then be studied. The solutions for the crack problem are obtained by setting the minor axis of the ellipse approach to zero. The stress intensity factors, crack opening displacement, and strain energy release rate are expressed in terms of the fundamental elasticity matrix $\mathbf{L}$ *and thermal vector* $\tilde{\gamma}_2^*$ *introduced in this paper. The validity of the fully open crack assumption is also discussed.*

1 Introduction

Thermal stress concentration occurs when a uniform heat flow is disturbed by a hole. As the hole reduces to a crack, the stresses induced by heat flow become singular at the tips of crack, which is the same as isothermal condition. Of various holes the elliptic shape has evoked the most interest among researchers for isothermal problems because of its flexibility to include the other special shapes such as circles or cracks. To the author's knowledge, however, very little work has been done for the thermal stresses disturbed by elliptic holes in materials of general anisotropy. Florence and Goodier (1959, 1960) studied this problem for an isotropic medium containing a circular or ovaloid hole by the method of Muskhelishvili (1953). Based upon the complex variable technique developed by Green and Zerna (1954) and extended to steady-state thermoelasticity, Chen (1967) studied the orthotropic medium with a circular or elliptic hole, and obtained a complex form solution for the hoop stress around the hole.

Unlike holes, cracks receive relatively higher concern in the literature due to the mathematical feasibility. For the flaw-induced thermal stresses in the infinite isotropic regions, solutions have been obtained by Olesiak and Sneddon (1960), Sih (1962), and Florence and Goodier (1963). Applying the equations for the distribution of thermal stresses in an anisotropic elastic half-space (Clements, 1973), Atkinson and Clements (1977) gave a solution for the two-dimensional Griffith crack obstructing a uniform heat flux in a general anisotropic medium. Using the techniques of Fourier transforms and multiple integrations, Tsai (1983, 1984) studied the crack embedded in a transversely isotropic or orthotropic material. Recently, Sturla and Barber (1988) reconsidered the same problem in general anisotropic materials by using a Green's function formulation, and extended their method to the case where the crack is partially close.

For plane deformations in a general anisotropic material, the most convenient and powerful approach appears to be that introduced by Stroh (1958). The improvement and maturity of Stroh formulation relies on the latter development of identities among the elasticity constants (Barnett and Lothe, 1973; Chadwick and Smith, 1977; Ting, 1988a; Ting and Hwu, 1988), which makes the mathematical formulation and manipulation simpler and easier. Otherwise, a complicated form solution will be obtained or an intractable mathematical problem will be left. The success of this improvement can be seen in various anisotropic elasticity problems, e.g., Ting, 1986; Hwu and Ting, 1989a, 1989b; Li and Ting, 1989; Hwu, 1990, etc. An extended version dealing with thermoelasticity has been given by Wu (1984), in which special attentions were given to the cases where the heat eigenvalue becomes equal to a single or double elasticity eigenvalue.

Contributed by the Applied Mechanics Division of THE AMERICAN SOCIETY OF MECHANICAL ENGINEERS for presentation at the Winter Annual Meeting, Dallas, Texas, Nov. 25–30, 1990.

Discussion on this paper should be addressed to the Technical Editor, Leon M. Keer, The Technological Institute, Northwestern University, Evanston, IL 60208; and will be accepted until two months after final publication of the paper itself in the JOURNAL OF APPLIED MECHANICS. Manuscript received by the ASME Applied Mechanics Division, Sept. 1989; final revision, Feb. 1990.

Paper No. 90-WA/APM-29.

Copyright © 1990 by ASME
Downloaded 03 May 2010 to 171.66.16.244. Redistribution subject to ASME license or copyright; see http://www.asme.org/terms/Terms_Use.cfm

Based upon the Stroh formalism in anisotropic elasticity (Hwu, 1990), a simple and compact version of general solutions for plane anisotropic thermoelasticity is presented in this paper. By applying this newly derived solution and using the technique of conformal mapping, the stresses, displacements, heat flux, and temperature in the whole domain disturbed by an elliptic hole can be obtained. The hoop stress is then obtained in an explicit form through the use of identities. If the minor axis of the ellipse is chosen to be zero, we get the solution for the crack problem. The crack opening displacement, stress intensity factors, and energy release rate can also be obtained in an explicit form. The effect of geometry, heat flow, elastic and thermal anisotropy, and heat conductivity on the stress concentration (or stress intensity) can then be studied through this explicit form solution.

The explicit form solutions shown in this paper do not contain the complex eigenvectors. Hence, the solutions are valid for degenerate materials and the problem of repeated eigenvalues considered by Wu (1984) is circumvented. An example has been given for the isotropic materials for which all the elasticity eigenvalues and heat eigenvalues are equal to $\pm i$. The comparison with solutions given in the literature (Florence and Goodier, 1960; Sih, 1962) shows that the solutions presented here are exact, simple, and general.

2 Basic Equations for Plane Anisotropic Thermoelasticity

In a fixed rectangular coordinate system x_i, $i = 1, 2, 3$, let u_i, σ_{ij}, ϵ_{ij}, T, and h_i be, respectively, the displacement, stress, strain, temperature, and heat flux. The heat conduction, energy equation, strain displacement relation, constitutive law, and the equations of equilibrium for the uncoupled steady-state thermoelastic problems are (Nowacki, 1962)

$$h_i = -k_{ij}T_{,j}, \tag{1}$$

$$h_{i,i} = -k_{ij}T_{,ij} = 0, \tag{2}$$

$$\epsilon_{ij} = \frac{1}{2}(u_{i,j} + u_{j,i}), \tag{3}$$

$$\sigma_{ij} = C_{ijks}\epsilon_{ks} - \beta_{ij}T = C_{ijks}u_{k,s} - \beta_{ij}T, \tag{4}$$

$$\sigma_{ij,j} = C_{ijks}u_{k,sj} - \beta_{ij}T_{,j} = 0, \tag{5}$$

where repeated indices imply summation, a comma stands for differentiation, and C_{ijks}, k_{ij}, β_{ij} are the elastic constants, heat conduction coefficients, and thermal moduli, respectively. In general, C_{ijks} and β_{ij} are assumed to be symmetric, while k_{ij} need not to be symmetric for anisotropic materials. For two-dimensional problems, u_i and T are independent of x_3. The solutions to equation (2) may be expressed as (Clements, 1973; Wu, 1984)

$$T = 2\mathrm{Re}\{g'(z_t)\}, \tag{6}$$

$$z_t = x_1 + \tau x_2, \tag{7}$$

where Re stands for the real part, g is an arbitrary function and the prime(′) denotes differentiation with respect to its argument. τ is the heat eigenvalue with positive imaginary part of

$$k_{22}\tau^2 + (k_{12} + k_{21})\tau + k_{11} = 0. \tag{8}$$

Substituting equation (6) into equation (1), the distribution of heat flux can be written as

$$h_i = -2\mathrm{Re}\{(k_{i1} + \tau k_{i2})g''(z_t)\}. \tag{9}$$

By using equations (5) and (6), a general expression for the displacement components may be written in matrix notations as (Clements, 1973, Wu, 1984)

$$\mathbf{u} = \mathrm{Re}\left\{\sum_{\alpha=1}^{3} \mathbf{a}_\alpha f_\alpha(z_\alpha) + \mathbf{c}g(z_t)\right\}, \tag{10}$$

$$z_\alpha = x_1 + p_\alpha x_2, \ \alpha = 1, 2, 3, \tag{11}$$

where f is an arbitrary function, p_α, $\mathbf{a}_\alpha$ are the elasticity eigenvalues with positive imaginary part and the associated eigenvectors of

$$\left.\begin{aligned} \mathbf{D}(p)\mathbf{a} &= 0 \\ \mathbf{D}(p) &= \mathbf{Q} + p(\mathbf{R} + \mathbf{R}^T) + p^2\mathbf{T} \end{aligned}\right\}, \tag{12}$$

where the superscript T stands for the transpose and $\mathbf{Q}$, $\mathbf{R}$, $\mathbf{T}$ are 3×3 matrices given by

$$Q_{ik} = C_{i1k1}, \ R_{ik} = C_{i1k2}, \ T_{ik} = C_{i2k2}. \tag{13}$$

$\mathbf{c}$ is determined by

$$\mathbf{D}(\tau)\mathbf{c} = \beta_1 + \tau\beta_2, \tag{14}$$

$$\beta_1 = \begin{Bmatrix} \beta_{11} \\ \beta_{21} \\ \beta_{31} \end{Bmatrix}, \ \beta_2 \begin{Bmatrix} \beta_{12} \\ \beta_{22} \\ \beta_{32} \end{Bmatrix}. \tag{15}$$

Note that the general solution equation (10) is obtained under the assumption that $p_1 \neq p_2 \neq p_3 \neq \tau$. The special cases in which the heat eigenvalue τ becomes equal to a single or double elasticity eigenvalue, p_α, have been studied by Wu (1984). We hasten to add that the explicit form solutions presented in this paper do not contain the eigenvectors $\mathbf{a}_\alpha$ and $\mathbf{c}$. Hence, the solutions are valid for the special cases considered by Wu (1984).

The stress σ_{ij} obtained by substituting equations (6) and (10) into (4) can be written as

$$\sigma_{i1} = -\phi_{i,2}, \ \sigma_{i2} = \sigma_{i,1}, \ i = 1, 2, 3, \tag{16}$$

where ϕ is the stress function

$$\phi = 2\mathrm{Re}\left\{\sum_{\alpha=1}^{3} \mathbf{b}_\alpha f_\alpha(z_\alpha) + \mathbf{d}g(z_t)\right\}. \tag{17}$$

$\mathbf{b}$ and $\mathbf{d}$ are defined by

$$\mathbf{b} = (\mathbf{R}^T + p\mathbf{T})\mathbf{a} = -\frac{1}{p}(\mathbf{Q} + p\mathbf{R})\mathbf{a}, \tag{18}$$

$$\mathbf{d} = (\mathbf{R}^T + \tau\mathbf{T})\mathbf{c} - \beta_2 = -\frac{1}{\tau}(\mathbf{Q} + \tau\mathbf{R})\mathbf{c} + \frac{1}{\tau}\beta_1, \tag{19}$$

where the second equalities of equations (18) and (19) come from (12) and (14), respectively.

In many applications including the present one, the arbitrary function $f_\alpha(\alpha_\alpha)$ are chosen to be the same function form

$$f_\alpha(z_\alpha) = q_\alpha f(z_\alpha), \ \alpha \text{ not summed},$$

where q_α, $\alpha = 1, 2, 3$, are arbitrary complex constants. Introducing the diagonal matrix

$$\mathbf{F}(\mathbf{Z}) = \mathrm{diag}[f(z_1)\ f(z_2)\ f(z_3)] \tag{20}$$

and the 3×3 complex matrices

$$\mathbf{A} = [\mathbf{a}_1\ \mathbf{a}_2\ \mathbf{a}_3], \ \mathbf{B} = [\mathbf{b}_1\ \mathbf{b}_2\ \mathbf{b}_3], \tag{21}$$

the general solutions for the displacement components, $\mathbf{u}$, and stress function, ϕ, can be written as

$$\left.\begin{aligned} \mathbf{u} &= 2\mathrm{Re}\{\mathbf{A}\mathbf{F}(\mathbf{Z})\mathbf{q} + \mathbf{c}g(z_t)\}, \\ \phi &= 2\mathrm{Re}\{\mathbf{B}\mathbf{F}(\mathbf{Z})\mathbf{q} + \mathbf{d}g(z_t)\}, \end{aligned}\right. \tag{22}$$

in which $\mathbf{q}$ is the 3×1 matrix whose elements are q_α, $\alpha = 1, 2, 3$.

Equations (18) and (19) can be reconstructed into the following standard eigenrelations

$$\mathbf{N}\xi = p\xi, \tag{23}$$

$$\mathbf{N}\eta = \tau\eta + \gamma, \tag{24}$$

where

Downloaded 03 May 2010 to 171.66.16.244. Redistribution subject to ASME license or copyright; see http://www.asme.org/terms/Terms_Use.cfm

$$\mathbf{N}=\begin{bmatrix}\mathbf{N}_1 & \mathbf{N}_2\\ \mathbf{N}_3 & \mathbf{N}_1^T\end{bmatrix},\quad \xi=\begin{Bmatrix}\mathbf{a}\\ \mathbf{b}\end{Bmatrix},$$

$$\gamma=-\begin{bmatrix}\mathbf{0} & \mathbf{N}_2\\ \mathbf{I} & \mathbf{N}_1^T\end{bmatrix}\begin{Bmatrix}\beta_1\\ \beta_2\end{Bmatrix},\quad \eta=\begin{Bmatrix}\mathbf{c}\\ \mathbf{d}\end{Bmatrix} \tag{25}$$

$$\mathbf{N}_1=-\mathbf{T}^{-1}\mathbf{R}^T,\ \mathbf{N}_2=\mathbf{T}^{-1}=\mathbf{N}_2^T,$$
$$\mathbf{N}_3=\mathbf{R}\mathbf{T}^{-1}\mathbf{R}^T-Q=\mathbf{N}_3^T.$$

A generalized form of equations (23) and (24), which is related to the coordinate transformation and is useful for the development of identities, is written as (see Appendix)

$$\mathbf{N}(\omega)\xi=p(\omega)\xi, \tag{26}$$

$$\mathbf{N}(\omega)\eta(\omega)=\tau(\omega)\eta(\omega)+\gamma(\omega), \tag{27}$$

where

$$\eta(\omega)=\lambda(\omega)\eta,\ \lambda(\omega)=(\cos\omega+\tau\sin\omega). \tag{28}$$

The corresponding matrices $\mathbf{Q}(\omega)$, $\mathbf{R}(\omega)$, $\mathbf{T}(\omega)$, and $\beta_i(\omega)$ are defined by

$$Q_{ik}(\omega)=C_{ijks}n_jn_s,\ R_{ik}(\omega)=C_{ijks}n_jm_s,\ T_{ik}(\omega)=C_{ijks}m_jm_s, \tag{29}$$

$$\beta_{i1}(\omega)=\beta_{ij}n_j,\ \beta_{i2}(\omega)=\beta_{ij}m_j, \tag{30}$$

in which ω is an arbitrary real parameter and

$$n_i=(\cos\omega,\ \sin\omega,\ 0),\ m_i=(-\sin\omega,\ \cos\omega,\ 0). \tag{31}$$

$p(\omega)$ and $\tau(\omega)$ are related to p and τ by

$$p(\omega)=\frac{p\cos\omega-\sin\omega}{p\sin\omega+\cos\omega},\ \tau(\omega)=\frac{\tau\cos\omega-\sin\omega}{\tau\sin\omega+\cos\omega}. \tag{32}$$

Note that ξ in equation (26) is independent of ω, which has been shown by Chadwick and Smith (1977). However, $\eta(\omega)$ is related to η by equation (28) and is proved in the Appendix. When $\omega = 0$, equations (26) – (30) reduce to (23), (24), (13), and (15). By using equations (23) and (26), the following identities which will be used in this paper can be derived (Ting, 1988a, 1988b)

$$2\mathbf{BP}(\theta)\mathbf{A}^T=\mathbf{N}_1^T(\theta)-i[\mathbf{N}_1^T(\theta)\mathbf{S}^T+\mathbf{N}_3(\theta)\mathbf{H}],$$
$$2\mathbf{BP}(\theta)\mathbf{B}^T=\mathbf{N}_3(\theta)-i[\mathbf{N}_3(\theta)\mathbf{S}-\mathbf{N}_1^T(\theta)\mathbf{L}],$$
$$2\mathbf{BPP}(\theta)\mathbf{A}^T=\mathbf{N}_1^T\mathbf{N}_1^T(\theta)+\mathbf{N}_3\mathbf{N}_2(\theta)$$
$$-i\{\mathbf{N}_1^T[\mathbf{S}^T\mathbf{N}_1^T(\theta)-\mathbf{L}\mathbf{N}_2(\theta)]+\mathbf{N}_3[\mathbf{H}\mathbf{N}_1^T(\theta)+\mathbf{S}\mathbf{N}_2(\theta)]\}, \tag{33}$$
$$2\mathbf{BPP}(\theta)\mathbf{B}^T=\mathbf{N}_1^T\mathbf{N}_3(\theta)+\mathbf{N}_3\mathbf{N}_1(\theta)$$
$$-i\{\mathbf{N}_1^T[\mathbf{S}^T\mathbf{N}_3(\theta)-\mathbf{L}\mathbf{N}_1(\theta)]+\mathbf{N}_3[\mathbf{H}\mathbf{N}_3(\theta)+\mathbf{S}\mathbf{N}_1(\theta)]\},$$

where $\mathbf{P}$ and $\mathbf{P}(\theta)$ are the diagonal matrices defined by

$$\mathbf{P}=\mathrm{diag}[p_1\ p_2\ p_3],$$
$$\mathbf{P}(\theta)=\mathrm{diag}[p_1(\theta)\ p_2(\theta)\ p_3(\theta)]. \tag{34}$$

$\mathbf{S}$, $\mathbf{H}$, $\mathbf{L}$ are 3×3 real matrices introduced by Barnett and Lothe (1973) as

$$\mathbf{S}=i(2\mathbf{A}\mathbf{B}^T-\mathbf{I})=\frac{1}{\pi}\int_0^\pi \mathbf{N}_1(\omega)d\omega,$$
$$\mathbf{H}=2i\mathbf{A}\mathbf{A}^T=\frac{1}{\pi}\int_0^\pi \mathbf{N}_2(\omega)d\omega, \tag{35}$$
$$\mathbf{L}=-2i\mathbf{B}\mathbf{B}^T=\frac{-1}{\pi}\int_0^\pi \mathbf{N}_3(\omega)d\omega$$

in which $\mathbf{I}$ is the unit matrix. $\mathbf{H}$ and $\mathbf{L}$ are symmetric and positive definite and $\mathbf{SH}$, $\mathbf{LS}$, $\mathbf{H}^{-1}\mathbf{S}$, $\mathbf{S}\mathbf{L}^{-1}$ are antisymmetric.

We can also prove that

$$\mathbf{HL}-\mathbf{SS}=\mathbf{I}. \tag{36}$$

Another identity which also comes from equation (26) is that the product of $\mathbf{N}(\omega)$ and $\mathbf{N}(\omega^*)$ commutes (Kirchner and Lothe, 1986), i.e.,

$$\mathbf{N}(\omega)\mathbf{N}(\omega^*)=\mathbf{N}(\omega^*)\mathbf{N}(\omega). \tag{37}$$

Integrating and using equation (35), we have

$$\mathbf{N}(\omega)\tilde{\mathbf{N}}=\tilde{\mathbf{N}}\mathbf{N}(\omega) \tag{38}$$

where

$$\tilde{\mathbf{N}}=\frac{1}{\pi}\int_0^\pi \mathbf{N}(\omega)\,d\omega=\begin{bmatrix}\mathbf{S} & \mathbf{H}\\ -\mathbf{L} & \mathbf{S}^T\end{bmatrix}. \tag{39}$$

By applying equations $(32)_2$, and (35) and knowing that $\mathbf{N}(\omega)$ is periodic in ω with periodicity π which can be seen from equation (29), the integration of equation (27) from 0 to 2π gives

$$\mathbf{S}\mathbf{c}+\mathbf{H}\mathbf{d}=i\mathbf{c}+\tilde{\gamma}_1^*,$$
$$-\mathbf{L}\mathbf{c}+\mathbf{S}^T\mathbf{d}=i\mathbf{d}+\tilde{\gamma}_2^*, \tag{40}$$

where

$$\tilde{\gamma}_1^*=\frac{1}{2\pi}\int_0^{2\pi}\lambda^{-1}(\omega)\gamma_1(\omega)d\omega,\quad \gamma_1(\omega)=-\mathbf{N}_2(\omega)\boldsymbol{\beta}\mathbf{m}(\omega),$$
$$\tilde{\gamma}_2^*=\frac{1}{2\pi}\int_0^{2\pi}\lambda^{-1}(\omega)\gamma_2(\omega)d\omega,\quad \gamma_2(\omega)=-\boldsymbol{\beta}\mathbf{n}(\omega)-\mathbf{N}_1^T(\omega)\boldsymbol{\beta}\mathbf{m}(\omega), \tag{41}$$

and

$$\boldsymbol{\beta}=[\beta_1\ \beta_2\ \beta_3]. \tag{42}$$

3 Uniform Heat Flow Disturbed by an Elliptic Hole

In an infinite anisotropic plate, heat is flowing uniformly in the direction of the positive x_2-axis. The uniform steady heat flow is disturbed by the presence of an insulated elliptic hole whose boundary is given by

$$x_1=a\cos\psi,\ x_2=b\sin\psi, \tag{43}$$

where ψ is a real parameter and a, b are the half length of the major and minor axes of the ellipse (Fig. 1). If the hole is assumed to be free of tractions, the boundary conditions for this problem can be written as

$$h_m=0,\quad \mathbf{t}_m=0;\ \text{along the hole boundary},$$
$$h_2\to h_0,\quad \sigma_{ij}\to 0;\ \text{at infinity}, \tag{44}$$

where h_m is the heat flux in the direction of $\mathbf{m}$ which is normal to the surface of the elliptic hole (Fig. 1). $\mathbf{t}_m$ is the surface traction along the hole boundary of which the normal is $\mathbf{m}$. By using the coordinate transformation and applying equations (8), and (9), h_m is obtained as

$$h_m=-h_1\sin\theta+h_2\cos\theta$$
$$=2k\mathrm{Im}\{(\cos\theta+\tau\sin\theta)g''(z_t)\}, \tag{45}$$

where Im stands for the imaginary part, $k = k_{22}(\tau - \bar{\tau})/2i$ is a real constant, and the angle θ (Fig. 1) is related to ψ by

$$\rho\cos\theta=a\sin\psi,\ \rho\sin\theta=-b\cos\psi$$
$$\rho=\sqrt{a^2\sin^2\psi+b^2\cos^2\psi}. \tag{46}$$

Note that equation $(45)_2$ is a simplified equation for k_{ij} to be symmetric, which can easily be modified for k_{ij} nonsymmetric.

Downloaded 03 May 2010 to 171.66.16.244. Redistribution subject to ASME license or copyright; see http://www.asme.org/terms/Terms_Use.cfm

The relation between $\mathbf{t}_m$ and ϕ is (Stroh, 1958; Hwu, 1990)

$$\mathbf{t}_m = \phi_{,n} = \cos\theta\phi_{,1} + \sin\phi_{,2}. \tag{47}$$

Due to the linear property, the principle of superposition can be used and the solution can be represented as the sum of a uniform heat flux in an unnotched solid and corrective solution, for which the boundary conditions are

$$h_m = -h_0\cos\theta,\ \mathbf{t}_m = \mathbf{0};\ \text{along the hole boundary},$$
$$h_2 \to 0,\ \sigma_{ij} \to 0;\ \text{at infinity}. \tag{48}$$

To satisfy equation (48) the choice of arbitrary functions $f(z_\alpha)$ and $g(z_t)$ becomes critical in the solution procedures. A comparison with the isothermal problem under uniform loading (Lekhnitskii, 1968; Hwu, 1990) may give us some idea on the proper choice. The boundary conditions of the heat flux shown in equation (48) is similar to those of the stresses in the isothermal condition. The general solutions for the heat flux shown in equation (9) and isothermal stresses in equation (22) with the last term neglected, are proportional to $g''(z_t)$ and $f'(z_\alpha)$, respectively. Therefore, by referring the solutions for the isothermal problem, we may choose $g(z_t)$ as

$$g(z_t) = g_0\int\zeta^{-1}(z_t)dz_t, \tag{49}$$

where

$$\zeta(z_t) = \frac{z_t + \sqrt{z_t^2 - (a^2+\tau^2b^2)}}{a - i\tau b}, \tag{50}$$

and g_0 is a complex constant to be determined. After taking the inverse and integrating, we obtain

$$g(z_t) = \frac{g_0}{a+i\tau b}\left\{\frac{1}{2}z_t^2 - \frac{1}{2}z_t\sqrt{z_t^2-(a^2+\tau^2b^2)} + \frac{a^2+\tau^2b^2}{2}\log(z_t + \sqrt{z_t^2-(a^2+\tau^2b^2)})\right\}. \tag{51}$$

The only requirement for the choice of $f(z_\alpha)$ is the satisfaction of boundary conditions. Owing to the fact that $f(z_\alpha)$ and $g(z_t)$ have the same order to affect the displacements and stresses in equation (22), possible function forms come from the partition of $g(z_t)$. That is

$$f_1(z_\alpha) = \frac{1}{a+ip_\alpha b}\left\{\frac{1}{2}z_\alpha^2 - \frac{1}{2}z_\alpha\sqrt{z_\alpha^2-(a^2+p_\alpha^2b^2)}\right\},$$
$$f_2(z_\alpha) = \frac{a-ip_\alpha b}{2}\log(z_\alpha + \sqrt{z_\alpha^2-(a^2+p_\alpha^2b^2)}), \tag{52}$$

where the subscripts 1 and 2 are the indices for the different possible functions. The general solutions for the displacements and stress functions shown in equation (22) can now be written as

$$\mathbf{u} = 2\sum_{k=1}^{2}\mathrm{Re}\{\mathbf{A}\mathbf{F}_k(Z)\mathbf{A}^T\}\mathbf{q}_{ka} + 2\sum_{k=1}^{2}\mathrm{Re}(\mathbf{A}\mathbf{F}_k(Z)\mathbf{B}^T\}\mathbf{q}_{kb} + 2\mathrm{Re}\{\mathbf{c}g(z_t)\},$$
$$\phi = 2\sum_{k=1}^{2}\mathrm{Re}\{\mathbf{B}\mathbf{F}_k(Z)\mathbf{A}^T\}\mathbf{q}_{ka} + 2\sum_{k=1}^{2}\mathrm{Re}(\mathbf{B}\mathbf{F}_k(Z)\mathbf{B}^T\}\mathbf{q}_{kb} + 2\mathrm{Re}\{\mathbf{d}g(z_t)\}, \tag{53}$$

where

$$\mathbf{F}_k(Z) = \mathrm{diag}[f_k(z_1)\ f_k(z_2)\ f_k(z_3)]. \tag{54}$$

$\mathbf{q}_{ka}$ and $\mathbf{q}_{kb}$, $k = 1, 2$, are real constants which are related to the complex constant $\mathbf{q}_k$ by

$$\mathbf{q}_k = \mathbf{A}^T\mathbf{q}_{ka} + \mathbf{B}^T\mathbf{q}_{kb}. \tag{55}$$

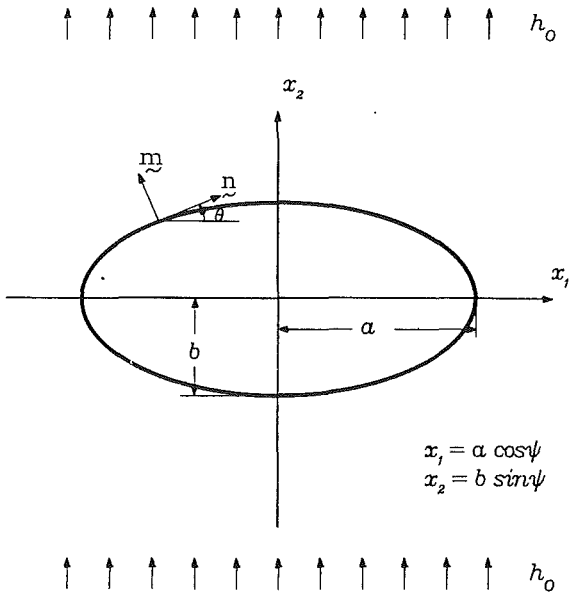


Fig. 1 Elliptic hole under uniform heat flow

The problem now reduces to the determination of the unknown constants g_0, $\mathbf{q}_{ka}$, and $\mathbf{q}_{kb}$ which should satisfy the boundary conditions equations (48). Differentiating equations (51) and (52) with respect to their arguments, we obtain

$$g'(z_t) = g_0\zeta_t^{-1},\ g''(z_t) = -g_0\zeta_t^{-2}\frac{d\zeta_t}{dz_t},$$
$$f_1'(z_\alpha) = \zeta_\alpha^{-1} - \frac{a-ip_\alpha b}{2\sqrt{z_\alpha^2-(a^2+p_\alpha^2b^2)}},\ f_2'(z_\alpha) = \frac{a-ip_\alpha b}{2\sqrt{z_\alpha^2-(a^2+p_\alpha^2b^2)}}, \tag{56}$$

where ζ_t, ζ_α are the simplified notations of $\zeta(z_t)$ and $\zeta(z_\alpha)$. Since $g'(z_t)$, $g''(z_t)$ and $f_k'(z_a) \to 0$ when $|z_t|$ or $|z_\alpha| \to \infty$, the boundary conditions at infinity equation $(48)_2$ are satisfied. To satisfy equation $(48)_1$, one should evaluate $g''(z_t)$, $g_{,n}(z_t)$ and $f_{k,n}(z_\alpha)$ along the hole boundary. Knowing that $\zeta = \zeta_t = \zeta_\alpha = e^{i\psi}$, $d\zeta_t/dz_t = -ie^{i\psi}/\rho(\cos\theta + \tau\sin\theta)$ and the relation equation (46) when $x_1 = a\cos\psi$, $x_2 = b\sin\psi$, we have

$$g''(z_t) = \frac{ig_0(\cos\psi - i\sin\psi)}{\rho(\cos\theta + \tau\sin\theta)},$$
$$g_{,n}(z_t) = (\cos\theta + \tau\sin\theta)g'(z_t) = \frac{ig_0}{2\rho}\{(a+i\tau b)(\cos 2\psi - i\sin 2\psi) - a + i\tau b\}, \tag{57}$$
$$f_{1,n}(z_\alpha) = (\cos\theta + p_\alpha\sin\theta)f_1'(z_\alpha) = \frac{a+ip_\alpha b}{2\rho}(\sin 2\psi + i\cos 2\psi),$$
$$f_{2,n}(z_a) = \frac{-i}{2\rho}(a - ip_\alpha b).$$

By using equations $(45)_2$ and $(57)_1$ and the heat flux boundary condition in equation $(48)_1$, we obtain

$$g_0 = \frac{-ah_0i}{2k}. \tag{58}$$

To calculate the surface traction $\mathbf{t}_m$, equations $(47)_1$, $(53)_2$, $(57)_{2,3,4}$, and (58) are used. The identities equations (33) and $(35)_{1,3}$ are now utilized to convert the complex form into a real form. Satisfaction of the traction free boundary condition in equation $(48)_1$ will then give us

Downloaded 03 May 2010 to 171.66.16.244. Redistribution subject to ASME license or copyright; see http://www.asme.org/terms/Terms_Use.cfm

$$b(\mathbf{N}_3\mathbf{S}-\mathbf{N}_1^T\mathbf{L})\mathbf{q}_{1b}+[a\mathbf{I}+b(\mathbf{N}_1^T\mathbf{S}^T+\mathbf{N}_3\mathbf{H})]\mathbf{q}_{1a}$$

$$=-\frac{ah_0}{k}\,\mathrm{Im}\,\{(a+ib\tau)\,\mathbf{d}\},$$

$$-(a\mathbf{L}+b\mathbf{N}_3)\mathbf{q}_{1b}+(a\mathbf{S}^T-b\mathbf{N}_1^T)\mathbf{q}_{1a}=\frac{-ah_0}{k}\mathrm{Re}\{(a+ib\tau)\mathbf{d}\},$$

$$(a\mathbf{L}-b\mathbf{N}_3)\mathbf{q}_{2b}-(a\mathbf{S}^T+b\mathbf{N}_1^T)\mathbf{q}_{2a}=\frac{-ah_0}{k}\,\mathrm{Re}\{(a-ib\tau)\mathbf{d}\}. \tag{59a}$$

Due to the multivalued characteristics of logarithmic functions contained in $g(z_t)$ and $f_2(z_\alpha)$, the requirement of single valuedness of displacements provides

$$(a\mathbf{S}+b\mathbf{N}_1)\mathbf{q}_{2b}+(a\mathbf{H}+b\mathbf{N}_2)\mathbf{q}_{2a}=-\frac{ah_0}{k}\,\mathrm{Re}\{(a-ib\tau)\mathbf{c}\}. \tag{59b}$$

Applying the antisymmetric property of $\mathbf{LS}$ and identities equations (36) and (38), the manipulation $\mathbf{L}^{-1}\,[\mathbf{S}^T\,(59a)_2+(59a)_1]$ gives a simplified equation to replace equation $(59a)_1$, which is,

$$(a\mathbf{S}-b\mathbf{N}_1)\mathbf{q}_{1b}+(a\mathbf{H}-b\mathbf{N}_2)\mathbf{q}_{1a}$$

$$=\frac{-ah_0}{k}\,\mathbf{L}^{-1}\mathrm{Re}\{(a+ib\tau)\,(\mathbf{S}^T-i\mathbf{I})\mathbf{d}\}. \tag{59c}$$

Combining equations $(59c)$, $(59a)_2$, $(59b)$, and $(59a)_3$, we obtain

$$\begin{Bmatrix}\mathbf{q}_{1b}\\ \mathbf{q}_{1a}\end{Bmatrix}=\frac{-ah_0}{k}\,(a\tilde{\mathbf{N}}-b\mathbf{N})^{-1}\begin{Bmatrix}\mathbf{L}^{-1}\mathrm{Re}\{(a+ib\tau)(\mathbf{S}^T-i\mathbf{I})\mathbf{d}\}\\ \mathrm{Re}[(a+ib\tau)\mathbf{d}]\end{Bmatrix} \tag{60}$$

$$\begin{Bmatrix}\mathbf{q}_{2b}\\ \mathbf{q}_{2a}\end{Bmatrix}=\frac{-ah_0}{k}\,(a\tilde{\mathbf{N}}+b\mathbf{N})^{-1}\mathrm{Re}\{(a-ib\tau)\eta\}.$$

Note that the matrices $(a\tilde{\mathbf{N}}\pm b\mathbf{N})$ will become singular when one of their eigenvalues $ai\pm bp_\alpha$ equals to zero. This is the limiting case for the choice of $f_1(z_\alpha)$ in equation (52), which can be obtained through applying L'Hospital rule by differentiating both the denominator and numerator with respect to p_α. However, the final expressions given in the following two sections do not contain eigenvalues p_α and any possible singular matrices. Hence, the solutions are valid for any limiting cases.

4 The Hoop Stress

Using the stress functions ϕ obtained in the previous section, the hoop stress ϕ_{nn} is determined from (Hwu, 1990)

$$\phi_{nn}=\mathbf{n}^T(\theta)\mathbf{t}_n,$$

$$\mathbf{t}_n=-\boldsymbol{\phi}_{,m}=\sin\theta\boldsymbol{\phi}_{,1}-\cos\theta\boldsymbol{\phi}_{,2}. \tag{61}$$

Similar to the calculation of $\mathbf{t}_m$, one should evaluate $g_{,m}(z_t)$ and $f_{k,m}(z_\alpha)$ along the hole boundary. By comparing equations (47) and $(61)_2$, and using the relations given in equation (32), one obtains

$$g_{,m}(z_t)=\tau(\theta)g_{,n}(z_t),$$

$$f_{k,m}(z_\alpha)=p_\alpha(\theta)f_{k,n}(z_\alpha), \tag{62}$$

where $g_{,n}(z_t)$ and $f_{k,n}(z_\alpha)$ are given in equation (57). Substituting equations (62) and $(57)_{2,3,4}$ into equations (61) and (53), one can find the hoop stress σ_{nn} with the constants g_0, $\mathbf{q}_{ka}$, $\mathbf{q}_{kb}$ given in equations (58), (59), and (60). Applying equation (33) the complex form solution is then converted into real form. To have a simplified result, the identities equations (37), (38), (27), and $(40)_2$ are used. The final simplified expression is

$$\sigma_{nn}=\mathbf{n}^T(\theta)\mathbf{t}_n,$$

$$\mathbf{t}_n=\frac{-ah_0}{2k\rho}\,\{2\rho\,\sin\,\psi\gamma_2(\theta)-\mathbf{N}_3(\theta)\mathbf{L}^{-1}\mathrm{Re}[e^{-2i\psi}(a+ib\tau)\tilde{\gamma}_2^*]\}. \tag{63}$$

The above result can easily be checked by calculating σ_{mn}, which should be zero along the hole boundary if we use

$$\sigma_{mn}=\mathbf{m}^T(\theta)\mathbf{t}_n \tag{64}$$

and the identities (Ting, 1988b)

$$\mathbf{N}_1(\theta)\mathbf{m}(\theta)=-\mathbf{n}(\theta),$$

$$\mathbf{N}_3(\theta)\mathbf{m}(\theta)=0. \tag{65}$$

Note that the explicit closed-form solution for the hoop stress given in equation (63) does not contain the elasticity eigenvalues, eigenvectors, and heat eigenvectors. Hence, the solution is valid for degenerate materials and the special treatment given by Wu (1984) for the repeated eigenvalues is circumvented. Solution equation (63) shows that the hoop stress σ_{nn} is influenced by the elasticity and thermal anisotropy through $\mathbf{N}_3$, $\mathbf{L}$, γ_2 and $\tilde{\gamma}_2^*$. The shape of the elliptic opening is represented by a, b, and ρ. The effect of heat conductivity is reflected by k and the heat eigenvalue τ. The magnitude of uniform heat flow which is perpendicular to the x_1-axis is given by h_0. To find the location of maximum or minimum hoop stress, we differentiate σ_{nn} with respect to θ and set the result to zero. Note that ψ and ρ are functions of θ, which can be seen in equation (46).

For isotropic materials, $\beta_{ij}=\dfrac{E\alpha}{1-2\nu}\,\delta_{ij}$, $k_{ij}=k\delta_{ij}$, where E, ν, α and k are the Young's modulus, Poisson's ratio, thermal expansion coefficient, and heat conductivity, respectively. δ_{ij} is the Kronecker symbol. The fundamental elasticity matrices $\mathbf{N}_1$, $\mathbf{N}_3$, $\mathbf{L}$ can be calculated by using equations $(25)_{3,4}$, (29) and $(35)_3$, or be found in (Hwu, 1990). The heat eigenvalue τ is determined by equation (8) and the root with positive imaginary part is obtained to be i, which is equal to the triple elasticity eigenvalue p_α, $\alpha=1, 2, 3$, determined by equation (12) or (23). Therefore, the isotropic materials belong to the special cases discussed by Wu (1984) and cannot be reduced from the solutions for general anisotropic materials. The solutions given by Chen (1967) for orthotropic materials also have this restriction. As stated in the previous paragraph, however, the solution given in equation (63) is valid for any kind of anisotropy. The determination of the hoop stress in equation (63) is now relied on the calculations of $\gamma_2(\theta)$ and $\tilde{\gamma}_2^*$, which are obtained by using β_{ij}, $\mathbf{N}_1(\theta)$ and equation $(41)_2$. The results are

$$\gamma_2(\theta)=\frac{-E_\alpha}{1-\nu}\begin{Bmatrix}\cos\theta\\ \sin\theta\\ 0\end{Bmatrix},\quad \tilde{\gamma}_2^*=\frac{E\alpha}{2(1-\nu)}\begin{Bmatrix}-1\\ i\\ 0\end{Bmatrix}. \tag{66}$$

Substituting equations (66) and the fundamental elasticity matrices $\mathbf{N}_3$, $\mathbf{L}$ (Hwu, 1990) into equation (63), we obtain

$$\sigma_{nn}=\frac{Eh_0\alpha a^2(a+b)}{2k\rho^2(1-\nu)}\sin\,\psi,$$

which is identical to the one given in the literature (Florence and Goodier, 1960).[1]

5 Cracks

An elliptic hole can be made into a crack of length $2a$ by letting b approach zero. The solutions for the uniform heat

[1]There is a typing error in equation (41) which should be corrected to $h=[\rho^4-2\rho^2m\cos 2\theta+m^2]^2$.

Downloaded 03 May 2010 to 171.66.16.244. Redistribution subject to ASME license or copyright; see http://www.asme.org/terms/Terms_Use.cfm

flux obstructed by a plane crack in a general anisotropic body can then be obtained from Section 3 by letting $b = 0$. Using the identities $\tilde{\mathbf{N}}^2 = -\mathbf{I}$ (Chadwick and Smith, 1977), equation (60) can be simplified to

$$\mathbf{q}_{1a} = -\frac{ah_0}{k} I_m\{\mathbf{d}\},$$

$$\mathbf{q}_{1b} = \frac{ah_0}{k} \mathbf{L}^{-1}\mathrm{Re}\{(\mathbf{I}+i\mathbf{S}^T)\mathbf{d}\},$$

$$\mathbf{q}_{2a} = \frac{ah_0}{k} \mathrm{Re}\{-\mathbf{Lc}+\mathbf{S}^T\mathbf{d}\}, \tag{67}$$

$$\mathbf{q}_{2b} = \frac{ah_0}{k} \mathrm{Re}\{\mathbf{Sc}+\mathbf{Hd}\}.$$

Substituting equations (56), (58), and (67) with $x_2 = 0$, $|x_1| > a$ into equations $(16)_2$, $(53)_2$ and using the identities equations $(35)_{1,3}$ and $(40)_2$, the stresses σ_{i2} ahead of the crack tip along the x_1-axis are obtained as

$$\sigma_{i2} = \frac{h_0}{2k} \frac{a^2}{\sqrt{x_1^2 - a^2}} \mathrm{Re}\{\tilde{\gamma}_2^*\}. \tag{68}$$

As in the isothermal problems, the above solution shows that the stresses are singular near the crack tip. With the usual definition, the stress intensity factors are given by

$$\begin{Bmatrix} K_{II} \\ K_I \\ K_{III} \end{Bmatrix} = \lim_{x_1 \to a} \sqrt{2\pi(x_1 - a)}\sigma_{i2} = \frac{\sqrt{\pi}h_0}{2k} a^{\frac{3}{2}} \mathrm{Re}\{\tilde{\gamma}_2^*\}. \tag{69}$$

Similarly, by using equation $(53)_1$ and setting $x_2 = 0^{\pm}$, $|x_1| < a$ where $\pm$ denotes the upper and lower surface of the crack, the crack opening displacements, $\Delta\mathbf{u}$, are obtained as

$$\Delta\mathbf{u} = \mathbf{u}(x_1, 0^+) - \mathbf{u}(x_1, 0^-) = \frac{h_0}{k} x_1 \sqrt{a^2 - x_1^2}\mathbf{L}^{-1}\mathrm{Re}\{\tilde{\gamma}_2^*\}. \tag{70}$$

It can be seen that Δu_2 will always be negative in either $-a < x_1 < 0$ or $0 < x_1 < a$ if the second component of $\mathbf{L}^{-1}\,\mathrm{Re}\{\tilde{\gamma}_2^*\}$ is not equal to zero, which violates the assumption of fully open crack and the solution is invalid. Sturla and Barber (1988) discussed this situation and gave a solution with partial contact crack. If $\{\mathbf{L}^{-1}\,\mathrm{Re}(\tilde{\gamma}_2^*)\}_{(2)} = 0$, $\Delta u_2 = 0$ for all x_1 within the crack, and hence there is no tendency for the crack to open or close. However, a relative tangential displacement may exist between the crack faces. Therefore, equation (70) is valid if $\Delta u_2 = 0$ or the negative Δu_2 is increased to a positive value by an applied tensile load.

By applying the virtual crack closure method (Irwin, 1957), the total strain energy release rate G can then be calculated as

$$G = \lim_{\Delta a \to 0} \frac{1}{2\Delta a}\int_0^{\Delta a} \Delta u_i(x - \Delta a)\sigma_{i2}(x)dx = \frac{\pi h_0^2 a^3}{8k^2} \mathrm{Re}\{\tilde{\gamma}_2^*\}^T\mathbf{L}^{-1}\mathrm{Re}\{\tilde{\gamma}_2^*\}. \tag{71}$$

Note that the integration variable x represents the distance ahead of the crack tip.

For isotropic materials, substituting equation $(66)_2$ and the fundamental matrix $\mathbf{L}$ into equation (70), we have $\Delta u_2 = 0$ which validates the following solutions. From equations (69) and (71),

$$K_{II} = -\frac{\sqrt{\pi}E\alpha h_0 a^{\frac{3}{2}}}{4(1-\nu)k}, \quad K_I = K_{III} = 0,$$
$$G = \frac{\pi E\alpha^2 h_0^2 a^3(1+\nu)}{16(1-\nu)k^2}, \tag{72}$$

which is identical to the solutions given in the literature (Sih, 1962).

6 Conclusions

Based upon the Stroh formalism, the general solutions for plane anisotropic thermoelasticity are derived and expressed in a matrix form. Some new identities concerning the heat eigenvalues and eigenvectors are developed in this paper, which is useful in replacing the complex eigenvectors by the basic material properties like C_{ijks}, k_{ij}, and β_{ij}. Hence, the problems of repeated eigenvalues considered by Wu (1984) is circumvented. Note that almost all the solutions for plane anisotropic thermoelasticity given in the literature (e.g., Chen, 1967; Atkinson and Clements, 1977; Sturla and Barber, 1988) cannot be reduced directly to the isotropic materials due to the repeated eigenvalues. The hoop stress around the elliptic hole, the stress intensity factor, crack opening displacement, and the strain energy release rate for the crack obtained in this paper do not contain the eigenvectors and hence can be reduced for any degenerate materials. Comparison with the solutions found for the isotropic materials shows that the solution presented here is exact, simple, and general. Due to the simplicity and generality of the solutions, the effect of geometry (a, b), heat flow (h_0), elastic and thermal anisotropy ($\mathbf{N}_3$, $\mathbf{L}$, γ_2, $\tilde{\gamma}_2^*$), heat conductivity (k, τ), and location (θ, ψ, ρ) can be studied clearly and easily.

References

Atkinson, C., and Clements, D. L., 1977, "On Some Crack Problems in Anisotropic Thermoelasticity," *Int. J. Solids Structures*, Vol. 13, pp. 855–864.

Barnett, D. M., and Lothe, J., 1973, "Synthesis of the Sextic and the Integral Formalism for Dislocation, Green's Function and Surface Waves in Anisotropic Elastic Solids," *Phys. Norv.*, Vol. 7, pp. 13–19.

Chadwick, P., and Smith, G. D., 1977, "Foundations of the Theory of Surface Waves in Anisotropic Elastic Materials," *Adv. Appl. Mech.*, Vol. 17, pp. 303–376.

Chen, W. T., 1967, "Plane Thermal Stress at an Insulated Hole Under Uniform Heat Flow in an Orthotropic Medium," ASME JOURNAL OF APPLIED MECHANICS, Vol. 34, pp. 133–136.

Clements, D. L., 1973, "Thermal Stress in an Anisotropic Elastic Half-Space," *SIAM J. Appl. Math.*, Vol. 24, No. 3, pp. 332–337.

Florence, A. L., and Goodier, J. N., 1959, "Thermal Stress at Spherical Cavities and Circular Holes in Uniform Heat Flow," ASME JOURNAL OF APPLIED MECHANICS, Vol. 26, pp. 293–294.

Florence, A. L., and Goodier, J.N., 1960, "Thermal Stresses Due to Disturbance of Uniform Heat Flow by an Insulated Ovaloid Hole," ASME JOURNAL OF APPLIED MECHANICS, Vol. 27, pp. 635–639.

Florence, A. L., and Goodier, J. N., 1963, "The Linear Thermoelastic Problem of Uniform Heat Flow Disturbed by a Penny-Shaped Insulated Crack," *Int. J. Eng. Sci.*, Vol. 1, pp. 533–540.

Green, A. E., and Zerna, W., 1954, *Theoretical Elasticity*, Oxford University Press, London, England.

Hwu, C., and Ting, T. C. T., 1989, "Solutions for the Anisotropic Elastic Wedge at Critical Wedge Angles," to appear in *J. Elasticity*.

Hwu, C., and Ting, T. C. T., 1989, "Two-Dimensional Problems of the Anisotropic Elastic Solid with an Elliptic Inclusion," to appear in the *Q. J. Mech. Appl. Math.*.

Hwu, C., 1989, "Anisotropic Plates With Various Openings Under Uniform Loading or Pure Bending," to appear in ASME JOURNAL OF APPLIED MECHANICS.

Irwin, G. R., 1957, "Analysis of Stresses and Strains Near the End of a Crack Transversing a Plate," ASME JOURNAL OF APPLIED MECHANICS, Vol. 24, pp. 361–364.

Kirchner, H. O. K., and Lothe, J., 1986, "On the Redundancy of the N-Matrix of Anisotropic Elasticity," *Phi. Mag., A*, Vol. 53, pp. L1-L10.

Lekhnitskii, S. G., 1968, *Anisotropic Plates*, Gordon and Breach.

Li, Q., and Ting, T. C. T., 1989, "Line Inclusions in Anisotropic Elastic Solids," ASME JOURNAL OF APPLIED MECHANICS, Vol. 56, pp. 556–563.

Muskhelishvili, N. I., 1953, "Some Basic Problems of Mathematical Theory of Elasticity," Noordhoff Pub., Groningen.

Nowacki, W., 1962, *Thermoelasticity*, Addison Wesley, Reading, Mass.

Olesiak, Z., and Sneddon, I. N., 1960, "The Distribution of Thermal Stress in an Infinite Elastic Solid Containing a Penny-Shaped Crack," *Arch. Rational Mech. Anal.*, Vol. 4, pp. 238–254.

Sih, G. C., 1962, "On the Singular Character of Thermal Stresses Near a Crack Tip," ASME JOURNAL OF APPLIED MECHANICS, Vol. 29, pp. 587–589.

Stroh, A. N., 1958, "Dislocations and Cracks in Anisotropic Elasticity," *Phil. Mag.*, Vol. 7, pp. 625–646.

Downloaded 03 May 2010 to 171.66.16.244. Redistribution subject to ASME license or copyright; see http://www.asme.org/terms/Terms_Use.cfm

Sturla, F. A., and Barber, J. R., 1988, "Thermal Stresses Due to a Plane Crack in General Anisotropic Material," ASME JOURNAL OF APPLIED MECHANICS, Vol. 55, pp. 372–376.

Tsai, Y. M., 1983, "Transversely Isotropic Thermoelastic Problem of Uniform Heat Flow Disturbed by a Penny-Shaped Crack," *J. Thermal Stresses*, Vol. 6, pp. 379–389.

Tsai, Y. M., 1984, "Orthotropic Thermoelastic Problem of Uniform Heat Flow Disturbed by a Central Crack," *J. Comp. Mat.*, pp. 122–131.

Ting, T. C. T., 1982, "Effects of Change of Reference Coordinates On the Stress Analyses of Anisotropic Elastic Materials," *Int. J. Solids Structures*, Vol. 18, pp. 139–152.

Ting, T. C. T., 1986, "Explicit Solution and Invariance of the Singularities at an Interface Crack in Anisotropic Composites," *Int. J. Solids Structures*, Vol. 22, pp. 965–983.

Ting, T. C. T., 1988, "Some Identities and the Structures of N_i the Stroh Formalism of Anisotropic Elasticity," *Q. Appl. Math.*, Vol. 46, pp. 109–120.

Ting, T. C. T., 1988, "The Anisotropic Elastic Wedge Under a Concentrated Couple," *Q. J. Mech. Appl. Math.*, Vol. 41, pp. 563–578.

Ting, T. C. T., and Hwu, C., 1988, "Sextic Formalism in Anisotropic Elasticity for Almost Non-Semisimple Matrix N," *Int. J. Solids Structures*, Vol. 24, pp. 65–76.

Wu, C. H., 1984, "Plane Anisotropic Thermoelasticity," ASME JOURNAL OF APPLIED MECHANICS, Vol. 51, pp. 724–726.

APPENDIX

Generalized Stroh Formalism for Plane Anisotropic Thermoelasticity

If the solution to equation (2) is assumed to be

$$T = g'(z_t^*),\ z_t^* = x_1^* + \tau(\omega)x_2^*, \tag{A1}$$

where

$$x_1^* = x_1 \cos\omega + x_2 \cos\omega,$$

$$x_2^* = -x_1 \sin\omega + x_2 \cos\omega,$$

and substituting (A1) into equation (2) we obtain

$$k_{11}(\omega) + [k_{12}(\omega) + k_{21}(\omega)]\tau(\omega) + k_{22}(\omega)\tau^2(\omega) = 0, \tag{A2}$$

$$k_{11}(\omega) = k_{ij}n_in_j,\ k_{12}(\omega) = k_{ij}n_im_j,\ k_{21}(\omega) = k_{ij}m_jn_j,$$

$$k_{22}(\omega) = k_{ij}m_im_j. \tag{A3}$$

To find the solution of equation (5), we assume

$$u_k = u_k^{(h)} + u_k^{(p)}, \tag{A4}$$

$$u_k^{(h)} = a_k^* f(z_\alpha^*),\ z_\alpha^* = x_1^* + p_\alpha(\omega)x_2^*, \tag{A5}$$

$$u_k^{(p)} = c_k^* g(z_t^*),$$

where (h) denotes the homogeneous solution and (p) is a particular solution. The homogeneous solutions are obtained by substituting $(A5)_1$ into equation (5) with T neglected.

$$\{\mathbf{Q}(\omega) + p(\omega)[\mathbf{R}(\omega) + \mathbf{R}^T(\omega)] + p^2(\omega)\mathbf{T}(\omega)\}\mathbf{a}^* = \mathbf{0}, \tag{A6}$$

where

$$Q_{ik}(\omega) = C_{ijks}n_jn_s,\ R_{ik}(\omega) = C_{ijks}n_jm_s,\ T_{ik}(\omega) = C_{ijks}m_jm_s. \tag{A7}$$

Substituting equation $(A5)_2$ into equation (5), we obtain

$$\{\mathbf{Q}(\omega) + \tau(\omega)[\mathbf{R}(\omega) + \mathbf{R}^T(\omega)] + \tau^2(\omega)\mathbf{T}(\omega)\}\mathbf{c}^* = \beta_1(\omega) + \tau(\omega)\beta_2(\omega), \tag{A8}$$

where

$$\beta_{i1}(\omega) = \beta_{ij}n_j,\ \beta_{i2}(\omega) = \beta_{ij}m_j. \tag{A9}$$

The eigenvalue $p(\omega)$ shown in (A6) is a function of ω and is related to the one given in equation (12) by (Lekhnitskii, 1968, Ting, 1982)

$$p(\omega) = \frac{p\cos\omega - \sin\omega}{p\sin\omega + \cos\omega}. \tag{A10}$$

Similarly, the relation of $\tau(\omega)$ given in (A8) and equation (14) can also be obtained as

$$\tau(\omega) = \frac{\tau\cos\omega - \sin\omega}{\tau\sin\omega + \cos\omega}. \tag{A11}$$

The eigenvector $\mathbf{a}^*$ in (A6) is independent of ω, which was proved by Chadwick and Smith (1977). However, the independency of $\mathbf{c}^*$ in (A8) cannot be assumed unless one proves it. The equivalent forms of equations (A6) and (A8) are now written as

$$\mathbf{N}(\omega)\xi = p(\omega)\xi, \tag{A12}$$

$$\mathbf{N}(\omega)\eta(\omega) = \tau(\omega)\eta(\omega) + \gamma(\omega), \tag{A13}$$

where

$$\mathbf{N}(\omega) = \begin{bmatrix} \mathbf{N}_1(\omega) & \mathbf{N}_2(\omega) \\ \mathbf{N}_3(\omega) & \mathbf{N}_1^T(\omega) \end{bmatrix},\ \xi = \begin{Bmatrix} \mathbf{a} \\ \mathbf{b} \end{Bmatrix},$$

$$\gamma(\omega) = -\begin{bmatrix} \mathbf{0} & \mathbf{N}_2(\omega) \\ \mathbf{I} & \mathbf{N}_1^T(\omega) \end{bmatrix}\begin{Bmatrix} \beta_1(\omega) \\ \beta_2(\omega) \end{Bmatrix},\ \eta(\omega) = \begin{Bmatrix} \mathbf{c}(\omega) \\ \mathbf{d}(\omega) \end{Bmatrix},$$

$$\mathbf{N}_1(\omega) = -\mathbf{T}^{-1}(\omega)\mathbf{R}^T(\omega), \tag{A14}$$

$$\mathbf{N}_2(\omega) = \mathbf{T}^{-1}(\omega) = \mathbf{N}_2^T(\omega),$$

$$\mathbf{N}_3(\omega) = \mathbf{R}(\omega)\mathbf{T}^{-1}(\omega)\mathbf{R}^T(\omega) - \mathbf{Q}(\omega) = \mathbf{N}_3^T(\omega),$$

$$\beta_1(\omega) = \beta\mathbf{n}(\omega),\ \beta_2(\omega) = \beta\mathbf{m}(\omega),$$

$$\beta = [\beta_1\ \beta_2\ \beta_3].$$

In the following, we will find the relation between $\eta(\omega)$ and η. Differentiating both sides of equation (A13) and using the following identities, which can be proved by direct differentiation (Barnett and Lothe, 1973),

$$\mathbf{N}'(\omega) = -\mathbf{I} - \mathbf{N}^2(\omega), \tag{A15}$$

we obtain

$$[\tau'(\omega) + 1 + \tau^2(\omega)]\eta(\omega) + [\mathbf{N}(\omega)\gamma(\omega) + \gamma'(\omega)] + \tau(\omega)\gamma(\omega) = [\mathbf{N}(\omega) - \tau(\omega)\mathbf{I}]\eta'(\omega). \tag{A16}$$

The first term of the left-hand side of equation (A16) vanishes through the use of equation (A11). Applying $(A14)_3$ and (A15) we can show that

$$\gamma'(\omega) = -\mathbf{N}(\omega)\gamma(\omega). \tag{A17}$$

Equation (A16) now becomes

$$\mathbf{N}(\omega)\eta'(\omega) = \tau(\omega)\eta'(\omega) + \tau(\omega)\gamma(\omega). \tag{A18}$$

Comparison with equation (A13) suggests that

$$\eta'(\omega) = \tau(\omega)\eta(\omega). \tag{A19}$$

Dividing both sides of the six equations by $\eta_i(\omega)$, $i = 1, 2, \ldots, 6$, integrating and using equation (A11), we obtain

$$\eta(\omega) = \lambda(\omega)\eta,\ \lambda(\omega) = \cos\omega + \tau\sin\omega, \tag{A20}$$

where $\eta = \eta(0)$.

Downloaded 03 May 2010 to 171.66.16.244. Redistribution subject to ASME license or copyright; see http://www.asme.org/terms/Terms_Use.cfm

G. R. Liu
Graduate Student,
Graduate School of Engineering,
Tohoku University,
Sendai, 980, Japan

J. Tani
Professor,
Institute of Fluid Science,
Tohoku University,
Sendai, 980, Japan
Mem. ASME

K. Watanabe
Associate Professor,
Department of Mechanical Engineering,
Yamagata University,
Yonezawa, 992, Japan

T. Ohyoshi
Professor,
Department of Mechanical Engineering,
Mining College,
Akita University,
Akita, 010, Japan

Lamb Wave Propagation in Anisotropic Laminates

The wave propagation in arbitrary anisotropic laminates is investigated on the basis of an exact theory. The dispersion relations of Lamb waves are determined for graphite/epoxy symmetric angle-ply laminates and hybrid composite ones which consist of carbon/epoxy and glass/epoxy layers. The dispersion and anisotropy of phase velocities for fundamental modes are discussed in detail. The energy distributions in the thickness direction of laminates are calculated for each kind of Lamb wave. A hybrid composite laminate is found to have better capability in absorbing impact energy by analyzing the strain energy distribution during the wave propagation. The results of the strain energy distribution are useful in determining the arrangement and the fiber orientation of the layers of hybrid composite laminates.

1 Introduction

Composite materials are ideal for structural applications where high strength-to-weight and stiffness-to-weight ratios are required. Aircraft are typical weight-sensitive structures in which composite materials are cost effective. The most important practical composite structure is laminated plate structure. Hence, the studies of impact and wave propagation in the composite laminated plate become very important. To improve the energy absorbing ability of the laminated plate during the wave propagation, the hybrid composite materials, which consist of more than two kinds of composites, are used. In the hybrid composite laminate, some of the layers have the higher property for static loads and some of them have the higher capability in absorbing impact energy. It is desirable that during the wave propagation the strain energy concentrates in the layers which have the higher capability in absorbing impact energy. Hence, the distribution of the strain energy in the thickness direction of the laminate may be important data to design hybrid composite laminates.

Solutions to the plane wave propagation in unbounded homogeneous layered media have been well known, and many methods have been proposed. The exact dispersion relations can be found in many good books or papers (Brekhovskikh, 1960) and a continuum theory has been proposed (Sun, Achenbach, and Herrmann, 1968). A mixture theory has been used to investigate the infinite periodically layered anisotropic media (Murakami and Akiyama, 1985). For bounded layered isotropic media, an exact method was proposed by Thomson (1950). Wave types occurring in bounded layered anisotropic media are more complicated. Hence, a numerical method has been used to examine these waves (Kausel, 1986), but they have not been investigated exactly. In order to obtain the dispersion relations for the wave propagation in a hybrid composite laminate and the distribution of strain energy in the thickness direction of the laminate, the problem about the wave propagation in the laminate which consists of anisotropic layers is solved exactly in this paper.

2 Formulation

Consider a laminate which consists of N layers of anisotropic materials as shown in Fig. 1. The thickness, the angle of fiber-orientation and elastic coefficients of nth layers are denoted by h_n, ϕ_n, and $C_{ijkl}^{(n)}$, respectively. The total thickness of the laminate is H. A rectangular Cartesian reference system x_1, x_2, and x_3 is selected with x_3 normal to the plane of laminate defined by x_1 and x_2.

The relations governing each layer are given as follows.

(a) Constitutive relations for anisotropic materials

$$\sigma_{ij}^{(n)} = C_{ijkl}^{(n)} \epsilon_{kl}^{(n)}, \tag{1}$$

Contributed by the Applied Mechanics Division of THE AMERICAN SOCIETY OF MECHANICAL ENGINEERS for publication in the JOURNAL OF APPLIED MECHANICS.

Discussion on this paper should be addressed to the Technical Editor, Leon M. Keer, The Technological Institute, Northwestern University, Evanston, IL 60208, and will be accepted until two months after final publication of the paper itself in the JOURNAL OF APPLIED MECHANICS. Manuscript received by the ASME Applied Mechanics Division, July 19, 1988; final revision, Aug. 20, 1989.

Copyright © 1990 by ASME
Downloaded 03 May 2010 to 171.66.16.244. Redistribution subject to ASME license or copyright; see http://www.asme.org/terms/Terms_Use.cfm

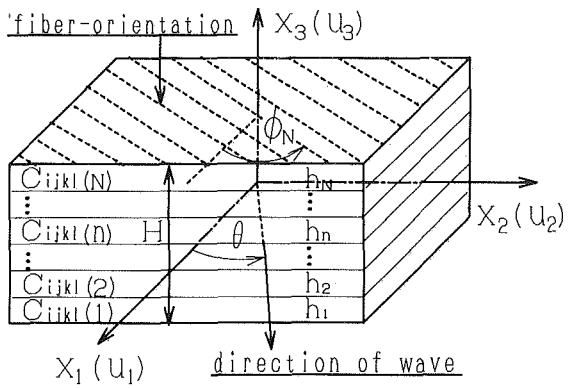


Fig. 1 A laminate and coordinate system

where the superscript (n) means nth layer, $\sigma_{ij}^{(n)}$ and $\epsilon_{ij}^{(n)}$ are the stress and strain tensors, respectively, and the fourth-order tensor of the elasticity $C_{ijkl}^{(n)}$ satisfies the (Green) symmetry conditions:

$$C_{ijkl}^{(n)} = C_{klij}^{(n)} = C_{ijlk}^{(n)} = C_{jikl}^{(n)}. \tag{2}$$

Hence, 21 independent constants are used to describe the anisotropic elastic solid.

(b) Equations of motion

$$\frac{\partial \sigma_{ij}^{(n)}}{\partial x_j} = \rho_n \frac{\partial^2 u_i^{(n)}}{\partial t^2}, \tag{3}$$

where ρ_n is the density of the nth layer, t is time, $u_i^{(n)}$ is the displacement in the x_i direction.

(c) Strain-displacement relations

$$\epsilon_{ij}^{(n)} = \frac{1}{2}\left(\frac{\partial u_i^{(n)}}{\partial x_j} + \frac{\partial u_j^{(n)}}{\partial x_i}\right). \tag{4}$$

(d) The continuity of displacement and stress at the interface

$$\mathbf{S}^{(n)}(h_n) = \mathbf{S}^{(n+1)}(0)$$
$$\mathbf{D}^{(n)}(h_n) = \mathbf{D}^{(n+1)}(0), \tag{5}$$

where

$$\mathbf{S}^{(n)}(x_3) = \{\bar{\sigma}_{13}\ \bar{\sigma}_{23}\ \bar{\sigma}_{33}\}$$
$$\mathbf{D}^{(n)}(x_3) = \{\bar{u}_1\ \bar{u}_2\ \bar{u}_3\} \tag{6}$$

and the bar means the amplitudes of the stress and displacement which are the function of x_3 only.

(e) The boundary condition on the laminate surfaces

$$\mathbf{S}^{(1)}(0) = \mathbf{0} \tag{7}$$
$$\mathbf{S}^{(N)}(h_N) = \mathbf{0}, \tag{8}$$

where $\mathbf{0}$ is zero vector.

Substituting equations (1) and (4) into equation (3), equations of motion are expressed by displacement as follows:

$$C_{ijkl}^{(n)} \frac{\partial^2 u_k^{(n)}}{\partial x_j \partial x_l} = \rho_n \frac{\partial^2 u_i^{(n)}}{\partial t^2}. \tag{9}$$

3 Analysis

Assume that solutions to equation (9) are expressed by

$$u_i^{(n)} = U_i^{(n)} \exp\{j\xi(n_1x_1 + n_2x_2 + n_3x_3 - ct)\}$$
$$(i = 1, 2, 3) \tag{10}$$

where $U_i^{(n)}$ are the constants related to the amplitude of displacement, n_k $(k = 1, 2, 3)$ are the components of the unit vector giving the direction of propagation, c is the phase velocity, and ξ is the wave number.

Substituting equation (10) into equation (9), we have

$$\Pi_{ik}^{(n)} U_k^{(n)} = 0 \tag{11}$$

where

$$\Pi_{ik}^{(n)} = \Gamma_{ik}^{(n)} - \rho_n c^2 \delta_{ik}, \tag{12}$$

and where δ_{ik} is the Kronecker delta, and Γ_{ik} are the Christoffel stiffness as follows:

$$\Gamma_{ik}^{(n)} = \Gamma_{ki}^{(n)} = C_{ijkl}^{(n)} n_j n_l. \tag{13}$$

For a nontrivial solution, we have

$$\det(\Pi_{ik}^{(n)}) = 0. \tag{14}$$

For an infinite anisotropic body, when n_i are given, three phase velocities can be obtained by equation (14). For the finite thickness laminate, we can obtain n_3 from equation (14), when n_1 and n_2 are given. On the other hand, equation (14) can be written as a polynomial equation of n_3.

$$\det(a_{ik}^{(n)} + b_{ik}^{(n)} n_3 + d_{ik}^{(n)} n_3^2) = 0 \tag{15}$$

The degree of this polynomial equation is six. We can solve it numerically and obtain six roots $n_3 = \alpha_l^{(n)}$ $(l = 1, \ldots 6)$, and write the displacement as follows:

$$u_i^{(n)} = \sum_{l=1}^{6} q_{i(l)}^{(n)} A_l^{(n)} \exp(j\xi\alpha_l^{(n)} x_3) \exp\{j\xi(n_1x_1 + n_2x_2 - ct)\} \tag{16}$$

where

$$q_{1(l)}^{(n)} = 1$$
$$q_{2(l)}^{(n)} = \{\Gamma_{12}^{(n)}\Gamma_{13}^{(n)} - \Gamma_{23}^{(n)}(\Gamma_{11}^{(n)} - \rho_n c^2)\} / \{\Gamma_{12}^{(n)}\Gamma_{23}^{(n)} - \Gamma_{13}^{(n)}(\Gamma_{22}^{n} - \rho_n c^2)\}$$
$$q_{3(l)}^{(n)} = (\rho_n c^2 - \Gamma_{11}^{(n)})/\Gamma_{13}^{(n)} - (\Gamma_{12}^{n}/\Gamma_{13}^{(n)}) q_{2(l)}^{(n)}. \tag{17}$$

Equation (16) satisfies equation (9) and contains six undefined constants. From equations (16) and (4) the strain tensors can be expressed as follows:

$$\epsilon_{ik}^{(n)} = \sum_{l=1}^{6} p_{ik(l)}^{(n)} A_l^{(n)} \exp(j\xi\alpha_l^{(n)} x_3) \exp\{j\xi(n_1x_1 + n_2x_2 - ct)\} \tag{18}$$

where

$$p_{ik(l)}^{(n)} = j\xi(n_k q_{i(l)}^{(n)} + n_i q_{k(l)}^{(n)})/2 \quad (i, k = 1, 2, 3). \tag{19}$$

The stress tensors are

$$\sigma_{ik}^{(n)} = \sum_{l=1}^{6} r_{ik(l)}^{(n)} A_l^{(n)} \exp(j\xi\alpha_l^{(n)} x_3) \exp\{j\xi(n_1x_1 + n_2x_2 - ct)\} \tag{20}$$

where

$$r_{ik(l)}^{(n)} = C_{ikpq}^{(n)} p_{pq(l)}^{(n)}$$
$$(i, k, p, q = 1, 2, 3). \tag{21}$$

In equations (19) and (21), $n_3 = \alpha_l^{(n)}$ $(l = 1, \ldots 6)$. With equations (16) and (20) we have

$$u_i^{(u)} = \bar{u}_{i(l)}^{(n)} \exp\{j\xi(n_1x_1 + n_2x_2 - ct)\} \tag{22}$$
$$\sigma_{i3}^{(n)} = \bar{\sigma}_{i3(l)}^{(n)} \exp\{j\xi(n_1x_1 + n_2x_2 - ct)\} \tag{23}$$

where

$$\bar{u}_i^{(n)} = \sum_{l=1}^{6} q_{i(l)}^{(n)} \exp(j\xi\alpha_l^{(n)} x_3) A_l^{(n)} \tag{24}$$

Downloaded 03 May 2010 to 171.66.16.244. Redistribution subject to ASME license or copyright; see http://www.asme.org/terms/Terms_Use.cfm

$$\bar{\sigma}_{i3}^{(n)} = \sum_{l=1}^{6} r_{i3(l)}^{(n)} \exp(j\xi\alpha_l^{(n)} x_3) A_l^{(n)}. \tag{25}$$

Equations (24) and (25) can be expressed by the following matrix form:

$$\begin{bmatrix} \mathbf{S} \\ \mathbf{D} \end{bmatrix}^{(n)} = \begin{bmatrix} \mathbf{K}_1 & \mathbf{K}_2 \\ \mathbf{K}_3 & \mathbf{K}_4 \end{bmatrix}^{(n)} \begin{bmatrix} \mathbf{A}_1 \\ \mathbf{A}_2 \end{bmatrix}^{(n)} \tag{26}$$

where $\mathbf{S}^{(n)}$ and $\mathbf{D}^{(n)}$ are given by equation (6), $\mathbf{A}_1^{(n)}$ and $\mathbf{A}_2^{(n)}$ are given by

$$\mathbf{A}_1^{(n)} = \{A_1\ A_2\ A_3\}^{(n)};\ \mathbf{A}_2^{(n)} = \{A_4\ A_5\ A_6\}^{(n)}. \tag{27}$$

On the upper and lower surfaces of the nth layer, equation (26) can be expressed as follows: On the lower surface,

$$\begin{bmatrix} \mathbf{S} \\ \mathbf{D} \end{bmatrix}_{x_3=0}^{(n)} = \begin{bmatrix} \mathbf{G}_1 & \mathbf{G}_2 \\ \mathbf{G}_3 & \mathbf{G}_4 \end{bmatrix}^{(n)} \begin{bmatrix} \mathbf{A}_1 \\ \mathbf{A}_2 \end{bmatrix}^{(n)}. \tag{28}$$

On the upper surface,

$$\begin{bmatrix} \mathbf{S} \\ \mathbf{D} \end{bmatrix}_{x_3=h_n}^{(n)} = \begin{bmatrix} \mathbf{Q}_1 & \mathbf{Q}_2 \\ \mathbf{Q}_3 & \mathbf{Q}_4 \end{bmatrix}^{(n)} \begin{bmatrix} \mathbf{A}_1 \\ \mathbf{A}_2 \end{bmatrix}^{(n)}, \tag{29}$$

where

$$\mathbf{G}_i^{(n)} = \mathbf{K}_i^{(n)}(x_3 = 0);\ \mathbf{Q}_i^{(n)} = \mathbf{K}_i^{(n)}\ (x_3 = h_n)\ (i = 1, \ldots 4). \tag{30}$$

According to equations (7) and (28), $\mathbf{A}_2^{(1)}$ can be expressed by $\mathbf{A}_1^{(1)}$.

$$\mathbf{A}_2^{(1)} = -(\mathbf{G}_2^{(1)})^{-1}\mathbf{G}_1^{(1)}\mathbf{A}_1^{(1)} \tag{31}$$

Substituting equation (31) into equation (29), $\mathbf{S}^{(1)}$ (h_1) and $\mathbf{D}^{(1)}$ (h_1) can be expressed by $\mathbf{A}_1^{(1)}$.

$$\mathbf{S}^{(1)}(h_1) = \mathbf{Z}_s^{(1)}\mathbf{A}_1^{(1)} \tag{32}$$

$$\mathbf{D}^{(1)}(h_1) = \mathbf{Z}_d^{(1)}\mathbf{A}_1^{(1)} \tag{33}$$

where

$$\mathbf{Z}_s^{(1)} = \mathbf{Q}_1^{(1)} - \mathbf{Q}_2^{(1)}(\mathbf{G}_2^{(1)})^{-1}\mathbf{G}_1^{(1)} \tag{34}$$

$$\mathbf{Z}_d^{(1)} = \mathbf{Q}_3^{(1)} - \mathbf{Q}_4^{(1)}(\mathbf{G}_2^{(1)})\mathbf{G}_1^{(1)}. \tag{35}$$

According to the continuity condition at the interface between the first and second layers we have

$$\mathbf{G}_1^{(2)}\mathbf{A}_1^{(2)} + \mathbf{G}_2^{(2)}\mathbf{A}_2^{(2)} = \mathbf{Z}_s^{(1)}\mathbf{A}_1^{(1)} \tag{36}$$

$$\mathbf{G}_3^{(2)}\mathbf{A}_1^{(2)} + \mathbf{G}_4^{(2)}\mathbf{A}_2^{(2)} = \mathbf{Z}_d^{(1)}\mathbf{A}_1^{(1)}. \tag{37}$$

From equations (36) and (37) the constants of the second layer $\mathbf{A}_1^{(2)}$ and $\mathbf{A}_2^{(2)}$ can be expressed by $\mathbf{A}_1^{(1)}$, and with equation (29), $\mathbf{S}^{(2)}$ (h_2) and $\mathbf{D}^{(2)}$ (h_2) can be expressed by $\mathbf{A}_1^{(1)}$ also.

$$\mathbf{S}^{(2)}(h_2) = \mathbf{Z}_s^{(2)}\mathbf{A}_1^{(1)} \tag{38}$$

$$\mathbf{D}^{(2)}(h_2) = \mathbf{Z}_d^{(2)}\mathbf{A}_1^{(1)} \tag{39}$$

With the continuity condition at the interface between the second and third layers, $\mathbf{S}^{(3)}$ (h_3) and $\mathbf{D}^{(3)}$ (h_3) can be expressed by $\mathbf{A}_1^{(1)}$ also. By this procedure, $\mathbf{S}^{(N)}$ (h_N) and $\mathbf{D}^{(N)}$ (h_N) of Nth layer can be expressed, finally, by $\mathbf{A}_1^{(1)}$ of the first layer.

$$\mathbf{S}^{(N)}(h_N) = \mathbf{Z}_s^{(N)}\mathbf{A}_1^{(1)} \tag{40}$$

$$\mathbf{D}^{(N)}(h_N) = \mathbf{Z}_d^{(N)}\mathbf{A}_1^{(1)} \tag{41}$$

With the boundary condition on the upper surface of the laminate given by equation (8), we have

$$\mathbf{Z}_s^{(N)}\mathbf{A}_1^{(1)} = 0. \tag{42}$$

For a nontrivial solution, the determinant of $\mathbf{Z}_s^{(N)}$ must vanish.

$$\det(\mathbf{Z}_s^{(N)}) = 0 \tag{43}$$

In general, $\mathbf{Z}_s^{(N)}$ is a complex matrix, equation (43) means that the absolute value of the determinate of $\mathbf{Z}_s^{(N)}$ must be equal to zero.

The determinant of $\mathbf{Z}_s^{(N)}$ is a function of phase velocity c and wave number ξ. When the wave number is assumed, the phase velocity can be obtained from equation (43). Consequently, the dispersion of the phase velocity is given by equation (43).

For any c and ξ which satisfy equation (43), the vector $\mathbf{A}_1^{(1)}$ can be determined. With the inverse process, $\mathbf{A}_1^{(n)}$ and $\mathbf{A}_2^{(n)}$ $(n = 1, \ldots N)$ can be obtained, and then the displacement, as well as stress and strain tensors, can be determined easily.

By selecting the real parts of the stress and strain, and omitting the superscript (n), the stress and strain can be written as follows:

$$\{\sigma_{11}\ \sigma_{22}\ \sigma_{33}\ \sigma_{12}\ \epsilon_{11}\ \epsilon_{22}\ \epsilon_{33}\ \epsilon_{12}\} = \{\bar{\sigma}_{11}\ \bar{\sigma}_{22}\ \bar{\sigma}_{33}\ \bar{\sigma}_{12}\ \bar{\epsilon}_{11}\ \bar{\epsilon}_{22}\ \bar{\epsilon}_{33}\ \bar{\epsilon}_{12}\} \cos\xi(n_1x_1 + n_2x_2 - ct) \tag{44}$$

$$\{\sigma_{13}\ \sigma_{23}\ \epsilon_{13}\ \epsilon_{23}\} = \{\bar{\sigma}_{13}\ \bar{\sigma}_{23}\ \bar{\epsilon}_{13}\ \bar{\epsilon}_{23}\} \sin\xi(n_1x_1 + n_2x_2 - ct). \tag{45}$$

The equation of the strain energy per unit volume is

$$E = (\sigma_{11}\epsilon_{11} + \sigma_{22}\epsilon_{22} + \sigma_{33}\epsilon_{33} + 2\sigma_{12}\epsilon_{12} + 2\sigma_{13}\epsilon_{13} + 2\sigma_{23}\epsilon_{23})/2. \tag{46}$$

Substituting equations (44) and (45) into equation (46) we have

$$E = E_c \cos^2\xi(n_1x_1 + n_2x_2 - ct) + E_s\sin^2\xi(n_1x_1 + n_2x_2 - ct), \tag{47}$$

where

$$E_c = (\bar{\sigma}_{11}\ \bar{\epsilon}_{11} + \bar{\sigma}_{22}\ \bar{\epsilon}_{22} + \bar{\sigma}_{33}\ \bar{\epsilon}_{33} + 2\ \bar{\sigma}_{12}\ \bar{\epsilon}_{12})/2 \tag{48}$$

$$E_s = \bar{\sigma}_{13}\ \bar{\epsilon}_{13} + \bar{\sigma}_{23}\bar{\epsilon}_{23}. \tag{49}$$

4 Numerical Results and Discussion

Numerical calculations of phase velocity spectra are carried out for a unidirectional graphite/epoxy laminate, angle-ply graphite/epoxy ones, and hybrid ones which consist of carbon/epoxy and glass/epoxy layers. The material properties are shown in Table 1 (from the papers given by Murakami and Akiyama, 1985; Takahashi and Chou, 1987). Each layer of

Table 1 Material properties of composites

property / composite	E_1	E_2	G_{12}	ν_{12}	ν_{23}	ρ
graphite/epoxy	30.0	0.75	0.375	0.250	0.250	1.90
carbon/epoxy	142.17	9.255	4.795	0.3340	0.4862	1.90
glass/epoxy	38.49	9.367	3.414	0.2912	0.5071	2.66

Downloaded 03 May 2010 to 171.66.16.244. Redistribution subject to ASME license or copyright; see http://www.asme.org/terms/Terms_Use.cfm

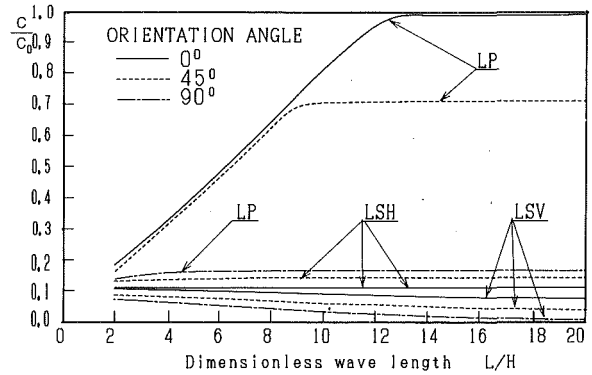


Fig. 2 Phase velocity spectra for unidirectional laminates (graphite/epoxy composite $\theta = 0$)

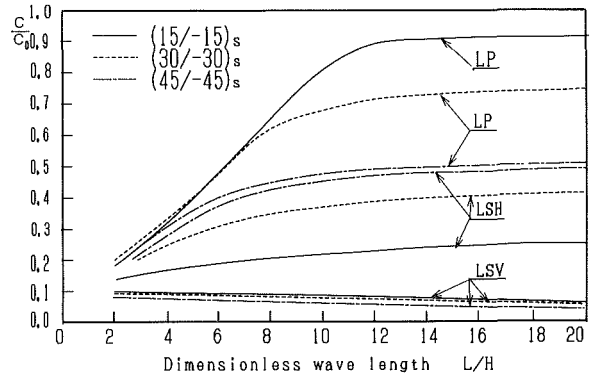


Fig. 3 Phase velocity spectra for symmetric angle-ply laminates (graphite/epoxy composite $\theta = 0$)

these laminates is made of fiber-reinforced composite, and in general, it is regarded as transverse isotropic material. Hence, we have

$$E_2 = E_3;\ \nu_{21} = \nu_{31};\ \nu_{12} = \nu_{13};\ \nu_{23} = \nu_{32}. \tag{50}$$

The elastic coefficients $C_{ijkl}^{(n)}$ can be calculated from the moduli shown in Table 1 and the fiber orientation angle ϕ_n (Jones, 1975).

In an infinite anisotropic body there are three kinds of waves which are denoted by QP, QSV, and QSH. Similarly, we name the three fundamental modes of Lamb wave LP, LSV, and LSH in this paper. Let c_0 be the phase velocity of QP wave in the strongest layer, i.e.,

$$c_0 = \sqrt{C_{1111}(0)/\rho_0} \tag{51}$$

where $C_{1111}(0)$ is the elastic coefficient of the strongest layer with the fiber orientation angle equal to zero, and ρ_0 is the density of this layer. The wavelength is denoted by L, and L/H is the dimensionless wavelength.

4.1 Dispersion and Anisotropy of Phase Velocity. The phase velocity dispersion curves for unidirectional graphite fiber-reinforced composite material are shown in Fig. 2. When the wave propagates along the symmetric axis (for 0 and 90 degrees) the LSH wave has no dispersion and the phase velocity is equal to that of the QSH wave. Otherwise, the LSH wave has weak dispersion. For the LP wave, the closer the direction of the wave propagation is to the fiber orientation, the stronger the dispersion becomes, and when the wave propagates along the fiber orientation, the strongest dispersion is observed. But when $L > 13H$, the phase velocity of the LP wave approaches that of the QP wave. For the LSV wave, the closer the direction of the wave propagation is to the fiber orientation, the weaker

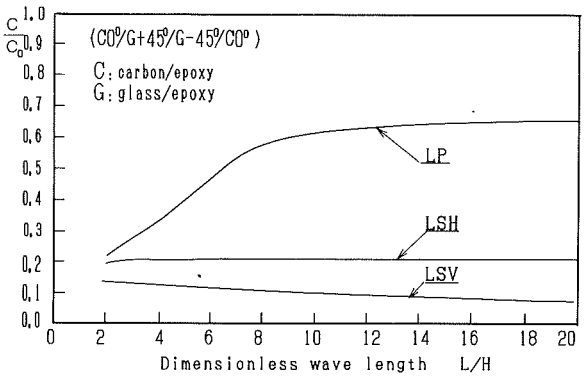


Fig. 4 Phase velocity spectra for hybrid laminates (graphite/epoxy and glass/epoxy composite $\theta = 0$)

the dispersion becomes. When L/H approaches to zero, the phase velocity of the LSV wave approaches that of the Rayleigh wave.

For symmetric angle-ply laminates $(15/-15)_s$, $(30/-30)_s$, $(45/-45)_s$ which consist of four layers of graphite/epoxy composite, the dispersion occurs for all kinds of the fundamental mode waves as shown in Fig. 3, when the wave propagates along the x-axis. For the LP wave, the smaller the fiber orientation angle is, the stronger the dispersion becomes. Conversely, for the LSH wave, the smaller the fiber orientation angle is, the weaker the dispersion becomes.

The dispersion of the hybrid composite laminate which consists of carbon/epoxy and glass/epoxy layers is shown in Fig. 4. The wave propagates along the x_1-axis. To keep the static strength, the stronger carbon/epoxy layers are laid on the surfaces of the laminate, and, to improve the impact strength, the glass/epoxy layers with the better capability in absorbing impact energy are laid in the inner part of the laminate. From Fig. 4 it can be seen that the weak dispersion occurs for the LSH wave, and the strong dispersion is observed for the LP wave when $L/H < 10$.

For the LSV wave, it can be found from Figs. 2–4 that for all the laminates the phase velocity decreases almost linearly with the increase in L/H.

Phase velocity contours versus wave direction ($0 < \theta < 90$ deg) are computed for the unidirectional laminate and are shown in Fig. 5 for nondimensional wavelengths $L/H = 4$, 8, and 19. This is a different view of the spectra in Fig. 2. From Fig. 5 the strong anisotropy is observed for all the waves. Since the dispersion of the LSH wave is weak (see Fig. 2), the curves for $L/h = 4$, 8, and 19 are very close and can not be distinguished. When $L/H = 19$ (solid line), the shapes of the curves for LP and LSH waves are close to those given by Murakami and Akiyama (1985) (in the wave guide type), and the values are smaller than those. Because the laminate discussed by Murakami and Akiyama was unbounded, the waves have no dispersion. When $L/H = \infty$ the curves for LP and LSH waves will approach those obtained by Murakami and Akiyama.

For the symmetric angle-ply laminates $(15/-15)_s$, $(30/-30)_s$, and $(45/-45)_s$, the anisotropy of the phase velocity are shown in Figs. 6-8. One angle-ply laminate considered here just corresponds to one cell of the unbounded angle-ply laminate discussed by Murakai and Akiyama. Comparing the unbounded laminate with the finite thickness, one with the same fiber orientation angle, it can be found that the curves of finite thickness laminate for $L/H = 19$ are close to those of unbounded laminate for $L/H = \infty$, and the phase velocity of the finite thickness laminate is smaller than that of unbounded laminate. The smaller the fiber orientation angle is, the greater the difference of phase velocity becomes. For the LP wave in laminate $(15/-15)_s$, when $L/H = 8$ the difference is about 21

Downloaded 03 May 2010 to 171.66.16.244. Redistribution subject to ASME license or copyright; see http://www.asme.org/terms/Terms_Use.cfm

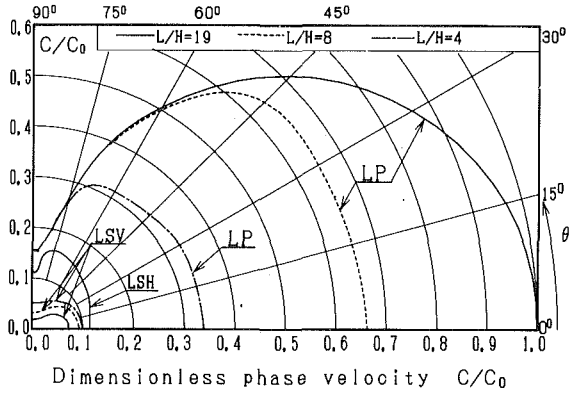


Fig. 5 Phase velocity contours for unidirectional laminates (graphite/epoxy composite)

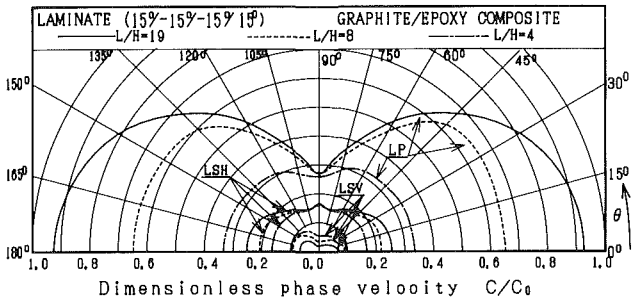


Fig. 6 Phase velocity contours for ±15 deg symmetric angle-ply laminate

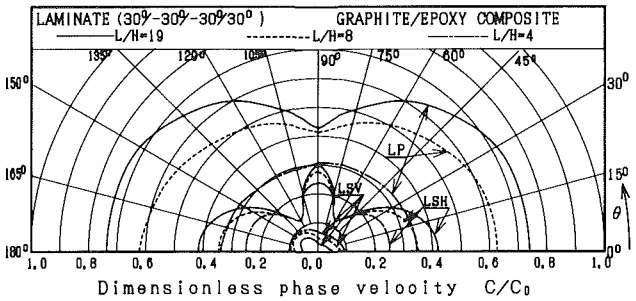


Fig. 7 Phase velocity contours for ±30 deg symmetric angle-ply laminate

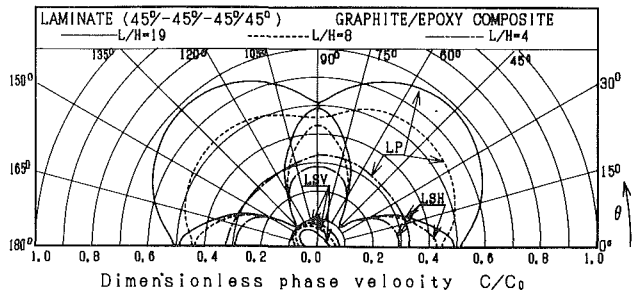


Fig. 8 Phase velocity contours for ±45 deg symmetric angle-ply laminate

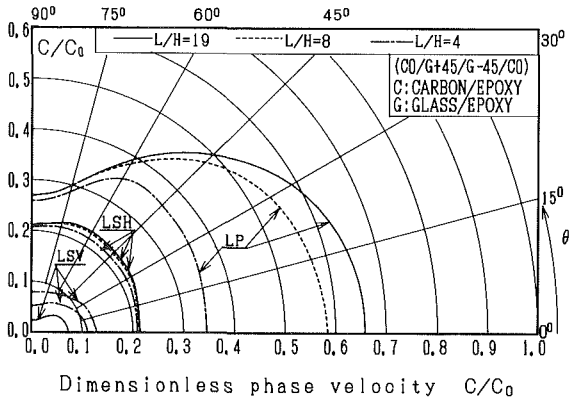


Fig. 9 Phase velocity contours for hybrid laminate

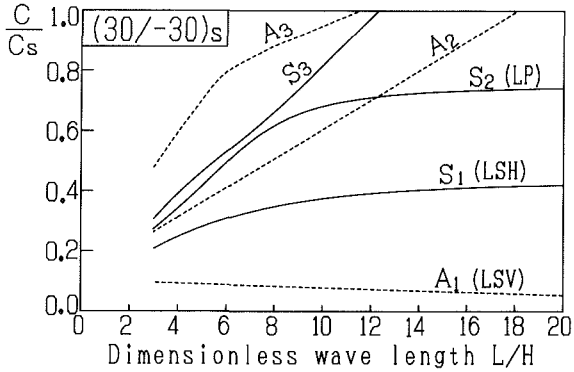


Fig. 10 Phase velocity contours of higher modes for ±30 deg symmetric angle-ply laminate

percent, and when $L/H=4$ it is about 26 percent. That is to say, the dispersion of the finite laminate is much stronger than that of unbounded one, when the wavelength is short and the number of layers is small.

For the LSV wave, the phase velocity has obviously both anisotropy and dispersion (see Figs. 5–9) in the finite thickness laminate, but has neither anisotropy nor dispersion in the unbounded laminate.

It is noted that the phase velocity of any wave changes in the range of $\theta = 0 \sim 180$ degrees. It means that there is only one symmetric (or antisymmetric) axis for the phase velocity as shown in Figs. 6–8. But for the unbounded angle-ply laminate, the phase velocity changes only in the range of $\theta = 0 \sim 90$ degrees.

The anisotropy of phase velocity of the hybrid composite laminate which consists of carbon/epoxy and glass/epoxy layers is shown in Fig. 9. Since the laminate is antisymmetric, the phase velocity changes in the range of $\theta = 0 \sim 90$ degrees. The phase velocity of the LSH wave has not only weak dispersion but also weak anisotropy.

In Figs. 5–9, it can be observed that when the wavelength is long, the phase velocities of LP and LSH waves depend on the direction of wave propagation, and when the wavelength is short, the dispersion becomes strong and the anisotropy becomes weak. It may mean that the dispersion weakens the anisotropy of phase velocity of the LP and LSH waves for the short wavelength.

In the finite thickness laminate, there are infinite wave modes. As an example, the phase velocity spectra for the lower six modes are shown in Fig. 10 for the graphite/epoxy angle-ply laminate $(30/-30)_s$. Because the displacement of the higher mode becomes complicated, the dispersion curves are divided into antisymmetric (dot line) and symmetric (solid line) modes.

4.2 Strain Energy Distribution. The distributions of the strain energies E_c and E_s are calculated and shown in Figs. 11–13. For the LP wave E_c in a laminate $(C0)_4$, concentrates within the surface layer, but E_c in a hybrid laminate (C0/G0/G0/C0) (where C and G denote carbon/epoxy and glass/epoxy layer, respectively, and 0 means $\phi = 0$) concentrates within the inner glass/epoxy layers which have the better capability in absorbing impact energy. And E_s in this hybrid laminate is very small. For the LSV wave, E_c concentrates within the surface layers

Downloaded 03 May 2010 to 171.66.16.244. Redistribution subject to ASME license or copyright; see http://www.asme.org/terms/Terms_Use.cfm

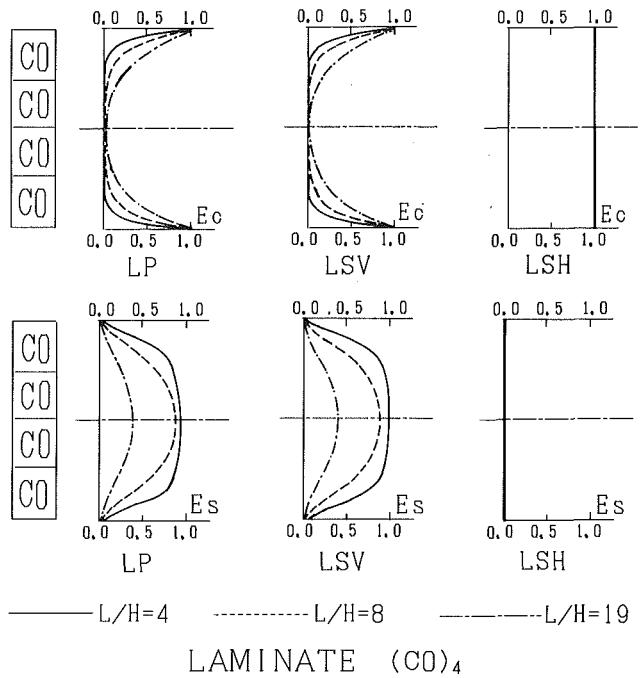


Fig. 11 Distributions of strain energy amplitudes in the thickness direction of unidirectional laminate (carbon/epoxy composite)

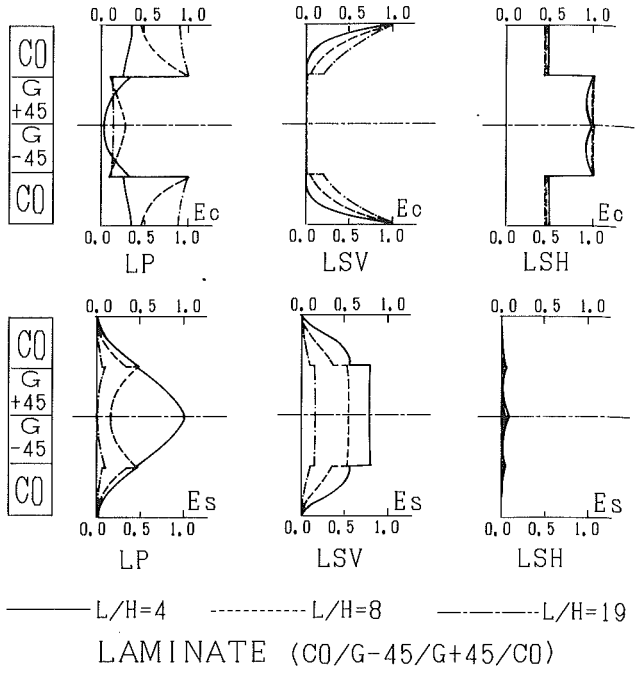


Fig. 13 Distributions of strain energy amplitudes in the thickness direction of hybrid composite laminate (C:carbon/epoxy; G:glass/epoxy)

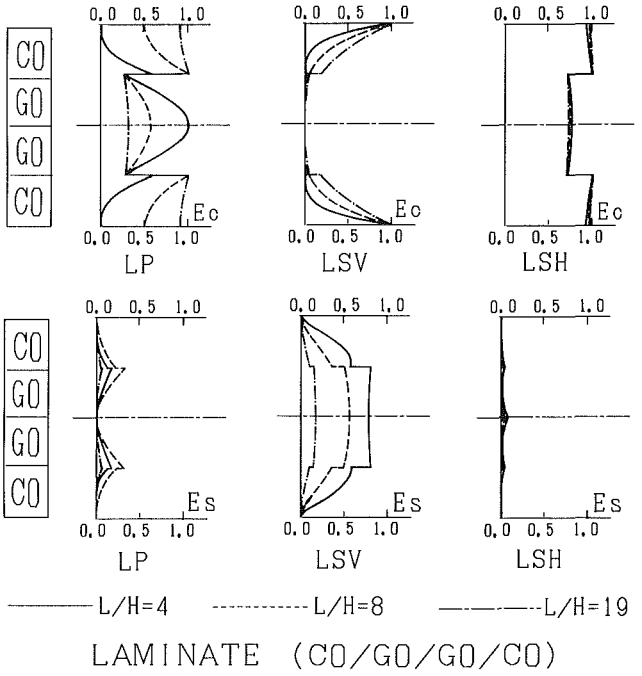


Fig. 12 Distributions of strain energy amplitudes in the thickness direction of hybrid composite laminate (C:carbon/epoxy; G:glass/epoxy)

in both the laminates $(C0)_4$ and (C0/G0/G0/C0), but E_s in the laminate (C0/G0/G0/C0/) concentrates within the two inner layers more than in the $(C0)_4$. This is what we are looking forward to. For the LSH wave, E_s is very small in both the laminates $(C0)_4$ and (C0/G0/G0/C0), and E_c in the laminate $(C0)_4$ is uniform in the thickness direction of the laminate. But in the laminated (C0/G0/G0/C0), the inner layers contain smaller strain energy than the surface layers. This is what we did not expect.

Next, we change the fiber orientation of the inner layers, such as (C0/G+45/G−45/C0), and calculate the energy distribution in the thickness direction of the laminate. The results are shown in Fig. 13. It can be seen that not only for the LP and LSV waves but also for the LSH wave the strain energy concentrates within inner layers. This laminate may be expected to have the better capability in absorbing impact energy.

It is well known that the energy tends to concentrate in the soft layer during wave propagation, but it is not true for any kind of waves. The strain energies of LP and LSV waves concentrate in the inner part where the softer layers are laid. On the contrary, the strain energy of the LSH wave concentrates in the inner part where the harder layers are laid. For example, the two inner layers of the laminate $(C0)_4$ are harder than those in the laminate (C0/G0/G0/C0), and the energy E_c) contained in the two inner layers of the laminate $(C0)_4$ is more than in the laminate (C0/G0/G0/C0). Compared with the laminates (C0/G+45/G−45/C0) and $(C0)_4$, the same phenomenon can be found. Since the shear module of the inner layers (G+45/G−45) in the laminate (C0/G+45/−45/C0) is greater than that of the inner layers (C0/C0) in the laminate $(C0)_4$, the strain energy (E_c), which concentrates in the two inner layers of the laminate (C0/G+45/G−45/C0), is more than that of the laminate $(C0)_4$. That is to say, the strain energy of the LSH wave concentrates in the hard layer.

It may be mentioned that the present approach has limitations due to the numerical truncation errors. The limitations depend on the materials of the laminate. For example, for an isotropic plate with Poisson's ratio of 0.3, our program still works, even if the wave number is equal to 40. But for the unidirectional graphite fiber-reinforced laminate ($\phi = 0$), the program fails when the wave number is greater than 11.

5 Conclusion

There are two methods in the practical numerical computation to find the phase velocity for a given wave number. One of them has been mentioned previously, but needs a complicated subroutine to find the phase velocity from the complex transcendental equation (43). In another method, a real matrix similar to that in equation (43) can be obtained by means of expressing the displacement using exponential, sine, and cosine functions with real arguments instead of equation (16). Hence,

Downloaded 03 May 2010 to 171.66.16.244. Redistribution subject to ASME license or copyright; see http://www.asme.org/terms/Terms_Use.cfm

a general method such as the secant method or the Newton-Raphson method can be used to find the phase velocity from a real transcendental equation. But the subroutine which generates the real matrix becomes very complicated. In the present work, the two methods have been used and verified to be equivalent. The results shown in Section 4 are obtained using the second method. But the formulations of the first method have compact forms and are easy to understand.

From the numerical results, the following conclusions can be drawn.

(1) In general, the phase velocity of anisotropic laminates changes in the range of $\theta = 0 \sim 180$ degrees, even for the fiber-reinforced composite laminates for which each layer material has three symmetric axes.

(2) When the wavelength is long, the phase velocities of the LP and LSH waves depend on the direction of wave propagation in the anisotropic laminate. When the wavelength is short, the dispersion becomes strong and the anisotropy of the phase velocity becomes weak.

(3) By analyzing the distribution of strain energy in the thickness direction of laminates, we can determine the sequence of the layers and the fiber orientation of each layer in order to let the strain energy concentrate within the layers which have better capability in absorbing impact energy. By this method the better hybrid laminate may be obtained.

References

Brekhovskikh, L. M., 1960, *Waves in Layered Media*, Academic Press, p. 79.

Jones, R. M., 1975, *Mechanics of Composite Materials*, Scripta, Washington, D.C.

Kausel, E., 1986, "Wave Propagation in Anisotropic Layered Media," *Int. J. Numer. Methods Eng.*, Vol. 23, pp. 1567–1578.

Murakami, H., 1985, "A Mixture Theory for Wave Propagation in Angle-Ply Laminates, Part 1: Theory," ASME JOURNAL OF APPLIED MECHANICS, Vol. 52, pp. 331–337.

Murakami, H., and Akiyama, A., 1985, "A Mixture Theory for Wave Propagation in Angle-Ply Laminates, Part 2: Application," ASME JOURNAL OF APPLIED MECHANICS, Vol. 52, pp. 338–344.

Sun, C. T., Achenbach, J. D., and Herrmann, G., 1968, "Time-Harmonic Waves in a Stratified Medium Propagating in the Direction of the Layering," ASME JOURNAL OF APPLIED MECHANICS, Vol. 35, pp. 408–411.

Sun, C. T., Achenbach, J. D., and Herrmann, G., 1968, "Continuum Theory for a Laminated Medium," ASME JOURNAL OF APPLIED MECHANICS, Vol. 35, September, pp. 467–475.

Takahashi, K., and Chou, Tsu-Wei, 1987, "Non-linear Deformation and Failure Behavior of Carbon/Glass Hybrid Laminates," *J. Compos. Mater.*, Vol. 21, p. 396.

Thomson, W., 1950, "Transmission of Elastic Waves Through a Stratified Medium," *J. Appl. Phys.*, Vol. 21, pp. 89–93.

Downloaded 03 May 2010 to 171.66.16.244. Redistribution subject to ASME license or copyright; see http://www.asme.org/terms/Terms_Use.cfm

Kazuyuki Sasaki
Research Engineer,
Nagasaki Research and Development Center,
Mitsubishi Heavy Industries, Ltd.,
1-1, Akunoura-cho, Nagasaki 850-90, Japan

Yukio Iwashimizu
Professor,
Department of Mechanical Engineering,
Faculty of Science and Engineering,
Ritsumeikan University,
56-1 Tojiin-kitamachi,
Kita-ku, Kyoto 603, Japan

Osami Kobori
Associate Professor,
Department of Mechanical Engineering,
Faculty of Engineering,
Osaka Sangyo University,
3-1-1, Nakagaito,
Daito-shi,
Osaka 574, Japan

Strain-Induced Elastic Anisotropy Measured With Ultrasonic Waves

Measurements on ultrasonic velocities were performed to define elastic anisotropy produced in steel by plastic compressive deformation. Cylindrical blocks cut from a SS41 steel bar were compressed plastically along the bar axis, and then used to make specimens available for different propagation directions. Velocity variations with plastic strain were shown linear in the strain range from 0.09 to 0.22, and, the strain-induced transverse isotropy of slight degree was determined by analyzing their direction dependences.

1 Introduction

In polycrystalline metals, macroscopic elasticity is anisotropic in some degree principally due to metallurgical textures, and such elastic anisotropy has attracted attention increasingly through its effect on the propagation of ultrasonic waves. For example, the ultrasonic determination of elastic anisotropy is available for the macroscopic evaluation of textures. This was suggested by Papadakis (1964), and the quantitative study was recently performed by Sayers (1982). He derived the relations to determine some expansion coefficients of a crystallite orientation distribution function from ultrasonic velocities, and Allen et al. (1983) examined the validity of these relations experimentally. The ultrasonic texture evaluation based on these works was subsequently studied by Johnson (1985), Hirao et al. (1987), Clark et al. (1988), and Smith et al. (1988). Moreover, the evaluation of Lankford value, an important parameter of plastic anisotropy in thin plates, was also studied from a similar viewpoint by Hirao et al. (1988).

In these studies, the growth of elastic anisotropy, especially with plastic deformation, has not yet been studied systematically, but such investigation seems helpful to understand the elastic anisotropy more positively, and to obtain the fundamental relations based on which the growth of deformation texture is evaluated macroscopically. In the present study, therefore, we intend to define the elastic anisotropy produced in a steel bar by plastic uniaxial compression. To this end, the velocity of ultrasonic waves was measured, and its dependence on the propagation direction and plastic compressive strain was analyzed to determine the elastic constants expressing the strain-induced anisotropy.

Since the elastic anisotropy is equivalent to the deviatoric part of the fourth-rank elasticity tensor, a transverse isotropy, for instance, is generally expressed by three anisotropic elastic constants, the independent components of the deviatoric tensor. If these constants are (a, b, c), the type, and degree of the transverse isotropy may be defined by the ratio $a : b : c$, and the magnitude $(a^2+b^2+c^2)^{1/2}$, respectively. It is also convenient to define the transverse isotropy with opposite sign by the constants $(-a, -b, -c)$.

In the aforementioned studies on the ultrasonic texture evaluation, the type of elastic anisotropy is not general, but necessarily subjected to some restriction originating from the assumption that macroscopic elastic constants are given by the orientation averages of elastic constants of crystallites. Hence, the number of anisotropic elastic constants is reduced from three to one in the case of transverse isotropy. Though simplification due to such restriction is much preferable for further development of related ultrasonic studies including acoustoelasticity, its validity is to be examined in more detail. This point was also considered in the present study.

2 Elastic Waves in a Material With Slight Transverse Isotropy

In this section, we briefly summarize the theoretical results

Contributed by the Applied Mechanics Division of THE AMERICAN SOCIETY OF MECHANICAL ENGINEERS for publication in the JOURNAL OF APPLIED MECHANICS.

Discussion on this paper should be addressed to the Technical Editor, Leon M. Keer, The Technological Institute, Northwestern University, Evanston, IL 60208, and will be accepted until two months after final publication of the paper itself in the JOURNAL OF APPLIED MECHANICS. Manuscript received by the ASME Applied Mechanics Division, April 10, 1989; final revision, Aug. 31, 1989.

Copyright © 1990 by ASME
Downloaded 03 May 2010 to 171.66.16.244. Redistribution subject to ASME license or copyright; see http://www.asme.org/terms/Terms_Use.cfm

used to consider experimental results given later. A transversely isotropic material is assumed, and a set of orthogonal axes is taken with the X_3-axis along its symmetry axis. The elastic constants referred to these axes are denoted by either C_{ijkl} or C_{mn} (Voigt notation), and decomposed into the isotropic parts $C^0{}_{ijkl}$, and anisotropic parts $C'{}_{ijkl}$ defined by the following equations.

$$C_{ijkl} = C^0{}_{ijkl} + C'{}_{ijkl}, \tag{1}$$

$$C'{}_{mmpp} = C'{}_{mpmp} = 0, \tag{2}$$

$$C^0{}_{ijkl} = \lambda\delta_{ij}\delta_{kl} + \mu(\delta_{ik}\delta_{jl} + \delta_{il}\delta_{jk}),$$

$$\lambda = (C_{11} + C_{33} + 8C_{13} + 5C_{12} - 4C_{44})/15, \tag{3}$$

$$\mu = (7C_{11} + 2C_{33} - 4C_{13} - 5C_{12} + 12C_{44})/30.$$

The usual summation convention is applied to equation (2), and later to equation (7). Since C'_{ijkl} characterizing the anisotropy have three independent constants, these are chosen as

$$B = C'_{44},\ C = C'_{33},\ G = (8C'_{44} - C'_{33} + 4C'_{23})/16. \tag{4}$$

The other nonzero constants are expressed in terms of these as follows:

$$C'_{11} = C'_{22} = -(C + 4G)/2,$$

$$C'_{12} = C'_{21} = (C'_{11} - 4C'_{23} + 4C'_{44})/3$$

$$= -(-8B + C + 12G)/2, \tag{5}$$

$$C'_{23} = C'_{32} = C'_{31} = C'_{13} = (-8B + C + 16G)/4,$$

$$C'_{66} = (C'_{11} - C'_{12})/2 = 2(-B + G).$$

When the transverse isotropy is of slight degree, the anisotropic elastic constants C'_{kl} are small compared with the isotropic ones, λ and μ, i.e.,

$$|C'_{kl}|/\lambda,\ |C'_{kl}|/\mu \ll 1. \tag{6}$$

The velocity and polarization of elastic waves can be analyzed (Auld, 1973) by assuming the displacement u_k as

$$u_k = U_k \exp\{i\omega(n_m X_m/v - t)\}, \tag{7}$$

where U_k, ω, n_m, and v are, respectively, the displacement amplitude, angular frequency, propagation direction (unit vector), and propagation velocity. Since propagation directions at the same angle θ from the symmetry axis of transverse isotropy are equivalent, n_k in equation (7) may be taken as shown in Fig. 1, that is, as

$$n_1 = \sin\theta,\ n_2 = 0,\ n_3 = \cos\theta, \tag{8}$$

without loss of generality. Then elastic analysis yields the result that the plane harmonic wave expressed by equation (7) has three modes, i.e., the quasi-transverse, pure transverse, and quasi-longitudinal modes, and the respective velocities v_1, v_2, and V, and mutually orthogonal polarization directions are given by the following equations:

$$v_1(\theta) = [(C_{11}n_1{}^2 + C_{33}n_3{}^2 + C_{44} - A^{1/2})/(2\rho)]^{1/2},$$

$$U_3/U_1 = -\{C_{11}n_1{}^2 - C_{33}n_3{}^2 + C_{44}(2n_3{}^2 - 1) + A^{1/2}\}/ \tag{9}$$

$$\{2(C_{13} + C_{44})n_1 n_3\},\ U_2 = 0,$$

$$v_2(\theta) = [\{(C_{11} - C_{12})n_1{}^2 + 2C_{44}n_3{}^2\}/(2\rho)]^{1/2},$$

$$U_1 = U_3 = 0, \tag{10}$$

$$V(\theta) = [(C_{11}n_1{}^2 + C_{33}n_3{}^2 + C_{44} + A^{1/2})/(2\rho)]^{1/2},$$

$$U_3/U_1 = -\{C_{11}n_1{}^2 - C_{33}n_3{}^2 + C_{44}(2n_3{}^2 - 1) - A^{1/2}\}/ \tag{11}$$

$$\{2(C_{13} + C_{44})n_1 n_3\},\ U_2 = 0,$$

where

$$A = \{(C_{11} - C_{44})n_1{}^2 + (C_{44} - C_{33})n_3{}^2\}^2$$

$$+ 4(C_{13} + C_{44})^2 n_1{}^2 n_3{}^2. \tag{12}$$

For slight transverse isotropy, equations (9)–(12) can be approximated by neglecting the second and higher powers of C'_{ijkl} on account of equation (6), and the results are given as follows:

$$v_1(\theta) = a_1 - b_1(1 - \cos 4\theta), \tag{13}$$

$$U_3/U_1 = -\tan\theta[1 - \{3C/4 + G(1 - 5\cos 2\theta)\}/(\lambda + \mu)],$$

$$U_2 = 0, \tag{14}$$

$$v_2(\theta) = a_2 - b_2(1 - \cos 2\theta), \tag{15}$$

$$U_1 = U_3 = 0, \tag{16}$$

$$V(\theta) = a - b(1 - \cos 2\theta) - c(1 - \cos 4\theta), \tag{17}$$

$$U_3/U_1 = \cot\theta[1 + \{3C/4 + G(1 - 5\cos 2\theta)\}/(\lambda + \mu)],$$

$$U_2 = 0, \tag{18}$$

where $a's$, $b's$, and c are defined by

$$a_1 = a_2 = v_0 + TB,\ b_1 = 5TG/4,\ b_2 = T(3B/2 - G), \tag{19}$$

$$a = V_0 + LC,\ b = L(3C/4 + G),\ c = -5LG/4, \tag{20}$$

$$T = v_0/(2\mu), \qquad v_0 = (\mu/\rho)^{1/2} \tag{21}$$

$$L = V_0/[2(\lambda + 2\mu)],\ V_0 = [(\lambda + 2\mu)/\rho]^{1/2}. \tag{22}$$

v_0, and V_0 in equations (21) and (22) are, respectively, equal to the angular averages of $[v_1(\theta) + v_2(\theta)]/2$, and $V(\theta)$, which may be referred to as isotropic velocities. Since the polarization directions given by equations (14) and (18), both lying in the X_1X_3-plane, are almost perpendicular, and parallel to the propagation direction, respectively, equations (13) and (15) give two transverse velocities, and equation (17) gives the longitudinal velocity.

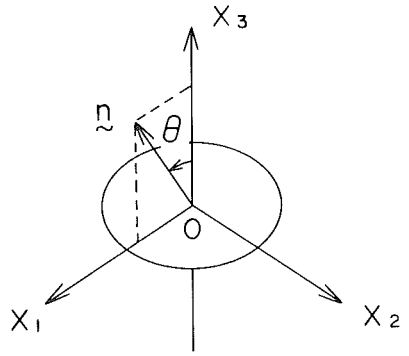


Fig. 1 Orthogonal axes and propagation direction

Downloaded 03 May 2010 to 171.66.16.244. Redistribution subject to ASME license or copyright; see http://www.asme.org/terms/Terms_Use.cfm

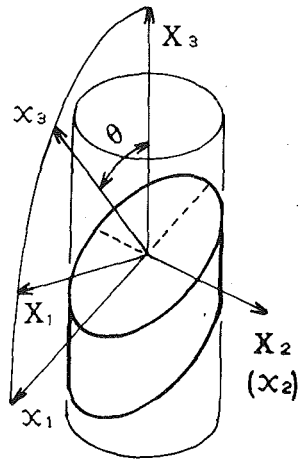


Fig. 2 Schematic of a specimen

3 Experiment

In the present experiment, an as-received 30-mm diameter bar of steel SS41 was used. Cylindrical blocks with 50-mm height cut from this were compressed along the bar axis for different plastic strains, and then machined for specimens as shown in Fig. 2. The nominal compressive plastic strain of the blocks, e, was chosen as $e=0$, 9.2, 15.5, 22.0, and 29.4 percent. In Fig. 2, the X_3-axis is the axis of the original bar, and θ is the angle from this to the x_3-axis which is normal to a pair of plane parallel faces. The thickness along the x_3-axis was about 19 mm, and an identical plane in the bar was taken as the X_3x_3-plane in each specimen.

For different propagation directions of ultrasonic waves, the face angle θ was chosen as $\theta=0$, 22.5, 45, 60 deg, and, as for the specimens $\theta=0$ deg, another pair of plane parallel faces was also machined perpendicularly to the X_2-axis. These specimens originally prepared were finally supplemented by five ones, ($\theta=30$ deg, $e=0$) and ($\theta=0$ deg, 45 deg, $e=19.6$, 26.0 percent).

The ultrasonic measurements were performed by a single transducer pulse echo method. Transducers for transverse, and longitudinal waves were, respectively, plated 4 mm, and 4.5-mm square ceramics with resonant frequency 5 MHz (from Fuji Ceramics). In order to obtain two transverse and one longitudinal velocities $v_1(\theta)$, $v_2(\theta)$, and $V(\theta)$ in the propagation direction at the angle θ from the bar axis, the transducer was attached to a plane of each specimen, and the relative time delay of the first and second echoes from the opposite plane face was measured by the sing-around device (UVM-2 from Cho-onpa Kogyo). It should be noted that the velocities $v_1(90\ \text{deg})$, $v_2(90\ \text{deg})$, and $V(90\ \text{deg})$ were measured in the specimens $\theta=0$ by using the parallel faces perpendicular to the X_2-axis.

In transverse velocity measurements by the sing-around method, the relative time delay of two successive echoes varies by rotating the transducer, and the peaks, or midpoints in nearly flat portions of such variation give two polarization directions and corresponding velocities $v_1(\theta)$ and $v_2(\theta)$. Hence, deviations of the transducer direction from the polarization directions introduce some errors to the obtained velocities, and, in the present case, the errors due to deviations within 15 deg were ascertained to be less than 0.4 m/s. It was also confirmed that the polarization directions except for the waves $\theta=90$ deg had some deviations from the x_1 and X_2-axes, and their maximum was about 13 deg for the waves with $\theta=0$ deg. Based on these observations, the present measurements of $v_1(\theta)$, and $v_2(\theta)$ were performed by setting the transducer direction along the x_1 and X_2-axes, respectively. Since the waves with $\theta=90$ deg polarized into the X_1, and X_3-axes, the transducer was set along these directions to obtain the respective velocities, $v_1(90\ \text{deg})$, and $v_2(90\ \text{deg})$.

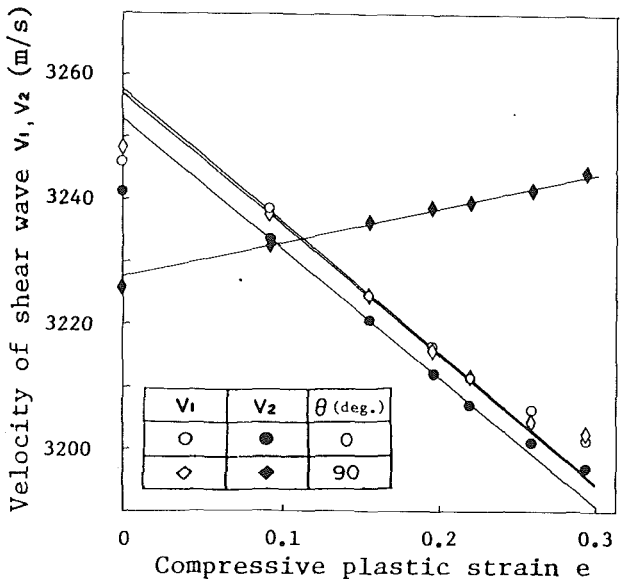


Fig. 3 Transverse velocities v_1 and v_2 versus plastic strain e for propagation directions $\theta=0$ deg and 90 deg

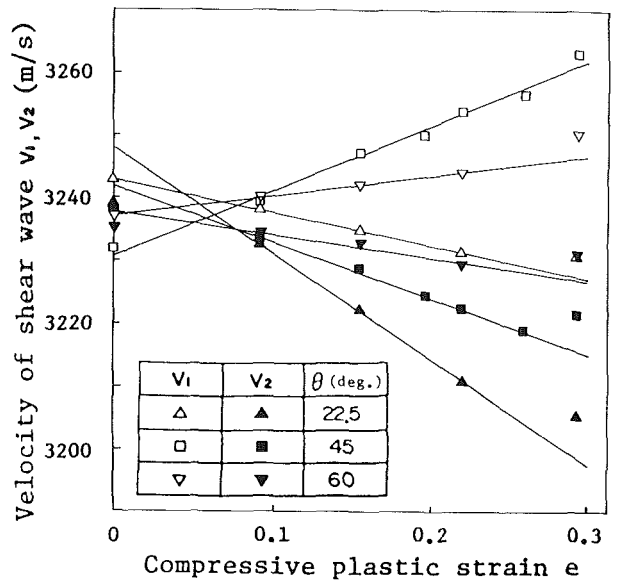


Fig. 4 Transverse velocities v_1 and v_2 versus plastic strain e for propagation directions $\theta=22.5$ deg, 45 deg and 60 deg

Since measuring temperatures were different between 22 ± 3°C, the obtained data were modified to the values at the reference temperature 22°C by using the constant rates of velocity changes due to temperature. These rates measured beforehand were -0.4(m/s)/°C for transverse waves, and -0.7(m/s)/°C for longitudinal waves. By repeated measurements including the use of different coupling media between transducers and specimens, the extent of measurement errors was estimated as ±1 m/s for transverse velocities, and ±2 m/s for longitudinal velocities. In this estimation, the inaccuracy in thickness measurements was also taken into account.

In interpreting measured velocities in anisotropic materials, it is generally important to take the effect of beam skewing into account (Allen et al., 1985). In the present study, this effect was estimated by using later given equations (31), (32), (34), and (35) to equations (13), (15), and (17), and it was confirmed

Downloaded 03 May 2010 to 171.66.16.244. Redistribution subject to ASME license or copyright; see http://www.asme.org/terms/Terms_Use.cfm

Table 1 Coefficients α's and β's (m/s)

θ	α_1	β_1	α_2	β_2	α	β
0°	3257.7	-211	3252.7	-207	5924.1	65
22.5°	3242.9	-53	3248.0	-168	5925.5	13
45°	3230.8	103	3241.8	-89	5932.2	-94
60°	3237.1	31	3237.7	-37	5933.5	-97
90°	3257.4	-214	3227.2	54	5913.1	53

that the correction of velocity data due to this could be neglected.

4 Transverse Velocities

Figures 3 and 4 are the plots of the measured velocities v_1 and v_2 versus the compressive plastic strain e, and show that, in the strain range $0.09<e<0.22$, both velocities varied directly with the strain variation irrespective of the propagation direction θ. The lines in the figures were determined by these linear variations, the coefficients of their equations

$$v_1=\alpha_1+\beta_1 e,\ v_2=\alpha_2+\beta_2 e \tag{23}$$

being given in Table 1 for later use. Figure 3 shows another distinctive feature that the difference between v_1(0 deg) and v_2(0 deg) kept a nearly constant value of about 5 m/s, and v_1(90 deg) was almost coincident with v_1(0 deg), irrespective of the strain e. This and the fact that the initial difference between v_1(90 deg) and v_2(90 deg) was about five times larger than the difference 5 m/s above suggest that the initial anisotropy of the bar was an orthotropy very akin to a transverse isotropy, and another transverse isotropy grew with the plastic strain.

In Figs. 5 and 6, the data are plotted with respect to the propagation direction θ with the strain e as the parameter, and the auxiliary curves obeying equations (13) and (15) are also drawn to make the figures easy to see. These figures clearly show that the initial anisotropy of the bar was almost offset by an anisotropy induced by the strain e of about 0.09, and this strain-induced anisotropy was developed furthermore. Since the curves except for $e=0$ are in good agreement with the data, this anisotropy may be regarded as a transverse isotropy as already suggested.

5 Longitudinal Velocities

The measured longitudinal velocities V are plotted in Fig. 7 with respect to the strain e, and in Fig. 8 with respect to the propagation direction θ. As in the case of transverse waves, the relations between V and e in the range $0.09<e<0.22$ were linear irrespective of θ. The lines in Fig. 7 express these linear relations

$$V=\alpha+\beta e, \tag{24}$$

whose coefficients are also listed in Table 1. In Fig. 8, where the auxiliary curves obeying equation (17) are also drawn, the offsetting between the initial and strain-induced anisotropies is not seen so clearly as in Figs. 5 and 6, but the growth of the latter is evident.

6 Strain-Induced Elastic Anisotropy

Since the experimental data showed that the specimens were almost transversely isotropic, it is appropriate to analyze them quantitatively based on the theoretical relations, equations (13), (15), and (17). To do this, we confine ourselves to the linear velocity variations due to the strain in the range $0.09<e<0.22$, because parabolic velocity variations in $e<0.09$, though interesting, can be inferred from only two

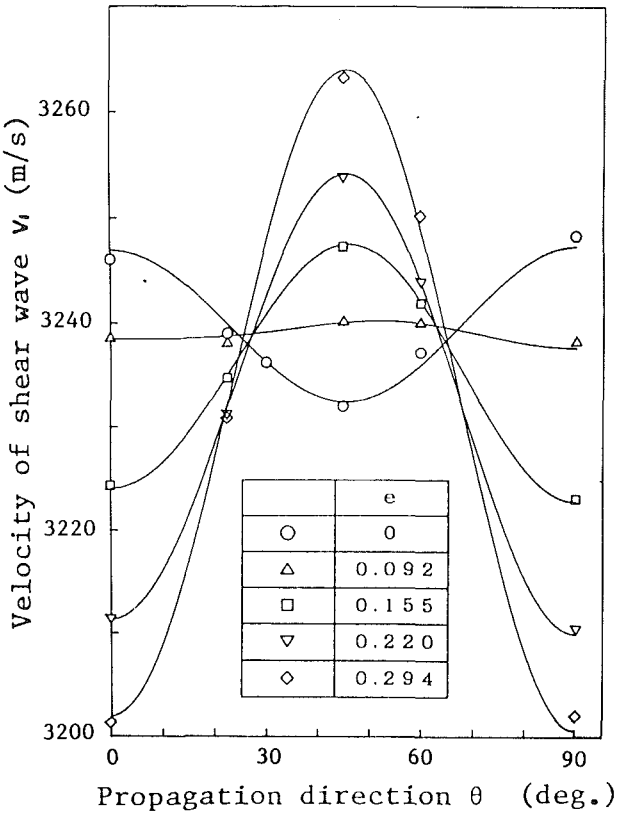


Fig. 5 Transverse velocity v_1 versus propagation direction θ

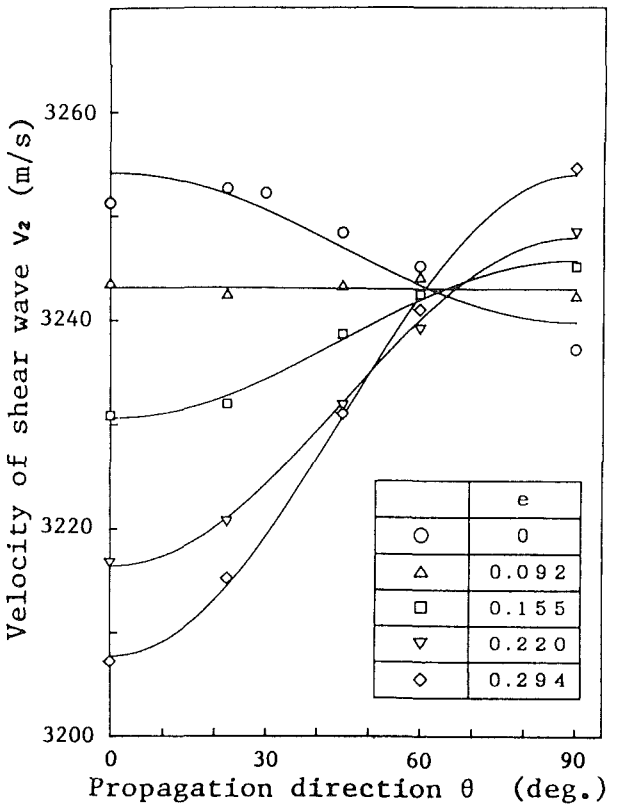


Fig. 6 Transverse velocity v_2 versus propagation direction θ

data at $e=0$ and 0.09, and those in $e>0.22$ seem to have been affected by nonuniformity of large compressive deformations.

This confinement makes it possible to treat the coefficients

Downloaded 03 May 2010 to 171.66.16.244. Redistribution subject to ASME license or copyright; see http://www.asme.org/terms/Terms_Use.cfm

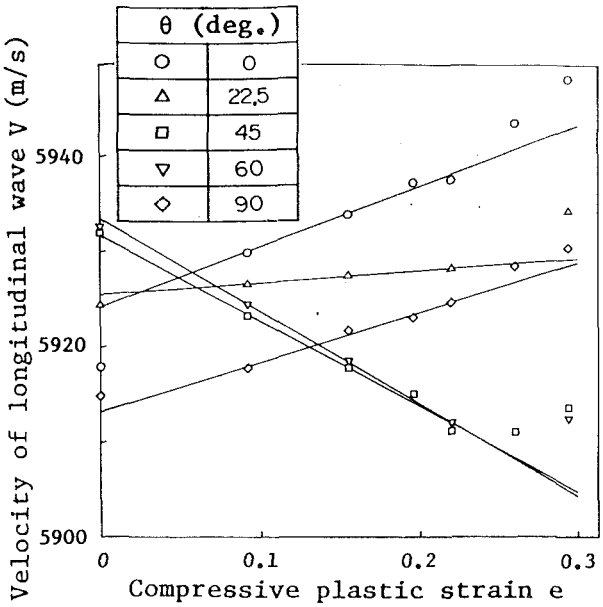


Fig. 7 Longitudinal velocity V versus plastic strain e

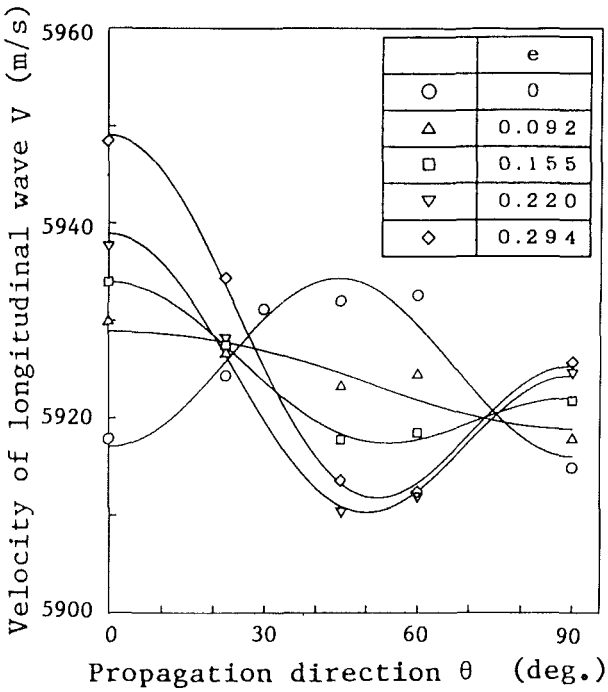


Fig. 8 Longitudinal velocity V versus propagation direction θ

$a's$, $b's$, and c in the theoretical relations as linear functions of the strain, that is, for instance,

$$a_1 = p_{10} + p_{11}e,\ b_1 = q_{10} + q_{11}e. \tag{25}$$

Hence, equation (13) becomes

$$v_1 = [p_{10} - q_{10}(1 - \cos 4\theta)] + [p_{11} - q_{11}(1 - \cos 4\theta)]e,$$

and the comparison of this with equation (23) yields

$$\alpha_1 = p_{10} - q_{10}(1 - \cos 4\theta),$$

$$\beta_1 = p_{11} - q_{11}(1 - \cos 4\theta). \tag{26}$$

Since the experimental values of α_1 and β_1 for each θ are listed in Table 1, $p's$ and $q's$ in the above equations can be determined by the least square method, and then used to determine

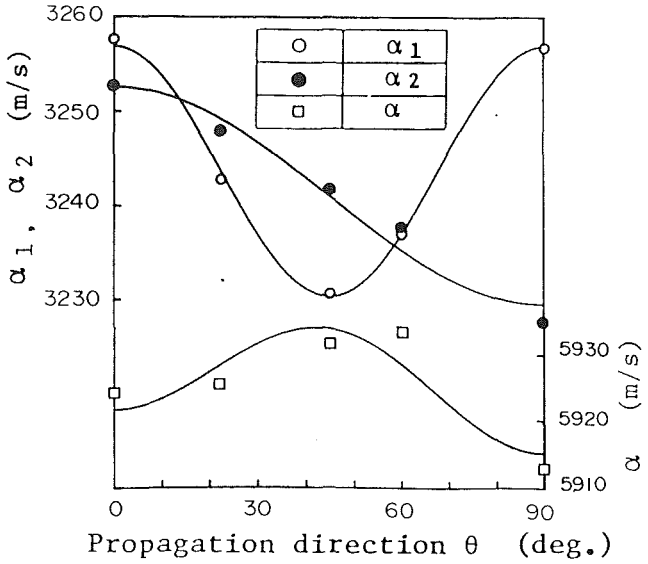


Fig. 9 Dependences of α_1, α_2 and α on propagation direction θ

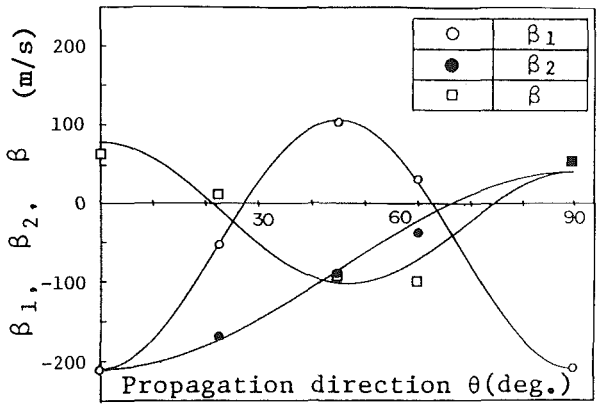


Fig. 10 Dependences of β_1, β_2 and β on propagation direction θ

a_1 and b_1 in equation (25). In this manner, $\alpha's-\theta$ and $\beta's-\theta$ curves in Figs. 9 and 10, and the following results for $a's$, $b's$ and c (m/s) are obtained.

$$a_1 = a_0 + \delta,\ b_1 = 13.5 - 159\,e, \tag{27}$$

$$a_2 = a_0 - \delta,\ b_2 = 11.7 - 125\,e, \tag{28}$$

$$a_0 = 3255.0 - 211\,e,\ \delta = 2.3 - 2e, \tag{29}$$

$$a = 5921.6 + 81e,\ b = 3.2 + 19e,\ c = -7.9 + 83\,e \tag{30}$$

As for the transverse waves, $\alpha's$ and $\beta's$ curves in the figures are in good agreement with the experimental plots, which shows that equations (27)–(29) are much reliable in the strain range considered. It is seen from the second of equation (29) that the terms $\pm\delta$ in equations (27) and (28), which are inconsistent with transverse isotropy, keep nearly constant and small magnitude of about 2 m/s. This means that the initial anisotropy, corresponding to $\alpha's$, differs a little from transverse isotropy. The neglection of δ and comparison of equations (27)–(29) with equation (19) yield

$$v_0 = 3240.0 - 43e, \tag{31}$$

$$TB = 15.0 - 168e,\ TG_T = 10.8 - 127e \tag{32}$$

(m/s), where G_T is used instead of G. The use of equations (21) and (31) to equation (32) finally gives

Downloaded 03 May 2010 to 171.66.16.244. Redistribution subject to ASME license or copyright; see http://www.asme.org/terms/Terms_Use.cfm

$$B = 7.6 - 86e,\ G_T = 5.5 - 65e\ (\times 10^2 \text{MPa}), \tag{33}$$

where the constant density $\rho = 7.86 \times 10^3 \text{kg/m}^3$ is assumed.

In contrast, α and β curves for the longitudinal wave, especially the former, have deviations from the experimental plots, and this seems closely related to the aforementioned nature of the initial anisotropy. However, these deviations are not so large compared with the extent of the measurement error, so that it seems allowable to use equation (30) for the determination of the elastic anisotropy. Equations (20) and (30) give

$$V_0 \doteq 5925.8 - 33e, \tag{34}$$

$$LC = -4.2 + 114e,\ LG_L = 6.3 - 67e \tag{35}$$

(m/s), where G_L is used instead of G. It follows from these and equation (22) that

$$C = -3.9 + 106e,\ G_L = 5.9 - 62e\ (\times 10^2\ \text{MPa}). \tag{36}$$

Since G_T and G_L, determined by the independent data, are well coincident, the mean value of them gives

$$G = 5.7 - 64e\ (\times 10^2\ \text{MPa}). \tag{37}$$

From equations (33), (36), and (37), it is concluded that the elastic anisotropy in question is composed of the initial transverse isotropy given by

$$B_0 = 7.6,\quad G_0 = 5.7,\quad C_0 = -3.9\quad (\times 10^2\ \text{MPa}), \tag{38}$$

and the strain-induced transverse isotropy given by

$$\bar{B} = -86\,e,\quad \bar{G} = -64e,\quad \bar{C} = 106e\quad (\times 10^2\ \text{MPa}). \tag{39}$$

Concerning this, it should be again noted that the strain range is limited, and that some discrepancy of the initial anisotropy from transverse isotropy is neglected, which lowers the validity of the obtained values of B_0, G_0, and, especially, C_0. Equation (39) seems to be the first result expressing the strain-induced elastic anisotropy systematically, and, in further study, it is desired to interpret this based on the texture development expected by the polycrystalline plasticity theory.

7 Discussion

Since the initial and strain-induced transverse isotropies given by the previous equations have opposite signs, the former is offset by the latter as the compressive plastic strain increases, However, the ratios defining the types of them, i.e.,

$$B_0 : G_0 : C_0 = 1 : 0.75 : -0.51, \tag{40}$$

$$\bar{B} : \bar{G} : \bar{C} = 1 : 0.74 : -1.23, \tag{41}$$

are different on account of C_0 and $\bar{C}$, so that $C = C_0 + \bar{C}$ does not vanish at $e = 0.09$ giving $B = B_0 + \bar{B} = 0$ and $G = G_0 + \bar{G} = 0$. In the previous study in S18C steel with transverse waves (Toriyama et al., 1988), the results corresponding to equations (39) and (41) are

$$\bar{B} = -74e,\quad \bar{G} = -60e\quad (\times 10^2\ \text{MPa})$$

$$\bar{B} : \bar{G} = 1 : 0.81,$$

and these are similar to the present results.

For theoretical evaluation of macroscopic elastic constants of polycrystalline materials (Musgrave, 1970), the Voigt method is simple and frequently used. Since this assumes that the macroscopic stiffness is equal to the orientation average of those of crystallites, the constants B, G, and C obtained for any transversely isotropic aggregate of cubic crystallites obey the restriction

$$B^V : G^V : C^V = 1 : 0.875 : -2. \tag{42}$$

When transverse isotropy is of slight degree, the Reuss method, which averages the compliances of crystallites in a similar way, also gives equation (42). The experimental ratios $B_0 : G_0$ and $\bar{B} : \bar{G}$ are relatively close by $B^V : G^V$, while $\bar{B} : \bar{C}$ seems a little more different from $B^V : C^V$. Much difference of $B_0 : C_0$ from this seems due to the approximation of the initial anisotropy.

Isotropic elastic constants $\lambda = \lambda_0 + \bar{\lambda}$ and $\mu = \mu_0 + \bar{\mu}$ are also obtained from equations (21), (22), (31), and (34) as

$$\lambda_0 = 110,\ \mu_0 = 83\qquad (\text{GPa}), \tag{43}$$

$$\bar{\lambda} = 13e,\ \bar{\mu} = -22e\qquad (\times 10^2\text{MPa}), \tag{44}$$

where the density is assumed to be constant. These give the following bulk modulus $K = K_0 + \bar{K}$, and Young's modulus $E = E_0 + \bar{E}$.

$$K_0 = 166,\ E_0 = 212\qquad (\text{GPa}) \tag{45}$$

$$\bar{K} = 2e,\ \bar{E} = -49e\qquad (\times 10^2\text{MPa}). \tag{46}$$

Equations (44) and (46) show that the variations of these isotropic constants with the plastic strain are small compared with those of the anisotropic constants B, C, and G. In particular, $\bar{K}$ is much smaller, so that the bulk modulus K may be regarded to be independent of the plastic strain. This agrees well with the theoretical result (Hill, 1952) that the bulk modulus of a polycrystalline aggregate of cubic crystallites is equal to that of the single crystal.

Finally, the acoustic birefringence defined by

$$D(\theta) = \{v_1(\theta) - v_2(\theta)\}/v_0$$

is briefly mentioned. This is an important quantity in acoustoelasticity, and its change with plastic deformation was studied by Toda et al. (1982) and Taniguchi and Iwashimizu (1987). The respective results for SS41 steel plates compressed along the rolling directions give $dD/de = -6.6 \times 10^{-2}$, and -9.7×10^{-2} in the strain range $e < 0.2$. $dD(90)/de$ obtained from the study by Toriyama et al. (1988) and the present study are -6.8×10^{-2}, and -7.7×10^{-2}, respectively. The present value is equal to the average of these.

References

Allen, A. J., Hutchings, M. T., and Sayers, C. M., 1983, "Use of Neutron Diffraction Texture Measurement to Establish a Model for Calculation of Ultrasonic Velocities in Highly Oriented Austenitic Weld Material," *Journal of Applied Physics*, Vol. 54, pp. 555–560.

Allen, D. R., Langman, R., and Sayers, C. M., 1985, "Ultrasonic SH Wave Velocity in Textured Aluminum Plates," *Ultrasonics*, Vol. 23, pp. 215–222.

Auld, B. A., 1973, *Acoustic Fields and Waves in Solids*, Vol. 1, John Wiley and Sons, New York, Chapter 7 and Appendix 3.

Clark, A. V., Jr., Reno, R. C., Thompson, R. B., Smith, J. F., Blessing, G. V., Fields, R. J., Delasanto, P. P., and Mignogna, R. B., 1988, "Texture Monitoring in Aluminum Alloys: A Comparison of Ultrasonic and Neutron Diffraction Measurement," *Ultrasonics*, Vol. 26, pp. 189–197.

Hill, R., 1952, "The Elastic Behavior of a Crystalline Aggregate," *Proceedings of the Physical Society, London*, Vol. A65, pp. 349–354.

Hirao, M., Aoki, K., and Fukuoka, H., 1987, "Polycrystalline Metals Characterized by Ultrasonic Velocity Measurements," *Journal of the Acoustical Society of America*, Vol. 81, pp. 1434–1440.

Hirao, M., Hara, N., Fukuoka, H., and Fujisawa, K., 1988, "A Non-Destructive Evaluation of Texture in Cold-Rolled Steel Sheets Using Ultrasonic (Plastic Strain Ratio and Ultrasonic Pole Figure)," *Transactions of the Japan Society of Mechanical Engineers A*, Vol. 54, pp. 1814–1819 (in Japanese).

Johnson, G. C., 1985, "The Acoustoelastic Response of a Rolled Plate: Theoretical Estimate vs. Experiment," *Review of Progress in Quantitative NDE*, Vol. 4B, pp. 1043–1050.

Musgrave, M. J. P., 1970, *Crystal Acoustics*, Holden-Day, San Francisco, Calif., Chapter 15.

Papadakis, E. P., 1964, "Ultrasonic Study of Simulated Crystal Symmetries in Polycrystalline Aggregates," *IEEE Transactions on Sonic and Ultrasonics*, Vol. SU-11, pp. 19–29.

Downloaded 03 May 2010 to 171.66.16.244. Redistribution subject to ASME license or copyright; see http://www.asme.org/terms/Terms_Use.cfm

Sayers, C. M., 1982, "Ultrasonic Velocities in Anisotropic Polycrystalline Aggregates," *Journal of Physics D*, Vol. 54, pp. 2157–2167.

Smith, J. F., Thompson, R. B., Rehbein, D. K., and Negel, T. J., 1988, "Illustration of Texture with Ultrasonic Pole Figure," *Review of Progress in Quantitative NDE*, Vol. 6B, pp. 1541–1548.

Taniguchi, M., and Iwashimizu, Y., 1987, "Ultrasonic Study on the Change in Elastic Anisotropy with Plastic Deformation," *Ultrasonics*, Vol. 25, pp. 160–165.

Toda, H., Fukuoka, H., and Ohmori, H., 1982, "Variations in Texture-Induced Acoustic Anisotropy Due to Compressive Deformations (Influence of Strain-Rate and Temperature)," *Journal of the Society of Materials Science Japan*, Vol. 31, pp. 238–243 (in Japanese).

Toriyama, T., Iwashimizu, Y., and Kobori, O., 1988, "An Ultrasonic Study on Variations of Elastic Anisotropy with Plastic Compression," *Transactions of Japan Society of Mechanical Engineers A*, Vol. 54, pp. 1842–1846 (in Japanese, to be published in English in the International Journal of JSME).

Downloaded 03 May 2010 to 171.66.16.244. Redistribution subject to ASME license or copyright; see http://www.asme.org/terms/Terms_Use.cfm

On the Wave Propagation in Elastic Multilayer Periodic Media With Nonlocal Interactions[1]

J.L. Nowinski
H. Fletcher Brown Professor Emeritus,
Department of Mechanical Engineering,
University of Delaware,
Newark, DE 19716

After a brief review of the main concepts of the nonlocal theory of elasticity, the equations of the nonlocal elastic moduli are derived, and the constitutive equations of the nonlocal medium established. Propagation of a longitudinal time-periodic wave normal to the laminae of the layered medium is then analyzed, and the equation of the wave dispersion determined. The dispersion originates from two sources: the configuration (discreteness) of the structure, and the nonlocal constitution of the material of the laminae. A numerical example accompanied by a graph illustrates the dependence of the effective wave velocity on the wave number in the entire Brillouin zone. It is found that for very short waves the wave velocity decreases to about 64 percent of its conventional value established for waves of long wavelength.

Introduction

Since its very inception some 150 years ago, the classical theory of elasticity has been remarkably successful in the predictions of the behavior of material bodies acted upon by mechanical forces and heat. This is true in spite of the fact that the theory adopts an abstract continuum model for the material bodies under study. For all the accomplishments of the classical approach, however, there are instances in which its predictions must be called into question, evidently owing to the failure of the continuum model to provide a rational explanation in those cases.

To the credit of the classical theory it must be pointed out that, as a rule, its shortcomings come to light when the analysis touches upon the internal structure of matter. This should come as no surprise, inasmuch as the questions concerning the submicrostructure of bodies lie beyond the range of validity of any theory founded on the continuum concept.[2]

Even the founders of the theory of elasticity recognized its limitations, but nothing was done to remedy the situation until the early part of this century, when the brothers Cosserat (1909) introduced a new concept, that of the so-called couple stresses. More recently, efforts in the same direction were made by Mindlin and Tiersten (1967), providing a rigorous presentation of the couple stress theory, Mindlin (1968), exploring the connections between the crystal lattice and the continuum theories, Green and Rivlin (1964), examining higher-order gradients of displacement and velocity, and Eringen (1968), studying micropolar and micromorphic materials, to mention but a few.

A radical step forward was proposed in the 1960s by Edelen (1976), Eringen (1976), Kroener (1976), and Kunin (1983), with the formulation of a new, "nonlocal" theory of elasticity. This substantial generalization of the conventional theory rejects the fundamental classical assumption that the intermolecular forces within the bodies are contact forces possessing an infinitesimal range of influence. Rather, the new theory extends the action of cohesion over the entire body—an assumption more realistic than the classical one, in that, according to the experimental evidence, the cohesive interactions may reach to 15 (Cochran, 1965) and even 20 intermolecular distances (i.e., approximately 60 Å, or $6. \times 10^{-7}$ cm).

The introduction of a nonlocal structure into the concept of a continuum has two welcome consequences. First, it narrows the gap between the postulates of the classical elasticity and the dogma of modern physics asserting that matter has a discrete, and certainly not a continuous, structure. Second, owing to its more realistic approach, the new theory enables one to clarify some of the disputable points in the classical solutions. The following examples may serve to illustrate the latter claim.

(a) In agreement with actual observations, but in contrast to the conclusions of the classical theory, a nonlocal medium occupying an unbounded region exhibits dispersion of undulatory motions. The dispersion in this case has a constitutive character, i.e., derives from an internal ("pseudo-discrete") structure of the nonlocal medium.

(b) Stress singularities predicted by the classical theory at the tips of cracks and at the cores of dislocations are smoothed in their nonlocal aspect, being transformed into regular stress distributions.

[1]Prepared with the partial support of the University of Delaware.

[2]We recall the well-known fact that a continuum theory provides an adequate approximation as long as the wavelength is large compared with the intermolecular distance. For short waves, the influence of the discrete structure of matter can no longer be ignored (cf., e.g., Lindsay, 1960, Sect. 6.6, or Brillouin, 1963).

Contributed by the Applied Mechanics Division of THE AMERICAN SOCIETY OF MECHANICAL ENGINEERS for publication in the JOURNAL OF APPLIED MECHANICS.

Discussion on this paper should be addressed to the Technical Editor, Leon M. Keer, The Technological Institute, Northwestern University, Evanston, IL 60208, and will be accepted until two months after final publication of the paper itself in the JOURNAL OF APPLIED MECHANICS. Manuscript received by the ASME Applied Mechanics Division, Oct. 17, 1988; final revision, May 25, 1989.

Copyright © 1990 by ASME
Downloaded 03 May 2010 to 171.66.16.244. Redistribution subject to ASME license or copyright; see http://www.asme.org/terms/Terms_Use.cfm

(c) No less significant a point is that the analysis of the wave motion in the classical setting involves long (theoretically, infinitely long) wavelengths Λ alone. On the other hand, the nonlocal theory permits study of mechanical radiation of waves of any wavelength Λ, from the infinite down to as short as two interatomic distances (cf., Kittel, 1962).

Prompted by these and various other facts, it seems natural to inquire concerning the effects of nonlocal cohesive interactions on wave transmission through multilayer structures. As is well known, this topic is of primary importance in the area of composite materials, and has already been discussed at great length in its conventional aspect. In the present study we wish to examine the structural side of the problem alone, leaving aside both the question of sound filtration and the related matters of pass and stop bands (cf., e.g., Lindsay, 1938 or 1960). We also confine ourselves to an analysis of laminated media consisting of alternating layers of two isotropic materials. It is known that such structures behave effectively in gross as transversely isotropic materials, and are characterized by five elastic constants.

Regarding earlier work in this connection, mention should be made of the papers by Bruggeman (1937) and Riznichenko (1948). The former gives expressions for all five constants, but the values of two of these are questionable. In Riznichenko (1948) longitudinal waves parallel and normal to the layers are studied, and one constant remains undetermined. Later, Postma (1950) recomputed all of the effective constants and formulated an effective-modulus theory. A rigorous analysis of layered composites was proposed by Rytov (1956), Sun et al., (1968), and Sve (1968). The first two of these gave the exact dispersion relation for a one-dimensional wave traveling normal to the layering; Sve was able to consider an arbitrary direction of the wave. A continuum theory called "the effective-stiffness theory" was proposed in a series of publications by Achenbach et al., (1967, 1968, and 1969). In the formulation of these authors the representative moduli combine the geometric and elastic characteristics of both the matrix and the reinforcement layers. An extension of the effective-stiffness theory to higher-order accuracy, allowing the evaluation of displacements and stresses, was carried out by Drumheller and Bedford (1974). Also, Drumheller and Sutherland (1973) demonstrated that some composite materials can be modeled successfully by one-dimensional Bravais lattices. A rather different continuum theory was set forth by Hegemeier and Nayfeh (1973), in which use is made of expansion in series of both stresses and displacements. Interesting remarks on the question of the attenuation of waves in layered media have been made by Christensen (1973), whose text (1979), like those of Achenbach (1973) and Brekhovshikh (1960), gives a comprehensive account of the state of research into composites.

In the present paper, as already noted, we wish to shed some light, however limited, on the problem of wave propagation in a laminated medium displaying a long-range cohesion. Following a review of the main concepts of the nonlocal theory, the equations for the nonlocal elastic moduli are derived and the constitutive relations for the nonlocal medium established. Propagation of a longitudinal time-periodic wave normal to the laminae of the layered medium is then analyzed, and the equation determining the wave dispersion is derived. The dispersion arises from two sources, viz., the configuration (discreteness) of the structure and the nonlocal constitution of the laminae. A numerical example accompanied by a graph illustrates the dependence of the effective wave velocity on the wave number in the entire Brillouin zone. It is found that for very short waves the wave velocity decreases to about 64 percent of its long-wave value.

1 Geometry: Constitutive Equations. Let a laminated medium be composed of parallel layers of two different homogeneous, isotropic, and elastic materials denoted 1 and 2, respectively.

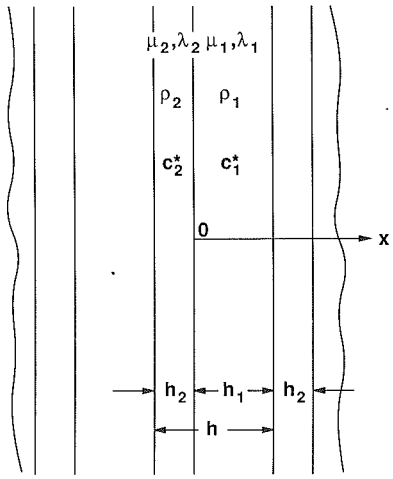


Fig. 1 Multilayer periodic medium

The thickness, mass density and the Lamé constants of the layers are h_1, ρ_1, λ_1, μ_1, and h_2, ρ_2, λ_2, μ_2, respectively. The layers alternate, and their distribution is periodic (Fig. 1). The x-axis of a rectangular cartesian coordinate system x, y, z is directed normal to the faces of the layers, and the origin of coordinates is located at the left face of a layer 1. The structure is unbounded in all three directions x, y, z, and the materials manifest a long-range cohesion.

The first ingredient needed for a meaningful solution of the problem under consideration is evidently the establishment of the constitutive equations defining the mechanical properties of the materials of the layers. With the nonlocal character of the latter in the mind, we adopt the equations in the form proposed by Eringen (1976) and Kroener (1976). For the normal stress component, τ_{xx}, in the x-direction — the only one of interest in the assumed state of plane strain — we have

$$\tau_{xx}(x,t) = (2\mu+\lambda)e_{xx}(x,t) + \int_V [2\mu'(|x-x'|) + \lambda'(|x-x'|)]e'_{xx}(x',t)dv'. \quad (1)$$

Here, $e_{xx} = \partial u/\partial x$, where $u(x, t)$ is the displacement in the x-direction; μ and λ are the classical Lamé constants, and μ' and λ' are the nonlocal moduli; x is the point of observation, and a superscribed prime denotes (here and throughout the text) a generic point of the medium; moreover t is the time, and V the volume of the body.

We assume that the conventional moduli, λ and μ, of the materials of the laminae are known. In order to determine the nonlocal moduli, λ' and μ', we refer to the paper of Nowinski (1989), in which using the principle of correspondence established between the dispersion equation of the nonlocal theory (in the long-wave limit) and its counterpart in the lattice dynamics, it is found that

$$\omega^2 = \frac{4}{\rho a^3}\sum_{n=1}^{N} C_n \sin^2\frac{nka}{2}. \quad (2)$$

Here, ω is the wave frequency of a longitudinal wave propagating in an unbounded nonlocal medium, a the lattice constant (i.e., the interparticle distance), C_n the force parameter, k the wave number, and the distance Na determines the accepted range of the cohesive forces.

Writing the foregoing equation in a slightly different form we obtain the formula exhibiting the dependence of the wave velocity (in a nonlocal unbounded medium) on the wave number,

Downloaded 03 May 2010 to 171.66.16.244. Redistribution subject to ASME license or copyright; see http://www.asme.org/terms/Terms_Use.cfm

$$c^2_{\text{nonloc}} = \frac{1}{\rho a}\sum_{n=1}^{N} C_n n^2 \frac{\sin^2 \frac{nka}{2}}{\left(\frac{nka}{2}\right)^2}. \tag{3a}$$

Equation (3*a*) clearly exhibits the constitutional nature of the dispersion brought about by the nonlocality of the medium.

It should be noted that if one sets $N = 1$ and demands that $a \to 0$, then the nonlocal cohesive force reduces to the classical contact force, and the phase velocity,

$$c = \frac{\omega}{k} = \frac{C_1}{\rho a}, \tag{3b}$$

becomes the classical velocity, $c_1 = (\lambda + 2\mu)/\rho$. It follows immediately from this that $C_1 = (\lambda + 2\mu)a$. In the specific case considered we also find that (Nowinski, 1984)

$$c_{\text{nonloc}} = c_1 \sin\frac{ka}{2}/(ka/2). \tag{4}$$

In a general case, as shown by Nowinski (1989), a longer argument leads to the conclusion that

$$\frac{\lambda'(|x-x'|)+2\mu'(|x-x'|)}{\lambda+2\mu} = \frac{1}{\lambda+2\mu}\sum_{n=1}^{N} C_n \frac{n}{a^2}\left(1-\frac{|x-x'|}{na}\right), \tag{5}$$

where $|x-x'| \le na$. In addition to that it is found that

$$\tau_{xx}(x,t) \equiv \tau(x,t) = \frac{1}{a^2}\int_{x-na}^{x+na}\sum_{n=1}^{N} C_n n \times \times\left(1-\frac{|x-x'|}{na}\right)\frac{\partial u'(x',t)}{\partial x'}\,dx'. \tag{6}$$

This completes the derivation of the state of stress, inasmuch as the only stress component of interest in the problem under scrutiny is just the component τ_{xx}.

In the subsequent section we return to the title problem, and examine the wave propagation in a layered medium with long-range cohesion.

2 Layered Medium. Suppose now that a longitudinal harmonic wave propagates across a nonlocal laminated medium defined in Section 1. The wave travels in the x-direction normal to the layers, and its effective velocity is v, say. In each of the materials 1 and 2 of the structure, the wave generates the displacements in the x-direction, which we choose to represent in the form

$$u_m(x,t) = U_m(x)\, e^{i\omega\left(x-\frac{t}{v}\right)}. \tag{7}$$

Here, $m = 1, 2$ corresponds to the layers 1 and 2, respectively, and $U_m(x)$, $m = 1, 2$, are functions which, on account of the periodicity of the structure, we select in the form (cf., also Rytov, 1956)

$$U_m(x) = A_m e^{i\omega\left(\frac{1}{v}-\frac{1}{c_m}\right)x} + B_m e^{i\omega\left(\frac{1}{v}+\frac{\omega}{c_m}\right)x}, \tag{8}$$

where $m = 1, 2$, and A_m and B_m are constants; furthermore, c_m, $m = 1, 2$, are the wave velocities associated with the materials 1 and 2, respectively, and denoted earlier as c_{nonloc} in equation (3).

We now substitute the expression (8) into the equation (6), and after lengthy but straightforward calculations arrive at the equation

$$\tau_{xxm} = \frac{\omega}{i} c_m \rho_m (A_m \alpha_m - B_m \beta_m), \tag{9}$$

where $m = 1, 2$,

$$\alpha_m(x) = e^{i\omega\left(\frac{1}{v}-\frac{1}{c_m}\right)x} e^{i\omega\left(t-\frac{x}{v}\right)},$$
$$\beta_m(x) = e^{i\omega\left(\frac{1}{v}+\frac{1}{c_m}\right)x} e^{i\omega\left(t-\frac{x}{v}\right)}, \tag{10}$$

i is the imaginary unit, and τ_{xxm} denotes the stress in the material m. Again, taking into account the periodicity of the structure (cf., e.g., Christensen, 1979, p. 232) we demand:

(a) that the displacements and stresses be continuous at the plane $x = 0$ (Fig. 1). This gives

$$A_1 + B_1 = A_2 + B_2,$$
$$A_1 - B_1 = K(A_2 - B_2), \tag{11}$$

where

$$K = c_2\rho_2/c_1\rho_1. \tag{12}$$

(*b*) That the continuity of stress and displacement is also observed at $x = h_1$, so that $U_1(h_1) = U_2(-h_2)$. This finally gives

$$A_1\alpha_1(h_1) + B\beta_1(h_1) = A_2\alpha_2(-h_2) + B_2\beta_2(-h_2),$$
$$A_1\alpha_1(h_1) + B\beta_1(h_1) = \mathrm{K}[A_2\alpha_2(-h_2) - B_2\beta_2(-h_2)]. \tag{13}$$

Evidently, for the system of four equations (11) and (13) linear in the four coefficients A_m and B_m, $m = 1, 2$, to have a nontrivial solution, the principal determinant of the system should vanish. This, after some manipulations, leads to the central equation of the problem,

$$\cos\frac{\omega h}{v} = \cos\frac{\omega h_1}{c_1}\cos\frac{\omega h_2}{c_2} - \frac{1+K^2}{2K}\sin\frac{\omega h_1}{c_1}\sin\frac{\omega h_1}{c_1}\sin\frac{\omega h_2}{c_2}, \tag{14}$$

determining the wave velocity v as a function of the frequency or, via the relation $\omega = vk$, as a function of the wave number. It should be recalled that c_m, $m = 1, 2$, are here the *nonlocal* velocities associated with the materials of the layers.

The following remarks, with regard to the equation (14), are now both interesting and informative.

(1) First, if as noted in Section 1 one reduces the nonlocal medium to a classical continuum by setting $N = 1$ and demands the lattice constant a go to zero, then the nonlocal velocities c_m, $m = 1, 2$, become those of the classical elasticity, and the equation (14) transforms into the well-known classical dispersion equation for the periodically laminated medium (cf., e.g., Christensen, 1979, p. 234).

(2) Second, the dispersion displayed in equation (14) ensues from two different sources: (a) the heterogeneity of the configuration (or of the geometry) of the structure manifested in the dependence of the frequency ω on the wave number k (in view of the relation $\omega = vk$); (b) the nonlocality of the materials of the laminae discernible in the presence of the nonlocal velocities c_m, $m = 1, 2$, depending in turn on the wave number (see equation (4)).

(3) Third, and even more important, the range of validity of the theory of propagation of the nonlocal waves extends over the entire Brillouin zone, that is to say, from the long (theoretically, infinitely long) waves up to the waves whose length equals twice the interatomic distance (Brillouin, 1963). In contrast to that, the classical theory, as commonly known, loses its applicability beyond the range of (infinitely) long waves.

3 Illustrative Example. So far our discussion had a general character, and it seems desirable at this stage to complement the theory by some more tangible and down-to-earth results. In order to do this, and not to obscure the main points of the subject by nonessential calculations, we decide to assume that the materials of the layers possess equal *nonlocal* acoustic resistances,

$$c_1\rho_1 = c_2\rho_2. \tag{15}$$

Downloaded 03 May 2010 to 171.66.16.244. Redistribution subject to ASME license or copyright; see http://www.asme.org/terms/Terms_Use.cfm

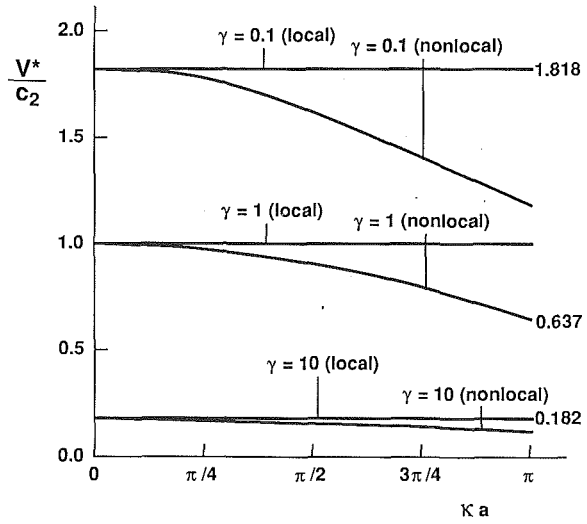


Fig. 2 Nondimensional effective wave velocity versus nondimensional wave number

This, of course, does not necessarily imply that the materials of the layers are identical, but simply removes the reflections of waves at the interfaces between the layers.

The foregoing relation implies now that

$$(1(+K^2)/2K=1, \tag{16}$$

or that

$$\frac{h_1}{c_1}+\frac{h_2}{c_2}=\frac{h}{v}, \tag{17}$$

where $h = h_1 + h_2$. Since the velocities c_m, $m = 1, 2$, depend on the wave number (cf., equation (3)), then the equation (17) exhibits the dispersive character of the nonlocal structure in question. This, of course, is not the case if the medium happens to be local.

It should be noted that the relation (17) may also be obtained by a simple reasoning that the sum of the times $\Delta t_m = h_m/c_m$, $m = 1, 2$, of wave transmission across each of two neighboring layers has to be equal to the time of transmission of the wave across the entire distance $h = h_1 + h_2$ with an effective velocity v, (cf., e.g., Christensen, 1979, p. 229). Figure 2 displays the graphs of the ratio $v/c_{2\text{loc}}$ in function of the wave number k in the entire Brillouin zone, assuming $h_1 = h_2$. Here again v is the effective wave velocity, and $c_{2\text{loc}}$ the wave velocity pertaining to the unbounded medium 2 considered local. Evidently, by virtue of the assumed equality of the acoustic resistances equation (15), there is

$$\frac{v}{c_{2\text{loc}}}=\frac{2}{1+\gamma}\,\frac{\sin\dfrac{ka}{2}}{\dfrac{ka}{2}}, \tag{11}$$

where $\gamma = (\lambda_2 + 2\mu_2) / (\lambda_1 + 2\mu_1)$, and by assumption $N = 1$.

The graphs in Fig. 2 are depicted for three drastically different values of the parameter γ, namely 0.1; 1; and 10. A glance at the figure reveals a substantial deviation of the effective wave velocity, v, in the nonlocal case from its classical value. For long waves the difference goes to zero, as it should according to the correspondence principle mentioned in Section 1. However, in the limiting case of the shortest acceptable wavelength, $2a$, the difference reaches about 36 percent independent of the value of the parameter γ.

It is of interest to note that an order of magnitude analysis carried out within the framework of the classical elasticity confirms the decrease of the wave velocity with an increasing frequency (Christensen, 1979, p. 235; cf., also Sve, 1971, Fig. 2). This, of course, was determined for the low frequency range (range of long wavelength), the only one in which the classical elastodynamics retains its validity.

Acknowledgment

The author thanks his wife, Maria, for her assistance in preparation of this paper.

References

Achenbach, J. D., Sun, C. T., and Herrmann, G., 1968, "On the Vibrations of a Laminated Body," ASME JOURNAL OF APPLIED MECHANICS, Vol. 35, pp. 689–693.

Achenbach, J. D., 1973, *A Theory of Elasticity with Microstructure for Directionally Reinforced Composites*, International Center for Mechanical Sciences, Courses and Lectures No. 167, Springer, New York.

Brekhovskikh, L. M., 1960, *Waves in Layered Media*, Academic Press, New York.

Brillouin, L., 1963, *Wave Propagation in Periodic Structures*, Dover, New York.

Bruggeman, D. A. G., 1937, "Calculation of Different Physical Constants of Heterogeneous Substances, III," (in German), *Annalen der Physik*, Vol. 29, pp. 160–178.

Christensen, R. M., 1973, "Attenuation of Harmonic Waves in Layered Media," ASME JOURNAL OF APPLIED MECHANICS, Vol. 40, pp. 155–160.

Christensen, R. M., 1979, *Mechanics of Composite Materials*, John Wiley and Sons, New York.

Cochran, W., 1965, "Interpretation of Phonon Dispersion Curves," *Lattice Dynamics*, Proceedings of the International Conference, Copenhagen, August 5–9, 1963, R. F. Wallis, ed., Pergamon Press, Oxford, pp. 75–84.

Cosserat, E., and F., 1909, *Theory of Deformable Bodies* (in French), Herrmann, Paris.

Drumheller, D. S., and Sutherland, H. J., 1973, "A Lattice Model for Stress Wave Propagation in Composite Materials," ASME JOURNAL OF APPLIED MECHANICS, Vol. 40, pp. 149–154.

Drumheller, D. S., and Bedford, A., 1974, "Wave Propagation in Elastic Laminates Using a Second-Order Microstructure Theory," *International Journal of Solids and Structures*, Vol. 10, pp. 67–76.

Edelen, D. G. B., 1976, "Nonlocal Field Theories," *Continuum Physics*, Vol. 4, A. C. Eringen, ed., Academic Press, New York, pp. 76–204.

Eringen, A. C., 1968, "Mechanics of Micromorphic Continua," *Mechanics of Generalized Continua*, Proceedings of the IUTAM-Symposium, Freudenstadt and Stuttgart, 1967, E. Kroener, ed., Springer, New York, pp. 18–35.

Eringen, A. C., 1976, "Nonlocal Polar Field Theories," *Continuum Physics*, Vol. 4, A. C. Eringen, ed., Academic Press, New York, pp. 205–267.

Green, A. E., and Rivlin, R. S., 1964, "Multipolar Continuum Mechanics," *Archive for Rational Mechanics and Analysis*, Vol. 17, pp. 113–147.

Hegemeier, G. A., and Nayfeh, A. H., 1973, "A Continuum Theory for Wave Propagation in Laminated Composites," ASME JOURNAL OF APPLIED MECHANICS, Vol. 40, pp. 503–510.

Herrmann, G., and Achenbach, J. D., 1967, "On Dynamic Theories of Fiber-Reinforced Composites," *Proceedings of the AIAA-ASME Eighth Structures, Structural Dynamics and Materials Conference*, New York, pp. 112–118.

Kittel, C., 1962. *Introduction to Solid State Physics*, John Wiley and Sons, New York.

Kroener, E., 1976, "Continuum Mechanics and Range of Atomic Cohesion Forces," *Proceedings of International Conference on Fracture*, Vol. 1, Sendai, Japanese Society for Strength and Fracture of Materials.

Kunin, I. A., 1982 and 1983, *Elastic Media with Microstructure*, Vols. 1 and 2, Springer, Berlin.

Lindsay, R. B., 1938, "Filtration of Sound, I," *Journal of Applied Physics*, Vol. 9, pp. 612–622.

Lindsay, R. B., 1960, *Mechanical Radiation*, McGraw-Hill, New York.

Mindlin, R. D., and Tiersten, H. F., 1967, "Effect of Couple-Stresses in Linear Elasticity," *Archive for Rational Mechanics and Analysis*, Vol. 11, pp. 415–448.

Mindlin, R. D., 1968, "Theories of Elastic Continua and Crystal Lattice Theories," *Mechanics of Generalized Continua*, Proceedings of the IUTAM-Symposium, Freudenstadt and Stuttgart, 1967, E. Kroener, ed., Springer, Berlin, pp. 312–320.

Nowinski, J. L., 1984, "On the Nonlocal Aspects of the Propagation of Love Waves," *International Journal of Engineering Science*, Vol. 22, pp. 383–392.

Nowinski, J. L., 1989, "On the Wave Transmission Across the Interface of Two Elastic Half-Spaces with Nonlocal Cohesion Forces," *Acta Mechanica*, Vol. 78, pp. 209–218.

Postma, G. W., 1950, "Wave Propagation in Stratified Medium," *Geophysics*, Vol. 20, pp. 780–806.

Riznichenko, I. V., 1948, "The Propagation of Seismic Waves in Discrete and Heterogeneous Media," *Bulletin of the Academy of Sciences, USSR*, Geographical and Geophysical Series, Vol. 13, No. 2, pp. 115–128.

Rytov, S. M., 1956, "Acoustic Properties of a Thinly Laminated Medium," *Soviet Physical Acoustics*, Vol. 2, pp. 68–80.

Sun, C. T., Achenbach, J. D., and Herrmann, G., 1968, "Continuum Theory of a Laminated Medium," ASME JOURNAL OF APPLIED MECHANICS, Vol. 35, pp. 468–475.

Sun, C. T., Achenbach, J. D., and Herrmann, G., 1969, "Time Harmonic Waves in a Stratified Medium, Propagating in the Direction of the Layers," ASME JOURNAL OF APPLIED MECHANICS, Vol. 35, pp. 408–411.

Sve, C., 1971, "Time-Harmonic Waves Travelling Obliquely in a Periodically Laminated Medium," ASME JOURNAL OF APPLIED MECHANICS, Vol. 38, pp. 477–487.

Downloaded 03 May 2010 to 171.66.16.244. Redistribution subject to ASME license or copyright; see http://www.asme.org/terms/Terms_Use.cfm

Thermal Dynamic Problems of Reinforced Composite Cylinders

Victor Birman
Engineering Education Center,
University of Missouri-Rolla,
St. Louis, MO 63121
Mem. ASME

Thermal dynamic problems of circular cylindrical composite shells reinforced in the axial and circumferential directions and subject to variations of temperature are considered. Nonlinear governing equations are formulated based on the extension of Donnell shell theory. These equations are used to determine the response of geometrically nonlinear and linear shells to a thermal loading represented by the Heaviside step function (thermal shock). The solution of the nonlinear problem obtained by the assumption that displacements are single-term functions of coordinates is discussed. The analysis of the linear problem illustrates different types of response to thermal shock. The condition of thermally-induced buckling of shells is formulated. Numerical analysis results in conclusions regarding the behavior of shells subject to thermal shock if the temperature is uniformly distributed throughout the shell and stiffeners.

Introduction

Reinforced cylindrical shells represent one of the principal elements of aerospace and ship structures, pressure vessels, etc. Increasing application of composite materials in design makes investigation of static and dynamic behavior of composite shells very important. Studies of reinforced composite cylindrical shells were published by Thielemann (1960), Block (1968), Bogdanovich and Koshkina (1983, 1984), Bogdanovich (1986), and Birman (1988a,b, 1990).

Composite shells used in practical applications are often subject to uniform or nonuniform thermal fields. The research of effects of temperature on response of isotropic structures has been pursued for a long time; see the book of Boley and Weiner (1962) which outlines the principle elements of this research and the paper of Tauchert (1986) concentrating on plated structures. The response of composite material structures subject to thermal effects has been also investigated. In particular, thermal problems of composite cylinders were considered by Birger (1971), Tauchert (1980), and Hyer and Cooper (1986). However, the behavior of reinforced composite shells in thermal fields has not been considered.

In this paper geometrically nonlinear dynamic equations for reinforced circular cylindrical shells subject to nonuniform elevated temperature are formulated. These equations represent the generalization of the Donnell shell theory to composite material cylinders. The solution of geometrically nonlinear and linear problems of reinforced composite cylinders subject to instantaneous increase of temperature (thermal shock) is discussed. A method of experimental prediction of the temperature resulting in thermally-induced buckling is proposed. This method can be used for nondestructive evaluation of shells subject to thermal shock if the boundary conditions are not specified. The response of a graphite/epoxy shell is illustrated in numerical analysis which also elucidates the importance of ring stiffeners for prevention of thermally-induced buckling.

Governing Equations

Consider a cylindrical shell reinforced by axial and ring stiffeners as shown in Fig. 1. The shell is composed of many identical layers symmetrically arranged about its middle surface. In this case the behavior of the real shell can be modeled by an equivalent orthotropic shell. The geometry of the shell is such that the Donnell-type theory is applicable. The stiffeners are supposed to work independently; i.e., axial stiffeners do not affect deformations of ring stiffeners and visa versa. Such an assumption is often used in the studies of reinforced shell structures. An example of a structure where this assumption is justified is a shell with riveted reinforcements in both axial and circumferential directions which are not connected to each other (Timashev, 1974). The torsional stiffness of the stiffeners is neglected according to the conclusion of Birman (1988b).

The shell is subject to a nonuniform thermal field $T(x, y, z, t)$, x and y being the axial and circumferential coordinates; z

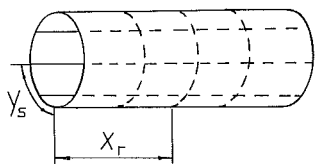


Fig. 1 Shell geometry. Internal stiffeners are indicated by broken lines; x_r and y_s are the coordinates of stiffeners.

Contributed by the Applied Mechanics Division of THE AMERICAN SOCIETY OF MECHANICAL ENGINEERS for publication in the JOURNAL OF APPLIED MECHANICS.

Discussion on this paper should be addressed to the Technical Editor, Leon M. Keer, The Technological Institute, Northwestern University, Evanston, IL 60208, and will be accepted until two months after final publication of the paper itself in the JOURNAL OF APPLIED MECHANICS. Manuscript received by the ASME Applied Mechanics Division, Apr. 17, 1989; final revision, Oct. 14, 1989.

Copyright © 1990 by ASME
Downloaded 03 May 2010 to 171.66.16.244. Redistribution subject to ASME license or copyright; see http://www.asme.org/terms/Terms_Use.cfm

is the radial coordinate positive in the inward direction and t time. The webs and the flanges of the stiffeners are supposed to be thin so that temperature is uniform in the thickness directions of the elements of each profile.

The strain-displacement relationships in Donnell's theory of geometrically nonlinear shells are assumed to be

$$\begin{aligned}
&\epsilon_x^0 = u_{,x} + 1/2 w_{,x}^2 \\
&\epsilon_y^0 = v_{,y} + 1/2 w_{,y}^2 - \frac{w}{R} \\
&\gamma_{xy}^0 = u_{,y} + v_{,x} + w_{,x} w_{,y} \\
&\kappa_x = -w_{,xx} \quad \kappa_y = -w_{,yy} \quad \kappa_{xy} = -2w_{,xy} \\
&\epsilon_x = \epsilon_x^0 + z\kappa_x \\
&\epsilon_y = \epsilon_y^0 + z\kappa_y \\
&\gamma_{xy} = \gamma_{xy}^0 + z\kappa_{xy}
\end{aligned} \tag{1}$$

where ϵ_x^0, ϵ_y^0, γ_{xy}^0 denote strains in the middle surface, κ_x, κ_y, and κ_{xy} are the changes of the middle surface curvature and twist, and ϵ_x, ϵ_y, γ_{xy} are strains at the distance z from the middle surface. Axial, circumferential, and radial displacements of the middle surface are denoted by u, v, and w, respectively, w being positive in the inward direction, and R is the radius of the middle surface.

The linear thermoelastic orthotropic constitutive relations for the kth layer of the shell are

$$\begin{Bmatrix} \sigma_1 \\ \sigma_2 \\ \sigma_6 \end{Bmatrix}_k = \begin{bmatrix} Q_{11} & Q_{12} & Q_{16} \\ Q_{12} & Q_{22} & Q_{26} \\ Q_{16} & Q_{26} & Q_{66} \end{bmatrix}_k \begin{Bmatrix} \epsilon_x - \alpha_1 T \\ \epsilon_y - \alpha_2 T \\ \gamma_{xy} - \alpha_6 T \end{Bmatrix}_k \tag{2}$$

where σ_1 and σ_2 are the axial and circumferential stresses, σ_6 is the shearing stress, and Q_{ij} are transformed reduced stiffness of the layer. The thermal expansion coefficients of the layer are related to the principal coefficients in the fiber and transverse directions (α_L, α_T), and to the lamination angle θ_k by

$$\begin{aligned}
&\alpha_1 = \alpha_L \cos^2\theta_k + \alpha_T \sin^2\theta_k \\
&\alpha_2 = \alpha_L \sin^2\theta_k + \alpha_T \cos^2\theta_k \\
&\alpha_6 = (\alpha_L - \alpha_T)\sin\theta_k \cos\theta_k.
\end{aligned} \tag{3}$$

If the shell is manufactured from an orthotopic material with the fiber direction parallel to the x-axis, $\alpha_1 = \alpha_L$, $\alpha_2 = \alpha_T$, $\alpha_6 = 0$ in equation (2). The stresses in the stiffeners obtained by the assumption that the stiffeners in the axial and circumferential directions do not affect each other directly are:

$$\begin{aligned}
&\sigma_1^s = E_s(\epsilon_x - \alpha_s T) \\
&\sigma_2^r = E_r(\epsilon_y - \alpha_r T)
\end{aligned} \tag{4}$$

where E_s and E_r are the moduli of elasticity of the axial (s) and ring (r) stiffener materials in the respective stiffener length directions, α_s and α_r are the corresponding thermal expansion coefficients.

The stress resultants and stress couples can be obtained by integration of the stresses given by equation (2) and (4) with respect to the thickness (radial) coordinate:

$$\begin{aligned}
N_1 &= A_{11}\epsilon_x^0 + A_{12}\epsilon_y^0 - N_1^T + \sum_s \delta(y - y_s) E_s A_s (\epsilon_x^0 + z_s \kappa_x) \\
N_2 &= A_{12}\epsilon_x^0 + A_{22}\epsilon_0^y - N_2^T + \sum_r \delta(x - x_r) E_r A_r (\epsilon_y^0 + z_r \kappa_y) \\
N_6 &= A_{66}\gamma_{xy}^0 - N_6^T \\
M_1 &= D_{11}\kappa_x + D_{12}\kappa_y - M_1^T + \sum_s \delta(y - y_s) E_s (A_s z_s \epsilon_x^0 + I_{os}\kappa_x) \\
M_2 &= D_{12}\kappa_x + D_{22}\kappa_y - M_2^T + \sum_r \delta(x - x_r) E_r (A_r z_r \epsilon_y^0 + I_{or}\kappa_y) \\
M_6 &= D_{66}\kappa_{xy} - M_6^T.
\end{aligned} \tag{5}$$

In equations (5), $\delta(\ldots)$ is the Dirac delta function, y_s and x_r are the coordinates of the axial and ring stiffeners, respectively, A_{ij} and D_{ij} are extensional and bending stiffnesses of the shell, z_s and z_r are the distances from the centroids of the corresponding stiffeners to the middle surface positive for inside reinforcement, A_s and A_r are the cross-sectional areas of the respective stiffeners, and I_{os}, I_{or} are their moments of inertia with respect to the middle surface. The thermal terms in equation (5) are:

$$\begin{aligned}
N_1^T &= \int_{-h/2}^{h/2} (Q_{11}\alpha_1 + Q_{12}\alpha_2 + Q_{16}\alpha_6) T dz \\
&\quad + \sum_s \delta(y - y_s) E_s \alpha_s \int_z \beta_s(z) T_s dz \\
N_2^T &= \int_{-h/2}^{h/2} (Q_{12}\alpha_1 + Q_{22}\alpha_2 + Q_{26}\alpha_6) T dz \\
&\quad + \sum_s \delta(x - x_r) E_r \alpha_r \int_z \beta_r(z) T_r dz \\
N_6^T &= \int_{-h/2}^{h/2} (Q_{16}\alpha_1 + Q_{26}\alpha_2 + Q_{66}\alpha_6) T dz \\
M_1^T &= \int_{-h/2}^{h/2} (Q_{11}\alpha_1 + Q_{12}\alpha_2 + Q_{16}\alpha_6) T z dz \\
&\quad + \sum_s \delta(y - y_s) E_s \alpha_s \int_z \beta_s(z) T_s z dz \\
M_2^T &= \int_{-h/2}^{h/2} (Q_{12}\alpha_1 + Q_{22}\alpha_2 + Q_{26}\alpha_6) T z dz \\
&\quad + \sum_r \delta(x - x_r) E_r \alpha_r \int_z \beta_r(z) T_r z dz \\
M_6^T &= \int_{-h/2}^{h/2} (Q_{16}\alpha_1 + Q_{26}\alpha_2 + Q_{66}\alpha_6) T z dz
\end{aligned} \tag{6}$$

where T_s and T_r denote temperature distributions in the stiffeners, $\beta_s(z)$, $\beta_r(z)$ are the widths of the stiffeners, and h is the thickness of the shell.

If the temperature is constant throughout the stiffener cross-sections, the corresponding terms in equation (6) are simplified as follows:

$$\begin{aligned}
&\sum_s \delta(y - y_s) E_s \alpha_s \int_z \beta_s(z) T_s dz \to \sum_s \delta(y - y_s) E_s A_s \alpha_s T_s \\
&\sum_r \delta(x - x_r) E_r \alpha_r \int_z \beta_r(z) T_r dz \to \sum_r \delta(x - x_r) E_r A_r \alpha_r T_r \\
&\sum_s \delta(y - y_s) E_s \alpha_s \int_z \beta_s(z) T_s z dz \to \sum_s \delta(y - y_s) E_s F_s \alpha_s T_s \\
&\sum_s \delta(x - x_r) E_r \alpha_r \int_z \beta_r(z) T_r z dz \to \sum_r \delta(x - x_r) E_r F_r \alpha_r T_r
\end{aligned} \tag{7}$$

where F_s and F_r are the first moments of the respective stiffeners about the shell middle surface. Note that the term N_6^T is equal to zero if temperature is independent on the z-coordinate.

Equations of motion, in terms of stress resultants and stress couples, are

$$\begin{aligned}
&N_{1,x} + N_{6,y} = 0 \\
&N_{6,x} + N_{2,y} = 0 \\
&M_{1,xx} + 2M_{6,xy} + M_{2,yy}\frac{N_2}{R} + (N_1 w_{,x} + N_6 w_{,y})_{,x} \\
&\quad + (N_6 w_{,x} + N_2 w_{,y})_{,y} = \rho_{eq} h w_{,tt}
\end{aligned} \tag{8}$$

where

$$\rho_{eq} h = \rho h + \sum_s \delta(y - y_s)\rho_s A_s + \sum_r \delta(x - x_r)\rho_r A_r. \tag{9}$$

In equation (9), ρ, ρ_s, and ρ_r are the mass densities of the materials of the shell, axial, and ring stiffeners, respectively.

The substitution of equations (5) and (6) into (8) and neglect of the in-surface inertias yield the following equations of motion in terms of displacements:

Downloaded 03 May 2010 to 171.66.16.244. Redistribution subject to ASME license or copyright; see http://www.asme.org/terms/Terms_Use.cfm

$$[A_{11}+\sum_s \delta(y-y_s)E_sA_s]u_{,xx}+A_{66}u_{,yy}+(A_{12}+A_{66})v_{,xy}$$
$$-A_{12}w_{,x}/R-\sum_s \delta(y-y_s)E_sA_sz_sw_{,xxx}$$
$$+[A_{11}+\sum_s \delta(y-y_s)E_sA_s]w_{,x}w_{,xx}$$
$$+(A_{12}+A_{66})w_{,y}w_{,xy}+A_{66}w_{,x}w_{,yy}=N^T_{1,x}+N^T_{6,y}$$
$$(A_{12}+A_{66})u_{,xy}+[A_{22}+\sum_r \delta(x-x_r)E_rA_r]v_{,yy}+A_{66}v_{,xx}$$
$$-[A_{22}+\sum_r \delta(x-x_r)E_rA_r]w_{,y}/R-\sum_r \delta(x-x_r)E_rA_rz_rw_{,yyy}$$
$$+[A_{22}+\sum_r \delta(x-x_r)E_rA_r]w_{,y}w_{,yy}$$
$$+(A_{12}+A_{66})w_{,x}w_{,xy}+A_{66}w_{,xx}w_{,y}=N^T_{6,x}+N^T_{2,y}$$
$$-D_{11}w_{,xxxx}-2(D_{12}+2D_{66})w_{,xxyy}-D_{22}w_{,yyyy}$$
$$+\sum_s \delta(y-y_s)E_s\{A_sz_s[u_{,xxx}+w_{,x}w_{,xxx}$$
$$+w^2_{,xx}]-I_{os}w_{,xxxx}\}+\sum_r \delta(x-x_r)E_r\{A_rz_r[v_{,yyy}$$
$$-w_{,yy}/R+w_{,y}w_{,yyy}+w^2_{,yy}]$$
$$-I_{or}w_{,yyyy}\}+A_{12}(u_{,x}+1/2w^2_{,x})/R$$
$$+[A_{22}+\sum_r \delta(x-x_r)E_rA_r](v_{,y}-w/R+1/2w^2_{,y})/R$$
$$-\sum_r \delta(x-x_r)E_rA_rz_rw_{,yy}/R+\{\{[A_{11}+\sum_s \delta(y-y_s)E_sA_s]$$
$$(u_{,x}+1/2w^2_{,x})+A_{12}(v_{,y}-w/R+1/2w^2_{,y})$$
$$-\sum_s \delta(y-y_s)E_sA_sz_sw_{,xx}\}w_{,x}+A_{66}(u_{,y}+v_{,x}+w_{,x}w_{,y})w_{,y}\}_{,x}$$
$$+\{A_{66}(u_{,y}+v_{,x}+w_{,x}w_{,y})w_{,x}$$
$$+\{A_{12}(u_{,x}+1/2w^2_{,x})+[A_{22}$$
$$+\sum_r \delta(x-x_r)E_rA_r](v_{,y}-w/R+1/2w^2_{,y})$$
$$-\sum_r \delta(x-x_r)E_rA_rz_rw_{yy}\}w_{,y}\}_{,y}=M^T_{1,xx}+2M^T_{6,xy}$$
$$+M^T_{2,yy}+N^T_2/R+(N^T_1w_{,x}$$
$$+N^T_6w_{,y})_{,x}+(N^T_6w_{,x}+N^T_2w_{,y})_{,y}+\rho_{eq}hw_{,tt}. \quad (10)$$

As follows from equations (10), the shell will experience radial deflections when subject to a nonuniform temperature even if other loads are absent. This conclusion applies to both linear and nonlinear problems. Even if the distribution of temperature is uniform, the shell will bend in the radial direction; this follows from the presence of the term N^T_2/R on the right side of the last equation (10).

Thermal Shock-Geometrically Nonlinear Problem

If the temperature increases very rapidly so that the thermal ramp occurs over a small time compared to the fundamental period of the structure, it is convenient to treat these temperature increases as instantaneous. Consider the case where the temperature is represented by the Heaviside step function, i.e., it increases to a certain level and remains constant after that. Shells subject to such thermal fields may experience dynamic deformations. Suppose that displacements u, v, and w can be expressed as single-term functions of the in-surface coordinates:

$$u = U(t)f_1(x, y)$$
$$v = V(t)f_2(x, y)$$
$$w = W(t)f_3(x, y) \quad (11)$$

where $f_i(x, y)$ satisfy boundary and periodicity conditions. Then the substitution of equations (11) into (10) and the application of the Galerkin procedure yield a set of nonlinear equations for the functions $U(t)$, $V(t)$, and $W(t)$. The first two of these functions can be expressed in terms of $W(t)$ from the first two equations of the set. Then the remaining equation, which corresponds to the last equation in equations (10), can be represented in terms of $W(t)$ only:

$$W_{,tt}+(\beta_1+\beta_1^1T_1)W+\beta_2W^2+\beta_3W^3+\beta_0T_1=0, \quad (12)$$

where β_i and β_1^1 are coefficients and T_1 is a characteristic of the thermal field. An example of the coefficients in equation (12) is shown in the Appendix. As follows from equation (12), the shell may exhibit two types of behavior. If $\beta_1+\beta_1^1T_1>0$ the shell will oscillate periodically while if $\beta_1+\beta_1^1T_1<0$ the behavior is aperiodic, and is referred to as a thermal instability phenomenon.

In the following the analysis is concerned with limited variations of temperature so that the resulting motion is oscillatory. The exact solution of equation (12) can be sought in terms of elliptic integrals and functions similar to the approach used in the problems of free vibrations of perfect and imperfect bars (Woinowsky-Krieger, 1950; Burgreen, 1950; Elishakoff et al., 1985; Birman 1986). However, note that in these references the solution was simplified for the case where $\beta_2=0$.

Multiplication of equation (12) by dW and the subsequent integration yield

$$W_{,t}^2=-(\beta_1+\beta_1^1T_1)W^2-2/3\beta_2W^3-1/2\beta_3W^4-2\beta_0T_1+C \quad (13)$$

where C is a constant found from the condition that $W_{,t}=0$ at $W=W_{\max}$. Then substituting the value of C into equation (13), separating variables and integrating, one obtains

$$t-t_0=\int_{\bar{W}0}^{\bar{W}} \frac{d\bar{W}}{\sqrt{(\beta_1+\beta_1^1T_1)(1-\bar{W}^2)+2/3\beta_2W_{\max}(1-\bar{W}^3)+1/2\beta_3W^2_{\max}(1-\bar{W}^4)+2(\beta_0/W_{\max})T_1(1-\bar{W})}} \quad (14)$$

where

$$\bar{W}=W/W_{\max} \text{ and } \bar{W}_0=\bar{W}(t_0). \quad (15)$$

The right side of equation (14) can often be represented as a tabulated elliptic integral. Then $\bar{W}$ can be found as an elliptic function of time. The value $W_{\max}$ should be specified using the initial conditions.

Note that the scenario discussed previously involves laborious transformations. Moreover, the value of $W_{\max}$ is necessary for evaluation of the integral in equation (14). However, in the solution just described, $W_{\max}$ can be specified only after $\bar{W}(t)$ has already been determined. Hence, the solution must be iterative.

Therefore, an approximate solution of equation (12) may be quite attractive. For example, the difference between the exact solution for the frequencies of free vibration of imperfect elastic bars and a timewise, two-term Galerkin approximation was shown to be less than 5 percent (Elishakoff et al. 1985). The approach similar to that used by Elishakoff et al. (1985) is used in this paper. Assuming

$$W=W_0+W_1\cos\omega t \quad (16)$$

Downloaded 03 May 2010 to 171.66.16.244. Redistribution subject to ASME license or copyright; see http://www.asme.org/terms/Terms_Use.cfm

and applying the Galerkin procedure to equation (12), one obtains

$$-\omega^2 W_1 + (\beta_1 + \beta_1{}^1 T_1) W_1 + 2\beta_2 W_0 W_1 + 3\beta_3 W_0{}^2 W_1 + 3/4\beta_3 W_1{}^3 = 0$$

$$(\beta_1 + \beta_1^1 T_1) W_0 + \beta_2 W_0{}^2 + \beta_3 W_0{}^3 + 1/2\beta_2 W_1{}^2 + 3/2\beta_3 W_0 W_1{}^2 + \beta_0 T_1 = 0. \quad (17)$$

Equations (17) include three unknowns: W_0, W_1 and ω. If the shell is at rest at the instant of thermal shock,

$$W(0) = 0 \qquad W_{,t}(0) = 0. \quad (18)$$

The substitution of equation (16) in the first equation (18) yields $W_0 = -W_1$, the second condition (18) is identically satisfied. Then the relationship between W_1 and T_1 as well as the corresponding frequency of oscillations can be determined from equation (17).

Thermal Shock-Geometrically Linear Problem

If displacements remain small so that nonlinear effects can be neglected, the equation of motion equation (12) is reduced to

$$W_{,tt} + (\beta_1 + \beta_1{}^1 T_1) W + \beta_0 T_1 = 0 \quad (19)$$

with the obvious solution

$$W = A\sin\tilde{\omega}t + B\cos\tilde{\omega}t - \frac{\beta_0 T_1}{\beta_1 + \beta_1{}^1 T_1} \quad (20)$$

where $\tilde{\omega} = \sqrt{\beta_1 + \beta_1{}^1 T_1}$.
Initial conditions (18) yield

$$A = 0,\ B = \frac{\beta_0 T_1}{\beta_1 + \beta_1{}^1 T_1} \quad (21)$$

Note that β_1 is proportional to the linear buckling load of the shell subject to axial compression, say $\beta_1 = N_{cr}\psi$, where N_{cr} is the buckling load and ψ is a coefficient. Then introducing a nondimensional time parameter τ so that $(\ldots)_{,tt} = (\ldots)_{,\tau\tau}\omega_0{}^2$ where $\omega_0 = \sqrt{\beta_1}$ is the natural frequency of the shell at the room temperature, one obtains from equation (19):

$$\tilde{W}_{,\tau\tau} + \left(1 + \frac{\beta_1{}^1 T_i}{\psi N_{cr}}\right)\tilde{W} = -\frac{\beta_0 T_1}{\beta_1 h} \quad (22)$$

where $\tilde{W} = W/h$.

Equation (22) includes only nondimensional parameters. Denote

$$\frac{\beta_1{}^1 T_1}{\psi N_{cr}} = \lambda_1 \bar{N}_1{}^T \qquad \frac{\beta_0 T_1}{\beta_1 h} = \lambda_2 \bar{N}_1{}^T \quad (23)$$

where λ_1 and λ_2 are coefficients and $\bar{N}_1{}^T = N_1{}^T/N_{cr}$.

Then equation (22) yields

$$\tilde{W}_{,\tau\tau} + (1 + \lambda_1 \bar{N}_1{}^T)\tilde{W} = -\lambda_2 \bar{N}_1{}^T. \quad (24)$$

The solution of equation (24) subject to zero initial condition is

$$\tilde{W} = \frac{\lambda_2 \bar{N}_1{}^T}{1 + \lambda_1 \bar{N}_1{}^T}\left(\cos\sqrt{1 + \lambda_1 \bar{N}_1{}^T}\,\tau - 1\right). \quad (25)$$

The validity of this solution is limited to the values of $\bar{N}_1{}^T$ which satisfy the inequality $1 + \lambda_1 \bar{N}_1{}^T > 0$. The convenience of equation (25) is that it enables us to determine the amplitude of motion as a function of a dimensionless thermal load $\bar{N}_1{}^T$ and two nondimensional parameters which can be easily evaluated in particular cases. For example, if the ends of the shell are simply supported so that

$$w = \sum_{mn} W_{mn}(t)\sin\frac{m\pi x}{L}\sin\frac{ny}{R}, \quad (26)$$

and the thermal field is uniform, i.e., $T(x, y, z) = T_r = T_s = T$,

$$\rho_{eq} h\psi = \left(\frac{m\pi}{L}\right)^2 \qquad \rho_{eq} h\beta_0 T_1 = \frac{N_2{}^T}{R}$$

$$\rho_{eq} h\beta_1{}^1 T_1 = -\left(\frac{m\pi}{L}\right)^2\left[1 + \left(\frac{\bar{L}n}{m\pi}\right)^2 n_2{}^T\right] N_1{}^T \quad (27)$$

where

$$\bar{L} = \frac{L}{R} \qquad n_2{}^T = \frac{N_2{}^T}{N_1{}^T}. \quad (28)$$

Then

$$\lambda_1 = -\left[1 + \left(\frac{\bar{L}n}{m\pi}\right)^2 n_2{}^T\right]$$

$$\lambda_2 = \frac{n_2{}^T \bar{L}}{(m\pi)^2 \bar{h}} \quad (29)$$

where $\bar{h} = \frac{h}{L}$.

Note that the relationship $\tilde{W}(\bar{N}_1{}^T)$ can be obtained even without specifying the in-surface boundary conditions. The change of the response from steady-state oscillations to a periodic motion, which can be conveniently called thermally-induced buckling, occurs if

$$\bar{N}_1{}^T > \frac{1}{1 + \left(\frac{\bar{L}n}{m\pi}\right)^2 n_2{}^T}. \quad (30)$$

Therefore, even if in-surface boundary conditions are not known but the axial buckling load the corresponding buckling mode shape are determined from experiments, the value of temperature corresponding to thermal buckling can be cal-

Table 1 Critical temperatures and nondimensional buckling loads of shells

Type of Reinforcement	Thermally induced buckling			Buckling due to axial loading		
	Critical temperature T K	Mode shape m	n	Critical load $\lvert N_{cr}/E_t h\rvert$	Mode shape m	n
Stiffeners in both directions	2110	1	2	0.41	3	3
Ring Stiffeners	1152	12	3	6.95×10^{-2}	12	3
Axial Stiffeners	60	1	4	6.01×10^{-2}	1	4
Unstiffened shell	56	1	4	4.60×10^{-2}	11	2

Downloaded 03 May 2010 to 171.66.16.244. Redistribution subject to ASME license or copyright; see http://www.asme.org/terms/Terms_Use.cfm

Table 2 Comparison of the amplitudes of harmonics of oscillations of the shell reinforced in both directions $|100\ W_{mn}/h|$; $T=100$ K

m	n					
	2	3	4	5	6	7
1	50.30	16.51	5.87	2.36	1.16	0.62
2	15.38	13.69	5.24	2.37	1.14	0.63
3	7.09	8.00	4.41	2.05	1.09	0.60
4	3.55	4.59	2.94	1.67	0.92	0.55
5	2.02	2.36	1.92	1.19	0.75	0.46

Table 3 Comparison of the amplitudes of harmonics of oscillations of the shell reinforced in both directions $|100\ W_{mn}/h|$; $T=200$ K

m	n					
	2	3	4	5	6	7
1	105.86	31.97	11.98	4.66	2.35	1.23
2	30.04	28.38	10.27	4.80	2.36	1.27
3	14.44	15.56	9.01	4.04	2.20	1.20
4	7.01	9.38	5.77	3.39	1.82	1.12
5	4.09	4.65	3.89	2.34	1.51	0.92

culated. Similar conclusions can be obtained using nondestructive vibration testing with the critical load related to the natural frequency by $N_{cr}=\frac{\omega_0^2}{\psi}$.

Numerical Analysis

The calculations were performed for a simply-supported multilayered cylindrical shell symmetrically laminated about the middle surface with the angle ± 30 deg. Both the shell and the stiffeners were manufactured from graphite/epoxy AS/3501 which has the following properties at room temperature (Tsai and Hahn, 1980):

$E_L=138$ GPa, $E_T=8.96$ GPa, $G_{LT}=7.1$ GPa, $\nu_{LT}=0.30$, $\alpha_L=0.18$ μm/m/K, $\alpha_T=22.50$ μm/m/K.

It is well known that mechanical properties are functions of temperature. In the problem of thermal shock, temperature increases very rapidly and remains constant thereafter. In the following examples all properties have been taken as indicated previously. This is justified if the temperature increase is moderate and the thermal field is uniform as was assumed in the numerical analysis.

The geometry of the shell was $L=2$ m, $R=0.5$ m, $h=0.01$ m, the internal reinforcements in both directions were 0.05-m high and 0.01-m wide with the spacing 0.1 m (the spacing of the axial reinforcements should be 0.1013 m to provide 31 stiffeners). The fiber directions coincided with the axes of the corresponding stiffeners.

Critical temperatures corresponding to thermally-induced buckling, i.e., to the change of dynamic response character of the shell were calculated for the shells whose axial buckling loads have been determined in the previous paper (Birman, 1988b). The results of calculations are summarized in Table 1. As follows from this table the mode shape of thermally-induced buckling does not necessarily coincide with the mode shape of buckling due to axial loading, although they can be close. The presence of ring stiffeners appears to have a very significant effect on the response to the thermal shock. The shells, even reinforced in the axial direction, experience thermally-induced buckling at very small elevations of temperature. On the contrary, ring-reinforced shells exhibit stable oscillatory response at very high temperatures. Note that thermally-induced buckling does not necessarily mean failure of the shell. However, it results in large deflections and the response has to be analyzed using nonlinear theory.

The results obtained for high temperatures are unreliable since the properties of material will be different at such temperatures. However, the conclusion that can be drawn from Table 1, i.e., that the shells will exhibit steady-state oscillations even if the temperature "jumps" to several hundred degrees, is very important.

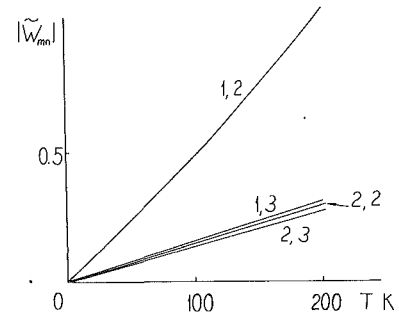


Fig. 2 Increase of the amplitudes of harmonics of oscillations of the shell reinforced in both directions with temperature. The numbers m and n are shown at the corresponding curves.

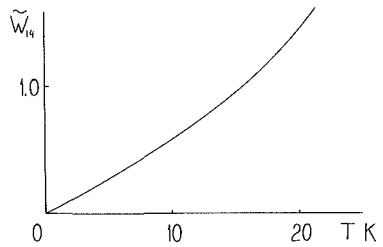


Fig. 3 Increase of the amplitude of the dominant harmonic of oscillations of the shell reinforced in the axial direction only with temperature

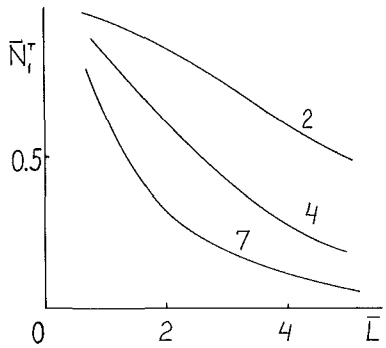


Fig. 4 Nondimensional critical thermal loads of reinforced shells; $n_2^T=0.1$

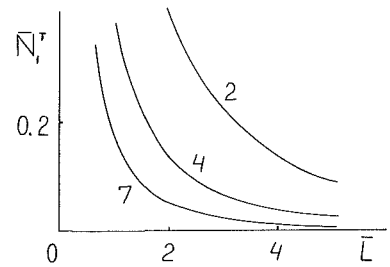


Fig. 5 Nondimensional critical thermal loads of reinforced shells; $n_2^T=1.0$

Downloaded 03 May 2010 to 171.66.16.244. Redistribution subject to ASME license or copyright; see http://www.asme.org/terms/Terms_Use.cfm

The comparison of the amplitudes of harmonics in the series (26) representing radial oscillations of the shell is given in Tables 2 and 3 for different temperatures. The comparison of these two tables illustrates that the same harmonics remain dominant at various temperatures. The increase of the amplitudes of these harmonics with temperature is shown in Fig. 2. The rapid increase of the amplitude of the dominant harmonic is shown in Fig. 3 for the axially-reinforced shell. Finally, variations of the nondimensional critical thermal load with the ratio $L = L/R$ are shown in Figs. 4 and 5. These figures illustrate that the ratio of the thermal term $N_1{}^T$ corresponding to thermally-induced buckling to the critical axial load associated with the same mode shape decreases for longer shells.

Conclusions

The analysis presented in the paper illustrates that an elevated temperature results in bending deflections of reinforced circular cylindrical shells manufactured from composite materials. Naturally, this conclusion remains valid for isotropic shells as well. If a shell is subject to an instantaneous increase of temperature (thermal shock) it can exhibit steady-state oscillations. However, if the temperature exceeds a certain critical level, associated with thermally-induced buckling, the character of response changes and the deflections can increase dramatically.

Shells reinforced in the circumferential direction have much higher temperature corresponding to thermally-induced buckling than shells without such reinforcements. On the contrary, axial stiffening does not show a significant effect on the thermally-induced buckling temperature. However, it should be emphasized that the conclusions regarding relative effectiveness of stiffeners were obtained for a particular material and boundary conditions; shells manufactured from other composites may behave differently. The mode shape of thermally-induced buckling does not always coincide with the mode shape of buckling due to axial loading. However, in the examples considered here these mode shapes were remarkably similar for reinforced shells. The thermally-induced buckling of shells subjected to uniform temperature can be predicted based on the static buckling loads in axial compression and/or the natural frequencies.

Acknowledgment

The discussions with Prof. Charles W. Bert of the University of Oklahoma are warmly appreciated.

References

Birger, B. I., 1971, "Thermal Stresses in an Anisotropic Cylinder," *Izvestia Vuzov, Aviatsionnaya Technika*, Vol. 14, pp. 24–28.

Birman, V., 1986, "On the Effect of Nonlinear Elastic Foundation on Free Vibration of Beams," ASME JOURNAL OF APPLIED MECHANICS, Vol. 53, pp. 471–473.

Birman, V., 1988a, "Axisymmetric Divergence of Ring-Stiffened Composite Cylindrical Shells Subject to Axial Compression," ASME JOURNAL OF APPLIED MECHANICS, Vol. 55, pp. 984–985.

Birman, V., 1988b, "Divergence Instability of Reinforced Composite Cylindrical Shells," *Recent Advances in the Macro and Micro-Mechanics of Composite Materials Structures*, AD-Vol. 13, D. Hui, and J. R. Vinson, ASME, New York, pp. 169–176.

Birman, V., 1990, "On Post-Buckling Behavior of Reinforced Cylindrical Shells," *Journal of Ship Research*, in press.

Block, D. L., 1968, "Influence of Discrete Ring Stiffeners and Prebuckling Deformations on the Buckling of Eccentrically Stiffened Orthotropic Cylinders," NASA TN D-4283.

Bogdanovich, A. E., and Koshkina, T. B., 1983, "Deformation and Strength of Ring-Reinforced Orthotropic Cylindrical Shells Subject to Dynamic Compressive Loads," *Mechanics of Composite Materials*, No. 3, pp. 476–488, (in Russian).

Bogdanovich, A. E., and Koshkina, T. B., 1984, "Deformation and Strength of Orthotropic Cylindrical Shells Reinforced by Axial Stiffeners and Subject to Dynamic Compressive Loads," *Mechanics of Composite Materials*, No. 5, pp. 866–876, (in Russian).

Bogdanovich, A. E., 1986, "Nonlinear Problems of the Dynamic Buckling of Reinforced Laminar Cylindrical Shells," *Soviet Applied Mechanics*, Vol. 22, pp. 745–753.

Boley, B. A., and Weiner, J. H., 1962, *Theory of Thermal Stresses*, 2nd printing, John Wiley and Sons, New York.

Burgreen, D., 1951, "Free Vibrations of Pin-Ended Column with Constant Distance Between Pin-Ends," ASME JOURNAL OF APPLIED MECHANICS, Vol. 18, pp. 135–139.

Elishakoff, I., Birman, V., and Singer, J., 1985, "Influence of Initial Imperfections on Nonlinear Free Vibration of Elastic Bars," *Acta Mechanics*, Vol. 55, pp. 191–202.

Hyer, M. W., and Cooper, D. E., 1986, "Stresses and Deformations in Composite Tubes Due to a Circumferential Temperature Gradient," ASME JOURNAL OF APPLIED MECHANICS, Vol. 53, pp. 757–764.

Tauchert, T. R., 1980, "Thermal Stresses in Coal Conversion Pressure Vessels Built of Layered Construction," *Thermal Stresses in a Severe Environment*, D. P. H. Hasselman, and R. Heller, eds., Plenum Press, New York, pp. 183–205.

Tauchert, T. R., 1986, "Thermal Stresses in Plates-Statical Problems," *Thermal Stresses*, Vol. I, R. B. Hetnarski ed., North-Holland, Amsterdam, pp. 23–141.

Thielmann, W. F., 1960, "New Developments in the Nonlinear Theories of the Buckling of Thin Cylindrical Shells," *Proceedings of Durand Centennial Conference*, Stanford University, Pergamon Press, Oxford.

Timashev, S. A., *Stability of Reinforced Shells*, Stroyizdat, Moscow, p. 11, (in Russian).

Tsai, S. W., and Hahn, H. T., 1980, *Introduction to Composite Materials*, Technomic, Westport, Conn., p. 18.

Woinowsky-Krieger, S., 1950, "The Effect of an Axial Force on the Vibration of Hinged Bars," ASME JOURNAL OF APPLIED MECHANICS, Vol. 17, pp. 35–36.

APPENDIX

Coefficients of Equation (12)

The substitution of equations (11) into equations (10) and Galerkin procedure yield a set of three algebraic equations for $U(t)$, $V(t)$, and $W(t)$. These equations can be represented in a nondimensional form:

$$a_1\bar{U}+a_2\bar{V}+a_3\bar{W}+a_4\bar{W}^2=n_1T_1$$
$$b_1\bar{U}+b_2\bar{V}+b_3\bar{W}+b_4\bar{W}^2=n_2T_1$$
$$c_1\bar{W}+c_2\bar{U}+c_3\bar{V}+c_4\bar{W}^2+c_5\bar{W}^3+c_6\bar{U}\bar{W}+c_7\bar{V}\bar{W} = n_3t_1+n_4\bar{W}T_1+\bar{\rho}\,\bar{W}_{,\tau\tau} \tag{A1}$$

where

$$\{\bar{U},\ \bar{V},\ \bar{W}\}=\{U(t),\ V(t),\ W(t)\}/h. \tag{A2}$$

T_1 is a dimensionless characteristic of the thermal field, $T_1=\alpha T_1{}^0$, where α is an arbitrary thermal expansion coefficient and $T_1{}^0$ is temperature. A nondimensional time scale τ is introduced by

$$\tau=\omega t, \tag{A3}$$

ω being a normalizing frequency which can be chosen arbitrarily. Accordingly,

$$\bar{\rho}=\frac{\rho_{eq}h^2\omega^2}{E} \tag{A4}$$

where E is a reference modulus of elasticity.

The values of $\bar{U}$ and $\bar{V}$ can be evaluated from the first two equations (A1). The substitution of these values into the third equation (A1) yields a nondimensional version of equation (12):

$$\bar{W}_{,\tau\tau}+(\bar{\beta}_1+\bar{\beta}_1{}^1T_1)\,\bar{W}+\bar{\beta}_2\bar{W}^2+\bar{\beta}_3\bar{W}^3+\bar{\beta}_0T_1=0 \tag{A5}$$

where

$$\begin{aligned}
\bar{\rho}\bar{\beta}_0 &= n_3-(c_2s_3+c_3s_6)\\
\bar{\rho}\bar{\beta}_1 &= -(c_1+c_1s_1+c_3s_4)\\
\bar{\rho}\bar{\beta}_1{}^1 &= n_4-(c_6s_3+c_7s_6)\\
\bar{\rho}\bar{\beta}_2 &= -(c_1s_2+c_3s_5+c_4+c_6s_1+c_7s_4)\\
\bar{\rho}\bar{\beta}_3 &= -(c_6s_2+c_7s_5+c_5).
\end{aligned} \tag{A6}$$

In equation (A6)

$$\begin{aligned}
s_1 &= (b_3a_2-b_2a_3)/s & s_2 &= (a_2b_4-a_4b_2)/s\\
s_3 &= (b_2n_1-a_2n_2)/s & s_4 &= (a_3b_1-a_1b_3)/s\\
s_5 &= (a_4b_1-a_1b_4)/s & s_6 &= (a_1n_2-b_1n_1)/s\\
s &= a_1b_2-a_2b_1.
\end{aligned} \tag{A7}$$

Downloaded 03 May 2010 to 171.66.16.244. Redistribution subject to ASME license or copyright; see http://www.asme.org/terms/Terms_Use.cfm

The coefficients of equation (12) can be expressed in terms of the coefficients of equation (A5) as follows:

$$\begin{aligned}&\beta_0=\bar{\beta}_0\omega^2h\\&\{\beta_1,\ \beta_1{}^1\}=\{\bar{\beta}_1,\ \bar{\beta}_1{}^1\}\omega^2\\&\beta_2=\bar{\beta}_2\omega^2/h\\&\beta_3=\bar{\beta}_3\omega^2/h^2.\end{aligned}\tag{A8}$$

Particular Case: Thermal Shock of a Plate Reinforced in One Direction

Consider a simply-supported plate reinforced in the x-direction. The tangential movements of the edges are restricted but the in-plane displacements in the directions normal to the edges are permitted. Therefore, the boundary conditions are:

$$\begin{aligned}&x=0,\ x=a:\ w=v=M_1=N_1=0\\&y=0,\ y=b:\ w=u=M_2=N_2=0\end{aligned}\tag{A9}$$

where a and b are the lengths of the edges in the x and y directions, respectively.

The thermal field is represented by

$$T(x,\ y,\ t)=T_1{}^0(t)\sin\frac{m\pi x}{a}\sin\frac{n\pi y}{b}\tag{A10}$$

m and n being integers.

Thermal terms corresponding to the thermal field equation (A10) can be written as

$$\begin{aligned}&\{N_1{}^T,\ N_2{}^T,\ N_6{}^T,\ M_1{}^T,\ M_2{}^T,\ M_6{}^T\}T_1\\&\quad=\{\bar{n}_1{}^T,\ \bar{n}_2{}^T,\ \bar{n}_6{}^T,\ \bar{m}_1{}^T,\ \bar{m}_2{}^T,\ \bar{m}_6{}^T\}\sin\frac{m\pi x}{a}\sin\frac{n\pi y}{b}\end{aligned}\tag{A11}$$

where $\bar{n}_1{}^T$, $\bar{n}_2{}^T$, . . . are coefficients which can be easily evaluated using equation (6).

Boundary conditions (A9) can be satisfied if the displacements are given by

$$\begin{aligned}u&=U(t)\cos\frac{m\pi x}{a}\sin\frac{n\pi y}{b}\\v&=V(t)\sin\frac{m\pi x}{a}\cos\frac{n\pi y}{b}\\w&=W(t)\sin\frac{m\pi x}{b}\sin\frac{n\pi y}{b}.\end{aligned}\tag{A12}$$

The substitution of equations (A11) and (A12) into the equations of motion (10), the Galerkin procedure, and some transformations yield the equation (A5). The coefficients in equations of the set of equations (A1) used to evaluate $\bar{\beta}_1$ and $\bar{\beta}_1{}^1$ are:

$$\begin{aligned}a_1&=-(m\pi h_a)^2\left[\bar{A}_{11}+\left(\frac{\lambda n}{m}\right)^2\bar{A}_{66}\right]\\&\quad-2(m\pi h_a)^2h_a\lambda\sum_s\bar{E}_s\bar{A}_s\sin^2\frac{n\pi y_s}{b}\\a_2&=-mn\pi^2h_a{}^2\lambda(\bar{A}_{12}+\bar{A}_{66})\\a_3&=2(m\pi h_a)^3h_a\lambda\sum_s\bar{E}_s\bar{A}_s\bar{z}_s\sin^2\frac{n\pi y_s}{b}\\a_4&=\frac{16}{9mn\pi^2}[-2(m\pi h_a)^3\bar{A}_{11}\\&\quad+mn^2\pi^3h_a{}^3\lambda^2(\bar{A}_{12}-\bar{A}_{66})]f(m)f(n)\\&\quad-\frac{8h_a\lambda}{3m\pi}(m\pi h_a)^3\sum_s\bar{E}_s\bar{A}_s\sin^3\frac{n\pi y_s}{b}f(m)\\n_1&=m\pi h_a\frac{\bar{n}_1{}^T}{Eh}\\n_2&=n\pi h_a\lambda\frac{\bar{n}_2{}^T}{Eh}\\c_1&=-[(m\pi h_a)^4\bar{D}_{11}+2(m\pi h_a)^2(n\pi h_a\lambda)^2(\bar{D}_{12}+2\bar{D}_{66})\\&\quad+(n\pi h_a\lambda)^4\bar{D}_{22}]-2\sum_s(m\pi h_a)^4\bar{E}_s\bar{I}_{0s}\sin^2\frac{n\pi y_s}{b}\\c_2&=(m\pi h_a)^3\sum_s\bar{E}_s\bar{A}_s\bar{z}_sh_a\lambda\sin^2\frac{n\pi y_s}{b}\\c_3&=0\\c_4&=0\\c_5&=-\left[\frac{9}{32}(m\pi h_a)^4\bar{A}_{11}+\frac{1}{8}(m\pi h_a)^2(n\pi h_a\lambda)^2\left(\frac{\bar{A}_{12}}{2}+\bar{A}_{66}\right)\right.\\&\quad\left.+\frac{9}{32}(n\pi h_a\lambda)^4\bar{A}_{22}\right]-\frac{1}{4}(m\pi h_a)^4h_a\lambda\sum_s\bar{E}_s\bar{A}_s\sin^2\frac{n\pi y_s}{b}\\c_6&=\frac{32(m\pi h_a)^3}{9mn\pi^2}[\bar{A}_{11}+\left(\frac{n\lambda}{m}\right)^2(\bar{A}_{12}-\bar{A}_{66})]f(m)f(n)\\&\quad-\frac{8}{3}(m\pi h_a)^3\frac{h_a\lambda}{m\pi}\sum_s\bar{E}_s\bar{A}_s\sin^3\frac{n\pi y_s}{b}f(m)\\c_7&=\frac{32(n\pi h_a\lambda)^3}{9mn\pi^2}[\bar{A}_{22}+\left(\frac{m}{n\lambda}\right)^2(\bar{A}_{12}-\bar{A}_{66})]f(m)f(n)\\n_3&=-(m\pi h_a)^2\left[\frac{\bar{m}_1{}^T}{Eh^2}+\left(\frac{n\lambda}{m}\right)^2\frac{\bar{m}_2{}^T}{Eh^2}\right]\\n_4&=-\frac{32}{9}(m\pi h_a)^2\left[\frac{\bar{n}_1{}^T}{Eh}+\left(\frac{n\lambda}{m}\right)^2\frac{\bar{n}_2{}^T}{Eh}\right]f(m)f(n).\end{aligned}\tag{A13}$$

The coefficients b_i can be obtained from a_i by the following rotation of symbols:

$$m\Leftrightarrow n,\ \bar{A}_{11}\rightarrow\bar{A}_{22},\ \sum_s=0,\ h_a\rightarrow h_a\lambda,\ h_a\lambda\rightarrow h_a.$$

Additional notation used in equation (A13) is:

$$\begin{aligned}\bar{A}_{ij}&=A_{ij}/Eh & \bar{D}_{ij}&=_{ij}/Eh^3\\h_a&=h/a & \lambda&=a/b\\\bar{E}_s&=E_s/E & \bar{A}_s&=A_s/h^2\\\bar{z}_s&=z_s/h & \bar{I}_{0s}&=I_{0s}/bh^3\end{aligned}$$

$$f(i)=\begin{cases}0 \text{ if } i=\text{even}\\1 \text{ if } i=\text{odd}.\end{cases}\tag{A14}$$

Downloaded 03 May 2010 to 171.66.16.244. Redistribution subject to ASME license or copyright; see http://www.asme.org/terms/Terms_Use.cfm

A Three-Dimensional Constitutive Theory for Fiber Composite Laminated Media[1]

R. M. Christensen
Department of Applied Science,
University of California, and
Lawrence Livermore National Laboratory.
Fellow, ASME

E. Zywicz
Mem. ASME

Lawrence Livermore National Laboratory,
Ceramics and Composite Section,
Livermore, CA 94550

A three-dimensional elastic constitutive theory is developed for application to fiber composite laminated media. The lamina level constitutive relationship is a specific subset of general, transversely isotropic media behavior. This special class of lamina behavior permits the development of an exact lamination procedure for systems assembled from a single lamina type. The three-dimensional constitutive form for the laminate is determined in terms of the subscale lamina properties and the orientations of each lamina. The extension of this specific constitutive relationship to general transversely isotropic lamina involves separation of the five lamina-scale properties into fiber-dominated versus matrix-dominated classifications and the development of a generalized averaging procedure for the matrix-dominated properties. The resulting three-dimensional constitutive/lamination theory is evaluated through comparisons between exact solutions, using data bases appropriate for graphite and glass epoxy systems in quasi-isotropic layups. The theory remains highly effective through the transition from thin laminate to thick laminate behavior and even beyond that through the transition from thick laminate behavior to fully and strongly three-dimensional elastic behavior. The generalized averaging procedure for the matrix-dominated properties produces variations in results that are the same or less than the variations in results due to the experimental uncertainty in the matrix-dominated properties themselves. The theory is fairly simple and extremely versatile in its application.

1 The Problem

The means and mechanism for translating lamina level properties into laminate properties has been available for many years under strongly limited conditions loosely referred to as those of a "thin" laminate. This procedure is known as classical lamination theory, and it neglects the interface conditions between individual lamina and directly sums, by algebraic formulas, the in-plane lamina properties to obtain the integrated in-plane laminate properties. This two-dimensional procedure is widely used and has contributed greatly to the effectiveness of fiber composites. Unfortunately, the two-dimensional procedure provides little guidance on how to proceed in the much more complicated three-dimensional case. However, Pagano (1974) has provided a complete and general three-dimensional lamination procedure, and it has been implemented by Sun and Li (1988). The two-dimensional classical lamination procedure is approximate in the sense that it implies plane-stress conditions. It is the intention here to develop a three-dimensional lamination procedure which retains the essential simplicity of the two-dimensional procedure. Of course, it will not be possible to assume plane-stress conditions in the three-dimensional case, and some other approximations will need to be introduced here to accomplish the objective.

The starting point in the material's characterization is the properties state at the unidirectional lamina level. Taking these properties to be characterized by a state of transversely isotropic symmetry leads to the properties specification through five independent properties. These five independent elastic properties can be specified by the longitudinal Young's modulus, E_l, meaning the modulus in the fiber direction, the longitudinal Poisson's ratio, ν_l, meaning the transverse strain response when the composite is strained in the longitudinal direction to determine E_l, as well as the transverse Young's modulus, E_t, the longitudinal shear modulus, μ_l, and finally the transverse shear modulus, μ_t. These five lamina level properties can be differentiated by grouping them into fiber-dominated versus matrix-dominated properties. The two groupings are:

[1]Work performed under the auspices of the U.S. Department of Energy by the Lawrence Livermore National Laboratory under Contract No. W-7405-ENG-48.

Contributed by the Applied Mechanics Division of THE AMERICAN SOCIETY OF MECHANICAL ENGINEERS for presentation at the Winter Annual Meeting, Dallas, Texas, Nov. 25-30, 1990.

Discussion on this paper should be addressed to the Technical Editor, Leon M. Keer, The Technological Institute, Northwestern University, Evanston, IL 60208, and will be accepted until two months after final publication of the paper itself in the JOURNAL OF APPLIED MECHANICS. Manuscript received by the ASME Applied Mechanics Division, Aug. 4, 1989; final revision, Feb. 5, 1990.

Paper No. 90-WA/APM-32.

Copyright © 1990 by ASME
Downloaded 03 May 2010 to 171.66.16.244. Redistribution subject to ASME license or copyright; see http://www.asme.org/terms/Terms_Use.cfm

Fiber Dominated	Matrix Dominated
E_l	E_t
ν_l	μ_l
	μ_t

For the fiber-dominated properties, the fibers act as the direct load transfer agent. In the matrix-dominated properties, the fibers effectively act as "inclusions" in a continuous matrix phase. This distinction is fundamental, and reveals itself in all credible micromechanics models of fiber composites. High performance fibers translate into a fiber-property dominated composite. Accordingly, in a fiber-dominated composite, the matrix-dominated properties are of less importance than are the fiber-dominated properties. Leaving the fiber-dominated properties unchanged, we specifically seek to develop an averaging procedure for the less important three matrix-dominated properties. The procedure is intended to simplify the constitutive form, but it must not significantly alter basic physical behavior. Needless to say, the matrix-dominated properties averaging procedure will be of no interest or use if it does not permit the development of a three-dimensional lamination theory and the subsequent detailed evaluation thereof. Furthermore, it remains possible that the entire procedure could be "exact" in special cases, as will turn out to be true.

2 The Formal Method

The macroscopic elastic properties for the aligned fiber-reinforced medium are taken to be those of transversely isotropic symmetry with

$$[C_{ij}] = \begin{bmatrix} C_{11} & C_{12} & C_{12} & 0 & 0 & 0 \\ & C_{22} & C_{23} & 0 & 0 & 0 \\ & & C_{22} & 0 & 0 & 0 \\ & & & (C_{22}-C_{23})/2 & 0 & 0 \\ & & & & C_{66} & 0 \\ & & & & & C_{66} \end{bmatrix}, \quad (1)$$

where $\sigma_i = C_{ij}\epsilon_j$ and with

$$\sigma_1=\sigma_{11},\ \sigma_2=\sigma_{22},\ \sigma_3=\sigma_{33},\ \sigma_4=\sigma_{23},\ \sigma_5=\sigma_{31},\ \sigma_6=\sigma_{12}$$

and

$$\epsilon_1=\epsilon_{11},\ \epsilon_2=\epsilon_{11},\ \epsilon_3=\epsilon_{33},\ \epsilon_4=2\epsilon_{23},\ \epsilon_5=2\epsilon_{31},\ \epsilon_6=2\epsilon_{12}.$$

The five independent properties in equation (1), with axis 1 in the fiber direction, can be written in terms of the usual measurable properties, E_{11}, ν_{12}, E_{22}, μ_{12}, and μ_{23} through:

$$\begin{aligned} C_{11} &= E_{11} + 4\nu_{12}^2\kappa_{23}, \\ C_{12} &= 2\kappa_{23}\nu_{12}, \\ C_{22} &= \mu_{23} + \kappa_{23}, \\ C_{23} &= -\mu_{23} + \kappa_{23}, \\ C_{66} &= \mu_{12}. \end{aligned} \quad (2)$$

Here,

$$\kappa_{23} = \frac{E_{22}}{4[1-\nu_{12}^2 E_{22}/E_{11}] - E_{22}/\mu_{23}}, \quad (3)$$

with E_{11} and E_{22} being uniaxial moduli, ν_{12}, the axial Poisson's ratio, and μ_{12} and μ_{23} the shear moduli.

The grouping of five independent properties, E_{11}, ν_{12}, E_{22}, μ_{12}, and μ_{23} contains the three matrix-dominated moduli, E_{22}, μ_{12}, and μ_{23} which were discussed previously. To permit developing a formalism, two interrelations are taken between the three matrix-dominated properties. After obtaining the relevant forms, considerations will be returned to material systems for which the two interrelationships do not apply, which is the case of primary interest.

Begin by taking the two shear moduli μ_{12} and μ_{23} as being equal, i.e.,

$$\mu_{12} = \mu_{23}. \quad (4)$$

The second relationship between the matrix-dominated moduli is taken as

$$\mu_{23} = \frac{(1-\nu_{12})E_{22}}{2(1-\nu_{12}^2 E_{22}/E_{11})}. \quad (5)$$

(This form actually results from a corresponding relationship between the C_{ij} moduli, namely $C_{12} = C_{23}$.) Examining modulus C_{11} in light of the two forms, equations (4) and (5), C_{11} can be expressed as

$$C_{11} = E_{11} - E + \hat{C}_{11}, \quad (6)$$

where

$$E = \frac{(1-\nu_{12}^2)E_{22}}{1-\nu_{12}^2 E_{22}/E_{11}} = 2(1+\nu_{12})\mu_{12} = 2(1+\nu_{12})\mu_{23} \quad (7)$$

and

$$\hat{C}_{11} = \frac{(1-\nu_{12})^2 E_{22}}{(1-\nu_{12}^2 E_{22}/E_{11})(1-2\nu_{12})} = \frac{2(1-\nu_{12})\mu_{12}}{(1-2\nu_{12})} = \frac{2(1-\nu_{12})\mu_{23}}{(1-2\nu_{12})}. \quad (8)$$

With $\hat{C}_{11}$ so defined, for the other C_{ij}'s take

$$\hat{C}_{ij} = C_{ij}, \quad \text{when} \quad i, j \neq 1, 1. \quad (9)$$

Then the full vector of $\hat{C}_{ij}$'s subject to equations (4) and (5) can be written as

$$\begin{bmatrix} \frac{1-2\nu_{12}}{2(1-\nu_{12})}\hat{C}_{11} \\ \frac{1-2\nu_{12}}{2\nu_{12}}\hat{C}_{12} \\ \frac{1-2\nu_{12}}{2(1-\nu_{12})}\hat{C}_{22} \\ \frac{1-2\nu_{12}}{2\nu_{12}}\hat{C}_{23} \\ \hat{C}_{66} \end{bmatrix} = \frac{(1-\nu_{12})E_{22}}{2(1-\nu_{12}^2 E_{22}/E_{11})} \begin{bmatrix} 1 \\ 1 \\ 1 \\ 1 \\ 1 \end{bmatrix} = \mu_{12} \begin{bmatrix} 1 \\ 1 \\ 1 \\ 1 \\ 1 \end{bmatrix} = \mu_{23} \begin{bmatrix} 1 \\ 1 \\ 1 \\ 1 \\ 1 \end{bmatrix}. \quad (10)$$

The form equation (10) rigorously applies only when equations (4) and (5) are satisfied, but it does provide a guiding formalism in the more general case of interest here.

At this point consideration is returned to fiber-reinforced systems which do not satisfy the two interrelationships equations (4) and (5) and accordingly accommodate five independent properties. For such systems, it is our intention to develop an averaging procedure for E_{22}, μ_{12}, and μ_{23} which depends explicitly on all three properties. Of course, these moduli cannot be averaged directly since E_{22} is a uniaxial modulus, while the other two are shear moduli. From equation (10), however, a format is evident by which E_{22} can be compared with μ_{12} and μ_{23}. Define generalized moduli by:

$$\mathcal{E}_1 = \frac{(1-\nu_{12})E_{22}}{2(1-\nu_{12}^2 E_{22}/E_{11})},$$

Downloaded 03 May 2010 to 171.66.16.244. Redistribution subject to ASME license or copyright; see http://www.asme.org/terms/Terms_Use.cfm

$$\mathfrak{L}_2 = \mu_{12}, \qquad (11)$$
$$\mathfrak{L}_3 = \mu_{23}.$$

An averaged, generalized modulus, $\mathfrak{L}$, could be established from equation (11) by arbitrarily writing $\mathfrak{L} = (\mathfrak{L}_1 + \mathfrak{L}_2 + \mathfrak{L}_3)/3$. However, a better and more physically meaningfully averaging procedure now will be developed.

To establish a base line accessible case for physical interpretation, examine the special form of transverse isotropy which results when the two Poisson's ratios are taken as vanishing, i.e.,

$$\nu_{12} = 0 \text{ and } \nu_{23} = 0. \qquad (12)$$

From equation (2) it immediately follows for $\nu_{12} = 0$ that $C_{12} = 0$. The identity $E_{22} = 2(1 + \nu_{23})\mu_{23}$ combined with equation (12) produces $E_{22} = 2\mu_{23}$. Using this latter result in equation (3) and then equation (2) results in $C_{23} = 0$. Finally, using $E_{22} = 2\mu_{23}$ again in equations (3) and (2) gives $C_{22} = E_{22}$, so that equation (12) with equation (2) yields $C_{11} = E_{11}$. Combining all these results into equation (1) gives it the diagonal form

$$[C_{ij}] = \begin{bmatrix} E_{11} & 0 & 0 & 0 & 0 & 0 \\ & E_{22} & 0 & 0 & 0 & 0 \\ & & E_{22} & 0 & 0 & 0 \\ & & & \mu_{23} & 0 & 0 \\ & & & & \mu_{12} & 0 \\ & & & & & \mu_{12} \end{bmatrix}. \qquad (13)$$

Thus, equation (13), with $E_{22} = 2\mu_{23}$, is the form assumed by transverse isotropy for vanishing Poisson's ratios, equation (12), with no other restrictions.

Now form the strain energy density, U, associated with equation (13). This gives

$$2U = (E_{11} - E_{22})\epsilon_{11}^2 + E_{22}\epsilon_{11}^2 + E_{22}\epsilon_{22}^2 + E_{22}\epsilon_{33}^2 + 2\mu_{12}\epsilon_{12}^2 + 2\mu_{23}\epsilon_{23}^2 + 2\mu_{12}\epsilon_{31}^2. \qquad (14)$$

The term $(E_{11} - E_{22})\epsilon_{11}^2$ is the fiber-dominated effect, which obviously must vanish as the fiber reinforcement contribution goes to zero in an isotropic matrix phase. For the remaining matrix-dominated terms in equation (14) let

$$\hat{U} = U_{\text{Matrix-Dominated}} = \frac{E_{22}}{2}(\epsilon_{11}^2 + \epsilon_{22}^2 + \epsilon_{33}^2) + \mu_{23}\epsilon_{23}^2 + \mu_{12}(\epsilon_{12}^2 + \epsilon_{31}^2). \qquad (15)$$

In the spirit of considering fully three-dimensional deformation conditions take all strain components as $\epsilon_{ij} = \mathcal{O}(\delta)$, and using this in equation (15) gives

$$\hat{U} \approx \mathcal{O}\left(\left[3\frac{E_{22}}{2} + 2\mu_{12} + \mu_{23}\right]\delta^2\right). \qquad (16)$$

It is seen that the three matrix-dominated moduli contribute to the strain energy, equation (16), in the proportions

$$\frac{E_{22}}{2} : \mu_{12} : \mu_{23} \quad \text{as} \quad 3 : 2 : 1. \qquad (17)$$

Returning to the generalized moduli, equation (11), an acceptable generalized averaging procedure must recover the result just found. Specifically, for the generalized moduli in equation (11) (specialized to $\nu_{12} = \nu_{23} = 0$) to recover the results, equations (16) and (17), it is necessary that the moduli be averaged with the weighting factors shown below:

$$\mathfrak{L}_1 : \mathfrak{L}_2 : \mathfrak{L}_3 \quad \text{as} \quad 3 : 2 : 1. \qquad (18)$$

Thus, this generalized averaging procedure gives the generalized shear modulus, μ, as

$$\mu = \frac{1}{6}\left[\frac{3(1-\nu_{12})E_{22}}{2(1-\nu_{12}^2\, E_{22}/E_{11})} + 2\mu_{12} + \mu_{23}\right]. \qquad (19)$$

Finally, then the $\hat{C}_{ij}$ coefficients formalized by equation (10) are now taken as

$$\begin{bmatrix} \frac{1-2\nu_{12}}{2(1-\nu_{12})}\hat{C}_{11} \\ \frac{1-2\nu_{12}}{2\nu_{12}}\hat{C}_{12} \\ \frac{1-2\nu_{12}}{2(1-\nu_{12})}\hat{C}_{22} \\ \frac{1-2\nu_{12}}{2\nu_{12}}\hat{C}_{23} \\ \hat{C}_{66} \end{bmatrix} = \mu \begin{bmatrix} 1 \\ 1 \\ 1 \\ 1 \\ 1 \end{bmatrix}, \qquad (20)$$

where μ is now given by equation (19). Relation (20) also applies in the "exact" case when equations (4) and (5) are identically satisfied.

Next, write the $\hat{C}_{ij}$'s in equation (20) in matrix form and compare them with the appropriate isotropic material form in Green and Zerna (1963). It is quickly seen that the forms in equation (20) are those for isotropic behavior with isotropic shear modulus given by μ and with isotropic λ given by

$$\lambda = \frac{2\nu_{12}}{1-2\nu_{12}}\mu. \qquad (21)$$

The relation between $\hat{C}_{ij}$ and C_{ij} is given by equations (6) and (9). The $\hat{C}_{ij}$ form is isotropic, as just established. Thus, using equation (9), the C_{ij} form is isotropic to within the presence of the $(E_{11} - E)$ part of C_{11}. It directly follows that the stress constitutive relation, corresponding to the C_{ij} form, is given by

$$\sigma_{ij} = \lambda\epsilon_{kk}\delta_{ij} + 2\mu\epsilon_{ij} + (E_{11} - E)\delta_{1i}\delta_{1j}\epsilon_{11}, \qquad (22)$$

where λ is given by equation (21), μ by equation (19), and E is given by

$$E = 2(1 + \nu_{12})\mu. \qquad (23)$$

The form equation (22) was previously identified by Christensen (1988); however, in that work the associated interrelationships equations (4) and (5) were taken as restrictions, rather than being developed into the generalized averaging procedure given here and culminating in expression (19). Also, in the work of Christensen (1988), emphasis was given to using equation (22) to develop an associated failure criterion. Attention here is given to using the form equation (22) to identify a specific three-dimensional lamination procedure and to evaluate it.

The lamina level constitutive formulation is now complete with the forms equations (19) and (21)–(23). It should be emphasized that the lamina constitutive equation (22) does not imply the interrelations equations (4) and (5), although it only is "exact" when they are satisfied. In the most general case, all five transversely isotropic properties enter the constitutive form equation (22). The two fiber-dominated properties enter the constitutive forms directly, while all three matrix-dominated properties enter through the generalized averaging procedure result equation (19). Using the form equation (22) to specify the lamina-level behavior, the corresponding laminated medium characterization will be now found. This is the so-called three-dimensional lamination theory or procedure.

Express constitutive relation equation (22) in coordinates other than in the fiber direction. Take the angle of rotation of the coordinate system as θ from the fiber direction, rotated

Downloaded 03 May 2010 to 171.66.16.244. Redistribution subject to ASME license or copyright; see http://www.asme.org/terms/Terms_Use.cfm

about axis x_3. With a_{ij} being the direction cosines matrix, the constitutive relation equation (22) takes the rotated form

$$\sigma_{ij} = \lambda\epsilon_{kk}\delta_{ij} + 2\mu\epsilon_{ij} + (E_{11} - E)a_{1i}a_{1j}a_{1k}a_{1l}\epsilon_{kl}, \tag{24}$$

where

$$[a_{1i}] = [\cos\theta, \quad -\sin\theta, \quad 0], \tag{25}$$

with equation (25) being the first row of a_{ij}. Now, take N similar lamina in bonded contact, each with its individual direction, θ_n. The three-dimensional form equation (24) for each lamina is directly combined to give the three-dimensional medium constitutive form

$$\sigma_{ij} = \lambda\epsilon_{kk}\delta_{ij} + 2\mu\epsilon_{ij} + \frac{(E_{11} - E)}{N}\sum_{n=1}^{N} m_i^{(n)}m_j^{(n)}m_k^{(n)}m_l^{(n)}\epsilon_{kl}, \tag{26}$$

wherein from equation (25),

$$[m_i^{(n)}] = [\cos\theta_n, \quad \sin\theta_n, \quad 0]. \tag{27}$$

Equation (26) along with equations (19), (21), (23), and (27) constitute the three-dimensional constitutive theory for fiber composite laminated media assembled from a single lamina type, and involves all five independent properties.

It is readily verified from equation (26) that the interlaminar stress components σ_{33}, σ_{32}, and σ_{31} are continuous across the interfaces between lamina because the last term in equation (26) vanishes for these three stress components. By definition, the displacements are continuous across the interfaces since the entire constitutive form equation (26) is expressed in terms of the single strain tensor, ϵ_{ij}. Thus, the laminated medium constitutive form equation (26), as derived from the lamina constitutive form equation (22), is an exact three-dimensional result. No approximations are involved in satisfying interface conditions. It is implicit in obtaining equation (26) from equation (22) that the strain gradients are small over the number of lamina of interest, N. This condition will be generalized (relaxed) in the section on utilization. Although form equation (26) takes all lamina to be of equal thickness, it is easily extended by including thickness related weighting functions in it.

The constitutive form equation (26) for the laminated medium is extraordinarily compact and easy to use. If the two interrelations equations (4) and (5) are satisfied (to within experimental accuracy) by a given set of five transversely isotropic properties, then the entire procedure up through and including the final constitutive result, equation (26), is "exact" within the theory of linear elasticity. In this case the results are identical to the C_{ij} matrix in Pagano (1974). If the two interrelations equations (4) and (5) are not satisfied, then the result, equation (26), is an approximation based upon the generalized averaging procedure for the three matrix-dominated properties. Under this condition it will be necessary to carefully evaluate the nature of the approximation as will be done in the next two sections.

3 A Test Case

Judging the total accuracy of the proposed constitutive relationship against the exact form necessitates comparing more than just the resulting effective lamina moduli. Although direct comparisons between individual moduli show the differences expected from "uni-axial" load states, they do not accurately capture the coupling between components which occurs naturally under a general three-dimensional load state. This section formulates a specific BV problem which: (1) allows direct comparisons of various field quantities obtained by using both the exact and proposed constitutive relationships, and (2) shows the finite regimes where classical long-wavelength (LW) theory (essentially plane-stress or classical flat lamination theories) is appropriate. To aid the reader in distinguishing variables associated with the constitutive formulation from those associated with the BV problem, direction notation and an X-Y-Z coordinate frame are employed in defining and solving the test problem.

In adopting a test case for the three-dimensional lamination theory, it is necessary to select a particular lay-up pattern. There are two limiting cases for lay-up patterns. At one extreme is the degenerate case of all lamina being aligned, thus the laminate retains aligned-axis character. At the other extreme is a quasi-isotropic lay-up involving the most dispersed pattern of directions. The aligned laminate is a trivial application of lamination theory, since there are no true interfaces. The quasi-isotropic lay-up is in fact the most extreme case, and provides the most severe test of a lamination theory. It requires the highest degree of interactive coupling between all lamina properties to produce laminate behavior.

3.1 The Boundary Value Problem. The problem considered herein is a "homogenized" solid lying parallel to the X-Z plane. The laminated solid consists of many identical transversely isotropic laminae oriented in a repetitive [0 deg, $\pm$60 deg] order and is considered to be quasi-isotropic in the X-Z plane. A sufficient number of laminae exist through the thickness, in the Y-direction, such that the macroscopic composite properties are well represented by those of a homogenized single [0 deg, $\pm$60 deg] sublaminate.

Without loss of generality, the coordinate positions X, Y, and Z are nondimensionalized to the coordinates x, y, and z by half the thickness of the solid, $h/2$, (i.e., $x = 2X/h$, $y = 2Y/h$, and $z = 2Z/h$) so that the upper and lower surfaces lie in the planes $y = 1$ and $y = -1$, respectively. Displacements in the z-direction, as well as all derivatives taken with respect to z, are taken to vanish identically (yielding plane-strain conditions). Imposed on the lower surface, $y = -1$, are traction-free boundary conditions; while on the upper surface, $y = 1$, a sinusoidal normal traction is applied which has the form

$$t_n = -P\sin(\alpha x). \tag{28}$$

Here,

$$\alpha = \frac{h\pi}{2L}, \tag{29}$$

P, the load magnitude, has units of stress, $2L$ is the loading wavelength, and the convention that positive normal tractions produce normal tensile stresses is employed. The solid extends "infinitely" in the x-direction, but only the region from $x = 0$ to $x = 2L/h$ need be examined, due to periodicity. Furthermore, all body forces are identically zero. This problem has been chosen because by varying α, essentially the ratio of h to L, many different loading conditions can be achieved. For values of $h/L \ll 1$, classical LW conditions result and as h/L increases fully, three-dimensional load states develop.

3.2 Material Formulation. Using the homogenizing procedure used by Sun and Li (1988), the effective sublaminate stiffnesses are assembled. Using the appropriate tensor transformations the $\pm$60 deg material stiffness tensor components are expressed in the 0 deg lamina material coordinate frame. (For transversely isotropic lamina whose plane of isotropy lies perpendicular to the lamina or ply-plane, Christensen (1988) gives the explicit stiffness tensor components in any cartesian coordinate frame where the rotated in-plane axes remain parallel to the original ply-plane.) Unit macro strains are individually imposed along the boundaries of a combined (unit-square) $\pm$60 deg lamina pair. After enforcing continuity of interlaminar displacements and tractions, the resulting net forces yield the effective $\pm$60 deg stiffness components when properly normalized. Next, the 0 deg and effective $\pm$60 deg laminae are weighted appropriately and assembled using the same

Downloaded 03 May 2010 to 171.66.16.244. Redistribution subject to ASME license or copyright; see http://www.asme.org/terms/Terms_Use.cfm

method to produce the effective properties of the entire sublaminate.

The quasi-isotropic lay-up produces a set of transversely isotropic properties in three dimensions. With x_3 being the axis of symmetry for the laminate, the nonzero effective stiffness properties, c_{ij}, for the [0 deg, ±60 deg] quasi-isotropic laminate are given by these newly derived (exact) closed-form expressions:

$$c_{11}=c_{22}=\frac{3}{8}(C_{11}+C_{22})+\frac{1}{4}C_{12}+\frac{1}{2}C_{66}-\frac{1}{8C_{22}}(C_{12}-C_{23})^2, \tag{30}$$

$$c_{12}=\frac{1}{8}(C_{11}+C_{22})+\frac{3}{4}C_{12}-\frac{1}{2}C_{66}+\frac{1}{8C_{22}}(C_{12}-C_{23})^2, \tag{31}$$

$$c_{13}=c_{23}=\frac{1}{2}(C_{12}+C_{23}), \tag{32}$$

$$c_{33}=C_{22}, \tag{33}$$

$$c_{44}=c_{55}=\frac{2C_{66}(C_{22}-C_{23})}{2C_{66}+C_{22}-C_{23}}, \tag{34}$$

$$c_{66}=\frac{1}{2}(c_{11}-c_{12}). \tag{35}$$

Here, the upper case C_{ij} refers to the individual lamina components given in the lamina coordinate frame; i.e., axis 1 in the fiber direction. Substituting equations (2) and (3) into (30)–(35) allows the quasi-isotropic stiffnesses to be expressed in terms of the usual five properties, specifically E_{11}, E_{22}, ν_{12}, μ_{12}, and μ_{23}.

3.3 Solution Formulation. The general solution to the test case BV problem has been fully derived, following the method employed by Timoshenko and Goodier (1970) to solve a similar isotropic problem. First, the equilibrium equations, infinitesimal strain-displacement relationships, and compatibility equations are reduced by incorporating the plane-strain assumption. Next, the individual stress component forms are found by using the reduced equilibrium equations and by assuming a separable solution where a Fourier series represents the x-dependence and some function of $F(y)$ represents the y-dependence. The strain component forms, determined by substituting the stress forms into the constitutive relationship along with the sole remaining compatibility equation, yield the governing differential equation for $F(y)$. Solving the linear homogeneous differential equation and matching the original boundary conditions uniquely determines $F(y)$ which, when substituted back into the original stress and strain forms, yields the complete closed-form BV problem solution.

The effective laminate properties and BV problem, in conjunction with actual material properties, allow an objective and realistic evaluation of the proposed constitutive relationship in a fully three-dimensional load state. In the following section, laminate properties and solutions to the BV problem will be compared for two specific composite systems, and the effectiveness of the proposed lamination procedure relationships will be demonstrated.

Table 1 Lamina properties used in evaluation

	Gr/Ep[1]	Gl/Ep[2]
E_{11}GPa	144	53.7
$E_{22}=E_{33}$ GPa	9.65	17.9
ν_{12}	0.31	0.25
ν_{23}	0.52	0.25
μ_{12} GPa	5.24	8.96
μ_{23} GPa	3.17	7.17

[1]Data from Kim, Abrams, and Knight, 1988
[2]Data from Sun and Li, 1988

4 Evaluation

4.1 Properties. To evaluate the proposed constitutive relationship, two sets of lamina properties are chosen, which approximately satisfy the restrictions of transverse isotropy. A graphite/epoxy (Gr/Ep) composite [AS4/3501-6] is chosen for its extremely anisotropic (axial to transverse) moduli, along with a glass/epoxy (Gl/Ep) composite, chosen as representative of a lesser fiber-dominated system. Table 1 lists the elastic lamina constants for both systems, and to satisfy the restrictions of transverse isotropy, namely $\mu_{23} = E_{22}/2(1+\nu_{23})$, the actual moduli are adjusted slightly from the reported values.

Table 2 contains the effective quasi-isotropic laminate properties calculated via equations (30)–(35) using the proposed forms from Section 2, namely the C_{ij} properties corresponding to the lamina constitutive equation (22), and, for comparison, using the exact C_{ij} properties from equation (2) and (3). (The proposed C_{ij} properties are explicitly given by equations (6), (9), (19)–(21), and (23).) The ratios of these results are shown in Table 2 as well. Generally less discrepancy exists between the in-plane moduli (1 and 2 directions) than the out-of-plane components. Also tabulated in Table 2 are the quantities $E_{11}/(1-\nu_{12}^2)$ and $E_{11}/(1-\nu_{12})$ which represent uni-axial and bi-axial in-plane extensional stiffnesses, respectively, associated with classical flat lamination theory. For the two composite systems examined, the exact and proposed quasi-isotropic moduli and in-plane extensional stiffnesses differ typically by less than ≈ 10 percent.

4.2 Test BV Problem. The previously formulated BV problem is now explored, utilizing the Gr/Ep and Gl/Ep laminate properties listed in Table 2, to quantify results from a three-dimensional problem. By judiciously selecting several variables at two locations, a meaningful and representative comparison is possible without having to examine the entire

Table 2 Effective quasi-isotropic laminate elastic constants and in-plane extensional stiffnesses calculated using the exact transversely isotropic and proposed lamina constitutive relationships for Gr/Ep and Gl/Ep systems

	Gr/Ep			Gl/Ep		
	Proposed	Exact	Proposed / Exact	Proposed	Exact	Proposed / Exact
$E_{11}=E_{22}$ GPa	55.0	55.5	0.99	30.7	31.1	0.99
E_{33} GPa	13.4	12.5	1.07	20.4	18.3	1.11
ν_{12}	0.329	0.309	1.06	0.283	0.245	1.16
$\nu_{13}=\nu_{23}$	0.302	0.348	0.87	0.239	0.225	1.06
μ_{12} GPa	20.7	21.2	0.98	11.9	12.5	0.95
$\mu_{13}=\mu_{23}$ GPa	3.95	3.95	1.00	7.61	8.00	0.95
$E_{11}/(1-\nu_{12}^2)$ GPa	61.7	61.3	1.01	33.4	33.1	1.01
$E_{11}/(1-\nu_{12})$ GPa	82.0	80.0	1.02	42.8	41.1	1.04

Downloaded 03 May 2010 to 171.66.16.244. Redistribution subject to ASME license or copyright; see http://www.asme.org/terms/Terms_Use.cfm

Table 3 Normalized flexural stresses for Gr/Ep and Gl/Ep systems versus thickness to length ratio h/L. Normalizing values, σ_{xx-LW}, represent the asymptotic solution obtained as $h/L \to 0$; i.e., LW theory.

$$\sigma_{xx}(y=1,\ x=L/h)/\sigma_{xx-LW}(y=1,\ x=L/h)$$

	Gr/Ep		Gl/Ep	
h/L	Proposed	Exact	Proposed	Exact
0.01	1.000	1.000	1.000	1.000
0.05	1.006	1.006	1.001	1.001
0.10	1.023	1.023	1.006	1.006
0.50	1.663	1.638	1.221	1.216
1.00	3.824	3.965	2.319	2.406
5.00	86.18	90.39	51.60	54.78
10.0	343.1	359.8	205.4	218.1

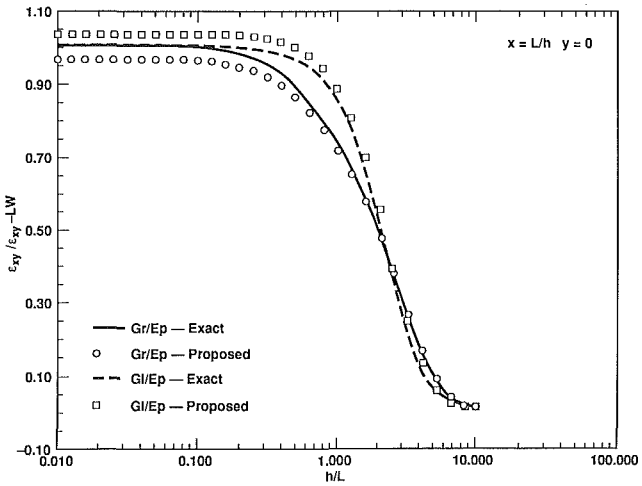


Fig. 1 Midplane shear strains, normalized by the exact asymptotic solution, versus thickness-to-loading wavelength ratio for a quasi-isotropic laminate

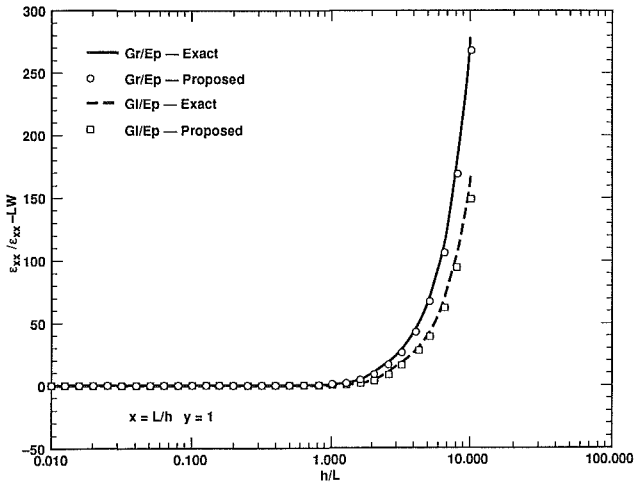


Fig. 2 Flexural strains, normalized by the exact asymptotic solution, versus thickness-to-loading wavelength ratio for a quasi-isotropic laminate

field. The variables chosen for comparison are: (1) the flexural stress and strain, σ_{xx} $(y=1,\ x=L/h)$ and ϵ_{xx} $(y=1,\ x=L/h)$; (2) the upper-surface normal displacement, u_y $(y=1, x=L/h)$; and (3) the midplane shear stress and shear strain, σ_{xy} $(y=0,\ x=L/h)$ and ϵ_{xy} $(y=0,\ x=L/h)$. At these locations, these variables are the dominant components present as well as the minimum or maximum values achieved by these variables (almost) anywhere in the body. The normal displacement probably best captures the three-dimensional aspects in that it reflects an integrated value, whereas the other terms are more

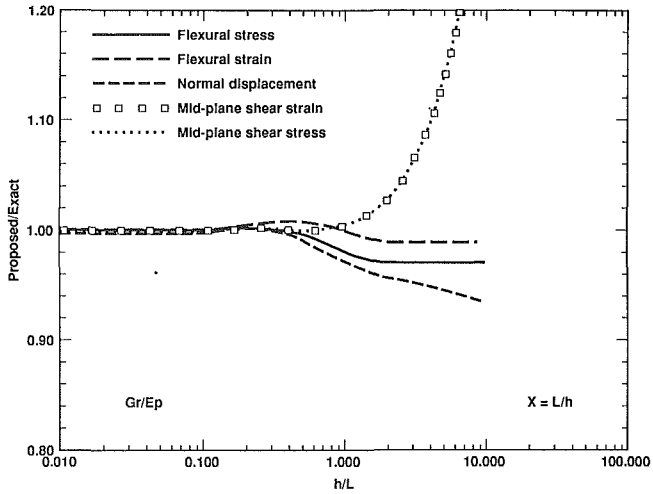


Fig. 3 Normalized field quantities, as a function of the thickness-to-loading wavelength ratio, calculated using the proposed constitutive relationship and normalized by their corresponding exact values, for Gr/Ep

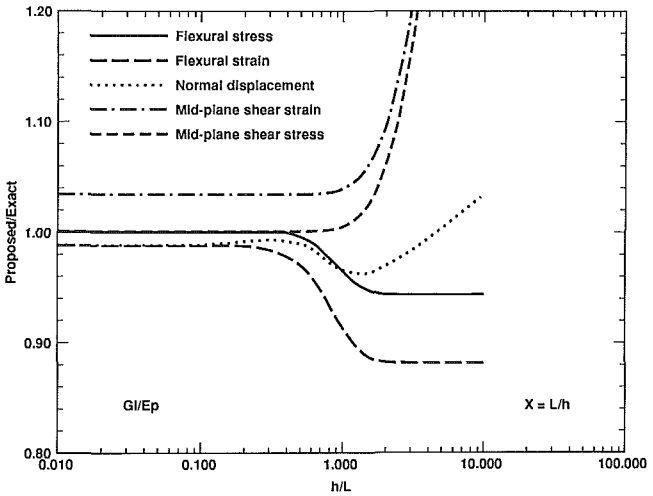


Fig. 4 Normalized field quantities, as a function of the thickness-to-loading wavelength ratio, calculated using the proposed constitutive relationship and normalized by their corresponding exact values, for Gl/Ep

indicative of the material properties directly associated with that particular component.

Table 3 lists the normalized flexural stresses, as a function of the thickness-to-length ratio, h/L, evaluated using both the proposed and exact constitutive relationships for both composite systems. The stresses have been normalized by the asymptotic solution obtained as $h/L \to 0$, i.e., essentially LW or classical plate theory, using the exact transversely isotropic lamina relationship. Reasonable agreement exists between the two solutions from $h/L = 0$ to an astonishing value of $h/L = 10$. Note how rapidly the BV solution deviates from classical LW theory as h/L increases beyond approximately 0.10. Figures 1 and 2 show the midplane shear strain and flexural strain, respectively, normalized by their LW solution for both composite systems as a function of h/L. The agreement between the results shown in Figs. 1 and 2 is typical of all the variables considered. Examining the figures reveals that the components calculated from the proposed and exact constitutive relationship differ only slightly even as $\epsilon_{xy} \to 0$ as $h/L \to \infty$. Unfortunately, plotted at this scale it is not evident how drastically the BV and LW solutions drift apart, e.g., $\epsilon_{xx} > 2\epsilon_{xx-LW}$ for $h/L > 0.75$ and $\epsilon_{xy} < 0.75\epsilon_{xy-LW}$ for $h/L > 1.0$. Nonetheless, the proposed lamina relationship captures remarkably well all

Downloaded 03 May 2010 to 171.66.16.244. Redistribution subject to ASME license or copyright; see http://www.asme.org/terms/Terms_Use.cfm

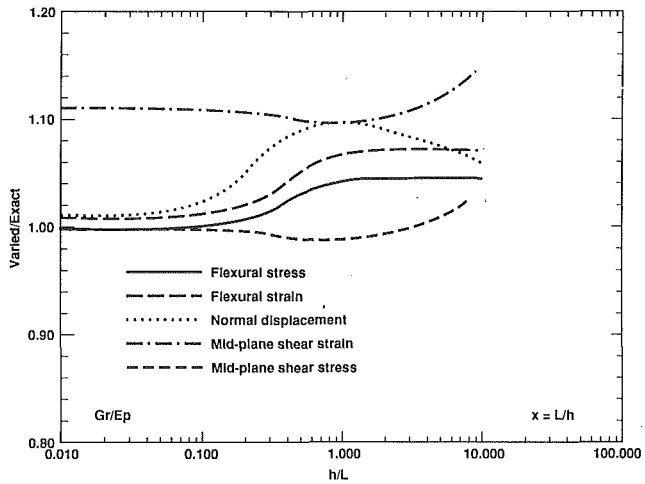


Fig. 5 Field quantities, normalized by the exact solution, versus the thickness-to-loading wavelength ratio. Values obtained using the exact constitutive relationship but by decreasing the three matrix-dominated properties by 10 percent, for Gr/Ep.

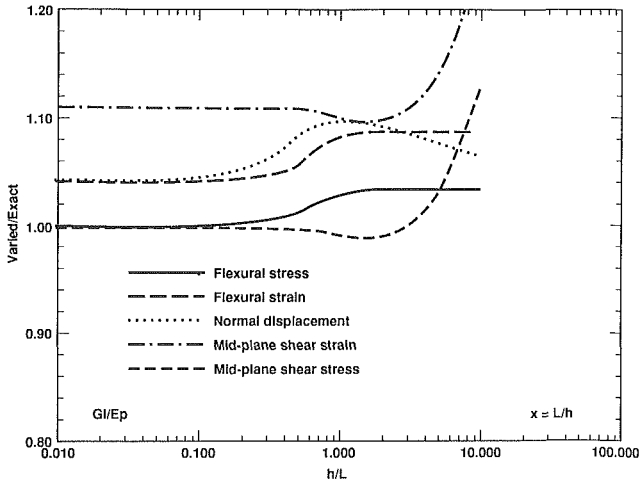


Fig. 6 Field quantities, normalized by the exact solution, versus the thickness-to-loading wavelength ratio. Values obtained using the exact constitutive relationship but by decreasing the three matrix-dominated properties by 10 percent, for Gl/Ep.

characteristics of the BV problem, neglecting small differences in numerical values.

To quantify precisely the differences arising from the proposed relationship, the five field quantities have been normalized by their corresponding exact values and plotted versus h/L in Figs. 3 and 4 for the Gr/Ep and Gl/Ep systems, respectively. Recognize that as $h/L \to \infty$, $\sigma_{xy} \to 0$ and $\epsilon_{xy} \to 0$, and thus their normalized ratios for increasing h/L represent differences in decreasingly smaller numbers. Ignoring the regions where σ_{xy} and ϵ_{xy} approach zero, the errors in the five normalized field quantities for $h/L < 10$ are less than 11 percent in the Gl/Ep system and 7 percent in the fiber-dominated Gr/Ep system.

Overall, the BV problem results invariably reflect the differences in effective lamina properties between the proposed and exact constitutive idealization. Keeping in mind that the BV problem is intrinsically stress controlled, underestimated properties, like Gl/Ep μ_{13}, produce overestimated strain values and vice versa.

This test problem is ideally suited to discriminate thin laminate conditions (LW theory) from thick laminate conditions. The ratio of laminate thickness to the loading wavelength (h/L) directly gives the parameter of variation. As $h/L \to 0$, long wavelength, thin laminate conditions are recovered as a limiting case. As h/L becomes larger, more complex physical effects enter the BV problem. Somewhere in the range $0.1 < h/L < 1$ a transition from thin laminate conditions to thick laminate conditions occurs (e.g. see Figs. 1 and 2). Certainly in the neighborhood of $h/L = 1$, fully three-dimensional deformation conditions exist in the laminate. The lamination theory developed herein properly models all major effects, and it even remains effective up through $h/L = 10$.

4.3 Constitutive Error Relative to Experimental Uncertainties. As stated in Section 2, this work aims to formulate a practical and workable three-dimensional lamination theory which retains algebraic simplicity while providing "reasonable and useful" composite representation. In actual application both constitutive approximations and material property variations, arising from experimental uncertainties, contribute to overall analysis inaccuracies. Thus, comparing the absolute mathematical error from the constitutive approximations with that from the material properties appears appropriate. This section compares the magnitude of experimental uncertainties to the resulting constitutive error in quantifying the lamina properties.

Large scatter in measured lamina properties is common, especially with all the difficulties encountered in obtaining them; for example, Kim, Abrams, and Knight (1988) report coefficients of variations in measured unidirectional Gr/Ep lamina moduli between 2.0 percent and 12.2 percent even though 3 to 10 specimens were used in each test. Clearly, the lamina constants most difficult to experimentally determine and most prone to uncertainties are the three matrix-dominated moduli, namely E_{22}, μ_{12}, and μ_{23}.

The differences between the proposed and exact lamina relationships stem solely from assumptions made regarding the matrix-dominated properties. Since variations in fiber-dominated properties produce (nearly) identical results in either constitutive relationship, attention is focused only upon uncertainties associated with the matrix-dominated properties. Plotted in Figs. 5 and 6 are the normalized BV problem quantities for the Gr/Ep and Gl/Ep systems, respectively, calculated by decreasing the three matrix-dominated lamina properties by 10 percent (an amount typical of their actual variation) from their base values given in Table 1. As before, the BV problem values are normalized by their corresponding exact quantities. The variations in field quantities and, thus, lamina properties caused by uncertainties in the three matrix-dominated properties are the same order of magnitude as those introduced by the proposed constitutive relationship; i.e., compare Figs. 5 and 6 with Figs. 3 and 4. Therefore, we conclude that use of the proposed method in actual engineering analyses should produce results with uncertainties which, for all practical purposes, cannot be realistically differentiated from inherent experimental error in the matrix-dominated lamina properties.

5 Utilization

This section explores how the proposed constitutive relationship can be beneficially utilized in analyzing both thin and thick composite structures.

5.1 Classical Lamination Theory. The proposed lamina relationship can be incorporated into classical lamination theory. Using the previous averaging approach on the four constants required by classical lamination theory, the generalized shear modulus becomes

$$\mu = \frac{1}{5}\left[\frac{3(1-\nu_{12})E_{22}}{2(1-\nu_{12}^2 E_{22}/E_{11})} + 2\mu_{12}\right]. \tag{36}$$

Downloaded 03 May 2010 to 171.66.16.244. Redistribution subject to ASME license or copyright; see http://www.asme.org/terms/Terms_Use.cfm

Using equations (6), (9), (20), and (36) the transformed nth lamina stiffness matrix, Q_{ij}^n, defined such that

$$\begin{Bmatrix} \sigma_1 \\ \sigma_2 \\ \sigma_6 \end{Bmatrix}^n = \begin{bmatrix} Q_{11} & Q_{12} & Q_{16} \\ Q_{12} & Q_{22} & Q_{26} \\ Q_{16} & Q_{26} & Q_{66} \end{bmatrix}^n \begin{Bmatrix} \epsilon_1 \\ \epsilon_2 \\ \epsilon_6 \end{Bmatrix}^n, \tag{37}$$

is directly obtainable. Because of the lamina relationship form, Q_{ij}^n is decomposable into an effectively isotropic and homogeneous term, Q_{ij-H}^n, and a reinforcement term, Q_{ij-R}^n, as

$$Q_{ij}^n = Q_{ij-H}^n + Q_{ij-R}^n, \tag{38}$$

where

$$[Q_{ij-H}]^n = \begin{bmatrix} 2\mu+\lambda & \lambda & 0 \\ \lambda & 2\mu+\lambda & 0 \\ 0 & 0 & \mu \end{bmatrix} \tag{39}$$

and

$$[Q_{ij-R}]^n = (E_{11} - E) \begin{bmatrix} \cos^4\theta_n & \cos^2\theta_n\sin^2\theta_n & \cos^3\theta_n\sin\theta_n \\ \cos^2\theta_n\sin^2\theta_n & \sin^4\theta_n & \cos\theta_n\sin^3\theta_n \\ \cos^3\theta_n\sin\theta_n & \cos\theta_n\sin^3\theta_n & \cos^2\theta_n\sin^2\theta_n \end{bmatrix}. \tag{40}$$

Since μ_{23} does not enter into classical lamination theory, the form of μ given in equation (36) should be used. When evaluating the extensional, coupling, and bending stiffness matrices for a laminate composed of a single lamina type, the contribution of equation (39) factors through the integration, as a homogeneous isotropic material, leaving only the reinforcement contribution to be calculated on a ply-by-ply basis.

5.2 Finite Element Procedures For Thick Composite Structures. Currently, to analyze a thick composite structure, either each lamina in the component is discretized and assigned its own material constants, or the laminae are homogenized, represented by a single or several sets of effective properties, allowing the component to be discretized as an equivalent "homogeneous" solid. When defining each lamina as its own continuum layer, obtaining a satisfactory solution with modest to large through thickness gradients generally requires several elements through each lamina thickness; and because typical composite structures contain tens to hundreds of plies and because element aspect ratios must be maintained, the total problem size, i.e., degrees-of-freedom (DOF), quickly escalates. In structures where adjacent parts mandate nonlinear, presumably iterative, solution procedures and contain thousands to hundreds of thousands of DOF, implicit FE methods become economically unfeasible. On the other hand, when dynamic responses necessitate explicit FE schemes, e.g. impact loadings, the maximum time increment permitted is limited by approximately the minimum time required for a wave to propagate across the smallest element (Bathe, 1982). With such small elements, an unacceptable large number of time steps results and may render the solution technique impractical.

To circumvent some of these difficulties, consider incorporating the lamina constitutive equation (24) into displacement-based solid elements, using conventional FE methodologies. Following the usual procedures, the laminated structure to be analyzed would be discretized as a homogeneous solid (presuming it is manufactured from a single composite system). However, when evaluating the elemental stiffness matrix K_{ij}, C_{ij} is allowed to vary with position representing the differently oriented lamina within the element. Symbolically, K_{ij} is thus calculated as

$$K_{ij} = \int_v B_{li} C_{lm}(x,y,z) B_{mj}\, dv, \tag{41}$$

where v designates the element volume, $C_{ij}(x, y, z)$ is the position-dependent stiffness matrix whose form is given by equation (24), and B_{ij} is the strain-displacement transformation matrix. Note that equation (41) homogenizes the laminate material within each element to the same kinematic order as the element, without sacrificing stacking sequence-related behavior. This procedure guarantees continuity of interlaminar displacements and tractions while ensuring that both the global solution and homogenization method converge, in the FE sense, as the number of elements increases. Simplifications in calculating equation (41) can be made by requiring the elements be oriented so that one surface is parallel to the plane of the lamina. Although the resulting strains would be the individual lamina strains, some postprocessing is necessary to recover the in-plane lamina stresses. In general, this approach should make analyzing thick laminates involve nearly the same degree of (analysis) difficulties as encountered in analyzing thick homogeneous solids.

6 Conclusions

A three-dimensional theory, which rigorously enforces continuity of interlaminar tractions and displacements, is developed for thick laminated media and is evaluated by direct comparisons with exact solutions. The lamina constitutive relationship, almost isotropic in mathematical form but arbitrarily anisotropic in physical content, simplifies lamination theory without sacrificing physical meaning or even significant accuracy. The accuracy level of this theory is well inside the range of experimental uncertainty contained in the properties themselves.

Acknowledgments

RMC would like to acknowledge support from the Office of Naval Research, Dr. Y. Rajapakse, and the Ballistics Research Laboratory, Dr. Bruce Burns.

References

Bathe, K. J., 1982, *Finite Element Procedures in Engineering Analysis*, Prentice-Hall, Englewood Cliffs, N.J., pp. 532–556.

Christensen, R. M., 1988, "Tensor Transformations and Failure Criteria for the Analysis of Fiber Composite Materials," *Journal of Composite Materials*, Vol. 22, pp. 874–897.

Green, A. E., and Zerna, W., 1963, *Theoretical Elasticity*, Oxford University Press, p. 161.

Kim, R. Y., Abrams, F., and Knight, M., 1988, "Mechanical Characterization of a Thick Composite Laminate," *Proceedings of the American Society for Composites, 3rd Technical Conference*, Sept. 25–29, 1988, Seattle, Wash., Technomic Publishing, pp. 711–718.

Pagano, N. J., 1974, "Exact Moduli of Anisotropic Laminates," *Mechanics of Composite Materials*, Vol. 2, G. P. Sendeckyj, ed., Academic Press, New York, pp. 23–44.

Sun, C. T., and Li, S., 1988, "Three-Dimensional Effective Elastic Constants for Thick Laminates," *Journal of Composite Materials*, Vol. 22, pp. 629–639.

Timoshenko, S. P., and Goodier, J. N., 1970, *Theory of Elasticity*, 3rd ed., McGraw-Hill, New York, pp. 53–60.

Downloaded 03 May 2010 to 171.66.16.244. Redistribution subject to ASME license or copyright; see http://www.asme.org/terms/Terms_Use.cfm

Effect of Interphases on Micro and Macromechanical Behavior of Hexagonal-Array Fiber Composites

J. D. Achenbach
Fellow ASME

H. Zhu
Post-Doctoral Fellow

Center for Quality Engineering and Failure Prevention,
Northwestern University,
Evanston, IL 60208-3020

The effect of interphase stiffness on microstresses and macromechanical behavior has been investigated for transverse loading of an hexagonal-array unidirectional fiber composite. The interphase is modeled by a layer which resists radial extension and circumferential shear deformation. Taking advantage of the periodicity of the medium, the states of stress, and deformation in a basic cell have been analyzed numerically by the use of the boundary element method. The circumferential tensile stress along the matrix side of the interphase and the radial stress in the interphase have been analyzed for various values of the interphase parameters and the fiber volume ratio. The micromechanical results have also been used to determine the effect of interphase stiffness on the effective moduli. The calculated values have been compared with analytical results that were adjusted for interphase stiffness.

Introduction

In many fiber-reinforced composites, the bond between the fibers and the matrix material is not of the perfect kind that can be modeled by continuity of tractions and displacements across a discrete fiber-matrix interface. Instead, the bond is effected across a thin interfacial zone, an interphase, which has its own stiffness properties. Clearly such an interphase may significantly affect the mechanical properties as well as the strength of fiber-reinforced composites.

The influence of an interfacial zone on a composite's mechanical and thermal behavior has been investigated by a number of authors. It was shown by Walpole (1978) that a thin coating on an inclusion has a pronounced effect on the fields just outside the inclusion. The stress field in and around a coated short fiber has been investigated by Mikata and Taya (1985a). These authors (1985b) also investigated a continuous fiber composite subjected to thermomechanical loading. A computer simulation of the strength of metal-matrix composites with a reaction layer at the interfaces has been presented by Ochiai and Osamura (1987).

In related studies two analytical models have been considered. Broutman and Agarwal (1974), Theocaris et al. (1985), Maurer et al. (1986), Sideridis (1988), and Benveniste et al. (1989) have described the interphase as a layer between fiber (or inclusion) and matrix, of specified thickness and of elastic constants different from those of the matrix and the fiber. In an alternate model a very thin interfacial zone of unspecified thickness has been considered. In this model it is assumed that the radial and the tangential tractions are continuous across the interphase, but the displacements may be discontinuous from fiber to matrix due to the presence of the interphase in between. The tractions are assumed to be proportional to the corresponding displacement discontinuities. The proportionality constants then characterize the stiffness of the interphase. This spring layer model was employed by Lene and Leguillar (1982), Benveniste (1985), Aboudi (1987), Steif and Hoysan (1987), Achenbach and Zhu (1989), and Hashin (1990). Both models mentioned above were studied by Jasiuk and Tong (1989).

The selection of an appropriate interphase model is important, but it is also essential that a suitable method is employed to account for the presence of other fibers. A very useful approximate approach has been provided by Mori and Tanaka (1973). In an alternate scheme, which is conceptually more elementary but gives rigorous results, a periodic configuration of fibers is assumed, and micromechanical calculations are carried out for a basic cell. This cell contains a single fiber and adjoining matrix material, and its bounding surfaces are subjected to appropriate surface tractions and/or displacements which are consistent with the structural periodicity and the far-field loading. For transverse loading and perfect fiber-matrix bonds, such calculations have been carried out by Adams (1987) and Zywicz (1986) for rectangular and hexagonal arrays, respectively. Within the context of the periodic model of a rectangular array, the effect of an interphase has been investigated in this manner by Achenbach and Zhu (1989). These authors found that variation of the interphase parameters causes pronounced changes in the stress fields in the

Contributed by the Applied Mechanics Division of THE AMERICAN SOCIETY OF MECHANICAL ENGINEERS for presentation at the Winter Annual Meeting Dallas, Texas, November 25–30, 1990.

Discussion on this paper should be addressed to the Technical Editor, Leon M. Keer, The Technological Institute, Northwestern University, Evanston, IL 67208, and will be accepted until two months after final publication of the paper itself in the JOURNAL OF APPLIED MECHANICS. Manuscript received by the ASME Applied Mechanics Division, Sept. 8, 1989; final revision, Mar. 1, 1990.

Paper No. 90-WA/APM-44.

Copyright © 1990 by ASME
Downloaded 03 May 2010 to 171.66.16.244. Redistribution subject to ASME license or copyright; see http://www.asme.org/terms/Terms_Use.cfm

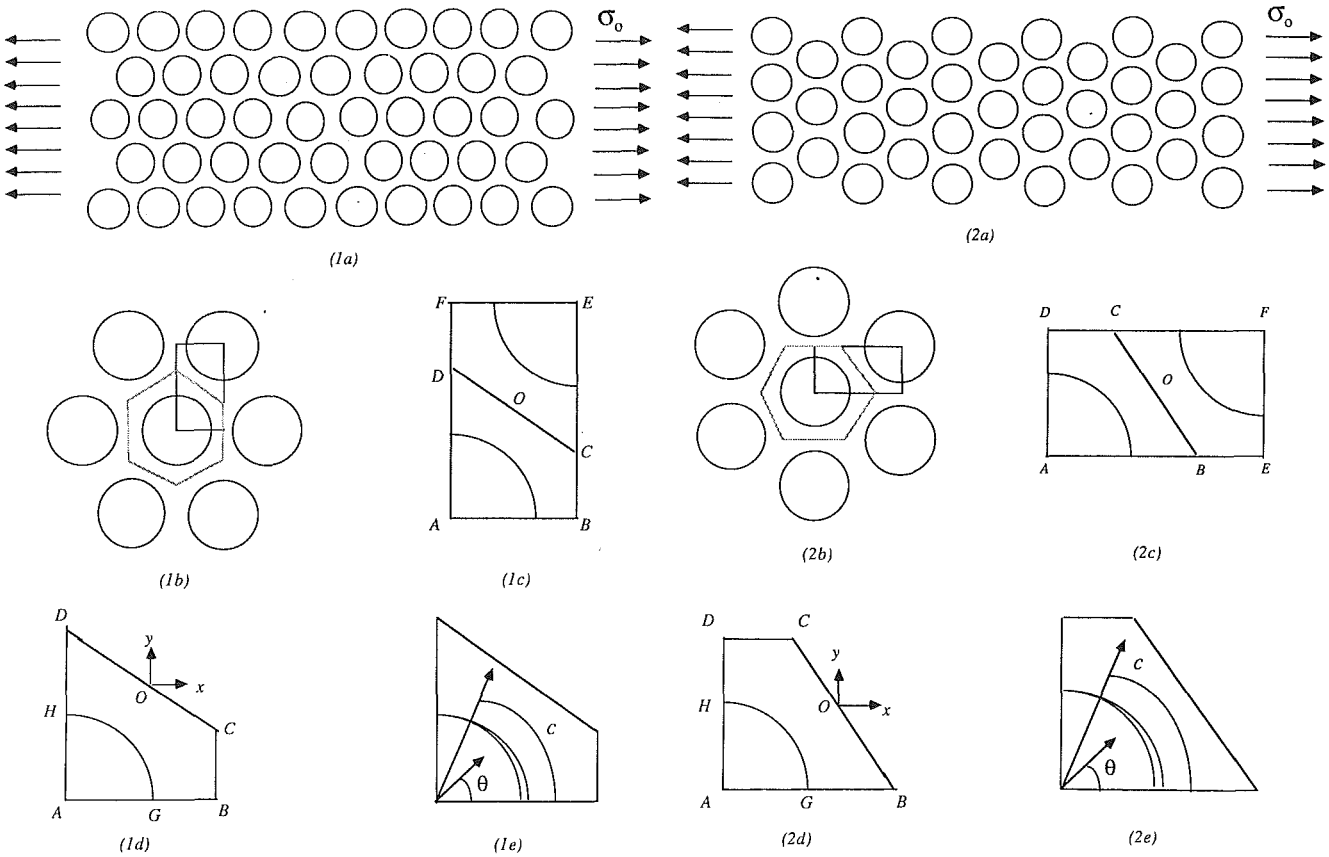


Fig. 1(*a*) Hexagonal array subjected to far-field uniform tensile stress in the closest packing direction (CPD), (*b*) basic cell, (*c*) quarter region of basic cell, (*d*) trapezoidal domain for numerical calculations, (*e*) interphase crack

Fig. 2(*a*) Hexagonal array subject to far-field uniform tensile stress in the mid-closest packing direction (Mid-CPD), (*b*) basic cell, (*c*) quarter region of basic cell, (*d*) trapezoidal domain for numerical calculations, and (*e*) interphase crack

fibers, the matrix, and the interphase. Achenbach and Zhu (1989) also analyzed the propagation and arrest of interphase cracks based on a criterion of critical strain energy density in the interphase.

In the present paper the spring-layer interphase model has been employed in conjunction with transverse loading of an hexagonal-array fiber composite. By the use of the boundary element method a numerical analysis for a basic cell of trapezoidal shape provides results for the micromechanical fields of stress and deformation, with and without partial interphase failure. It is shown that the maximum value of the circumferential stress, σ_θ, along the matrix side of the interphase, which may be assumed to control the development of radial matrix cracks, strongly depends in magnitude and position on the interphase stiffness and the fiber volume ratio.

The micromechanical results of this paper have also been employed to determine the effect of the interphase stiffness parameters on the overall elastic moduli prior, as well as subsequent to, the development of interphase failure. Finally, the numerical results for the effective elastic constants in the presence of interphases have been compared with analytical results. For perfect bond this can be done directly by using results obtained by Hashin (1979) and Christensen and Lo (1979). For the case of interphase stiffness, a slight adjustment of these results is required by the use of "effective" moduli for the fibers, which take into account the interphase effect. Details have been worked out for a transverse elastic constant, and it is shown that the numerically calculated values, as a function of fiber volume ratio, agree very well with the adjusted analytical results.

Formulation

Figures 1(*a*) and 2(*a*) show cross-sectional views of a fiber-reinforced composite. The fibers, which are all of equal radius, a, are periodically spaced in a hexagonal array. It is assumed that at some large distance, the composite is subjected to uniform stresses, σ_o, applied in the x-direction. The loading direction in Fig. 1(*a*) is called a closest packing direction (CPD), and the one in Fig. 2(*a*), which is along the bisectrix of the CPD directions, is called the mid-closest packing direction (mid-CPD). The spacing of the fiber centers in the mid-CPD direction is $3b$. The basic cell of the composite is a hexagonal with sides b, as shown in Figs. 1(*b*) and 2(*b*) (the regions enclosed by dashed lines). The periodicity of the composite then implies that the state of stress and deformation in the composite will be completely defined by the stresses and strains in a quarter region of a basic cell. This quarter region is shown in Fig. 1(*d*) for the CPD case and Fig. 2(*d*) for the mid-CPD case.

To give the boundary conditions on the external surfaces of the trapezoid in Fig. 1(*d*) for the CPD case, let us consider Fig. 1(*c*). The lines AF, FE, EB, and BA are lines of symmetry for the composite configuration shown in Figs. 1(*a*) and 1(*b*). This means that the shear stresses vanish on the lines AB, BE, EF, and FA, and the rectangle ABEF remains a rectangle after deformation. If this rectangle is being considered separately as being loaded by its surface tractions, then the displacement of the center point, O, of the rectangle may be taken as zero. A rigid body motion of the rectangle is being ignored in this manner, since the actual displacement of point O will not vanish when the rectangle is part of the composite. The point O is located on a side of the hexagon shown in Fig. 1(*b*), and this side, CD, which is of length b, is also indicated in the rectangle shown in Fig. 1(*c*).

Relative to a Cartesian coordinate system centered at O, the boundary conditions on sides AB, BC, and DA of the domain

Downloaded 03 May 2010 to 171.66.16.244. Redistribution subject to ASME license or copyright; see http://www.asme.org/terms/Terms_Use.cfm

ABCD may be expressed in terms of unknown but constant displacements C_1 and C_2 as:

$$-\frac{\sqrt{3}}{4}b \le x \le \frac{\sqrt{3}}{4}b,\ y=-\frac{3}{4}b: \quad \sigma_{yx}=0,\ v=C_2 \tag{1a,b}$$

$$x=\frac{\sqrt{3}}{4}b,\ -\frac{3}{4}b \le y \le -\frac{1}{4}b: \quad \sigma_{xy}=0,\ u=\frac{C_1}{2} \tag{2a,b}$$

$$x=-\frac{\sqrt{3}}{4}b,\ -\frac{3}{4}b \le y \le \frac{1}{4}b: \quad \sigma_{xy}=0,\ u=-\frac{C_1}{2}. \tag{3a,b}$$

The displacement components (u, v) and traction components (t_x, t_y) on line DC obey the following relations:

$$u(-x,-y)=-u(x,y),\ v(-x,-y)=-v(x,y) \tag{4a,b}$$

$$t_x(-x,-y)=t_x(x,y),\ t_y(-x,-y)=t_y(x,y). \tag{5a,b}$$

These relations can be verified by rotating the trapezoid ABCD in Fig. 1(*c*) 180 deg around the point O, so that it will coincide with the trapezoid CEFD. The displacement at a point on line OC will then have the same magnitude, but opposite sign than the one at the corresponding symmetric point on line OD, while the tractions at these two symmetric points will have both the same magnitude and sign, because the unit normal to DC in trapezoid ABCD is opposite to the normal on trapezoid CEFD.

By similar arguments the following boundary conditions for the Mid-CPD case shown in Fig. 2(*d*) can be derived

$$-\frac{3}{4}b \le x \le \frac{1}{4}b,\ y=-\frac{\sqrt{3}}{4}b:\ \sigma_{yx}=0,\ v=-\frac{C_2}{2} \tag{6a, b}$$

$$\mathbf{x} \in \text{CB}:\ u(-x,\ -y)=-u(x,y),\ v(-x,\ -y)=-v(x,y) \tag{7a,b}$$

$$\mathbf{x} \in \text{CB}:\ t_x(-x,-y)=t_x(x,\ y),\ t_y(-x,-y)=t_y(x,y) \tag{8a,b}$$

$$-\frac{3}{4}b \le x \le -\frac{1}{4}b,\ y=\frac{\sqrt{3}}{4}b:\ \sigma_{yx}=0,\ v=\frac{C_2}{2} \tag{9a,b}$$

$$x=-\frac{3}{4}b,\ -\frac{3}{4}b \le y \le \frac{\sqrt{3}}{4}b:\ \sigma_{yx}=0,\ u=C_1. \tag{10a,b}$$

From equilibrium in the x-direction, the following additional conditions on t_x and t_y follow for the CPD case shown in Figs. 1(*a*)–(*d*)

$$\int_{\text{AD}}+\int_{\text{DF}} t_x(s)\,ds=-\frac{3}{2}b\sigma_o \tag{11}$$

$$\int_{\text{AD}}+\int_{\text{CD}}+\int_{\text{BC}} t_x(s)\,ds=0. \tag{12}$$

Also,

$$\int_{\text{DF}} t_x(s)\,ds=-\int_{\text{BC}} t_x(s)\,ds \tag{13}$$

$$\int_{\text{CO}} t_x(s)\,ds=\int_{\text{OD}} t_x(s)\,ds. \tag{14}$$

By combining equations (11)–(14), we then obtain

$$\int_{\text{BC}}+\int_{\text{OC}} t_x(s)=\frac{3}{4}b\sigma_o. \tag{15}$$

Since there is no far-field stress, in the y-direction

$$\int_{\text{CD}} t_y(s)\,ds=0. \tag{16}$$

In an analogous manner we obtain for the mid-CPD case:

$$\int_{\text{CB}} t_x(s)\,ds=\frac{\sqrt{3}}{2}b\sigma_o \tag{17}$$

$$\int_{\text{DC}}+\int_{\text{CO}} t_y(s)\,ds=0. \tag{18}$$

Following an earlier paper by Achenbach and Zhu (1989), the compliant interphase between fibers and matrix is modeled by a distribution of mechanical springs. With respect to local polar coordinates, the relations between the relevant stress and displacement components may then be expressed as

$$\sigma_r^m=\sigma_r^f=k_r(u_r^m-u_r^f),\ \text{if } u_r^m \ge u_r^f \tag{19}$$

$$\sigma_r^m=\sigma_r^f \text{ and } u_r^m=u_\theta^f,\ \text{if } u_r^m \text{ not } > u_r^f \tag{20}$$

$$\sigma_{r\theta}^m=\sigma_{r\theta}^f=k_\theta(u_\theta^m-u_\theta^f) \tag{21}$$

where σ_r is the interfacial radial stress and $\sigma_{r\theta}$ is the interfacial shear stress. Quantities with upper index 'm' and 'f' are defined in the matrix and the fiber regions, respectively. The constants k_r and k_θ are the coefficients of the springs. The addition of equation (20) insures that the model will not allow an unrealistic radial overlap of the two materials in the interfacial zone.

It will be difficult to measure the constants k_r and k_θ directly, even though certain techniques have recently been developed, as discussed by Narkis et al. (1988). In an alternative approach it may be possible to obtain k_r and k_θ by using the results of this paper in conjunction with measurements of two effective elastic constants governing deformation in the xy-plane. As shown later in this paper, it is possible to calculate such constants for specific choices of k_r and k_θ. Conversely, given the transverse elastic constants, it may be possible to solve the inverse problem for k_r and k_θ. The values for k_r and k_θ that have been used in the numerical calculations of the present paper have been selected over a broad range for illustrative purposes.

The interface conditions equations (19)–(21) apply when the interphase layer is intact all around the fiber. If on the other hand, due to interphase failure the surfaces of the fiber and the adjacent matrix material are not connected, say over a region $r = a,\ -\theta_c < \theta < \theta_c$ and $\pi - \theta_c < \theta < \pi + \theta_c$, then in the quarter region shown in Figs. 1(*e*) and 2(*e*), the conditions of equations (19)–(21) are valid for $r = a,\ \theta_c \le \theta < \pi/2$, while for $r = a,\ 0 \le \theta < \theta_c$ we would have

$$\sigma_r^f=\sigma_r^m=\sigma_{r\theta}^f=\sigma_{r\theta}^m=0. \tag{22}$$

It should be noted that the compliant conditions (19)–(21) include the case of perfect contact ($k_r = \infty,\ k_\theta = \infty$), when the stresses and displacements are continuous, and the case of no contact ($k_r = k_\theta \equiv 0$), when the stresses vanish. The conditions equation (22) define an interface crack. At the transition from the crack surface to the bonded area (the crack tip) the interface stresses for perfect contact are totally different from the ones for flexible contact. For the transition to perfect contact, the interface stresses show oscillatory singularities (see Williams (1959)). On the other hand, for the transition to compliant contact, the stresses remain bounded. This conclusion follows immediately from equations (19)–(21) and the boundedness of the displacements.

Boundary Integral Equations

It is well known that the displacement components in an elastic region can be expressed in terms of a representation integral over the boundary of that region. In a first application, this integral is applied to the domain of the matrix material enclosed by $\overline{\text{GBCDH}}$, shown in Fig. 1(*d*). In the limit as the point of observation approaches the boundary, the integral yields:

$$\frac{1}{2}u_i^m(\mathbf{x})=\int_{\Gamma_1+\Gamma_2} U_{ij}^m(\mathbf{x},\ \xi)t_j^m(\xi)\,d\Gamma(\xi) - \int_{\Gamma_1+\Gamma_2} T_{ij}^m(\mathbf{x},\xi)u_j^m(\xi)\,d\Gamma(\xi),\ \mathbf{x}\in\Gamma_1+\Gamma_2 \tag{23}$$

where

Downloaded 03 May 2010 to 171.66.16.244. Redistribution subject to ASME license or copyright; see http://www.asme.org/terms/Terms_Use.cfm

$$U_{ij}^m(\mathbf{x},\xi)=\frac{1}{8\pi\mu^m(1-\nu^m)}\left[(3-4\nu^m)\ln\left(\frac{1}{R}\right)\delta_{ij}+\frac{\partial R}{\partial x_i}\frac{\partial R}{\partial x_j}\right] \quad (24)$$

$$T_{ij}^m(\mathbf{x},\xi)=-\left[\lambda^m\frac{\partial}{\partial x_\ell}U_{il}^m\delta_{jk}+\mu^m\frac{\partial}{\partial x_k}U_{ij}^m+\mu^m\frac{\partial}{\partial x_j}U_{ik}^m\right]n_k(\xi) \quad (25)$$

and

$$\Gamma_1\equiv\overline{GB}+\overline{BC}+\overline{CD}+\overline{DH} \quad (26)$$

$$\Gamma_2=\overline{HG}. \quad (27)$$

Here, $R=|\mathbf{x}-\xi|$, $t_j^m(\xi)$ is the traction, and $n(\xi)$ is the outward normal on the contour of interest. The Lamé constant, λ^m, may be expressed in terms of the shear modulus, μ^m, and Poisson's ratio, ν^m, as

$$\lambda^m=2\nu^m\mu^m/(1-2\nu^m). \quad (28)$$

The coefficient of $u_j^m(\mathbf{x})$ in the left-hand side of equation (23) is $\frac{1}{2}$ because the material is isotropic and $\Gamma_1+\Gamma_2$ is a smooth curve.

The corresponding integral representation for the displacement components in the fiber may be written as:

$$\frac{1}{2}u_i^f(\mathbf{x})=\int_{\Gamma_2+\Gamma_3}U_{ij}^f(\mathbf{x},\xi)t_j^f(\xi)d\Gamma(\xi)$$

$$-\int_{\Gamma_2+\Gamma_3}T_{ij}^f(\mathbf{x},\xi)u_j^f(\xi)d\Gamma(\xi),\quad \mathbf{x}\in\Gamma_2+\Gamma_3 \quad (29)$$

where

$$\Gamma_3=\overline{HA}+\overline{AG}. \quad (30)$$

Here, the fundamental solutions $U_{ij}^f(\mathbf{x},\xi)$ and $T_{ij}^f(\mathbf{x},\xi)$ are also defined by equations (24) and (25), but with elastic constants λ^f and μ^f of the fiber, and the unit normal is now pointing out from the fiber material. For convenience we employ indicial notation in this section; where $x_1=x$ and $x_2=y$, and the summation convention is implied for repeated indices.

The boundary integral equations (23) and (29) also apply to the mid-CPD case shown in Fig. 2(*d*).

Numerical Procedure

To solve the systems of integral equations, the contours are divided in elements, and the fields are assumed to be uniform over these elements. For the CPD case, let us suppose that $\Gamma_1-\overline{CD}$ is divided into N_1 elements, $\overline{CD}$ into N_2 elements, Γ_2 into N_3 elements, and Γ_3 into N_4 elements. From the integration over Γ_2 we then have $8N_3$ unknowns, since there are two unknown tractions and two unknown displacements on each side of Γ_2. It follows from equations (1)–(5) that the integrations over $\Gamma_1-\overline{DC}$ and Γ_3 involve $2(N_1+N_4)+2$ unknowns (normal tractions, tangential displacements, and C_1, C_2). The integration over $\overline{DC}$ involves $2N_2$ unknowns (normal and tangential tractions and displacements only on $\overline{OC}$ or $\overline{OD}$). Hence, the total number of unknowns is $2N_1+2N_2+8N_3+2N_4+2$. Now, equation (23) yields $2(N_1+N_2+N_3)$ equations, while equation (29) yields $2(N_3+N_4)$ equations. The conditions (19)–(21) will produce $4N_3$ equations. An additional two equations are provided by the equilibrium conditions equations (15) and (16). The total number of equations thus is $2N_1+2N_2+8N_3+2N_4+2$, which is the same as the number of unknowns. Therefore, the discretized system of equations can be solved numerically. Similar conclusions can be drawn for the mid-CPD case.

An additional complication in the calculation derives from the presence of the alternative interface conditions given by equations (19) and (20). In the initial phase of the calculations, the radial interface stress σ_r^m $(=\sigma_r^f)$ is computed under the assumption that equation (19) applies. A positive value for the computed stress component indicates that the initial assumption was correct. If a negative value is obtained over one or more interface elements, equations (19) is replaced by equation (20) for those elements, and the calculation is redone. The radial interfacial stress should still be obtained as negative in this adjusted calculation.

The numerical calculations have been carried out for solids with the following material properties:

$$\text{matrix:}\quad \mu^m=14.2\ \text{Msi},\ \nu^m=0.22$$

$$\text{fibers:}\quad \mu^f=30\ \text{Msi},\quad \nu^f=0.22.$$

The results will actually apply for any pair of solids, which have the stated Poisson's ratios, and whose ratio of the shear moduli is the same as for the above materials. The interphase constants k_r and k_θ were rendered dimensionless by division by μ^m/a, where a is the radius of the fibers. In the computations, the two interphase constants were taken equal in magnitude, and thus

$$k_r/(\mu^m/a)=k_\theta/(\mu^m/a)=k. \quad (31)$$

The following values were considered $k=1$, $k=10$, and $k=\infty$. These values represent an increasingly stiff interphase, with $k=\infty$ corresponding to a perfect bond.

The area of the trapezoid in either Fig. 1(*d*) or Fig. 2(*d*) is $3\sqrt{3}b^2/8$ and the fiber volume ratio, V_f, was chosen as 0.4; hence

$$\frac{\pi a^2}{4}\Big/\frac{3\sqrt{3}b^2}{8}=0.4, \quad (32)$$

and thus:

$$\frac{b}{a}=\left[\frac{5\pi}{3\sqrt{3}}\right]^{1/2}.$$

Calculations were carried out for both a completely intact interphase, and for an interphase containing a crack. The crack configuration is shown in Fig. 1(*e*) and Fig. 2(*e*), where

$$c=a\theta_c. \quad (34)$$

It should be noted that the cracked configuration applies to a composite for which all fibers contain the same symmetrically-oriented interphase cracks. The lengths of the boundary elements for all calculations were chosen as $0.04a$ or smaller.

Numerical Results

For an interphase without a crack and for three values of k, the radial interphase stresses, σ_r, and the interphase shear stresses, $\sigma_{r\theta}$, are shown in Figs. 3(*a*) and 3(*b*) for the CPD and the mid-CPD cases, respectively. These figures show that the largest radial stress is obtained at $\theta=0$ deg, while the magnitude of the shear stress shows minimum absolute values at both $\theta=0$ deg and $\theta=90$ deg. We can also see from these results that the maximum radial stress is smaller for the mid-CPD case than for the CPD case. The sharp drop in σ_r near $\theta=75$ deg for $k=1$ is caused by the transition of the interphase condition from equation (19) to equation (20).

The values of the circumferential stresses, σ_θ, along the matrix side of the interphase (which are of great interest because they may control the development of radial matrix cracks) are plotted in Figs. 4(*a*) and 4(*b*). By using Hooke's law for ϵ_θ^m in terms of σ_r^m, σ_θ^m and σ_z^m, where $\sigma_z^m=\nu^m(\sigma_r^m+\sigma_\theta^m)$ from the plane-strain condition, and by subsequently replacing ϵ^m by its relation in terms of u_θ^m and u_r^m, we can write

$$\sigma_\theta^m=\frac{\nu^m}{1-\nu^m}\sigma_r^m+\frac{2\mu^m}{a(1-\nu^m)}\left(u_r^m+\frac{\partial u_\theta^m}{\partial\theta}\right) \quad (35)$$

and $\partial u_\theta^m/\partial\theta$ can be obtained by a numerical differentiation method. The maximum value of σ_θ is at $\theta=90$ deg for large values of k. For the CPD case, σ_θ reaches a maximum at $\theta\simeq$

Downloaded 03 May 2010 to 171.66.16.244. Redistribution subject to ASME license or copyright; see http://www.asme.org/terms/Terms_Use.cfm

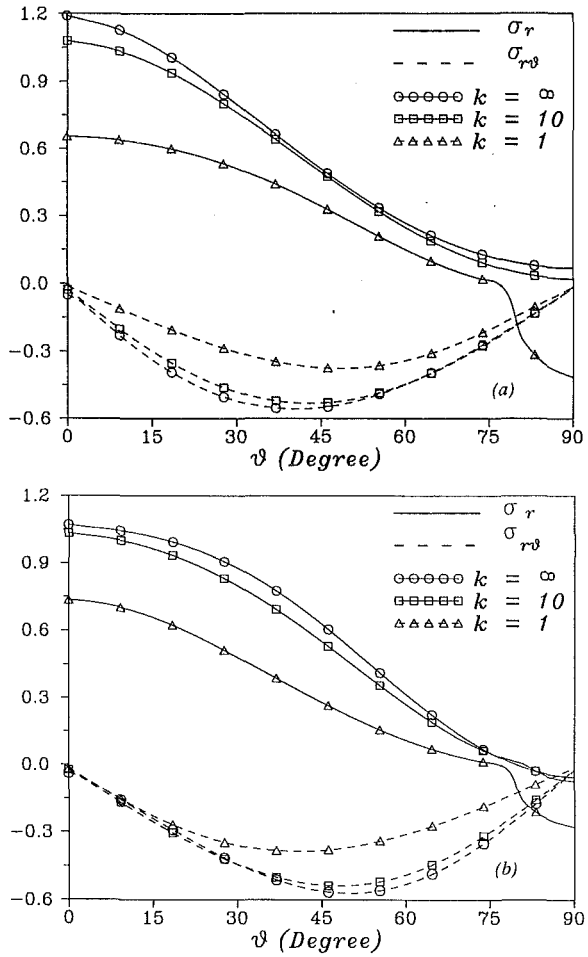


Fig. 3 Radial stress, σ_r, and circumferential shear stress, $\sigma_{r\theta}$, in the interphase; (*a*) CPD case and (*b*) mid-CPD case

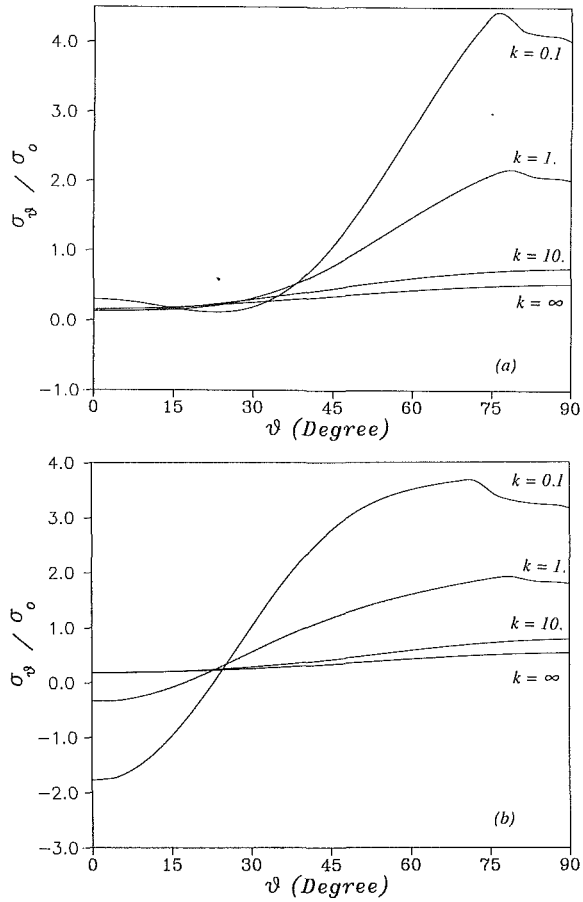


Fig. 4 Circumferential stress, σ_θ, at the matrix side of the interphase; (*a*) CPD case and (*b*) mid-CPD case

77 deg for smaller values of k, but for the mid-CPD case, the point at which σ_θ is a maximum moves to about $\theta = 72.5$ deg for $k = 0.1$. In order to study this shift in more detail, Figs. 5(*a*) and 5(*b*) show σ_θ versus the fiber volume ratio, V_f, for $k = 0.1$. For the CPD case the maximum remains at $\theta \simeq 77$ deg for the three values of V_f. For the mid-CPD case, it can be seen that when $V_f = 0.5$, there is a peak at about $\theta = 57$ deg, and for $V_f = 0.6$ the maximum is at $\theta = 50$ deg. Figure 5 reveals that the maximum value of σ_θ is very sensitive to an increase of V_f if the interphase stiffness is small. The results of Fig. 5(*b*) suggests that for small interphase stiffness and higher fiber volume ratio, radial matrix cracks may be expected at angles much smaller than $\theta = 90$ deg, in accordance with the experimental observations of Daniel et al. (1989).

The results of Figs. 3(*a*) and 3(*b*) suggest that interphase cracks, if they do develop, will be located near $\theta = 0$ deg because σ_r has its largest value at that location. The investigations of interphase cracks, specifically of their initiation, propagation and arrest, requires the adoption of an appropriate criterion. In the present paper, an energy density criterion is employed. For the simple interphase model considered here, an energy criterion is particularly appropriate since it includes the effects of both radial and shear tractions across the interphase. The energy per unit interphase, U, is defined as:

$$U = \frac{\sigma_r^2}{2k_r} + \frac{\sigma_{r\theta}^2}{2k_\theta}. \tag{36}$$

By introducing $\bar{\sigma}_r = \sigma_r/\sigma_o$ and $\bar{\sigma}_{r\theta} = \sigma_{r\theta}/\sigma_o$, we find in dimensionless form:

$$\bar{U} = \frac{\mu^m}{\sigma_o^2 a} U = \frac{\bar{\sigma}_r^2 + \bar{\sigma}_{r\theta}^2}{2k} \tag{37}$$

where k is the dimensionless number defined by equation (31).

It is now reasonable to assume that the interface will break when U reaches a critical value, U_{cr}, in the region where σ_r is positive, or σ_o reaches a critical positive value, σ_o^{cr}, defined by,

$$\sigma_o^{cr} = \left[\frac{\mu^m}{a}\frac{U_{cr}}{\bar{U}}\right]^{1/2}. \tag{38}$$

It is of interest to display the radial stress across the interphase for the case that the interphase contains a crack. For various crack lengths, the results are shown in Fig. 6. The radial stress vanishes across the interphase crack, but shows a tensile peak at the crack tip, and becomes compressive as θ increases further. As the crack becomes larger, the tensile peak first increases in magnitude but then becomes smaller, while the zone of compressive stresses becomes larger.

Figures 7(*a*) and 7(*b*) show the values of $\bar{U}$ at the crack tips versus the interphase crack length, for two values of the interphase stiffness parameter k. The presence of a crack gives rise to larger near-tip values of $\bar{U}$ than would exist in an intact interphase. Hence, if the critical value of $\bar{U}$ is reached for the uncracked interphase, and if a crack will develop, then the cracked interphase will be unstable, since it gives rise to an increased value of $\bar{U}$ at the crack tip. The near-tip energy does, however, first increase and then decrease with crack length, in consort with the change of the tensile stresses shown in Fig. 6. This implies that the crack can arrest once the crack length reaches the value denoted by $a\theta_a$, at which $\bar{U}$ again equals the

Downloaded 03 May 2010 to 171.66.16.244. Redistribution subject to ASME license or copyright; see http://www.asme.org/terms/Terms_Use.cfm

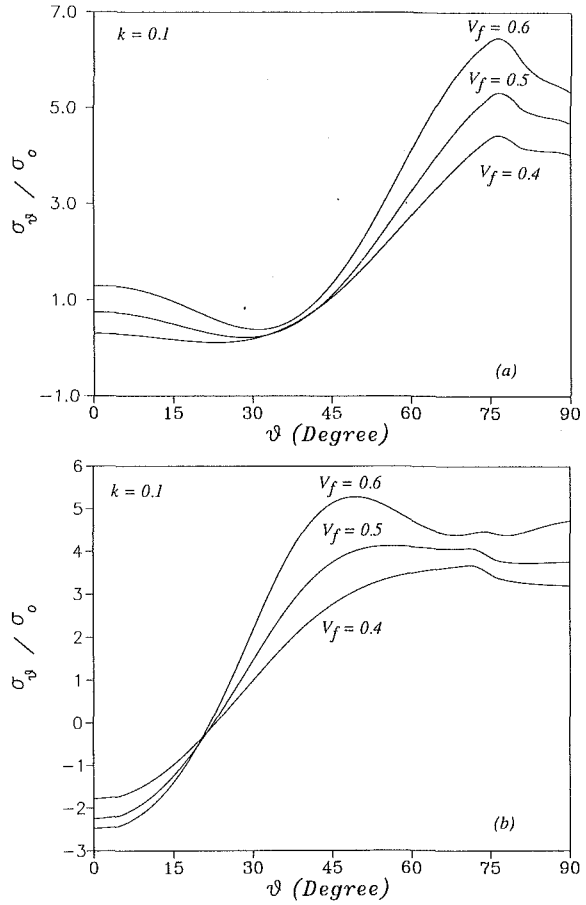


Fig. 5 Circumferential tensile stress, σ_θ, at the matrix side of the interphase; (*a*) CPD case and (*b*) mid-CPD case

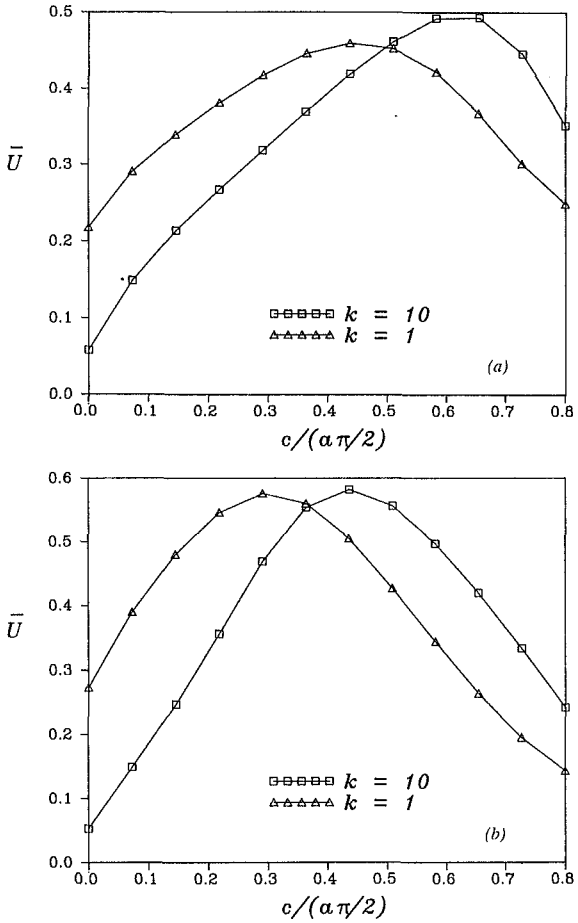


Fig. 7 Near-tip strain energy density in the interphase versus crack length; (*a*) CPD case and (*b*) mid-CPD case

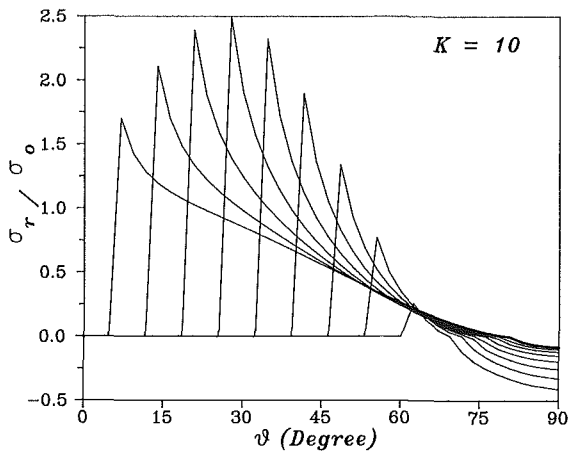


Fig. 6 Radial stress, σ_r, in an interphase containing a crack, for nine crack lengths corresponding to θ = 6.75 deg, 13.5 deg, etc. The stress vanishes on the crack and shows a tensile peak at the crack tip; mid-CPD case.

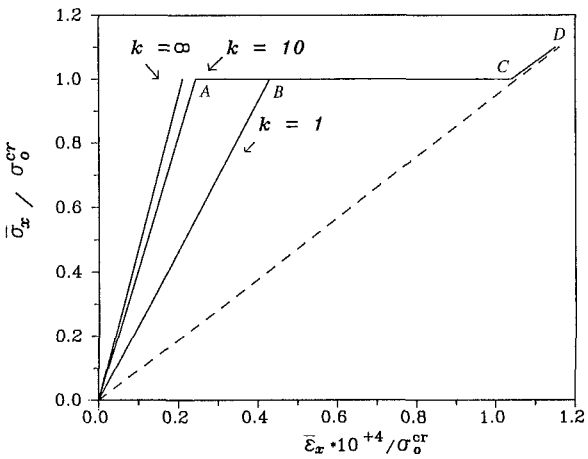


Fig. 8 Effective stress-strain relations for various values of *k* for an uncracked (solid line) and a cracked (dashed line) interphase

critical value. In fact, due to the development of negative radial stresses, the interphase crack generally will not span the full circumference of the fiber, even as σ_o is increased well beyond σ_o^{cr}.

The results of this paper also provide information for the formulation of effective stress-strain curves for the composite, with and without cracks in the interphase. For the CPD case, the average strain for uniform tensile stress, σ_o, applied in the x-direction, may be expressed as:

$$(\bar{\epsilon}_x)_o = C_1/\frac{\sqrt{3}}{2}\, b,\ (\bar{\epsilon}_y)_o = -C_2/\frac{3}{4}\, b \qquad (39a,b)$$

while for the mid-CPD cases, we have

$$(\bar{\epsilon}_x)_o = -C_1/\frac{3}{4}\, b,\ (\bar{\epsilon}_y)_o = C_2/\frac{\sqrt{3}}{2}\, b \qquad (40a,b)$$

where C_1 is defined by equations (2.3*a*, *b*) and (10*b*) for the CPD and the mid-CPD cases, respectively, and C_2 is defined by equations (1*a*, *b*) and (6.9*a*, *b*).

Downloaded 03 May 2010 to 171.66.16.244. Redistribution subject to ASME license or copyright; see http://www.asme.org/terms/Terms_Use.cfm

For a specified value of σ_o, the value of C_1 is calculated as part of the numerical work described in this paper. For $\sigma_o < \sigma_o^{cr}$, where σ_o^{cr} is defined by equation (38), the value of C_1 is proportional to σ_o, and hence by the use of equation (39*a*) a linear stress-strain follows as

$$\bar{\sigma}_x = \frac{b\sqrt{3}}{2C_1}\,\sigma_o\,\bar{\epsilon}_x \tag{41}$$

where $\bar{\sigma}_x$ is the average stress. Figure 8 includes the linear parts of the relations between $\bar{\sigma}_x$ and $\bar{\epsilon}_x$ for three values of k: $k = 1$, $k = 10$, and $k = \infty$. As expected, the slope is steeper, i.e., the composite is stiffer for larger k. The calculations of the linear relations showed no significant differences between the CPD and mid-CPD cases, and hence Fig. 8 is valid for both cases. When $\bar{\sigma}_x$ is increased beyond σ_o^{cr}, the interphase instantaneously develops an unstable crack, and C_1 suddenly increases (see Figs. 7(*a*) and 7(*b*)). Consequently, the strain $\bar{\epsilon}_x$ jumps. As noted before, an interphase crack will generally not cover the complete circumference of a fiber due to the development of compressive radial stresses. The dashed line in Fig. 8 shows the effective stress-strain relation for maximum crack length. Now, if the stress is increased beyond σ_{cr} the crack length will increase, and the stress-strain curve will follow BC and approach the linear relation for maximum crack length indicated by the dashed line.

As previously noted, the linear relations between $\bar{\sigma}_x$ and $\bar{\epsilon}_x$ displayed in Fig. 8 show no significant differences between the CPD and mid-CPD cases. This result confirms the validity of the assumption of macro-isotropic behavior in the *xy*-plane, which is employed in the formulation of an effective modulus theory for an unidirectional fiber-reinforced composite. From the point of view of macroelastic behavior, a unidirectional fiber-reinforced composite may be considered as transversely isotropic, with the axis of symmetry in the fiber direction. The state of stress and deformation that has been considered in this paper then corresponds to

$$\bar{\sigma}_x = \sigma_o,\ \bar{\sigma}_y \equiv 0,\ \bar{\epsilon}_z \equiv 0,\ \bar{\sigma}_{xy} \equiv 0,\ \bar{\sigma}_{xz} \equiv 0,\ \bar{\sigma}_{yz} \equiv 0 \tag{42}$$

where the bars indicate the averaged field quantities that appear in effective stress-strain relations. The relevant relations have been stated by Hashin (1983, equations (3.2.1)-(3.2.2)). For the case defined by equation (42), these equations reduce to

$$\bar{\sigma}_x = (K + G_T)\bar{\epsilon}_x + (K - G_T)\bar{\epsilon}_y \tag{43}$$

$$0 = (K - G_T)\bar{\epsilon}_x + (K + G_T)\bar{\epsilon}_y. \tag{44}$$

In equations (43)–(44), K and G_T are the transverse bulk modulus and the transverse shear modulus, respectively.

The numerical results obtained in this paper can be interpreted in terms of the effective modulus theory. The slopes of the $\bar{\sigma}_x - \bar{\epsilon}_x$ curves in Fig. 8 (here defined by constants $\tilde{E}$) are numerically obtained as

$$\tilde{E} = \frac{b\sqrt{3}}{2C_1}, \tag{45}$$

see equation (41). This constant can be related to K and G_T by

$$\tilde{E} = 4(1/K + 1/G_T), \tag{46}$$

which is obtained by eliminating $\bar{\epsilon}_y$ from equation (43) by the use of equation (44).

It is now of interest to compare the values of $\tilde{E}$, numerically calculated in this paper, with theoretical predictions. By employing the so-called CCA model (Composite Cylinder Assemblage model), Hashin (1979) has derived explicit expressions for four of the five transverse elastic constants of a fiber-reinforced composite, in terms of the elastic constants of the two phases and the fiber volume fraction. These four elastic constants include the transverse bulk modulus K (Hashin 1979, equation (31)), but not the transverse shear modulus G_T. Chris-

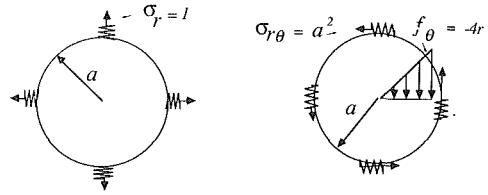


Fig. 9 Configurations for the calculations of "effective" fiber moduli (Note: springs are all around the circumference); (*a*) radial loading and (*b*) circumferential loading

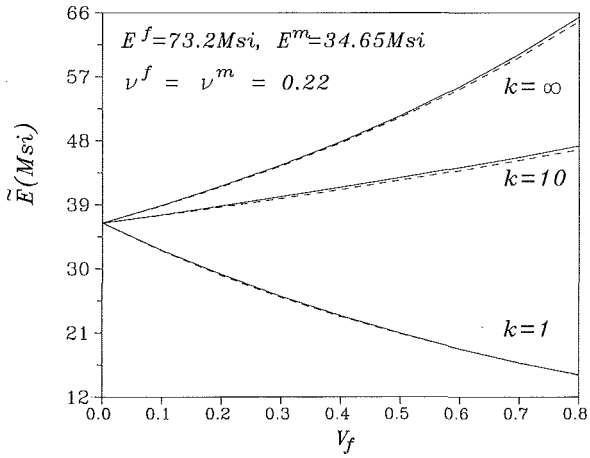


Fig. 10 Comparison of computed elastic constant $\tilde{E}$ (solid lines) with theoretical results that have been adjusted for the interphase stiffness (dashed line)

tensen and Lo (1979, equations (4.11)-(4.14)) have obtained G_T of a fiber-reinforced composite by employing the so-called Three-Phase model. These authors have derived a quadratic equation for G_T, with explicit expressions for the coefficients in terms of the elastic constants of the fibers and the matrix and the fiber volume fraction. The expression for K from Hashin (1979) and the transverse shear modulus G_T from Christensen and Lo (1979) can now be substituted in equation (46). For a perfect bond between the fibers and the matrix, the results can be compared directly with the numerical results of this paper. For the case of interphase stiffness, a slight adjustment is required. If the interphase does have its own stiffness, the constants E^f and ν^f which appear in the expression for K and in the coefficients of the equation for G_T should be replaced by an effective Young's modulus $\bar{E}^f$ and Poisson's ratio, $\bar{\nu}^f$, which take into account the spring constants in the interphase in an averaged manner, see Hashin (1990). To calculate $\bar{E}^f$ and $\bar{\nu}^f$ we consider the two model problems shown in Fig. 9(*a*) and 9(*b*). Figure 9(*a*) shows a two-dimensional configuration for a cylinder with a spring layer (constant k_r per unit length) subjected to radial stresses $\sigma_r = 1$. The radial displacement at $r = a$ is easily calculated as

$$u_r = \frac{1 - (\nu^f)^2}{E^f}\left(1 - \frac{\nu^f}{1 - \nu^f}\right)a + \frac{1}{k_r}. \tag{47}$$

For a cylinder without a spring layer, but of elastic constants $\bar{E}_f$ and $\bar{\nu}_f$, we would find $\bar{u}_r$ of the same form as equation (47) but without the last term. By imposing $u_r = \bar{u}_r$, we then obtain a first relation of the form

$$\frac{1 - (\bar{\nu}^f)^2}{\bar{E}^f}\left(1 - \frac{\bar{\nu}^f}{1 - \bar{\nu}^f}\right)a = \frac{1 - (\nu^f)^2}{E^f}\left(1 - \frac{\nu^f}{1 - \nu^f}\right)a + \frac{1}{k_r}. \tag{48}$$

To calculate the effective shear modulus $\bar{\mu}^f$, the slightly more complicated state of loading shown in Fig. 9(*b*) must be considered. Here, we have a linear distribution of circumferential

Downloaded 03 May 2010 to 171.66.16.244. Redistribution subject to ASME license or copyright; see http://www.asme.org/terms/Terms_Use.cfm

body forces, $f_\theta = -4r$, which are equilibrated by circumferential shear stresses at $r = a$, $\sigma_{r\theta} = a^2$, which are applied via a layer of circumferential springs of stiffness k_θ per unit length. Equating the circumferential displacements for the fiber + spring layer and the effective fiber yields the relation

$$\frac{a^3}{2\mu^f}+\frac{a^2}{k_\theta}=\frac{a^3}{2\bar{\mu}^f}. \tag{49}$$

Using, in addition the relation $\bar{E}^f = 2\bar{\mu}^f(1 + \bar{\nu}^f)$, the following expressions can be obtained from equations (48) and (49):

$$\bar{\nu}^f = 0.5 - \frac{ak_\theta\mu^f}{ak_\theta+2\mu^f}\left[\frac{1}{2\mu^f}(1-2\nu^f)+\frac{1}{ak_r}\right] \tag{50}$$

$$\bar{E}^f = \frac{2ak_\theta\mu^f(1+\bar{\nu}^f)}{ak_\theta+2\mu^f}. \tag{51}$$

These expressions for $\bar{E}^f$ and $\bar{\nu}^f$ can subsequently be substituted in the expressions for the K and the coefficients of the equation for G_T. For three values of k, where k is defined by equation (31), the results are plotted versus V_f in Fig. 10 as dashed lines. Also plotted in Fig. 10, as solid lines, are the values of $\tilde{E}$ according to equation (45) and the numerical values of C_1 calculated in this paper. It is noted that the calculated $\tilde{E}$ shows excellent agreement with the adjusted theoretical results.

Acknowledgment

This work was carried out in the course of research sponsored by the Air Force Office of Scientific Research under Grant AFOSR-88-0124. The authors would like to acknowledge helpful discussions with Michael Gosz and Professors Moran and Daniel. Helpful suggestions from Prof. Zvi Hashin are also gratefully acknowledged.

References

Aboudi, J., 1987, "Damage in Composites Modeling of Imperfect Bonding," *Composite Science and Technology*, Vol. 28, pp. 103–128.

Achenbach, J. D., and Zhu, H., 1989, "Effect of Interfacial Zone on Mechanical Behavior and Failure of Fiber-Reinforced Composites," *J. Mech. Phys. Solids*, Vol. 37, No. 3, pp. 381–393.

Adams, D. F., 1987, "A Micromechanics Analysis of the Influence of the Interface on the Performance of Polymer-Matrix Composites," *Journal of Reinforced Plastics and Composites*, Vol. 6, pp. 66–87.

Benveniste, Y., 1985, "The Effective Mechanical Behavior of Composite Materials with Imperfect Contact between the Constituents," *Mechanics of Material*, Vol. 4, pp. 197–208.

Broutman, L. J., and Agarwal, B. D., 1974, "A Theoretical Study of the Effect of an Interfacial Layer on the Properties of Composites," *Polymer Engineering Science*, Vol. 14, pp. 581–588.

Christensen, R. M., 1979, *Mechanics of Composite Materials*, John Wiley and Sons, New York.

Christensen, R. M., and Lo, K. H., 1979, "Solutions for Effective Shear Properties in Three Phase Sphere and Cylinder Models," *J. Mech. Phys. Solids*, Vol. 27, pp. 315–330.

Daniel, I. M., Anastassopoulos, G., and Lee, J. W., 1989, "Failure Mechanics in Ceramic Matrix Composites," *Proc. of 1989 SEM Spring Conference on Experimental Mechanics*, Cambridge, Mass., pp. 832–838.

Hashin, Z., 1979, "Analysis of Properties of Fiber Composites with Anisotropic Constituents," ASME JOURNAL OF APPLIED MECHANICS, Vol. 46, pp. 543–550.

Hashin, Z., 1983, "Analysis of Composites Materials—A Survey," ASME JOURNAL OF APPLIED MECHANICS, Vol. 50, pp. 481–505.

Hashin, Z., 1990, "Thermoelastic Properties of Fiber Composites with Imperfect Interface," *Mechanics of Materials*, Vol. 8, p. 333.

Jasiuk, I., and Tong, Y., 1989, "The Effect of Interface on the Elastic Stiffness of Composites," *Mechanics of Composite Materials and Structures*, J. N. Reddy et al. ed., ASME AMD-Vol. 100, pp. 49–54.

Lene, F., and Leguillon, D., 1982, "Homogenized Constitutive Law for a Partially Cohesive Composite Material," *Int. J. Solids and Structures*, Vol. 18, pp. 443–458.

Maurer, F. H. J., Simha, R., and Jain, R. K., 1986, "On the Elastic Moduli of Particulate Composites: Interlayer versus Molecular Model," *Composites Interfaces*, H. Ishida et al., ed., North-Holland, pp. 367–374.

Mikata, Y., and Taya, M., 1985a, "Stress Field in and Around a Coated Short Fiber in an Infinite Matrix Subjected to Uniaxial and Biaxial Loadings," ASME JOURNAL OF APPLIED MECHANICS, Vol. 52, pp. 19–26.

Mikata, Y., and Taya, M., 1985b, "Stress Field in a Coated Continuous Fiber Composite Subjected to Thermo-Mechanical Loadings," *Journal of Composite Materials*, Vol. 19, pp. 554–578.

Mori, T., and Tanaka, K., 1973, "Average Stress in Matrix and Average Elastics Energy of Materials with Misfitting Inclusions," *Acta Metallurgica*, Vol. 21, pp. 571–574.

Narkis, M., Chen, E. J. H., and Pipes, R. B., 1988, "Review of Methods for Characterization of Interfacial Fiber-Matrix Interactions," *Polymer Composites*, Vol. 9, pp. 245–251.

Ochiai, S., and Osamura, K., 1987, "A Computer Simulation of Strength of Metal Matrix Composites with a Reaction Layer at the Interface," *Metallurgical Transactions*, Vol. 18A, pp. 673–679.

Sideridis, E., 1988, "The In-Plane Shear Modulus of Fiber Reinforced Composites as Defined by the Concept of Interphase," *Composite Science and Technology*, Vol. 31, pp. 35–53.

Steif, P., and Hoysan, S. F., 1987, "An Energy Method for Calculating the Stiffness of Aligned Short-Fiber Composites," *Mechanics of Materials*, Vol. 6, pp. 197–210.

Theocaris, P. S., Sideridis, E. P., and Papanicolaou, G. C., 1985, "The Elastic Longitudinal Modulus and Poisson's Ratio of Fiber Composites," *Journal of Reinforced Plastics and Composites*, Vol. 4, pp. 396–418.

Walpole, L. J., 1978, "A Coated Inclusion in an Elastic Medium," *Math. Proc. Camb. Phil. Soc.*, Vol. 83, pp. 495–506.

Williams, M. L., 1959, "The Stresses Around a Fault or Crack in Dissimilar Media," *Bulletin of Seismological Society of America*, Vol. 49, pp. 199–204.

Zywicz, E., 1986, "Local Stress and Deformation Due to Fabrication and Transverse Loading in an Ideal Continuously Reinforced Graphite/Aluminum Metal Matrix Composite," M. Sc. Thesis, Department of Mechanical Engineering, MIT.

Downloaded 03 May 2010 to 171.66.16.244. Redistribution subject to ASME license or copyright; see http://www.asme.org/terms/Terms_Use.cfm

A New Method for Determination of Bending Rigidities of Thin Anisotropic Plates

M. Grédiac

A. Vautrin

Département Mécanique et Matériaux,
Ecole Nationale Supérieure des Mines,
42023 St. Etienne Cedex 2, France

The paper presents a new method to determine the six elastic bending rigidities of thin anisotropic plates. The experimental procedure only requires one plate specimen submitted to several bending tests performed on the same testing device. The data processing is based on the principle of virtual work and it is shown that simple linear relationships between the bending rigidities, applied loads, and plate curvature can be derived using particular virtual displacement fields. The unknown plate rigidities are the solution of a set of linear equations. The numerical simulations of various relevant bending configurations of anisotropic laminated plates point out the efficiency of this new approach.

Introduction

The measurement of the elastic properties of anisotropic plates is an important problem—but a difficult task—since the development of composite materials. When restricting the subject to symmetric plates, it is well known that the elastic behavior of such structures is characterized by a set of six in-plane rigidities and six flexural rigidities.

Much work has been done on the experimental characterization of the in-plane behavior; such a problem is now usually solved by performing different tensile off-axis tests. When redundant tests are carried out, optimum values can be derived from the minimization of a relevant error function (Vong and Verchery, 1980). On the contrary, just a few papers concern the practical determination of the bending rigidities of anisotropic plates. This latter problem is more difficult than the previous one because flexural stiffnesses are generally completely anisotropic, even though the in-plane stiffnesses are orthotropic; for instance, the well-known stacking sequence $[0, 90, 45, -45]_s$ leads to a completely anisotropic flexural behavior although its in-plane one is quasi-isotropic. Unfortunately, most of the presented methods are limited to orthotropic plates whose orthotropic axis have been previously determined (Tsai, 1965; Lee and Biblis, 1977; Kernevez et al., 1978). Masuda (1982) presents a method which determines the orthotropic axis in flexure, nevertheless, it fails to evaluate the four unknown rigidities. These methods often require several specimens, so the accuracy of the results strongly depends on the scatter of the specimen characteristics. To our knowledge, only two methods can be used to characterize the complete anisotropy of the flexural behavior of anisotropic plates. Sol (1986) proposes a method based on the measurement of resonant frequencies of a rectangular test plate; however, the numerical data processing needs an iterative calculation which requires a set of initial values in the vicinity of the true ones. Foudjet (1981) uses static bending tests and a moiré method to measure the plate deflections but his results seem to be very sensitive to experimental errors.

This paper deals with the numerical optimization of the completely anisotropic flexural rigidities of thin symmetric plates. This method only requires one plate specimen tested in different static bending configurations on the same testing device. The experimental data are the fields of the two plate deflection slopes.

The paper has two parts:

- the application of the principle of virtual work to the determination of the flexural rigidities, and
- the numerical simulation of the determination of plate characteristics taking into account the effects of the anisotropy and experimental errors as well.

Theoretical Principle

We consider an anisotropic elastic thin plate of any shape simply supported at three points located along two mutually perpendicular x and y-axes (Fig. 1). Then, the constitutive relations reduce to:

$$\begin{pmatrix} M_{xx} \\ M_{yy} \\ M_{xy} \end{pmatrix} = - \begin{pmatrix} D_{11} & D_{12} & D_{16} \\ D_{12} & D_{22} & D_{26} \\ D_{16} & D_{26} & D_{66} \end{pmatrix} \begin{pmatrix} \dfrac{\partial^2 w}{\partial x^2} \\ \dfrac{\partial^2 w}{\partial y^2} \\ \dfrac{2\,\partial^2 w}{\partial x \partial y} \end{pmatrix} \quad (1)$$

Contributed by the Applied Mechanics Division of The American Society of Mechanical Engineers for presentation at the Winter Annual Meeting, Dallas, Texas, Nov. 25-30, 1990.

Discussion on this paper should be addressed to the Technical Editor, Leon M. Keer, The Technological Institute, Northwestern University, Evanston, IL 60208, and will be accepted until two months after final publication of the paper itself in the Journal of Applied Mechanics. Manuscript received by the ASME Applied Mechanics Division, July 26, 1988; final revision, Oct. 5, 1989.

Paper No. 90-WA/APM-27.

Copyright © 1990 by ASME

Downloaded 03 May 2010 to 171.66.16.244. Redistribution subject to ASME license or copyright; see http://www.asme.org/terms/Terms_Use.cfm

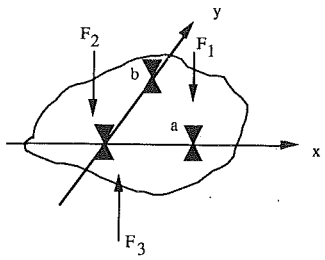


Fig. 1 Bending of a plate under normal load

where:
- M_{xx}, M_{yy}, and M_{xy} are the bending moments,
- the D_{ij} are the bending rigidities, and
- w is the deflection of the plate.

The principle of virtual work can be applied and leads to the following equation (Leknitskii, 1968; Dym and Shames, 1973):

$$\sum_{i=1}^{N} F_i w^*{}_i = \int\int_S \left(\frac{\partial^2 w^*}{\partial x^2}, \frac{\partial^2 w^*}{\partial y^2}, 2\frac{\partial^2 w^*}{\partial x \partial y}\right) \times \begin{pmatrix} D_{11} & D_{12} & D_{16} \\ D_{12} & D_{22} & D_{26} \\ D_{16} & D_{26} & D_{66} \end{pmatrix} \begin{pmatrix} \frac{\partial^2 w}{\partial x^2} \\ \frac{\partial^2 w}{\partial y^2} \\ 2\frac{\partial^2 w}{\partial x \partial y} \end{pmatrix} dxdy \quad (2)$$

where F_i, $i = 1..N$ are the applied loads.

This relationship is verified for any kinematically compatible deflection field w^* of the plate. The left side of this equation is the external virtual work and the right side is the internal virtual work.

A necessary and sufficient condition for equilibrium is that the external virtual work must equal the internal virtual work for any kinematically compatible field w^*. Such a relation is quite general and independent of any constitutive law. It usually introduces variational principles of elasticity and the finite element method. To our knowledge, no application based on any particular choice of the virtual displacement field has been made. This paragraph presents the use of virtual displacement fields which leads to simple linear relationships between the bending rigidities, applied loads, and plate curvatures.

We can choose the following three virtual displacements: $w^*{}_1 = k_1 x(x-a), w^*{}_2 = k_2 y(y-b)$, $w^*{}_3 = k_3 xy$, (k_1, k_2, k_3 are three real numbers) whose second derivatives are constant.

Then, expressing equation (2) for each field, we easily get:

$$\begin{pmatrix} D_{11} & D_{12} & D_{16} \\ D_{12} & D_{22} & D_{26} \\ D_{16} & D_{26} & D_{66} \end{pmatrix} \begin{pmatrix} 2\int\int_S \frac{\partial^2 w}{\partial x^2} dxdy \\ 2\int\int_S \frac{\partial^2 w}{\partial y^2} dxdy \\ 4\int\int_S \frac{\partial^2 w}{\partial x \partial y} dxdy \end{pmatrix} = \begin{pmatrix} \sum_{i=1}^{N} F_i x_i (x_i - a) \\ \sum_{i=1}^{N} F_i y_i (y_i - b) \\ \sum_{i=1}^{N} F_i x_i y_i \end{pmatrix}. \quad (3)$$

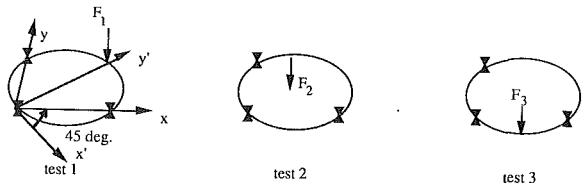


Fig. 2 Bending tests

Next, we make the following substitutions for the three integrals:

$$\overline{\epsilon_{xx}} = \frac{-h}{2S}\int\int_S \frac{\partial^2 w}{\partial x^2} dxdy \quad y\overline{\epsilon_{yy}} = \frac{-h}{2S}\int\int_S \frac{\partial^2 w}{\partial y^2} dxdy\ \overline{\epsilon_{xy}}$$

$$\overline{\epsilon_{xy}} = \frac{-h}{2S}\int\int_S \frac{\partial^2 w}{\partial x \partial y} dxdy \quad (4)$$

where h and S are the thickness and the surface of the plate, respectively, and $\overline{\epsilon_{xx}}$, $\overline{\epsilon_{yy}}$, and $\overline{\epsilon_{xy}}$ are the mean values of the strain of the upper surface of the plate.

Finally, we form the system as follows:

$$\begin{pmatrix} \overline{\epsilon_{xx}} & 0 & \overline{\epsilon_{yy}} & 0 & 2\overline{\epsilon_{xy}} & 0 \\ 0 & \overline{\epsilon_{yy}} & \overline{\epsilon_{xx}} & 0 & 0 & 2\overline{\epsilon_{xy}} \\ 0 & 0 & 0 & 2\overline{\epsilon_{xy}} & \overline{\epsilon_{xx}} & \overline{\epsilon_{yy}} \end{pmatrix} \begin{pmatrix} D_{11} \\ D_{22} \\ D_{12} \\ D_{66} \\ D_{16} \\ D_{26} \end{pmatrix} = \frac{-h}{4S} \begin{pmatrix} \sum_{i=1}^{N} F_i x_i (x_i - a) \\ \sum_{i=1}^{N} F_i y_i (y_i - b) \\ \sum_{i=1}^{N} F_i x_i y_i \end{pmatrix}. \quad (5)$$

The unknown plate rigidities are the solution of a set of three linear equations. Obviously, the identification of these rigidities requires more equations which can be obtained through two ways performing:
- one single bending test and developing equation (2) using additional admissible fields, or
- several bending tests, each test giving rise to a new set of three equations (5)

The next paragraph will now examine these two possibilities through two numerical simulations.

Numerical Simulations

Principle.

(*a*) *Choice of One or More Test Configurations.* Three basic tests have been selected (Fig. 2) and simulated with a finite element program developed in our laboratory (Ali, 1986).The plate is circular with a radius of 75 mm and is 2 mm thick. Such a shape has been chosen because a rotation of the specimen in the mechanical device will lead to different mechanical configurations when the plate is anisotropic. The first test is similar to the well-known anticlastic bending test of a square plate. It emphasizes the shear behavior of the plate and leads to estimates of the flexural compliance coefficients d_{66}, d_{16}, and d_{26} in the x and y-axes ($[d] = [D]^{-1}$). The second test refers to the three-point bending test usually performed on beams; it allows the determination of d'_{11}, d'_{12}, and d'_{16} along the x' and y'-axes. Finally, the third test does not look like any usual test; it has been selected because it can be easily performed on the same experimental device as the two pre-

Downloaded 03 May 2010 to 171.66.16.244. Redistribution subject to ASME license or copyright; see http://www.asme.org/terms/Terms_Use.cfm

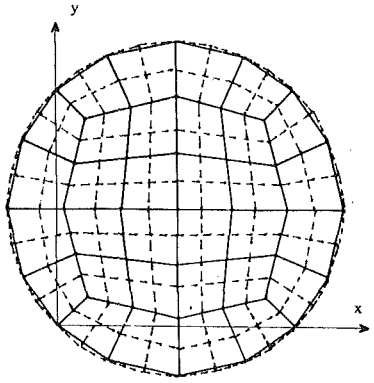


Fig. 3 Mesh of the plate with 32 (full line) and 128 (dashed line) quadrilateral elements

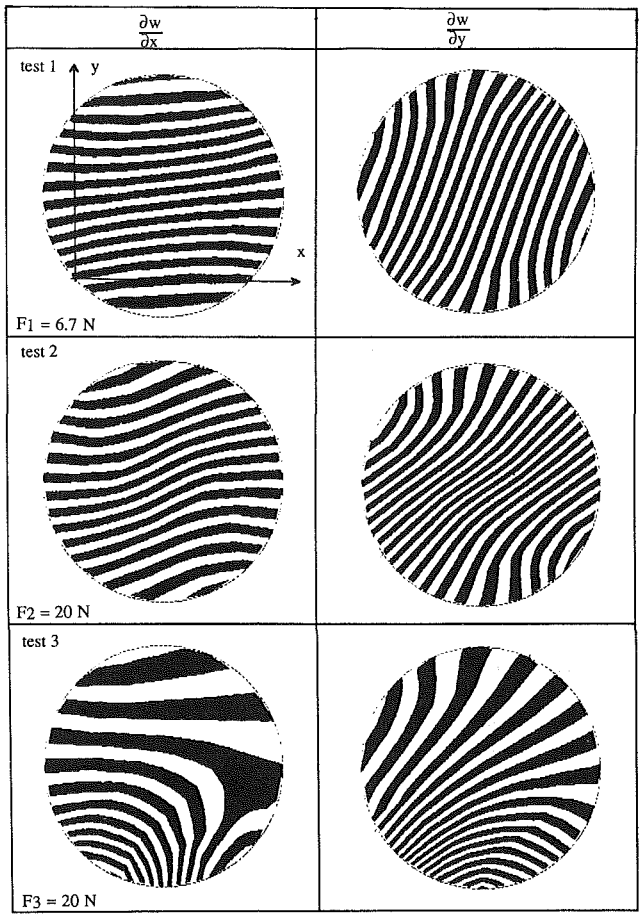


Fig. 4 Patterns of the slope contours for the plate 3

ceding tests. Considering a completely anisotropic plate, test 1 presents two planes of symmetry, test 2 only one plane of symmetry, and test 3 none. They can be used to get a large number of mechanical configurations associated with a rotation angle of less than 90 deg.

(*b*) *Choice of the Material.* A steel plate (plate 1), a $[0]_{8S}$ T300/5208 (plate 2) and a $[0, 45, 0, 90, 0, -45, 90, 0]_S$ T300/5208 (plate 3) stacking sequences are tested. They are isotropic, orthotropic and anisotropic in bending respectively. The stacking sequence of plate 3 is frequently used in aeronautical structures. The values of the D_{ij} are computed within the framework of the classical laminated plate theory (Tsai, 1987).

(*c*) *Finite Element Program.* The finite element program uses a mesh shown in Fig. 3 which has 145 nodes with 3 degrees-of-freedom by node and 32 quadrilateral lagrangian elements. This 9-noded plate bending element is described by Hinton and Bicanic (1979).

(*d*) *Reading of the Simulated Experimental Points.* The output file gives the deflection w and the two slopes $\frac{\partial w}{\partial x}$ and $\frac{\partial w}{\partial y}$ at each node and the simulated experimental points are chosen among the nodes of the mesh.

(*e*) *Determination Program.* Our identification program constructs the system with different admissible fields w^*_i. The different integrals (4) of the equation (2) are computed on the surface of the plate meshed with 128 quadrilateral elements with 4 nodes and 2 degrees-of-freedom by nodes (Fig. 3). This element is usually used for plane stress problems (Zienkiewicz, 1977). The two degrees-of-freedom are here the two slopes which can be measured in practice with a reflected image moiré method presented by Theocaris (1966). The choice of slopes instead of deflections as mechanical parameters is justified because deflections lead to results which are too much influenced by experimental errors (Foudjet et al., 1981). The main reason is that the curvatures in equation (1) have to be computed using interpolation functions deduced from experimental points; the slopes only require one differentiation while the deflections require two differentiations. Note that direct measurement of the curvatures is theoretically possible (Subramanian and Nair, 1985), but much more complicated than measuring slopes in practice.

Determination of Bending Rigidities From One Single Test. Figure 4 shows the two slope contours $\frac{\partial w}{\partial x}$ and $\frac{\partial w}{\partial y}$ of plate 3 submitted to the three selected tests. Note that equidistant fringe patterns for both $\frac{\partial w}{\partial x}$ and $\frac{\partial w}{\partial y}$ lead to a uniform state of strain which is incompatible with a determination from a single test. Indeed, assuming that the mechanical strain field is uniform, equation (2) reduces to:

$$\sum_{i=1}^{N} F_i w^*_i = (\alpha_1 D_{11} + \alpha_2 D_{12} + 2\alpha_3 D_{16}) \iint_S \frac{\partial^2 w^*}{\partial x^2}\, dxdy + (\alpha_1 D_{12} + \alpha_2 D_{22} + 2\alpha_3 D_{26}) \iint_S \frac{\partial^2 w^*}{\partial y^2}\, dxdy + 2(\alpha_1 D_{16} + \alpha_2 D_{26} + 2\alpha_3 D_{66}) \iint_S \frac{\partial^2 w^*}{\partial x \partial y}\, dxdy \qquad (6)$$

where $\alpha_1 = \frac{\partial^2 w}{\partial x^2}$, $\alpha_2 = \frac{\partial^2 w}{\partial y^2}$, $\alpha_3 = \frac{\partial^2 w}{\partial x \partial y}$

and only three groups of rigidities are determined whatever the virtual displacement fields. The effect of the anisotropy can be detected on Fig. 4: The rigidities D_{16} and D_{26} of plate 3 incline the fringes of test 1. The third test has been retained because it fundamentally leads to a nonuniform strain field whatever the material and ensures the independence of the linear equations.

The choice at best of the complementary virtual field is a very difficult task because it clearly depends on the material (Tables 1, 2, and 3). However, relevant fields well suited to some particular conditions can be pointed out as it will be shown next. In the present case, we suggest to base the computation on the ten following virtual fields:

$$w^*_1 = k_1 x(x-a)$$

$$w^*_2 = k_2 y(y-a)$$

Downloaded 03 May 2010 to 171.66.16.244. Redistribution subject to ASME license or copyright; see http://www.asme.org/terms/Terms_Use.cfm

Table 1 Bending rigidities of plate 1, in *mN*

	D11	D22	D12	D66	D16	D26
true value	155	155	48.0	53.4	0	0
one single test	178	179	73.2	56.3	-1.97	1.17
three tests, 25 pts	152	152	48.6	52.1	-0.14	0.19
three tests, 145 pts	154	153	48.3	52.3	0.01	-0.01

Table 2 Bending rigidities of plate 2, in *mN*

	D11	D22	D12	D66	D16	D26
true value	121	6.67	1.93	4.67	0	0
one single test	127	6.88	2.73	4.68	0.88	0.05
three tests, 25 pts	120	6.78	2.43	4.69	0.05	<0.01
three tests, 145 pts	120	6.79	2.07	4.70	<0.01	<0.01

Table 3 Bending rigidities of plate 3, in *mN*

	D11	D22	D12	D66	D16	D26
true value	82.0	30.9	9.40	12.3	6.03	6.03
one single test	89.0	32.6	12.2	13.1	6.50	7.20
three tests, 25 pts	79.3	30.4	9.55	12.0	5.92	6.00
three tests, 145 pts	81.2	30.5	9.57	12.1	5.99	5.94

$$w^*_3 = k_3 xy$$

$$w^*_4 = k_4 xy(x-a)(y-a)$$

$$w^*_5 = k_5 x(x-a)\exp\left(\frac{2x-a}{R}\right)$$

$$w^*_6 = k_6 w^{*2}_2$$

$$w^*_7 = k_7 w^{*3}_2$$

$$w^*_8 = k_8 w^{*4}_2$$

$$w^*_9 = k_9\left[\left(x-\frac{a}{2}\right)^2 + \left(y-\frac{a}{2}\right)^2 - R^2\right]^3$$

$$w^*_{10} = k_{10}\left[16\left(x-\frac{a}{2}\right)^4 - 16\,a\left|x-\frac{a}{2}\right|^3 + a^4\right]$$

where R is the radius of the tested plate and k_i, $i = 1..10$, is a real number.

Note that the virtual fields can be considered as filters which emphasize the contribution to the virtual works of some rigidities or regions of the plate. For instance, w^*_3 eliminates the contribution of D_{11}, D_{22}, D_{12} to the virtual work, w^*_1, w^*_6, w^*_7, and w^*_8 the one due to D_{22}, D_{26}, D_{66}, and w^*_2 the one due to D_{11}, D_{16}, and D_{66}. w^*_5 emphasizes the contribution of the strain field of the plate for $x > \frac{a}{2}$. Eventual perturbations due to edge effects are suppressed for particular plate shapes such as a circular disk using virtual fields whose second derivatives are zero at the edge. For example, the field w^*_9 satisfies these conditions. Notice that eventual perturbations due to local effect in the vicinity of the loaded points can be smoothed off using fields whose second derivatives are zero at these points. For instance, w^*_{10} satisfies this condition for a three-point bending test (Fig. 5).

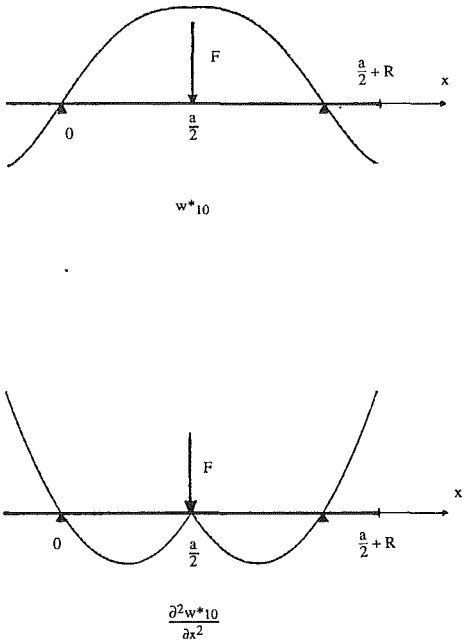


Fig. 5 w^*_{10} and $\frac{\partial^2 w^*_{10}}{\partial x^2}$ curves

These fields lead to an overdetermined set of ten linear equations whose interdependence is checked a posteriori. The solution is derived through the least squares method. Tables 1, 2, and 3 give the final bending rigidities obtained considering the whole set of 145 nodes of the mesh as simulated experimental points. The major observation is that the accuracy of the results depend on the plates and the rigidities, with a large error on D_{12}. One of the main reasons is probably the small contribution of D_{12} to the strain field.

As a matter of fact, the best choice of mechanical configuration and the set of virtual fields is a function of the anisotropy of the plate; in practice, it would need a lot of computations. However, we have computed the internal and external virtual works for the ten chosen fields and the true rigidity values and we have established that the three simplest fields w^*_1, w^*_2, and w^*_3 systematically lead to the lowest difference between these two works. This result means that these three fields can be considered as well suited to the present case. It is due to the uniform distribution of the simulated experimental points imposed by the regular mesh of the plate. With these fields, all the experimental points have the same weight, although the other fields tend to increase the contribution of some particular regions. For instance, Fig. 5 shows that w^*_{10} emphasizes the contribution in the vicinity of the points located at $x = \frac{a}{2} - R, x = \frac{a}{4}, x = \frac{3a}{4}, x = \frac{a}{2} + R$. Hence, in practice, we should have to increase the number of experimental points in these domains and the numerical simulation of such an experimental procedure would have to be based on irregular meshes.

All these comments lead us to select several tests associated with the three fields described previously.

Determination of Bending Rigidities From Three Tests. The three tests of Fig. 2 associated with the fields w^*_1, w^*_2, and w^*_3 give a set of nine linear equations. Two cases are considered to simulate each test:

- 25 regularly spaced nodal values from 145 are selected and
- the whole set of 145 nodal values is selected

in order to examine the effect of the number of experimental points.

From Tables 1, 2, and 3, it appears that the determination

Downloaded 03 May 2010 to 171.66.16.244. Redistribution subject to ASME license or copyright; see http://www.asme.org/terms/Terms_Use.cfm

Table 4 Influence of experimental errors, in percentages

	p11	p22	p12	p66	p16	p26
plate 1	0.96	1.05	2.24	0.50	–	–
plate 2	4.13	0.75	27.10	0.60	–	–
plate 3	1.43	1.38	6.31	0.94	4.41	3.67
plate 2, 45°	0.83	0.16	2.10	0.41	–	–

using only 25 selected nodal values could lead to reasonable accurate results for plate 1 and 3; as a matter of fact, in these two cases, the rigidities are obtained with an error less than 3,3 percent for 25 points and 2 percent for 145 points. However, for the most anisotropic plate, i.e., plate 2, the accuracy on D_{12} considerably decreases from 145 points (7,3 percent) to 25 points (25,9 percent): It is probably due to the quite small contribution of this rigidity to the strain field for the three tests.

In this particular case, the use of several mechanical tests and three very simple virtual fields obviously gives better results than one single test associated with a large number of fields, but the accuracy of the determination depends on the experimental errors as well.

Influence of Experimental Errors. It is necessary to estimate the effect of location errors of the n experimental points on the identified bending rigidities. We assume that the coordinates (x'_k, y'_k) of each experimental point k $(k = 1..N)$ have the form $x'_k = x_k + \mu_k$ and $y'_k = y_k + \beta_k$ where (x_k, y_k) is the true location of the point k.

The corresponding identified rigidities are: $D'_{ij} = D_{ij} + \Omega_{ij}$ where the D_{ij} are the values obtained at points (x_k, y_k). The relations between Ω_{ij} and (μ_k, β_k) are not simple and have to be considered from a statistical point of view. The errors μ_k and β_k are simulated through a Gaussian random number generator routine. The parameter considered here is the magnitude A of the distribution, whose average equals zero and whose standard deviation is approximately $0.3A$. We finally compute the mean value M_{ij} and the standard deviation Σ_{ij} of the errors Ω^l_{ij}, $1 = 1..n$ corresponding to n simulations.

For each plate, a set of four magnitudes A is successively tested: 1, 2, 3, 4 mm. At first, we have noted that M_{ij} can be considered as equal to zero. The best parameter to describe the sensitivity of the method to experimental errors is the standard deviation Σ_{ij}. The results obtained with the three plates are presented in Table 4, with $N = 145$, $n = 50$, and $p_{ij} = \dfrac{\Sigma_{ij}}{D_{ij}}$ in percent. The relationships between p_{ij} and A are linear to a first approximation. Only the result for $A = 4$ mm has been reported. We observe that the sensitivity to experimental errors depends on the rigidities. Generally, the value of p_{ij} is less than 6,5 percent for an error of 4 mm. D_{66} is the least sensitive rigidity. The reason is that D_{66} has the major contribution in test 1. On the other hand, D_{12} is the most sensitive rigidity, as discussed previously. In particular, we notice the high sensitivity of D_{12} for plate 2, where $p_{12} = 27.1$ percent with $A = 4$ mm. However, these results are very influenced by the position of the plate specimen in the mechanical device. For instance, let us rotate the plate through 45 deg about the z-axis. Table 4 gives the values of p_{ij} for this configuration (plate 2,45 deg). The contribution of each D_{ij} is different from the preceding case and it appears that the final results are far less sensitive to experimental errors. This point justifies the circular shape of the plate specimen, so that each rotation gives a new mechanical configuration. An optimization of all experimental results obtained for different values of θ can be performed by suppressing the data which are far from the final values if necessary (Babut and Brandt, 1977).

Conclusion

The main characteristics of a new determination method have been presented. The different numerical simulations have proved its reliability for materials with different degrees of anisotropy. The influence of experimental errors on the determined values has been estimated and we have established that the sensitivity to errors depends on the orientation of the plate specimen in the mechanical device.

Finally, it is worth pointing out the interest of numerical simulations in experimental mechanics, which lead to a better knowledge of the experimental procedures. In our case, we have both determined the rigidities which are identified with the best accuracy and obtained information on the sensitivity of our method to the number of experimental points or to experimental errors.

The implementation of the bending device and of the reflected image moiré method is actually developed.

References

Ali, M., 1986, "Calcul Statique et Dynamique Par Éléments Finis Sur Microordinateur de Structures Composites et Metalliques," Thèse de doctorat de l'université Paris 6.

Babut, R., and Brandt, M., 1977, "Measurements of Internal Strains by Nine-Gauge Devices," *Strain*, Vol. 1, pp. 18–21.

Dym, C. L., and Shames, I. H., 1973, *Solid Mechanics, A Variational Approach*, International Student ed., McGraw-Hill, Kogakusha, Tokyo.

Foudjet, A., Duhau, R., Surry, C., and Jullien, J. F., 1981, "Identification Methods of Elastic Constants of Wood," *Proceedings of the International Symposium on the Mechanical Behaviour of Structured Media*, Ottawa, pp. 463–477.

Hinton, E., and Bicanic, N., 1979, ,"A Comparison of Lagrangian and Serendipity Mindlin Plate Elements for Free Vibration Analysis," *Computer and Structures*, Vol. 100, pp. 483–493.

Kernevez, J. P., Knopf-Lenior, C., Touzot, G., and Verchery, G., 1978, "An Identification Method Applied to an Orthotropic Plate Bending Experiment," *Int. Jour. for Num. Meth.in Eng.*, Vol. 12, pp. 129–139.

Lee, W. C., and Biblis, E. J., 1977, "New Approach for Determination of Elastic Constants of Orthotropic Wood Base Plates by Strip Bending and Plate Twisting," *Wood Science*, Vol. 9, No. 4, pp. 160–166.

Lekhnistskii, S. G., 1968, *Anisotropic Plates*, Gordon and Breach, New York.

Masuda, Y., 1982, "A New Method to Determine the Bending Rigidities of Anisotropic Plates," *Proceedings of the I.C.C.M. 4*, Tokyo, pp. 1733–1740.

Sol, H., 1986, "Identification of Anisotropic Plate Rigidities Using Free Vibration Data," Doc. Thesis. Vrije Universiteit Brussel.

Subramanian, G., and Nair, S. M., 1985, "Direct Determination of Curvatures of Bent Plates Using a Double Glass Plate Shearing Interferometer," *Experimental Mechanics*, pp. 376–380.

Theocaris, P. S., 1966, *Proc. of the Second S.E.S.A. Int. Cong. Exp. Mech.*, B. E. Rossi ed., p. 56.

Tsai, S. W., 1965, "Experimental Determination of the Elastic Behaviour of Orthotropic Plates," ASME *Journal of Engineering for Industry*, pp. 315–318.

Tsai, S. W., 1987, *Composites Design*, 3rd ed., Think Composites, Dayton, Ohio.

Vong, T., and Verchery, G., 1980, "Optimal Use of Redundant Measurements of Constrained Quantities. Application to Elastic Module of Anisotropic Composite Materials," *Proceedings of the I.C.C.M. 3*, pp. 1783–1795.

Zienkiewicz, O. C., 1977, *The Finite Element Method*, 3rd ed., McGraw-Hill, Maidenhead.

Downloaded 03 May 2010 to 171.66.16.244. Redistribution subject to ASME license or copyright; see http://www.asme.org/terms/Terms_Use.cfm

Relationship Between the Elastic Buckling of Square Tubes and Rectangular Plates

S. Li[1]

S. R. Reid
Mem. ASME

Department of Mechanical Engineering,
UMIST,
Manchester M60 1QD, U.K.

The buckling behavior of axially compressed square tubes is investigated by introducing realistic edge conditions for the panels which correspond to symmetry or antisymmetry in the modes of deformation of the tube cross-section with regard to the diagonals of the section. The results show a number of differences between the buckling behavior of square tubes and of simply-supported plates. This vanishes only for very thin tubes and plates. The comparison between the buckling mode for thinner and thicker tubes suggests an explanation for the existence of compact and noncompact crushing modes in the subsequent crushing of tubes.

1 Introduction

The buckling problems of square tubes and simply-supported plates under axial compression have long been considered equivalent. In his classical work, Timoshenko (1961) suggested that simply-supported edge conditions for rectangular plates were realized by means of thin square tubes for buckling analysis. Indeed, experimental results for the buckling of simply-supported plates have been obtained by conducting experiments on square tubes (Gerard, 1957). Conversely, in seeking to understand the buckling behavior of square tubes under axial compression, several workers (for example, Meng et al., 1983; Reid et al., 1986; Hui, 1986) have studied the behavior of simply-supported plates. The equivalence of the buckling behaviors of square tubes and simply-supported plates under axial compression is always implied in the literature. However, it is shown in this paper that this is only the case for very thin tubes and plates.

In the past few years the axial crushing behavior of square tubes has been studied extensively in an attempt to understand the use of such components as impact energy absorbers, where large elastoplastic deformation is involved. As the first stage of the whole complicated deformation process, the buckling behavior should have a significant influence on the later crushing behavior. However, when the panels of square tubes are treated as simply-supported plates in the usual way, some important phenomena, which have remained unexplained hitherto, seem unrelated to the buckling behavior. For example, thick-walled tubes tend to crush in a compact mode while thin tubes deform in a noncompact mode (Reid et al., 1986; Mahmood et al., 1981) as show in Fig. 1(*a*, *b*), respectively. The present paper will describe certain features of the elastic buckling mode which could have an influence on the subsequent crushing behavior.

The essential feature of this analysis is the utilization of more realistic edge conditions for the panels of square tubes which differ from the commonly accepted simply-supported conditions.

2 Symmetric and Antisymmetric Edge Conditions for the Buckling of Square Tubes

In claiming the equivalence between the behavior of the panels of a square tube and simply-supported plates, one of the basic assumptions is that the four vertical edges of the tube remain straight when buckling. In this section this will be discarded. Instead, two sets of substitute and completely realistic edge conditions are proposed which correspond to symmetric and antisymmetric deformation with respect to the two diagonals in any cross-section. It is helpful to reexamine the

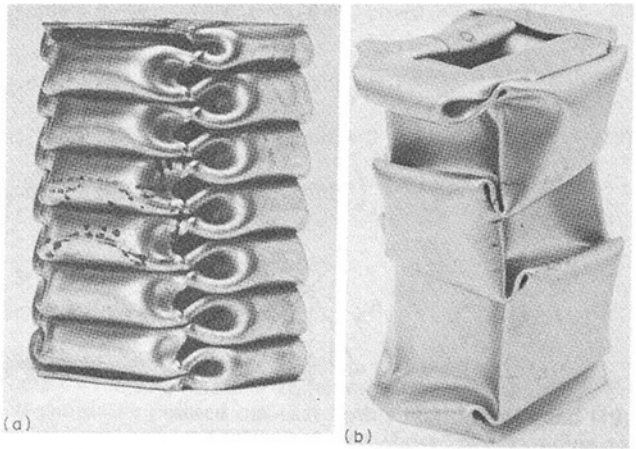


Fig. 1 Axially crushed square tubes; (*a*) compact mode ($b/t = 32.4$) and (*b*) noncompact mode ($b/t = 100$) (from Reid et al., 1986)

[1]Permanent address: Department of Aircraft Engineering, Nanjing Aeronautical Institute, Nanjing, People's Republic of China.

Contributed by the Applied Mechanics Division of THE AMERICAN SOCIETY OF MECHANICAL ENGINEERS for publication in the JOURNAL OF APPLIED MECHANICS.

Discussion on this paper should be addressed to the Technical Editor, Leon M. Keer, The Technological Institute, Northwestern University, Evanston, IL 60208, and will be accepted until two months after final publication of the paper itself in the JOURNAL OF APPLIED MECHANICS. Manuscript received by the ASME Applied Mechanics Division, Apr. 21, 1989; final revision, Oct. 20, 1989.

Copyright © 1990 by ASME
Downloaded 03 May 2010 to 171.66.16.244. Redistribution subject to ASME license or copyright; see http://www.asme.org/terms/Terms_Use.cfm

problem of the buckling of square tubes under axial compression afresh in order to establish these conditions.

Figure 2(*a*) shows a square tube and Fig. 2(*b*) shows an arbitrary cross-section of it. The axial compressive load is distributed uniformly over the top and bottom edges of the four panels. Obviously, the geometry of the tube is symmetric about its diagonal planes D_1 and D_2 as is the load. For any symmetric structure, the deformation is bound to be symmetric if the load applied over it is symmetric and the deformation will be antisymmetric if the load is antisymmetric. In buckling problems, buckling equations are set up in incremental form (e.g., incremental displacements) with respect to incremental loads. By definition (Timoshenko, 1961), buckling corresponds to zero load increment while there exist nonvanishing incremental displacements which give the buckling mode. The above symmetry and antisymmetry principle holds true also for incremental analysis. However, if as in buckling analysis the load increment is zero, we have a neutral situation in which the load increment can be considered either symmetric or antisymmetric. Consequently, the buckling mode could be symmetric or antisymmetric depending on which mode then minimizes the buckling load.

By introducing the above symmetric or antisymmetric conditions, a tube can be separated into four panels and each of them can be treated as a plate under some particular edge conditions. To assist with the formulation of these edge conditions, diagrams of two separated adjacent panels are shown in Fig. 3 in which all of the kinematic and generalized force variables along the edges are shown. The directions of those parameters displayed which relate to the y-z plane are chosen normal and tangential to the diagonal plane so that the continuity conditions are satisfied identically. By using conventional notation the unconventional parameters, which appear in Fig. 3, can be expressed as

$$\begin{aligned}
\sqrt{2}u_t &= \mp v - w \\
\sqrt{2}u_n &= v \mp w \\
\theta &= \mp w_{,y} \\
\sqrt{2}N_t &= \mp N_y - T_y \\
\sqrt{2}N_n &= N_y \mp T_y \\
M &= M_y
\end{aligned} \tag{1}$$

where $T_y = Q_y + M_{xy,x}$ is the equivalent lateral shear force (Timoshenko, 1961) of thin plate theory and a comma denotes partial differentiation. The two alternative signs in the above expressions correspond to $y = \pm b/2$, respectively. The edge conditions at $y = \pm b/2$ are as follows

Symmetric mode

$$\begin{aligned}
\sqrt{2}u_n &= v \mp w = 0 \\
\theta &= \mp w_{,y} = 0 \\
\sqrt{2}N_t &= \mp N_y - T_y = 0 \\
N_{xy} &= 0
\end{aligned} \tag{2}$$

Antisymmetric mode

$$\begin{aligned}
\sqrt{2}u_t &= \mp v - w = 0 \\
u &= 0 \\
M &= M_y = 0 \\
\sqrt{2}N_n &= N_y \mp T_y = 0
\end{aligned} \tag{3}$$

Along the loaded edges, simply-supported conditions are assumed as in the literature, i.e.,

$$w = 0 \quad \text{and} \quad M_x = 0 \qquad \text{at } x = 0, l. \tag{4}$$

Thus, in postulating an equivalent plate problem for buckling analysis, two sets of admissible edge conditions are obtained. Which of them corresponds to the actual buckling mode is yet to be determined.

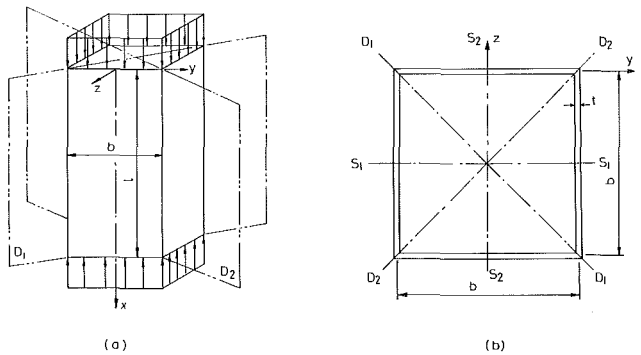


Fig. 2 Square tube under uniform axial load; (*a*) diagonal planes, D_1 and D_2, and (*b*) typical cross section

3 Buckling Equations and Their Solutions

In buckling problems of plates, the deflection w and the in-plane displacements u and v are uncoupled in the buckling equations. Therefore, for conventional plates, it is sufficient to solve the equation for w to obtain the corresponding buckling load and buckling mode. For tubes, however, since the edge conditions are coupled, all the equations have to be solved in order to impose the edge conditions.

The buckling equations for tubes can be obtained by combining the governing equations for plane stress analysis and the buckling equation for conventional plates, i.e.,

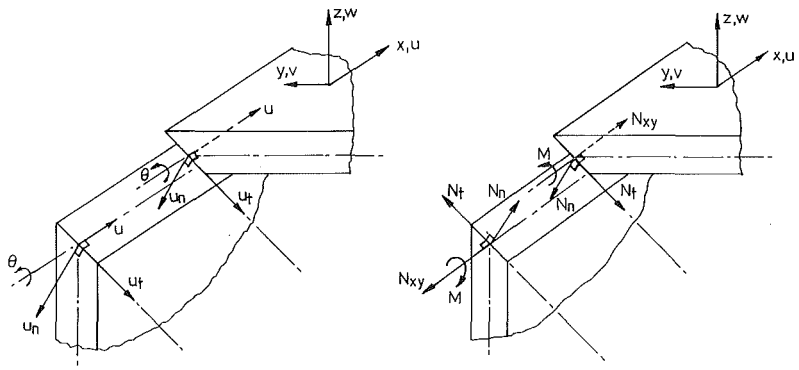


Fig. 3 Definitions of parameters describing conditions at the panel edges

Downloaded 03 May 2010 to 171.66.16.244. Redistribution subject to ASME license or copyright; see http://www.asme.org/terms/Terms_Use.cfm

$$u_{,xx}+\frac{1-\nu}{2}u_{,yy}+\frac{1+\nu}{2}v_{,xy}=0$$
$$v_{,yy}+\frac{1-\nu}{2}v_{,xx}+\frac{1+\nu}{2}u_{,xy}=0 \qquad (5)$$

$$w_{,xxxx}+2w_{,xxyy}+w_{,yyyy}-\frac{N_x}{D}w_{,xx}=0 \qquad (6)$$

where u, v, and w are all *incremental* displacements. N_x is the axial in-plane force per unit length, D is the flexural rigidity, and ν is Poisson's ratio.

The following forms for the solution satisfy the edge conditions (4) identically.

$$u=U(y)\cos\alpha x$$
$$v=V(y)\sin\alpha x \qquad (7)$$
$$w=W(y)\sin\alpha x \qquad (8)$$

where

$$\alpha=m\pi/l \qquad (9)$$

and m is an integer half-wave number. Equations (5) and (6) then reduce to the following ordinary differential equations.

$$\frac{1-\nu}{2}U''-\alpha^2U+\frac{1+\nu}{2}V'=0$$
$$V''-\frac{1-\nu}{2}\alpha^2V-\frac{1+\nu}{2}U'=0 \qquad (10)$$

$$W''''-2\alpha^2W''+\alpha^4\left(1-\frac{k^2}{m^2}K\right)W=0 \qquad (11)$$

where $k=l/b$, $K=-N_xb^2/\pi^2D$ and primes represent derivatives with respect to y.

The solutions of equations (10) can be found in the following form

$$U=A_1\cosh\alpha y+A_2y\sinh\alpha y$$
$$V=B_1\sinh\alpha y+B_2y\cosh\alpha y \qquad (12)$$

Obviously, the constants A_1 and A_2 are dependent on B_1 and B_2. The relationships between them are readily obtained by substituting equations (12) into (10).

$$A_1=B_1+\frac{1}{\alpha}\frac{3-\nu}{1+\nu}B_2$$
$$A_2=B_2 \qquad (13)$$

To solve equation (11), it should be noted that the form of the solution depends on the value of K. However, as will be discussed next, it can be verified that K always satisfies the following condition

$$K>m^2/k^2.$$

Thus, the solution is obtained as

$$W=C_1\cosh\beta y+C_2\cos\gamma y \qquad (14)$$

where

$$\beta=\alpha\sqrt{\sqrt{K}\frac{k}{m}+1}\ \text{and}\ \gamma=\alpha\sqrt{\sqrt{K}\frac{k}{m}-1}. \qquad (15)$$

In obtaining solutions (12) and (14), symmetry about the S_1 and S_2 axes in any cross-section (Fig. 2(*b*)) has been assumed. According to the statement in the last section about the neutral nature of the conditions that pertain at the point of buckling, antisymmetric deformation about these axes is also admissible as a buckling mode. However, it can be shown that such deformation always corresponds to a higher load level and therefore will not be the buckling mode.

4 Application of the Symmetric and Antisymmetric Edge Conditions

After solving the buckling equations (5) and (6), the buckling mode is known in the following form, which is obtained by substituting equations (12)–(14) into (7) and (8).

$$u = \left[B_1\cosh\alpha y+B_2\left(\frac{1}{\alpha}\frac{3-\nu}{1+\nu}\cosh\alpha y+y\sinh\alpha y\right)\right]\cos\alpha x$$
$$v = (B_1\sinh\alpha y+B_2y\cosh\alpha y)\sin\alpha x \qquad (16)$$
$$w = (C_1\cosh\beta y+C_2\cos\gamma y)\sin\alpha x$$

Following plate theory, after some manipulation all the other field quantities appearing in the edge conditions (2) and (3) can be obtained.

$$w_{,y} = (C_1\beta\sinh\beta y-C_2\gamma\sin\gamma y)\sin\alpha x$$

$$N_{xy} = \frac{Et}{1+\nu}\left[B_1\alpha\sinh\alpha y+B_2\left(\frac{2}{1+\nu}\sinh\alpha y+\alpha y\cosh\alpha y\right)\right]\cos\alpha x$$

$$N_y = \frac{Et}{1+\nu}\left[B_1\alpha\cosh\alpha y+B_2\left(\frac{1-\nu}{1+\nu}\cosh\alpha y+\alpha y\sinh\alpha y\right)\right]\sin\alpha x$$

$$M_y = -\frac{Et^3}{12(1-\nu^2)}[C_1(\beta^2-\nu\alpha^2)\cosh\beta y - C_2(\gamma^2+\nu\alpha^2)\cos\gamma y]\sin\alpha x$$

$$T_y = -\frac{Et^3}{12(1-\nu^2)}[C_1\beta(\beta^2-(2-\nu)\alpha^2)\sinh\beta y + C_2\gamma(\gamma^2+(2-\nu)\alpha^2)\sin\gamma y]\sin\alpha x \qquad (17)$$

where B_1, B_2, C_1, and C_2 are constants. Imposing the symmetric and antisymmetric edge conditions (2) and (3), respectively, results in the following two sets of homogeneous equations for B_1, B_2, C_1, and C_2.

$$\begin{aligned}
&B_1\sinh\theta+B_2\frac{1}{\alpha}\theta\cosh\theta-C_1\cosh\xi\theta-C_2\cos\eta\theta=0\\
&C_1\xi\sinh\xi\theta-C_2\eta\sin\eta\theta=0\\
&B_1\cosh\theta+B_2\frac{1}{\alpha}\left(\frac{1-\nu}{1+\nu}\cosh\theta+\theta\sinh\theta\right)\\
&-\frac{\theta^2}{3(1-\nu)h^2}[C_1\xi(\xi^2-2+\nu)\sinh\xi\theta\\
&+C_2\eta(\eta^2+2-\nu)\sin\eta\theta]=0\\
&B_1\sinh\theta+B_2\frac{1}{\alpha}\left(\frac{2}{1+\nu}\sinh\theta+\theta\cosh\theta\right)=0
\end{aligned} \qquad (18)$$

or

$$\begin{aligned}
&B_1\sinh\theta+B_2\frac{1}{\alpha}\theta\cosh\theta+C_1\cosh\xi\theta+C_2\cos\eta\theta=0\\
&B_1\cosh\theta+B_2\frac{1}{\alpha}\left(\frac{3-\nu}{1+\nu}\cosh\theta+\theta\sinh\theta\right)=0\\
&C_1(\xi^2-\nu)\cosh\xi\theta-C_2(\eta^2+\nu)\cos\eta\theta=0\\
&B_1\cosh\theta+B_2\frac{1}{\alpha}\left(\frac{1-\nu}{1+\nu}\cosh\theta+\theta\sinh\theta\right)\\
&+\frac{\theta^2}{3(1-\nu)h^2}[C_1\xi(\xi^2-2+\nu)\sinh\xi\theta\\
&+C_2\eta(\eta^2+2-\nu)\sin\eta\theta]=0
\end{aligned} \qquad (19)$$

where $\theta=\alpha b/2$, $\xi=\beta/\alpha$, $\eta=\gamma/\alpha$, $h=b/t$.

It should be pointed out that both equations (18) and (19) correspond to the edge $y=b/2$ and those corresponding to $y=-b/2$ are automatically satisfied, since symmetry is implied in solution (12) and (14).

Downloaded 03 May 2010 to 171.66.16.244. Redistribution subject to ASME license or copyright; see http://www.asme.org/terms/Terms_Use.cfm

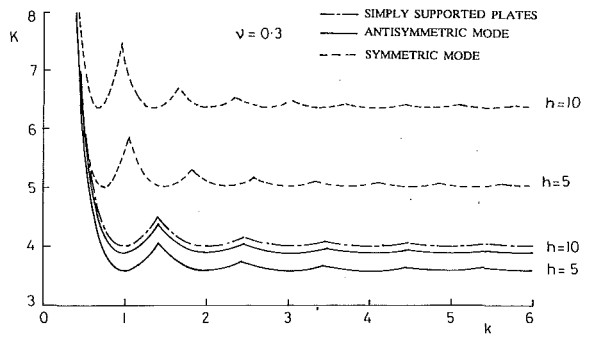


Fig. 4 Nondimensional buckling load, K, versus aspect ratio, k

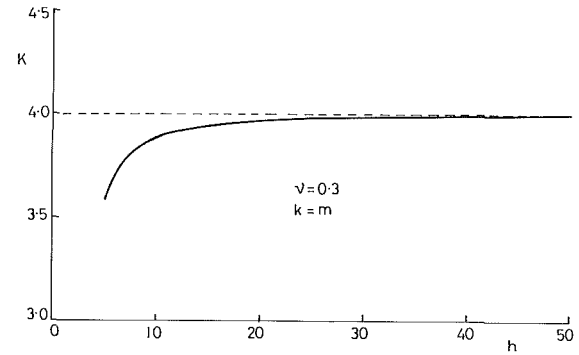


Fig. 5 Dependence of nondimensional buckling load, K, on relative width $h = b/t$ for $k = m$ (integer)

The buckling criterion requires the existence of nontrivial solutions for B_1, B_2, C_1, and C_2 from equations (18) or (19), which leads to

$$\xi\eta(\xi^2+\eta^2)\tanh\theta\tanh\xi\theta\sin\eta\theta - \frac{3}{2}\frac{h^2}{\theta^2}(1-\nu^2)(\xi\tanh\xi\theta\cos\eta\theta+\eta\sin\eta\theta)=0 \tag{20}$$

or

$$\left(\theta-\frac{3-\nu}{1+\nu}\tanh\theta-\theta\tanh^2\theta\right)[(\xi^2-2+\nu)(\eta^2+\nu)\xi\tanh\xi\theta\cos\eta\theta + (\eta^2+2-\nu)(\xi^2-\nu)\eta\sin\eta\theta]+\frac{1-\nu}{1+\nu}\frac{6h^2}{\theta^2}(\xi^2+\eta^2)\cos\eta\theta=0. \tag{21}$$

For any given geometry (aspect ratio k and relative width h), (20) and (21) are equations which give K in terms of m for symmetric and antisymmetric modes, respectively. Denoting their solutions by K_m^s and K_m^a, the buckling load corresponds to the minimum of K_m^s and K_m^a for $m = 1, 2, \ldots$, and, consequently, the buckling mode can be determined.

If $K \leqq m^2/k^2$, other forms of equations (20) and (21) can be obtained. However, these equations do not lead to values of K which are less than the values obtained from equations (20) and (21). Thus, the solutions of equations (20) and (21) above are the appropriate values of K.

Following the above approach, buckling loads were obtained numerically for a range of values of the aspect ratio k for some typical relative widths h and these are plotted in Fig. 4.

5 Discussion

5.1 Buckling Mode and Buckling Loads. In Fig. 4 it is clear that the symmetric mode gives a higher value of K than does the antisymmetric mode, except for very short tubes for which the values of K are far beyond the scale of the diagram. Therefore, in most cases, buckling is in the antisymmetric mode and most of the following discussions will relate to this mode.

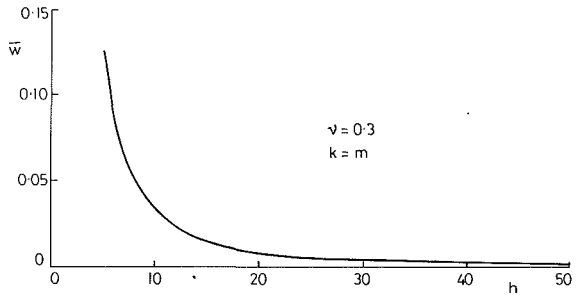


Fig. 6 Dependence of relative deflection, $\bar{w}$ (ratio of transverse deflection at center of panel to deflection at edge), on relative width, $h = b/t$ for $k = m$ (integer)

For short tubes (approximately $k < 0.3$), the values of K for both the symmetric and antisymmetric modes tend towards each other and also towards the values for simply-supported plates. This means that the buckling of short tubes is of double-mode type. In such cases the particular mode they buckle into depends on physical conditions such as any initial imperfections involved. Sometimes in experiments combinations of the two modes can be observed. Such irregular modes are therefore not surprising in the light of the double-mode buckling type, although to explain how such modes develop one has to deal with the mode interaction problem in initial postbuckling theory, Koiter (1945), which is beyond the scope of the present paper.

5.2 Effect of Thickness. The analysis of the buckling of simply-supported plates based on the Kirchhoff hypothesis leads to the conclusion that the nondimensional buckling load K and buckling mode are not affected by thickness. However, by contrast, the buckling behavior of tubes as described by the present theory is affected significantly by their thickness. The buckling loads and the buckling modes appropriate to the new boundary conditions given in Section 2 are discussed in turn next.

From Fig. 4, it is seen that the buckling load for tubes is always lower than that of simply-supported plates. As the thickness decreases (increase in h), K approaches that of simply-supported plates. This tendency is clearly shown in Fig. 5 which is drawn for a particular aspect ratio $k = m$ or for a long tube. In fact if t tends to zero, i.e., h tends to infinity, equations (20) and (21) become

$$\xi\sinh\xi\theta\cos\eta\theta+\eta\cosh\xi\theta\sin\eta\theta=0 \tag{22}$$

and

$$\cos\eta\theta=0, \tag{23}$$

respectively. These are exactly the same equations as for plates. The former is for plates with the two loaded edges simply supported and the other two opposite edges clamped, while the latter corresponds to completely simply-supported plates. Of course, in this case, buckling always corresponds to the latter case, i.e., the antisymmetric tube mode or simply-supported plates. Therefore simply-supported plates can be used to represent square tubes exactly only for very thin tubes and vice versa. If they are not very thin, the equivalence between square tubes and simply-supported plates cannot be taken for granted.

5.3 Compact and Noncompact Behavior. It is interesting to examine the buckling modes of square tubes (equation (16)) in comparison to that of rectangular plates. An extra hyperbolic term $\cosh\beta y$ appears in the expression for the transverse deflection in the third equation of (16), which results in a nonvanishing deflection along the edges $y = \pm b/2$. In fact, for the antisymmetric mode, the relative deflection along $y = b/2$ has the following expression

Downloaded 03 May 2010 to 171.66.16.244. Redistribution subject to ASME license or copyright; see http://www.asme.org/terms/Terms_Use.cfm

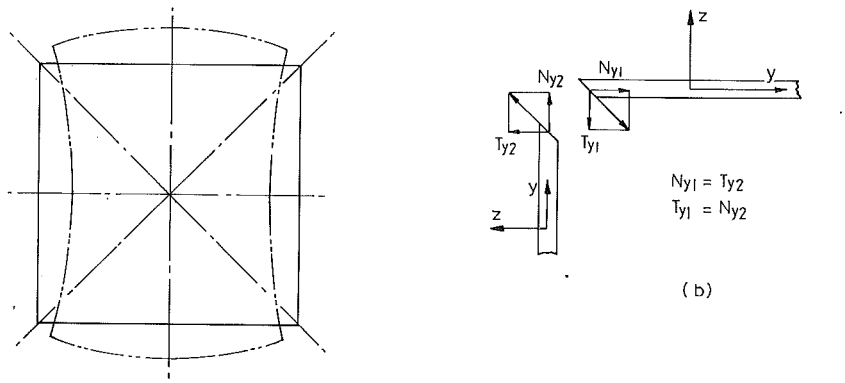


Fig. 7 Forces on edges of distorted panels: (*a*) distorted cross-section, (*b*) forces generated

$$\overline{w}=\frac{w\left(y=\frac{b}{2}\right)}{w(y=0)}=\frac{(\xi^2+\eta^2)\cosh\xi\theta\cos\eta\theta}{(\xi^2-\nu)\cosh\xi\theta+(\eta^2+\nu)\cos\eta\theta}, \qquad (24)$$

which is plotted in Fig. 6 against the relative width h for some particular aspect ratio $k=m$ or for a long tube. Obviously, the deflection along the edges $y=\pm b/2$ with respect to that along the central line ($y=0$) increases with thickness, while for very thin tubes $\overline{w}$ tends to vanish. Therefore, during buckling, the edges do not remain straight, instead, they deflect in some way. Only for very thin tubes can these deflections be neglected, which again implies equivalence between tubes and simply-supported plates.

How the edges of square tubes deflect is an important factor which might be related to the nature of the subsequent crushing modes. From the buckling mode (equation (16)), remembering the first edge condition in (3) for the antisymmetric mode, the edges deflect into sinusoidal curves which lie in planes perpendicular to the diagonals of the cross-section, i.e., at 45 deg to the panels of the tube. Of course, this is only for the buckling phase. In the postbuckling stage they seem likely to deviate from these planes. Because of such deflections of the edges, it is evident that the panels of square tubes undergo a degree of circumferential extension or compression, see Fig. 7. Where the transverse deflection of the panels is outwards, it is accompanied by displacements and forces at the two edges $y=\pm b/2$ which act towards each other, see the horizontal panel in Fig. 7(*a*) and (*b*). This favors further deflection and promotes bending in both longitudinal and circumferential directions. Where the panel deflection is inwards, a degree of circumferential stretching is produced in that part of the panel so that the bending in the circumferential direction is somewhat constrained, however, it can bend longitudinally along with the edges. This tendency coincides with experimental observations of compact crushing modes very well. However, the degree of such behavior is affected by the thickness of the tubes significantly.

The implication of Fig. 6 is that, for a given level of peak transverse panel deflection, there is a greater degree of edge deflection for a thicker tube. This in turn is likely to lead to the earlier development of the combined stretching-bending mechanisms described by Wierzbicki and Abramowicz (1983) and so is more likely to generate a compact mode response for thick tubes; while for thin tubes, the four nearly straight vertical edges allow only a noncompact mode. Examples of compact and noncompact modes of deformation in crushed tubes are shown in Fig. 1. Thus, the deflection of the vertical edges of the tube gives some insight into what triggers compact and noncompact crushing modes. In order to follow the development of this an elastic-plastic postbuckling analysis is required and it needs to be recognized that the buckling process itself could be in the plastic range. This will be discussed in a subsequent publication.

6 Conclusions

The buckling problems of square tubes and simply-supported plates under axial compression are essentially different and only for very thin tubes and plates do they approach each other. The subsequent axial crushing mode, whether compact or noncompact, of square tubes would seem to be closely related to their buckling mode.

References

Gerard, G., et al., 1957, *Handbook of Structural Stability—Part I—Buckling of Flat Plates*, NACA TN3781.

Hui, D., 1986, "Design of Beneficial Geometric Imperfections for Elastic Collapse of Thin-Walled Box Columns," *Int. J. Mech. Sci.*, Vol. 28, pp. 163–172.

Koiter, W. T., 1970, "On the Stability of Elastic Equilibrium," Thesis, Delft, H. J. Paris, Amsterdam 1945, AFFDL-TR-70-25, 1970, (AD704124).

Mahmood, H. F., and Paluszny, A., 1981, "Design of Thin-Walled Columns for Crush Energy Management—Their Strength and Mode of Collapse," *Proc. 4th Int. Conf. Vehicle Struct. Mech.*, SAE, pp. 7–18.

Meng, Q., Al-Hassani, S. T. S., and Soden, P., 1983, "Axial Crushing of Square Tubes," *Int. J. Mech. Sci.*, Vol. 25, pp. 747–773.

Reid, S. R., Reddy, T. Y., and Gray, M. D., 1986, "Static and Dynamic Axial Crushing of Foam-Filled Sheet Metal Tubes," *Int. J. Mech. Sci.*, Vol. 28, pp. 295–322.

Timoshenko, S. T., and Gere, J. M., 1961, *Theory of Elastic Stability*, 2nd. ed., McGraw-Hill Book Company, New York.

Wierzbicki, T., and Abramowicz, W., 1983, "On the Crushing Mechanics of Thin-Walled Structures," ASME JOURNAL OF APPLIED MECHANICS, Vol. 50, pp. 727–734.

Downloaded 03 May 2010 to 171.66.16.244. Redistribution subject to ASME license or copyright; see http://www.asme.org/terms/Terms_Use.cfm

J. P. Dempsey
Professor,
Mem. ASME

Z. G. Zhao
Research Assistant.

L. Minnetyan
Associate Professor.

H. Li
Visiting Assistant Professor.

Department of Civil and Environmental Engineering,
Clarkson University,
Potsdam, NY 13676

Plane Contact of an Elastic Layer Supported by a Winkler Foundation

Plane contact problems of an elastic, homogeneous, and isotropic layer supported by a Winkler foundation are studied in this paper. The elastic layer has a finite depth and infinite in-plane dimensions. The upper surface of the layer is in plane contact with a rigid indenter. The particular applications studied in this paper are formulated by first providing the solution for a line load. For the case of a rigid cylinder, the upper portion of the load deflection response is modeled using beam theory with wrapping. The contact pressure distributions for the relatively flexible foundation cases can be accurately determined from the wrapping theory.

Introduction

Solutions to problems involving a layer supported by foundations modeled as a Winkler medium have many applications, particularly in geophysics, and the geotechnical and ice engineering fields (Westergaard, 1926; Hetényi, 1946; Timoshenko and Woinowsky-Krieger, 1959; Selvadurai, 1979; Turcotte, 1979; Ashton, 1986). Rather surprisingly, there has apparently been no general treatment of a layer supported by a Winkler foundation. A survey of the literature revealed, however, that there have been a considerable number of studies involving plates on Winkler foundations. Unfortunately, beam or plate theories can not readily furnish an accurate representation of the associated contact pressure distributions, the indentation and applied load versus extent of the contact, and the local stresses, moments, and shears.

In this paper the fundamental line load solution for an elastic layer supported by a Winkler medium is first obtained. A crucial feature of this basic solution is the derivation of an accurate series approximation for several analytically intractable infinite integrals. This fundamental solution is used to solve for the contact pressure and deformation produced by the surface indentation of both a rigid unbonded cylinder and a rigid bonded strip.

Fundamental Line Load Solution

In the downward line load case (Fig. 1(*a*)), the boundary conditions are given by

$$\tau_{xz}(x,h)=0, \quad \sigma_z(x,h)=-kw(x,h), \tag{1a,b}$$

$$\tau_{xz}(x,0)=0, \quad \sigma_z(x,0)=-P\delta(x) \tag{1c,d}$$

where k is the stiffness of the foundation, $\delta(x)$ is the Dirac delta function, and P is the line load per unit length in the y-direction. The stresses and displacements under a unit line load are derived and presented in the Appendix. The formulation assumes a state of plane-stress deformation. For the plane-strain case, the solution may be obtained by replacing Poisson's ratio ν by $\nu/(1-\nu)$, the elastic modulus E by $E/(1-\nu^2)$, and the layer thickness in the y-direction b by a unit length.

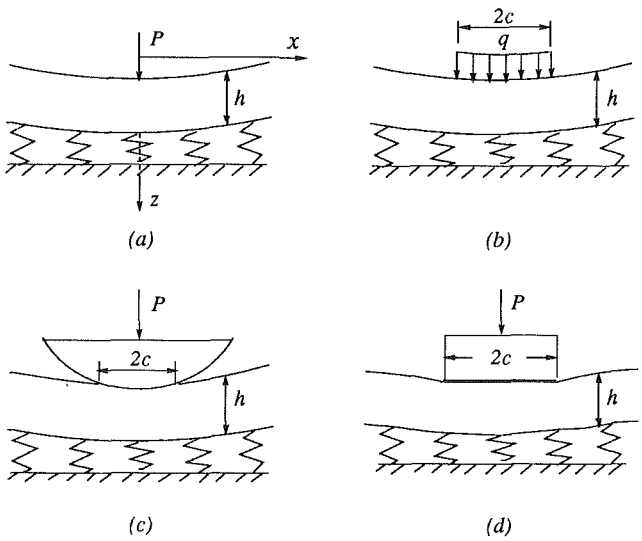


Fig. 1 **Problem configuration; (*a*) a line load acting on an infinite layer, (*b*) a uniform load acting on an infinite layer, (*c*) an infinite layer indented by a rigid cylinder, and (*d*) an infinite layer indented by a rigid strip**

Contributed by the Applied Mechanics Division of THE AMERICAN SOCIETY OF MECHANICAL ENGINEERS for publication in the JOURNAL OF APPLIED MECHANICS.

Discussion on this paper should be addressed to the Technical Editor, Prof. Leon M. Keer, The Technological Institute, Northwestern University, Evanston, IL 60208, and will be accepted until two months after final publication of the paper itself in the JOURNAL OF APPLIED MECHANICS. Manuscript received by the ASME Applied Mechanics Division, April 21, 1989; final revision, Aug. 10, 1989.

Copyright © 1990 by ASME
Downloaded 03 May 2010 to 171.66.16.244. Redistribution subject to ASME license or copyright; see http://www.asme.org/terms/Terms_Use.cfm

Table 1 Typical range of *l/h* for different material combinations

	E(GPa)	k(MN/m^3)	h(m)	l/h
lithosphere/mantle	20 – 100	0.025 – 0.035	$10^5 - 2\times10^5$	0.7 – 1.4
steel/concrete	207	5000 – 20000	0.02 – 0.1	1.7 – 3.6
concrete/soil	20 – 30	50 – 220	0.1 – 1	1.7 – 4.6
freshwater ice/water	3 – 7	0.01	0.05 – 1	12 – 33
steel/rubber	207	0.03 – 0.1	0.02 – 0.1	36 – 73

After substituting $z = 0$ and $z = h$ into equation (A7), the displacements of the upper and lower surface under the downward line load P reduce to

$$w(x,0) = \frac{2P}{\pi E}\int_0^\infty L_u(\beta)\cos(\beta x/h)d\beta, \tag{3}$$

$$w(x,h) = \frac{2P}{\pi E}\int_0^\infty L_l(\beta)\cos(\beta x/h)d\beta, \tag{4}$$

where

$$L_u(\beta) = \frac{1}{\beta D(\beta)}\left(\beta + \sinh\beta\cosh\beta + \frac{h^4}{6\beta l^4}\sinh^2\beta\right), \tag{5}$$

$$L_l(\beta) = \frac{1}{\beta D(\beta)}(\sinh\beta + \beta\cosh\beta), \tag{6}$$

$$D(\beta) = \sinh^2\beta - \beta^2 + \frac{h^4}{6\beta l^4}(\beta + \sinh\beta\cosh\beta), \tag{7}$$

$$l^4 = EI/k, \qquad I = h^3/12. \tag{8a,b}$$

Note that neither $L_u(\beta)$ nor $L_l(\beta)$ depend on Poisson's ratio. The parameter l is usually called the "characteristic length" or the "radius of relative stiffness" (Westergaard, 1926). When the Winkler foundation is infinitely rigid, $l = 0$, and equation (3) reduces to the fundamental solution for a layer on a rigid smooth base (Hannah, 1951).

The parameter l/h is useful in this paper to characterize the interaction between the layer and the underlying foundation. To give a general idea of the possible variation of l/h, a few typical ranges are presented in Table 1, in which $l/h = (E/12hk)^{1/4}$. However, it should be pointed out that for an elastic foundation, the Winkler foundation model is only a convenient approximation and the stiffness parameter k is not well defined. The value of k depends on the load distribution and intensity as well as on the depth of the underlying material. A rigid smooth base can be considered a special case of a Winkler foundation with $k \to \infty$ ($l/h \to 0$).

Since $L_u(\beta) \to 1/\beta$ as $\beta \to \infty$, the integral in equation (3) has a logarithmic singularity at $x = 0$. This singularity is extracted using the relation

$$\int_0^\infty \frac{e^{-2\beta}-1}{\beta}\cos(\beta\alpha)d\beta - \log|\alpha| + \frac{1}{2}\log[4+\alpha^2] = 0. \tag{9}$$

The upper surface displacement due to the line load is now given by

$$w(x,0) = \frac{2P}{\pi E}\left\{-\log|x| + \frac{1}{2}\log(4h^2 + x^2) + \int_0^\infty L_u^*(\beta)\cos(\beta x/h)d\beta\right\}, \tag{10}$$

where

$$L_u^*(\beta) = L_u(\beta) + \frac{e^{-2\beta}-1}{\beta}. \tag{11}$$

Both $L_u^*(\beta)$ and $L_l(\beta)$ decay exponentially for large β. These two functions are both approximated here by exponential series as

$$L_u^*(\beta) = \sum_{m=1}^{M} a_m e^{-m\gamma_a\beta}, \quad L_l(\beta) = \sum_{m=1}^{M} b_m e^{-m\gamma_b\beta}, \tag{12a,b}$$

where the coefficients a_m, b_m, γ_a, and γ_b are determined by a least-squares criterion (Dempsey et al., 1988). Once these constants are obtained, the integrals in equation (4) and (10) are evaluated analytically since

$$\int_0^\infty e^{-m\gamma\beta}\cos(\beta\alpha)d\beta = \frac{m\gamma}{(m\gamma)^2+\alpha^2}. \tag{13}$$

The physical quantities of interest are thereby reduced to expressions involving finite summations

$$\frac{w(x,0)EI}{Pl^3} = \frac{h^3}{6\pi l^3}\left\{-\log|x| + \frac{1}{2}\log(4h^2+x^2) + \sum_{m=1}^{M} a_m\frac{m\gamma_a}{(m\gamma_a)^2+(x/h)^2}\right\}, \tag{14}$$

$$\frac{w(x,h)EI}{Pl^3} = \frac{h^3}{6\pi l^3}\sum_{m=1}^{M} b_m\frac{m\gamma_b}{(m\gamma_b)^2+(x/h)^2}. \tag{15}$$

$$\frac{Q(x)}{P} = -\frac{1}{2} + \frac{k}{P}\int_0^x w(\eta,h)d\eta = -\frac{1}{2} + \frac{1}{6\pi}\left(\frac{h}{l}\right)^4\sum_{m=1}^{M} b_m\arctan\left(\frac{x}{m\gamma_b h}\right), \tag{16}$$

$$\frac{M(x)}{Pl} = \frac{1}{Pl}\left[M(0) - \frac{1}{2}P|x| + k\int_0^x w(\eta,h)(x-\eta)d\eta\right] = \frac{M(0)}{Pl} - \frac{|x|}{2l} + \frac{1}{6\pi}\left(\frac{h}{l}\right)^5\sum_{m=1}^{M} b_m m\gamma_b\left\{\frac{x}{m\gamma_b h}\arctan\left(\frac{x}{m\gamma_b h}\right) - \frac{1}{2}\log\left[1+\left(\frac{x}{m\gamma_b h}\right)^2\right]\right\}, \tag{17}$$

$$\frac{M(0)}{Pl} = \frac{h}{\pi l}\int_0^\infty\left\{1 - \frac{h^4}{6l^4\beta D(\beta)}(\sinh\beta + \beta\cosh\beta)\right\}\frac{d\beta}{\beta^2}. \tag{18}$$

$M(0)$ is obtained by integrating the moment of stress at the section $x = 0$ and can be calculated using Gaussian quadrature.

When the transverse deformations are neglected, the elastic layer can also be treated as a beam. The associated displacement, moment, and shear force have been derived either by using Euler-Bernoulli beam theory (Hetényi, 1946) or by using Reissner's plate theory (Frederick, 1957).

For the displacements at the upper and lower surface, comparisons are made between the layer solution and the Euler-Bernoulli beam solution in Fig. 2. The difference between the elasticity solution and the beam solution are caused by the shear deformation and transverse deformation which were neglected in the above beam theory. Since these deformations become smaller for larger l/h values, implying either a smaller layer depth or a softer foundation, the beam solution becomes more applicable for larger l/h values. There is a logarithmic singularity within the elasticity solution of the upper surface displacement equation (14). However, this singular term quickly loses significance as the ratio l/h increases. The differences are negligible when $l/h \geq 8$. Frederick (1957) presented results for $l/h = 1$. From Fig. 2 it is evident that for such a low l/h value, the displacements from the Euler-Bernoulli beam theory and from the elasticity theory are noticeably different. For small distances from the line load, since the displacement is maximum at the upper surface and minimum at the lower surface, the elasticity solutions can be used as the upper and lower bound to check the improved beam solution. The displacement given by Frederick (1957) indeed falls in between these two bounds. Curiously, the maximum bending moment obtained from Reissner's plate theory is only 52 percent of that obtained from the Euler-Bernoulli beam theory. However, Simmonds (1989) has recently explored the pathological be-

Downloaded 03 May 2010 to 171.66.16.244. Redistribution subject to ASME license or copyright; see http://www.asme.org/terms/Terms_Use.cfm

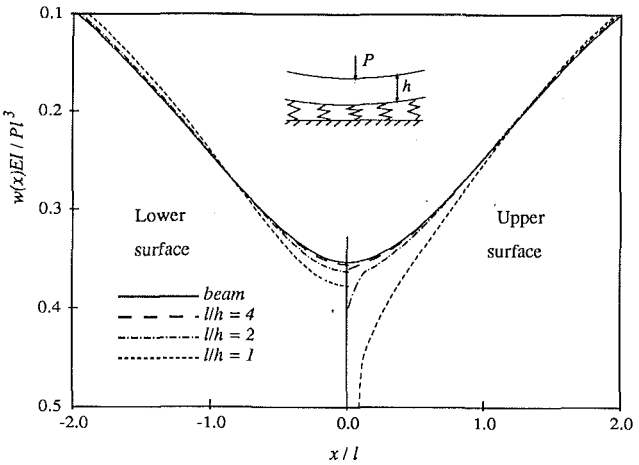


Fig. 2 Surface deflection under line load

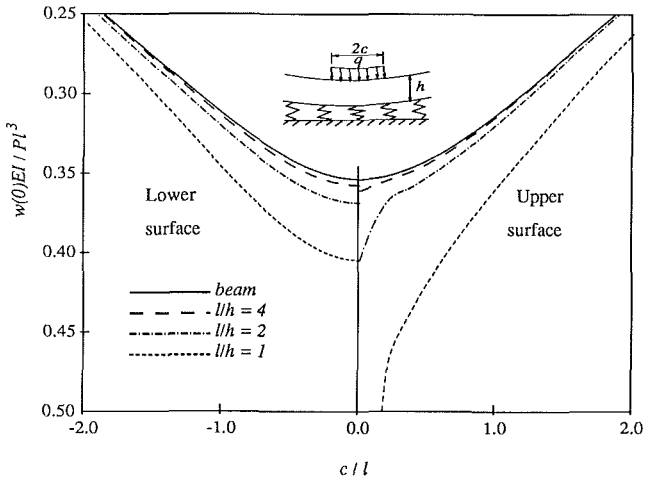


Fig. 3 Deflection at $x = 0$ under uniform load

havior of Reissner's plate theory, emphasizing the fact that this higher-order theory is "good for smooth loads, but detrimental for (nearly) singular loads."

Once the solution for a line load is obtained, superposition may be used for any other loading conditions. For a layer under a uniform load (Fig. 1(*b*)), the surface displacements at the center are presented in Fig. 3. The singularity disappears as the load changes from a line load to a uniform load. The differences between the elasticity solution and the beam solution are substantial only for $l/h \leq 4$. Such low l/h ratios imply either very low layer moduli, very stiff foundations, or very deep layers.

For the bending moments and shear forces, the differences are smaller than those for the vertical displacement. For a line load the maximum shear force is calculated from the equilibrium condition, and thus is the same for all cases. The maximum bending moments for a line load calculated from the elasticity solution, for $l/h = 1$, 2, and 4, respectively, are 97.0 percent, 98.9 percent, and 99.6 percent of that from the beam solution. The maximum tensile stress at the lower surface may also be calculated. For $l/h = 1$, 2, and 4, respectively, the values from the elasticity solution are 80.3 percent, 91.4 percent, and 96.1 percent of that from the beam solution. For a distributed load, the differences between the elasticity solution and the beam solution for bending moment and shear force are even smaller.

Unbonded Contact With a Rigid Cylinder

When the upper surface of the layer is indented by a rigid smooth cylinder (Fig. 1(*c*)), the contact pressure between the indenter and the layer is the unknown function to be solved. Since the extent of contact increases with increasing load, this cylindrical indentation problem can be characterized as an advancing contact problem (Dundurs, 1975). Within the contact region, the displacement of the layer $w(x, 0)$ is the same as the profile of the indenter. The boundary conditions on the upper surface are

$$w(x,0) = \delta - x^2/2R, \ |x| \leq c; \quad \sigma_z(x,0) = 0, \ |x| > c \qquad (19a,b)$$

where δ is the displacement of the indenter and R is the radius of the cylindrical indenter. The foregoing contact is assumed to be frictionless and tensionless. The latter condition indicates that $p(x) \geq 0$ for $|x| < c$.

The condition in equation (19), noting (14) and (A8), may be restated as an integral equation,

$$\frac{2}{\pi E}\int_{-c}^{c} p(\eta)\{-\log|x-\eta| + H(x-\eta)\}d\eta = \delta - \frac{x^2}{2R}, \ |x| \leq c; \qquad (20)$$

where $p(x)$ is the unknown contact pressure and

$$H(u) = \frac{1}{2}\log[4h^2+u^2] + \sum_{m=1}^{M} a_m \frac{m\gamma_a}{(m\gamma_a)^2 + (u/h)^2}. \qquad (21)$$

This integral equation is solved using the method formalized by Gladwell (1976). The details are provided in the report by Dempsey et al., (1988). This method reduces the contact problem to a set of linear equations in which the unknowns define the contact pressure distribution. Once the contact pressure is found, the displacement, bending moment, and shear force distributions may be obtained by integration of the line load solutions in equations (14)–(18).

When the values of l/h become large and the transverse deformation become less significant, this indentation problem may also be solved by using the Euler-Bernoulli beam theory to provide a checking solution. Based on beam theory, there are two kinds of contact: line contact and area contact or "wrapping," as it is called. The line contact occurs when the indenter load and displacement are small ($PRl/EI \leq 2\sqrt{2}$ and $\delta R/l^2 \leq 1$). In this case, the line load solution (Hetényi, 1946) still applies and the load displacement relation is linear, being given by

$$PRl/EI = 2\sqrt{2R\delta/l^2}. \qquad (22)$$

For larger indenter loads and displacements ($PRl/EI > 2\sqrt{2}$ and $\delta R/l^2 > 1$) wrapping occurs and the load displacement relation becomes nonlinear. The derivation proceeds as follows.

Because of the constant curvature of the cylindrical indenter, the bending moment is constant within the contact region. The shear force is zero for $|x| < c$, and the upper surface contact pressure is the same as the lower surface support reaction. Outside the contact region, the layer is treated as an end loaded, semi-infinite beam on a Winkler foundation. The end displacement and shear force of the beam follow from the slope and curvature for a given contact half-length c. The displacement δ of the indenter may be calculated from the end displacement. The end shear force P_c is equilibrated by a concentrated contact force at the edge of the contact region. The total load is the summation of the distributed pressure and the concentrated forces. The wrapping solution so derived is given by

$$R\delta/l^2 = [1 + (c/\sqrt{2}l)]^2 = \xi^2, \quad R\delta/l^2 \geq 1 \qquad (23a)$$

Downloaded 03 May 2010 to 171.66.16.244. Redistribution subject to ASME license or copyright; see http://www.asme.org/terms/Terms_Use.cfm

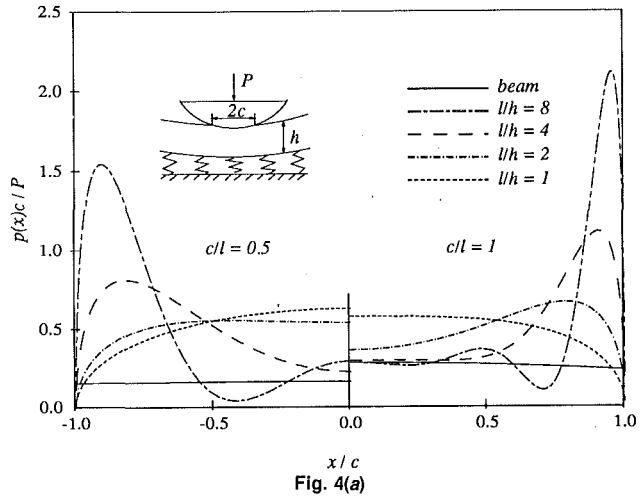


Fig. 4(*a*)

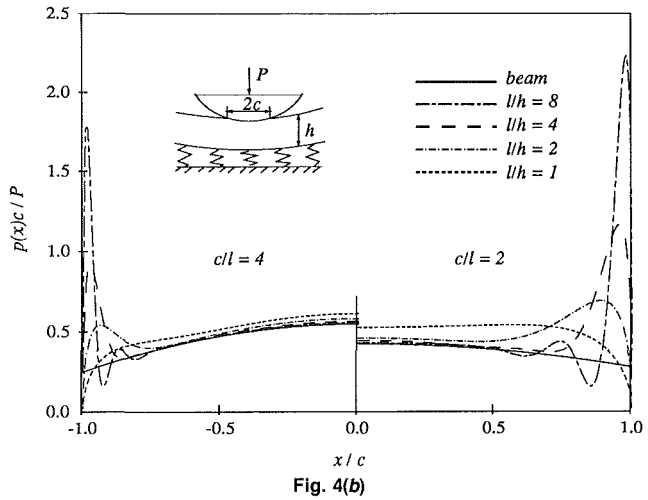


Fig. 4(*b*)

Fig. 4 Contact pressure under cylindrical indenter

$$PRl/EI = 2\sqrt{2}(1+2\xi^3)/3, \quad PRl/EI \geq 2\sqrt{2} \tag{23b}$$

$$PRl/EI = 2\sqrt{2}[1+2(R\delta/l^2)^{3/2}]/3, \quad R\delta/l^2 \geq 1 \tag{23c}$$

$$cp(x)/P = (3/4\sqrt{2})(c/l)[2\xi^2-(x/l)^2]/(1+\xi^2), \quad |x|<c \tag{23d}$$

$$P_c/P = 3\xi/[2(1+2\xi^3)], \tag{23e}$$

where P_c is the concentrated force at each edge of the contact region and $p(x)$ is the contact pressure.

Results for Cylindrical Indentation

In solving equation (20), it is convenient to consider l/h and c/l as two controlling parameters in the cylindrical indentation problem: All other physical quantities may be calculated once these two values are given. For the beam theory (equations (22)–(23)), only one parameter c/l is involved. The greater the value of l/h, the more flexible the Winkler foundation or the thinner the layer; the greater the value of c/l, the greater the contact region. For larger values of l/h and c/l, the influence of transverse deformation becomes less significant and, correspondingly, the beam solution becomes more accurate in this instance.

The contact pressure calculated from the elasticity theory equation (20) and beam theory (22), (23) are compared in Figs. 4(*a*), 4(*b*). Clearly, the beam solution approaches the elasticity solutions as both the ratio l/h and the ratio c/l increase. Based on the beam theory, there are two concentrated forces P_c acting at the edges of the contact region. Correspondingly, from the elasticity theory, there are concentrations of contact pressure at the edges of the contact region for relatively flexible layers.

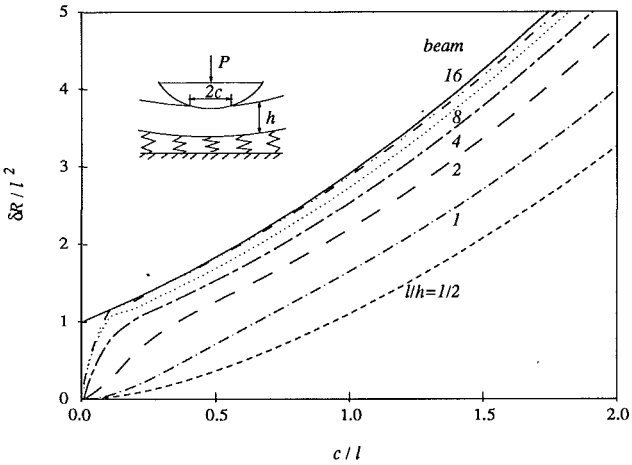


Fig. 5(*a*) Displacement of indenter versus contact length

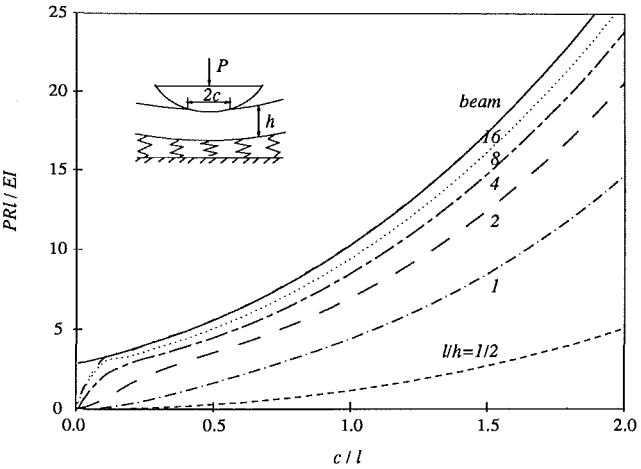


Fig. 5(*b*) Total load on indenter versus contact length

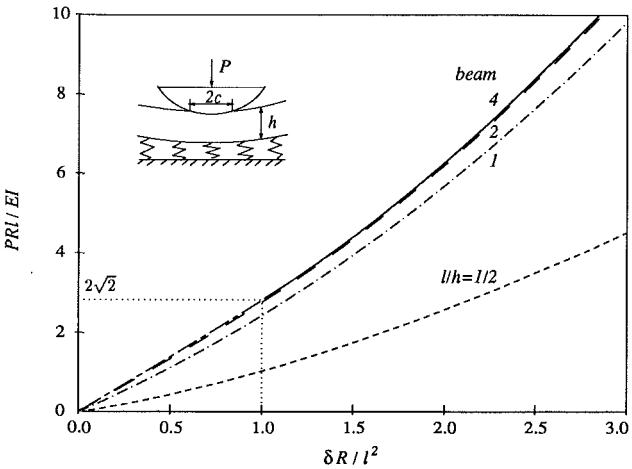


Fig. 5(*c*) Total load versus displacement of indenter

Fig. 5 Relations for the cylindrical indenter

When the elasticity solution is well approximated by the wrapping solution ($l/h \geq 8$), the contact pressure oscillates near the edges. Since essentially an attempt is being made to approximate a discontinuous function by a Fourier series, this oscillation is a type of Gibbs phenomenon. Therefore, the oscillation can not be eliminated by increasing the order of the polynomials. Fortunately, this phenomenon occurs only for large l/h values when the elasticity solution is well approximated by the beam solution.

The relations among the displacements of the indenter, total

Downloaded 03 May 2010 to 171.66.16.244. Redistribution subject to ASME license or copyright; see http://www.asme.org/terms/Terms_Use.cfm

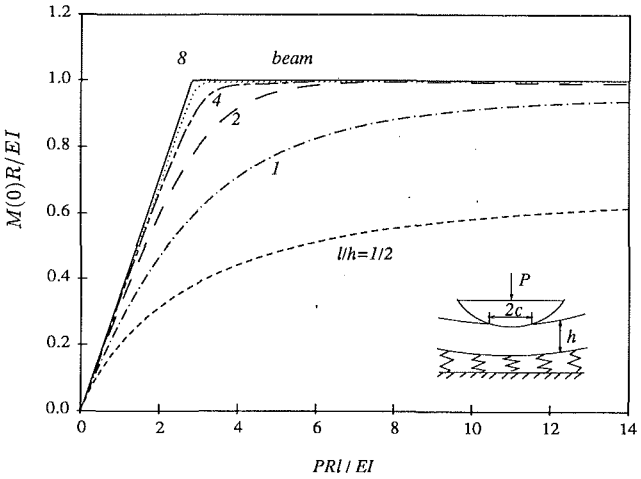


Fig. 6(*a*) Moment under the cylindrical indenter

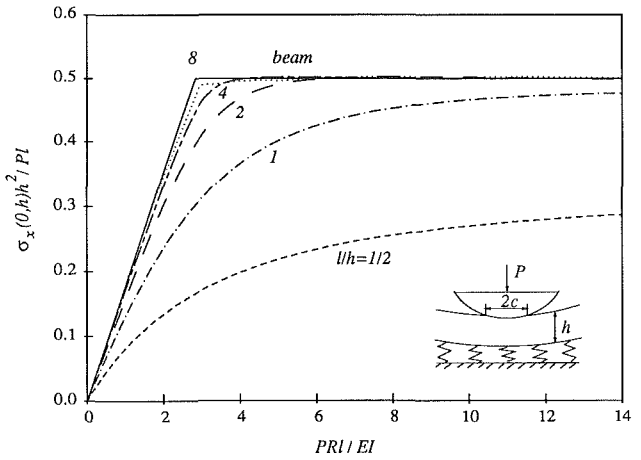


Fig. 6(*b*) Maximum tensile stress under the cylindrical indenter

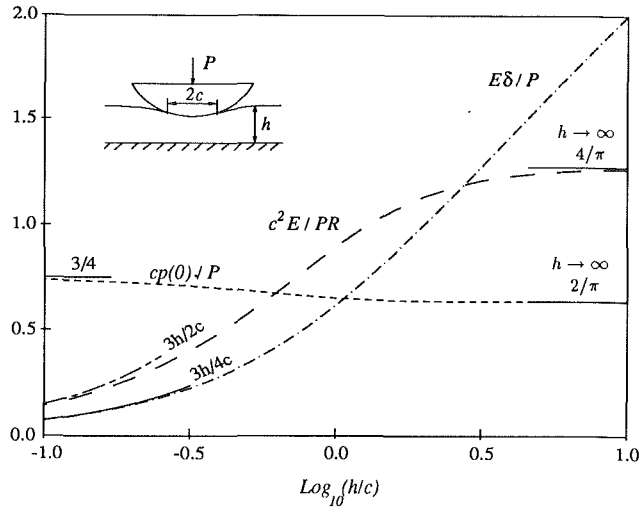


Fig. 7 Cylindrical indenter on a layer underland by a rigid smooth base

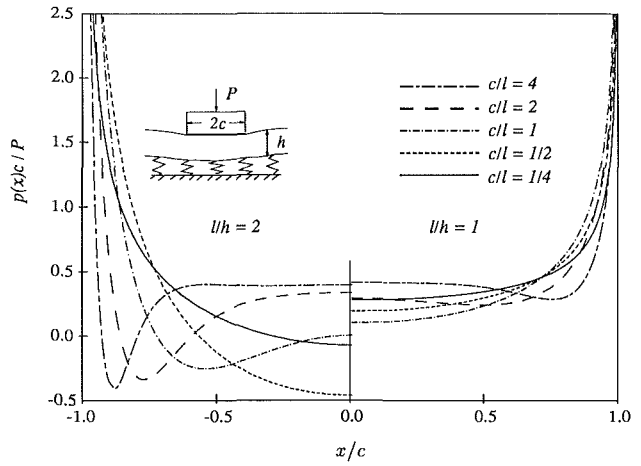


Fig. 8 Contact pressure under the flat-ended indenter

load, and contact length are shown in Fig. 5. The load displacement relation is nonlinear. The beam solutions become more accurate for large l/h ($l/h \geq 8$). However, as seen from Figs. 5(*a*), 5(*b*), and more clearly from 5(*c*), the differences are relatively independent of the c/l values. The differences are caused mainly by the transverse deformation of the layer which is most significant for thicker layers or harder foundations (l/h small). Because of integration, the spurious oscillation in the contact pressure for $l/h \geq 8$ has little influence over the values of the total load and displacement. The indenter load versus displacement (Fig. 5(*c*)) is predicted remarkably well by beam theory (equations (22) and (23*c*)) for $l/h \geq 4$.

Once the contact pressure distribution is found, the other physical quantities may be evaluated using the integration formula equation (A8). The bending moment under the center of the indenter is particularly interesting and is presented in Fig. 6(*a*). Note that the differences between the elasticity solution and the beam solution are large when l/h is small. As is evident from Fig. 6(*b*), the exact values of the maximum tensile stress at the lower surface are extremely close to those calculated directly from the bending moments in Fig. 6(*a*) and the flexure formula. This follows because under the distributed contact pressure, the normal stress σ_x is distributed nearly linearly with depth. As shown in Figs. 6(*a*), 6(*b*) the beam solution provides the upper bound for each case.

The present method may also be extended to the case of a layer in smooth contact with a rigid base on the lower surface by letting the foundation stiffness k in equation (8*a*) approach infinity (in which case $l \to 0$). The contact pressure distributions are then very similar to those given by Meijers (1968), although the latter studied a layer bonded to a rigid base. The associated displacement, contact region, and pressure at the center are calculated and presented in Fig. 7. Knowing the contact pressure at the center from $cp(0)/P$ in Fig. 7, the contact pressure distribution can be approximated quite accurately as

$$\frac{cp(x)}{P} = \left\{\frac{cp(0)}{P} + \left(\frac{8}{\pi} + \frac{4cp(0)}{P}\right)\left(\frac{x}{c}\right)^2\right\}\sqrt{1-(x/c)^2}. \tag{24}$$

This expression has the same center pressure value, resultant force, and singularity at the ends of the contact region as the exact solution; also, equation (24) is exact when the layer is deep enough to be well approximated by a half plane (that is, for $h \to \infty$). Furthermore, when the layer depth becomes small in comparison to the contact region ($h < c/3$), the following approximate relations can be used,

$$\frac{cp(0)}{P} \approx \frac{3}{4}, \quad \frac{E\delta}{P} \approx \frac{3}{4}\frac{h}{c}, \quad \frac{c^2E}{RP} \approx \frac{3}{2}\frac{h}{c}. \tag{25}$$

These equations are obtained by neglecting the influence of the material outside the contact region.

Bonded Contact With a Rigid Strip

When the upper surface of the layer is indented by a rigid strip (Fig. 1(*d*)), the boundary conditions on the upper surface are given by

$$w(x,0) = \delta, \ |x| \leq c; \ \sigma_z(x,0) = 0, \ |x| > c, \tag{26}$$

Downloaded 03 May 2010 to 171.66.16.244. Redistribution subject to ASME license or copyright; see http://www.asme.org/terms/Terms_Use.cfm

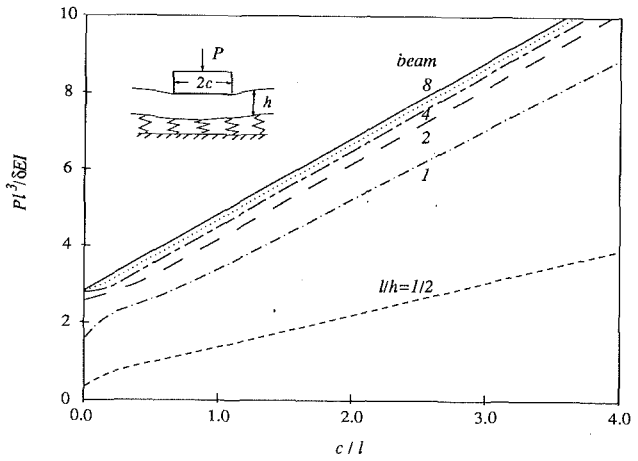


Fig. 9 Load displacement ratio under the flat-ended indenter

where c is the half-width of the strip. The rigid strip is assumed to be bonded to the top surface. The possibility of contact separation and multiple regions of contact is thereby excluded.

The solution procedure is as outlined for the cylindrical indenter, except that there is no quadratic term in equation (19*a*), or (20). Also, the contact pressure is now unbounded as $|x| \to c^-$ (Sadowsky, 1928; Li and Dempsey, 1989).

Typical contact pressure distributions are shown in Fig. 8, while the load displacement ratio is plotted in Fig. 9 as a function of c/l. Clearly, the contact pressure is negative in different regions for different c/l and l/h combinations. Multiple contact regions would occur in the case of tensionless contact. The latter receding contact problem (Dundurs, 1975) is not readily treated by the formulation in this paper and requires a separate study. By using the Euler-Bernoulli beam theory and assuming that the beam is bonded to the rigid strip and that the slope at the edges is zero as $|x| \to c^-$, the following load displacement relation is found

$$\frac{Pl^2}{EI} = \left(2\sqrt{2} + 2\frac{c}{l}\right)\frac{\delta}{l}. \tag{27}$$

As is evident from Fig. 9, equation (27) is reasonable unless $l/h \leq 2$. For stiffer foundations, or deeper layers, shear deformation and transverse deformation become more important.

The case of a rigid strip indenting a layer underlaid by a rigid base was investigated by Li and Dempsey (1989). The latter study corresponds here to the case of a zero characteristic length ($l \to 0$).

Conclusions

The fundamental line load solution for an elastic layer supported by a Winkler medium is first obtained. The basic solution is presented in full detail in the Appendix. Prior to obtaining explicit expressions for the top and bottom surface vertical displacement distributions, as well as the shear force and moment, accurate series approximations of several analytically intractable hyperbolic functions are presented.

Superposition of the above line load solution facilitates a direct formulation of the rigid cylindrical indentation problem and the indentation of a rigid strip. The cylinder is unbonded, while the strip is assumed to be bonded, the contact pressure is thereby nonsingular and singular, and the contact type is advancing and receding, respectively. The solution procedure in both cases is efficient.

Solutions obtained using beam theory are presented as well; it is useful to know in which instances it is accurate to use the analytical beam theory solutions. The latter solutions also suggest the appropriate normalizations that should be used in the plots presented. As is evident from the results presented, a problem in which the characteristic length-to-layer-depth ratio exceeds eight is well approximated by beam theory.

Finally, note that all of the results presented are independent of Poisson's ratio.

Acknowledgments

This work has been supported in part by the U. S. Army Cold Regions Research and Engineering Laboratory under Grant No. DACA 89-86-K-0018.

References

Ashton, G. D., Ed., 1986, *River and Lake Ice Engineering*, Water Resources Publications, Colo.

Dempsey, J. P., Zhao, Z. G., Minnetyan, L., and Li, H., 1988, "Plane Contact of a Winkler Supported Elastic Layer," Report No. 88-10, Department of Civil and Environmental Engineering, Clarkson University, Potsdam, N.Y.

Dundurs, J., 1975, "Properties of Elastic Bodies in Contact," *The Mechanics of the Contact Between Deformable Bodies*, A. D. De Pater and J. J. Kalker, eds., Delft University Press.

Frederick, D., 1957, "Thick Rectangular Plates on an Elastic Foundation," *ASCE Transactions*, Vol. 122, pp. 1069–1085.

Gladwell, G. M. L., 1976, "On Some Unbonded Contact Problems in Plane Elasticity Theory," ASME JOURNAL OF APPLIED MECHANICS, Vol. 43, pp. 263–267.

Hannah, M., 1951, "Contact Stress and Deformation in a Thin Elastic Layer," *Quarterly Journal of Mechanics and Applied Mathematics*, Vol. 4, pp. 95–105.

Hetényi, M., 1946,, *Beams on Elastic Foundation*, The University of Michigan Press, Ann Arbor, Mich.

Li, H., and Dempsey, J. P., 1990, "A Rigid Flat Indenter on an Elastic Layer Underlain by a Rigid Base," *Zeitschrift für angewandte Mathematik und Mechanik*, Vol. 70, No. 1, pp. 69–73.

Meijers, P., 1968, "The Contact Problem of a Rigid Cylinder on Elastic Layer," *Applied Scientific Research*, Vol. 18, pp. 353–383.

Sadowsky, M., 1928, "Zweidimensionale Probleme der Elastizitätstheorie," *Zeitschrift für angewandte Mathematik und Mechanik*, Vol. 8, pp. 107–121.

Selvadurai, A. P. S., 1979, *Elastic Analysis of Soil-Foundation Interaction*, Elsevier North-Holland, New York.

Simmonds, J. G., 1989, "Pointwise Errors in the Classical and in Reissner's Linear Theory of Plates, Especially for Concentrated Loads," *Journal of Elasticity*, in press.

Timoshenko, S., and Woinowsky-Krieger, S., 1959, *Theory of Plates and Shells*, 2nd ed., McGraw-Hill, New York.

Turcotte, D. L., 1979, "Flexure," *Advances in Geophysics*, Vol. 21, pp. 51–86.

Westergaard, H. M., 1926, "Stress in Concrete Pavements Computed by Theoretical Analysis," *Public Roads*, Vol. 7, pp. 25–35.

APPENDIX

Basic Line Load Solution

The two-dimensional problem of an infinite layer supported by a Winkler foundation and loaded by a unit line load is solved using a stress function approach as follows.

A stress function is assumed in the form of

$$\phi(x,z) = \int_0^\infty \{A_1(\alpha)\cosh(\alpha z) + A_2(\alpha)\sinh(\alpha z) + A_3(\alpha)\alpha z\cosh(\alpha z) + A_4(\alpha)\alpha z\sinh(\alpha z)\}\cos(\alpha x)d\alpha, \tag{A1}$$

which satisfies the biharmonic equation

$$\nabla^4\phi(x,z) = 0. \tag{A2}$$

The stresses and displacements can be calculated from $\phi(x,z)$ (Sneddon, 1951). The functions $A_1(\alpha)$, $A_2(\alpha)$, $A_3(\alpha)$, and $A_4(\alpha)$ can then be determined from the boundary conditions (1*a–d*). For a line load of unit intensity, the final expressions are found to be

$$\sigma_x^*(x,z) = \int_0^\infty \frac{\cos(\xi x)}{\pi D(\beta)}\Big\{\{\xi z\sinh^2\beta - (\beta + \sinh\beta\cosh\beta)\}\sinh(\xi z)$$

Downloaded 03 May 2010 to 171.66.16.244. Redistribution subject to ASME license or copyright; see http://www.asme.org/terms/Terms_Use.cfm

$$+\{\sinh^2\beta+\beta^2-\xi z(\beta+\sinh\beta\cosh\beta)\}\cosh(\xi z)$$
$$+\frac{h^4}{6l^4\beta}\Big\{(\xi z\sinh\beta\cosh\beta-\sinh^2\beta)\sinh(\xi z)$$
$$+\{\sinh\beta\cosh\beta-\beta-\xi z\sinh^2\beta\}\cosh(\xi z)\Big\}\Big\}d\xi, \quad \text{(A3)}$$

$$\sigma_z^*(x,z)=\int_0^\infty\frac{\cos(\xi x)}{\pi D(\beta)}\Big\{-\{\xi z\sinh^2\beta+(\beta+\sinh\beta\cosh\beta)\}\sinh(\xi z)$$
$$+\{\sinh^2\beta-\beta^2+\xi z(\beta+\sinh\beta\cosh\beta)\}\cosh(\xi z)$$
$$+\frac{h^4}{6l^4\beta}\{-(\xi z\sinh\beta\cosh\beta+\sinh^2\beta)\sinh(\xi z)$$
$$+\{\sinh\beta\cosh\beta+\beta+\xi z\sinh^2\beta\}\cosh(\xi z)\}\Big\}d\xi, \quad \text{(A4)}$$

$$\tau_{xz}^*(x,z)=\int_0^\infty\frac{\sin(\xi x)}{\pi D(\beta)}\Big\{\{\beta^2-\xi z(\beta+\sinh\beta\cosh\beta)\}\sinh(\xi z)+\xi z\sinh^2\beta\cosh(\xi z)$$
$$-\frac{h^4}{6l^4\beta}\{(\beta+\xi z\sinh^2\beta)\sinh(\xi z)-\xi z\sinh\beta\cosh\beta\cosh(\xi z)\}\Big\}d\xi, \quad \text{(A5)}$$

$$u^*(x,z)=\frac{1+\nu}{E}\int_0^\infty\frac{\sin(\xi x)}{\pi\xi D(\beta)}\Big\{\Big\{\xi z\sinh^2\beta-\frac{1-\nu}{1+\nu}(\beta+\sinh\beta\cosh\beta)\Big\}\sinh(\xi z)$$
$$-\Big\{\xi z(\beta+\sinh\beta\cosh\beta)-\frac{1-\nu}{1+\nu}\sinh^2\beta-\beta^2\Big\}\cosh(\xi z)$$
$$+\frac{h^4}{6l^4\beta}\Big\{\Big\{\xi z\sinh\beta\cosh\beta-\frac{1-\nu}{1+\nu}\sinh^2\beta\Big\}\sinh(\xi z)$$
$$-\Big\{\xi z\sinh^2\beta+\beta-\frac{1-\nu}{1+\nu}\sinh\beta\cosh\beta\Big\}\cosh(\xi z)\Big\}\Big\}d\xi, \quad \text{(A6)}$$

$$w^*(x,z)=\frac{1+\nu}{E}\int_0^\infty\frac{\cos(\xi x)}{\pi\xi D(\beta)}\Big\{\Big\{\frac{2}{1+\nu}\sinh^2\beta-\beta^2+\xi z(\beta+\sinh\beta\cosh\beta)\Big\}\sinh(\xi z)$$
$$-\Big\{\frac{2}{1+\nu}(\beta+\sinh\beta\cosh\beta)+\xi z\sinh^2\beta\Big\}\cosh(\xi z)$$
$$+\frac{h^4}{6l^4\beta}\Big\{\Big\{\frac{2}{1+\nu}\sinh\beta\cosh\beta+\beta+\xi z\sinh^2\beta\Big\}\sinh(\xi z)$$
$$-\Big\{\frac{2}{1+\nu}\sinh^2\beta+\xi z\sinh\beta\cosh\beta\Big\}\cosh(\xi z)\Big\}\Big\}d\xi, \quad \text{(A7)}$$

where $\beta = \xi h$, the characteristic length $l^4 = EI/k$, and $D(\beta)$ is defined in equation (7).

An arbitrary upper surface loading $p(x)$ on a layer supported by a Winkler medium may now be treated by using the above line load solution as follows:

$$f(x,z)=\int_\Omega p(\eta)f^*(|x-\eta|,z)d\eta, \quad \text{(A8)}$$

where Ω is the loaded region while f and f^* symbolically represent the physical quantity of interest.

Downloaded 03 May 2010 to 171.66.16.244. Redistribution subject to ASME license or copyright; see http://www.asme.org/terms/Terms_Use.cfm

Buckling and Post-Buckling Behavior of Elliptical Plates: Part I—Analysis

Herzl Chai
Polymers Division,
Materials Science and Engineering Laboratory,
National Institute of Standards and Technology,
Gaithersburg, MD 20899

A polynomial series expansion for displacements is used in conjunction with the Rayleigh-Ritz energy method to produce buckling and post-buckling stress solutions for an elliptically-shaped surface layer that has been delaminated from the main load-bearing body. Plate deformations are induced by a combined in-plane displacement field applied to the plate boundary and normal pressure. Convergence of the plate solution is assessed by systematically increasing the number of displacement terms in the series expansion. The convergence of membrane and bending stresses at the plate boundary was generally slow and nonuniform. The degrees-of-freedom necessary for a satisfactory solution typically increase with increasing complexity or magnitude of the plate deformations. By employing as many as 77 displacement terms, practically exact stress solutions are obtained for a wide variety of basic delamination plate problems. The proposed solution procedure is highly efficient and economical, and it may be easily extended to other plate geometries or loading conditions.

I Introduction

The ability of thin plates to carry load beyond their buckling stress has been long exploited in the design of aerospace structural components where weight savings is critical. More recently, the stress and deformation characteristics of thin plate elements have become of interest also in the analysis of delamination or debonding of subsurface layers; such failure is common in applications concerning protective or functional coatings (Gille, 1985), adhesion measurements (Dannenberg, 1961), and primary composite structures subjected to impact damage (Starnes and Williams, 1982; Chai, Knauss, and Babcock, 1983). Figure 1 shows a high-speed photo record of the collapse process of a multidirectional composite laminate under uniaxial compression following impact by a foreign object (Chai, Knauss and Babcock, 1983); the Moiré fringes in this print are contours of equal out-of-plane deformations. The bulge appearing in the second and third frames of this photo sequence is believed to represent a buckled group of surface plies that have been delaminated from the main laminate after impact. This initial damage has progressed to undamaged areas of the plate through a process of further delamination and buckling; thus leading to structural disintegration at a load which is only a fraction of the ultimate load of the undamaged laminate.

Figure 2 shows a simplified model of the delamination buckling problem discussed above. To successfully analyze the conditions for delamination propagation or arrest for this model problem in accordance with linear fracture mechanics concepts, it is first necessary to understand the deformation and

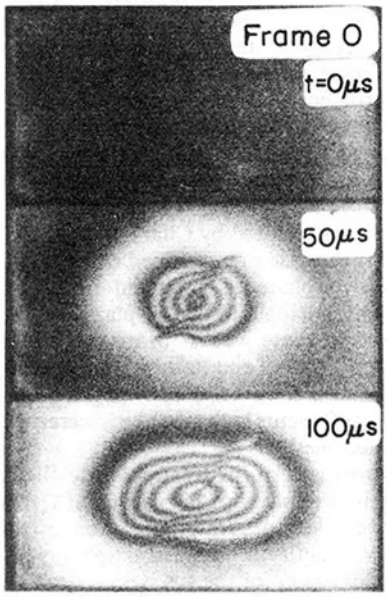


Fig. 1 A photo record showing propagation of delamination damage in a composite laminate following impact by a foreign object (Chai, Knauss, and Babcock, 1983). The laminate was loaded in compression along its vertical axis before the impactor struck. The dark and light bands are out-of-plane Moiré fringes; fringe constant = 0.33 mm.

Contributed by the Applied Mechanics Division of THE AMERICAN SOCIETY OF MECHANICAL ENGINEERS for presentation at the Winter Annual Meeting, Dallas, Texas, Nov. 25–30, 1990.

Discussion on this paper should be addressed to the Technical Editor, Leon M. Keer, The Technological Institute, Northwestern University, Evanston, IL 60208, and will be accepted until two months after final publication of paper itself in the JOURNAL OF APPLIED MECHANICS. Manuscript received by the ASME Applied Mechanics Division, May 26, 1989; final revision, Jan. 25, 1990.

Paper No. 90-WA/APM-36.

Copyright © 1990 by ASME
Downloaded 03 May 2010 to 171.66.16.244. Redistribution subject to ASME license or copyright; see http://www.asme.org/terms/Terms_Use.cfm

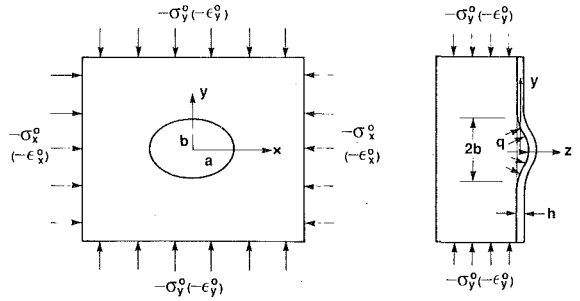


Fig. 2 Front (left) and sectional (right) views of an elliptically-shaped subsurface debond

stress behavior of the delaminated layer in both the buckling and the post-buckling regimes. The present plate problem differs from traditional large-deformation plate problems in a number of ways. First, because of the thinness of the surface layer, very large deformations ($w/h \gg 1$) may occur prior to crack propagation. Second, the layer is attached to the main material body, which may give rise to complex boundary conditions. Third, "sinusoidal" film deformations may occur leading to contact between the film surface and the substrate. Fourth, because the analysis of debond growth requires accurate solution for the square of bending and membrane stresses at the plate boundary (Chai, 1990), approximate plate solutions based on limited number of displacement terms may not be adequate. As a first step towards a mixed-mode fracture analysis of delamination growth, the present work is concerned with developing economical yet accurate large-deflection stress solution for the elliptical plate section of the structure shown in Fig. 2.

Geometrically nonlinear solutions for thin plates are typically available only in an approximate way. The majority of works deal with circular or rectangular plates (Timoshenko and Woinowsky-Krieger, 1959; Chia, 1980). The first large-deflection treatment of elliptical plates seems to be due to Weil and Newmark (1956), who have considered a clamped plate subjected to normal pressure. Motivated by the exact, small-deflection plate solution, Weil and Nemark employed a polynomial series expansion for the displacement field incorporating three out-of-plane and eight in-plane displacement terms. The displacement coefficients were then determined from the requirement that the potential energy of the system be stationary with respect to variations in any one of them. The same plate problem was later treated by Nash and Cooley (1959) using a polynomial series expansion consisting of five out-of-plane and 12 in-plane displacement terms, the nominal values of the displacement coefficients that were determined from the perturbation method. The solution approach by Weil and Newmark was adopted by Chai (1982) and Chai and Babcock (1985) for the case of a clamped elliptical plate subjected to a prescribed in-plane displacement field at its boundary. Only three out-of-plane and two-in-plane displacement terms were employed in these works. More recently, Kassapoglou (1988) has extended Chai and Babcock's solution by employing five out-of-plane and two-in-plane displacement terms. The displacement coefficients in that analysis were determined from the perturbation method.

The main drawback of the treatments detailed above is that the rather limited number of displacement terms used, while allowing for relatively accurate prediction of such quantities as buckling load, deflection and strain energy, typically leads to poor approximation for the stresses or strains, the accuracy that is generally worsened with increasing plate deformations. Moreover, the great computational effort involved in the above analyses makes a refinement of the solution through the addition of extra displacement terms practically impossible.

In this work a computing strategy is developed which allows for a treatment of virtually unlimited number of displacement terms in the polynomial series expansion. The nonlinear equations associated with solution of the displacement coefficients are expressed in closed form, with the total number of degrees-of-freedom being a user-controlled parameter. This makes it possible to obtain practically exact stress solutions for a wide range of plate problems in an economical and efficient way. Following the peer review of this paper, the author has become aware of a recent publication (Yin and Jane, 1989) dealing with the buckling and postbuckling behavior of elliptical plates. The analysis in that work was also based on the Rayleigh-Ritz energy method, with as many as 33 terms included in the displacement series. Both isotropic as well as anisotropic plates have been considered by Yin and Jane.

II. Problem Formulation and Solution

The problem considered is shown in Fig. 2. The thin, elliptical plate section is part of a large material body that is subjected to a biaxial strain field ("load") defined by ϵ_x^o and ϵ_y^o or, alternatively, by the following stress field:

$$\sigma_x^o = \frac{E}{(1-\nu^2)}(\epsilon_x^o + \nu\epsilon_y^o), \quad \sigma_y^o = \frac{E}{(1-\nu^2)}(\epsilon_y^o + \nu\epsilon_x^o) \tag{1}$$

where E and ν are the Young's modulus and Poisson's ratio, respectively, of the substrate or film. In addition, the plate may deform by a normal pressure, q. It is assumed that the thickness of the delaminated layer is negligibly small compared to the ellipse axes or all substrate dimensions. Under these conditions it is reasonable to assume that the delaminated layer can be treated as a clamped plate subjected to in-plane deformations at its boundary which are fully dictated by the substrate. These simplifying assumptions ("thin film" assumptions) have been adopted by a number of investigators treating one-dimensional strip (Chai, 1982), circle (Kachanov, 1976; Bottega and Maewal, 1983; Evans and Hutchinson, 1984; Yin, 1985) and elliptic (Chai, 1982; Chai and Babcock, 1985; Kassapoglou, 1988) debond geometry. The constraint conditions on the plate boundary are thus given by

$$u = x\epsilon_x^o$$

$$v = y\epsilon_y^o$$

$$w = \partial w/\partial x = \partial w/\partial y = 0 \tag{2a-c}$$

where u, v, and w are the displacements in the x, y, and z direction, respectively, and "a" and "b" are the ellipse semi-axes. Large deflection solution (in the von Karman sense) for this plate problem is desired. Let ϕ be a boundary function given by

$$\phi = -1 + x^2/a^2 + y^2/b^2. \tag{3}$$

Considering only symmetrical modes of deformations, the following displacement series satisfying equation (2) shall be assumed as an approximate solution to the problem at hand (Chai, 1982):

$$u = a\bar{x}\epsilon_x^o + \frac{\bar{x}h^2}{a\eta^4}(a_{1,1} + a_{1,2}\bar{y}^2 + \ldots + a_{1,N+1}\bar{y}^{2N} + a_{2,1}\bar{x}^2 + a_{2,2}\bar{x}^2\bar{y}^2 + \ldots + a_{N+1,1}\bar{x}^{2N})\phi$$

$$v = b\bar{y}\epsilon_y^o + \frac{\bar{y}h^2}{b}(b_{1,1} + \ldots b_{N+1,1}\bar{x}^{2N})\phi$$

$$w = h(c_{1,1} + c_{1,2}\bar{y}^2 + \ldots + c_{1,M+1}\bar{y}^{2M} + c_{2,1}\bar{x}^2 + c_{2,2}\bar{x}^2\bar{y}^2 + \ldots + c_{M+1,1}\bar{x}^{2M})\phi^2 \tag{4a-c}$$

where h is the plate thickness, $a_{1,1}\ldots$, $b_{1,1}\ldots$, $c_{1,1}\ldots$ are displacement coefficients, M and N are arbitrary summation integers, and

Downloaded 03 May 2010 to 171.66.16.244. Redistribution subject to ASME license or copyright; see http://www.asme.org/terms/Terms_Use.cfm

$$\bar{x} \equiv x/a,\ \bar{y} \equiv y/b,\ \eta \equiv b/a. \tag{5}$$

The total number of in-plane terms, N_T, and out-of-plane terms, M_T, are given by

$$N_T = (N+1)(N+2)$$
$$M_T = (M+1)(M+2)/2. \tag{6a-b}$$

It is advantageous to express ϕ and ϕ^2 as

$$\phi = \sum_{p=0}^{1}\sum_{q=0}^{1-p} \bar{f}_{p+1,\,q+1}\,\bar{x}^{2p}\bar{y}^{2q};\ \bar{f}_{1,\,1} = -1,\ \bar{f}_{1,\,2} = \bar{f}_{2,\,1} = 1$$

$$\phi^2 = \sum_{p=0}^{2}\sum_{q=0}^{2-p} f_{p+1,\,q+1}\,\bar{x}^{2p}\bar{y}^{2q};\ f_{1,\,1} = f_{1,\,3} = f_{3,\,1} = 1,$$
$$f_{1,\,2} = f_{2,\,1} = -f_{2,\,2} = -2. \tag{7a-b}$$

The displacements can then be expressed in the following compact form:

$$u = \left[\eta^2\lambda_x + \sum_{p=0}^{1}\sum_{q=0}^{1-p}\sum_{m=0}^{N}\sum_{n=0}^{N-m} \times \bar{f}_{p+1,\,q+1}a_{m+1,\,n+1}\,\bar{x}^{2(p+m)}\bar{y}^{2(q+n)}\right]\frac{\bar{x}h^2}{a\eta^4}$$

$$v = \left[\lambda_y + \ldots\ldots\ldots\ldots b_{m+1,\,n+1}\ldots\ldots\ldots\right]\frac{\bar{y}h^2}{b}$$

$$w = h\sum_{p=0}^{2}\sum_{q=0}^{2-p}\sum_{m=0}^{M}\sum_{n=0}^{M-m} f_{p+1,\,q+1}\,c_{m+1,\,n+1}\,\bar{x}^{2(p+m)}\,\bar{y}^{2(q+n)} \tag{8a-c}$$

where

$$\lambda_x \equiv \epsilon_x^o b^2/h^2,\ \lambda_y \equiv \epsilon_y^o b^2/h^2. \tag{9}$$

The potential energy due to pressure is

$$V = \iint_A qw\,dx\,dy, \tag{10}$$

where A is the ellipse area. The strain energy of the plate, U, can be expressed in terms of displacements and their derivatives (Timoshenko and Woinowsky-Krieger, 1959). The results for a specially orthotropic plate whose material axes are aligned in the x and y-axes are (Chai and Babcock, 1985):

$$U/\frac{E_y h}{2(1-\nu_{xy}\nu_{yx})} = \iint_A \Big\{k_1\,u_{,x}^{2} + v_{,y}^{2} + 2\nu_{xy}u_{,x}v_{,y} + \frac{(k_2-\nu_{xy})}{2}(u_{,y}+v_{,x})^2 + (k_2-\nu_{xy})(u_{,y}+v_{,x})\,w_{,x}\,w_{,y} + \nu_{xy}\,(u_{,x}\,w_{,y}^2 + v_{,y}\,w_{,x}^2) + (k_1u_{,x}w_{,x}^2 + v_{,y}w_{,y}^2) + \frac{1}{4}[k_1w_{,x}^4 + w_{,y}^4 + 2k_2w_{,x}^2\,w_{,y}^2] + \frac{h^2}{12}[k_1w_{,xx}^2 + w_{,yy}^2 + 2k_2w_{,xx}w_{,yy}]\Big\}dA \tag{11}$$

where comma indicates partial differentiation,

$$k_1 \equiv E_x/E_y,\ k_2 \equiv \nu_{xy} + \frac{2G_{xy}}{E_y}(1-\nu_{xy}\nu_{yx}),\ \nu_{yx} = \nu_{xy}E_y/E_x \tag{12}$$

and E_x, E_y, G_{xy} and ν_{xy} are the four orthotropic elastic constants. Note that terms associated with $w_{,xy}$ were omitted from equation (11) because their contributions vanish. For simplicity reasons in the analysis, yet without loss of generality, we shall assume in the present study that the plate is isotropic. Thus:

$$k_1 = k_2 = 1,\ \nu_{xy} = \nu_{yx} \equiv \nu,\ E_x = E_y \equiv E. \tag{13}$$

Consider next the contribution to U from a typical term in equation (11) such as $(\partial^2 w/\partial x^2)^2$. A double-derivation operation on w from equation (8c) leads to

$$R \equiv \iint_A \left(\frac{\partial^2 w}{\partial x^2}\right)^2 dA = \frac{64\eta h^2}{a^2}\int_0^1\int_0^{\sqrt{1-\bar{x}^2}} \sum_{m_1=0}^{M}\sum_{n_1=0}^{M-m_1}\sum_{m_2=0}^{M} \times \sum_{n_2=0}^{M-m_2}\sum_{p_1=0}^{2}\sum_{q_1=0}^{2-p_1}\sum_{P_2=0}^{2}\sum_{q_2=0}^{2-p_2} \times f_{p_1+1,\,q_1+1}\,f_{p_2+1,\,q_2+1}\,(p_1+m_1)\,(p_2+m_2)\,(p_1 + m_1 - 0.5)(p_2+m_2-0.5)\,c_{m_1+1,\,n_1+1}c_{m_2+1,\,n_2+1} \times \bar{x}^{2(p_1+m_1+p_2+m_2-2)}\,\bar{y}^{2(q_1+n_1+q_2+n_2)}d\bar{x}\,d\bar{y}. \tag{14}$$

The integrand in equation (14) can be integrated term by term. Noting that

$$4\int_0^1\int_0^{\sqrt{1-\bar{x}^2}} \bar{x}^{2i}\bar{y}^{2j}\,d\bar{x}\,d\bar{y} = \frac{\Gamma(i+0.5)\Gamma(j+0.5)}{\Gamma(i+j+2)} \equiv \pi B(i,j) \tag{15}$$

where i and j are integers, Γ is the Gamma function and "B" is used for abbreviation, one easily finds

$$R = \frac{16\pi\eta h^2}{a^2}\sum_{m_1,\,n_1}^{c}\sum_{m_2,\,n_2}^{c}\psi_{11}\,(m_1,\,n_1,\,m_2,\,n_2). \tag{16}$$

The symbol ψ_{11} in equation (16) represents a fourth-order array of constant numbers, the values are given in Appendix A, equation (A1). Also, the following shorthand notation is made:

$$\sum_{m_i,\,n_i}^{c} \equiv \sum_{m_i=0}^{M}\sum_{n_i=0}^{M-m_i} c_{m_i+1,\,n_i+1}. \tag{17}$$

Equation (16) shows that R is merely a summation of all the displacement coefficients, with the components of ψ_{11} serving as "weight" functions. By proceeding similarly with all other contributions to U, equation (11) is reduced to

$$U(\epsilon_x^o/\epsilon_y^o,\,\lambda_y,\,\eta,\,k_1,\,k_2,\,\nu_{xy})/\left[\frac{2\pi E_y h^5 a/b^3}{(1-\nu_{xy}\nu_{yx})}\right] = \sum_{e=1}^{3}\Bigg\{\sum_{m_1,\,n_1}^{c}\sum_{m_2,\,n_2}^{c}\Big[F_{1e}\,\psi_{1e}\,(m_1,\,n_1,\,m_2,\,n_2) + \lambda_y\,F_{1e}^{*}\psi_{1e}^{*}\,(m_1,\,n_1,\,m_2,\,n_2)\Big] + \sum_{m_3,\,n_3}^{c}\sum_{m_4,\,n_4}^{c} F_{2e}\psi_{2e}(m_1,\,n_1,\,m_2,\,n_2,\,m_3,\,n_3,\,m_4,\,n_4) + \sum_{m_3,\,n_3}^{a} F_{3e}\,\psi_{3e}(m_1,\,n_1,\,m_2,\,n_2,\,m_3,\,n_3) + \sum_{m_3,\,n_3}^{b} F_{4e}\,\psi_{4e}\,(m_1,\,n_1,\,m_2,\,n_2,\,m_3,\,n_3)\Big] + \sum_{m_1,\,n_1}^{a}\sum_{m_2,\,n_2}^{a} G_{1e}\Psi_{1e}(m_1,\,n_1,\,m_2,\,n_2) + \sum_{m_1,\,n_1}^{b}\sum_{m_2,\,n_2}^{b} G_{2e}\Psi_{2e}(m_1,\,n_1,\,m_2,\,n_2) + \sum_{m_1,\,n_1}^{a}\sum_{m_2,\,n_2}^{b} G_{3e}\,\Psi_{3e}(m_1,\,n_1,\,m_2,\,n_2)\Bigg\} + (k_1\lambda_x^2 + \lambda_y^2 + 2\nu_{xy}\lambda_x\lambda_y)/4 \tag{18}$$

where the following shorthand notations are made:

Downloaded 03 May 2010 to 171.66.16.244. Redistribution subject to ASME license or copyright; see http://www.asme.org/terms/Terms_Use.cfm

$$\sum_{m_i,\, n_i}^{a} \equiv \sum_{m_i=0}^{N} \sum_{n_i=0}^{N-m_i} a_{m_i+1,\, n_i+1}$$

$$\sum_{m_i,\, n_i}^{b} \equiv \sum_{m_i=0}^{N} \sum_{n_i=0}^{N-m_i} b_{m_i+1,\, n_i+1}. \qquad (19a\text{-}b)$$

As shown in Appendix A, the ψ's and Ψ's are arrays of known constants whose rank is defined by the number of variables enclosed by the corresponding parentheses. These arrays were evaluated *a priori* over the full range of their indices, i.e., m_1, $m_2 \ldots = 0\text{-}M$ (or $0\text{-}N$) and n_1, n_2, $\ldots = 0\text{-}M(0\text{-}N)$, and the results stored on a magnetic tape for later uses. The quantities F's and G's in equation (18) are arrays of constants that depend only on the problem parameters (see Appendix B).

The potential energy due to pressure is similarly evaluated from equations (10) and (8*c*) to be

$$V = \pi abqh \sum_{m,\, n}^{c} \psi_v\,(m,n) \qquad (20)$$

where

$$\psi_v(m,n) \equiv B(m,n) - 2B(m,n+1) + B(m,n+2) - 2B(m+1,n) + 2B(m+1,\, n+1) + B(m+2,\, n). \qquad (21)$$

The requirement that the total energy of the system be independent of variations with respect to any of the displacement coefficients leads to the following sets of nonlinear algebraic equations:

$$0 = F_a(i,j) \equiv \frac{\partial U}{\partial a_{i+1,\, j+1}} = \sum_{e=1}^{3} \left[\sum_{m_1,\, n_1}^{c} \sum_{m_2,\, n_2}^{c} \times F_{3e}\, \psi_{3e}(m_1,\, n_1,\, m_2,\, n_2,\, i,\, j) + 2 \sum_{m_1,\, n_1}^{a} G_{1e} \Psi_{1e}(m_1,\, n_1,\, i,\, j) + \sum_{m_1,\, n_1}^{b} G_{3e}\, \Psi_{3e}(i,\, j,\, m_1,\, n_1) \right], \quad i = 1, \ldots, N,\ j = 1, \ldots, N \qquad (22)$$

$$0 = F_b(i,j) \equiv \frac{\partial U}{\partial b_{i+1,\, j+1}} = \sum_{e=1}^{3} \left[\sum_{m_1,\, n_1}^{c} \sum_{m_2,\, n_2}^{c} \times F_{4e}\, \psi_{4e}(m_1,\, n_1,\, m_2,\, n_2,\, i,\, j) + 2 \sum_{m_1,\, n_1}^{b} G_{2e} \Psi_{2e}(m_1,\, n_1,\, i,\, j) + \sum_{m_1,\, n_1}^{a} G_{3e}\, \Psi_{3e}(m_1,\, n_1,\, i,\, j) \right], \quad i = 1, \ldots, N,\ j = 1, \ldots, N \qquad (23)$$

$$0 = F_c(i,j) \equiv \frac{\partial (U - V)}{\partial c_{i+1,\, j+1}} = \sum_{m_1,\, n_1}^{c} \sum_{e=1}^{3} \times \Big[F_{1e}\, [\psi_{1e}(m_1,\, n_1,\, i,\, j) + \psi_{1e}(i,j,\, m_1,n_1)] + 2\lambda_y F_{1e}^{*} \psi_{1e}^{*}\,(m_1,\, n_1,\, i,\, j) + 2 \sum_{m_2,\, n_2}^{c} \sum_{m_3,\, n_3}^{c} F_{2e}\, [\psi_{2e}\,(m_1,\, n_1,\, m_2,\, n_2,\, m_3,\, n_3,\, i,\, j) + \psi_{2e}\,(m_1,\, n_1,\, i,\, j,\, m_2,\, n_2,\, m_3,\, n_3)] + \sum_{m_3,\, n_3}^{a} F_{3e}\, [\psi_{3e}(m_1,\, n_1,\, i,\, j,\, m_3,\, n_3) + \psi_{3e}(i,\, j,\, m_1,\, n_1,\, m_3,\, n_3)] + \sum_{m_3,\, n_3}^{b} F_{4e}\, [\psi_{4e}(m_1,\, n_1,\, i,\, j,\, m_3,\, n_3) + \psi_{4e}(i,\, j,\, m_1,\, n_1,\, m_3,\, n_3)] \Big] - \frac{(1 - \nu_{xy}\nu_{yx})}{2} \gamma\, \psi_v\,(i,\, j),\ i = 1, \ldots, M,\ j = 1, \ldots, M, \qquad (24)$$

where

$$\gamma \equiv \frac{qb^4}{E_y h^4}.$$

For given problem parameters, the sets of equations (22)-(24) constitute the necessary conditions for solution of the displacement coefficients. In the numerical solution of these equations, it is advantageous to use the Jacobian associated with equation (24). The latter is easily found to be

$$J(i,\, j,\, k,\, l) \equiv \frac{\partial F_c(i,\, j)}{\partial c_{k+1,\, l+1}} = \sum_{e=1}^{3} \Big[2 \sum_{m_1,\, n_1}^{c} \sum_{m_2,\, n_2}^{c} \times F_{2e} [\psi_{2e}(m_1,\, n_1,\, m_2,\, n_2,\, k,\, l,\, i,\, j) + \psi_{2e}(k,\, l,\, i,\, j,\, m_2,\, n_2,\, m_1,\, n_1) + 2\psi_{2e}(m_1,\, n_1,\, i,\, j,\, m_2,\, n_2,\, k,\, l) + 2\psi_{2e}(m_1,\, n_1,\, k,\, l,\, i,\, j,\, m_2,\, n_2)] + 2\lambda_y F_{1e}^{*} \psi_{1e}^{*}\,(k,\, l,\, i,\, j) + F_{1e}\, [\psi_{1e}(k,\, l,\, i,\, j) + \psi_{1e}(i,\, j,\, k,\, l)] + \sum_{m_3,\, n_3}^{a} F_{3e}\, [\psi_{3e}(k,\, l,\, i,\, j,\, m_3,\, n_3) + \psi_{3e}(i,\, j,\, k,\, l,\, m_3,\, n_3)] + \sum_{m_3,\, n_3}^{b} F_{4e} [\psi_{4e}(k,\, l,\, i,\, j,\, m_3,\, n_3) + \psi_{4e}(i,\, j,\, k,\, l,\, m_3,\, n_3)] \Big].$$

$$i = 1, \ldots, M,\ j = 1, \ldots, M$$
$$k = 1, \ldots, M,\ l = 1, \ldots, M \qquad (26)$$

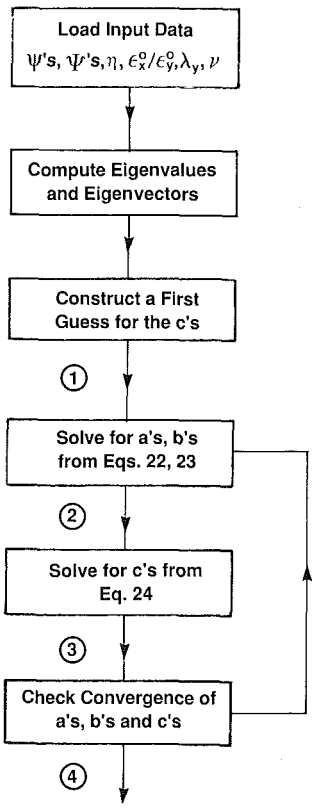


Fig. 3 *Computer flow chart of the numerical solution for the displacement coefficients*

Downloaded 03 May 2010 to 171.66.16.244. Redistribution subject to ASME license or copyright; see http://www.asme.org/terms/Terms_Use.cfm

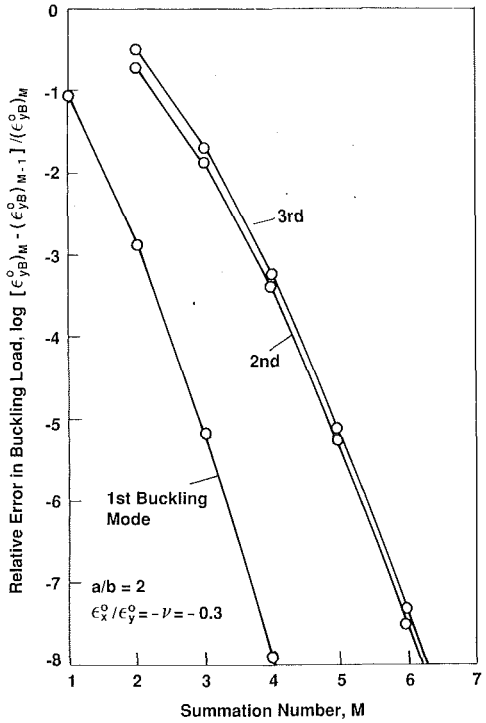


Fig. 4 The variations of first three buckling loads with number of displacement terms retained in the series expansion. Results are shown for an elliptical plate deforming under the action of a far-field, uniaxial compressive stress applied along the short axis of the ellipse. Lines connecting data points in this and all subsequent figures have only illustrative significance.

The buckling condition is obtained from equation (24) by setting γ and all the in-plane coefficients $a_{m,n}$, $b_{m,n}$ to zero, and neglecting all but first-order terms in the coefficients $c_{m,n}$. Equation (24) then reduces to the following eigenvalue problem:

$$\det \tilde{A} = 0, \tag{27}$$

where the components of the matrix A have the form

$$A_{rs} = \sum_{e=1}^{3} \Big[F_{1e} [\psi_{1e}(m_1, n_1, i, j) + \psi_{1e}(i, j, m_1, n_1)] + 2\lambda_y F^*_{1e} \Psi^*_{1e} (m_1, n_1, i, j) \Big]. \quad i = 1, \ldots, M, j = 1, \ldots, M \quad r = 1, \ldots, M_T, s = 1, \ldots, M_T \tag{28}$$

Equation (27) is a standard eigenvalue problem in λ_y provided the parameters η and $\epsilon^o_x/\epsilon^o_y$ are predetermined.

III Numerical Solution

Equations (27) and (22)–(24) were solved numerically on a Cyber 205 supercomputer. A flow chart of the computing procedure is shown in Fig. 3. This part of the work focuses on the convergence behavior of the solution. A rather detailed study of buckling and post-buckling deformations and stresses in the plate is given in Part II. All data to be presented herein were generated for an isotropic plate, with ν taken as 0.3.

Buckling Analysis. The buckling equations were solved using available computer routines. Both eigenvalues and eigenvectors were determined. Convergence of buckling loads was examined for a range of problem parameters utilizing up to 45 out-of-plane displacement terms ($M = 8$). The buckling stress

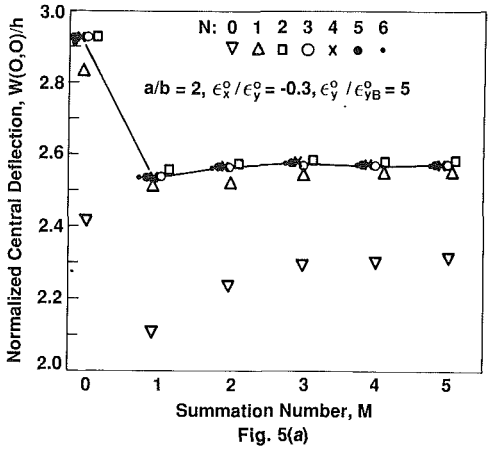


Fig. 5(*a*)

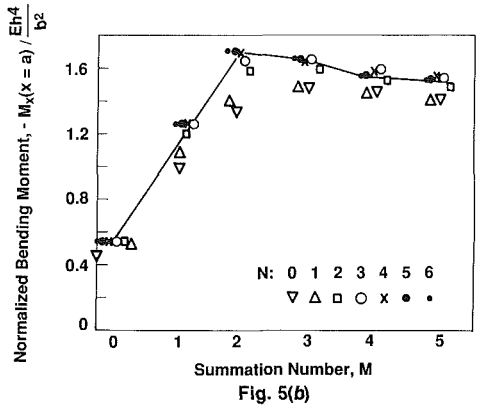


Fig. 5(*b*)

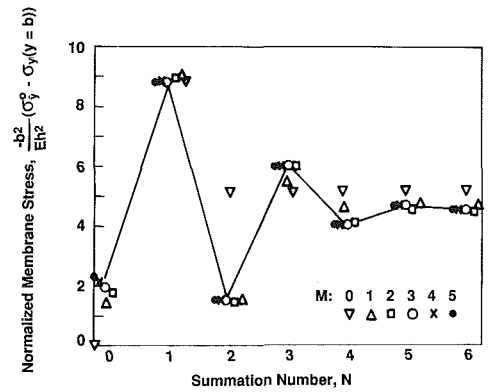


Fig. 5(*c*)

Fig. 5 Convergence behavior of normalized central deflection (*a*), bending moment at the end of the ellipse major axis (*b*), and "jump" in membrane normal stress at the end of the ellipse minor axis for an elliptical plate (η = 0.5) deforming under the action of a far-field, uniaxial compressive stress applied along its short axis. The applied strain is five times the buckling strain, which is given by $\epsilon^o_{yb} = -1.24h^2/b^2$.

for a uniformally loaded circular plate was found to agree with the exact solution given in Timoshenko and Woinowsky-Kreiger (1959). Figure 4 shows the dependence of buckling load on the number of displacement terms employed for a uniaxially loaded ellipse. Results are given for the first three buckling modes. For illustrative purposes only, the data in this and all subsequent figures were connected by straight lines. All buckling loads in Fig. 4 exhibit an initial phase of slow convergence which is followed by a more rapid one as M becomes large. The number of terms needed for a given accuracy seems to increase with increasing the buckling mode number, which is due to the increasing complexity of the associated plate deformations (Chai, Part II.)

Downloaded 03 May 2010 to 171.66.16.244. Redistribution subject to ASME license or copyright; see http://www.asme.org/terms/Terms_Use.cfm

Large-Deflection Analysis. Post-buckling solutions were obtained using an iterative scheme that employed available algorithms for solving linear and nonlinear algebraic equations. As shown in Fig. 3, the solution procedure consisted of first solving equations (22) and (23) as linear equations in the unknowns $a_{m,n}$ and $b_{m,n}$, with the values of $c_{m,n}$ being provided as a guess. Using the so obtained values of the in-plane coefficients and the initial guess for the out-of-plane displacement coefficients, equation (24) was then used to solve for $c_{m,n}$ using a standard nonlinear algorithm. This iterative process was repeated until sufficient convergence of the displacement coefficients was achieved. This solution technique, which is commonly used in structural plate problems (e.g., Chia, 1980), has greatly reduced computing time and computer storage requirements.

Error is defined as the largest relative difference between two successive iterations among all the displacement coefficients, i.e.,

$$E = \max\ |E_a, E_b, E_c| \tag{29}$$

where

$$E_a \equiv |[(a_{m+1,n+1})_k - (a_{m+1,n+1})_{k-1}]/(a_{m+1,n+1})_k|,$$
$$m = 0,\ldots, N,\ n = 0,\ldots, N \tag{30}$$

and k denotes the iteration number; similar expressions as in equation (30) apply for E_b and E_c. As many as 40 iterations were used to ensure that the error "E" in equation (29) was less than 0.001. To start the iteration process, an initial guess to the c's is needed. The selection of these coefficients is critical when the plate deflection is complex. Initial guess for the c's was obtained from the corresponding eigenvector solution, with all displacement coefficients normalized by a common factor whose value, determined by trial and error, was dictated by the ratio of applied load to buckling load. The initial load was typically set at about 40 percent above the buckling load. The desired load level was then reached by incrementing the load in sufficiently small steps. Convergence of the plate solution was assessed by systematically increasing the number of in-plane and out-of-plane displacement terms. As many as 77 displacement terms were used to insure practically exact stress and deformation values for all plate configurations analyzed in this work.

Bending and membrane stresses at the plate boundary are useful in predicting the individual components of the energy release rate which are responsible for delamination growth or arrest (Chai, 1990). Figure 5 shows the convergence behavior of boundary membrane stresses and central deflection for a uniaxially loaded ellipse, the applied load being five times the buckling load. The normal-to-the-boundary bending moment, M_n, and the "jump" in membrane normal stress across the crack border, $\sigma_n^o - \sigma_n$, given in this figure are specified at $(\bar{x}, \bar{y}) = (1, 0)$ and $(0, 1)$, respectively, where these quantities attain their respective maximum. These stresses were calculated from the following equations which were derived from equation (8) and Timoshenko and Woinowsky-Kreiger (1959):

$$\left.\begin{aligned}
(\sigma_n^o - \sigma_n)\frac{b^2}{Eh^2} &= \frac{-2}{(1-\nu^2)}\sum_{m=0}^{N}\sum_{n=0}^{N-m}\bar{x}^{2m}(1-\bar{x}^2)^n \\
&\times\left(\frac{\bar{x}^2}{\eta^2}a_{m+1,n+1} + \bar{y}^2 b_{m+1,n+1}\right) \\
(\tau_{nt}^{\sigma} - \tau_{nt})\frac{b^2}{Eh^2} &= \frac{\eta\bar{x}\bar{y}}{(1+\nu)}\sum_{m=0}^{N}\sum_{n=0}^{N-m}\bar{x}^{2m}(1-\bar{x}^2)^n\left(\frac{a_{m+1,n+1}}{\eta^4} - b_{m+1,n+1}\right) \\
M_n\frac{b^2}{Eh^4} &= \frac{-2}{3(1-\nu^2)}[1-(1-\eta^2)\bar{x}^2]\sum_{m=0}^{M}\sum_{n=0}^{M-m} \\
&\times c_{m+1,n+1}\bar{x}^{2m}(1-\bar{x}^2)^n \\
&\bar{x} = 0 - 1
\end{aligned}\right\} \tag{31}$$

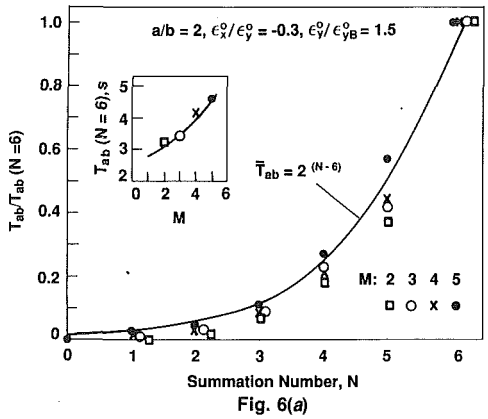


Fig. 6(*a*)

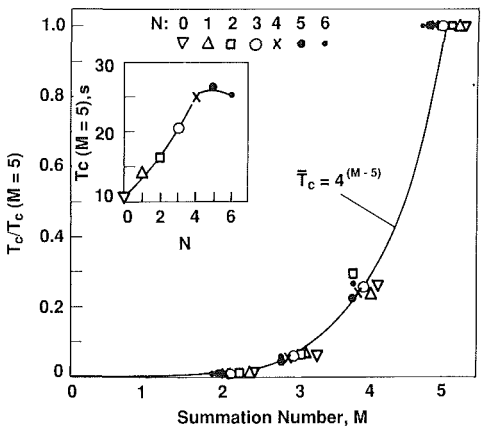


Fig. 6(*b*)

Fig. 6 Dependence of computer run time associated with solution of the displacement coefficients on the number of terms used in the series expansion. Results are presented for a 2 to 1 ellipse loaded uniaxially along the minor axis. Referring to Fig. 3 for notation, T_{ab} (Fig. 6(*a*)) is the run time associated with solution of the in-plane coefficients (equations (22)–(23)), while T_c (Fig. 6(*b*)) is the run time for the out-of-plane coefficients, (equation (24)).

where n and t denote, respectively, normal and tangential coordinates. The central deflection (Fig. 5(*a*)) seems to converge rapidly with increasing M or N, with error that is less than one percent when M and N are increased beyond 2. In contrast, convergence of the normal membrane stress (Fig. 5(*c*)) is slow and nonuniform, resembling an interesting "sinusoidal" variation with an "exponential" decay as N is increased. The bending moment (Fig. 5(*b*)) seems to be largely controlled by the out-of-plane displacement terms while the normal stress (Fig. 5(*c*)) is largely dictated by the in-plane terms. The influence of the latter terms was found to increase with increasing the ratio of applied load to buckling load.

Downloaded 03 May 2010 to 171.66.16.244. Redistribution subject to ASME license or copyright; see http://www.asme.org/terms/Terms_Use.cfm

Computer run time and computer memory requirements become critical when large number of displacement terms are employed. Figure 6 provides information on the variation of computing time with increasing number of degrees-of-freedom. Referring to Fig. 3 for notation, T_{ab} and T_c denote the total computing time spent on solving the set of linear equations associated with the in-plane terms, equations (22)–(23), and the set of nonlinear equations associated with the out-of-plane terms, equation (24), respectively. Note from Fig. 3 that $T_4 - T_1 = T_{ab} + T_c$. Figure 6 shows that the dependence of computer run time on the summation parameters M and N is reasonably well described by the following empirical relationships:

$$\bar{T}_{ab} \equiv T_{ab}(M, N)/T_{ab}(M, N=6) = 2^{(N-6)}$$
$$\bar{T}_c \equiv T_c(M, N)/T_c(M=5, N) = 4^{(M-5)} \qquad (32a\text{–}b)$$

where T_{ab} $(M, N=6)$ and T_c $(M=5, N)$ are the run times for the particular choice $N=6$ and $M=5$, respectively. The variations of T_{ab} $(N=6)$ with M and of T_c $(M=5)$ with N are also given in Fig. 6. Figure 6 and equation (32) show that both T_{ab} and T_c increase rapidly with increasing the number of displacement terms used in the series expansion. However, the rate of increase as well as the absolute magnitude are much greater for T_c than T_{ab}. This is readily understood from the fact that T_{ab} is associated with solution of linear equations while T_c with nonlinear equations. Taking advantage of this, one may thus construct a solution of a comparable accuracy for the plate problem of Fig. 5 by first determining the normal and tangential membrane stresses using $M=2$, $N=5$, and then determining the bending moment from a different computer run using $M=4$, $N=5$. The combined run time for these two operations is nine seconds (Fig. 6), which is much less than for a single run based on $M=5$, $N=6$ (30 s (Fig. 6)).

V Summary and Conclusions

A polynomial series expansion was used in conjunction with the Rayleigh-Ritz energy method to obtain buckling and large-deflection solutions for thin elliptical plates deforming under edge thrust or normal pressure. The governing equations necessary for a solution of the displacement coefficients were expressed in a closed form, with the number of degrees-of-freedom in the series expansion being a user-controlled parameter.

A convergence study utilizing up to 77 displacement terms shows that the boundary stresses in the plate tend to converge in a slow and nonuniform fashion as the number of degrees-of-freedom is increased, but excellent engineering accuracy could always be obtained economically if sufficient displacement terms are retained in the series expansion. The bending stresses are influenced much more by the out-of-plane displacement terms than the in-plane terms, while the opposite holds true for the membrane stresses. It was also found that the in-plane terms become more and more dominating as the loading or plate deformations are increased. The overall solution could be constructed much more efficiently by combining partial solutions from repeated computer runs.

The solution technique developed in this work can be readily extended to other plate problems, including plates undergoing nonsymmetrical deformations which may be induced either by material anisotropy or by application of far-field shear stresses. The present equations for solution of the displacement coefficients hold true also for other plate geometries such as rectangular, triangular, oblong, etc., provided only that the boundary function ϕ is appropriately modified.

References

Bottega, W. J., and Maewal, A., 1983, "Delamination Buckling and Growth in Laminates," ASME Journal of Applied Mechanics, Vol. 50, pp. 184–189.

Chai, H., 1982, "The Growth of Impact Damage in Compressively Loaded Laminates," Ph.D. Thesis, California Institute of Technology.

Chai, H., Knauss, W. G., and Babcock, C. D., 1983, "Observation of Damage Growth in Compressively Loaded Laminates," *Experimental Mechanics*, Vol. 23, No. 3, pp. 329–337.

Chai, H., and Babcock, C. D., 1985, "Two-Dimensional Modelling of Compressive Failure in Delaminated Laminates," *Journal of Composite Materials*, Vol. 19, pp. 67–98.

Chai, H., 1990, "Buckling and Post-Buckling Behavior of Elliptical Plates: Part II—Results," ASME Journal of Applied Mechanics, Vol. 57, pp. 989–994.

Chai, H., 1990, "Three-Dimensional Fracture Analysis of Thin-Film Debonding," *International Journal of Fracture*, in press.

Chia, Chuen-Yuan, *Nonlinear Analysis of Plates*, McGraw-Hill, New York, 1980.

Dannenberg, H., 1961, "Measurement of Adhesion by a Blister Method," *Journal of Applied Polymer Science*, Vol. 5, pp. 125–134.

Evans, A. G., and Hutchinson, J. W., 1984, "On the Mechanics of Delamination and Spalling in Compressed Films," *International Journal of Solids and Structures*, Vol. 20, pp. 455–466.

Gille, G., 1985, "Strength of Thin Films and Coatings," *Current Topics in Materials Science*, E. Kaldis, ed., Vol. 12, North-Holland, pp. 421–449.

Kachanov, L. M., 1976, "Separation Failure of Composite Materials," *Polymer Mechanics*, Vol. 12, pp. 812–815.

Kassapoglou, C., 1988, "Buckling, Post-Buckling and Failure of Elliptical Delaminations in Laminates Under Compression," *Composite Structures*, Vol. 9, pp. 139–159.

Nash, W. A., and Cooley, I. D., 1959, "Large Deflections of a Clamped Elliptical Plate Subjected to Uniform Pressure," ASME Journal of Applied Mechanics, pp. 291–293.

Starnes, J. H., Jr., and Williams, J. G., 1982, "Failure Characteristics of Graphite-Epoxy Structural Components Loaded in Compression," *Mechanics of Composite Materials: Recent Advances*, Z. Hashin, ed., Pergamon Press, pp. 283–306.

Timoshenko, S., and Woinowsky-Krieger, S., 1959, *Theory of Plates and Shells*, McGraw-Hill, New York.

Weil, N. A., and Newmark, N. M., 1956, "Large Deflections of Elliptical Plates," ASME Journal of Applied Mechanics, Vol. 23, pp. 21–26.

Yin, W. L., 1985, "Axisymmetric Buckling and Growth of a Circular Delamination in a Compressed Laminate," *International Journal of Solids and Structures*, Vol. 21, pp. 503–514.

Yin, W. L., and Jane, K. C., 1989, "Postbuckling Analysis of Laminated Elliptical Plates with Application to Delamination Growth," *Proceedings AIAA/ASME/ASCE/AHS 30th SDM Conference*, Mobile, Ala., Apr. 3–5, 1989, pp. 121–134.

APPENDIX A

The arrays ψ's and Ψ's in equation (18) are given as follows. The functions "B", f, and $\bar{f}$ in these expressions are defined in equations (15) and (7), respectively.

$$\psi_{1e}(m_1, n_1, m_2, n_2) = \sum_{p_1=0}^{2} \sum_{q_1=0}^{2-p_1} \sum_{p_2=0}^{2} \sum_{q_2=0}^{2-p_2} \times f_{p_1+1,\, q_1+1} f_{p_2+1,\, q_2+1}\, T_{1e} B(p_1+m_1+p_2 + m_2-3+e,\ q_1+n_1+q_2+n_2-e+1),\ e=1-3 \qquad \text{(A1)}$$

$$T_{11} = (p_1+m_1)(p_2+m_2)(p_1+m_1-0.5)(p_2+m_2-0.5)$$
$$T_{12} = (p_1+m_1)(p_1+m_1-0.5)(q_2+n_2)(q_2+n_2-0.5)$$
$$T_{13} = (q_1+n_1)(q_2+n_2)(q_1+n_1-0.5)(q_2+n_2-0.5)$$

$$\psi^*_{1e}(m_1, n_1, m_2, n_2) = \sum_{p_1=0}^{2} \sum_{q_1=0}^{2-p_1} \sum_{p_2=0}^{2} \sum_{q_2=0}^{2-p_2} f_{p_1+1,\, q_1+1} \times f_{p_2+1,\, q_2+1}\, T^*_{1e} B(p_1+m_1+p_2+m_2 - e+1,\ q_1+n_1+q_2+n_2-2+e),\ e=1, 2 \qquad \text{(A2)}$$

$$T^*_{11} = (q_1+n_1)(q_2+n_2)$$
$$T^*_{12} = (p_1+m_1)(p_2+m_2)$$

$$\psi_{2e}(m_1, n_1, m_2, n_2, m_3, n_3, m_4, n_4) = \sum_{p_1=0}^{2} \sum_{q_1=0}^{2-p_1} \sum_{p_2=0}^{2} \sum_{q_2=0}^{2-p_2} \sum_{p_3=0}^{2} \sum_{q_3=0}^{2-p_3} \sum_{p_4=0}^{2} \sum_{q_4=0}^{2-p_4} \times f_{p_1+1,\, q_1+1} f_{p_2+1,\, q_2+1} f_{p_3+1,\, q_3+1} f_{p_4+1,\, q_4+1}$$

Downloaded 03 May 2010 to 171.66.16.244. Redistribution subject to ASME license or copyright; see http://www.asme.org/terms/Terms_Use.cfm

$$\times T_{2e}\, B(-3+e+\sum_{i=1}^{4}(p_i+m_i),\ -e+1+\sum_{i=1}^{4}(q_i+n_i)),$$

$$e=1-3 \quad \text{(A3)}$$

$$T_{21}=(p_1+m_1)(p_2+m_2)(p_3+m_3)(p_4+m_4)$$
$$T_{22}=(p_1+m_1)(p_2+m_2)(q_3+n_3)(q_4+n_4)$$
$$T_{23}=(q_1+n_1)(q_2+n_2)(q_3+n_3)(q_4+n_4)$$
$$\psi_{ie}(m_1, n_1, m_2, n_2, m_3, n_3)$$
$$=\sum_{p_1=0}^{2}\sum_{q_1=0}^{2-p_1}\sum_{p_2=0}^{2}\sum_{q_2=0}^{2-p_2}\sum_{p_3=0}^{1}\sum_{q_3=0}^{1-p_3}$$
$$\times f_{p_1+1,\,q_1+1}\, f_{p_2+1,\,q_2+1}\, \bar{f}_{p_3+1,\,q_3+1}\, T_{ie}\, B(\alpha_i(e)$$
$$+\sum_{i=1}^{3}(p_i+m_i),\ \beta_i(e)+\sum_{i=1}^{3}(q_i+n_i))$$
$$e=1,2,\ i=3,4 \quad \text{(A4)}$$

$$\alpha_3(1)=\alpha_3(3)=\beta_3(2)=0,\ \alpha_3(2)=\beta_3(1)=\beta_3(3)=-1$$
$$\alpha_4(1)=\beta_4(2)=\beta_4(3)=0,\ \alpha_4(2)=\alpha_4(3)=\beta_4(1)=-1$$
$$T_{31}=(q_1+n_1)(q_2+n_2)(p_3+m_3+0.5)$$
$$T_{32}=(p_1+m_1)(p_2+m_2)(p_3+m_3+0.5)$$
$$T_{33}=(p_1+m_1)(q_2+n_2)(q_3+n_3)$$
$$T_{41}=(q_1+n_1)(q_2+n_2)(q_3+n_3+0.5)$$
$$T_{42}=(p_1+m_1)(p_2+m_2)(q_3+n_3+0.5)$$
$$T_{43}=(p_1+m_1)(q_2+n_2)(p_3+m_3)$$

$$\Psi_{ie}(m_1, n_1, m_2, n_2)=\sum_{p_1=0}^{1}\sum_{q_1=0}^{1-p_1}\sum_{p_2=0}^{1}\sum_{q_2=0}^{1-p_2}$$
$$\times \bar{f}_{p_1+1,\,q_1+1}\, \bar{f}_{p_2+1,\,q_2+1}\, S_{ie}$$
$$\times B(p_1+m_1+p_2+m_2+\phi_i,\ q_1+n_1+q_2+n_2-\phi_i)$$
$$e=1,2,\ i=1-3 \quad \text{(A5)}$$

$$\phi_1=e-1,\ \phi_2=-\phi_1,\ \phi_3=0$$
$$S_{11}=(p_1+m_1+0.5)(p_2+m_2+0.5)$$
$$S_{12}=(q_1+n_1)(q_2+n_2)$$
$$S_{21}=(q_1+n_1+0.5)(q_2+n_2+0.5)$$
$$S_{22}=(p_1+m_1)(p_2+m_2)$$
$$S_{31}=(p_1+m_1+0.5)(q_1+n_1+0.5)$$
$$S_{32}=(q_1+n_1)(p_2+m_2)$$

APPENDIX B

The arrays F's and G's in equation (18) are given as follows:

$$\left.\begin{aligned}
&[F_{11}, F_{12}, F_{13}]=[k_1\eta^4,\ 2k_2\eta^2,\ 1]/3\\
&[F^*_{11}, F^*_{12}, F^*_{13}]=[\nu_{xy}\epsilon^o_x/\epsilon^o_y+1,\ \eta^2(\nu_{xy}+k_1\epsilon^o_x/\epsilon^o_y),\ 0]\\
&[F_{21}, F_{22}, F_{23}]=[k_1\eta^4,\ 2k_2\eta^2,\ 1]\\
&[F_{31}, F_{32}, F_{33}]=2[\nu_{xy},\ k_1\eta^2,\ k_2-\nu_{xy}]/\eta^2\\
&[F_{41}, F_{42}, F_{43}]=2[1, \nu_{xy}\eta^2,\ (k_2-\nu_{xy})\eta^2]\\
&[G_{11}, G_{12}, G_{13}, G_{21}, G_{22}, G_{31}, G_{32}, G_{33}]\\
&=[k_1/\eta^2,\ (k_2-\nu_{xy})/2\eta^4,\ 0,\ \eta^2,\\
&(k_2-\nu_{xy})\eta^4/2, 0, 2\nu_{xy},\ k_2-\nu_{xy},\ 0]/\eta^2
\end{aligned}\right\} \quad \text{(B1)}$$

Downloaded 03 May 2010 to 171.66.16.244. Redistribution subject to ASME license or copyright; see http://www.asme.org/terms/Terms_Use.cfm

Buckling and Post-buckling Behavior of Elliptical Plates: Part II—Results

Herzl Chai
Polymers Division,
Materials Science and Engineering Laboratory,
National Institute of Standards and Technology,
Gaithersburg, MD 20899

The large-deflection plate solution developed in Part I is used here to study the buckling and post-buckling deformation and stress characteristics of an elliptically-shaped surface layer that has been delaminated from a large material body. The economical, yet accurate nature of this solution, together with available graphic routines, has made it possible to present, figuratively, a comprehensive description of the plate behavior. The conditions for a layer-substrate overlap and the variations of membrane and bending stresses along the plate boundary are emphasized. Deformations were induced either by a normal pressure or a biaxial displacement field applied to the plate boundary. The problem variables are plate size and shape, details of load biaxiality, and load level.

I Introduction

In Part I of this work, a large-deflection plate analysis was developed to account for deformations and stresses in the elliptical plate section ("film") of the delaminated structure ("substrate") shown in Fig. 1. The plate was assumed to be thin, homogeneous, and isotropic, with a clamp-type boundary support. The elastic constants of the film and substrate were assumed to be identical. Deformations in the plate were induced by a normal pressure, q, and/or in-plane displacements applied to the plate boundary. In accordance with the "thin film" approximation (Chai and Babcock, 1985), the following constraints thus hold on the plate boundary which is defined by $x^2/a^2 + y^2/b^2 = 1$.

$$u = x\epsilon_x^o$$
$$v = y\epsilon_y^o$$
$$w = \partial w/\partial x = \partial w/\partial y = 0 \qquad (1a\text{–}c)$$

where "a" and "b" are the semi-major and semi-minor axis of the ellipse, respectively, u, v, and w are the displacements in the x, y, and z direction, in that order, and ϵ_x^o and ϵ_y^o are the far-field strains ("loads"). Approximate large-deflection plate solutions in the von Karman sense were obtained (Chai, Part I) by employing a polynomial series expansion for the displacement field, with the displacement coefficients determined from a Rayleigh-Ritz type energy approach. Only symmetrical modes of deformations were considered. The numerical analysis was formulated such that the number of displacement terms could be arbitrarily controlled, which made it easy to study systematically the convergence properties of all field quantities of interest. By employing as many as 77 displacement terms in the series expansion, convergence of all quantities to be presented here was insured to be better than a few percent.

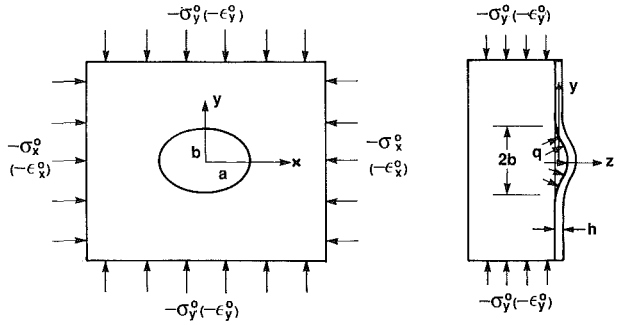


Fig. 1 Thin film delamination buckling model

Following the peer review of this paper, the author has become aware of a parallel publication (Yin and Jane, 1989) dealing with the buckling and post-buckling behavior of elliptically-shaped delamination plates. In their work, Yin and Jane studied the convergence behavior of central deflection, boundary force, boundary moment, and total energy release rate at select points on the delamination boundary for a number of plate configurations by utilizing up to 33 terms in the series expansion for displacements.

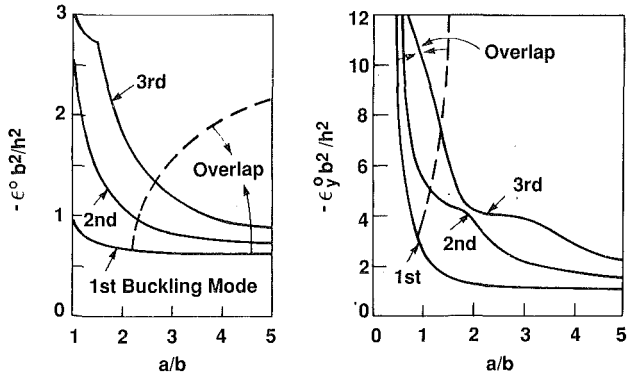
In this part the deformation and stress characteristics of the delaminated film are presented with an eye towards application to delamination crack problems. Special emphasis is placed on elucidating the conditions at which the film and substrate may overlap, and on the behavior of membrane and bending stresses at the plate boundary; these stresses are directly related to the stress intensity factors of the delamination crack (Chai, 1990).

Contributed by the Applied Mechanics Division of THE AMERICAN SOCIETY OF MECHANICAL ENGINEERS for presentation at the Winter Annual Meeting, Dallas, Texas, Nov. 25–30, 1990.

Discussion on this paper should be addressed to the Technical Editor, Leon M. Keer, the Technological Institute, Northwestern University, Evanston, IL 60208, and will be accepted until two months after final publication of the paper itself in the JOURNAL OF APPLIED MECHANICS. Manuscript received by the ASME Applied Mechanics Division, May 26, 1989; final revision, Jan. 25, 1990.

Paper No. 90-WA/APM-37.

Copyright © 1990 by ASME
Downloaded 03 May 2010 to 171.66.16.244. Redistribution subject to ASME license or copyright; see http://www.asme.org/terms/Terms_Use.cfm



(a) Uniform Compression, $\epsilon_x^o = \epsilon_y^o \equiv \epsilon^o$

(b) Uniaxial Compression, $\epsilon_x^o/\epsilon_y^o = -\nu = -0.3$

Fig. 2 Buckling load as a function of ellipse aspect ratio, (*a*) uniform load case, (*b*) uniaxial load case. Results are shown for the first three buckling modes. The conditions for a film substrate overlap in the post-buckling regime for the first buckling mode are identified in the figure by dashed curves. These overlap regions were obtained from the plate analysis. More accurate interaction regions, predicted from a combined plate/elasticity solution, are given in Chai, 1990.

The effect of stress biaxiality is highlighted by considering two loading cases of practical interest, namely "uniform" and "uniaxial." For the uniform case,

$$\epsilon_x^o = \epsilon_y^o \equiv \epsilon^o, \quad \sigma_x^o = \sigma_y^o \equiv \sigma^o = E\epsilon^o/(1-\nu). \tag{2}$$

For the uniaxial load case,

$$\sigma_x^o = 0, \quad \sigma_y^o = E\epsilon_y^o, \quad \epsilon_x^o = -\nu\epsilon_y^o, \tag{3}$$

where E and ν are the Young's modulus and Poisson's ratio, respectively, of the plate or substrate, and σ_x^o and σ_y^o are the stresses applied to the substrate. In all subsequent illustrations, the Poisson's ratio is taken to be 0.3. Note that the uniform load case would be identical to the case where the film is deformed under a temperature gradient if

$$\epsilon^o \equiv -(\alpha_f - \alpha_s)\Delta T, \tag{4}$$

where α_f and α_s are the thermal coefficients of expansion of the film and the substrate, respectively, ΔT is the temperature gradient, and $\alpha_f > \alpha_s$.

II Buckling Behavior

Figure 2 shows the variations of the first three buckling loads with plate aspect ratio for uniaxial and uniform loadings. For both cases, the buckling load corresponding to the first buckling mode seems to vary only little for large aspect ratios ($a/b > 2$) while increasing sharply as a/b is decreased from unity. The behavior for the higher buckling modes differs from that of the first mode in that the variations with a/b may not be monotonic. It is also apparent that for moderate aspect ratios the buckling resistance of the higher-order modes may considerably exceed that of the fundamental buckling mode.

The dependence of the first buckling load on the detail of loading is shown in Fig. 3 for three aspect ratios, namely $a/b = 1$, 2, and 4. In the first quadrant both loadings are compressive, while in the second and fourth quadrants one loading is compressive while the other is tensile. For a given value of b, the buckling strength is seen to increase with decreasing a/b. It is also apparent that the least buckling resistance for a circular plate occurs under uniform loading, i.e., when $\epsilon_x^o = \epsilon_y^o$.

The range in tensile loading that can be applied along the a axis of the ellipse while the plate remains in a buckled form is defined by the solid curve in Fig. 4; as shown, buckling may occur only in the region above that curve. Buckling is seen to occur more easily when the compressive load is applied along

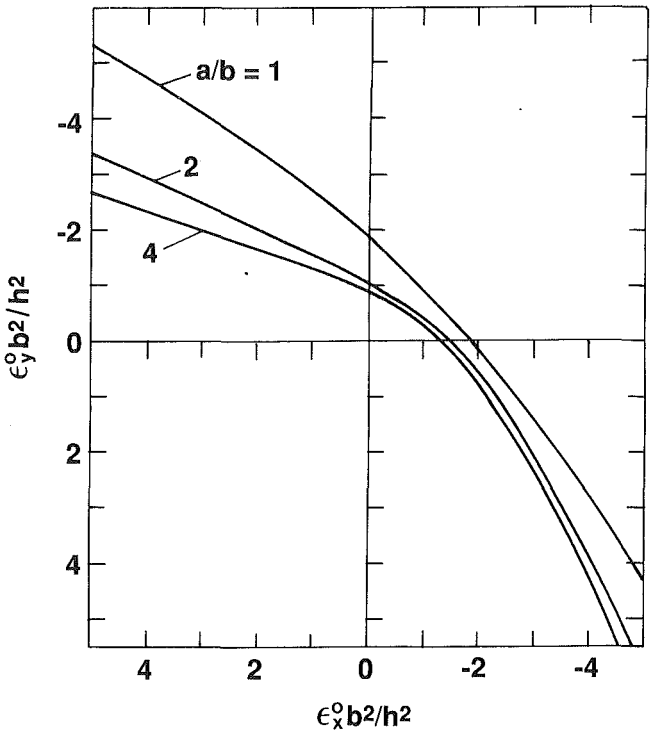


Fig. 3 Variation of buckling load (first buckling mode) with details of load biaxiality. Results are shown for three different ellipse aspect ratios.

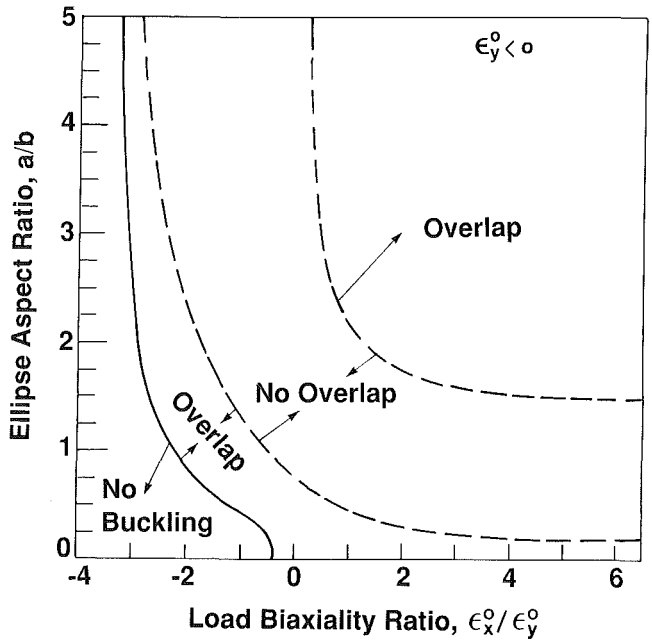


Fig. 4 Dependence of buckling and the conditions for overlap between film and substrate at buckling on the details of load biaxiality and ellipse aspect ratio. $\epsilon_y^o < 0$. Results pertain to the first buckling mode.

the minor axis of the ellipse while the tensile load along the major axis; for a very narrow ellipse, the applied tensile load may be as large as three times the compressive load. It is interesting to note that buckling of an elliptically-shaped, specially orthotropic delamination layer was also found to occur under purely tensile loading (Shivakumar and Whitcomb, 1985; Chai and Babcock, 1985). The reason for that buckling was attributed to the induction of relatively large compressive deformations over a region at the plate boundary which is normal to the load axis; such deformations result from the mismatch

Downloaded 03 May 2010 to 171.66.16.244. Redistribution subject to ASME license or copyright; see http://www.asme.org/terms/Terms_Use.cfm

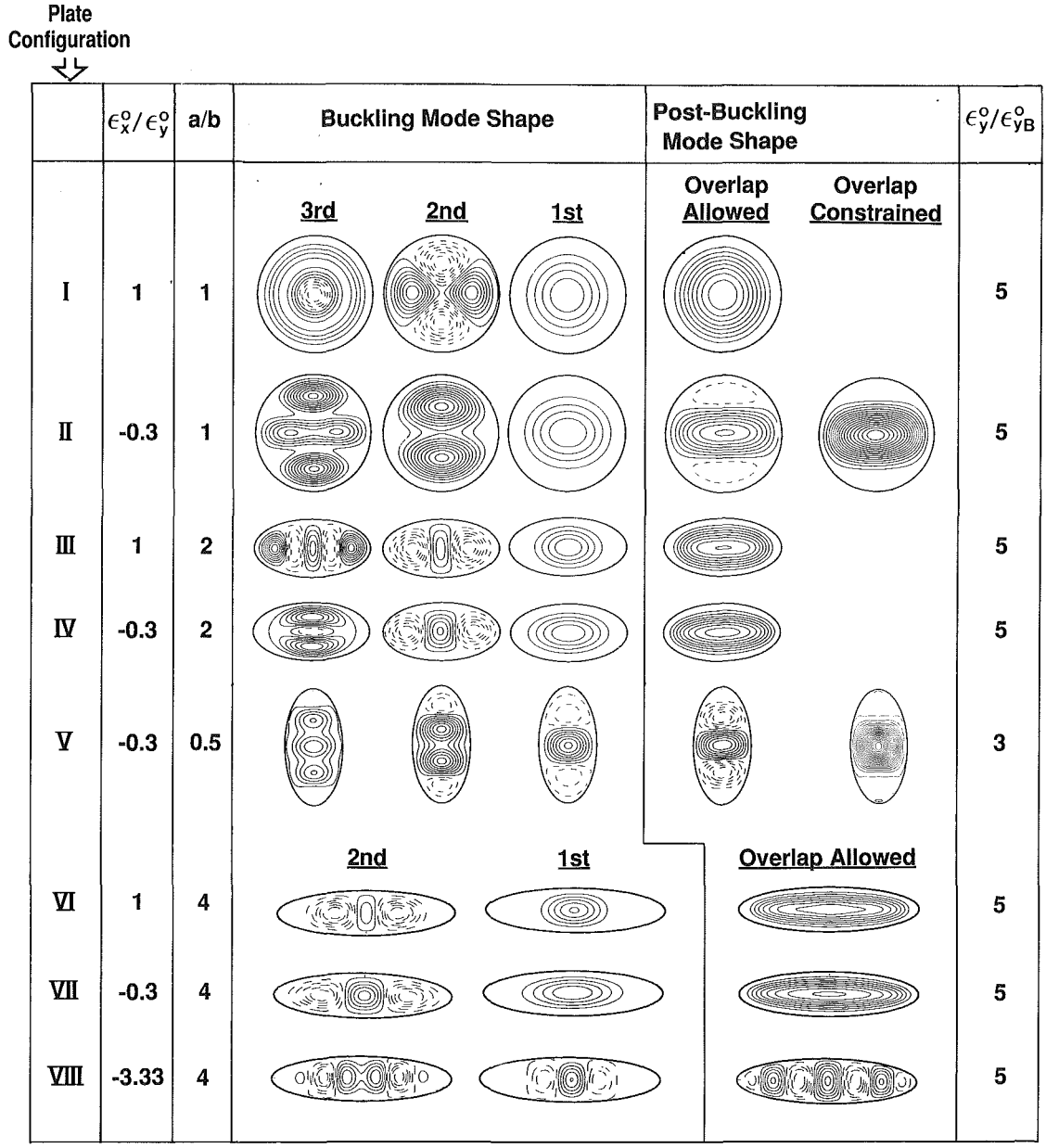


Fig. 5 Contour plots (lines of equal out-of-plane deformations) for several plate configurations. Solid curves and dashed curves denote positive and negative deformations, respectively. Shown are results for buckling deformations (first three buckling modes in configurations I-V, first two in VI-VIII), post-buckling deformations, and post-buckling deformations obtained from the contact analysis. The post-buckling deformations were extended from the mode shape of the first buckling mode. Post-buckling fringe constant = 0.3h. Note that for configurations I-VII, $\epsilon_y^o < 0$ while for configuration VIII, $\epsilon_y^o > 0$.

in elastic constants between the orthotropic layer and the isotropic base laminate.

Buckling contour plots, obtained from solution of the eigenvector problem (Chai, Part I), are shown in Fig. 5 for a number of plate configurations. Nominal buckling loads for all these illustrations are given in Table 1. The deformation for the first three buckling modes (configurations I–V) or first two (VI–VIII) are presented. For plate configurations I–VII, $\epsilon_y^o < 0$, while for configuration VIII, $\epsilon_y^o > 0$. The out-of-plane deformations for all buckling patterns were normalized by an appropriate factor. Convergence of the deflection solution was assessed by discretizing the plate area into 100 elemental points, and by comparing $w(x, y)$ in every such point among plate solutions employing increasing number of displacement terms. The worst relative difference among all the plate elements between two successive approximations was taken as the error. By employing as many as 45 displacement terms in the expansion series for $w(x, y)$, the error was kept below a few percent of the plate thickness for all cases shown.

The buckling contours in Fig. 5 display a number of interesting features:

(a) For the majority of plate configurations (i.e., I–IV, VI–VII), the plate deformations associated with the first buckling mode vary monotonically, the largest deflection occurring at the plate center.

(b) For narrow plates in which the compressive load is

Downloaded 03 May 2010 to 171.66.16.244. Redistribution subject to ASME license or copyright; see http://www.asme.org/terms/Terms_Use.cfm

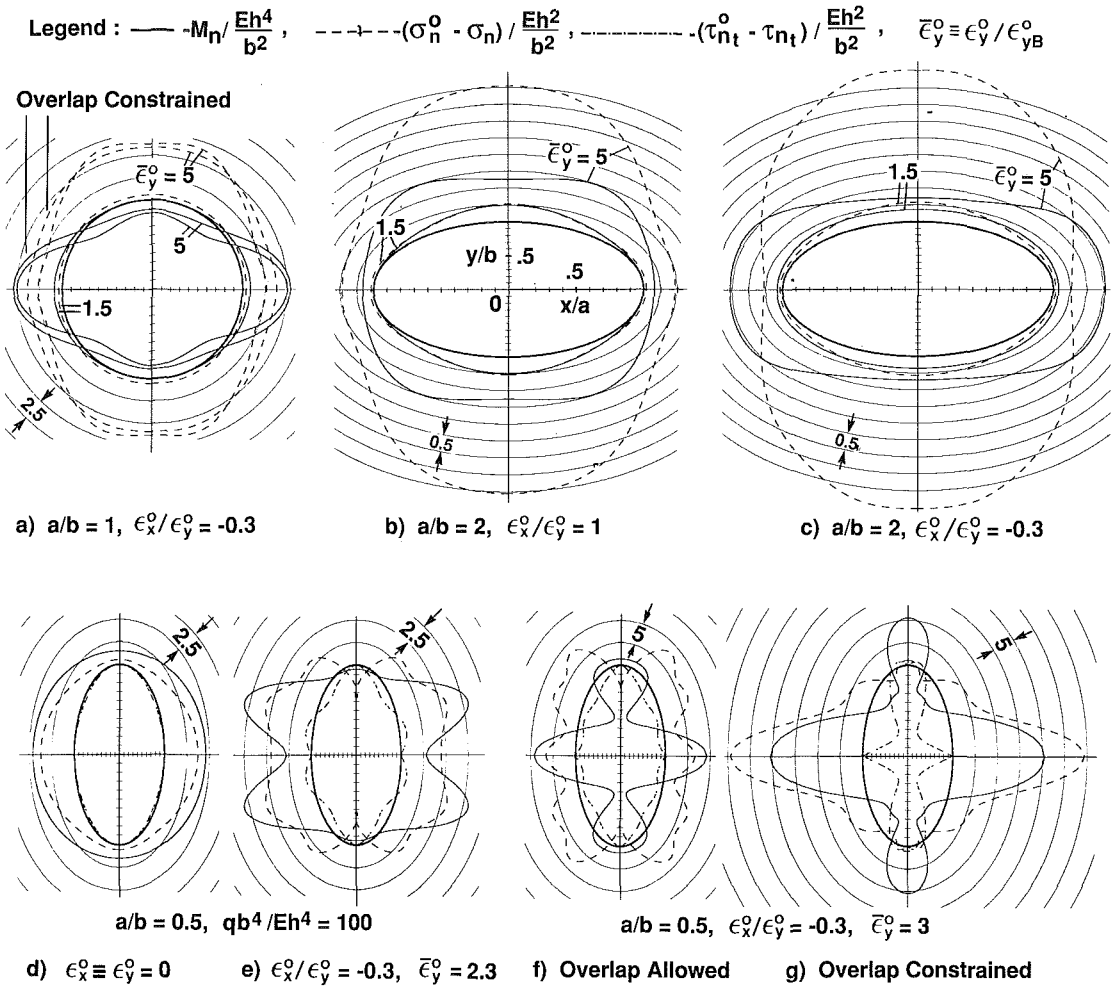


Fig. 6 Distribution of normal, tangential, and bending stresses around the plate boundary for a number of plate configurations

aligned along the major axis of the ellipse (i.e., configuration V, VIII), "sinusoidal" type deformations occur.

(c) Higher buckling modes are associated with increasing surface waviness. The corresponding "bulges" apparently act to convert the in-plane displacements applied to the plate boundary into bending deformations associated with less strain energy. Note that plate waviness may be due either to purely outward deformations (second and third buckling modes in configuration II, third mode in IV and V) or a combination of negative (inward) and positive (outward) deformations.

(d) Reinforcement along nodal lines is a viable means to suppress the first buckling mode in favor of higher modes associated with larger buckling resistance. In the case of configuration I, it is apparent that the third buckling mode may be realized if the plate is reinforced by a ring of radius r such that $r/b = 0.3$. As shown in Fig. 2(a), this would increase the buckling strength by a factor of 3.

In applications to delamination problems it is necessary to establish the conditions at which the film and substrate may overlap. It has been shown (Whitcomb, 1988; Chai, 1990) that a contact between the film and substrate may significantly alter the distribution of each of the components of the energy release rate around the delamination front. The dependence of overlap conditions on ellipse aspect ratio and load level has been determined for a uniaxially loaded ellipse based on a rather limited number of displacement terms (Chai and Babcock, 1985). The availability of virtually unlimited number of degrees-of-freedom in the present analysis allows for an accurate determination of the overlap regions. The latter were established by analyzing the deformation pattern of the plates, and the results, pertaining to the first buckling mode, are given in Fig. 4 as function of aspect ratio and detail of load biaxiality. The data in this figure correspond to the choice $\epsilon_y^o < 0$. As shown, the out-of-plane deformations are positive everywhere in the plate only in the domain enclosed by the two dashed curves. When both loadings are compressive (i.e., $\epsilon_x^o/\epsilon_y^o > 0$), overlap is seen to be restricted to either relatively small or relatively large aspect ratios. On the other hand, when the load in the x direction is tensile (i.e., $\epsilon_x^o/\epsilon_y^o < 0$), overlap may occur for more common plate shapes.

III Post-buckling Behavior

As discussed in Part I of this work, post-buckling solutions were obtained by utilizing the displacement coefficients at buckling (after an appropriate normalization) as initial guess in the iterative solution process. Solution for a given load ratio (i.e., ratio of applied stress to buckling stress) was then constructed by incrementing the load in small steps. Figure 5 shows post-buckling deformation contours for all the plate configurations of this figure. These deformation patterns were obtained by incrementing the load from the first buckling mode. The height difference between two adjacent contours ("fringe constant") is 30 percent of the plate thickness, h. Except for configuration V, the applied stresses are five times the buckling stresses; the nominal values of the applied loads can be easily deduced from Table 1. The post-buckling deformations are generally similar to their buckling (first-mode) counterparts, whether they are simple (configurations I, III–IV, VI–VII) or

Downloaded 03 May 2010 to 171.66.16.244. Redistribution subject to ASME license or copyright; see http://www.asme.org/terms/Terms_Use.cfm

sinusoidal (V, VIII). In the latter cases as well as for a uniaxially loaded circle (II), additional bulges are formed upon increasing the load from buckling. These bulges apparently act to convert the additional axial deformations applied to the plate boundary into bending deformations.

The conditions for film-substrate overlap in the post-buckling regime were determined as a function of load ratio and the results, corresponding to an extension of the plate deformation from the first buckling mode, are given by the dashed curves in Fig. 2. As shown, for the uniform load case overlap may occur only if the aspect ratio is large (i.e., $a/b > 2.2$). This overlap is seen to disappear once the load is sufficiently increased from the buckling load. For the uniaxial load case, overlap may occur only if $a/b < 1.4$; for $a/b < 0.9$, this overlap develops right at buckling, while in the intermediate range, $0.9 < a/b < 1.4$, the overlap starts when the applied load becomes sufficiently large. Whitcomb (1988) has recently developed a geometrically nonlinear, finite element analysis based on three-dimensional elasticity for the delamination problem which is of concern in this work. His analysis of a 2-to-1 elliptical delamination deforming under a uniaxial compressive load applied along the ellipse minor axis shows that unlike the present results (Fig. 2(*b*)), a film substrate overlap does occur for this plate problem. This overlap, which is confined to the immediate vicinity of the plate border, is clearly not expected to be accurately predicted by any plate analysis. More recently, a simplified hybrid analysis was developed (Chai, 1990) to account for the elastic behavior in the immediate vicinity of the delamination border. In this analysis, the boundary stresses from the plate solution serve as input parameters in a crack-tip singularity solution pertaining to the delamination border. This hybrid analysis has indeed predicted overlap regions at the delamination border, which are in addition to the overlap in the plate interior predicted by the plate analysis (see Fig. 6 of Chai, 1990). However, it was found that for many delamination problems of interest, the local overlap has only marginal effect on the dominant pointwise value of the energy release rate.

Figure 6 shows the variation along the plate boundary of bending stress and "jump" in membrane stresses across the plate border for a number of plate configurations, some of which appear in Fig. 5. "*n*" and "*t*" are the coordinates normal and parallel to the plate boundary. The tangential stresses are shown only for those configurations in which they are not negligible. Numerical values for stresses and central deflection are given in Table 2 for select cases. The normal membrane stresses in Figs. 6(*a–c*) (dashed curves) seem to be localized over a boundary region near the end of the vertical axis of the plate, which is the axis of compressive load. The behavior for the bending stresses (solid curves) is more involved. For a uniaxially loaded circle (*a*), these stresses tend to concentrate in a region normal to the load axis, while for a uniaxially-loaded ellipse (*c*), the locus of intense bending stresses seems to shift from the end of the minor axis to the end of the major axis of the ellipse as the load ratio is increased. It can also be seen in these illustrations that all stress components tend to spread over a larger and larger boundary region as the load is increased. For an ellipse loaded compressively along its major axis, Fig. 6(*f*), all three stress components exhibit periodic variations along the plate boundary, which is in accord with the sinusoidal variations of the post-buckling deformation pattern in Fig. 5, configuration V.

For pressure loading, Fig. 6(*d*), the membrane and bending stresses vary monotonically along the plate boundary; the maximum and minimum occurs at the end of the minor axis and major axis, respectively. The effect of a combined normal pressure and uniaxial compression applied along the long axis of the ellipse is shown in Fig. 6(*e*)). The particular load ratio chosen (i.e., $\epsilon_y^o \equiv \epsilon_y^o/\epsilon_{yB}^o = 2.3$, ϵ_{yB}^o is the buckling load) is the largest load ratio that can be applied, yet the out-of-plane deformations remain positive everywhere in the plate. The resulting stress patterns are again wavy, but unlike Fig. 6(*f*), which corresponds to a purely compressive loading, the bending stress is negative essentially everywhere along the plate boundary.

Table 1* Buckling data, $\nu = 0.3$

a/b	$\epsilon_x^o/\epsilon_y^o$	$-\epsilon_{yB}^o b^2/h^2$ Buckling Mode		
		First	Second	Third
1	1	0.941	2.61	3.16
2	1	0.669	1.11	1.88
4	1	0.628	0.753	0.967
0.1	-0.3	210	292	421
0.25	-0.3	28.6	35.9	45.0
0.5	-0.3	8.22	12.7	18.5
1	-0.3	2.49	5.34	9.81
2	-0.3	1.24	3.74	4.15
4	-0.3	1.03	1.69	2.83
10	-0.3	0.947	1.27	1.85

* ϵ_{yB}^o is the buckling strain.

Table 2* Large-deflection data, $\nu = 0.3$

a/b	$\frac{q}{E}\frac{b^4}{h^4}$	$\epsilon_x^o/\epsilon_y^o$	$\epsilon_y^o/\epsilon_{yB}^o$	w(0,0)/h	$-(\sigma_x^o-\sigma_x)b^2/Eh^2$	$-(\sigma_y^o-\sigma_y)b^2/Eh^2$	$-M_x b^2/Eh^4$	$-M_y b^2/Eh^4$
1	0	1	1.5	0.973	0.421	0.421	0.409	0.409
1	0	1	5	2.67	3.69	3.69	1.66	1.66
1	0	-0.3	1.5	0.992	0.38	0.547	0.848	-0.056
1	0	-0.3	5	2.294	2.68	6.29	5.00	-1.47
2	0	1	1.5	0.966	0.074	0.529	0.008	0.486
2	0	1	5	2.418	0.933	4.05	0.315	1.26
2	0	-0.3	1.5	0.966	0.067	0.576	0.149	0.357
2	0	-0.3	5	2.574	0.535	4.53	1.54	0.707
2	25	---	0	2.202	0.537	3.26	1.18	3.00

* ϵ_{yB}^o is the buckling strain. The data for stresses and bending moments pertain to the plate boundary.

Downloaded 03 May 2010 to 171.66.16.244. Redistribution subject to ASME license or copyright; see http://www.asme.org/terms/Terms_Use.cfm

IV Contact Analysis

In applications to delamination or debonding problems, inward plate deformations are prevented by the substrate. To gain an insight into how the stresses redistribute as a result of contact between the film and substrate, a simplified contact analysis was developed which is based on the following assumptions:

(a) Frictionless contact.
(b) The contact regions are limited to isolated points.
(c) At a contact point, $w = \partial w/\partial x = \partial w/\partial y = 0$.
(d) The reaction normal stress at a contact point is compressive, i.e., $q < 0$; the mathematical expression for this condition is given by equation (217) of Timoshenko and Woinowsky-Krieger (1959).

Contact solutions were obtained for configurations II and V of Fig. 5. It was assumed that the contact region is limited to two isolated points, y_c and $-y_c$, which lie on the y axis. The expression for $w(x, y)$ from Part I is

$$w(\bar{x},\bar{y}) = h(1-\bar{x}^2-\bar{y}^2)^2 \sum_{m=0}^{M}\sum_{n=0}^{M-m} c_{m+1,n+1}\bar{x}^{2m}\bar{y}^{2n},$$

$$\bar{x} \equiv x/a,\ \bar{y} \equiv y/b, \tag{5}$$

where M and N are arbitrary integers and $c_{m,n}$ are displacement coefficients. Assumptions (c) imply that the following holds at $(x, y) = (0, y_c)$:

$$\sum_{n=0}^{M} c_{1,n+1}\bar{y}_c^{2n} = 0,$$

$$\sum_{n=0}^{M} [2\bar{y}_c^2 + n(\bar{y}_c^2 - 1)]c_{1,n+1}\bar{y}_c^{2n} = 0. \tag{6a,b}$$

Equation (6) provides two additional constraints on the equations for displacement coefficients given in Part I, while only one additional unknown, $(\bar{y}_c)$. Solutions were obtained by replacing the first equation in the set of equations for displacement coefficients, equation (24), Part I, with (6*a*) and by adding (6*b*) to that set. In practice, difficulties were encountered in choosing the initial guess for the displacement coefficients and in numerically fulfilling (6*b*). The solution strategy adopted was to start with the original solution where overlap is allowed, identify a value of $\bar{y}$ such that $w(0, \bar{y}) = 0$, and proceeds with varying $\bar{y}$ from that value towards the peak of the inward bulge until the quantity $\partial w/\partial y$ is minimized. The convergence of the so-obtained stress solution with increasing number of displacement terms was not very satisfactory, and the results from the contact analysis to be presented here are believed to be accurate only to within ± 30 percent. A more sophisticated approach such as the geometrically nonlinear finite element analysis employed by Whitcomb (1988) would probably be necessary for more accurate information. Results from the contact analysis are shown in Figs. 5 and 6 for a uniaxially loaded circle and a uniaxially loaded ellipse ($a/b = 0.5$). As shown in Fig. 5 (configurations II and V), in both these cases the post-buckling patterns from the contact analysis display no inward deformations. Figure 6 shows that the redistribution of stresses caused by contact is quite small for the circle (Fig. 6(*a*)) but considerable for the ellipse (Fig. 6(*f*) versus Fig. 6(*g*)). In the latter case the original wavy stress patterns of Fig. 6(*f*) are replaced by essentially monotonic ones, the largest bending and normal stresses that occur at the end of the a axis of the ellipse.

Summary and Conclusions

The buckling and post-buckling behavior of an elliptically-shaped surface layer that has been delaminated from a large material body was illustrated in detail. Emphasis was placed on elucidating the conditions under which the delaminated layer may interact with the main body, and on boundary stresses that are responsible for delamination growth. Results were presented graphically and numerically for a number of plate configurations that are at the same time of practical interest and illuminative of the range of behavior possible. The following findings of general interest are noted:

(a) Higher-order buckling modes are generally associated with increasing waviness of the buckled surface. This waviness is apparently due to a conversion of the in-plane deformations that are transmitted across the plate boundary into bending deformations associated with less strain energy.
(b) Buckling may occur even if one of the two axial loadings is tensile; for a narrow ellipse loaded compressively along its short axis, the tensile load applied along the long axis of the ellipse may exceed by a factor of three the compressive load.
(c) The post-buckling deformation patterns generally resemble the corresponding buckling patterns except at higher load levels in which additional surface waviness may develop.
(d) The jump in normal membrane stress across the plate border for plates undergoing simple deformations tends to be localized over the boundary region where the applied contraction is the largest. The behavior for bending moment is more complex. For narrow plates loaded compressively along their long axis, the out-of-plane deformations tend to be wavy. A simplified contact analysis developed in this work shows that prohibiting overlap between the film and substrate may lead to a substantial increase in the boundary stresses.

Material anisotropy and shear loadings are expected to significantly affect the deformations and stresses in the plate, and consequently the energy release rate. Consideration of these effects would be a natural extension of the present work.

References

Chai, H., and Babcock, C. D., 1985, "Two-Dimensional Modelling of Compressive Failure in Delaminated Laminates," *Journal of Composite Materials*, Vol.19, pp. 67–98.

Chai, H., 1990, "Buckling and Postbuckling Behavior of Elliptical Plates: Part I—Analysis," ASME JOURNAL OF APPLIED MECHANICS, Vol. 57, pp. 981–988.

Chai, H.,1990, "Three-Dimensional Fracture Analysis of Thin-Film Debonding," *International Journal of Fracture*, in press.

Shivakumar, K. N., and Whitcomb, J. D., 1985, "Buckling of a Sublaminate in a Quasi-Isotropic Composite Laminate," *Journal of Composite Materials*, Vol. 19, pp. 2–18.

Timoshenko, S., and Woinowsky-Krieger, S., 1959, "Theory of Plates and Shells," McGraw-Hill, New York.

Whitcomb, J. D., 1988, "Instability-Related Delamination Growth of Embedded and Edge Delaminations," Report No. NASA TM 100655.

Yin, W. L., and Jane, K. C., 1989, "Refined Buckling and Postbuckling Analysis of Two-Dimensional Delaminations," *Recent Developments in Buckling of Structures*, D. Hui, V. Birman, and D. Bushnell, eds., ASME, New York, pp. 31–40.

Downloaded 03 May 2010 to 171.66.16.244. Redistribution subject to ASME license or copyright; see http://www.asme.org/terms/Terms_Use.cfm

Free Vibration and Tension Buckling of Circular Plates With Diametral Point Forces

E. F. Ayoub

A. W. Leissa
Fellow ASME

Department of Engineering Mechanics,
Ohio State University,
Columbus, OH 43210

This paper presents the first known results for the free vibrations of a circular plate subjected to a pair of static, concentrated forces acting on the boundary at opposite ends of a diameter. The closed-form exact solution of the plane elasticity problem is used to provide the in-plane stress distribution for the vibration problem. A proper procedure using the Ritz method is developed for solving the latter problem for clamped, simply supported, or free boundary conditions. Numerical results are given for the vibration frequencies of a simply supported circular plate, which separate into four symmetry classes of mode shapes. Compressive buckling loads for each symmetry class are determined as a special case as the frequencies decrease to zero with increasing compressive force. Tracking the frequency versus loading data with increasing tensile forces shows that buckling due to tensile force can also occur, and the critical value of the force is found.

1 Introduction

Solutions of vibration and buckling problems for plates subjected to in-plane point forces are of interest to designers, for high intensity edge loadings are often encountered in practice. Generally speaking, tensile forces increase the free vibration frequencies, while compressive forces decrease them. As a frequency of zero is approached, this corresponds to approaching a buckling load.

Numerous solutions exist for the compressive buckling loads of rectangular plates (especially in the case of the square) subjected to a pair of point forces acting upon opposite edges. (Fourteen relevant publications are given by Leissa and Ayoub (1988) for a plate having all edges simply supported.) However, until recently, there has been considerable disagreement in the numerical results presented.

What makes the buckling and free vibration problem particularly difficult is that a plane elasticity solution must first be found, and that solution must be used in the subsequent eigenvalue problem. The complex nature of the internal stress field, which includes singularities at the point forces, makes exact solutions of these problems impossible. Moreover, for the rectangular plate, the plane elasticity problem is also intricate and has no exact solution. Thus, approximations arise in both stages of the overall problem in that case.

For the circular plate, the problem is less complicated because exact solutions (series and closed-form) of the plane stress part of the problem are known for two point forces acting diametrally along the boundary (Fig. 1). Yamaki (1956) used the series form of the solution to obtain the compressive buckling load for simply supported and clamped circular plates. Subsequently, Rózsa (1966) found the compressive buckling load for a point-loaded circular plate with free boundaries.

This paper presents the first known solution to the free vibration problem for the diametrally loaded circular plate. Vibration frequencies are obtained for simply supported boundaries. Yamaki's compressive buckling result is also verified as a special case of zero frequency.

The free vibration problem for circular plates subjected to partially distributed edge loads was analyzed by Narita (1985) using approaches different than in the present work for both the plane elasticity solution and in the subsequent vibration eigenvalue problem. An approximation to the concentrated forces of the present problem was obtained by Narita by applying uniformly distributed pressures over four degree arc lengths on opposite sides of the plate.

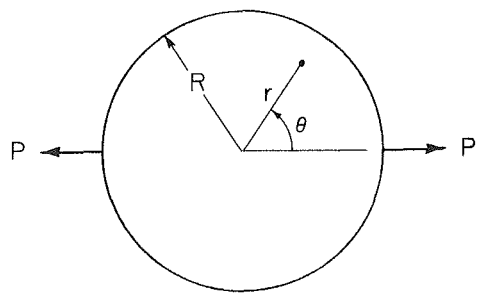


Fig. 1 Circular plate with diametral point forces

Contributed by the Applied Mechanics Division of THE AMERICAN SOCIETY OF MECHANICAL ENGINEERS for presentation at the Joint Applied Mechanics/Bioengineering Conference, Ohio State University, Columbus, OH, June 16-19, 1991.

Discussion on this paper should be addressed to the Technical Editor, Leon M. Keer, The Technological Institute, Northwestern University, Evanston, IL 60208, and will be accepted until final publication of the paper itself in the JOURNAL OF APPLIED MECHANICS. Manuscript received by the ASME Applied Mechanics Division, June 19, 1989; final revision, Sept. 15, 1989.

Paper No. 91-APM-24.

Copyright © 1990 by ASME

Downloaded 03 May 2010 to 171.66.16.244. Redistribution subject to ASME license or copyright; see http://www.asme.org/terms/Terms_Use.cfm

Further, a study of the vibration eigenvalue spectrum shows the existence of zero frequencies for diametral forces which are tensile. These correspond to tension buckling loads. The possibility of tension buckling due to oppositely directed point forces was previously shown by Durban (1977) for clamped circular plates. The phenomenon was also demonstrated recently by Leissa and Ayoub (1989) for simply supported rectangular plates.

Analysis

The solution of the plane elasticity problem for a circulate plate subjected to diametrical tensile forces P (Fig. 1) is exact, and may be obtained in either of two ways:

(1) Expanding the boundary stresses in terms of Fourier series in θ, which are used to determine the coefficients of the well-known Airy stress function in polar coordinates (cf., Timoshenko and Goodier, 1970, p. 132). This solution yields infinite series for the stress components σ_r, σ_θ, and $\tau_{r\theta}$.

(2) Superposition of two solutions for point forces acting upon infinite half planes with a hydrostatic loading (cf., Timoshenko and Goodier, 1970, p. 122). This solution yields closed-form expressions for the stress components.

The second solution is found to be less complicated, and is used in the subsequent vibration and buckling analysis.

The closed-form expressions for the stresses are available in quite simple forms when bipolar coordinates with origins at points of force application are used. Transformed to the single set of polar coordinates shown in Fig. 1, they are:

$$\frac{\sigma_r Rh}{P}=\frac{2R}{\pi}\left[\frac{(R-r\cos\theta)(r-R\cos\theta)^2}{(R^2+r^2-2Rr\cos\theta)^2}+\frac{(R+r\cos\theta)(r+R\cos\theta)^2}{(R^2+r^2+2Rr\cos\theta)^2}\right]-\frac{1}{\pi}$$

$$\frac{\sigma_\theta Rh}{P}=\frac{2R}{\pi}\left[\frac{(R-r\cos\theta)(R\sin\theta)^2}{(R^2+r^2-2Rr\cos\theta)^2}+\frac{(R+r\cos\theta)(R\sin\theta)^2}{(R^2+r^2+2Rr\cos\theta)^2}\right]-\frac{1}{\pi}$$

$$\frac{\tau_{r\theta} Rh}{P}=\frac{2R}{\pi}\left[\frac{(R-r\cos\theta)(r-R\cos\theta)R\sin\theta}{(R^2+r^2-2Rr\cos\theta)^2}+\frac{(R+r\cos\theta)(r+R\cos\theta)R\sin\theta}{(R^2+r^2+2Rr\cos\theta)^2}\right] \quad (1)$$

where h is the plate thickness.

The equation of motion for free, transverse vibration is

$$D(\nabla^2 w)^2-h\left[\sigma_r\frac{\partial^2 w}{\partial r^2}+\sigma_\theta\left(\frac{1}{r}\frac{\partial w}{\partial r}+\frac{1}{r^2}\frac{\partial^2 w}{\partial\theta^2}\right)+2\tau_{r\theta}\frac{\partial}{\partial r}\left(\frac{1}{r}\frac{\partial w}{\partial\theta}\right)\right]=\rho h\frac{\partial^2 w}{\partial t^2} \quad (2)$$

where

$$\nabla^2=\frac{\partial^2}{\partial r^2}+\frac{1}{r}\frac{\partial}{\partial r}+\frac{1}{r^2}\frac{\partial^2}{\partial\theta^2}, \quad (3)$$

ρ is the mass density per unit volume, and $D=Eh^3/12(1-\nu^2)$ is the flexural rigidity of the plate. Because σ_r, σ_θ, and $\tau_{r\theta}$ are the relatively complicated functions of r and θ given by equations (1), an exact solution of equation (2) is unavailable. Therefore, the problem will be solved by the Ritz method.

The Ritz procedure requires minimizing the functional $T_{\max}-V_{\max}$ where $T_{\max}$ and $V_{\max}$ are the maximum values of the kinetic energy (T) and potential energy (V) of the system during a vibratory cycle. The kinetic energy is

$$T=\frac{\rho h}{2}\int_0^{2\pi}\int_0^R\left(\frac{\partial w}{\partial t}\right)^2 r\,dr\,d\theta. \quad (4)$$

The potential energy is the sum of the bending strain energy (V_s) and the load potential (V_L). That is,

$$V=V_s+V_L \quad (5)$$

where

$$V_s=\frac{D}{2}\int_0^{2\pi}\int_0^R\left\{(\nabla^2 w)^2-2(1-\nu)\left[\frac{\partial^2 w}{\partial r^2}\left(\frac{1}{r}\frac{\partial w}{\partial r}+\frac{1}{r^2}\frac{\partial^2 w}{\partial\theta^2}\right)-\left[\frac{\partial}{\partial r}\left(\frac{1}{r}\frac{\partial w}{\partial\theta}\right)\right]^2\right]\right\}r\,dr\,d\theta \quad (6)$$

$$V_L=\frac{h}{2}\int_0^{2\pi}\int_0^R\left\{\sigma_r\left(\frac{\partial w}{\partial r}\right)^2+\sigma_\theta\left(\frac{1}{r}\frac{\partial w}{\partial\theta}\right)^2+2\tau_{r\theta}\frac{\partial w}{\partial r}\left(\frac{1}{r}\frac{\partial w}{\partial\theta}\right)\right\}r\,dr\,d\theta. \quad (7)$$

Assuming harmonic motion for the time response in free vibrations,

$$w(r,\theta,t)=W(r,\theta)\sin(\omega t+\phi), \quad (8)$$

where ω is a natural frequency and ϕ is a phase angle to permit arbitrary initial conditions, $T_{\max}$ is obtained from equation (4) as

$$T_{\max}=\frac{\rho h\omega^2}{2}\int_0^{2\pi}\int_0^R W^2\,r\,dr\,d\theta. \quad (9)$$

$V_{\max}$ is obtained from equations (5), (6), and (7) by replacing w by W.

It is assumed that the boundary conditions are uniform around the plate or, if they vary with θ, that they are symmetric with respect to θ. Then the vibration mode shapes will separate into four classes, depending upon whether they are symmetric or antisymmetric with respect to $\theta=0$ and $\theta=\pi/2$. Displacement functions for each of these symmetry classes may then be assumed as follows:

Doubly symmetric (S-S) modes:

$$W(r,\theta)=\psi(r)\sum_{m=0,2}^{M}\sum_{n=0,2}^{N}C_{mn}r^m\cos n\theta \quad (n\le m). \quad (10a)$$

Symmetric-antisymmetric (S-A) modes:

$$W(r,\theta)=\psi(r)\sum_{m=1,3}^{M}\sum_{n=1,3}^{N}C_{mn}r^m\cos n\theta \quad (n\le m). \quad (10b)$$

Antisymmetric-symmetry (A-S) modes:

$$W(r,\theta)=\psi(r)\sum_{m=1,3}^{M}\sum_{n=1,3}^{N}C_{mn}r^m\sin n\theta \quad (n\le m). \quad (10c)$$

Antisymmetric-antisymmetric (A-A) modes:

$$W(r,\theta)=\psi(r)\sum_{m=2,4}^{M}\sum_{n=2,4}^{N}C_{mn}r^m\sin n\theta \quad (n\le m). \quad (10d)$$

It should be noted that requiring $n\le m$ in equations (10) eliminates the possibility of singularities at the coordinate origin ($r=0$).

In equations (10) the $\psi(r)$ are functions chosen so as to satisfy the boundary conditions for the plate. For the three most important cases they are:

Free edge	$\psi(r)=1$	(11a)
Simply supported edge:	$\psi(r)=R^2-r^2$	(11b)
Clamped edge:	$\psi(r)=(R^2-r^2)^2$.	(11c)

Equations (10) and (11) define mathematically complete sets of functions for each symmetry class. Thus, the solutions will converge to the exact solutions as sufficient terms in the series of equations (10) are used (cf., Kantorovich and Krylov, 1964; Mikhlin, 1964). This will be demonstrated in the next section.

Substituting equations (10) and (11) into the energy functionals, the following minimizing operations are carried out:

$$\frac{\partial(T_{\max}-V_{\max})}{\partial C_{pq}}=0 \quad (12)$$

Downloaded 03 May 2010 to 171.66.16.244. Redistribution subject to ASME license or copyright; see http://www.asme.org/terms/Terms_Use.cfm

Table 1 Comparison of nondimensional frequencies $\omega R^2\sqrt{\rho h/D}$ from the Ritz method with exact values for the unloaded plate ($\nu = 0.3$)

Mode	Exact [10]	Ritz method (and percent error)	
		10 terms	15 terms
0,0	4.9351	4.9352 (0.00)	4.9351 (0.00)
2,0	25.613	25.619 (0.02)	25.614 (0.00)
0,1	29.720	29.736 (0.05)	29.720 (0.00)
4,0	56.842	58.760 (3.37)	56.911 (0.12)
2,1	70.117	75.964 (8.34)	70.476 (0.51)
0,2	74.156	81.902 (10.45)	74.706 (0.74)
1,0	13.898	13.898 (0.00)	13.898 (0.00)
3,0	39.957	39.981 (0.06)	39.957 (0.00)
1,1	48.479	48.581 (0.21)	48.479 (0.00)
5,0	76.203	79.513 (4.35)	76.362 (0.21)
3,1	94.549	105.29 (11.36)	95.404 (0.90)
1,2	102.77	119.12 (11.28)	104.28 (1.47)

where p and q range over all integers m and n, to M and N. This yields a set of linear, algebraic equations in the C_{pq}, which are homogeneous. Setting the determinant of the coefficient matrix equal to zero results in the desired eigenvalues. It is found to be computationally more efficient to perform the differentiations of equation (12) before carrying out the integrals over the plate area.

The method will now be demonstrated for the circular plate having a simply supported boundary.

Comparisons for the Unloaded Plate

For the simply supported circular plate having no in-plane forces, all free vibration modes are accounted for by equations (10*a*) and (10*b*). In this case equations (10*c*) and (10*d*) yield the same mode shapes as (10*a*) and (10*b*) for $n > 0$.

An exact solution of the free vibration problem is also available as (cf., Leissa, 1969)

$$W_n(r, \theta) = [A_n J_n(kr) + C_n I_n(kr)]\cos n\theta \qquad (13)$$
$$(n = 0, 1, 2 \ldots)$$

where $J_n(kr)$ and $I_n(kr)$ are ordinary and modified Bessel functions of the first kind, respectively, k is related to the circular frequency, ω by

$$k^4 = \frac{\rho h \omega^2}{D} \qquad (14)$$

and, for the simply supported edge conditions, the coefficients A_n and C_n are related by

$$\frac{C_n}{A_n} = -\frac{J_n(\lambda_n)}{I_n(\lambda_n)}. \qquad (15)$$

The eigenvalues λ_n are expressed in terms of the frequencies by

$$\lambda^2 = \omega R^2 \sqrt{\rho h/D} \qquad (16)$$

and are found to be the roots of the characteristic equation

$$\frac{J_{n+1}(\lambda)}{J_n(\lambda)} + \frac{I_{n+1}(\lambda)}{I_n(\lambda)} = \frac{2\lambda}{1-\nu} \qquad (17)$$

which depend upon Poisson's ratio (ν) for the material.

Comparisons between approximate frequencies obtained by the Ritz method, using equations (10*a*) and (10*b*), and the exact results from equation (17) as obtained by Leissa and Narita (1980), are made in Table 1 for $\nu = 0.3$. The first six frequencies are listed for both the S-S and S-A modes. Mode shapes are identified by (n, s) where n and s are the numbers of nodal diameters and nodal circles, respectively. It is seen that using only ten terms in the displacement series ($M = N = 6$ in equation (10*a*), and $M = N = 7$ in equation (10*b*)) results in accurate frequencies for the first three modes of each symmetry classes, but the fourth and higher frequencies are quite inaccurate in each case. Increasing M and N one additional step results in 15 terms in the series. Table 1 shows that the frequencies of the fourth, fifth, and sixth modes are then improved considerably, and are reasonably accurate.

Frequencies for the Simply Supported Plate with Point Forces

The convergence study for the unloaded plate (Table 1) showed that accurate frequencies for the first three modes of each symmetry class are obtainable with ten terms of the corresponding displacement series. If negative (i.e., compressive) values of the concentrated forces (P) are applied, the lowest frequency for each displacement symmetry class will decrease. When the frequency becomes zero, buckling occurs in a mode consistent with that symmetry class. The corresponding negative value of P will be called the "critical load" for that symmetry class, for there will be additional buckling loads (larger in absolute values) for other modes. A convergence study for these critical loads is shown in Table 2. Again, it is seen that ten terms of the displacement series yields sufficiently accurate results. The lowest of the four critical loads, $P_{cr}R/D = 13.15$ agrees well with Yamaki's (1956) results of 13.14.

The studies described above suggest that ten terms of the displacement series of equations (10) is sufficient to obtain reasonably accurate vibration frequencies over a rather wider range of loading parameters. These data are presented in Table 3, where the first three frequencies for each of the four symmetry classes over the loading range $-1.0 \leq P/P_{cr} < 1.0$. Pertinent values of P_{cr} are those given previously in Table 2. A

Downloaded 03 May 2010 to 171.66.16.244. Redistribution subject to ASME license or copyright; see http://www.asme.org/terms/Terms_Use.cfm

Table 2 Nondimensional compressive critical loads $P_{cr}R/D$ for simply supported circular plates subjected to diametral point forces ($\nu = 0.3$)

Symmetry class	Number of terms in series		
	6	10	15
S-S*	13.149	13.148	13.148
S-A	20.099	20.041	20.018
A-S	138.60	119.30	116.09
A-A	127.17	117.17	115.08

* Yamaki (1956) obtained 13.14.

Table 3 Nondimensional frequencies $\omega R^2\sqrt{\rho h/D}$ for simply supported circular plates subjected to diametral point forces ($\nu = 0.3$)

Symmetry class	P/P_{cr}				
	-1.0	-0.5	0	0.5	1.0
S-S	0.00	3.493	4.935	6.039	6.970
	20.29	23.45	25.62	26.66	26.99
	28.82	29.04	29.74	31.20	33.11
S-A	0.00	9.904	13.90	16.92	19.43
	31.93	37.00	39.98	41.62	42.66
	43.92	45.76	48.58	52.02	55.51
A-S	0.00	13.29	13.90	13.60	12.82
	19.80	31.27	39.98	43.10	41.85
	50.49	49.41	48.58	50.98	56.19
A-A	0.00	19.47	25.62	30.03	33.66
	32.43	47.32	56.91	62.00	64.57
	64.17	66.74	70.48	76.16	82.58

Table 4 Extension of Table 3 to large values of P/P_{cr} for the A-S modes ($\omega R^2\sqrt{\rho h/D}$)

P/P_{cr}		
1.5	2.0	2.66
11.26	9.39	0.00
39.26	37.09	33.37
61.94	65.64	70.77

value of $P/P_{cr} = 1.0$ describes a pair of *tensile* forces, equal in magnitude to the compressive buckling load in that mode. Tensile forces, with one exception (which will be discussed in the next section), are seen to increase the frequencies relative to the unloaded case, at least for the range of P/P_{cr} shown in Table 3. Thus, for example, for $P = 13.15\ D/R$ (from Table 2), the fundamental (i.e., lowest) frequency of the plate is increased by 41.2 percent. More results are available in the recent dissertation by Ayoub (1989).

Tension Buckling

Returning to the exception mentioned in the preceding section, Table 3 indicates that tensile concentrated forces decrease the lowest frequency for the A-S mode. Indeed, a set of tensile forces of $P = 116.09\ D/R$ (corresponding to $P/P_{cr} = 1.0$) causes the frequency to decrease by 7.8 percent. One wonders what would happen if P were increased further.

Table 4 is an extension of Table 3 for the A-S modes only, as P/P_{cr} is increased beyond unity. It is seen that, with increasing P/P_{cr}, the frequency decreases at an increasing rate until it becomes zero at $P = 318\ D/R$ (corresponding to $P/P_{cr} = 2.66$). This indicates a tension buckling load for A-S modes. The tension buckling is a consequence of the compressive stress generated in the direction transverse to the applied tensile forces. This may be observed in equations (1) for σ_θ with $\theta = 0$.

Table 5 Convergence study for tension buckling (A-S critical mode)

M,N	Number of terms in series	$\frac{PR}{D}$
9	15	293.8
11	21	285.2
13	27	281.5
15	36	279.8
17	45	278.8
19	55	278.2

Further investigation shows that considerably more terms of the displacement series are needed for accurate representation of tension buckling, and that the ten-term result given above is far from converged. A convergence study for the A-S mode tension buckling load is displayed in Table 5. It is seen that at least 55 terms in the series (requiring finding the roots of a characteristic determinant of order 55) are needed to determine the tension buckling load with reasonable accuracy. The value thus determined is $P = 278\ D/R$.

Consider next the behavior of the *second* frequency for A-S modes. It is observed from Tables 3 and 4 that the maximum frequency occurs for a small amount of tensile force in the vicinity of $P/P_{cr} = 0.5$, and that subsequent increase in the forces causes the frequency to decrease at an increasing rate. This indicates the existence of a second tensile buckling load in excess of $278\ D/R$ for this mode symmetry class.

Tensile buckling can also occur in the modes of the other symmetry classes. This is shown in Table 6, where a three-step convergence study is made for the smallest tensile buckling load of each symmetry class. It is observed that the tensile buckling loads converge at different rates for the different symmetry classes. Table 6 also verifies that the smallest tensile buckling load for all symmetry classes is that for the A-S mode, as discussed above. Thus, $P = 278\ D/R$ is the *critical* tensile buckling load for the simply supported plate with $\nu = 0.3$.

Concluding Remarks

A proper procedure has been demonstrated for obtaining free vibration frequencies and buckling loads to any desired degree of accuracy for circular plates subjected to a pair of diametral point forces. The procedure uses the well-known Ritz method, but depends upon choosing proper displacement function which:

(1) recognize the symmetries of possible mode shapes,
(2) do not include terms causing undesired singularities, and
(3) form a mathematically complete set, thereby guaranteeing convergence to the correct results.

A study of the frequency spectrum with varying tensile point forces showed decreasing frequency with increasing force for some of the modes. Tracking of the decreasing frequency with increasing loads to its zero value determines a tension buckling load unequivocally. Theoretically, one could simply take the complete set of loading parameter eigenvalues which are the roots of the characteristic determinant for the buckling problem, with all positive values of corresponding to tension buckling loads. However, careful tracking reduces the likelihood of having meaningless extraneous roots caused by numerical anomalies in dealing with determinants of large order.

The mode shapes for tension buckling tend to have node lines the direction of the applied forces. The lowest (i.e., critical) tension buckling load is for an A-S mode having a single

Downloaded 03 May 2010 to 171.66.16.244. Redistribution subject to ASME license or copyright; see http://www.asme.org/terms/Terms_Use.cfm

Table 6 Smallest values of nondimensional loads PR/D for tension buckling for each mode symmetry class ($\nu = 0.3$)

Number of terms in series	Mode symmetry class			
	S-S	S-A	A-S	A-A
21	329.4	2209	285.2	1845
36	319.3	1440	279.8	1368
55	317.1	1274	278.2	1252

Table 7 Variation of compression and tension buckling loads with Poisson's ratio

ν	Compression buckling		Tension buckling	
	P_{cr} R/D	P_{cr} R/Eh^3	P_{cr} R/D	P_{cr} R/Eh^3
0	10.636	0.8863	275.4	22.95
0.1	11.503	0.9683	276.4	23.27
0.2	12.340	1.0712	277.3	24.07
0.3	13.148	1.2040	278.2	25.48
0.4	13.924	1.3813	279.0	27.68
0.5	14.677	1.6308	279.8	31.09

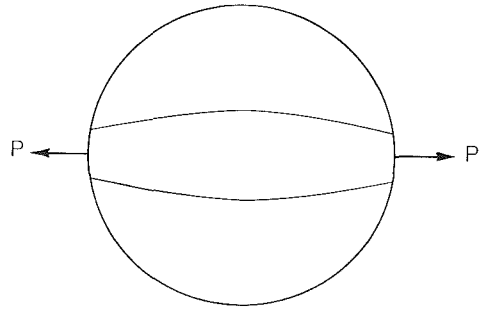


Fig. 2 Doubly symmetric tension buckling node lines

nodal diameter joining the load application points (i.e., the line $\theta = 0$, 180 deg, in Fig. 1). The next lowest value is for an S-S mode having two node lines which, although not straight, are also in the direction of the forces, as shown in Fig. 2. Thus, the compressive transverse stress components caused by the tensile forces tend to cause wrinkling in the transverse direction. This is in contrast with buckling mode shapes due to compressive point forces, which involve more curvature change in the direction of the loading.

Although transverse compressive stresses are caused by tensile point forces, equations (1) show that they do not depend upon Poisson effects. The strain energy of bending, as given by equation (6) and used in the vibration and buckling problems, does depend upon Poisson's ratio (ν). Hence, the vibration frequencies and buckling loads also depend upon ν. For modes dominated by terms having small numbers of circumferential waves (e.g., $n = 0$ and 1), the dependence of results upon ν is expected to be strong (cf., Leissa and Narita, 1980). This is demonstrated in Table 7, where the variation of nondimensional buckling parameters with ν is shown for both compressive and tensile loads. The parameters $P_{cr}R/D$ used in the previous tables is shown there for comparison. However, since $D = Eh^3/12(1-\nu^2)$, this parameter contains ν. The dependence of critical load upon ν is shown clearly by the other tabulated parameter, $P_{cr}R/Eh^3$. Both tension and compression buckling loads are seen to increase significantly as ν is increased from zero to its upper limiting value of 0.5. This is particularly the case for the compression buckling load, which nearly doubles. For the entire spectrum of ν, the critical compression buckling was found to occur in an S-S mode, whereas critical tension buckling was in an A-S mode. Except for the value of $P_{cr}R/D = 13.14$ obtained by Yamaki (1956) for compression buckling with $\nu = 0.3$, as discussed earlier, all data in Table 7 represents previously unknown information.

Because the vibration frequencies obtained by the Ritz method are all known to be upper bounds to the exact values, it may be easily proven that the tension buckling loads (as well as the compressive ones) are also upper bounds to the exact values. This was demonstrated numerically in Tables 5 and 6.

The tension buckling load for the simply supported circular plate was determined above to be $P = 278\ D/R$. For the circumscribing square plate of dimensionless $2R \times 2R$, which is also simply supported, the tension buckling load was found to be slightly larger—$P = 312\ D/R$. This is in contrast with the situation for buckling due to compressive point loads, where the critical load for the square plate was found to be slightly smaller (cf., Leissa and Ayoub, 1988).

References

Ayoub, E. F., 1989, "Vibration and Buckling of Plates Subjected to Inplane Concentrated Forces," Ph.D. Dissertation, Ohio State University.

Durban, D., 1977, "Instability of an Elastic Circular Plate Subjected to Nonuniform Loads," *AIAA Journal*, Vol. 15, No. 3, pp. 360–365.

Kantorovich, L. V., and Krylov, V. I., 1964, *Approximate Methods of Higher Analysis*, P. Noordhoff Ltd., Gronigen.

Leissa, A. W., 1969, *Vibration of Plates*, NASA SP-160, U.S. Government Printing Office, Washington, DC.

Leissa, A. W., and Ayoub, E. F., 1988, "Vibration and Buckling of a Simply Supported Rectangular Plate Subjected to a Pair of In-Plane Concentrated Forces," *Journal of Sound and Vibration*, Vol. 127, No. 1, pp. 155–171.

Leissa, A. W., and Ayoub, E. F., 1989, "Tension Buckling of Rectangular Sheets Due to Concentrated Forces," *ASCE Journal of Engineering Mechanics*, to appear.

Leissa, A. W., and Narita, Y., 1980, "Natural Frequencies of Simply Supported Plates," *Journal of Sound and Vibration*, Vol. 70, No. 2, pp. 221–229.

Mikhlin, S. G., 1964, *Variational Methods in Mathematical Physics*, Pergamon Press, Oxford, U.K.

Narita, Y., 1985, "Vibration and Stability of Circular Plates Under Partially Distributed or Concentrated Inplane Loads," ASME JOURNAL OF APPLIED MECHANICS, Vol. 52, pp. 549–552.

Rózsa,l M., 1966, "Stability Analysis of a Circular Plate Submitted to Two Compressive Forces Acing along a Diameter," *Acta Technica Academiae Scientiarum Hungaricae*, Vol. 55, pp. 153–172.

Timoshenko, S. P., and Goodier, J. N., 1970, *Theory of Elasticity*, 3rd ed., McGraw-Hill, New York.

Yamaki, N., 1956, "Buckling of a Circular Plate under Locally Distributed Forces," *Transactions of the Japanese Society of Mechanical Engineers*, Vol. 22, No. 115, pp. 119–123.

Downloaded 03 May 2010 to 171.66.16.244. Redistribution subject to ASME license or copyright; see http://www.asme.org/terms/Terms_Use.cfm

Analytical Estimation for Static Deformation of Wire Ropes With Fibrous Core

K. Kumar
Professor of Aerospace Engineering,
Indian Institute of Technology,
Kanpur-208016 UP, India

J. E. Cochran, Jr.
Professor of Aerospace Engineering,
Auburn University,
Auburn University, AL 36849

This papers develops closed-form solutions for the extension of twisted wire ropes with fibrous cores which are subjected to axial forces as well as axial moments. The analytical results are compared with the corresponding numerical results obtained by Costello and Phillips. A close agreement between the two establishes validity of the analytical solutions. Finally, an expression for the effective rigidity modulus of wire ropes with fibrous core is obtained in terms of the helix angle and the number of helical wires in the rope for each of the two end conditions.

Introduction

The usefulness of wire rope in conventional engineering applications is well recognized. Recently, interest has been expressed in its use for augmentation of structural damping in large space structures. However, any serious attempt for such applications must be preceded by detailed investigations of the various aspects of the wire rope dynamics. These in turn require having a better insight into the static behavior of wire rope under the influence of external loads.

The problem of extension of wire ropes, or "cables," under static loads has been investigated by several authors. In the earlier theoretical works, often simplifying assumptions of questionable validity were made. Hall (1951) assumed that each wire in the cable is subjected to simple tension. Hruska (1951, 1952, 1953) also included in his analysis the radial and tangential forces. Leissa (1959) and Starkey and Cress (1959) were the first ones to consider the contact stresses. The effects of bending and twisting moments in the wires were recognized by Machida and Durelli (1973) and Bert and Stein (1962). Chi (1974) studied the problem of extension of wire ropes with fixed-end strands; however, he ignored the effects of contact forces. Phillips and Costello (1973, 1985) adopted a more fundamental approach to study the various aspects of static behavior of the wire ropes including the contact forces. They treated the cable as a group of separate curved rods in the form of helices. The general, nonlinear equilibrium equations were obtained for each rod. The governing set of equations was solved using an iterative Newton-Raphson approach to obtain the axial force-strain characteristics. The "linearization" subsequently proposed by Velinski et al. (1984), and Phillips and Costello (1985) achieves some economy of computational time without altering the basic numerical character of their simulations.

More recently, Kumar and Cochran (1987) applied Costello's theory in conjunction with the assumption of small geometric changes to develop closed-form solutions for static elastic deformations of multilayered strands with metallic core. This same approach is applied in this paper to develop corresponding analytical results for single strand cables with *fibrous cores*. To assess the accuracy of the closed-form solution thus obtained, the analytical results are compared with the earlier numerical results of Costello and Phillips (1976).

Analysis

The wire rope considered here is a single strand formed by

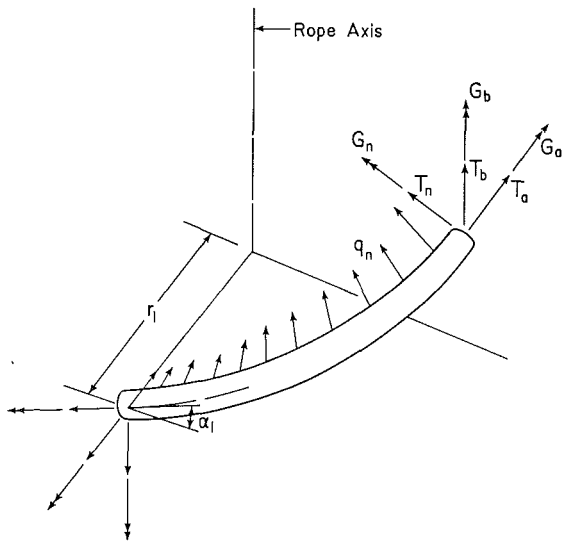


Fig. 1 Components of the resultant forces and moments acting on the helical wires

Contributed by the Applied Mechanics Division of THE AMERICAN SOCIETY OF MECHANICAL ENGINEERS for publication in the JOURNAL OF APPLIED MECHANICS.

Discussion on this paper should be addressed to the Technical Editor, Leon M. Keer, The Technological Institute, Northwestern University, Evanston, IL 60208, and will be accepted until two months after final publication of the paper itself in the JOURNAL OF APPLIED MECHANICS. Manuscript received and accepted by the ASME Applied Mechanics Division, June 29, 1989.

Copyright © 1990 by ASME
Downloaded 03 May 2010 to 171.66.16.244. Redistribution subject to ASME license or copyright; see http://www.asme.org/terms/Terms_Use.cfm

an arbitrary number of thin helical wires around a fibrous core. The core does not directly contribute to the strength of the rope. The initial wire helix angle and helix radius are denoted by α and r, respectively. We assume that when the wire rope is subjected to an external pull F and an axial moment M, the helical character of the wires is retained and the new helix angle and radius are denoted by α_1 and r_1, respectively, as shown in Fig. 1. The equilibrium conditions for the new configuration, as stated by Love (1944) are used as a starting point for our analysis. Love's equations, included here in order that the present development be as self-contained as possible, are:

$$\begin{aligned}
&\frac{dT_n}{ds} - T_b\tau_1 + T_a\kappa_1' + q_n = 0\\
&\frac{dT_b}{ds} - T_a\kappa_1 + T_n\tau_1 + g_b = 0\\
&\frac{dT_a}{ds} - T_n\kappa_1' + T_b\kappa_1 + q_a = 0\\
&\frac{dG_n}{ds} - G_b\tau_1 + G_a\kappa_1' + T_b + n_n = 0\\
&\frac{dG_b}{ds} - G_a\kappa_1 + G_n\tau_1 + T_n + n_b = 0\\
&\frac{dG_a}{ds} - G_n\kappa_1' + G_b\kappa_1 + n_a = 0
\end{aligned} \tag{1}$$

where

T, G = the resultant internal and external force and moment, respectively, acting on each helical wire.

q, n = the resultant constant force and moment per unit length, respectively.

r, r_1 = the initial and final helix radii, respectively.

V_n, V_b, V_a = the components of the vector V along the wire normal, binormal, and axis, respectively; $V = T, G, q$ and n.

G_n, G_b, G_a = $A(\kappa_1 - \kappa)$, $A(\kappa_1' - \kappa')$ *and* $C(\tau_1 - \tau)$, respectively.

T_a = $D\xi$ where ξ denotes the longitudinal strain of helical wire.

A, C, D = $(\pi ER^4/4)$, $[\pi ER^4/\{4(1+\nu)\}]$ and πER^2, respectively.

E = modulus of rigidity of the material of the helical wires.

R = radius of helical wires.

α, α_1 = the initial and final helix angles, respectively.

κ, κ' = 0, $(\cos^2\alpha/r)$; the components of initial curvature of the centerline of helical wire in normal and binormal directions, respectively.

κ_1, κ_1' = 0, $(\cos^2\alpha_1/r_1)$; the components of final curvature of the centerline of helical wire in normal and binormal directions, respectively.

τ, τ_1 = $(\sin\alpha\ \cos\alpha/r)$, $(\sin\alpha_1\ \cos\alpha_1/r_1)$; the initial and final angles of twist per unit length, respectively, along the helical wire.

s = distance along the centerline of the deformed wire.

Some new notation used here has been adopted because it seems less cumbersome than that used by Love (1944).

The equations of equilibrium are valid provided ξ, the longitudinal strain of the helical wire, is small. We further assume that the tension in the cable is constant along the length of the cable and that the individual wires in the cables are not subjected to internal bending moments through contact; i.e., $n_n = n_b = 0$. Using these assumptions, we may reduce equations (1) to

$$\begin{aligned}
q_n &= -T_a(\cos^2\alpha_1/r_1) + T_b(\sin\alpha_1\ \cos\alpha_1/r_1)\\
T_b &= G_a(\cos^2\alpha_1/r_1) + G_b(\sin\alpha_1\ \cos\alpha_1/r_1)\\
q_b &= q_n = n_a = 0.
\end{aligned} \tag{2}$$

Now, considering the equilibrium of a rope consisting of all the m helical wires—when the nonzero contact forces denoted by q become internal and hence vanish—the expressions for the total axial force F and the twisting moment M can be written as:

$$\begin{aligned}
F &= m(T_a\sin\alpha_1 + T_b\cos\alpha_1)\\
M &= m(G_a\sin\alpha_1 + G_b\cos\alpha_1) + T_a r_1\cos\alpha_1 - T_b r_1\sin\alpha_1).
\end{aligned} \tag{3}$$

From the geometry of the wires in the rope, we can write

$$(r/R) = [1 + \cot^2(\pi/m)\sin^2\alpha]^{1/2} \tag{4}$$

where

R = wire radius.

For the practical range of α limited to the interval, $\pi/3 < \alpha \le \pi/2$, equation (4) simplifies to:

$$(R/r) = \sin\alpha\ \sin(\pi/m)[1 + (1/2)\sin^2(\pi/m)\cos^2\alpha]. \tag{5}$$

Similarly, the corresponding relation for the deformed cable configuration can be written as

$$(R_1/r_1) = \sin\alpha_1\sin(\pi/m)[1 + (1/2)\sin^2(\pi/m)\cos^2\alpha_1] \tag{6}$$

where

$$R_1 = R(1 - \nu\xi).$$

By dividing equation (5) by equation (6), we get $(r_1/r) = 1 - \xi_r$ where

$$\begin{aligned}
\xi_r &= f\cot\alpha\Delta\alpha + \nu\xi\\
\nu &= \text{Poisson's ratio}\\
f &= 1 - \sin^2\alpha\sin^2(\pi/m) - \sin^2\alpha\cos^2\alpha\sin^4(\pi/m).
\end{aligned}$$

Considerations of compatibility lead to the following relations:

$$\begin{aligned}
&\text{Axial strain, } \epsilon = (1+\xi)(\sin\alpha_1/\sin\alpha) - 1\\
&\text{Rotational strain, } \beta = (r/r_1)(1+\epsilon)\cot\alpha_1 - \cot\alpha.
\end{aligned} \tag{7}$$

Assuming $\Delta\alpha = (\alpha_1 - \alpha)$ to be small in magnitude, expanding the right-hand sides as power series in $\Delta\alpha$ and neglecting the second and higher-power terms in $\Delta\alpha$, we get,

$$\xi = \epsilon - \Delta\alpha\cot\alpha \tag{8}$$

$$\begin{aligned}
\beta = {} & \epsilon(1+\nu)\cot\alpha - (\Delta\alpha/\sin^2\alpha)\\
& \times \{1 - (1 - \nu - \sin^2\alpha\sin^2(\pi/m)\\
& - \sin^2\alpha\cos^2\alpha\sin^4(\pi/m))\cos^2\alpha\}.
\end{aligned} \tag{9}$$

From equation (9), it is easy to see that

$$\Delta\alpha = [\epsilon(1+\nu)\sin\alpha\ \cos\alpha - \beta\ \sin^2\alpha]g \tag{10}$$

where

$$g = 1 + \{\cos^2(\pi/m) - \nu\}\cos^2\alpha + (1 - 2\nu)\cos^4\alpha.$$

Our objective now is to solve the above set of equations in order to obtain a closed-form solution for the axial force and moment required for the specified axial cable strains. That is why the expressions for forces and moments in helical wires are first obtained. Utilizing the small $\Delta\alpha$ assumption for simplifications, these expressions can be approximated as follows:

$$\begin{aligned}
T_a \doteq {} & \pi R^2 E[\epsilon h + \beta g\ \sin\alpha\ \cos\alpha]\\
T_b \doteq {} & [\pi R^4 E/(4r^2)]\sin^3\alpha\ \cos^2\alpha[(1+2\nu)\cos\alpha\\
& + \{(1+\nu) + 2(1-\nu)\cos^2\alpha\}\sin\alpha]\\
G_a \doteq {} & -[\pi R^4 E/(4r)]\sin\alpha[\epsilon\{-\cos 2\alpha - \nu_f - \cos^4\alpha\\
& \times((2-\nu)\cos^2\pi/m - \nu - (1-\nu)\sin^2\alpha\sin^2\pi/m)\}\cos\alpha\\
& + \beta\{\sin\alpha/(1+\nu)\}\{\cos 2\alpha + \cos^4\alpha\\
& \times((2-\nu)\cos^2\pi/m - \nu - (1-\nu)\sin^2\alpha\sin^2\pi/m)\}]\\
G_b \doteq {} & -[\pi R^4 E/(4r)\cos\alpha[\epsilon\ \cos\alpha\ \{2\sin^2\alpha - \nu\cos 2\alpha\\
& - (1+\nu)((1-\nu)\cos 2\alpha + \sin^2\alpha\sin^2\pi/m)\cos^2\alpha\\
& + (-(1-\nu)\cos 2\alpha - 4\nu^2\sin^2\alpha + (1+\sin^2\alpha)\\
& \times\sin^2\pi/m)\cos^4\alpha\} + \beta\sin\alpha\{2\sin^2\alpha\\
& - \cos^2\alpha((1-\nu)\cos^2\alpha + \sin^2\alpha\sin^2\pi/m)
\end{aligned}$$

Downloaded 03 May 2010 to 171.66.16.244. Redistribution subject to ASME license or copyright; see http://www.asme.org/terms/Terms_Use.cfm

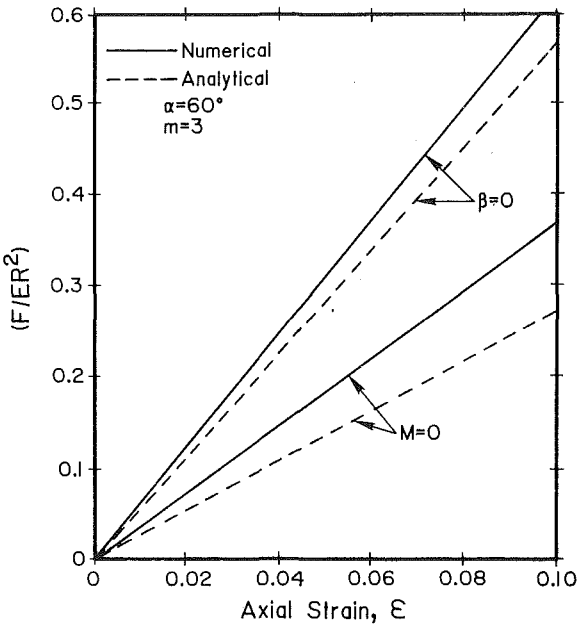


Fig. 2 Typical plots comparing analytical and numerical results for wire rope extension characteristics when $m=3$

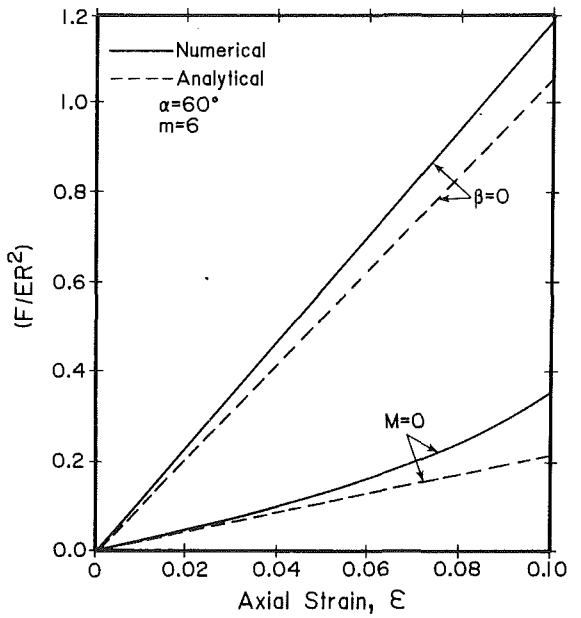


Fig. 3 Typical plots comparing analytical and numerical results for wire rope extension characteristics when $m=6$

$$+(1-\nu)\cos^4\alpha(-(1-\nu)\cos 2\alpha+\sin^2\pi/m \times(1+\sin^2\alpha))\}] \quad (11)$$

where

$$h=1-(1+\nu)\cos^2\alpha-(1+\nu)(\cos^2\pi/m-\nu)\cos^4\alpha.$$

Utilizing these in equations (3) and (4) and performing the necessary algebra enables us to obtain the following results:

$$F/(m\pi R^2E)=F_\epsilon\epsilon+F_\beta\beta \quad (12)$$

$$M/(m\pi R^3E)=M_\epsilon\epsilon+M_\beta\beta \quad (13)$$

where

$$\begin{aligned} F_\epsilon &= h\sin\alpha \\ F_\beta &= [g-(1/4)(1+\nu)\sin^2\pi/m\sin^4\alpha\cos^2\alpha]\cos\alpha\sin^2\alpha \\ M_\epsilon &= (r/R)[h-(1/4)(1+\nu\sin^2 2\alpha)(\sin^2\alpha \times\sin^2\pi/m)/(1+\nu)]\cos\alpha \\ M_\beta &= (r/R)[g\cos^2\alpha+(1/4)\sin^4\alpha\sin^2\pi/m \times\{(1+\nu_f\cos 2\alpha)+(1+\nu)\sin^2\alpha\cos^2\alpha\}]\sin\alpha \end{aligned} \quad (14)$$

with

$$\nu_f=\nu/(1+\nu).$$

To illustrate the use of these results, in what follows, we provide examples of their application in studying the static elastic deformations of wire ropes in two commonly encountered situations (Cases 1 and 2). In the first case, the ends of the ropes are constrained against rotation while in the second, the ropes are free to rotate. Next, the effective dimensionless modulus of rigidity of the wire rope, ($\bar{E}$), defined as

$$\bar{E}=d[F/(m\pi R^2E)]/d\epsilon.$$

is determined.

Case 1 No end rotation permitted, i.e., $\beta=0$.

In this practical situation, using equations (8), (10), (12), and (14), it can be easily shown that:

$$\begin{aligned} &\Delta\alpha=\epsilon g(1+\nu)\sin\alpha\cos\alpha \\ &\xi=\epsilon[1-(1+\nu)g\cos^2\alpha] \\ &[F/(ER^2)]|_{\beta=0}=\epsilon m\pi h\sin\alpha \\ &[M/(ER^3)]|_{\beta=0}=(m\pi r/R)\epsilon[h-(1/4)\sin^2\alpha \sin^2\pi/m(1+\nu\sin^2 2\alpha)/(1+\nu)]\cos\alpha \\ &\bar{E}=h\sin\alpha. \end{aligned}$$

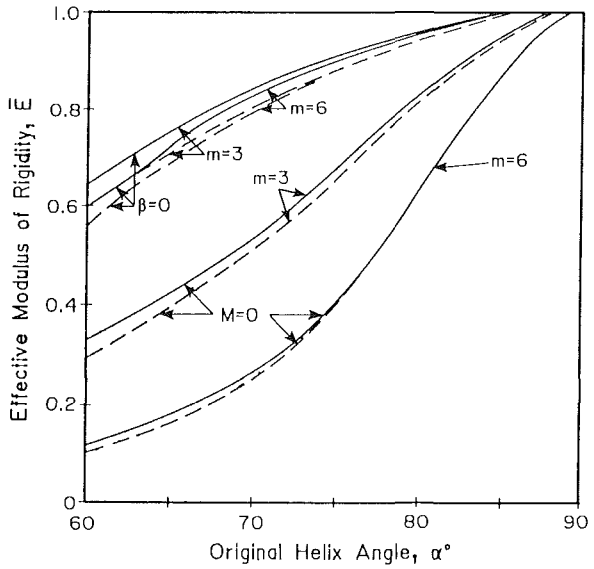


Fig. 4 Plots comparing the analytical and numerical values of effective moduli of rigidity of wire rope

Case 2 Rope ends are free to rotate.

In several applications, the ropes are not restrained against rotation, a condition for which the end moments can be assumed to be zero. On substituting $M=0$ in equation (13) for this case, we obtained the following expression for the rotational strain:

$$\beta=-\epsilon\cot\alpha[h-(1/4)\sin^2\alpha\sin^2\pi/m (1+\nu\sin^2 2\alpha)/(1+\nu)]/[g\cos^2\alpha+ (1/4)\sin^4\alpha\sin^2\pi/m\{1+\nu_f\cos 2\alpha+ (1+\nu)\sin^2\alpha\cos^2\alpha\}]. \quad (16)$$

Finally, by putting this β into equation (12) and performing the necessary algebra, we find the following results:

$$\begin{aligned} &[F/(ER^2)]|_{M=0}=\epsilon m\pi h\sin^3\alpha\sin^2(\pi/m)u \\ &\bar{E}|_{M=0}=hu\sin^3\alpha\sin^2\pi/m \end{aligned} \quad (17)$$

Downloaded 03 May 2010 to 171.66.16.244. Redistribution subject to ASME license or copyright; see http://www.asme.org/terms/Terms_Use.cfm

where

$$u = [1 + \nu_f \cos 2\alpha + \{(1+\nu)\sin^2\alpha + g\}\cos^2\alpha(1+\cos^2\alpha)]/[g\cos^2\alpha + (1/4)\sin^2\alpha\sin^2\pi/m\{1 + \nu_f\cos 2\alpha + (1+\nu)\sin^2\alpha\cos^2\alpha\}.$$

Results and Discussion

Figures 2 and 3 show the results computed for three and six wire ropes of initial helix angle 60 deg for the two stated end conditions. To investigate the accuracy of the analytical results obtained here, the corresponding numerical results of Costello and Phillips (1976) are included for comparison. The results for relatively smaller axial strains are found to be in a reasonable agreement. Even for the "worst case" of low helix angles considered here, the discrepancies observed are not too significant. The importance of the approximate analytical results cannot be overemphasized as these can be used in explicit assessment of the influence of design parameters such as α, m, and ν.

For a specified axial strain, the axial load taken up by the cable is strongly affected by α, while the number of helical wires seem to have significant influence only in the case of no end moments; i.e., when $M=0$. The analytical expressions clearly show that the Poisson's ratio hardly affects the axial force in the wire rope for the case of no rotation. Even in the zero moment case, the dependence of the extension characteristics on this property appears to be rather weak and the computations for $\nu=0.26$ and 0.31 produce virtually identical results.

The analytical results expressing ξ, $\Delta\alpha$, and β in terms of the axial strain, ϵ, may also be quite useful, particularly in formulations of governing equations of motion for wire rope systems.

Figure 4 compares the values of effective moduli of rigidity for the wire ropes obtained using the above analytical results with the corresponding numerical results of Costello and Phillips (1976) over the entire feasible design range of α. A generally excellent agreement between the two is noted, thus establishing the validity of the approximate analytical results.

Acknowledgment

The support of this work under NASA Grant NAG8-532 through the Marshall Space Flight Center is gratefully acknowledged.

References

Bert, C. W., and Stein, R. A., 1962, "Stress Analysis of Wire Rope in Tension and Torsion," *Wire and Wire Products*, Vol. 37, pp. 769–770.

Chi, M., 1974, "Analysis of Multi-Wire Strands in Tension and Combined Tension and Torsion," *Developments in Theoretical and Applied Mechanics, Proceedings of the Seventh Southeastern Conference and Theoretical and Applied Mechanics*, Vol. 7, pp. 599–639.

Costello, G. A., and Phillips, J. W., 1973, "Contact Stresses in Thin Twisted Rods," *Journal of Applied Mechanics Division*, Trans. ASME, Trans. Series E, Vol. 40, pp. 629–630.

Costello, G. A., and Phillips, J. W., 1974, "Contact Stresses in Thin Twisted Rods," *Journal of Applied Mechanics Division*, ASCE, Vol. 100, pp. 1069–1099.

Costello, G. A., and Phillips, J. W., 1976, "Effective Modulus of Twisted Wire Cables," *Journal of Engineering Mechanics Division*, ASCE, Vol. 102, pp. 171–181.

Hall, H. M., 1951, "Stresses in Small Wire Ropes," *Wire and Wire Products*, Vol. 26, pp. 228, 257–259.

Hruska, F. H., 1951, "Calculations Stresses in Wire Rope, *Wire and Wire Products*, Vol. 26, pp. 766–767, 799–801.

Hruska, F. H., 1952, "Radial Forces in Wire Ropes," *Wire and Wire Products*, Vol. 27, pp. 459–463.

Hruska, F. H., 1953, "Tangential Forces in Wire Ropes," *Wire and Wire Products*, Vol. 28, pp. 455–460.

Kumar, K., and Cochran, J. E., Jr., 1987, "Closed-Form Analysis for Elastic Deformations of Multilayered Strands," ASME JOURNAL OF APPLIED MECHANICS, Vol. 109, pp. 898–903.

Leissa, A. W., 1959, "Contact Stresses in Wire Ropes," *Wire and Wire Products*, Vol. 34, pp. 307–316, 372–373.

Love, A. E. H., 1944, *A Treatise on the Theory of Elasticity*, Dover Publications, Inc., New York, Chapters 18 and 19.

Machida, S., and Durelli, A. J., 1973, "Response of a Strand to Axial and Torsional Displacements," *Journal of Mechanical Engineering Science*, Vol. 15, pp. 241–251.

Phillips, J. W., and Costello, G. A., 1973, "Contact Stresses in Twisted Wire Cables," *Journal of the Engineering Mechanics Division*, ASCE, Vol. 99, pp. 331–341.

Phillips, J. W., and Costello, G. A., 1985, "Analysis of Wire Ropes with International Wire-Rope Cores," ASME JOURNAL OF APPLIED MECHANICS, Vol. 52, pp. 510–516.

Starkey, W. L., and Cress, H. A., 1959, "An Analysis of Critical Stresses and Mode of Failure of a Wire Rope," ASME *Journal of Engineering for Industry*, Vol. 81, pp. 307–316.

Velinsky, S. A., Anderson, G. L., and Costello, G. A., 1984, "Wire Rope with Complex Cross Sections," *Journal of the Engineering Mechanics Division*, ASCE, Vol. 110, pp. 380–391.

Downloaded 03 May 2010 to 171.66.16.244. Redistribution subject to ASME license or copyright; see http://www.asme.org/terms/Terms_Use.cfm

The Maggi or Canonical Form of Lagrange's Equations of Motion of Holonomic Mechanical Systems

John G. Papastavridis
School of Mechanical Engineering,
Georgia Institute of Technology,
Atlanta, GA 30332

This paper formulates the simplest possible, or canonical, form of the Lagrangean-type of equations of motion of holonomically constrained mechanical systems. This is achieved by introducing a new special set of n *holonomic (system) coordinates in terms of which the* m(<n) *holonomic constraints are expressed in their simplest, or uncoupled, form: the first* m *of these new coordinates vanish; the remaining* (n-m) *(nonvanishing) new coordinates of the* (n-m) *degree-of-freedom system are then independent. From the resulting equations of motion: (a) The last* (n-m) *are reactionless canonical equations (the holonomic counterpart of the linear or nonlinear equations, either of Maggi (in the old variables), or of Boltzmann/Hamel (in the new variables)) whose solution yields the motion, while (b) the first* m *supply the system reactions, in the old or new coordinates, once the motion is known. Special forms of these equations and a simple example are also given. The geometrical interpretation of the above, in modern vector/linear algebra language is summarized in the Appendix.*

1 Introduction[1]

Consider a mechanical system described by a set of n holonomic positional system generalized coordinates $q = \{q_1, \ldots, q_n\}$. These q are not independent, in general, but are restricted by $m(<n)$ finite or holonomic, independent[2] constraints

$$f_k = f_k(q,t) = 0 \ (k = 1, \ldots, m). \tag{1}$$

Next, we define, as customary, the (covariant) components of the system impressed (or applied, or active) force as the coefficients

$$Q = \{Q_1, \ldots, Q_n\}$$

of the (first-order) impressed virtual work expression

$$\delta' W = \sum_{l=1}^{n} Q_l \delta q_l, \tag{2}$$

where the

$$\delta q = \{\delta q_1, \ldots, \delta q_n\}$$

are arbitrary fixed-time differentials of the q's, but they satisfy the virtual forms of the constraints (equation (1))

$$\delta f_k \equiv \sum_{l=1}^{n} \frac{\partial f_k}{\partial q_l} \delta q_l = 0 \qquad (k = 1, \ldots, m). \tag{3}$$

No additional constraints are imposed on the system.

Then, as is well known (see e.g., Hamel, 1949) the equations of motion of this system are the following Lagrangean-type Routh/Voss (R/V) equations

$$M_l = Q_l^{(r)} \qquad (l = 1, \ldots, n); \tag{4}$$

where

$$M_l \equiv E_l(T) - Q_l \qquad [= M_l(t,q,\dot{q})],$$

$$Q_l^{(r)} \equiv \sum_{k=1}^{m} \lambda_k \frac{\partial f_k}{\partial q_l}$$

$= $ Covariant components of system constraint reaction vector, in the q-coordinates,

$$E_l(\ldots) \equiv \frac{d}{dt}\left(\frac{\partial \ldots}{\partial \dot{q}_l}\right) - \left(\frac{\partial \ldots}{\partial q_l}\right) \tag{4a}$$

$= $ Euler-Lagrange operator,

$T = T(q, \dot{q}, t) = $ Kinetic Energy of System (relative to an inertial frame),

$\lambda = \{\lambda_1, \ldots, \lambda_m\} = $ Lagrangean multipliers.

Contributed by the Applied Mechanics Division of THE AMERICAN SOCIETY OF MECHANICAL ENGINEERS for publication in the JOURNAL OF APPLIED MECHANICS.

Discussion on this paper should be addressed to the Technical Editor, Leon M. Keer, The Technological Institute, Northwestern University, Evanston, IL 60208, and will be accepted until two months after final publication of the paper itself in the JOURNAL OF APPLIED MECHANICS. Manuscript received by the ASME Applied Mechanics Division, Dec. 21, 1988; final revision, June 22, 1989.

[1]The main body of the paper has been, deliberately, written in the simplest possible, standard, engineering notation. A more precise summary, in the language of vectors/tensors/linear algebra, is given in the Appendix, for the benefit of the more advanced readers.

[2]Analytically, this means that the $m \times n$ matrix $(\partial f_k/\partial q_l)$ $(k = 1, \ldots, m; l = 1, \ldots, n)$ has maximal rank, i.e., m, at each (q, t).

Copyright © 1990 by ASME
Downloaded 03 May 2010 to 171.66.16.244. Redistribution subject to ASME license or copyright; see http://www.asme.org/terms/Terms_Use.cfm

Equations (4) plus (1), plus appropriate initial conditions, constitute a set of $(n + m)$ equations for the $(n + m)$ functions $q = q(t)$, $\lambda = \lambda(t)$.

The objective of this paper is to seek new systems of generalized (system) coordinates in which equations (4) take their simplest form. It is in this original and literal sense that we use the term "canonical,"[3] and not in the customary one, i.e., of Hamiltonian equations in terms of q, and generalized momenta, etc.

2 The Basic Theory

Guided by the method of quasi-coordinates/quasi-velocities of Hamel et al., which applies to both holonomic and nonholonomic systems alike, we introduce the following new system of holonomic coordinates $e = \{e_1, \ldots e_n; e_{n+1}\}$

$$\begin{cases} e_d \equiv f_d(q,t) & = 0 \quad (d = 1, \ldots, m; \text{ for } \textit{dependent}), \\ e_i \equiv f_i(q,t) & \neq 0 \quad (i = m+1, \ldots, n; \text{ for } \textit{independent}), \\ e_{n+1} \equiv q_{n+1} & = t \end{cases} \tag{5}$$

where the second set of equation (5) is arbitrary but such that when all these equations are solved for the n q's in terms of the e's (and t) and then these results are substituted back into the first of equation (5), they satisfy them identically.[4] Thus, inverting equation (5), we obtain

$$q_l = q_l(e_i, t) \qquad \begin{pmatrix} l = 1, \ldots, n; \\ i = m+1, \ldots, n \end{pmatrix}, \tag{6}$$

and since

$$\delta e_1 = \ldots = \delta e_m = 0, \text{ or } \delta e_d = 0, \tag{7}$$

and

$\delta e_{n+1} = \delta q_{n+1} = \delta t = 0$ (by the d'Alembert/Lagrange Principle)

finally, equation (6) yields

$$\delta q_l = \sum_{i=m+1}^{n} \frac{\partial q_l(e,t)}{\partial e_i} \delta e_i \quad (l = 1, \ldots, n). \tag{8}$$

Inserting now this δq representation into Lagrange's Principle (LP)

$$\sum_{l=1}^{n} M_l \delta q_l = 0, \tag{9}$$

yields

$$\sum_{l=1}^{n} M_l \left(\sum_{i=m+1}^{n} \frac{\partial q_l}{\partial e_i} \delta e_i \right) = \sum_{i=m+1}^{n} M_i^* \delta e_i = 0, \tag{10}$$

where

$$\begin{aligned} M_i^* &\equiv \sum_{l=1}^{n} \frac{\partial q_l}{\partial e_i} M_l \\ &= M_i^*(e, \dot{e}, t) \\ &\text{(covariant—like transformation of } M_l \text{ between } q \text{ and } e) \end{aligned} \quad , \tag{11}$$

from which, since the $(n\text{-}m)$ δe's are independent, we find the $(n\text{-}m)$ canonical, or holonomic Maggi's equations of motion

$$\sum_{l=1}^{n} \frac{\partial q_l}{\partial e_i} M_l = 0, \tag{12}$$

or, in extenso,

$$\sum_{l=1}^{n} \frac{\partial q_l}{\partial e_i} \left[\frac{d}{dt} \left(\frac{\partial T}{\partial \dot{q}_l} \right) - \frac{\partial T}{\partial q_l} - Q_l \right] = 0, \tag{13}$$

or

$$\underbrace{\sum_{l=1}^{n} \frac{\partial \dot{q}_l}{\partial \dot{e}_i} E_l(T)}_{E_i^*(T^*)} = \underbrace{\sum_{l=1}^{n} \frac{\partial q_l}{\partial e_i} Q_l}_{Q_i^*}, \quad (i = m+1, \ldots, n)$$

where

$$E_i^*(T^*) \equiv \frac{d}{dt} \left(\frac{\partial T^*}{\partial \dot{e}_i} \right) - \frac{\partial T^*}{\partial e_i},$$

and

$$\begin{aligned} T &= T(q, \dot{q}, t) \\ &= T[q(e,t), \dot{q}(e, \dot{e}, t), t] \\ &\equiv T^*(e, \dot{e}, t) \\ &\equiv T^*, \end{aligned} \tag{13a}$$

and similarly for Q_i^* (see also Woodhouse, 1987, pp. 57–59).

Critical Comments

(1) The fact that not only $M_l \equiv E_l(T) - Q_l$, but also $E_l(T)$ and Q_l, separately, transform as the covariant components of a vector under arbitrary (mathematically meaningful) time-dependent holonomic coordinate transformations $q \rightarrow e(q, t)$ is well known (see e.g., Woodhouse, 1987 and the Appendix). But equations (11)–(13) have an additional advantage over (4) in that they are reactionless: In equation (4)

$$Q_l^{(r)} \equiv \sum_{d=1}^{m} \lambda_d \frac{\partial f_d}{\partial q_l} \neq 0,$$

but in equation (13),

$$Q_i^{(r)*} = 0 \qquad (i = m+1, \ldots, n).$$

We shall show next that

$$Q_k^{(r)*} \begin{cases} = \lambda_d \neq 0 & (d = 1, \ldots, m) \\ = 0 & (i = m+1, \ldots, n; \\ & \text{see equation (21).} \end{cases} \tag{14}$$

This is important if one is only interested in the motion under the given forces $\{Q_k\}$.

(2) Differentiating equation (6) totally in time yields

$$\dot{q}_l = \sum_{i=m+1}^{n} \frac{\partial q_l}{\partial e_i} \dot{e}_i + \frac{\partial q_l}{\partial t}, \tag{15}$$

and, therefore,

$$\frac{\partial \dot{q}_l}{\partial \dot{e}_i} = \frac{\partial q_l}{\partial e_i} \equiv q_{l,i} \qquad \begin{pmatrix} l = 1, \ldots, n; \\ i = m+1, \ldots, n \end{pmatrix}, \tag{16}$$

and with the proper precautions for $q_{l,k}$ $(l, k = 1, \ldots, n)$. Similarly, we can show the purely *kinematical* result:

$$\text{(a)} \quad q_{l,i} = \frac{\partial \ddot{q}_l}{\partial \ddot{e}_i} = \frac{\partial \dddot{q}_l}{\partial \dddot{e}_i} = \ldots . \tag{17}$$

and

$$\text{(b)} \quad e_{k,l} \equiv \frac{\partial e^k}{\partial q^l} = \frac{\partial \dot{e}^k}{\partial \dot{q}^l} = \frac{\partial \ddot{e}^k}{\partial \ddot{q}^l} = \ldots \quad (\text{for } k,l = 1, \ldots n).$$

[3] Suggested to us by Dr. L. Y. Bahar of Drexel University.

[4] For the computational problems arising from arbitrary choices of the second, or independent, set of e's (e.g., poorly conditioned Jacobians of the f's) see the comparative study by Kurdila et al. (1989). This paper tries to clarify the theoretical aspects of the problem.

Downloaded 03 May 2010 to 171.66.16.244. Redistribution subject to ASME license or copyright; see http://www.asme.org/terms/Terms_Use.cfm

Thus, equations (12), (13) can be written, respectively, as

$$\left.\begin{aligned}&\sum_{l=1}^{n}\frac{\partial\dot{q}_l}{\partial\dot{e}_i}M_l=0,\\&\sum_{l=1}^{n}E_l(T)\frac{\partial\dot{q}_l}{\partial\dot{e}_i}=\sum_{l=1}^{n}Q_l\frac{\partial\dot{q}_l}{\partial\dot{e}_i}\quad(i=m+1,\ldots,n).\end{aligned}\right\}\tag{18}$$

These are Maggi's equations, and hold for kinematical, linear or nonlinear, holonomic or nonholonomic, constraints (see, e.g., Hamel, 1938). They are reactionless, but since they still contain all the original variables (i.e., t, q, $\dot{q}$), they may not be as useful as the new-variable equations M_i^* $(t, e, \dot{e}) = 0$. It should also be pointed out here that the latter are the holonomic constraint and coordinate—counterparts, or specialization, of the famous Boltzmann-Hamel equations (see Hamel, 1949, pp. 480–482).

(3) Equations (12) have an interesting geometrical interpretation (see Appendix): They represent the projection (or dot product) of the system vector $\{E_l(T)\text{-}Q_l\neq 0\}$ onto the virtual hyperplane of the system at the point $(q, t) \rightarrow (e, t)$ of the $[(n\text{-}m) + 1]$—dimensional configuration space of $\{e_{m+1}, \ldots, e_n; t\}$. And since the system *reaction* vector

$$Q_l^{(r)}=\sum_{d=1}^{m}\lambda_d\frac{\partial e_d}{\partial q_l}\quad(l=1,\ldots,n)$$

is perpendicular to this hyperplane, at every point of the e-space (by the d'Alembert/Lagrange principle), its projection to it

$$\sum_{l=1}^{n}Q_l^{(r)}\frac{\partial q_l}{\partial e_i}\quad(i=m+1,\ldots,n;\text{ see equation (29)})$$

vanishes. The virtual hyperplane is the tangent plane to the $(n\text{-}m)$-dimensional surface, described by equation (6) and t = constant ($\rightarrow \delta t = 0$), at a given point of the system's configuration space; the latter can be specified either in the q or the e (curvilinear) coordinates. This latter's equation in the q-variables is the virtual differential form of the first of equation (5)

$$\delta e_d=\sum_{l=1}^{n}\frac{\partial e_d}{\partial q_l}\delta q_l=0\quad(d=1,\ldots,m).$$

The $[(n + 1)\text{-}m]$-dimensional e_I-surface is a subspace (or constraint surface) obtained from the original $(n + 1)$-dimensional (q, t) unconstrained extended configuration space by imposing the m constraints equation (1)/first of equation (5). Finally, the tip of the vector that describes the virtual changes of the system, for a given (q, t) point, lies on the virtual hyperplane at that point and has (curvilinear) coordinates $\{q_l + \delta q_l\}$ where the $\{\delta q_l\}$ are given by equation (8); we note that $\delta e_{n+1} \equiv \delta t = 0$, although $de_{n+1} \equiv dt \neq 0$ (see also Papastavridis, 1988b).

The Holonomic Maggi Equations for d = *1, . . . ,* m. Here, we must use LP in e-coordinates/δe-variations

$$\sum_{k=1}^{n}M_k^*\delta e_k=0,\tag{19}$$

where now the n δe's are not free but are subject to the m constraints equation (7)

$$1\cdot\delta e_1=0,\ \ldots,\ 1\cdot\delta e_m=0;\tag{20}$$

also, we can think of the $(n\text{-}m)$ $\{\delta e_i\}$ as if they are subject to

$$0\cdot\delta e_{m+1}=0,\ \ldots,\ 0\cdot\delta e_n=0.\tag{21}$$

This is achieved with Lagrange's method of undetermined multipliers: multiplying each of equation (20) by a multiplier λ_k $(k = 1, \ldots, m)$, and similarly for equations (21), and adding them to equation (19) yields

$$\sum_{k=1}^{m}(M_K^*-\lambda_k)\delta e_k+\sum_{k=m+1}^{n}M_k^*\delta e_k=0,\tag{22}$$

where, now the n δe's behave as if they were unrestricted (see Hamel, 1949, pp. 85–87). The variational equation (22) produces the two sets of equations

$$\left.\begin{aligned}&M_d^*=\lambda_d\quad(d=1,\ldots,m),\\&M_i^*=0\quad(i=m+1,\ldots,n),\end{aligned}\right\}\tag{23}$$

where, in general

$$M_k^*\equiv\sum_{l=1}^{n}\frac{\partial q_l}{\partial e_k}M_l\quad(k=1,\ldots,n),\tag{24}$$

but for $k \rightarrow d = 1, \ldots, m$: First, we differentiate q_l with respect to e_d, and then we set $e_d = 0$. The second set of equation (23) is, naturally, identical with equations (12), (13). The first set does contain on its right side the reactions λ_d generated by the constraints $\delta e_d = 0$. The foregoing procedure constitutes, in effect, an application of Hamel's "Befreiungsprinzip," freely translated as "Principle of Relaxation of the Constraints" (see Hamel, 1927, 1949; and Papastavridis 1988a).

Remarks. Since coordinates, like e, that satisfy the first of equation (5) are sometimes called adapted to the constraints, we could call the first set of equation (23) adapted equations of motion (see, e.g., Woodhouse, 1987).

To understand better the meaning of the multipliers λ, we express the vanishing of the total virtual work of the system reactions, in both q and e coordinates:

$$\begin{aligned}\delta' W^{(r)}&=\sum_{l=1}^{n}Q_l^{(r)}\delta q_l\\&=\sum_{k=1}^{n}Q_k^{(r)*}\delta e_k=0,\end{aligned}\tag{25}$$

from which

$$\begin{aligned}0&=\sum_{l=1}^{n}Q_l^{(r)}\left(\sum_{k=1}^{n}\frac{\partial q_l}{\partial e_k}\delta e_k\right)\\&=\sum_{k=1}^{n}Q_k^{(r)*}\delta e_k,\end{aligned}$$

and, thus

$$Q_k^{(r)*}=\sum_{l=1}^{n}\frac{\partial q_l}{\partial e_k}Q_l^{(r)}\quad(k=1,\ldots,n).\tag{26}$$

Conversely, from

$$\begin{aligned}0&=\sum_{k=1}^{n}Q_k^{(r)*}\delta e_k=\sum_{k=1}^{n}Q_k^{(r)*}\left(\sum_{l=1}^{n}\frac{\partial e_k}{\partial q_l}\delta q_l\right)\\&=\sum_{l=1}^{n}Q_l^{(r)}\delta q_l,\end{aligned}$$

we find

$$Q_l^{(r)}=\sum_{k=1}^{n}\frac{\partial e_k}{\partial q_l}Q_k^{(r)*}.\tag{27}$$

Downloaded 03 May 2010 to 171.66.16.244. Redistribution subject to ASME license or copyright; see http://www.asme.org/terms/Terms_Use.cfm

Equations (26), (27) represent covariant laws of transformation of the reaction components, from the q to the e, and vice versa. Comparing the second of equation (4*a*) with (27), while recalling (5), we see that

$$Q_k^{(r)*}\begin{cases}=\lambda_d & (d=1,\ldots,m),\\ =0 & (k\to i=m+1,\ldots,n).\end{cases} \tag{28}$$

Thus:

(a) in equation (26), k runs from 1 to m; for $k = m + 1, \ldots, n$ we recover the second set of equation (23), and

(b) in equation (27), k runs from 1 to m, and l from 1 to n;

(c) the q's and e's must, of course, satisfy the compatibility conditions (see the Appendix).

$$\left.\begin{aligned}\sum_{k=1}^{n}\frac{\partial q_l}{\partial e_k}\frac{\partial e_k}{\partial q_s}&=\delta_{ls}\quad(l,s=1,\ldots,n),\\ \sum_{l=1}^{n}\frac{\partial e_k}{\partial q_l}\frac{\partial q_l}{\partial e_s}&=\delta_{ks}\quad(k,s=1,\ldots,n)\end{aligned}\right\} \tag{29}$$

($\delta\ldots$ = Kronecker deltas).

A Special Choice of Coordinates: Special choices of e's in equations (5) result in special forms of equations (12), (13), and (23). An interesting and common choice is the following

$$\left.\begin{aligned}e_d\equiv f_d(q,t)&=0\quad(d=1,\ldots,m),\\ e_i\equiv q_i&\neq 0\quad(i=m+1,\ldots,n),\end{aligned}\right\} \tag{30}$$

in other words, the last $(n\text{-}m)$ q's are taken as the new independent coordinates. In this case:

(a) for $i=m+1,\ldots,n$:

$$0=M_i^*=\sum_{l=1}^{n}\frac{\partial q_l}{\partial e_i}M_l$$

$$=\sum_{l=1}^{n}\frac{\partial q_l}{\partial q_i}M_l$$

$$=\sum_{l=1}^{m}\frac{\partial q_l}{\partial q_i}M_l+\sum_{l=m+1}^{n}\frac{\partial q_l}{\partial q_k}M_l,$$

or finally,

$$M_i+\sum_{d=1}^{m}\frac{\partial q_d}{\partial q_i}M_d=0\quad(i=m+1,\ldots,n). \tag{31}$$

In this equation $(\partial q_d/\partial q_i)$ signifies the derivatives of the first m-dependent q's with respect to the last $(n\text{-}m)$-independent q's: This functional relation is obtained from the first group of equation (30)

$$q_d=q_d(q_{m+1},\ldots,q_n;t)\qquad(d=1,\ldots,m); \tag{32}$$

(b) for $d=1,\ldots,m$:

$$\lambda_d=M_d^*=\sum_{l=1}^{m}\frac{\partial q_l}{\partial q_d}M_l+\sum_{l=m+1}^{n}\frac{\partial q_l}{\partial q_d}M_l$$

$$=\sum_{l=1}^{m}\delta_{ld}M_l+\sum_{l=m+1}^{n}0\cdot M_l,$$

or finally,

$$M_d=\lambda_d\quad(d=1,\ldots,m). \tag{33}$$

Remarks:

(1) The constraints equation (32) can also be viewed as the following special case of (1) and (5):

$$\left.\begin{aligned}e_d\equiv f_d\equiv q_d-q_d(q_{m+1},\ldots,q_n;t)&=0\\ e_i\equiv q_i&\\ (d=1,\ldots,m),&\\ (i=m+1,\ldots,n).&\end{aligned}\right\} \tag{34}$$

Then,

$$\frac{\partial f_k}{\partial q_l}\begin{cases}=\delta_{kl} & (k,l=1,\ldots,m),\\ =-\dfrac{\partial q_k}{\partial q_l} & \begin{matrix}k=1,\ldots,m;\\ l=m+1,\ldots,n\end{matrix},\end{cases} \tag{35}$$

and therefore equations (4) reduce to

$$M_l\begin{cases}=\lambda_d & (d=1,\ldots,m),\\ =-\displaystyle\sum_{d=1}^{m}\lambda_d\frac{\partial q_d}{\partial q_i} & (i=m+1,\ldots,n);\end{cases} \tag{36}$$

eliminating the m λ's among these two groups of equations (36), we recover (31).

(2) Recalling equations (15), (16), we see that equations (31) are the holonomic counterpart of the Hadamard equations (1895, 1899).

$$M_i+\sum_{d=1}^{m}\frac{\partial\dot q_d}{\partial\dot q_i}M_d=0\quad(i=m+1,\ldots,n), \tag{37}$$

originally formulated for the linear nonholonomic constraint case

$$\dot q_d=\sum_{i=m+1}^{n}b_{di}(q,t)\dot q_i+b_d(q,t)\quad(d=1,\ldots,m). \tag{38}$$

2 An Example

If (l, m, n) are the direction cosines of a thin homogeneous bar moving in any manner in space, with respect to fixed axes, and if V be its potential energy, show that

$$\frac{1}{l}\left(I\ddot l+\frac{\partial V}{\partial l}\right)=\frac{1}{m}\left(I\ddot m+\frac{\partial V}{\partial m}\right)=\frac{1}{n}\left(I\ddot n+\frac{\partial V}{\partial n}\right)$$

where I = moment of inertia of bar about an axis through its center of mass C, perpendicular to its length (see Smart, 1951).

Choosing axes C-xyz through C continuously parallel to the inertial ones O-xyz, we find (see Fig. 1):

$$\left.\begin{aligned}l&=\sin\theta\cos\phi,\\ m&=\sin\theta\sin\phi,\\ n&=\cos\theta,\end{aligned}\right\} \tag{39}$$

where these three cosines are subject to the constraint

$$l^2+m^2+n^2=1. \tag{40}$$

Clearly here only the rotational kinetic energy of the bar about C in the nonrotating axes C-xyz is needed; we shall denote it by T. It is not hard to show that

$$2T=I(\dot\theta^2+\dot\phi^2\sin^2\theta); \tag{41}$$

(see, e.g., Spiegel, 1967). We shall express T in terms of (l, m, n) and their derivatives. Next:

$$\sin^2\theta=l^2+m^2,$$

$$\dot n^2=(l^2+m^2)\dot\theta^2,$$

$$l\dot m-\dot l m=(l^2+m^2)\dot\phi,$$

Downloaded 03 May 2010 to 171.66.16.244. Redistribution subject to ASME license or copyright; see http://www.asme.org/terms/Terms_Use.cfm

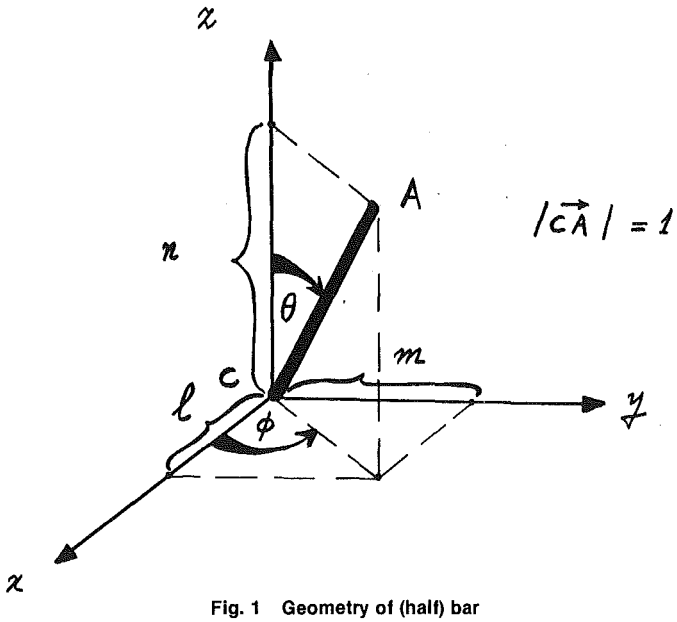


Fig. 1 Geometry of (half) bar

(due to $\dot{l} = (\cos\theta \cdot \cos\phi)\dot{\theta} - m\dot{\phi}$, $\dot{m} = (\cos\theta \cdot \sin\phi)\dot{\theta} + l\dot{\phi}$, etc.)

$$(l\dot{m} - \dot{l}m)^2 + \underbrace{(l\dot{l} + m\dot{m})^2}_{(-n\dot{n})^2} = l^2 + m^2)(\dot{l}^2 + \dot{m}^2)$$

from which

$$\dot{n}^2 + (l\dot{m} - \dot{l}m)^2 = (l^2 + m^2)(\dot{l}^2 + \dot{m}^2 + \dot{n}^2).$$

Therefore,

$$2T = I\left[\frac{\dot{n}^2}{l^2 + m^2} + \frac{(l\dot{m} - \dot{l}m)^2}{l^2 + m^2}\right]$$

and, finally,

$$2T = I(\dot{l}^2 + \dot{m}^2 + \dot{n}^2), \tag{42}$$

under equation (40).

With $q_1 = l$, $q_2 = m$, $q_3 = n$, we introduce the new e-coordinates

$$\begin{cases} e_1 \equiv l^2 + m^2 + n^2 - 1 = 0, \\ e_2 \equiv m, \\ e_3 \equiv n, \end{cases} \tag{43}$$

and inverting

$$\begin{cases} l^2 = 1 + e_1 - e_2^2 - e_3^2, \\ m = e_2, \\ n = e_3. \end{cases} \tag{44}$$

Thus, the holonomic Maggi's equations yield:

(a) $k = 2$: $\dfrac{\partial l}{\partial e_2} M_l + \dfrac{\partial m}{\partial e_2} M_m + \dfrac{\partial n}{\partial e_2} M_n = 0,$

or, employing equation (44),

$$\left(-\frac{m}{l}\right) M_l + M_m = 0, \tag{45}$$

(b) $k = 3$: $\dfrac{\partial l}{\partial e_3} M_l + \dfrac{\partial m}{\partial e_3} M_m + \dfrac{\partial n}{\partial e_3} M_n = 0,$

or

$$\left(-\frac{n}{l}\right) M_l + M_n = 0, \tag{46}$$

(c) $k = 1$: $\dfrac{\partial l}{\partial e_1} M_l + \dfrac{\partial m}{\partial e_1} M_m + \dfrac{\partial n}{\partial e_1} M_n = \lambda_1,$

or

$$\left(\frac{1}{2l}\right) M_l = \lambda_1. \tag{47}$$

Since $V = V(l, m, n)$ and (l, m, n) and their derivatives appear only in the rotational kinetic energy T, equations (45)–(47) read explicitly:

$$(58) \quad \rightarrow \frac{1}{l}\left(I\ddot{l} + \frac{\partial V}{\partial l}\right) = \frac{1}{m}\left(I\ddot{m} + \frac{\partial V}{\partial m}\right), \tag{48}$$

$$(59) \quad \rightarrow \frac{1}{l}\left(I\ddot{l} + \frac{\partial V}{\partial l}\right) = \frac{1}{n}\left(I\ddot{n} + \frac{\partial V}{\partial n}\right), \tag{49}$$

$$(60) \quad \rightarrow \frac{1}{l}\left(I\ddot{l} + \frac{\partial V}{\partial l}\right) = 2\lambda_1, \text{ q.e.d.} \tag{50}$$

The first two are clearly reactionless, while the third is not. If only the motion is sought, we combine equations (48)–(49) with the constraint equation (40); the reaction $\lambda_1(t)$ can be found afterwards from equation (50), if needed.

Remarks

(a) The customary three Routh/Voss equations of this problem would be

$$\left.\begin{aligned} M_l &= \lambda_1(2l), \\ M_m &= \lambda_1(2m), \\ M_n &= \lambda_1(2n); \end{aligned}\right\} \tag{51}$$

they are, obviously, equivalent with equations (45)–(47).

(b) Other choices of e-coordinates are of course possible, and lead to different values of λ but, overall, equivalent equations of motion.

Acknowledgment

The author would like to thank the unknown reviewers for their constructive comments for improvement on the first version of this paper.

References

Hamel, G., 1927, "Die Axiome der Mechanik," pp. 1-42, in Vol. 5 of (old) *Handbuch der Physik*, Springer, Berlin, pp. 26-27.

Hamel, G., 1938, "Nichtholonome Systeme hoeherer Art," *Sitzungsberichte d. Berl. Math. Ges.*, Vol. 37, pp. 41-52.

Hamel, G., 1949, *Theoretische Mechanik*, Springer, Berlin, pp. 91; 131; 152; 464-465.

Kurdila, A., Papastavridis, J. G., and Kamat, M. P., 1989, "Role of Maggi's Equations in Computational Methods for Constrained Multi-body Systems," *Journal of Guidance, Dynamics and Control*, Vol. 13, No. 1, pp. 113-120.

Papastavridis, J. G., 1988a, "On the Nonlinear Appell's Equations and the Determination of Generalized Reaction Forces," *International Journal of Engineering Science*, Vol. 26, No. 6, pp. 609-625.

Papastavridis, J. G., 1988b, "A Method of Eliminating Lagrangian Multipliers from the Equations of Motion of Interconnected Mechanical Systems," discussion, ASME JOURNAL OF APPLIED MECHANICS, Vol. 55, pp. 250-251.

Smart, E. H., 1951, *Advanced Dynamics*, Vol. 2, MacMillan, London, pp. 272-273.

Spiegel, M. R., 1967, *Theoretical Mechanics*, Schaum, New York, pp. 268, 301.

Wang, C.-C., 1979, *Mathematical Principles of Mechanics and Electromagnetism, Part A: Analytical and Continuum Mechanics*, Plenum, New York, pp. 15-22; 27-39.

Woodhouse, N. M. J., 1987, *Introduction to Analytical Dynamics*, Clarendon Press, Oxford, U.K., pp. 44-48; 56-57.

APPENDIX

A Geometrical Interpretation of the Maggi Equations

Consider a rheonomic holonomic mechanical system, S, originally with n degrees-of-freedom. Its motion can be viewed either as the motion of a point in an n-dimensional configuration space, V_n, with time-dependent metric (a flexible, or breathing V_n), or as the motion of the system event-point, P,

Downloaded 03 May 2010 to 171.66.16.244. Redistribution subject to ASME license or copyright; see http://www.asme.org/terms/Terms_Use.cfm

in an $(n+1)$-dimensional, generally curved (pseudo-Riemannian) event space, V_{n+1}. In V_{n+1} we consider a set of curvilinear (system) coordinates $\{q \equiv (q^1, \ldots, q^n), q^{n+1} \equiv t; k = 1, \ldots, n\}$; then a P is described by the $(n+1)$-tuple (q, t). The system virtual displacement, at $P(q, t)$ is defined as the vector (with summation convention, and, from now on, with all latin indices, except i and d, running from 1 to n)

$$\delta\mathbf{q} = \mathbf{a}_k \delta q^k \qquad (\delta q^{n+1} \equiv \delta t = 0). \tag{A1}$$

The n linearly independent vectors $\{\mathbf{a}_k\}$ are tangent to the coordinates $\{q^k\}$, at P, and constitute a covariant natural basis there (see, e.g., Wang, 1979). The contravariant natural basis $\{\mathbf{a};\mathrm{kk}\}$ at P defined by:

$$\mathbf{a}_k \cdot \mathbf{a}^l = \delta_k^l \qquad \text{(Kronecker delta)}, \tag{A2}$$

is called the dual or reciprocal to the $\{\mathbf{a}_k\}$ (and vice versa). The vectors of these two bases are related by

$$\mathbf{a}_k = g_{kl}\mathbf{a}^l, \ \mathbf{a}^k = g^{kl}\mathbf{a}_l, \tag{A3}$$

where

$$g_{kl} \equiv \mathbf{a}_k \cdot \mathbf{a}_l, \ g^{kl} \equiv \mathbf{a}^k \cdot \mathbf{a}^l \tag{A4}$$

are the corresponding covariant and contravariant metric tensors, respectively, in the q-variables.

The vector $\mathbf{a}^k$ is perpendicular to the surface obtained by keeping only q^k constant, and varying all the other $(n-1)$ q's. We also define

$$\delta q_k = g_{kl}\delta q^l \ (\leftrightarrow \delta q^l = g^{lk}\delta q_k), \tag{A5}$$

from which

$$\delta\mathbf{q} = \mathbf{a}^k \delta q_k. \tag{A6}$$

Next, we define, at P, the following system vectors: $\mathbf{Q}$ = impressed force, $\mathbf{Q}^{(r)}$ = constraint reaction force, $\mathbf{I}$ = inertia force. In the q-system and associated bases $\{\mathbf{a}_k\}$, $\{\mathbf{a}^k\}$ these vectors have the following covariant and contravariant representations:

$$\begin{aligned} &\mathbf{Q} = Q_k \mathbf{a}^k = Q^k \mathbf{a}_k, \\ &\mathbf{Q}^{(r)} = Q_k^{(r)} \mathbf{a}^k = Q^{(r)k} \mathbf{a}_k, \\ &\mathbf{I} = I_k \mathbf{a}^k = I^k \mathbf{a}_k, \end{aligned} \tag{A7}$$

where the Q_k are defined as the coefficient $(-s)$ of the (coordinate-invariant) impressed force virtual work

$$\delta' W = Q_k \delta q^k \ (= Q^k \delta q_k), \tag{A8}$$

and

$$Q_k^{(r)} = \lambda_k (\partial f^d / \partial q^k) \qquad \{d = 1, \ldots, m(<n)\}, \tag{A9}$$

when a certain number $m(<n)$ of (additional) rheonomic holonomic constraints $f^d \equiv f^d(q, t) = 0$ are imposed on the system, and

$$\begin{aligned} &I_k \equiv E_k(T) = d/dt(\partial T/\partial \dot{q}^k) - \partial T/\partial q^k, \\ &T = T(t, q, \dot{q}) = \text{kinetic energy of } S. \end{aligned} \tag{A10}$$

The indices of all these forces are raised/lowered with the $\{g^{kl}/g_{kl}\}$, for e.g.,

$$Q^l = g^{lk} Q_k \leftrightarrow Q_k \equiv g_{kl} Q^l. \tag{A11}$$

Let us now introduce the following special curvilinear coordinates e^k.

$$e^k \begin{cases} e^d \equiv f^d(q,t) = 0 & \{d = 1, \ldots, m(<n)\} \\ e^i \equiv g^i(q,t) \neq 0 & \{i = m+1, \ldots, n\} \end{cases}. \tag{A12}$$

The motivation for introducing the m dependent coordinates e^d is so that they vanish on the constraint surface $f^d = 0$. The $(n\text{-}m)$ independent coordinates e^i are chosen arbitrarily, but in such a way that when the n equations (A12) are solved for the q^k in terms of the e^i: $q^k = q^k(e, t)$, and then this result is inserted back into the constraints $f^d = 0$, they satisfy them identically. In the e-coordinates, the aforementioned system of vectors have the representations:

$$\begin{cases} \delta\mathbf{q} = \mathbf{A}_k \delta e^k = \mathbf{A}^k \delta e_k \{ = \mathbf{A}_i \delta e^i = \mathbf{A}^i \delta e_i — \text{see (A19)}\}, \\ \mathbf{Q} = Q_k^* \mathbf{A}^k = Q^{*k} \mathbf{A}_k, \\ \mathbf{Q}^{(r)} = \overset{*}{Q}_k^{(r)} \mathbf{A}^k = \overset{*}{Q}^{(r)k} \mathbf{A}_k \{ = \lambda_d \mathbf{A}^d = \lambda^d \mathbf{A}_d — \text{see (A29)}\}, \\ \mathbf{I} = I_k^* \mathbf{A}^k = \overset{*}{I}{}^k \mathbf{A}_k, \end{cases} \tag{A13}$$

where

$$\begin{cases} I_k^* \equiv E_k^*(T^*) = d/dt(\partial T^*/\partial \dot{e}^k) - \partial T^*/\partial e^k, \\ T^* = T\{t, q(t,e), \dot{q}(t,e,\dot{e})\} = T^*(t,e,\dot{e}). \end{cases}$$

The two (mutually dual or reciprocal) e-bases at P, $\{\mathbf{A}^k\}$ and $\{\mathbf{A}_k\}$, are defined by

$$\begin{aligned} &\mathbf{A}^k = e_l^k \mathbf{a}^l \leftrightarrow \mathbf{a}; kl = q_k^l \mathbf{A}^k, \\ &\mathbf{A}_k = q_k^l \mathbf{a}_l \leftrightarrow \mathbf{a}_l = e_l^k \mathbf{A}_k, \end{aligned} \tag{A14}$$

where their direction cosines are

$$\partial q^k / \partial e^l \equiv q_l^k, \ \partial e^l / \partial q^k \equiv e_k^l. \tag{A15}$$

The $\{\mathbf{A}_k\}$ are tangent to the $\delta e^k = e_l^k \delta q^l$, at P; while the vector $\mathbf{A}^k$ is perpendicular to the surface $\delta e^k = 0$ there. Clearly, the nonsingular $(n \times n)$ matrices $\mathbf{q} \equiv (q_l^k)$ and $\mathbf{e} \equiv (e_l^k)$ are inverse:

$$q_l^k e_s^l = \delta_s^k, \ q_l^k e_k^s = \delta_l^s. \tag{A16}$$

With their help, one can relate the components of the system vectors. For example,

$$Q_k^* = q_k^l Q_l \leftrightarrow Q_l = e_l^k Q_k^* \tag{A17}$$

(covariant transformation), and

$$\overset{*}{Q}{}^k = e_l^k Q^l \leftrightarrow Q^l = q_k^l \overset{*}{Q}{}^k \tag{A18}$$

(contravariant transformation), etc. Now, the system virtual hyperplane (VHP) at P {or tangent space to the constraint surface $f^d = 0$ there, or null space of the constraint matrix (f_k^d) $(d = 1, \ldots, m; k = 1, \ldots, n)$, or space orthogonal to the range of the transpose of (f_k^d)—null space and range are mutually orthogonal, or complementary, subspaces} is defined in the q and e coordinates, by the m equations

$$e_k^d \delta q^k = 0, \quad \underset{(d=1,\ldots,m)}{\text{and}} \quad \delta e^d = 0, \tag{A19}$$

or, in vector notation,

$$\delta e^d = \mathbf{A}^d \cdot \delta\mathbf{q} = 0, \tag{A20}$$

i.e., $\delta\mathbf{q}$ must be perpendicular to the m (independent) vectors $\mathbf{A}^d = e_l^d \mathbf{a}^l$, or belong to the (n-m)-dimensional null (sub-) space and thus be perpendicular to the m-dimensional range (sub-) space. Next, the elements of the matrix $\mathbf{q} = (q_l^k)$, as (A14) indicate, have the following double interpretation: They can be viewed either (a) as the covariant components of $\mathbf{a}^k$ along the basis $\{\mathbf{A}^l\}$:

$$\mathbf{a}^k = q_l^k \mathbf{A}^l, \tag{A21}$$

or (b) as the contravariant components of $\mathbf{A}_l$ along the $\{\mathbf{a}_k\}$

$$\mathbf{A}_l = q_l^k \mathbf{a}_k; \tag{A22}$$

in short:

$$q_l^k = \mathbf{a}^k \cdot \mathbf{A}_l. \tag{A23}$$

Similarly, the elements (e_l^k) can be viewed either (c) as the covariant components of $\mathbf{A}^k$ along the $\{\mathbf{a}^l\}$, or (d) as the contravariant components of the $\mathbf{a}_l$ along the $\{\mathbf{A}_k\}$:

$$e_l^k = \mathbf{A}^k \cdot \mathbf{a}_l. \tag{A24}$$

So, the matrices $\mathbf{q}$ and $\mathbf{e}$ can be written as

Downloaded 03 May 2010 to 171.66.16.244. Redistribution subject to ASME license or copyright; see http://www.asme.org/terms/Terms_Use.cfm

$$(q_i^k) = \begin{pmatrix} \bar{a}^1 \\ \cdot \\ \cdot \\ \cdot \\ \bar{a}^n \end{pmatrix} = (\bar{A}_1 \ldots \bar{A}_n), \quad \text{(column vectors)} \tag{A25}$$

and (row vectors)

$$(e_i^k) = \begin{pmatrix} \bar{A}^1 \\ \cdot \\ \cdot \\ \cdot \\ \bar{A}^n \end{pmatrix} = (\bar{a}_1 \ldots \bar{a}_n), \quad \text{(column vectors)} \tag{A26}$$

(row vectors)

Then equations (A16) simply state that

$$\mathbf{a}^k \cdot \mathbf{a}_s = \delta_s^k, \text{ and } \mathbf{A}_l \cdot \mathbf{A}^s = \delta_l^s, \tag{A27}$$

as expected. Now we are ready to translate the earlier found dynamical equations in simple geometrical language. The equation of motion of the system (Newton's second law summed over all the particles), equation (4*a*), is

$$\begin{matrix} \mathbf{I} & = & \mathbf{Q} + \mathbf{Q}^{(r)} \\ \text{(Inertial "Force")} & & \text{(Impressed + Reaction Forces).} \end{matrix} \tag{A28}$$

But successively,

$$\mathbf{Q}^{(r)} = Q_k^{(r)} \mathbf{a}^k = (\lambda_d e_k^d) \mathbf{a}^k = \lambda_d \mathbf{A}^d, \tag{A29}$$

i.e., $\mathbf{Q}^{(r)}$ is perpendicular to the VHP at P. The above shows that the m multipliers $\{\lambda_d;\ d = 1, \ldots, m\}$ are simply the covariant components of $\mathbf{Q}^{(r)}$ along $\mathbf{A}^d$ (see Fig. 2) then, clearly, $\lambda_i = 0$. Therefore, projecting equation (A28) onto the VHP, spanned by the $(n\text{-}m)$ vectors $\mathbf{A}_i = q_i^k a_k$, yields $\mathbf{I} \cdot \mathbf{A}_i = \mathbf{Q} \cdot \mathbf{A}_i + \mathbf{Q}^{(r)} \cdot \mathbf{A}_i$, or since $\mathbf{Q}^{(r)} \cdot \mathbf{A}_i = \{\lambda_d e_k^d) \mathbf{a}^k\} \cdot \mathbf{A}_i = \lambda_d (\mathbf{A}^d \cdot \mathbf{A}_i) = \lambda_d \delta_i^d = \lambda_i = 0$, finally

$$\mathbf{I} \cdot \mathbf{A}_i = \mathbf{Q} \cdot \mathbf{A}_i, \tag{A30}$$

and, explicitly,

$$q_i^k I_k = q_i^k Q_k \qquad \begin{pmatrix} k = 1, \ldots, n; \\ i = m+1, \ldots, n \end{pmatrix}. \tag{A31}$$

This is the holonomic case counterpart of the Maggi Equations, equations (18). We shall call them holonomic reactionless Maggi Equations, or M_i. Projecting, next, equation (A28) onto the range subspace, at P, spanned by the m vectors $\mathbf{A}_d$ (dual to the m vectors $\mathbf{A}^d$ i.e., $\mathbf{A}^d \cdot \mathbf{A}_{d'} = \delta_{d'}^d$; $d, d' = 1, \ldots, m$—orthogonal complement of the null space of the constraint matrix), we find

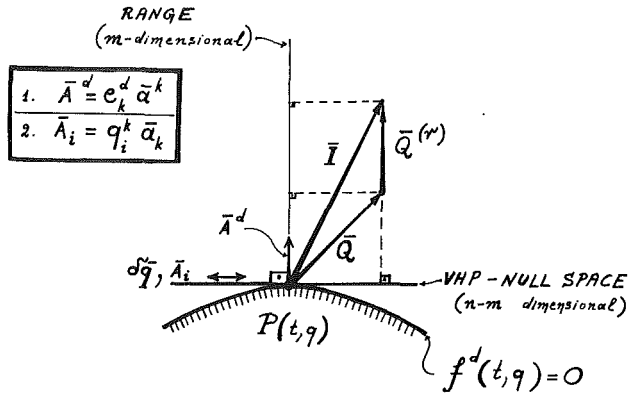


Fig. 2 Balance of system vectors: inertia = force (impressed + reaction) in configuration/event space—special case: $n = 2$, $m = 1$

$$\mathbf{I} \cdot \mathbf{A}_d = \mathbf{Q} \cdot \mathbf{A}_d + \mathbf{Q}^{(r)} \cdot \mathbf{A}_d, \tag{A32}$$

or, explicitly,

$$q_d^k I_k = q_d^k Q_k + \lambda_d, \tag{A33}$$

since now $\mathbf{Q}^{(r)} \cdot \mathbf{A}_d = (\lambda_{d'} \mathbf{A}^{d'} \cdot \mathbf{A}_d) = \lambda_{d'} \delta_d^{d'} = \lambda_d$ ($d, d' = 1, \ldots, m$: dependent indices). Equations (A32) and (A33) we shall call holonomic reaction—containing Maggi Equations, or M_d, although they were not given by Maggi. In the simpler e-variables equations $M_{i,d}$ read simply

$$\left.\begin{aligned} I_i^* &= Q_i^* \quad (i = m+1, \ldots, n) \\ I_d^* &= Q_d^* + \lambda_d \quad (d = 1, \ldots, m) \end{aligned}\right\}, \tag{A34}$$

where $I_k^* \equiv E_k^*(T^*)$ ($k = 1, \ldots, n$)—recall equations (23) and (24). The first set of (A34) can be viewed as the holonomic reactionless Boltzmann/Hamel Equations; the second set we shall call the holonomic reaction-containing *BH* Equations, although, again, they were not given by *B*, *H*. Fig. 2 helps explain the foregoing theory.

Both M_i and M_d can be extended to nonholonomic constraints (in holonomic variables) with slight modifications.

Downloaded 03 May 2010 to 171.66.16.244. Redistribution subject to ASME license or copyright; see http://www.asme.org/terms/Terms_Use.cfm

N. S. Namachchivaya
Mem. ASME

Gerard Leng

Department of Aeronautical and Astronautical Engineering, University of Illinois, Urbana, IL 61801

Equivalence of Stochastic Averaging and Stochastic Normal Forms

The equivalence of the methods of stochastic averaging and stochastic normal forms is demonstrated for systems under the effect of linear multiplicative and additive noise. It is shown that both methods lead to reduced systems with the same Markovian approximation. The key result is that the second-order stochastic terms have to be retained in the normal form computation. Examples showing applications to systems undergoing divergence and flutter instability are provided. Furthermore, it is shown that unlike stochastic averaging, stochastic normal forms can be used in the analysis of nilpotent systems to eliminate the stable modes. Finally, some results pertaining to stochastic Lorenz equations are presented.

1 Introduction

In the analysis of dynamical systems it is often necessary to reduce the dimensions of the problem in order to study the nonlinear system behavior. Often certain variables which are asymptotically stable can be eliminated as being unimportant with the essential behavior of the system restricted to the dynamics of the remaining critical variables. For deterministic systems the theory of normal forms, center manifold, and averaging are particularly useful. Similar ideas have been used for the study of stochastic systems. In this paper we will compare two such methods, namely stochastic averaging and stochastic normal forms. The method of stochastic averaging, which was established by Stratonovich (1963) by a physically rigorous analysis, has been widely used to approximate physical processes with certain smoothness and differentiability conditions by a diffusive Markov process. A mathematically rigorous proof of this result was given by Khasminskii (1966). Since then, several authors have extended the theory into various directions using various assumptions. Papanicolaou and Kohler (1974) and Borodin (1977) provided the same results under essentially less stringent assumptions. The results of Papanicolaou and Kohler (1975), pertaining to the analysis of equations whose solutions have rapidly oscillating and decaying components along with rapidly varying stochastic components, is of primary interest to us in this investigation.

The ideas of center manifold and normal forms were extended to stochastic systems by Knobloch and Wiessenfeld (1983) and Coulett (1985), respectively. The applicability of the method of normal forms to nonlinear stochastic systems was demonstrated by Sri Namachchivaya and Hilton (1988). However, these extensions were unsuccessful in capturing the contributions of the stable modes stochastic components to the critical mode drift terms. Such effects were shown to exist by Sri Namachchivaya and Lin (1988) using extended stochastic averaging. The goal of this work is to present the method of stochastic normal forms developed by the authors in order to reduce the dimensionality of nonlinear stochastic systems near bifurcation points. Unlike stochastic averaging, stochastic normal forms can be used in the analysis of nilpotent systems to reduce the dimension. However, for the purposes of this paper, such systems will not be considered. The goal of this paper is to show that these two methods are in fact equivalent for a specific class of nonlinear systems. We also wish to add that an alternate approach has been used by Caughey (1988) to analyze nonlinear stochastic systems. This approach replaces a nonlinear stochastic system without an exact solution by an "equivalent" system with an exact solution chosen in some optimal fashion. There need not be any reduction in dimension. The method of stochastic normal forms differs because it replaces the original system by an "equivalent" system of *lower* dimension by the elimination of stable modes. The paper is organized as follows: A short introduction to stochastic averaging is given in the next section followed by the theory of stochastic normal forms in Section 3. Section 4 deals with the equivalence of the two techniques, and we conclude with an example which demonstrates the idea explicitly.

2 Stochastic Averaging

In a few words, the method of averaging is a method of approximating the solution of a weakly perturbed dynamical system over a large time interval. The deterministic averaging theorem of Bogoliubov and Mitropolskii (see, e.g., Guckenheimer and Holmes (1983)) states that the solution of the system of differential equations

$$\dot{x} = \epsilon F(x,t,\epsilon) \qquad x(0) = x_o \tag{1}$$

Contributed by the Applied Mechanics Division of THE AMERICAN SOCIETY OF MECHANICAL ENGINEERS for publication in the JOURNAL OF APPLIED MECHANICS.

Discussion on this paper should be addressed to the Technical Editor, Leon M. Keer, The Technological Institute, Northwestern University, Evanston, IL 60208, and will be accepted until two months after final publication of the paper itself in the JOURNAL OF APPLIED MECHANICS. Manuscript received by the ASME Applied Mechanics Division, Apr. 17, 1989; final revision, Aug. 22, 1989.

Copyright © 1990 by ASME
Downloaded 03 May 2010 to 171.66.16.244. Redistribution subject to ASME license or copyright; see http://www.asme.org/terms/Terms_Use.cfm

can be approximated under some fairly general conditions by a solution of

$$\dot{\hat{x}} = \epsilon \bar{F}(\hat{x}) \qquad \hat{x}(0) = x_o \tag{2}$$

over a time interval of order $O(1/\epsilon)$ where

$$\bar{F}(\hat{x}) = \underset{t}{M}(F(x,t,0)) = \lim_{T\to\infty} \frac{1}{\bar{T}} \int_0^T F(x,t,0)dt. \tag{3}$$

The extension of this idea to stochastic systems was performed by Stratonovich (1983) and rigorously proven by Khasminskii (1966). Loosely, it states that the system

$$\dot{x} = \epsilon^2 f(x,t) + \epsilon g(x,t,\xi(t)) \tag{4}$$

where $\xi(t)$ are random processes, has a Markovian approximation valid over a time interval of the order $O(1/\epsilon^2)$ with the drift and diffusion terms given by:

$$m_i(x) = \underset{t}{M}\left\{E[f_i(x,t)] + \int_{-\infty}^{0} E\left[\frac{\partial}{\partial x_j} g_i(t)\ g_j(t+\tau)\right] d\tau\right\} \tag{5}$$

$$(\sigma\sigma^T)_{jk} = \underset{t}{M}\{E[g_j(t+\tau)\ g_k(t)]\}. \tag{6}$$

A review of this technique and its applications can be found in Sri Namachchivaya (1990) and the references cited therein. A modification of the above technique to account for systems with rapidly decaying components is given in Papanicolaou and Kohler (1975). This extended averaging theorem of Papanicolaou and Kohler considers systems of the form:

$$\begin{aligned} \dot{x} &= \epsilon^2 F^1(x,y,t) + \epsilon F^o(x,y,t,\xi(t)) \\ \dot{y} &= Ay + \epsilon^2 G^1(x,y,t) + \epsilon G^o(x,y,t,\xi(t)) \end{aligned} \tag{7}$$

where without loss of generality, A is taken to be a diagonal matrix whose eigenvalues have negative real parts. The drift and diffusion terms of the corresponding Markovian approximation for the slow component x is given by:

$$\begin{aligned} m(x) = \underset{t}{M}\Big\{ & F^1(x,0,t) + \int_{-\infty}^{0} E\Big[\frac{\partial F^o}{\partial x}\ (x,y,t,\xi(t)) F^o(x,y,t \\ & + \tau, \xi(t+\tau))\Big]_{y=0} d\tau \end{aligned} \tag{8}$$

$$\begin{aligned} + \int_{-\infty}^{0} E\Big[\frac{\partial F^o}{\partial y}\ (x,y,t,\xi(t))\ e^{-A\tau} G^o(x,y,t \\ + \tau, \xi(t+\tau))\Big]_{y=0} d\tau\Big\} \end{aligned}$$

$$\begin{aligned} (\sigma\sigma^T) = \underset{t}{M}\Big\{ & \int_{-\infty}^{\infty} E[F^o(x,y,t,\xi(t)) F^{T_o}(x,y,t \\ & + \tau, \xi(t+\tau))]_{y=0} d\tau\Big\}. \end{aligned} \tag{9}$$

We observe that the rapidly decaying components lead to additional contributions to the drift term. An example of the application of this theorem to study systems with large damping can be found in the work of Sri Namachchivaya and Lin (1988).

3 Stochastic Normal Forms

The theory of normal forms for deterministic systems is a method of simplifying a system of differential equations of the form:

$$\dot{x} = Ax + f(x) \tag{10}$$

by the use of successive formal, near-identity change of coordinates. It can be shown (Arnold, 1983) that for the case where A is diagonalizable and its eigenvalues $\lambda_1, \lambda_2, \ldots\ldots, \lambda_n$ satisfy the nonresonance condition

$$\lambda_i \neq \sum_{k=1}^{n} n_k \lambda_k \quad \text{for all } n_k \geqq 0,\ \Sigma n_k \geqq 2,\ i = 1 \ldots n, \tag{11}$$

the nonlinear system can be reduced to

$$\dot{y} = Ay. \tag{12}$$

However, in bifurcation problems, where the nonresonance condition is not satisfied, the system can be reduced to:

$$\dot{y} = Ay + g(y) \tag{13}$$

where $g(y)$ is of a simpler form than the original $f(x)$. Computational techniques for determining normal forms can be found in Guckenheimer and Holmes (1983) and a recursive formulation suitable for symbolic manipulation is given by Hsu and Fanretto (1984).

This idea of finding a simple system representation has been applied to stochastic problems by several researchers. Knobloch and Wiessenfeld (1983) studied systems excited by both additive and multiplicative Gaussian white noise. They applied the idea of normal forms to the Fokker-Planck equation and concluded that the classification of deterministic bifurcation problems carry over to the stochastic case. On the other hand, Coulett et al. (1985) performed the normal transformation directly on the system equations and found additional terms which cannot be eliminated due to "stochastic resonance." In this paper, we shall work directly with the system equations and we will not assume Gaussian white noise. In order to study the interplay between the deterministic and stochastic parts of the system we shall derive the normal form for systems scaled as follows:

$$\dot{x} = Ax + \epsilon^2 f(x) + \epsilon g(x,\xi(t)) \tag{14}$$

where A is diagonal and $\xi(t)$ are stationary processes with zero means.

The nonlinear function f is a vector function smooth in its arguments and its rth order polynomial can be represented by

$$f(x) = \sum_m f^r_{i;m} x^m = \sum_m f^r_{i;m_1,m_2,\ldots m_n} x_1^{m_1} x_2^{m_2} \ldots x_n^{m_n}$$

where $m = (m_1, m_2, \ldots, m_n)$ are non-negative integers, $x^m = x_1^{m_1} x_2^{m_2} \ldots x_n^{m_n}$ is an rth order monomial such that $\Sigma m_j = r$, $f^r_{i;m}$ are the coefficients of the monomial with a particular combination of $(m_1, m_2, \ldots, m_n)$, and the summation is over all such monomials. Similarly, the rth order polynomial of the stochastic part can be represented as

$$g(x,\xi(t)) = \sum_m g^r_{i;m} x^m \cdot \xi(t)$$

where $g_{i;m}$ are the time-dependent coefficients of the monomials. With hindsight, we find that it is necessary to consider a near-identity transformation *up to second order in the stochastic terms.*

$$x = y + \epsilon^2 h(y) + \epsilon V_o(y,t) + \epsilon^2 V_1(y,t) \tag{15}$$

Furthermore, let the desired normal form be represented by:

$$y = Ay + \epsilon^2 F(y) + \epsilon W_o(y,t) + \epsilon^2 W_1(y,t). \tag{16}$$

Making the appropriate substitutions and ignoring terms of order $0(\epsilon^3)$ and higher, the transformations which yield the desired normal form are given by:

$$L[h, A] = f(y) - F(y) \tag{17}$$

$$\frac{\partial V_o}{\partial t} + L[V_o, A] = g(y,\xi(t)) - W_o(y,t) \tag{18}$$

$$\frac{\partial V_1}{\partial t} + L[V_1, A] = \frac{\partial g}{\partial y} V_o - \frac{\partial V_o}{\partial y} W_o - W_1 \tag{19}$$

Downloaded 03 May 2010 to 171.66.16.244. Redistribution subject to ASME license or copyright; see http://www.asme.org/terms/Terms_Use.cfm

where the operator L, is defined as:

$$L[*, A] = \frac{\partial(*)}{\partial y} Ay - A(*). \tag{20}$$

If we take the nonlinear terms in equations (15) and (16) as monomials of the form

$$(y_1^{m_1} y_2^{m_2} \ldots . y_n^{m_n}),\ (y_1^{m_1} y_2^{m_2} \ldots . y_n^{m_n}) \xi(t),$$

then by using the fact that A is diagonal, the operator L on $h(y)$ can be written as

$$L_A \cdot h = L[h,A] = [(m,\lambda) - \lambda_i] h^n_{i;m}\, y^m,\ (m,\lambda) = \sum_k m_k \lambda_k.$$

Here we denote, by $H_k(R^n)$, the vector space of homogeneous polynomials of degree k on R^n. Since L_A maps $H_k(R^n)$ to $H_k(R^n)$, L_A is called the homological operator. Moreover, L_A is a linear operator and the image of L_A, $\mathrm{Im}(L_A)$, and the kernel of the adjoint, $\ker(L_A^*)$, span the whole space. Consequently, the r.h.s. of equation (17) has to belong to $\mathrm{Im}(L_A)$. This gives a condition that $F^n_{k;m}$ may be chosen in $\ker(L_A^*)$, and the resonance condition reduces for the deterministic terms to:

$$\sum_{k=1}^{n} m_k \lambda_k - \lambda_i = 0 \text{ for all } i = 1,2, \ldots . n. \tag{21}$$

After taking Fourier transforms, the resonance condition for the stochastic terms becomes:

$$j\Omega + \sum_{k=1}^{n} m_k \lambda_k - \lambda_i = 0 \text{ for all } i = 1,2, \ldots n. \tag{22}$$

It should be noted that for stochastic terms in the critical modes, containing only the critical variables, there is always some value of Ω for which the condition equation (22) (stochastic resonance) is satisfied since the values of the λ's are zero or pure imaginary. In order to facilitate a comparison with stochastic averaging the system is partitioned into critical and stable modes, such that

$$A = \begin{bmatrix} A_c & \vdots & 0 \\ \cdots & \cdots & \cdots \\ 0 & \vdots & A_s \end{bmatrix} \tag{23}$$

where the eigenvalues of A_c are pure imaginary or zero and the eigenvalues of A_s have negative real parts. Similarly the state variables, the nonlinear vector, and the stochastic components can be partitioned as

$$x = \{x_c, x_s\},\ f(x) = \{f_c(x_c,x_s),\ f_s(x_c,x_s)\} \tag{24}$$

$$g(x_c,x_s,\xi(t)) = \begin{bmatrix} B_{cc}(t) & \vdots & B_{cs}(t) \\ \cdots & \cdots & \cdots \\ B_{sc}(t) & \vdots & B_{ss}(t) \end{bmatrix} \begin{Bmatrix} x_c \\ \\ x_s \end{Bmatrix}. \tag{25}$$

From Appendix B, we know that noise terms in the critical modes, which contain the stable variables, can be eliminated, and for the case of linear multiplicative noise, the same goes for the $B_{sc}(t)\ x_c$ terms in the stable mode equations. Hence, performing the normal form transformation described earlier we obtain:

$$\begin{Bmatrix} \dot{y}_c \\ \\ \dot{y}_s \end{Bmatrix} = \begin{bmatrix} A_c & \vdots & 0 \\ \cdots & \cdots & \cdots \\ 0 & \vdots & A_s \end{bmatrix} \begin{Bmatrix} y_c \\ \\ y_s \end{Bmatrix} + \epsilon^2 \begin{bmatrix} F_c(y_c) \\ \cdots \\ F_s(y_c,y_s) \end{bmatrix}$$

$$+ \epsilon \begin{bmatrix} B_{cc}(t) & \vdots & 0 \\ \cdots & \cdots & \cdots \\ 0 & \vdots & B_{ss}(t) \end{bmatrix} \begin{Bmatrix} y_c \\ -- \\ y_s \end{Bmatrix}$$

$$+ \epsilon^2 \begin{bmatrix} B_{cs}(t)\ V_{sc}(t) & \vdots & 0 \\ \cdots & \cdots & \cdots \\ 0 & \vdots & B_{sc}(t)\ V_{cs}(t) \end{bmatrix} \begin{Bmatrix} y_c \\ -- \\ y_s \end{Bmatrix} \tag{26}$$

where

$$\dot{V}_{cs} = A_c V_{cs} - V_{cs} A_s + B_{cs}(t) \tag{27}$$

$$\dot{V}_{sc} = A_s V_{sc} - V_{sc} A_c + B_{sc}(t). \tag{28}$$

Thus, using normal forms we have effectively uncoupled the critical modes from the stable ones. We also wish to point out that the deterministic part of the uncoupled system is the same as the deterministic normal form for the system unperturbed by noise. The nonlinear vector function $F_c(y_c)$ for various codimension one and two bifurcations are given in Arnold (1983) and Guckenheimer and Holmes (1983). It remains now to solve equations (27)–(28) to completely obtain the stochastic components of the normal form.

4 Equivalence of Stochastic Averaging and Stochastic Normal Forms

In this section, the foregoing lower dimensional equations are replaced by diffusive Markov processes whose transition probabilities at time intervals $\Delta t\ (\Delta t \gg \tau_{\mathrm{cor}})$ are approximately the same as those of the original processes. There are two ways of deriving the drift and diffusion coefficients which completely describe the Markov process. In the first method the increments $x(t_2) - x(t_1)$ and $x(t_4) - x(t_3)$, where $t_1 < t_2 < t_3 < t_4$, are assumed independent when the correlation time of the smooth process is much smaller than the relaxation time of the reduced system (Stratonovich, 1963). The second method Roberts and Spanos (1986) deals with the asymptotic behavior of the solution of the lower dimensional system when τ_{cor} tends to zero. In Appendix A of this paper we show the use of the first method to calculate the drift and diffusion terms. A physical interpretation of this approach, which is more appealing to engineers, is given by Lin (1986). It will be shown that the approximation of the solution of the lower dimensional equations by a Markov process gives rise to the same drift and diffusion terms as those obtained in the extended stochastic averaging technique. However, in order to demonstrate the equivalence we shall consider two cases where equations (27)–(28) will be solved explicitly.

4.1 Case 1: $A_c = 0$ (divergence instability)

In this case equations (27)–(28) reduce to:

$$\dot{V}_{cs} = -V_{cs} A_s + B_{cs}(t) \tag{29}$$

$$\dot{V}_{sc} = A_s V_{sc} + B_{sc}(t). \tag{30}$$

We require a particular solution for the normal form transformation,

$$V_{cs}(t) = -\left(\int_t^{\infty} B_{cs}(s) e^{A_s s} ds\right) e^{-A_s t} \tag{31}$$

$$V_{sc}(t) = e^{A_s t} \left(\int_{-\infty}^{t} e^{-A_s s} B_{sc}(s)\ ds\right). \tag{32}$$

Hence, the reduced system is (where x_c now represents the variable after transformation)

$$\dot{x}_c = \epsilon^2 F_c(x_c) + \epsilon\ B_{cc}(t) x_c + \epsilon^2 \left\{\left(B_{cs}(t) \int_{-\infty}^{t} e^{-A_s(s-t)} B_{sc}(s) ds\right) x_c\right\}. \tag{33}$$

Downloaded 03 May 2010 to 171.66.16.244. Redistribution subject to ASME license or copyright; see http://www.asme.org/terms/Terms_Use.cfm

Using the Markovian approximation shown in Appendix A and performing a time-translation, we find that the drift contribution from the stable modes to the drift term of the critical modes is

$$M_t\left\{E\left[\left(\int_{-\infty}^{0} B_{cs}(t)e^{-A_s\tau}B_{sc}(t+\epsilon)d\tau\right)x_c\right]\right\}, \tag{34}$$

which agrees with that obtained from the extended averaging theorem.

4.2 Case 2: $A_c = \text{diag}\ \{-j\omega_1,\ j\omega_1,\ \ldots\ldots,-j\omega_n,\ j\omega_n\}$ (flutter instability).

In this case, in addition to multiplicative noise, the effect of additive noise is also considered, i.e.,

$$g(x_c,x_s,\xi(t)) = \left[\begin{array}{c:c} B_{cc}(t) & B_{cs}(t) \\ \hdashline B_{sc}(t) & B_{ss}(t) \end{array}\right]\left\{\begin{array}{c} x_c \\ \hdashline x_s \end{array}\right\} + \left\{\begin{array}{c} D_c(t) \\ \hdashline D_s(t) \end{array}\right\}$$

and the solutions of equations (27)–(28) for this case are:

$$V_{cs}(t) = -e^{A_c t}\left(\int_t^{\infty} e^{-A_c s}B_{cs}(s)e^{A_s s}ds\right)e^{-A_s t} \tag{35}$$

$$V_{sc}(t) = e^{A_s t}\left(\int_{-\infty}^{t} e^{-A_s s}B_{sc}(s)e^{A_c s}ds\right)e^{-A_c t}. \tag{36}$$

As before, the second-order correction to the drift from the stable modes is:

$$M_t\left\{E\left[\left(\int_{-\infty}^{0} e^{-A_c t}B_{cs}(t)e^{-A_s\tau}B_{sc}(t+\tau)e^{A_c(t+\tau)}d\tau\right)x_c + \int_{-\infty}^{0} e^{-A_c t}B_{cs}(t)e^{-A_s\tau}D_s(t+\tau)d\tau\right]\right\}, \tag{37}$$

which agrees with that obtained from the extended averaging theorem. It is worthy to point out that the second term in equation (37) vanishes since $M_t\{e^{-A_c t}\} = 0$.

In both examples, we have assumed that the deterministic part has been reduced to a normal form. This assumption does not invalidate the equivalence in any way, since it has been shown that deterministic normal form and deterministic averaging methods are equivalent for non-nilpotent systems (Sethna, 1988). We will outline the proof here for convenience in Appendix C.

In the foregoing discussions we have assumed that the linear operator is diagonalizable. However, when it is not diagonalizable, the method of averaging cannot be applied due to the fact that the matrix e^{At} contains terms that are polynomials in t and the time average does not exist. Unlike averaging, normal forms can be used in the analysis of such nilpotent systems. Results for a system with a double zero bifurcation is presented by Sri Namachchivaya (1989) for a two-dimensional case.

5 Example: Stochastic Version of the Lorenz Equations

The results of the previous section are applied to a stochastic version of the Lorenz equations of fluid convection (Sri Namachchivaya and Hilton, 1988). This model is described by a three-parameter family of three-dimensional ordinary differential equations

$$\dot{u} = \rho(v-u),\ \dot{v} = \sigma u - v - uw,\ \dot{w} = -\beta w + uv. \tag{38}$$

Roughly speaking, the variables u, v, and w measure the rate of convective overturning, the horizontal temperature variation, and the vertical temperature variations, respectively. The three parameters, ρ, β, and σ are, respectively, proportional to the Prandtl number, to a geometric factor, and to the Rayleigh number. We assume that σ, the parameter associated with the Rayleigh number, fluctuates about a mean value σ_o, i.e.,

$$\sigma = \sigma_o(1+\epsilon\ \xi(t)) \tag{39}$$

where $\xi(t)$ is a stationary, zero-mean stochastic process. The fixed point (0,0,0) loses its stability by a simple bifurcation at $\sigma_o = 1$ in the absence of noise. For $\sigma_o = 1$, we apply the following transformation:

$$\left\{\begin{array}{c} u \\ v \\ w \end{array}\right\}^{\cdot} = \epsilon\left[\begin{array}{ccc} 1 & \rho & 0 \\ 1 & -1 & 0 \\ 0 & 0 & 1 \end{array}\right]\left\{\begin{array}{c} x_1 \\ x_2 \\ x_3 \end{array}\right\} \tag{40}$$

to obtain

$$\left\{\begin{array}{c} \dot{x}_1 \\ \dot{x}_2 \\ \dot{x}_3 \end{array}\right\} = \left[\begin{array}{ccc} 0 & 0 & 0 \\ 0 & -\alpha & 0 \\ 0 & 0 & -\beta \end{array}\right]\left\{\begin{array}{c} x_1 \\ x_2 \\ x_3 \end{array}\right\} + \epsilon\left\{\begin{array}{c} -\rho/\alpha(x_1+\rho x_2)x_3 \\ 1/\alpha(x_1+\rho x_2)x_3 \\ (x_1+\rho x_2)(x_1-x_2) \end{array}\right\}$$

$$+\epsilon\left[\begin{array}{ccc} \rho/\alpha & \rho^2/\alpha & 0 \\ -1/\alpha & -\rho/\alpha & 0 \\ 0 & 0 & 0 \end{array}\right]\left\{\begin{array}{c} x_1 \\ x_2 \\ x_3 \end{array}\right\}\xi(t) \tag{41}$$

where $\alpha = (1+\rho)$. The deterministic quadratic terms can be eliminated using the near identity transformations

$$x_1 = z_1 + \epsilon\{(\rho/\alpha\beta)z_1z_3 + (\rho^2/\alpha(\alpha+\beta))z_2z_3\},$$

$$x_2 = z_2 + \epsilon\{(1/\alpha(\alpha-\beta))z_1z_3 - (\rho/\alpha\beta)z_2z_3\},$$

$$x_3 = z_3 + \epsilon\left\{\frac{1}{\beta}z_1^2 + \frac{(1-\rho)}{(\alpha-\beta)}z_1z_2 + (\rho/(2\alpha-\beta))z_2^2\right\}$$

and the normal form transformations result in the creation of cubic terms. Details can be found in Sri Namachchivaya and Hilton (1988). Here we shall concentrate on the normal form calculation for the stochastic terms. In this example, z_1 is the critical mode and z_2 and z_3 are the two stable modes. The near-identity transformation to second order in the stochastic terms is

$$\left\{\begin{array}{c} z_1 \\ z_2 \\ z_3 \end{array}\right\} = \left\{\begin{array}{c} y_c \\ y_{s1} \\ y_{s2} \end{array}\right\} + \epsilon\left\{\begin{array}{c} V_{01}(t)y_{s1} \\ V_{02}(t)y_c \\ 0 \end{array}\right\} + \epsilon^2\left\{\begin{array}{c} V_{11}(t)y_{s1} \\ V_{12}(t)y_c \\ 0 \end{array}\right\} \tag{42}$$

which leads to:

$$\left\{\begin{array}{c} \dot{y}_c \\ \dot{y}_{s1} \\ \dot{y}_{s2} \end{array}\right\} = \left[\begin{array}{ccc} 0 & 0 & 0 \\ 0 & -\alpha & 0 \\ 0 & 0 & -\beta \end{array}\right]\left\{\begin{array}{c} y_c \\ y_{s1} \\ y_{s2} \end{array}\right\} + \epsilon^2\left\{\begin{array}{c} \text{cubic nonlinear} \\ \text{terms in } y_c, y_{s1}, y_{s2} \end{array}\right\}$$

$$+\epsilon\left[\begin{array}{ccc} \rho/\alpha & 0 & 0 \\ 0 & -\rho/\alpha & 0 \\ 0 & 0 & 0 \end{array}\right]\left\{\begin{array}{c} y_c \\ y_{s1} \\ y_{s2} \end{array}\right\}\xi(t)$$

$$+\epsilon^2\left[\begin{array}{ccc} \rho^2/\alpha\ V_{02}(t)\ \xi(t) & 0 & 0 \\ 0 & -1/\alpha\ V_{01}(t)\ \xi(t) & 0 \\ 0 & 0 & 0 \end{array}\right]\left\{\begin{array}{c} y_c \\ y_{s1} \\ y_s{}^2 \end{array}\right\}.$$

Corresponding to equations (27)–(28) we require that:

$$\dot{V}_{01}(t) = \alpha\ V_{01}(t) + \frac{\rho^2}{\alpha}\xi(t),$$

$$\dot{V}_{02}(t) = -\alpha\ V_{02}(t) - \frac{1}{\alpha}\xi(t) \tag{43a}$$

and to uncouple the second-order stochastic terms,

Downloaded 03 May 2010 to 171.66.16.244. Redistribution subject to ASME license or copyright; see http://www.asme.org/terms/Terms_Use.cfm

$$\dot{V}_{11}(t) = \alpha\, V_{11}(t) + \frac{2\rho}{\alpha}\, V_{01}(t),$$

$$\dot{V}_{12}(t) = -\alpha\, V_{12}(t) - \frac{2\rho}{\alpha}\, V_{02}(t). \tag{43b}$$

A particular solution for equation (43*a*) is

$$V_{01}(t) = -\frac{\rho^2}{\alpha}\int_t^\infty e^{\alpha(t-s)}\xi(s)\, ds,$$

$$V_{02}(t) = -\frac{1}{\alpha}\int_{-\infty}^t e^{-\alpha(t-s)}\xi(s)\, ds. \tag{44}$$

Similarly, we can solve equation (43*b*), but to $O(\epsilon^2)$ it is not necessary to do so explicitly (refer to equation (26). Thus, the reduced system for the critical mode alone is:

$$\dot{y}_c = \epsilon^2\eta\, y_c - \epsilon^2\frac{\rho}{\alpha\beta}\, y_c{}^3 + \epsilon\frac{\rho}{\alpha}\, y_c\, \xi(t)$$

$$-\epsilon^2\left(\frac{\rho^2}{\alpha^2}\int_{-\infty}^t e^{-\alpha(t-s)}\xi(t)\xi(s)ds\right)y_c. \tag{45}$$

$\epsilon^2\eta$ is included as an unfolding parameter. The Markov approximation for the reduced system equation (45) can now be obtained and the drift and diffusion terms are:

$$m(x) = \epsilon^2 M_t\left\{\eta y_c - \frac{\rho}{\alpha\beta}\, y_c{}^3 - \left(\frac{\rho^2}{\alpha^2}\int_{-\infty}^0 e^{+\alpha\tau}R_{\xi\xi}(\tau)d\tau\right)y_c\right.$$

$$\left. + \left(\frac{\rho^2}{\alpha^2}\int_{-\infty}^0 R_{\xi\xi}(\tau)\, d\tau\right)y_c\right\} \tag{46}$$

$$\sigma\sigma^T = \epsilon^2\frac{\rho^2}{\alpha^2}\, M_t\left\{\int_{-\infty}^\infty R_{\xi\xi}(\tau)\, y_c{}^2\, d\tau\right\}.$$

Solution of the time-independent Fokker-Planck equation yields the stationary density function as:

$$p_{st}(y_c) = \left[\frac{1}{\beta\, S_o}\right]^\nu \frac{|y_c|^{2\nu-1}}{\Gamma(\nu)}\exp\left[-y_c{}^2/<\beta\, S_o\right] \tag{47}$$

where $S_o = 2\int_{-\infty}^0 R_{\xi\xi}(\tau)d\tau$, $S_1 = 2\int_{-\infty}^0 R_{\xi\xi}(\tau)e^{\alpha\tau}d\tau$

$$\nu = (\eta - S_1/2)S_o \geqq 0 \quad \text{and} \quad \beta > 0$$

and the results are identical to those obtained using the extended stochastic averaging method in Sri Namachchivaya and Hilton (1988).

6 Conclusions

We have demonstrated the equivalence of stochastic normal forms and stochastic averaging for systems under the effect of linear multiplicative and additive noise. Equivalence is defined in the sense that the normal form transformations lead to a reduced system with the same Markovian approximation as that obtained directly from the extended stochastic averaging theorem. The key result is that one has to retain second-order stochastic terms in the normal form computation. To our knowledge this has been ignored by previous investigations. The method of stochastic normal forms is applied to the stochastic version of Lorenz model of fluid convection. Unlike stochastic averaging, stochastic normal forms can be used in the analysis of nilpotent systems since equations (35) and (36) do not depend in anyway on A_c being a diagonal matrix and the $O(\epsilon^2)$ contribution from the stable modes can be obtained from equation (26) for the class of systems considered.

Acknowledgment

This research is supported by a grant from the Air Force Office of Scientific Research under Grant No. AFOSR-88-0233. Dr. Spencer Wu is the Program Director.

References

Arnold, V. I., 1983, *Geometric Methods in the Theory of Ordinary Differential Equations*, Springer-Verlag, New York.

Borodin, A. N., 1977, "A Limit Theorem for the Solution of Differential Equations with Radom Right Hand Side," *Theory of Probability and its Applications*, Vol. 22, No. 3, pp. 482–497.

Caughey, T. K., 1986, "On the Response of Non-Linear Oscillations to Stochastic Excitation," *Probabilistic Engineering Mechanics*, Vol. 1, No. 1, pp. 2–4.

Coulett, P. H., Elphick, C., and Tircepegui, E., 1985, "Normal Form of a Hopf Bifurcation with Noise," *Physics Letters*, Vol. 111A, No. 6, pp. 277–282.

Guckenheimer, J., and Holmes, P., 1983, *Nonlinear Oscillations Dynamical Systems and Bifurcations of Vector Fields*, Springer-Verlag, New York.

Hsu, L., and Fanretto, L., 1984, "Recursive Bifurcation Formulae for Normal Form and Center Manifold Theory," *Journal of Mathematical Analysis and Applications*, Vol. 101, pp. 562–574.

Khasminskii, R. Z., 1963, "Principle of averaging for Parabolic and Elliptic Differential Equations and for Markov Processes with Small Diffusion," *Theory of Probability and its Applications*, Vol. 8, No. 1, pp. 1–21.

Khasminskii, R. Z., 1966, "A Limit Theorem for the Solutions of Differential Equations with Random Right Hand Sides," *Theory of Probability and its Applications*, Vol. 11, No. 3, pp. 390–405.

Knobloch, E., and Wiessenfeld, K. A., 1983, "Bifurcations in Fluctuating Systems: the center manifold Approach," *Journal of Statistical Physics*, Vol. 33, No. 3, pp. 612–637.

Lin, Y. K., 1986, "Some Observations on the Stochastic Averaging Method," *Probability Engineering Mechanics*, Vol. 1, pp. 23–27.

Papanicolaou, G. C., and Kohler, W., 1974, "Asymptotic Theory of Mixing Stochastic Ordinary Differential Equations," *Communications on Pure Applied Mathematics*, Vol. 27, pp. 641–668.

Papanicolaou, G. C., and Kohler, W., 1975, "Asymptotic Analysis of Deterministic and Stochastic Equations with Rapidly Varying Components," *Communications in Mathematical Physics*, Vol. 45, pp. 217–232.

Roberts, J. B., and Spanos, P. D., 1986, "Stochastic Averaging: An Approximate Method of Solving Random Vibration Problems," *International Journal of Nonlinear Mechanics*, Vol. 21, pp. 111–136.

Sethna, P. R., 1988, "On the equivalence of averaged and normal form equations," preprint.

Sri Namachchivaya, N., 1989, "Co-dimension Two Bifurcations in the Presence of Noise," ASME JOURNAL OF APPLIED MECHANICS, to appear.

Sri Namachchivaya, N., 1990, "Stochastic Bifurcation," *Journal of Applied Mathematics and Computation*, to appear.

Sri Namachchivaya, N., and Hilton, Harry H., 1988, "Stochastically perturbed Bifurcations," *Nonlinear Stochastic Dynamic Engineering Systems*, Ziegler and Schueller, eds., Springer-Verlag, New York, pp. 169–180.

Sri Namachchivaya, N., and Lin, Y. K., 1988, "Applications of Stochastic Averaging for Systems with High Damping," *Probabilitic Engineering Mechanics*, Vol. 3, No. 3, pp. 159–167, see also *Stochastic Structural Mechanics* (Lecture notes in Engineering, 31), Y. K. Lin and G. I. Schueller, eds., 1987, Springer-Verlag, New York, pp. 282–310.

Stratonovich, R. L., 1967, *Topics in the Theory of Random Noise*, Vol. 1, Gordon and Breach, New York.

APPENDIX A

Approximation to Markov Process

Following the discussion in Section 4, it is necessary to evaluate the solutions of equations (26)–(28) and then compute the drift and diffusion coefficients given as

$$m(x,t) = \lim_{\Delta t\to 0} E\left\{\frac{[x(t_o+\Delta t) - x(t_o)]}{\Delta t}\middle| x = x(t_o)\right\} \tag{A1}$$

$$\sigma(x,t)\sigma^T(x,t) = B(x,t)$$

$$= \lim_{\Delta t\to 0} E\left\{\frac{[x(t_o+\Delta t) - x(t_o)]^2}{\Delta t}\middle| x = x(t_o)\right\}. \tag{A2}$$

Since the above conditional moments do not require the exact solution of equations (26)–(28), the solution is obtained on a small interval $\Delta t \gg \tau_{\text{cor}}$. To this end we consider case 1, the solution of which can be written formally as

$$x(t_o+\Delta t) = x(t_o) + \epsilon\left\{\int_{t_o}^{t_o+\Delta t} B_{cc}(\eta)x(\eta)d\eta\right\}$$

$$+\epsilon^2\left\{\int_{t_o}^{t_o+\Delta t}\left[F(x(\eta))\right.\right.$$

$$\left.\left. + \left(B_{cs}(\eta)\int_{t_o}^{\eta} e^{A_s(\eta-s)}B_{sc}(s)ds\right)x(\eta)\right]d\eta\right\}. \tag{A3}$$

Downloaded 03 May 2010 to 171.66.16.244. Redistribution subject to ASME license or copyright; see http://www.asme.org/terms/Terms_Use.cfm

Substituting for $x(\eta)$ in r.h.s. of equations (A3), we obtain

$$x(t_o+\Delta t)=x(t_o)+\epsilon\left\{\int_{t_o}^{t_o+\Delta t} B_{cc}(\eta)x(t_o)d\eta\right\}$$

$$+\epsilon^2\left\{\int_{t_o}^{t_o+\Delta t}[F(x(t_o))+(B_{cc}(\eta)\int_{t_o}^{\eta} B_{cc}(\xi)d\xi$$

$$+B_{cs}(\eta)\int_{t_o}^{\eta} e^{A_s(\eta-s)}B_{sc}(s)ds)x(t_o)\Big]d\eta\right\}.$$

Thus, the drift and diffusion terms are evaluated as

$$m(x,t)=\epsilon^2\Big\{F(x)$$

$$+\lim_{\Delta t\to 0}\left(\frac{1}{\Delta t}\right)\left\{x\int_{t_o}^{t_o+\Delta t}\left[\int_{t_o-\eta}^{o}<B_{cc}(\eta)B_{cc}(\eta+\tau)>d\tau\right.\right.$$

$$\left.\left.+\int_{t_0-\eta}^{0}<B_{cs}(\eta)e^{-A_s\tau}B_{sc}(\eta+\tau)>d\tau\right]d\eta\right\}\Big\}$$

$$B(x,t)=\lim_{\Delta t\to 0}\epsilon^2\left\{\int_{t_o}^{t_o+\Delta t}d\eta\left[\int_{t_o}^{t_o+\Delta t}<B_{cc}(\eta)xx^TB_{cc}^T(\xi)>d\xi\right]\right\}.$$

Now, for $\Delta t\gg\tau_{cor}$, taking into consideration the stationarity of the processes, the conditional moments reduce to

$$m(x,t)=\epsilon^2[F(x)+x\left\{\int_{-\infty}^{o}<B_{cc}(\eta)B_{cc}(\eta+\tau)>d\tau\right.$$

$$\left.+\int_{-\infty}^{o}<B_{cs}(\eta)e^{-A_s\tau}B_{sc}(\eta+\tau)>d\tau\right\}] \tag{A4}$$

$$\sigma(x,t)=\epsilon^2\left[\int_{-\infty}^{\infty}<B_{cc}(\eta)xx^TB_{cc}^T(\eta+\tau)>d\tau\right] \tag{A5}$$

where we have approximated, e.g.,

$$\frac{1}{\Delta t}\int_{t_o}^{t_o+\Delta t}d\eta\int_{t_o-\eta}^{o}<B_{cs}(\eta)e^{-A_s\tau}(\eta+\tau)>d\tau$$

$$\simeq\int_{-\infty}^{o}<B_{cs}(\eta)e^{-A_s\tau}B_{cs}(\eta+\tau)>d\tau$$

for $\Delta t t\gg\tau_{cor}$. The associated diffusion proccess is given by

$$\frac{\partial u}{\partial t}=L_\epsilon u=\epsilon^2\left\{m_i(x,t)\frac{\partial u}{\partial x_i}+\frac{1}{2}B_{ij}(x,t)\frac{\partial^2 u}{\partial x_i\partial x_j}\right\}.$$

Now, applying the deterministic averaging as shown by Khasminskii (1963), the averaged operator is obtained as

$$\frac{\partial u^o}{\partial t}=L_3^o u^o=\lim_{T\to\infty}\frac{1}{T}\int_t^{t+T}L_\epsilon(\cdot,t)dt$$

$$=\epsilon^2\left\{m_i^o(x)\frac{\partial u^o}{\partial x_i}+\frac{1}{2}B_{ij}^o(x)\frac{\partial^2 u^o}{\partial x_i\partial x_j}\right\}$$

and the solutions u_ϵ^o and u_ϵ are uniformly close on a time interval $O(1/\epsilon^2)$. The averaged drift and diffusion coefficients are

$m^o(x)=\underset{t}{M}[m(x,t)]$ and $B^o(x)=\underset{t}{M}[B(x,t)]$.

APPENDIX B

We will show that noise terms in the critical modes, which contain stable variables, can be eliminated. Let the noise term be of the form

$$(y_{c_1}^{m_1}\cdot\cdot\cdot\cdot\cdot y_{c_p}^{m_p})(y_{s_1}^{n_1}\cdot\cdot\cdot\cdot y_{s_a}^{n_a})\xi(t)$$

then the resonance condition equation (22) is

$$j\Omega+\sum_{j=1}^{p}m_j\lambda_{cj}+\sum_{j=1}^{q}n_j\lambda_{sj}-\lambda_{ci}=0$$

where the λ_{cj}'s are either zero or pure imaginary and the λ_{sj}'s have negative real parts. Since at least one of the n_j's is a non-negative integer, it is obvious that the resonance condition can never be satisfied for any value of Ω. Hence, we can always remove noise terms containing the stable variables from the critical modes.

Similarly, in the case of linear multiplicative noise, noise terms of the form $y_{cj}\,\xi(t)$ can be removed from the stable modes. Checking the resonance condition,

$$j\Omega+(1)\lambda_{cj}-\lambda_{si}=0$$

since λ_{cj} is zero or pure imaginary and λ_{si} has a negative real part, the resonance condition cannot be satisfied for any Ω. This allows us to decouple the stochastic terms in equation (26) leading to equations (27)–(28) which provides the $O(\epsilon^2)$ contribution from the stable modes to the critical modes.

We wish to add that for higher-order noise terms such a decoupling may not be possible because of "stochastic resonance."

Example: $\lambda_{cj}=j\omega$, $\lambda_{c2}=-j\omega$ (Hopf bifurcation). $\lambda_{s1}=\gamma$. Let the stable mode contain a noise term of the form $y_{c_1}^{m_1}\,y_{c_2}^{m_2}\,y_{s_1}\,\xi(t)$.

The resonance condition is

$$j\Omega+m_1(j\omega)+m_2(-j\omega)+1(-\gamma)-(-\gamma)=0$$

$$\text{i.e., } j(\Omega+(m_1-m_2)\omega)=0$$

which is satisfied for $\Omega=(m_2-m_1)\,\omega$. Thus, it is not always possible to remove such terms unless the noise $\xi(t)$ has no energy at the frequencies $\Omega=(m_2-m_1)\omega$.

APPENDIX C

We need to show that

$$F_c(\bar{x}_c)=\underset{t}{M}\{e^{-A_ct}f_c(e^{A_ct}\bar{x}_c,0)\}$$

where $x_c=e^{A_ct}\bar{x}_c$

and $$\dot{x}=A_cx+\epsilon^2f_c(x,0). \tag{C1}$$

Using the fact that the normal form $F_c(\bar{x}_c)$ lies in the null-space of the L operator, i.e.,

$$\frac{\partial F_c}{\partial x_c}A_cx_c-A_cF_c(x_c)=0, \tag{C2}$$

we can write

$$\frac{d}{dt}[F_c(e^{A_ct}\bar{x}_c)]=\frac{\partial F_c}{\partial x_c}A_ce^{A_ct}\bar{x}_c=A_cF_c(x_c), \tag{C3}$$

which is a linear first-order O.D.E in $F_c(x_c)$. The solution of equation (C3) is

$$F_c(x_c)=e^{A_ct}F_c(x_c,t=0)\ \text{ or }\ F_c(e^{A_ct}\bar{x}_c)=e^{A_ct}F_c(\bar{x}_c). \tag{C4}$$

Thus, averaging the system in normal form

$$\dot{x}_c=A_cx_c+\epsilon^2F_c(x_c)$$

yields

$$\dot{\bar{x}}=\epsilon^2F_c(\bar{x}_c). \tag{C5}$$

On the other hand, if we were to average equation (C3), we obtain

$$\dot{\bar{x}}=\epsilon^2\underset{t}{M}\{e^{-A_ct}f_c(e^{A_ct}\bar{x}_c,0)\}. \tag{C6}$$

Since both the normal form and the averaged system are unique we conclude that

Downloaded 03 May 2010 to 171.66.16.244. Redistribution subject to ASME license or copyright; see http://www.asme.org/terms/Terms_Use.cfm

$$F_c(\bar{x}_c) = \underset{t}{M}\{e^{-A_c t} f_c(e^{A_c t}\bar{x}_c, 0)\}. \tag{C7}$$

For the case where the deterministic terms are nonautonomous and are of the form

$$f^{(r)}_{i,m,\omega} e^{j\omega t}$$

where $f^{(r)}_{i,m,\omega}$ as a monomial is defined in Section 3, we can still show that the equivalence holds. In this case, taking the deterministic terms in the normal form computation to be

$$F^{(r)}_{i,m,\omega} e^{j\omega t}$$

yields equations corresponding to equations (17) and (21) as

$$\frac{\partial h}{\partial t} + L[h,A] = f(y,t) - F(y,t) \tag{C8}$$

$$j\omega + \sum_{k=1}^{n} m_k \lambda_k - \lambda_i = 0. \tag{C9}$$

Similarly, it can be shown that

$$F_c(e^{A_c t}\bar{x}_c, t) = e^{A_c t} F_c(\bar{x}_c, 0) \tag{C10}$$

and the equivalence of deterministic normal forms and deterministic averaging follows.

Downloaded 03 May 2010 to 171.66.16.244. Redistribution subject to ASME license or copyright; see http://www.asme.org/terms/Terms_Use.cfm

The Generalized Cell Mapping Method in Nonlinear Random Vibration Based Upon Short-Time Gaussian Approximation

J. Q. Sun
Research Associate,
Mem. ASME

C. S. Hsu
Professor,
Fellow ASME

Department of Mechanical Engineering,
University of California,
Berkeley, CA 94720

A short-time Gaussian approximation scheme is proposed in the paper. This scheme provides a very efficient and accurate way of computing the one-step transition probability matrix of the previously developed generalized cell mapping (GCM) method in nonlinear random vibration. The GCM method based upon this scheme is applied to some very challenging nonlinear systems under external and parametric Gaussian white noise excitations in order to show its power and efficiency. Certain transient and steady-state solutions such as the first-passage time probability, steady-state mean square response, and the steady-state probability density function have been obtained. Some of the solutions are compared with either the simulation results or the available exact solutions, and are found to be very accurate. The computed steady-state mean square response values are found to be of error less than 1 percent when compared with the available exact solutions. The efficiency of the GCM method based upon the short-time Gaussian approximation is also examined. The short-time Gaussian approximation renders the overhead of computing the one-step transition probability matrix to be very small. It is found that in a comprehensive study of nonlinear stochastic systems, in which various transient and steady-state solutions are obtained in one computer program execution, the GCM method can have very large computational advantages over Monte Carlo simulation.

1 Introduction

More than 20 years ago, an important iterative method based upon the cellular discretization of the state space was first developed and applied to the first-passage problem of linear oscillators by Crandall and his co-workers (Crandall et al., 1966). This article is the most frequently cited one on this subject. The results of some first-passage problems of linear oscillators published in the article are often taken as benchmarks against which other approximate solutions are compared.

In the attempt of solving this and many other difficult problems in nonlinear random vibration, a number of numerical techniques have been developed over the years. Toland and Yang (1971) developed a random walk model for solving the Fokker-Planck-Kolmogorov (FPK) equation. The method was applied, with success, to the first-passage problem of the Duffing system and the "bang-bang" system (Toland and Yang, 1971; Toland et al., 1972). Being an explicit finite difference scheme in mathematical terms, the random walk model was later improved by Roberts (1986) using a Crank-Nicolson type implicit finite difference algorithm. Roberts (1986) applied his new algorithm to the first-passage problem of one-dimensional energy envelope process of nonlinear oscillators under light damping. A very powerful finite element method for the first-passage problem of nonlinear oscillators, originally proposed by Heinrich et al. (1977), was developed by Bergman and Heinrich (1982) and by Bergman and Spencer (1983). This method is found well suited for solving the backward Kolmogorov equation for the first-passage time probability, and the Pontriagin-Vitt equations for moments of the time to first passage. A large number of results of the first-passage problems for linear and nonlinear oscillators are compiled in (Bergman and Spencer, 1983). A different finite element scheme was proposed by Langley (1985) for solving the forward FPK equation. He applied the method to a couple of nonlinear systems, and obtained the stationary probability density of the system. The discussion on literature given previously is not meant to be exhaustive. An interested reader should consult, for example, the review article by Crandall and Zhu (1983) for other approximate methods.

Contributed by the Applied Mechanics Division of THE AMERICAN SOCIETY OF MECHANICAL ENGINEERS for presentation at the Winter Annual Meeting, Dallas, Texas, Nov. 25-30, 1990.

Discussion on this paper should be addressed to the Technical Editor, Leon M. Keer, The Technological Institute, Northwestern University, Evanston, IL 60208, and will be accepted until two months after final publication of the paper itself in the JOURNAL OF APPLIED MECHANICS. Manuscript received by the ASME Applied Mechanics Division, May 24, 1989; final revision, Nov. 13, 1989.

Paper No. 90-WA/APM-28.

Copyright © 1990 by ASME
Downloaded 03 May 2010 to 171.66.16.244. Redistribution subject to ASME license or copyright; see http://www.asme.org/terms/Terms_Use.cfm

Upon examining the existing numerical methods in nonlinear random vibration, it appears that little has been done along the line of Crandall's original iterative approach. In 1981, Hsu (1981) developed a generalized cell mapping (GCM) method for global analysis of nonlinear deterministic systems. When the GCM method is applied to stochastic systems, it is realized that the GCM method is literally a generalization of Crandall's iterative method for linear stochastic systems to nonlinear systems. What also becomes apparent is that when the computation by the GCM method covers a sufficiently large domain in the state space, essentially all transient and steady-state solutions of the system, including the first-passage time probability, can be obtained in one computer program execution. Since it is built upon the theory of finite Markov chains, which include random walk as a special case, the GCM method can also be considered as a generalization of Toland and Yang's random walk model. However, the GCM method has certain advantages over the random walk model, as discussed in (Sun and Hsu, 1988a). The GCM method has been applied to various random vibration problems, such as moments of the steady-state response, the steady-state probability density function, and the first-passage problem (Chiu, 1984; Chiu and Hsu, 1986; Sun and Hsu, 1988a, 1989a). The GCM method is quite general in the sense that it can yield a wide range of solutions, transient and steady-state, of the system, and it is applicable to the systems which are either weakly or strongly nonlinear, and either lightly or highly damped. In particular, the GCM method may be applied to the stochastic systems which don't necessarily admit a Fokker-Planck equation (Chiu, 1984; Soong, 1973; Sun and Hsu, 1988b), while most of the existing numerical techniques in nonlinear random vibration are designed to solve either the forward or backward Fokker-Planck equation. The most interesting feature of the GCM method is that once the one-step transition probability matrix is computed, the dynamical evolution of the system is controlled by a discrete finite Markov chain. That is to say, the complete response history of the system can be computed simply by iterating the evolution equation of the Markov chain. Further, the structure of the steady-state solutions can be predicted, to some extent, by examining the topological property of the transition probability matrix without doing any iteration (Hsu, 1987). Up to now, the transition probability matrix of the GCM method for nonlinear systems has been mainly computed by Monte Carlo simulation. The computation is quite intensive. The transition probability matrix is also subject to statistical errors due to finite samples used in the simulation (Sun and Hsu, 1987b). Nevertheless, the results reported in the aforementioned references are accurate when large number of samples are used in the simulation, and the cell sizes are properly chosen. The GCM method is found to be more efficient than Monte Carlo simulation only when global or comprehensive studies of the system are desired.

In this paper we introduce an analytical approach for computing the short-time one-step transition probability density function, which is then used to compute numerically the one-step transition probability matrix of the GCM method. The approach is based upon a short-time Gaussian approximation of the one-step conditional probability density function. The GCM method based upon this short-time Gaussian approximation is then applied to several nonlinear systems under external and parametric Gaussian white noise excitations. Various transient and steady-state response statistics, and the probability density function are obtained with amazingly high accuracy. To show that the method can stand on its own merits, we validate it by comparing its results with available exact solutions or with simulation results when exact solutions are not available. No attempt is made in the paper to compare the results of this method with those from other existing numerical techniques. There is also no attempt here to discuss the theoretical aspects of the new method, such as error analyses and so forth. These theoretical underpinnings await further study in the future. With these aims in view, the paper is arranged as follows. In Section 2 we briefly describe the basic idea of the GCM method. In Section 3 we introduce the short-time Gaussian approximation scheme. In Section 4 we present examples of application. A discussion on the efficiency of the GCM method based upon the short-time Gaussian approximation will be presented along with many interesting numerical results obtained by the GCM method. For convenience of reference we shall refer to this GCM method using short-time Gaussian approximation as the GCM/STGA method.

2 A Brief Description of the GCM Method

Let $\mathbf{x}(t)$ be the response process of state variables of an N-dimensional nonlinear dynamical system under Gaussian white noise excitation. $\mathbf{x}(t)$ is known to be a stationary Markov process. Let $p(\mathbf{x},t)$ be the probability density function of the process $\mathbf{x}(t)$ at time t, and $p(\mathbf{x},t\,|\mathbf{x}_0,t_0)$ the probability density function of $\mathbf{x}(t)$ at time t conditional on $\mathbf{x}_0$ at time $t_0 (t_0 < t)$, which satisfies the following condition:

$$p(\mathbf{x},t\,|\mathbf{x}_0,t_0) = p(\mathbf{x},t-t_0\,|\mathbf{x}_0,0), \quad \text{for } t-t_0>0. \tag{1}$$

Under condition (1), we have

$$p(\mathbf{x},t) = \int_{R^N} p(\mathbf{x},t-t_0\,|\mathbf{x}_0,0)p(\mathbf{x}_0,t_0)d\mathbf{x}_0. \tag{2}$$

Let $t_0 = (n-1)\tau$ and $t = n\tau$. Then, equation (2) can be cast into a form of function mapping

$$p(\mathbf{x},n\tau) = \int_{R^n} p(\mathbf{x},\tau\,|\mathbf{x}_0,0)p(\mathbf{x}_0,(n-1)\tau)d\mathbf{x}_0. \tag{3}$$

Consider a discretized space $\mathbf{R}^N$ consisting of countable many cells of finite but small volume $(h_1 \times h_2 \times \ldots \times h_N)$. Because of countability, each cell in the discretized space can be indexed by an integer. Equation (3) can be approximated by the evolution equation of a discrete Markov chain in the discretized space as follows:

$$p_i(n) = \sum_{j=1}^{\infty} P_{ij}p_j(n-1), \quad n=1,2,\ldots \tag{4}$$

where $p_i(n)$ represents the probability of the system being in the ith cell at time $n\tau$, and P_{ij} the probability of the system being in the ith cell at time τ when the system is initially in the jth cell with probability one. $p_i(n)$ and P_{ij} are given by

$$p_i(n) = \int_{C_i} p(\mathbf{x},n\tau)d\mathbf{x}, \quad P_{ij} = \int_{C_i} p(\mathbf{x},\tau\,|\mathbf{x}_j,0)d\mathbf{x}, \tag{5}$$

where C_i is the domain occupied by the ith cell in $\mathbf{R}^N$, and $\mathbf{x}_j$ the center of the jth cell. In real computation, the infinite summation in equation (4) is inevitably truncated. In this paper we truncate the summation so that in each mapping step, 99.97 percent of the probability is captured.

The above is the basic idea of the GCM method for stochastic systems. In implementing the method, computation of the one-step transition probability matrix P_{ij} involving all i's and j's is a key task. When $\mathbf{x}(t)$ is the response process of a linear oscillator to Gaussian white noise excitation, P_{ij} can be computed based upon the exact conditional probability density function of $\mathbf{x}(t)$ (Crandall et al., 1966; Sun and Hsu, 1988a). For nonlinear stochastic systems, on the other hand, exact conditional probability density function of the response process is rarely available, and Monte Carlo simulation has been a common approach for computing P_{ij} (Chiu, 1984; Hsu and Chiu, 1986; Sun and Hsu, 1988a). In the simulation, one

Downloaded 03 May 2010 to 171.66.16.244. Redistribution subject to ASME license or copyright; see http://www.asme.org/terms/Terms_Use.cfm

generates a large number of sample trajectories of time duration τ out of each cell, and then construct a histogram estimator of P_{ij}. The computation is quite intensive when large number of cells are involved and large number of sample trajectories are simulated out of each cell. Furthermore, the estimated P_{ij} is still subjected to statistical error which converges to zero at the rate of $m^{-1/2}$, where m is the number of sample trajectories (Sun and Hsu, 1987b).

3 Short-Time Gaussian Approximation

To avoid the time-consuming Monte Carlo simulation in computing P_{ij}, one naturally seeks for an analytical approximation of $p(\mathbf{x},\tau\,|\mathbf{x}_0,0)$, with which the computation of P_{ij} is simplified to an integration over a cell according to equation (5). Such an approximation can be devised based upon the following result.

Result 1. $p(\mathbf{x},\tau\,|\mathbf{x}_0,0)$ is approximately Gaussian when τ is sufficiently small.

In fact, $\lim_{\tau\to 0} p(\mathbf{x},\tau\,|\mathbf{x}_0,0)=\delta(\mathbf{x}-\mathbf{x}_0)$, and $\delta(\mathbf{x}-\mathbf{x}_0)$ is a special case of Gaussian probability density function. Furthermore, it can be shown that when $\tau \ll 1$, $p(\mathbf{x},\tau\,|\mathbf{x}_0,0)$, known as the small-time solution to the Fokker-Planck equation, is approximately Gaussian within an error of order $O(\tau^2)$ (Risken, 1984). We have done some simulation of nonlinear systems to validate and appreciate Result 1. It is observed that for small τ (say, $\tau \le 0.1$), the short-time Gaussian approximation is indeed valid and accurate in almost all cases we studied; for τ being of order one, the short-time Gaussian approximation is still good for some cases, but no longer adequate for others. Some of the simulation tests will be reported elsewhere in the paper. A motivation of Result 1 comes from the observation of the results obtained by Gaussian approximations reported in the literature. It has been shown, for example, in (Wu and Lin, 1984; Sun and Hsu, 1989b), that the transient solutions of response moments, starting from an initial condition $\mathbf{x}=\mathbf{x}_0$ at time t_0, obtained by Gaussian approximation agree very well with the simulation results for some small-time increment $t-t_0$, and the deviation of the approximate solutions from the simulation results gradually grows with time. It can be shown that the probability density function at this small-time increment $t-t_0$ also agrees with the simulated probability density function very well.

An important remark on Result 1 is that the Gaussian approximation of the conditional probability density function $p(\mathbf{x},\tau\,|\mathbf{x}_0,0)$ depends on or varies with the initial condition $\mathbf{x}_0$. That is to say, the approximating Gaussian probability density function $p(\mathbf{x},\tau\,|\mathbf{x}_0,0)$ will, in general, take on different "shapes" for different initial conditions $\mathbf{x}_0$. This might be a very obvious observation. Nevertheless, this retained spacewise adaptive character appears to be the key to the success of the short-time Gaussian approximation to capture the global nonlinear system behavior when it is applied in conjunction with the GCM method.

Strictly speaking, P_{ij} needs to satisfy the boundary conditions when the GCM method is applied to the first-passage problem (Roberts, 1976, 1978). However, it has been demonstrated in (Crandall et al., 1966; Sun and Hsu, 1988a) that when the mapping time-step τ is small, the first-passage time probability can be accurately predicted by using equation (4) of the GCM method, where P_{ij} is computed from equation (5) without imposition of the boundary conditions in the first-passage problem. This approximation also implies that the first-passage failure can only occur at the discrete times $n\tau$ ($n=0,1,2,\ldots$). Hence, it is not totally undesirable to have small τ as required by Result 1. However, too small a τ does add more computations in iterating equation (4) for long-term steady-state solutions. Analytical study to find a proper mapping time-step in order to achieve maximum efficiency and accuracy seems warranted. In the paper, we choose the mapping time-step based upon the simulation studies and past experience, and find that τ, being about 0.5, provides a good balance of efficiency and accuracy.

Since $p(\mathbf{x},\tau\,|\mathbf{x}_0,0)$ is assumed to be Gaussian, we need to evaluate only the first and second-order moments of $\mathbf{x}(t)$ in order to completely specify the conditional probability density function. This can be done by integrating the first and second-order moment equations from $t=0$ to $t=\tau$. By using this Gaussian approximation of the conditional probability density function, we can virtually treat any type of nonlinearities. When the nonlinear terms of the system are polynomials in the components of $\mathbf{x}$, however, the first and second-order moment equations can be readily closed by applying the Gaussian closure method (Wu and Lin, 1984; Ibrahim, 1985; Sun and Hsu, 1987a).

4 Examples of Application

In this introductory paper, without going into detail studies of theoretical aspects of the proposed method, we present here some examples to show the effectiveness and computational advantages of the method.

Example 1. Consider a one-dimensional nonlinear system

$$\dot{x}+\alpha x+\beta x^3 = w(t), \tag{6}$$

where $w(t)$ is a Gaussian white noise satisfying

$$E[w(t)]=0,\ E[w(t)w(t')]=2D_w\delta(t-t'). \tag{7}$$

An exact steady-state probability density function of x can be obtained by solving the Fokker-Planck equation associated with the system, and is given by

$$p_s(x)=C\exp\left\{-\frac{1}{2D_w}(\alpha x^2+1/2\beta x^4)\right\}, \tag{8}$$

where C is a normalization constant. In the subsequent discussion we take $\alpha=-1$ and $\beta=2$. Hence, the system is highly nonlinear and has two stable equilibria at $x_s=\pm 1/\sqrt{2}$, which render $p_s(x)$ to be a bimodal probability density function.

We shall demonstrate the validity of the short-time Gaussian approximation for this highly nonlinear system. Equations for the mean $m(t)$ and variance $v(t)$ of $x(t)$ can be derived as

$$\begin{aligned}\dot{m} &= -\alpha m-\beta m(3v+m^2)\\ \dot{v} &= -2\alpha v-6\beta v(v+m^2)+2D_w.\end{aligned} \tag{9}$$

The initial conditions are given by

$$m(0)=x_0,\ v(0)=0. \tag{10}$$

In deriving equation (9), moment relations of Gaussian random variables are used to close the equation. For a given initial value x_0, we numerically integrate equation (9) to obtain $m(\tau)$ and $v(\tau)$, and then to construct a Gaussian probability density function by using $m(\tau)$ and $v(\tau)$. For comparison, the corresponding conditional probability density function $p(x,\tau\,|x_0,0)$ is also computed by using Monte Carlo simulation of 5000 samples. The Gaussian probability density function is found to be in very good agreement with simulation results for various combinations of parameters α, β, and x_0. The approximation by Gaussian probability density function is seen to deteriorate as τ becomes large. Some of the results discussed above are shown in Figs. 1 and 2.

We then make use of the GCM method based upon the short-time Gaussian approximation to compute the steady-state probability density function and the first-passage time probability. The computation domain is taken to be $[-2, 2]$. It is divided into 300 cells of length 0.0133 unit. The mapping step-time τ is chosen to be 0.1, based upon the knowledge gained in testing the validity of the short-time Gaussian ap-

Downloaded 03 May 2010 to 171.66.16.244. Redistribution subject to ASME license or copyright; see http://www.asme.org/terms/Terms_Use.cfm

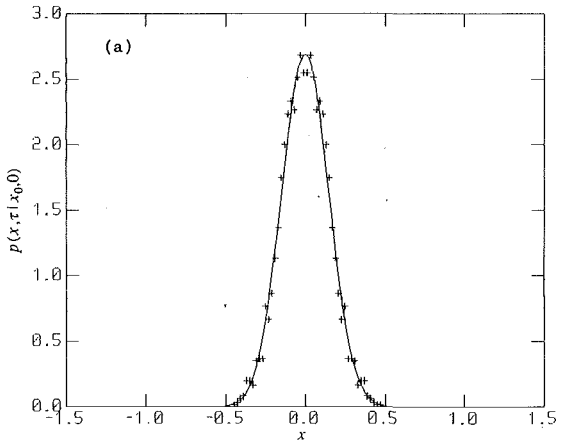


Fig. 1(a)

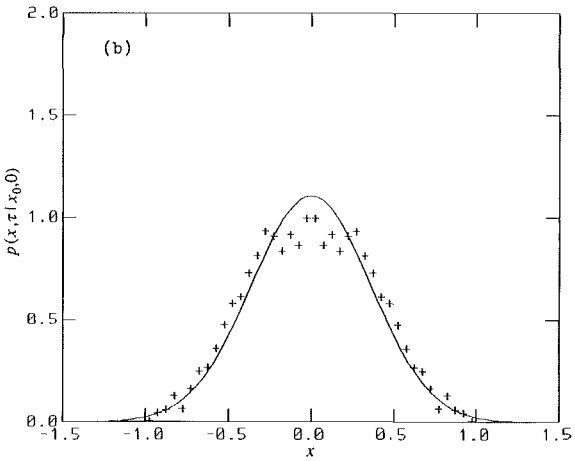


Fig. 1(b)

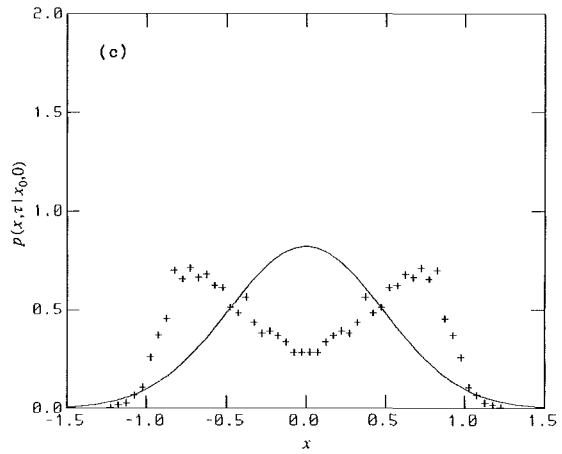


Fig. 1(c)

Fig. 1 One-step conditional probability density function of system (6). $x_0 = 0$. (a) $\tau = 0.1$; (b) $\tau = 0.5$; (c) $\tau = 2.0$. Solid line: Gaussian approximation; "+": simulation results.

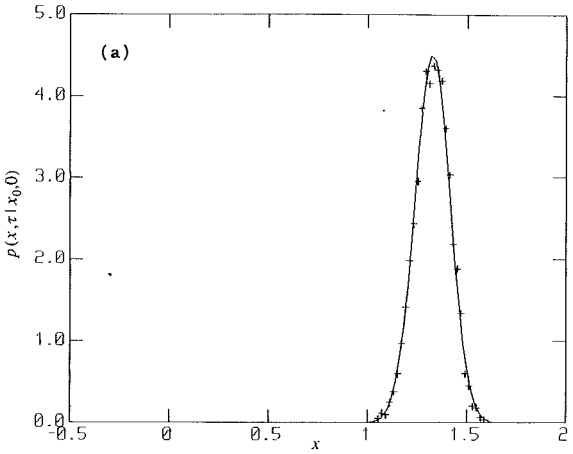


Fig. 2(a)

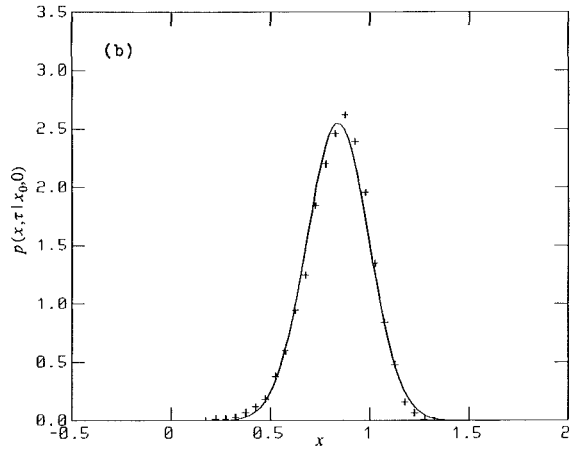


Fig. 2(b)

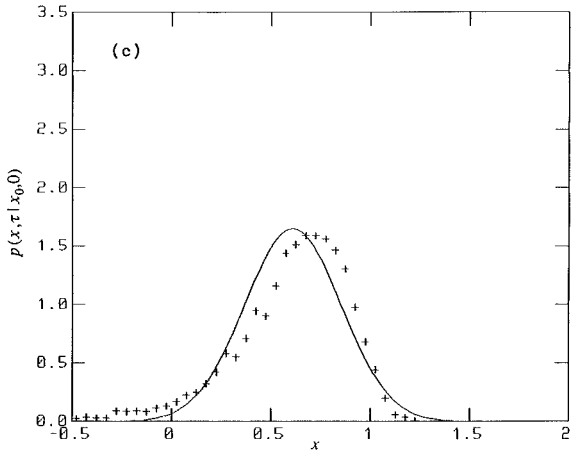


Fig. 2(c)

Fig. 2 One-step conditional probability density function of system (6). $x_0 = 2$. (a) $\tau = 0.1$; (b) $\tau = 0.5$; (c) $\tau = 2.0$. Solid line: Gaussian approximation; "+": simulation results.

proximation approach. An optimal τ may be, in principle, determined by considering the worst initial condition x_0 with regard to the accuracy of the short-time Gaussian approximation. However, no optimalization of any kind is adapted in the computations reported herein.

The steady-state probability density function computed by the GCM/STGA method is virtually indistinguishable from the exact one, as shown in Fig. 3. The steady-state mean square value of x is also computed to be 0.414696 with 0.18 percent error compared with the exact value 0.415448. Next, we consider a transient problem. The probability of the time when the system, initially at an equilibrium $x_s = 1/\sqrt{2}$, crosses over the energy barrier at $x = 0$ for the first time, i.e., the first-passage time probability, is computed by the GCM/STGA method, and is shown in Fig. 4 together with the simulation result of 2000 samples. The agreement between both results is excellent. It is noted that all the transient and steady-state solutions discussed here are obtained by the GCM/STGA

Downloaded 03 May 2010 to 171.66.16.244. Redistribution subject to ASME license or copyright; see http://www.asme.org/terms/Terms_Use.cfm

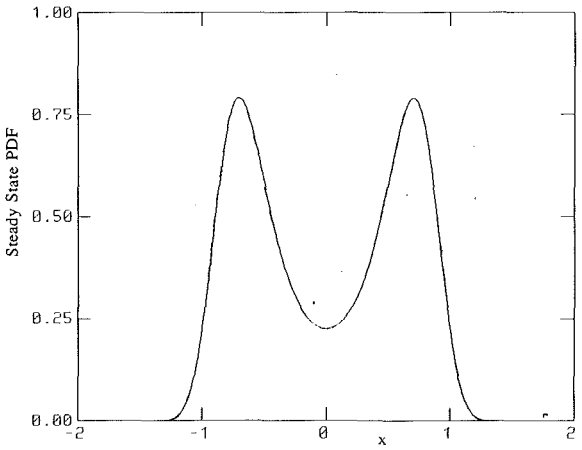


Fig. 3 Steady-state probability density function of system (6). $\alpha = -1.0$; $\beta = 2.0$. The exact and computed solutions are indistinguishable.

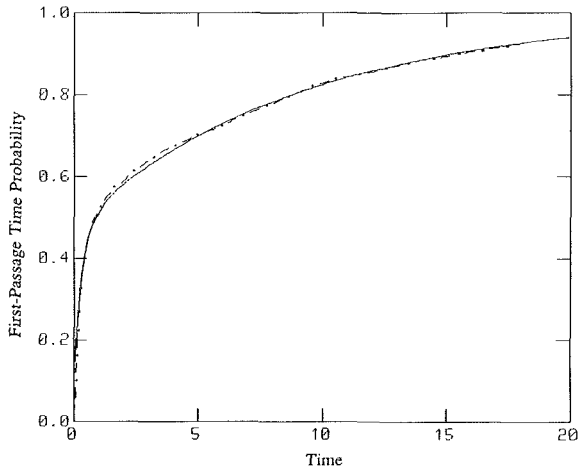


Fig. 4 First-passage time probability of system (6). $\alpha = -1.0$; $\beta = 2.0$. Solid line: GCM/STGA result; Dot-Dash line: simulation result.

method in one computer program execution, and the whole computation takes about 19 seconds CPU time, which represents a very large saving of computational efforts, compared with that required by Monte Carlo simulation for the same number of solutions. This CPU time is on VAX 780. The same is true for all CPU time data reported in the other parts of the paper.

Finally, we show in Fig. 5 various approximations of the steady-state probability density function $p_s(x)$ by conventional methods such as the stochastic equivalent linearization, the fourth-order cumulant-neglect closure, the 6-term Gram-Charlier expansion, and 4-term Edgeworth expansion. Apparently, these methods are not adequate for this system.

Example 2. Consider the well-known van der Pol oscillator under Gaussian white noise excitation

$$\ddot{x} + 2\zeta(\epsilon x^2 - 1)\dot{x} + x = w(t), \tag{11}$$

where $w(t)$ satisfies equation (7). This system has received a good deal of attention in the past. An up-to-date summary of the studies of this system can be found in (Zhu and Yu, 1987). In this article, a controversy regarding different approximations to the steady-state solutions of van der Pol oscillator under white noise excitation was resolved. It appears, according to Zhu and Yu (1987), that the stochastic averaging method can yield the best approximation of the response of van der Pol oscillator provided the damping is very light ($\zeta \ll 1$). When the damping is not light, however, the system

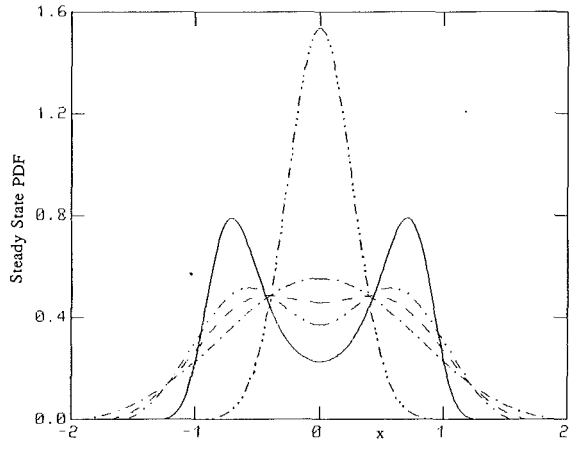


Fig. 5 Various approximations of the steady-state probability density function of system (6). $\alpha = -1.0$; $\beta = 2.0$. Solid line: exact solution; Dash-3-Dots-Dash line: stochastic equivalent linearization; Dash-Dot-Dash line: Fourth-order cumulant-neglect closure; Dash line: 6-term Gram-Charlier expansion; Dash-2-Dots-Dash line: 4-term Edgeworth expansion.

becomes very hard to deal with by the stochastic averaging method and by other conventional methods. Earlier, the steady-state probability density function and mean square response of van der Pol oscillator were studied in a range of damping parameters by the GCM method based upon Monte Carlo simulation (Chiu, 1984; Chiu and Hsu, 1986). While the overall results by the GCM method are accurate when large number of samples are used in the simulation, the computation is intensive, and the steady-state probability density function is not smooth due to random error associated with Monte Carlo simulation with limited number of samples.

Here, we apply the GCM method based upon the short-time Gaussian approximation. To save space, we shall not list the equations for the first and second-order moments of x and $\dot{x}$. They are, however, very easy to derive, and to be closed by using the Gaussian closure method. We report only two cases here. In the first case, we take $\zeta = 0.05$, $\epsilon = 1$, and $D_w = 0.01$. The domain of interest is $[-4.5, 4.5] \times [-4.5, 4.5]$. The cell dimensions are $h_1 = h_2 = 0.1$. $\tau = 0.5$. In one computer program execution, we have obtained six records of the first-passage time probability distribution curve for three types (B, D and E) of barriers with barrier level $b = 1.5$ and $b = 2.0$, the asymptotic decay parameters (not presented in this paper) of the first-passage time probability (Sun and Hsu, 1988a), the steady-state mean square response of x and $\dot{x}$, and the steady-state probability density function. Some of the results are shown in Figs. 6–8. The simulation results of the first-passage time probability using 4000 samples are also shown in Figs. 6–7. The agreement between the results by the GCM/STGA method and by Monte Carlo simulation is very good. The initial state of the system for all the first-passage problem studied in this paper is taken to be (0, 0). The total CPU time for the GCM/STGA results mentioned above is 2103 seconds, while the total direct simulation CPU time for six records of the first-passage time probability is 11,668 seconds. Based upon the report in (Spanos, 1979), to simulate the steady-state probability density function, using 3000 samples can easily consume the CPU time of order 10^4 seconds. This suggests that the GCM/STGA method can achieve computational advantages of ten folds over Monte Carlo simulation provided a comprehensive study such as the one discussed previously is carried out in one computer program execution. It is important to note that out of 2103 seconds of the total CPU time for the GCM/STGA method, only 188 seconds are spent on computing the one-step transition probability matrix. Clearly, the overhead of CPU time for the GCM/STGA

Downloaded 03 May 2010 to 171.66.16.244. Redistribution subject to ASME license or copyright; see http://www.asme.org/terms/Terms_Use.cfm

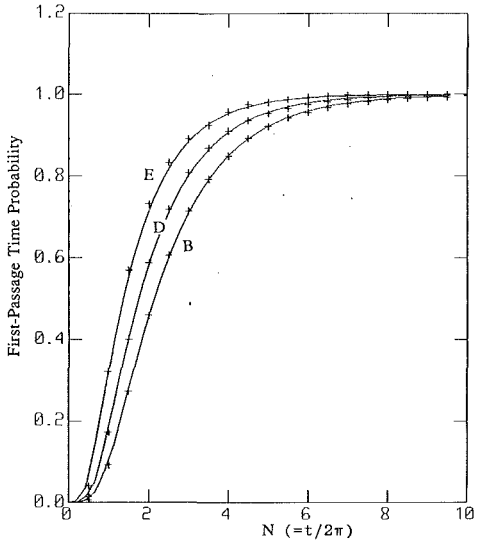


Fig. 6 First-passage time probability of van der Pol oscillator (11). $\zeta = 0.05$; $\epsilon = 1.0$; $D_w = 0.1$. Barrier lever $b = 1.5$ for all three types of barrier. " + ": simulation results; Solid line: GCM/STGA results.

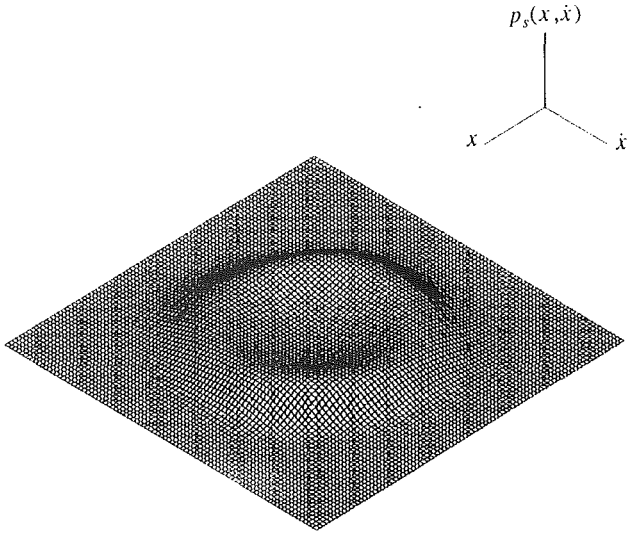


Fig. 8 Steady-state probability density function of van der Pol oscillator (11). $\zeta = 0.05$; $\epsilon = 1.0$; $D_w = 0.1$. Ranges of the figure: $(x,\dot{x}) \in [-4.5, 4.5] \times [-4.5, 4.5]$; $p_s(x,\dot{x}) \in [0, 0.05662]$.

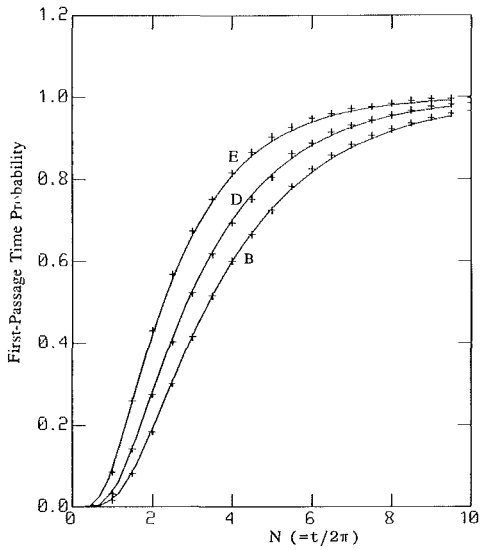


Fig. 7 First-passage time probability of van der Pol oscillator (11). $\zeta = 0.05$; $\epsilon = 1.0$; $D_w = 0.1$. Barrier lever $b = 2.0$ for all three types of barrier. " + ": simulation results; Solid line: GCM/STGA results.

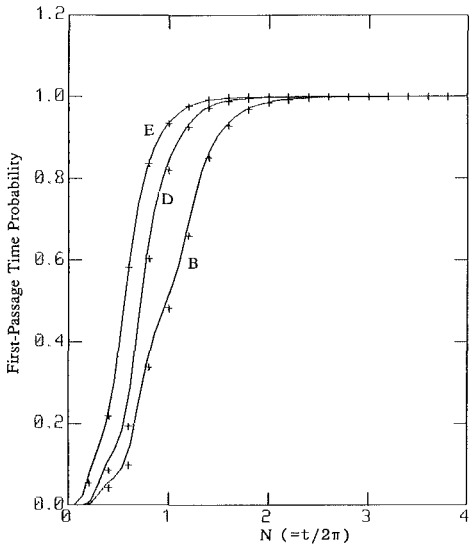


Fig. 9 First-passage time probability of van der Pol oscillator (11). $\zeta = 0.5$; $\epsilon = 1.0$; $D_w = 0.1$. Barrier lever $b = 1.5$ for all three types of barrier. " + ": simulation results; Solid line: GCM/STGA results.

method spent on computing the transition probability matrix based upon the short-time Gaussian approximation is small, and becomes less significant as more solutions are computed in one computer program execution. It is of interest to note that the shape of the steady-state probability density function shown in Fig. 8 is not exactly axial symmetrical, but nearly so about the origin, and the distribution is nearly uniform along the limit cycle of the corresponding deterministic van der Pol oscillator. This explains why the stochastic averaging method can yield good approximations of lightly damped van der Pol oscillator.

In the second case, we take $\zeta = 0.5$, $\epsilon = 1$, and $D_w = 0.1$. The domain of interest is $[-4.5, 4.5] \times [-6, 6]$. $h_1 = 0.09$. $h_2 = 0.075$. $\tau = 0.5$. The same set of solutions, as in the first case, are computed and shown in Figs. 9–11. Once again, the agreement of the first-passage time probabilities shown in Figs. 9–10 by the GCM/STGA method and by Monte Carlo simulation is good. The steady-state probability distribution in this case is highly nonuniform along the deterministic limit cycle. The shape of it is distorted far away from a circle. The CPU time and the computational advantages of the GCM/STGA method over Monte Carlo simulation are nearly the same as in the first case. Hence, they are not reported here. It is noted that the exact steady-state probability density function of van der Pol oscillator is not available, and the approximations of the density function as smooth and accurate as the ones presented in this paper have not been seen before.

Example 3. Finally, we study a nonlinear system under both external and parametric random excitations

$$\ddot{x} + 2\alpha[1 + \eta(t)]\dot{x} + \beta_1(x^2 + \dot{x}^2/\Omega^2)\dot{x} + \Omega^2[1 + \xi(t)]x = \zeta(t), \quad (12)$$

where $\eta(t)$, $\xi(t)$, and $\zeta(t)$ are independent Gaussian white noise satisfying

$$\begin{aligned} &E[\eta(t)] = 0, E[\eta(t)\eta(t')] = D_\eta \delta(t - t') \\ &E[\xi(t)] = 0, E[\xi(t)\xi(t')] = D_\xi \delta(t - t') \\ &E[\zeta(t)] = 0, E[\zeta(t)\zeta(t')] = D_\zeta \delta(t - t'). \end{aligned} \quad (13)$$

This system was originally studied by Dimentberg (1982). He found that when

Downloaded 03 May 2010 to 171.66.16.244. Redistribution subject to ASME license or copyright; see http://www.asme.org/terms/Terms_Use.cfm

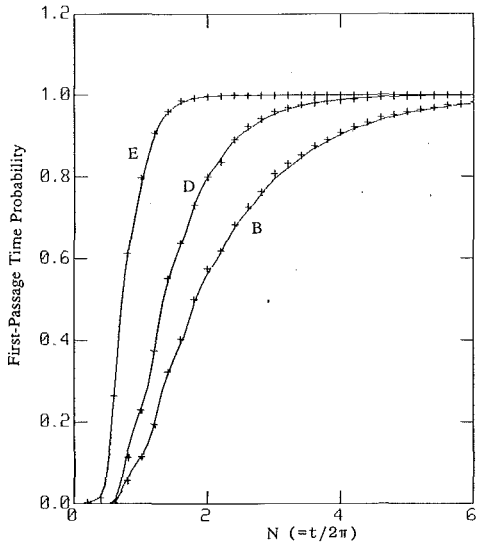


Fig. 10 First-passage time probability of van der Pol oscillator (11). $\zeta = 0.5$; $\epsilon = 1.0$; $D_w = 0.1$. Barrier lever $b = 2.0$ for all three types of barrier. "+": simulation results; Solid line: GCM/STGA results.

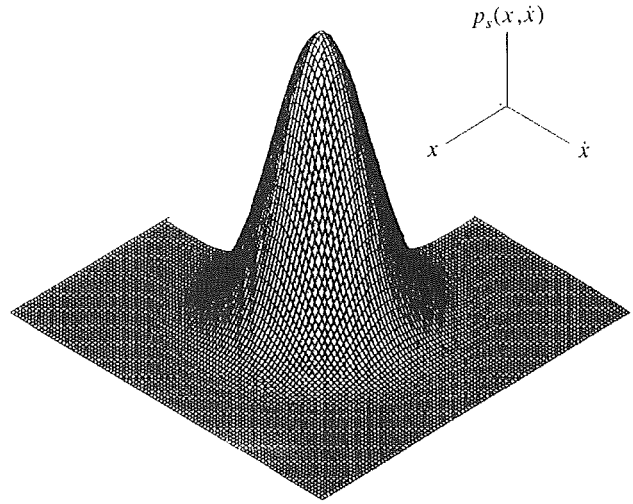


Fig. 12 Computed steady-state probability density function of system (12) by the GCM/STGA method (with the left-back quarter removed). $\alpha = 0.1$; $\beta_1 = 0.1$; $\Omega = 1.0$; $D_\eta = 2.5$; $D_\zeta = 0.1$; $D_\xi = 0.3$. Ranges of the figure: $(x,\dot{x}) \in [-4.0, 4.0] \times [-4.0, 4.0]$; $p_s(x,\dot{x}) \in [0, 0.2769]$.

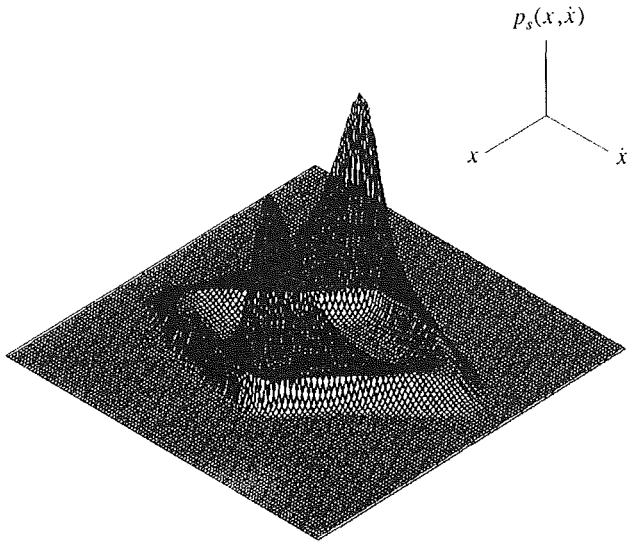


Fig. 11 Steady-state probability density function of van der Pol oscillator (11). $\zeta = 0.5$; $\epsilon = 1.0$; $D_w = 0.1$. Ranges of the figure: $(x,\dot{x}) \in [-4.5, 4.5] \times [-4.5, 4.5]$; $p_s(x,\dot{x}) \in [0, 0.4590]$

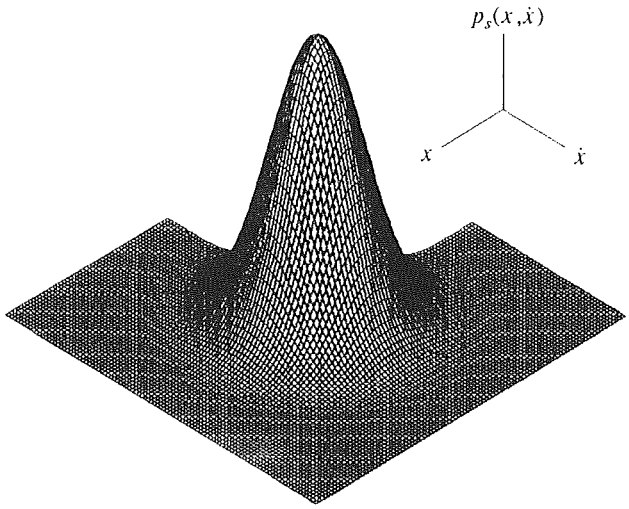


Fig. 13 Exact steady-state probability density function of system (12) corresponding to the case in Fig. 12 (with the left-back quarter removed). The parameters and ranges of the figure are the same as in Fig. 12.

$$\Omega^2 D_\xi = 4\alpha^2 D_\eta, \tag{14}$$

an exact steady-state probability density function can be obtained from the Fokker-Planck equation as

$$p_s(x,\dot{x}) = C \frac{e^{-\beta(x^2 + \dot{x}^2/\Omega^2)}}{(\kappa + x^2 + \dot{x}^2/\Omega^2)^{\delta - \kappa\beta}}, \tag{15}$$

where C is a normalization constant, and

$$\kappa = \frac{D_\zeta}{\Omega^4 D_\xi}, \quad \delta = \frac{2\alpha}{\Omega^2 D_\xi} + 1/2, \quad \beta = \frac{\beta_1}{\Omega^2 D_\xi}.$$

This system is in general very difficult to handle. In case of light damping, the stochastic averaging method can obtain certain satisfactory approximate solutions. However, to obtain transient and steady-state solutions of the system presents a tough problem to other conventional methods. Monte Carlo simulation will certainly be even more expensive for this system due to added uncertainties of three random excitations. It turns out that the GCM method based upon the short-time Gaussian approximation can deal with this system just as easi-

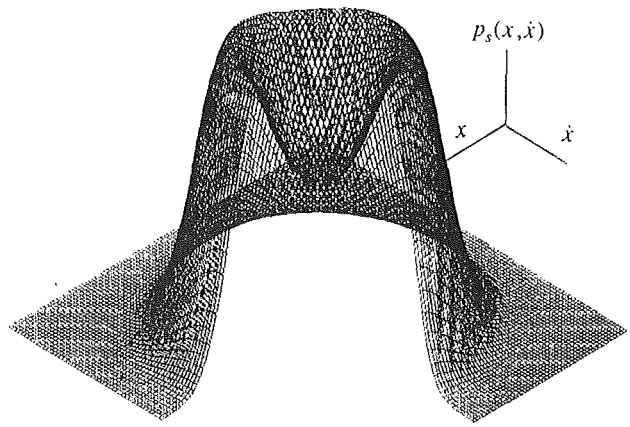


Fig. 14 Steady-state probability density function of system (12) by the GCM/STGA method (with the right-front quarter removed). $\alpha = -0.1$; $\beta_1 = 0.1$; $\Omega = 1.0$; $D_\eta = D_\zeta = 0.1$; $D_\xi = 0.3$. Ranges of the figure: $(x,\dot{x}) \in [-3.5, 3.5] \times [-3.5, 3.5]$; $p_s(x,\dot{x}) \in [0, 0.07823]$.

Downloaded 03 May 2010 to 171.66.16.244. Redistribution subject to ASME license or copyright; see http://www.asme.org/terms/Terms_Use.cfm

ly, efficiently, and accurately as with other systems we have studied. The same set of transient and steady-state solutions as in Example 2 can be computed by the GCM/STGA method in one computer program execution. In this example, however, we shall only present the results of steady-state probability density function. First, we consider a case where the exact probability density function exists. Let $\alpha = 0.1$, $\beta_1 = 0.1$, $\Omega = 1$, $D_\xi = 0.1$, and $D_\zeta = 0.3$. D_η is found to be 2.5 from equation (14). The domain of interest is taken to be $[-3.5, 3.5] \times [-3.5, 3.5]$. $h_1 = h_2 = 0.07$. $\tau = 0.25$. The first and second-order moment equations can be found in (Sun and Hsu, 1987a). The computed and exact stady-state probability density functions are shown in Figs. 12 and 13. They are hardly distinguishable. In order to have a readable graph the left-back quarter of the three-dimensional surface has been removed in Figs. 12 and 13. The mean square values of x and $\dot{x}$ are computed, and can be taken as an indication of how accurate the probability density function computed by the GCM/STGA method is. The computed mean square values of x and $\dot{x}$ are 0.558154 and 0.557403, respectively. The exact ones are given by $E[x^2] = E[\dot{x}^2] = 0.555307$. The errors of the computed mean square values are 0.51 percent and 0.38 percent. The CPU time for these steady-state solutions by the GCM/STGA method is 1567 seconds, out of which 469 seconds are spent on computing the one-step transition probability matrix.

Next, we change the parameters so that the exact solution is no longer available. We take $\alpha = -0.1$ and $D_\eta = 0.1$, and let the rest of parameters remain the same as before. Other computational settings are also unchanged. The steady-state probability density function obtained by the GCM/STGA method is shown in Fig. 14, where the right-front quarter of the three-dimensional surface has been deleted. The CPU time is 1898 seconds, out of which 365 seconds are spent on computing the one-step transition probability matrix.

5 Concluding Remarks

A short-time Gaussian approximation scheme is proposed in the paper. This scheme provides a very efficient and accurate way of computing the one-step transition probability matrix of the GCM method in nonlinear random vibration. The GCM method based upon this short-time Gaussian approximation scheme is then applied to some nonlinear systems under external and parametric Gaussian white noise excitations. Certain transient and steady-state solutions such as the first-passage time probability, steady-state mean square response, and the steady-state probability density function have been obtained. Some of the solutions are compared with either the simulation results or the available exact solutions, and are found to be very accurate. The computed steady-state mean square response values are found to be of error less than 1 percent when compared with the available exact solutions. The efficiency of the GCM method based upon the short-time Gaussian approximation is also examined. First of all, the short-time Gaussian approximation renders the overhead of computing the one-step transition probability matrix to be very small, and to become less significant as more solutions are obtained in one computer program execution. It is found that in a comprehensive study of nonlinear stochastic systems, in which various transient and steady-state solutions are obtained in one computer program execution, the GCM method can have computational advantages up to ten folds over Monte Carlo simulation for the same set of solutions.

There are many possible extensions of the proposed short-time Gaussian approximation scheme. Further studies of the scheme in conjunction with the GCM method are now under investigations.

Acknowledgment

This material is based upon work supported by the National Science Foundation under Grant No. MSM-8519950.

References

Bergman, L. A., and Heinrich, J. C., 1982, On the Reliability of the Linear Oscillator and Systems of Coupled Oscillators," *Int. J. for Num. Methods in Eng.*, Vol. 18, pp. 1271–1295.

Bergman, L. A., and Spencer, B. F., 1983, "Solution of the First-Passage Problem for Simple Linear and Nonlinear Oscillators by the Finite Element Method," *Department of Theoretical and Applied Mechanics*, University of Illinois at Urbana-Champaign, T.A.&M. Report No. 461.

Chiu, H. M., 1984, "Random Vibration Analysis by Cell Mapping Methods," Ph.D. Thesis, Mechanical Engineering, University of California, Berkeley.

Chiu, H. M., and Hsu, C. S., 1986, "A Cell Mapping Method for Nonlinear Deterministic and Stochastic Systems—Part II: Examples of Application," ASME JOURNAL OF APPLIED MECHANICS, Vol. 53, pp. 702–710.

Crandall, S. H., Chandiramani, K. L., and Cook, R. G., 1966, "Some First-Passage Problems in Random Vibration," ASME JOURNAL OF APPLIED MECHANICS, Vol. 33, pp. 532–538.

Crandall, S. H., and Zhu, W. Q., 1983, "Random Vibration: A Survey of Recent Developments," ASME JOURNAL OF APPLIED MECHANICS, Vol. 50, pp. 953–962.

Dimentberg, M. F., 1982, "An Exact Solution to a Certain Non-Linear Random Vibration Problem," *Int. J. Non-Linear Mechanics*, Vol. 17, No. 4, pp. 231–236.

Heinrich, J. C., Huyakarn, P. S., Zienkiewicz, O. C., and Mitchell, A. R., 1977, "An "upwind" Finite Element Scheme for Two Dimensional Convective Transport Equations," *Int. J. for Num. Methods in Eng.*, Vol. 11, pp. 131–143.

Hsu, C. S., 1981, A Generalized Theory of Cell-to-Cell Mapping for Nonlinear Dynamical Systems, ASME JOURNAL OF APPLIED MECHANICS, Vol. 48, pp. 634–642.

Hsu, C. S., and Chiu, H. M., 1986, "A Cell Mapping Method for Nonlinear Deterministic and Stochastic Systems—Part I: The Method of Analysis," ASME JOURNAL OF APPLIED MECHANICS, Vol. 53, pp. 695–701.

Hsu, C. S., 1987, *Cell-to-Cell Mapping—A Method of Global Analysis for Nonlinear Systems*, Springer-Verlag, New York.

Ibrahim, R. A., 1985, *Parametric Random Vibration*, Research Studies Press Ltd., U.K.

Langley, R. S., 1985, "A Finite Element Method for the Statistics of Non-Linear Random Vibration," *J. of Sound Vib.*, Vol. 101, No. 1, pp. 41–54.

Risken, H., 1984, "The Fokker-Planck Equation—Methods of Solution and Applications," *Springer Series in Synergetics*, Vol. 18, Springer-Verlag, New York.

Roberts, J. B., 1976, "First-Passage Time for the Envelope of a Randomly Excited Linear Oscillator," *J. of Sound Vib.*, Vol. 46, No. 1, pp. 1–14.

Roberts, J. B., 1978, "First-Passage Time for Oscillators With Nonlinear Damping," ASME JOURNAL OF APPLIED MECHANICS, Vol. 45, pp. 175–180.

Roberts, J. B., 1986, "First-Passage Time for Randomly Excited Nonlinear Oscillators," *J. of Sound Vib.*, Vol. 109, No. 1, pp. 33–50.

Soong, T. T., 1973, *Random Differential Equations in Science and Engineering*, Academic Press, New York.

Spanos, P-T. D., 1980, "Numerical Simulations of a van der Pol Oscillator," *Comp. and Maths. with Appls.*, Vol. 6, pp. 135–145.

Sun, J. Q., and Hsu, C. S., 1987a, Cumulant-Neglect Closure Method for Nonlinear Systems Under Random Excitations, ASME JOURNAL OF APPLIED MECHANICS, Vol. 54, pp. 649–655.

Sun, J. Q., and Hsu, C. S., 1987b, "A Statistical Study of Generalized Cell Mapping," ASME JOURNAL OF APPLIED MECHANICS, Vol. 55, pp. 694–701.

Sun, J. Q., and Hsu, C. S., 1988a, "First-Passage Time Probability of Nonlinear Stochastic Systems by Generalized Cell Mapping Method," *J. Sound Vib.*, Vol. 124, No. 2, pp. 233–248.

Sun, J. Q., and Hsu, C. S., 1988b, Effects of Small Random Uncertainties on Nonlinear Systems Studied by the Generalized Cell Mapping Method, to appear in the *J. Sound Vib.*

Sun, J. Q., and Hsu, C. S., 1989a, "Random Vibration of a Hinged Shallow Arch," *J. Sound Vib.*, Vol. 132, No. 2, pp. 299–315.

Sun, J. Q., and Hsu, C. S., 1989b, "Cumulant-Neglect Closure Method for Asymmetric Nonlinear Systems Driven by Gaussian White Noise," to appear in the *J. Sound Vib.*

Toland, R. H., and Yang, C. Y., 1971, "Random Walk Model for First-Passage Probability," *ASCE J. of Eng. Mech. Div.*, Vol. 97, (EM3), pp. 791–807.

Toland, R. H., Yang, C. Y., and Hsu, C. K.-C., 1972, "Non-stationary Random Vibration of Nonlinear Structures," *Int. J. Non-Lin. Mech.*, Vol. 7, pp. 395–406.

Wu, W. F., and Lin, Y. K., 1984, "Cumulant-Neglect Closure for Non-Linear Oscillators Under Parametric and External Excitations," *Int. J. Non-Linear Mechanics*, Vol. 9, No. 4, pp. 349–362.

Zhu, W. Q., and Yu, J. S., 1987, "On the Response of van der Pol Oscillator to White Noise Excitations," *J. Sound Vib.*, Vol. 117, No. 3, pp. 421–431.

Downloaded 03 May 2010 to 171.66.16.244. Redistribution subject to ASME license or copyright; see http://www.asme.org/terms/Terms_Use.cfm

Ye Zhiming
Associate Professor,
Department of Civil Engineering,
Shanghai University of Technology,
Shanghai 200072,
People's Republic of China

Yeh Kaiyuan
Professor,
Department of Mechanics,
Lanzhou University,
Lanzhou, Gansu 730001,
People's Republic of China

A Study of Belleville Spring and Diaphragm Spring in Engineering

This paper deals with the static response of a Belleville spring and a diaphragm spring by using the finite rotation and large deflection theories of a beam and conical shell, and an experimental method as well. The authors propose new mechanical analysis mathematical models. The exact solution of a variable width cantilever beam is obtained. By using the integral equation method and the iterative method to solve the simplified equations and Reissner's equations of finite rotation and large deflection of a conical shell, this paper has calculated a great number of numerical results. The properties of loads, strains, stresses and displacements, and the distribution rules of strains and stresses of diaphragm springs are investigated in detail by means of the experimental method. The unreasonableness of several assumptions in traditional theories and calculating method is pointed out.

Introduction

A Belleville spring and a diaphragm spring have found wider applications in engineering, such as in metallurgy and mining machinery, automobile, tractor, universal machine, cannon, mine, and nuclear industry, and have been taken a shock absorber, damping device, forced device in clutch and brake, pressure controller in valve, contact in mine, and energy storage device in nuclear industry, and so on (see Fig. 1). Because of the simplifications made in the development of the traditional theory and calculation of those springs, there exist many errors between theoretical analysis and practical use. As is known from the literature, Almen and Laszlo (1936) proposed a spring approximate model, based on the following two assumptions: (1) the rigid section moved around the turning center of the spring and (2) the radial stress was equal to zero. Their theories have been adopted in engineering since 1936. Curti and Orlando (1979, 1980) discovered that there was one mistake in Almen-Laszlo's model, its second assumption should be the radial strain disappearance other than the radial stress. As for correct theory, they developed Almen-Laszlo's theory. Contributions by Lutz and Wennitz (1967), Timoshenko (1942), Schmidt and Wempner (1958, 1959), Wempner (1961, 1971), Hübner (1982), and many others are also found in the references.

In the current paper, a study of a Belleville spring and a diaphragm spring is presented. By this research, the theoretical analytic method and the design method of those springs may be obtained. A new mechanical model is proposed first, and takes into consideration the finite rotation and large deflection problems of a beam and an annular conical shell. This new model is different from the traditional ones. We note that, in the references, only an infinite deflection problem of a beam and the quite approximate shell theory, such as Almen-Laszlo's, are considered. Further, based on the experimental results of springs studied and the theories of finite rotation and large deflection of beam and revolutional shell, the mathematical model of springs is discussed in detail, and the new equations and their simplified forms are obtained as investigating problems. The exact solution of a large deflection of a variable width cantilever beam under the action of arbitrary transverse loads was obtained by the authors in 1989. Using Green's function method the conical shell, fundamental equations, including their simplified forms, can be changed into integral equations, and their iterative solutions can be made and cal-

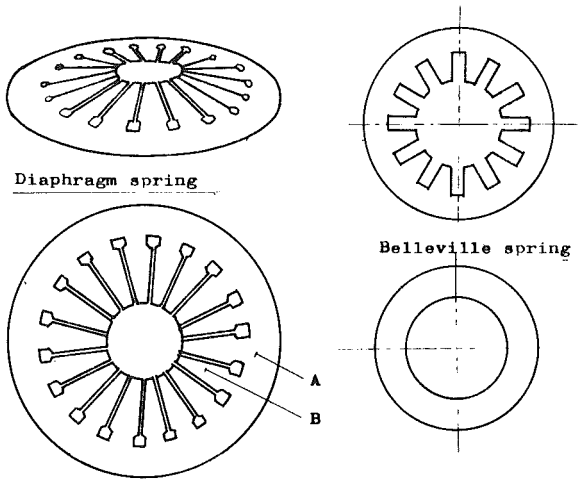


Fig. 1 Examples of Belleville and diaphragm springs

Contributed by the Applied Mechanics Division of THE AMERICAN SOCIETY OF MECHANICAL ENGINEERS for presentation at the Winter Annual Meeting, Dallas, Texas, Nov. 25-30, 1990.

Discussion on this paper should be addressed to the Technical Editor, Leon M. Keer, The Technological Institute, Northwestern University, Evanston, IL 60208, and will be accepted until two months after final publication of the paper itself in the JOURNAL OF APPLIED MECHANICS. Manuscript received by the ASME Applied Mechanics Division, Sept. 21, 1989; final revision, Jan. 23, 1990.

Paper No. 90-WA/APM-45.

Copyright © 1990 by ASME
Downloaded 03 May 2010 to 171.66.16.244. Redistribution subject to ASME license or copyright; see http://www.asme.org/terms/Terms_Use.cfm

culated by a computer. In order to get the reasonable mechanical and mathematical models and to examine the solutions solved in the paper, the properties of loads, strains, stresses, and displacements, and the distribution rules of strains and stresses of springs are investigated in detail by using the experimental method. The theoretical solutions coincide very well with the results of experimental investigation, which shows that the study in this paper is satisfactory in engineering application. Finally, the unreasonableness of several assumptions in traditional theories and calculation methods is pointed out.

Mechanical and Mathematical Models

In general, in Fig. 1, part A is called the conical portion of the spring and part B the separative bar. The number of separative bars is more than 18. The working state of the spring is an axisymmetric deformation.

A new mechanical model in this paper is given as follows: Part A is taken as an axisymmetrical finite rotation and large deflection problem of an annular conical shell and part B is a large deflection problem of a cantilever beam with variable width.

For boundary conditions we consider that the inner boundary is free and the outer is simply supported for a conical shell, and the sliding friction between two support surfaces is neglected, and that the built-in cantilever with a small inclination is taken as a beam.

When considering the mathematical model, we adopt the nonlinear theory of the revolving shell. In engineering, Belleville and diaphragm springs are made of steel limited in elastic range, and the spring deformation must be considered as the large displacement and rotation problem. Thus, a new mathematical model is in the form:

Part A: Reissner's theory on the axisymmetric finite rotation and large deflection of revolutional shell;

Part B: Euler-Bernoulli's theory on large deflection of a beam.

The Governing Equations

For a conical shell problem the axisymmetric finite rotation and deflection theory of a revolutional shell was given by E. Reissner in 1958.

We take the relations on the conical shell as follows:

$$\begin{cases} \phi = \text{constant} \\ \phi' = \theta', \ \phi'' = \theta'' \end{cases} \tag{1}$$

and

$$\begin{cases} r = s\cos\phi & r' = \cos\phi \\ z = s\sin\phi & z' = \sin\phi \end{cases} \tag{2}$$

and Reissner's equations in a conical shell are as follows:

$$\theta'' + \frac{1}{s}\theta' + \frac{\cos\Phi}{s^2\cos^2\phi}(\sin\Phi - \sin\phi) = \frac{1}{Ds\cos\phi}(\psi_h \sin\Phi - \psi_v \cos\Phi), \tag{3a}$$

$$\psi_h'' + \frac{1}{s}\psi_h' - \frac{1}{s^2}\psi_h = \frac{C}{s\cos\phi}(\cos\Phi - \cos\phi) + \frac{\sin\phi}{s\cos\phi}\psi_v' + \frac{\sin\phi}{s^2\cos\phi}\psi_v \tag{3b}$$

in which $D = Eh^3/(12(1-\mu^2))$, $C = Eh$, $\Phi = \phi + \theta$, and $(\,)' = d(\,)/ds$.

The middle surface deflection expression of a shell is

$$w = \int(\sin\Phi - \sin\phi)\, ds. \tag{4}$$

Introducing the following dimensionless parameters:

$$\left.\begin{aligned} &x = \frac{s\cos\phi}{a}, \ W = \sqrt{12(1-\mu^2)}\,\frac{w}{h\cos\phi}, \ \theta = \frac{dW}{ds}, \\ &\theta = -\lambda\tilde{\theta}, \ \lambda = \frac{h\cos\theta}{a\sqrt{12(1-\mu^2)}}, \ K = \frac{f}{a\lambda} = \frac{1}{\lambda}\,tg\phi, \\ &Q = \frac{[12(1-\mu^2)]^{\frac{3}{2}}a^2}{2\pi Eh^4\cos^2\phi}P, \ S = \frac{12(1-\mu^2)a}{Eh^3\cos\phi}\psi_h, \end{aligned}\right\} \tag{5}$$

and considering the following design parameters of springs

$$\left.\begin{aligned} &\frac{H_1}{h} = 1.3 \sim 2.2, \ \frac{a}{b} \geq 2.5, \ \frac{a}{c} = 1.15 \sim 1.5 \\ &\phi = 10° \sim 15°, \ h = 0.1 \sim 5(\text{mm}), \ \frac{h}{a} = 0.02 \sim 0.03, \end{aligned}\right\} \tag{6}$$

we have two shell geometric parameters, λ and K, in which $\lambda = 0.005 \sim 0.008$ and $K = 22 \sim 36$. Examining the experimental results, we find the maximum rotation angle of a shell is $\theta = \pi/9 \sim \pi/6$. In equation (3), if we expand $\cos\Phi$ and $\sin\Phi$ into a trigonometric function series and take the above geometric parameters λ and K, we have the fundamental equations which describe the static response of a Belleville spring and the conical portion of a diaphragm spring;

$$\left.\begin{aligned} &\mathcal{L}(x\theta) = \frac{3\lambda^2K}{2x^2}\theta^2 - \frac{S}{x}\left(k - \theta - \frac{\lambda^2K}{2}\theta^2\right) - \frac{Q}{x}(1 + \lambda^2K\theta) \\ &\mathcal{L}(xS) = \frac{1}{x}\left(K\theta - \frac{1}{2}\theta^2 - \frac{\lambda^2K}{6}\theta^3\right) + \frac{\lambda^2K}{x^2}Q \end{aligned}\right\} \tag{7}$$

and the boundary conditions:

$$\left.\begin{aligned} &\theta' + \frac{\mu}{x}\left(\theta - \frac{\lambda^2K}{2}\theta^2\right) = -m, \ S = 0, \text{ at } x = \beta \\ &\theta' + \frac{\mu}{x}\left(\theta - \frac{\lambda^2K}{2}\theta^2\right) = 0, \ S = 0, \text{ at } x = 1 \end{aligned}\right\} \tag{8}$$

and

$$\left.\begin{aligned} W &= \int\left(\theta + \frac{\lambda^2K}{2}\theta^2\right)dx \\ W_\beta &= \int_\beta^1\left(\theta + \frac{\lambda^2K}{2}\theta^2\right)dx \end{aligned}\right\} \tag{9}$$

where $\mathcal{L}(\,) = (\,)'' + (\,)'/x - (\,)/x^2$. By neglecting the barrel terms in the equations and boundary conditions above, we get the simplified equations and boundary conditions.

For the cantilever beam with variable width, the equations are

$$\frac{d^2v}{dz^2} = \frac{M(z)}{EI(z)}\left[1 + \left(\frac{dv}{dz}\right)^2\right]^{\frac{3}{2}} \tag{10a}$$

Nomenclature

- D = bending rigidity
- E = modulus of elasticity
- μ = Poisson's ratio
- h = thickness of a shell
- W = deflection of a shell in the z-direction
- f = height of the arch of a shell
- a = outer radius
- c = inner radius
- u = displacement of a beam in a horizontal direction
- v = deflection of a beam

Downloaded 03 May 2010 to 171.66.16.244. Redistribution subject to ASME license or copyright; see http://www.asme.org/terms/Terms_Use.cfm

$$\int_0^{1-u_m}\left[1+\left(\frac{dv}{dz}\right)^2\right]^{\frac{1}{2}}dx=1 \tag{10b}$$

$$v(0)=0,\ \frac{dy(o)}{dz}=tg\alpha_o. \tag{10c,d}$$

The exact solution of a cantilever beam problem was obtained by the authors in 1989 and some examples were given. The exact solution included the existing solution in the special cases of references, because it was obtained under general conditions.

The Solutions of a Conical Shell

For a simplified equation we use the Green's function method (which was adopted by Wempner (1961)) to change the simplified equation into the following integral equations:

$$\left.\begin{aligned}\theta(x)&=f(x)Q_1+\frac{K}{x}\int_\beta^1\frac{S(\xi)}{\xi}K_1(x,\xi)d\xi\\&\quad-\frac{1}{x}\int_\beta^1\frac{S(\xi)\theta(\xi)}{\xi}K_1(x,\xi)d\xi\\S(x)&=-\frac{K}{x}\int_\beta^1\frac{\theta(\xi)}{\xi}K_2(x,\xi)d\xi+\frac{1}{2x}\int_\beta^1\frac{\theta^2(\xi)}{\xi}K_2(x,\xi)d\xi\end{aligned}\right\} \tag{11}$$

where $K_1(x,\xi)$ and $K_2(x,\xi)$ are the integral kernel functions:

$$K_1(x,\xi)=\begin{cases}\dfrac{1}{2(1-\beta^2)}\left(\dfrac{1-\mu}{1+\mu}x^2+\beta^2\right)\left(\xi^2+\dfrac{1+\mu}{1-\mu}\right) & (\beta\le x\le\xi)\\ \dfrac{1}{2(1-\beta^2)}\left(\dfrac{1-\mu}{1+\mu}x^2+\beta^2\right)\left(\xi^2+\dfrac{1+\mu}{1-\mu}\right) & (\xi\le x\le 1)\end{cases} \tag{12}$$

$$K_2(x,\xi)=\begin{cases}-\dfrac{1}{2(1-\beta^2)}(x^2-\beta^2)(\xi^2-1) & (\beta\le x\le\xi)\\ -\dfrac{1}{2(1-\beta^2)}(\xi^2-\beta^2)(\chi^2-1) & (\xi\le x\le 1).\end{cases} \tag{13}$$

Because the integral equations are nonlinear in character, their solutions are intricate. Various numerical methods for solutions to these equations have been followed by works cited in the references, but they were confined to the numerical solutions and problem results only. In this paper, we propose a new semi-numerical and semi-analytical method, which gives analytical expressions to solutions and is different from the ones in the references.

Solving equations (11) by the iterative procedure and taking W_β, the maximum deflection $W(\beta)=W_\beta$, as an iterative parameter, we obtain the following iterative solutions:

$$\left.\begin{aligned}Q_1&=\sum_{i=1}^{3^n-1}e_i\,W_\beta^i\\ \theta_{n-1}&=\sum_{i=1}^{3^n-2}\theta_i^{(n-1)}\,W_\beta^i,\quad \theta_n=\sum_{i=1}^{3^n-1}\theta^{(n-1)}\,W_\beta^i\\ S_{n-1}&=\sum_{i=1}^{2.3^n-2}S_i^{(n-1)}\,W_\beta^i,\ S_n=\sum_{i=1}^{2.3^n-1}S_i^{(n)}\,W_\beta^i\end{aligned}\right\} \tag{14}$$

where n is an iterative number, e_i are constants to be determined, and $\theta_i^{(n-1)}$, $\theta_i^{(n)}$, $S_i^{(n-1)}$, and $S_i^{(n)}$ are functions to be determined. In solving the problems by substituting equation (14) into the integral equations (11), all constants and functions to be determined can be obtained and calculated by a computer.

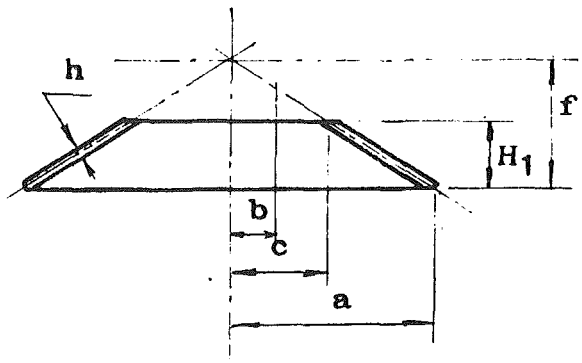


Fig. 2 Geometric relation of conical shell

When $n=2$, we get the iterative analytical expression

$$Q_1=e_1W+e_2W^2+e_3W^3 \tag{15}$$

in which

$$\left.\begin{aligned}e_1&=e_{11}\,(1+K^2e_{11}I_1)\\ e_2&=e_{11}^3\,KI_2\\ e_3&=e_{11}^4I_3\\ e_{11}&=1/\textstyle\int_\beta^1 f(x)dx\end{aligned}\right\} \tag{16}$$

and

$$I_1=\int_\beta^1\frac{1}{x}\int_\beta^1\frac{K_1(x,\xi_2)}{\xi_2^2}\int_\beta^1\frac{f(\xi_1)K_2(\xi_2,\xi_1)}{\xi_1}d\xi_1\,d\xi_2\,dx \tag{17a}$$

$$I_2=\int_\beta^1\frac{1}{x}\left(\int_\beta^1\frac{K_1(x,\xi_2)}{2\xi_2^2}\int_\beta^1\frac{f^2(\xi_1)\,K_2(\xi_2,\xi_1)}{\xi_1}d\xi_1d\xi_2+\int_\beta^1\frac{K_1(x,\xi_2)f(\xi_2)}{\xi_2^2}\int_\beta^1\frac{f(\xi_1)K_2(\xi_2,\xi_1)}{\xi_1}d\xi_1d\xi_2\right)dx \tag{17b}$$

$$I_3=\int_\beta^1\frac{1}{x}\int_\beta^1\frac{f(\xi_2)K_1(x,\xi_2)}{2\xi_2^2}\int_\beta^1\frac{f^2(\xi_1)K_2(\xi_2,\xi_1)}{\xi_1}d\xi_1d\xi_2\,dx. \tag{17c}$$

From the foregoing expressions, we can obtain the relative function on displacement load, load rotation angle, displacement rotation angle, and inner force displacement of the shell to be conveniently applied to the engineering problem.

For Reissner's equation, the iterative solution expressions are in the form

$$\begin{aligned}\theta_n&=fQ_1\\&\quad+\frac{\mu\lambda^2K}{2}\left[C_3\left(\frac{\theta_{n-1}^2(1)}{\beta^2}-\frac{\theta_{n-1}^2(\beta)}{\beta}\right)x+C_4\left(\theta_{n-1}^2(1)-\frac{\theta_{n-1}^2(\beta)}{\beta}\right)x^{-1}\right]\\&\quad+\frac{1}{x}\int_\beta^1\frac{\lambda^2Kn_1Q_1}{\xi}\theta_{n-1}K_1(x,\xi)d\xi\\&\quad-\frac{1}{x}\int_\beta^1\left[\frac{3\lambda^2K}{2\xi^2}\theta_{n-1}^2-\frac{S_{n-1}}{\xi}\left(K-\theta_{n-1}-\frac{\lambda^2K}{2}\theta_{n-1}^2\right)\right]K_1(x,\xi)d\xi\end{aligned} \tag{18a}$$

$$W_\beta=\int_\beta^1\left(\theta_n+\frac{\lambda^2K}{2}\theta_{n-1}^2\right)dx$$

$$S_n=-\frac{1}{x}\int_\beta^1\left[\frac{1}{\xi}\left(K\theta_{n-1}-\frac{\theta_{n-1}^2}{2}-\frac{\lambda^2K}{6}\theta_{n-1}^3\right)+\frac{\lambda^2Kn_1Q_1}{\xi^2}\right]K_2(x,\xi)\,d\xi, \tag{18b}$$

where $f(x)$, $K_1(x,\xi)$, and $K_2(x,\xi)$ are the same as mentioned previously. In the iterative formulas equations (18), to multiply θ_n and Q_1, it is necessary that the $n-1$ iterative solution $Q_1=Q_1$ (W_β) be substituted into the terms on Q_1 in formula (18).

Some results are shown in Figs. 3, 4, 8, 9, 10, and 11. In Fig. 3, the following solution is obtained (when $n=2$)

Downloaded 03 May 2010 to 171.66.16.244. Redistribution subject to ASME license or copyright; see http://www.asme.org/terms/Terms_Use.cfm

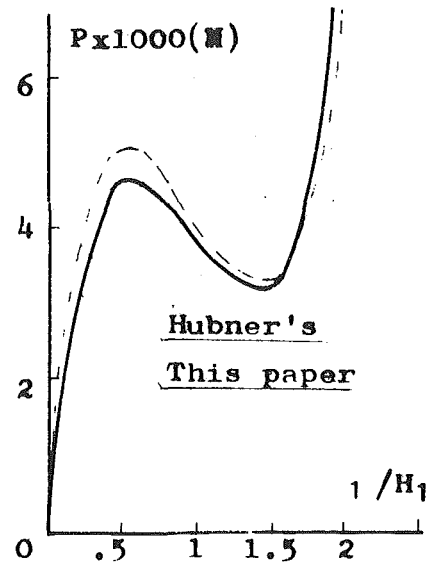


Fig. 3 Rigidity characteristics of Belleville spring

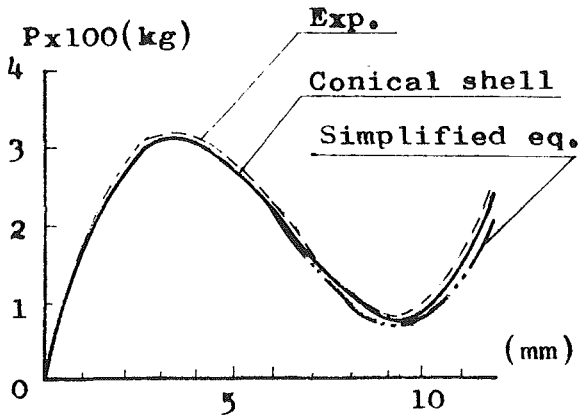


Fig. 4 A comparison: conical shell and shallow shell

$$Q_1 = 12.2341 W_\beta - 2.1889 W_\beta^2 + 0.10954 W_\beta^3 + \\ + 0.89423 \times 10^{-5} W_\beta^4 + 1.734 \times 10^{-8} W_\beta^5. \quad (19)$$

The Hübner's result was obtained by the Ronge-Kutta and Shooting methods. In his work, the boundary value problem of equations was changed into the initial value problem to be solved. Hence, the results would be affected by the calculating initial value. But it is clear that the method used in this paper is to solve the boundary value problem directly.

The Combination Solution of a Diaphragm Spring

Before calculating the combination solution, we have to take into consideration the compatibility relation between the beam and the conical shell (see Fig. 5).

The force compatibility can be written as

$$M_b = M_s,\ Q_b = Q_s,\ N_b = N_s \quad (20)$$

in which M_b, Q_b, and N_b are the moment, shearing force, and membrane force of beam, and M_s, and Q_s, and N_s are those of shell, respectively. Then the compatibility of deformation can be written as

$$\alpha_b = \theta_s,\ u_b = u_s \quad (21)$$

and the deflection is zero.

The load displacement expression of diaphragm spring can be taken as (see Fig. 5)

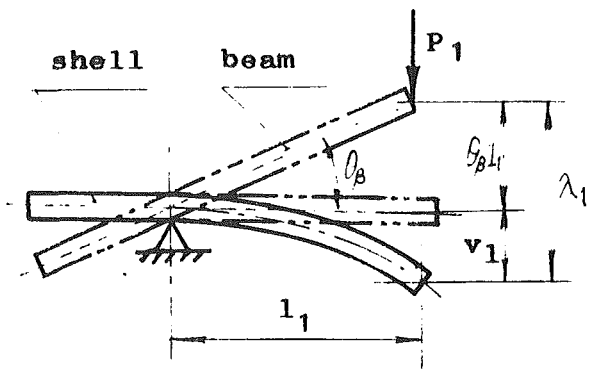


Fig. 5 Compatibility of beam and shell

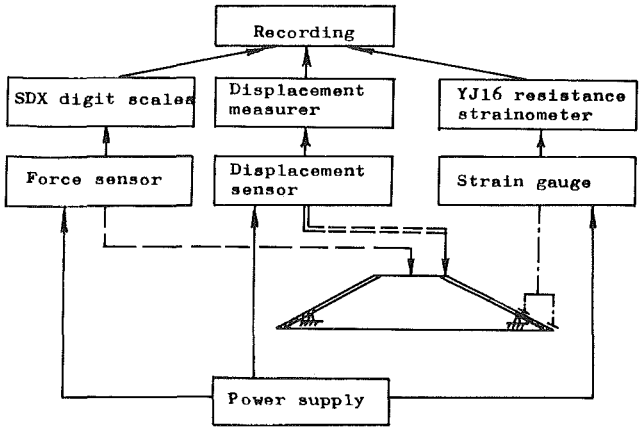


Fig. 6 Measurement system

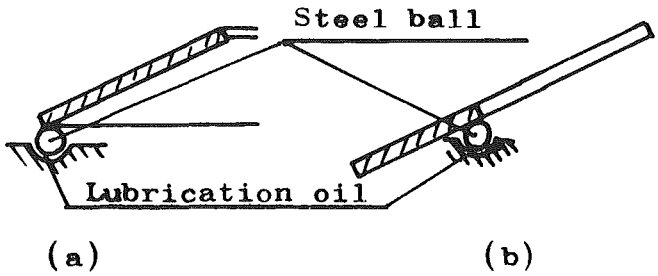


Fig. 7 Spring support used in the experiment

$$\lambda_1 = \theta_\beta l_1 + v_1 \quad (22)$$

and the solution of the shell,

$$M_s = F(\theta_\beta). \quad (23)$$

The procedure for solving is as follows:

(*i*) P_{total} is given, calculate P_1 (load on beam).

(*ii*) From P_1, calculate the exact solution of cantilever beam, and obtain v_1, l_1 and $M_1 = P_1 l_1$.

(*iii*) From M_1, get M_s, acting upon the inner boundary of shell.

(*iv*) From formula (23), solve θ_β.

(*v*) Using formula (22), calculate λ_1.

(*vi*) Repeat (i)-(v), and obtain the $P_{\text{total}} - \lambda_1$ relation behavior.

Experimental Investigation and Results

In this paper, the static response of some diaphragm springs are investigated in detail by the experimental method. The experimental contents covered in the paper are as follows:

Downloaded 03 May 2010 to 171.66.16.244. Redistribution subject to ASME license or copyright; see http://www.asme.org/terms/Terms_Use.cfm

Table 1 Rotation angle displacement behavior at the inner and outer radii

λ_1 (mm)	1.0	2.0	3.0	4.0	5.0	6.0	7.0	8.0	9.0
$\theta(a)$(deg)	1.95	3.89	5.83	7.76	9.70	11.6	13.6	15.5	17.5
$\theta(c)$(deg)	2.11	4.21	6.32	8.41	10.5	12.6	14.7	16.8	18.9

Table 2 $M_r - \lambda_1$ behavior at the turning center

λ_1 (mm)	1.0	2.0	3.0	4.0	5.0	6.0	7.0	8.0	9.0
M_r(kg)	−.274	−.432	−.481	−.486	−.475	−.483	−.547	−.703	−.988

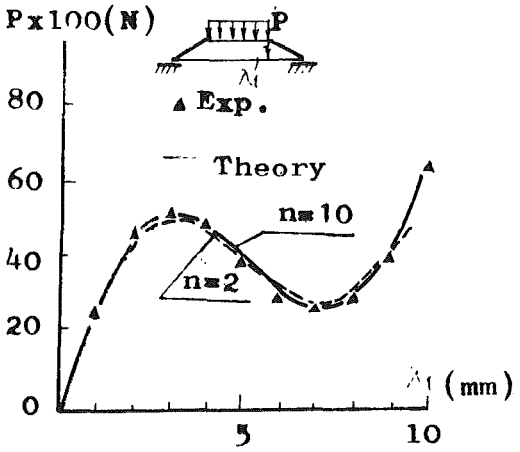


Fig. 8 Rigidity characteristics of Belleville spring

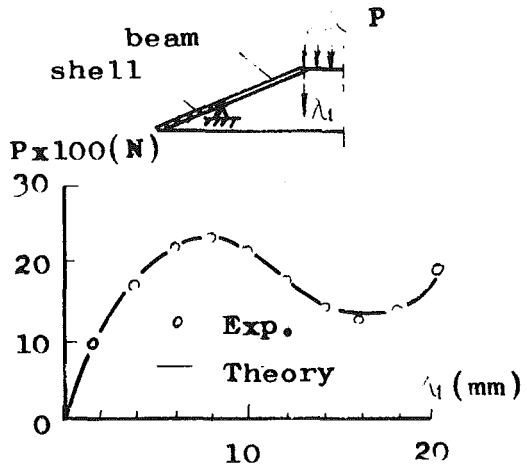


Fig. 9 Rigidity characteristics of diaphragm spring

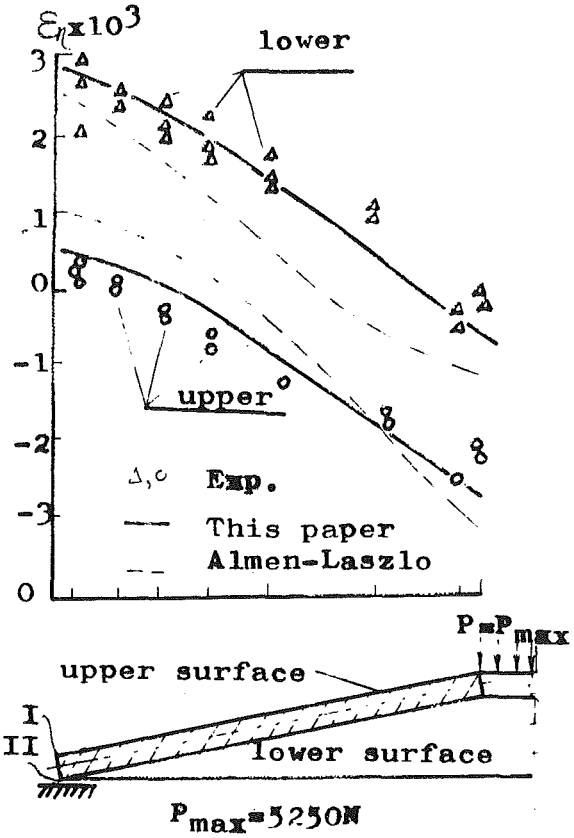


Fig. 10 Encircle strain distribution of upper and lower surfaces of spring

(1) strain distribution on surfaces of springs,

(2) the stress concentration of a shell exerts influence on strains of various parts of springs,

(3) strain distribution on the root of a separative bar when the bar is acted upon by force,

(4) maximum stress displacement characteristics, and

(5) load displacement characteristics.

Figure 6 shows the measurement system of an experimental investigation. Figure 7 is a plot of the spring support used in the experiment. This coincides with the theory: The sliding friction is neglected.

Figures 7, 8, 9, 10, 11, 12, and 13, and Tables 1 and 2 display a portion of the results of an experimental investigation. In Figs. 12 and 13, the radial strain ϵ_ξ is nonuniformly distributed along the width of the root of beam, and the encircle strain ϵ_η is very different from various points on the inner radius on a strain displacement relation. This is in fact due to the stress concentration. These results cannot be obtained by theoretical calculation.

From Figs. 8, 9, 10, 11, 12, 13 and Tables 1, 2, we can see that the analysis methods and results in this paper are satisfactory in an engineering application.

By means of the theoretical solutions and experimental results obtained, we know that the radial moment M_r is not equal to zero at the turning center. In traditional theory there is $M_r = 0$, and the rigid section assumed by Almen-Laszlo produces the big errors in stress calculation.

In engineering application, we can use the iterative formulas when $n = 2$ instead of the general iterative expressions. Some results plotted in Fig. 8 show that the foregoing analysis can be applied satisfactorily in practice.

Acknowledgment

This work was supported by Shanghai's Youth Science Fund.

References

Almen, J. O., and Laszlo, A., 1936, "The Uniform-section Disc Spring," *Transactions of the ASME*, Vol. 58, pp. 305–314.

Berry, W. R., 1956, "Spring Design XXY, *Mechanical World and Engineering Record*, Vol. 136, pp. 758–767.

Chironis, N. P., 1969, "New Equations Simplify Belleville Spring Design," *Product Engineering*, No. 1, pp. 14–20.

Curti, G., and Orlando, M., 1979, "New Calculation of Coned Annular Disk Springs," *Wire*, Vol. 30, pp. 356–361.

Downloaded 03 May 2010 to 171.66.16.244. Redistribution subject to ASME license or copyright; see http://www.asme.org/terms/Terms_Use.cfm

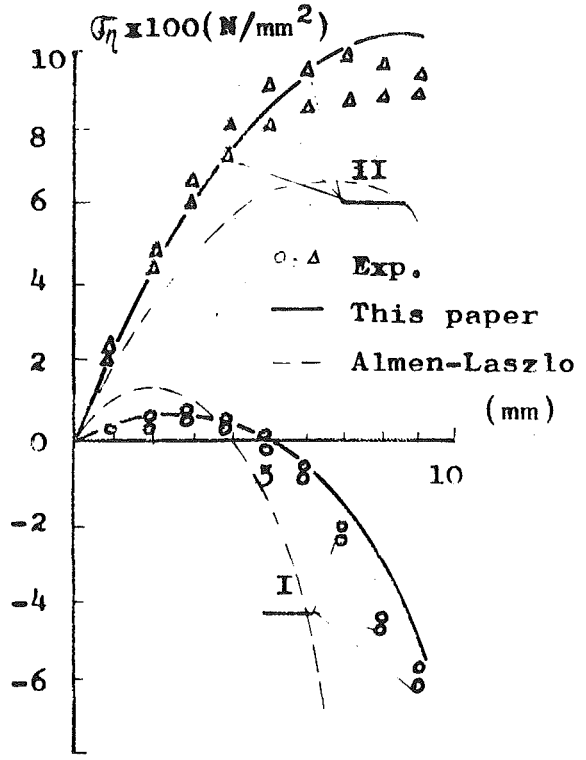


Fig. 11 Encircle stress displacement behavior at I and II points

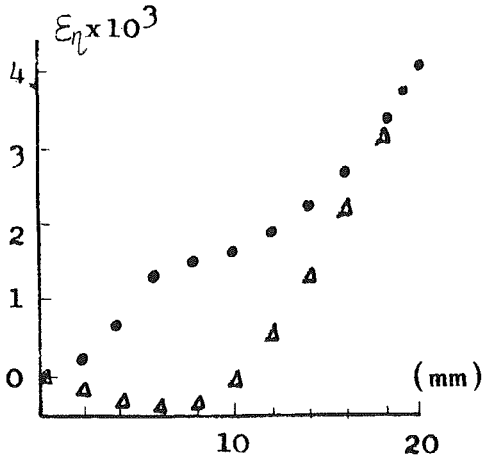


Fig. 12 Encircle strain displacement behavior at the inner radius

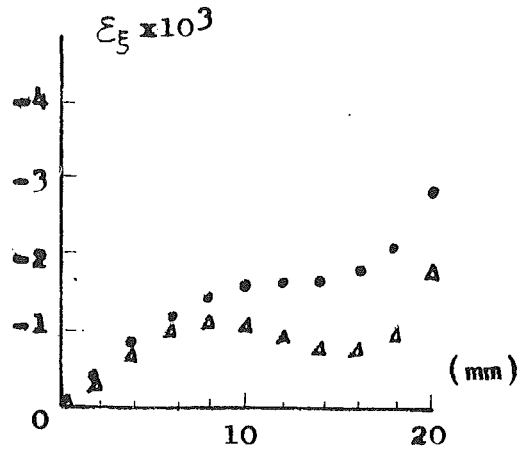


Fig. 13 Radial strain displacement behavior at the root of beam

Curti, G., 1979, "New Calculation Method for Disc Springs," *Wire*, Vol. 30, pp. 17–22.

Curti, G., 1980, "Experimental Investigation with a New Design Calculation for Disc Springs," *Wire*, Vol. 31, pp. 26–29.

Durton, R., 1967, "Diaphragm Spring Clutch Design," *Automobile Design Engineering*, No. 8, pp. 845–853.

Hübner, W., 1982, "Deformation and Stress of Belleville Springs," *Construction*, Vol. 34, pp. 387–392.

Ling, S. Y., 1965, "The Design of Disc Springs of Automobile and Tractor," *Chinese Industrial Press*, in Chinese.

Pothier, N. E., 1976, "The Application of Belleville Springs as Energy Storage Devices on Packed Valve Steam Seals in Candu Power Reactor Service," *Proc. 3rd. Symp. Engr. Appl. of Solid Mechanics*, Vol. 1, pp. 687–692.

Reissner, E., 1963, "On the Equation for Finite Symmetrical Deflections of Thin Shells of Revolution," *Proc. Appl. Mech.*, Macmillan, New York Co., pp. 171–177.

Reissner, E., 1958, "Rotationally Symmetric Problems in the Theory of Thin Elastic Shells," *Proc. 3rd. U.S. Congr. Appl. Mech.*, ASME, New York, pp. 51–69.

SAE Standard, 1955, *Manual on Design and Manufacture of Coned Disc Springs or Belleville Springs*, 2nd. ed. SAE, New York.

Schremmer, G., 1973, "The Slotted Conical Disk Spring," ASME *Journal of Engineering of Industry*, Vol. 8, pp. 765–770.

Schmidt, R., and Wempner, G., 1959, "The Nonlinear Conical Spring," ASME Journal of Applied Mechanics, Vol. 14, pp. 681–682.

Wahl, A. M., 1963, *Mechanical Springs*, 2nd ed., McGraw-Hill Book Co., New York.

Wempner, G. A., 1958, "The Conical Spring," *Proc. 3rd. U.S. Congr. of Appl. Mech.*, ASME, New York, pp. 473–478.

Wempner, G. A., 1961, "Axisymmetric Deflection of Shallow Conical Shells," *Journal of Engineering Mechanics*, EM2, ASCE, New York, pp. 181–193.

Wempner, G. A., 1971, "Discrete Approximations Related to Nonlinear Theories of Solids," *Int. Jour. Solids and Structures*, Vol. 7, pp. 1581–1598.

Ye, Z. M., 1987, "Finite Deformation Analysis and Experimental Investigation of Beam-Shell Structures in Engineering," Ph.D. Thesis, Lanzhou University, P.R. China.

Ye, Z. M., and Yeh, K. Y., 1989, "Exact Solution for Finite Deformation Problems of Cantilever Beam with Variable Section under the Action of Arbitrary Transverse Loads," *Acta Mechanical Sinica*, Vol. 5, pp. 152–158.

Yeh, K. Y., and Ye, Z. M., 1989, "Advances on Belleville Springs and Diaphragm Springs—Nonlinear Elastic Elements in Engineering," *Mechanics and Practice*, Vol. 11, pp. 5–10.

Downloaded 03 May 2010 to 171.66.16.244. Redistribution subject to ASME license or copyright; see http://www.asme.org/terms/Terms_Use.cfm

Density Effects in Two-Dimensional Bins

N. P. Kruyt
Department of Mechanical Engineering,
University of Twente,
Enschede, The Netherlands

Various theories exist for predicting the pressure on the walls of bins filled with granular material. These theories, such as Janssen's (1895) theory, usually neglect the effect of the compressibility of the granular material, which is relevant for many materials. Here this effect is studied numerically, and the results are compared with a new approximate theory. This comparison shows that the agreement is excellent.

Introduction

The various theories for predicting the pressure on the walls of bins filled with granular material (for example: Janssen, 1895; Savage and Yong, 1970; Walters, 1973) include the assumption of incompressibility. However, as is noted by Jenike (1987), all solids are compressible to some degree. This compressibility effect is most prominent in fine powders and materials consisting of soft particles. Theoretical considerations (Schofield and Wroth, 1968) and experimental results (Schofield and Wroth, 1968; Clower et al., 1973; Loewer et al., 1977; Sundaram and Cowin, 1985) show that for many materials, the density varies with pressure. This density increase can be more than 10 percent in the pressure range up to 80 kPa.

The effect of the density variation on the wall pressure was studied by Cowin (1979), who developed an approximate relation that takes this into account. Here this theory will be extended and in order to judge the accuracy of the new theory, the results will be compared with a numerical simulation by a finite difference method.

A noncohesive granular material in a two-dimensional bin is considered. It is assumed that it satisfies the Coulomb yield criterion. Compressive stresses are positive and the stress conditions will be active in the bin.

Equilibrium Conditions

The quasi-static equilibrium equations are:

$$\frac{\partial}{\partial x}\sigma_{xx}+\frac{\partial}{\partial y}\sigma_{xy}=\rho\, g \tag{1}$$

$$\frac{\partial}{\partial x}\sigma_{xy}+\frac{\partial}{\partial y}\sigma_{yy}=0 \tag{2}$$

where ρ is the bulk density of the material and g is the acceleration due to gravity. The x-axis is directed vertically downwards.

The material satisfies the Coulomb yield criterion. The stresses are given by Sokolovski (1965):

$$\sigma_{xx}=p[1+\sin(\phi)\cos(2\psi)] \tag{3}$$

$$\sigma_{yy}=p[1-\sin(\phi)\cos(2\psi)] \tag{4}$$

$$\sigma_{xy}=p\,\sin(\phi)\sin(2\psi). \tag{5}$$

Here, p denotes the mean pressure, ϕ is the internal friction angle, and ψ is the angle between the x-axis and the direction of the major principal stress.

Substituting equations (3)–(5) into (1) and (2) gives, after some algebra:

$$\frac{\partial}{\partial x}\begin{bmatrix}p\\ \psi\end{bmatrix}=\frac{1}{\cos(2\psi)+\sin(\phi)}\begin{bmatrix}-\sin(2\psi) & -2p\,\sin(\phi)\\ \dfrac{-\cos^2(\phi)}{2p\,\sin(\phi)} & -\sin(2\psi)\end{bmatrix}\frac{\partial}{\partial y}\begin{bmatrix}p\\ \psi\end{bmatrix}$$

$$+\frac{1}{\cos(2\psi)+\sin(\phi)}\begin{bmatrix}\rho g\,\cos(2\psi)\\ -\rho g\,\sin(2\psi)/(2p)\end{bmatrix}. \tag{6}$$

Or, symbolically:

$$\frac{\partial}{\partial x}\mathbf{w}=\mathbf{A}(\mathbf{w})\frac{\partial}{\partial y}\mathbf{w}+\mathbf{s}(\mathbf{w}). \tag{7}$$

At the horizontal free surface the normal and shear stress equal zero so:

$$\psi_{\text{top}}=0 \text{ and } p_{\text{top}}=0. \tag{8}$$

Because of the symmetry at the center line ψ satisfies:

$$\psi_{\text{center}}=0. \tag{9}$$

Assuming that wall friction is fully developed at the wall, ψ is given by:

$$\psi_{\text{wall}}=\frac{1}{2}\left\{\arcsin\left(\frac{\sin(\delta)}{\sin(\phi)}\right)-\delta\right\} \tag{10}$$

where δ is the wall friction angle.

It is assumed that the density depends only on the mean pressure. This dependence is modeled by (see also Fig. 1):

$$\rho(p)=\begin{cases}\rho_0+(\rho_\infty-\rho_0)\left[2\left(\dfrac{p}{p^c}\right)-\left(\dfrac{p}{p^c}\right)^2\right] & ,\ p\le p^c\\ \rho_\infty & ,\ p\ge p^c\end{cases}. \tag{11}$$

Contributed by the Applied Mechanics Division of THE AMERICAN SOCIETY OF MECHANICAL ENGINEERS for publication in the JOURNAL OF APPLIED MECHANICS.

Discussion on this paper should be addressed to the Technical Editor, Leon M. Keer, The Technological Institute, Northwestern University, Evanston, IL 60208, and will be accepted until two months after final publication of the paper itself in the JOURNAL OF APPLIED MECHANICS. Manuscript received and accepted by the ASME Applied Mechanics Division, June 20, 1989.

Copyright © 1990 by ASME
Downloaded 03 May 2010 to 171.66.16.244. Redistribution subject to ASME license or copyright; see http://www.asme.org/terms/Terms_Use.cfm

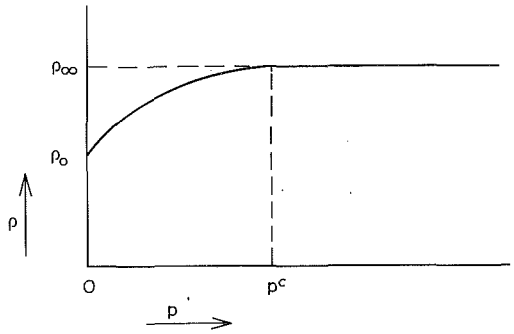


Fig. 1 The relation between mean pressure and density

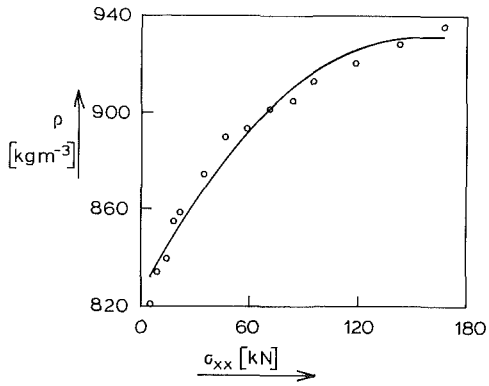


Fig. 2 The relation between vertical stress and density for coal; *o*, experimental data from (Sundaram and Cowin, 1985);—, curve fit according to equation (18)

According to Sundaram and Cowin (1985), the relation between density and pressure is well described by a quadratic relation. A disadvantage of this relation is that it predicts a decrease in density for large pressure, which is physically unacceptable. Therefore, the quadratic relation is cut off at its maximum $\rho = \rho_\infty$ for $p = p^c$, and is continued as a constant.

Other relations between pressure and density have been proposed. Schofield and Wroth (1968) have suggested a logarithmic relation between voidage and pressure:

$$\frac{1}{\rho} = A - B \ln(p). \tag{12}$$

This relation does not give realistic results for low pressures. An empirical power-law relation is given by Jenike (1961 and 1987):

$$\rho = C(p - p_0)^\beta. \tag{13}$$

According to Jenike (1987) the value of β is smaller than 0.05 for minerals, but for "spongy" materials it may exceed 0.1.

The three relations (11)–(13) are all curve fits to experimental data. Since both relations (12) and (13) are not suitable for developing an analytical theory, equation (11) is used in the sequel. This relation fits experimental data from (Sundaram and Cowin, 1985) with acceptable accuracy (see Figs. 2 and 3).

A New Approximate Analytical Theory

In developing an approximate analytical theory, Janssen's approach is followed. Although apparently different, Walters' (1973) approach is equivalent to that of Janssen: Walters' equation for the wall pressure is a special case of Janssen's equation with a λ equal to $B'\ D/\tan(\delta)$, where B' and D are factors that were derived by Clague (1973).

Following Janssen's approach it is assumed that σ_{xx} and σ_{yy} are constant along a horizontal slice. The ratio of horizontal

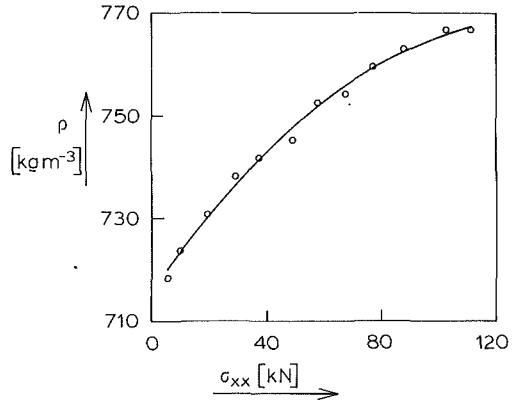


Fig. 3 The relation between vertical stress and density for whole shelled corn; *o*, experimental data from (Sundaram and Cowin, 1985);—, curve fit according to equation (18)

to vertical stress is denoted by λ. The vertical equilibrium condition leads to:

$$\frac{d}{dx}\sigma_{xx} + \frac{2}{B}\mu\,\lambda\,\sigma_{xx} = \rho(\sigma_{xx})g. \tag{14}$$

Here, B is the width of the bin and $\mu = \tan(\delta)$. The following relations for λ have been proposed:

$$\lambda = \frac{1 - \sin(\phi)\cos(2\chi)}{1 + \sin(\phi)\cos(2\chi)}. \tag{15}$$

Here, χ is the average (over a horizontal slice) of the direction of the major principal stress ψ; χ can be:

$$\chi = \psi_{\text{center}} \tag{16}$$

$$\chi = \psi_{\text{wall}}. \tag{17}$$

Experiments have shown that the influence of the pressure on ϕ and δ is usually slight. Therefore, λ will be treated as a constant. Cowin (1979), however, assumes that λ depends linearly on the vertical stress.

The relation between the density and the vertical stress is given by (compare (2.6)):

$$\rho(\sigma_{xx}) = \begin{cases} \rho_0 + (\rho_\infty - \rho_0)\left[2\left(\dfrac{\sigma_{xx}}{\sigma_{xx}^c}\right) - \left(\dfrac{\sigma_{xx}}{\sigma_{xx}^c}\right)^2\right] & ,\ \sigma_{xx} \le \sigma_{xx}^c \\ \rho_\infty & ,\ \sigma_{xx} \ge \sigma_{xx}^c \end{cases} \tag{18}$$

This relation is in better agreement with experimental results (Clower et al., 1973; Loewer et al., 1977; Sundaram and Cowin, 1985; for example) than the linear relation proposed by Cowin (1979). Note that equation (18) gives ρ as a function of σ_{xx}, while equation (11) relates ρ to p. These functions are different, since p^c and σ_{xx}^c are different.

Equation (14) is solved in two steps. In the first step $\sigma_{xx} \le \sigma_{xx}^c$, and in the second step $\sigma_{xx} \ge \sigma_{xx}^c$.

First Step: $\sigma_{xx} \le \sigma_{xx}^c$.

When $\sigma_{xx} \le \sigma_{xx}^c$ it follows from equations (14) and (18) that

$$\frac{d}{dx}\sigma_{xx} = q_1 + q_2\sigma_{xx} + q_3(\sigma_{xx})^2 \tag{19}$$

where

$$q_1 = \rho_0 g \tag{20}$$

$$q_2 = \frac{2(\rho_\infty - \rho_0)g}{\sigma_{xx}^c} - \frac{2}{B}\mu\,\lambda \tag{21}$$

$$q_3 = \frac{-(\rho_\infty - \rho_0)g}{\left(\sigma_{xx}^c\right)^2}. \tag{22}$$

Downloaded 03 May 2010 to 171.66.16.244. Redistribution subject to ASME license or copyright; see http://www.asme.org/terms/Terms_Use.cfm

This Riccati equation (Boyce and DiPrima, 1976) must be solved together with the initial condition that the top surface is stress-free:

$$\sigma_{xx}(0)=0. \tag{23}$$

The solution of equation (19), together with (23), is:

$$\sigma_{xx}=C\left[1-\frac{(q_2+2q_3C)}{(q_2+q_3C)\exp[-(q_2+2q_3C)x]+q_3C}\right], \tag{24}$$

where C is given by:

$$\text{If } q_3\neq 0: \quad C=\frac{-q_2+\sqrt{(q_2^2-4q_1q_3)}}{2q_3}. \tag{25}$$

$$\text{If } q_3=0: \quad C=\frac{-q_1}{q_2}. \tag{26}$$

The solution (24) is valid for $x \le x_c$, where x_c is the value of x for which $\sigma_{xx} = \sigma^c_{xx}$. It is given by:

$$x_c=\frac{-1}{q_2+2q_3C}\ln\left(\frac{C}{q_2+q_3C}\cdot\frac{q_2+q_3(C+\sigma^c_{xx})}{C-\sigma^c_{xx}}\right). \tag{27}$$

Second Step: $\sigma_{xx} \ge \sigma^c_{xx}$.

When $\sigma_{xx} \ge \sigma^c_{xx}$ it follows from equations (14) and (18) that:

$$\frac{d}{dx}\sigma_{xx}=\rho_\infty g-\frac{2}{B}\mu\lambda\sigma_{xx}. \tag{28}$$

This equation must be solved together with the initial condition:

$$\sigma_{xx}(x_c)=\sigma^c_{xx}. \tag{29}$$

The solution of equations (28) and (29) is:

$$\sigma_{xx}=\frac{\rho_\infty g B}{2\mu\lambda}+\left[\sigma^c_{xx}-\frac{\rho_\infty g B}{2\mu\lambda}\right]\exp\left[-\frac{2\mu\lambda}{B}(x-x_c)\right]. \tag{30}$$

This solution is valid for $x \ge x_c$.

The complete solution of equation (14) is given by (24) and (30). Janssen's relation is a special case of this solution. It is retrieved when $\rho_\infty = \rho_0$ and $\sigma^c_{xx} = 0$.

A Numerical Method

In order to judge the accuracy of the developed theory, a comparison will be made with a numerical simulation. Similar comparisons, using the method of characteristics, have been made for the incompressible case by (Savage and Yong, 1970; Horne and Nedderman, 1976).

A finite difference method is employed to solve equation (7) numerically. Advantages of finite difference methods over the method of characteristics are that they are simpler to implement and that the solution is obtained on a regular grid.

A modified version of the well-known McCormack (1969) method is employed. It consists of two steps. Starting from the known values $\mathbf{w}_i^n$ ($\mathbf{w}_i^n$ denotes $\mathbf{w}$ at the intersection of the nth level in the x-direction and the ith level in the y-direction), the values $\mathbf{w}_i^*$ at an intermediate level in the x-direction are computed from:

$$\mathbf{w}_i^*=\mathbf{w}_i^n+\frac{\Delta x}{\Delta y}\mathbf{A}^n_{i+1/2}\left(\mathbf{w}^n_{i+1}-\mathbf{w}^n_i\right)+\Delta x\,\mathbf{s}^n_i. \tag{31}$$

Here, Δx and Δy denote the size of the steps in the x and y-direction, respectively.

The values $\mathbf{w}_i^{n+1}$ at the next level in the x-direction are computed from:

$$\mathbf{w}_i^{n+1}=\frac{1}{2}\left\{\mathbf{w}_i^n+\mathbf{w}_i^*+\frac{\Delta x}{\Delta y}\mathbf{A}^*_{i-1/2}\left(\mathbf{w}_i^n-\mathbf{w}^n_{i-1}\right)+\Delta x\,\mathbf{s}_i^*\right\}. \tag{32}$$

Table 1 Average relative deviation in wall shear stress between numerical and analytical methods

ϕ	δ	Dev. Janssen percent		Dev. Walters percent
		λ_{center}	λ_{wall}	
30	10	1.5	3.1	2.2
30	20	3.3	8.9	4.6
30	25	4.6	14.4	6.2
45	10	1.7	2.4	2.0
45	20	2.9	5.6	4.0
45	30	4.5	10.6	6.5
60	10	1.7	1.9	1.8
60	20	3.2	4.2	3.7
60	30	4.6	7.2	5.8

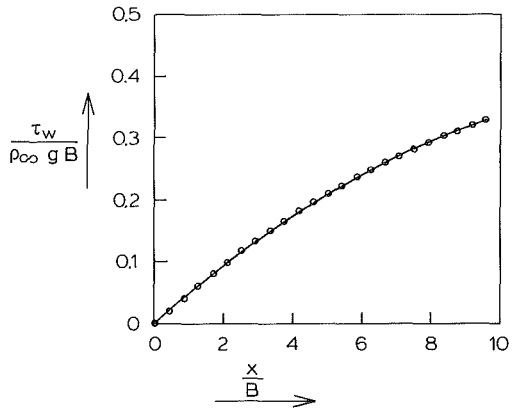


Fig. 4 The dimensionless shear stress at the wall as a function of the dimensionless depth; ϕ = 40 deg, δ = 15 deg, ρ_0 = 825 kg.m^{-3}, ρ_∞ = 930 kg.m^{-3}, σ^c_{xx} = 150 kPa; *o*, numerical;—, approximate

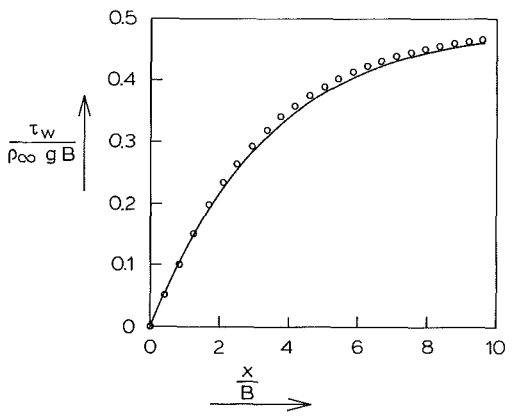


Fig. 5 The dimensionless shear stress at the wall as a function of the dimensionless depth; ϕ = 30 deg, δ = 25 deg, ρ_0 = 715 kg.m^{-3}, ρ_∞ = 770 kg.m^{-3}, σ^c_{xx} = 135 kPa; *o*, numerical;—, approximate

The boundary conditions equations (16) and (17) must be included in the computation of $\mathbf{w}_i^{n+1}$.

The step size Δx is chosen in such a way that it satisfies the Courant-Friedrichs-Lewy stability condition (Richtmeyer and Morton, 1967). By starting at the free surface and moving downwards the solution is obtained throughout the bin.

Comparison of the Two Methods

In experiments the density is often measured as a function of the mean pressure. The parameters ρ_0, ρ_∞, and p^c in equation (11) are determined from a least-squares fit of the test results. In the approximate theory the density depends on the vertical stress as given by equation (18). Parameter σ^c_{xx} is related to p^c by:

Downloaded 03 May 2010 to 171.66.16.244. Redistribution subject to ASME license or copyright; see http://www.asme.org/terms/Terms_Use.cfm

$$\sigma_{xx}^c = p^c\left[1+\sin(\phi)\cos(2\chi)\right]. \tag{33}$$

In order to find a suitable value for χ (and hence for λ), the incompressible case is considered first. Numerical results for the shear stress at the wall, and that of Janssen's relation (for two values of λ) and of Walter's relation, are compared. The average relative deviations, when compared with the numerical results (which can be regarded as exact), are given in Table 1. As can be seen from this Table, Janssen's relation is the most accurate when λ equals:

$$\lambda = \frac{1-\sin(\phi)}{1+\sin(\phi)} \tag{34}$$

and hence,

$$\chi = 0. \tag{35}$$

For the axisymmetric case it was also found by Benink (1989) that λ according to equation (34) gives the most accurate results. This is surprising since the stress ratio λ, according to equation (34), is valid at the *center line*, yet it gives the most accurate results at the *wall*.

The numerical and analytical approach were compared for many different sets of the parameters that describe the granular material and the bin. The agreement was always excellent. A typical result is shown in Fig. 4. Here the values of the dimensionless shear stress at the wall $\tau_w/(\rho_\infty\, g\, B)$ are given for both methods. The height and the width of the bin are 25 m and 2.5 m, respectively. The largest deviations occurred when the difference between the internal friction angle ϕ and wall friction angle δ was small ($\leq$ 5 deg), as in Fig. 5.

Acknowledgments

This work was performed while the author was staying at McGill University (Montréal, Canada). The author would like to thank Prof. S. B. Savage for very valuable discussions and encouragement. The financial support from the Netherlands Foundation for Technical Research (S.T.W.) is also gratefully acknowledged. The University of Twente (and especially Prof. F. J. C. Rademacher) is thanked for their cooperation and support.

References

Benink, E. J., 1989, "Flow and Stress Analysis of Cohesionless Bulk Materials in Silos Related to Codes," Ph.D. Thesis, University of Twente, Enschede.

Boyce, W. E., and DiPrima, R. C., 1976, *Elementary Partial Differential Equations and Boundary Value Problems*, John Wiley and Sons, New York, p. 50.

Clague, K., 1973, *The Effect of Stresses in Bunkers*, Ph.D. Thesis, University of Nottingham, Nottingham, U.K.

Clower, R. E., Ross, I. J., and White, G. M., 1973, "Properties of Compressible Granular Materials as Related to Forces in Bulk Storage Structures," *Trans. ASAE*, Vol. 16, pp. 478–481.

Cowin, S. C., 1979, "The Pressure Ratio in the Theory of Bin Pressures," ASME Journal of Applied Mechanics, Vol. 46, pp. 524–528.

Horne, R. M., and Nedderman, R. M., 1976, "Analysis of Stress Distribution in Two-Dimensional Bins by the Method of Characteristics," *Powder Technol.*, Vol. 14, pp. 93–102.

Janssen, H. A., 1895, "Versuche über Getreidedruck in Silozellen," *VDI-Zeitschrift*, Vol. 35, pp. 1045–1049.

Jenike, A. W., 1961, *Univ. Utah Exp. Stn. Bull. No. 108*, University of Utah, Salt Lake City.

Jenike, A. W., 1987, "A Theory of Flow of Particulate Solids in Converging and Diverging Channels Based on a Conical Yield Function," *Powder Technol.*, Vol. 50, pp. 229–236.

Loewer, O. J., Ross, I. J., Kratzer, D. D., and Walker, J. N., 1977, "Properties of Ground Shelled Corn as Related to Forces in Bulk Storage Structures," *Trans. ASAE*, Vol. 20, pp. 155–156.

McCormack, R. W., 1969, AIAA paper 69-354.

Richtmeyer, R. D., and Morton, K. W., 1967, *Difference Methods for Initial Value Problems*, Wiley Interscience, New York.

Savage, S. B., and Yong, R. N., 1970, "Stresses Developed by Cohesionless Granular Materials in Bins," *Int. J. Mech. Sci.*, Vol. 49, pp. 675–693.

Schofield, A. N., and Wroth, C. P., 1968, *Critical State Soil Mechanics*, McGraw-Hill, New York.

Sokolovski, V. V., 1965, *Statics of Granular Materials*, Pergamon Press, Oxford, U.K.

Sundaram, V., and Cowin, S. C., 1985, "The Experimental Evaluation of the Effect of Material Consolidation on Static Bin Pressures," *Powder Technol.*, Vol. 42, pp. 241–247.

Walters, J. K., 1973, "A Theoretical Analysis of Stresses in Silos with Vertical Walls," *Chem. Eng. Sci.*, Vol. 28, pp. 13–21.

Downloaded 03 May 2010 to 171.66.16.244. Redistribution subject to ASME license or copyright; see http://www.asme.org/terms/Terms_Use.cfm

Gravity-Driven Granular Flows of Smooth, Inelastic Spheres Down Bumpy Inclines

M. W. Richman
Mem. ASME

R. P. Marciniec

Department of Mechanical Engineering,
Worcester Polytechnic Institute,
Worcester, MA 01609

We employ a kinetic constitutive theory that includes the effects of particle transport and collisions to analyze steady, fully developed, gravity-driven flows of smooth, inelastic spheres down bumpy inclines. By replacing the solid fraction by its depth-averaged value wherever it occurs in the balance equations, we obtain a closed-form solution for the granular temperature profile, which when employed in the constitutive relations for the normal and shear stresses determines the solid fraction and mean velocity profiles. The solutions ensure that the stresses and energy flux vanish at the free surface and that the balance of momentum and energy are satisfied at the base. We also determine for fixed flow rates the ranges of inclinations within which steady flows are possible, and for fixed inclinations the depths of the resulting flows. Most striking are the inclinations and flow rates at which both a dilute, fast flow and a dense, slow flow are possible.

Introduction

Gravity-driven granular flows down inclined surfaces occur in contexts ranging from geophysical flows that comprise snow avalanches and rock landslides to industrial flows that are common in a variety of materials handling applications. As a result, these flows have been the subject of several experimental and theoretical investigations. In a typical experiment, for example, grains are fed onto an inclined at its peak, and through the use of either high-speed photography, fiber optic probes, or other more primitive means, measurements are made to estimate the flow depth and the profiles of solid fraction and velocity, as well as to determine their variations with inclination, flow rate, and position along the incline. Experimental investigation of this type have been carried out by Bagnold (1954), Ridgway and Rupp (1970), Augenstein and Hogg (1978), Ishida and Shira (1979), Savage (1979), Hungr and Morgenstern (1984), Campbell et al. (1985), and Patton et al. (1987). Most recently, Johnson and Jackson (1990) performed similar experiments and for the first time paid special attention to the dependence of the nature of the flow on the manner in which the grains were fed onto the incline.

The same flows have been analyzed by Goodman and Cowin (1971), Nunziato et al. (1980), Ogawa et al. (1980), McTigue (1982), and Sayed and Savage (1983) employing theories that did not account for the effects of velocity fluctuations, and by Savage (1982), Ahmadi and Shahinpoor (1983), and Ma and Ahmadi (1985) employing theories that did incorporate the effects of fluctuations. In all cases, an ad hoc boundary condition was applied to the mean velocity at the base of the incline, and for those theories in which a measure of the fluctuation energy was treated as an important mean field, an ad hoc condition was also applied to the energy flux at the base. Numerical solutions for the profiles of solid fraction, velocity, and granular temperature within these gravity flows have been obtained by Hutter et al. (1968a, b) and Johnson and Jackson (1990), and numerical simulations of the planar analog to these flows have been performed by Campbell and Brennen (1985).

Here we employ a kinetic theory and corresponding boundary conditions to analyze steady, fully developed, free surface, gravity-driven granular flows of identical, smooth, nearly elastic spheres down bumpy inclines. We simplify the solution procedure by replacing the solid fraction by its depth-averaged value wherever it occurs in the balance equations. In this manner, it is possible to obtain from the energy equation an approximate closed-form solution for the granular temperature, which when employed in the basal energy flux boundary condition determines the depth of flow, and when employed in the constitutive relations for the normal and shear stresses determines the solid fraction and velocity profiles. The solutions, which ensure that the stresses and energy flux vanish at the free surface and that the balances of momentum and energy are satisfied at the base, also determine the range of angles between which steady flows are possible for a fixed boundary geometry and flow rate. Because the results are based upon a closed-form solution for the granular temperature, they are obtained with no computational difficulties and are easy to interpret physically.

General Theory

In this section, we present a general theory for flows of

Contributed by the Applied Mechanics Division of the THE AMERICAN SOCIETY OF MECHANICAL ENGINEERS for publication in the JOURNAL OF APPLIED MECHANICS.

Discussion on this paper should be addressed to the Technical Editor, Prof. Leon M. Keer, The Technological Institute, Northwestern University, Evanston, IL 60208, and will be accepted until two months after final publication of the paper itself in the JOURNAL OF APPLIED MECHANICS. Manuscript received by the ASME Applied Mechanics Division, Aug. 23, 1988; final revision, Aug. 1, 1989.

Copyright © 1990 by ASME
Downloaded 03 May 2010 to 171.66.16.244. Redistribution subject to ASME license or copyright; see http://www.asme.org/terms/Terms_Use.cfm

identical, smooth, nearly elastic spheres of diameter, σ, and mass density, ρ_p. We consider only those flows in which the particle number density is low enough and the strain rate is high enough to neglect the effects of enduring contacts between particles. Under these circumstances, the transfer of momentum and energy in dense flows is due primarily to binary collisions between particles, and in dilute flows is due primarily to the transport of particles between collisions. In the intermediate range of flow density, both mechanisms may make significant contributions to the transfer of momentum and energy. The theory is based upon a statistical description of the particles' velocities in which a single particle distribution function is used to define the mean of any property and to construct the frequency of any binary collision. For flows of nearly elastic particles, the relevant mean fields are the solid fraction, ν, which when multiplied by ρ_p gives the flow density, ρ; the mean velocity, $\mathbf{u}$, about which the particles fluctuate; and the granular temperature, T, which is a measure of the kinetic energy per unit mass associated with the velocity fluctuations. The general theory consists of balance equations for mass, momentum, and energy; constitutive relations for stress, energy flux, and collisional rate of energy dissipation; and boundary conditions on the stress and energy flux.

The balance equations for mass and momentum have the familiar forms:

$$\dot{\rho} + \rho \nabla \cdot \mathbf{u} = 0, \tag{1}$$

where an overdot indicates the time derivative taken while following the mean motion; and

$$\rho \dot{\mathbf{u}} = -\nabla \cdot \boldsymbol{P} + \rho \mathbf{g}, \tag{2}$$

where $\boldsymbol{P}$ is the pressure tensor and $\mathbf{g}$ is the body force unit mass. The balance of energy is given by

$$(3/2)\rho \dot{T} = -\nabla \cdot \mathbf{Q} - tr(\boldsymbol{P} \cdot \boldsymbol{D}) - \gamma, \tag{3}$$

in which $\mathbf{Q}$ is the flux of fluctuation energy, γ is the collisional rate per unit volume of energy dissipation, and $\boldsymbol{D}$ is the symmetric part of the velocity gradient $\nabla \mathbf{u}$. The formal derivation of these equations for the dissipative flows of interest was first given by Jenkins and Savage (1983).

In order to relate the pressure tensor, $\boldsymbol{P}$, energy flux, $\mathbf{Q}$, and rate of dissipation, γ, to the mean fields of solid fraction, ν, velocity, $\mathbf{u}$, and temperature, T, we employ the constitutive theory of Jenkins and Richman (1985) for flows of identical, smooth, nearly elastic spheres. In this theory, the rate of dissipation is given by

$$\gamma = 15\mu(1-e)T/\sigma^2, \tag{4}$$

where e is the coefficient of restitution between flow particles and

$$\mu = 8\sigma\rho G T^{1/2}/5\pi^{1/2}, \tag{5}$$

in which $G(\nu) = \nu\,(2-\nu)\,/\,2(1-\nu)^3$. The pressure tensor is given by

$$\boldsymbol{P} = 4\rho G F T \boldsymbol{I} - 2\mu E \hat{\boldsymbol{D}}, \tag{6}$$

where $F(\nu) = 1 + 1/4G$, $E(\nu) = 1 + \pi\,(1+5/8G)^2/12$, and $\hat{\boldsymbol{D}}$ is the deviatoric piece of $\boldsymbol{D}$; and the energy flux is

$$\mathbf{Q} = -(5\mu/2)M \nabla T, \tag{7}$$

where $M(\nu) = 1 + 9\pi\,(1+5/12G)^2/32$. Because the theory includes contributions to the constitutive quantities from particle transport as well as from particle collisions, it applies to the full range of solid fraction.

In order to write down boundary conditions, we consider a unit area of a boundary that interacts with the flow and has a unit inward normal $\mathbf{n}$. Due to collisions between the flow particles and this segment of the boundary, momentum is supplied to the flow at a rate $\mathbf{M}$ and energy is dissipated at a rate D. The balance of momentum at the boundary requires that

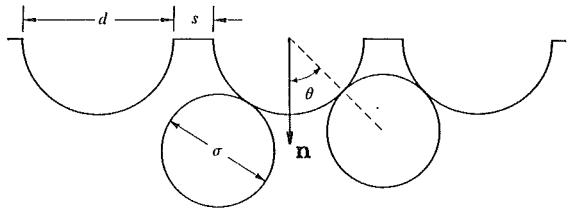


Fig. 1 The boundary as seen by a plane passing through the center of a wall particle and its average neighboring torus; also shown are two flow particles whose centers lie within the plane

$$\mathbf{M} = \boldsymbol{P} \cdot \mathbf{n}, \tag{8}$$

and the balance of energy requires that

$$\mathbf{M} \cdot \mathbf{v} - D = \mathbf{Q} \cdot \mathbf{n}, \tag{9}$$

where the slip velocity, $\mathbf{v}$, is the boundary velocity minus the flow velocity at the wall. The direction of the energy flux at the boundary is determined by the relative magnitudes of the slipwork, $\mathbf{M} \cdot \mathbf{v}$, which is due to equal tractions acting through velocities that differ by $\mathbf{v}$, and the dissipation, D, which is due to inelastic wall-flow particle collisions.

Expressions for $\mathbf{M}$ and D depend on the details of the boundary. Here we are concerned with a flat wall to which identical smooth hemispherical particles of diameter d are randomly attached an average distance s apart, as shown in Fig. 1. On average, the nearest neighbors of any hemisphere form a half-torus with inner diameter $d+2s$, outer diameter $3d+2s$, and height $d/2$. When a flow particle collides with a wall particle, the distance between their centers is $\bar{\sigma} \equiv (\sigma + d)/2$. Dimensionless measures of wall geometry are $r \equiv \sigma/d$ and $\Delta \equiv s/d$. In order to ensure that no flow particle ever collides with the flat part of the wall, we insist that Δ be less than $-1 + (1+2r)^{1/2}$. The boundary may be made effectively rougher either by increasing Δ or decreasing r. The fraction of surface area of each wall hemisphere that is accessible to any flow particle is $(1-\cos\theta)$, where θ is defined by the relation $\sin\theta = (1+\Delta)/(1+r)$. The coefficient of restitution that characterizes the energy dissipated in wall-flow particle collisions is e_w, and it is assumed that these collisions are nearly elastic.

The rates D and $\mathbf{M}$ are statistical averages of the changes per collision in the appropriate flow particle property weighted by the frequency of each wall-flow particle collision. To ensure that the boundary conditions are consistent with the constitutive theory given by equations (4) through (7), we must base all averaging at the wall on the improved Maxwellian of Jenkins and Richman (1985). In this manner, Richman (1988) has found that the rate of dissipation due to boundary interactions is, to lowest order, given by

$$D = (2/\pi)^{1/2} 2\rho\chi(1-e_w) T^{3/2}(1-\cos\theta)\csc^2\theta, \tag{10}$$

where the factor $\chi(\nu)$ accounts for excluded volume near the boundary and the shielding of flow particles from wall particles by other flow particles. Similarly, the Cartesian components M_i of the rate of momentum supply are, to within an error consistent with expression (6) for $\boldsymbol{P}$, given by

$$M_i = \rho\chi T\{n_i + (2^{3/2}v_i/3\sqrt{\pi T})[2\csc^2\theta(1-\cos\theta) - \cos\theta)] + (2^{1/2}\bar{\sigma}u_{k,j}/\sqrt{\pi T})[(1+\sigma B/\bar{\sigma})I_{ijk} + n_j I_{ik}]\}, \tag{11}$$

where $B(\nu) = \pi\,(1+5/8G)\,/\,12\sqrt{2}$, and I_{ik} and I_{ijk} arise naturally from the averaging procedure at the boundary and are defined in terms of the boundary geometry by

$$I_{ik} = (2/3)\{2[\csc^2\theta(1-\cos\theta) + \cos\theta)]n_i n_k + [2\csc^2\theta(1-\cos\theta) - \cos\theta](\tau_i\tau_k + t_i t_k)\}, \tag{12}$$

in which $\mathbf{t}$, τ, and $\mathbf{n}$ form a right-handed orthonormal triad, and

Downloaded 03 May 2010 to 171.66.16.244. Redistribution subject to ASME license or copyright; see http://www.asme.org/terms/Terms_Use.cfm

$$I_{ijk} = (\sin^2\theta - 2)n_i n_j n_k - (1/2)\sin^2\theta[n_i(\tau_j\tau_k + t_j t_k) + n_j(\tau_k\tau_i + t_k t_i) + n_k(\tau_i\tau_j + t_i t_j)]. \quad (13)$$

The physical implications of I_{ik} and I_{ijk} may be inferred from the work of Richman (1988), who used these tensors in expression (11) for M_i and found that in simple shear flows driven by bumpy boundaries, the slip velocity decreased as either Δ increased or r decreased.

When initial conditions are specified, the mean fields ρ, **u**, and T are determined by balance equations (1) through (3), constitutive relations (4) through (7), and boundary conditions (8) and (9) in which expressions (11) and (10) are used for **M** and D.

Steady Gravity-Driven Flows

Of interest here are steady, fully developed, gravity-driven granular flows down bumpy inclined surfaces. The vertical acceleration due to gravity is g, the angle between the incline and the horizontal is ϕ, and the perpendicular distance from the incline to the free surface is L. We introduce an $x_1 - x_2 - x_3$ Cartesian coordinate system in which x_1 measures parallel distances along the incline and x_2 measures perpendicular distances above the incline. If $y = (L - x_2)/\sigma$ is the dimensionless coordinate measured from the free surface and the flows are infinitely extended in the x_3-direction, then the solid fraction, ν, the dimensionless velocity, $u = u_1/(\sigma g)^{1/2}$, and the dimensionless measure, $w = (T/\sigma g)^{1/2}$, of granular temperature depend on y only.

In these flows, the balance of mass (1) and the x_3-component of the balance of momentum (2) are satisfied identically. In terms of the dimensionless shear stress $S = -P_{12}/\rho_p\sigma g$, the x_1-component of the momentum equation is

$$S' = \nu\sin\phi, \quad (14)$$

where a prime denotes differentiation with respect to y, and, in terms of the dimensionless normal pressure $N = P_{22}/\rho_p\sigma g$, the x_2-component of the momentum equation is

$$N' = \nu\cos\phi. \quad (15)$$

Regardless of $\nu(y)$, y may be eliminated between equations (14) and (15) to show that the ratio S/N is equal to $\tan\phi$ provided that both S and N vanish at the free surface. In order to simplify the energy equation, we introduce the dimensionless energy flux $q = Q_2/\rho_p(\sigma g)^{3/2}$ and energy dissipation $\Gamma = \gamma/\rho_p\sigma^{1/2}g^{3/2}$. In terms of these quantities, equation (3) reduces to

$$q' - Su' - \Gamma = 0. \quad (16)$$

It remains to write the constitutive relations in dimensionless form.

From the isotropic piece of the pressure tensor, N is given by

$$N = 4\nu GFw^2, \quad (17)$$

and from the deviatoric piece, S is given in terms of the dimensionless viscosity $\eta = \mu/\rho_p\sigma^{3/2}g^{1/2}$ by

$$S = -\eta Eu'. \quad (18)$$

The expression for η in terms of N is

$$\eta = 2N/5\pi^{1/2}Fw, \quad (19)$$

and may be employed in equation (18) to show that the relation between the velocity gradient u' and the stress ratio S/N is

$$u' = -5\pi^{1/2}FSw/2EN. \quad (20)$$

Furthermore, by differentiating equation (17) with respect to y, we find that ν' is related to w' and N' through

$$\nu' = [N'/N - 2w'/w]/d\ln(\nu GF)/d\nu]. \quad (21)$$

The constitutive relations for q and Γ are obtained from equations (7) and (4) for **Q** and γ. If equation (19) for η is used to eliminate the viscosity from each, then the resulting dimensionless relations are

$$q = (2MN/\pi^{1/2}F)w', \quad (22)$$

and

$$\Gamma = 6(1-e)Nw/\pi^{1/2}F. \quad (23)$$

In what follows, we employ equations (20), (21), (22), and (23) to eliminate u', ν', q, and Γ wherever they occur.

The energy equation may be written explicitly in terms of w and its derivatives. We first employ expressions (22), (20), and (23) to eliminate q, u', and Γ from equation (16), and next employ expression (21) to eliminate ν' from the intermediate result. The final form of the energy equation is then

$$(w''/w) + [(1-2H)N'/N]\,(w'/w) + 4H(w'/w)^2 - \lambda^2 = 0, \quad (24)$$

where λ^2 is defined by

$$\lambda^2 = [6(1-e) - 5\pi F^2S^2/2EN^2]/2M, \quad (25)$$

and H is the function of solid fraction, defined by

$$2H = -[d\ln(M/F)/d\nu)]/[d\ln(\nu GF)/d\nu], \quad (26)$$

that appears in the two terms of equation (24) that arise when ν' is eliminated through equation (21). The magnitude of $2H$ is a measure of the importance of the transport contributions to the fluxes of momentum and energy. In Fig. 2, we show the variation of H with ν and find that as ν increases from 0 to 1, $2H$ decreases from 1 to 0.

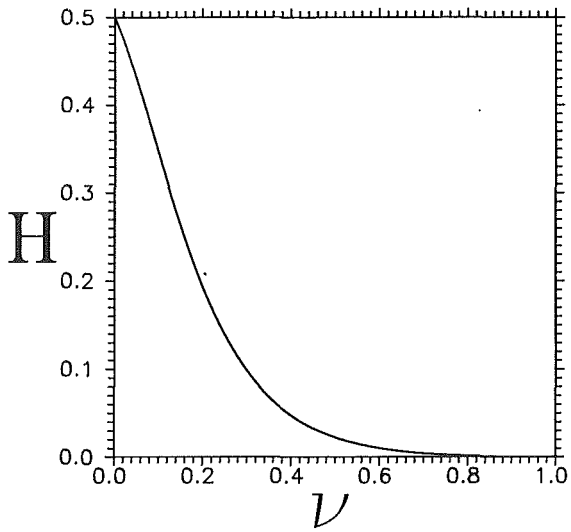


Fig. 2 The variation of H with ν

In principle, the mean fields $\nu(y)$, $u(y)$, and $w(y)$ and the variations of the stresses $S(y)$ and $N(y)$ are determined to within five constants of integration by equations (14), (15), (17), (20), and (24). The five constants and the dimensionless depth $\beta = L/\sigma$ are fixed by the normal stress, shear stress, and energy flux boundary conditions at the free surface ($y = 0$), the tangential momentum and energy flux boundary conditions at the base ($y = \beta$), and the mass flow rate.

In order to simplify the solution procedure, we replace ν by its depth-averaged value $\bar{\nu}$,

$$\bar{\nu} = (1/\beta)\int_0^\beta \nu dy, \quad (27)$$

wherever it occurs in the field equations (14), (15), and (24). Integrations of the momentum balances then yield the approximate stress variations,

$$S = y\bar{\nu}\sin\phi \text{ and } N = y\bar{\nu}\cos\phi, \quad (28)$$

in which we have ensured that the stresses vanish at the free surface. The energy balance becomes

Downloaded 03 May 2010 to 171.66.16.244. Redistribution subject to ASME license or copyright; see http://www.asme.org/terms/Terms_Use.cfm

$$(w''/w)+[(1-2H)/y](w'/w)+4H(w'/w)^2-\lambda^2=0, \quad (29)$$

in which H and λ are evaluated at $\bar{\nu}$. Equation (29) is a Riccati equation for w'/w, which is equivalent to a modified Bessel equation of order H for the variation of w^{1+4}/y^H with $\lambda(1+4H)^{1/2}y$. The solution of equation (29) subjected to the conditions that w' and therefore the energy flux vanish at the free surface is then,

$$w=A[y^H I_{-H}(ky)]^{\frac{1}{1+4H}}, \quad (30)$$

where I_{-H} is the modified Bessel function of order $-H$, k^2 is equal to $(1+4H)\lambda^2$, and A is a positive constant to be determined. Equation (30) applies when λ^2 is positive. In this case, the rate per unit volume at which energy is dissipated due to inelastic collisions between flow particles is greater than the rate at which energy is supplied to the flow by gravity. If the average solid fraction, $\bar{\nu}$, the angle of inclination, ϕ, and the coefficient of restitution, e, assume values for which λ^2 is negative, then the rate per unit volume at which energy is dissipated is less than the rate at which energy is supplied, and the corresponding solution for w is

$$w=A[y^H J_{-H}(Ky)]^{\frac{1}{1+4H}}, \quad (31)$$

where J_{-H} is the Bessel function of order $-H$, and K^2 is equal to $-(1+4H)\lambda^2$. According to equations (30) and (31), the granular temperature is nonzero at $y=0$ and either increases monotonically if λ^2 is positive or decreases monotonically if λ^2 is negative as y increases toward β.

With $w(y)$ known and when $\nu(y)$ is determined, equation (20) for u' may be integrated to yield the velocity profile,

$$u=v+\frac{5\pi^{1/2}S}{2N}\int_y^\beta \frac{F}{E}w(\xi)d\xi. \quad (32)$$

Here, the slip velocity v is equal to the velocity $u(\beta)$ at the base of the incline, and w is given by either expression (30) if λ^2 is positive or expression (31) if λ^2 is negative.

The remaining unknown constants are the dimensionless depth, β, the coefficient, A, and the slip velocity, v. The remaining boundary conditions are the momentum balance (8) and the energy balance (9) at the base of the incline. In these, we employ expressions (10) and (11) for D and the components of $\mathbf{M}$. Because v_2, I_{221}, and I_{21} all vanish, M_2 reduces to $\rho\chi T$ and the x_2-component of condition (8) has the simple dimensionless form

$$N=\nu\chi w^2. \quad (33)$$

With N also given by equation (17) and $\chi(\nu)$ equal to $4GF$, the normal stress boundary condition does not restrict the solid fraction at the base of the incline. In the expression for M_1, we employ equations (33), (20), (12), and (13) to eliminate, respectively, χ, u', I_{11}, and I_{121}. The x_1-component of condition (8) then yields

$$\frac{v}{w}=\sqrt{\frac{\pi}{2}\frac{S}{N}}f, \quad (34)$$

in which the dependence of f on boundary geometry and average solid fraction is given by

$$f=\frac{1-(5\bar{\nu}F/2^{3/2}\sigma E)(1+\sigma B/\bar{\nu})\sin^2\theta}{(2/3)[2\csc^2\theta(1-\cos\theta)-\cos\theta]}+\frac{5\bar{\nu}F}{\sqrt{2\sigma E}}. \quad (35)$$

From the energy flux condition (9), we eliminate the slip velocity, the factor χ, and the energy flux through equations (34), (33), and (22). In this manner, we find that at the base of the incline,

$$w'/w=b, \quad (36)$$

where b depends on boundary geometry and average solid fraction according to

$$b=(F/M\sqrt{2})[\pi(S/N)^2 f/2-2(1-e_w)(1.-\cos\theta)\csc^2\theta]. \quad (37)$$

The two terms on the right-hand side of equation (37) are the dimensionless measures of the slip work $\mathbf{M}\cdot\mathbf{v}$ and the boundary dissipation D. Consequently, the boundary supplies fluctuation energy to the flow when b is positive and absorbs energy when b is negative.

With the appropriate expression (30) or (31) for w, the energy flux boundary condition (36) becomes

$$I_{-H+1}(k\beta)/I_{-H}(k\beta)=(1+4H)b/k \quad (38)$$

when λ^2 is positive, or

$$J_{-H+1}(K\beta)/J_{-H}(K\beta)=-(1+4H)b/K \quad (39)$$

when λ^2 is negative. For fixed values of $\bar{\nu}$, e, e_w, r, and Δ, equations (38) and (39) determine the variation of dimensionless depth β with angle of inclination ϕ, and the range of angles ϕ for which steady flows are possible. The rate per unit area at which energy is transferred from the boundary to the flow determines the rate at which energy may be gained or lost throughout the entire flow. This in turn fixes the total volume and therefore the depth of flow. Equation (38) indicates that the boundary must supply energy ($b>0$) when the rate per unit volume at which energy is dissipated due to inelastic collisions between flow particles exceeds the rate per unit volume at which energy is supplied to the flow by gravity. Equation (39) indicates that the boundary must absorb energy ($b<0$) when the rate of energy dissipated within the flow is exceeded by the rate of energy supplied.

For fixed values of $\bar{\nu}$, e, e_w, r, Δ, and ϕ, the depth β is determined by either condition (38) or (39) and $w(y)$ is known to within the factor A. With $N(y)$ approximated by the variation (28), $w(y)$ given by either solution (30) or (31), and an initial guess made for A, constitutive relation (17) determines $\nu(y)$. The initial guess for A is then adjusted until $\bar{\nu}$ calculated according to its definition (27) agrees with its prescribed value. With $w(y)$ and $\nu(y)$ known completely, v is fixed by condition (34) and $u(y)$ is calculated according to equation (32).

When the mass flow rate, rather than the average solid fraction, is prescribed, the solution procedure is somewhat more complicated. For a given value of the dimensionless mass flow rate $\dot{m}$, defined by

$$\dot{m}=\int_0^\beta \nu u dy, \quad (40)$$

we guess at the corresponding value of $\bar{\nu}$, carry out the solution procedure described above, and iterate on $\bar{\nu}$ until $\dot{m}$ calculated according to its definition (40) agrees with its prescribed value. In this manner, the flow rate determines the average solid fraction and, in turn, the measure of free surface temperature A.

For fixed values of e, e_w, r, and Δ, equation (40) and either equation (38) or (39) are the two relations that must be satisfied by the four parameters ϕ, $\dot{m}$, $\bar{\nu}$, and β. The profiles $w(y)$, $\nu(y)$, and $u(y)$ are completely determined when any two of the four parameters are prescribed. In a typical experiment, for example, the parameters ϕ and $\dot{m}$ are controllable. With these fixed, measurements may be taken to determine $w(y)$, $\nu(y)$, $u(y)$, $\bar{\nu}$, and β.

Results and Discussion

In order to interpret further equations (38) and (39), we define ϕ_0, determined by $\tan^2\phi_0=12E(1-e)/5\pi F^2$, as the value of ϕ for which λ^2, k^2, and K^2 all vanish. "I-solutions" for w, given by equation (30), apply only when ϕ is less than ϕ_0 and

Downloaded 03 May 2010 to 171.66.16.244. Redistribution subject to ASME license or copyright; see http://www.asme.org/terms/Terms_Use.cfm

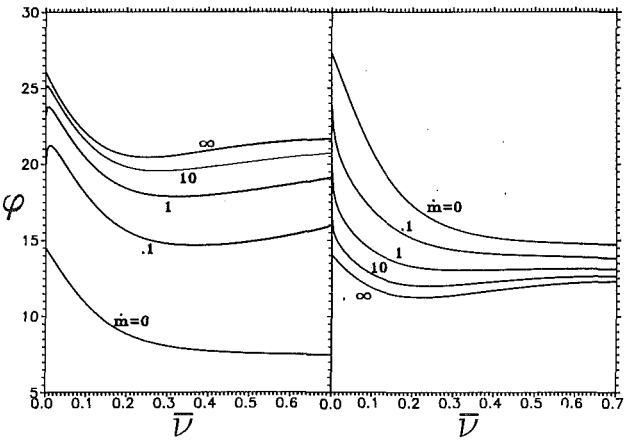


Fig. 3 The variations of ϕ (in degrees) with $\bar{\nu}$ when $\dot{m}=0$, .1, 1, 10, and ∞ for $e=.8$ and $e_w=.95$ (left panel); and $e=.95$ and $e_w=.8$ (right)—here $r=1/2$ and $\Delta=-1+\sqrt{2}$

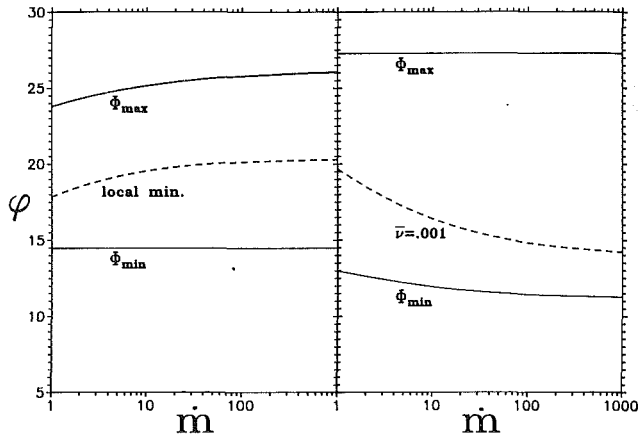


Fig. 4 The variations of Φ_{min} and Φ_{max} (in degrees) with $\dot{m}$ for $r=1$, $\Delta=-1+\sqrt{2}$ and $e=.8$ and $e_w=.95$ (left panel); and $e=.95$ and $e_w=.8$ (right)—dashed curves are the corresponding variations of the local minimum value of $\phi(\bar{\nu})$ (left panel) and the variations of $\phi(\bar{\nu}=.001)$ (right)

b (ϕ) is greater than zero. "J-solutions", given by equation (31), apply only when ϕ is greater than ϕ_0 and $b(\phi)$ is less than zero. Under all other circumstances no steady solutions are possible.

Moreover, as ϕ increases from zero, $b(\phi)$ increases monotonically from a negative value,

$$b(\phi=0)=-(\sqrt{2}F/M)(1-e_w)(1-\cos\theta)\csc^2\theta, \qquad (41)$$

and eventually assumes positive values that become unbounded as ϕ approaches $\pi/2$. Consequently, if $b(\phi=\phi_0)$, given by

$$b(\phi=\phi_0)=\sqrt{2}F[3E(1-e)f/5F^2 - (1-e_w)(1-\cos\theta)\csc^2\theta]/M \qquad (42)$$

is positive, then only I-solutions for w are possible, and if b ($\phi=\phi_0$) is negative then only J-solutions are possible.

Because the ratio of the modified Bessel functions in equation (38) varies between 0 when $k\beta$ is equal to 0, and 1 when $k\beta$ becomes large, the minimum angle ϕ_{min} and the maximum angle ϕ_{max} for which I-solutions are possible are, respectively, those values of ϕ for which $b=0$ and $(1+4H)b=k$. For fixed values of $\bar{\nu}$, the depth β increases monotonically from zero when ϕ is equal to ϕ_{min}, and becomes unbounded as ϕ approaches ϕ_{max}. For the J-solutions, we restrict attention to values of $K\beta$ that guarantee positive temperatures throughout the flow. In this range $J_{-H+1}(K\beta)$ has no zeroes other than $K\beta=0$, and the ratio from Bessel functions in equation (31) increases monotonically from zero when $K\beta$ is equal to zero until it becomes unbounded as $K\beta$ approaches the first zero of $J_{-H}(K\beta)$. The minimum and maximum angles for which J-solutions are possible are, respectively, the angle $\phi_{min}=\phi_0$ for which $K^2=0$ and the angle ϕ_{max} for which $b=0$. For fixed values of $\bar{\nu}$, the depth β increases monotonically from zero when ϕ is equal to ϕ_{max}, and becomes unbounded as ϕ decreases to ϕ_{min}.

Associated with every set of values for e, e_w, r, Δ, and $\bar{\nu}$ are the angles ϕ_{min} and ϕ_{max} between which steady flows are possible and for every angle ϕ between ϕ_{min} and ϕ_{max} there corresponds a fixed flow rate $\dot{m}$. In Fig. 3 the variations of ϕ with $\bar{\nu}$ for $\dot{m}=0$, .1, 1, 10, and ∞ are shown for two cases: $e=.8$ and $e_w=.95$; and $e=.95$ and $e_w=.8$. Here and in all figures that follow we have taken r equal to 1/2 and Δ equal to $-1+\sqrt{2}$. In the first case, w is given only by I-solutions over the full range of $\bar{\nu}$, and in the second case, w is given only by J-solutions. The depth β and therefore the flow rate $\dot{m}$ increase monotonically from 0 and become unbounded either when ϕ varies from ϕ_{min} to ϕ_{max} and an I-solution for w applies or when ϕ varies from ϕ_{max} to ϕ_{min} and a J-solution applies. In the Appendix we show that for all finite flow rates, as $\bar{\nu}$ approaches zero, steady flows are possible only if ϕ approaches ϕ_{min} ($\bar{\nu}=0$) when I-solutions apply or $\phi_{max}(\bar{\nu}=0)$ when J-solutions apply.

Figure 3 demonstrates the difference between the range $\phi_{min}<\phi<\phi_{max}$ of angles within which steady flows are possible for any prescribed value of $\bar{\nu}$ and the range $\Phi_{min}<\phi<\Phi_{max}$ within which steady flows are possible for any prescribed value of $\dot{m}$. In Fig. 4 the variations of Φ_{min} and Φ_{max} with $\dot{m}$ between 1 and 1000 are shown for two cases: $e=.8$ and $e_w=.95$; and $e=.95$ and $e_w=.8$. We have omitted results for values of $\dot{m}$ that are less than 1, because for these flow rates the theory predicts flow depths that are typically less than two particle diameters. In the first case Φ_{min} is equal to ϕ_{min} ($\bar{\nu}=0$) and in the second case Φ_{max} is equal to $\phi_{max}(\bar{\nu}=0)$. Based upon the variations of Φ_{min} and Φ_{max} with $\dot{m}$ we find that, depending upon the angle of inclination and because of its effect on the energetics within the flow and at the base, steady flows may be possible for all flow rates, no flow rates, or those flow rates above a critical value. In the first panel of Fig. 4, the dashed curve gives the angles that are local minima in the variations of ϕ with $\bar{\nu}$ for fixed values of $\dot{m}$ (see Fig. 3). The area between this curve and $\Phi_{min}(\dot{m})$ corresponds to circumstances under which steady flows occur only when $\bar{\nu}$ is less than 5×10^{-6}. We anticipate, therefore, that for values of $\dot{m}$ between 1 and 1000 the dashed curve and $\Phi_{max}(\dot{m})$ give the range of angles between which steady flows are physically realizable. The dashed curve also indicates that there are angles for which steady flows are physically possible only if the flow rate is below a critical value. In the second panel of Fig. 4, the dashed curve described the dependence of ϕ on $\dot{m}$ for $\bar{\nu}=.001$. The area between the dashed curve and $\Phi_{max}(\dot{m})$ corresponds to circumstances under which steady flows may be sustained only when $\bar{\nu}$ is less than .001. It is likely, then, that steady flows can be achieved only at angles and flow rates included in the area between $\Phi_{min}(\dot{m})$ and the dashed curve.

Equations (38) and (39) demonstrate that β is a single-valued function of ϕ for fixed values of $\bar{\nu}$. However, Fig. 3 demonstrates that $\bar{\nu}$ is a multivalued function of ϕ for high enough values of $\dot{m}$. Consequently, for a given angle of inclination and flow rate, there may be more than one possible steady flow depth. In Fig. 5, the variations of β with ϕ for $\dot{m}=10$, 50, and 250 are shown as solid curves for two cases: $e=.8$ and $e_w=.95$; and $e=.95$ and $e_w=.8$. The corresponding variations of $\bar{\nu}$, restricted between .001 and .7, are shown as dashed curves. Near the lowest inclinations two flows are physically possible. One is a relatively dilute flow that becomes deeper and more dilute as the inclination increases to its maximum value. The other is a relatively dense flow that becomes more

Downloaded 03 May 2010 to 171.66.16.244. Redistribution subject to ASME license or copyright; see http://www.asme.org/terms/Terms_Use.cfm

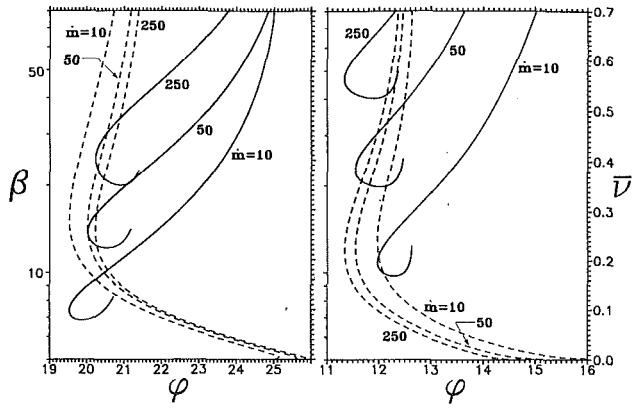


Fig. 5 The variations of β (solid curves) and $\bar{\nu}$ (dashed curves) with ϕ (in degrees) when $\dot{m} = 10$, 50, and 250 for $e = .8$ and $e_w = .95$ (left panel); and $e = .95$ and $e_w = .8$ (right)—here $r = 1/2$ and $\Delta = -1 + \sqrt{2}$

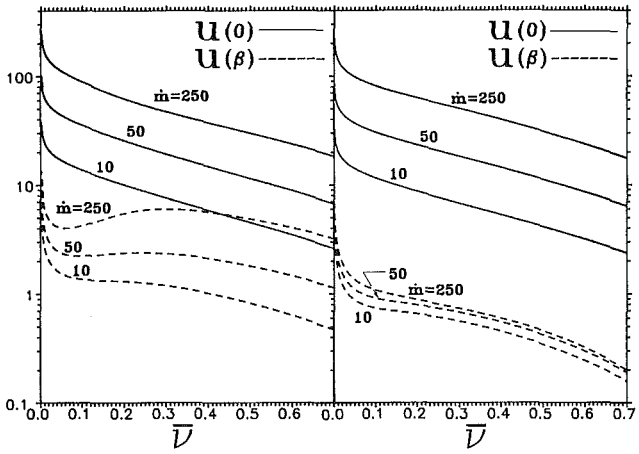


Fig. 6 The variations of $u(0)$ (solid curves) and $u(\beta)$ (dashed curves) when $\dot{m} = 10$, 50, and 250 for $e = .8$ and $e_w = .95$ (left panel); and $e = .95$ and $e_w = .8$ (right)—here $r = 1/2$ and $\Delta = -1 + \sqrt{2}$

dense as the inclination increases until, at an angle that is considerably lower than the maximum, the material can no longer be sheared.

In Fig. 6, the variations of the free surface velocity $u(0)$ and the slip velocity $u(\beta)$ with $\bar{\nu}$ when $\dot{m} = 10$, 50, and 250 are shown for $e = .8$ and $e_w = .95$, and for $e = .95$ and $e_w = .8$. The corresponding variations of the free surface temperature $w(0)$ and the basal temperature $w(\beta)$ are shown in Fig. 7. Typical velocities and temperatures increase with decreasing average solid fraction. For the relatively dilute flows of Fig. 5 this means that characteristic flow velocities and temperatures increase with increasing inclinations, as might be expected. However, the velocities and temperatures of the relatively dense flows actually decrease with increasing inclinations. Figure 7 also demonstrates that the free surface temperature is less than the basal temperature when w is given by an I-solution and is greater than the basal temperature when w is given by a J-solution.

Profiles of temperature, solid fraction, and velocity for $\dot{m} = 50$ are shown in Fig. 8 when $e = .8$ and $e_w = .95$ and in Fig. 9 when $e = .95$ and $e_w = .8$. In the first case, we plot the profiles corresponding to three inclinations: the minimum angle $\phi = 20.0$ deg which admits one possible flow (with $\bar{\nu} = .27$); an intermediate angle of $\phi = 20.7$ deg, which admits both a dilute ($\bar{\nu} = .16$) and a dense ($\bar{\nu} = .50$) flow; and a final angle $\phi = 21.8$ deg, which admits only a dilute flow ($\bar{\nu} = .10$). Similarly, in the second case profiles are shown for the minimum angle $\phi = 11.5$ deg, for which $\bar{\nu} = .22$; an intermediate angle $\phi = 12.2$

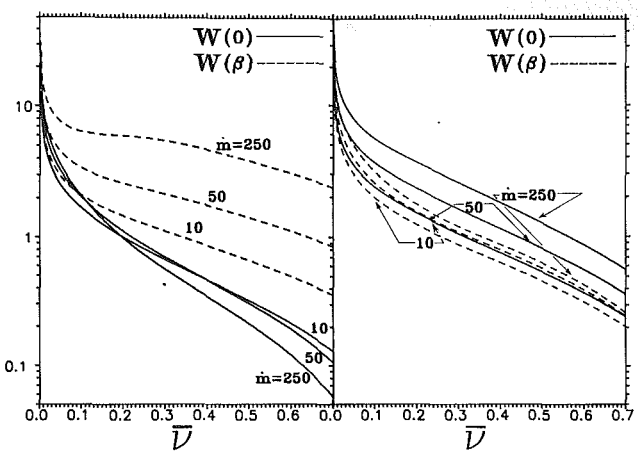


Fig. 7 The variatons of $w(0)$ (solid curves) and $w(\beta)$ (dashed curves) when $\dot{m} = 10$, 50, and 250 for $e = .8$ and $e_w = .95$ (left panel); and $e = .95$ and $e_w = .8$ (right)—here $r = 1/2$ and $\Delta = -1 + \sqrt{2}$

deg, for which $\bar{\nu} = .10$ or .50; and a final angle $\phi = 12.9$ deg, for which $\bar{\nu} = .06$. In all cases the temperature is nonzero at the free surface. In order to satisfy the stress-free condition there, both the solid fraction and velocity gradient must vanish. The qualitative differences between the solid fraction profiles of Fig. 8 and those of Fig. 9 are due to corresponding differences between I- and J-solutions for w. Only when $8\nu GFww'$ is greater than N', for example, will ν decrease with increasing distance from the free surface. Consequently, only when w is given by an I-solution is it possible for ν to reach a maximum other than at the base.

The stress-free boundary condition could also be satisfied by requiring that the temperature vanish at the free surface. In this case, w would be given by expressions analogous to equations (30) and (31) involving Bessel functions of positive order H. However, as y approaches zero, the gradient w' becomes unbounded at a rate that would exceed the rate at which w^2 vanishes. Consequently, the energy flux, which is proportional to w^2w', would not vanish at the free surface.

Conclusion

We have employed a kinetic theory to analyze steady, fully developed, gravity-driven, free surface flows of identical, smooth, inelastic spheres down roughened inclines. It was necessary to include, in the constitutive theory, the transport contributions to the stress and energy flux because even relatively dense flows contain a region near the free surface in which the solid fraction is small. For this reason, and because the normal stress within the flow varies with distance from the free surface, the solid fraction could not be eliminated from the energy equation. We have accounted for these effects in the simplest manner by first employing equation (21) to write the gradient of solid fraction ν' in terms of N' and w' wherever it occurred in the energy equation, and then by replacing the solid fraction by its depth-averaged value wherever it occurred in the balance equations. Through the terms involving the function of solid fraction H, the energy equation (29) and the general solution procedure maintain sensitivity to the gradient of solid fraction even though ν is replaced by $\bar{\nu}$. In this way, we have obtained an analytic expression for the granular temperature, an algebraic relation satisfied by the solid fraction, and a simple numerical integration for the velocity. We have employed the resulting profiles to calculate, for either a fixed flow rate or average solid fraction, the range of angles between which steady flows are physically possible and, for angles within the range, the corresponding depths of flow. The solution procedure is

Downloaded 03 May 2010 to 171.66.16.244. Redistribution subject to ASME license or copyright; see http://www.asme.org/terms/Terms_Use.cfm

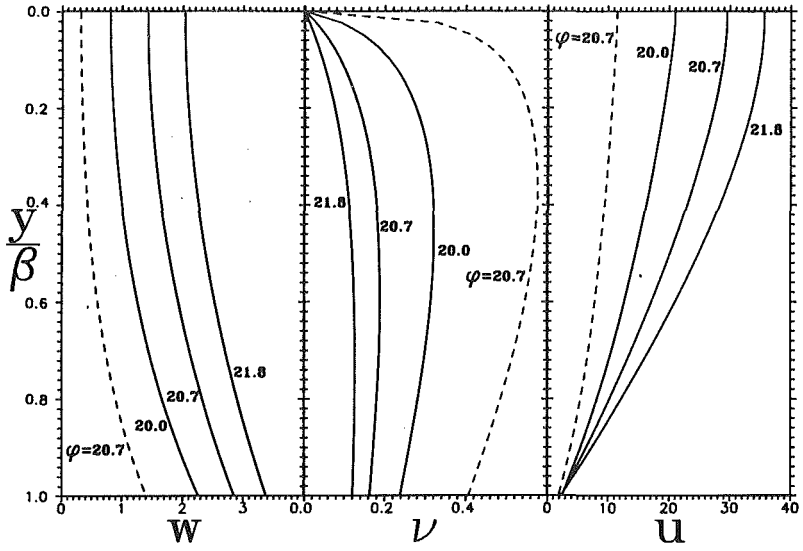


Fig. 8 The variations of w, ν, and u with y/β for $\phi = 20.0$ deg, 20.7 deg, and 21.8 deg when $e = .8$, $e_w = .95$, $\dot{m} = 50$, $r = 1/2$, and $\Delta = -1 + \sqrt{2}$

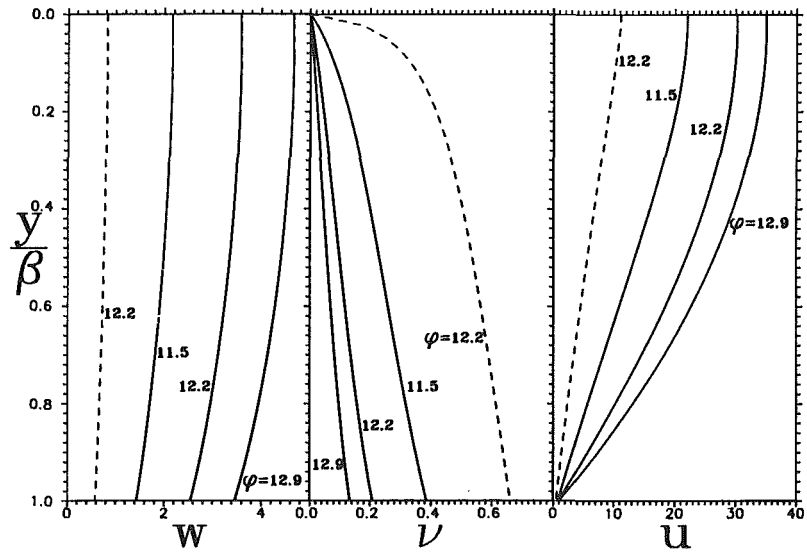


Fig. 9 The variations of w, ν, and u with y/β for $\phi = 11.5$ deg, 12.2 deg, and 12.9 deg when $e = .95$, $e_w = .8$, $\dot{m} = 50$, $r = 1/2$, and $\Delta = -1 + \sqrt{2}$

not computationally demanding and lends itself to simple physical interpretations.

We have focused special attention on the factors that determine the flow depth. The total rate at which energy is supplied by gravity and dissipated by collisions within the flow must be balanced by the rate at which energy is supplied by slipwork and dissipated by collisions at the boundary. For a given boundary and inclination, this balance may be satisfied by an infinite number of flows, each with its own depth and flow rate. Most striking are the inclinations at which two of these flows, each with different average solid fractions and characteristic velocities and temperatures, yield the same flow rate. At these inclinations, the flow rate does not uniquely determine the nature of the steady flow that might result. In particular, the theory predicts that both a relatively dilute, fast flow and a relatively dense, slow flow are possible. This result is consistent with the experimental results of Johnson and Jackson (1990), which demonstrated that at fixed inclinations and high enough flow rates, the flows that developed were either loosely or closely packed depending upon how the incline was loaded.

The first panel of Fig. 3 demonstrates that the lowest flow rate at which two steady solutions are possible increases with increasing angle. Furthermore, according to the dashed curve in the first panel of Fig. 4, when the boundary supplies energy to the flow there are inclinations at which no flows are physically possible beyond a critical flow rate. Moreover, we may infer from the first panel of Fig. 5 that for fixed inclinations, as the flow rate increases, the depths and average solid fractions of the relatively dilute flows increase. These features are in qualitative agreement with the experimental results of Johnson and Jackson (1990). For the most part, it is the details of the dense flows predicted here that do not agree with the observations of Johnson and Jackson (1990). At a given flow rate, for example, their dense flows were deeper than the corresponding dilute flows, whereas those predicted here were more shallow. However, such inconsistencies are not unexpected because we have not accounted for the effects of enduring

Downloaded 03 May 2010 to 171.66.16.244. Redistribution subject to ASME license or copyright; see http://www.asme.org/terms/Terms_Use.cfm

contacts between grains that are significant in the closely packed flows observed.

Acknowledgments

The authors would like to thank the National Science Foundation for its support of this work through Grant MSM-8707911. The authors are also grateful to Jim Jenkins of Cornell University and Les Schaffer of the University of London for several insightful conversations and John Lamach of Worcester Polytechnic Institute for his efforts in the early stages of this work.

References

Ahmadi, G., and Shahinpoor, M., 1983, "A Kinetic Model for Rapid Flows of Granular Materials," *Int. J. Non-Lin. Mech.*, Vol. 19, pp. 177–186.

Augenstein, D. A., and Hogg, R., 1978, "An Experimental Study of Dry Powders on Inclined Surfaces," *Powder Technology*, Vol. 19, pp. 205–215.

Bagnold, R. A., 1954, "Experiments on a Gravity-Free Dispersion of Large Solid Spheres in a Newtonian Fluid Under Shear," *Proc. R. Soc., London*, Vol. A255, pp. 49–63.

Campbell, C. S., and Brennen, C. E., 1985, "Chute Flows of Granular Material: Some Numerical Simulations," ASME JOURNAL OF APPLIED MECHANICS, Vol. 172, pp. 172–178.

Campbell, C. S., Brennen, C. E., and Sabersky, R. H. 1985, "Flow Regimes in Inclined Open-Channel Flows of Granular Materials," *Powder Technology*, Vol. 41, pp. 77–82.

Goodman, M. A., and Cowin, S. C., 1971, "Two Problems in Gravity Flow of Granular Materials," *J. Fluid Mech.*, Vol. 45, pp. 321–339.

Hungr, O., and Morgenstern, N. R., 1984, "Experiments on the Flow Behaviour of Granular Materials at High Velocity in an Open Channel," *Geotechnique*, Vol. 34, pp. 405–413.

Hutter, K., Szidarovsky, F., and Yakowitz, S., 1968a, "Plane Steady Shear Flow of a Cohesionless Granular Material Down an Inclined Plane. A Model for Flow Avalanches Part I: Theory," *Acta Mechanica*, Vol. 63, pp. 87–112.

Hutter, K., Szidarovksy, F., and Yakowitz, S., 1986b, "Plane Steady Shear Flow of Cohesionless Granular Material Down an Inclined Plane. A Model for Flow Avalanches Part II: Numerical Results," *Acta Mechanica*, Vol. 65, pp. 239–261.

Ishida, M., and Shira, T., 1979, "Velocity Distributions in the Flow of Solid Particles in an Inclined Open Channel," *J. Chem. Eng. of Japan*, Vol. 12, pp. 46–50.

Jenkins, J. T., and Richman, M. W., 1985, "Grad's 13-Moment System for a Dense Gas of Inelastic Spheres," *Arch. Rat. Mech.*, Vol. 87, pp. 355–377.

Jenkins, J. T., and Savage, S. B., 1983, "A Theory for the Rapid Flow of Identical Smooth, Nearly Elastic Particles," *J. Fluid Mech.*, Vol. 130, pp. 187–202.

Johnson, P. C., and Jackson, R., 1990, "Frictional-Collisional Equations of Motion for Particulate Flows and their Applications to Chutes," *J. Fluid Mech.*, in press.

Ma, D., and Ahmadi, G., 1985, "A Turbulence Model for Rapid Flows of Granular Materials Part II. Simple Shear Flows," *Powder Technology*, Vol. 44, pp. 269–279.

McTigue, D. F., 1982, *A Nonlinear Constitutive Model for Granular Materials: Application to Gravity Flow*, Vol. 49, pp. 291–296.

Nunziato, J. W., Passman, S. L., and Thomas, J. R., 1980, "Gravitational Flows of Granular Materials with Incompressible Grains," *J. Rheology*, Vol. 24, pp. 395–420.

Ogawa, S., Umemura, A., and Oshima, N., 1980, "On the Equations of Fully Fluidized Granular Materials," *ZAMP*, Vol. 31, pp. 483–493.

Patton, J. S., Brennen, C. E., and Sabersky, R. H., 1987, "Shear Flows of Rapidly Flowing Granular Materials," ASME JOURNAL OF APPLIED MECHANICS, Vol. 54, pp. 801–805.

Richman, M. W., 1988, "Boundary Conditions Based Upon a Modified Maxwellian Velocity Distribution for Flows of Identical, Smooth, Nearly Elastic Spheres," *Acta Mechanica*, Vol. 75, pp. 227–240.

Ridgway, K., and Rupp, R., 1970, "Flow of Granular Materials Down Chutes," *Chem. Proc. Eng.*, Vol. 51, pp. 82–85.

Savage, S. B., 1979, "Gravity Flow of Cohesionless Granular Materials in Chutes and Channels," *J. Fluid Mech.*, Vol. 92, pp. 53–96.

Savage, S. B., 1982, "Granular Flows at High Shear Rates," *Proc. of Advanced Seminar on Dispersed Multiphase Flows*, Math. Res. Cen., University of Wisconsin, Academic Press, New York, pp. 339–358.

Sayed, M., and Savage, S. B., 1983, "Rapid Gravity Flow of Cohesionless Granular Materials Down Inclined Chutes," *ZAMP*, Vol. 34, pp. 81–100.

APPENDIX

We are concerned here with flows in which the average solid fraction approaches zero. In this limit the following approximations apply: λ^2 is given by equation (25) with $F^2/E = 48/25\pi$ and $1/M = 512\bar{\nu}^2/25\pi$; H approaches $1/2$ so that $k^2 = 3\lambda^2$ and $K^2 = -3\lambda^2$; and b is given by equation (37) with $F/M = 128\bar{\nu}/25\pi$ and

$$f = \frac{1-(1/2)\sin^2\theta}{(2/3)[2\csc^2\theta(1-\cos\theta)-\cos\theta]}. \tag{A1}$$

In terms of the normalized coordinate $z \equiv y/\beta$, w may be written as $\alpha\omega(z)$, where α is a constant and either

$$\omega(z) = \cosh^{1/3}(k\beta z), \tag{A2}$$

when the boundary supplies energy to the flow, or

$$\omega(z) = \cos^{1/3}(K\beta z), \tag{A3}$$

when the boundary absorbs energy. The corresponding energy flux conditions at $z = 1$ are, respectively,

$$k\beta = \tanh^{-1}(3b/k), \tag{A4}$$

or

$$K\beta = \tan^{-1}(-3b/K). \tag{A5}$$

From equation (17) with $4\nu GF = \nu$ and $N = y\bar{\nu}\cos\phi$, the solid fraction profile is

$$\nu(z) = \frac{(\bar{\nu}\beta\cos\phi)z}{\alpha^2\omega^2(z)}, \tag{A6}$$

which yields the proper value of $\bar{\nu}$ provided that

$$\alpha^2 = \beta\cos\phi\int_0^1 \frac{z\,dz}{\omega^2(z)}. \tag{A7}$$

From equation (32) with v given by condition (34), $F/E = 192\nu/25\pi$, and ν described by equation (A6), the velocity profile is

$$u(z) = \sqrt{\frac{\pi}{2}}\alpha\tan\phi\left[f\omega(z=1) + \frac{192\bar{\nu}\beta^2\cos\phi}{5\sqrt{2}\pi\alpha^2}\int_z^1 \frac{\zeta\,d\zeta}{\omega(\zeta)}\right]. \tag{A8}$$

Employing profiles (A6) and (A8), and noting from equation (A7) that α is proportional to $\beta^{1/2}$, we find that the flow rate,

$$\dot{m} = \beta\int_0^1 \nu(z)u(z)\,dz, \tag{A9}$$

is proportional to $\bar{\nu}\beta^{3/2}$. That is, for the flow rate to remain fixed as the average solid fraction approaches zero, β must become unbounded with $(\dot{m}/\bar{\nu})^{2/3}$. In the same limit, the coefficient α, and therefore u and w, will become unbounded with $(\dot{m}/\bar{\nu})^{1/3}$. Under these circumstances, the second term on the right-hand side of equation (A8) remains finite, and as a result the velocity throughout the flow is, at lowest order, equal to the slip velocity.

Energy balances (A4) or (A5) are satisfied as k or K vanish with $\bar{\nu}$, and either $k\beta$ and b/k or $K\beta$ and b/K vanish with $(\dot{m}^2\bar{\nu})^{1/3}$. Because b given by equation (37) involves a coefficient that is proportional to $\bar{\nu}$, $\tan^2\phi$ must approach $(4/\pi f)(1-e_w)(1-\cos\theta)\csc^2\theta$ in the same manner that $(\dot{m}^2\bar{\nu})^{1/3}$ approaches zero. This means that as $\bar{\nu}$ vanishes, nonzero flow rates can be maintained only if $\phi = \phi_{\min}(\bar{\nu} = 0)$ when the boundary supplies energy to the flow and only if $\phi = \phi_{\max}(\bar{\nu} = 0)$ when the boundary absorbs energy.

Downloaded 03 May 2010 to 171.66.16.244. Redistribution subject to ASME license or copyright; see http://www.asme.org/terms/Terms_Use.cfm

Flows Inside and Around a Vaporizing/Condensing Drop Translating in an Electric Field

H. D. Nguyen
Graduate Student.

J. N. Chung
Professor,
Mem. ASME

Department of Mechanical and Materials Engineering,
Washington State University
Pullman, WA 99164

The flow behavior inside and around a translating liquid drop that simultaneously experiences a large interfacial radial mass flux as a result of evaporation or condensation, and the influence of a uniform electric field is analyzed in this paper. The steady-state equations of continuity and momentum of both continuous and drop phases are transformed, by a perturbation technique, into a series of systems of linear partial differential equations which are then solved analytically. The flow structure and the drag force are computed to the first order in $\epsilon (= U_\infty R/\nu)$*, the perturbed parameter. Interfacial velocity profiles are represented by Legendre polynomials up to second order to accommodate the electric-field-induced shear stress. It is found that the presence of an electric field does not contribute to the total drag force, but greatly modifies the flow patterns. The droplet internal flow is dominated by the electric field such that the double loop Taylor flow appears at relatively high field strength. The outside flow is dominated by the interfacial mass flux and the recirculation zone only shows up for an evaporating drop under a negative electric field. The electric field also moves the dividing streamline toward to or away from the surface depending on the direction of the electric field and the velocity direction at the interface. Also the effects of an electric field on the flow field are more pronounced for a drop with outward interfacial mass flux because the electric field helps restore the strength of internal circulation weakened by the outward interfacial mass flux.*

I Introduction

The flow behavior around a liquid sphere has been one of the most interesting classical problems in fluid mechanics that have received a great deal of attention from engineers and scientists. Because of its practical implications, detailed knowledge of fluid-droplet interactions is necessary in modeling transport processes involving a direct contact between the fluid and the droplet. In the literature, a large number of investigations of flow over a spherical particle have been reported, among which the book by Clift et al. (1978) has been considered as an excellent source of useful information in this area.

Early theoretical studies on a fluid sphere are confined to creeping motion in an infinite medium. By setting the normal and shear stresses at both sides of the interface equal, both Hadamard (1911) and Rybczynski (1911) independently presented the exact analytical solutions for steady, axisymmetric flows inside and around a fluid sphere without interfacial mass transfer at low Reynolds numbers. Even though their result is of fundamental importance in the field of fluid mechanics of bubbles and drops, its applications are restricted to creeping regime where viscous actions are dominant. Sadhal and Ayyaswamy (1983) employed a perturbation technique to examine the effects of the nonlinear inertial terms arising in their study of flow generated by a combination of the slowly-translating motion of a liquid drop and its nonuniform radial velocity, resulting from condensation/evaporation at the drop surface, which is taken to be one order of magnitude larger than the former. Analysis of the motion about a spherical fluid particle beyond the creeping regime has been attempted by Chao (1962) who followed a boundary layer approach to investigate the flow field caused by the buoyancy-induced translation of a spherical gas bubble rising steadily at a high Reynold's number in a quiescent viscous liquid. Other class of treatment aiming at the solution of the Navier–Stokes equation includes the finite diference numerical method as applied in the investigation of a rain drop falling in air by gravitation (Woo and Hamielec, 1971; LeClair et al., 1972). In contrast, only limited success has been achieved with approximate methods based on Galerkin's formulation. In this method, the flow field is represented by an assumed trial function that is then forced to satisfy the boundary conditions and the governing equation in such a way that the residual is minimized (Hamielec and Johnson, 1962; Hamielec et al., 1963; and Nakano and Tien, 1967). The success of these methods

Contributed by the Applied Mechanics Division of THE AMERICAN SOCIETY OF MECHANICAL ENGINEERS for publication in the JOURNAL OF APPLIED MECHANICS.

Discussion on this paper should be addressed to the Technical Editor, Leon M. Keer, The Technological Institute, Northwestern University, Evanston, IL 60208, and will be accepted until two months after final publication of the paper itself in the JOURNAL OF APPLIED MECHANICS. Manuscript received and accepted by the Applied Mechanics Division, Sept. 25, 1988.

Copyright © 1990 by ASME
Downloaded 03 May 2010 to 171.66.16.244. Redistribution subject to ASME license or copyright; see http://www.asme.org/terms/Terms_Use.cfm

depends strongly on the form of the trial function chosen. In large-scale computations Oliver and Chung (1987) used a series truncation method, in that the stream function is expanded in the form of a series of Legendre functions in the angular coordinates so that the highly nonlinear governing equations are reduced to a set of ordinary differential equations whose solutions were obtained by a cubic finite element method.

Recently, there exists a growing interest in applying an electric field to enhance the rate of momentum and heat and mass transfer associated with droplets. To assess such a promise, it is necessary to understand the two-phase flow/electric-field interactions. The pioneering theoretical work on droplet electrohydrodynamics was credited to Taylor (1966) who studied the motion generated inside and outside a stationary drop under the influence of an electric field. His classical work was subsequently refined by researchers in an effort to explore the deformation of the drop during the transient period (Sozou, 1973). Further extensions have also been made by Chang and his co-workers for the case where Taylor flow was superimposed by a translational motion (Chang et al., 1982). The effects of the nonlinear convective acceleration term was later considered in a separate work of Chang and Berg (1983) by using a Galerkin's method.

For drops under an electric field, the published reports discussed thus far all have made a common assumption that the drop is not subjected to any interfacial mass transfer that would result in a non-negligible radial flow component. This is not particularly true for many processes under which the drop experiences a large evaporation/condensation velocity as dictated by the thermodynamics of the two-phase system. For these systems, the use of an electric field may result in an even larger interfacial radial velocity or modify the interfacial velocity profile due to the electro-convective enhancement. The preliminary study on heat and mass transfer indicated that the presence of the field would alter the temperature and concentration along the drop surface (Nguyen and Chung, 1989). These changes in interfacial mass flux, interfacial velocity profile, and flow patterns, markedly different from those with negligible interfacial mass flux (Chang et al., 1982), might affect the transport characteristics such as the flame shape and the combustion efficiency. Before an assessment of such speculations is made, it is beneficial to have a full understanding of this flow field. The current work is intended to bridge the classical work of Taylor (1966) and the recent work of Sadhal and Ayyaswamy (1983), and to exploit the enhancement mechanisms the electric field may induce during the transfer processes of a vaporizing/condensing drop.

II Mathematical Formulation

In our present formulation it is assumed that the Weber number, the ratio of the dynamic force to the surface-tension force, being low enough (≤ 10) for the droplet to maintain its sphericity at all times, the physical properties of the two phases are constant, and that the fluids possess Newtonian behaviors. With these assumptions, we now consider a fluid sphere of radius R, density $\hat{\rho}$, viscosity $\hat{\mu}$ experiencing a nonuniform radial velocity due to translational motion and traveling steadily at U_∞ in a quiescent fluid of density ρ, viscosity μ, and the two-phase system is subjected under the action of an electric field. In this paper, the field strength is assumed to be small enough to justify the removal of the electric-magnetic couplings. Also, the drop phase is required to have a small electrical relaxation time compared to that of the gas phase in order to keep the charge leakage minimum. A spherical coordinates system shown in Fig. 1, with the origin fixed at the center of the drop, is employed in this analysis. As usual, the governing equations for this two-phase system are the continuity and momentum equations written as

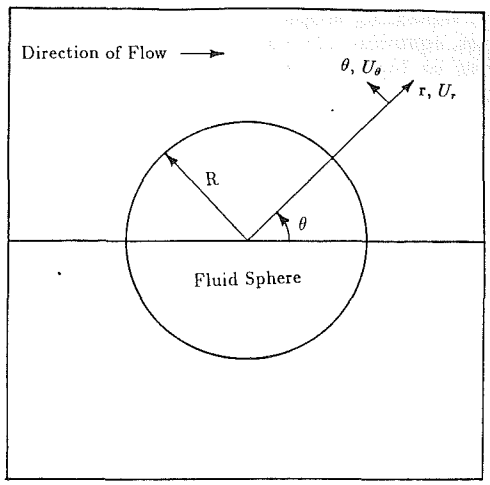


Fig. 1 Coordinate system

Continuity:

$$\nabla \cdot U = 0 \tag{1}$$

$$\nabla \cdot \hat{U} = 0. \tag{2}$$

Momentum:

$$\rho U \cdot \nabla U + \nabla \Pi = \mu \nabla^2 U \tag{3}$$

$$\hat{\rho} \hat{U} \cdot \nabla \hat{U} + \nabla \hat{\Pi} = \hat{\mu} \nabla^2 \hat{U}. \tag{4}$$

In the above, $U=(U_r,U_\theta)$ is the velocity vector and Π is the pressure. For completeness, the boundary conditions which must supplement the above system are the following:

At the free stream ($r \to \infty$):

$$U_r = U_\infty \cos\theta \tag{5}$$

$$U_\theta = -U_\infty \sin\theta. \tag{6}$$

At the interface ($r=R$):

$$U_r = A_0 + a_1(\theta) \tag{7}$$

$$\hat{U}_r = 0 \tag{8}$$

$$U_\theta = \hat{U}_\theta \tag{9}$$

$$\mathfrak{I}_{r\theta} - \hat{\mathfrak{I}}_{r\theta} = -\mathfrak{I}_{r\theta_e}. \tag{10}$$

At the origin ($r \to 0$):

$$\hat{U} \quad \text{is finite.} \tag{11}$$

In equation (7), the interfacial normal velocity of the drop is composed of two terms. The first term, A_0 a constant, represents the zeroth-order, large uniform, interfacial velocity determined by the prevailing thermodynamics of the system for an equivalent stationary drop. The term $a_1(\theta)$ is the interfacial normal velocity which is induced by the translational motion of the droplet and the motion generated by the electrical field. Since both are in the range of creeping motion, $a_1(\theta)$ is therefore one order of magnitude smaller than A_0, and is assumed a velocity variation of the type

$$a_1(\theta) = a_{01}P_0(\cos\theta) + a_{11}P_1(\cos\theta) + a_{21}P_2(\cos\theta) \tag{12}$$

where P_i is the Legendre polynomial of order i. In equation (12), the first term on the RHS is responsible for the first-order uniform normal velocity, the second is due to translational motion of the drop, and the third term is caused by the electric-field-generated motion. $a_1(\theta)$, without the third term, was adopted in the past (Hamielec et al., 1967); Sadhal and Ayyaswamy, 1983; Chung et al., 1984) for similar transport study in an electric-field-free environment. This paper is the first to study the interfacial velocity profile up to and including the second-order Legendre polynomial along with the effects of the electric field upon the fluid mechanics of a con-

Downloaded 03 May 2010 to 171.66.16.244. Redistribution subject to ASME license or copyright; see http://www.asme.org/terms/Terms_Use.cfm

densing/vaporizing droplet. For more complicated interfacial velocities, equation (12) may still be used by adding Legendre functions of higher order. Under those circumstances, the present analysis can still be extended in a straightforward manner. We also emphasize that though the drop motion is assumed to be in the creeping regime, the combined motion is not, and may well be non-Stokesian.

In the above equations, the liquid phase is distinguished from the gas phase by a "hat" ($\hat{}$). $\Im_{r\theta_e}$ is the tangential electrically-generated surface stress which, as a consequence of the accumulation of charged species at the drop surface, is produced from the interaction between the electric field and the surface charges.

III Method of Solution

First, the velocities and the pressures of both phases are written in the perturbed form consisting of two terms: the first is due to interfacial mass transport, while the second is due to droplet translation, i.e.,

$$U = U_0 + U', \quad \hat{U} = \hat{U}' \tag{13a,b}$$

$$\Pi = \Pi_0 + \Pi', \quad \hat{\Pi} = \hat{\Pi}'. \tag{14a,b}$$

In equation (13*a*), U_0 is the leading-order velocities and are assumed purely radial, and U' and $\hat{U}'$ are the corrections for the rectilinear motion of the drop with one order of magnitude smaller than the corresponding leading terms.

In order to work with a nondimensional system of governing equations, it is instructive to scale U_0 with A_0, U' and $\hat{U}'$ with U_∞. Thus the following dimensionless variables, denoted by superscript*, are introduced: $U_0^* = U_0/A_0$, $U'^* = U'/U_\infty$, $\hat{U}'^* = \hat{U}'/U_\infty$, $A_{01}P_0(\cos\theta) + A_{11}P_1(\cos\theta) + A_{21}P_2(\cos\theta) = \{a_{01}P_0(\cos\theta) + a_{11}P_1(\cos\theta) + a_{21}P_2(\cos\theta)\}/U_\infty$, $r^* = r/R$, $\epsilon = (U_\infty R)/\nu$, $A_{00} = A_0 R/\nu$, $\hat{A}_{00} = A_0 R/\hat{\nu}$, $\Phi_\mu = \mu/\hat{\mu}$, $\Pi_0^* = \Pi_0/(A_0\mu/R)$, $\Pi'^* = \Pi'/(U_\infty\mu/R)$, $\hat{\Pi}'^* = \hat{\Pi}'/(U_\infty\hat{\mu}/R)$, $\nabla^* = R\nabla$. For notational simplicity, the kinematic viscosity ν was used alternately with the dynamic viscosity μ in the above definitions. In terms of the newly defined variables, the velocities then become

$$U^* = A_{00}U_0^* + \epsilon U'^* \tag{15}$$

$$\hat{U}^* = \hat{\mathrm{Re}}\hat{U}'^* \tag{16}$$

where U^* and $\hat{U}^*$ are defined by the groups $(UR)/\nu$ and $(\hat{U}R)/\hat{\nu}$, respectively. $\hat{\mathrm{Re}} = U_\infty R/\hat{\nu}$ is the Reynolds number for the droplet phase. In a similar manner, the pressures may be scaled as $\Pi^* = (\Pi R^2)/(\nu\mu)$, and $\hat{\Pi}^* = (\hat{\Pi}R^2)/\hat{\nu}\hat{\mu}$ so that

$$\Pi^* = A_{00}\Pi_0^* + \epsilon\Pi'^* \tag{17}$$

$$\hat{\Pi}^* = \hat{\mathrm{Re}}\hat{\Pi}'^*. \tag{18}$$

Before substituting these quantities into the governing equations (1)–(4), a regular perturbation expansion scheme using the translating motion as the perturbed parameter is introduced

$$U'^* = U_1^* + \epsilon U_2^* + \epsilon^2 U_3^* + \ldots \tag{19}$$

$$\Pi'^* = \Pi_1^* + \epsilon\Pi_2^* + \epsilon^2\Pi_3^* + \ldots. \tag{20}$$

Equations (15)–(20) are now used to rewrite the continuity and momentum equations in terms of dimensionless variables. The results, with asterisks omitted, are

$$A_{00}\nabla\cdot U_0 + \epsilon\nabla\cdot U_1 + \ldots = 0 \tag{21}$$

$$\hat{\mathrm{Re}}\nabla\cdot\hat{U}' = 0 \tag{22}$$

$$[A_{00}^2 U_0\cdot\nabla U_0 + A_{00}\nabla\Pi_0] + \epsilon[A_{00}(U_0\cdot\nabla U_1 + U_1\cdot\nabla U_0) + \nabla\Pi_1] + \ldots = A_{00}\nabla^2 U_0 + \epsilon\nabla^2 U_1 + \ldots \tag{23}$$

$$\hat{\mathrm{Re}}\hat{U}'\cdot\nabla U' + \nabla\hat{\Pi}' = \nabla^2\hat{U}' \tag{24}$$

and the boundary constraints (5)–(11) are transformed as the following:

At the free-stream ($r\to\infty$):

$$A_{00}U_{0r} + \epsilon U_{1r} + \ldots = \epsilon\cos\theta \tag{25}$$

$$A_{00}U_{0\theta} + \epsilon U_{1\theta} + \ldots = -\epsilon\sin\theta. \tag{26}$$

At the interface ($r=1$):

$$A_{00}U_{0r} + \epsilon U_{1r} + \ldots = A_{00} + \epsilon[A_{01}P_0(\cos\theta) + A_{11}P_1(\cos\theta) + A_{21}P_2(\cos\theta)] \tag{27}$$

$$\hat{U}_r' = 0 \tag{28}$$

$$A_{00}U_{0\theta} + \epsilon U_{1\theta} + \ldots = \epsilon\hat{U}_\theta' \tag{29}$$

$$\Phi_\mu A_{00}\left[r\frac{\partial}{\partial r}\left(\frac{U_{0\theta}}{r}\right) + \frac{1}{r}\frac{\partial U_{0r}}{\partial\theta}\right] + \epsilon\left[\Phi_\mu\left(r\frac{\partial}{\partial r}\left(\frac{U_{1\theta}}{r}\right) + \frac{1}{r}\frac{\partial U_{1r}}{\partial\theta}\right) - \left(r\frac{\partial}{\partial r}\left(\frac{\hat{U}_\theta'}{r}\right) + \frac{1}{r}\frac{\partial\hat{U}_r'}{\partial\theta}\right)\right] = \frac{5}{4}\epsilon W\cos\theta\sin\theta. \tag{30}$$

At the origin ($r\to 0$):

$$\hat{U}_r' \text{ and } \hat{U}_\theta' \text{ are finite} \tag{31}$$

where W is defined as

$$W = \frac{4V_{cr}(1+\Phi_\mu)}{U_\infty} \tag{32}$$

and

$$V_{cr} = \frac{9\hat{\beta}\mathrm{RE}_0^2\left(1 - \dfrac{\beta\sigma}{\hat{\beta}\hat{\sigma}}\right)}{10\hat{\mu}(1+\Phi_\mu)\left(2+\dfrac{\sigma}{\hat{\sigma}}\right)^2}. \tag{33}$$

In the above equation, V_{cr} is the maximum speed generated by the electric field in the dispersed phase, σ and β are the electrical resistivity and electrical permittivity, respectively, and E_0 is the electric field strength. Careful examination of equation (33) indicates that the negative sign in the numerator results in two possible directions of internal circulation, either from the pole to the equator ($+V_{cr}$) or from the equator to the pole ($-V_{cr}$) depending on the physical properties of the two phases. Under normal circumstances, the gas-liquid system usually exhibits a $-V_{cr}$. However, there is situation where, in an attempt to increase the gas conductivity, the surrounding gas is seeded with metal powder it may result in $a + V_{cr}$. With W so defined in equation (32), it may be interpreted as the relative strength between the electric field-induced flow and the translational flow. The expression on the right-hand side of equation (30) represents the electrical stress, a derivation of which is given elsewhere (Taylor, 1966; Sozou, 1973).

Following the usual procedure in perturbation theory, all the terms of powers of ϵ on the left-hand side are equated to the corresponding terms on the right to yield systems of partial differential equations. For the leading order, ϵ^0, solutions to the following equations are needed

$$\nabla\cdot U_0 = 0 \tag{34}$$

$$A_{00}U_0\cdot\nabla U_0 + \nabla\Pi_0 = \nabla^2 U_0. \tag{35}$$

The same procedure is repeated on the boundary conditions to obtain

$$U_{0r} = 0 \quad \text{and} \quad U_{0\theta} = 0 \quad \text{at the free stream}$$

$$U_{0r} = 1 \quad \text{and} \quad U_{0\theta} = 0 \quad \text{at the interface.}$$

Since the zeroth order of the flow field was assumed purely radial, U_{0r} is the only nonzero velocity component. Owing to this special feature of the flow, equations (34) and (35) are no

Downloaded 03 May 2010 to 171.66.16.244. Redistribution subject to ASME license or copyright; see http://www.asme.org/terms/Terms_Use.cfm

longer coupled; hence, they may be integrated to give the velocity

$$U_{0r} = \frac{1}{r^2}. \tag{36}$$

Equating the coefficients of ϵ leads to the equations in the form

$$D^4\Psi_1 = A_{00}\frac{1}{r^2}\left(\frac{\partial}{\partial r} - \frac{2}{r}\right)D^2\Psi_1 \tag{37}$$

$$D^4\hat{\Psi} = \hat{\mathrm{Re}}\left[\frac{1}{r^2}\frac{\partial(\hat{\Psi}, D^2\hat{\Psi})}{\partial(r,\hat{\mu})} + \frac{2}{r^2}D^2\hat{\Psi} \times \left(\frac{\bar{\mu}}{1-\bar{\mu}^2}\frac{\partial\hat{\Psi}}{\partial r} + \frac{1}{r}\frac{\partial\hat{\Psi}}{\partial\bar{\mu}}\right)\right] \tag{38}$$

where $\bar{\mu} = \cos\theta$, $D^2 = \partial^2/\partial r^2 + 1 - \bar{\mu}^2/r^2\ \partial^2/\partial\bar{\mu}^2$, and $\partial(\ ,\ )/\partial(\ ,\ )$ is the usual notation representing the Jacobian. The boundary conditions now become:

At the free stream ($r \to \infty$):

$$\Psi_1 = \frac{1}{2}r^2(1-\bar{\mu}^2). \tag{39}$$

At the interface ($r = 1$):

$$-\frac{1}{r^2}\frac{\partial\Psi_1}{\partial\bar{\mu}} = A_{01}P_0(\bar{\mu}) + A_{11}P_1(\bar{\mu}) + A_{21}P_2(\bar{\mu}) \tag{40}$$

$$-\frac{1}{r^2}\frac{\partial\hat{\Psi}}{\partial\bar{\mu}} = 0 \tag{41}$$

$$\frac{\partial\Psi_1}{\partial r} = \frac{\partial\hat{\Psi}}{\partial r} \tag{42}$$

$$\Phi_\mu\left[-r\frac{\partial}{\partial r}\left(\frac{1}{r^2}\frac{\partial\Psi_1}{\partial r}\right) + \frac{1-\bar{\mu}^2}{r^3}\frac{\partial^2\Psi_1}{\partial\bar{\mu}^2}\right] - \left[-r\frac{\partial}{\partial r}\left(\frac{1}{r^2}\frac{\partial\hat{\Psi}}{\partial r}\right) + \frac{1-\bar{\mu}^2}{r^3}\frac{\partial^2\hat{\Psi}}{\partial\bar{\mu}^2}\right] = \frac{5}{4}W\bar{\mu}(1-\bar{\mu}^2). \tag{43}$$

At the origin ($r \to 0$):

$$\frac{1}{r^2}\hat{\Psi} \quad \text{is finite} \tag{44}$$

where Ψ_1 and $\hat{\Psi}$ are the stream functions defined in such a way that the continuity equations for first order in ϵ are satisfied identically. In mathematical notation, they are expressed as

$$U_{1r} = -\frac{1}{r^2}\frac{\partial\Psi_1}{\partial\bar{\mu}} \tag{45}$$

$$U_{1\theta} = -\frac{1}{r(1-\bar{\mu}^2)^{1/2}}\frac{\partial\Psi_1}{\partial r} \tag{46}$$

$$\hat{U}_r' = -\frac{1}{r^2}\frac{\partial\hat{\Psi}}{\partial\bar{\mu}} \tag{47}$$

$$\hat{U}_\theta' = -\frac{1}{r(1-\bar{\mu}^2)^{1/2}}\frac{\partial\hat{\Psi}}{\partial r}. \tag{48}$$

If the electric field is not present, equations (37)–(44) would be identical to the ones presented in the paper by Sadhal and Ayyaswamy (1983). The fact that the present study distinguishes itself from their work is the addition of an electrical force as appeared in the force balance on the drop surface. Because of the lack of the proper eigenfunctions needed to satisfy the boundary condition (43), their solutions are now modified to the following forms:

$$\Psi_1 = -A_{01}\bar{\mu} + \frac{1}{2}F(r)(1-\bar{\mu}^2) + F_e(r)(1-\bar{\mu}^2)\bar{\mu} \tag{49}$$

$$\hat{\Psi} = \frac{1}{2}G(r)(1-\bar{\mu}^2) + G_e(r)(1-\bar{\mu}^2)\bar{\mu} \tag{50}$$

where $F(r)$ and $G(r)$ are solutions for the case without an electric field and are given in the paper by Sadhal and Ayyaswamy (1983). These expressions, for convenience, are reproduced below. Further detail is discussed in the referred article.

$$F(r) = r^2 + \frac{B}{r} + C\left[\frac{A_{00}}{r}\int_{\frac{1}{A_{00}}}^{\frac{r}{A_{00}}}(\xi^4+\xi^3)e^{-\frac{1}{\xi}}d\xi - \frac{1}{5}\left(\frac{r}{A_{00}}\right)^4 + \frac{1}{6}\left(\frac{r}{A_{00}}\right)^2\right] \tag{51}$$

$$G(r) = \hat{B}(r^4 - r^2) \tag{52}$$

where the constants B, C, and $\hat{B}$ depend on the viscosity ratio of host fluid to liquid drop and the parameters characterizing the radial velocity at the drop surface,

$$B = \frac{(1-A_{11})\left[1 - \frac{1}{5}(3+2\Phi_\mu) - \left(1 + A_{00} - \frac{1}{3}\Phi_\mu A_{00}^2\right)e^{-A_{00}}\right] + 2A_{11}\left(-\frac{1}{5} + \frac{1}{6}A_{00}^2\right)}{-1 + \frac{1}{6}(3+2\Phi_\mu)A_{00}^2 + \left(1 + A_{00} - \frac{1}{3}\Phi_\mu A_{00}\right)e^{-A_{00}}} \tag{53}$$

$$C = \frac{-[(3+2\Phi_\mu) - A_{11}(1+2\Phi_\mu)]A_{00}^4}{-1 + \frac{1}{6}(3+2\Phi_\mu)A_{00}^2 + \left(1 + A_{00} - \frac{1}{3}\Phi_\mu A_{00}^2\right)e^{-A_{00}}} \tag{54}$$

$$\hat{B} = \frac{\Phi_\mu(1-A_{11})\left[1 + \frac{1}{3}A_{00}^2 - \left(1 + A_{00} + \frac{1}{6}A_{00}^2\right)e^{-A_{00}} + \frac{1}{3}A_{00}^2(1-e^{-A_{00}})\right]}{-1 + \frac{1}{6}(3+2\Phi_\mu)A_{00}^2 + \left(1 + A_{00} - \frac{1}{3}\Phi_\mu A_{00}^2\right)e^{-A_{00}}}. \tag{55}$$

In equations (49) and (50), the functions $F_e(r)$ and $G_e(r)$ are incorporated for modeling the presence of the electric field. Replacements of Ψ_1 and $\hat{\Psi}$ in equation (37) and the creeping version of equation (38) by equations (49) and (50), respectively, result in a pair of fourth-order linear ordinary differential equations

$$\left[\frac{d^2}{dr^2} - \frac{A_{00}}{r^2}\left(\frac{d}{dr} - \frac{2}{r}\right) - \frac{6}{r^2}\right]$$

Downloaded 03 May 2010 to 171.66.16.244. Redistribution subject to ASME license or copyright; see http://www.asme.org/terms/Terms_Use.cfm

$$\times\left[\frac{d^2}{dr^2}-\frac{6}{r^2}\right]F_e(r)=0 \tag{56}$$

$$\left[\frac{d^2}{dr^2}-\frac{6}{r^2}\right]^2 G_e(r)=0 \tag{57}$$

and the boundary conditions are:

$$F_e(r)=0 \quad @r\to\infty \tag{58}$$

$$\frac{dF_e}{dr}=\frac{dG_e}{dr} \quad @r=1 \tag{59}$$

$$F_e=\frac{A_{21}}{2} \quad \text{and } G_e=0 \quad @r=1 \tag{60a, b}$$

$$\Phi_\mu\left[-r\frac{d}{dr}\left(\frac{1}{r^2}\frac{dF_e}{dr}\right)-\frac{6F_e}{r^3}\right]$$

$$+\left[r\frac{d}{dr}\left(\frac{1}{r^2}\frac{dG_e}{dr}\right)+\frac{6G_e}{r^3}\right]=\frac{5}{4}W \quad @r=1 \tag{61}$$

$$G_e(r) \quad \text{is finite} \quad @r\to 0. \tag{62}$$

The general solutions to equations (56) and (57) can be found in closed forms by first applying the method of Frobenius to obtain one solution, then using the method of reduction of order to get the other solution. With the particular set of conditions (58)–(62), they become

$$F_e(r)=B_e\left(\frac{A_{00}}{r}\right)^2+C_e\left[\left(\frac{A_{00}}{r}\right)^2\int_{A_{00}}^{\frac{r}{A_{00}}}(12\xi^6+6\xi^5+\xi^4)e^{-\frac{1}{\xi}}d\xi-\frac{12}{7}\left(\frac{r}{A_{00}}\right)^5+\left(\frac{r}{A_{00}}\right)^4-\frac{1}{5}\left(\frac{r}{A_{00}}\right)^3\right] \tag{63}$$

$$G_e(r)=\hat{B}_e(r^5-r^3) \tag{64}$$

with the constants B_e, C_e, and $\hat{B}_e$ given as

$$B_e=\frac{A_{21}}{2A_{00}^2}+\frac{\left[\frac{5}{4}W+(8\Phi_\mu+5)A_{21}\right]\left[\frac{1}{5}A_{00}^2-A_{00}+\frac{12}{7}\right]}{A_{00}^2\Omega_e} \tag{65}$$

$$C_e=\frac{A_{00}^5\left[\frac{5}{4}W+(8\Phi_\mu+5)A_{21}\right]}{\Omega_e} \tag{66}$$

$$\hat{B}_e=-\frac{A_{21}}{2}+\frac{\left[\frac{5}{4}W+(8\Phi_\mu+5)A_{21}\right]\left[\left(\frac{A_{00}^2}{2}+3A_{00}+6\right)e^{-A_{00}}-\frac{A_{00}^2}{2}+3A_{00}-6\right]}{\Omega_e} \tag{67}$$

and the quantity, Ω_e, in the denominator is defined as

$$\Omega_e=-\Phi_\mu A_{00}^3e^{-A_{00}}+60(e^{-A_{00}}-1)$$

$$+(-6\Phi_\mu e^{-A_{00}}+30e^{-A_{00}}+6\Phi_\mu+30)A_{00}$$

$$+(-4\Phi_\mu e^{-A_{00}}+5e^{-A_{00}}-2\Phi_\mu-5)A_{00}^2. \tag{68}$$

In obtaining equation (63), the integral had been expanded asymptotically for large value of r. This was done by successive integration by parts and that all the terms leading to nonzero velocity in the far field were removed as required by the constraint equation (58). With the functions $F_e(r)$ and $G_e(r)$ known, the velocities of both phases may now be calculated from the definition of stream functions. After some differentiation, the results are:

$$U_r=\frac{A_{00}}{r^2}+\epsilon\left\{\frac{A_{01}}{r^2}+\left[1+\frac{B}{r^3}+\frac{C}{r^2}\right.\right.$$

$$\times\left(\frac{A_{00}}{r}\int_{A_{00}}^{\frac{r}{A_{00}}}(\xi^4+\xi^3)e^{-\frac{1}{\xi}}d\xi\right.$$

$$\left.-\frac{1}{5}\left(\frac{r}{A_{00}}\right)^4+\frac{1}{6}\left(\frac{r}{A_{00}}\right)^2\right)\Big]\cos\theta-\Big[\frac{B_e}{r^4}+\frac{C_e}{r^2}$$

$$\times\left(\left(\frac{A_{00}}{r}\right)^2\int_{A_{00}}^{\frac{r}{A_{00}}}(12\xi^6+6\xi^5+\xi^4)e^{-\frac{1}{\xi}}d\xi\right.$$

$$\left.\left.-\frac{12}{7}\left(\frac{r}{A_{00}}\right)^5+\left(\frac{r}{A_{00}}\right)^4-\frac{1}{5}\left(\frac{r}{A_{00}}\right)^3\right)\Big](1-3\cos^2\theta)\right\} \tag{69}$$

$$U_\theta=-\epsilon\left\{\left[1-\frac{B}{2r^3}+\frac{C}{2r^2}\left(-\frac{A_{00}}{r}\int_{A_{00}}^{\frac{r}{A_{00}}}(\xi^4+\xi^3)e^{-\frac{1}{\xi}}d\xi\right.\right.\right.$$

$$\left.+\left[\left(\frac{r}{A_{00}}\right)^4+\left(\frac{r}{A_{00}}\right)^3\right]e^{-\frac{A_{00}}{r}}-\frac{4}{5}\left(\frac{r}{A_{00}}\right)^4\right.$$

$$\left.\left.+\frac{1}{3}\left(\frac{r}{A_{00}}\right)^2\right)\Big]\sin\theta+\Big[-2\frac{B_e}{r^4}+\frac{C_e}{r^2}\right.$$

$$\times\left(-2\left(\frac{A_{00}}{r}\right)^2\int_{A_{00}}^{\frac{r}{A_{00}}}(12\xi^6+6\xi^5+\xi^4)e^{-\frac{1}{\xi}}d\xi\right.$$

$$\left.+\left[12\left(\frac{r}{A_{00}}\right)^5+6\left(\frac{r}{A_{00}}\right)^4+\left(\frac{r}{A_{00}}\right)^3\right]e^{-\frac{A_{00}}{r}}\right.$$

$$\left.\left.-\frac{60}{7}\left(\frac{r}{A_{00}}\right)^5+4\left(\frac{r}{A_{00}}\right)^4-\frac{3}{5}\left(\frac{r}{A_{00}}\right)^3\right)\Big]\sin\theta\cos\theta\right\} \tag{70}$$

$$\hat{U}_r=\hat{B}(r^2-1)\cos\theta-\hat{B}_e(r^3-r)(1-3\cos^2\theta) \tag{71}$$

$$\hat{U}_\theta=-\hat{B}(2r^2-1)\sin\theta+\hat{B}_e(5r^3-3r)\sin\theta\cos\theta. \tag{72}$$

Since all the parameters with subscript "e" are proportional to W and A_{21}, they all vanish in the limit W and A_{21} approaching zero; hence, the velocity components inside and outside the fluid sphere, without an external electric field, are recovered as would be expected (Sadhal and Ayyaswamy, 1983). In an electric-field-free environment, $W=0$, but with a

Downloaded 03 May 2010 to 171.66.16.244. Redistribution subject to ASME license or copyright; see http://www.asme.org/terms/Terms_Use.cfm

nonzero A_{21} in equation (27), the present results may be viewed as an extension of their work by adding more flexibility to the modeling of the interfacial velocity with second-order Legendre polynomials.

IV Drag Forces

A translating droplet with a radial mass efflux experiences a dynamic force on its surface as a result of three factors. First, viscous stresses due to viscosity and velocity gradients cause forces tangential to the surface. Second, asymmetrical pressure distribution due to dynamical effects creates a form drag on the fluid sphere. Third, the droplet also experiences another force due to interfacial momentum flux. Thus, the total dimensionless drag F_D, is merely equal to the sum of all three contributions:

$$F_D = F_\mu + F_\pi + F_m \tag{73}$$

in which each component has been nondimensionalized by $(\mu U_\infty R)$. The subscripts μ, π, and m denote the viscous, pressure, and momentum components, respectively. These forces can be calculated as follows:

$$F_\mu = \frac{2\pi}{\epsilon}\int_0^\pi \left\{2\frac{\partial U_r}{\partial r}\cos\theta\sin\theta - \left[r\frac{\partial}{\partial r}\left(\frac{U_\theta}{r}\right) + \frac{1}{r}\frac{\partial U_r}{\partial\theta}\right]\sin^2\theta\right\}\Big|_{r=1} d\theta$$

$$= \frac{4}{3}\pi C\left\{\left(\frac{2}{A_{00}^4}+\frac{2}{A_{00}^3}+\frac{1}{A_{00}^2}\right)e^{-A_{00}} - \frac{2}{A_{00}^4}\right\}. \tag{74}$$

To calculate the pressure drag, the pressure distribution is integrated from the momentum equation. It should be noted that the leading order pressure, Π_0, makes no contribution to the drag; hence, only Π_1 is needed in the calculation. The θ-component of the momentum equation for the first order in ϵ may be extracted from equation (23) to yield

$$\frac{1}{r}\frac{\partial\Pi_1}{\partial\theta} = \left(E^2 U_{1\theta} + \frac{2}{r^2}\frac{\partial U_{1r}}{\partial\theta} - \frac{U_{1\theta}}{r^2\sin^2\theta}\right) - \frac{A_{00}}{r^3}\left(\frac{\partial U_{1\theta}}{\partial r}+\frac{U_{1\theta}}{r}\right) \tag{75}$$

and the operator, E^2, is defined as

$$E^2 = \frac{1}{r^2}\left[\frac{\partial}{\partial r}\left(r^2\frac{\partial}{\partial r}\right)+\frac{1}{\sin\theta}\frac{\partial}{\partial\theta}\left(\sin\theta\frac{\partial}{\partial\theta}\right)\right]. \tag{76}$$

Integration of equation (75), with respect to θ, leads to

$$\Pi_1(r=1) = \epsilon\left\{\left[-A_{00}A_{11} + C\left(\left(\frac{2}{A_{00}^4}+\frac{1}{A_{00}^3}\right)e^{-A_{00}} - \frac{2}{A_{00}^4}+\frac{1}{A_{00}^3}\right)\right]\cos\theta + \left[-3B_e A_{00} + C_e\left(\left(\frac{36}{A_{00}^5} + \frac{18}{A_{00}^4}+\frac{3}{A_{00}^3}\right)e^{-A_{00}} - \frac{36}{A_{00}^5}+\frac{162}{7A_{00}^4} - \frac{6}{A_{00}^3} + \frac{3}{5A_{00}^2}\right)\right]\cos^2\theta\right\} \tag{77}$$

and the constant of integration—the reference pressure—is taken to be zero, since it does not contribute to net drag when integrating over the surface. The dimensionless pressure drag is now computed to give

$$F_\pi = \frac{2\pi}{\epsilon}\int_0^\pi -\Pi_1(r=1)\cos\theta\sin\theta d\theta$$

$$= \frac{4}{3}\pi\left\{A_{00}A_{11} - C\left[\left(\frac{2}{A_{00}^4}+\frac{1}{A_{00}^3}\right)e^{-A_{00}} - \frac{2}{A_{00}^4}+\frac{1}{A_{00}^3}\right]\right\}. \tag{78}$$

The drag due to momentum flux at the interface can be found from the following equation:

$$F_m = \frac{2\pi}{\epsilon}\int_0^\pi -(U_r U_r\cos\theta - U_r U_\theta\sin\theta)\,|_{r=1}\sin\theta d\theta$$

$$= -\frac{4}{3}\pi\left\{A_{00}A_{11} + 3A_{00} + C\left[\left(\frac{1}{A_{00}^3}+\frac{1}{A_{00}^2}\right)e^{-A_{00}} - \frac{1}{A_{00}^3}+\frac{1}{2A_{00}}\right]\right\}. \tag{79}$$

The total drag acting on a fluid sphere now becomes

$$F_D = -\frac{4}{3}\pi\left(3A_{00}+\frac{C}{2A_{00}}\right)$$

$$= \frac{4}{3}\pi\left\{-3A_{00} + \frac{\frac{1}{2}[(3+2\Phi_\mu) - A_{11}(1+2\Phi_\mu)]A_{00}^3}{-1+\frac{1}{6}(3+2\Phi_\mu)A_{00}^2 + \left(1+A_{00}-\frac{1}{3}\Phi_\mu A_{00}^2\right)e^{-A_{00}}}\right\}. \tag{80}$$

It should be pointed out that equation (80) is identical to equation (64) of Sadhal and Ayyaswamy (1983), and is consistent with the fact that was revealed from the analysis of Chang et al. (1982). From our present analysis, it is seen that the presence of an electric field has no influence on any components of the drag, and hence the total drag—even though it has significant impacts on the flow patterns and possibly the transport rates of heat and mass. This may mean that the droplet residence time or the intraction time would stay unchanged while more intensive transport rates are experienced by the droplet. This could result in a higher efficiency in spray combustion.

V Results and Discussion

In this section we present some typical numerical calculations from this analysis for both cases of inward and outward mass fluxes. As mentioned throughout the previous sections, a major contribution of this paper is the addition of an electric field on the purely hydrodynamic flow field of a translating droplet. As demonstrated, the electric field significantly modifies the flow patterns but adds no effect on the total drag, therefore the sample results presented are designed to show the variations of the flow fields due to the electric field.

Representative results for the velocity fields for both inward and outward radial flows with $\epsilon = 0.5$ and $\Phi_\mu = 0.1$ are illustrated in Figs. 2 and 3, respectively. In all cases, the integrals in equations (51) and (63) are evaluated by first approximating the integrands using Taylor's expansion, then followed by a term-by-term integration, and the value of the integral is taken as the sum of all terms with relative magnitude $\geq 10^{-10}$. As an example of the rate of convergence, no more than 16 terms are necessary to achieve the desired accuracy at all locations outside the fluid sphere. As the radial distance from the drop surface becomes larger, the series truncates much more rapidly.

Downloaded 03 May 2010 to 171.66.16.244. Redistribution subject to ASME license or copyright; see http://www.asme.org/terms/Terms_Use.cfm

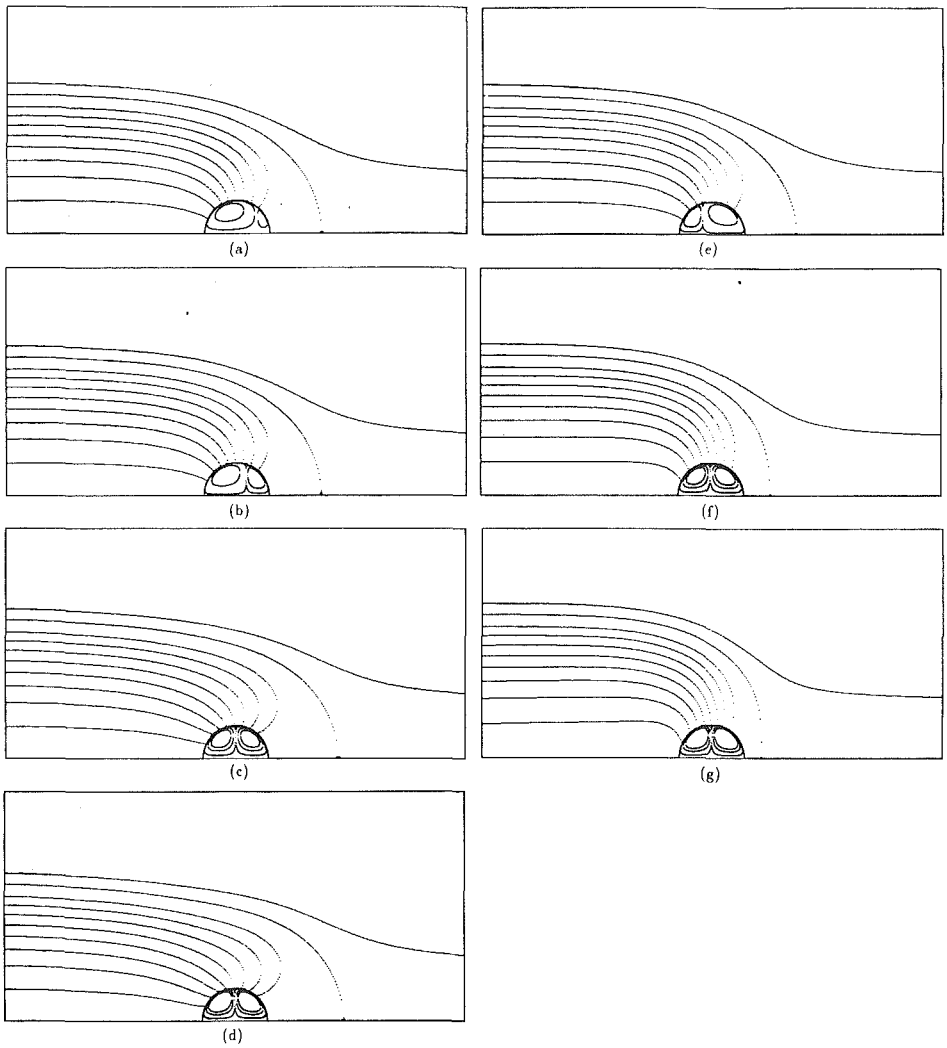


Fig. 2 Flow patterns of a translating drop with inward radial velocity; (a) $W = -0.5$, (b) $W = -1.0$, (c) $W = -25.0$, (d) $W = -35.0$, (e) $W = 1.0$, (f) $W = 25.0$, (g) $W = 35.0$

In Figs. 2, we examine the case of a radially inward mass flux ($A_{00} = -2.$, a condensing droplet). The other parameters are: $A_{01} = -0.5$, $A_{11} = .25$, and $A_{21} = .10$. The parameter, $|W|$, varies from 0.5 where the electric flow field is weak, compared to the translational flow field to 35 where the electric flow field is dominant. Due to symmetry to the direction of translation, only the upper half of the streamline patterns are shown. In Fig. 2(*a*), for $W = -0.5$, the streamline patterns are very similar to those of Fig. 2(*b*) in Sadhal and Ayyaswamy (1983) (except that a secondary loop directing from the equator to the pole starts to develop within the droplet). As W is increased, the size of the secondary loop gets larger and eventually becomes symmetric, about $\theta = \pi/2$, as seen from Fig. 2(*d*). Under this condition, the electric field has established a total dominance inside the droplet where the two circulating loops are equal in size, which is similar to the flow pattern predicted by Taylor (1966) for a nontranslating suspended droplet (for example, a droplet in zero-gravity environment) within an electric field. On the outside, the streamlines resemble the case of flow past a condensing droplet; however, as the field strength becomes stronger, the dividing streamline seems to be pushed further from the downstream stagnation region. This displacement is believed to be due to the pressure gradient generated by the field along a vertical section. For the cases of a positive W, the internal motion near the surface runs from the pole toward the equator and this seems to cause the dividing streamline in the wake region to move closer toward the rear stagnation as shown in Figs. 2(*e*), 2(*f*), and 2(*g*). The effects of the electric field on the dividing streamlines could have significant impact on the transport profiles and flame shapes in a burning drop. It is interesting to note that the condensing interfacial mass flux seems to suppress the flow separation, and the reversed flow was not predicted for a condensing droplet unless the interfacial velocity is vanishingly small (Chang et al., 1982; Chang and Berg, 1983).

For the case of a droplet with radially outward mass flux ($A_{00} = 2.$, $A_{01} = .5$, $A_{11} = -.25$, and $A_{21} = -.1$, an evaporating drop), different flow patterns for various values of W are plotted in Figs. 3 to show the relative effects of an electric field. Apparently the effects of an electric field on the flow patterns are more pronounced for an evaporating drop. For $W = -.5$, the size of the circulation loops indicates a closer state of symmetry than that for the condensing drop. This is believed to be due to the mechansim that the outward mass flux reduces the strength of internal circulation induced by the translation of the droplet. When the translation-induced internal circulation is weakened, it is easier for the electric-field-induced internal circulation to develop dominance. At $W \approx -20$, a recirculation zone begins to develop behind the drop and is enlarged very rapidly, by a factor of about 10 at $W = -25$. This recirculation zone is believed

Downloaded 03 May 2010 to 171.66.16.244. Redistribution subject to ASME license or copyright; see http://www.asme.org/terms/Terms_Use.cfm

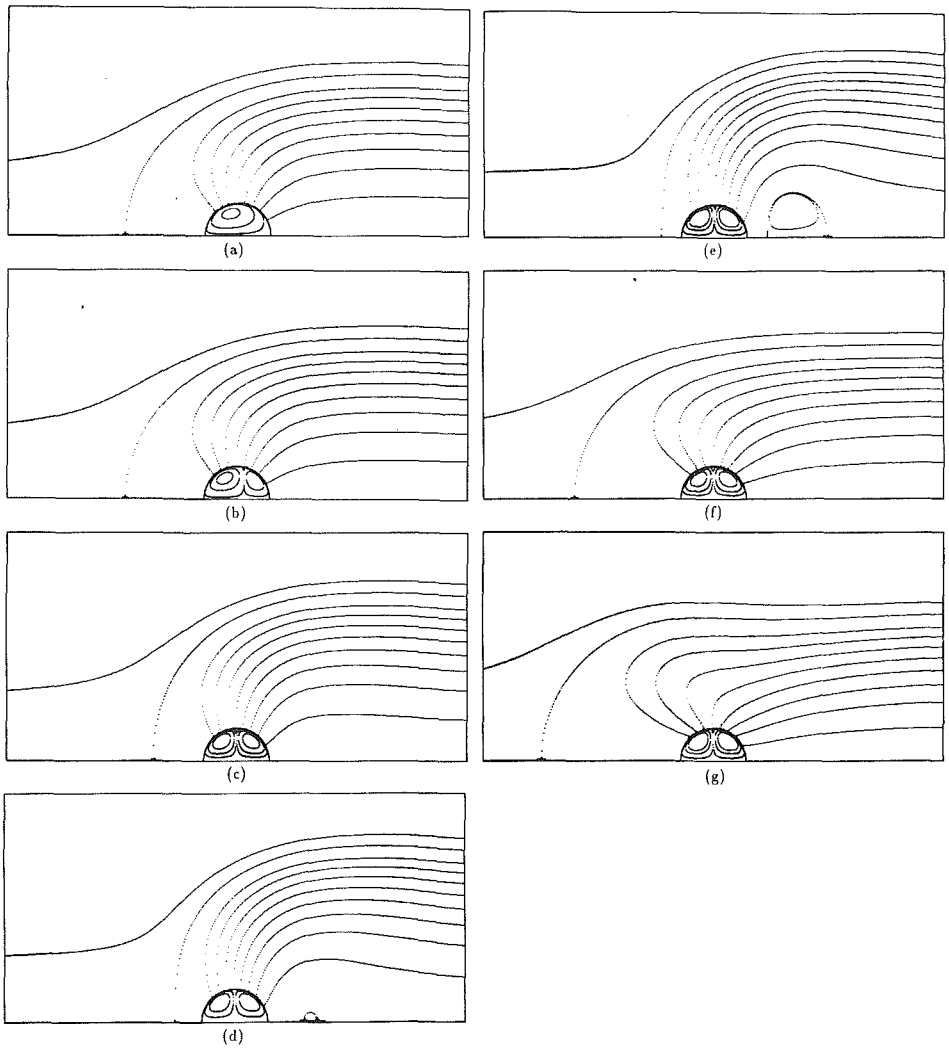


Fig. 3 Flow patterns of a translating drop with outward radial velocity; (a) $W = -0.1$, (b) $W = -0.5$, (c) $W = -10.0$, (d) $W = -20.0$, (e) $W = -25.0$, (f) $W = 10.0$, (g) $W = 25.0$

to be predicted for the first time for an evaporating droplet in an electric field. Such recirculating patterns were not predicted without the field (Sadhal and Ayyaswamy, 1983). It is clear that the strong evaporation in the frontal portion of the drop causes a relocation of this low pressure region that would occur upstream if the drop were nonevaporating. As we change W from negative to positive, the reversed flow region seems to disappear indicating its inability to resist the adverse stress under electrically-induced flow heading from the pole to the equator. This suggests a convenient way of controlling the flow separation by simply changing the sign of the electric field. It is also worthwhile to note that a positive W causes the dividing streamline in the upstream to move away from the front stagnation point as compared to a negative W for an evaporating droplet. The trend is reversed for a condensing drop as shown in Figs. 2. This is due to the fact that the dividing streamline is in the wake for a condensing droplet while it is in the upstream of an evaporating droplet. To examine the effects of the strength of evaporation upon the flows, we provide the results for two different values of W at 2.2 and 5.0 in Figs. 4(a) and 4(b), respectively. The differences are quite remarkable, spherically symmetric evaporation becomes more pronounced with further increase in evaporation rate. Unlike the results reported earlier (Chang et al., 1982; Chang and Berg, 1983) which addressed a droplet with no interfacial velocity, the presence of strong blowing/suction (evaporation/condensation) clearly restructures the flow patterns, and the occurrence of reversed flows seem to delay until much higher W is reached and are observed only for negative W. The shape of the wake zone is very different and is relatively far away from the surface which is favorable for effective transfer. In general, the flow pattern inside the drop is influenced more by the electric field as evidenced by the sample plots. For higher electric-field strength, the double-loop recirculation, similar to those of Taylor's, appears. Whereas for the external flow field, the flow pattern hardly bears any resemblance to those of Taylor (1966) even under high-field strength. The outside flow field is dominated by the condensing/evaporating mass flux such that its pattern is similar to that of a condensing/evaporating droplet in an electric-field-free environment.

From equation (80) of the total drag, there is no doubt that the flow induced by an electric field contributes no net force to the drop; hence, the terminal velocity of a falling drop under an electric field would remain the same as that falling under gravity alone. For more information, we plotted some more cases including the variations of each drag component. As we are dealing with a droplet translating in a gaseous environment, the viscosity ratio, Φ_μ, usually falls in the range of 0.01 (water drop in air) to 0.1 (methanol droplet in air) for most of

Downloaded 03 May 2010 to 171.66.16.244. Redistribution subject to ASME license or copyright; see http://www.asme.org/terms/Terms_Use.cfm

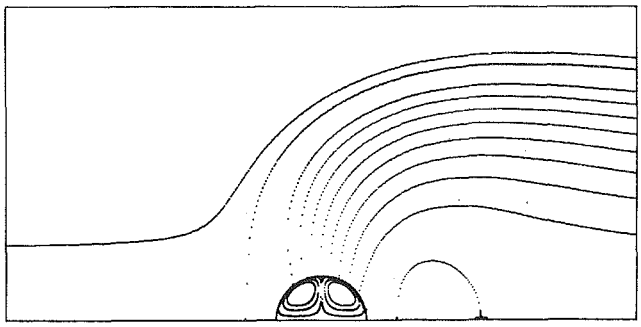


Fig. 4(a)

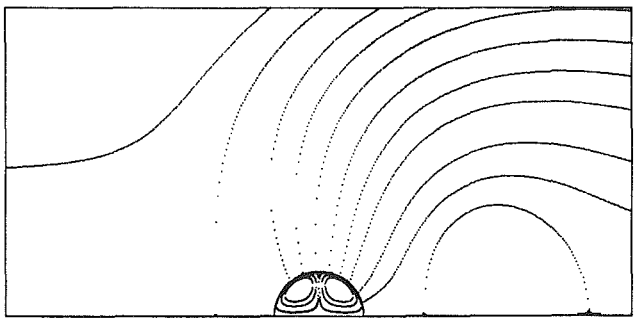


Fig. 4(b)

Fig. 4 Effects of mass flux level on the flow patterns for a fixed $W = -25.0$; (a) $A_{00} = 2.2$, (b) $A_{00} = 5.0$

the practical systems. In Figs. 5(*a*) and 5(*b*), the drag, nondimensionalized by that of a solid sphere ($\Phi_\mu = 0$) with no interfacial mass flux, is shown as a function of the outward interfacial velocity (A_{00} is positive) for $\Phi_\mu = 0.01$ and 0.1. Only negligibly small difference exists between Figs. 5(*a*) and 5(*b*). Therefore, for most of the droplet-gas systems, the total drag of an evaporating droplet is not sensitive to the viscosity ratio and it may be closely approximated by the drag of a sublimating solid sphere. The above is explained through equation (80) that $2\Phi_\mu$ is small as compared to 3 for a droplet-gas system. Another point of interest with regard to the trends of Figs. 5(*a*) and 5(*b*) is that the drag force increases with increasing A_{00} after A_{00} is larger than $O(10)$. The practical implication is that for an evaporating droplet of nonuniform radial mass flux ($A_{11} \neq 0$), the increased drag may keep the droplet in the system longer allowing more time for reaction. For the case of a condensing droplet (A_{00} is negative), again we show the drag for $\Phi_\mu = 0.01$ and 0.1 in Figs. 6(*a*) and 6(*b*). Similar to an evaporating droplet, the drag does not vary significantly with the viscosity ratio. The drag increases monotonically with increasing condensation velocity ($-A_{00}$). Also, the drag is not very sensitive to the change in angular variations of interfacial velocity (A_{11}).

It is informative to examine the characteristics of each drag component for both evaporating and condensing droplets. In Fig. 7(*a*), the contribution of viscous drag, momentum flux drag, and pressure drag relative to the total drag force are plotted against the leading order of the interfacial velocity (A_{00}) for an evaporating drop (positive A_{00}) for $\Phi_\mu = 0.01$. Two sets of curves are given, one for the case of a droplet with uniform interfacial velocity ($A_{11} = 0$) and the other for nonuniform interfacial velocity. The viscosity drag decreases monotonically with increasing blowing velocity (A_{00}) for both cases. As A_{00} is increased, the pressure drag increases for a uniform blowing case and decreases for a nonuniform blowing droplet. The reason for the existence of a minimum for the total drag for a nonuniform evaporating droplet is made clear

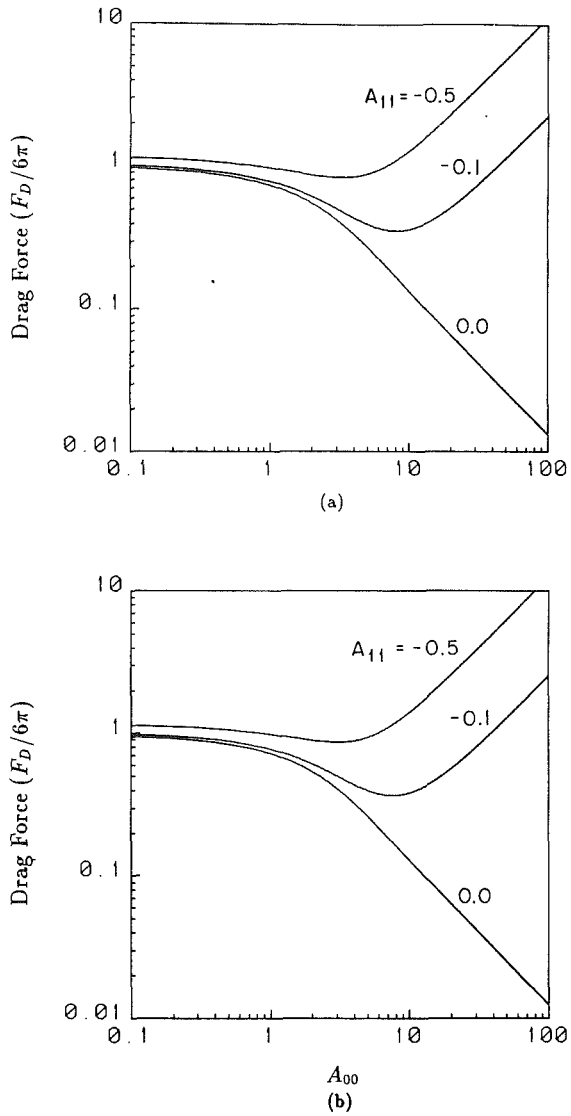


Fig. 5 Drag as a function of outward radial velocity; (a) $\Phi_\mu = 0.01$, (b) $\Phi_\mu = 0.1$

by the momentum drag. This drag increases rapidly as A_{00} is increased for a nonuniformly evaporating droplet whereas it is always zero for a uniformly evaporating droplet. This interesting behavior indicates that a droplet with nonuniform evaporating mass flux may not always experience a reduced drag as A_{00} is increased, and this behavior is mainly due to the contribution from the momentum flux drag. In actual applications, the increased drag may be used to keep the evaporating droplets in the reaction zone longer for a more complete process. In Fig. 7(*b*), component drags are plotted for a condensing drop. The viscous drag first increases until A_{00} reaches about 4, and beyond this value it decreases relatively slowly. However, no such increase is observed for drop with invariant condensing velocity. For the pressure drag, it decreases monotonically with increasing condensing velocity ($-A_{00}$) for both cases. The momentum flux drag increases rapidly for droplets of both uniform and nonuniform interfacial mass fluxes unlike the evaporating droplet. For small $-A_{00}$, the decrease in pressure drag is offset by the increase of the momentum flux drag, but as $-A_{00}$ increases, the rapid rise of the momentum flux drag is the main reason for the total drag to be monotonically increasing with $-A_{00}$. Therefore, for both evaporating and condensing droplets, the momentum flux drag plays a dominant role on the variation of total drag with the interfacial velocity.

Downloaded 03 May 2010 to 171.66.16.244. Redistribution subject to ASME license or copyright; see http://www.asme.org/terms/Terms_Use.cfm

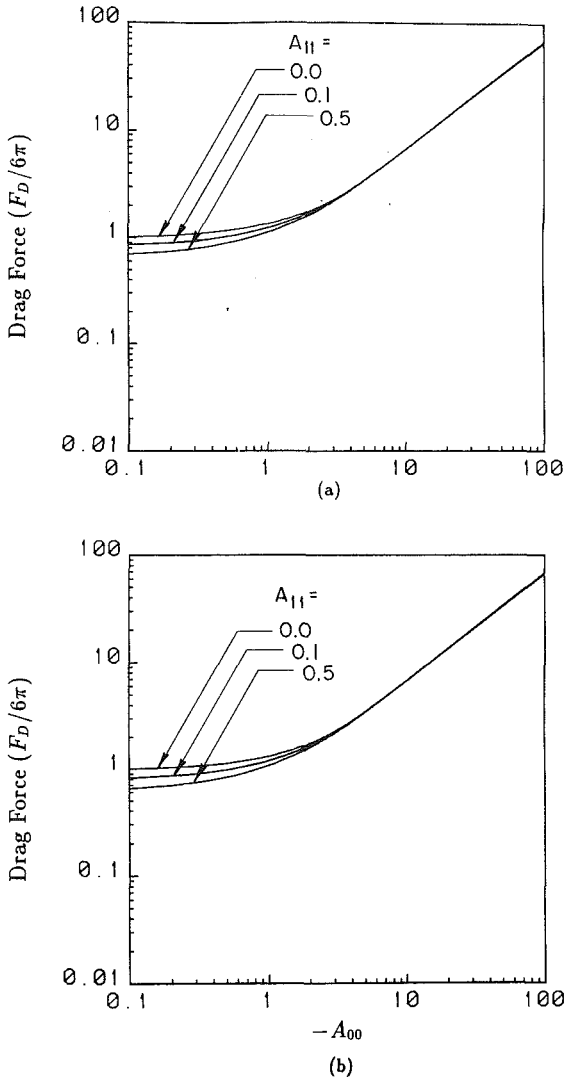


Fig. 6 Drag as a function of inward radial velocity; (*a*) $\Phi_\mu = 0.01$, (*b*) $\Phi_\mu = 0.1$

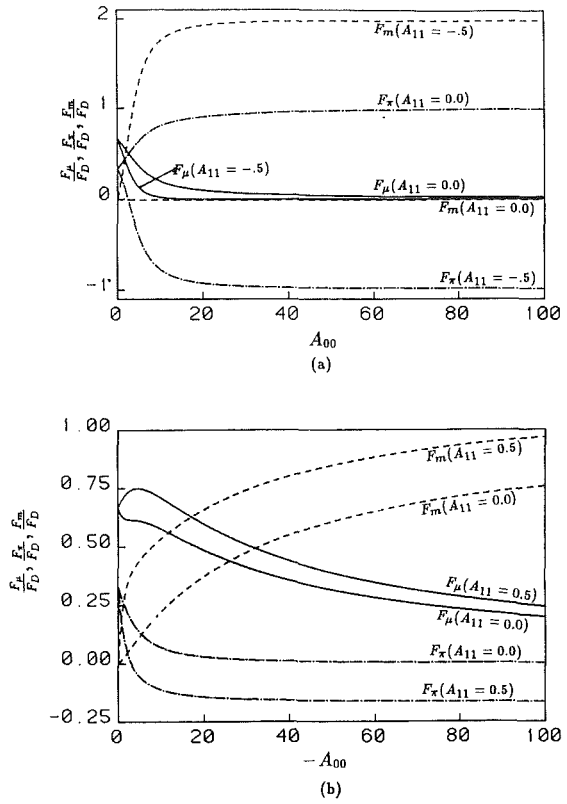


Fig. 7 Effect of radial velocity on drags; (*a*) $\Phi_\mu = 0.01$, (*b*) $\Phi_\mu = 0.1$

In Figs. 8, the strength of the vortices within the drop arising from the electric field is illustrated as a function of the interfacial velocity A_{00} for various values of A_{21} and W. Both Figs. 8(*a*) and 8(*b*) exhibit a general behavior in that $\hat{B}_e$ is a strong function of W with a relatively weak dependence on A_{21}. With a set of values A_{21} and W given, the intensity of the electric-field-induced circulation tends to increase as the condensation velocity becomes weak. However, that trend is reversed for the case of evaporation. That is, the evaporation process enhances the internal circulation generated by the electric field. Such phenomenon can be explained by the exchange of momentum between the fluid particles carrying the radial velocity and those travelling with the translational velocity. During the course of their collisions, the fluid particles near the drop surface, as in the case of evaporation, lose some of their kinetic energy, and consequently the drop will experience a weaker shear force on its surface. As a result, the electric field becomes more fully established in order to compensate for the reduction in surface shear. It is also interesting to note that the condensation process possesses a point at which the strength of the vortices due to the electric field becomes insensitive with respect to A_{21}. By inspection, this point seems to locate at $A_{00} = -4.6$. Physically, this point may be interpreted as the deficient point where the enhanced circulation gives rise to very little change, if not at all, in the interfacial mass flux.

As far as the solution is concerned, nothing has been said about the magnitude of the parameter A_{21}. In fact, it must be a function of the electric field strength. Since this study is of parametric nature, there is no need to know the explicit form describing the dependence of A_{21} upon E_0. However, one can get some useful information on A_{21} by inspecting a special case when U_∞ is zero, a situation that may be encountered in space, for example. Under this circumstance, ϵ becomes zero identically, and hence ϵA_{21} must be on the order of W in order to maintain the consistency as well as the generality of the model without reformulating the problem. That is,

$$A_{21} = O(V_{cr}), \tag{81}$$

and consequently the flow patterns can be visualized as the Taylor type of motion (Taylor, 1966) within the drop domain, whereas the outside is almost spherically symmetric with streamlines emanating from the gas-liquid interface. For a clear demonstration, the motions are depicted in Figs. 9(*a*) and 9(*b*) for $(RV_{cr}/\nu) = .5$ and $-.5$, respectively, with other parameters ($\Phi_\mu = 0.1$, $A_{00} = 2.0$, and $A_{21} = 0.2$) remaining invariant. From these figures, it appears that the change of sign in V_{cr} does not affect the structure of the flow, but its direction. Due to the symmetry of the flow lines caused by electrical forces and of the source (droplet obeying the d^2-Law during evaporation), the combined motion is symmetrical about both x and y-axes. The foregoing discussion, in fact, follows from the superposition principle which also holds when the strength of evaporation, A_{00}, and the electric field intensity are of the same order. This corresponds to a drop experiencing a small temperature difference, and hence small A_{00}. Therefore, there exists stagnation points near the drop surface and on the $x(y)$-axis depending on the direction of the electric-field-driven motion, and the dividing streamlines will align themselves to form a shape similar to a plume on a horizontal surface.

VI Conclusion

Analytical solutions based on perturbation techniques are obtained for a translating droplet with large, nonuniform in-

Downloaded 03 May 2010 to 171.66.16.244. Redistribution subject to ASME license or copyright; see http://www.asme.org/terms/Terms_Use.cfm

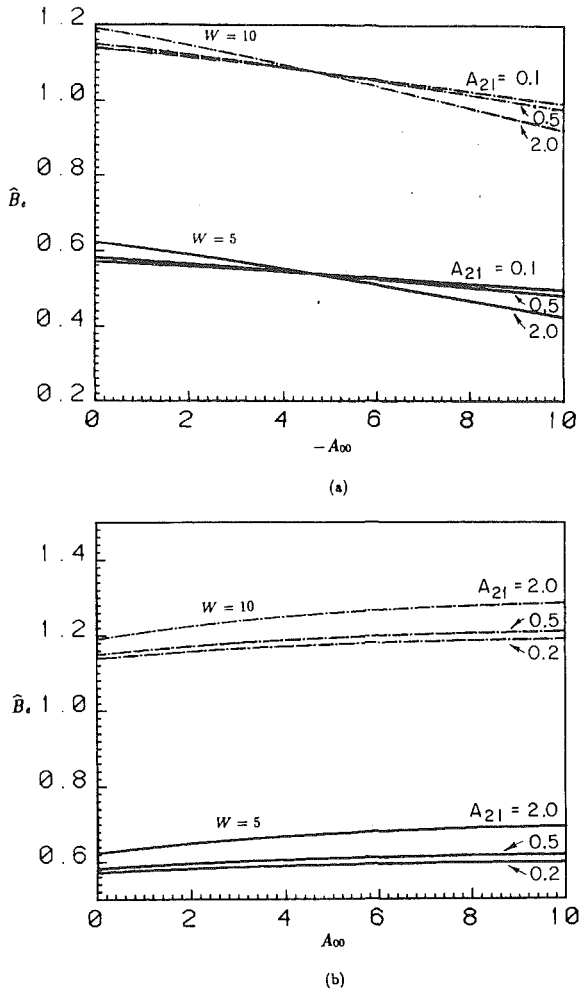


Fig. 8 Strength of vortices due to electric field for $\Phi_\mu = 0.1$

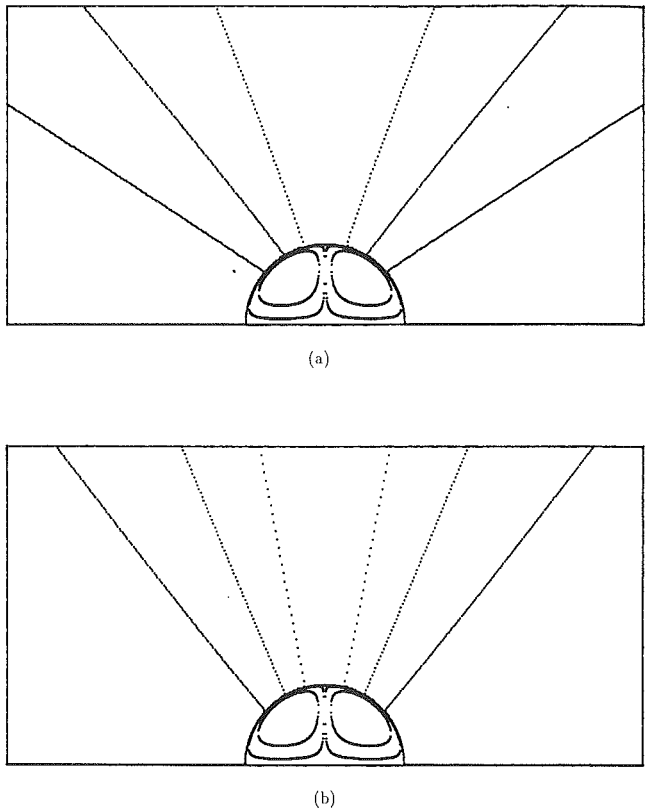


Fig. 9 Streamlines of a vaporizing drop suspended in an electric field. (a) $RV_{cr}/\nu = 0.5$, (b) $RV_{cr}/\nu = -0.5$

terfacial mass flux and simultaneously the droplet is subjected under the influence of an electric field. Flow fields both inside and outside the droplet have been plotted for typical cases. The main purpose of this work is intended to bridge the gap between the classical work of Taylor (1966) and the recent work of Sadhal and Ayyaswamy (1983).

The key contribution of this work is the development of a procedure for the first time that accommodates the interfacial velocity profile up to the second-order Legendre polynomials which is required for the electric-field-induced interfacial shear stress.

As expected, there is no change in total drag, but significant modification to the flow patterns have been predicted. In general, at high electric field strength, only the internal circulation resembles that of the Taylor droplet. This indicates that the external flow is dominated by the momentum flux of interfacial velocities. The effect of the electric field on the external flow is seen basically with the dividing streamlines. For a condensing droplet, the dividing streamline in the wake will be moved closer to the droplet if W is positive, and further away fom the droplet if W is negative. No recirculation bubble was calculated for a condensing droplet. For an evaporating droplet, the effect of an electric field is more pronounced. The electric field establishes its dominance on the internal flow with less strength than the condensing droplet case. The recirculation bubbles were only predicted for an evaporating droplet with large negative W, and that phenomenon is believed to be predicted for the first time. No recirculating bubble was calculated for an evaporating drop with positive W, no matter how large it gets. As a result, substantially different flow patterns could take place only with the change of the direction of the electric field. The electric field established its dominance on the internal flow with less strength than the condensing droplet case. The recirculation bubbles were only predicted for an evaporating droplet with large negative W, and that phenomenon is believed to be predicted for the first time. No recirculating bubble was calculated for an evaporating drop with positive W, no matter how large it gets. As a result, substantially different flow patterns could take place only with the change of the direction of the electric field. The electric field also affects the dividing streamlines in the upstream of the droplet. A positive W causes the dividing streamline to move away from the droplet, and vice versa for a negative W.

For both evaporating and condensing droplets, the momentum flux drag plays a dominant role. In a condensing droplet the total drag increases monotonically with increasing condensing velocity, whereas it decreases montonically with increasing evaporation rates for a uniformly evaporating drop. With a translating drop undergoing evaporation, the drag first decreases as the evaporating rates are increased for a nonuniformly evaporating droplet, and it starts to increase as the evaporation rate is further increased ($A_{00} > O(10)$) when the momentum flux takes dominance. The results on the strength of the electric-field-induced vortices also indicate that the intensity of those vortices is enhanced as the strength of those vortices, generated by translation, is lessened.

References

Chang, L. E., Carleson, T. E., and Berg, J. C., 1982, "Heat and Mass Transfer to a Translating Drop in an Electric Field," *Int. J. Heat Mass Transfer*, Vol. 25, pp. 1023–1030.

Chang, L. S., and Berg, J. C., 1983, "Fluid Flow and Transfer Behavior of a

Downloaded 03 May 2010 to 171.66.16.244. Redistribution subject to ASME license or copyright; see http://www.asme.org/terms/Terms_Use.cfm

Drop Translating in an Electric Field at Intermediate Reynolds Numbers," *Int. J. Heat Mass Transfer*, Vol. 26, pp. 823–831.

Chao, B. T., 1962, "Motion of Spherical Gas Bubbles in a Viscous Liquid at Large Reynolds Numbers," *Phys. Fluids*, Vol. 5, pp. 69–79.

Chung, J. N., Ayyaswamy, P. S., and Sadhal, S. S., 1984, "Laminar Condensation on a Moving Drop. Part 1. Singular Perturbation Technique," *J. Fluid Mech.*, Vol. 139, pp. 105–130.

Clift, R., Grace, J. R., and Weber, M. E., 1978, *Bubbles, Drops, and Particles*, Academic Press, New York.

Hadamard, C. R., 1911, "Mouvement Permanent Lent d'une Sphere Liquide et Visqueuse dans un Liquid Visqueux," *Acad. Sci. Paris*, Vol. 152, pp. 1735–1738.

Hamielec, A. E., and Johnson, A. I., 1962, "Viscous Flow Around Fluid Spheres at Intermediate Reynolds Numbers," *Can. J. Chem. Eng.*, Vol. 40, pp. 41–45.

Hamielec, A. E., Storey, S. H., and Whitehead, J. M., 1963, "Viscous Flow Around Fluid Spheres at Intermediate Reynolds Number (II)," *Can. J. Chem. Eng.*, Vol. 41, pp. 246–251.

Hamielec, A. E., Hoffman, T. W., and Ross, L. L., 1967, "Numerical Solution to the Navier-Stokes Equation for Flow Past Spheres: Part I. Viscous Flow Around Spheres With and Without Radial Mass Efflux," *J. A.I.Ch.E.*, Vol. 13, pp. 212–219.

LeClair, B. P., Hamielec, A. E., Pruppacher, H. R., and Hall, H. R., 1972, "A Theoretical and Experimental Study of the Internal Circulation in Water Drops Falling at Terminal Velocity in Air," *J. Atmos. Sci.*, Vol. 29, pp. 728–740.

Nakano, Y., and Tien, C., 1967, "Approximate Solutions of Viscous Incompressible Flow Around Fluid Spheres at Intermediate Reynolds Numbers," *Can. J. Chem. Eng.*, Vol. 4, pp. 135–140.

Nguyen, H. D., and Chung, J. N., 1989, "Evaporation From a Translating Drop in an Electric Field," submitted to *J. Fluid Mech.*

Oliver, D. L. R., and Chung, J. N., 1987, "Flow About a Fluid Sphere at Low to Moderate Reynolds Numbers," *J. Fluid Mech.*, Vol. 177, pp. 1–18.

Rybczynski, W., 1911, "On the Translatory Motion of a Fluid Sphere in a Viscous Medium," *Bull. Int. Acad. Pol. Sci. Lett. Cl. Sci. Math. Nat.*, Series A, pp. 40–46.

Sadhal, S. S., and Ayyaswamy, P. S., 1983, "Flow Past a Liquid Drop with a Large Non-Uniform Radial Velocity," *J. Fluid Mech.*, Vol. 133, pp. 65–81.

Sozou, C., 1973, "Electrohydrodynamics of a Liquid Drop: The Development of the Flow Field," *Proc. R. Soc., Lond.*, Vol. A334, pp. 343–356.

Taylor, G. I., 1966, "Studies in Electrohydrodynamics. I. The Circulation Produced in a Drop by an Electric Field," *Pro. R. Soc., Lond.*, Vol. A291, pp. 159–166.

Woo, S. E., and Hamielec, A. E., 1971, "A Numerical Method of Determining the Rate of Evaporation of Small Water Drops Falling at Terminal Velocity in Air," *J. Atmos. Sci.*, Vol. 28, pp. 1448–1454.

Downloaded 03 May 2010 to 171.66.16.244. Redistribution subject to ASME license or copyright; see http://www.asme.org/terms/Terms_Use.cfm

Effect of Finite Thickness Flexible Boundary Upon the Stability of a Poiseuille Flow

Mauro Pierucci
Professor of Aerospace Engineering and Engineering Mechanics

Pedro G. Morales
Assoc. Mem. ASME

Department of Aerospace Engineering and Engineering Mechanics,
College of Engineering,
San Diego State University,
San Diego, CA 92182

The stability behavior, the stress, and velocity distributions for a plane Poiseuille flow bounded by a finite thickness elastic layer is studied. The analysis is performed by utilizing the coupled relationships between the Orr-Sommerfeld stability equation for the fluid and the Navier equations for the solid. The numerical instabilities experienced in the solution of the Orr-Sommerfeld equation have been overcome with the use of Davey's orthonormalization technique. This study focuses only on the Tollimen-Schlichting instabilities. This mode is the most unstable of the three different types of instabilities. The results show that certain combinations of parameters can lead to improved stability conditions. Under these conditions the normal and shear stress distributions may behave completely different in certain regions of the fluid.

Introduction

The delay and/or control of transition of a laminar into a turbulent boundary layer has received wide attention over the last quarter of a century.

At first, fluid suction through porous walls and fluid cooling were investigated. In 1960, M. O. Kramer found that considerable reduction of skin-friction drag could be obtained on circular cylinders coated with flexible materials; he reported up to a 50 percent reduction in certain cases for Reynolds numbers of 10^6 to 10^7. In this paper, the role played by a flexible layer adjacent to a plane Poiseuille flow and the resulting stability and control of Tollmien-Schlichting waves (TSI) is presented.

The TSI waves, which were reported by Kramer to be damped out by the flexible layer, are directly associated with transition. Kaplan (1964) has analyzed the stability of this problem; however, the highly stiff nature of the linearized Orr-Sommerfeld equation associated with this problem prevented the extraction of the eigenfunctions for all cases and the extension of the analysis to more general cases. Orszag (1971) and Tsvelodub (1978) and more recently Carpenter (1985) have also studied different aspects of this problem. Davey (1983) has recently developed a numerical orthonormalization technique which allows the numerical integration of very stiff linear differential systems; not only does Davey's technique allow the evaluation of the eigenvalue, but it also gives the values of the eigenfunctions (i.e., velocity and stress distribution) to a high degree of accuracy.

Contributed by the Applied Mechanics Division of THE AMERICAN SOCIETY OF MECHANICAL ENGINEERS for publication in the JOURNAL OF APPLIED MECHANICS.

Discussion on this paper should be addressed to the Technical Editor, Leon M. Keer, The Technological Institute, Northwestern University, Evanston, IL 60208, and will be accepted until two months after final publication of the paper itself in the JOURNAL OF APPLIED MECHANICS. Manuscript received by the ASME Applied Mechanics Division, July 29, 1988; final revision, July 31, 1989.

The Hydrodynamic Stability Equation

For the fluid, the Navier-Stokes equations can be linearized with respect to the mean flow field.

$$U = U_m\left[1 - \left(\frac{y}{D}\right)^2\right] \tag{1}$$

The axial velocity component is then composed of the mean component plus a perturbation term u; the transverse velocity is then composed of the perturbed value only. Define a potential function ϕ such that

$$\begin{aligned} u &= \phi' \exp i(\alpha x - \omega t) \\ v &= -i\alpha\phi \exp i(\alpha x - \omega t). \end{aligned} \tag{2}$$

Introducing the function ϕ in the linearized form of the Navier-Stokes equations gives the Orr-Sommerfeld equation

$$(U-c)(\phi'' - \alpha^2\phi) - U''\phi = -\frac{i}{\alpha \mathrm{Re}}(\phi^{iv} - 2\alpha^2\phi'' + \alpha^4\phi). \tag{3}$$

In equation (3), U is the mean flow profile given by equation (1). The Reynolds number is $U_m\, \rho_f D/\mu$, (ρ_f being the fluid density and μ its viscosity) and D is the half width of the channel (Fig. 1). The derivatives are, with respect to the transverse coordinate, y, α is the wave number, and ϕ is the potential function. The speed c at which the fluid disturbances propagate in the fluid is given by ω/α. The value c is the eigenvalue of the problem and is a complex number such that if $\mathrm{Im}(c) < 0$ the flow is stable, while for $\mathrm{Im}(c) > 0$ the fluid disturbances are unstable. The solution to equation (3) has been shown to be very stiff at high Reynolds numbers. Davey's orthonormalization technique will, however, overcome this problem.

The boundary conditions for the Poiseuille flow are split and are taken to be

$$\left.\begin{aligned} \phi'(0) &= 0 \\ \phi'''(0) &= 0 \end{aligned}\right\} \tag{4}$$

Copyright © 1990 by ASME
Downloaded 03 May 2010 to 171.66.16.244. Redistribution subject to ASME license or copyright; see http://www.asme.org/terms/Terms_Use.cfm

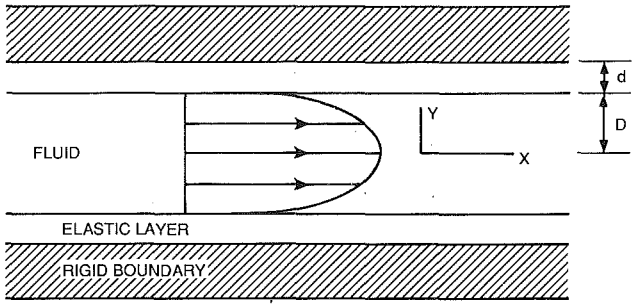


Fig. 1 Sketch of Poiseuille flow with elastic walls

with continuity of displacement and stresses occurring at the fluid-solid interface. In order to properly define these interface conditions, one has to consider the governing equations and the solution for the elastic solid.

Elastic Layer Equations

For the elastic medium the governing equations are:

$$c_t^2(u_{1,xx}+u_{1,yy})+(c_l^2-c_t^2)(u_{1,xx}+u_{2,yx})=u_{1,tt} \tag{5}$$

$$c_t^2(u_{2,xx}+u_{2,yy})+(c_l^2-c_t^2)(u_{1,xy}+u_{2,yy})=u_{2,tt}, \tag{6}$$

where u_1 and u_2 are axial and normal displacements in the solid, and c_t, c_l are the transverse and longitudinal wave speeds in the solid. The coupled equations (5) and (6) are solved by assuming displacements of the type

$$u_1 = \sum_{j=1}^{4} B_j \exp(\lambda_j y)\exp i(\alpha x-\omega t)$$
$$u_2 = \sum_{j=1}^{4} A_j \exp(\lambda_j y)\exp i(\alpha x-\omega t), \tag{7}$$

where

$$\lambda_{1,2}=\pm\alpha r_1$$
$$\lambda_{3,4}=\pm\alpha r_2 \tag{8}$$
$$r_1^2=1-(c/c_t)^2$$
$$r_2^2=1-(c/c_l)^2.$$

After one introduces the assumed solutions of the solid layer displacements, equations (7) and (8) in the Navier equations a relation can be found between the coefficients A_j and B_j.

$$B_{1,2}=\pm ir_1 A_{1,2}$$
$$B_{3,4}=\pm i/r_2 A_{3,4}. \tag{9}$$

The boundary conditions, continuity of normal and shear stress, and continuity of normal and longitudinal velocity at the fluid solid interface are given by

$$-3\mu\alpha i\phi'+\frac{i\mu}{\alpha}\phi'''+\rho_f\phi'(U-c)-\rho_f\phi U'=2\rho_s c_t^2 u_{2,y}$$
$$+\rho_s(c_l^2-2c_t^2)(u_{1,u}+u_{2,y})$$
$$\mu(\alpha^2\phi+\phi'')=\rho_s c_t^2(u_{1,y}+u_{2,x}) \tag{10}$$
$$v_f=v_s$$
$$u_f=u_s.$$

At the outer boundary of the elastic layer, the conditions are zero normal and longitudinal displacements.

$$u_1(D)=0$$
$$u_2(D)=0 \tag{11}$$

By taking four of the conditions stated above corresponding to the continuity of velocities and zero rigid wall displacement, one can solve for the A_j (see Appendix) substitute back into the remaining two equations evaluated at the interface giving the following result:

$$\phi'(D)=A_1\psi_1(\alpha, r_1, r_2, D, c, d)+A_2\psi_2(\alpha, r_1, r_2, D, c, d) \tag{12}$$
$$\phi(D)=A_1\psi_3(\alpha, r_1, r_2, D, c, d)+A_2\psi_4(\alpha, r_1, r_2, D, c, d).$$

The ψ_i are complex functions given in the Appendix and are functions of the indicated parameters. The values of A_j's are then substituted into equations (12) and after considerable manipulation one obtains:

$$-2g_1+g_2f_1(\alpha, \mathrm{Re}, c)-g_4f_2(\alpha, \mathrm{Re})$$
$$+A_1f_3(\alpha, r_1, c_t, c_l, \rho)+\ldots A_4f_6=0 \tag{13}$$

$$-2g_1f_7(\alpha, \mathrm{Re})-g_3f_5(\mathrm{Re})+A_1f_9$$
$$+\ldots A_4f_{12}(\alpha, r_2, c_t, c, \rho)=0. \tag{14}$$

In equation (13), the g_i's are given by

$$g_1=\phi$$
$$g_2=\phi' \tag{15}$$
$$g_3=\phi''-\alpha^2\phi$$
$$g_4=\phi'''-\alpha^2\phi'.$$

In terms of g_1, the Orr-Sommerfeld equations can be written in the matrix form

$$\begin{Bmatrix} g_1 \\ g_2 \\ g_3 \\ g_4 \end{Bmatrix} = \begin{pmatrix} 0 & 1 & 0 & 0 \\ \alpha^2 & 0 & 1 & 0 \\ 0 & 0 & 0 & 1 \\ 2i\alpha\mathrm{Re} & 0 & \alpha^2+i\alpha\mathrm{Re}(U-c) & 0 \end{pmatrix} \begin{Bmatrix} g_1 \\ g_2 \\ g_3 \\ g_4 \end{Bmatrix}. \tag{16}$$

Equation (16) is now solved by Davey's technique subject to the split boundary conditions as given by equations (4) and (13)–(14). The split boundary conditions are satisfied by guessing at a value of c and the magnitude of the normal and tangential velocity at the fluid solid interface until the left-hand side of equation (13) and equation (14) are equal to zero.

Discussion of Results

It is a well-documented fact that solutions for values of α equal to unity correspond to the most interesting cases (i.e., transition at the lowest Reynolds number); therefore, in all of the subsequent results, the value of α has been set equal to unity.

In order to analyze the effect of wall compliance upon the stability problem, one is concerned with the effect of the wall compliance parameter ($\bar{c}_t=c_t/U_m$), the elastic layer thickness ($\bar{h}=d/D$), the solid to fluid density ratio ($\bar{\rho}$), and the Reynolds number Re. In Fig. 2 the effect of the wall compliance on the stability of the flow for several values of Reynolds number is shown. Values Im(c) greater than zero constitute instability while values less than zero lead to stable flow conditions. As the value of $\bar{c}_t$ is increased, a stabilizing effect exists at the lower Reynolds numbers. For higher Reynolds numbers, this stabilizing effect is slowly lost for the same increase in wall rigidity.

Large values of the wall compliance parameter $\bar{c}_t$ correspond to a very rigid layer, while smaller values correspond to more compliant surfaces. From Fig. 2 one sees that values of $\bar{c}_t$ greater than about three give results very similar to the rigid wall cases. At the lower Reynolds numbers, the effect of the wall compliance is seen to lead to less stable conditions. The solution corresponding to a Reynolds number of 5000 is seen to be affected less than the case corresponding to 500. As the Reynolds number is increased further, the effect of the wall compliance diminishes until at a value of 15,000, the wall compliance has no effect on the eigenvalue c. At values greater than 15,000, the wall compliance tends to lower the value of Im(c), thus increasing the stability of the flow field. At a Reynolds number of 20,000, the rigid wall Poiseuille flow is unstable; wall compliance is seen to lower the value of Im(c),

Downloaded 03 May 2010 to 171.66.16.244. Redistribution subject to ASME license or copyright; see http://www.asme.org/terms/Terms_Use.cfm

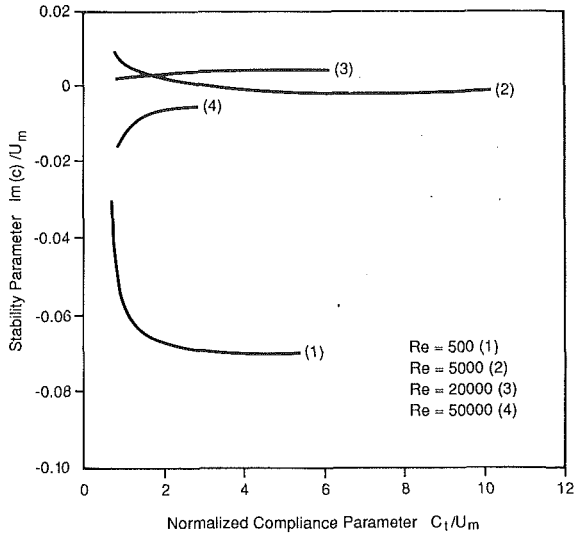


Fig. 2 Effect of the wall compliance and the Reynolds number on the stability parameter $\mathrm{Im}(c)/U_m$, $\bar{h} = 5$

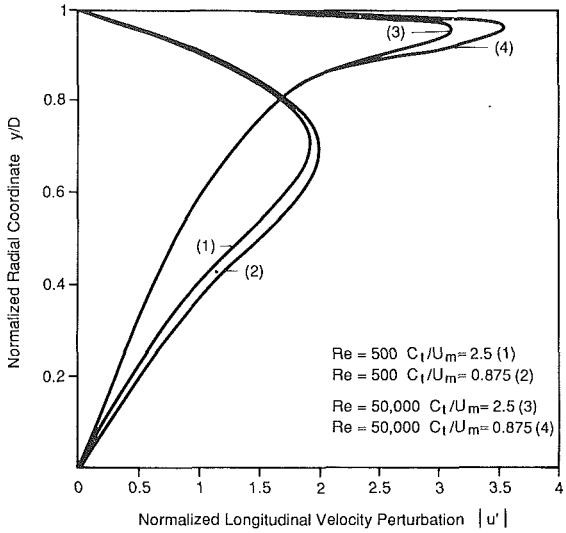


Fig. 4 Effect of the Reynolds number and wall compliance on the longitudinal velocity profile, $\bar{h} = 5$

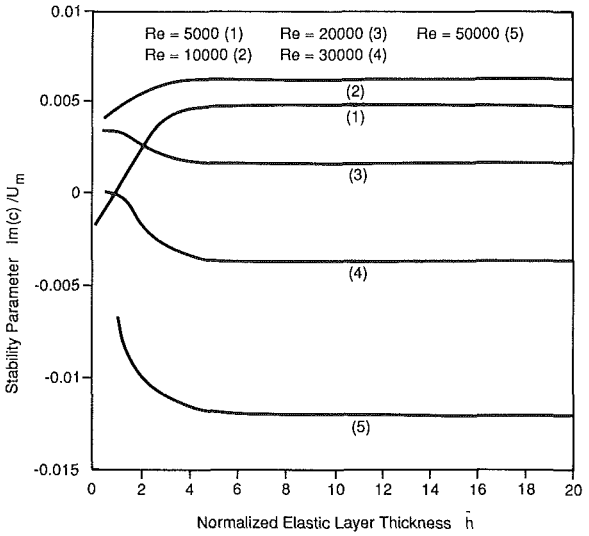


Fig. 3 Effect of the elastic layer thickness and the Reynolds number on the stability parameter $\mathrm{Im}(c)/U_m$, $c_t = 1$

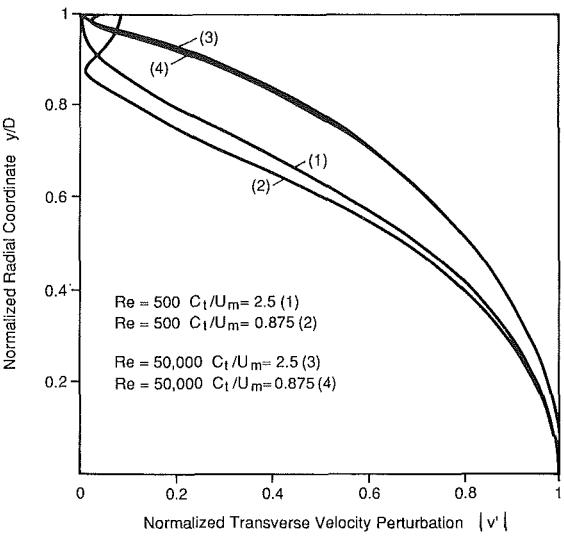


Fig. 5 Effect of the Reynolds number and wall compliance on the transverse velocity profile, $\bar{h} = 5$

indicating a less unstable situation. The result also seems to indicate that possible stable solutions may exist at values of $\bar{c}_t$ lower than any value used in this study. At a Reynolds number of 50,000, the classical flow field is already stable, and the wall compliance is seen to make the fluid disturbances more stable by a factor of two. Figure 3 shows the effect of varying the thickness of the elastic layer upon the value of $\mathrm{Im}(c)$. Note that in the limit as $\bar{h}$ goes to zero, due to the outer wall conditions, the rigid wall solutions are always recovered. The same general conclusions drawn from Fig. 2 can be applied to Fig. 3. The effect of increasing the wall thickness is to destabilize the flow field for Reynolds numbers less than 15,000, while at higher Reynolds numbers thicker layers will make the flow more stable.

Horizontal Velocity Perturbation. In the fluid, the overall trend of the horizontal velocity perturbation is similar for all cases independent of any parameter variation. The normalized longitudinal perturbation velocity (u/U_m) increases steadily from zero at the centerline until it reaches a maximum, and then decreases until the velocity becomes compatible to that of the solid at the interface. Increasing the Reynolds numbers has the effect of producing larger velocity gradients in the region close to the wall and of shifting the velocity maximum toward the wall. For the example illustrated in Fig. 4 it is seen that at a Reynolds number equal to 500, values of the longitudinal velocity are greater near the centerline than for the case corresponding to a Reynolds number of 50,000. Near the wall the opposite exists, the higher Reynolds number case gives higher values for the horizontal velocity component. It can also be noted that the effect of wall compliance does not radically influence the velocity profile. Although more noticeable at larger Reynolds number, an increase in wall compliance (i.e. decrease $\bar{c}_t$) does contribute to an increase of the profile of u.

In general, it was noted that for values of $\bar{c}_t$ greater than 2.5 the rigid wall solutions are recovered, while an increase in the magnitude of the u profile is seen for cases corresponding to wall compliance less than 2.5.

Transverse Velocity Perturbation. Figure 5 shows the typical behavior of the transverse velocity perturbation (v/U_m). The velocity is unity at the centerline and it decreases as the elastic wall is approached. In the $0.8 \leq \bar{y} \leq 1$ region, a minimum and a maximum occurs; the maximum occurs at the interface of the fluid and the flexible boundary with the value being

Downloaded 03 May 2010 to 171.66.16.244. Redistribution subject to ASME license or copyright; see http://www.asme.org/terms/Terms_Use.cfm

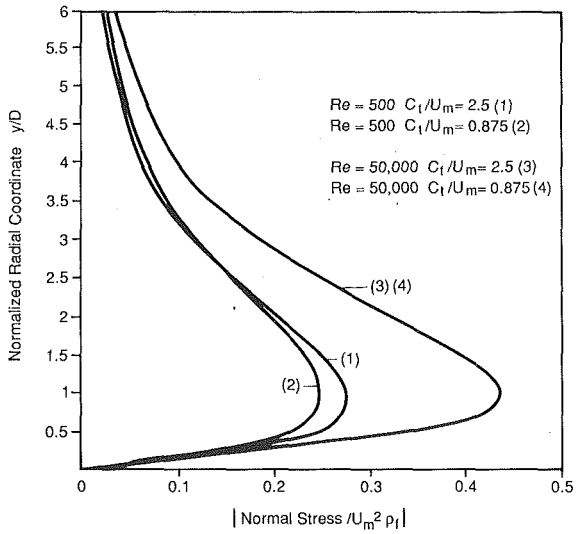


Fig. 6 Effect of the Reynolds number and wall compliance on the normal stress distribution, $\bar{h} = 5$

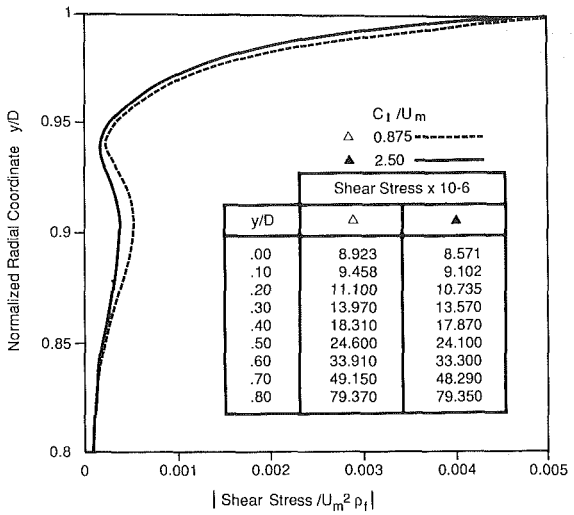


Fig. 7(*a*) Effect of the Reynolds number and wall compliance on the shear stress distribution, $\bar{h} = 5$, Re = 50,000

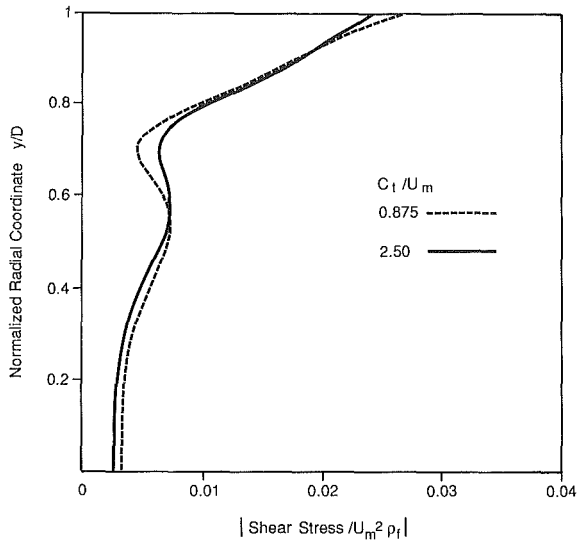


Fig. 7(*b*) Effect of the Reynolds number and wall compliance on the shear stress distribution, $\bar{h} = 5$, Re = 500

larger for the low Reynolds number cases. The minimum in the velocity profile occurs in the region close to the wall, and it gets closer to the wall as the value of the Reynolds number increases. The flexibility of the wall is seen to play a large role within the fluid region. As seen in Fig. 5 for the case of Reynolds number equal to 500, a more flexible wall ($\bar{c}_t$ of 0.875) reduces the magnitude of transverse velocity in the region closer to the centerline, while in the wall region the compliance, as expected, increases the perturbation velocity component.

Normal Stress. The normal stress in the fluid and in the solid can be shown to be related to ϕ and u_i by

$$P_f = -3\mu\alpha i\phi' + \frac{i\mu}{\alpha}\phi''' + \rho_f\phi'(U-c) - \rho_f\phi U' \qquad (17)$$

$$-\sigma_n = 2\rho_s c_t^2 u_{2,y} + \rho_s(c_l^2 - 2c_t^2)(u_{1,x} + u_{2,y}). \qquad (18)$$

The effect of the Reynolds number upon the normal stress distribution within the fluid and the solid is shown in Fig. 6 (note that values of $\bar{y}$ less than unity correspond to the fluid region while greater than unity represent the elastic layer). For the case of the Reynolds number equal to 50,000, the maximum value of the fluid normal stress increases from 0.25 to 0.45 when compared to the value for the Reynolds number equal to 500. The maximum stress point is always found at the fluid solid interface ($\bar{y}$ equal to 1). The effect of making the solid more compliant is to decrease the normal stress distribution near the interface in both the fluid and the solid while at the same time increasing the normal stress distribution near the wall. It was determined that a thinner flexible layer transmits larger values of the normal stress closer to the rigid wall.

Shear Stress. The shear stresses in the fluid and in the solid can be obtained from the velocity profiles and are given by:

$$\tau_f = \mu(u_{,y} + v_{,x}) \qquad (19)$$

$$\tau_s = \rho_s c_t^2 (u_{1,y} + u_{2,x}). \qquad (20)$$

As expected, in the fluid region it was found that an increase in the Reynolds number is followed by a reduction in the shear stress proportional to 1/Re. Figure 7 shows typical results for different values of compliance parameter $\bar{c}_t$. Wall compliance are seen to increase the shear stress in the region close to the channel centerline while decreasing it in the region close to the wall. As the fluid disturbances propagate in the fluid they cause a maximum and a minimum in the shear stress profile. The location of these extrema are directly related to the velocity perturbations u' and v', are seen to move closer to the wall, and are reduced in amplitude for increasing values of the Reynolds number. In Fig. 7 one sees that at a Reynolds number of 500, the effect of a more compliant wall is to decrease the local maximum values by four percent and also to decrease the local minimum located at a value of y equal to 0.71 by 28 percent. The location of the extrema is not seen to vary as a function of the compliance of the elastic layer. For the case corresponding to a Reynolds number of 50,000, the maximum occurs at a value of $\bar{y}$ equal to 0.9 and the minimum occurs at a value of 0.94. The values of the peak and minimum stress are seen to increase with increasing compliance; this is in contrast to the lower Reynolds number case. Wall compliance is thus seen to affect different sections of the fluid in different ways. Very large variations in the stress distributions occur within a distance of four percent of the channel dimensions. The large stress fluctuations near the wall are produced by the large velocity profile fluctuations seen in Fig. 4. Most of the shear stress profile is governed by the $u_{,y}$ term of equation (19). The only regions where the transverse term $v_{,x}$ dominates the magnitude of the shear stress profile is in the region where the transverse velocity profile is at a maximum (i.e., $u_{,y}$ equal to zero).

Conclusions

In this paper the attention has been focused on the hydro-

Downloaded 03 May 2010 to 171.66.16.244. Redistribution subject to ASME license or copyright; see http://www.asme.org/terms/Terms_Use.cfm

dynamic stability of plane Poiseuille flow linked to a flexible boundary coating.

The four influence parameters investigated in this paper are: the compliance parameter $\bar{c}_t$, the flexible layer thickness $\bar{h}$, the Reynolds number, and the solid-to-fluid-density ratio $\bar{\rho}$. From the results, it has been determined that there exists a stability plateau at an approximate Reynolds number of 15,000 where the effect of the parameters on the stability of the flow are reversed. In the low Reynolds number regime it has been found that wall compliance reduces the stability of the flow field. This behavior remains for Reynolds numbers up to 15,000. In the region $15{,}000 \le \mathrm{Re} \le 50{,}000$ wall compliance and thicker elastic layers have a positive effect on the stability of the flow. The layer thickness parameter was found to have a beneficial effect for values of $\bar{h}$ up to about seven (i.e., the flexible layer being seven times thicker than the half-width of the channel). Any further increase in the thickness does not increase the stability of the flow. The velocity and stress distribution in the channel were found to be directly affected by the variation of the Reynolds number in the fluid. Large velocity fluctuations near the wall have been seen to exist at large Reynolds numbers. The wall compliance has also been shown not to affect the longitudinal velocity profile appreciably. The transverse velocity profile is altered by the wall compliance only in a small region close to the wall. In this region a point exists where the transverse velocity has a very small value (almost zero). The exact location of this point can be shifted by varying the properties of the solid. This property could have interesting implications, because it implies that certain key boundary layer locations can be influenced dramatically by a suitable selection of elastic layer properties. The stress distribution (both normal and shear) variation as a function of Reynolds number and wall are affected differently. The wall properties can be selected to either increase or decrease the shear stress at a particular fluid location.

In summary, the wall compliance has been shown to be an additional tool that the fluid mechanician can use to alter the fluid properties at a particular location. The implications of the present results are beyond the scope of this work and are left to the reader to ponder.

References

Baxley, P. A., 1983, "The Stability of Plane Poiseuille Flow with Compliant Boundaries," San Diego State University Aerospace and Engineering Mechanics Report, TR-83-02.

Carpenter, P. W., 1985, "The Hydrodynamic Stability of Flow Over Kramer-Type Compliant Surfaces, Part 1," *Journal of Fluid Mechanics*, Vol. 155.

Davey, A., 1983, "An Automatic Orthonormalization Method for Solving Stiff Boundary-Value Problems," *Journal of Comp. Physics*, Vol. 51, pp. 343–356.

Kaplan, R. E., 1964, "The Stability of Laminar Incompressible Boundary Layers in the Presence of Compliant Boundaries," MIT Aeroelastic and Structures Research Laboratory Report, No. ASRL-TR 116-1.

Kramer, M. O., 1960, "Boundary Layer Stabilization by Distributed Damping," *Journal of the American Society of Naval Engineers*, Vol. 72, pp. 25–33.

Orszag, S. A., 1971, "Accurate Solution of the Orr-Sommerfeld Equation," *Journal of Fluid Mechanics*, Vol. 50, pp. 689–703.

Tsvelodub, O. Y., 1978, "Stability of Poiseuille Flow in an Elastic Channel," ASME JOURNAL OF APPLIED MECHANICS, Vol. 18, pp. 650–655.

APPENDIX

The solution to the coefficients A_j may be found by considering the following boundary conditions:

$$\begin{aligned} v_f &= (D) = v_s(D) \\ u_f(D) &= u_s(D) \\ u_1(D+d) &= 0 \\ u_2(D+d) &= 0. \end{aligned} \tag{A1}$$

By evaluating (A1) with the help of equations (2), (8), (9), and (10), one will obtain the following equations for A_j:

$$\begin{aligned} &A_1\exp(\alpha r_1 D) + A_2\exp(-\alpha r_1 D) + A_3\exp(\alpha r_2 D) \\ &\qquad + A_4\exp(-\alpha r_2 D) = \phi/c \\ &A_1 r_1\exp(\alpha r_1 D) - A_2 r_1\exp(-\alpha r_1 D) + A_3/r_2\exp(\alpha r_2 D) \\ &\qquad - A_4/r_2\exp(-\alpha r_2 D) = \phi'/\alpha c \\ &A_1\exp(\alpha r_1(D+d)) + A_2\exp(-\alpha r_1(D+d)) \\ &\qquad + A_3\exp(\alpha r_2(D+d)) + A_4\exp(-\alpha r_2(D+d)) = 0 \\ &A_1 r_1 r_2\exp(\alpha r_1(D+d)) - A_2 r_1 r_2\exp(-\alpha r_1(D+d) \\ &\qquad + A_3\exp(\alpha r_2(D+d)) + A_4\exp(-\alpha r_2(D+d)) = 0. \end{aligned} \tag{A2}$$

After some manipulation, the above equations may be resolved into the following definitions for A_j:

$$A_1 = \frac{\phi'\psi_4 - \phi\psi_2}{\psi_1\psi_4 - \psi_3\psi_2} \tag{A3}$$

$$A_2 = \frac{\phi\psi_1 - \phi'\psi_3}{\psi_1\psi_4 - \psi_3\psi_2} \tag{A4}$$

$$A_3 = \frac{A_2}{2}(r_2 r_1 - 1)\exp[-\alpha(1+\bar{h})(r_2 + r_1)] - \frac{A_1}{2}(r_2 r_1 + 1)\exp[\alpha(1+\bar{h})(r_1 - r_2)] \tag{A5}$$

$$A_4 = \frac{A_1}{2}(r_2 r_1 - 1)\exp[+\alpha(1+\bar{h})(r_2 + r_1)] - \frac{A_2}{2}(r_2 r_1 + 1)\exp[-\alpha(1+\bar{h})(r_1 - r_2)] \tag{A6}$$

$$\psi_1 = \frac{\alpha c}{2r_2}\Big\{2r_2 r_1\exp(\alpha r_1) - (r_2 r_1 + 1)\exp[\alpha(1+\bar{h})(r_1 - r_2) + \alpha r_2] - (r_2 r_1 - 1)\exp[\alpha(1+\bar{h})(r_1 + r_2) - \alpha r_2]\Big\} \tag{A7}$$

$$\psi_2 = \frac{\alpha c}{2r_2}(-2r_2 r_1\exp(-\alpha r_1) + (r_2 r_1 - 1)\exp[-\alpha(1+\bar{h})(r_2 + r_1) + \alpha r_2] + (r_2 r_1 + 1)\exp[-\alpha(1+\bar{h})(r_1 - r_2) - \alpha r_2] \tag{A8}$$

$$\psi_3 = \frac{c}{2}\Big\{2\exp(\alpha r_1) - (r_2 r_1 + 1)\exp[\alpha(1+\bar{h})(r_1 - r_2) + \alpha r_2] + (r_2 r_1 - 1)\exp[\alpha(1+\bar{h})(r_2 + r_1) - \alpha r_2]\Big\} \tag{A9}$$

$$\psi_4 = \frac{c}{2}\Big\{2\exp(-\alpha r_1) + (r_2 r_1 - 1)\exp[-\alpha(1+\bar{h})(r_2 + r_1) + \alpha r_2] - (r_2 r_1 + 1)\exp[-\alpha(1+\bar{h})(r_1 - r_2) - \alpha r_2]\Big\} \tag{A10}$$

$$f_1 = 2(i\alpha/\mathrm{Re}) + c \tag{A11}$$

$$f_2 = i/\alpha\mathrm{Re} \tag{A12}$$

$$f_3 = 2\theta_{1l}\exp(\alpha r_1) \tag{A13}$$

$$f_4 = -2\theta_{1l}\exp(-\alpha r_1) \tag{A14}$$

$$f_5 = (\theta_{2l} - \theta_{2l}/r_2^2 + 2(\theta_{2t}/r_2^2))\exp(\alpha r_2) \tag{A15}$$

$$f_6 = (\theta_{2l}/r_2^2 - \theta_{2l} - 2(\theta_{2t}/r_2^2))\exp(-\alpha r_2) \tag{A16}$$

$$f_7 = \alpha^2/\mathrm{Re} \tag{A17}$$

$$f_8 = 1/\mathrm{Re} \tag{A18}$$

$$f_9 = i\alpha\rho_s c_t^2(1 + r_1^2)\exp(\alpha r_1) \tag{A19}$$

$$f_{10} = i\alpha\rho_{sx} c_t^2(1 + r_1^2)\exp(-\alpha r_1) \tag{A20}$$

$$f_{11} = 2i\alpha\rho_s c_t^2\exp(\alpha r_2) \tag{A21}$$

$$f_{12} = 2i\alpha\rho_s c_t^2\exp(-\alpha r_2) \tag{A22}$$

$$\theta_{1l} = \alpha\rho_s r_1 c_t^2 \tag{A23}$$

$$\theta_{2l} = \theta_{1l}(r_2/r_1) \tag{A24}$$

$$\theta_{1t} = \alpha\rho_s r_1\, c_t^2(c_t/c_l)^2 \tag{A25}$$

$$\theta_{2t} = \theta_{1t}(r_2/r_1). \tag{A26}$$

Downloaded 03 May 2010 to 171.66.16.244. Redistribution subject to ASME license or copyright; see http://www.asme.org/terms/Terms_Use.cfm

Transient Stokes Flow in a Channel Driven by Moving Sleeves

P. Carbonaro
Department of Mathematics,
University of Catania,
95125 Catania, Italy

Erik B. Hansen
Laboratory of Applied Mathematical Physics,
The Technical University of Denmark,
DK-2800 Lyngby, Denmark

A two-dimensional, nonstationary Stokes flow in an infinite channel with plane, parallel walls is considered. The flow is driven by two sleeves forming parts of the walls and moving with a constant velocity starting at t = 0. *The exact Laplace transform of the stream function is determined and an approximate inversion, valid for* t *small, is performed. The resulting approximate formula for the stream function is used to study numerically the nonstationary flow as it approaches the stationary state in which an infinite system of Moffatt eddies is fully developed. The results are presented as a series of streamline plots.*

Introduction

When interpreted as the stream function for the flow of a Newtonian fluid in the Stokes approximation, some solutions to the biharmonic equation in wedge-shaped regions describe infinite systems of eddies the size and intensity of which decrease as the vertex is approached. This was first noticed by Moffatt (1964a). Moffatt also devised an exactly soluble problem where such a system of eddies is found (Moffatt 1964b). In the problem the flow is driven by a pair of sleeves which replace a strip of the wall on each side of a wedge and slide with constant velocities in the directions toward or away from the vertex. Later similar eddy systems have been shown to exist in a number of other Stokes flow situations. As an example we mention the flow past a cylinder touching a plane wall (Schubert, 1967). Here the eddies occur in the wedgelike regions between the cylinder and the wall. An experimental demonstration of the existence of systems of eddies in slow flows in wedge-shaped regions was made by Taneda (1979). Taneda was only able to observe two eddies of the infinite system predicted by theory, but this limitation is understandable when it is realized that in the geometry used by Taneda, the ratio between the velocities of the flow in two successive eddies is about 10^{-3}. A more recent demonstration of such eddy systems was made by Coutanceau et al. (1984). In their experiment the eddies were caused by a cylinder rotating at the center of a channel with parallel walls, a geometry which resembles somewhat the one considered in the present paper.

The theoretical investigations of Stokes flows in wedge-shaped regions, which have been referred to in this paper all deal with stationary flows. It seems of interest, however, also to study the transient development of an eddy system from the start of a fluid motion to the stationary state. A first step in this direction was taken by Carbonaro (1985). He investigated the flow between two plane, parallel walls when a part of each wall was replaced by a sleeve oscillating in the direction perpendicular to the sides of the sleeve. Thus, the geometry considered by Carbonaro was the limiting case of the one considered in (Moffatt, 1964b), when the distance between the sleeves is fixed and the wedge angle goes to zero. Xu and Hansen (1987) investigated the transient flow in a sector region bounded by two intersecting planes and a circular cylinder with axis on the line of intersection of the planes, when the cylinder rotates with a constant angular velocity starting at, say, $t = 0$. However, the fact that their approach was purely numerical somewhat limited the detail with which they were able to analyze the development of the eddy system in which the intensities of the eddies differed by orders of magnitude. Xu and Hansen also pointed out that the transient development of flows in the geometry considered by Carbonaro (e.g., when the sleeves move with a constant velocity starting at $t = 0$) can be found exactly by means of the method of integral transforms. In this paper we shall do so and use the results to compute streamline plots at various instants of time during the transient development. In the next section we formulate the problem mathematically and determine the Laplace transform of its solution. From the Laplace transform we obtain an expression for the stream function in the stationary state. We also show how the Laplace transform can be expressed as an infinite series which can be inverted termwise. The resulting series for the stream function converges the more rapidly the smaller t is, so it is well suited for our purpose. We determine explicitly the first few terms of the series. In the final section we present some streamline plots computed from the formula obtained in this way and discuss the results.

The Problem and Its Solution

We consider a Newtonian fluid between two plane, parallel walls at distance $2h$ as shown in Fig. 1. Parts of the walls are replaced by infinite sleeves with half width ah, which move in

Contributed by the Applied Mechanics Division of THE AMERICAN SOCIETY OF MECHANICAL ENGINEERS for presentation at the Winter Annual Meeting, Dallas, Texas, Nov. 25–30, 1990.

Discussion on this paper should be addressed to the Technical Editor, Leon M. Keer, The Technological Institute, Northwestern University, Evanston, IL 60208, and will be accepted until two months after final publication of the paper itself in the JOURNAL OF APPLIED MECHANICS. Manuscript received and accepted by the ASME Applied Mechanics Division, Oct. 24, 1988.

Paper No. 90-WA/APM-48.

Copyright © 1990 by ASME
Downloaded 03 May 2010 to 171.66.16.244. Redistribution subject to ASME license or copyright; see http://www.asme.org/terms/Terms_Use.cfm

the directions indicated in the figure. The fluid is at rest until time $t = 0$, when the sleeves start moving with the constant speed v, which is assumed to be so small that Stokes approximation is valid. When all distances are measured in units of h, all times in units of the quantity h^2/ν, where ν is the kinematic viscosity), and we choose v to be unity (this causes no loss of generality since the problem is linear), the stream function $\psi = \psi(x, y, t)$ satisfies the equation

$$\Delta\Delta\psi = \frac{\partial\Delta\psi}{\partial t} \tag{1}$$

for $-\infty < x < \infty$ and $-1 < y < 1$, the boundary conditions

$$\psi(x, \pm 1, t) = 0 \text{ for } -\infty < x < \infty,\ \psi_y(x, \pm 1, t) = \begin{cases} \mp 1 \text{ for } |x| < a \\ 0 \text{ for } a < |x| \end{cases} \tag{2}$$

for $t > 0$, and the initial condition

$$\psi(x, y, 0) = 0 \tag{3}$$

for $-\infty < x < \infty$ and $-1 < y < 1$. The coordinate system (x, y) is indicated in Fig. 1 and the stream function is defined in the usual manner so that the velocity is equal to $(\psi_y, -\psi_x)$.

The Laplace transform, $\Psi = \Psi(x, y, s)$ of ψ, satisfies the boundary conditions in equations (2), and it follows from equations (1) and (3) that it satisfies the equation $\Delta\Delta\Psi - s\Delta\Psi = 0$ for $-\infty < x < \infty$ and $-1 < y < 1$. From this equation and the conditions in equation (2) it is found by standard Fourier transform technique that Ψ can be expressed as

$$\Psi(x, y, s) = L\{P(x+a, 1-y, t)\} + L\{P(x+a, 1+y, t)\} - L\{P(x-a, 1-y, t)\} - L\{P(x-a, 1+y, t)\} \tag{4}$$

where

$$L\{P(u, y, t)\} = \pi^{-1} \int_0^\infty \frac{\sin(ku)}{k} \left[\frac{\cosh q}{\cosh k} \cosh(ky) - \cosh(qy) \right] \frac{dk}{D}. \tag{5}$$

Here, $q = (s + k^2)^{1/2}$, and

$$D = s(q \sinh q - k \tanh k \cosh q). \tag{6}$$

By means of the limit value theorem for Laplace transforms, the stream function in the stationary state, $\psi_\infty(x, y)$, is found from formulas (4) and (5) to be

$$\psi_\infty(x, y) = P_\infty(x+a, 1-y) + P_\infty(x+a, 1+y) - P_\infty(x-a, 1-y) - P_\infty(x-a, 1+y) \tag{7}$$

where

$$P_\infty(u, v) = \frac{v}{\pi} \int_0^\infty \frac{\sin(ku)}{k} \frac{\sinh k(2-v)}{\sinh(2k) + 2k}\, dk. \tag{8}$$

When $|u|$ is small, it is convenient to evaluate P_∞ from formula (8). When $|u|$ increases, it becomes more convenient to use the following series, which is derived from formula (8) by contour deformation in the complex k-plane:

$$P_\infty(u, v) = \frac{v(2-v)}{8} + \frac{v}{2} \sum_{n=0}^{\infty} \text{Re} \left[\frac{\sin k_n(2-v)}{k_n \cosh^2 k_n} \exp(i k_n u) \right]. \tag{9}$$

Here, k_n, $n = 1, 2, \ldots$, are the roots of the equation $\sin(2k) + 2k = 0$ located in the first quadrant of the complex k-plane, and it is assumed that $u > 0$.

We now consider the transient flow.

In view of the complexity of the integrand in formula (5), we have not attempted to invert the Laplace transform in closed form. Instead we rewrite the integrand as a sum of four infinite series, which converge for all positive values of s, and can be

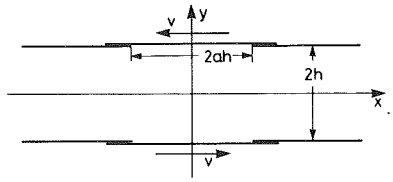


Fig. 1 The fluid in an infinite, two-dimensional channel with parallel walls at distance 2*h* is set into motion by two sleeves of length 2*ah*, which slide in the indicated directions with the constant speed *v* starting at *t* = 0

inverted term-by-term to any desired order. The series converge more rapidly, the larger s is. Therefore, with a fixed number of terms included, the approximation to ψ can be expected to be better, the smaller t is. Thus, this approach is particularly well suited for our purpose, to study the initial part of the transient motion.

To carry out the procedure outlined above, we first write D in equation (6) as

$$D = \frac{1}{2} s\, [q - b - (q + b) \exp(-2q)] \exp q. \tag{10}$$

In equation (10) and in the following formulas, $b = k \tanh k$. For $k = 0$ and $s > 0$, the square bracket in formula (10) is equal to $s^{1/2}\, [1 - \exp(-2s^{1/2})]$, while for $k > 0$ and $s > 0$, it is easily verified that

$$0 < \frac{q+b}{q-b} \exp(-2q) < \frac{k+b}{k-b} \exp(-2q) = \exp(-2(q-k)) < 1. \tag{11}$$

Consequently, in either case D^{-1} may be expanded as the convergent series

$$D^{-1} = 2\, s^{-1} \sum_{n=0}^{\infty} \frac{(q+b)^n}{(q-b)^{n+1}} \exp(-\alpha q), \tag{12}$$

where $\alpha = 2n + 1$. When formula (12) is inserted into formula (5), the integrand becomes a sum of four series each of which is multiplied by a factor, which depends on k but not on s. The four series are given by formula (12) with $\alpha = 2n$, $2n + 2$, and $2n + 1 \pm y$, respectively. Next, we apply the binomial formula to the numerator $(q - b + 2b)^n$ in formula (12). Thereby the nth term becomes a linear combination of the $n + 1$ functions

$$s^{-1}(q-b)^{-m} \exp(-\alpha q), \tag{13}$$

where $m = 1, 2, \ldots, n+1$, with coefficients which do not depend on s. It follows from the Laplace transform rules of attenuation and integration that

$$L^{-1}\{s^{-1}(q-b)^{-m} \exp(-\alpha q)\} = \int_0^t \exp(-k^2\tau) \phi_m(\tau, \alpha, b)\, d\tau, \tag{14}$$

if

$$\phi_m(t, \alpha, b) = L^{-1}\{(s^{1/2} - b)^{-m} \exp(-\alpha s^{1/2})\}. \tag{15}$$

It now only remains to determine the functions ϕ_m. This can be done for any given m. The first one, ϕ_1, is found in (Erdelyi et al., 1953). The others are derivable from ϕ_1 by differentiation, since it follows from formula (15) that $m\phi_{m+1} = \partial\phi_m/\partial b$ for $m \geqq 1$. Thus, by means of the foregoing we can invert the terms in the series in formula (12) and, hence, the integrand in formula (5) to any desired order. It turns out that for all m, Φ_m is of the form

Downloaded 03 May 2010 to 171.66.16.244. Redistribution subject to ASME license or copyright; see http://www.asme.org/terms/Terms_Use.cfm

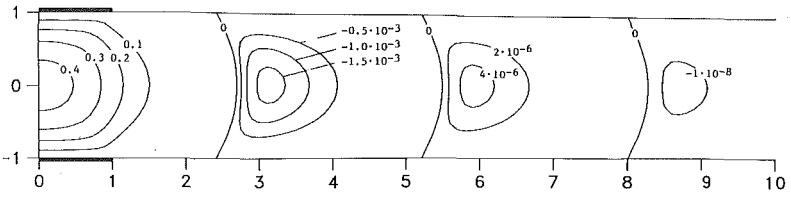


Fig. 2 The stationary flow in the section $0 < x < 10$ of the channel. On each streamline the value of the stream function is indicated. The streamlines $\psi = 0$ are the boundaries between consecutive eddies. Note that in the four eddies the streamlines are shown with different densities.

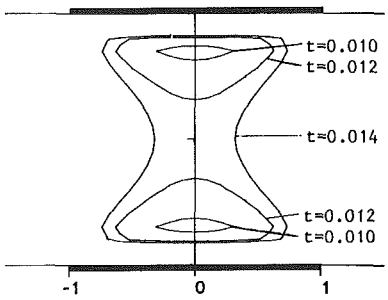


Fig. 3 The start of the central eddy. The streamline $\psi = 0.1$ is shown at times $t = 0.010$, 0.012, and 0.014.

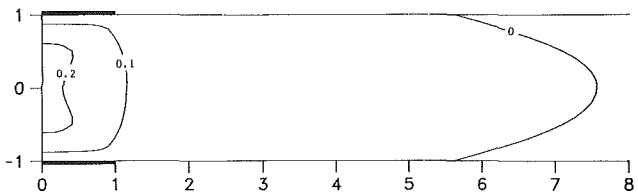


Fig. 4 The flow at $t = 0.05$

$$\phi_m(t,\alpha,b) = t^{-1/2} Q_m \exp\left(-\frac{1}{4}\alpha^2/t\right)$$

$$+ R_m \exp(-\alpha b + b^2 t) erfc\left(\frac{1}{2}\alpha t^{-1/2} - bt^{1/2}\right) \qquad (16)$$

where Q_m and R_m are polynomials of degree $m - 1$ in t with coefficients, which are powers of α and b. For example, $Q_1 = \pi^{1/2}$ and $R_1 = b$. In order to obtain the results presented in the next section, in turned out to be necessary to work out the explicit expressions for ϕ_2 and ϕ_3 also. Since they are rather complicated we shall not give them here.

When the integrand in formula (5) is inverted by means of an approximate Laplace inversion formula based on the first few of the functions ϕ_m, $P(u,v,t)$ becomes expressed as a Fourier sine integral, the integrand of which is itself an integral over the interval $[0, t]$. It is possible and convenient to rewrite somewhat this double integral by means of Fourier sine transform inversion formulas found in (Erdelyi et al., 1953). Thereby $P(u, v, t)$ becomes expressed as a sum of an integral over $[0, t]$ and a term which is still a double integral—but with an integrand which decreases more rapidly with increasing transform variable, k, than does the original one.

Results and Discussion

The formulas for the stream function, of which the derivation was described in the previous section, were used to compute stream line plots of the flow at various instants of time. Some of the plots are shown in Figs. 2 through 7. The numerical computations were carried out on the IBM 3081 computer at the Lyngby branch of the UNI•C Computing Centre.

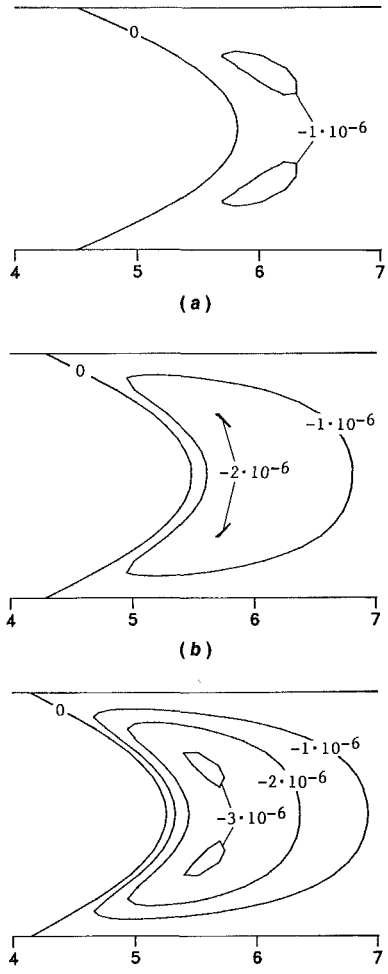


Fig. 5 The start of the second eddy. The streamline $\psi = 0$ is the boundary of the central eddy. The three plots correspond to times $t = 0.077$ (*a*), $t = 0.085$ (*b*), and $t = 0.091$ (*c*), respectively.

In all our computations the half-width of the sleeves was $a = 1$.

To compute the stream function in the stationary state we used formula (8) in the interval $|x| < 3$ and formula (9) for $2 < |x| < 10$. The Fourier sine integral in formula (8) was evaluated by means of the subroutine DQDAWF of the IMSL-MATH/LIBRARY. In the interval $2 < |x| < 3$, where both formulas were used, the agreement was complete. As mentioned before, the approximate expression for the stream function in the transient state is a sum of an integral over the interval $[0, t]$, and a Fourier sine integral of which the integrand itself is an integral over $[0, t]$. In the integrals the interval $[0, t]$ was divided into n subintervals of equal length, and each integral over a subinterval was evaluated by means of an *l*-

Downloaded 03 May 2010 to 171.66.16.244. Redistribution subject to ASME license or copyright; see http://www.asme.org/terms/Terms_Use.cfm

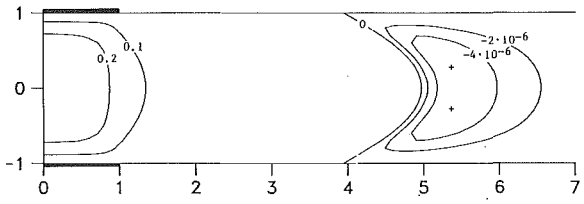


Fig. 6 The flow at $t = 0.1$. The second eddy still consists of two symmetric ones with centers at the crosses.

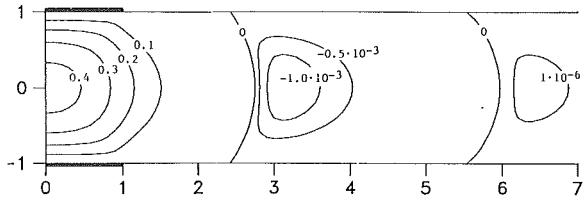


Fig. 7 The flow at $t = 0.5$

point Gauss formula. Before the production runs were carried out, the approximate stream function was evaluated for a number of t-values and at a set of test stations in the channel using $n = 2$ and $l = 6$ as well as $n = 4$ or 8 and $l = 12$. Since the discrepancies between the results were insignificant for all times and all stations the values $n = 2$ and $l = 6$ were used in all subsequent calculations. As anticipated, the larger t is, the more the functions $\phi_1, \phi_2, \ldots$ have to be included in the approximation to the stream function. It was found sufficient to include ϕ_1 for $t \leqq 0.1$ and ϕ_1 and ϕ_2 for $t \leqq 0.6$. Since the largest finite time we considered was $t = 0.5$, it was therefore sufficient to include ϕ_1 and ϕ_2 in the computations by means of which the streamline plots were produced.

A streamline plot of the stationary flow is found in Fig. 2. In the interval shown ($0 < x < 10$) four eddies can be seen. The flow structure resembles the one which Moffatt (1964b) found in a wedge region. The existence of such a flow structure in wedge or channel geometries is by now a well-established fact, but one may still feel a need for a qualitative explanation why the flow splits up in an infinite system of eddies, rather than forming a single eddy, which dies out as the distance from the source of agitation increases. In the authors' opinion the observed structure can be understood by the following argument. When fluid particles near one of the sleeves reach the edge of the sleeve, their forward motion is blocked by the almost stagnant fluid next to the immobile part of the channel wall. Therefore, the particles are forced to move towards the other channel wall, and in this way the central eddy is formed. The central eddy acts on the rest of the fluid with viscous stresses creating a shear force which tends to pump around the fluid body outside the eddy. Recently Hansen (1988) found that in the transient Stokes flow in a fluid half-space bounded by plane containing a sleeve, an eddy exists in the region close to the sleeve. In that case, however, no other eddies are found. In a half-space the fluid, which is pumped in or out by the central eddy, can easily be supplied from or disposed of in directions in the fluid body, which are far away from the fixed boundary. In the channel, the impeding forces from the walls have to be overcome in order that the fluid can move around. Therefore, the necessary shear stresses exerted by the central eddy and by Newton's third law, the reactive shear stresses from the rest of the fluid have to be larger. The shear stress is proportional to the velocity gradient, which is the ratio between a velocity drop and the distance over which it takes place. The drop from the velocity at the edge of the central eddy to the velocity 0 (at infinity) cannot exceed the velocity 1 of the sleeves. Therefore, the velocity gradient in the direction of the channel axis can only be increased enough by reducing the distance over which the available velocity drop takes place. Consequently, a stagnation point must exist near the edge of the central eddy, and this stagnation point is the center of the second eddy. The existence of the eddies further out can be understood by the same argument.

We now consider the transient flow. Although strictly all the fluid is immediately set into motion, just after $t = 0$ the motion is essentially concentrated to the regions close to the sleeves, and in each of these regions the flow should resemble the one outside a sleeve in a plane wall bounding a fluid half-space. Indeed, in the channel the streamlines $\psi = 0.1$ emerge outside the sleeves a little before $t = 0.01$ (see Fig. 3), while in the case of the half-space Hansen (1988) found that the streamline $\psi = 0.1$ emerges between $t = 0.01$ and $t = 0.011$. (Since $a = 1$, the dimensionless length of a sleeve, the unit of length, and the unit of time are pairwise identical in this paper and in (Hansen, 1988).) The smallness of the time difference suggests that the interaction between the sleeves is weak at this point of the development. On the other hand, at $t = 0.01$, the local maximum value of ψ (which is assumed at the center of the eddies) is 0.102, and the value of ψ at the center of the channel is 0.087. This means that even at this early stage 85 percent of the fluid, which passes between a sleeve and center of the neighboring eddy, also passes between the other sleeve and its eddy. The development towards a merger of the two eddies is illustrated in Fig. 3 where the streamline $\psi = 0.1$ is shown at different instances. It was found that the centers of the eddies move rather slowly, and that the formation of a single, central eddy (i.e., when the local maxima reach $(x, y) = (0, 0)$) does not take place until $t = 0.085$.

In the beginning the central eddy is very large. Thus, at $t = 0.01$ it stretches beyond the interval $-10 < x < 10$, where computations were performed. Its size at $t = 0.05$ can be seen in Fig. 4, and Figs. 6 and 7 show that the eddy continues to shrink during the transient period giving room for the second and following eddies. Xu and Hansen (1987) found that in a sector region bounded by two intersecting lines and a rotating circle with its center at the vertex, a similar development takes place during the transient period after the circle has started to rotate. In that case an eddy, which originally seems to occupy the whole sector, later withdraws from the region closest to the vertex to be replaced by new and weaker eddies. The observed behavior shows that in the beginning of the fluid motion the impeding influence of the immobile walls is smaller than later on. This is in agreement with the fact that the flow velocities in the central eddy, and hence the velocity gradients, increase with time.

The slow merger of the two initial eddies into a central one also affects the development of the next eddy further out in the channel. This is demonstrated in Figs. 5(a–c). It is seen that outside the edge of the central eddy the streamlines $\psi = -1 \cdot 10^{-6}$, $-2 \cdot 10^{-6}$ and $-3 \cdot 10^{-6}$ all start as symmetric pairs in which the two streamlines expand in the direction of the channel axis so that the pair eventually becomes one streamline. This shows that the eddy next to the central one is also developed by a merger of two eddies. Our numerical results show that at $t = 0.1$, there are still two local minima of ψ in $x > 0$. Their approximate locations are shown in Fig. 6. Thus, at $t = 0.1$ a single, second eddy has not yet been formed.

The further development towards the stationary state is illustrated in Figs. 6, and 7. A comparison between Figs. 2 and 7 shows that at $t = 0.5$, the central eddy has almost reached its stationary state and that the next eddy is not far from it either. Indeed, at $t = 0.5$, the intersection of the channel axis and the boundary between the central eddy and the next one is at $x = 2.74$, while it is at 2.70 in the stationary state, and the total fluxes (the absolute values of the stream function in

Downloaded 03 May 2010 to 171.66.16.244. Redistribution subject to ASME license or copyright; see http://www.asme.org/terms/Terms_Use.cfm

the center of the eddy) are 0.444 and 0.447, respectively. At $t = 0.5$ and $t = \infty$, the intersection of the axis and the boundary between the second and the third eddies is at 5.97 and 5.49, respectively, and the fluxes in the second eddy are $1.41 \cdot 10^{-3}$ and $1.67 \cdot 10^{-3}$, respectively. In the third eddy the flux is $1.38 \cdot 10^{-6}$ at $t = 0.5$, while it is $4.69 \cdot 10^{-6}$ in the stationary state. Thus, the third eddy is still rather far from its stationary state, and we may conclude that the transient time of the central eddy and its next neighbors is about 0.5 time units, which is a real time equal to $0.5h^2/\nu$.

Acknowledgments

The work presented in this paper was carried out during two visits of one of the authors (EBH) to the University of Palermo and the University of Catania, respectively. He is grateful to Al Consiglio Nationale delle Richerche and to Julie Damm's Studiefond whose support made the two visits possible. Thanks are also due to the Danish Technical Research Council for partial coverage of the computing expenses under grant No. 16-4287.M.

References

Carbonaro, P., 1985, "Sequences of Eddies in Oscillatory Stokes Flow," *Journal de Méchanique Théoretique et Appliquée*, Vol. 4, pp. 425–432.

Coutanceau, M., Bouard, R., Bourot, J.-M., and Hellou, M., 1984, "Visualization of the Cellular Structure of the Two-Dimensional Stokes Flow Induced by the Rotation of a Circular Cylinder in a Rectangular Tank" (in French), *Comptes Rendus Acad., Ser. II*, Vol. 298, pp. 767–770.

Erdelyi, A., et al., 1954, *Tables of Integral Transforms*, Vol I, McGraw-Hill Book Co., New York, pp. 73, 246.

Hansen, E. B., 1988, "Transient Stokes Flow Over a Plane with a Moving Sleeve," *Journal of Applied Mathematics and Physics*, Vol. 39, pp. 762–767.

Moffatt, H. K., 1964a, "Viscous and Resistive Eddies Near a Sharp Corner," *Journal of Fluid Mechanics*, Vol. 18, pp. 1–18.

Moffatt, H. K., 1964b, "Viscous Eddies Near a Sharp Corner," *Archivum Mechaniki Stosowanej*, Vol. 2, pp. pp. 365–372.

Schubert, G., 1967, "Viscous Flow Near a Cusped Corner," *Journal of Fluid Mechanics*, Vol. 27, pp. 647–656.

Taneda, S., 1979, "Visualization of Separating Stokes Flow," *Jour. Phys. Soc. Japan*, Vol. 46, pp. 1935–1942.

Xu, B., and Hansen, E. B., 1987, "Transient Stokes Flow in a Wedge," ASME JOURNAL OF APPLIED MECHANICS, Vol. 54, pp. 203–208.

Downloaded 03 May 2010 to 171.66.16.244. Redistribution subject to ASME license or copyright; see http://www.asme.org/terms/Terms_Use.cfm

On the Disturbance of a Thin Layer of Liquid by a Moving Obstruction

Roger F. Gans
Professor,
Mem. ASME

Chung-Hai Wang
Graduate Student.

Department of Mechanical Engineering,
University of Rochester,
Rochester, NY 14627

We calculate the free surface shapes upstream and downstream of an obstacle obstructing a thin liquid layer on a moving surface, taking into account gravity and surface tension. We assume low Reynolds number viscous flow, a two-dimensional layer, and small ratio of vertical to horizontal length scale. The upstream and downstream shapes are very different. The upstream liquid piles up against the obstacle to provide an overpressure sufficient to drive the Poiseuille component of the lubrication flow under the obstacle. The downstream liquid is disturbed only by surface tension.

1 Introduction

The problem of a solid object moving in a liquid at the free surface of that liquid has applications ranging from yacht racing to the behavior of starved bearings. In the case where the liquid lies in a thin layer on top of a solid surface, so that viscous forces are important, the applications are primarily to starved bearings, lubrication/friction testing devices, and blade coating. One of the outstanding issues for these problems is the behavior of the liquid and in the inlet and exit regions. As Bonneau and Frene (1983) remark, ". . .an inlet zone analysis under starved conditions appears to be badly needed. Such a study should take into account surface tension, gravity and inertia effects." To our knowledge no such study exists. Indeed, no study including correctly both gravity and surface tension exists, and it is the purpose of this paper to provide one.

Both the coating and lubrication communities recognize the distinction between low and "high" Reynolds numbers. The latter case requires inertial terms to be included. Both communities use a vertically integrated streamwise momentum equation as a first approximation. A good exposition of this approach for roll coating is given by Cerro and Scriven (1980). The use of inertia terms for the entrance region in bearings is apparently limited to the case of fully flooded bearings, for which gravity is irrelevant. Recent work in this area has been pursued by Tichy and coworkers (Tichy, 1986; Tichy and Bougin, 1985). The latter has a good set of references to earlier work.

The low Reynolds number bearing case can be examined at two levels of detail. A problem similar to that worked here, but neglecting gravity, was attacked by Tipei (1978). One difficulty with this work is the apparent contradiction between the assumption of Bernoulli's law on the free surface and the imposition of shear stress continuity. These are incompatible conditions.

For the thin layers that occur in starved bearing analyses, Bernoulli's law is likely to be a bad approximation even outside the gap. It is likely to be much better in the case of fully flooded conditions where shear is small outside the immediate entrance region. A similar approach was taken by Wong et al. (1985) for the classical problem of the cylinder rotating above a plane. The same Bernoulli assumption is made. They neglect the effect of coating of the cylinder, so their work can be compared with that presented here.

Bonneau and Frene (1983) have examined in great detail the immediate entrance region, including surface tension, but neglect gravity and inertia. They conclude that the major adjustment between the upstream layer and the gap takes place in a region of perhaps two gap widths extending upstream with one into the gap. They do not discuss in detail how this region is to be matched to the free stream far upstream. Their work is complementary to the work we report.

By far the most detailed work, including experiments that measure layer thickness, comes from the coating community. (Hsu et al., 1985; Sullivan and Middleman, 1986; Sullivan et al., 1987) Their basic system is a cylinder rotating in a bath of liquid. The liquid is drawn up the cylinder and interacts with a blade at or near the top of the system. Their interest is focused on the thickness of the layer after the interaction, the coating thickness, and on how this is affected by the liquid constitutive law. They neglect gravity. They use the large Reynolds number results for simple roll coating as upstream conditions (Cerro and Scriven, 1980; Campanella and Cerro, 1984), and make a tacit assumption that the downstream flow intersects the blade at a corner.

We introduce a direct method for the complete analysis of the flow on the moving plate under a fixed obstacle. (Fig. 1.)

Contributed by the Applied Mechanics Division of THE AMERICAN SOCIETY OF MECHANICAL ENGINEERS for publication in the JOURNAL OF APPLIED MECHANICS.

Discussion on this paper should be addressed to the Technical Editor, Prof. Leon M. Keer, The Technological Institute, Northwestern University, Evanston, IL 60208, and will be accepted until two months after final publication of the paper itself in the JOURNAL OF APPLIED MECHANICS. Manuscript received by the ASME Applied Mechanics Division, Dec. 12, 1988; final revision, June 2, 1989.

Copyright © 1990 by ASME
Downloaded 03 May 2010 to 171.66.16.244. Redistribution subject to ASME license or copyright; see http://www.asme.org/terms/Terms_Use.cfm

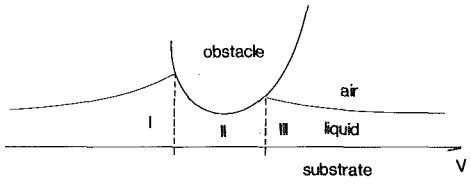


Fig. 1 General obstacle on substrate; the slopes are exaggerated, the analysis holding only in the limit of small slopes

We show that the entrance and exit heights can be determined by reference to a Reynolds equation outside the lubrication region if one includes gravity in the analysis. We show the influence of surface tension for the specific obstacle model of a blade. (See Fig. 2.).

The plan of the paper is:

(1) to formulate the general problem of an obstacle partially obstructing a liquid layer on a uniformly moving substrate;

(2) to show that the qualitative behavior of the liquid outside the gap is independent of the shape of the obstacle (in particular, the usual condition for reversed flow appears, and we find a condition for gravity capillary waves upstream of the obstacle); and

(3) to calculate liquid behavior over a range of a four-parameter space.

2 Formulation and Some General Results

Consider the flow under an obstacle partially obstructing a layer of incompressible liquid. The liquid lies on a moving, rigid surface, referred to as the substrate. Denote the viscosity and density of the liquid by μ and ρ, respectively. Denote the surface tension between the liquid and the overlying air by γ. Denote the thickness of the liquid layer far from the obstacle by h_∞, and let the closest separation of the obstacle from the substrate be h_0. Choose a coordinate system attached to the obstacle, and denote the velocity of the substrate by V. Let the substrate surface be $z=0$, with $x=0$ centered under the lowest point of the obstacle and z positive upwards. Figure 1 shows a sketch of the system.

We consider a purely two-dimensional problem and seek steady solutions. The basic equations of motion are conservation of momentum and mass

$$\rho\{uu_x + wu_z\} + p_x = \mu\{u_{zz} + u_{xx}\}$$

$$\rho\{uw_x + ww_z\} + p_z = \mu\{w_{zz} + w_{xx}\} - \rho g$$

$$u_x + w_z = 0 \tag{1}$$

where the subscripts denote partial derivatives, u and w denote the horizontal and vertical components of the velocity, p is the pressure, and g is the acceleration of gravity.

The liquid layer is divisible into three regions. Region I, to the left of the obstacle, is the entrance—or leading edge region. Region II is the region under the obstacle. Region III, to the right of the obstacle, is the exit—or trailing edge region. The lower boundary condition (on $z=0$) is the same in all three regions: the no-slip, $u=V$, $w=0$, condition. The upper surface conditions in regions I and III are the continuity of stress and the kinematic condition relating the vertical velocity and the free surface shape. The upper surface conditions in region II are simple no-slip, $u=0=w$, conditions.

The problem is more easily understood if one scales the variables. This will be done here in anticipation of a lubrication analysis under the obstacle so that $h(x)$, the thickness of the layer is supposed to be small everywhere, compared to the characteric horizontal dimension; and variation in the horizontal direction will be slow compared to that in the vertical. This suggests scaling h and z by h_0 and x by L, where L is a characteristic length related to the horizontal extent of the obstacle. The choice of L is obstacle dependent. The ratio of these two scales will be denoted by $\epsilon \ll 1$. This is the fundamental small parameter for a lubricationlike analysis.

The horizontal velocity u will be scaled by V and the vertical velocity by ϵV, as is common. The pressure scale will be denoted by P. The scaled differential equations become:

$$\epsilon\mathrm{Re}\{uu_x + wu_z\} + \Pi p_x = \{u_{zz} + \epsilon^2 u_{xx}\}$$

$$\epsilon^3\mathrm{Re}\{uw_x + ww_z\} + \Pi p_z = \epsilon^2\{w_{zz} + \epsilon^2 w_{xx}\} - c^2\mathrm{Re}\epsilon$$

$$u_x + w_z = 0 \tag{2}$$

where $\mathrm{Re} = \rho V h_0/\mu$ is the Reynolds number, $c^2 = gh_0/V^2$ is the square of the ratio of gravity wave speed to the speed of the substrate, and

$$\Pi = \epsilon\mathrm{Re}P/(\rho V^2) \tag{3}$$

is a dimensionless representation of the pressure scale. If, as is common in incompressible lubrication analysis, we work with the gage pressure and take P to be $\mu LV/h_0^2$, then $\Pi = 1$. It will prove useful later to have defined $G = \epsilon\mathrm{Re}c^2$, as the gravity scale. When P is taken to be $\mu LV/h^2$, $G = \rho g h_0/P$—the ratio of the overburden pressure to the lubrication pressure. In bearing applications this is a small number.

The variables appearing in equations (2) are dimensionless. As the remainder of the paper uses these dimensionless forms exclusively, no ambiguity should arise from the use of the same symbols for dimensional and dimensionless quantities.

Solutions to this set will be sought in the limit that both ϵ and the product $\epsilon\mathrm{Re}$ are small. G is left a 0(1) parameter. This is equivalent to requiring that

$$(\mathrm{Re}/\epsilon)c^2 = \rho g h L/\mu V \gg 1,$$

and it allows us to neglect the viscous term in the vertical momentum equation in comparison to the gravity term. These approximations reduce the order of the system in the x-dimension, which reduces the number of boundary conditions that can be applied at boundaries in x.

In all three regions no slip boundary conditions apply on the bottom of the layer. At the top of the layer in regions I and III, vanishing shear stress and continuous pressure are required. The pressure condition can be converted to one on the velocity using the kinematic condition: that the vertical velocity be equal to the total derivative of the surface with respect to time. In region II, no-slip boundary conditions on the velocity can be applied at $z=0$ and at $z=h(x)$, leading to the usual Reynolds equation obtained by a vertical integration of the mass conservation equation. The horizontal boundary conditions on the Reynolds equation will be the continuity of pressure at the entrance and exit boundaries. We will discuss this issue further in Section 3.

The introduction of gravity made necessary by the appearance of free surfaces makes this problem different from the usual lubrication problem. Gravity becomes the key to the entrance region.

We begin with an assessment of the flow under the free surfaces. Integrating the second equation in the set (2) gives

$$\Pi p = G(c(x) - z) \tag{4}$$

where $c(x)$ is an arbitrary of function of x. The boundary conditions in z are that $u=1$ on $z=0$, and that $u_z=0$ on the upper surface, $z=h$. In addition, the gage pressure at the upper surface is reduced below zero by the effects of surface tension, giving a pressure boundary condition

$$\Pi p = -\Gamma[K_1 + K_2] \tag{5}$$

where K_1 and K_2 denote the principal curvatures of the surface and

Downloaded 03 May 2010 to 171.66.16.244. Redistribution subject to ASME license or copyright; see http://www.asme.org/terms/Terms_Use.cfm

$$\Gamma = \gamma\epsilon^2 \mathrm{Re}/\rho L V^2 = \epsilon^2\gamma/\mu V \tag{6}$$

is the appropriate dimensionless representation of the surface tension.

The principal curvatures simplify in this two-dimensional lubrication setting. $K_1 = 0$, and $K_2 = h_{xx} + 0(\epsilon^2)$. With these simplifications, the gage pressure under the free surface becomes

$$\Pi p = G(h(x) - z) - \Gamma h_{xx}. \tag{7}$$

The horizontal momentum equation can be be integrated to find u:

$$u = (Gh_x - \Gamma h_{xxx})z(z/2 - h) + 1, \tag{8}$$

where we have applied the no-slip condition on the bottom and the zero shear condition on the top.

An equation for h can be found in either of two equivalent ways. One can either solve equation (2c) for w, applying a no-slip boundary condition on $z = 0$ and the kinematic condition on $z = h$, or integrate equation (2c) for the flux, q, which is constant for this incompressible system. The result is the same third-order ordinary differential equation of the height $h(x)$ in regions I and III:

$$h^3(Gh_x - \Gamma h_{xxx}) = 3(h - q) \tag{9}$$

where q is the flux per unit length, numerically equal to the thickness of the layer at $\pm\infty$. The boundary conditions for equation (9) are that $h \to q$ as $x \to \pm\infty$, that h_x match the slope fixed by the contact angle, and a condition relating h and h_{xx} derived from the pressure matching conditions at $x = -1$ and $x = 0$. (Note that $h = q$ is a solution, but it is in general not acceptable because of the contact angle boundary condition.)

This is a difficult third-order nonlinear boundary value problem. We can understand more of the physics by considering first the (singular) limit $\Gamma \to 0$, and then the linearized version, valid when $(h - q)/h \ll 1$, before moving on the full problem. In the singular limit the equation becomes

$$Gh^3 h_x = 3(h - q) \tag{10}$$

and we must discard the conditions on the slope at the boundaries.

There are two possible solutions to this equation. The simple solution $h = q$ describes a level surface satisfying the boundary conditions at ∞, now acceptable with the loss of the contact angle boundary condition. The second solution, implicit in x, is obtained by separation of variables.

$$x - x_0 = G\{h^3 + (3/2)qh^2 + 3q^2h + 3q^3 \log(h - q)\}/9$$

$$= GH(h,q)/9 \tag{11}$$

where x_0 is a constant of integration. Neither x_1 nor h_1, the intersection height of the liquid at the leading edge, is known in general. However, x_0 must equal $x_1 - GH(h_1,q)/9$. As the intersection of the surface with the obstacle is on the surface, x_1 and h_1 are related by the equation of the surface, so that x_1 and h_1 together represent only one undetermined constant.

The log term in equation (11) shows that $h > q$. As $h \to q$, the right-hand side approaches $-\infty$, so that $x \to \infty$. Thus, the solution (11) can represent the flow in the leading edge region, region I, but cannot be used in the trailing edge region, region III. Thus, we see, *without working out the flow under the obstacle*, that when $\Gamma \to 0$ there is a pileup of fluid in front of the obstacle, and a flat sheet behind.

We note also (compare Tipei, 1978) that the simple formulation predicts a region of reversed flow. Combining equations (8) and (9) gives

$$u = 3(h - q)z(z/2 - h)h^3 + 1. \tag{12}$$

As $h \to q$, we obtain the uniform solution $u = 1$, as required. The horizontal velocity is a monotonically decreasing function of z, reversing at

$$z = h\{1 \pm [(h - 3q)/3(h - q)]^{1/2}\}. \tag{13}$$

The onset of reversal is at $h = 3q$. For $h > 3q$ there is a lens-shaped region of reversed flow.

We can learn more about the general situation with surface tension by examining a linearized version of the full problem. We can expect that the qualitative behavior of the full solutions will be similar to that of the solutions to the linearized problem.

To linearize, let $h = q + d$, where $d/h \ll 1$. Equation (9) becomes

$$(q + d)^3(Gd_x - \Gamma d_{xxx}) = 3d, \tag{14}$$

which can be linearized to

$$q^3(Gd_x - \Gamma d_{xxx}) = 3d. \tag{15}$$

The linear equation admits simple exponential solutions, of the form e^{kx}, and k satisfies a cubic characteristic equation

$$\Gamma k^3 - Gk + 3/q^3 = 0. \tag{16}$$

From Descartes' rule of signs it can be seen that there is at most one negative and at most two positive roots. The Cardan solution shows that there is always one negative root. There can be two positive roots, or a pair of conjugates. In the latter case, the real parts of the conjugate pair are positive. All of this means that in region III, where $x > 0$, the linear version of the problem admits the only single solution

$$d_{\mathrm{III}} = (\tan\phi/k)e^{-kx} \tag{17}$$

where $-k$ is the single negative real root of equation (16) and ϕ denotes the complement to the angle between the outward normal to the liquid surface and the outward normal to the solid (blade) surface, taken positive (negative) if the inner product of the normals is positive (negative). Thus, $\phi > 0$ (< 0) implies capillary rise (depression) in both regions I and III. (For a vertical bounding surface, ϕ is $\pi/2$ less than the contact angle, θ. For nonvertical surfaces the situation is more complicated. There is the possibility of a reentrant surface and a non-single-valued d_{III}.) This is clearly a simple modification of the downstream flat sheet we found in the $\Gamma \to 0$ limit. The capillary rise is independent of the dynamics. Surface tension does not alter the fundamental difference between the leading edge and trailing edge regions. (In the limit that $\Gamma \to 0$, the amplitude of the rise and the e-folding length over which the rise is nonzero tend to zero.)

It is easy to see from equation (16) that the real root $-k < -\sqrt{(G/\Gamma)}$, so that the rise on the trailing edge $d_{\mathrm{III}}(0)$ is less than $\tan\phi\sqrt{(\Gamma/G)}$, and a sufficient condition that the linear solution be a good approximation in region III is that $\tan\phi\sqrt{(\Gamma/G)}/q \ll 1$. If $3/\Gamma q^3$ is large compared to $(G/\Gamma)^{3/2}$, then the negative root is approximately equal to $-(3/\Gamma)^{1/3}q$, and a better estimate for linearity is that $q \tan\theta\, \Gamma^{1/3} \ll 1$. The choice of criterion depends on the ratio

$$9\Gamma/(Gq^2)^3 = [9\gamma(\mu V)^2]/[q^6(\rho g h_0^2)^3]. \tag{18}$$

Two solutions are possible in region I, so that we can match the solution at the trailing edge through the intermediate region II solution. The character of these two solutions at a large distance from the obstacle, where the linear approximation can be expected to hold in region I as well, depends on the magnitude of the parameters G, q, and Γ. For $\Gamma < 4G^3q^6/243 = \Gamma_{\mathrm{crit}}$, the three roots k are all real, and the surface cannot sustain any wavelike behavior. At larger values of Γ, the two non-negative roots become complex. The decay rate and frequency are proportional to $(3/2\Gamma)^{1/3}/q$. The proportionality constants depend solely on the ratio $\Gamma/\Gamma_{\mathrm{crit}}$.

In region II one can write $\Pi p = -Gz + \Pi p^*(x)$, where p^* satisfies the usual Reynolds equation. The Reynolds equation, being one-dimensional and steady, can be integrated once to give

Downloaded 03 May 2010 to 171.66.16.244. Redistribution subject to ASME license or copyright; see http://www.asme.org/terms/Terms_Use.cfm

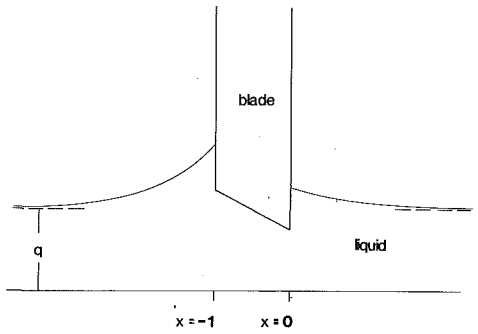


Fig. 2 The blade obstacle; there is a vertical exaggeration of $1/\epsilon$ in the figure

$$\Pi p_x^* = 6/h^2 - 12q/h^3. \tag{19}$$

The next integration depends on the specific obstacle under consideration. It will introduce a single constant of integration. There are two boundary conditions for equation (19), the continuity of pressure at each end of the region. These two conditions determine that constant of integration here, and the free constant associated with the rise at the leading edge. The downstream intersection of the layer with the obstacle is determined by equation (17). The details are best explored in the context of a specific problem.

3 Analysis of a Simple Example

The general analysis of the previous section will be clearer in the context of a simple, well-understood geometry. We use a simple plane wedge, which can model a starved slider bearing or a coating blade. Figure 2 shows the geometry of this system. Figure 2 is drawn in scaled coordinates. The apparent steep slope is not steep. We have introduced an informal vertical exaggeration of $1/\epsilon$. This is also true of the figures displaying the results, discussed in Section 4. The length scale L is the thickness of the blade. We show the liquid intersecting the vertical sides on both the upstream and downstream sides, and we will limit the analysis to cases where this applies. As we will show next, this restricts the values G, Γ, q, ϕ, and β that are permissible.

Some words about the lacing together of the three regions are appropriate at this point. The approximations used in this paper lead to an apparent contradiction: The normal velocity does not vanish on the vertical surface of the blade. In a typical hydrodynamic setting, one expects to be able to impose at least normal boundary conditions of the velocity. It is counterintuitive to allow apparent penetration of the boundary by the liquid. This is, however, the correct boundary condition in the present circumstance, as we shall attempt to explain. The governing equations for the flow in regions I and III, when reduced to a single equation in x, are of first-order in the pressure, and zeroth-order in the x velocity; a pointwise boundary condition cannot be imposed on the velocity. We can impose only a single pressure condition and an integrated velocity condition. The latter is just the conservation of mass flow, which is guaranteed within the formulation used. Thus, the nonsatisfaction of the normal velocity boundary condition on the vertical leading and trailing edges of the blade is appropriate, and presumably correctable by a more detailed analysis near these two solid surfaces. (For an example of such an analysis, see Bonneau and Frene, 1983). This detailed analysis will not affect the nature of the solution found next at the highest order. Our solution remains a correct first approximation.

The point of closest approach is the trailing edge. Let that be $x=0$. Then the leading edge becomes $x=-1$. Denote the slope of the blade by $-\beta$, where β is a positive number, so that the height of the gap at $x=-1$ is $1+\beta$. The gage pressure in the gap is governed by equation (19), with $h=1-\beta x$. The integration is straightforward leading to

$$\Pi p^* = -6\{q-h\}/\beta h^2 + \Lambda \tag{20}$$

where Λ is a constant of integration. The boundary conditions for the lubrication region are the continuity of the pressure across the gap. All three pressure expressions have the term $-Gz$ in common, so that the match can be imposed on p^*—we require p^* to be continuous at $x=-1$ and $x=0$.

Recall that $\Pi p^* = Gh - \Gamma h_{xx}$ in regions I and III. Use subscripts 1 and 2 to refer to the leading and trailing edges, respectively, and use h, here, to refer to the free surface height. Then we have the two boundary conditions

$$-6\{q-1-\beta\}/\beta(1+\beta)^2 + \Lambda = Gh_1 - \Gamma(h_{xx}) \tag{21a}$$

$$-6\{q-1\}/\beta + \Lambda = Gh_2 - \Gamma(h_{xx})_2 \tag{21b}$$

where we have used $h=1$ and $h=1+\beta$ at the two boundaries.

The two boundary conditions can be uncoupled if the linear approximation can be applied downstream. In that case

$$h_{\mathrm{III}} = q + \tan\phi \exp(-kx)/k \tag{22}$$

where, again, $-k$ is the negative root of the characteristic equation (16). The downstream boundary condition on the pressure becomes

$$\Pi p^* = Gq + G\tan\phi/k - \Gamma k\tan\phi = Gq + \Theta(G,\Gamma,q,\phi). \tag{23}$$

Substitution into equation (21*b*) gives the constant in terms of the capillary rise on the downstream side. That leads to an expression for the pressure

$$\Pi p^* = 6[(q-1) - (q-h)/h^2]/\beta + Gq - \Theta(G,\Gamma,q,\phi). \tag{24}$$

The quantity $G/k - k\Gamma > 0$, so that the sign of Θ is the same as that of ϕ. When Θ is positive (negative), it represents the decrease (increase) in pressure caused by the curvature at the downstream end. Substitution of this into equation (21*a*) provides the third boundary condition for equation (9).

The general matching, when neither upstream or downstream equations can be linearized, requires the determination of the constant Λ appearing in equation (21) as an eigenvalue.

While it is reasonable to expect the linearization to be applicable at the downstream end, we can expect a large rise at the leading edge, so it is necessary to solve the full nonlinear problem in region I. This requires a numerical approach, which we outline briefly here.

Our problem is to solve equation (9), subject to the pressure boundary condition

$$Gh_1 - \Gamma(h_{xx})_1 = 6[(q-1) - (q-1-\beta)/(1+\beta)^2]/\beta + Gq - \Theta$$

$$= B(G,\Gamma,q,\phi,\beta) + Gq \tag{25}$$

and the contact angle condition $h_x = \tan\phi$ at $x=-1$, as well as the condition at infinity, $h \to q$ as $x \to -\infty$.

It is convenient for computation to map the infinite range of x into a finite range. In addition, because $h \to q$ as $x \to -\infty$, it is convenient to let $h = d + q$. Put

$$y = 1 - e^{x+1} \tag{26}$$

and rewrite the governing equation for d with y as the independent variable

$$(y-1)(d+q)^3\{Gd_y - \Gamma[(y-1)^2 d_{yyy} + 3(y-1)^2 d_{yy} + d_y]\} = 3d. \tag{27}$$

The boundary conditions become

$$d_y + \tan\phi = 0 = Gd - \Gamma(d_{yy} - d_y) - B \tag{28}$$

at $y=0$ and $d=0$ at $y=1$.

The linearized differential equation has three solutions, two of which are acceptable and one of which is not. This means that a shooting technique to integrate numerically is doomed

Downloaded 03 May 2010 to 171.66.16.244. Redistribution subject to ASME license or copyright; see http://www.asme.org/terms/Terms_Use.cfm

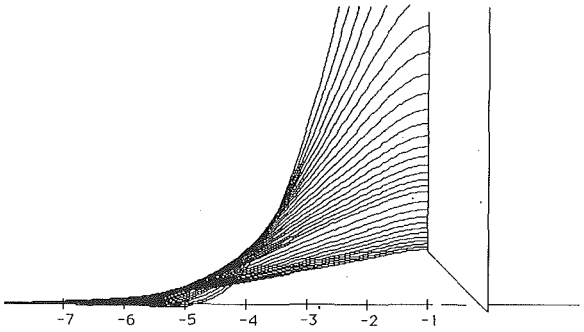


Fig. 3 Variation of gravity; profiles are depressed with increasing G; $G = 0.05$, 1.0 (0.05) and 1.0, 2.0 (0.2); $\Gamma = 0.1$, $f = 0.1$, $\phi = 0$, $\beta = 1$

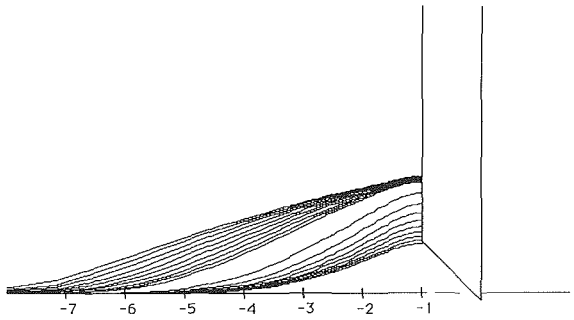


Fig. 4 Variation of surface tension; profiles are depressed with increasing Γ; $\Gamma = 0.01$, 0.1 (0.01) and 1.0, 1.9 (0.1); $G = 1.0$, $f = 0.1$, $\phi = 0$, $\beta = 1$

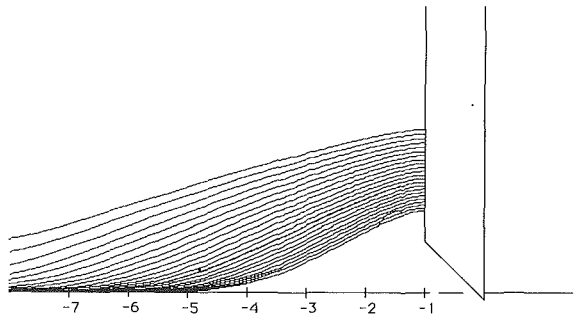


Fig. 5 Variation of penetration; profiles rise with increasing f; $f = 0.01$, 0.1 (0.01) and 0.1, 0.23 (0.1); $G = 1.0$, $\Gamma = 0.1$, $\phi = 0$, $\beta = 1$

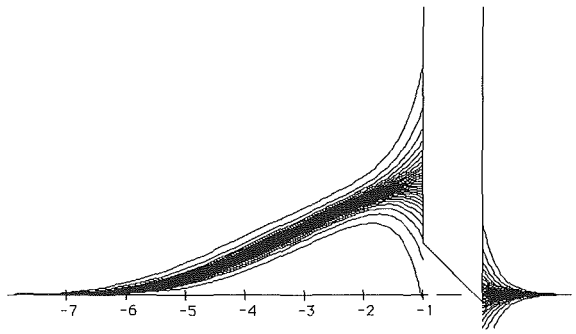


Fig. 6 Variation of contact angle; $\phi = -84$ deg, 84 deg (6 deg); $G = 1.0$, $\Gamma = 0.1$, $f = 0.1$, $\beta = 1$

to failure. After some experimentation, we have found that the (implicit) relaxation routines in Press et al. (1986) can be adapted to yield a useful numerical scheme. These implement a Newton-Raphson scheme making use of some tricks to simplify the matrix operations and reduce the storage requirements. We have implemented our scheme successfully using MacPascal on a MacIntosh Plus.

Apparently because of the strong singular point at $y = 1$, points need to be concentrated there, and the controlling term for convergence is the second derivative d_{yy} at the last mesh point. We normalize d by q, d_y by q/m and d_{yy} by q/m^2, where m is the number of mesh points. Our most successful assignment of grid points is the uneven grid given by

$$y_j = \sin\{(j-1)\pi/2(m-1)\} \quad j = 1,2, \ldots \tag{29}$$

which we call "asymmetric Chebyshev." Results of these computations will be discussed in the next section.

4 Results and Discussion

This is a five-parameter problem, and a complete survey is out of the question. We attempt, in this section, to isolate the influence of the parameters singly. We take as a base $G = 1$, $\Gamma = 0.1$, $f = 0.1$, $\theta = 0$ and $\beta = 1$, and examine in turn the effects of varying G, Γ, f, and ϕ. We have introduced the parameter $f = (q-1)/q$, the fraction of the free stream thickness obstructed, as a more easily visualized parameter than q. Note that f can be less than zero. Our results are shown in a series of figures, in which there is a vertical exaggeration of $1/\epsilon$, which comes from the scaling. Apparent slopes of order unity in the figures are actually small, and the lubrication hypothesis is not violated.

Variation of β is a separate issue, one we will not investigate in this paper. As can be seen from equation (25), the constant $B(G, \Gamma, q, \phi, \beta)$ is singular in the limit that $\beta \to 0$. As the squeeze film effect diminishes with a smaller and smaller squeeze angle, the pressure buildup at the leading edge required to drive the flow through the gap increases. This is not an issue in the usual fully flooded situation, for which no attention is paid to the source of lubricant, nor the amount that is transported through the gap. (Large β, of course, is contrary to the original lubrication hypothesis.)

Figure 3 shows the effect of varying G. At small G the rise at the leading edge is high. As G increases, the rise decreases. We have shown the first "impossible" case in the figure. $G = 2$ is the largest value for which the surface intersects the leading edge above the slope surface.

Figure 4 shows the influence of Γ. At $\Gamma = 0.01$, the solution is essentially that for zero surface tension when, as here, the angle $\phi = 0$. (We have done the calculation for zero surface tension using the implicit exact solution. We do not present those results here.) In this range of Γ, surface tension is unimportant even near the blade, the height h_1 hardly changing with Γ. At larger Γ, the surface tension reduces the rise everywhere. At Γ between 1.8 and 1.9 the "impossible" situation is reached here.

As one would expect, increasing penetration of the blade into the layer increases the rise of the liquid at the leading edge. Figure 5 shows the influence of f. The present numerical routine breaks down at f greater than 0.23, but the trend is clear from the calculations shown. (The breakdown in the computation comes from oscillations far upstream. It is impractical to use enough points to resolve essentially unimportant small ripples far from the blade. We prefer to stop the calculation rather than introduce an artificial boundary condition (or a match to the exact linear solution) at a finite distance upstream.) As f increases, the upstream influence increases greatly. As f decreases, a limiting situation is reached. As noted previously, at $f = 0$, $q = 1$, there is a possible solution that has a rise at the leading edge. In the limit that $f \to 0$, the leading edge rise is $h_1 = 1.5$, approximately the result shown for $f = 0.01$, $q = 0.1$. For nonzero surface tension with $\phi > 0$, q can be less than unity. Indeed, this is the usual circumstance in coating problems.

Finally, the influence of contact angle is shown in Fig. 6. Since the contact angle enters in the form of $\tan \phi$, it is not surprising that the effect is strongest at ϕ near $\pm\pi/2$.

Downloaded 03 May 2010 to 171.66.16.244. Redistribution subject to ASME license or copyright; see http://www.asme.org/terms/Terms_Use.cfm

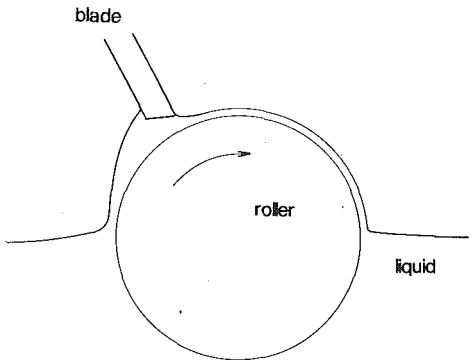


Fig. 7 Idealized roller/blade coating apparatus

We have been unable to find any experimental work in the literature with which we can compare our predictions. The blade cited previously is part of a series of experimental and analytical papers dealing with roller-blade coating, and are the closest candidates. Even these papers, however, are far from the range of parameters considered in this paper, G and Γ being both quite small. The geometry of all three is the same, shown in Fig. 7. The shape of the wedge region is very different from our linear blade, and the effective β is large. The first paper reports calculations and measurements of the forces on the blade, the second detailed measurements of the thickness of the coating as a function of blade spacing, blade angle, and liquid type. The third reports a finite element analysis of the experiment.

The analysis neglects both gravity and surface tension, rightly so, in view of the smallness of G and Γ. In Hsu et al. and Sullivan and Middleman, a zeroth-order lubrication theory, neglecting both curvature and inertial effects, is used to find the flow under the blade. For Newtonian fluids the solution is analytic. For non-Newtonian fluids, a numerical scheme is used. Ambient pressure is imposed at each end of the blade, and the flux is found. As the flux must equal the thickness sufficiently far downstream, this is used to predict the coating thickness. No effort is made to predict or to measure the upstream profile, though it is noted that the experiment gives strong constraints on both roller speed and viscosity necessary to ensure a fully flooded entrance.

The results are presented as coating thickness versus blade spacing. They obtain good results compared to their predictions for a "long" blade, with our $\epsilon \approx 0.003$, with progressively worsening agreement as the blade becomes "shorter," and ϵ increases. They explain this, quite reasonably, as caused by the increasing influence of entrance and exit effects, not considered by the lubrication analysis. They find coating thickness independent of both viscosity and roller speed, but strongly dependent on blade angle.

Most of the experiments using a Newtonian liquid used glycerol. From Hsu et al., where specific values of viscosity (7 poise) are given, and the stated lower limit of 3 poise for viscosity, solutions in the range of 90 to 95 wt percent glycerol and water were apparently used (Weast, 1975). We use a density of 1.25 gm/cm^3 and a surface tension of 60 dynes/cm[12], the latter allowing for some contamination of the surface. A typical value of the product μV is 100 gm/s^2. We take the effective gravity to be the component normal to the roller at the trailing edge, $981\cos(30\ \text{deg}) = 845$ cm/s^2. Three lengths of blade were used: 1.7, 6.35, and 12.7 mm. The gaps were in the range of 20 μm to 1.3 mm, giving a large range of ϵ. Figures 8, 9, and 10 of Sullivan and Middleman show the Newtonian data for all three blade widths at two different blade angles. Agreement between prediction and experiment is very good for the longest blade, even at the widest separation, for which $\epsilon \approx 0.1$. The others show deviation from the lubrication prediction at about the same value of ϵ.

Using these values we can obtain typical values for G, Γ, and the ratio G/Γ, a key to the linear solution. For the smaller gaps, G and Γ are both very small. As they depend on the cube of the gap, they increase rapidly, and at the wider gaps, of the order of 1 mm, they are $G \geq 0.005$ and $\Gamma \geq 4.7 \times 10^{-4}$, still quite small. Their ratio is independent of gap: $G/\Gamma \geq 11$. (The numerical values given are for the longest blades.)

For the experiments reported, $q < 1$, typically 0.75, and linearity is not a good approximation. Indeed, if q is $\approx 3/4$, then d will be 1/3 at the trailing edge, hardly small.

If we are willing to impose the condition that the intersection of the free surface on the downstream side of the blade is at the corner of the blade, an assumption apparently made tacitly in the works under discussion (see, particularly, Figs. 1 and 2 in Sullivan et al., and the accompanying discussion) we can use their results to assess our downstream solution qualitatively. If we set $x = 0$ in equation (22), and set $h_{III}(0) = 1$, to put the free surface at the corner, we obtain

$$q \approx 1 - \tan\phi / k. \tag{30}$$

The constant k is as above; $-k$ is the real root of equation (16). This depends on two parameters, G/Γ, independent of both viscosity and speed, and $3/\Gamma q^3$, linearly dependent on both μ and V. In the range of parameter space in which the experiments were performed, $k \approx -(3/\Gamma)^{1/3}/q$, and equation (30) can be rearranged to give

$$q \approx 1/\{1 + (\gamma/3\mu V)^{1/3} \tan\phi\} \tag{31}$$

a weak dependence on the product μV. Given the tenuous relevance of the theory worked out here to the experiments, the most we can say is that this result is not in conflict with the experiments.

In sum, we have constructed a new formalism, which governs the behavior of a liquid layer perturbed by a moving obstacle under the assumption that the motion is slow, so that inertial effects can be neglected in the liquid, and that the length scale for variations in the direction parallel to the layer is much greater than the thickness of the layer, so that a lubrication analysis can be applied. Account has been taken of both gravity and surface tension. The problem is inherently nonlinear. We have given sample results for one obstacle, a blade similar to that used in blade coating processes, in the limited case that the downstream perturbation is small.

The choice of parameters for this survey was dictated primarily for numerical convenience, to allow observation of the influence of each parameter in turn in a domain where such influence can be seen. Direct application of these results would require smaller values of the product μV than appear in the current coating literature. The regime is accessible experimentally, however, even in as simple a setting as phonograph-top experiment. A blade 5 mm long running at a height of 500 μm at a radius of 70 mm from the center of a phonograph turntable turning at 33 rpm will have $G \approx 1$ and $\Gamma \approx 0.09$, using 1 cS silicon oil (Dow Corning 200 Fluid: $\rho = 970$ kg/m^3, $\gamma = 21$ mPa-m, $\mu = 0.97$ mPa-s).

We note that the analysis here supposes an unlimited supply of liquid, so that the height of rise at the inlet is controlled only by gravity and surface tension. This is thus only qualitatively applicable to the case of bearing starvation. We have done some preliminary analysis of a finite volume system: a large rotating disk of radius $R \gg L$, with a fixed volume of liquid in a fixed channel like the phonograph-top experiment just mentioned. This system is apparently delicate numerically, and a full treatment of that problem together with experiments will be deferred to another paper.

5 Acknowledgments

This work has been supported in part by the National In-

Downloaded 03 May 2010 to 171.66.16.244. Redistribution subject to ASME license or copyright; see http://www.asme.org/terms/Terms_Use.cfm

stitute of Dental Research under grant number ROI DEO 8511 and such support is gratefully acknowledged.

References

Bonneau, D., and Frene, J., 1983, "Film Formation and Flow Characteristics at the Inlet of a Starved Contact—Theoretical Study," *ASME Journal of Lubrication Technology*, Vol. 105, pp. 178–186.

Campanella, O. H., and Cerro, R. L., 1984, Viscous Flow on the Outside of a Horizontal Rotating Cylinder: The Roll Coating Regime with a Simple Fluid," *Chemical Engineering Science*, Vol. 39, pp. 1443–1449.

Cerro, R. L., and Scriven, L. E., 1980, "Rapid Free Surface Film Flows: an Integral Approach,"*Industrial and Engineering Chemistry Fundamentals*, Vol. 19, pp. 40–50.

Hsu, T. C., Malone, M., Laurence, R. L., and Middleman, S., 1985, "Separating Forces in Blade Coating of Viscous and Viscoelastic Liquids," *Journal of Non-Newtonian Fluid Mechanics*, Vol. 18, pp. 273–294.

Press, W. H., Flannery, B. P., Teukolsky, S. A., and Vetterling, W. T., 1986, *Numerical Recipes: The Art of Scientific Computing*, Cambridge University Press, pp. 588–607.

Sullivan, T. M., and Middleman, S., 1986, "Film Thickness in Blade Coating of Viscous and Viscoelastic Liquids," *Journal of Non-Newtonian Fluid Mechanics*, Vol. 21, p. 13–38.

Sullivan T. M., Middleman, S., and Keunings, R., 1987, "Use of a Finite-Element Method to Interpret Rheological Effects in Blade Coating," *American Institute of Chemical Engineers Journal*, Vol. 33, pp. 2047–2056.

Tichy, J. A., 1986, "Entry Flow in a Narrow Channel of Varying Gap with One Sliding Surface," *ASME Journal of Tribology*, Vol. 108, pp. 288–293.

Tichy, J. A., and Bourgin, P., 1985, "The Effect of Inertia in Lubrication Flow Including Entrance and Initial Conditions," ASME JOURNAL OF APPLIED MECHANICS, Vol. 52, pp. 759–765.

Tipei, N., 1978, "Flow Characteristics and Pressure Build-up at the Inlet of Narrow Passages," *ASME Journal of Lubrication Technology*, Vol. 100, pp. 47–55.

Weast, R. C., ed., 1975, *The Handbook of Chemistry and Physics*, 56th ed., CRC Press, Cleveland, pp. D230–D231.

Wong, K. K. Y., Kennedy, J. S., and Rodkiewicz, M., 1985, "On the Localization of Inlet Boundary for Hydrodynamically Lubricated Infinite Cylinder Rotating Over a Flat Surface," *ASME Journal of Tribology*, Vol. 107, pp. 249–251.

Downloaded 03 May 2010 to 171.66.16.244. Redistribution subject to ASME license or copyright; see http://www.asme.org/terms/Terms_Use.cfm

M. A. Ebadian
Department of Mechanical Engineering,
Florida International University,
The State University of Florida at Miami,
Miami, FL 33199
Mem. ASME

Rate of Flow in a Curved Concentric Pipe of Circular Cross-Section

1 Introduction

The problem considered here is the steady laminar flow of an incompressible viscous fluid in a curved concentric annulus. A literature survey, including Berger, Talbot, and Yao (1983) indicates that flows in curved pipes have been extensively investigated. In the analysis of the study by Thomas and Walters (1965), only the secondary flow is investigated by using Dean's (1927, 1928) formulation, in which the simplified forms of the momentum and continuity equation have been used. However, their solution does not contain the rate of flow and is for a simple curved pipe which is different from the geometry considered in this paper. The solution presented by Hamakiotes and Berger (1988) is the fully developed region of periodic flows through curved pipes of circular cross and arbitrary curvature. This has been solved numerically, which again is different from the method proposed in this paper. In Prusa and Yao (1982), the fully developed laminar flow for a horizontal heated curved tube is studied numerically. Again, their solution is for a simple curved tube which is different from the geometry considered in this paper. Therefore, very little work is available for the case of a curved concentric annulus. One attempt is found in Kapur, Tyagi and Srivastava (1965) in which the simplified momentum and continuity equations were used. Consequently, the full two loops of secondary flow have not been found. In addition, the analysis was not continued to include the rate of flow. Another attempt is due to Topakoglu (1967) in which the correct form of the secondary flow is obtained, but the analysis was not pursued to include the rate of flow in the curved concentric pipe of circular cross-section.

This paper is an attempt to extend the latter to obtain the flow field and the rate of flow in a curved pipe of concentric annulus. The method of analysis is based on the double expansion procedure of Topakoglu and Ebadian, (1985). Hence, no approximation is involved in any step other than the natural limitation of the finite number of the calculated terms for the primary and secondary flows. It has been verified that in the limiting case of zero core size, which is the case of simple curved pipe of circular cross-section, the velocity field, and the rate of flow expression, reduce to those obtained by Topakoglu and Ebadian (1987).

2 Governing Equations for Primary and Secondary Flows

The dimensionless primary flow velocity component, w, and the dimensionless stream function, ϕ, satisfy the following equations (cf., Topakoglu and Ebadian (1985)):

$$\nabla^2 w = \frac{1}{(y+\sigma)^2} w(1-\sigma\phi_x) + \frac{1}{y+\sigma}\left[\sigma \frac{\partial(\phi, w)}{\partial(y, x)} - w_y - \sigma k_0\right]$$

$$\nabla^4 \phi = \frac{1}{\sigma}(w^2)_x + \frac{1}{y+\sigma}\left[2\nabla^2\phi_y + \sigma \frac{\partial(\phi, \nabla^2\phi)}{\partial(y, x)}\right] - \frac{1}{(y+\sigma)^2}\left[3\phi_{yy} + \sigma \frac{\partial(\phi, \phi_y)}{\partial(y, x)} - 2\sigma\phi_x\nabla^2\phi\right] + 3\frac{1}{(y+\sigma)^3}\phi_y(1-\sigma\phi_x) \quad (1)$$

where

$$\nabla^2 = \frac{\partial^2}{\partial y^2} + \frac{\partial^2}{\partial x^2},\ y = r\cos\alpha,\ ,\ x = r\sin\alpha,\ k_0 = 4(\mathrm{Re}). \quad (2)$$

The Reynolds number (Re) used in equation (2) is a dimensionless parameter which indicates a measure of the intensity of the average primary flow velocity. It is defined as the Reynolds number obtained for a simple straight pipe with full circular cross-section of radius A and subjected to a longitudinal pressure gradient which is the same as that measured along the center line of a concentric curved pipe.

3 Expansion of Flow in Terms of Curvature

Following the well-known expansion procedure, the primary and secondary flows are expanded in terms of the curvature, $\lambda = \frac{1}{\sigma}$ into power series as

$$w = w_0 + \lambda\, w_1 + \lambda^2 w_2 + \ldots,\ \phi = \lambda\, \phi_1 + \lambda^2\phi_2 + \ldots. \quad (3)$$

Each term of these expansions satisfies the following boundary conditions:

$$w_i = 0,\ \phi_i = \phi_i' = 0 \text{ for } r = 1 \text{ and } r = \omega \quad (4)$$

Contributed by the Applied Mechanics Division of THE AMERICAN SOCIETY OF MECHANICAL ENGINEERS for publication in the JOURNAL OF APPLIED MECHANICS.

Discussion on this paper should be addressed to the Technical Editor, Leon M. Keer, The Technological Institute, Northwestern University, Evanston, IL 60208, and will be accepted until two months after final publication of the paper itself in the JOURNAL OF APPLIED MECHANICS. Manuscript received by the ASME Applied Mechanics Division, Mar. 3, 1989; final revision, Aug. 4, 1989.

Copyright © 1990 by ASME
Downloaded 03 May 2010 to 171.66.16.244. Redistribution subject to ASME license or copyright; see http://www.asme.org/terms/Terms_Use.cfm

where a prime indicates differentiation with respect to r. Also, ω is the dimensionless inner separation radius of the annulus.

The first term of the expansion of the primary flow corresponds to the flow in a straight concentric pipe and is given in Topakoglu (1967) as:

$$w_0 = f_0 = (\mathrm{Re})(1 - r^2 - m\ln r) \text{ with } m = (1-\omega^2)/\ln\omega. \quad (5)$$

The first term of the expansion of the secondary flow is obtained as:

$$\phi_1 = g_1 \sin\alpha \quad (6)$$

$$g_1 = \frac{1}{288}(\mathrm{Re})^2[r^8 + 2(3m\ln r - 2m - 3)r^6 + 9(2m\ln r - 5m - 4)mr^4\ln r + Nr^4 + (M + M_1\ln r)r^2 + N_2]\frac{1}{r} \quad (7)$$

where the constants N, M, M_1, and N_1 are calculated explicitly in terms of m and ω, but due to their complexities are not given here.

4 Second Term of Primary Flow

The substitution of the expansions of equation (3) into the first equation of (1) and the comparison of the coefficients of λ yield

$$\nabla^2 w_1 = \frac{1}{r}\frac{\partial(\phi_1, w_0)}{\partial(r, \alpha)} - w_{0y} + k_o r\cos\alpha. \quad (8)$$

This can further be written as

$$\nabla^2 w_1 = F_1 \cos\alpha \text{ with } F_1 = k_o r - \left(1 + \frac{1}{r}g_1\right)f_0'. \quad (9)$$

The solution of equation (9) with the boundary conditions of equation (4) will have the following form:

$$w_1 = f_1 \cos\alpha \quad (10)$$

where f_1 is subject to the boundary conditions

$$f_1 = 0 \text{ for } r = 1 \text{ and } r = \omega. \quad (11)$$

Substituting f_0 and g_1 and omitting the steps of integration, the following solution is obtained:

$$f_1 = \frac{(\mathrm{Re})}{4}\left\{[3r^2 + mr(2\ln r - 1)]r + (\mathrm{Re})^2(u_2 r^2\ln^2 r + u_4\ln r + \tilde{u}_4)\frac{1}{r}\right\} \quad (12)$$

where u_2, u_4, and $\tilde{u}_4$ are polynomials in r^2 and their orders are indicated by their indices.

5 Second Term of Secondary Flow

The substitution of the expansion of equation (3) into the second equation of (1) and the comparison of the coefficients of λ^2 yield

$$\nabla^4\phi_2 = 2(w_0 w_1)_x + 2\nabla^2\phi_{1y} + \frac{1}{r}\frac{\partial(\phi_1, \nabla^2\phi_1)}{\partial(r, \alpha)}. \quad (13)$$

This can further be written as

$$\nabla^4\phi_2 = G_2 \sin 2\alpha, \text{ where,} \quad (14)$$

$$G_2 = r\left(\frac{1}{r}f_0 f_1\right)' + r\left\{\frac{1}{r}\left[\frac{1}{r}(rg_1)'\right]'\right\}' + \frac{1}{2}\frac{1}{r}\left\{g_1'\left[\frac{1}{r}(rg_1)'\right]' - g_1\left[\frac{1}{r}(rg_1)'\right]''\right\}. \quad (15)$$

The solution of equation (14) with the boundary conditions of equation (4) will have the following form:

$$\phi_2 = g_2 \sin 2\alpha \quad (16)$$

where g_2 is subject to the boundary conditions

$$g_2 = 0 \text{ and } g_2' = 0 \text{ for } r = 1 \text{ and } r = \omega. \quad (17)$$

Substituting f_0, g_1, and f_1 and omitting the steps of integration, the following solution is obtained:

$$g_2 = \frac{(\mathrm{Re})^4}{(288)(576)}[mr^6\ln^4 r + x_1\ln^3 r + x_2\ln^2 r + x_5\ln r + x_6] + (\mathrm{Re})^2\left[\tilde{x}_2\ln^2 r + \tilde{x}_5\ln r + x_7 r^2 + x_8\frac{1}{r^2}\right] \quad (18)$$

where x_1, x_2, x_5, x_6, $\tilde{x}_2$, $\tilde{x}_5$, x_7, x_8 are polynomials in r^2 and their orders are indicated by their indices.

6 Third Term of Primary Flow

The substitution of the expansion of equation (3) into the first equation of (1) and the comparison of the coefficients of λ^2 yields

$$\nabla^2 w_2 = w_0(1 - \phi_{1x}) + \left[rw_{0y} - \frac{\partial(\phi_1, w_0)}{\partial(r, \alpha)}\right]\cos\alpha + \frac{1}{r}\left[\frac{\partial(\phi_2, w_0)}{\partial(r, \alpha)} + \frac{\partial(\phi_1, w_1)}{\partial(r, \alpha)}\right] - w_{1y} - \frac{1}{2}k_o r^2(1 + \cos 2\alpha). \quad (19)$$

This can further be written as

$$\nabla^2 w_2 = F_{20} + F_{22}\cos 2\alpha, \text{ where,} \quad (20)$$

$$F_{20} = \frac{1}{2}\left\{-k_o r^2 + 2f_0 + (r + g_1)f_0' - \frac{1}{r}f_0(rg_1)' - \frac{1}{r}[f_1(r + g_1)]'\right\}, \text{ and} \quad (21)$$

$$F_{22} = \frac{1}{2}\left[-k_o r^2 + rf_0' + r\left(\frac{1}{r}f_0 g_1\right)' - r\left(\frac{1}{r}f_1\right)' + \frac{1}{r}(f_1 g_1' - f_1' g_1 - 4f_0' g_2)\right]. \quad (22)$$

The solution of equation (20) with the boundary conditions of equation (4) will have the following terms:

$$w_2 = f_{20} + f_{22}\cos 2\alpha \quad (23)$$

where f_{20} and f_{22} are subject to the boundary conditions

$$f_{20} = 0 \text{ and } f_{22} = 0 \text{ for } r = 1 \text{ and } r = \omega. \quad (24)$$

Substituting f_0, g_1, and omitting the steps of integration, the following solution for f_{20} and f_{22} is obtained as:

$$f_{20} = \frac{(\mathrm{Re})}{256}\left[v_1\ln r + v_2 + (\mathrm{Re})^2\left(m^3 r^4\ln^3 r + v_3\ln^2 r + v_4\ln r + v_6\frac{1}{r^2}\right) + (\mathrm{Re})^4\left(\tilde{v}_2 r^4\ln^4 r + v_5\ln^3 r + \tilde{v}_6\ln^2 r + v_8\frac{1}{r^2}\ln r + v_9\frac{1}{r^2}\right)\right], \text{ and} \quad (25)$$

$$f_{22} = \frac{(\mathrm{Re})}{256}\left\{(y_1\ln r + y_2) + (\mathrm{Re})^2(y_3 r^2\ln^2 r + y_4\ln r + y_6) + (\mathrm{Re})^4(\tilde{y}_2 r^2\ln^4 r + \tilde{y}_5 r^2\ln^3 r + \tilde{y}_6\ln^4 r + \tilde{y}_8\ln r) + \left(y_6 r^2 + y_7\frac{1}{r^2}\right)\right\} \quad (26)$$

where v_1, v_2, v_3, v_4, v_6, $\tilde{v}_2$, v_5, $\tilde{v}_6$, v_8, v_9, and y_1, y_2, y_3, y_4, y_6, $\tilde{y}_2$, $\tilde{y}_5$, $\tilde{y}_6$, $\tilde{y}_8$, y_6, and y_7 are polynomials in r^2 and their orders are indicated by their indices.

7 Rate of Flow

Using the calculated terms of the expansion of the primary flow, the dimensionless normal velocity component can now be expressed as

Downloaded 03 May 2010 to 171.66.16.244. Redistribution subject to ASME license or copyright; see http://www.asme.org/terms/Terms_Use.cfm

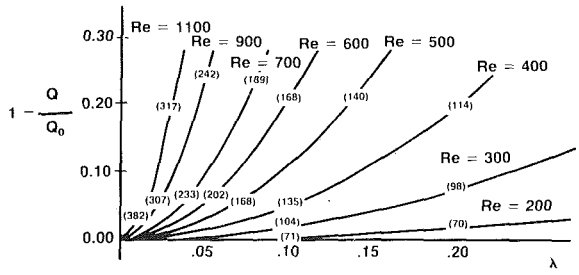


Fig. 1 Reduction of rate of flow (ω = 0.2)

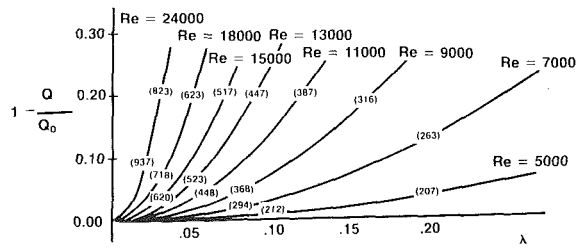


Fig. 2 Reduction of rate of flow (ω = 0.6)

$$w = f_o + \lambda f_1 \cos\alpha + \lambda^2 (f_{20} + f_{22} \cos 2\alpha). \tag{27}$$

Noting that only the function f_0 and f_{20} contribute to the mass flow rate, Q, one obtains $Q = Q_0 + \lambda^2 Q_2$, where

$$Q_0 = 2\pi \mu A \int_\omega^1 r f_0 dr,\ Q_2 = 2\pi \mu A \int_\omega^1 r f_{20} dr. \tag{28}$$

The integration of Q_0 and Q_2 yields

$$Q_0 = \frac{1}{2} \pi \mu A(\mathrm{Re})(1-\omega^2)(1+\omega^2+m),\ Q_2$$

$$= \pi \mu A[(\mathrm{Re})q_1 + (\mathrm{Re})^3 q_3 + (\mathrm{Re})^5 q_5]. \tag{29}$$

8 Reduction Ratio of Rate of Flow

The ratio of the rate of flow in a curved pipe of concentric annulus to that of a straight pipe having the same cross-section and the same pressure gradient as that measured along the center line of the curved pipe, maintaining only the most significant term of the curvature is

$$\frac{Q}{Q_0} = 1 + \frac{1}{\sigma^2} \frac{Q_2}{Q_0}. \tag{30}$$

Equation (30) involves only the most significant contribution of the effect of the curvature. The effect of the other terms can be obtained when further terms of the expansions are calculated. It is seen that the rate-of-flow ratio, besides depending on the dimensionless inner separation radius of the annulus and the curvature, also depends on the Reynolds number, Re.

9 Results and Discussion

It is seen from equation (29) that the ratio $\frac{Q_2}{Q_0}$, depends not only on the dimensionless radius of the inner periphery, ω, and the curvature, λ, but also on the Reynolds number, Re. It is verified that for the special case of a simple circular curved pipe, ω = 0, the result of equation (30) reduces to the corresponding form of a simple circular section (Topakoglu and Ebadian (1987)).

To be able to observe the rate of flow variation with curvature and the Reynolds number, Re, the reduction ratio of the rate of flow, $1 - \frac{Q}{Q_0}$, is plotted against the curvature, $\lambda = \frac{1}{\sigma}$, for various values of ω and Re.

To plot the representative curves, two ω values are selected as 0.20 and 0.60. The results are presented in Figs. 1 and 2. The values of the selected Reynolds numbers are shown in each figure. In each case, the Reynolds numbers are selected as such so that a fairly wide coverage is obtained. The Reynolds number, Re, used in the analysis does not correspond to the real Reynolds number of actual flow. However, the true Reynolds number, based on the hydraulic diameter of the annular section, can be calculated as

$$(\mathrm{Re})_{\mathrm{True}} = \left(\frac{Q}{Q_0}\right)(\mathrm{Re}) \frac{\beta}{1+\omega} \text{ with } \beta$$

$$= (1-\omega^2)(1+\omega^2+m). \tag{31}$$

The true Reynolds numbers are written in parenthesis at the indicated points of each curve. Experiments by White (1929), Taylor (1929), and Adler (1934) have confirmed that the flow in a curved pipe or tube is much more stable than that in a straight pipe or tube. Whereas the critical Reynolds number for the latter is typically 2000 in a curved tube of even smaller curvature, it may be larger by a factor of two or more. For example, Taylor found that the critical Reynolds number for a simple circular curved pipe was about 5000. Thus, it is noticed that in Figs. 1 and 2 the largest true Reynolds number value is 937. This number is well below the critical Reynolds number of 5000. One can argue that a curved pipe with concentric annuli will have a larger critical Reynolds number than this value.

References

Adler, M., 1934, "Strömung in gekrümmten Rohren," *Z. Angew. Math. Mech.*, Vol. 14, pp. 257–275.

Berger, S. A., Talbot, L., and Yao, L. S., 1983, "Flow in Curved Pipes," *Ann. Rev. Fluid Mech.*, Vol. 15, pp. 461–512.

Dean, W. R., 1927, "Notes on the Motion of Fluid in a Curved Pipe," *Phil. Mag.*, Vol. 30, pp. 208–223.

Dean, W. R., 1928, "The Streamline Motion of Fluid in a Curved Pipe," *Phil. Mag.*, Vol. 30, pp. 673–695.

Kapur, J. W., Tyagi, V. P., and Srivastava, R. C., 1965, "Streamline Flow Through a Curved Annulus," *Applied Scientific Research*, Section A, Vol. 14, pp. 253–267.

Hamakiotes, C. C., and Berger, S. A., 1988, "Fully Developed Pulsatile Flow in a Curved Pipe," *J. Fluid Mechanics*, Vol. 195, pp. 23–55.

Prusa, J., and Yao, L. S., 1982, "Numerical Solution for Fully Developed Flow in Heated Curved Tubes," *J. Fluid Mechanics*, Vol. 123, pp. 503–522.

Taylor, G. I., 1929, "The Criterion for Turbulence in Curved Pipes," *Proc. R. Soc. London*, Vol. A124, pp. 243–249.

Thomas, R. H., and Walters, K., 1965, "On the Flow of an Elastico-Viscous Liquid in a Curved Pipe under a Pressure Gradient," *J. Fluid Mechanics*, Vol. 16, pp. 228–242.

Topakoglu, H. C., 1967, "Steady Laminar Flows of an Incompressible Viscous Fluid in Curved Pipes," *J. Maths Mech.*, Vol. 16, pp. 1321–1338

Topakoglu, H. C., and Ebadian, M. A., 1985, "On the Steady Laminar Flows of an Incompressible Viscous Fluid in Curved Pipe of Elliptical Cross-Section," *J. Fluid Mechanics*, Vol. 158, pp. 329–340.

Topakoglu, H. C., and Ebadian, M. A., 1987, "Viscous Laminar Flow in a Curved Pipe of Elliptical Cross Section," *J. Fluid Mechanics*, Vol. 184, pp. 571–580.

White, C. M., 1929, "Streamline Flow through Curved Pipes," *Proc. R. Soc. London*, Vol.A123, pp. 645–663.

Downloaded 03 May 2010 to 171.66.16.244. Redistribution subject to ASME license or copyright; see http://www.asme.org/terms/Terms_Use.cfm

ERRATA

Errata on "Crack Extension Force in a Piezoelectric Material," by Y. Eugene Pak and published in the Sept. 1990 issue of the ASME JOURNAL OF APPLIED MECHANICS, Vol. 57, pp. 647–653.

The sentence immediately following equation (5) should read:

With these symmetry relations, ε_{ij} in (3) can be replaced by $u_{i,j}$.

Equation (8) should read:

$$\sigma_{ij} = \frac{\partial H}{\partial_{ij}} = C_{ijkl}\varepsilon_{kl} - e_{kij}E_k$$
$$D_i = -\frac{\partial H}{\partial E_i} = e_{ikl}\varepsilon_{kl} + \epsilon_{ik}E_k. \tag{8}$$

Equation (15) should read:

$$\begin{Bmatrix} \sigma_{xx} \\ \sigma_{yy} \\ \sigma_{zz} \\ \sigma_{zy} \\ \sigma_{zx} \\ \sigma_{xy} \end{Bmatrix} = \begin{bmatrix} c_{11} & c_{12} & c_{13} & 0 & 0 & 0 \\ c_{12} & c_{11} & c_{13} & 0 & 0 & 0 \\ c_{13} & c_{13} & c_{33} & 0 & 0 & 0 \\ 0 & 0 & 0 & c_{44} & 0 & 0 \\ 0 & 0 & 0 & 0 & c_{44} & 0 \\ 0 & 0 & 0 & 0 & 0 & \frac{1}{2}(c_{11}-c_{12}) \end{bmatrix} \begin{Bmatrix} \varepsilon_{xx} \\ \varepsilon_{yy} \\ \varepsilon_{zz} \\ 2\varepsilon_{zy} \\ 2\varepsilon_{zx} \\ 2\varepsilon_{xy} \end{Bmatrix} - \begin{bmatrix} 0 & 0 & e_{31} \\ 0 & 0 & e_{31} \\ 0 & 0 & e_{33} \\ 0 & e_{15} & 0 \\ e_{15} & 0 & 0 \\ 0 & 0 & 0 \end{bmatrix} \begin{Bmatrix} E_x \\ E_y \\ E_z \end{Bmatrix} \tag{15}$$

Equation (A7) should read:

$$c_{44}\varepsilon_{zy} - e_{15}E_y^{(p)} = 0. \tag{A7}$$

Equation (A8) should read:

$$e_{15}\varepsilon_{zy} \quad \epsilon_{11}E_y^{(p)} = \epsilon_0 E_y^{(c)}. \tag{A8}$$

Copyright © 1990 by ASME
Downloaded 03 May 2010 to 171.66.16.244. Redistribution subject to ASME license or copyright; see http://www.asme.org/terms/Terms_Use.cfm

Journal of Applied Mechanics

Brief Notes

A Brief Note is a short paper that presents a specific solution of technical interest in mechanics but which does not necessarily contain new general methods or results. A Brief Note should not exceed 1500 words *or equivalent* (a typical one-column figure or table is equivalent to 250 words; a one line equation to 30 words). Brief Notes will be subject to the usual review procedures prior to publication. After approval such Notes will be published as soon as possible. The Notes should be submitted to the Technical Editor of the JOURNAL OF APPLIED MECHANICS. Discussions on the Brief Notes should be addressed to the Editorial Department, ASME, United Engineering Center, 345 East 47th Street, New York, N. Y. 10017, or to the Technical Editor of the JOURNAL OF APPLIED MECHANICS. Discussions on Brief Notes appearing in this issue will be accepted until two months after publication. Readers who need more time to prepare a Discussion should request an extension of the deadline from the Editorial Department.

Dynamic Plastic Response of Circular Plates With Transverse Shear

Q. M. Li[1] and Y. G. Huang[2]

Introduction

In this paper, the motion of a thin, circular plate made of a rigid-perfectly material is studied. The plate is subjected to a descending load, which is uniformly distributed over the plate. The behavior of the material of the plate is in conformity with the yield criterion proposed by Sawczuk and Duszek (1963). This paper is an extension of earlier investigations achieved both by Jones and Gomes de Oliveira (1980), who first considered the effects of the transverse shear under an impulsive load indicating that the pattern of the velocitiy profile depends on the parameter $\nu = RQ_0/2M_0$, and by Kumar and Krishna Reddy (1986), who gave an analytic solution to rectangular load, in which the shear sliding condition depends on the value of $p(P/P_0,\ P_0 = 6M_0/R^2)$ and parameter ν.

Results

Class I, $0 < \nu \le 3/2$, the velocity field throughout the plate is

$$\dot{\bar{w}} = \int_o^\tau p(\tau)d\tau - 2\nu\tau/3 \tag{1}$$

where $\dot{\bar{w}} = \dot{w}/(I^*/\mu)$ is the moving velocity of the plate whose mass per unit area is μ; $\tau = t/(I^*/P_0)$; I' is the impulse of the load.

Class II, $3/2 < \nu \le 2$.

Case (a), $1 < p < 2(\nu - 1)$, the velocity field is

$$\dot{\bar{w}} = 2(1-\xi)\left(\int_o^\tau p(\tau)d\tau - \tau\right) \tag{2}$$

in which, $\xi = r/R$. Thus, the motion ceases when

$$\int_o^{\tau_f} p(\tau)d\tau = \tau_f. \tag{3}$$

Case (b), $2(\nu - 1) \le p$.

Phase (1), $0 \le \tau \le \tau_1$, the velocity field may be written as:

$$\dot{\bar{w}} = 2(1-\nu)\tau + 2(2\nu - 3)(1-\xi)\tau + \int_o^\tau p(\tau)d\tau. \tag{4}$$

τ_1 is determined by

$$2(1-\nu)\tau_1 + \int_o^{\tau_1} p(\tau)d\tau = 0. \tag{5}$$

Phase (2), $\tau_1 \le \tau \le \tau_f$, the results are similar to those of Case (a) in Class I.

Class III, $\nu \ge 2$.

Case (a), $p < 2\nu/(1-y)(2+y)$, $y = [4(\nu^2 - 8\nu + 1)^{1/2} - 1]/2\nu$.

Phase (1), $0 \le \tau \le \tau_1$, the transverse velocity field is given by

$$\dot{\bar{w}} = \int_0^\tau p(\tau)d\tau, \qquad 0 \le \xi \le x \tag{6a}$$

$$\dot{\bar{w}} = (1-\xi)\int_0^\tau p(\tau)d\tau/(1-x), \qquad x \le \xi \le 1 \tag{6b}$$

in which x satisfies the following equation:

$$(1 + x^3 - x^2 - x)\int_0^\tau p(\tau)d\tau = 2\tau. \tag{7}$$

$x = 0$ leads to $\int_0^{\tau_1} p(\tau)d\tau = 2\tau_1$. This equation requires $p < 2$, otherwise the results would be similar to those of Case (a) in Class II.

Phase (2), $\tau_1 \le \tau \le \tau_f$, the results of Case (a) in Class II may be used to describe the motion of this phase.

Case (b), $p \ge 2\nu/(1-y)(2+y)$, y is given in Case (a).

Phase (1), $0 \le \tau \le \tau_1$, the velocity field may be expressed as follows:

$$\dot{\bar{w}} = \int_0^\tau p(\tau)d\tau, \qquad 0 \le \xi \le x \tag{8a}$$

$$\dot{\bar{w}} = \int_0^\tau p(\tau)d\tau + 2\nu\tau(\xi - x)/(2 - x^2 - x)(/x - 1), \quad x \le \xi \le 1 \tag{8b}$$

here, $x = y$. $\dot{\bar{w}}\,|_{\xi=1} = 0$ can be used to determine τ_1.

$$\int_0^{\tau_1} p(\tau)d\tau = 2\nu\tau_1/(2 - x^2 - x) \tag{9}$$

Phase (2) and Phase (3) in this case are similar to Phase (1) of Case (a) in Class III and Case (a) in Class II, respectively.

[1]Department of Applied Mathematics and Mechanics, Taiyuan University of Technology, Taiyuan, Shanxi Province, People's Republic of China.

[2]Division of Applied Sciences, Harvard University, Cambridge, MA 02139.

Manuscript received by the ASME Applied Mechanics Division, June 6, 1988; final revision, Nov. 10, 1989.

Copyright © 1990 by ASME

Downloaded 03 May 2010 to 171.66.16.244. Redistribution subject to ASME license or copyright; see http://www.asme.org/terms/Terms_Use.cfm

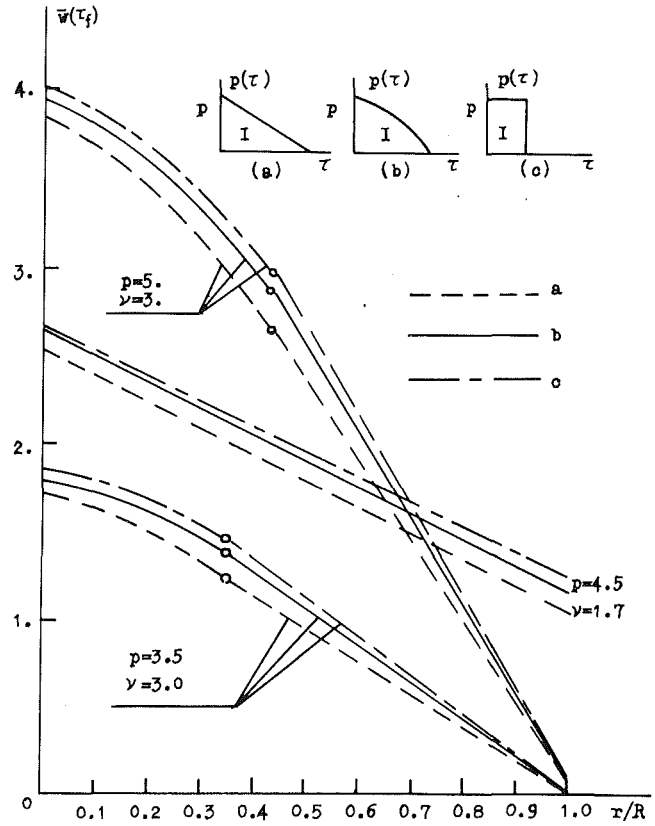


Fig. 1

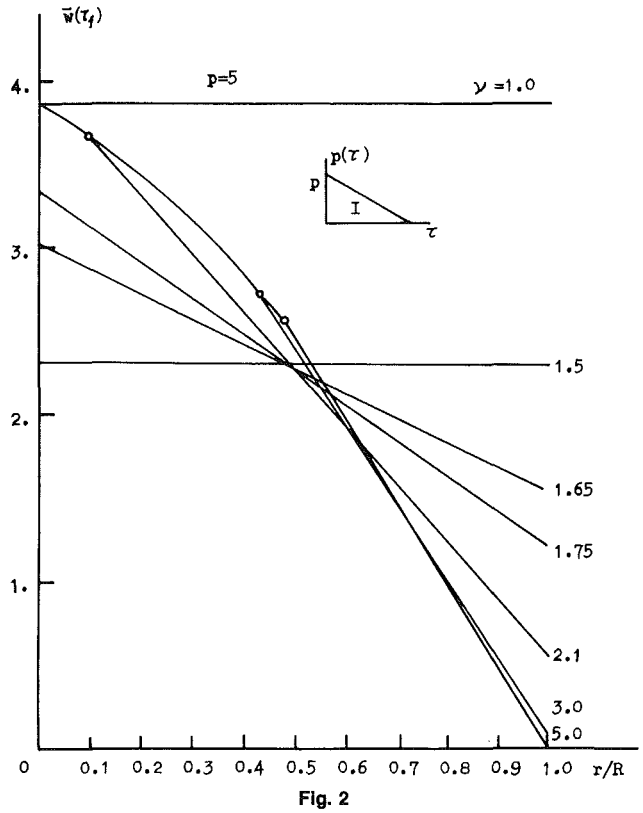


Fig. 2

Discussion

Figure 1 shows that the effects of the loading shape on the final deflection are small and that the parameter I (here, $I=p/2$, which is the dimensionless impulse of load) and p may be used to represent the loading character. In Fig. 2 the variation of dimensionless transverse deflections versus radius is plotted. It can be seen that the shear deformation decreases with the value of ν and the shear sliding causes the final transverse deflection near the central region to decrease. For any given p, there exists a value of the dimensionless radius, at which the final transverse deflections have the near value when $\nu \leq 2$. Figure 3 shows the variation of the dimensionless central and edge final deflections ($\dot{\bar{w}}_0$ and $\dot{\bar{w}}_1$) versus ν. It can be seen that when $\nu \leq 1.5$, which gives $\dot{\bar{w}}_0 = \dot{\bar{w}}_1$, the plate will yield only at the supports. The final central deflections at $\nu=1$ and $\nu=2$ have the same value. When $\nu>2$, the edge final deflection is much less than the central final deflection, which coincides with the bending results. The previous results obtained by the aforementioned scholars may be regarded as special results of the solution presented in this paper. $p\to\infty$ and $I=$ constant give the results of Jones and Gomes de Oliveira (1980), $p=$ constant gives Kumar and Krishna Reddy's results (1986), and $\nu\to\infty$ gives Youngdahl's results (1971) when $t_m=0$.

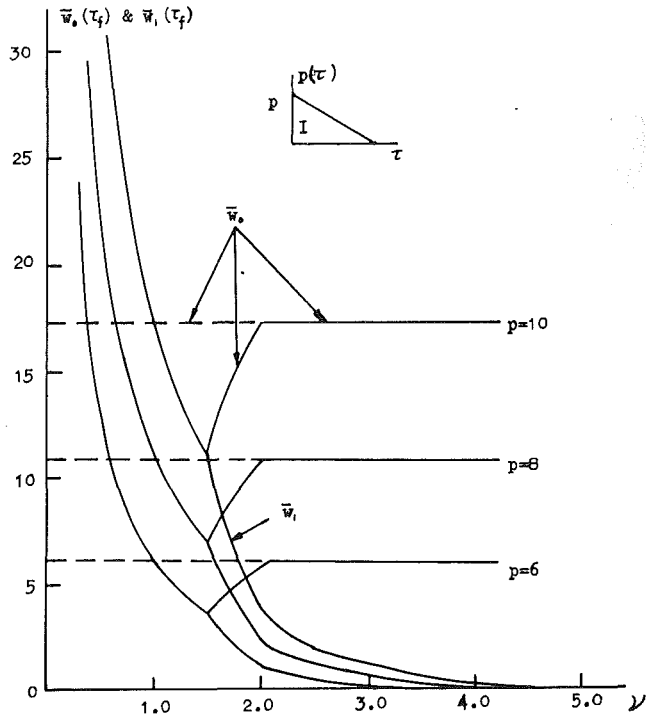


Fig. 3

Acknowledgment

The authors gratefully acknowledge the support of the National Science Foundation of Shanxi Province in China.

References

Jones, N., and Gomes de Oliveira, J., 1980, "Dynamic Plastic Response of Circular Plates With Transverse Shear and Rotatory Inertia," ASME JOURNAL OF APPLIED MECHANICS, Vol. 47, pp. 27–34.

Kumar, A., and Krishna Reddy, V. V., 1986, "Dynamic Plastic Response of Circular Plates With Transverse Shear," ASME JOURNAL OF APPLIED MECHANICS, Vol. 53, pp. 952–953.

Sawczuk, A., and Duszek, M., 1963, "A Note on the Interaction of Shear and Bending in Plastic Plates," *Arch. Mech. Stosow.*, Vol. 15, pp. 411–426.

Youngdahl, C. K., 1971, "Influence of Pulse Shape on the Final Plastic Deformation of a Circular Plate," *International Journal of Solid Structures*, Vol. 7, pp. 1127–1141.

Downloaded 03 May 2010 to 171.66.16.244. Redistribution subject to ASME license or copyright; see http://www.asme.org/terms/Terms_Use.cfm

A Central Crack in a Finite Rectangular Plate With Four Hinged Edges Under the Opening Mode

S. W. Ma[3] and Y. G. Tsuei[3]

By combining linearly the Fourier transform and Fourier series, the stress intensity factor of a central crack in a finite rectangular plate with four hinged edges under the opening mode is expressed as the Fredholm integral equation of the second kind. The uniform loading case is considered in detail. The numerical results include the predictions by Koiter and Fichter as limiting cases.

I Introduction

Since Irwin put forward the concept of stress intensity factor, the research of stress intensity factors for the Griffith's crack of model I is the most detailed one. The references (Sih, 1973; Tada, 1973; Rooke, 1976) have collected a lot of research results in this aspect. Historically, Sneddon (1951) solved the problems for infinite cracked bodies by Fourier integral transform. Sneddon and Srivastav (1971) investigated the strip under the combined bending and tensile load. Lowengrub (1966) and Fichter (1967) considered various kinds of strips with different boundary conditions. Sih and Chen (1981) obtained several analytical solutions about composite materials which have been extensively used in industry.

All these analytical solutions in these references are based on the assumption that the cracked body or strip is infinite in dimension in comparison with the crack. But this assumption may lead to various degrees of inaccuracy because practically cracked bodies or strips are finite in dimension. So far the closed-form solution of a finite cracked body under the opening mode (model) has not yet been obtained. Brock (1986) points out that "Cracks in plates of finite size are of great practical interest, but for these cases no closed-form solutions are available. The problems are difficult because of the boundary conditions."

Because of this difficulty, many numerical techniques have been developed since the 1960s; for instance, Sih (1973) discussed the finite element method and boundary collocation process. This process has been used extensively by Isida (1972) to solve various boundary problems. However, we should be careful when drawing a conclusion comparing the results from numerical and analytical methods. Sih (1973) has pointed out the shortcomings of the collocation process, saying, "At present, there is no general proof that collocation solutions will converge by increasing the number of boundary points. The accuracy of the solution must depend largely on the experience and judgement of the analyst." This shows clearly the limitations of using this method of engineering.

In order to meet the needs of engineering and theoretic research, this paper considers the solution of the central crack in a finite rectangular plate with four hinged edges under the opening mode without customary assumption. The solution to this problem may be obtained through the work of Delameter et al. (1975, 1977), but their method, which considers double periodic cracks in an infinite plate, has its limitations; that is, the work can not been extended in general, especially for a finite plate with a stress-free-boundary, composite material, and dynamics. Aboudi (1987) reconsidered this problem with the aid of stiffness reduction, but the method is numerical and shows some discrepancy compared with exact solution.

By use of the basic theorem of Fourier transform and Fourier series, the exact solution of this problem is obtained. This method was initially introduced by Zhang (1984) when he solved the problem of a cracked sheet under the tearing (mode III). However, the solution of a cracked plate under the opening mode (model I) was investigated by (Ma, 1988a). Recently, this method has been extensively used to solve various finite cracked bodies such as composite plates (Ma, 1988b) and dynamics of plates (Zhang and Ma, 1986).

The governing equations and boundary conditions are discussed in Section 2. It follows with the solution of this problem expressed in the Fredholm integral equation of the second kind by use of Fourier transform and Fourier series in Section 3. In Section 4, the numerical results are obtained through solving the integral equation for comparison. It will be shown that two kinds of strips reported by Fitcher (1967) and Koiter (Sih, 1973) are the special cases in this paper.

II Basic Equations

Consider a crack of length $2a$ in a finite rectangular plate $2h \times 2b$ with four edges hinged as shown in Fig. 1. In the case of a two-dimensional plane strain, the displacement components u_x and u_y along x-axis and y-axis directions are the functions of Cartisian coordinates x and y only. The stress-strain relations may be written in the form

$$\sigma_x = \frac{2\mu}{1-2\nu}\left[(1-\nu)\frac{\partial u_x}{\partial x} + \nu\frac{\partial u_y}{\partial y}\right] \tag{1}$$

$$\sigma_y = \frac{2\mu}{1-2\nu}\left[(1-\nu)\frac{\partial u_y}{\partial y} + \nu\frac{\partial u_x}{\partial x}\right] \tag{2}$$

$$\tau_{xy} = \mu\left(\frac{\partial u_x}{\partial y} + \frac{\partial u_y}{\partial x}\right) \tag{3}$$

where μ is shear modulus and ν is Poisson's ratio. In the absence of body forces the equations of elastic equilibrium are reduced to the form

$$2(1-\nu)\frac{\partial^2 u_x}{\partial x^2} + (1-2\nu)\frac{\partial^2 u_x}{\partial y^2} + \frac{\partial^2 u_y}{\partial x \partial y} = 0 \tag{4}$$

$$(1-2\nu)\frac{\partial^2 u_y}{\partial x^2} + 2(1-\nu)\frac{\partial^2 u_y}{\partial y^2} + \frac{\partial^2 u_x}{\partial x \partial y} = 0. \tag{5}$$

Although all of the above results are derived from the state of plane strain, for plane stress they may also be obtained

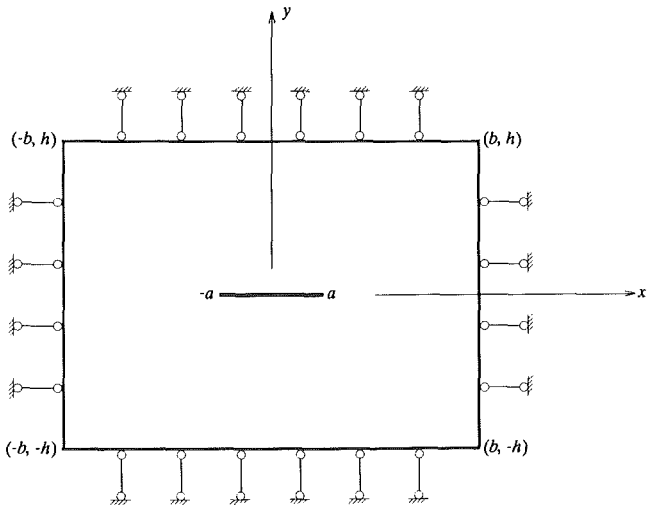


Fig. 1 The central cracked plate with four hinged boundary under the opening mode

[3]Department of Mechanical and Industrial Engineering, University of Cincinnati, Cincinnati, OH 45221-0072.

Manuscript received by the ASME Applied Mechanics Division, Mar. 9, 1988; final revision, Feb. 10, 1989.

Copyright © 1990 by ASME
Downloaded 03 May 2010 to 171.66.16.244. Redistribution subject to ASME license or copyright; see http://www.asme.org/terms/Terms_Use.cfm

easily by replacing the Poisson's ratio wherever it occurs by $\nu/(1+\nu)$. Since the crack surfaces are subjected to a pair of compression loading, the boundary conditions can be expressed as

$$\tau_{xy}(x,0)=0, \qquad 0\le x\le b \tag{6}$$
$$\tau_{xy}(x,h)=0, \qquad 0\le x\le b \tag{7}$$
$$u_y(x,h)=0, \qquad 0\le x\le b \tag{8}$$
$$u_x(b,y)=0, \qquad 0\le y\le h \tag{9}$$
$$\tau_{xy}(b,y)=0, \qquad 0\le y\le h \tag{10}$$
$$\sigma_y(x,0)=-p(x), \qquad 0\le x<a \tag{11}$$
$$u_y(x,0)=0, \qquad a<x\le b. \tag{12}$$

The goal is to find the suitable displacement expressions $u_x(x,y)$ and $u_y(x,y)$ which satisfy the stress-strain relations (1)–(3), the equilibrium equations (4) and (5), and boundary conditions (6)–(12).

III Analytical Solution

By using the linear combination of the Fourier transform and Fourier series, the solutions of both partial differential equations (4) and (5) may be written

$$u_x=\frac{1}{2\mu}\int_0^\infty [(\kappa B+C+D\xi y)\cosh(\xi y) + (A+\kappa D+B\xi y)\sinh(\xi y)]\sin(\xi x)d\xi + \frac{1}{2\mu}\sum_{n=0}^{\infty}{}' \left[\kappa(G-E)\sinh\frac{n\pi x}{h}-G\frac{n\pi x}{h}\cosh\frac{n\pi x}{h}\right]\cos\frac{n\pi y}{h} \tag{13}$$

$$u_y=-\frac{1}{2\mu}\int_0^\infty [(A+B\xi y)\cosh(\xi y)+(C+D)\sinh(\xi y)]\cos(\xi x)d\xi + \frac{1}{2\mu}\sum_{n=0}^{\infty}{}' \left[E\cosh\frac{n\pi x}{h}+G\frac{n\pi x}{h}+G\frac{n\pi x}{h}\sinh\frac{n\pi x}{h}\right]\sin\frac{n\pi y}{h} \tag{14}$$

where the prime in the symbol Σ' stands for taking a half when $n=0$, the constant κ is defined by the expression

$$\kappa=3-4\nu, \tag{15}$$

and the unknown functions

$$\left(A,B,C,D,E,G\right)=\left(A(\xi),B(\xi),C(\xi),D(\xi),E)(n),G(n)\right) \tag{16}$$

will be determined through the boundary conditions (6)–(12). From (1)–(3), the corresponding stress components may be found

$$\sigma_x=\int_0^\infty \xi\Big\{[(3-2\nu)B+C+D\xi y]\cosh(\xi y)+[A+(3-2\nu)D+B\xi y]\times\sinh(\xi y)\Big\}\cos(\xi\chi)d\xi+\sum_{n=0}^{\infty}{}'\frac{n\pi}{h}\left\{[(2-2\nu)G-E]\cos\frac{n\pi x}{h} - G\frac{n\pi x}{h}\sinh\frac{n\pi x}{h}\right\}\cos\frac{n\pi y}{h} \tag{17}$$

$$\sigma_y=\int_0^\infty \xi\Big\{[-A-B\xi y-(1-2\nu)D]\sinh(\xi y+[-C-D\xi y - (1-2\nu)B]\cosh(\xi y)\Big\}\cos(\xi x)d\xi + \sum_{n=0}^{\infty}{}'\frac{n\pi}{h}\left[(E+2\nu G)\cosh\frac{n\pi x}{h}+G\frac{n\pi x}{h}\sinh\frac{n\pi x}{h}\right]\cos\frac{n\pi y}{h} \tag{18}$$

$$\tau_{xy}=\int_0^\infty \xi\Big\{[(2-2\nu)B+C+D\xi y]\sinh(\xi y)+[A+B\xi y + (2-2\nu)D]\cosh(\xi y)\Big\}\sin(\xi x)d\xi + \sum_{n=0}^{\infty}{}'\frac{n\pi}{h}\left\{[E-(1-2\nu)G]\sinh\frac{n\pi x}{h}+G\frac{n\pi x}{h}\cosh\frac{n\pi x}{h}\right]\sin\frac{n\pi y}{h}\right\}. \tag{19}$$

Putting (18) into (14) into boundary conditions (11) and (12), the following pair of dual integral equations is obtained

$$\frac{d}{dx}\int_0^\infty D\sin(\xi x)d\xi+\int_0^\infty \xi[C+(1-2\nu)B-D]\cos(\xi x)d\xi - \sum_{n=0}^{\infty}{}'\frac{n\pi}{h}\left[([E+2\nu G)\cosh\frac{n\pi x}{h}+G\frac{n\pi x}{h}\sinh\frac{n\pi x}{h}\right] = p(x),\ 0\le x<a \tag{20}$$

$$\int_0^\infty A\cos(\xi x)d\xi=0, \quad a<x\le b \tag{21}$$

where the unknown functions $A(\xi),\ldots,G(n)$ are not independent. Their relations may be obtained through boundary conditions (6)–(10). From (6), (7), and (8), the functions A, B, and C can be expressed in terms of D as

$$A=-(2-2\nu)D \tag{22}$$
$$B=-\coth(\xi h)D \tag{23}$$
$$C=[(2-2\nu)\coth(\xi h)+\xi h\ csch^2(\xi h)]D. \tag{24}$$

By the Fourier transform from (9) and (10), the expressions of G and $E+2\nu G$ may be written

$$G(n)=\frac{2}{h\sinh\dfrac{n\pi b}{h}}\int_0^\infty \frac{\xi\sin(\xi b)D}{\xi^2+\left(\dfrac{n\pi}{h}\right)^2} \tag{25}$$

and

$$E(n)+2\nu G(n)=\frac{2}{h\sinh\dfrac{n\pi b}{h}}\left(1-\frac{n\pi b}{h}\coth\frac{n\pi b}{h}\right)\int_b^a\frac{\xi\sin(\xi b)D}{\xi^2+\left(\dfrac{n\pi}{h}\right)^2}d\xi + \frac{4}{h\sinh\dfrac{n\pi b}{h}}\int_0^\infty\frac{\xi^2\sinh(\xi b)D}{\left[\xi^2+\left(\dfrac{n\pi}{h}\right)^2\right]^2}d\xi. \tag{26}$$

Now, substitute (22)–(26) into the above dual integral equations (20) and (21). This problem has been reduced to determine the only unknown function D, if we assume that D can be expressed by another unknown function $\phi(\zeta)$.

$$D=\int_0^a \zeta\phi(\zeta)J_0(\xi\zeta)d\zeta \tag{27}$$

where J_0 stands for the zero-order Bessel function of the first kind. It can be seen that (21) will be satisfied automatically if (27) and (22) are substituted into equation (21) according to the formula (Gradshteyn 1980)

$$\int_0^\infty J_0(\xi\zeta)\cos(\xi x)d\xi=\begin{cases}(\zeta^2-x^2)^{-1/2} & 0<x<\zeta\\ 0 & 0<\zeta<x.\end{cases} \tag{28}$$

Similarly, by using the following relations

$$\int_0^\infty J_0(\xi\zeta)\sin(\xi x)d\xi=\begin{cases}0 & 0<x<\zeta\\ (\zeta^2-x^2)^{-1/2} & 0<\zeta<x,\end{cases} \tag{29}$$

equation (20) can be expressed as

$$\frac{d}{dx}\int_0^x\frac{\zeta\phi(\zeta)}{(x^2-\zeta^2)^{1/2}}d\zeta + \int_0^\infty\frac{\xi h+\exp(-\xi h)\sinh(\xi h)}{\sinh^2(\xi h)}\left[\int_0^a\eta\phi(\eta)J_0(\xi\eta)d\eta\right]\cos(\xi x)d\xi$$

Downloaded 03 May 2010 to 171.66.16.244. Redistribution subject to ASME license or copyright; see http://www.asme.org/terms/Terms_Use.cfm

$$-\sum_{n=0}^{\infty}{}' \frac{\pi}{h}\frac{n\pi}{h}\frac{\exp\left(-\frac{n\pi b}{h}\right)}{\sinh\frac{n\pi b}{h}}\int_0^a \eta\phi(\eta)d\eta W = p(x) \quad (30)$$

where

$$W=\left\{\left[\left(3-\frac{n\pi b}{h}\frac{\exp\frac{n\pi b}{h}}{\sinh\frac{n\pi b}{h}}\right)I_0\left(\frac{n\pi\eta}{h}\right)+\frac{n\pi\eta}{h}I_1\left(\frac{n\pi\eta}{h}\right)\right]\times\cosh\frac{n\pi x}{h}+I_0\left(\frac{n\pi\eta}{h}\right)\frac{\eta\pi x}{h}\sinh\frac{n\pi x}{h}\right\}$$

and where I_0 and I_1 stand for the modified Bessel function of the first kind of order zero and of order one, respectively. With the aid of the Abel equation pair in Sneddon (1975)

$$\frac{2}{\pi}\frac{d}{dx}\int_0^x\frac{\zeta\phi(\zeta)}{(x^2-\zeta^2)^{1/2}}d\zeta=F(x);\quad \phi(\zeta)=\int_0^\zeta\frac{F(x)}{(\zeta^2-x^2)^{1/2}}dx, \quad (31)$$

we may find that the auxiliary function $\phi(\zeta)$ in the Abel integral equation (30) is governed by a Fredholm integral equation of the second kind

$$\phi(\zeta)+\int_0^a\eta\phi(\eta)(F_1-F_2)d\eta=\frac{2}{\pi}\int_0^\zeta\frac{p(x)}{(\zeta^2-x^2)^{1/2}}dx \quad (32)$$

where

$$F_1=\int_0^\infty\xi\frac{\xi h+\exp(-\xi h)\sinh(\xi h)}{\sinh^2(\xi h)}J_0(\xi\zeta)J_0(\xi\eta)d\xi \quad (33)$$

$$F_2=\sum_{n=0}^{\infty}{}'\frac{\pi}{h}\frac{n\pi}{h}\frac{\exp\left(-\frac{n\pi b}{h}\right)}{\sinh\frac{n\pi b}{h}}\times\left\{\left[3-\frac{\frac{n\pi b}{h}\exp\frac{n\pi b}{h}}{\sinh\frac{n\pi b}{h}}\right]I_0\left(\frac{n\pi\zeta}{h}\right)I_0\left(\frac{n\pi n}{h}\right)+\frac{n\pi n}{h}I_1\left(\frac{n\pi\eta}{h}\right)I_0\left(\frac{npie\zeta}{h}\right)+\frac{n\pi\zeta}{h}I_1\left(\frac{n\pi\zeta}{h}\right)I_0\left(\frac{n\pi n}{h}\right)\right\}. \quad (34)$$

It is noted that the equation (30) comes from the boundary condition (11). Hence, when x is larger than a crack length a, the normal stress is

$$\sigma_y(x,0)=-\frac{d}{dx}\int_0^a\frac{\zeta\phi(\zeta)}{(x^2-\zeta^2)^{1/2}}d\zeta+l_2 \quad (35)$$

in which l_2 stands for the second term on the left-hand side of the equation (30). Because it does not have a singularity $x\to a$, it may be eliminated when we seek the stress intensity factory of this problem

$$K_I=\lim_{x\to a}[2(x-a)]^{1/2}\sigma_y(x,0)$$

$$=\lim_{x\to a}[2(x-a)]^{1/2}\left[-\frac{d}{dx}\int_0^a\frac{\zeta\phi(\zeta)}{(x^2-\zeta^2)^{1/2}}d\zeta\right]. \quad (36)$$

Integrating by parts once, the solution of the stress intensity factor of the rectangular plate with a central crack is obtained

$$K_I=\phi(a) \quad (37)$$

where $\phi(a)$ is the solution of the Fredholm integral equation of the second kind (32).

Table 1 The stress intensity factor $\psi(1)$ from $K_I = \psi(1)\, p\, a^{1/2}$

	ratio of crack length to plate width a:b					
a:h	1:1.2	1:1.5	1:2	1:5	1:10	1:∞
1:0.25	1.3759	0.7774	0.5403	0.3488	0.3119	0.2821
1:0.5	1.5880	1.0142	0.7330	0.4879	0.4389	0.3989
1:1	1.6751	1.2176	0.9620	0.6817	0.6210	0.5702
1:2	1.6884	1.2840	1.1133	0.8999	0.8412	0.7896
1:4	1.6885	1.2861	1.1283	1.0029	0.9662	0.9309
1:10	1.6886	1.2861	1.1284	1.0170	1.0028	0.9879
1:∞	1.6885	1.2861	1.1284	1.0170	1.0041	1.0000

IV Numerical Solution

To solve the equation (32) on the computer for the unknown $\phi(\zeta)$, it is convenient to nondimensionalize some variables. Assuming uniform compression on the crack opening, i.e., $p(x)$ = constant, and making the suitable substitute of variables, such as $\zeta\to\zeta/a$, $\xi\to\xi a$, and $\phi(\zeta)\to\psi(\zeta/a)$, (32) and (37) have the following forms

$$\psi(\zeta)+\int_0^1(\zeta\eta)^{1/2}\psi(\eta)(F_1-F_2)d\eta=\zeta^{1/2} \quad (38)$$

where

$$F_1=\int_0^\infty\xi\frac{\frac{\xi h}{a}+\exp\left(-\frac{\xi h}{a}\right)\sinh\left(\frac{\xi h}{a}\right)}{\sinh^2\left(\frac{\xi h}{a}\right)}J_0(\xi\zeta)J_0(\xi\eta)d\xi \quad (39)$$

$$F_2=\sum_{n=0}^{\infty}{}'\frac{\pi a}{h}\frac{n\pi a}{h}\frac{\exp\left(-\frac{n\pi b}{h}\right)}{\sinh\frac{n\pi b}{h}}\left\{\left[3-\frac{\frac{n\pi b}{h}\exp\frac{n\pi b}{h}}{\sinh\frac{n\pi b}{h}}\right]I_0\times\left(\frac{n\pi\zeta}{h}\right)T_0\left(\frac{n\pi n}{h}\right)+\frac{n\pi\eta}{h}I_1\left(\frac{n\pi\eta}{h}\right)I_0\left(\frac{m\pi\xi}{h}\right)+\frac{n\pi\eta}{h}I_1\left(\frac{n\pi\zeta}{h}\right)I_0\frac{n\pi\eta}{h}\right\} \quad (40)$$

$$K_I=\psi(1)p\,a^{1/2}. \quad (41)$$

Using the seven point Gauss-Radau quadrature formula (Davis 1975), the integral equation (40) can been converted into a system of linear algebraic equations which have been solved for a dimensionless $\psi(1)$. Its numerical value has been listed in Table 1 for all kinds of rectangular sheets. The values of the last line (a: h = 1: ∞) in Table 1 are consistent with ones derived by Koiter (Sih, 1973) although he discussed the problem of colinear cracks in an infinite plate. The last column (a : b = 1:∞) is the same as the results according to Fichter (1967).

V Conclusions

The techniques of linearly combining the Fourier transform and Fourier series is used for investigating a finite rectangular plate with crack for various ratios of crack length to plate height, a : h, and crack length to plate width, a : b. The results for the stress intensity factor, $\psi(1)$, include the predictions by Koiter and Fichter as limiting cases.

References

Aboudi, J., 1987, "Stiffness Reduction of Cracked Solids," *Engineering Fracture Mechanics*, Vol. 26, pp. 637–650.

Broek, D., 1986, *Elementary Engineering Fracture Mechanics*, Martinus Nijhoff Publishers, Dordrecht, p. 81.

Davis, P. J., and Rabinowitz, P., 1975, *Methods of Numerical Integration*, Academic Press, New York, pp. 73–82.

Delameter, W. R., Herrmann, G., and Barnett, D. M., 1975, "Weakening

Downloaded 03 May 2010 to 171.66.16.244. Redistribution subject to ASME license or copyright; see http://www.asme.org/terms/Terms_Use.cfm

of an Elastic Solid by a Rectangular Array of Cracks," ASME JOURNAL OF APPLIED MECHANICS, Vol. 42, pp. 74–80 and Vol. 44, 1977, pp. 190.

Fichter, W. B., 1967, "Stresses at the Tip of a Longitudinal Crack in a Plate Strip," NASA TR R-265.

Gradshteyn, I. S., and Ryzhik, I. M., 1980, *Table of Integrals, Series, and Products*, Academic Press, New York, p. 731.

Isida, M., 1972, "Effects of Specimen Geometry and Loading Conditions on the Crack Tip Plastic Zone," *Mechanical Behavior of Materials*, Vol. 1, Society of Material Science, Japan, pp. 394–407.

Lowengrub, M., 1966, "Some Dual Trigonometric Equations with an Application to Elasticity," *International Journal of Engineering Science*, Vol. 4, pp. 79–76.

Ma, S. W., 1988*a*, "A Central Crack in a Finite Rectangular Plate with Constrained Edges Parallel to the Crack under the Opening Mode," *Engineering Fracture Mechanics*" Vol. 31, pp. 493–500.

Ma, S. WQ., 1988*b*, "A Central Crack Normal to the Interface between Two Different Materials in a Rectangular Sheet under an Anti-Plane Shear Stress," *Engineering Fracture Mechanics*, Vol. 30, pp. 759–765.

Rooke, D. P., and Cartwright, D. J., 1976, *Compendium of Stress Intensity Factors*, London, Her Majesty's Stationary Office.

Sih, G. C., 1973, *Handbook of Stress Intensity Factor*, Lehigh University, Bethlehem, Penn.

Sih, G. C., and Chen, E. P., 1981, *Cracks in Composite Materials*, Martinus Nijhoff Publishers.

Analytical Solution for a Pinched Laminated Cylinder

K. Bhaskar[4,6] and T. K. Varadan[5,6]

Introduction

The problem of a cylindrical shell pinched by two concentrated loads at diametrically opposite points is often used as a benchmark for assessment of new shell finite elements and has found its way into textbooks on finite elements (Cook, 1981). The analytical solution for this problem is generally obtained using the classical shell theory equations of Flugge (1967) which do not account for shear deformation effects.

The current trend in shell finite elements is to use the concept of degeneration (Ahmed et al., 1970; Panda and Natarajan, 1981) wherein three-dimensional isoparametric elements are reduced to two-dimensional shell elements. In such an analysis, the different shell theory variants are circumvented and the only assumption involved is that normals to the middle surface remain straight (not necessarily normal) and unstretched after deformation. Thus, the analysis accounts for shear deformation and is applicable to thick as well as thin shells.

For assessment of degenerated shell elements, the analytical solution of a test problem should be based on a first-order shear deformation theory and should be free of the assumptions like thinness, shallowness, etc. usually employed in shell theory. Such a solution for the pinched cylinder, for both laminated and isotropic shells, is the objective of the present work.

Formulation

Let the cylindrical shell of length, L, mean radius, R_o, and thickness, h, be referred to a cylindrical polar coordinate system x, θ, z (Fig. 1). The displacements $\bar{u}$, $\bar{v}$, $\bar{w}$ along these axes of any point of the shell are given for a first-order theory by

$$(\bar{u},\ \bar{v}) = (u,\ v) + z(\phi,\ \psi),\ \bar{w} = w \tag{1}$$

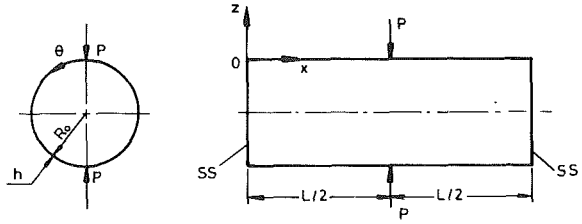


Fig. 1 The pinched cylindrical shell

where u, v, w refer to the displacements of the point $(x, \theta, 0)$ and ϕ and ψ are the rotations of the normal about θ and x directions, respectively. u, v, w, ϕ, ψ are functions of x and θ only.

The strain-displacement relations of elasticity are

$$\begin{aligned} e_x &= \bar{u}_{,x} & e_\theta &= (\bar{v}_{,\theta} + \bar{w})/R \\ e_z &= \bar{w}_{,z} & \gamma_{x\theta} &= \bar{v}_{,x} + \bar{u}_{,\theta}/R \\ \gamma_{xz} &= \bar{w}_{,x} + \bar{u}_{,z} & \gamma_{\theta z} &= \bar{v}_{,z} + (\bar{w}_{,\theta} - \bar{v})/R \end{aligned} \tag{2}$$

where $R = R_o + z$ and a comma denote differentiation.

These, in terms of u, v, w, ϕ, ψ, are

$$\begin{aligned} e_x &= u_{,x} + z\phi_{,x} & e_\theta &= (v_{,\theta} + z\psi_{,\theta} + w)/R \\ e_z &= 0 & \gamma_{x\theta} &= v_{,x} + z\psi_{,x} + (u_{,\theta} + z\phi_{,\theta})/R \\ \gamma_{xz} &= w_{,x} + \phi & \gamma_{\theta z} &= (R_o\psi + w_{,\theta} - v)/R. \end{aligned} \tag{3}$$

The shell is made of either an isotropic material or of layers of orthotropic material with the material axes coinciding with the x, θ directions. The stress-strain law for the ith layer is

$$\begin{Bmatrix} \sigma_x \\ \sigma_\theta \end{Bmatrix}_{(i)} = \begin{bmatrix} Q_{11} & Q_{12} \\ Q_{12} & Q_{22} \end{bmatrix}_{(i)} \begin{Bmatrix} e_x \\ e_\theta \end{Bmatrix}_{(i)} \text{ and} \tag{4a}$$

$$\begin{Bmatrix} \tau_{\theta z} \\ \tau_{xz} \\ \tau_{x\theta} \end{Bmatrix}_{(i)} = \begin{bmatrix} k^2Q_{44} & 0 & 0 \\ 0 & k^2Q_{55} & 0 \\ 0 & 0 & Q_{66} \end{bmatrix}_{(i)} \begin{Bmatrix} \gamma_{\theta z} \\ \gamma_{xz} \\ \gamma_{x\theta} \end{Bmatrix}_{(i)}, \tag{4b}$$

where Q_{ij} are the plane-stress reduced stiffness coefficients and k^2 is the shear correction factor.

The following generalized force resultants are defined:

$$\begin{aligned} (N_x,\ N_{x\theta},\ N_{xz}) &= \int (\sigma_x,\ \tau_{x\theta},\ \tau_{xz})(1 + z/R_o)\,dz \\ (N_\theta,\ N_{\theta x},\ N_{\theta z}) &= \int (\sigma_\theta,\ \tau_{x\theta},\ \tau_{\theta z})\,dz \\ (M_x,\ M_{x\theta}) &= \int (\sigma_x,\ \tau_{x\theta}) z\,(1 + z/R_o)\,dz \\ (M_\theta,\ M_{\theta x}) &= \int (\sigma_\theta,\ \tau_{x\theta}) z\,dz. \end{aligned} \tag{5}$$

Using equations (3), (4), and (5), the force resultants can be expressed in terms of the generalized variables u, v, ϕ, ψ, w. The integrations over z are carried out *exactly, retaining logarithmic terms as they occur*, without any simplification. Thus, the analysis remains free of the usual classical theory approximation of neglecting z/R_o, or its higher powers as being small compared to unity. The expressions for the force resultants are easy to derive and are not given here for the sake of brevity.

The governing equations for the shell loaded by a transverse radial load $Q(x, \theta)$ per unit area of the middle surface are derived using the principle of minimum total potential given by

[4]Research Scholar.

[5]Professor.

[6]Department of Aerospace Engineering, Indian Institute of Technology, Madras, India.

Manuscript received and accepted by the ASME Applied Mechanics Division, October 16, 1989.

Downloaded 03 May 2010 to 171.66.16.244. Redistribution subject to ASME license or copyright; see http://www.asme.org/terms/Terms_Use.cfm

of an Elastic Solid by a Rectangular Array of Cracks," ASME JOURNAL OF APPLIED MECHANICS, Vol. 42, pp. 74–80 and Vol. 44, 1977, pp. 190.

Fichter, W. B., 1967, "Stresses at the Tip of a Longitudinal Crack in a Plate Strip," NASA TR R-265.

Gradshteyn, I. S., and Ryzhik, I. M., 1980, *Table of Integrals, Series, and Products*, Academic Press, New York, p. 731.

Isida, M., 1972, "Effects of Specimen Geometry and Loading Conditions on the Crack Tip Plastic Zone," *Mechanical Behavior of Materials*, Vol. 1, Society of Material Science, Japan, pp. 394–407.

Lowengrub, M., 1966, "Some Dual Trigonometric Equations with an Application to Elasticity," *International Journal of Engineering Science*, Vol. 4, pp. 79–76.

Ma, S. W., 1988*a*, "A Central Crack in a Finite Rectangular Plate with Constrained Edges Parallel to the Crack under the Opening Mode," *Engineering Fracture Mechanics*" Vol. 31, pp. 493–500.

Ma, S. WQ., 1988*b*, "A Central Crack Normal to the Interface between Two Different Materials in a Rectangular Sheet under an Anti-Plane Shear Stress," *Engineering Fracture Mechanics*, Vol. 30, pp. 759–765.

Rooke, D. P., and Cartwright, D. J., 1976, *Compendium of Stress Intensity Factors*, London, Her Majesty's Stationary Office.

Sih, G. C., 1973, *Handbook of Stress Intensity Factor*, Lehigh University, Bethlehem, Penn.

Sih, G. C., and Chen, E. P., 1981, *Cracks in Composite Materials*, Martinus Nijhoff Publishers.

Analytical Solution for a Pinched Laminated Cylinder

K. Bhaskar[4,6] and T. K. Varadan[5,6]

Introduction

The problem of a cylindrical shell pinched by two concentrated loads at diametrically opposite points is often used as a benchmark for assessment of new shell finite elements and has found its way into textbooks on finite elements (Cook, 1981). The analytical solution for this problem is generally obtained using the classical shell theory equations of Flugge (1967) which do not account for shear deformation effects.

The current trend in shell finite elements is to use the concept of degeneration (Ahmed et al., 1970; Panda and Natarajan, 1981) wherein three-dimensional isoparametric elements are reduced to two-dimensional shell elements. In such an analysis, the different shell theory variants are circumvented and the only assumption involved is that normals to the middle surface remain straight (not necessarily normal) and unstretched after deformation. Thus, the analysis accounts for shear deformation and is applicable to thick as well as thin shells.

For assessment of degenerated shell elements, the analytical solution of a test problem should be based on a first-order shear deformation theory and should be free of the assumptions like thinness, shallowness, etc. usually employed in shell theory. Such a solution for the pinched cylinder, for both laminated and isotropic shells, is the objective of the present work.

Formulation

Let the cylindrical shell of length, L, mean radius, R_o, and thickness, h, be referred to a cylindrical polar coordinate system x, θ, z (Fig. 1). The displacements $\bar{u}$, $\bar{v}$, $\bar{w}$ along these axes of any point of the shell are given for a first-order theory by

$$(\bar{u},\ \bar{v}) = (u,\ v) + z(\phi,\ \psi),\ \bar{w} = w \tag{1}$$

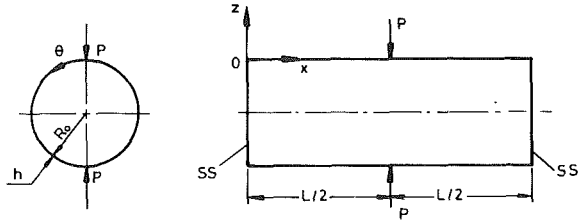


Fig. 1 The pinched cylindrical shell

where u, v, w refer to the displacements of the point $(x, \theta, 0)$ and ϕ and ψ are the rotations of the normal about θ and x directions, respectively. u, v, w, ϕ, ψ are functions of x and θ only.

The strain-displacement relations of elasticity are

$$\begin{aligned} e_x &= \bar{u}_{,x} & e_\theta &= (\bar{v}_{,\theta} + \bar{w})/R \\ e_z &= \bar{w}_{,z} & \gamma_{x\theta} &= \bar{v}_{,x} + \bar{u}_{,\theta}/R \\ \gamma_{xz} &= \bar{w}_{,x} + \bar{u}_{,z} & \gamma_{\theta z} &= \bar{v}_{,z} + (\bar{w}_{,\theta} - \bar{v})/R \end{aligned} \tag{2}$$

where $R = R_o + z$ and a comma denote differentiation.

These, in terms of u, v, w, ϕ, ψ, are

$$\begin{aligned} e_x &= u_{,x} + z\phi_{,x} & e_\theta &= (v_{,\theta} + z\psi_{,\theta} + w)/R \\ e_z &= 0 & \gamma_{x\theta} &= v_{,x} + z\psi_{,x} + (u_{,\theta} + z\phi_{,\theta})/R \\ \gamma_{xz} &= w_{,x} + \phi & \gamma_{\theta z} &= (R_o\psi + w_{,\theta} - v)/R. \end{aligned} \tag{3}$$

The shell is made of either an isotropic material or of layers of orthotropic material with the material axes coinciding with the x, θ directions. The stress-strain law for the ith layer is

$$\begin{Bmatrix} \sigma_x \\ \sigma_\theta \end{Bmatrix}_{(i)} = \begin{bmatrix} Q_{11} & Q_{12} \\ Q_{12} & Q_{22} \end{bmatrix}_{(i)} \begin{Bmatrix} e_x \\ e_\theta \end{Bmatrix}_{(i)} \text{ and} \tag{4a}$$

$$\begin{Bmatrix} \tau_{\theta z} \\ \tau_{xz} \\ \tau_{x\theta} \end{Bmatrix}_{(i)} = \begin{bmatrix} k^2Q_{44} & 0 & 0 \\ 0 & k^2Q_{55} & 0 \\ 0 & 0 & Q_{66} \end{bmatrix}_{(i)} \begin{Bmatrix} \gamma_{\theta z} \\ \gamma_{xz} \\ \gamma_{x\theta} \end{Bmatrix}_{(i)}, \tag{4b}$$

where Q_{ij} are the plane-stress reduced stiffness coefficients and k^2 is the shear correction factor.

The following generalized force resultants are defined:

$$\begin{aligned} (N_x,\ N_{x\theta},\ N_{xz}) &= \int (\sigma_x,\ \tau_{x\theta},\ \tau_{xz})(1 + z/R_o)\,dz \\ (N_\theta,\ N_{\theta x},\ N_{\theta z}) &= \int (\sigma_\theta,\ \tau_{x\theta},\ \tau_{\theta z})\,dz \\ (M_x,\ M_{x\theta}) &= \int (\sigma_x,\ \tau_{x\theta}) z\,(1 + z/R_o)\,dz \\ (M_\theta,\ M_{\theta x}) &= \int (\sigma_\theta,\ \tau_{x\theta}) z\,dz. \end{aligned} \tag{5}$$

Using equations (3), (4), and (5), the force resultants can be expressed in terms of the generalized variables u, v, ϕ, ψ, w. The integrations over z are carried out *exactly, retaining logarithmic terms as they occur*, without any simplification. Thus, the analysis remains free of the usual classical theory approximation of neglecting z/R_o, or its higher powers as being small compared to unity. The expressions for the force resultants are easy to derive and are not given here for the sake of brevity.

The governing equations for the shell loaded by a transverse radial load $Q(x, \theta)$ per unit area of the middle surface are derived using the principle of minimum total potential given by

[4]Research Scholar.

[5]Professor.

[6]Department of Aerospace Engineering, Indian Institute of Technology, Madras, India.

Manuscript received and accepted by the ASME Applied Mechanics Division, October 16, 1989.

Copyright © 1990 by ASME
Downloaded 03 May 2010 to 171.66.16.244. Redistribution subject to ASME license or copyright; see http://www.asme.org/terms/Terms_Use.cfm

Table 1 Displacements and force resultants at different points

Parameter	90°/0°/90°		90°/0°		Isotropic	
	$R_o/h=100$	$R_o/h=10$	$R_o/h=100$	$R_o/h=10$	$R_o/h=100$	$R_o/h=10$
$w'(0.1L,0)$*	- 53.943	- 8.240	-122.520	- 15.118	- 21.395	- 1.328
$w'(0.2L,0)$	-112.470	- 17.200	-255.911	- 31.682	- 43.795	- 2.825
$w'(0.3L,0)$	-183.460	- 28.456	-420.466	- 51.520	- 68.612	- 4.765
$w'(0.4L,0)$	-292.010	- 46.643	-686.117	- 77.555	-100.013	- 7.461
$w'(L/2,0)$	-672.336	-120.489	-1241.390	-151.796	-165.630 (-164.247)	-11.351 (- 9.456)
$w'(L/2,\pi/8)$	-288.906	- 55.634	-403.570	- 78.037	- 56.321	- 7.664
$w'(L/2,\pi/4)$	143.575	9.608	132.050	21.367	15.661	1.899
$w'(L/2,3\pi/8)$	6.694	26.794	- 49.422	32.442	- 11.970	2.089
$w'(L/2,\pi/2)$	- 51.245	31.715	- 12.309	31.615	- 0.463	1.531
$N_x'(0.4L,0)$	- 3.908	- 7.641	- 8.443	- 11.733	- 7.362 (- 7.370)	-12.267 (-12.189)
$N_\theta'(0.4L,0)$	1.885	- 1.311	1.808	- 5.700	2.222 (2.216)	- 9.761 (-10.315)
$M_x'(0.4L,0)$	0.227	1.328	3.254	1.899	- 0.365 (- 0.361)	- 2.463 (- 2.496)
$M_\theta'(0.4L,0)$	- 4.682	-14.934	- 3.719	- 11.798	- 4.176 (- 4.174)	- 8.640 (- 8.675)

* $w'=(E_L h w)/P$; $(N_x', N_\theta')=(100h/P)(N_x, N_\theta)$; $(M_x', M_\theta')=(100/P)(M_x, M_\theta)$
Values in parantheses refer to Flugge's theory.

$$\int(\sigma_x\delta e_x+\sigma_\theta\delta e_\theta+\tau_{x\theta}\delta\gamma_{x\theta}+\tau_{\theta z}\delta\gamma_{\theta z}+\tau_{xz}\delta\gamma_{xz})\times(1+z/R_o)dzdA-\int Q\delta w dA=0, \tag{6}$$

where $dA=R_o dx d\theta$.

After integration through the thickness, this gives

$$\int[N_x\delta u_{,x}+M_x\delta\phi_{,x}+N_\theta(\delta v_{,\theta}+\delta w)/R_o+M_\theta\delta\psi_{,\theta}/R_o+N_{x\theta}\delta v_{,x}+M_{x\theta}\delta\psi_{,x}+N_{\theta x}\delta u_{,\theta}/R_o+M_{\theta x}\delta\phi_{,\theta}/R_o+N_{\theta z}(\delta w_{,\theta}-\delta v+R_o\delta\psi)/R_o+N_{xz}(\delta w_{,x}+\delta\phi)-Q\delta w]dA=0. \tag{7}$$

The equations of equilibrium are then as follows:

$$\begin{aligned}
&N_{x,x}+N_{\theta x,\theta}/R_o=0\\
&N_{x\theta,x}+N_{\theta,\theta}/R_o+N_{\theta z}/R_o=0\\
&M_{x,x}+M_{\theta x,\theta}/R_o-N_{xz}=0\\
&M_{x\theta,x}+M_{\theta,\theta}/R_o-N_{\theta z}=0\\
&N_{xz,z}+N_{\theta z,\theta}/R_o-N_\theta/R_o=-Q.
\end{aligned} \tag{8}$$

Solution

The shell is assumed to be simply supported at both ends with the following boundary conditions:

$$N_x=M_x=w=v=\psi=0.$$

For a sinusoidal distribution of the transverse load, (i.e., $Q=\bar{Q}\sin m\pi x/L\cos n\theta$) a closed-form solution satisfying boundary conditions can be obtained by assuming

$$\begin{aligned}
(u/h,\phi) &= (U, P)\cos m\pi x/L\cos n\theta\\
(v/h, \psi) &= (V, S)\sin m\pi x/L\sin n\theta\\
w/h &= W\sin m\pi x/L\cos n\theta.
\end{aligned} \tag{9}$$

Solving the set of linear algebraic equations resulting from substitution of equations (9) into equations (8) yields U, V, W, P, S.

For the pinched cylinder problem, the applied load is expanded in a double Fourier series as

$$Q(x,\theta)=\sum_m\sum_n Q_{mn}\sin m\pi x/L\cos n\theta \tag{10}$$

where $m = 1, 3, 5, \ldots$; $n = 0, 2, 4, 6, \ldots$; $Q_{m0} = -2P(-1)^{(m-1)/2}/(\pi R_o L)$; $Q_{mn} = -4P(-1)^{(m-1)/2}/(\pi R_o L)$; P = each point load.

Corresponding to each component Q_{mn} of equation (10), the solution vector (U, V, W, P, S) has to be calculated. The displacements and stresses at any point of the shell are then obtained by a summation of the different Fourier components.

Numerical Results

Results are presented in Table 1 for two laminated shells, (90 deg/0 deg) and (90 deg/0 deg/90 deg), and an isotropic shell, with $L/R_o=2$, $R_o/h=10$, 100, and the following material properties:

(*i*) $\nu=0.3$ for the isotropic shell, and

(*ii*) $E_L/E_T = 25$, $G_{LT}/E_T = 0.5$, $G_{TT}/E_T = 0.2$, $\nu_{LT}=\nu_{TT} = 0.25$ for the laminated shells.

The value of k^2 has been taken as 5/6. The number of terms taken for m or n in equation (10) has been progressively increased from 35 in steps of 15 to such a value that the results vary by less than 1 percent by addition of 15 more terms for each of m and n. The series for the force resultants are not convergent directly below the concentrated load and hence these results are presented at a nearby point. All calculations have been performed in double precision on a Siemens 7580-E computer.

The maximum deflections and the force resultants for the isotropic case, obtained by the classical equations of Flugge (1967) are included for comparison. It can be seen that the maximum deflections predicted by the two theories are significantly different for the thicker shell. However, the force resultants are almost the same, even for the thicker shell. This is as expected since it has been shown earlier (Whitney and Pagano, 1970) that inclusion of shear deformation effects using a first-order theory results in a very little change in stresses compared to the classical approach.

Conclusion

An analytical solution for the pinched laminated cylinder with diaphragmed ends is presented here. This is based on a first-order shear deformation theory without any shell theory assumptions. Comparison with Flugge's classical solution shows the significance of shear deformation. The results presented are useful for assessment of degenerated shell finite elements.

References

Ahmed, S., Irons, B. M., and Zienkiewicz, O. C., 1970, "Analysis of Thick and Thin Shell Structures by Curved Finite Elements," *International Journal of Numerical Methods in Engineering*, Vol. 2, pp. 419–451.

Cook, R. D., 1981, *Concepts and Applications of Finite Element Analysis*, John Wiley and Sons, Inc., New York.

Flugge, W., 1967, *Stresses in Shells*, Springer-Verlag, New York.

Panda, S., and Natarajan, R., 1981, "Analysis of Laminated Composite Shell Structures by Finite Element Method," *Computers and Structures*, Vol. 14, pp. 225–230.

Whitney, J. M., and Pagano, N. J., 1970, "Shear Deformation in Heterogeneous Anisotropic Plates," ASME JOURNAL OF APPLIED MECHANICS, Vol. 37, pp. 1031–1036.

Downloaded 03 May 2010 to 171.66.16.244. Redistribution subject to ASME license or copyright; see http://www.asme.org/terms/Terms_Use.cfm

Finite Element Transient Response of Composite and Sandwich Plates With a Refined Higher-Order Theory

Mallikarjuna[7,9] and T. Kant[8,9]

Introduction

A finite element formulation for transient dynamics of a symmetrically laminated plate based on a higher-order displacement model and a three-dimensional state of stress and strain is presented here. This higher-order theory incorporates linear variation of transverse normal strain and parabolic variation of transverse shear strains through the plate thickness. The solution of the discrete system of ordinary differential equations in time is obtained using the explicit central difference scheme with a special mass lumping procedure. Numerical results for deflections and stresses are presented showing the effect of plate side-to-thickness ratio, material orthotropy, finite element mesh, and lamination scheme. Apparently, the present study constitutes the first one to analyze the transient response of composite sandwich plates using a higher-order theory.

Theoretical Formulation

The development of the present theory starts with the assumption of the displacement field in the following form:

$$\begin{aligned} u(x,y,z,t) &= z\theta_x(x,y,t) + z^3\theta_x^*(x,y,t) \\ v(x,y,z,t) &= z\theta_y(x,y,t) + z^3\theta_y^*(x,y,t) \\ w(x,y,z,t) &= w_o(x,y,t) + z^2 w_o^*(x,y,t) \end{aligned} \tag{1}$$

in which t is the time, w_o denotes the transverse displacement of the midplane, and θ_x and θ_y are the rotations of normals to midplane about the y and x-axes, respectively. The terms w_o^*, θ_x^*, and θ_y^* are the corresponding higher-order terms in the Taylor's series expansion and are also defined at the midplane. Thus, the generalized displacement vector δ of the midplane is defined as,

$$\delta = (w_o, \theta_x, \theta_y, w_o^*, \theta_x^*, \theta_y^*)^T. \tag{2}$$

The relevant mathematical details are available in Pandya and Kant (1988).

With the finite element discretization scheme in space, the dynamic problem (in the absence of damping) gives rise to a set of ordinary differential equations of the form

$$\mathbf{M}\,\mathbf{d} + \mathbf{K}\,\mathbf{d} = \mathbf{F}(t) \tag{3}$$

in which the dots denote differentiation in time, t, $\mathbf{d}$ is the nodal displacement vector, $\mathbf{M}$ is the mass matrix and $\mathbf{F}(t)$ is the vector of forces which varies with time, t.

In the C^0 finite element theory the continuum displacement vector within the element is discretized such that,

$$\delta(x,y,t) = \sum_{i=1}^{NN} N_i(x,y)\delta_i(t) \tag{4}$$

in which the term $N_i(x, y)$ is the interpolating shape function associated with node i, $\delta_i(t)$ is the value of $\delta(t)$ corresponding to node i, and NN is the number of nodes in the element.

With the generalized displacement vector $\delta(t)$ known at all points within the element as per equation (4), the generalized strain vector $\epsilon(t)$ at any point is expressed as follows (Pandya and Kant, 1988):

$$\epsilon(x,y,t) = \sum_{i=1}^{NN} \mathbf{B}_i\delta_i(t). \tag{5}$$

The element stiffness matrix is readily computed using the standard relation (Pandya and Kant, 1988):

$$\mathbf{K}_{ij}^e = \int_{-1}^{+1}\int_{-1}^{+1} \mathbf{B}_i^T\mathbf{D}\,\mathbf{B}_j|\mathbf{J}|\,d\xi\,d\eta. \tag{6}$$

The mass matrix $\mathbf{M}$ in equation (3) is given by

$$\mathbf{M} = \int_{\text{Area}} \mathbf{N}^T\bar{\mathbf{m}}\mathbf{N}d(\text{Area}) \tag{7}$$

$$\text{where } \bar{\mathbf{m}} = \begin{bmatrix} I_1 & & & & & 0 \\ & I_2 & & & & \\ & & I_2 & & & \\ & & & I_3 & & \\ & & & & I_4 & \\ 0 & & & & & I_4 \end{bmatrix} \tag{8}$$

$$\text{and } (I_1,I_2,I_3,I_4) = \sum_{L=1}^{n}\int_{h_L}^{h_{L+1}} (I,z^2,z^4,z^6)\rho^L dz \tag{9}$$

in which (I_1, I_2) and (I_3, I_4) are normal inertia, rotary inertia, and higher-order inertias, respectively. ρ^L is the material density of the Lth layer and $\mathbf{N}$ is the shape function matrix.

The integration in time of equation (3) is performed using the explicit central difference scheme,

$$\mathbf{d}^{n+1} = \mathbf{M}^{-1}\left[(\Delta t)^2(-\mathbf{K}\,\mathbf{d}^n + \mathbf{F}^n) - \mathbf{M}\,\mathbf{d}^{n-1} + 2\mathbf{M}\,\mathbf{d}^n\right] \tag{10}$$

with a suitable starting formula. The superscripts $n-1$, n, $n+1$ stand for three successive time stages and Δt is the time-step length. With diagonalized mass matrix $\mathbf{M}$, the computation at

Table 1 Comparison of transverse deflections obtained in the present study with those obtained by the classical plate theory and closed-form solution (Reddy, 1982) for a composite square plate (Material-1, a/h = 5) under suddenly applied sinusoidal pulse load, (cross-ply, 0 deg/90 deg/0 deg/ . . . . . , q = 10 N/cm^2).

E_1/E_2	Source	Layers 1	3	5	7
25	HOST	0.3484 (85)	0.3309 (83)	0.2902 (77)	0.2796 (75)
	FOST	0.3582 (85)	0.3399 (83)	0.2929 (77)	0.2825 (75)
	CFS	0.3566 (90)	0.3386 (85)	0.2924 (80)	0.2817 (80)
	CPT	0.1272 (55)	0.1272 (55)	0.1272 (55)	0.1272 (55)
40	HOST	0.3129 (81)	0.2907 (77)	0.2474 (71)	0.2362 (69)
	FOST	0.3243 (82)	0.2993 (78)	0.2473 (70)	0.2376 (69)
	CFS	0.3233 (85)	0.2985 (80)	0.2473 (75)	0.2376 (70)

Values in the parenthesis denote the time (in μ-sec) at which the maximum center deflection occurred.
HOST—Higher-order shear deformation theory
FOST—First-order shear deformation theory
CFS —Closed-form solution
CPT —Classical plate theory

[7]Research scholar.
[8]Professor.
[9]Department of Civil Engineering, Indian Institute of Technology, Powai, Bombay 400 076, India.

Contributed by the ASME Applied Mechanics Division. Manuscript received Oct. 10, 1988; final revision, Sept. 21, 1988.

Copyright © 1990 by ASME
Downloaded 03 May 2010 to 171.66.16.244. Redistribution subject to ASME license or copyright; see http://www.asme.org/terms/Terms_Use.cfm

Table 2 Convergence of center deflection ($w_o \times 10^3$) and stress (σ_x^{top}) for different time steps and meshes, (Material-2, 5 layers, $a/h = 10$, 0 deg/90 deg/core/90 deg/0 deg, $h_o = h_{90} = 0.25$, $h_{core} = 1.5$, $q = 1$ N/cm^2)

Time (μ-sec)	$w_o \times 10^3$ σ_x^{top}	$\Delta t = 0.5$ μ-sec			$\Delta t = 1$ μ-sec			$\Delta t = 2$ μ-sec	
		2×2	3×3	4×4	2×2	3×3	4×4	2×2	3×3
40	w	0.4759	0.4677	0.4677	0.4759	0.4677	0.4677	0.4759	
	σ	34.927	39.135	40.494	35.709	39.950	41.416	41.029	
80	w	1.9826	1.9785	1.9796	1.9826	1.9784	1.9798	1.9827	
	σ	233.27	221.14	224.63	232.21	219.13	221.52	223.72	
120	w	4.8914	4.8602	4.8593	4.8913	4.8602	4.8594	4.8919	
	σ	765.09	747.38	740.50	768.88	748.35	742.84	776.72	
160	w	8.6191	8.6355	8.6380	8.6194	8.6356	8.6383	8.6200	
	σ	1464.1	1468.9	1459.9	1463.7	1470.1	1460.8	1455.4	UNSTABLE
200	w	11.528	11.558	11.568	11.528	11.558	11.568	11.528	
	σ	1877.3	1876.1	1894.2	1869.3	1870.7	1885.6	1884.4	
240	w	12.953	12.877	12.847	12.953	12.877	12.848	12.953	
	σ	2084.2	2002.8	1980.8	2055.4	2009.1	1994.7	2053.1	
280	w	13.119	13.089	13.108	13.119	13.089	13.108	13.120	
	σ	2147.3	2131.4	2128.4	2132.3	2126.3	2117.0	2132.9	
320	w	12.198	12.228	12.224	12.198	12.228	12.223	12.199	
	σ	2048.4	2064.5	2063.9	2053.4	2063.7	2064.7	2066.4	
360	w	9.9341	9.8972	9.8752	9.9337	9.8924	9.8746	9.9321	
	σ	1643.5	1605.9	1599.1	1654.8	1615.7	1611.3	1635.2	

every time step becomes trivial (Hinton, Rock, and Zienkiewicz, 1976).

Numerical Results and Discussion

Two sets of materials are used in the numerical examples, viz.,

Material-1

$$\frac{E_1}{E_2} = \frac{E_2}{E_3} = 25,\ G_{12} = G_{23} = G_{13} = 0.5\,E_2$$

$$E_2 = 2.1 \times 10^6 \text{N/cm}^2,\ \nu_{12} = \nu_{23} = \nu_{13} = 0.25$$

$$\rho = 0.8 \times 10^{-5}\ \text{N-sec}^2/\text{cm}^4$$

Material-2

Face sheets:

$$E_1 = 1.308 \times 10^7 \text{N/cm}^2,\ E_2 = E_3 = 1.06 \times 10^6 \text{N/cm}^2$$

$$G_{12} = G_{13} = 0.6 \times 10^6 \text{N/cm}^2,\ G_{23} = 0.39 \times 10^6 \text{N/cm}^2$$

$$\nu_{12} = \nu_{13} = 0.28,\ \nu_{23} = 0.34,\ \rho = 0.158 \times 10^{-4} \text{N-sec}^2/\text{cm}^4$$

Core:

$$G_{13} = 0.5206 \times 10^5 \text{N/cm}^2,\ G_{23} = 0.1772 \times 10^5 \text{N/cm}^2$$

$$\rho = 0.1009 \times 10^{-5} \text{N-sec}^2/\text{cm}^4$$

A square plate of side length equal to 25 cm is used throughout. The selective integration scheme, i.e., 3 × 3 Gauss rule for bending energy and inertia terms and 2 × 2 Gauss rule for shear terms in the energy expression were employed in the numerical integration. In all the numerical examples, the plate is discretized with nine-noded Lagrangian quadrilateral elements. Due to the biaxial symmetry of the problems discussed, only one quadrant of the plate was analyzed except for angle ply laminates which are analyzed as full plates. In all the cases, zero initial conditions on displacements and their time derivatives were assumed. The finite element evaluations of stresses are at the nearest Gauss points. All the computations were carried in single precision on CYBER 180/840 computer.

Reddy (1982) has given analytical solution of the first-order shear deformation theory. The problem consists of a simply-supported composite square plate (with Material-1) subjected to a suddenly applied sinusoidal pulse loading. The plate center deflections from the present higher-order theory are compared with those of Reddy's results (Reddy, 1982) in Table 1. It is clear that the classical thin plate theory predicts significantly lower values of deflections.

Next, simply-supported laminated composite sandwich plates subjected to a uniformly distributed pulse load as shown in Fig. 1 were analyzed. Table 2 presents the center deflection and normal stress for different meshes and time steps. In estimating the time step Δt, the emperical formula given by Tsui and Tong (1971) was used with minor modification given as follows:

$$\Delta t \le \left[\rho(1-\nu^2)/\left(E_2 R\left\{2+(1-\nu)\frac{\pi^2}{12}\left(1+1.5\left(\frac{\Delta x}{h}\right)^2\right)\right\}\right)\right]^{1/2}\Delta x \tag{11}$$

in which $R = E_1/E_2$, Δx is the smallest distance between adjacent nodes in a parabolic element used. E_1 and E_2 are the Young's moduli, where subscript 1 refers to the direction of fibers and subscript 2 refers to the transverse direction. The main purpose of tabulating these results is to provide an easy means for future comparisons by other investigators.

Further, the clamped composite sandwich plates (0 deg/90 deg/core/90 deg/0 deg) subjected to a suddenly applied pulse loading (Fig. 1) were analyzed. From the results shown in Figs. 2–4, it was found that Mindlin's theory predicted significantly lower values of deflection and period for thick composite sandwich plates. It is also apparent, from the results of these theories, that the deflection and period increase with increasing value of the side-thickness ratio of the plate. The effect of transverse shear and plate thickness on the amplitude and

Downloaded 03 May 2010 to 171.66.16.244. Redistribution subject to ASME license or copyright; see http://www.asme.org/terms/Terms_Use.cfm

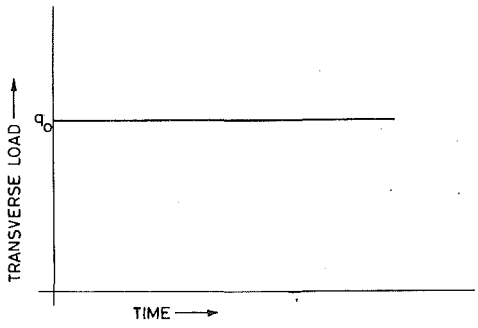


Fig. 1 Pulse or step load

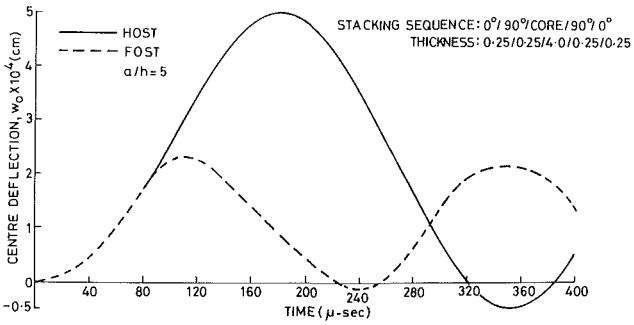


Fig. 2 Center deflection versus time for a clamped plate under uniform pulse loading (material 2, Δt = 1.0 μ-sec; q = 1N/cm²)

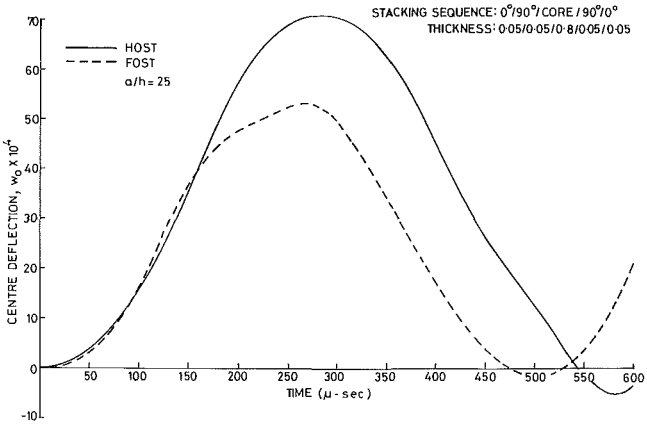


Fig. 3 Center deflection versus time for a clamped plate under uniform pulse loading (material 2, Δt = 1.0 μ-sec; q = 1N/cm²)

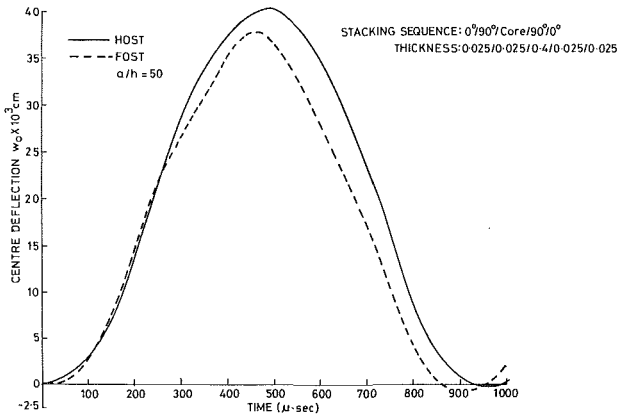


Fig. 4 Center deflection versus time for a clamped plate under uniform pulse loading (material 2, Δt = 0.5 μ-sec; q = 1N/cm²)

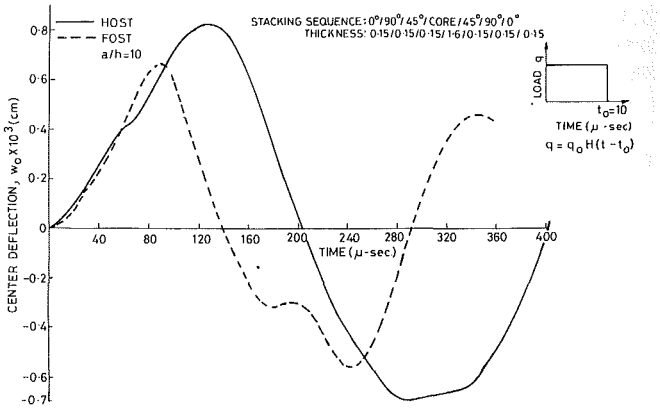


Fig. 5 Center deflection versus time (material 2, Δt = 1.0 μ-sec; q = 10N/cm, considering full plate with 4 × 4 mesh)

period of the deflection is clear on sandwich plates. It is also observed that, as the side-thickness ratio increases, the difference in the results of Mindlin's theory and present higher-order theory decreases.

The last example is concerned with transient response of a seven-layer (0 deg/90 deg/45 deg/core/45 deg/90 deg/0 deg) clamped composite sandwich plate subjected to an impulsive loading. Figure 5 shows the variation of the center deflection with respect to time. Since no damping is included in the present model, the solutions do not decay with time.

Conclusions

A refined higher-order theory and first-order shear deformation theory are used for transient response of symmetrically laminated composite and sandwich plates. Numerical results are presented for various commonly used boundary conditions and dynamic loading cases, some of which should serve as bench marks for future investigators. In contrast to the classical shear deformation theories, the present higher-order theory does not require shear correction coefficient due to more realistic representation of the cross-sectional deformation. In addition, the present theory includes the effect of direct normal stress (σ_z) which is, though negligible, very important to study the delamination mode of failure in laminated composites. The results bring out the difference in the solutions of higher-order theory from the Mindlin's plate theory, particularly for composite sandwich plates.

Acknowledgment

Partial support of this research by the Aeronautics Research and Development Board, Ministry of Defence, Government of India through its grant Nos. Aero/RD-134/100/84-85/362, 518, and 534 is gratefully acknowledged.

References

Hinton, E., Rock, T., and Zienkiewicz, O. C., 1976, "A Note on Mass Lumping and Related Processes in the Finite Element Method," *Earthquake Engineering and Structural Dynamics*, Vol. 4, pp. 245–249.

Pandya, B. N., and Kant, T., 1988, "Flexural Analysis of Laminated Composites Using Refined Higher-Order C° Plate Bending Elements," *Computer Methods in Applied Mechanics and Engineering*, Vol. 66, pp. 173–193.

Reddy, J. N., 1982, "On the Solutions to Forced Motions of Rectangular Composite Plates," ASME Journal of Applied Mechanics, Vol. 49, pp. 403–408.

Tsui, T. Y., and Tong, P., 1971, "Stability of Transient Solution of Moderately Thick Plates by Finite Difference Methods," *American Institute of Aeronautics and Astronautics Journal*, Vol. 9, pp. 2062–2063.

Downloaded 03 May 2010 to 171.66.16.244. Redistribution subject to ASME license or copyright; see http://www.asme.org/terms/Terms_Use.cfm

Shearing Stress Intensity Factors of a Cracked and Perforated Plate

Fu Bin[10] and Zhang Xiangzhou[10]

The Problem

An infinite plate containing a circular hole and a radial crack is depicted in Fig. 1. The stress intensity factors at the crack tips when the plate is stretched uniformly at infinity have been considered by some researchers, and related numerical data can be found in standard handbooks (see Tada et al., 1973, for instance). This note is concerned with the shearing stress intensity factors of the cracked and perforated plate when the plate is subjected to a uniform shearing stress $\tau_{xy}=\sigma_{II}=$ const. at infinity.

The Solution

The problem is solved with use of an equivalent procedure version of the alternating method. The basic idea of the equivalent procedure has been presented in Chang (1983) where a similar problem, i.e., the stress intensity factors of a radial crack contained in a circular disk, was discussed. Omitting the details of the development of the solution to the present problem, which are fairly like those presented in Chang (1983), the final expressions for the shearing stress intensity factors are given as follows:

$$\frac{K_{II}(t_0)}{\sigma_{II}\sqrt{\pi a}}=1-\frac{r}{2a}\left[R-\sum_{m=1}^{\infty}B_m\left(\frac{r}{t_0}\right)^m\right] \tag{1}$$

$$\frac{K_{II}(t_1)}{\sigma_{II}\sqrt{\pi a}}=1+\frac{r}{2a}\left[R-\sum_{m=1}^{\infty}B_m\left(\frac{r}{t_1}\right)^m\right] \tag{2}$$

$$R=\sum_{k=1}^{\infty}\gamma_k \tag{3}$$

$$B_m=\sum_{k=1}^{\infty}b_{m,k} \tag{4}$$

$$\gamma_k=\frac{r}{\sqrt{h^2-a^2}}\sum_{n=1}^{\infty}b_{n,k}C_{n-1} \tag{5}$$

$$b_{m,k}=\sum_{n=0}^{\infty}S_{m+n,k}g_n \tag{6}$$

$$C_m=\frac{1}{4^m}\sum_{n=0}^{m}\frac{(2n)!(2m-2n)!r^m}{[n!(m-n)!]^2t_0^{\,n}t_1^{\,m-n}} \tag{7}$$

$$g_m=\frac{1}{4^m}\sum_{n=0}^{m}\frac{(2n)!(2m-2n)!r^m}{[n!(m-n)!]^2(2n-1)(2m-2n-1)t_0^{\,n}t_1^{\,m-n}} \tag{8}$$

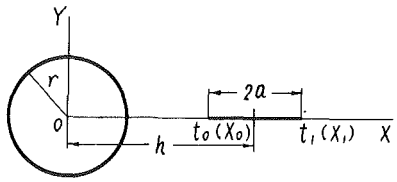


Fig. 1 The cracked and perforated plate

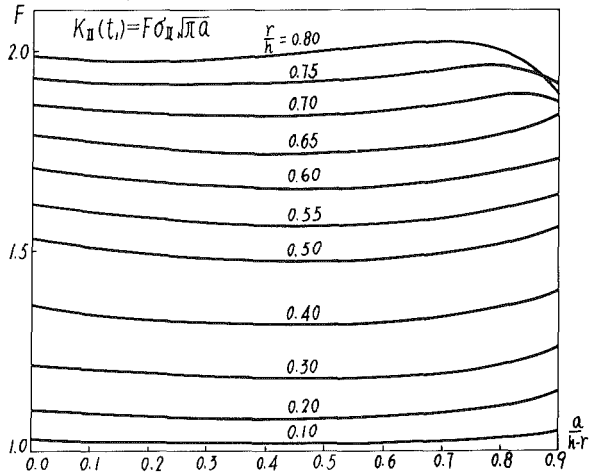


Fig. 2 Values of the stress intensity factors $K_{II}(t_1)$

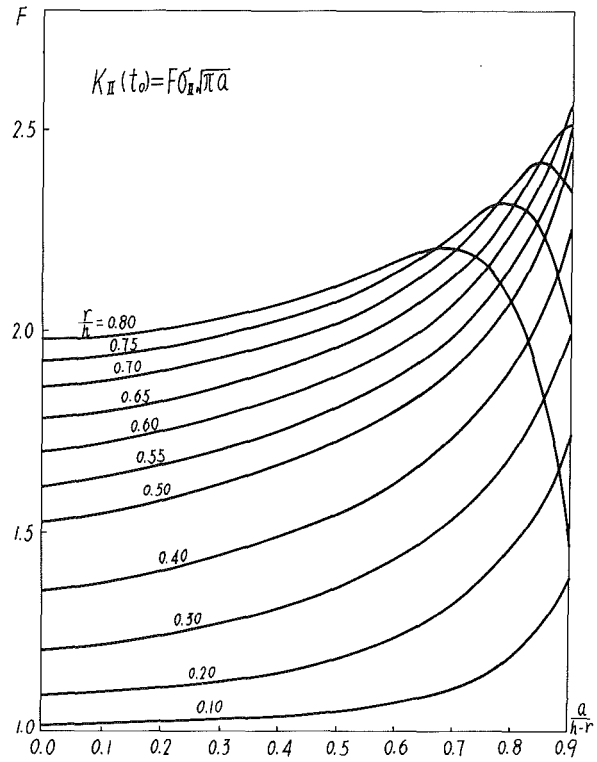


Fig. 3 Values of the stress intensity factors $K_{II}(t_0)$

$$S_{m,k}=\begin{cases}0, & m=1\\ Q_{0,k-1}-2Q_{-2,\,k-1}, & m=2\\ -mQ_{-m,k-1}+(m-1)Q_{-(m-2),k-1}\\ \quad+Q_{m-2,\,k-1}, & m\geq 3\end{cases} \tag{9a-c}$$

[10]Department of Aircraft Engineering, Northwestern Polytechnical University, Xian, 710072, People's Republic of China.

Contributed by the Applied Mechanics Division of The American Society of Mechanical Engineers. Manuscript received July 13, 1988; final revision, July 1, 1989.

Copyright © 1990 by ASME
Downloaded 03 May 2010 to 171.66.16.244. Redistribution subject to ASME license or copyright; see http://www.asme.org/terms/Terms_Use.cfm

Table 1 Values of stress intensity factors ($\alpha = a/(h-r)$, $F = K_{II}/\sigma_{II}\sqrt{\pi a}$, $\beta = r/h$)

Values of F for $K_{II}(t_0)$

β \ α	0.010	0.100	0.200	0.300	0.400	0.500	0.600	0.700	0.800	0.900
0.10	1.0251	1.0275	1.0314	1.0369	1.0450	1.0576	1.0780	1.1148	1.1910	1.3935
0.20	1.0984	1.1066	1.1190	1.1360	1.1598	1.1937	1.2441	1.3233	1.4592	1.7356
0.30	1.2143	1.2291	1.2507	1.2791	1.3168	1.3675	1.4377	1.5389	1.6962	1.9946
0.40	1.3636	1.3837	1.4120	1.4479	1.4937	1.5528	1.6308	1.7384	1.9014	2.2217
0.50	1.5335	1.5559	1.5866	1.6247	1.6721	1.7320	1.8099	1.9171	2.0842	2.4318
0.55	1.6212	1.6433	1.6735	1.7108	1.7570	1.8155	1.8919	1.9988	2.1702	2.5140
0.60	1.7077	1.7286	1.7572	1.7926	1.8368	1.8931	1.9680	2.0756	2.2531	2.5546
0.65	1.7903	1.8091	1.8352	1.8680	1.9097	1.9640	2.0380	2.1480	2.3263	2.5193
0.70	1.8664	1.8824	1.9054	1.9351	1.9744	2.0273	2.1021	2.2133	2.3682	2.3624
0.75	1.9328	1.9456	1.9652	1.9924	2.0298	2.0822	2.1563	2.2540	2.3259	2.0252
0.80	1.9863	1.9958	2.0123	2.0371	2.0723	2.1194	2.1743	2.2066	2.0952	1.4396

Values of F for $K_{II}(t_1)$

β \ α	0.010	0.100	0.200	0.300	0.400	0.500	0.600	0.700	0.800	0.900
0.10	1.0246	1.0230	1.0219	1.0213	1.0213	1.0220	1.0236	1.0266	1.0323	1.0447
0.20	1.0969	1.0912	1.0869	1.0845	1.0839	1.0853	1.0892	1.0964	1.1093	1.1336
0.30	1.2115	1.2008	1.1923	1.1870	1.1849	1.1860	1.1910	1.2009	1.2181	1.2488
0.40	1.3597	1.3446	1.3322	1.3240	1.3197	1.3197	1.3244	1.3350	1.3538	1.3875
0.50	1.5291	1.5119	1.4973	1.4872	1.4814	1.4803	1.4843	1.4946	1.5138	1.5482
0.55	1.6268	1.5998	1.5852	1.5750	1.5692	1.5680	1.5720	1.5824	1.6018	1.6344
0.60	1.7036	1.6875	1.6738	1.6644	1.6593	1.6586	1.6631	1.6741	1.6943	1.7211
0.65	1.7867	1.7725	1.7607	1.7530	1.7495	1.7502	1.7561	1.7685	1.7891	1.8031
0.70	1.8633	1.8519	1.8430	1.8380	1.8371	1.8404	1.8488	1.8631	1.8814	1.8716
0.75	1.9305	1.9225	1.9174	1.9163	1.9191	1.9261	1.9375	1.9519	1.9594	1.9108
0.80	1.9849	1.9806	1.9801	1.9835	1.9906	2.0006	2.0115	2.0162	1.9944	1.8897

$$Q_{m,0} = \begin{cases} -(m+1)q_{-m,0} + mq_{-(m+2),0}, & m \le -3 \\ q_{2,0} - 2q_{0,0} - 2\sqrt{h^2 - a^2}/r, & m = -2 \\ 0, & m = -1,\ 0 \\ -q_{m,0}, & m \ge 1 \end{cases} \quad (10a\text{–}d)$$

$$Q_{m,k} = \begin{cases} (m+1)q_{-m,k} - mq_{-(m+2),k}, & k \ge 1,\ m \le -3 \\ -q_{2,k} + 2q_{0,k}, & k \ge 1,\ m = -2 \\ 0, & k \ge 1,\ m = -1,\ 0 \\ -q_{m,k}, & k \ge 1,\ m \ge 1 \end{cases} \quad (11a\text{–}d)$$

$$q_{m,0} = \begin{cases} h/r - \sqrt{h^2 - a^2}/r, & m = 0 \\ hC_m/r - C_{m-1}, & m \ge 1 \end{cases} \quad (12a,\ b)$$

$$q_{m,k} = \frac{1}{2}\left[\sum_{n=0}^{m} b_{n,k}C_{m-n} + \gamma_k C_m\right],\ k \ge 1,\ m = 0,\ 1,\ 2,\ \ldots \quad (13)$$

All these expressions are exact formulas.

Numerical Results

Numerical values of the stress intensity factors are given in Table 1, Fig. 2, and Fig. 3. For small r/h and $a/(h-r)$, that is, for relatively short cracks located a long way from the hole, the stress intensity factors at both the crack tips are nearly $\sigma_{II}\sqrt{\pi a}$, the canonical value of the shearing stress intensity factor for a single crack contained in an infinite plate. On the other hand, for large r/h and $a/(h-r)$, that is, for short cracks near the hole, a sharp decrease in stress intensity factors is observed in Fig. 3. This remarkable trend is in contrast to the case of stretching stress intensity factors, which increase monotonically as the crack tips approach the hole. The explanation is that, since the circumference of the hole is a free boundary, the shearing stress on the x-axis and in the neighborhood of the hole is small and has little effect on the shearing deformation at the crack tips.

References

Chang Shangchow, 1983, "An Equivalent Procedure for the Evaluation of the Stress Intensity Factors of a Radial Crack in a Disc," *International Journal of Engineering Science*, Vol. 21, pp. 1247–1252.

Tada, H., Paris, C. P., and Irwin, G. R., 1973, *The Stress Analysis of Cracks Handbook*, Del Research Corp.

On Kinematical Assumptions of Refined Theories of Plates: A Survey

G. Jemielita[11]

The paper presents a survey of the kinematical hypotheses and the governing equations of the refined theories of plates. By carrying out a comparative analysis of various, apparently different, kinematical hypotheses proposed by various authors, it is shown that the kinematical hypothesis by Vlasov (1957) is a pattern for all of them.

1 Introduction

A large class of improved theories of plates is based upon kinematic hypotheses. The simplest leading to a sixth-order plate theory is that of Hencky-Bollé (1947), according to which the straight material fibers orthogonal to the plate midsurface in the reference configuration are assumed not to change their length and to remain straight in the deformed configuration. Simplicity is the virtue of this hypothesis, one of vices being the necessity of introducing a shear correction factor into the equations of the theory. In the past, theoretical investigations have aimed at relaxing the Hencky-Bollé assumptions. The in-plane displacements, $u_\alpha(x^\beta, z)$, $\alpha = 1, 2$, are usually assumed in a form that assures the transverse shear stresses $\sigma_{\alpha 3}(x^\beta, z)$, to be second-order polynomials with respect to the variable z—the distance from a given point of the plate to its middle plane.[12]

The first kinematical hypothesis of this type was explicitly put forward by B. F. Vlasov in 1957. Since then many theories of plates based on several (sometimes sophisticated) variants of the Vlasov hypothesis have been developed. Until now, many authors have not known who to credit for devising and applying the theory based on the aforementioned kinematical hypothesis.

On pp. 249–250, Vol. 55, of the ASME JOURNAL OF APPLIED MECHANICS several notes appear discussing Z. Rychter's paper (1987) in which theories of plates, which are based on certain kinematical assumptions, are referred to as theories of Levinson type. R. Schmidt (1988) writes "The theory of plates to which the author refers to as 'Levinson's theory' and cites Levinson (1980) as his reference is nothing else but a linearized version of the nonlinear theory published by Schmidt (1977) . . . In the name of fairness, this oversight should be acknowledged and corrected." Thus, R. Schmidt claims that not Levinson but he is a discoverer of the kinematical assumptions used in the papers of Rychter (1987), Schmidt (1977), and Levinson (1980).

In the review article by E. Reissner (1985), among other aspects of plate modeling, some problems of the sixth-order plate theories have been dealt with. Unfortunately, in this outstanding article some important works written in Polish and Russian languages have not been referred to.

To set the record straight, I wish to point out that the kinematical hypothesis used by the aforementioned authors, as well as by other contributors, was a starting point in the Vlasov's theory dated from 1957. Below, given in a chronological

[11]Warsaw University of Technology, Faculty of Civil Engineering, Institute of Structural Mechanics, Warsaw, Poland 00-637.

[12]It is the Kirchhoff's plate theory that provides an inspiration for such assumptions. In this theory the equilibrium equations imply a parabolic distribution of stresses $\sigma_{\alpha 3}$ across the plate thickness.

Manuscript received by the ASME Applied Mechanics Division, Feb. 3, 1989; final revision, Aug. 18, 1989.

Downloaded 03 May 2010 to 171.66.16.244. Redistribution subject to ASME license or copyright; see http://www.asme.org/terms/Terms_Use.cfm

Table 1 Values of stress intensity factors ($\alpha = a/(h-r)$, $F = K_{II}/\sigma_{II}\sqrt{\pi a}$, $\beta = r/h$)

Values of F for $K_{II}(t_0)$

β \ α	0.010	0.100	0.200	0.300	0.400	0.500	0.600	0.700	0.800	0.900
0.10	1.0251	1.0275	1.0314	1.0369	1.0450	1.0576	1.0780	1.1148	1.1910	1.3935
0.20	1.0984	1.1066	1.1190	1.1360	1.1598	1.1937	1.2441	1.3233	1.4592	1.7356
0.30	1.2143	1.2291	1.2507	1.2791	1.3168	1.3675	1.4377	1.5389	1.6962	1.9946
0.40	1.3636	1.3837	1.4120	1.4479	1.4937	1.5528	1.6308	1.7384	1.9014	2.2217
0.50	1.5335	1.5559	1.5866	1.6247	1.6721	1.7320	1.8099	1.9171	2.0842	2.4318
0.55	1.6212	1.6433	1.6735	1.7108	1.7570	1.8155	1.8919	1.9988	2.1702	2.5140
0.60	1.7077	1.7286	1.7572	1.7926	1.8368	1.8931	1.9680	2.0756	2.2531	2.5946
0.65	1.7903	1.8091	1.8352	1.8680	1.9097	1.9640	2.0380	2.1480	2.3263	2.6793
0.70	1.8664	1.8824	1.9054	1.9351	1.9744	2.0273	2.1021	2.2133	2.3982	2.7624
0.75	1.9328	1.9456	1.9652	1.9924	2.0298	2.0822	2.1563	2.2540	2.3259	2.0252
0.80	1.9863	1.9958	2.0123	2.0371	2.0723	2.1194	2.1743	2.2066	2.0952	1.4396

Values of F for $K_{II}(t_1)$

0.10	1.0246	1.0230	1.0219	1.0213	1.0213	1.0220	1.0236	1.0266	1.0323	1.0447
0.20	1.0969	1.0912	1.0869	1.0845	1.0839	1.0853	1.0892	1.0964	1.1093	1.1336
0.30	1.2115	1.2008	1.1923	1.1870	1.1849	1.1860	1.1910	1.2009	1.2181	1.2488
0.40	1.3597	1.3446	1.3322	1.3240	1.3197	1.3197	1.3244	1.3350	1.3538	1.3875
0.50	1.5291	1.5119	1.4973	1.4872	1.4814	1.4803	1.4843	1.4946	1.5138	1.5482
0.55	1.6268	1.5998	1.5852	1.5750	1.5692	1.5680	1.5720	1.5824	1.6018	1.6344
0.60	1.7036	1.6875	1.6738	1.6644	1.6593	1.6586	1.6631	1.6741	1.6943	1.7211
0.65	1.7867	1.7725	1.7607	1.7530	1.7495	1.7502	1.7561	1.7685	1.7891	1.8031
0.70	1.8633	1.8519	1.8430	1.8380	1.8371	1.8404	1.8488	1.8631	1.8814	1.8716
0.75	1.9305	1.9225	1.9174	1.9163	1.9191	1.9261	1.9375	1.9519	1.9594	1.9108
0.80	1.9849	1.9806	1.9801	1.9835	1.9906	2.0006	2.0115	2.0162	1.9944	1.8897

$$Q_{m,0} = \begin{cases} -(m+1)q_{-m,0} + mq_{-(m+2),0}, & m \le -3 \\ q_{2,0} - 2q_{0,0} - 2\sqrt{h^2 - a^2}/r, & m = -2 \\ 0, & m = -1,\ 0 \\ -q_{m,0}, & m \ge 1 \end{cases} \tag{10a-d}$$

$$Q_{m,k} = \begin{cases} (m+1)q_{-m,k} - mq_{-(m+2),k}, & k \ge 1,\ m \le -3 \\ -q_{2,k} + 2q_{0,k}, & k \ge 1,\ m = -2 \\ 0, & k \ge 1,\ m = -1,\ 0 \\ -q_{m,k}, & k \ge 1,\ m \ge 1 \end{cases} \tag{11a-d}$$

$$q_{m,0} = \begin{cases} h/r - \sqrt{h^2 - a^2}/r, & m = 0 \\ hC_m/r - C_{m-1}, & m \ge 1 \end{cases} \tag{12a, b}$$

$$q_{m,k} = \frac{1}{2}\left[\sum_{n=0}^{m} b_{n,k}C_{m-n} + \gamma_k C_m\right], \quad k \ge 1,\ m = 0,\ 1,\ 2,\ \ldots \tag{13}$$

All these expressions are exact formulas.

Numerical Results

Numerical values of the stress intensity factors are given in Table 1, Fig. 2, and Fig. 3. For small r/h and $a/(h-r)$, that is, for relatively short cracks located a long way from the hole, the stress intensity factors at both the crack tips are nearly $\sigma_{II}\sqrt{\pi a}$, the canonical value of the shearing stress intensity factor for a single crack contained in an infinite plate. On the other hand, for large r/h and $a/(h-r)$, that is, for short cracks near the hole, a sharp decrease in stress intensity factors is observed in Fig. 3. This remarkable trend is in contrast to the case of stretching stress intensity factors, which increase monotonically as the crack tips approach the hole. The explanation is that, since the circumference of the hole is a free boundary, the shearing stress on the x-axis and in the neighborhood of the hole is small and has little effect on the shearing deformation at the crack tips.

References

Chang Shangchow, 1983, "An Equivalent Procedure for the Evaluation of the Stress Intensity Factors of a Radial Crack in a Disc," *International Journal of Engineering Science*, Vol. 21, pp. 1247-1252.

Tada, H., Paris, C. P., and Irwin, G. R., 1973, *The Stress Analysis of Cracks Handbook*, Del Research Corp.

On Kinematical Assumptions of Refined Theories of Plates: A Survey

G. Jemielita[11]

The paper presents a survey of the kinematical hypotheses and the governing equations of the refined theories of plates. By carrying out a comparative analysis of various, apparently different, kinematical hypotheses proposed by various authors, it is shown that the kinematical hypothesis by Vlasov (1957) is a pattern for all of them.

1 Introduction

A large class of improved theories of plates is based upon kinematic hypotheses. The simplest leading to a sixth-order plate theory is that of Hencky-Bollé (1947), according to which the straight material fibers orthogonal to the plate midsurface in the reference configuration are assumed not to change their length and to remain straight in the deformed configuration. Simplicity is the virtue of this hypothesis, one of vices being the necessity of introducing a shear correction factor into the equations of the theory. In the past, theoretical investigations have aimed at relaxing the Hencky-Bollé assumptions. The in-plane displacements, $u_\alpha(x^\beta, z)$, $\alpha = 1, 2$, are usually assumed in a form that assures the transverse shear stresses $\sigma_{\alpha 3}(x^\beta, z)$, to be second-order polynomials with respect to the variable z—the distance from a given point of the plate to its middle plane.[12]

The first kinematical hypothesis of this type was explicitly put forward by B. F. Vlasov in 1957. Since then many theories of plates based on several (sometimes sophisticated) variants of the Vlasov hypothesis have been developed. Until now, many authors have not known who to credit for devising and applying the theory based on the aforementioned kinematical hypothesis.

On pp. 249-250, Vol. 55, of the ASME JOURNAL OF APPLIED MECHANICS several notes appear discussing Z. Rychter's paper (1987) in which theories of plates, which are based on certain kinematical assumptions, are referred to as theories of Levinson type. R. Schmidt (1988) writes "The theory of plates to which the author refers to as 'Levinson's theory' and cites Levinson (1980) as his reference is nothing else but a linearized version of the nonlinear theory published by Schmidt (1977) . . . In the name of fairness, this oversight should be acknowledged and corrected." Thus, R. Schmidt claims that not Levinson but he is a discoverer of the kinematical assumptions used in the papers of Rychter (1987), Schmidt (1977), and Levinson (1980).

In the review article by E. Reissner (1985), among other aspects of plate modeling, some problems of the sixth-order plate theories have been dealt with. Unfortunately, in this outstanding article some important works written in Polish and Russian languages have not been referred to.

To set the record straight, I wish to point out that the kinematical hypothesis used by the aforementioned authors, as well as by other contributors, was a starting point in the Vlasov's theory dated from 1957. Below, given in a chronological

[11]Warsaw University of Technology, Faculty of Civil Engineering, Institute of Structural Mechanics, Warsaw, Poland 00-637.

[12]It is the Kirchhoff's plate theory that provides an inspiration for such assumptions. In this theory the equilibrium equations imply a parabolic distribution of stresses $\sigma_{\alpha 3}$ across the plate thickness.

Manuscript received by the ASME Applied Mechanics Division, Feb. 3, 1989; final revision, Aug. 18, 1989.

Copyright © 1990 by ASME
Downloaded 03 May 2010 to 171.66.16.244. Redistribution subject to ASME license or copyright; see http://www.asme.org/terms/Terms_Use.cfm

order, are the basic assumptions and equations of theories based on Vlasov's or Vlasov-like kinematic assumptions. To show clearly the interrelations between various apparently different hypotheses of kinematical type, a unified description of them is assumed. Different notations for the various two-variable functions of x^α are introduced.

2 B. F. Vlasov's Theory

In 1957, B. F. Vlasov proposed a theory based on the following kinematical assumptions:

$$u_\alpha(x^\beta,z) = -zt_\alpha(x^\beta) - \frac{4z^3}{3h^2}(w_{,\alpha} - t_\alpha),$$

$$u_3(x^\alpha,z) = w(x^\alpha), \tag{1}$$

where h denotes the plate thickness, $z = x^3$, $\alpha, \beta = 1, 2$.

The constitutive equations are simplified by the assumption

$$\sigma_{33} = 0. \tag{2}$$

By the direct method, Vlasov (1957) obtained the following sixth-order set of three differential equations involving three field functions of two variables $w(x^\alpha)$ and $t_\alpha(x^\beta)$:

$$D\nabla^4 w = (1 - K_1 h^2 \nabla^2) p_3,$$

$$\left(\nabla^2 - \frac{12K}{h^2}\right)\Phi = 0 \tag{3}$$

where $D = \dfrac{\mu h^3}{6(1-\nu)}$ is the bending stiffness of the plate, ν is Poisson's ratio, μ is the shear modulus, $\Phi = t_{1,2} - t_{2,1}$ is the rotational part of the displacement, p_3 is the component of the vector load perpendicular to the midsurface and K_1, K are coefficients—the latter being the so-called shear factor. In Vlasov's theory, $K_1 = \dfrac{1}{5(1-\nu)}$, $K = \dfrac{5}{6}$.

The majority of linear sixth-order plate theories are described (in the static case) by equation (3). They differ in the values of the K_1 and K and in the physical interpretation of the functions $w(x^\alpha)$ and $t_\alpha(x^\beta)$.

In the same year, P. Narasimhamurthy made the more general kinematical constraint assumptions

$$u_\alpha = -zv_{,\alpha} + \left(1 - \frac{4z^2}{3h^2}\right)\varphi_\alpha - \frac{h^2(1-\nu)}{8\mu(1-2\nu)}\left(1 - \frac{4z^2}{h^2}\right)p_{3,\alpha}$$

$$u_3 = v - \frac{\nu h^2}{8(1-\nu)}\left(1 - \frac{4z^2}{h^2}\right)\nabla^2 v + \frac{1}{6}\left(5 - 24\frac{z^2}{h^2} + 16\frac{z^4}{h^4}\right)\varphi^\alpha{}_{,\alpha}$$

$$- \frac{hp_3(1-\nu)}{8(1-2\nu)\mu}\left(1 + 8\frac{z}{h} - 16\frac{z^4}{h^4}\right). \tag{4}$$

The author then derived a set of reduced equations assuming the vertical load, $p_3 = 0$. Unfortunately, the function multiplying p_3 in equation $(4)_2$ is mistakenly chosen so that the distribution of the stress σ_{33} that follow from equation (4) is incorrect. If $p_3 = 0$, the function $v(x^\alpha) = u_3\left(x^\alpha, \pm\dfrac{h}{2}\right)$ stands for the deflection of plate faces.

3 S. A. Ambartsumyan's Theory

In 1958, Ambartsumyan put forward a theory of anisotropic plates based upon the stress-displacement hypothesis

$$\sigma_{\alpha 3} = -\frac{h^2}{8}\left(1 - 4\frac{z^2}{h^2}\right)\varphi_\alpha(x^\beta)$$

$$u_3 = w(x^\alpha). \tag{5}$$

These assumptions, upon imposing equation (2) in the isotropic case, lead to the displacement distribution

$$u_\alpha = -zw_{,\alpha} - \frac{h^2}{8}z\left(1 - \frac{4}{3}\frac{z^2}{h^2}\right)\frac{\varphi_\alpha}{\mu}$$

$$u_3 = w(x^\alpha). \tag{6}$$

On setting

$$t_\alpha = w_{,\alpha} + \frac{h^2}{8}\frac{\varphi_\alpha}{\mu} \tag{7}$$

in the Vlasov assumptions, one obtains the assumptions (6) while the set of equations (3) remains valid with the same coefficients K_1 and K. In his book Ambartsumyan (1967) gave up the assumption (2). He assumed the same distribution of σ_{33} as in Reissner's theory. Thus, he arrived at the set of equations (3) with coefficients $K_1 = \dfrac{2-\nu}{10(1-\nu)}$, $K = 5/6$—the same as in Reissner's (1947) theory.

4 Z. Kaczkowski's Theory

In 1968, in a noteworthy monograph on the statics of plates, Kaczkowski (1968) assumed the following distribution of displacements

$$u_\alpha(x^\beta,z) = u^o_\alpha(x^\beta) - zw_{,\alpha}$$

$$+ z\left(1 - \frac{4}{3}\frac{z^2}{h^2}\right)\vartheta_\alpha + \frac{h\overset{+}{p}_\alpha}{24}\left(24\frac{z^3}{h^3} + 12\frac{z^2}{h^2} - 6\frac{z}{h} - 1\right)$$

$$+ \frac{h\overline{p}_\alpha}{24}\left(24\frac{z^3}{h^3} - 12\frac{z^2}{h^2} - 6\frac{z}{h} + 1\right)$$

$$u_3(x^\alpha,z) = w(x^\alpha), \tag{8}$$

where $\overset{+}{p}_\alpha$, $\overline{p}_\alpha$ denote the tangential loads on the lower and upper surfaces of the plate.

The constitutive equations are simplified according to equation (2). It is readily seen that the assumptions (8) are generalizations of Vlasov's hypotheses, and the interrelation between the fields t_α, ϑ_α is

$$t_\alpha = w_{,\alpha} - \vartheta_\alpha. \tag{9}$$

5 E. Reissner's and V. Panc's Consideration

In 1975, Reissner proposed to determine u_α with $u_3 = w(x^\alpha)$, on the basis of the constitutive relations for transverse shear, with parabolic distributions for $\sigma_{\alpha 3}$ (equation $(5)_1$) in the form

$$u_\alpha = -zw_{,\alpha} + \frac{3z}{2\mu h}\left(1 - \frac{4}{3}\frac{z^2}{h^2}\right)Q_\alpha$$

$$u_3 = w(x^\alpha). \tag{10}$$

In the same year Panc (1975) assumed the distribution equation (10). As a result, he arrived at equations (3). One can easily verify that assuming

$$t_\alpha = w_{,\alpha} - \frac{3}{2}\frac{Q_\alpha}{\mu h}. \tag{11}$$

In equation (1) one obtains the distribution equation (10).

6 G. Jemielita's Theory

In 1975, Jemielita generalized the hypothesis by Kaczkowski by imposing, for the bending state, the following distribution of displacements[13]

[13] In Jemielita's work (1975), only the loads antisymmetric with respect to the midplane have been considered. For such loads, $u_3\left(x^\alpha, \dfrac{h}{2}\right) = u_3\left(x^\alpha, -\dfrac{h}{2}\right)$.

Downloaded 03 May 2010 to 171.66.16.244. Redistribution subject to ASME license or copyright; see http://www.asme.org/terms/Terms_Use.cfm

$$u_\alpha = -t'(z)v_{,\alpha} + s'(z)\Theta_\alpha + \frac{f'(z)}{\mu}p_\alpha$$

$$u_3 = v(x^\alpha) - \Gamma(x^\alpha, z), \tag{12}$$

where

$$\Gamma(x^\alpha,z) = \frac{\nu}{1-\nu}\left[s(z)\Theta^\alpha{}_{,\alpha} - t(z)\nabla^2 v + \frac{f(z)}{\mu}p^\alpha{}_{,\alpha}\right] - \frac{1-2\nu}{2\mu(1-\nu)}\left[g_1(z)p_3 + g_2(z)\int_{-h/2}^{h/2} X_3 dx\right], \tag{13}$$

$( )' = \dfrac{d( )}{dz}$ and X_3 are normal components of the body force.

The functions $t(z), s(z), f(z), g_1(z), g_2(z)$ satisfy the following conditions at $z = \pm h/2$

$$t\left(\pm\frac{h}{2}\right) = s\left(\pm\frac{h}{2}\right) = s''\left(\pm\frac{h}{2}\right) = f\left(\pm\frac{h}{2}\right) = g_1\left(\pm\frac{h}{2}\right) = g_2\left(\pm\frac{h}{2}\right) = g_2'\left(\pm\frac{h}{2}\right) = 0$$

$$f''\left(\pm\frac{h}{2}\right) = t''\left(\pm\frac{h}{2}\right) = 1,\ g_1'\left(\pm\frac{h}{2}\right) = \pm\frac{1}{2}. \tag{14}$$

Thus, the stress boundary conditions on the surfaces $z = \pm h/2$ are identically fulfilled. On using the direct method, one obtains the set of three differential equations of motion.[14]

The governing equations for the functions $v(x^\alpha)$ and $\Phi(x^\alpha)$ are, for $X_i = 0$, $i = 1, 2, 3$, $p_\alpha = 0$ and $p_3 \neq 0$,

$$D\nabla^4 v = \left[1 - \frac{h^2 k_2}{(1-\nu)k_1}\left(2 + \nu\frac{\hat{k}_4}{k_4} - 2\nu\frac{k_1 k_3}{k_2}\right)\times\nabla^2 - 2\frac{h^4 k_2 \hat{k}_3}{k_1}\nabla^4\right]p_3,$$

$$\left(\nabla^2 - \frac{k_1}{h^2 k_2}\right)\Phi = 0, \tag{15}$$

where

$$\Phi = \Theta_{1,2} - \Theta_{2,1},$$

$$k_1 = \frac{1}{h}\int_0^{h/2} s''(z)dz,\ k_2 = \frac{1}{h^3}\int_0^{h/2} zs'(z)dz,$$

$$k_3 = \frac{1}{h^2}\int_0^{h/2} zg_1'(z)dz,\ k_4 = \frac{1}{h^3}\int_0^{h/2} zt'(z)dz,$$

$$\hat{k}_3 = \frac{1}{h^2}\int_0^{h/2} g_1(z)dz,\ \hat{k}_4 = \frac{1}{h^3}\int_0^{h/2} t(z)dz. \tag{16}$$

One can check that the following identities hold:

$$\hat{k}_3 = -k_3,\ \hat{k}_4 = -k_4. \tag{17}$$

Due to the introduction of the coefficients $\hat{k}_3$, $\hat{k}_4$, one can consider some particular cases of the kinematical assumptions (12) in which $k_3, k_4 \neq 0$ and $\hat{k}_3, \hat{k}_4 = 0$. Thus, one obtains a family of theories of plates of the sixth order. By changing the functions of z or the values of the coefficients $k_i, \hat{k}_i$ $(i = 1, 2, 3, 4)$, one can arrive at the equations of the various theories of plates by E. Reissner (1947), E. Hencky (1947), L. Bollé (1947), B. F. Vlasov (1957), Ch. M. Muštari (1959), Z. Kaczkowski (1968), W. L. Berdichevski (1972) and others.

Criteria for choosing the functions of the z variable and values of the coefficients k_i and $\hat{k}_i$ are given in Jemielita's paper (1975). For the functions of z considered in Jemielita's paper, and for the following fields which describe the plate deflection,

$$\hat{w} \equiv u_3\left(x^\alpha, \pm\frac{h}{2}\right),\ \underset{*}{w} \equiv u_3(x^\alpha, 0),\ \overset{*}{w} \equiv \frac{1}{h}\int_{-h/2}^{h/2} u_3(x^\alpha, z)dz,$$

$$\underset{*}{w} \equiv \frac{3}{2h}\int_{-h/2}^{h/2}\left(1 - 4\frac{z^2}{h^2}\right)u_3(x^\alpha, z)dz. \tag{18}$$

The counterpart of equation $(15)_1$ is asymptotically exact in the case when the function $p_3(x^\alpha)$ is biharmonic. For instance, the functions $\hat{w}$ and $\underset{*}{w}$ satisfy

$$D\nabla^4\hat{w} = \left(1 - \frac{h^2}{5}\nabla^2 + \frac{28}{2800}h^4\nabla^4\right)p_3$$

$$D\nabla^4\underset{*}{w} = \left[1 - \frac{h^2(8-3\nu)}{40(1-\nu)}\nabla^2 - \frac{29-19\nu}{9600(1-\nu)}h^4\nabla^4 + \frac{\nu h^6}{19200(1-\nu)}\nabla^6\right]p_3. \tag{19}$$

For the loads p_3 which satisfy the equation $\nabla^6 p_3 = 0$, equation $(19)_1$ differs in the coefficient of $h^4\nabla^4$ from the exact value of 27/2800. Similarly, in equation $(19)_2$, the coefficient at $h^4\nabla^4$ is nearly exact.

7 R. Schmidt's Theory

In 1977 Schmidt proposed the nonlinear theory of plates by assuming the following hypothesis for displacements[5]

$$u_\alpha = u_\alpha^o - zw_{,\alpha} + \frac{3}{2}z\left(1 - \frac{4}{3}\frac{z^2}{h^2}\right)\gamma_\alpha,$$

$$u_3 = w(x^\alpha), \tag{20}$$

where $\gamma_\alpha = Q_\alpha/\mu h$.

It is readily seen that in bending, this distribution of displacements is exactly the same as in the approach of Reissner (1975) and Panc (1975). This distribution can be obtained from Vlasov's hypothesis by assuming

$$t_\alpha = w_{,\alpha} - \frac{3}{2}\gamma_\alpha, \tag{21}$$

from Ambartsumyan's assumption (in the isotropic case) by setting

$$\varphi_\alpha = -12\mu\gamma_\alpha, \tag{22}$$

and from Kaczkowski's assumptions by setting

$$\overset{+}{p}_\alpha = \overline{p}_\alpha = 0,\ \vartheta_\alpha = \frac{3}{2}\gamma_\alpha. \tag{23}$$

8 M. Levinson's Consideration

In 1980 Levinson put forward the following kinematical hypothesis

$$u_\alpha = z\psi_\alpha - \frac{4}{3}\frac{z^3}{h^2}(\psi_\alpha + w_{,\alpha}),\ u_3 = w(x^\alpha), \tag{24}$$

which can be obtained directly from Vlasov's assumptions by assuming

[14]The variational approach based on hypothesis (12) has been put forward by T. Lewiński (1987).

[15]On using the hypothesis (5), Ambartsumyan (1967) derived the nonlinear equations of the anisotropic plates (cf., pp. 67–81). In the isotropic case the assumptions (5) result in equation (6). However, in this case the nonlinear equations by Ambartsumyan differ from those of Schmidt, since both authors assumed different simplifications of the strain-displacement relationships.

Downloaded 03 May 2010 to 171.66.16.244. Redistribution subject to ASME license or copyright; see http://www.asme.org/terms/Terms_Use.cfm

$$t_\alpha = -\psi_\alpha. \tag{25}$$

Similarly, one can prove that the hypothesis (24) can be arrived at from all hypotheses discussed previously. Nevertheless, the author of the paper (1980) named his approach a "new theory" (cf., pp. 344, 349).

9 M. V. V. Murthy's Theory

In 1981 Murthy proposed the following kinematical constraints:

$$u_\alpha = u_\alpha^o + \frac{z}{4}\left(1 - \frac{20}{3}\frac{z^2}{h^2}\right) w_{,\alpha} + \frac{5}{4} z \left(1 - \frac{4}{3}\frac{z^2}{h^2}\right) \beta_\alpha,$$

$$u_3 = w(x^\alpha). \tag{26}$$

This hypothesis can be obtained from the hypotheses mentioned previously, e.g., from the hypotheses by Kaczkowski, by assuming

$$\overset{+}{p}_\alpha = \overline{p}_\alpha = 0,\ \vartheta_\alpha = \frac{5}{4}(w_{,\alpha} + \beta_\alpha).$$

Moreover, one can show that many plate models developed after 1981 are based on the hypotheses previously mentioned.

References

Ambartsumyan, S. A., 1958, "On a Theory of Bending of Anisotropic Plates" (in Russian), *Izv. A. N. SSSR, OTN*, No. 5, pp. 69–77.

Ambartsumyan, S. A., 1967, "Theory of Anisotropic Plates" (in Russian), *Izd., Nauka, Moskva*; "Theory of Anisotropic Plates," J. E. Ashton, and T. Cheron, eds., Technomic, Stanford, 1969.

Berdichevskii, V. L., 1972, "On the Equations Describing Transversally Vibrations of Thin Elastic Plates" (in Russian), *Izv. A.N.SSSR, MTT*, No. 6, pp. 152–155.

Bollé, L., 1947, "Contribution au Probléme Linéaire de Flexion d'une Plaque Élastique," *Bull. Tech. Suisse Romande*, Vol. 73, No. 21, pp. 281–285; No. 22, pp. 293–298.

Hencky, H., 1947, "Über die Berücksichtigung der Schubverzerrung in ebenen Platten," *Ing. Archiv.*, Vol. 16, pp. 72–76.

Hutchinson, J. R., 1987, "A Comparison of Mindlin and Levinson Plate Theories," *Mech. Res. Comm.*, Vol. 14, No. 3, pp. 165–170.

Jemielita, G., 1975, "Technical Theory of Plates with Moderate Thickness" (in Polish), *Rozprawy Inż.*, Vol. 23, No. 3, pp. 483–499.

Kaczkowski, Z., 1968, *Plates: Statical Calculations* (in Polish), Arkady, Warszawa.

Levinson, M., 1980, "An Accurate, Simple Theory of Statics and Dynamics of Elastic Plates," *Mech. Res. Comm.*, Vol. 7, No. 6, pp. 342–350.

Lewiński, T., 1987, "On Refined Plate Models Based on Kinematical Assumptions," *Ing. Archiv.*, Vol. 57, pp. 133–146.

Murthy, M. V. V., 1981, "An Improved Transverse Shear Deformation Theory for Laminated Anisotropic Plates," NASA Technical Paper No. 1903.

Muštari, Ch. M., 1959, "Theory of Bending of Plates of Moderate Thickness" (in Russian), *Izv. A. N. SSSR, OTN*, No. 2, pp. 107–113.

Narasimhamurthy, P., 1957, "The Effect of Transverse Shear Deformation and Rotatory Inertia in Wave Propagation and Vibration of Thin Elastic Plates," *Proc. 3rd Congr. Theor. Appl. Mech.*, Bangalore, India, pp. 351–360.

Panc, V., 1975, *Theories of Elastic Plates*, Academia, Prague, p. 51.

Reissner, E., 1947, "On Bending of Elastic Plates," *Q. Appl. Math.*, Vol. 5, pp. 55–68.

Reissner, E., 1975, "On Transverse Bending of Plates, Including the Effect of Transverse Shear Deformation," *Int. J. Solids Struct.*, Vol. 11, No. 5, pp. 569–573.

Reissner, E., 1985, "Reflections on the Theory of Elastic Plates," *Appl. Mech. Rev.*, Vol. 38, ASME, New York, pp. 1453–1464.

Rychter, Z., 1987, "A Sixth-Order Plate Theory-Derivation and Error Estimates," ASME JOURNAL OF APPLIED MECHANICS, Vol. 54, pp. 275–279.

Schmidt, R., 1977, "A Refined Nonlinear Theory of Plates with Transverse Shear Deformation," *Industrial Mathematics*, Vol. 27, No. 1, pp. 23–38.

Schmidt, R., 1988, discussion, ASME JOURNAL OF APPLIED MECHANICS, Vol. 55, p. 250.

Vlasov, B. F., 1957, "On the Equations of Bending of Plates" (in Russian), *Doklady AN Azerbaidzhanskoi SSR*, Vol. 13, No. 9, pp. 955–959.

Vlasov, B. F., 1957, "On the Equations of Theory of Bending of Plates" (in Russian), *Izv. AN SSSR, OMN*, No. 12, pp. 57–60.

On the Propagation Pressure of Buckles in Cylindrical Confined Shells

F. S. Li[16] and S. Kyriakides[16,17]

Introduction

In a number of engineering applications, long cylindrical structures are lined with a thin inner shell. The liner is used to seal the outer structures, or to protect it from caustic contents. Under some circumstances a pressure difference can develop between the outer structure and the inner shell. In the presence of imperfections this can lead to collapse of the liner. Collapse is typically local in nature and will occur in the region of the structure with the largest initial imperfections. If enough fluid is available, this initially local collapse propagates and in the process destroys large sections of the liner shell. The lowest pressure which will sustain the propagation of the collapse, known as confined propagation pressure (P_{pc}), is usually much smaller than the pressure required to cause the initial instability.

The special case of the problem where the outer structure is stiff enough so that it can be considered rigid was studied by Kyriakides (1986). It was demonstrated that for this case a propagating instability can occur for linearly elastic as well as elastic-plastic liner shell materials (for the latter see also Caladine, 1986). Figure 1, taken from this study, demonstrates how a thin mylar liner shell buckles and propagates inside a relatively thick, transparent acrylic tube. It was also shown that if the liner is elastic, the confined propagation pressure can be established from a simple energy balance known as Maxwell construction (see Chater and Hutchinson, 1984). This can be carried out by calculating the pressure volume response of a long, confined shell collapsing uniformly in a circular cavity (Kyriakides and Youn, 1984).

In this Note we consider the effect of the rigidity of the outer structure on the confined propagation pressure of the inner shell. This is done by making use of the recently developed solution (Li and Kyriakides, 1989) for the large deflection collapse of two concentric, elastic rings under external pressure.

The Problem

We consider a long, thin-walled cylindrical structure consisting of a circular outer shell of radius R and wall thickness t_0, and an inner shell of wall thickness t_I. The two shells are linearly elastic and have modulus and Poisson's ratio (E_0, ν_0) and (E_I, ν_I). The inner shell is in smooth contact with the outer one, but has a small initial geometric imperfection as shown in Fig. 2.

The composite structure is loaded by hydrostatic pressure (P) which is applied in two ways as shown in Fig. 2. For load type I, pressure is applied on the outer surface of the structure, as well as in the cavity formed by the initial imperfection. For load type II, pressure is only applied in the imperfection cavity.

The large deflection, nonlinear response of these structures was calculated numerically using a formulation and a numerical procedure developed by the authors (1991). The procedure addressed the inherent contact problem as well as instability issues governing the problem. The pressure deforms the two rings and causes the inner one to detouch from the outer one

[16]Engineering Mechanics Research Laboratory, Department of Aerospace Engineering and Engineering Mechanics, University of Texas at Austin, Austin, TX 78712.

[17]Assoc. Mem. ASME.

Manuscript received by the ASME Applied Mechanics Division, Oct. 17, 1989; final revision, Dec. 22, 1989.

Downloaded 03 May 2010 to 171.66.16.244. Redistribution subject to ASME license or copyright; see http://www.asme.org/terms/Terms_Use.cfm

$$t_\alpha = -\psi_\alpha. \tag{25}$$

Similarly, one can prove that the hypothesis (24) can be arrived at from all hypotheses discussed previously. Nevertheless, the author of the paper (1980) named his approach a "new theory" (cf., pp. 344, 349).

9 M. V. V. Murthy's Theory

In 1981 Murthy proposed the following kinematical constraints:

$$u_\alpha = u_\alpha^o + \frac{z}{4}\left(1 - \frac{20}{3}\frac{z^2}{h^2}\right) w_{,\alpha} + \frac{5}{4} z \left(1 - \frac{4}{3}\frac{z^2}{h^2}\right) \beta_\alpha,$$

$$u_3 = w(x^\alpha). \tag{26}$$

This hypothesis can be obtained from the hypotheses mentioned previously, e.g., from the hypotheses by Kaczkowski, by assuming

$$\overset{+}{p}_\alpha = \overline{p}_\alpha = 0, \ \vartheta_\alpha = \frac{5}{4}(w_{,\alpha} + \beta_\alpha).$$

Moreover, one can show that many plate models developed after 1981 are based on the hypotheses previously mentioned.

References

Ambartsumyan, S. A., 1958, "On a Theory of Bending of Anisotropic Plates" (in Russian), *Izv. A. N. SSSR, OTN*, No. 5, pp. 69–77.

Ambartsumyan, S. A., 1967, "Theory of Anisotropic Plates" (in Russian), *Izd., Nauka, Moskva*; "Theory of Anisotropic Plates," J. E. Ashton, and T. Cheron, eds., Technomic, Stanford, 1969.

Berdichevskii, V. L., 1972, "On the Equations Describing Transversally Vibrations of Thin Elastic Plates" (in Russian), *Izv. A.N.SSSR, MTT*, No. 6, pp. 152–155.

Bollé, L., 1947, "Contribution au Probléme Linéaire de Flexion d'une Plaque Élastique," *Bull. Tech. Suisse Romande*, Vol. 73, No. 21, pp. 281–285; No. 22, pp. 293–298.

Hencky, H., 1947, "Über die Berücksichtigung der Schubverzerrung in ebenen Platten," *Ing. Archiv.*, Vol. 16, pp. 72–76.

Hutchinson, J. R., 1987, "A Comparison of Mindlin and Levinson Plate Theories," *Mech. Res. Comm.*, Vol. 14, No. 3, pp. 165–170.

Jemielita, G., 1975, "Technical Theory of Plates with Moderate Thickness" (in Polish), *Rozprawy Inż.*, Vol. 23, No. 3, pp. 483–499.

Kaczkowski, Z., 1968, *Plates: Statical Calculations* (in Polish), Arkady, Warszawa.

Levinson, M., 1980, "An Accurate, Simple Theory of Statics and Dynamics of Elastic Plates," *Mech. Res. Comm.*, Vol. 7, No. 6, pp. 342–350.

Lewiński, T., 1987, "On Refined Plate Models Based on Kinematical Assumptions," *Ing. Archiv.*, Vol. 57, pp. 133–146.

Murthy, M. V. V., 1981, "An Improved Transverse Shear Deformation Theory for Laminated Anisotropic Plates," NASA Technical Paper No. 1903.

Muštari, Ch. M., 1959, "Theory of Bending of Plates of Moderate Thickness" (in Russian), *Izv. A. N. SSSR, OTN*, No. 2, pp. 107–113.

Narasimhamurthy, P., 1957, "The Effect of Transverse Shear Deformation and Rotatory Inertia in Wave Propagation and Vibration of Thin Elastic Plates," *Proc. 3rd Congr. Theor. Appl. Mech.*, Bangalore, India, pp. 351–360.

Panc, V., 1975, *Theories of Elastic Plates*, Academia, Prague, p. 51.

Reissner, E., 1947, "On Bending of Elastic Plates," *Q. Appl. Math.*, Vol. 5, pp. 55–68.

Reissner, E., 1975, "On Transverse Bending of Plates, Including the Effect of Transverse Shear Deformation," *Int. J. Solids Struct.*, Vol. 11, No. 5, pp. 569–573.

Reissner, E., 1985, "Reflections on the Theory of Elastic Plates," *Appl. Mech. Rev.*, Vol. 38, ASME, New York, pp. 1453–1464.

Rychter, Z., 1987, "A Sixth-Order Plate Theory-Derivation and Error Estimates," ASME JOURNAL OF APPLIED MECHANICS, Vol. 54, pp. 275–279.

Schmidt, R., 1977, "A Refined Nonlinear Theory of Plates with Transverse Shear Deformation," *Industrial Mathematics*, Vol. 27, No. 1, pp. 23–38.

Schmidt, R., 1988, discussion, ASME JOURNAL OF APPLIED MECHANICS, Vol. 55, p. 250.

Vlasov, B. F., 1957, "On the Equations of Bending of Plates" (in Russian), *Doklady AN Azerbaidzhanskoi SSR*, Vol. 13, No. 9, pp. 955–959.

Vlasov, B. F., 1957, "On the Equations of Theory of Bending of Plates" (in Russian), *Izv. AN SSSR, OMN*, No. 12, pp. 57–60.

On the Propagation Pressure of Buckles in Cylindrical Confined Shells

F. S. Li[16] and S. Kyriakides[16,17]

Introduction

In a number of engineering applications, long cylindrical structures are lined with a thin inner shell. The liner is used to seal the outer structures, or to protect it from caustic contents. Under some circumstances a pressure difference can develop between the outer structure and the inner shell. In the presence of imperfections this can lead to collapse of the liner. Collapse is typically local in nature and will occur in the region of the structure with the largest initial imperfections. If enough fluid is available, this initially local collapse propagates and in the process destroys large sections of the liner shell. The lowest pressure which will sustain the propagation of the collapse, known as confined propagation pressure (P_{pc}), is usually much smaller than the pressure required to cause the initial instability.

The special case of the problem where the outer structure is stiff enough so that it can be considered rigid was studied by Kyriakides (1986). It was demonstrated that for this case a propagating instability can occur for linearly elastic as well as elastic-plastic liner shell materials (for the latter see also Caladine, 1986). Figure 1, taken from this study, demonstrates how a thin mylar liner shell buckles and propagates inside a relatively thick, transparent acrylic tube. It was also shown that if the liner is elastic, the confined propagation pressure can be established from a simple energy balance known as Maxwell construction (see Chater and Hutchinson, 1984). This can be carried out by calculating the pressure volume response of a long, confined shell collapsing uniformly in a circular cavity (Kyriakides and Youn, 1984).

In this Note we consider the effect of the rigidity of the outer structure on the confined propagation pressure of the inner shell. This is done by making use of the recently developed solution (Li and Kyriakides, 1989) for the large deflection collapse of two concentric, elastic rings under external pressure.

The Problem

We consider a long, thin-walled cylindrical structure consisting of a circular outer shell of radius R and wall thickness t_0, and an inner shell of wall thickness t_I. The two shells are linearly elastic and have modulus and Poisson's ratio (E_0, ν_0) and (E_I, ν_I). The inner shell is in smooth contact with the outer one, but has a small initial geometric imperfection as shown in Fig. 2.

The composite structure is loaded by hydrostatic pressure (P) which is applied in two ways as shown in Fig. 2. For load type I, pressure is applied on the outer surface of the structure, as well as in the cavity formed by the initial imperfection. For load type II, pressure is only applied in the imperfection cavity.

The large deflection, nonlinear response of these structures was calculated numerically using a formulation and a numerical procedure developed by the authors (1991). The procedure addressed the inherent contact problem as well as instability issues governing the problem. The pressure deforms the two rings and causes the inner one to detouch from the outer one

[16]Engineering Mechanics Research Laboratory, Department of Aerospace Engineering and Engineering Mechanics, University of Texas at Austin, Austin, TX 78712.

[17]Assoc. Mem. ASME.

Manuscript received by the ASME Applied Mechanics Division, Oct. 17, 1989; final revision, Dec. 22, 1989.

Copyright © 1990 by ASME
Downloaded 03 May 2010 to 171.66.16.244. Redistribution subject to ASME license or copyright; see http://www.asme.org/terms/Terms_Use.cfm

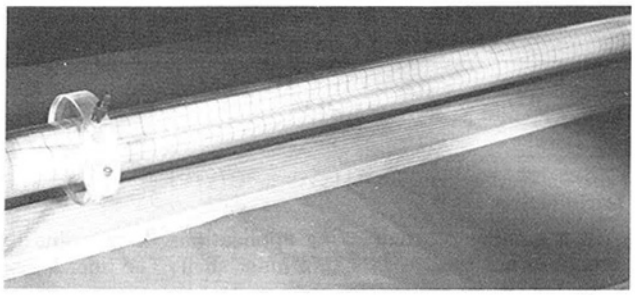


Fig. 1(*a*) Initiation of a propagating buckle in a confined mylar shell

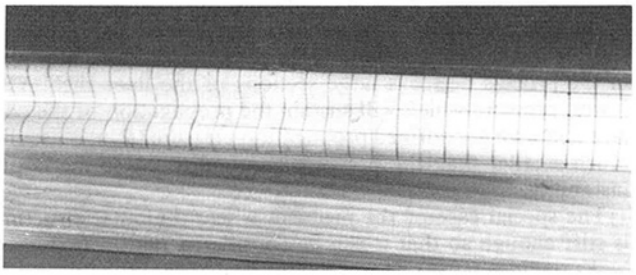
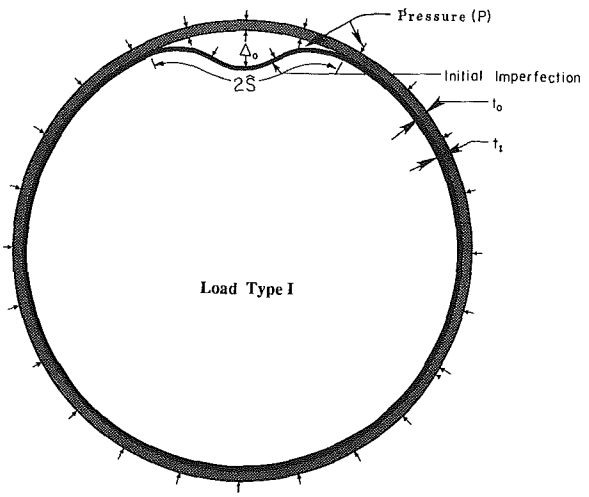


Fig. 1(*b*) Propagating buckle transition zone



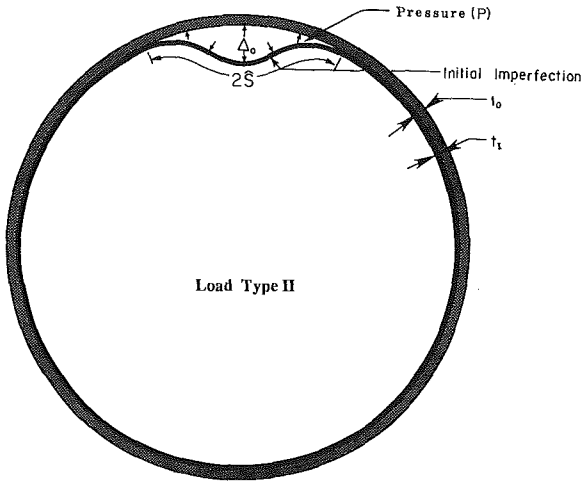


Fig. 2 Problem geometry

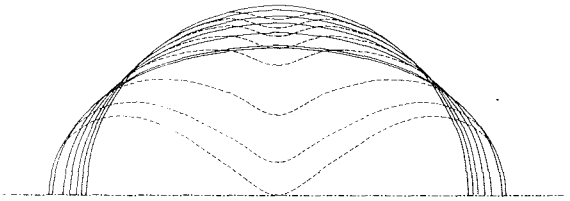


Fig. 3(*a*) Sequence of calculated response configurations for doubly symmetric case ($(t_o/t_i)^3 = 3$, load type I)

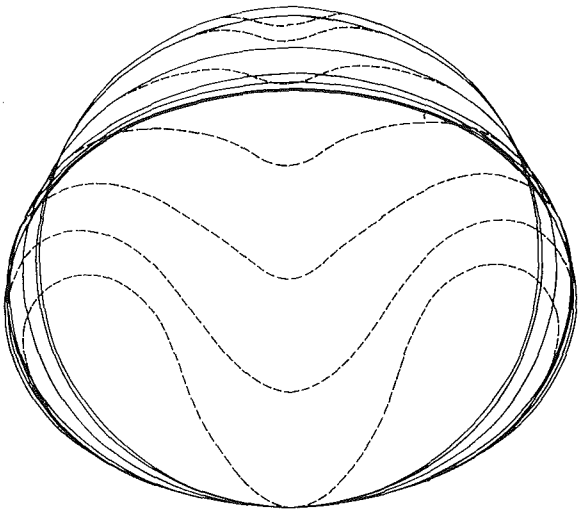


Fig. 3(*b*) Sequence of calculated response configurations for singly symmetric case ($(t_o/t_i)^3 = 3$, load type I)

and collapse. Two possible deformation patterns were considered. The first has two planes of symmetry and the second has one plane of symmetry. Sequences of collapse configurations for the two modes of collapse are shown in Fig. 3. These were calculated for load type I and tube rigidity ratio of $(t_0/t_I)^3 = 3$.

Figure 4 shows pressure volume responses for the two types of loading considered (ΔV is the increase in the volume of the cavity formed between the two rings during deformation; $V = \pi R^2$; $E' = E/(1-\nu^2)$). A particular imperfection defined in the preceding paper (1991) with amplitude $\Delta_0 = .025R$ was used in these calculations. Results for various tube rigidity ratios are presented. The presence of the outer shell clearly has a stiffening effect on the response of the composite structure for both types of loads considered. In the case of load type I if the bending rigidity of the outer shell is relatively small, the response is similar to that of a single tube under external pressure. Beyond a certain pressure (critical buckling pressure) the structure experiences a substantial loss of stiffness but continues to deform under increasing pressure. For higher relative bending rigidities the response becomes initially stiffer, but a limit load instability develops. The value of the limit pressure increases as the outer tube rigidity increases. For any given imperfection there is an upper bound to the limit pressure. This is achieved when the outer ring is rigid. Following the maximum, the pressure drops sharply to a pressure plateau at which most of the deformation takes place. The calculations were stopped when the crown point of the inner tube touched the opposite wall as shown in Fig. 3.

These general features are also exhibited in the responses calculated for load type II. However, in this case a limit load instability was found to occur even for relatively small bending rigidity ratios.

Downloaded 03 May 2010 to 171.66.16.244. Redistribution subject to ASME license or copyright; see http://www.asme.org/terms/Terms_Use.cfm

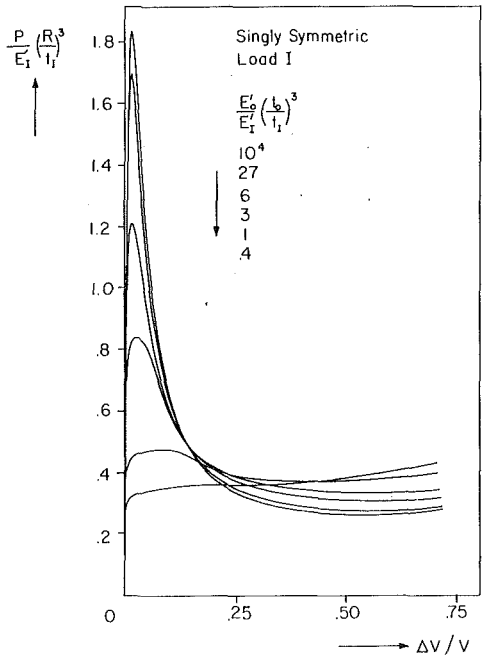


Fig. 4(*a*) Pressure volume responses for various bending rigidity ratios: load type I

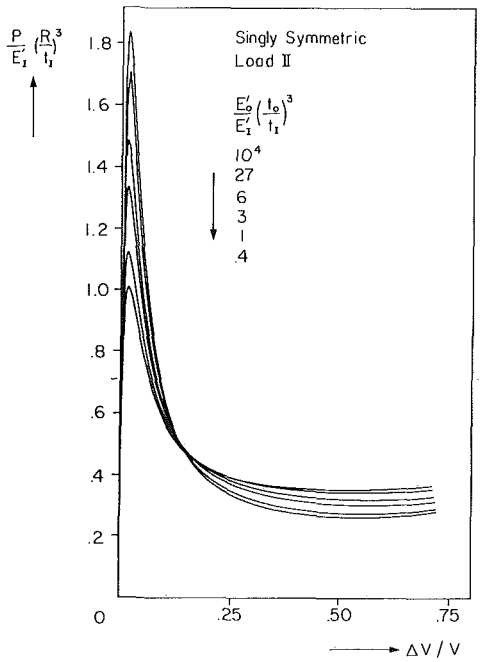


Fig. 4(*b*) Pressure volume responses for various bending rigidity ratios: load type II

The responses for the corresponding problems deforming in a doubly symmetric fashion are also qualitatively similar. The limit pressure for this mode of collapse was found to be lower for smaller bending rigidity ratios, whereas the structure was found to collapse in the singly symmetric mode for higher bending rigidity ratios.

In the case where the outer shell is rigid it was shown (Kyriakides and Youn, 1984) that the pressure required to continue deformation of the shell past the point of first touchdown of the crown point, rises sharply (i.e., the response becomes stable again under prescribed pressure). Motivated by this previous result this part of the response was approximated as rigid in

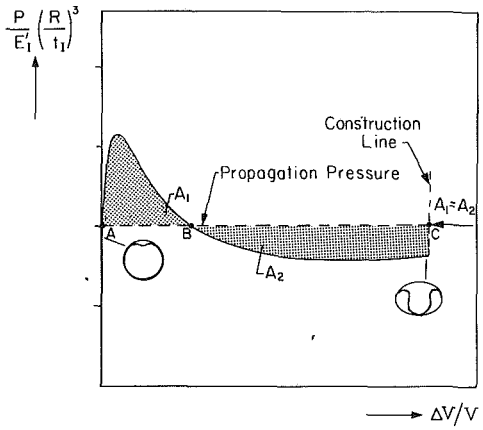


Fig. 5 Typical pressure volume response and Maxwell construction for calculating the propagation pressure

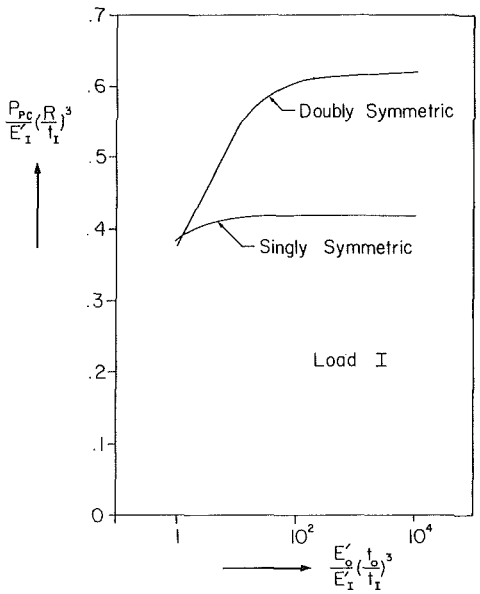


Fig. 6(*a*) Propagation pressure as a function of bending rigidity ratio: load type I

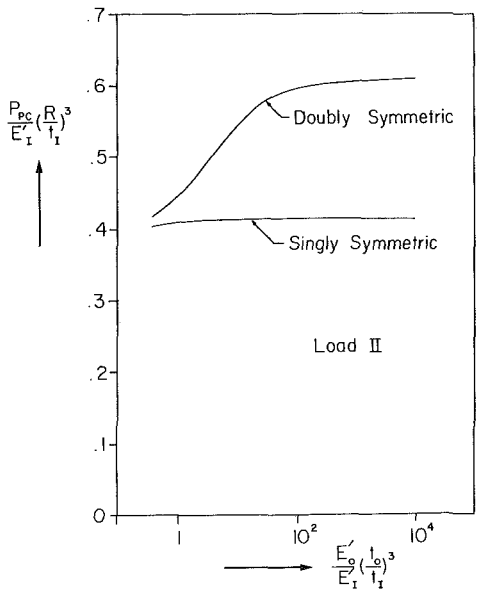


Fig. 6(*b*) Propagation pressure as a function of bending rigidity ratio: load type II

Downloaded 03 May 2010 to 171.66.16.244. Redistribution subject to ASME license or copyright; see http://www.asme.org/terms/Terms_Use.cfm

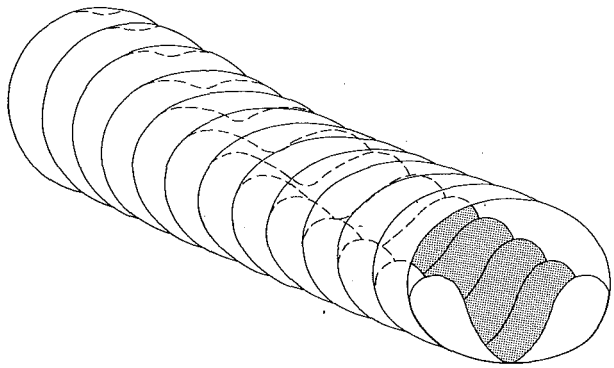


Fig. 7 Schematic representation of transition zone of confined propagating buckle

the present analysis (vertical construction line in Fig. 5). Thus, for a range of pressures the structure has three possible equilibrium states, A, B, and C. A and C are stable whereas B is unstable for a prescribed value of pressure. In view of this, given a large enough disturbance, the structure can "jump" from equilibrium state A to equilibrium state C. At C the structure is essentially in a collapsed state. In practice the disturbance can come from an imperfection which locally reduces the critical pressure of the structure. This can lead to local collapse. The locally collapsed section, in turn, acts as imperfection for the adjacent sections of the long structure. Thus, given a high enough pressure, the local buckle can initiate one that propagates. In a case like the one considered here, where the inner shell is confined inside the outer one, enough fluid flow must be provided in order for the buckle to continue propagating.

The lowest pressure which can sustain quasi-static propagation of the buckle can be obtained by the Maxwell construction shown in Fig. 5. This can be derived from a simple energy balance between the work done by the external pressure and the elastic energy stored in the structure when the buckle moves forward by a unit distance (in the process, the structure moves from equilibrium state A to equilibrium state C). More details on this calculation can be found in Chater and Hutchinson (1984) and Kyriakides (1986). It can be shown that the propagation pressure is the value of pressure which makes the two shaded areas in Fig. 5 equal.

This method was used to calculate the confined propagation pressure, as a function of the bending rigidity ratio of the two shells, for the two load types mentioned. Results for both the singly symmetric and doubly symmetric collapse modes are presented in Fig. 6.

The following observations can be made from these results:

(a) The propagation pressure for the singly symmetric case is seen to be lower for nearly all values of variables considered. It can thus be concluded that this is the prevalent mode of deformation for the phenomenon. The propagation pressure for the doubly symmetric mode of deformation is lower only for very small values of bending rigidity ratios for load type I.

(b) The normalized propagation process is relatively insensitive to the bending rigidity ratio of the two rings.

(c) For load type I, the propagating instability stops being a problem for small values of bending rigidity ratios because of the change in the nature of the response, discussed earlier. For load type II this change does not occur.

(d) The values of P_{pc} for the two loads differ by only a small amount with load type II yielding slightly lower values.

(e) The amplitude of the initial geometric imperfection used in the analysis strongly influences the limit pressure exhibited in the response but was found to have only a small effect on the calculated propagation pressure.

The expected profile of propagation of the buckle is shown schematically in Fig. 7. Its calculation requires a more complete treatment of the problem.

Acknowledgment

The work presented was carried out with support from the National Science Foundation under the PYI award MSM-8352370.

References

Calladine, C. R., 1986, "Analysis of Large Plastic Deformations in Shell Structures," *Proc. IUTAM Symposium: Inelastic Behavior of Plates and Shells*, Bevilacqua et al., ed., Springer, New York, pp. 69–101.

Chater, E., and Hutchinson, J. W., 1984, "On the Propagation of Bulges and Buckles," ASME JOURNAL OF APPLIED MECHANICS, Vol. 106, pp. 269–277.

Kyriakides, S. and Youn, S. K., 1984, "On the Collapse of Circular Confined Rings Under External Pressure," *Int'l. J. Solids and Structures*, Vol. 20, pp. 699–713.

Kyriakides, S., 1986, "Propagating Buckles in Long Confined Cylindrical Shells," *Int'l. J. Solids and Structures*, Vol. 22, pp. 1579–1597.

Li, F. S., and Kyriakides, S., 1991, "On the Response and Stability of Two Concentric Contacting Rings Under External Pressure," *Int'l. J. Solids and Structures*, Vol. 27, pp. 1–14.

On Spatial Chaos, Asymptotic Modal Analysis, and Turbulence

Earl H. Dowell[18,20] and Lawrence N. Virgin[19,20]

Introduction

A great deal of interesting and valuable work has been accomplished on temporal chaos in low-dimensional systems. (See references. Dowell (1988) provides a useful recent summary.) These studies, for the most part, deal with systems of relatively low order, although numerical simulations of Duffing-like systems of the order of 20 to 30 (say, 10–15 coupled Duffings equations) have been carried out by Dowell (1982, 1983). Also, higher-order versions of the Lorenz equations of similar total order have been studied by several authors (Sparrow, 1982). For Duffing-like systems, it is known that spatially converged solutions can be obtained for certain interesting physical parameter ranges using systems of low order, say ten or less (Dowell, 1982, 1983). For the Lorenz equations the (minimum) needed order (for spatial convergence) is not yet known, but is thought to be very large. It is also known, moreover, that by a suitable change in the physical parameters in a Duffing-like system, the needed order for spatial convergence (resolution) increases, apparently without bound.

All of this background is relevant to the question of the relationship between chaos and turbulence. It is generally agreed that the order of a system needed to describe turbulence is large (Manley, 1985; Sparrow, 1982). The question is, how large? Also, in what sense does "true turbulence" differ from low-dimensional or low-order chaos?

Some recent work (Dowell and Kubota, 1985; Kubota and

[18]Dean of Engineering, Mem. ASME.
[19]Assistant Professor, Mechanical Engineering and Materials Science.
[20]Duke University, Durham, NC 27706.
Manuscript received by the ASME Applied Mechanics Division, Nov. 18, 1988; final revision, Nov. 16, 1989.

Downloaded 03 May 2010 to 171.66.16.244. Redistribution subject to ASME license or copyright; see http://www.asme.org/terms/Terms_Use.cfm

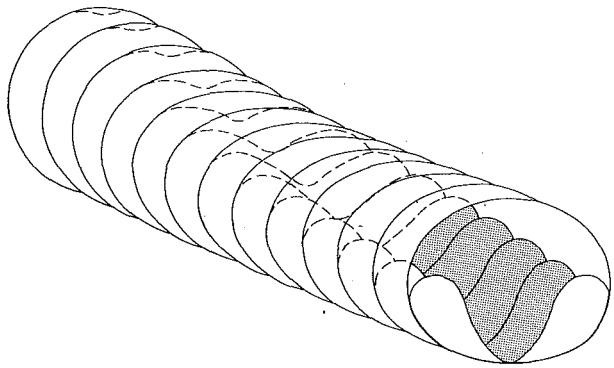


Fig. 7 Schematic representation of transition zone of confined propagating buckle

the present analysis (vertical construction line in Fig. 5). Thus, for a range of pressures the structure has three possible equilibrium states, A, B, and C. A and C are stable whereas B is unstable for a prescribed value of pressure. In view of this, given a large enough disturbance, the structure can "jump" from equilibrium state A to equilibrium state C. At C the structure is essentially in a collapsed state. In practice the disturbance can come from an imperfection which locally reduces the critical pressure of the structure. This can lead to local collapse. The locally collapsed section, in turn, acts as imperfection for the adjacent sections of the long structure. Thus, given a high enough pressure, the local buckle can initiate one that propagates. In a case like the one considered here, where the inner shell is confined inside the outer one, enough fluid flow must be provided in order for the buckle to continue propagating.

The lowest pressure which can sustain quasi-static propagation of the buckle can be obtained by the Maxwell construction shown in Fig. 5. This can be derived from a simple energy balance between the work done by the external pressure and the elastic energy stored in the structure when the buckle moves forward by a unit distance (in the process, the structure moves from equilibrium state A to equilibrium state C). More details on this calculation can be found in Chater and Hutchinson (1984) and Kyriakides (1986). It can be shown that the propagation pressure is the value of pressure which makes the two shaded areas in Fig. 5 equal.

This method was used to calculate the confined propagation pressure, as a function of the bending rigidity ratio of the two shells, for the two load types mentioned. Results for both the singly symmetric and doubly symmetric collapse modes are presented in Fig. 6.

The following observations can be made from these results:

(a) The propagation pressure for the singly symmetric case is seen to be lower for nearly all values of variables considered. It can thus be concluded that this is the prevalent mode of deformation for the phenomenon. The propagation pressure for the doubly symmetric mode of deformation is lower only for very small values of bending rigidity ratios for load type I.

(b) The normalized propagation process is relatively insensitive to the bending rigidity ratio of the two rings.

(c) For load type I, the propagating instability stops being a problem for small values of bending rigidity ratios because of the change in the nature of the response, discussed earlier. For load type II this change does not occur.

(d) The values of P_{pc} for the two loads differ by only a small amount with load type II yielding slightly lower values.

(e) The amplitude of the initial geometric imperfection used in the analysis strongly influences the limit pressure exhibited in the response but was found to have only a small effect on the calculated propagation pressure.

The expected profile of propagation of the buckle is shown schematically in Fig. 7. Its calculation requires a more complete treatment of the problem.

Acknowledgment

The work presented was carried out with support from the National Science Foundation under the PYI award MSM-8352370.

References

Calladine, C. R., 1986, "Analysis of Large Plastic Deformations in Shell Structures," *Proc. IUTAM Symposium: Inelastic Behavior of Plates and Shells*, Bevilacqua et al., ed., Springer, New York, pp. 69–101.

Chater, E., and Hutchinson, J. W., 1984, "On the Propagation of Bulges and Buckles," ASME JOURNAL OF APPLIED MECHANICS, Vol. 106, pp. 269–277.

Kyriakides, S. and Youn, S. K., 1984, "On the Collapse of Circular Confined Rings Under External Pressure," *Int'l. J. Solids and Structures*, Vol. 20, pp. 699–713.

Kyriakides, S., 1986, "Propagating Buckles in Long Confined Cylindrical Shells," *Int'l. J. Solids and Structures*, Vol. 22, pp. 1579–1597.

Li, F. S., and Kyriakides, S., 1991, "On the Response and Stability of Two Concentric Contacting Rings Under External Pressure," *Int'l. J. Solids and Structures*, Vol. 27, pp. 1–14.

On Spatial Chaos, Asymptotic Modal Analysis, and Turbulence

Earl H. Dowell[18,20] and Lawrence N. Virgin[19,20]

Introduction

A great deal of interesting and valuable work has been accomplished on temporal chaos in low-dimensional systems. (See references. Dowell (1988) provides a useful recent summary.) These studies, for the most part, deal with systems of relatively low order, although numerical simulations of Duffing-like systems of the order of 20 to 30 (say, 10–15 coupled Duffings equations) have been carried out by Dowell (1982, 1983). Also, higher-order versions of the Lorenz equations of similar total order have been studied by several authors (Sparrow, 1982). For Duffing-like systems, it is known that spatially converged solutions can be obtained for certain interesting physical parameter ranges using systems of low order, say ten or less (Dowell, 1982, 1983). For the Lorenz equations the (minimum) needed order (for spatial convergence) is not yet known, but is thought to be very large. It is also known, moreover, that by a suitable change in the physical parameters in a Duffing-like system, the needed order for spatial convergence (resolution) increases, apparently without bound.

All of this background is relevant to the question of the relationship between chaos and turbulence. It is generally agreed that the order of a system needed to describe turbulence is large (Manley, 1985; Sparrow, 1982). The question is, how large? Also, in what sense does "true turbulence" differ from low-dimensional or low-order chaos?

Some recent work (Dowell and Kubota, 1985; Kubota and

[18]Dean of Engineering, Mem. ASME.
[19]Assistant Professor, Mechanical Engineering and Materials Science.
[20]Duke University, Durham, NC 27706.
Manuscript received by the ASME Applied Mechanics Division, Nov. 18, 1988; final revision, Nov. 16, 1989.

Copyright © 1990 by ASME
Downloaded 03 May 2010 to 171.66.16.244. Redistribution subject to ASME license or copyright; see http://www.asme.org/terms/Terms_Use.cfm

Dowell, 1986) on asymptotic modal analysis for *linear* systems of high dimension, combined with our present understanding of chaos for low-dimensional systems, suggests some possible answers to these questions. These are explored in the present paper, along with some supportive numerical results for a nonlinear system.

To fix ideas we will deal with the chaotic motions and asymptotic modal analysis of a beam or plate, simply because our present understanding is most advanced for this system and the available analytical, numerical, and (physical) experimental evidence most complete.

Discussion

The chaotic motions of a beam or plate due to a periodic (sinusoidal) input can be described by the following mathematical model (Dowell, 1982)

$$\ddot{a}_i+\gamma_i\dot{a}_i+\omega_i^2 a_i+\lambda\sum_j B_{ji}a_j+\sum_j\sum_k\sum_l C_{ijkl}a_j a_k a_l=F_o\sin\omega\tau. \quad (1)$$

This is the modal description of a series of spring-mass-damper oscillators coupled through a follower force, λ, and also by nonlinear (cubic) stiffness terms. Physically it describes, for example, the response of a beam or plate fixed on all edges against in-plane or out-of-plane deflections, with a sinusoidal force applied normal to the beam or plate as well as an in-plane follower force. The follower force may physically arise due to fluid dynamic forces acting on the plate, for example.

The transverse displacement of the plate at point x,y and time t is given by $w(x,y,t)$. w can be expressed in terms of the modal generalized coordinates, a_i, and corresponding modal eigenfunctions, $\phi_i(x,y)$,

$$w(x,y,t)=\sum_{i=1}^{\infty}a_i(t)\phi_i(x,y). \quad (2)$$

It has been shown by Dowell (1982, 1984) that by a suitable choice of physical parameters, say ω_i and λ, the number of significant modes participating can be systematically increased; i.e., the a_i are of similar magnitude for $i=1\rightarrow I$ and I increases for suitable choices of ω_i and λ. ω_i can be varied by changing the in-plane compressive force in the plate, for example.

The question then arises, what happens as $I\rightarrow\infty$? Asymptotic modal analysis (Dowell and Kubota, 1985; Kubota and Dowell, 1986) provides a possible answer. From asymptotic modal analysis it is known that the physical deflection, w, due to a large number of spatially deterministic modes, when each modal response is random in time, becomes spatially uncorrelated as the number of modes in a given frequency bandwidth tends to infinity. In practice, typically more than ten, but less than one hundred, modes are required to obtain a significant degree of spatial randomness. As might be expected, the correlation length scales roughly with modal wavelength and tends to zero as the wavelength tends to zero. However, more importantly, a sufficiently large number of modes of finite wavelength in a given frequency bandwidth also leads to diminished spatial correlation.

Hence, it is possible that spatial *and* temporal chaos (i.e., "turbulence" if you will) is or can be a result of a large number of temporally chaotic, but spatially deterministic, modes interacting in a given frequency bandwidth.

Thus, Landau's hypothesis (1944) that turbulence is a result of many spatially and temporally deterministic modes interacting may not be altogether wrong. Temporal periodicity needs to be replaced by temporal randomness or chaos, but spatial determinism, per se, need not be abandoned in order to produce turbulence, *if* there is a sufficiently large number of modes actively participating.

Supporting Analysis

It is observed in a Duffing-like system that each temporal mode in a chaotic oscillation responds as though it were a single linear spring-mass-damper oscillator responding to a random input (Dowell, 1982, 1984, 1988; Pezeshki and Dowell, 1987). The universality of this result for other systems exhibiting chaos is still an open question, of course. Be that as it may, for present purposes it is sufficient to invoke the results of asymptotic modal analysis (AMA) (Dowell and Kubota, 1985; Kubota and Dowell, 1986) for a linear system (e.g., a plate) responding to a random input. The essential elements are summarized here.

Previously it has been shown that the cross-temporal mean-square of the plate deflection, $w(x,y,t)$ due to a point force acting normal to the plate and random in time, is given by

$$\overline{w^2}(x,y;x^*,y^*)=\frac{\pi}{4}\sum_{m=M}^{M+\Delta M}\frac{\psi_m(x,y)\psi_m(x^*,y^*)}{M_m^2\omega_m^3\zeta_m}\psi_m^2(x_F,y_F)\Phi_{FF}(\omega_m). \quad (3)$$

Here, x_F,y_F are the coordinates of the point of force application; x,y and x^*,y^* are two different sets of coordinates of the plate response; $\psi_m(x,y)$ the mth plate eigenmode; M_m the mth generalized mass; ω_m the mth eigenfrequency and ζ_m the mth eigenmode critical damping ratio. Φ_{FF} is the power spectral density of the applied force and $\overline{w^2}(x,y;x^*,y^*)$ is the cross mean-square response of two different response points. ΔM is the number of modes excited in a given frequency bandwidth, $\Delta\omega$.

Each term in the sum on the right-hand side of equation (3) is the individual modal contribution of the mth mode to the response. As the number of modes, Δm, in a given frequency bandwidth becomes large, it can be shown that

$$\frac{\overline{w^2}(x,y;x^*,y^*)}{\overline{w^2}(x,y;x,y)}\rightarrow 0 \text{ as } \Delta M\rightarrow\infty \text{ for } x,y\neq x^*,y^*. \quad (4)$$

For a more detailed discussion, consult (Dowell and Kubota, 1985).

The basic idea in deriving equation (4) is that as $\Delta M\rightarrow\infty$ for a given frequency bandwidth, $\Delta\omega$; M_m, ω_m, and ζ_m are relatively slowly varying compared to the variations of ψ_m. Thus, equation (3) can be approximated as follows for $\Delta M\rightarrow\infty$.

$$\overline{w^2}(x,y;x^*,y^*)=\frac{\pi}{4}\frac{\Phi_{FF}(\omega_c)}{M_c^2\omega_c^3\zeta_c}\sum_{m=M}^{M+\Delta M}\psi_m(x,y)\psi_m(x^*,y^*)\psi_m^2(x_F,y_F) \quad (5)$$

where the subscript c denotes the modal conditions corresponding to the center of the frequency bandwidth.

Consider now the summation term in equation (5),

$$\text{SUM}\equiv\sum_{m=M}^{M+\Delta M}\psi_m(x,y)\psi_m(x^*,y^*)\psi_m^2(x_F,y_F). \quad (6)$$

In Dowell and Kubota (1985) it has been shown that

$$\text{SUM}\rightarrow\left[<\psi_c^2>\right]^2\Delta M \quad (7)$$

for $x,y=x^*,y^*$. $<\bullet\bullet\bullet>$ denotes spatial average. Equation (7) is true independent of the point of response x,y *and* the point of force application, x_F,y_F *provided* that these points, (x,y), (x_F,y_F) are not near a (structural) domain boundary or near each other. For the exceptional cases see Dowell and Kubota, (1985).

The *key* point, however, is that for $x,y=x^*,y^*$,

$$\text{SUM}\sim\Delta M$$

even for the exceptional cases. By contrast for $x,y\neq x^*,y^*$, SUM oscillates about zero and remains bounded even for $\Delta M\rightarrow\infty$. Thus,

$$\frac{\text{SUM}(x,y;x^*,y)}{\text{SUM}(x,y;x,y)}\rightarrow 0 \text{ as } \Delta M\rightarrow\infty$$

and equation (4) then follows.

Downloaded 03 May 2010 to 171.66.16.244. Redistribution subject to ASME license or copyright; see http://www.asme.org/terms/Terms_Use.cfm

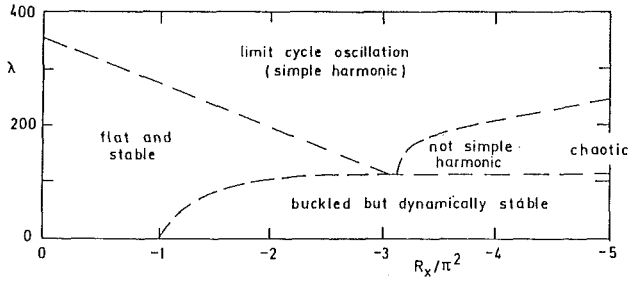


Fig. 1 Sketch of stability regions

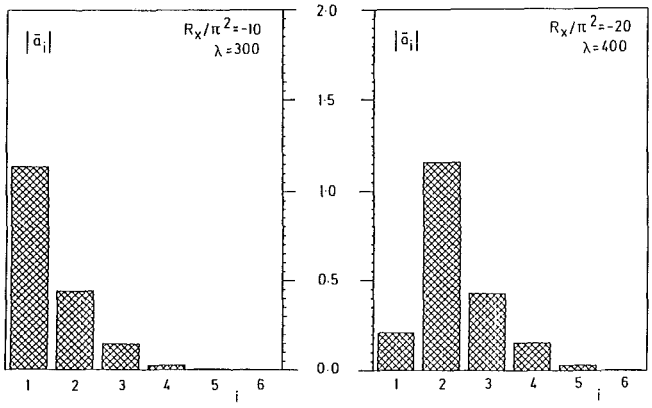


Fig. 2 Mean absolute deviations of Fourier coefficients

The essential meaning of equation (4) is that the spatial responses of two distinct points in the response domain tend to become uncorrelated as the number of modes participating in the response increases without bound.

Supporting Numerical Experiments

To investigate the conjecture of the previous sections of this paper, a simple version of the nonlinear system described by Dowell (1982, 1984) has been studied. The governing equations are

$$a_i(i\pi)^4/2+6(1-\nu^2)\left[\sum_r a_r^2(r\pi)^2/2\right]a_i(i\pi)^2/2 + R_x a_i(i\pi)^2/2+\ddot{a}_i/2 +\lambda\left\{\sum_r [ir/(i^2-r^2)][1-(-1)^{i+r}]a_r + \frac{1}{2}(\mu/M\lambda)^{1/2}\dot{a}_i\right\}=0 \tag{8}$$

and

$$w(x,t)=\sum_{i=1}^{\infty} a_i(t)\phi_i(x) \tag{9}$$

where

$$\phi_i(x)=\sin i\pi x.$$

Note that we consider here only a single spatial dimension, x, for simplicity plus time. Physically, the nonlinear system is a one-dimensional plate with a high-speed supersonic flow over one of the plate surfaces. The nonlinear terms in equation (8) model the in-plane tension induced by the plate bending. The several nondimensional parameters are ν, Poisson's ratio; R_x, the initial externally applied in-plane force that is positive in tension and negative in compression; λ, the ratio of flow dynamic pressure to plate stiffness; and μ/M, the fluid-to-plate mass ratio.

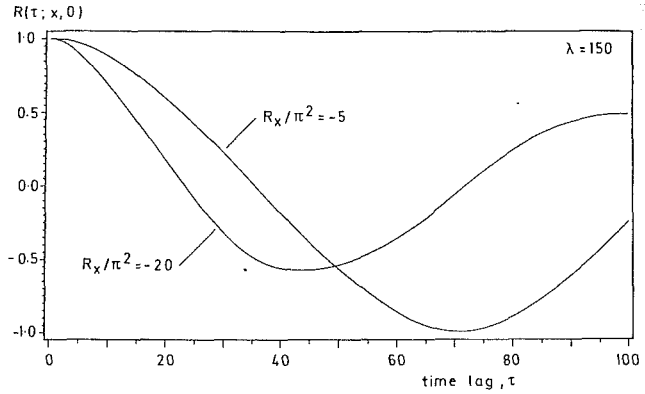


Fig. 3 Loss of temporal correlation

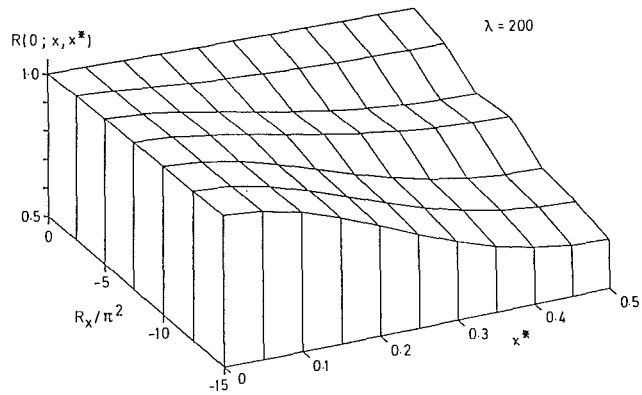


Fig. 4 Loss of spatial correlation (x^* is measured from center of plate)

In this work, $\nu=0.3$, $\mu/M=0.1$, or 0.4, and λ and R_x are varied. In Fig. 1, $\mu/M=0.1$ and otherwise it is .4. The latter value decreases the transients in the computer simulation. Fortunately, Fig. 1 is not sensitive to the precise value of this parameter. Several distinct types of motion are possible for this system depending on the values of λ and R_x, as shown in Fig. 1. The steady-state motion may be a flat and stable (motionless) plate, a buckled but dynamically stable plate, a simple harmonic limit cycle motion (flutter), or a periodic but not simple harmonic limit cycle motion. In recent years, within the last regime, chaotic motions have also been observed. For say, $\lambda=150$ and R_x/π^2 sufficiently negative, chaotic motion occurs and as R_x becomes more negative the higher modes of the plate become increasingly prominent. In Fig. 2 the modal absolute mean deviations, $|\bar{a}_i|$, are shown for $(R_x/\pi^2, \lambda)=(-10, 300)$ and $(-20, 400)$; these are calculated after the decay of initial transients.

To confirm our previous conjectures about loss of spatial correlation as the number of modes becomes large, the following correlation function is defined:

$$R(\tau;x,x^*)\equiv\frac{\lim_{T\to\infty}\frac{1}{2T}\int_{-T}^{T} w(t,x)w(t+\tau,x+x^*)dt}{\lim_{T\to\infty}\frac{1}{2T}\int_{-T}^{T} w^2(t,x)dt}. \tag{10}$$

By examining $R(\tau;x,0)$, the loss of temporal correlation may be investigated. This is shown in Fig. 3 for $\lambda=150$, $R_x/\pi^2=-5$ and $R_x/\pi^2=-20$, and $x=0.5$. By examining $R(0;x,x^*)$, the loss of spatial correlation may be investigated. This is shown in Fig. 4 where $\lambda=200$ and R_x/π^2 ranges from 0 to -15, and x^* is measured from the center of the plate, i.e., $x=0.5$.

Comparing Figs. 1, 2, 3, and 4 it is seen that indeed a loss of temporal correlation occurs when the motion is chaotic. Moreover, the increasing prominence of more and higher modes

Downloaded 03 May 2010 to 171.66.16.244. Redistribution subject to ASME license or copyright; see http://www.asme.org/terms/Terms_Use.cfm

leads to a loss of spatial correlation as well. Thus, our conjectures are confirmed for this example.

A final remark concerning the higher modes that were not retained in the numerical analysis may be made. In the numerical analysis, one only need retain those terms of 0(1) in amplitude, i.e., those physical modal amplitudes that are of the order of the plate thickness. Once the time histories and power spectra of these order-one modes are determined, the response in the higher modes, whose amplitudes by definition are in the *linear* response range, may be determined by *standard linear* vibration theory where now the higher linear modes are driven by the numerically determined lower nonlinear, chaotic modes. Further, over a given bandwidth of frequency in which many linear mode resonances lie, the classical, linear random vibration theory result may be well approximated by asymptotic modal analysis. See equations (5) and (7). This suggests that the mean-square deflection at higher frequencies scales with frequency as follows:

$$\overline{w^2} \sim \frac{\Phi(\omega_c)}{\omega_c^3 \zeta_c}$$

where $\Phi(\omega_c)$ is the power spectra of the nonlinear modal excitation, ω_c is the bandwidth center frequency, and ζ_c is the structural damping ratio, which may depend upon ω_c.

Concluding Remarks

In low-dimensional systems exhibiting chaos the response is temporally random (uncorrelated), but spatially deterministic (correlated). In this Note, a mechanism has been identified by which the response of a continuum system may be both temporally *and* spatially uncorrelated, i.e., "turbulent." The explanation of the mechanism is based upon recent work in chaos of low-to-moderate dimensional systems and also asymptotic modal analysis of high-dimensional systems. The conjectured mechanism and explanation has been confirmed by numerical experiments for a nonlinear system previously studied in the literature.

It is not claimed that this is the only mechanism by which turbulence may be produced or even the most common. Nevertheless, it is encouraging that one such mechanism has been identified, for moderate dimensional systems (10–100) for which there is supporting theoretical and experimental evidence. Even so, further work is required on Duffing-like systems as well as other systems. In particular, systematic numerical and physical experiments would be helpful.

Acknowledgments

This work was supported in part by the Army Research Office, Contract DAAL03-87K0023 and the National Science Foundation, Grant MSM-8504105. Drs. Gary Anderson and Elbert Marsh are the program directors.

References

Curry, J. H., Herring, J. R., Loncaric, J., and Orszag, S. A., 1984, "Order and Disorder in Two- and Three-Dimensional Benard Convection," *Journal of Fluid Mechanics*, Vol. 147, pp. 1–38.

Dowell, E. H., 1982, "Flutter of a Buckled Plate as an Example of Chaotic Motion of a Deterministic Autonomous System," *Journal of Sound and Vibration*, Vol. 85, pp. 333–344.

Dowell, E. H., 1984, "Observation and Evolution of Chaos in an Autonomous System," ASME JOURNAL OF APPLIED MECHANICS, Vol. 51, pp. 664–673.

Dowell, E. H., 1988, "Chaotic Oscillations in Mechanical Systems," *Computational Mechanics*, Vol. 3, pp. 199–216.

Dowell, E. H., and Kubota, Y., 1985, "Asymptotic Modal Analysis and Statistical Energy Analysis of Dynamical Systems," ASME JOURNAL OF APPLIED MECHANICS, Vol. 52, pp. 949–957.

Feigenbaum, M. J., 1978, "Quantitative Universality for a Class of Nonlinear Transformations," *Journal Stat. Physics*, Vol. 19, pp. 25–52.

Guckenheimer, J., and Holmes, P. J., 1983, *Nonlinear Oscillations, Dynamical Systems and Bifurcations of Vector Fields*, Springer-Verlag, Berlin.

Holmes, P. J., 1979, "A Nonlinear Oscillator With a Strange Attractor," *Philosophical Transactions of the Royal Society, London*, Vol. A292, pp. 419–448.

Holmes, P. J., and Moon, F. C., 1983, "Strange Attractors and Chaos in Nonlinear Mechanics," ASME JOURNAL OF APPLIED MECHANICS, Vol. 108, pp. 1021–1032.

Kubota, Y., and Dowell, E. H., 1986, "Experimental Investigation of Asymptotic Modal Analysis for a Rectangular Plate," *Journal of Sound and Vibration*, Vol. 106, pp. 203–216.

Landau, L. D., 1944, "On the Problem of Turbulence," *Akand. Nauk. Doklady*, Vol. 44, pp. 339–343, (also see English translation in collected papers of L. D. Landau, 1965, pp. 387–391.)

Manley, O. P., 1985, "Determining Modes and Fractal Attractors of Turbulent Flows," *Chaos in Nonlinear Dynamical Systems*, J. Chandra, ed., SIAM.

Miles, J. W., 1984, "Strange Attractors in Fluid Dynamics," *Advances in Applied Mechanics*, J. W. Hutchinson and T. Y. Wu, eds., Academic Press, London.

Moon, F. C., 1980, "Experiments on Chaotic Motions of a Forced Nonlinear Oscillator: Strange Attractors," ASME JOURNAL OF APPLIED MECHANICS, Vol. 47, pp. 638–644.

Moon, F. C., 1987, *Chaotic Vibrations*, John Wiley and Sons, New York.

Pezeshki, C., and Dowell, E. H., 1987, "An Examination of Initial Condition Maps for the Sinusoidally Excited Buckled Beam Modeled by the Duffings Equation," *Journal of Sound and Vibration*, Vol. 117, pp. 219–232.

Pezeshki, C., and Dowell, E. H., 1989, "Generation and Analysis of Liapunov Exponents for the Duffings Equations," *International Journal of Nonlinear Mechanics*, Vol. 24, pp. 79–97.

Roux, J. L., Richetti, P., Arnedo, A., and Argoul, F., 1984, "Chaos in a Chemical System: Toward a Global Understanding," *Journal Mech. Theorique et Applique, 3 Numero Special*, pp. 77–100.

Sparrow, C., 1982, "The Lorenz Equations: Bifurcations, Chaos, and Strange Attractors," *Applied Mathematical Science*, Vol. 41, Springer-Verlag, Berlin.

Szemplinska-Stupnicka, W., and Bajkowski, J., 1986, "The 1/2 Subharmonic Resonance and its Transition to Chaotic Motion in a Nonlinear Oscillator," *International Journal of Nonlinear Mechanics*, Vol. 21, pp. 401–419.

Tang, D. M., and Dowell, E. H., 1988, "On the Threshold Force for Chaotic Motions," ASME JOURNAL OF APPLIED MECHANICS," Vol. 55, pp. 190–196.

Thompson, J. M. T., and Stewart, H. B., 1986, *Nonlinear Dynamics and Chaos*, John Wiley and Sons, London.

Tseng, W. Y., and Dugundjii, J., 1971, "Nonlinear Vibrations of a Buckled Beam Under Harmonic Excitation," ASME JOURNAL OF APPLIED MECHANICS, Vol. 38, pp. 467–476.

Ueda, Y., 1980, "Explosion of Strange Attractors Exhibited by Duffings Equation," *Nonlinear Dynamics*, H. G. Helleman, ed., New York Academy of Sciences, New York, pp. 422–434.

Wolf, A., Swift, J. B., Swinney, H. L., and Vastano, J., 1985, "Determining Lyapunov Exponents From a Time Series," *Physica D*, Vol. 16, pp. 285–317.

Monte Carlo Simulation of Coupled Nonlinear Oscillators Under Random Excitations

Wenlung Li[21,22] and R. A. Ibrahim[21,23]

The main objectives of this note are to examine the random response of nonlinear three degree-of-freedom systems in the neighborhood of combination internal resonance by using Monte Carlo simulation and to compare the results with those obtained by first-order non-Gaussian closure. The numerical simulation is found to support the main features of the nonlinear interaction in the neighborhood of internal resonance conditions. For example, the nonlinear interaction takes place in the form of a randomly continuous energy exchange between the modes involved. In addition, the results verify the existence of energy absorbing effect as predicted by

[21] Department of Mechanical Engineering, Wayne State University, Detroit, MI 48202.

[22] Presently at the Department of Mechanical Engineering, National Taipei Institute of Technology, Taipei, Taiwan 10626, People's Republic of China.

[23] Mem. ASME

Manuscript received by the ASME Applied Mechanics Division, June 5, 1989; final revision, Jan. 8, 1990.

Downloaded 03 May 2010 to 171.66.16.244. Redistribution subject to ASME license or copyright; see http://www.asme.org/terms/Terms_Use.cfm

leads to a loss of spatial correlation as well. Thus, our conjectures are confirmed for this example.

A final remark concerning the higher modes that were not retained in the numerical analysis may be made. In the numerical analysis, one only need retain those terms of 0(1) in amplitude, i.e., those physical modal amplitudes that are of the order of the plate thickness. Once the time histories and power spectra of these order-one modes are determined, the response in the higher modes, whose amplitudes by definition are in the *linear* response range, may be determined by *standard linear* vibration theory where now the higher linear modes are driven by the numerically determined lower nonlinear, chaotic modes. Further, over a given bandwidth of frequency in which many linear mode resonances lie, the classical, linear random vibration theory result may be well approximated by asymptotic modal analysis. See equations (5) and (7). This suggests that the mean-square deflection at higher frequencies scales with frequency as follows:

$$\overline{w^2} \sim \frac{\Phi(\omega_c)}{\omega_c^3 \zeta_c}$$

where $\Phi(\omega_c)$ is the power spectra of the nonlinear modal excitation, ω_c is the bandwidth center frequency, and ζ_c is the structural damping ratio, which may depend upon ω_c.

Concluding Remarks

In low-dimensional systems exhibiting chaos the response is temporally random (uncorrelated), but spatially deterministic (correlated). In this Note, a mechanism has been identified by which the response of a continuum system may be both temporally *and* spatially uncorrelated, i.e., "turbulent." The explanation of the mechanism is based upon recent work in chaos of low-to-moderate dimensional systems and also asymptotic modal analysis of high-dimensional systems. The conjectured mechanism and explanation has been confirmed by numerical experiments for a nonlinear system previously studied in the literature.

It is not claimed that this is the only mechanism by which turbulence may be produced or even the most common. Nevertheless, it is encouraging that one such mechanism has been identified, for moderate dimensional systems (10–100) for which there is supporting theoretical and experimental evidence. Even so, further work is required on Duffing-like systems as well as other systems. In particular, systematic numerical and physical experiments would be helpful.

Acknowledgments

This work was supported in part by the Army Research Office, Contract DAAL03-87K0023 and the National Science Foundation, Grant MSM-8504105. Drs. Gary Anderson and Elbert Marsh are the program directors.

References

Curry, J. H., Herring, J. R., Loncaric, J., and Orszag, S. A., 1984, "Order and Disorder in Two- and Three-Dimensional Benard Convection," *Journal of Fluid Mechanics*, Vol. 147, pp. 1–38.

Dowell, E. H., 1982, "Flutter of a Buckled Plate as an Example of Chaotic Motion of a Deterministic Autonomous System," *Journal of Sound and Vibration*, Vol. 85, pp. 333–344.

Dowell, E. H., 1984, "Observation and Evolution of Chaos in an Autonomous System," ASME JOURNAL OF APPLIED MECHANICS, Vol. 51, pp. 664–673.

Dowell, E. H., 1988, "Chaotic Oscillations in Mechanical Systems," *Computational Mechanics*, Vol. 3, pp. 199–216.

Dowell, E. H., and Kubota, Y., 1985, "Asymptotic Modal Analysis and Statistical Energy Analysis of Dynamical Systems," ASME JOURNAL OF APPLIED MECHANICS, Vol. 52, pp. 949–957.

Feigenbaum, M. J., 1978, "Quantitative Universality for a Class of Nonlinear Transformations," *Journal Stat. Physics*, Vol. 19, pp. 25–52.

Guckenheimer, J., and Holmes, P. J., 1983, *Nonlinear Oscillations, Dynamical Systems and Bifurcations of Vector Fields*, Springer-Verlag, Berlin.

Holmes, P. J., 1979, "A Nonlinear Oscillator With a Strange Attractor," *Philosophical Transactions of the Royal Society, London*, Vol. A292, pp. 419–448.

Holmes, P. J., and Moon, F. C., 1983, "Strange Attractors and Chaos in Nonlinear Mechanics," ASME JOURNAL OF APPLIED MECHANICS, Vol. 108, pp. 1021–1032.

Kubota, Y., and Dowell, E. H., 1986, "Experimental Investigation of Asymptotic Modal Analysis for a Rectangular Plate," *Journal of Sound and Vibration*, Vol. 106, pp. 203–216.

Landau, L. D., 1944, "On the Problem of Turbulence," *Akand. Nauk. Doklady*, Vol. 44, pp. 339–343, (also see English translation in collected papers of L. D. Landau, 1965, pp. 387–391.)

Manley, O. P., 1985, "Determining Modes and Fractal Attractors of Turbulent Flows," *Chaos in Nonlinear Dynamical Systems*, J. Chandra, ed., SIAM.

Miles, J. W., 1984, "Strange Attractors in Fluid Dynamics," *Advances in Applied Mechanics*, J. W. Hutchinson and T. Y. Wu, eds., Academic Press, London.

Moon, F. C., 1980, "Experiments on Chaotic Motions of a Forced Nonlinear Oscillator: Strange Attractors," ASME JOURNAL OF APPLIED MECHANICS, Vol. 47, pp. 638–644.

Moon, F. C., 1987, *Chaotic Vibrations*, John Wiley and Sons, New York.

Pezeshki, C., and Dowell, E. H., 1987, "An Examination of Initial Condition Maps for the Sinusoidally Excited Buckled Beam Modeled by the Duffings Equation," *Journal of Sound and Vibration*, Vol. 117, pp. 219–232.

Pezeshki, C., and Dowell, E. H., 1989, "Generation and Analysis of Liapunov Exponents for the Duffings Equations," *International Journal of Nonlinear Mechanics*, Vol. 24, pp. 79–97.

Roux, J. L., Richetti, P., Arnedo, A., and Argoul, F., 1984, "Chaos in a Chemical System: Toward a Global Understanding," *Journal Mech. Theorique et Applique, 3 Numero Special*, pp. 77–100.

Sparrow, C., 1982, "The Lorenz Equations: Bifurcations, Chaos, and Strange Attractors," *Applied Mathematical Science*, Vol. 41, Springer-Verlag, Berlin.

Szemplinska-Stupnicka, W., and Bajkowski, J., 1986, "The 1/2 Subharmonic Resonance and its Transition to Chaotic Motion in a Nonlinear Oscillator," *International Journal of Nonlinear Mechanics*, Vol. 21, pp. 401–419.

Tang, D. M., and Dowell, E. H., 1988, "On the Threshold Force for Chaotic Motions," ASME JOURNAL OF APPLIED MECHANICS," Vol. 55, pp. 190–196.

Thompson, J. M. T., and Stewart, H. B., 1986, *Nonlinear Dynamics and Chaos*, John Wiley and Sons, London.

Tseng, W. Y., and Dugundjii, J., 1971, "Nonlinear Vibrations of a Buckled Beam Under Harmonic Excitation," ASME JOURNAL OF APPLIED MECHANICS, Vol. 38, pp. 467–476.

Ueda, Y., 1980, "Explosion of Strange Attractors Exhibited by Duffings Equation," *Nonlinear Dynamics*, H. G. Helleman, ed., New York Academy of Sciences, New York, pp. 422–434.

Wolf, A., Swift, J. B., Swinney, H. L., and Vastano, J., 1985, "Determining Lyapunov Exponents From a Time Series," *Physica D*, Vol. 16, pp. 285–317.

Monte Carlo Simulation of Coupled Nonlinear Oscillators Under Random Excitations

Wenlung Li[21,22] and R. A. Ibrahim[21,23]

The main objectives of this note are to examine the random response of nonlinear three degree-of-freedom systems in the neighborhood of combination internal resonance by using Monte Carlo simulation and to compare the results with those obtained by first-order non-Gaussian closure. The numerical simulation is found to support the main features of the nonlinear interaction in the neighborhood of internal resonance conditions. For example, the nonlinear interaction takes place in the form of a randomly continuous energy exchange between the modes involved. In addition, the results verify the existence of energy absorbing effect as predicted by

[21]Department of Mechanical Engineering, Wayne State University, Detroit, MI 48202.

[22]Presently at the Department of Mechanical Engineering, National Taipei Institute of Technology, Taipei, Taiwan 10626, People's Republic of China.

[23]Mem. ASME

Manuscript received by the ASME Applied Mechanics Division, June 5, 1989; final revision, Jan. 8, 1990.

Copyright © 1990 by ASME
Downloaded 03 May 2010 to 171.66.16.244. Redistribution subject to ASME license or copyright; see http://www.asme.org/terms/Terms_Use.cfm

the non-Gaussian closure method. While the non-Gaussian closure exhibits regions of multiple solutions in the neighborhood of exact internal resonance, the numerical simulation gives only one solution depending on the assigned initial conditions. This observation requires further investigation to establish the domains of attraction in stochastic nonlinear dynamics.

Analysis

Consider a nonlinear dynamic system described by the set of ordinary differential equations

$$Y_i'' + 2\zeta_i r_{i3} Y_i' + r^2_{in} Y_i = h_i(Y) W(\tau) + \epsilon g_i(Y, Y'), \quad i = 1,2, \ldots n \tag{1}$$

where Y_i is the nondimensional normal coordinate of mode i, ζ_i is the damping ratio of mode i, r_{in} is the ratio of the natural frequency of mode i to the natural frequency of mode n, a prime denotes differentiation with respect to the nondimensional time parameter $\tau = \omega_3 t$, ω_3 is the natural frequency of the third mode, ϵ is a small nonlinear coupling parameter, and $W(\tau)$ is a white noise random process. h_i is a nonlinear function of the coordinates Y_i and g_i is a nonlinear function of the coordinates Y_i and their time derivatives.

If both h_i and g_i contain quadratic nonlinearities, the system may possess internal resonance of third order of the form

$$\Sigma\ k_i \omega_i = 0 \tag{2}$$

where $\Sigma |k_i| = K$ is referred to as the order of internal resonance.

For the case of three degree-of-freedom system, h_i and g_i may take the following forms:

$$h_i(.)) = f_i + c_{i1} Y_1 + c_{i2} Y_2 + c_{i3} Y_3 + c_{i4} Y_1 Y_2 + c_{i5} Y_1 Y_3 + c_{i6} Y_2 Y_3 + c_{i7} Y_1 + c_{i8} Y_2 + c_{i9} Y_3, \quad i = 1, 2, 3 \tag{3a}$$

$$g_i(.) = \alpha_2 / M_{ii} [(2\zeta_1 r_{13} Y_1' + r_{i3}{}^2 Y_1)(L_{i11} Y_1 + L_{i21} Y_2 + L_{i31} Y_3) + (2\zeta_2 r_{23} Y_2' + r_{23}{}^2 Y_2)(L_{i12} Y_1 + L_{i22} Y_2 + L_{i32} Y_3) + (2\zeta_3 Y_3' + Y_3)(L_{i13} Y_1 + L_{i23} Y_2 + L_{i33} Y_3) - (N_{i11} Y_1'^2 + N_{i22} Y_2'^2 + N_{i33} Y_3'^2 + N_{i12} Y_1' Y_2' + N_{i13} Y_1' Y_3' + N_{i23} Y_2 Y_3)]. \tag{3b}$$

Ibrahim and Li (1988) and Li and Ibrahim (1989) employed Gaussian and non-Gaussian closures to determine the random response of this system in the neighborhood of combination internal resonance $\omega_3 = \omega_1 + \omega_2$ and the principal internal resonance conditions: $\omega_2 = 2\omega_1$, $\omega_3 = 2\omega_1$, $\omega_3 = 2\omega_2$. For the case of combination internal resonance, the non-Gaussian closure solution reveals two interesting features. The first is a transfer of energy from the third mode to the first two modes while the second is the existence of multiple solutions, over a small range of the internal detuning parameter $r = \omega_3/(\omega_1 + \omega_2) > 1$, which are associated with jump and collapse phenomena. Away from the internal resonance $\omega_3/(\omega_1 + \omega_2) \neq 1.0$, the non-Gaussian and linear solutions coincide. In this Note the validity of the non-Gaussian closure results will be examined by running Monte Carlo simulations for the case of combination internal resonance.

The Monte Carlo simulation is carried out by generating a set of random numbers representing a Gaussian process $\xi(\tau)$ of zero mean and a unit standard deviation. The spectral density function $S(\eta)$ of such a process can be written as (Clough and Penzion, 1975)

$$S_\xi(\eta) = \frac{D}{\pi} \frac{6 - 8\cos(\eta\Delta\tau) + 2\cos(2\eta\Delta\tau)}{(\eta\Delta\tau)^4} \tag{4}$$

where η is a nondimensional frequency parameter and D stands for the spectral density of the target white process $W(\tau)$, which has the autocorrelation function $R_w(\Delta\tau) = 2D\delta(\Delta\tau)$. Relation (4) reveals that $S_\xi(\eta) \to S_0 = D/\pi$ as $\Delta\tau \to 0$. Thus, one can choose $\Delta\tau$ very small compared with any characteristic period of the system. Relation (4) indicates that the spectral density function $S_\xi(\eta)$ remains approximately constant over a large frequency range if $\Delta\tau$ is chosen to be less than 0.02. For this reason, $\Delta\tau = 0.015$ is selected for the present numerical simulation.

In view of the nonlinearity of the system equations of motion, the response process will be non-Gaussian even though the excitation is Gaussian. Thus, either an extremely long simulation record (when the target process is ergodic) or a large sample size is required if an accurate result is needed. In accordance with the central limit theorem and the concept of interval estimator in statistics, the sample size N can be determined by using the relationship (Hald, 1952): $N = Z^2\sigma^2/\gamma^2$, where γ is the maximum allowable error or uncertainty, σ is the standard deviation of the response, and Z is the Z-transformation in statistics. In the present study, the response mean value $E[Y(\tau)]$ is estimated from a simulation record with a 90 percent confidence level, i.e., $Z = 1.645$, and with a maximum allowable error of 0.105σ of the estimated response sample mean. From relation (14), the estimated value $N = (1.645\sigma)^2/(0.105\sigma)^2 = 245$ which is selected to be $N = 250$ sample records for the numerical simulation.

The IMSL subroutine RNGET (Normal or Gaussian Random Deviate Generator) is used to generate a sequence of random signals. Based on the time history responses of the non-Gaussian closure solution it is found that the mean square response reaches its steady-state after $\tau = 1000 - 1500$ and becomes time invariant. In the present study, the time duration of each record is taken as 2500 nondimensional time scale. The generated signal $\xi(\tau)$ is introduced in the system equations of motion for $W(\tau)$. These equations are then solved by using the IMSL subroutine DIVPRK (Initial Value Problem Solver, Runge-Kutta-Verner Fifth and Sixth-Order Numerical Integration Method) for $Y_i(\tau)$. The numerical integration is performed with double precision and with integration accuracy 0.10D-06. The response statistics such as mean squares may be evaluated from the response coordinates $Y_i(\tau)$ as

$$E[Y_i^2] = \frac{1}{T}\int_{T_1}^{T_2} Y_i^2(t)\,dt = \left\{\sum_{j=1}^{M} Y_i^2(T_1 + j\Delta t)\right\}/M \tag{5}$$

where $T = T_2 - T_1$ is the range over which the statistics are taken and M is the number of sampling points. The mean square response is computed starting from the end of the transient response, i.e., at $T = 1500$. This means that the mean square response of each record is taken from $T_1 = 1500$ to $T_2 = 2500$. It is found that each record requires approximately 2000 seconds CPU time on a SUN computer, or the equivalent of 139 hours for the total of 250 records.

Discussions and Conclusions

The mean squares of response displacements are estimated numerically from the sample records for selected values of internal detuning parameter. The results are plotted by full circles ● for the nonlinear system and by empty squares for the linear system in Fig. 1. The dotted and solid curves are belonging to analytical linear and non-Gaussian closure solutions, respectively. The Monte Carlo simulation results give only one branch of the steady-state solution corresponding to a zero set of initial conditions. In view of the lengthy computational time, no attempts have been made to establish different domains of attraction which may result in another branch of steady-state response. It is seen that there is a qualitative agreement between the non-Gaussian solution and Monte Carlo results in the vicinity of the critical combination internal

Downloaded 03 May 2010 to 171.66.16.244. Redistribution subject to ASME license or copyright; see http://www.asme.org/terms/Terms_Use.cfm

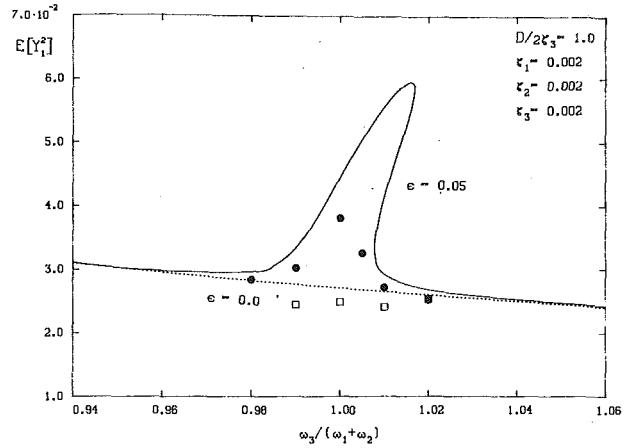


Fig. 1(*a*) First mode

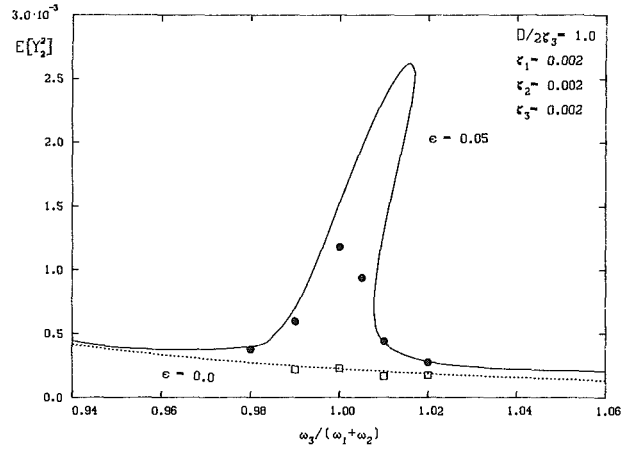


Fig. 1(*b*) Second Mode

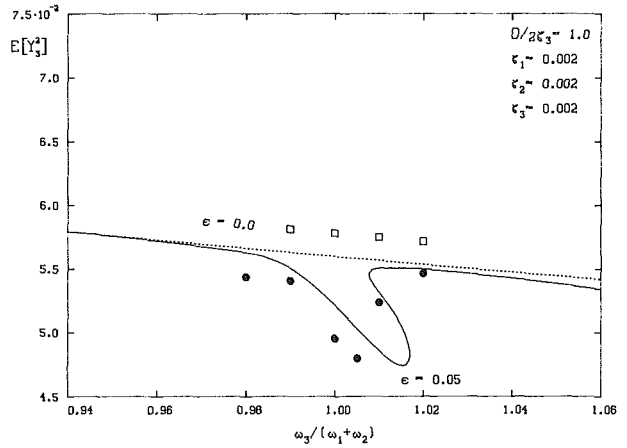


Fig. 1(c) Third mode

Fig. 1 Comparison of Monte Carlo results and cumulant-neglect closure solutions (: non-Gaussian, ...: linear solution, : simulated nonlinear, : simulated linear). Three mode interaction: $r=\omega_3/(\omega_1+\omega_2)=1$. $D/2\zeta_3=1.0$, $\zeta_j=0.002$

resonance condition. The agreement is mainly observed in the general trend of autoparametric interaction between the three modes.

Acknowledgment

This research is supported by a grant from the Air Force Office of Scientific Research under Grant No. AFOSR-85-0008 and an additional support from the Institute for Manufacturing Research.

References

Clough, R. W., and Penzien, J., 1975, *Dynamics of Structures*, McGraw-Hill, New York.

Hald, A., 1952, *Statistics Tables and Formulas*, John Wiley and Sons, New York.

Ibrahim, R. A., and Li, W., 1988, "Structural Modal Interaction with Combination Internal Resonance Under Wide-Band Random Excitation," *Journal of Sound and Vibration*, Vol. 123, No. 3, pp. 473–495.

Li, W., and Ibrahim, R. A., 1989, "Principal Internal Resonances in 3-DOF Systems Subjected to Wide-Band Random Excitation," *Journal of Sound and Vibration*, Vol. 130, No. 2.

Flexure of a Pressurized Tube

D. J. Steigmann[24]

In this note we study the theory of combined flexure and pressurization of an initially cylindrical elastic membrane of circular cross-section. For the case of homogeneous material and uniform pressure, we obtain first integrals of the equations of equilibrium.

Deformation

Position $\mathbf{x}$ of a material point on the reference surface is described parametrically by

$$\mathbf{x}(\theta, z) = r\mathbf{i}(\theta)+z\mathbf{k}, \tag{1}$$

where r is the constant cylinder radius, z measures distance along the generators $\theta=$ const., $\mathbf{k}$ is a fixed unit vector aligned with the generators, and $\mathbf{i}$ is the exterior unit normal to the cylindrical surface.

We consider deformations $(\theta,z)\rightarrow\mathbf{r}$ of the form

$$\mathbf{r}(\theta,z)=\mathbf{R}(s)+\xi(\theta)\mathbf{n}(s)+\eta(\theta)\mathbf{b}(s)\ ;\ s=f(z), \tag{2}$$

where $\mathbf{R}$ is the position of a point on a base curve with principal normal $\mathbf{n}$ and binormal $\mathbf{b}$ and s is an arclength parameter. We assume the parametrization to be such that $\alpha=f'(z)>0$. The principal curvature $\kappa(s)$ of the base curve is defined by $\mathbf{n}=\kappa^{-1}\mathbf{t}'(s)$, where $\mathbf{t}=\mathbf{R}'(s)$ is the unit tangent to the base curve. The binormal is then given by $\mathbf{b}=\mathbf{t}\times\mathbf{n}$.

The deformation equation (2) describes extension, flexure, and torsion of a tube in which every cross-section $s=$ const. suffers the same distortion. Henceforth, we restrict attention to the special case: $\mathbf{b}=$ const., $\alpha=$ const., $\kappa=|\mathbf{R}|^{-1}=$ const., corresponding to uniform, torsionless flexure in a plane with unit normal $\mathbf{b}$ (Fig. 1). In this description the center of curvature of the base curve and the origin of the vector $\mathbf{R}$ are taken to be coincident.

Let $\theta^1=\theta$ and $\theta^2=z$. Then the functions (1) and (2) induce the natural bases $\mathbf{A}_\alpha=\partial\mathbf{x}/\partial\theta^\alpha$ and $\mathbf{a}_\alpha=\partial\mathbf{r}/\partial\theta^\alpha$ $(\alpha=1,2)$ which span the tangent planes of the reference and deformed surfaces, respectively. From equations (1) and (2) we find

$$\mathbf{A}_1=r\mathbf{j}\ (\theta),\ \mathbf{A}_2=\mathbf{k}, \tag{3}$$

where $\mathbf{j}=\mathbf{i}'(\theta)$ is the azimuthal unit vector on the reference cylinder, and

$$\mathbf{a}_1=\xi'\mathbf{n}+\eta'\mathbf{b}\ ,\ \mathbf{a}_2=\alpha(1-\kappa\xi)\mathbf{t}. \tag{4}$$

The strain of the membrane is given by $\mathbf{C}=(\mathbf{a}_\alpha\cdot\mathbf{a}_\beta)\mathbf{A}^\alpha\otimes\mathbf{A}^\beta$,

[24]Department of Mechanical Engineering, University of Alberta, Edmonton, Alberta, Canada T6G 2G8.

Manuscript received and accepted by the ASME Applied Mechanics Division, July 6, 1989.

Downloaded 03 May 2010 to 171.66.16.244. Redistribution subject to ASME license or copyright; see http://www.asme.org/terms/Terms_Use.cfm

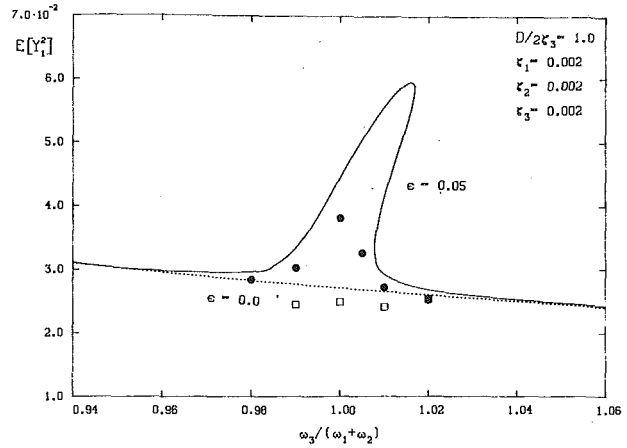


Fig. 1(*a*) First mode

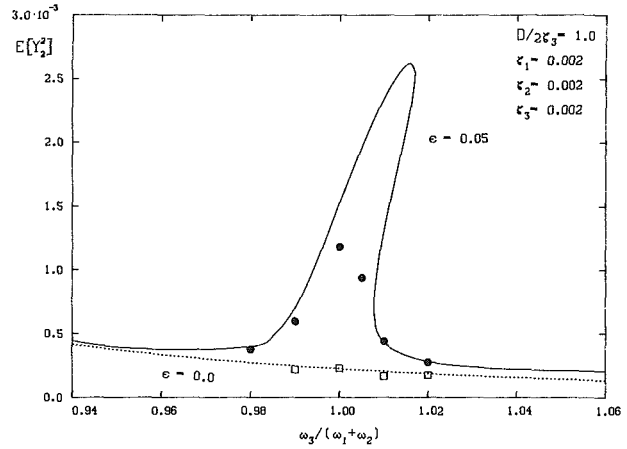


Fig. 1(*b*) Second Mode

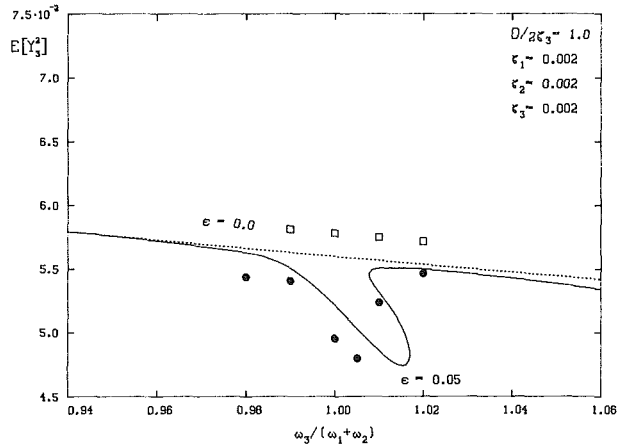


Fig. 1(c) Third mode

Fig. 1 Comparison of Monte Carlo results and cumulant-neglect closure solutions (: non-Gaussian, ...: linear solution, : simulated nonlinear, : simulated linear). Three mode interaction: $r=\omega_3/(\omega_1+\omega_2)=1$. $D/2\zeta_3=1.0$, $\zeta_j=0.002$

resonance condition. The agreement is mainly observed in the general trend of autoparametric interaction between the three modes.

Acknowledgment

This research is supported by a grant from the Air Force Office of Scientific Research under Grant No. AFOSR-85-0008 and an additional support from the Institute for Manufacturing Research.

References

Clough, R. W., and Penzien, J., 1975, *Dynamics of Structures*, McGraw-Hill, New York.

Hald, A., 1952, *Statistics Tables and Formulas*, John Wiley and Sons, New York.

Ibrahim, R. A., and Li, W., 1988, "Structural Modal Interaction with Combination Internal Resonance Under Wide-Band Random Excitation," *Journal of Sound and Vibration*, Vol. 123, No. 3, pp. 473–495.

Li, W., and Ibrahim, R. A., 1989, "Principal Internal Resonances in 3-DOF Systems Subjected to Wide-Band Random Excitation," *Journal of Sound and Vibration*, Vol. 130, No. 2.

Flexure of a Pressurized Tube

D. J. Steigmann[24]

In this note we study the theory of combined flexure and pressurization of an initially cylindrical elastic membrane of circular cross-section. For the case of homogeneous material and uniform pressure, we obtain first integrals of the equations of equilibrium.

Deformation

Position $\mathbf{x}$ of a material point on the reference surface is described parametrically by

$$\mathbf{x}(\theta, z) = r\mathbf{i}(\theta)+z\mathbf{k}, \tag{1}$$

where r is the constant cylinder radius, z measures distance along the generators $\theta=\text{const.}$, $\mathbf{k}$ is a fixed unit vector aligned with the generators, and $\mathbf{i}$ is the exterior unit normal to the cylindrical surface.

We consider deformations $(\theta,z)\rightarrow\mathbf{r}$ of the form

$$\mathbf{r}(\theta,z)=\mathbf{R}(s)+\xi(\theta)\mathbf{n}(s)+\eta(\theta)\mathbf{b}(s)\ ;\ s=f(z), \tag{2}$$

where $\mathbf{R}$ is the position of a point on a base curve with principal normal $\mathbf{n}$ and binormal $\mathbf{b}$ and s is an arclength parameter. We assume the parametrization to be such that $\alpha=f'(z)>0$. The principal curvature $\kappa(s)$ of the base curve is defined by $\mathbf{n}=\kappa^{-1}\mathbf{t}'(s)$, where $\mathbf{t}=\mathbf{R}'(s)$ is the unit tangent to the base curve. The binormal is then given by $\mathbf{b}=\mathbf{t}\times\mathbf{n}$.

The deformation equation (2) describes extension, flexure, and torsion of a tube in which every cross-section $s=\text{const.}$ suffers the same distortion. Henceforth, we restrict attention to the special case: $\mathbf{b}=\text{const.}$, $\alpha=\text{const.}$, $\kappa=|\mathbf{R}|^{-1}=\text{const.}$, corresponding to uniform, torsionless flexure in a plane with unit normal $\mathbf{b}$ (Fig. 1). In this description the center of curvature of the base curve and the origin of the vector $\mathbf{R}$ are taken to be coincident.

Let $\theta^1=\theta$ and $\theta^2=z$. Then the functions (1) and (2) induce the natural bases $\mathbf{A}_\alpha=\partial\mathbf{x}/\partial\theta^\alpha$ and $\mathbf{a}_\alpha=\partial\mathbf{r}/\partial\theta^\alpha$ $(\alpha=1,2)$ which span the tangent planes of the reference and deformed surfaces, respectively. From equations (1) and (2) we find

$$\mathbf{A}_1=r\mathbf{j}\ (\theta),\ \mathbf{A}_2=\mathbf{k}, \tag{3}$$

where $\mathbf{j}=\mathbf{i}'(\theta)$ is the azimuthal unit vector on the reference cylinder, and

$$\mathbf{a}_1=\xi'\mathbf{n}+\eta'\mathbf{b}\ ,\ \mathbf{a}_2=\alpha(1-\kappa\xi)\mathbf{t}. \tag{4}$$

The strain of the membrane is given by $\mathbf{C}=(\mathbf{a}_\alpha\cdot\mathbf{a}_\beta)\mathbf{A}^\alpha\otimes\mathbf{A}^\beta$,

[24]Department of Mechanical Engineering, University of Alberta, Edmonton, Alberta, Canada T6G 2G8.

Manuscript received and accepted by the ASME Applied Mechanics Division, July 6, 1989.

Copyright © 1990 by ASME
Downloaded 03 May 2010 to 171.66.16.244. Redistribution subject to ASME license or copyright; see http://www.asme.org/terms/Terms_Use.cfm

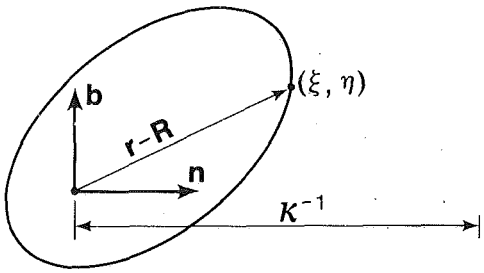


Fig. 1

where $\{\mathbf{A}^1,\mathbf{A}^2\}$ is the dual basis on the reference surface: $\mathbf{A}^1 = r^{-1}\mathbf{j}$, $\mathbf{A}^2 = \mathbf{k}$. Then equation (4) yields the spectral form $\mathbf{C} = \lambda^2\mathbf{M}\otimes\mathbf{M} + \mu^2\mathbf{N}\otimes\mathbf{N}$, where $\mathbf{M} = \mathbf{j}$, $\mathbf{N} = \mathbf{k}$ and λ and μ are the positive principal stretches:

$$\lambda = [(\xi'/r)^2 + (\eta'/r)^2]^{1/2}, \quad \mu = \alpha(1-\kappa\xi). \tag{5a,b}$$

Equilibrium

If the principal vectors $\mathbf{M},\mathbf{N}$ are the symmetry axes of the material, then the response of the membrane is specified by the strain energy function $w(\lambda,\mu)$, measured per unit area of the reference surface. This description includes isotropic materials, for which w is a symmetric function of its arguments.

The equations of equilibrium for a pressurized membrane are:

$$(\sqrt{A})^{-1}\,\partial(\sqrt{A}\,\mathbf{T}^\alpha)/\partial\theta^\alpha + pJ\mathbf{a}_3 = \mathbf{0}, \tag{6}$$

where A is the determinant of the matrix of inner products $(\mathbf{A}_\alpha\cdot\mathbf{A}_\beta)$, p is the pressure, $J\mathbf{a}_3 = \mathbf{a}_1\times\mathbf{a}_2/\sqrt{A}$ and $\mathbf{T}^\alpha$ are the stress vectors. Let w_λ and w_μ be the partial derivatives of w with respect to λ and μ. Then the stress vectors can be expressed in the form (Steigmann, 1990)

$$\mathbf{T}^\alpha = (\lambda^{-1}w_\lambda M^\alpha M^\beta + \mu^{-1}w_\mu N^\alpha N^\beta)\mathbf{a}_\beta, \tag{7}$$

where $M^\alpha = \mathbf{M}\cdot\mathbf{A}^\alpha$ and $N^\alpha = \mathbf{N}\cdot\mathbf{A}^\alpha$.

Assuming that w is not explicitly dependent on z, the foregoing results can be used to reduce equation (6) to

$$r^{-2}[(\lambda^{-1}w_\lambda\xi')'\mathbf{n} + (\lambda^{-1}w_\lambda\eta')'\mathbf{b}] + \mu^{-1}\alpha^2\kappa(1-\kappa\xi)w_\mu\mathbf{n} + r^{-1}\,p\alpha(1-\kappa\xi)(\eta'\mathbf{n} - \xi'\mathbf{b}) = \mathbf{0}. \tag{8}$$

From equations (5*b*) and (8) we derive the system

$$p\alpha(1-\kappa\xi)\eta'/r = -(\lambda^{-1}w_\lambda\xi'/r^2)' - \alpha\kappa w_\mu;$$
$$p\alpha(1-\kappa\xi)\xi'/r = (\lambda^{-1}w_\lambda\eta'/r^2)'. \tag{9a,b}$$

Equations (9), together with our restriction on w, imply that p is independent of z. If p is also independent of θ, then equation (9*b*) can be integrated at once to give $K = \text{const.}$, where

$$K = \lambda^{-1}w_\lambda\eta'/r - p\alpha\xi(1-\kappa\xi/2). \tag{10}$$

Conservation Law

We seek a second integral of the system equations (9). Our search is motivated by the observation that equations (9) are the Euler-Lagrange equations of a functional whose integrand is not explicitly dependent on θ when the material is homogeneous. For such problems it is well known that the Hamiltonian of the functional is conserved (Gelfand and Fomin, 1963). We obtain the Hamiltonian from equations (9) directly. The result can be used together with equation (10) to reduce the analysis of flexure to quadratures (Haseganu and Steigmann, 1990).

Multiplying equations (9*a*) and (9*b*) by ξ' and η', respectively, and equating the results leads to

$$(\lambda^{-1}w_\lambda)'[(\xi'/r)^2 + (\eta'/r)^2] + \lambda^{-1}w_\lambda(\xi'\xi'' + \eta'\eta'')/r^2 + \alpha\kappa\xi' w_\mu = 0. \tag{11}$$

From equation (5*a*), the first and second terms in (11) are

$$\lambda^2(\lambda^{-1}w_\lambda)' = \lambda(w_\lambda)' - \lambda' w_\lambda \tag{12}$$

and

$$(1/2)\lambda^{-1}w_\lambda(\lambda^2)' = \lambda' w_\lambda, \tag{13}$$

respectively. From equation (5*b*), the last term in equation (11) is $\alpha\kappa\xi' w_\mu = -\mu' w_\mu$. Then equation (11) becomes

$$w_\lambda\lambda' + w_\mu\mu' - (\lambda w_\lambda)' = 0. \tag{14}$$

If w is not explicitly dependent on θ, then equation (14) can be integrated to yield $H(\lambda,\mu) = \text{const.}$, where

$$H = w - \lambda w_\lambda. \tag{15}$$

A similar result was derived by Pipkin (1968) for the problem of axially symmetric deformation of a circular cylinder. In that context λ and μ are the stretches of meridians and circles of latitude, respectively.

Acknowledgment

This work was supported by a grant OGPIN 013 from the Natural Sciences and Engineering Research Council of Canada. I gratefully acknowledge this support.

References

Gelfand, I., and Fomin, S., 1963, *Calculus of Variations*, Prentice-Hall, Englewood Cliffs, N.J.

Haseganu, E., and Steigmann, D. J., 1990, "Flexural Response of Pressurized Membrane Tubes," forthcoming.

Pipkin, A. C., 1968, "Integration of an Equation in Membrane Theory," *ZAMP*, Vol. 19, pp. 818–819.

Steigmann, D. J., 1990, "Tension-Field Theory," *Proc. Royal Soc. Lond.*, Vol. A429, pp. 141–173.

Downloaded 03 May 2010 to 171.66.16.244. Redistribution subject to ASME license or copyright; see http://www.asme.org/terms/Terms_Use.cfm

Journal of Applied Mechanics

Discussion

Torsional Response of Rectangular Composite Laminates[1]

Yi-Yuan Yu.[2] It is gratifying to see the names of R. D. Mindlin and E. Reissner placed side by side to be given the credit jointly for the important contributions they both made to the theory of plates. Their contributions are of course closely related to each other. However, it is also important to recognize the differences between them. While Reissner (1945) deals with statics of plates, Mindlin (1951) is mainly concerned with dynamics and vibration of plates. Among other things, they treated the shear correction factor quite differently. By matching the frequency of the first antisymmetric mode of thickness-shear vibration given by his plate equations with that given by the exact elasticity theory, Mindlin (1951) arrived at a value of his shear factor equal to $\pi^2/12$, in contrast to the value of 5/6 given by Reissner. Mindlin later applied the same technique further to high frequency vibrations of crystal plates (1961). As pointed out recently by this writer (1989), Mindlin's later work (1961) on anisotropic plates has a close bearing upon laminated composites, although it does not seem to have been cited as such.

The authors stated that both Reissner (1945) and Mindlin (1951) had solved the torsion problem, but a solution to the problem cannot be found in Mindlin's paper. The author's analysis is thus essentially an extension of Reissner's bending analysis to a laminated composite plate, and they arrived at the same value of 5/6 for the shear correction factor as Reissner's. Although the book on dynamic properties of composites by Read and Dean (1978) is further referenced in this paper, any dynamic torsional response of a plate has not really been covered.

References

Mindlin, R. D., 1951, "Influence of Rotatory Inertia and Shear on Flexural Motions of Isotropic, Elastic Plates," ASME JOURNAL OF APPLIED MECHANICS, Vol. 18, pp. 31–38.

Mindlin, R. D., 1961, "High Frequency Vibrations of Crystal Plates," *Quarterly of Applied Mathematics*, Vol. 19, pp. 51–61.

Read, B. E., and Dean, G. D., 1973, *Determination of Dynamic Properties of Polymers and Composites*, John Wiley and Sons, New York.

Reissner, E., 1945, "The Effect of Transverse Shear Deformation on the Bending of Elastic Plates," ASME JOURNAL OF APPLIED MECHANICS, Vol. 12, pp. 69–77.

Yu, Y. Y., 1989, "Dynamics and Vibration of Layered Plates and Shells—A Perspective from Sandwiches to Laminated Composites," *Proceedings of the 30th AIAA/ASME/ASCE/AHS/ASC Structures, Structural Dynamics and Materials Conference*, pp. 2236–2245 (also presented at the First USSR-US Symposium on Mechanics of Composite Materials, Riga, Latvia, USSR, 1989, and to appear in the Proceedings to be published by ASME).

[1]By C.-L. Tsai, I. M. Daniel, and G. Yaniv and published in the June 1990 issue of the ASME JOURNAL OF APPLIED MECHANICS, Vol. 57, pp. 383–387.

[2]Professor of Mechanical Engineering, Department of Mechanical and Industrial Engineering, New Jersey Institute of Technology, Newark, New Jersey 07102. Life Fellow ASME.

Copyright © 1990 by ASME
Downloaded 03 May 2010 to 171.66.16.244. Redistribution subject to ASME license or copyright; see http://www.asme.org/terms/Terms_Use.cfm

Journal of Applied Mechanics

Book Reviews

The Behavior of Thin Walled Structures, Beams, Plates, and Shells, by J. R. Vinson. Kluwer Academic Publishers, Dordrecht, The Netherlands, 1989.

REVIEWED BY S. ABRATE[1]

This is a relatively small book (182 pages) but it is also of wide scope. It is intended to be used as a teaching text or guide for self-study and not as an exhaustive compilation of research results in this area.

Static deformations, thermal stresses, buckling, and free vibrations are treated for beams, rectangular and circular plates, and circular cylindrical shells. Isotropic linear elastic material behavior is assumed, and the reader is referred to another text by the same author for a treatment of laminated composite structures. The effect of shear deformation and rotatory inertia is neglected. To save time, some derivations are not presented; for example, the derivation of the equations of motion for a cylindrical shell are simply given as a starting point for the treatment that follows. In these cases, the reader can refer to the original research papers or to another text for which references are given. The approach taken is that while the literature on a given topic is usually voluminous, an introductory treatment is presented, and results are presented for common practical cases. For certain topics, only a general approach to the problem is given. For example, three pages are devoted to the vibration of cylindrical shells and the vibration of beams and plates is treated in five pages.

This book is very well written; the fundamental behavior of plates and shells is presented with an emphasis on physical behavior rather than mathematical intricacies. Basic assumptions in the development of equations of motion and boundary conditions are discussed, and methods for the solution of practical problems are clearly shown. For all but one of the 12 chapters, several carefully selected homework problems are given with the answers to most of these problems given in Appendix 2. This book is highly recommended as a text for a first course on plates and shells with emphasis on engineering applications. It can also be used for self-study and will provide a solid background for further learning.

Mécanique Vibratoire (Mechanical Vibrations), by M. Del Pedro and P. Pahud. Presses Polytechniques Romandes, 1989.

REVIEWED BY S. ABRATE[1]

This book deals with the vibration of discrete mechanical systems and is intended to be used as a textbook for a first course on the subject. Roughly half the book is devoted to analysis of the vibration of a single degree-of-freedom system. After a brief introduction and a general discussion of one degree-of-freedom systems, Chapter 3 deals with free vibration analysis of conservative and damped oscillators including viscous and dry damping. Steady-state response to a harmonic excitation is treated in Chapter 4 and steady-state response to a general periodic function using Fourier series expansions is presented in Chapter 5. In Chapter 6, transient response is determined using Laplace transforms and also using Fourier Transforms. Analogies with electrical circuits are briefly mentioned in Chapter 7.

The rest of the book treats the vibration of multi-degree-of-freedom systems starting with two degrees-of-freedom systems in Chapter 8, applications to the analysis of vibration absorbers in Chapter 9, and general discussion of multi-degree-of-freedom systems in Chapter 10. Chapters 11 and 12 cover the free vibration analysis of such systems and shows how modal analysis is used to uncouple the equations of motion. The analysis of transient response using modal analysis is treated in Chapter 13. The overall style is introductory, and presentation of the different topics is self-contained.

The discretization of distributed systems (beam, plates, shells) is not covered and the equations of motion for the multi-degree-of-freedom system are assumed to be given. Another criticism would be that numerical techniques of solving eigenvalue problems are not mentioned. These two drawbacks, which are common to many textbooks, may give the mistaken impression that the material presented here is of limited applicability because it cannot be applied to many important cases or that the equations obtained are too difficult to handle. This situation could easily be remedied.

The book is well written, uses clear standard notation, and is very well produced. One strength of the book is that for each section, several well-chosen practical examples are treated in detail. While it can be compared to several of the many existing introductory textbooks written in English, this book rates as one of the best written in French.

Knowledge-Based Control with Application to Robots (Lecture Notes in Control and Information Sciences), by C. W. de Silva and A. G. J. MacFarlane. Springer-Verlag, Berlin, 1989.

REVIEWED BY C. B. BROWN[2]

These lecture notes, which originated in the collaboration of the authors at Cambridge, present a view of robot control which consists of a crisp servo-control level, a knowledge-based inference system for each degree-of-freedom of the robot, and

[1]Department of Mechanical and Aerospace Engineering and Engineering Mechanics, University of Missouri, Rolla, MO 65401-0249.

[2]Department of Civil Engineering, University of Washington, Seattle, WA 98195.

Copyright © 1990 by ASME
Downloaded 03 May 2010 to 171.66.16.244. Redistribution subject to ASME license or copyright; see http://www.asme.org/terms/Terms_Use.cfm